Calendar of forthcoming meetings

7–11 September 2008
Bologna, Italy
ISLS 2008: XIIIth International Symposium on Luminescence Spectrometry. Contact: Professor Aldo Roda, Department of Pharmaceutical Sciences, Faculty of Pharmacy, University of Bologna, Italy. Tel. (+39-051) 343-398; Fax: (+39-051) 343-398; E-mail: isls2008@unibo.it; URL: http://www.isls2008.unibo.it

14–16 September 2008
Muenster, Germany
SIMS Europe 2008: 6th European Workshop on Secondary Ion Mass Spectrometry. URL: http://www.sims-europe.uni-muenster.de

5–10 October 2008
Dobogokö, Hungary
Matrafüred '08: International Conference on Electrochemical Sensors. URL: www.matrafured-08.ethz.ch

12–16 October 2008
San Diego, CA, USA
Microtas 2008: 12th International Conference on Miniaturized Systems for Chemistry and Life Sciences. URL: www.microtas2008.org

16–17 October 2008
Lisbon, Portugal
European Biomarkers Summit 2008. URL:https://selectbiosciences.com/conferences/EBS2008

16–17 October 2008
Lisbon, Portugal
Proteomics Europe 2008. URL: https://selectbiosciences.com/conferences/PE2008

16–17 October 2008
Lisbon, Portugal
Advances in Metabolic Profiling. URL: https://selectbiosciences.com/conferences/AMP2008

2–5 November 2008
Kaohsiung, Taiwan
APCE 2008: 8th Asia-Pacific International Symposium on Microscale Separations and Analysis. URL:http://www.tl.ntu.edu.tw/apce2008

2–5 December 2008
Kyoto, Japan
HPLC2008 Kyoto: 33rd International Symposium on High Performance Liquid Phase Separations and Related Techniques. URL:http://anchem.mc.kyotou.ac.jp/HPLC2008Kyoto/

26–30 January 2009
Amsterdam, The Netherlands
SCM-4: 4th International Symposium on the Separation and Characterization of Natural and Synthetic Macromole cules. Contact: scm@ordibo.be; URL: http://www.ordibo.be/scm

1–4 March 2009
Agra, India
PBA2009 India: 20th International Symposium on Pharmaceutical and Biomedical Analysis. E-mail: pba2009@gmail.com

11–15 May 2009
Frankfurt am Main, Germany
Achema 2009: 29th International Exhibition-Congress on Chemical Engineering, Environmental Protect ion and Biotechnology. URL: http://www.achema.de

21–25 June 2009
Denver, CO, USA
Transducers 2009: 15th International Conference on Solid-State Sensors, Actuators and Microsystems. URL: www.transducers09.org

6–10 September 2009
Innsbruck, Austria
Euroanalysis 2009. Contact: Euroanalysis 2009 Symposium Office, PCO Tyrol Congress, c/o Ina Kaehler, Rennweg 3, 6020 Innsbruck, Austria. Tel. (+43-512) 575-600; Fax: (+43-512) 575-607; E-mail: euroanalysis09@come-innsbruck.at; URL: www.euroanalysis2009.at

9–12 September 2009
Milan, Italy
RDPA 2009: 13th International Meeting on Recent Developments in Pharmaceutical Analysis. URL: www.rdpa2009.com

14–18 September 2009
Toronto, ON, Canada
SIMS XVII: 17th International Conference on Secondary Ion Mass Spectrometry. E-mail: email@simsxvii.org; URL: www.simsxvii.org/

11–14 October 2009
Orlando, FL, USA
PBA 2009: 21st International Symposium on Pharmaceutical and Biomedical Analysis

26–28 May 2010
Glasgow, UK
Biosensors 2010: The Eleventh World Congress on Biosensors.

20–23 September 2010
Antwerp, Belgium
Drug Analysis. URL: www.druganalysis.org

doi:10.1016/S0039-9140(08)00603-6

Talanta 76 (2008) I

Contents lists available at ScienceDirect

Talanta

journal homepage: www.elsevier.com/locate/talanta

3rd International IUPAC Symposium on Trace Elements in Food (TEF-3)

The 3rd International IUPAC Symposium on Trace Elements in Food (TEF-3) will be held 1–3 April 2009 in Rome, Italy, organized by the Istituto Superiore di Sanità. The meeting will consist in 2 and a half days of oral and poster presentations. Plenary lectures will be given by invited speakers in the following areas:

- Advances in trace element analysis in food matrices
- Sources and transfer of trace elements in the food chain
- Toxicology and risk assessment
- Trace element nutrition and human health.

The objective of this interdisciplinary symposium is to gather experts with different backgrounds to discuss all aspects of trace elements in relation to food, with special emphasis on biological effects of elements. The topics covered include essentiality, toxicity, bioaccessibility, bioavailability, speciation, sources and transfer in the food chain, effects of processing, food fortification, supplementation, international legislation and standards, analytical developments, analytical quality assurance and reference materials. Special emphasis will be placed on research and development efforts which have taken place in the last few years as well as on emerging issues in the area.

This meeting follows the previous ones, organized in Warsaw, Poland (2000), and in Brussels, Belgium (2004). Alike the two previous meetings of this series, TEF-3 aims at being a suitable forum for new ideas and experiences to be exchanged among researchers in the trace element area with a view to providing an evidence base for policy, advice on the development of improved foods and risk-management tools to protect public health.

Important dates include 30 September 2008, deadline for pre registration, 1 December 2008, deadline for submission of abstracts, and 15 January 2009, deadline for reduced fee payment. Further details are available on the symposium website (http://www.tef3-2009.it).

Dr. Francesco Cubadda
Symposium chair

doi:10.1016/S0039-9140(08)00629-2

Talanta

The International Journal of Pure and Applied Analytical Chemistry

Publication information: *Talanta* (ISSN 0039-9140). For 2008, volumes 74–76 (15 issues) are scheduled for publication. Subscription prices are available upon request from the Publisher or from the Regional Sales Office nearest you or from this journal's website (http://www.elsevier.com/locate/talanta). Further information is available on this journal and other Elsevier products through Elsevier's website: (http://www.elsevier.com). Subscriptions are accepted on a prepaid basis only and are entered on a calendar year basis. Issues are sent by standard mail (surface within Europe, air delivery outside Europe). Priority rates are available upon request. Claims for missing issues should be made within six months of the date of dispatch.

Orders, claims, and journal enquiries: please contact the Regional Sales Office nearest you:
Orlando: Elsevier, Customer Service Department, 6277 Sea Harbor Drive, Orlando, FL 32887-4800, USA; phone: (877) 8397126 [toll free within the USA]; (+1) (407) 5636022 [outside the USA]; fax: (+1) (407) 3631354; e-mail: JournalCustomerService-usa@elsevier.com
Amsterdam: Elsevier, Customer Service Department, PO Box 211, 1000 AE Amsterdam, The Netherlands; phone: (+31) (20) 4853757; fax: (+31) (20) 4853432; e-mail: JournalsCustomerServiceEMEA@elsevier.com
Tokyo: Elsevier, Customer Service Department, 4F Higashi-Azabu, 1-Chome Bldg, 1-9-15 Higashi-Azabu, Minato-ku, Tokyo 106-0044, Japan; phone: (+81) (3) 5561 5037; fax: (+81) (3) 5561 5047; e-mail: JournalsCustomerServiceJapan@elsevier.com
Singapore: Elsevier, Customer Service Department, 3 Killiney Road, #08-01 Winsland House I, Singapore 239519; phone: (+65) 63490222; fax: (+65) 67331510; e-mail: JournalsCustomerServiceAPAC@elsevier.com

USA mailing notice: *Talanta* (ISSN 0039-9140) is published monthly by Elsevier B.V. (Radarweg 29, 1043 NX Amsterdam, the Netherlands). Periodical postage paid at Rahway NJ and additional mailing offices.
USA POSTMASTER: Send change of address: Talanta, Elsevier, 6277 Sea Harbor Drive, Orlando, FL 32887-4800.
AIRFREIGHT AND MAILING in USA by Mercury International Limited, 365, Blair Road, Avenel, NJ 07001. .

Talanta 76 (2008) 1105–1112

Contents lists available at ScienceDirect

Talanta

journal homepage: www.elsevier.com/locate/talanta

Determination of motor gasoline adulteration using FTIR spectroscopy and multivariate calibration

Mohammad A. Al-Ghouti[a,*], Yahya S. Al-Degs[b], Mohammad Amer[a]

[a] Royal Scientific Society, Industrial Chemistry Centre, P.O. Box 1438, Al-Jubiha, Amman 11941, Jordan
[b] School of Chemistry, Hashemite University, Zarqa, Jordan

ARTICLE INFO

Article history:
Received 19 February 2008
Received in revised form 11 May 2008
Accepted 12 May 2008
Available online 23 May 2008

Keywords:
Motor gasoline
Adulteration
Distillation
Fourier transform infrared spectroscopy
Multivariate calibration

ABSTRACT

In this paper, an attempt has been made to develop a feasible procedure for the prediction of quality parameters of motor gasoline and to discriminate between the different adulterated motor gasoline samples using density values, distillation temperatures and Fourier transform infrared (FTIR) analyses along with multivariate calibrations without the need for using chromatographic separation or other expensive instruments such as an octane number analyser.

Ten blend mixtures of regular and super motor gasoline were prepared in order to study density, distillation temperatures and FTIR spectra characteristics for each blend. Distillation temperatures for the pure and blend mixtures of regular and super motor gasoline at initial boiling point (IBP) to final boling point (FBP) at 5%Vol. interval were obtained. Accurate and complete distillation data on the uncontaminated fuel would be essential for comparison. Thirteen peaks of the absorbance at the wavenumbers: 434, 461, 484, 673, 694, 1030, 1086, 1217, 1231, 1460, 1497, 1606 and 3028 cm^{-1} were chosen to perform the multivariate calibration. The results obtained were expected to be useful in determination and differentiation purposes, providing information on whether the density values, distillation temperatures and FTIR analyses along with multivariate method could be an appropriate feature for differentiating a particular pure motor gasoline sample from the others. The observed differences in the specific spectral bands are investigated and discussed. They have proven to be an effective combination in the pursuit of management's differentiation goals.

1. Introduction

Motor gasoline (MG) is a complex mixture of volatile flammable liquid hydrocarbons containing hundreds of different natural components (like benzene and toluene) and some additives like methyl *tert*-butyl ether (MTBE). The hydrocarbons present in MG may be classified, basically, into four classes: paraffins (normal and branched), cycloparaffins, olefins and aromatics. The exact composition of MG depends on the nature of the petroleum from which it originates [American Petroleum Institute (API) degree, chemical composition], the process through which the MG is obtained (distillation, alkylation, hydrocracking, catalytic cracking, etc.), the end use for which it is produced (automotive competitions, engine performance tests), and the legislation in place at the location of production and distribution (contents of benzene, aromatic, sulphur, lead, etc.) [1].

Fuel adulteration means the blending of a higher grade MG with other grades or solvents. Adulteration differs from contamination in that unacceptable materials are deliberately added to MG by unscrupulous people to enhance their profit. It may be as simple as adding regular-grade MG to the super-grade MG storage tank, which lowers the octane number of the super.

All engines are designed and manufactured to run on specified fuel. They will emit substantially more pollutants if the fuel specification is changed and poorly maintained. Often, but not always, the adulterated fuel leads to increased tailpipe emissions of harmful pollutants, reduces the life of engine components and also reduces performance of the engine. These practices lead to losses in several areas, which include some damaging of the engines and deterioration in air quality through increased emissions. The main driving force for this malpractice is the difference in the market prices of various petroleum products [2,3].

In Jordan, three main types of MG are sold in the service stations: regular leaded motor gasoline (RMG), super leaded motor gasoline (SMG) and unleaded motor gasoline (UMG). RMG is the cheapest one, while UMG has a higher price. This price differential is the main motivation for the illegal mixing of a cheaper fuel

* Corresponding author. Tel.: +962 65344701; fax: +962 65344806.
E-mail address: mghouti@rss.gov.jo (M.A. Al-Ghouti).

0039-9140/$ – see front matter © 2008 Elsevier B.V. All rights reserved.
doi:10.1016/j.talanta.2008.05.024

with a more expensive fuel. When RMG, SMG and UMG at 0.43, 0.60, 0.64 JD L^{-1} and kerosene is sold as low as 0.30 JD L^{-1} and the fuel pump merchant is given a small profit margin per litre, the temptation to adulterate the fuel is just too much. Most MG adulteration cases involve the illegal mixing of a cheaper leaded into an unleaded motor gasoline. Other common adulteration is the mixing of much cheaper heating fuel (such as kerosene) into MG. In the case of the adulteration of similar fuels (such as RMG into SMG), the main impact is increased emissions, whereas in the case of mixing dissimilar fuels (heating fuel into MG), long-term use may also lead to engine damage.

Determination of fuel adulteration in MG may be carried out by gas chromatography or other chromatographic techniques [5]. Other techniques may also use to uncover adulteration. Karoui and Baerdemaeker used various spectroscopic techniques, including the near infrared (NIR), mid-infrared (MIR), front face fluorescence spectroscopy (FFFS), stable isotope and nuclear magnetic resonance (NMR) in order to assess their suitability for the determination of the quality and/or geographical origins of dairy products [6]. Other workers have studied ^{13}C NMR spectra of olive oils from different regions and of different varieties to permit their discrimination using advanced chemometrics methods [7]. On the other hand, a limited number of publications were presented in the literature vis-à-vis gasoline adulteration using Fourier transform infrared (FTIR) with multivariate calibration. ASTM D86 distillation testing and/or ASTM D2699/ASTM D2700 [8,9] octane number testing may also be used to detect adulteration [10]. In some countries, dyes and markers are also used to deter the practice of adulteration. However, the determination of UMG adulteration with leaded motor gasoline is an easy task. It is usually undertaken by measuring the lead content in the sample using atomic absorption. ASTM D3237 [4] describes the procedure.

However, the chromatographic procedures and octane number testing are in general slow and time-consuming and it is generally too expensive to purchase. In this work, a procedure for the determination of SMG adulteration with RMG based on the use of density, distillation temperatures and FTIR analysis along with multivariate method was developed and tested. FTIR spectroscopy is the fastest and cheapest of the spectroscopic techniques used by scientists for identification purposes. It is based on the measurement of well defined and usually sharp characteristic fundamental frequencies associated with specific functional groups [11].

Recently, multivariate calibration has been applied for analysing many chemical systems including wastewater, foods, drugs formulations, and fuels without the need for separation of solutes prior to their analysis as the case in chromatographic analyses [12–14]. Multivariate calibration is an effective calibration method in which the chemical information (absorption, emission, transmission, etc.) of a set of standard mixtures recorded at different variables (wavenumbers) are related to the concentration of the chemical compounds present in the mixtures [12–13]. The popular calibration way used in chemical analysis is the univariate calibration in which the chemical information of a set of solution recorded at one variable (i.e. wavenumber) is related to the solute concentration in the solution. The most applied multivariate methods are classical least squares (CLS), inverse least squares (ILS), principal-component regression (PCR), partial least squares (PLS) and net-analyte signal (NAS) [12–14].

Therefore, the aim of this work was to develop a procedure, by means of the physical and chemical properties (density and distillation) and FTIR analyses along with PLS-1 calibration, for determination SMG adulteration with RMG. The results obtained are expected to be useful for determination purposes.

2. Experimental

The chemical and physical parameters analysed are based on the standardised analytical methods to provide an overall indication of the status of a fuel. Key American Standards for Testing and Materials (ASTM) chemical methods such as the determination of distillation (ASTM D86 [15]) and density (ASTM D1298 [16]) were carried out. The distillation and density tests were carried out in duplicate. The determination of the distillation curves was carried out with a manual distillation according to the norm ASTM D86. The density was determined with the aid of hydrometers (ASTM D1298).

Analytical spectra were taken using a Shimadzu IR Prestige-21/FTIR-8400S with a resolution of 4 cm^{-1} at 64 scans. The data interval provided by the instrument for a resolution of 4 cm^{-1} is 1 cm^{-1}. A small quantity (~2 μL) of the sample was deposited with the use of a Pasteur pipette between two well-polished KBr disks, creating a thin film. Duplicate spectra were collected for the same sample. All spectra were recorded from 4000 to 400 cm^{-1} and the spectra were collected using a Shimadzu IR Prestige-21 Windows Software. These tests were conducted at the laboratories of the Royal Scientific Society (RSS), Amman, Jordan. Then, the digitised absorbance values were transferred to a Pentium (IV) personal computer for subsequent analysis. The data treatment and the multivariate calculations were carried out using MATLAB (version 7.0).

Ten blend mixtures of RMG and SMG, to cover the percentage 0–100%Vol. for each individual component, were prepared to study the density, distillation temperatures and FTIR spectra for each blend. Ten samples were used to prepare the calibration set, while four samples were used for validation. Table 1 gives the composition of calibration and validation sets used in multivariate calibration. Five real samples of SMG were obtained from different local petrol stations.

2.1. Determination of MG adulteration using PLS-1 regression method

PLS-1 is a simple and convenient calibration method for resolving mixtures, which in principle could be applied for the current system. Due to the high collinearity in matrix **R**, the simple multivariate calibration method like CLS was invalid for determination of MG in the samples. Collinearity (i.e., the linear relationships between absorbances at multiple wavenumbers) is a serious drawback that may negatively affect the accuracy and precision of the calibration method. A good estimation of collinearity in a data

Table 1
Calibration and validation sets that used in multivariate calibration

Standard	RMG	SMG
Calibration set (Vol.%)		
1	1.0	99.0
2	2.0	98.0
3	3.0	97.0
4	4.0	96.0
5	15.0	85.0
6	35.0	65.0
7	55.0	45.0
8	70.0	30.0
9	100.0	0
10	0	100.0
Validation set (Vol.%)		
1	5.0	95.0
2	10.0	90.0
3	30.0	70.0
4	50.0	50.0

matrix is the condition number [12], matrices of high collinearity have high condition numbers and can not be involved in simple calibration methods. The condition number of matrix **R** was 300, which reflected the high degree of collinearity and the high spectral overlap between MGs as well. In PLS-1 regression, the high collinearity in matrix **R** could be eliminated and the calibration quality could be largely improved. Simply, in PLS-1 method, matrix **R** is decomposed using the concentrations vector of MG to be calibrated. With the aid of PLS-1 algorithm, $\mathbf{W}_{n\times h}$, $\mathbf{P}_{h\times n}$ matrixes and $\mathbf{q}_{h\times 1}$ vector were obtained, where h represents the number of optimum PLS-1 latent variables needed to perform accurate calibration. The calibration parameters **b** and b_o were obtained as following [13]:

$$\boldsymbol{b} = \boldsymbol{W}(\boldsymbol{P}^t\boldsymbol{W})\boldsymbol{q} \quad (1)$$

and,

$$b_o = \bar{c} - \boldsymbol{a}^t\boldsymbol{b} \quad (2)$$

where $\bar{c}$ and **a** are average concentration of MG in the calibration mixture and the average spectrum of the calibration mixtures, respectively. t stands for matrix transpose. To predict content of MG, c, from the spectrum of unknown sample, the following equation was used:

$$c = b_o + \boldsymbol{a}_{un}\boldsymbol{b} \quad (3)$$

where $\mathbf{a}_{un}$ is the measured spectrum of the unknown sample.

To improve the quality of PLS-1 calibration, the absorbances and concentrations were mean-centred before running the analysis [14]. The presence of outlier(s) was also investigated in calibration and prediction sets using Haaland and Thomas method [12]. PLS-1 method calculates the calibration parameters (**b** and b_o) for each MG separately; therefore, the earlier calculations were repeated for each MG.

The calibration matrix was obtained by recording the absorption spectra of standards over the spectral range 400–4000 cm^{-1}. Five factors were found to be the optimum for simultaneous determination of both MGs using PLS-1 calibration method. Thirteen peaks of the absorbance at the wavenumbers: 434, 461, 484, 673, 694, 1030, 1086, 1217, 1231, 1460, 1497, 1606 and 3028 cm^{-1} were chosen to perform the PLS-1 calibration. The chosen of these peaks was based on the main compositions in the MG and their importance in the multivariate calibration. Table 2 shows the 13 stretching vibration bands using FTIR.

Distillation temperatures for the pure and blend mixtures of RMG and SMG at initial boiling point (IBP) to final boling point (FBP) at 5%Vol. interval were obtained. Accurate and complete distillation data on the unadulterated fuels would be essential for comparison.

Table 2
stretching vibration bands of Jordanian MG [17]

Stretching vibration	Frequency (cm^{-1})
434	C–Cl stretch
461	Toluene (CCC inplane bending)
484	CCC out of plane bending
673	Benzene
694	*cis*-HC=C—H
1030	Pyridine
1086	C—H inplane bending
1217	C—H inplane bending
1231	C—H inplane bending
1460	C=C (aromatic) ring stretch
	Phenyl compounds
	C—H stretching antisymmetric
1497	C=C (aromatic) ring stretch
	Phenyl compounds
	degenerate pair
1606	C=C (aromatic) ring stretch
	sp^2 CH_2 (olefinic) Conjugation
3028	sp^2 CH_2 (olefinic) (non terminal = CH—C)

3. Results and discussion

Detection and determination of RMG and SMG adulteration are not simple everyday tasks. In this context, efforts to detect and determine adulteration in a traditional method could demand the determination of hundreds of organic compounds in MG samples, and further evaluation of a composition profile in comparison with typical unadulterated MGs in order to identify composition variation that could be related to adulteration. Thus, a fast and reliable method to screen large numbers of MG samples is required to classify and determine the adulterant amount added in the fuel.

The detection of fraud is difficult when the adulteration involves the addition of a hydrocarbon, or their mixtures, normally present in the composition of SMG. In such cases, if the quantity of adulterant added is beyond the detection limit (DL) of the instrument, not even the most sensitive techniques can be used to quantify the added compound due to the complexity of gasoline composition. The addition of RMG into SMG changes the original composition of the fuel, affecting its physicochemical properties in different ways. Distillation temperatures, density and octane rating are properties closely related to the fuel composition and the characteristics of its components.

The combination of density, distillation technique and infrared spectrometry along with multivariate method provides a powerful tool for monitoring a variety of processes and, as such, is arousing increase interest for quality control purposes. The fact that samples require virtually no treatment and the relative ease and speed with which spectra can be obtained have made infrared spectrometry a preferred choice over traditional techniques involving lengthy sample conditioning procedures.

In this work, an investigation was carried out into the observed changes in distillation curves and temperatures, density values and FTIR spectra along with multivariate calibration of SMG after the addition of different percentage of RMG.

3.1. Physical and chemical properties

The RMG and SMG were the typical fuel grades of the Jordanian market that are produced by Jordan Petroleum Refinery Company. Their specifications are presented in Table 3.

The following subsections will describe the effect of adulteration onto density values and distillation temperatures. The results of density and distillation temperatures of pure and adulterated SMG with different ratios of RMG are presented in Table 4.

Table 3
Typical Jordanian fuel properties (RMG and SMG)

Properties	Unit	Result		Test method
		RMG	SMG	
Distillation	°C			ASTM D86
10%Vol.		54	59	
50%Vol.		85	97	
90%Vol.		162	158	
Final boiling point		201	189	
Vapor pressure at 100 °F	$kg\,cm^{-2}$	0.629	0.571	ASTM D323
Total sulphur	%wt.	0.060	0.026	ASTM D1266
Density at 15 °C	$g\,mL^{-1}$	0.7319	0.7517	ASTM D1298
Octane number	–	87.4	95.3	ASTM D2699
Lead	$g\,L^{-1}$	0.097	0.194	ASTM D3341

Table 4
Density and distillation tests of adulterated SMG with RMG at different ratios

Properties	Unit	Result Percentage of RMG added, %Vol.						Test method
		0	4	5	10	20	50	
Density at 15 °C	g mL^{-1}	0.742	0.7550	0.7570	0.7600	0.7600	0.7625	ASTM D1298
Distillation	°C							ASTM D86
IBP		43.5	43.4	43.5	43.4	43.4	42.4	
10%Vol.		64.4	57.4	62.4	63.4	63.4	64.4	
20%Vol.		73.4	63.4	70.4	72.4	71.9	73.4	
30%Vol.		81.6	71.4	78.6	80.6	80.6	81.1	
40%Vol.		91.6	81.6	87.1	90.6	91.6	91.1	
50%Vol.		102.1	91.0	98.3	101.3	102.1	101.6	
60%Vol.		113.8	105.8	109.8	112.8	112.8	112.8	
70%Vol.		127.0	121.0	122.5	126.0	125.0	125.5	
80%Vol.		139.3	135.3	136.8	138.3	137.3	137.3	
90%Vol.		153.3	151.4	152.3	152.3	151.3	151.3	
95%Vol.		166.4	164.4	165.9	165.9	162.4	165.4	
FBP		185.6	184.6	190.9	189.6	187.6	185.6	

3.2. Density

Density is a significant property because it controls the amount of fuel that is burned in the combustion chamber. The higher the amount of fuel sprayed into the combustion chamber, the higher the output of partially oxidised products that is emitted.

MG density varies between summer and winter grades and from low octane to high octane. This variation takes into account the different performance requirements of MG at different temperatures. In order to maintain the "anti-knock" quality and octane ratings of MGs in the absence of lead, the portion of aromatic hydrocarbons used in MG was increased. MG contains various aromatic compounds which have a higher tendency of coke formation than paraffinic fuels [18]. Aromatic hydrocarbons take the form C_nH_{2n-6}, with a lower ratio of hydrogen to carbon than other hydrocarbons typically found in MG. Because carbon is much heavier than hydrogen, the lower ratio results in increased fuel density and higher shares of carbon [19]. As a result, the emissions coefficient for MG will rise. As shown in Table 4, the density of the adulterated MGs was varied between 0.7420 and 0.7625 g mL^{-1} and increased by 2.72% as the percentage of adulteration increases from 0 to 50%Vol. This means more emissions are obtained and this would not be sufficient to characterise exact adulteration.

The test result of density was compared with corresponding value prescribed as typical Jordanian MG specifications. The standard prescribed density for RMG and SMG is a value ranging from 0.729 to 0.736 and 0.740 to 0.760 g mL^{-1}, respectively. The observations from the experiment suggested that density was within the prescribed range immaterial of the extent of the SMG adulteration with RMG (Table 4). The presence of RMG did not appear to alter density of SMG appreciably and hence the application of the density test for adulteration with RMG is not appropriate.

3.3. Distillation characteristics

One of the most important features of a MG is the volatility that is measured by a distillation experiment [20]. MG is a mixture of hundreds of hydrocarbons, many of which have different boiling points. Thus MG boils or distills over a range of temperatures, unlike a pure compound, water, for instance, that boils at a single temperature. A MG's distillation profile or distillation curve is the set of increasing temperatures at which it evaporates for a fixed series of increasing volume percentages – 5, 10, 20, 30%, etc. – under specific conditions. (Alternatively, it may be the set of increasing evaporation volume percentages for a fixed series of increasing temperatures.) Fig. 1 shows the distillation profiles of average conventional summer and winter MGs.

Various ranges of a distillation profile have been correlated with specific aspects of MG performance. Front-end volatility is adjusted to provide: (a) easy cold starting, (b) easy hot starting, (c) freedom from vapor lock, and (d) low evaporation and running-loss emissions. Mid-range volatility is adjusted to provide: (a) rapid warm-up and smooth running, (b) good short-trip fuel economy, (c) good power and acceleration, and (d) protection against carburetor icing and hot stalling. Tail-end volatility is adjusted to provide: (a) good fuel economy after engine warm-up, (b) freedom from engine deposits, (c) minimal fuel dilution of crankcase oil, and (d) minimal volatile organic compound (VOC) exhaust emissions [10].

The most important points of the distillation curve are IBP, T10 (temperature at which 10% of distilled volume is recovered), T50 (temperature at which 50% of distilled volume is recovered), T90 (temperature at which 90% of distilled volume is recovered) and FBP. IBP and T10 are related to the amount of light compounds in the fuel, which are necessary for engine cold starting [21]. Never-

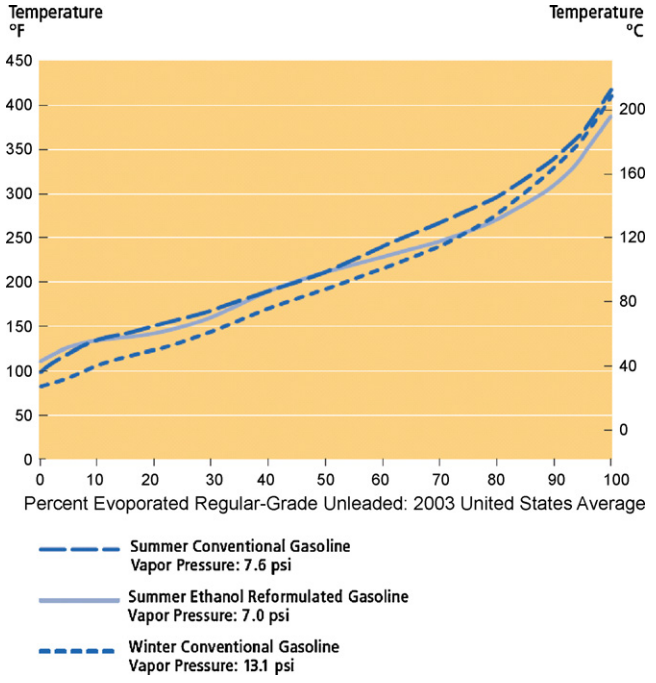

Fig. 1. Typical distillation profiles of summer and winter MGs (ASTM D86) [10].

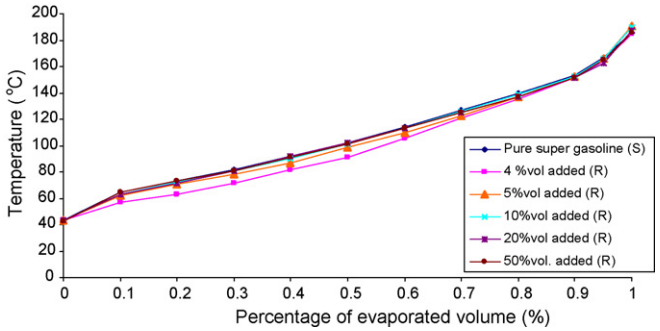

Fig. 2. Distillation curves of adulterated SMG (shortened as S) with different ratios of RMG (shortened as R).

theless, an excess of light hydrocarbons may cause vapor lock. The intermediary hydrocarbons are responsible for engine heating, and T50 is the parameter used to regulate this fraction. FBP and T90 are related to the amount of heavier substances with higher octane number, which provide fuel economy and detonation resistance.

Fig. 2 shows the results of distillation temperatures of the pure SMG, this curve is used as a reference in the analysis of the effect of the addition of RMG to SMG, and five other adulterated MG fuels obtained by blending of the SMG with an amount of 4, 5, 10, 20 and 50%Vol. of RMG.

Vaporisation at very narrow band of temperature is not desirable since it will result with an immediate burning and high rate of pressure rise. The burning of all the fuel increases the temperature and pressure of gas in the combustion chamber. This is a situation which can give rise to dangerous conditions for the engine components. It is necessary that a fuel sample burns gradually in a combustion chamber of an engine. When the RMG with an amount of 4–50%Vol. is mixed with the SMG, distillation temperature increases gradually at a finite rate. This gradual increment is important because starting ability and warm-up property of the fuel is evaluated by consideration of the evaporation temperatures of 20–70% vaporisation region of the distillation curves.

However, the change in density values and distillation temperatures is not proportional to the volume of RMG blended with SMG. This indicates that RMG is solved in the SMG and a new mixture has formed. It behaves as a new fuel according to the density and distillation tests results.

A simple visual inspection would not be sufficient to characterise MG adulteration, as can be observed from Fig. 2. The distillation curves show a continuous and smooth increase in temperature as the distillation process progresses. It can be observed in Fig. 2 that RMG additions tend to decrease the distillation temperatures of the mixture as a whole for 4 and 5%Vol. But, the behaviour of the distillation curves of 10, 20, and 50%Vol. is quite similar to the pure SMG. This behaviour could be explained by the properties and composition variations of the adulterated SMG samples. Probably, low intermolecular interactions were formed at lower percentages of adulteration while such interactions were increased at higher percentages. The distillation curves of the adulterated SMG did not affect, in a significant way, the distillation temperatures above 70% of the vaporised volume. On the other hand, the 50% of the vaporised volume was influenced by the addition of 4 and 5%Vol. RMG; this parameter may therefore be the strongest indication of the presence of this substance in SMG.

The distillation temperature that corresponds to 10% of the evaporated volume is related to the engine ignition. It appears from Fig. 2, that this phenomenon is not affected. The 50%Vol. distilled limit is monitored by its relation with the heating and accelerating of the engine and with the fuel economy. It can be clearly seen that the 50%Vol. distilled limit is affected by addition RMG into SMG to 4%Vol., a lesser extend to 5%Vol., and no effect was observed for 10, 20, and 50%Vol. It is also clear that no effect was observed after addition of RMG into SMG for tail-end volatility correspondence.

As a conclusion, it is quite difficult to differentiate the adulterate MG samples using distillation and density results. So, it continues to be a challenge when dealing with mixtures containing hundreds of components, as is the case for MG. This is of fundamental importance in relation to SMG adulteration through the addition of RMG. A better understanding of this phenomenon could aid in the establishment of more appropriate ranges for the quality parameters in order to detect adulterations with greater efficiency. FTIR along with multivariate calibration may be one of the best methods that may be used in determination and differentiation purposes. This method will be discussed in the following subsections.

3.4. Spectral overlap and importance of multivariate calibration

The present paper attempts to develop a feasible procedure for the prediction of quality parameters of MG and to discriminate between the different adulterated SMG samples using FTIR spectroscopy and multivariate methods, using principal-components analysis (PCA). PCA is used for finding patterns of correlations within large and complex data structures, such as the data matrix obtained for these fuels.

The FTIR spectra of RMG and SMG were recorded over the range (400–4000 cm^{-1}) and are illustrated in Fig. 3. For more clear FTIR graphics, the full spectra are divided into five regions: 3000–3100, 1400–1600, 1000–1300, 650–700, and 400–500 cm^{-1}. A broad spectral feature from 2800 to 3000 cm^{-1} for the "2% R" and "4% R" is produced by unknown interference. Ignore this peak as "interference". The difficulties that arise when mixtures of these fuels are to be determined are realised by studying the individual absorbance spectra given in Fig. 3. The spectra of the fuels were strongly overlapped within the entire spectral region and no certain wavenumber can be found where any of the fuel is the only absorber. This indicates that conventional calibration procedures would have a limited application for quantitative determinations. Therefore, the simultaneous determination of these overlapped fuels requires (a) the use of a separation technique (like high performance liquid chromatography or gas chromatography) prior to their determination, or (b) the application of a multivariate calibration technique for the resolution of the complex system. The second option was chosen in this study owing to its simplicity, rapidity and low cost. The concentrations of fuels in their mixtures were estimated using the popular multivariate method; PLS-1. During analysis, the RMG was given more attention than SMG because the former is the fuel that is regularly used in adulteration and usually added in variable amounts.

3.5. Selection of the optimum number of factors (h) for PLS-1 calibration method and leverage calculations

The optimum number of factors (h) should be selected in order to avoid overfitting when using PLS-1 method. This can be done by applying leave-one-out cross validation procedure as developed by Haaland and Thomas [12]. Basically, from a given set of m calibration samples, the PLS-1 calibration on $m-1$ calibration set is performed. Using this calibration, the concentration (%Vol.) of the sample left out during the calibration is predicted. This process was repeated m times, until each sample has been

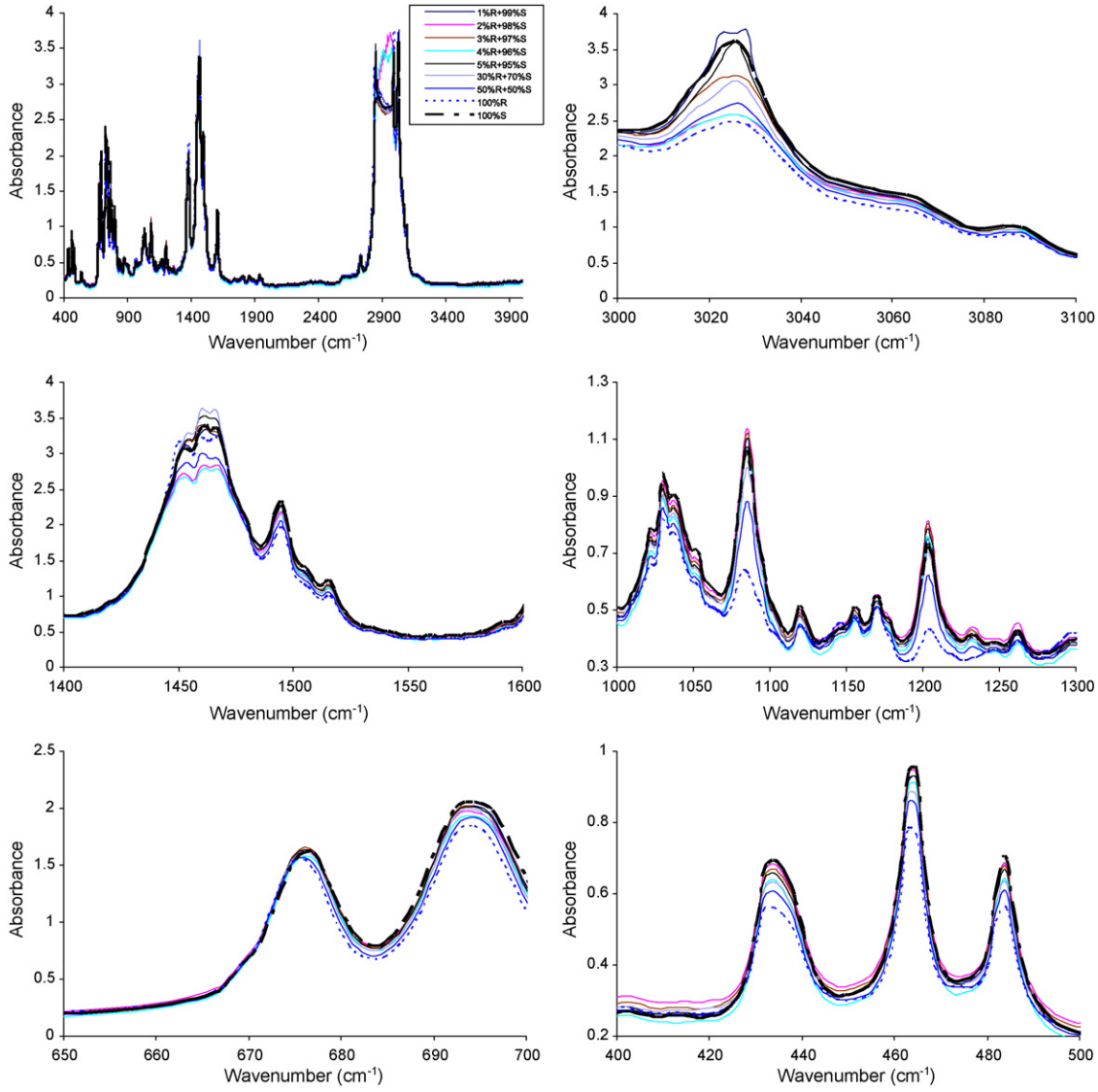

Fig. 3. Fourier transform infrared spectra of MG samples (RMG (R) and SMG (S)) at different mixing ratios.

left out once. The concentration (adulteration) predicted (C_{pred}) for each sample is then compared with the actual concentration (adulteration) (C_{act}) of this reference sample. The sum of squared prediction residual errors for all calibration samples, or PRESS = $\Sigma(C_{i,pred} - C_{i,act})^2$ was calculated each time a new factor (h) is added to the PLS-1 model. Usually, the optimum number of factors is obtained by computing the ratios $F = \text{PRESS}(h < h^*)/\text{PRESS}(h)$ (h^* corresponds to the minimum PRESS), and selecting the number of factors leading to a probability of less than 75% that $F > 1$ [12,13]. In our case, five factors were found to be optimum for simultaneous determination of fuels using PLS-1 calibration method. Fig. 4 shows the PRESS plot obtained by optimising the calibration matrix of the FTIR spectra of the samples with the PLS-1 method.

The regression coefficients that obtained from PLS-1 method using the optimum number of factors (6) was plotted against the wavenumbers used in calibration as depicted in Fig. 5.

The relative magnitude of the employed wavenumbers is apparent in Fig. 3, the wavenumbers at 673, 694, and 1029 cm^{-1} are more significant that the others and they are very important for the model. On the other hand, 433, 460, 484, 1230, 1460, and 3028 cm^{-1} have a little effect on the calibration method. The leverage plot was

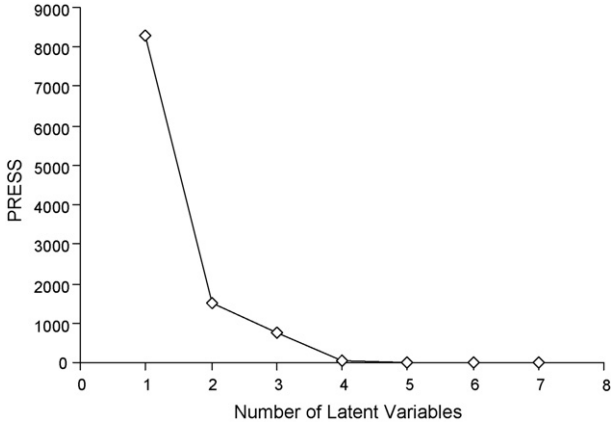

Fig. 4. A plot between numbers of latent variables vs. PRESS for analysis of SMG as obtained from cross-validation technique.

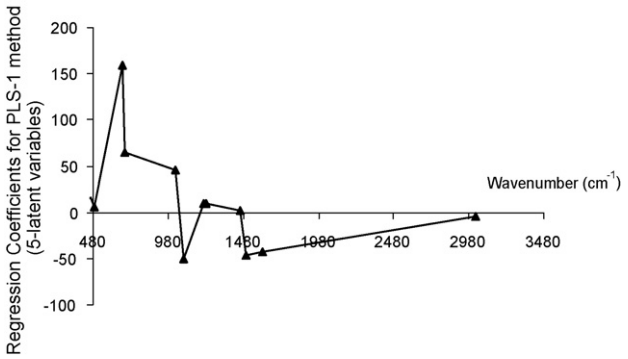

Fig. 5. Relative magnitude of the regression coefficients derived using a six-factors PLS-1 model for RMG.

also obtained for the RMG. Martens and Naes's method for leverage estimation was adopted in this work [14]. The obtained leverage plot is shown in Fig. 6.

As indicated in Fig. 6, there is a high leverage in samples 1 and 10 compare to the other samples used in the calibration set. This should not be a surprising because the concentration of RMG was at low levels in these samples. Low leverage values were obtained for the rest of the samples.

3.6. Determination of MG adulteration in the validation set and real samples and figures of merit of proposed method

The PLS-1 model has a high prediction power for determination of both fuels in the calibration and prediction sets. Figs. 7 and 8 show the plots between the actual and predicted concentration of RMG in the calibration and validation mixtures, respectively.

As indicated from both these figures, the PLS-1 methods has high prediction ability for determination of RMG in calibration (slope ≈ 1.0, $r^2 = 0.9997$) and validation (slope ≈ 0.97, $r^2 = 0.9992$) sets. The overall effectiveness of PLS-1 for prediction fuels in the validation set can be determined by calculating relative error of prediction (REP) values for each fuel as follows [22]:

$$\text{REP\%} = 100 \times \left(\frac{\sum_{i=1}^{n} (C_{i,\,\text{pred}} - C_{i,\,\text{act}})^2}{\sum_{i=1}^{n} (C_{i,\,\text{act}})^2} \right)^{1/2} \quad (4)$$

where n, C_{pred}, and C_{act} are the total number of validation samples, predicted concentration and the actual concentration of the fuel, respectively. The calibration results were collected in Table 5.

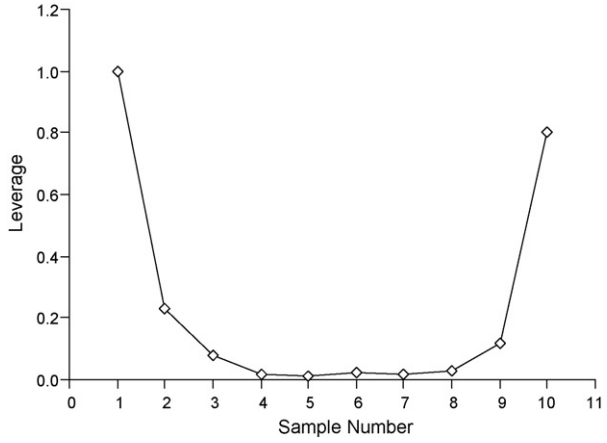

Fig. 6. Relative leverage exhibited by each sample in forming six-factors PLS-1 model for RMG.

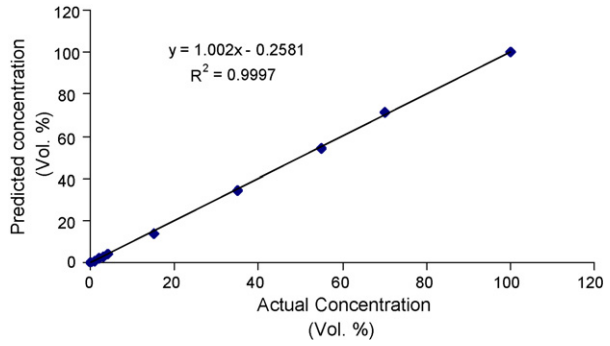

Fig. 7. Actual concentration vs. predicted concentration as obtained from the PLS-1 model for RMG (calibration set).

Table 5
Calibration results obtained from PLS-1 method

Calibration parameter	RMG	SMG
Spectral region (cm^{-1})	434–3028	434–3028
Number of factors (h)	5	5
PRESS	0.54	0.63
REP%	1.2	2.9
r^2 (validation)	0.9979	0.9965
LOD (Vol.%)	0.7	0.5

The reproducibility and detection limit of PLS-1 calibration method were also reported. Five replicate measurements of a fuel sample containing (5% RMG and 95% SMG, Vol.%) were carried out for validation set over a period of week to assess the precision of PLS-1 method. The steps of the analytical procedures including set preparation, FTIR-scanning and PLS-1 calibration were repeated under identical conditions. Accordingly, five replicate concentrations were obtained for each fuel.

The DL of the proposed multivariate calibration method for the fuels was estimated using the NAS calculations [23]:

$$\text{DL} = \frac{3||\varepsilon||}{||s_k^*||} \quad (5)$$

where ε and s_k^* are the spectrum of blank and the part of the spectrum of interest that is orthogonal to the space of spectra of other components, respectively. The symbol (|| ||) stands for the Euclidean norm for vector. The procedures of s_k^* estimation were outlined in Ref. [23]. $||\varepsilon||$ is a measure of instrumental noise.

As noted in Table 5, similar spectral regions were used in PLS-1 calibration for fuels. The high prediction ability of the PLS-1 method

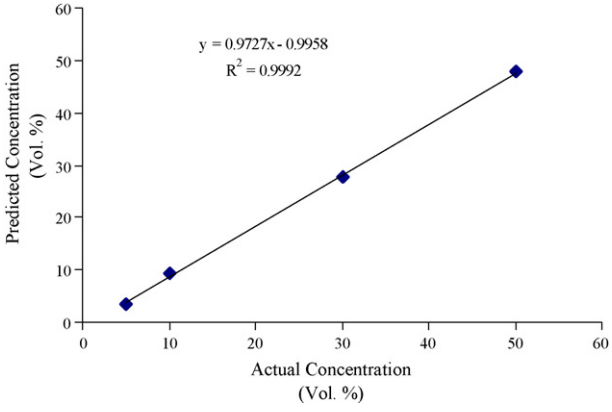

Fig. 8. Actual concentration vs. predicted concentration as obtained from the PLS-1 model for RMG (prediction set).

for RMG and SMG is as indicated by the values of r^2 and REP%. Using the proposed procedure, both fuels can be determined in their binary mixtures down to 0.5 and 0.7 Vol.% for RMG and SMG, respectively. Accordingly, the proposed PLS-1 multivariate method could be effectively used to find any adulteration of SMG with RMG. The multivariate method has a good reproducibility. In most cases, the values of relative standard deviation (R.S.D.) are lower than 6%. In a recent study, the PLS-1 method was applied to determine the levels of four adulterants (diesel oil, kerosene, turpentine spirit and thinner) which are frequently added to MG [24]. The earlier study indicated that PLS models based on FTIR spectra were shown to be practical analytical methods for predicting adulterants content in MG in the volume fraction range from 0 to 50%Vol. [24].

4. Conclusion

In this work, a practical procedure for the determination of fuel adulteration based on the use of density, distillation temperatures and FTIR analysis along with multivariate calibration was developed and tested. The following conclusions are drawn:

- RMG and SMG adulteration detection and determination are not straightforward tasks.
- The physical–chemical parameters (e.g. density and distillation) are not sufficient to establish if adulteration has occurred.
- The density of the adulterated MGs was increased by 2.72% at the percentage of adulteration increases from 0 to 50%Vol. This would not be sufficient to characterise exact adulteration.
- A simple visual inspection of the distillation curves would not be sufficient to characterise MG adulteration.
- The 50% of the vaporised volume was influenced by the addition of 4 and 5% RMG, this parameter may be the strongest indication of the presence of this substance in MG.
- Thirteen peaks of the absorbance at the wavenumbers: 434, 461, 484, 673, 694, 1030, 1086, 1217, 1231, 1460, 1497, 1606 and 3028 cm^{-1} were chosen to perform the multivariate calibration.
- The proposed PLS-1 multivariate method could be used effectively to find any adulteration of SMG with RMG.

Acknowledgements

The first author wishes to acknowledge the contribution of petrol and lubricants lab, Royal Scientific Society (Amman, Jordan), in conducting FTIR, distillation and density tests.

References

[1] E.V. Takeshita, R.V.P. Rezende, S.M.A. Guelli, U. de Souza, A.A.U. de Souza, Fuel 87 (2008) 2168.
[2] B.B. Ale, J. Inst. Eng. 3 (2003) 12.
[3] N. Pasadakis, A.A. Kardamakis, Anal. Chim. Acta 578 (2006) 250.
[4] ASTM D3237-06 Standard Test Method for Lead in Gasoline by Atomic Absorption Spectroscopy, Volume: 05.02.
[5] E. Lbpez-Anreus, S. Garrigues, M. de la Guardia, Anal. Chim. Acta 333 (1996) 157.
[6] R. Karoui, J. Baerdemaeker, Food Chem. 102 (2007) 621.
[7] A.D. Shawa, A. di Camillo, G. Vlahov, A. Jones, G. Bianchi, J. Rowland, D.B. Kell, Anal. Chim. Acta 348 (1997) 357.
[8] ASTM D2699-07 Standard Test Method for Research Octane Number of Spark-Ignition Engine Fuel, Volume: 05.05.
[9] ASTM D2700-07 Standard Test Method for Motor Octane Number of Spark-Ignition Engine Fuel, Volume: 05.05.
[10] Motor Gasoline Fuels, Technical Review, Chevron Products Company 1998, A Division of Chevron U.S.A. Inc.
[11] A. Iob, R. Buenafe, N.M. Abbas, Fuel 77 (1998) 1861.
[12] D. Haaland, E. Thomas, Anal. Chem. 60 (1988) 1193.
[13] H. Goicoechea, A. Olivieri, Talanta 47 (1998) 103.
[14] H. Martens, T. Naes, Multivariate Calibration, John Wiely & Sons, 1989.
[15] ASTM D86-07 Standard Test Method for Distillation of Petroleum Products at Atmospheric Pressure, Volume: 05.01.
[16] ASTM D1298-99 Standard Test Method for Density, Relative Density (Specific Gravity), or API Gravity of Crude Petroleum and Liquid Petroleum Products by Hydrometer Method, Volume: 05.01.
[17] D.W. Mayo, F.A. Miller, R.W. Hannah, Course Notes on the Interpretation of Infrared and Raman Spectra, John Wiley & Sons, 2003.
[18] I. Kang, J. Bae, G. Bae, J. Power Source 163 (2006) 538.
[19] National Institute of Petroleum and Energy Research, Motor Gasoline, Summer and Motor Gasoline, Winter (1984–1994), USA.
[20] R. Yumrutas, M.H. Alma, H. Özcan, K. Önder, Fuel 87 (2008) 252.
[21] L.C. Côcco, C.I. Yamamoto, O.F. von Meien, Chem. Intell. Lab. Syst. 76 (2005) 55.
[22] B. Hemmateenejad, M. Akhond, F. Samari, Spectrochim. Acta: Part A 67 (2007) 958.
[23] R. Boqué, N. Faber, F. Rius, Anal. Chim. Acta 423 (2000) 41.
[24] L.S.G. Teixeira, F.S. Oliveira, H.C. dos Santos, P.W.L. Cordeiro, S.Q. Almeida, Fuel 87 (2008) 346.

Talanta 76 (2008) 1241–1245

Contents lists available at ScienceDirect

Talanta

journal homepage: www.elsevier.com/locate/talanta

Utility of solid-phase spectrophotometry for determination of dissolved iron(II) and iron(III) using 2,3-dichloro-6-(3-carboxy-2-hydroxy-1-naphthylazo)quinoxaline

Alaa S. Amin [a,*], Ayman A. Gouda [b]

[a] Chemistry Department, Faculty of Science, Benha University, Benha, Egypt
[b] Chemistry Department, Faculty of Science, Zagazig University, Zagazig, Egypt

ARTICLE INFO

Article history:
Received 13 April 2008
Received in revised form 17 May 2008
Accepted 20 May 2008
Available online 7 July 2008

Keywords:
Iron determination
Quinoxaline azo dyes
Solid-phase spectrophotometry
Water analysis

ABSTRACT

A new simple, very sensitive, selective and accurate procedure for the determination of trace amounts of iron(II) by solid-phase spectrophotometry (SPS) has been developed. The procedure is based on fixation of iron(II) as 2,3-dichloro-6-(3-carboxy-2-hydroxy-1-naphthylazo)quinoxaline on a styrene-divinylbenzene anion-exchange resin. The absorbance of resin sorbed iron(II) complex is measured directly at 743 and 830 nm. Iron(III) was determined by difference measurements after reduction of iron(III) to iron(II) with hydroxylamine hydrochloride. Calibration is linear over the range 1.0–20 $\mu g\,L^{-1}$ of Fe(II) with relative standard deviation (R.S.D.) of 1.65% ($n = 10.0$). The detection and quantification limits for 100 mL sample system are 280 and 950 $ng\,L^{-1}$ using 0.5 g of the exchanger. The molar absorptivity and Sandell sensitivity are also calculated and found to be 2.86×10^6 L mol^{-1} cm^{-1} and 0.0196 ng cm^{-2}, respectively. The proposed procedure has been successfully applied to determine iron(II) and iron(III) in tap, mineral and well water samples.

1. Introduction

Iron is widely distributed in nature and is one of the most important elements in environmental and biological effectiveness influenced by its chemical properties, such as valence, solubility, and the degree of complex formation. The determination of iron(II) and iron(III) in aqueous solution is of great importance to evaluate the redox environment of natural waters. There is an increasing need for a highly sensitive method for analysis of iron speciation in environmental and biomedical studies [1]. The simultaneous determination of iron(II) and iron(III) has obtained particular attention [2–5].

Spectrophotometric determination of iron in different oxidation states in water has been reported [6–11]. For the determination of iron in $\mu g\,L^{-1}$ levels in natural waters, an appropriate preconcentration process is usually required [12]. This process is time consuming and the proportion of iron(II) and iron(III) may be altered by atmospheric oxygen in the course of analysis.

Solid-phase spectrophotometry (SPS) combines the preconcentration of the species of interest on a solid matrix, usually an ion-exchanger, with the aid of complexing agent and subsequent measurement of the absorbance of the complex in the solid phase. This provides an increase in selectivity and sensitivity with respect to conventional spectrophotometric method [13–18].

Many reagents are suggested for determination of iron by solid-phase spectrophotometry: 1,10-phenanthroline [19,20], bathophenanthroline [21], ferrozine [22,23], thioglycollic acid [24] and thiocyanic acid [25]. Some methods using these reagents are of low sensitivity and selectivity. 1,10-Phenanthroline is one of the most useful reagents for determining iron(II) and has been used to the determination of iron(II) and iron(III) [20], but Cu(II) and Zn(II) interfere.

2,3-Dichloro-6-(3-carboxy-2-hydroxy-1-naphthylazo)quinoxaline (DCHNAQ) is one of the quinoxaline reagents [26,27], it has been successfully used for spectrophotometric determination of gold(III) [26], scandium(III) [27], mercury(II) [28], vanadium(V) [29] and ruthenium(III) [18]. The goal of the present work is intended to study the possibilities of using DCHNAQ as a reagent for the determination of trace iron(II) and iron(III) by SPS. The optimum conditions have been established. Iron(II) reacts with DCHNAQ to give a coloured complex, which is easily sorbed on an anion-exchange resin and provides the basis for a relatively simple, accurate and rapid spectrophotometric method of iron(II) at $\mu g\,L^{-1}$ level, without a previous preconcentration step. The proposed method is free from many

* Corresponding author at: Faculty of Community, Department of Medical Science, Umm Al-Qura University, Makkah 1234, Saudi Arabia.
E-mail address: asamin2002@hotmail.com (A.S. Amin).

0039-9140/$ – see front matter © 2008 Elsevier B.V. All rights reserved.
doi:10.1016/j.talanta.2008.05.034

interferences and has been applied to the determination of iron(II) and iron(III) in tap, mineral and well water samples.

2. Experimental

2.1. Apparatus

A PerkinElmer Lambda 12 UV–vis spectrophotometer with a 5.0 mm quartz cell was used for all spectral measurements. An Orion research model 601A/digital ionalyzer pH meter was used for checking the pH of buffer solutions of pH values ranging from 2.5 to 12.0, prepared as recommended previously [28].

2.2. Reagent

Analytical reagent grade chemicals and doubly distilled water were used throughout. 2,3-Dichloro-6-(3-carboxy-2-hydroxy-1-naphthylazo)quinoxaline used in the present investigation was prepared according to the procedure described previously [24]. A 0.0826 g of DCHNAQ was dissolved in 100 mL of absolute ethanol (826 mg L^{-1}).

Iron(III) standard stock solution, 1000 mg L^{-1}, was prepared by dissolving 4.3175 g of $Fe(NH_4)(SO_4)_2 \cdot 12H_2O$ in 20 mL of 1:1 HCl and diluted to 500 mL with water. Iron(II) stock solution, 1000 mg L^{-1}, was prepared by dissolving 3.511 g of iron(II) ammonium sulphate hexahydrate in 50 mL of 1.0 M HCl and diluted to volume in a 500 mL calibrated flask. The working standard solutions were prepared freshly by dilution with water.

Hydroxylamine hydrochloride, 10% solution, was prepared by dissolving 10.0 g of hydroxylamine hydrochloride in 100 mL water. The solution was freshly prepared every day. Styrene-divinylbenzene anion exchange resin was used in the chloride form. The resin was soaked in alcohol for 12.0 h, then treated with 2.0 M HCl for 6.0 h, finally with distilled water until the washing was free from chloride. It was dried at 40 °C and stored in a brown reagent bottle.

2.3. Absorbance measurements

The absorbance of DCHNAQ–Fe^{2+} complex sorbed on the resin was measured in a 5.0 mm cell at 743 and 830 nm against a 5.0 mm cell packed with resin equilibrated with blank solution. The net absorbance (A_c) for the complex was obtained using the equation [30]:

$$A_c = A_{743} - A_{830}$$

where $A_{743} = A_{s\,743} - A_{b\,743}$ and $A_{830} = A_{s\,830} - A_{b\,830}$ and $A_{s\,xxx}$ and $A_{b\,xxx}$ are the absorbances of the sample and the blank (cell packed with resin equilibrated with blank solution), respectively at the indicated wavelength. When the absorbance was measured at two different wavelengths, one corresponding to absorption maximum of the complex (743 nm) and the other in a region where the complex absorbs very low (830 nm), the absorbance difference, $A_{743} - A_{830}$, could be assumed to be constant under the similar packing conditions.

2.4. General procedure

For the determination of total iron in a 100 mL sample containing 0.1–20.0 μg of total iron (II and III), 2.0 mL of 10% hydroxylamine hydrochloride solution, 2.0 mL of 826 mg L^{-1} DCHNAQ solution, 10.0 mL acetate buffer solution of pH 3.54 and 0.5 g of styrene-divinylbenzene resin were added. The mixture was stirred for 20 min. The coloured resin was collected and transferred to 5.0 mm quartz cell with the aid of a dropping pipette. A blank solution containing all reagents except iron was prepared and treated in the same way as the sample. The absorbance difference between sample and blank was measured after 5.0 min as described in Section 2.3.

For the determination of iron(II) in a 100 mL water sample containing 0.1–20 μg of iron(II), the same procedure was used but without the addition of 2.0 mL of 10% hydroxylamine HCl.

3. Results and discussion

3.1. Absorbance spectra

Iron(II) forms a deep red complex with DCHNAQ at the optimum conditions. Fig. 1 shows the absorption spectra of Fe^{2+}–DCHNAQ complex fixed on an anion-exchange resin and in solutions. The absorption maximum of Fe^{2+}–DCHNAQ complex is at 727 nm in solution, whereas it shifted to bathochromic direction at 743 nm in the solid phase. It is evident that the sensitivity increases when the complex is sorbed on the resin.

Investigations were carried out to establish the most favourable conditions to give a highly colour intensity and to achieve maximum colour development in the quantitative determination of iron. The influence of each of the following variables on the complexation reaction was tested.

3.2. Effect of pH

The optimum pH for the formation and fixation of the complex species was in the range 2.86–4.28 using different types of buffer solutions (universal, acetate, phosphate and thiel [28]). Acetate buffer solution was used to maintain the optimum one which give highest absorbance value in addition to the stability of the colour fixed species, so, all subsequent studies were performed at pH 3.54. Moreover, 10 mL of pH 3.54 acetate buffer solution was selected for 100 mL sample volume.

3.3. Effect of reagent concentration

The absorbance increases with DCHNAQ concentration increase. Maximum and constant absorbance was achieved with 1.5–2.5 mL

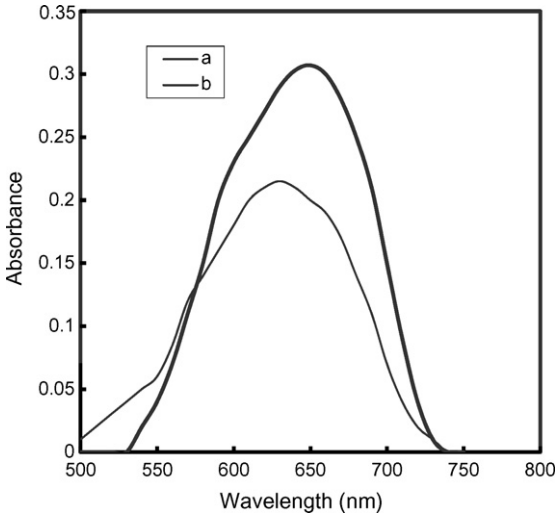

Fig. 1. Absorption spectra of Fe^{2+}–DCHNAQ complex: (a) in solution: $C_{Fe^{2+}} = 2.0$ mg L^{-1}, $C_{DCHNAQ} = 413$ mg L^{-1}, pH 3.54, 10 mm path length; (b) on the resin: $C_{Fe^{2+}} = 12$ μg L^{-1}, $C_{DCHNAQ} = 165.2$ mg L^{-1}, pH 3.54, 0.5 g resin, 5 mm optical path length.

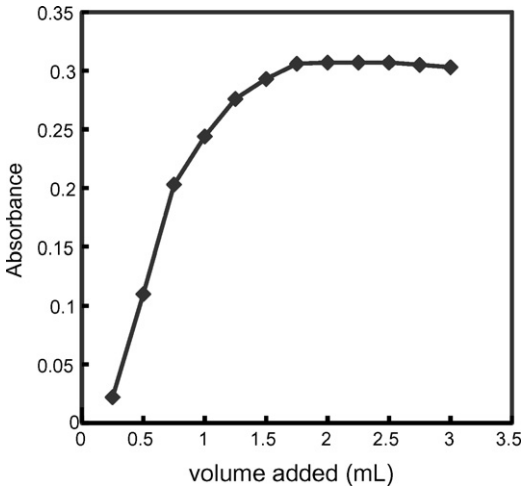

Fig. 2. Effect of 826 mg L^{-1} DCHNAQ volume on the complexation of 12 μg L^{-1} in sorbed form.

of 826 mg L^{-1}. Therefore, 2.0 mL was selected as the optimum volume (Fig. 2).

3.4. Effect of time

The effect of stirring time on colour intensity was investigation. The rate of equilibration was not influenced by the rate of reduction of iron(III) to iron(II). The colour development was complete within 15.0 min (Fig. 3). A stirring time of 20 min was chosen to keep the analysis time. The absorbance of ion-exchange resin phase became stable after ion-exchange resin was transferred into cell for 5.0 min and had no change for 6.0 h.

3.5. Effect of resin

The use of a large amount of resin lowered the absorbance as usual. Only the amount required filling the cell and to facilitate handling (i.e. 0.5 g) was used for all studies. Constant absorbance was obtained by adding 10% hydroxylamine HCl solution, in the range 0.5–4.0 mL, for the reduction of iron(II), 2.0 mL of 10% hydroxylamine HCl solution were employed.

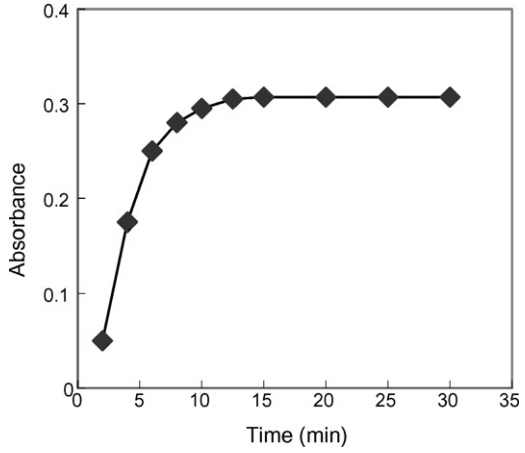

Fig. 3. Dependence of colour development in solid phase on stirring time, conditions: 12 μg L^{-1} of Fe^{2+}, 165.2 mg L^{-1} DCHNAQ, pH 3.54, 0.5 g resin for 100 mL sample.

3.6. Composition of the complex

The nature of the complex species fixed on the resin was established at the optimum conditions described above using the molar ratio and continuous variation methods. The plot of absorbance versus the molar ratio of DCHNAQ to Fe^{2+}, obtained by varying the DCHNAQ concentration, showed inflection at molar ratio 2.0, indicating presence of two DCHNAQ molecules in the fixed complex. Moreover, the Job method showed a ratio of DCHNAQ to iron(II) = 2.0. Consequently, the results indicated that the stoichiometric ratio was 2:1 [DCHNAQ:iron(II)]. The conditional formation constant ($\log K$), calculated using Harvey and Manning equation applying the data obtained from the above two methods, was found to be 7.88, whereas the true constant was 8.00.

3.7. Analytical data

The calibration graph for iron(II) ions was linear in the concentration range 1.0–20 μg L^{-1} for 100 mL volumes with r^2 of 0.9992 using 0.5 g of resin. The regression equation may be expressed by

$$A = 0.003 + 5.12 \times 10^{-3} C, \qquad r = 0.9996$$

where C is the concentration of iron in the sample solution in μg L^{-1}. The molar absorptivity, and Sandell sensitivity of the complex sorbed on the resin from 100 mL sample volume are recorded in Table 1.

Reproducibility was measured for a series of 10 independent determinations containing 12.0 μg L^{-1} of iron(II) in 100 mL sample using 0.5 g of the exchanger. The relative standard deviation was 1.65%.

The sensitivity expressed as molar absorptivity of the proposed method is compared in Table 2 with those of published spectrophotometric methods. The higher sensitivity of the proposed method is notable, greater even than that of the SPS [43] that used 1-(5-bromo-2-pyridylazo)-2-naphthol-6-sulphonic acid. Also, the proposed method is more sensitive than other method [19–25], that based on solid-phase spectrophotometry (Table 2).

The standard deviation (s) of the A_{blank}, the background absorbance measured for the blank, calculated as the average of 10 determinations and expressed as s units was 0.006. The IUPAC detection limit (K = 3.0) [30] and the quantification limit (K = 10) [31] were calculated for 100 mL sample (Table 1).

Table 1
Analytical parameters

Parameter	Value
pH	3.54
Amount of exchanger (g)	0.5
Optimum DCHNAQ concentration (mg L^{-1})	165.2
Optimum hydroxylamine concentration (%)	0.2
Stirring time (min)	20
Beer's law limit (μg L^{-1})	1.0–20
Ringbom optimum range (μg L^{-1})	2.5–18
Molar absorptivity ($\times 10^6$ L mol^{-1} cm^{-1})	2.86
Sandell sensitivity (ng cm^{-2})	0.0196
Detection limit (ng L^{-1})	280
Quantification limit (ng L^{-1})	950
Regression equation[a]	
Slope (b)	5.12×10^{-3}
Intercept (a)	0.003
Correlation coefficient (r)	0.9996
R.S.D. (%)	1.65

[a] $A = a + bC$, where C is the concentration of iron in μg L^{-1}.

Table 2
Comparison of the sensitivity of the methods for spectrophotometric determination of iron

Reagent	λ_{max} (nm)	ε ($\times 10^{-4}$ L mol^{-1} cm^{-1})	Reference
Ferrozine	562	2.79	[34]
2,4,6-Tri(2′-pyridyl)-1,3,5-triazine	595	2.15	[35]
2-(5-Bromo-2-pyridylazo)-5-diethylaminophenol	558	7.10	[36]
Azid—tetrahydrofuran	396	1.53	[37]
Thiocyanate—benzyltriethylammonium	476	2.79	[38]
Pyrocatechol violet—CTAB	595	6.55	[39]
2,4,6-Tris(2′-pyridyl)-1,3,5-triazine—picrate	600	22.0	[40]
Morin—Triton X-100	418	6.15	[41]
1-Nitroso-2-naphthol—Tween 80	446	1.69	[42]
Di-2-pyridylketone salicyloyl hydrazone	375	1.26	[9]
1-(5-Bromo-2-pyridylazo)-2-naphthol-6-sulphoric acid—SPS	765	47.7	[43]
DCHNAQ	743	286	This work

3.8. Effect of diverse ions

A systematic study of the effect of foreign ions on the determination of iron(II) was undertaken for a maximum W/W ratio value [foreign ion to iron(II)] of 18,000. Tolerance is defined as the foreign ion concentration causing an error smaller than ±3.0% in the determination of the analysis. The tolerance values for the ions studied are recorded in Table 3. The proposed method offers better selectivity than that proposed in other SPS methods [19–25].

In order to apply the method to determine iron in natural water samples, the interference from species commonly found in water was studied. The interference was negative for F^- and positive for other ions. Negative interference is due to decomposition of the formed complex with iron(II), whereas positive interference is due to formation of another complex with the examined ions with excess of DCHNAQ.

The most serious interference in the determination of iron in natural water due to their relatively high concentrations, were from Ca^{2+}, Mg^{2+} and SO_4^{2-}. However, the interference level can be reduced by diluting the sample, taking into account the sensitivity of the proposed method, without reducing the accuracy and whilst maintaining the simplicity and short duration of analysis.

Table 3
Effect of diverse ions on the determination of 12 μg L^{-1} of iron

Foreign ions	Tolerance limit (μg L^{-1})
Na^+, K^+, Li^+	18,000
NO_3^-, CH_3COO^-	13,500
Cl^-, ClO_4^-	11,000
SO_4^{2-}, PO_4^{3-}	9,000
$S_2O_3^{2-}$, SiO_3^{2-}	7,500
Ca^{2+}, Mg^{2+}, Sr^{2+}	6,000
Benzoate, citrate	5,000
Succinate, borate	3,750
Cu^{2+}, Co^{2+}, Ni^{2+}	2,500
Pd^{2+}, Pt^{4+}	1,800
Zn^{2+}, Cd^{2+}	1,100
Mo^{6+}, W^{6+}	800
Zr^{4+}, VO_2^+	500
Be^{2+}, Sc^{3+}	300
La^{3+}, Sm^{3+}, Gd^{3+}	250
Al^{3+}, Pb^{2+}	200
F^-	100

3.9. Analytical applications

The proposed method has been applied to the determination of iron(II) and iron(III) in water samples using the standard addition method. Sensitivity was modified by matrix effect and this fact can be evaluated from the ratio of the slope of the standard addition calibration graph. The ratios were 1.4 for tap water, 1.6 for river Nile water, 0.8 for mineral water and 1.1 for well water samples. The mean value (six determinations) of the iron found in the analysis for 100 mL sample system (taking into account the dilution factor) was 43.20 ± 0.006 μg L^{-1} for tap water, 140.5 ± 0.010 μg L^{-1} for river Nile water, 7.103 ± 0.005 μg L^{-1}

Table 4
Determination of iron(II) and iron(III) in water samples

Sample	Added		Proposed method[a] ((g L^{-1})				ICP-AES method[a] [32] (μg L^{-1})	
	Fe(II)	Fe(III)	Fe(II)	Fe(III)	t-value[b]	F-test[b]	Fe(II)	Fe(III)
Tap water	–	–	14.5	28.7	1.17	2.78	14.7	28.5
	2.0	4.0	16.6	32.6	1.29	3.13	16.6	32.5
	4.0	8.0	18.6	36.7	1.56	–	18.7	36.6
	6.0	12.0	20.5	40.5	–	3.27	20.6	40.5
Well water	–	–	46.3	94.2	1.34	3.46	46.5	94.0
	3.0	5.0	49.3	99.3	1.08		49.4	99.1
	6.0	10.0	52.4	104.3		2.71	52.4	104.2
	9.0	15.0	55.4	109.3	1.20	2.93	55.4	109.2
Mineral water	–	–	2.8	4.3	1.44	3.69	2.8	4.4
	4.0	6.0	6.7	10.4		3.25	6.8	10.4
	8.0	12.0	10.8	16.4	1.32		10.9	16.3
	12.0	18.0	14.9	22.3	1.26	3.07	14.8	22.3
Well water	–	–	36.2	78.9		2.85	36.3	79.0
	2.5	5.0	38.8	83.8	1.40	3.73	38.8	84.0
	5.0	10.0	41.3	88.9	1.52		41.2	88.9
	7.5	15.0	43.7	94.0		3.56	43.8	93.9

[a] Average of six determinations.
[b] Theoretical values for t- and F-values at 95% confidence level for five degrees of freedom are 2.57 and 5.05, respectively.

for mineral water and $115.10 \pm 0.012\ \mu g\ L^{-1}$ for well water samples.

In order to check the absolute accuracy of the proposed method, a recovery study was carried out on the water samples mentioned above using a competitive method. For this, different amounts of reference iron(II) material were added to water sample and the percentage recovery was determined. Table 4 showed the results obtained for all water samples. These results confirm the validity of the proposed method.

The performance of the proposed method was assessed by calculation of the *t*-value (for accuracy) and *F*-test (for precision) compared with ICP-AES method [32]. The mean values were obtained in a Student's *t*- and *F*-tests at 95% confidence limits for five degrees of freedom [33]. The results showed that the calculated values (Table 4) did not exceed the theoretical values. A wider range of determination, higher accuracy, more stability and less time consuming, shows the advantage of the proposed method over other methods. Also, there is no need for extraction or heating in the present method.

4. Conclusion

The proposed method permits the simultaneous determination of trace amounts of iron(II) and iron(III) by solid-phase spectrophotometry using DCHNAQ as complexing agent. Solid-phase spectrophotometry combines the preconcentration of the species of interest on a solid matrix and subsequent measurements of the absorbance of the complex in the solid phase. This provides an increase in selectivity and sensitivity with respect to conventional spectrophotometric method without requiring expensive and sophisticates instrumentation such as ICP, ETAAS. The method is highly sensitive, selective, simple and economical for the determination of iron(II). The proposed method has been applied to the determination of iron in natural water samples with good results. The proposed method is simple and more sensitive than other methods commonly used at microgram level, in addition to lower tolerance limits.

References

[1] K. Hirayama, N. Unohara, Anal. Chem. 60 (1988) 2573.
[2] J. Tamarit, V. Irazusta, A. Moreno-Cermeno, J. Ros, Anal. Biochem. 351 (2006) 149.
[3] X.-P. Yan, M.J. Hendry, R. Kerrich, Anal. Chem. 72 (2000) 1879.
[4] S. Oszwałdowski, D. Marchut, Anal. Chim. Acta 540 (2005) 207.
[5] G. Absalan, M. Nekoeinia, Anal. Chim. Acta 531 (2005) 293.
[6] W. Ruengsitagoon, Talanta 74 (2008) 1236.
[7] M. Hasani, A. Rezaei, H. Abdollahi, Spectrochim. Acta (A) 68 (2007) 414.
[8] P.K. Tarafder, R. Thakur, Microchem. J. 80 (2005) 39.
[9] M.C.C. Areias, L.H.S. Avila-Terra, I. Gaubeur, M.E.V. Suarez-Iha, Spect. Lett. 34 (2001) 289.
[10] M.J. Almendral, A. Alonso, M.J. Porras, M.A. Garcı, Y. Curto, Microchim. Acta 147 (2004) 117.
[11] M.A. Akl, Y. Mori, K. Sawada, Anal. Sci. 22 (2006) 1169.
[12] R.B. Willis, D. Sangster, Anal. Chem. 48 (1976) 59.
[13] F.C. Garcia, R. Checa, R. Avidad, L.F. Capitan-Vallvey, Talanta 42 (1995) 711.
[14] K. Yoshimura, S. Ohashi, Talanta 25 (1978) 103.
[15] L.S.G. Teixeira, F.R.P. Rocha, Talanta 71 (2007) 1507.
[16] M.C. Valencia, J. Garcia, L.F. Capitan-Vallvey, Anal. Lett. 23 (1990) 1095.
[17] A.S. Amin, Anal. Chim. Acta 437 (2001) 265.
[18] A.S. Amin, Spectrochim. Acta (A) 58 (2002) 1831.
[19] Z. Zhao, H. Liu, Huaxue Shiji 13 (1991) 123.
[20] S. Nigo, K. Yoshimura, T. Tarutani, Talanta 28 (1981) 669.
[21] K. Ohzeki, Y. Satoh, Y. Kawamara, T. Kambara, Bull. Chem. Soc. Jpn. 56 (1983) 2618.
[22] S. Li, W. Gao, Talanta 31 (1984) 844.
[23] M.L. Fernandez-de Cordova, A. Ruiz-Medina, A. Diaz, Fres. J. Anal. Chem. 357 (1997) 44.
[24] Y. Liu, X. Qu, B. Guo, J. Li, Fenxi Ceshi Xuebao 16 (1997) 35.
[25] R. Ga, Y. Liu, Fenxi Huaxue 24 (1996) 1309.
[26] A.S. Amin, S. Shakra, A.A. Abdalla, Bull. Chem. Soc. Jpn. 67 (1994) 1286.
[27] A.S. Amin, J. Saudi Chem. Soc. 3 (2000) 129.
[28] A.S. Amin, G.O. El-Sayed, Monatshefte 132 (2001) 587.
[29] A.S. Amin, Spectrochim. Acta (A) 59 (2003) 1025.
[30] IUPAC, Spectrochim. Acta (B) 33 (1978) 242.
[31] Analytical Methods Committee, Analyst 112 (1987) 199.
[32] M.G.D. Tamba, R. Falciani, T.D. Lopez, A.G. Coedo, Analyst 119 (1994) 2081.
[33] J.C. Miller, J.N. Miller, Statistics for Analytical Chemistry, 3rd edn., Ellis Horwood, Chichester, 1993.
[34] M.V. Dawson, S.J. Lyle, Talanta 37 (1990) 1189.
[35] G.S.R. Krishnamurti, P.M. Huang, Talanta 37 (1990) 745.
[36] J. Miura, Analyst 114 (1989) 1323.
[37] C.J. Chacarolli, J.F. Andrade, O.M. Guimaraes, V.R. Balbo, C.S. Venezuela, F.S. Teruel, Anal. Chim. Acta 411 (2000) 217.
[38] K.C. Bayan, H.K. Das, Talanta 35 (1988) 57.
[39] M.T.M. Zaki, W.H. Mahmoud, A.Y. El-Sayed, Talanta 35 (1988) 253.
[40] M.I. Toral, A.B. Barrera, Talanta 36 (1989) 1069.
[41] M.T.M. Zaki, A.M. El-Atrash, W.H. Mahmoud, A.Y. El-Sayed, Analyst 113 (1988) 937.
[42] J. Yun, H. Choi, Talanta 52 (2000) 893.
[43] J. Chen, J. Lin, Anal. Lett. 34 (2001) 2169.

Talanta 76 (2008) 1015–1021

Contents lists available at ScienceDirect

Talanta

journal homepage: www.elsevier.com/locate/talanta

Development and validation of reversed phase liquid chromatographic method utilizing ultraviolet detection for quantification of irinotecan (CPT-11) and its active metabolite, SN-38, in rat plasma and bile samples: Application to pharmacokinetic studies

Tripta Bansal[a,b,*], Anshumali Awasthi[b], Manu Jaggi[b], Roop K. Khar[a], Sushama Talegaonkar[a,*]

[a] Department of Pharmaceutics, Faculty of Pharmacy, Jamia Hamdard (Hamdard University), Hamdard Nagar, New Delhi 110062, India
[b] Dabur Research Foundation, 22, Site IV, Sahibabad, Ghaziabad, U.P. 201010, India

ARTICLE INFO

Article history:
Received 20 February 2008
Received in revised form 26 April 2008
Accepted 28 April 2008
Available online 4 May 2008

Keywords:
Irinotecan (CPT-11)
SN-38
Plasma
Bile
Ultraviolet detection
Pharmacokinetics

ABSTRACT

A new, simple, sensitive and specific reversed-phase high performance liquid chromatographic (HPLC) method using ultraviolet detection was developed and validated for the analysis of CPT-11 (λ_{max} = 254 nm, 365 nm) and its major active metabolite, SN-38 (λ_{max} = 380 nm) in rat plasma and bile. The sample pre-treatment from plasma involved a single protein precipitation step with cold acetonitrile. In case of bile, liquid–liquid extraction with dichloromethane: *tert*-butyl methyl ether (3:7) was carried out. Topotecan, a structurally related camptothecin, was used as an internal standard. An aliquot of 50 μL was injected onto a C-18 column. The chromatographic separation was achieved by gradient elution consisting of acetonitrile and water (pH 3.0 adjusted with 20% *o*-phosphoric acid) at a flow rate of 1.0 ml/min. Total run time for each sample was 30 min. All the analytes viz. topotecan, CPT-11, SN-38 were well separated with retention times of 11.4, 13.4 and 15.5 min, respectively. Method was found to be selective, linear ($R^2 \approx 0.999$), accurate (recovery ± 15%) and precise (<5% C.V.) in the selected concentration ranges for both the analytes. The quantification limit for CPT-11 was 40 ng ml^{-1} and for SN-38 was 25 ng ml^{-1}. The percent extraction efficiency was ~97% for CPT-11 and SN-38 from plasma while extraction recovery of CPT-11 and SN-38 from bile was ~70% and ~60%, respectively. The method was successfully used to determine plasma and biliary excretion time profiles of CPT-11 and SN-38, following oral and intravenous CPT-11 administration in rats. In the present study, irinotecan showed an absolute bioavailability of 30% as calculated from the pharmacokinetic data.

1. Introduction

Irinotecan (CPT-11), a notable water-soluble camptothecin derivative, is approved by FDA for treatment of colon and small cell lung malignancies. The mechanism of action of CPT-11 involves inhibition of mammalian DNA-topoisomerase-I, causing stabilization of complexes during DNA replication, leading to cell death. It has the most complex pharmacokinetic profile among the currently available camptothecin analogues. It is actually a prodrug with little inherent biological activity and gets rapidly hydrolysed by carboxylesterases to its 100–1000-fold more cytotoxic metabolite, 7-ethyl 10-hydroxy camptothecin (SN-38). At physiological pH, CPT-11 and SN-38 exist in two distinguishable forms, an active lactone ring (closed form) and inactive hydroxy acid (ring-opened form). Determination of separate lactone and carboxylate forms is hampered by inherent stability problems associated with lactone-acid inter-conversion. Besides this, it is also proved that monitoring the sum of the lactone and carboxylate forms is equally effective as determining the lactone form separately, with regard to measuring pharmacokinetic–pharmacodynamic outcome Fig. 1 [1].

Oral administration of CPT-11 in rodents resulted in peak plasma concentrations within 1–2 h post-dose with an absolute bioavailability of 20–30%. Preliminary study of CPT-11 elimination pathways indicate that less than 50–60% of administered dose is excreted unchanged into bile along with the minor contribution from SN-38 [2]. Further, the major dose-limiting toxicity after CPT-11 administration is severe diarrhea proposed to be caused by SN-38 intestinal exposure via biliary route [3]. Therefore, investigation on CPT-11 hepatobiliary transport and its metabolic disposition

* Corresponding author at: Dabur Research Foundation, 22, Site IV, Sahibabad, Ghaziabad, U.P. 201010, India. Tel.: +91 9212118120; fax: +91 120 4376902.
E-mail address: triptabansal@yahoo.co.in (T. Bansal).

0039-9140/$ – see front matter © 2008 Elsevier B.V. All rights reserved.
doi:10.1016/j.talanta.2008.04.058

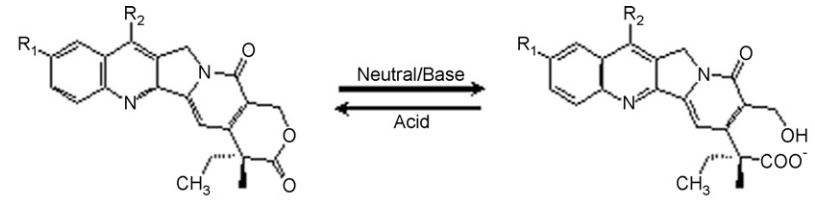

Compound	R_1	R_2
CPT-11	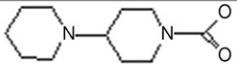	C_2H_5
SN-38	OH	C_2H_5
Topotecan	OH	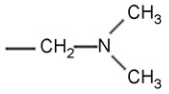

Fig. 1. Conversion of lactone and carboxylate forms of CPT-11, SN-38 and topotecan.

is of great interest. To facilitate such studies, a suitable assay for quantification of CPT-11 and SN-38 is necessary.

The availability of quantification methods for CPT-11 and SN-38 in biological fluids is limited. de Jong et al. described blood distribution of CPT-11 [4], Nakatomi et al. studied drug transport in membrane vesicles [5], Poujol et al. determined salivary pharmacokinetics [6] and Sparreboom et al. estimated drug concentration in urine and feces [7], but method development and validation in bile has not been described earlier. Myriads of sensitive high performance liquid chromatographic (HPLC) methods have been reported previously by various researchers to quantitate CPT-11 and SN-38 in plasma, using fluorescence method of detection [8–15]. Although these methods offer good sensitivity, fluorescence method suffers from constraints due to differences in native fluorescence of the analytes and their order of elution. It is interesting to note that camptothecins possess absorbance as reported for topotecan and 9-nitro camptothecin [16,17]. However, there is no report for analytical determination of CPT-11 and SN-38 using ultraviolet detection so far. Ultraviolet method is simple, more feasible and less time consuming over the existing methods of detection. The absorbance characteristics of all analytes were examined and the detector was set at the most favorable wavelength for each compound.

Therefore, the main objective of present study was to develop and validate a simple and sensitive HPLC method using ultraviolet detection to quantify CPT-11 and SN-38. Topotecan, a structurally related camptothecin is used as internal standard. The usefulness of the method was tested by determining CPT-11 and SN-38 concentration time profiles in plasma and bile following intravenous (20 mg/kg) and oral (80 mg/kg) administration in female wistar rats.

2. Experimental

2.1. Reagents and chemicals

CPT-11 (>99%), SN-38 (>96%) and topotecan (>98%) originated from Dabur Pharma Limited (U.P., India). Disodium ethylene diamine tetra acetic acid was purchased from Sigma–Aldrich (St. Louis, MO, USA). Acetonitrile of HPLC grade was obtained from J.T Baker (USA). *O*-phosphoric acid and DMSO were from Merck Ltd. (India). For pharmacokinetic studies, irinotecan hydrochloride injection (20 mg ml^{-1}) manufactured by Dabur Pharma Limited (U.P., India) was used. Ketamine (Aneket) and xylazine HCl (Xylaxin) were obtained from Neon Labs Ltd. (Mumbai, India) and Indian Immunologicals Ltd. (A.P., India), respectively. The water used was of Milli-Q grade purified by a Milli-Q UV Purification System (Millipore, Bedford, MA, USA). All other chemicals and reagents were of analytical or HPLC grade as appropriate and procured locally.

2.2. HPLC method development

2.2.1. Instrumentation

The liquid chromatographic system LC-2010C$_{HT}$ series (Shimadzu, Nakagyo-ku, Kyoto, Japan) consisting of gradient flow Control Pump, on-line Solvent Degasser, Autosampler, Diode Array Detector and Column Oven. All the parameters of HPLC were controlled by LC solutions software version 1.21 SP1.

2.2.2. Liquid chromatographic conditions

Chromatographic separations were achieved using YMC, C-18, ODS-A RP column (250 mm × 4.6 mm, 4 μm) stainless steel column, which was maintained at 35 °C. The samples of 50 μl were injected into HPLC system. The mobile phase consisted of 100% acetonitrile (mobile phase A) and Milli-Q water, adjusted to pH 3.0 with 20% *o*-phosphoric acid (mobile phase B) at a flow rate of 1.0 ml min^{-1}. The column was initially equilibrated at 10% solvent A and 90% solvent B. After injection, the concentration of solvent A was increased linearly to 80% and solvent B decreased linearly to 20% over 15 min. The A:B was then maintained at 80:20 for further 5 min. After 5 min, the system was returned to original conditions (solvent A at 10% and solvent B at 90%) linearly over 5 min and equilibrated for 5 min before the next injection. The total run time for each sample was 35 min. The mobile phase was filtered through 0.45 μm filter (Sartorius, Germany) and deaerated for 15 min by sonication.

2.2.3. Preparation of stock and working standard solutions

Primary stock solutions for CPT-11 and SN-38 were prepared separately in DMSO at a concentration of 2 mg ml^{-1}. A mixture of CPT-11 and SN-38 was obtained at a concentration of 1000 μg ml^{-1} by diluting the primary stock. Working standard solutions were prepared daily by serial dilution in acetonitrile containing 0.1% glacial acetic acid, to obtain analyte concentration from 500 μg ml^{-1} to 250 ng ml^{-1}.

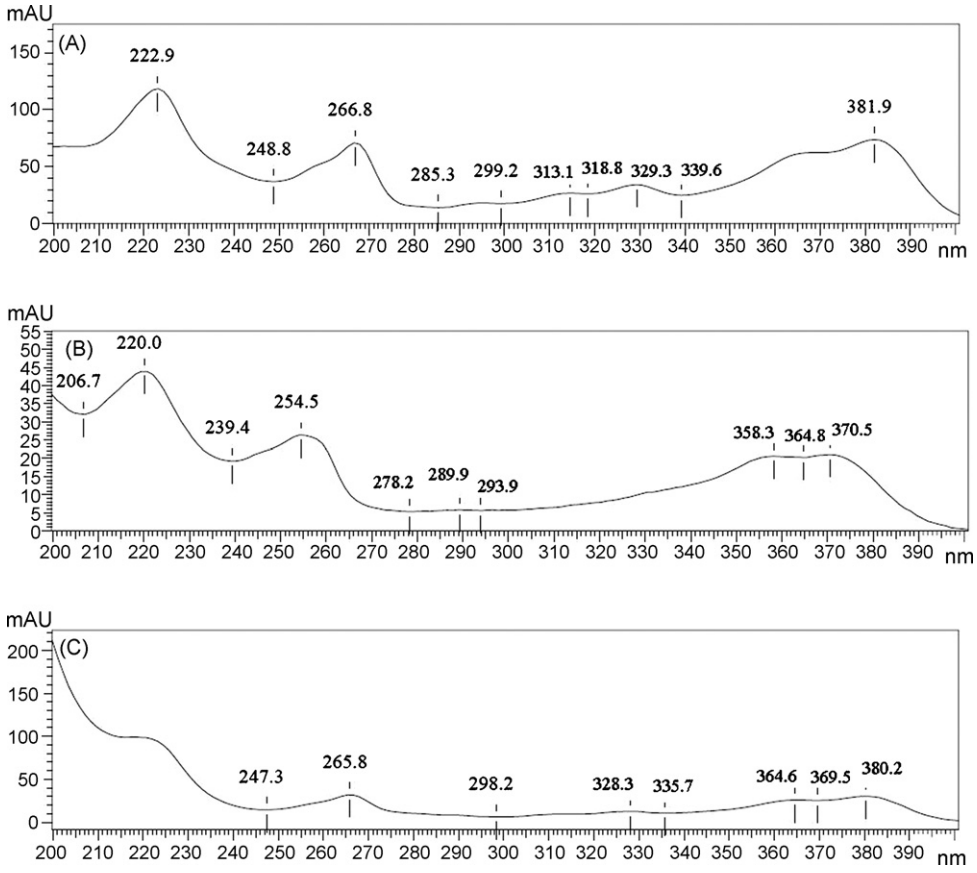

Fig. 2. Ultraviolet absorption scans of (A) topotecan (B) CPT-11 and (C) SN-38.

2.2.4. Plasma sample preparation

To 100 μl of plasma samples, 100 μl ice-cold acetonitrile containing 0.1% glacial acetic acid and 10 μg ml^{-1} topotecan (as internal standard) was added, resulting in protein precipitation. After rigorous vortex mixing for 5 min, the sample was centrifuged at 3000 × *g* for 10 min at 4 °C. An aliquot of 150 μl supernatant was transferred to a fresh tube and 50 μl was injected onto column for analysis.

2.2.5. Bile sample preparation

Feasibility of various solvent mixtures such as ethyl acetate, dichloromethane (DCM), *tert*-butyl methyl ether (TBME), diethyl ether, *n*-hexane were evaluated for extraction of analytes from bile. To 100 μl of bile sample, 10 μl of topotecan (100 μg ml^{-1}) was added as internal standard. A 1 ml aliquot of DCM:TBME (3:7) was added and the mixture was vortexed, followed by shaking for 10 min (MultiReax Heidolph, The Labware House, London, UK). Subsequently, centrifugation (3000 × *g* for 10 min) was performed to separate the aqueous and organic layer. A 900 μl of organic layer was transferred to a clean microtube and evaporated to dryness under vacuum (Savant DNA Speed-Vac, NJ, USA) at 40 °C. The dried extracts were redissolved by vortexing and sonication in 150 μl of 20:80 (v/v) acetonitrile:water (pH 3.0). A 50 μl volume was injected onto the HPLC system.

2.3. Validation procedures

The chromatographic method was further validated for specificity, linearity, sensitivity, precision and accuracy according to ICH guidelines [18].

2.3.1. Linearity

All validation runs were performed in triplicates on three consecutive days to assess inter-day and intra-day variation. Seven-point calibration curves were constructed in plasma and bile for the two analytes over the selected concentration range and tested for linearity. Plasma calibration standards were prepared at 25, 50, 100, 500, 1000, 5000 and 10,000 ng ml^{-1} whereas, bile calibration standards were of 100, 50, 20, 10, 2, 1 and 0.5 μg ml^{-1}.

2.3.2. Specificity, sensitivity, accuracy and precision

Specificity of the method was determined by analyzing six different batches of blank plasma or bile obtained from healthy rats. The reproducibility of the analytical procedure was determined by calculating intra- and inter-day coefficient of variation (C.V.). Accuracy was performed by five replicate analysis of spiked quality control samples at three concentrations using plasma (500, 100 and 50 ng ml^{-1}) and bile (50, 10 and 1 μg ml^{-1}) followed by their comparison with the calibration curves prepared on the same day and on different days. Limit of quantification (LOQ) is the lowest concentration at which precision expressed by % C.V. is less than 20% and accuracy expressed by relative difference of measured and nominal is also lower than 20%. Limit of detection (LOD) was determined at the lowest concentration to be detected, taking into consideration a signal-to-baseline noise ratio of 3.

2.3.3. Extraction efficiency

The extraction efficiency from plasma and bile was determined by comparison between areas of pure unextracted standards in the relevant concentration ranges plasma (500, 100 and 50 ng ml^{-1}) or bile (50, 10 and 1 μg ml^{-1}) prepared in mobile phase, with those of

extracted biological concentration containing the same amount of standards.

2.4. Application to pharmacokinetic studies

Healthy female wistar rats (180–200 g) used for pharmacokinetic studies were obtained from breeding stock of Dabur Research Foundation (Ghaziabad, U.P., India). All animal procedures were approved by Institutional Animal Ethics Committee (Dabur Research Foundation, U.P., India). Rats were fasted overnight before dose administration and approximately 3 h post-dose. The target dose was administered intravenous via the lateral tail vein (20 mg/kg) or orally via gavage (80 mg/kg) using a ball-tipped needle. Blood samples were withdrawn prior to dosing and at various time points till 24 h post-dosing from retro-orbital plexus into microtubes containing disodium ethylene diamine tetra acetic acid, to determine levels of CPT-11 and SN-38. Plasma was obtained by immediate centrifugation at 1500 × *g* for 10 min at 4 °C. Bile cannulation experiments were carried out as described previously [19]. Briefly, the abdominal cavity was opened after induction of anesthesia with ketamine (90 mg/kg, i.p.) and xylazine (10 mg/kg, i.p.). The common bile duct was ligated and cannulated with PE10 polyethylene tubing (inner diameter, 0.28 mm; outer diameter, 0.61 mm; Harvard Apparatus, Holliston, MA, USA). During the

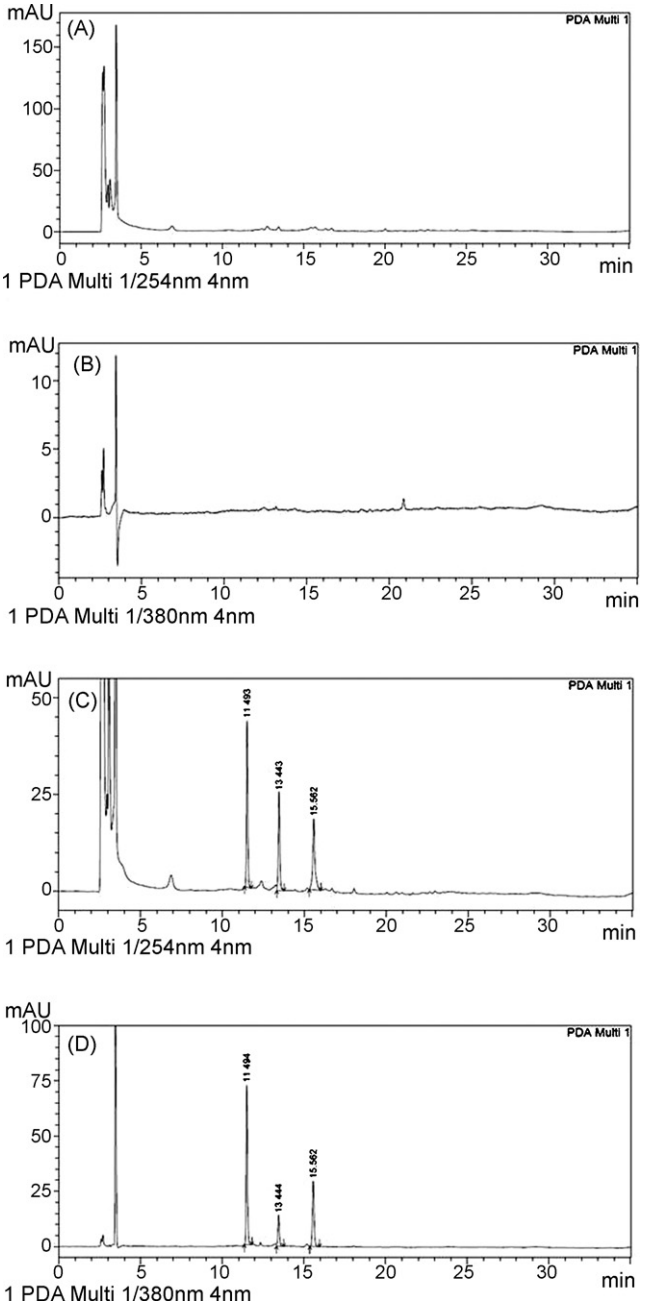

Fig. 3. Representative HPLC chromatograms of (A) Blank rat plasma sample at 254 nm, (B) blank rat plasma sample at 380 nm (C) rat plasma spiked with drug mixture at 254 nm and (D) rat plasma spiked with drug mixture at 380 nm. The peaks at 11.5, 13.4 and 15.6 min correspond to topotecan (internal standard), CPT-11 and SN-38, respectively.

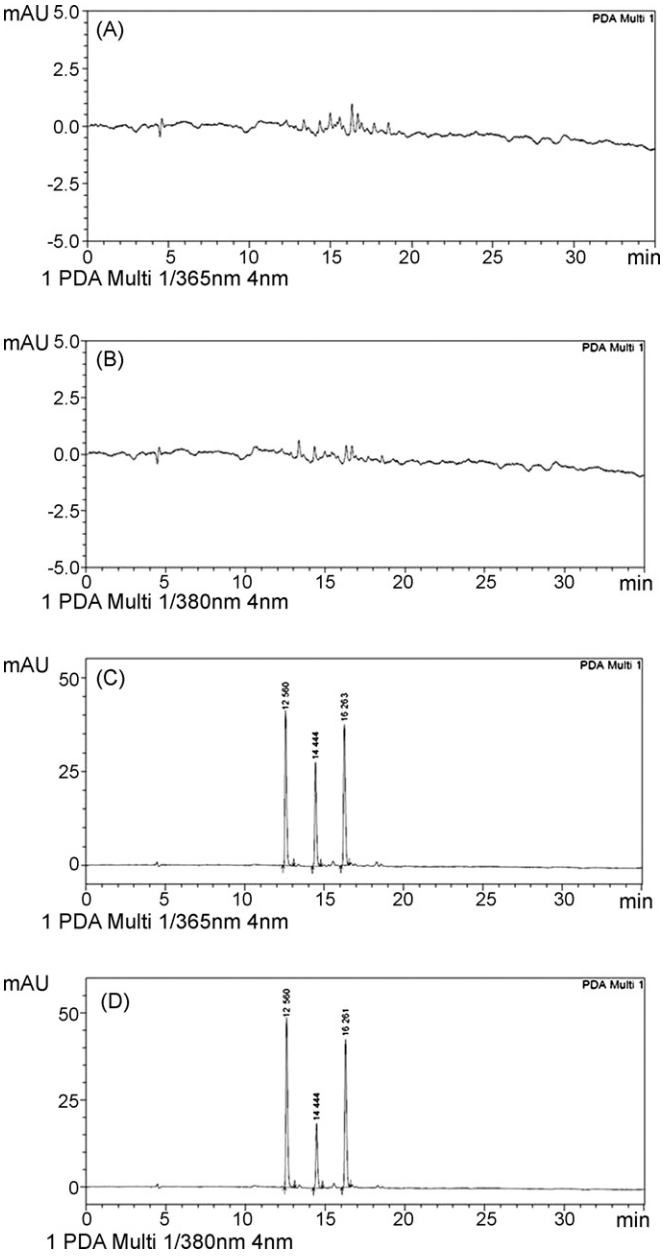

Fig. 4. Representative HPLC chromatograms of (A) blank rat bile sample at 365 nm, (B) blank rat bile sample at 380 nm, (C) rat bile spiked with drug mixture at 365 nm and (D) rat bile spiked with drug mixture at 380 nm. The peaks at 12.5, 14.4 and 16.2 min correspond to topotecan (internal standard), CPT-11 and SN-38, respectively.

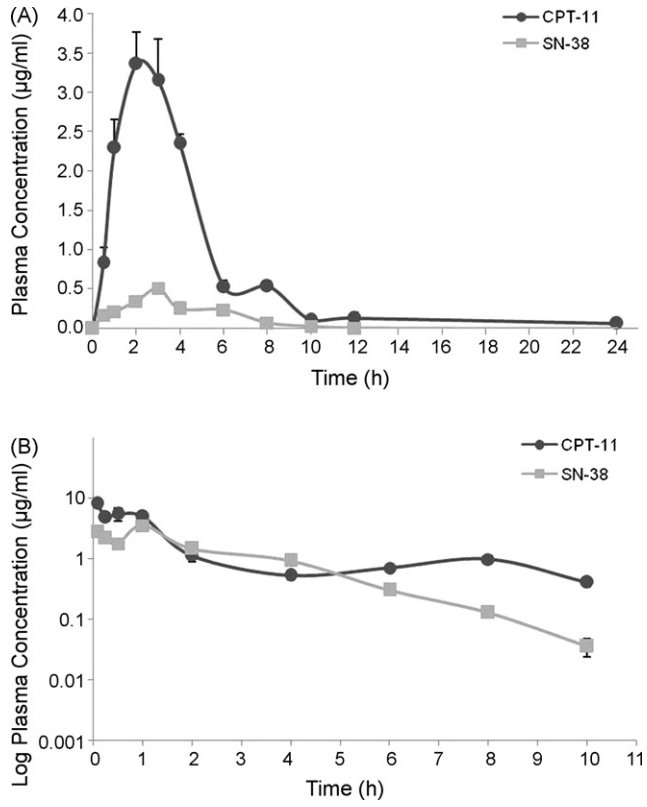

Fig. 5. Plasma concentration versus time curves following (A) CPT-11, 80 mg/kg, PO administration and (B) CPT-11, 20 mg/kg, i.v. adminstration in female wistar rats. Circles (-●-) denote CPT-11, and squares (-■-) denote SN-38. Each data point represents mean ± S.E.M. of five different rats.

experimental period body temperature of the rats was maintained at 37 °C with a heating pad. Bile (~1 ml at each time interval) was collected at 0–1, 1–2, 2–3, 3–4 and 4–5 h intervals and at 5 h, the rats were sacrificed.

The plasma CPT-11 and SN-38 concentration-versus-time curves were used to determine maximum plasma concentration (C_{max}), time to maximum plasma concentration (t_{max}), area under the concentration time curve to the final sampling point ($AUC_{0\text{-last}}$), volume of distribution (V_{ssobs}), elimination rate constant (K_{el}), half life ($t_{1/2}$) and total body clearance (Cl_{obs}). C_0 was the initial plasma concentration of drugs obtained by back-extrapolation to *y*-axis. Pharmacokinetic parameters were calculated by non-compartment model using WinNon-Lin 5.0 programme (Pharsight, Mountain View, CA, USA). The absolute bioavailability (*F*) of CPT-11 after the oral administration (80 mg/kg) compared to the intravenous (i.v.) administration (20 mg/kg) was calculated as follows:

$$F = \frac{AUC_{oral} \times \text{i.v. dose}}{AUC_{i.v.} \times \text{oral dose}} \quad (1)$$

2.5. Statistical analysis

Data of 3–5 independent experiments is reported as mean ± S.D. unless otherwise noted. Statistical analysis was performed using GraphPad prism software version 4.0 (San Diego, CA, USA).

3. Results and discussion

3.1. Method development

3.1.1. Ultraviolet wavelength (λ_{max}) selection

Ultraviolet (UV) is selected as method of detection because of being simple and more feasible. The UV absorption spectra of topotecan, CPT-11 and SN-38 are shown in Fig. 2A–C, respectively.

The criteria for λ selection were to allow maximum response at that wavelength and the absence of endogenous interfering peaks occurring from blank matrix. CPT-11 was measured at 254 nm and 365 nm for plasma and bile samples, respectively. For SN-38, λ_{max} of 380 nm was used.

3.2. Method validation

3.2.1. Specificity

Specificity was demonstrated by the absence of any endogenous interference at retention times of peaks of interest as evaluated by chromatograms of blank rat plasma and bile against those spiked with CPT-11, SN-38 and topotecan (Figs. 3A–D and 4A–D).

All the analytes viz. topotecan, CPT-11, SN-38 are well separated with retention times of 11.4, 13.4 and 15.5 min, respectively.

3.2.2. Range and linearity

Seven-point calibration curves were constructed for both the analytes on three consecutive days at specified concentrations. The calculated peak area ratios and concentration added showed linear relationship over selected concentration ranges in both bile and plasma. The linearity of the assay procedure was determined by calculation of regression line using the method of unweighted least square analysis. As evident from the coefficient of correlation (*r*), the calibration graphs were linear, for CPT-11 and SN-38 in the concentration ranges assayed; 25–10,000 ng ml^{-1} (for plasma) and 0.5–100 μg ml^{-1} (for bile). The slopes and intercepts were consistent throughout the validation runs and are listed in Table 1.

3.2.3. Accuracy and precision

The accuracy and precision data is shown in Table 2.

Quality control (QC) samples for each analyte were prepared in replicates ($n = 5$) at three different concentrations viz. low (LQC), medium (MQC) and high (HQC) from weighing independent of those used for preparing calibration curves. Both accuracy (recovery ± 15%) and precision (<5% C.V.) was found to be suitable and do not depend on the concentration assayed or on the day of the assay.

Table 1
Regression analysis of calibration curves for CPT-11 and SN-38 in plasma and bile over the specified concentration range

Matrix	Analyte	Range	Slope[a] ($m \pm$ S.D.)	Intercept[a] ($c \pm$ S.D.)	Correlation coefficient[b] (r)
Plasma	CPT-11	25–10,000 ng ml^{-1}	0.240 ± 0.011	0.011 ± 0.0015	0.9992
	SN-38	25–10,000 ng ml^{-1}	0.208 ± 0.010	0.055 ± 0.0070	0.9989
Bile	CPT-11	0.5–100 μg ml^{-1}	0.239 ± 0.017	0.081 ± 0.0083	0.9997
	SN-38	0.5–100 μg ml^{-1}	0.347 ± 0.009	0.048 ± 0.0027	0.9993

[a] Values are mean ± S.D. of three calibrations.
[b] *r* is the correlation coefficient obtained from seven-point calibration curve. The concentrations across the range were evenly distributed.

Table 2
Accuracy and precision data (inter-day and intra-day) of chromatographic method for analysis of CPT-11 and SN-38 in rat plasma and bile

Matrix	Analyte	Nominal concentration[a]	Intra-day			Inter-day		
			Measured concentration			Measured concentration		
			Mean	% Accuracy	C.V.	Mean	% Accuracy	C.V.
Plasma	CPT-11	500 ng ml^{-1}	505.1	101.0	1.91	510.7	102.1	1.26
		100 ng ml^{-1}	102.5	102.5	3.20	95.4	95.4	4.08
		50 ng ml^{-1}	52.4	104.8	4.08	52.7	105.4	3.32
	SN-38	500 ng ml^{-1}	502.8	100.6	1.34	491.2	98.2	2.14
		100 ng ml^{-1}	104.1	104.1	3.96	102.3	102.3	4.35
		50 ng ml^{-1}	53.2	106.4	3.14	51.4	102.8	3.42
Bile	CPT-11	50 μg ml^{-1}	50.36	100.7	1.11	51.48	103.0	1.48
		10 μg ml^{-1}	11.33	113.3	2.15	10.48	104.8	3.28
		1 μg ml^{-1}	1.10	109.5	3.60	1.10	109.8	2.51
	SN-38	50 μg ml^{-1}	51.68	103.4	0.79	49.53	99.1	1.55
		10 μg ml^{-1}	10.25	102.5	1.24	11.43	114.3	4.21
		1 μg ml^{-1}	1.04	103.7	3.67	0.94	94.2	3.14

[a] Selected concentrations represent the low, medium and high quality control concentrations viz. LQC, MQC and HQC. Intra-day and inter-day accuracy and precision was determined with replicates ($n = 5$) for each concentration. C.V. (coefficient of variation) = (S.D./mean) × 100.

Table 3
Percentage extraction efficiency of CPT-11 and SN-38 from plasma and bile samples done at different concentration levels

Analyte	Plasma			Bile		
	Theoretical concentration[a] (ng/ml)	% Extraction efficiency	C.V.	Theoretical concentration[a] (μg/ml)	% Extraction efficiency	C.V.
CPT-11	500	94.6 ± 4.1	4.2	50	65.1 ± 3.2	4.9
	100	93.1 ± 2.5	2.5	10	68.8 ± 4.9	7.1
	50	96.3 ± 1.3	1.3	1	70.2 ± 1.5	2.1
SN-38	500	92.1 ± 3.4	3.5	50	57.4 ± +3.6	6.3
	100	95.6 ± 1.8	1.9	10	60.2 ± 2.7	4.5
	50	96.6 ± 2.9	3.0	1	61.9 ± 2.6	4.2

[a] Values are the mean ± S.D. of three determinations.

3.2.4. Limit of quantitation

The limit of quantification (LOQ) was defined as the lowest drug concentration that could be determined with acceptable precision (i.e., C.V. < 20%) and accuracy (i.e., recovery 100 ± 20%). The limit of detection (LOD) is defined as the amount, which could be detected with a signal to noise ratio of 3. The LOQ for CPT-11 was 40 ng ml^{-1} and for SN-38 was 25 ng ml^{-1}. The detection limits were 15 and 10 ng ml^{-1} for CPT-11 and SN-38, respectively.

3.2.5. Extraction efficiency

Extraction efficiencies were calculated for CPT-11 and SN-38 in both biological matrices. Protein precipitation method yielded excellent recoveries (92–97%) for both CPT-11 and SN-38 from plasma. In case of bile, liquid–liquid (or, liquid phase or, solvent) extraction method resulted in much cleaner samples when compared with direct protein precipitation method. Selection of suitable solvent is a critical parameter in liquid–liquid extraction procedure. Ideally, the selected solvent should be compatible, immiscible with water, stable enough over the extraction time and have high solubility for the target analyte. A series of organic solvents and their mixtures of varying polarity (viz. ethyl acetate, dichloromethane (DCM), *tert*-butyl methyl ether (TBME), diethyl ether, *n*-hexane) were evaluated for extraction of CPT-11 and SN-38 from bile. Finally, DCM:TBME (3:7) mixture was selected since it provided adequate specificity and sensitivity. CPT-11 and its metabolite SN-38 have a moderate recovery of ∼70% and ∼60%, respectively in bile as a matrix (Table 3). Recovery of analyte need not be 100% but the extent of recovery of the analyte and its internal standard should be consistent, precise and reproducible [20,21]. Considering that the LOQ of CPT-11 and SN-38 is 40 and 25 ng ml^{-1}, respectively and the average recovery to be 60–70% for each of the compounds; 70–100 ng ml^{-1} of each compound in the original bile sample can be detected by UV.

3.3. Application

The present method allowed successful determination of CPT-11 and SN-38 in plasma and bile following oral and intravenous drug administration at therapeutically relevant doses.

3.3.1. Oral and intravenous pharmacokinetic study in female wistar rats

The plasma concentration time profiles of CPT-11 and its metabolite SN-38 determined by the described method are presented in Fig. 5A–B.

The main pharmacokinetic parameters are given in Table 4.

Plasma concentrations of CPT-11 gradually increased to reach peak levels within 2–3 h after oral dose and slowly began

Table 4
Pharmacokinetic parameters of CPT-11 and SN-38 after (i) CPT-11, 80 mg/kg, PO administration and (ii) CPT-11, 20 mg/kg, i.v. adminstration in female wistar rats. All values are mean ± S.E.M. in five different rats

Group	Parameters	CPT-11	SN-38
CPT-11, 20 mg/kg, intravenous	C_0 (μg/ml)	9.51 ± 1.4	3.35 ± 0.91
	$t_{1/2}$ (h)	3.1 ± 0.60	1.3 ± 0.20
	AUC_{last} (h μg/ml)	10.8 ± 2.0	9.3 ± 1.4
	V_{ssobs}(ml/kg)	4852.2 ± 703.8	–
	Cl_{obs} (ml/h/kg)	1206.4 ± 159.7	–
	K_{el}(h^{-1})	0.232 ± 0.05	–
CPT-11, 80 mg/kg, oral	C_{max} (μg/ml)	2.9 ± 0.37	0.48 ± 0.07
	t_{max} (h)	2.6 ± 0.89	2.8 ± 0.45
	$t_{1/2}$ (h)	1.24 ± 0.05	1.47 ± 0.35
	AUC_{last} (h μg/ml)	14.0 ± 2.18	1.81 ± 0.30
	Cl_{obs} (ml/h/kg)	5613.83 ± 1126.3	–
	V_{ssobs} (ml/kg)	32197.0 ± 8067.1	–
	K_{el} (h^{-1})	0.286 ± 0.25	–

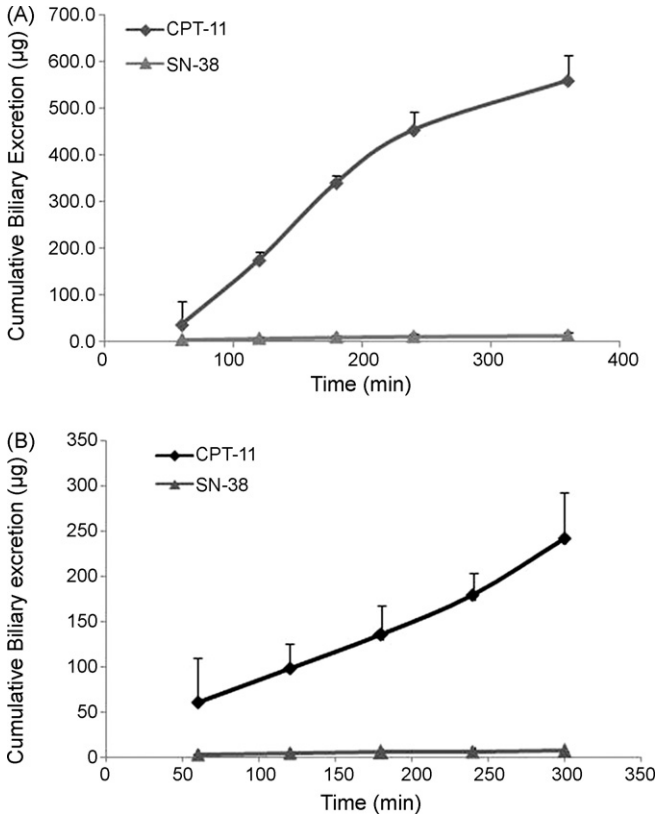

Fig. 6. Cumulative biliary excretion time profiles following (A) CPT-11, 80 mg/kg, PO administration and (B) CPT-11, 20 mg/kg, i.v. adminstration in bile duct cannulated female wistar rats. Diamonds (-♦-) denote CPT-11, and triangles (-▲-) denote SN-38. Each data point represents mean ± S.D. of three different rats.

to decline thereafter. A secondary peak appeared 7–8 h after dosing. SN-38 showed the similar profile. After intravenous administration, CPT-11 and SN-38 get eliminated showing a decreasing drug concentration with time. The absolute bioavailability of irinotecan calculated by the given formula was found to be 30% in rats, which is similar to the value reported earlier [3].

3.3.2. Biliary excretion study

The biliary excretion of CPT-11 and its metabolites was measured up to 5 h after drug administration. The cumulative biliary excretion curves of CPT-11 and SN-38 after oral and i.v. dosing of are presented in Fig. 6A–B.

The excretion increases linearly with time but gets saturated after 5 h. The amount of CPT-11 and SN-38 excreted in bile over 5 h can be expressed as percentages of the total CPT-11 dose administered in each rat. About 9% of the CPT-11 i.v. dose was recovered unchanged in the bile and 0.2% as SN-38 during the study period whereas when the drug was given orally, the amounts excreted decreased to 2 and 0.1% for CPT-11 and SN-38, respectively. The drug concentrations excreted in bile are lower than that reported previously in humans [22]. This could be because of intrinsic species differences and lesser duration of study.

4. Conclusions

In this paper, the absorbance characteristics of CPT-11 and SN-38 were studied and a simple HPLC-UV method for their quantification has been developed and validated for the first time. Ultraviolet method is simple, more feasible and less time consuming over the existing methods of detection. The optimal separation was achieved using a C-18 column using acetonitrile: water (pH 3.0) gradient as mobile phase. The proposed method is more feasible, uncomplicated and less time consuming over the existing methods. The method has shown to meet the current requirements of bio-analytical validation, providing good accuracy and precision. It is found to be sensitive enough to be implemented in real-time analysis of samples obtained from oral and intravenous pharmacokinetic studies in rats.

Acknowledgements

One of the authors (TB) is grateful to the Council of Scientific & Industrial Research (CSIR), New Delhi, India for providing senior research fellowship.

References

[1] E. Gupta, A.R. Safa, X. Wang, M.J. Ratain, Cancer Res. 56 (1996) 1309.
[2] C.F. Stewart, W.C. Zamboni, W.R. Crom, P.J. Houghton, Cancer Chemother. Pharmacol. 40 (1997) 259.
[3] R.H. Mathijssen, R.J. van Alphen, J. Verweij, W.J. Loos, K. Nooter, G. Stoter, A. Sparreboom, Clin. Cancer Res. 7 (2001) 2182.
[4] F.A. de Jong, R.H. Mathijssen, P. de Bruijn, W.J. Loos, J. Verweij, A. Sparreboom, J. Chromatogr. B Anal. Technol. Biomed. Life Sci. 795 (2003) 383.
[5] K. Nakatomi, M. Yoshikawa, M. Oka, Y. Ikegami, S. Hayasaka, K. Sano, K. Shiozawa, S. Kawabata, H. Soda, T. Ishikawa, S. Tanabe, S. Kohno, Biochem. Biophys. Res. Commun. 288 (2001) 827.
[6] S. Poujol, F. Pinguet, F. Malosse, C. Astre, M. Ychou, S. Culine, F. Bressolle, Clin. Chem. 49 (2003) 1900.
[7] A. Sparreboom, P. de Bruijn, M.J. de Jonge, W.J. Loos, G. Stoter, J. Verweij, K. Nooter, J. Chromatogr. B Biomed. Sci. Appl. 712 (1998) 225.
[8] D.F. Chollet, L. Goumaz, A. Renard, G. Montay, L. Vernillet, V. Arnera, D.J. Mazzo, J. Chromatogr. B Biomed. Sci. Appl. 718 (1998) 163.
[9] P. de Bruijn, J. Verweij, W.J. Loos, K. Nooter, G. Stoter, A. Sparreboom, J. Chromatogr. B Biomed. Sci. Appl. 698 (1997) 277.
[10] J. Escoriaza, A. Aldaz, C. Castellanos, E. Calvo, J. Giraldez, J. Chromatogr. B Biomed. Sci. Appl. 740 (2000) 159.
[11] W. Guo, A. Ahmad, S. Khan, F. Dahhani, Y.F. Wang, I. Ahmad, J. Chromatogr. B Anal. Technol. Biomed. Life Sci. 791 (2003) 85.
[12] N. Kaneda, Y. Hosokawa, T. Yokokura, Biol. Pharm. Bull. 20 (1997) 815.
[13] N.E. Schoemaker, H. Rosing, S. Jansen, J.H. Schellens, J.H. Beijnen, Ther. Drug Monit. 25 (2003) 120.
[14] H. Sumiyoshi, Y. Fujiwara, T. Ohune, N. Yamaoka, K. Tamura, M. Yamakido, J. Chromatogr. B Biomed. Appl. 670 (1995) 309.
[15] X. Yang, Z. Hu, S.Y. Chan, B.C. Goh, W. Duan, E. Chan, S. Zhou, J. Chromatogr. B Anal. Technol. Biomed. Life Sci. 821 (2005) 221.
[16] T. Bansal, M. Singh, G. Mishra, S. Talegaonkar, R.K. Khar, M. Jaggi, R. Mukherjee, J. Chromatogr. B Anal. Technol. Biomed. Life Sci. 859 (2007) 261.
[17] N.E. Schoemaker, H. Rosing, S. Jansen, P. Schoffski, J. Rizzo, J.H. Schellens, J.H. Beijnen, J. Chromatogr. B Anal. Technol. Biomed. Life Sci. 775 (2002) 231.
[18] Topic Q2B: Validation of analytical procedures: Methodology, in: International Conference on Harmonisation (ICH), 1996.
[19] X.Y. Chu, Y. Kato, K. Niinuma, K.I. Sudo, H. Hakusui, Y. Sugiyama, J. Pharmacol. Exp. Ther. 281 (1997) 304.
[20] G. Srinubabu, R.S. Patel, V.P. Shedbalkar, A.A. Rao, M.N. Rao, V.V.R. Bhandaru, J. Chromatogr. B 860 (2007) 202.
[21] http://www.fda.gov/cder/guidance/4252fnl.pdf.
[22] F. Lokiec, P. Canal, C. Gay, E. Chatelut, J.P. Armand, H. Roche, R. Bugat, E. Goncalves, A. Mathieu-Boue, Cancer Chemother. Pharmacol. 36 (1995) 79.

Talanta 76 (2008) 1183–1188

Contents lists available at ScienceDirect

Talanta

journal homepage: www.elsevier.com/locate/talanta

Analysis of metal-binding proteins separated by non-denaturating gel electrophoresis using matrix-assisted laser desorption/ionization mass spectrometry (MALDI-MS) and laser ablation inductively coupled plasma mass spectrometry (LA-ICP-MS)

J. Susanne Becker[a,*], Sandra Mounicou[a], Miroslav V. Zoriy[b], J. Sabine Becker[b], Ryszard Lobinski[a]

[a] Group of Bio-Inorganic Analytical Chemistry, CNRS UMR 5254, Hélioparc, 64053 Pau, France
[b] Central Division of Analytical Chemistry, Research Centre Jülich, D-52425 Jülich, Germany

ARTICLE INFO

Article history:
Received 10 March 2008
Received in revised form 29 April 2008
Accepted 14 May 2008
Available online 23 May 2008

Keywords:
BN-PAGE
LA-ICP-MS
Large laser ablation chamber
MALDI-TOF-MS
Rat tissue

ABSTRACT

Matrix-assisted laser desorption/ionization time-of-flight mass spectrometry (MALDI-TOF-MS) and laser ablation inductively coupled plasma mass spectrometry (LA-ICP-MS) have become established as very efficient and sensitive biopolymer and elemental mass spectrometric techniques for studying metal-binding proteins (metalloproteins) in life sciences. Protein complexes present in rat tissues (liver and kidney) were separated in their native state in the first dimension by blue native gel electrophoresis (BN-PAGE). Essential and toxic metals, such as zinc, copper, iron, nickel, chromium, cadmium and lead, were detected by scanning the gel bands using quadrupole LA-ICP-MS with and without collision cell as a microanalytical technique.

Several proteins were identified by using MALDI-TOF-MS together with a database search. For example, on one protein band cut from the BN-PAGE gel and digested with the enzyme trypsin, two different proteins – protein FAM44B and cathepsin B precursor – were identified. By combining biomolecular and elemental mass spectrometry, it was possible to characterize and identify selected metal-binding rat liver and kidney tissue proteins.

1. Introduction

Mineral elements essential for health that are found in animals or microorganisms, often at the trace and ultratrace concentration level, and play a vital role in biological systems (e.g. in single cells or cell organisms) and biological processes. The life of an organism is critically dependent on the proper regulation of the uptake, assimilation, intracellular and intercellular transport and translocation of trace metals (e.g. Cu, Fe, Zn, Ca). Knowledge of the chemical composition of metal-containing biomolecules (proteins and peptides or nucleic acids) and their chemical form (metallomics) and of metal–biomolecular interaction (metalloproteomics) within the cell or tissue is increasingly required to study biological processes and assess the extent and impact in life sciences [1–3].

Powerful bioanalytical techniques such as laser ablation inductively coupled plasma mass spectrometry (LA-ICP-MS) have been established as elemental mass spectrometric techniques and matrix-assisted laser desorption/ionization mass spectrometry (MALDI-MS) or electrospray ionization mass spectrometry (ESI-MS) as biomolecular mass spectrometric techniques in the characterization of proteins separated from complex protein mixtures by gel electrophoresis (in one and two dimensions). LA-ICP-MS has been employed in human brain research for the direct analysis of protein spot 2D gels to determine Cu, Zn, Al, Fe, S and P, for example in patients with Alzheimer's disease and healthy human brain sample [4,5]. By combining elemental and biomolecular mass spectrometry (LA-ICP-MS and MALDI-FTICR-MS, respectively), it was possible to characterize and identify several human Alzheimer brain proteins and to detect metal-containing peptides [6,7]. The formation of Cu-, Zn- and Fe-containing proteins was investigated by means of additional experiments on brain proteins of patients with Alzheimer's disease (including tau protein) using enriched stable isotopes (^{65}Cu, ^{67}Zn and ^{54}Fe) [8,9]. These tracer experiments showed that some metal bindings to proteins are stable enough during the denaturating gel electrophoresis steps. Some of the proteins are able to accumulate more metal ions or exchange their metal ions with the isotope tracers. In case of tau protein, it was shown that some

* Corresponding author. Present address: Varian Ltd., 10 Mead Road, Oxford Industrial Park, Yarnton, Oxford OX5 1QU, United Kingdom.
Tel.: +44 1865 291400; fax: +44 1865 291401.
E-mail address: susanne.becker@varianinc.com (J.S. Becker).

0039-9140/$ – see front matter © 2008 Elsevier B.V. All rights reserved.
doi:10.1016/j.talanta.2008.05.023

isoforms of the protein are able to bind metals such as Cu and Zn.

However, a main problem of denaturating SDS-PAGE is that metal-containing proteins are often not stable enough to survive the reducing (denaturating) condition during protein separation by 2D gel electrophoresis. Therefore, blue native (BN) PAGE is a powerful alternative technique for separating protein complexes with high molecular mass in their native state. Native PAGE combined with LA-ICP-MS was utilized for analysing Cd- and Zn-binding proteins in plants exposed to Cd (*Spinacia oleracea* L.) by Jakubowski and coworkers [10]. The authors study the uptake, the transport and protein binding capabilities of heavy metals in *Spinacia oleracea* L., a typical food plant with high susceptibility to cadmium uptake, and applied native PAGE to separate the metal-binding proteins. The detection of Cd and Zn in the proteins after PAGE separation and blotting onto membranes was demonstrated by LA-ICP-MS [11,12].

The aim of this work is to develop a non-denaturating separation technique via blue native gel electrophoresis (BN-PAGE) and to study the occurrence of metal-binding proteins in selected biological samples (in small amounts of rat kidney and liver samples). LA-ICP-MS will be utilized for the detection of essential and toxic metals in proteins after their gel electrophoretic separation. In a second step, as a specific biomolecular technique, MALDI-TOF-MS will be employed in searching for metal-containing proteins.

2. Experimental

2.1. Samples and sample preparation

Rat kidney and liver samples were analysed for metal content (Cu, Zn, Cr, Ni, etc.) by LA-ICP-MS after 1D native gel electrophoresis (BN-PAGE). The samples were lyophilized and homogenized to isolate the water-soluble proteins. The proteins were extracted in water by using an ultrasonic probe and afterwards separated by ultracentrifugation. Then BN-PAGE sample buffer (1 M Tris–HCl pH 6.8, 20% (v/v) glycerol, 0.01% (w/v) bromine phenol blue, from Sigma, Deisenhofen, Germany) was added and the proteins were separated by BN-PAGE according to their molecular weight.

2.2. Separation of proteins using native, non-denaturating gel electrophoresis

The rat kidney tissue was treated by BN-PAGE to separate the proteins according to their molecular weight in a polyacrylamide gel. The protein separation of the protein mixture by gel electrophoresis (Mini-Protein-Chamber V100, Biostep GmbH, Jahnsdorf, Germany) was performed in duplicate (one gel for LA-ICP-MS measurements and the other for MALDI-TOF-MS studies). The gels were stained with colloidal Coomassie and AmphiBlue Visopt® (Biostep GmbH, Jahnsdorf, Germany). For colloidal Coomassie 0.1% (w/v) brilliant blue R (Sigma, Deisenhofen, Germany), a solution of 25% (v/v) methanol (Fluka, Seelze, Germany) and 10% (v/v) acidic acid (Fluka, Seelze, Germany) in ultrapure water (Millipure water system, 18.2 MΩ) was added overnight to the gel after running. Afterwards the background of the gels was destained with 25% (v/v) methanol. For staining with AmphiBlue Visopt® the gels were fixated in 30% (v/v) in methanol for 1 h, and then stained with the AmphiBlue Visopt® colour for 1 h. The background of the gels was removed with 50 mM NaOAc (Sigma) in 20% (v/v) at pH 4.5 for 1 h and for 2 h 30 min to overnight with 20% (v/v) methanol. The same amount of sample was used for both staining procedures.

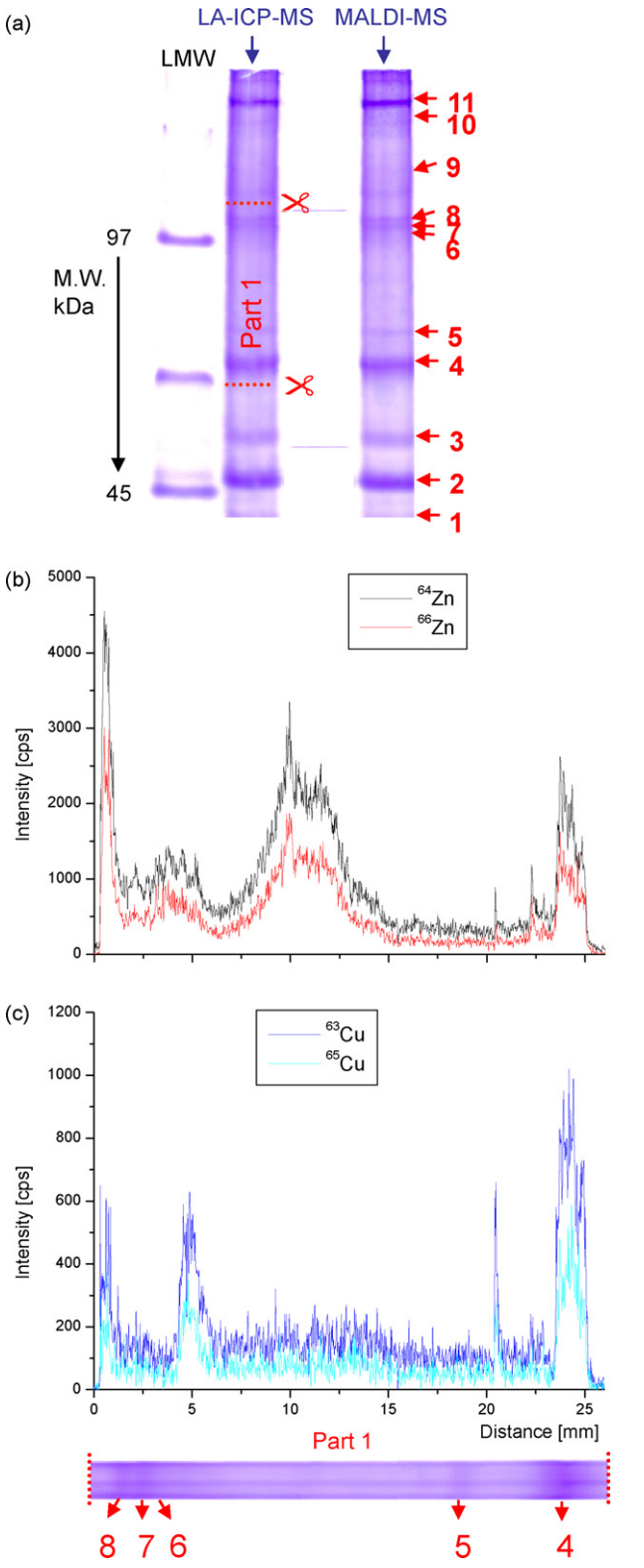

Fig. 1. (a) BN-PAGE of rat kidney water extract stained with colloidal Coomassie; right-hand side: BN-PAGE of rat kidney water extract stained with colloidal Coomassie with the protein bands that were cut and tryptic digested for MALDI-TOF-MS measurements. (b) Transient signals of $^{64}Zn^{+}$ and $^{66}Zn^{+}$ from part 1 of BN-PAGE gel of rat kidney (see Fig. 1a) using LA-ICP-MS. (c) Transient signals of $^{63}Cu^{+}$ and $^{65}Cu^{+}$ from part 1 of BN-PAGE gel of rat kidney (see Fig. 1a) using LA-ICP-MS.

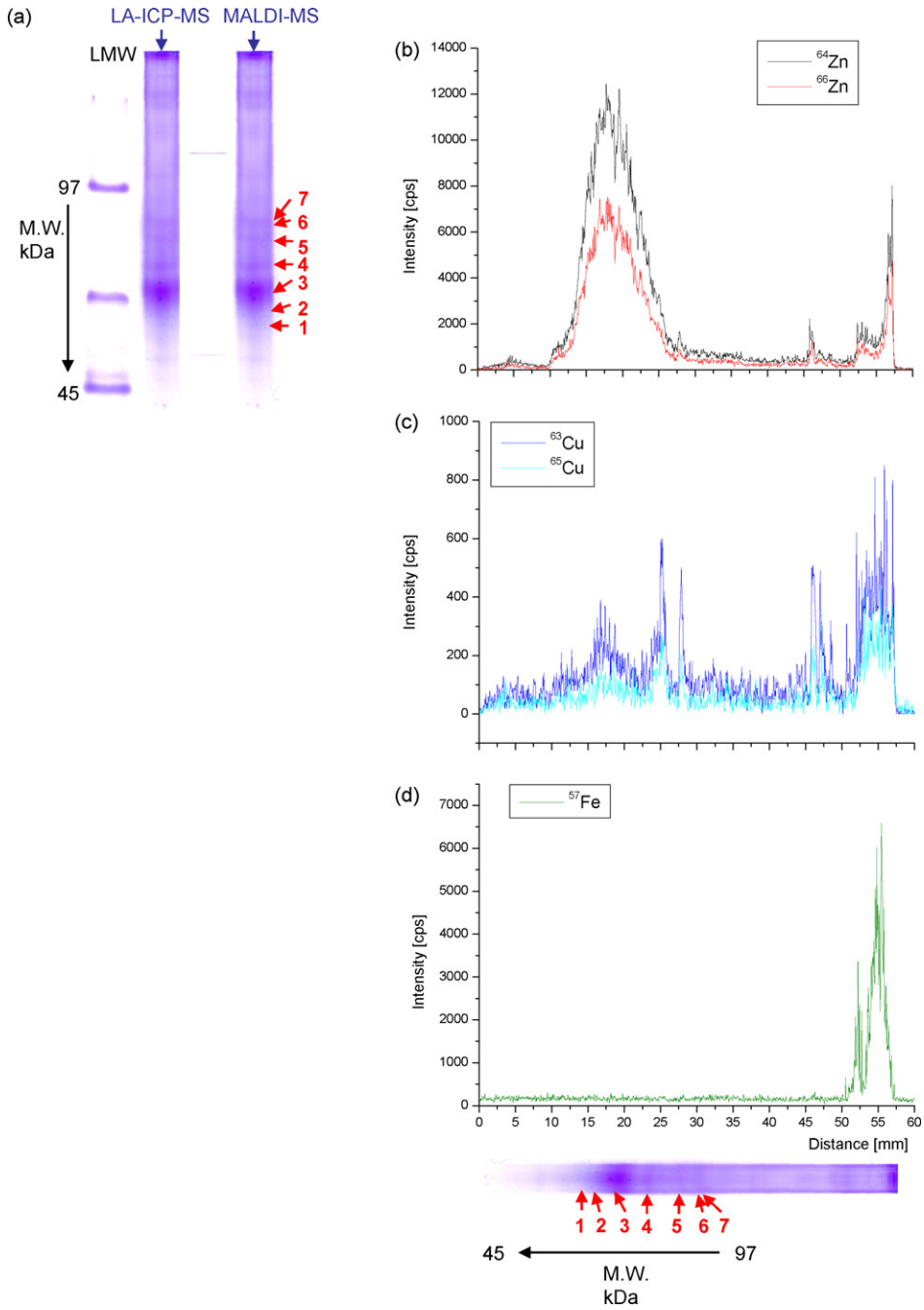

Fig. 2. (a) BN-PAGE of rat liver water extract stained with colloidal Coomassie; right-hand side: BN-PAGE of rat kidney water extract stained with colloidal Coomassie with the protein bands that were cut and tryptic digested for MALDI-TOF-MS measurements. (b) Transient signals of $^{64}Zn^{+}$ and $^{66}Zn^{+}$ from the whole BN-PAGE of rat liver (see Fig. 2a) using LA-ICP-MS. (c) Transient signals of $^{63}Cu^{+}$ and $^{65}Cu^{+}$ from the whole of BN-PAGE gel of rat liver (see Fig. 2a) using LA-ICP-MS. (d) Transient signals of $^{57}Fe^{+}$ from the whole of BN-PAGE gel of rat liver (see Fig. 2a) using LA-ICP-MS.

For the LA-ICP-MS measurements, the gels were dried on filter paper (chromatography paper 3MM CHR, Whatman, VWR, Fontenay-sous-Bois Cedex, France) by using a gel dryer (Model 583 Gel Dryer, BioRad, Marnes-la-Coquette, France).

The elements of interest were measured by LA-ICP-MS after 1D gel electrophoresis. The protein bands were cut in the second gel prepared under the same experimental conditions, digested with trypsin (Promega, Mannheim, Germany) and analysed by MALDI-TOF-MS as previously described [8,9]. For identification purposes a database search (www.matrixscience.com) was used with performed measurement.

2.3. Detection of metal-binding proteins (metalloproteins) using LA-ICP-MS

All LA-ICP-MS measurements for detecting the metal-binding proteins were performed by quadrupole-based ICP-MS at low mass resolution. A quadrupole-based ICP-MS (ELAN 6100, PerkinElmer, USA) coupled with a laser ablation system LSX 213 (CETAC LSX 213, Cetac Technologies, Omaha, NE, USA) was applied at the Research Centre Jülich (Germany) in searching for metal-binding proteins in gels. The direct element determination of the Cu, Zn, Ni, Cd and Pb detected in the protein bands of the one-dimensional gels was performed via several line scans. In order to validate the

measurements, a second quadrupole ICP-MS with collision cell (Agilent 7500 CE, Agilent) coupled to a laser ablation system LSX 100 (CETAC LSX 100, Cetac Technologies, Omaha, NE, USA) was utilized for element determination of Zn in protein bands in one-dimensional (1D) gels at CNRS in Pau (France). The background intensity of the ions analysed was determined after digestion of a small section of the blank gel with HNO_3 and the measurement was performed by using ICP-MS. For LA-ICP-MS measurements on gels at the Research Centre Jülich, a small laser ablation chamber was employed, and the performance of a large laser ablation chamber (from CETAC Technologies, Omaha, NE, USA) was tested. The chamber has an inner diameter of 7.86 cm × 10.40 cm (depth: 5.87 cm). The advantage of the large laser ablation chamber is that several gel samples can be arranged in the cell and measured under the same experimental conditions and it is therefore not necessary to cut the gel. The optimized experimental parameters for both instrumentations are described elsewhere [13].

2.4. Identification of proteins using MALDI-TOF-MS

MALDI-TOF-MS measurements on protein samples after separation by 1D native gel electrophoresis and subsequent tryptic in-gel digestion were performed with a Voyager-DETM STR instrument (Applied Biosystems). The pulsed nitrogen laser is operated at 337 nm, and ions are directly desorbed from the sample surface into the time-of-flight mass analyser. A solution of α-cyano-4-hydroxycinnamic acid (LaserBio Labs, Sophia Antipolis Cedex, France) in acetonitrile:0.1% TFA in water (2:1) was used as matrix. 0.7 μL matrix solution and 0.7 μL of sample solution were mixed on the stainless-steel MALDI sample target and allowed to dry. Calibration was performed with a standard peptide mixture with the *m*/*z* range of approximately 3000 (BioRad, Marnes-la-Coquette, France).

3. Results and discussion

3.1. Separation of proteins by blue native gel electrophoresis

Protein separation in small amounts of rat liver and kidney was carried out by blue native gel electrophoresis. Figs. 1a and 2a show two separations from two different gels of water-soluble proteins in rat kidney and rat liver in the BN-PAGE gel stained with colloidal Coomassie. The marker on the left-hand side demonstrates the mass range of the proteins investigated from 120 to 45 kDa. The three separations each of rat kidney and liver proteins were performed with good reproducibility with respect to the position and intensity of all protein bands. Each band contained at least one protein or even more.

Firstly, LA-ICP-MS measurements in the line scanning mode were performed to detect the metal-binding proteins. Secondly, water-soluble rat liver and rat kidney proteins were identified by measurements using MALDI-TOF-MS together with a database search.

3.2. LA-ICP-MS measurement

The dried gels were analysed in single line scan modus by LA-ICP-QMS with respect to the occurrence of a multitude of essential and toxic metals (Zn, Cu, Pb, Cd, Ni, and Cr). In our experiments in the separated protein bands of 1D blue native gels of rat kidney and liver, only Cu, Zn, Cd, Cr and Pb were detected by LA-ICP-MS using two different quadrupole mass spectrometers with and without collision cell. No Ni was found in the protein bands of rat kidney investigated. Of all the metals studied, zinc was observed in distinct protein bands with remarkable ion intensities. Transient signals of two zinc isotopes, namely $^{64}Zn^+$ and $^{66}Zn^+$, measured in three line scans over the whole one-dimensional gel by LA-ICP-QMS without collision cell of a rat kidney sample are plotted as a function of the length of the analysed the gel part in Fig. 1b. This graph shows the peaks for both zinc isotopes investigated in one protein band of the rat kidney gel at a mass of about 100 kDa. The maximum ion intensity for the most abundant $^{64}Zn^+$ isotope was found at about 4500 cps. The isotope ratio $^{66}Zn^+/^{64}Zn^+$ were determined by LA-ICP-MS as 0.59, which is close to the expected isotope ratio of 0.57. The whole gel from rat kidney water extract was analysed by LA-ICP-MS, but only in part 1 metal could be found. In the small Section 1 of the one-dimensional BN-PAGE of the rat kidney sample, an additional three Zn-containing protein bands were detected at around 95, 80 and 65 kDa by LA-ICP-MS. The width and the height of the bands are quite different. The widest peak with a maximum intensity of 3500 cps was observed at 80 kDa. The experimental findings of the occurrence of Zn-containing proteins in BN-PAGE gel of rat kidney sample were confirmed by LA-ICP-QMS with collision cell by the analysis of a selected Section 1 of the gel in the mass range of around 100–62 kDa. It is interesting to note that in this Zn-containing protein band at a molecular weight of the protein of 80 kDa, only Zn was found and none of the other metals investigated. However, Cu was clearly detected in the Zn-containing protein band with a mass at around 65 and 90 kDa. The maximum ion intensity of $^{63}Cu^+$ was determined as about 800 cps and the $^{65}Cu^+/^{63}Cu^+$ isotope ratio of about 0.5 is close to the expected IUPAC table value. Fig. 1c illustrates both Cu isotopes ($^{63}Cu^+$ and $^{65}Cu^+$) measured with smaller ion intensities in four protein bands of 1D gel of rat kidney at *m* = 100, 90, 70 and 65 kDa at the bands 8, 6, 5 and 4. In addition, LA-ICP-MS was employed to study the appearance of toxic elements such as Cd and Pb in proteins. In the 1D blue native gel, together with the occurrence of Zn and Cu traces of Cd and Pb in the protein bands of rat kidney at *m* = 65 kDa were detected. The measured ion intensities were significantly above the background signal. The measured ion intensities of the metals detected and the molecular weight of the proteins from the 1D gel of rat kidney are summarized in Table 1.

Table 1
Detected metals bonded to proteins and metal ion intensities for the most abundant isotope measured by LA-ICP-MS as a function their molecular weights (M.W.) from the protein bands determined in part 1 of BN-PAGE gel from rat kidney water extract (see Fig. 1a)

Metal ions measured (isotopic abundance)	Intensities of metal ion (cps)	M.W. of protein (kDa)
$^{64}Zn^+$ (48.63%)	4500	100
	1000–1500	95
	3000–3500	80
	2500	65
$^{63}Cu^+$ (69.17%)	600	100
	600	90
	650	70
	1000	65
$^{112}Cd^+$ (24.13%)	500	65
$^{208}Pb^+$ (52.4%)	180	65

In contrast to the BN-PAGE from the rat kidney sample, in the BN-PAGE from the rat liver sample Zn, Cu, Fe and Cr were detected in different proteins by LA-ICP-MS. In this experiment the whole gel band was measured directly by using the large laser ablation chamber. The experimental results of LA-ICP-MS measurements on 1D gel of rat liver with respect to Zn, Cu and Fe are illustrated in Fig. 2b–d. Whereas Zn-and Cu-containing proteins were detected at *m* = 200 and 65 kDa, Fe were found only in the protein band at highest mass. The highest intensity was observed for iron (via the

$^{57}Fe^{+}$ measurement). Chromium in the protein band at $m = 200$ kDa was measured by quadrupole ICP-MS without collision cell in the presence of a high background intensity of about 4000 cps at mass 52 u due to isobaric interference with $^{40}Ar^{12}C^{+}$ molecular ions.

The LA-ICP-MS results on gels using a small and a large laser ablation chamber are comparable with respect to the ion intensities measured and precision of analytical data obtained. The large laser ablation chamber is of advantage because the gels can be measured without cutting them into three pieces. Furthermore, standards for quantification and several samples can be measured under the same experimental conditions.

Quantification of metal-containing proteins by LA-ICP-MS using stable isotopes will be performed in a future study.

3.3. Identification of proteins by MALDI-TOF-MS and database search

The selected tryptic digested protein bands, shown in the right part of Figs. 1a and 2a, were analysed by using MALDI-TOF-MS and afterwards a database search was made for peptide mass fingerprinting (www.matrixscience.com, www.expasy.org, etc.). Several proteins were identified from the rat kidney and rat liver sample. All the identified proteins are summarized in Table 2 for rat kidney and Table 3 for rat liver. For example, band 1 from the rat kidney sample was identified as α-enolase and band 5 as the serine/threonine-protein phosphatase PP1-gamma catalytic subunit. Fig. 3a and b shows two MALDI-TOF-MS spectra of gel band 4 and 5 identified as Trans-Golgi network integral membrane protein TGN38 precursor

Table 2
Identified proteins after tryptic digestion and extraction from the gel bands of the BN-PAGE gel of rat kidney water extract sample measured by MALDI-MS (see Fig. 1a, right)

Band	Identified protein	M.W. (kDa)
1	α-Enolase	46.96
2	Major urinary protein precursor	20.72
3	Major urinary protein precursor	20.72
4	Trans-Golgi network integral membrane protein TGN38 precursor	38.28
5	Serine/threonine-protein phosphatase PP1-gamma catalytic subunit	36.96
6.1	*Protein FAM44B*	18.34
6.2	*Cathepsin B precursor*	37.45
7	Beta-synuclein (Phosphoneuroprotein 14)	14.50
8	Malate dehydrogenase, cytoplasmic	36.33
10	Ribonuclease UK114	14.16
11	Hydroxyacid oxidase 2	39.05

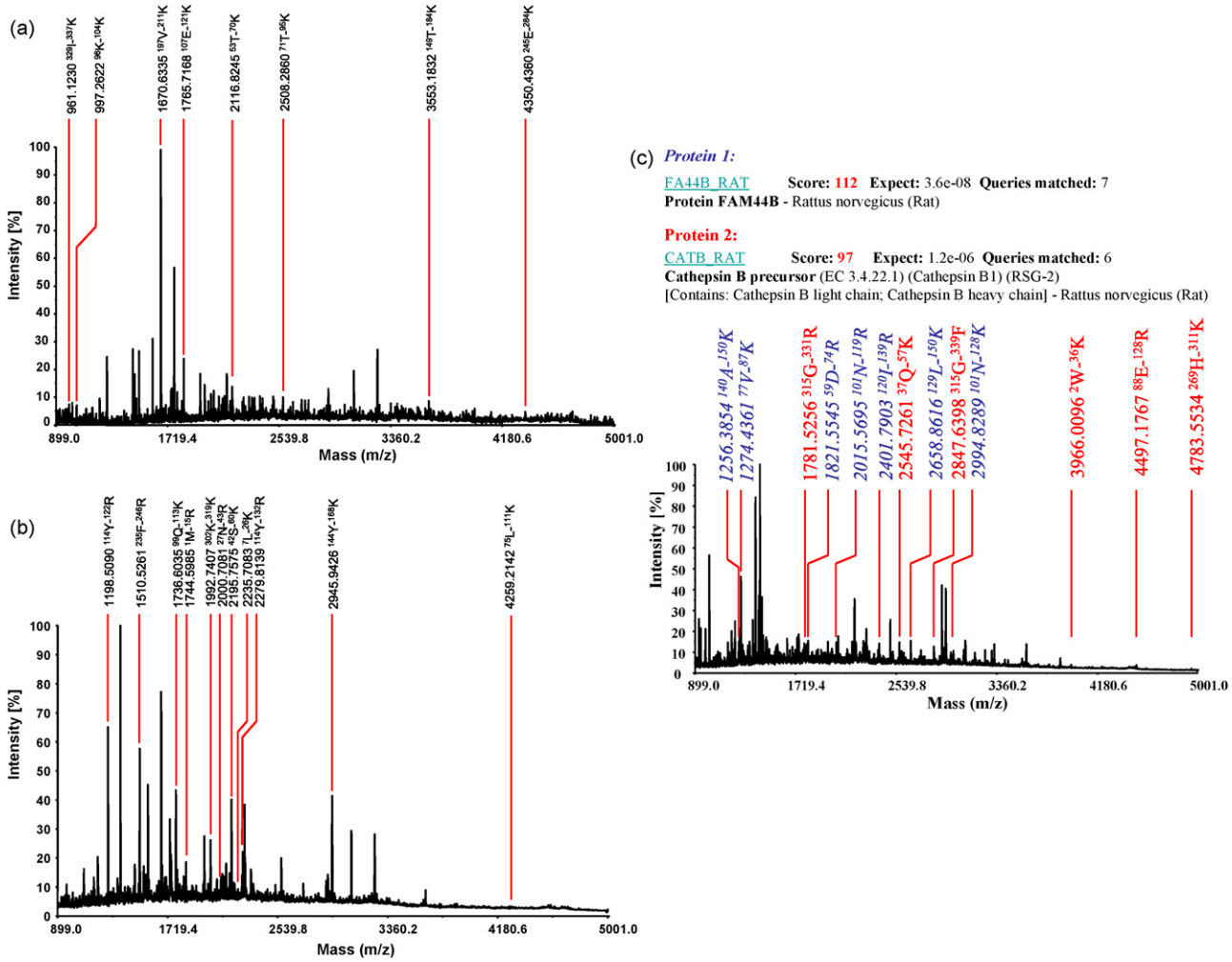

Fig. 3. (a) MALDI-TOF-MS spectra of protein band 4 of the rat kidney sample (see Fig. 1a, right side) showing the identified peptides of Trans-Golgi network integral membrane protein. (b) MALDI-TOF-MS spectra of protein band 5 of the rat kidney sample (see Fig. 1a, right side) showing the identified peptides of Serine/threonine-protein phosphatase PP1-gamma catalytic subunit. (c) MALDI-TOF-MS spectra of protein band 6 of the rat kidney sample (see Fig. 1a, right side) showing the identified peptides of two different proteins and the results from the database search using the Mascot database (www.matrixscience.com).

Table 3
Identified proteins after tryptic digestion and extraction from the gel bands of the BN-PAGE gel of rat liver water extract sample measured by MALDI-MS (see Fig. 2a, right)

Band	Identified protein	M.W. (kDa)
1	TP53RK-binding protein	17.6
2	Peroxisomal membrane protein 11A (Peroxin-11A)	27.9
3	Zinc finger protein SLUG (Neural crest transcription factor Slug) (Snail homolog 2)	29.9
4	Hemoglobin subunit beta-1	16.0
5	Regulator of G-protein signaling 4 (RGS4)	23.2
6	6-Phosphofructokinase, muscle type	85.6
7	Thyroid peroxidase precursor	101.5

and Serine/threonine-protein phosphatase PP1-gamma catalytic subunit with the identified peptides (www.matrixscience.com). In the gel band 6 of the rat kidney BN-PAGE gel two different proteins, protein FAM44B and cathepsin B precursor, were identified, as shown in Fig. 3c. In Fig. 3c, the results from the database search using the Mascot database (www.matrixscience.com) are shown and the identified peptides of the two peptides are indicated in the MALDI-TOF mass spectra. In the MALDI-TOF mass spectra there are still some peptides which are not contained in the two identified proteins. These fragments could come from another protein or could be peptides from the two identified proteins containing posttranslational modifications (PTM). Also in the other mass spectra there were unidentified peptide fragments, which could be from other proteins in the gel band and/or PTM's of the identified protein. Several other proteins from the rat kidney sample were identified, but no peptides containing metals could be found. From the BN-PAGE gel of the rat liver sample it was possible to identify some of the tryptic-digested proteins. For example, in the protein gel band 2 peroxisomal membrane protein 11A (Peroxin-11A) was identified with a molecular mass of 27.9 kDa and the protein in gel band 7 was identified as thyroid peroxidase precursor with a molecular mass of 101.5 kDa. In the Zinc finger protein SLUG found in gel band 3 from the rat liver sample (Fig. 2a) a quite high intensity of Zn could be measured (see Fig. 2b). This protein is known to contain Zn in small, independently folded domains that requires coordination of one or more zinc ions to stabilize its structure. In the database (http://www.ncbi.nlm.nih.gov) for the zinc finger protein SLUG several of these zinc finger regions are noted.

Not all the extracted and digested proteins from the two different samples could be identified. Also in the rat liver sample no metal-containing peptides could be found in the identified proteins. Not all of the identified proteins contained Zn, Cu or Fe.

In further studies, the other unidentified proteins, especially those containing metals, will be of interest and for better identification the proteins will be separated by 2D gel electrophoresis.

4. Conclusions

Blue native gel electrophoresis was successfully employed to separate protein complexes present in rat tissues (liver and kidney) in their native state. Essential and toxic metals (such as Zn, Cu, Fe, Cr, Cd and Pb) were detected in separated protein bands in a short analysis time using quadrupole LA-ICP-MS. The complementary data from MALDI-TOF-MS are particularly valuable for providing corresponding molecular information on proteins in the rat tissues investigated. The combination of MALDI-TOF-MS and LA-ICP-MS represents a powerful tool for studying metal-containing proteins in biological tissues. In the zinc finger protein SLUG from the rat liver sample identified by MALDI-TOF MS, Zn with a quite high intensity could be measured by LA-ICP-MS.

Acknowledgements

The authors would like to thank P. Krause (CETAC, Technologies, Omaha, NE, USA) for providing the LSX 213 laser ablation system with the large laser ablation chamber.

References

[1] D. Koppenaal, G. Hieftje, J. Anal. At. Spectrom. 22 (2007) 111.
[2] R. Lobinski, C. Moulin, R. Ortega, Biochimie 88 (2006) 1591.
[3] J. Szpunar, Analyst 103 (2005) 442.
[4] J.S. Becker, M. Zoriy, J.S. Becker, C. Pickhardt, E. Damoc, G. Juhacz, M. Palkovits, M. Przybylski, Anal. Chem. 77 (2005) 5851.
[5] J.S. Becker, M. Zoriy, J.S. Becker, C. Pickhardt, M. Przybylski, J. Anal. At. Spectrom. 19 (1) (2004) 149.
[6] J.S. Becker, S.F. Boulyga, J.S. Becker, C. Pickhardt, E. Damoc, M. Przybylski, Int. J. Mass Spectrom. 228 (2–3) (2003) 985.
[7] J.S. Becker, M. Zoriy, J.S. Becker, J. Dobrowolska, A. Matusch, J. Anal. At. Spectrom., 2007, published online (doi:10.1039/b701558e).
[8] J.S. Becker, M. Zoriy, C. Pickhardt, M. Przybylski, J.S. Becker, Int. J. Mass Spectrom. 242 (2–3) (2005) 135.
[9] J.S. Becker, M. Zoriy, M. Przybylski, J.S. Becker, Int. J. Mass Spectrom. 261 (2007) 68.
[10] A. Polatajko, M. Azzolini, I. Feldmann, T. Stuezel, N. Jakubowski, J. Anal. At. Spectrom., 2007, published online (doi:10.1039/b703245e).
[11] T.W.M. Fan, E.P. Shuttleworth, J. Anal. At. Spectrom. 17 (2002) 1621.
[12] A. Polatajko, N. Jakubowski, J. Szpunar, J. Anal. At. Spectrom. 21 (2006) 639.
[13] M. Dernovics, T. Garcia-Barrera, K. Bierla, H. Preud'homme, R. Lobinski, Analyst 132 (2007) 439.

Talanta 76 (2008) 965–977

Contents lists available at ScienceDirect

Talanta

journal homepage: www.elsevier.com/locate/talanta

Review

Response surface methodology (RSM) as a tool for optimization in analytical chemistry

Marcos Almeida Bezerra[a,b,*], Ricardo Erthal Santelli[a], Eliane Padua Oliveira[a], Leonardo Silveira Villar[a], Luciane Amélia Escaleira[a]

[a] Departamento de Geoquímica, Universidade Federal Fluminense, Outeiro São João Batista s/n, Centro, Niterói/RJ, 24020-150, Brazil
[b] Universidade Estadual do Sudoeste da Bahia, Laboratório de Química Analítica, Rua José Moreira Sobrinho s/n, Jequiezinho, Jequié/BA, 45206-190, Brazil

ARTICLE INFO

Article history:
Received 19 February 2008
Received in revised form 14 May 2008
Accepted 15 May 2008
Available online 21 May 2008

Keywords:
Response surface methodology
Three-level factorial design
Box–Behnken design
Central composite design
Doehlert design
Desirability function
Artificial neural network modeling

ABSTRACT

A review about the application of response surface methodology (RSM) in the optimization of analytical methods is presented. The theoretical principles of RSM and steps for its application are described to introduce readers to this multivariate statistical technique. Symmetrical experimental designs (three-level factorial, Box–Behnken, central composite, and Doehlert designs) are compared in terms of characteristics and efficiency. Furthermore, recent references of their uses in analytical chemistry are presented. Multiple response optimization applying desirability functions in RSM and the use of artificial neural networks for modeling are also discussed.

Contents

* Corresponding author at: Universidade Estadual do Sudoeste da Bahia, Laboratório de Química Analítica, Rua José Moreira Sobrinho s/n, Jequiezinho, Jequié/BA, 45206-190, Brazil.
E-mail address: mbezerra@uesb.br (M.A. Bezerra).

0039-9140/$ – see front matter © 2008 Published by Elsevier B.V.
doi:10.1016/j.talanta.2008.05.019

1. Introduction

Optimizing refers to improving the performance of a system, a process, or a product in order to obtain the maximum benefit from it. The term *optimization* has been commonly used in analytical chemistry as a means of discovering conditions at which to apply a procedure that produces the best possible response [1].

Traditionally, optimization in analytical chemistry has been carried out by monitoring the influence of one factor at a time on an experimental response. While only one parameter is changed, others are kept at a constant level. This optimization technique is called one-variable-at-a-time. Its major disadvantage is that it does not include the interactive effects among the variables studied. As a consequence, this technique does not depict the complete effects of the parameter on the response [2]. Another disadvantage of the one-factor optimization is the increase in the number of experiments necessary to conduct the research, which leads to an increase of time and expenses as well as an increase in the consumption of reagents and materials.

In order to overcome this problem, the optimization of analytical procedures has been carried out by using multivariate statistic techniques. Among the most relevant multivariate techniques used in analytical optimization is response surface methodology (RSM). Response surface methodology is a collection of mathematical and statistical techniques based on the fit of a polynomial equation to the experimental data, which must describe the behavior of a data set with the objective of making statistical previsions. It can be well applied when a response or a set of responses of interest are influenced by several variables. The objective is to simultaneously optimize the levels of these variables to attain the best system performance.

Before applying the RSM methodology, it is first necessary to choose an experimental design that will define which experiments should be carried out in the experimental region being studied. There are some experimental matrices for this purpose. Experimental designs for first-order models (e.g., factorial designs) can be used when the data set does not present curvature [3]. However, to approximate a response function to experimental data that cannot be described by linear functions, experimental designs for quadratic response surfaces should be used, such as three-level factorial, Box–Behnken, central composite, and Doehlert designs.

The present paper discusses the use of RSM for optimization in analytical chemistry. First, its basic principles are presented. Then, the approach to the applications of its more frequently used second-order experimental designs is broached, as well as the optimization of procedures that generate multiple responses.

2. Definition of some terms

Before beginning the discussion on the applications of response surface in the optimization of analytical methods, it is pertinent to introduce and define some key terms. Examples are also presented to illustrate each term.

Experimental domain is the experimental field that must be investigated. It is defined by the minimum and maximum limits of the experimental variables studied.
Experimental design is a specific set of experiments defined by a matrix composed by the different level combinations of the variables studied. Doehlert is an example of a second-order experimental design. This design defines a specific set of combinations for the levels of variables that must be applied experimentally to obtain the responses.
Factors or independent variables are experimental variables that can be changed independently of each other. Typical independent variables comprise the pH, temperature, reagents concentration, microwave irradiation time, flow rate, atomization temperature, and elution strength, among others.
Levels of a variable are different values of a variable at which the experiments must be carried out. The variable pH, for example, can be investigated at five levels: 4, 5, 6, 7 and 8 in the optimization of a spectrophotometric method.
Responses or dependent variables are the measured values of the results from experiments. Typical responses are the analytical signal (absorbance, net emission intensity, and electrical signal), recovery of an analyte, resolution among chromatographic peaks, percentage of residual carbon, and final acidity, among others.
Residual is the difference between the calculated and experimental result for a determinate set of conditions. A good mathematical model fitted to experimental data must present low residuals values.

3. Theory and steps for RSM application

Response surface methodology was developed by Box and collaborators in the 50s [4,10]. This term was originated from the graphical perspective generated after fitness of the mathematical model, and its use has been widely adopted in texts on chemometrics. RSM consists of a group of mathematical and statistical techniques that are based on the fit of empirical models to the experimental data obtained in relation to experimental design. Toward this objective, linear or square polynomial functions are employed to describe the system studied and, consequently, to explore (modeling and displacing) experimental conditions until its optimization [5].

Some stages in the application of RSM as an optimization technique are as follows: (1) the selection of independent variables of major effects on the system through screening studies and the delimitation of the experimental region, according to the objective of the study and the experience of the researcher; (2) the choice of the experimental design and carrying out the experiments according to the selected experimental matrix; (3) the mathematic–statistical treatment of the obtained experimental data through the fit of a polynomial function; (4) the evaluation of the model's fitness; (5) the verification of the necessity and possibility of performing a displacement in direction to the optimal region; and (6) obtaining the optimum values for each studied variable.

3.1. Screening of variables

Numerous variables may affect the response of the system studied, and it is practically impossible to identify and control the small contributions from each one. Therefore, it is necessary to select those variables with major effects. Screening designs should be carried out to determine which of the several experimental variables and their interactions present more significant effects. Full or fractional two-level factorial designs may be used for this objective principally because they are efficient and economical [2].

3.2. Choice of the experimental design

The simplest model which can be used in RSM is based on a linear function. For its application, it is necessary that the responses obtained are well fitted to the following equation:

$$y = \beta_0 \sum_{i=1}^{k} \beta_i x_i + \varepsilon, \quad (1)$$

where k is the number of variables, β_0 is the constant term, β_i represents the coefficients of the linear parameters, x_i represents the variables, and ε is the residual associated to the experiments.

Therefore, the responses should not present any curvature. To evaluate curvature, a second-order model must be used. Two-level factorial designs are used in the estimation of first-order effects, but they fail when additional effects, such as second-order effects, are significant. So, a central point in two-level factorial designs can be used for evaluating curvature. The next level of the polynomial model should contain additional terms, which describe the interaction between the different experimental variables. This way, a model for a second-order interaction presents the following terms:

$$y = \beta_0 + \sum_{i=1}^{k} \beta_i x_i + \sum_{1 \le i \le j}^{k} \beta_{ij} x_i x_j + \varepsilon \quad (2)$$

where β_{ij} represents the coefficients of the interaction parameters.

In order to determine a critical point (maximum, minimum, or saddle), it is necessary for the polynomial function to contain quadratic terms according to the equation presented below:

$$y = \beta_0 + \sum_{i=1}^{k} \beta_i x_i + \sum_{i=1}^{k} \beta_{ii} x_i^2 + \sum_{1 \le i \le j}^{k} \beta_{ij} x_i x_j + \varepsilon \quad (3)$$

where β_{ii} represents the coefficients of the quadratic parameter.

To estimate the parameters in Eq. (3), the experimental design has to assure that all studied variables are carried out at in at least three factor levels. Thus, two modeling, symmetrical response surface designs are available. Among the more known second-order symmetrical designs are the three-level factorial design, Box–Behnken design, central composite design, and Doehlert design. These symmetrical designs differ from one another with respect to their selection of experimental points, number of levels for variables, and number of runs and blocks. These experimental matrices are presented and discussed in Section 4.

3.2.1. Codification of the levels of the variable

Codification of the levels of the variable consists of transforming each studied real value into coordinates inside a scale with dimensionless values, which must be proportional at its localization in the experimental space. Codification is of concern because it enables the investigation of variables of different orders of magnitude without the greater influencing the evaluation of the lesser.

The following equation can be applied to transform a real value (z_i) into a coded value (x_i) according to a determinate experimental design:

$$x_i = \left(\frac{z_i - z_i^0}{\Delta z_i} \right) \beta_d \quad (4)$$

where Δz_i is the distance between the real value in the central point and the real value in the superior or inferior level of a variable, β_d is the major coded limit value in the matrix for each variable, and z^0 is the real value in the central point.

3.3. Mathematical–statistical treatment of data

After acquiring data related to each experimental point of a chosen design, it is necessary to fit a mathematical equation to describe the behavior of the response according to the levels of values studied. In other words, there must be estimates of the b parameters of Eqs. (1)–(3). Therefore, in matrix notation, Eqs. (1)–(3) can be represented as

$$y_{mX_i} = X_{mX_n} b_{nX_1} + e_{mX_1}, \quad (5)$$

where y is the response vector, X is the matrix of the chosen experimental design, b is the vector constituted by the parameters of the model, e is the residual, and m and n represent the numbers of lines and columns from the matrices, respectively.

Eq. (5) is solved by using a statistical approach called the method of least square (MLS) [6]. MLS is a multiple regression technique used to fit a mathematical model to a set of experimental data generating the lowest residual possible. After mathematical transformations of Eq. (5), a vector b containing the parameters can be obtained by the following equation:

$$b_{n\cdot 1} = (X_{n\cdot m}^T X_{m\cdot n})^{-1} (X_{n\cdot m}^T y_{m\cdot i}) \quad (6)$$

Eq. (6) is used in the construction of the response surface that describes the behavior of the response in the experimental domain. The great advantage of Eq. (6) is the low computational cost necessary to determine the b coefficients.

In the LSM, it is assumed that errors present a random distribution profile with a zero mean and a common unknown variance and that these errors are independent of each other. In this way, the variance estimate to each component of vector b is commonly obtained by authentic repetitions of the central point according to Eq. (7):

$$\hat{V}(b)_{n\cdot n} = (X_{n\cdot m}^T X_{m\cdot n})^{-1} s^2 \quad (7)$$

Thus, extracting the square root for each component of $\hat{V}(b)$ leads to obtaining the standard errors for the b coefficients that compose the equation of the response surface, allowing the evaluation of its significance.

3.4. Evaluation of the fitted model

The mathematical model found after fitting the function to the data can sometimes not satisfactorily describe the experimental domain studied. The more reliable way to evaluate the quality of the model fitted is by the application of analysis of variance (ANOVA). The central idea of ANOVA is to compare the variation due to the treatment (change in the combination of variable levels) with the variation due to random errors inherent to the measurements of the generated responses [7]. From this comparison, it is possible to evaluate the significance of the regression used to foresee responses considering the sources of experimental variance.

In ANOVA, the evaluation of data set variation is made by studying its dispersion. The evaluation of the deviation (d_i) that each observation (y_i) or its replicates (y_{ij}) present in relation to the media ($\bar{y}$), or, more precisely, the square of this deviation, is presented in Eq. (8):

$$d_i^2 = (y_{ij} - \bar{y})^2 \quad (8)$$

The sum of the square for all observation deviations in relation to the media is called the total sum of the square (SS_{tot}); it can be dismembered in the sum of the square due to the fitted mathematical model, that is, due to regression (SS_{reg}), and in the sum of the square due to residuals generated by the model (SS_{res}), as shown below:

$$SS_{tot} = SS_{reg} + SS_{res} \quad (9)$$

As replicates of the central point are made, it is possible to estimate the pure error associated with repetitions. Thus, the sum of the square for residuals can be dismembered into two more parcels: the sum of the square due to pure error (SS_{pe}) and the sum of the square due the lack of fit (SS_{lof}), as shown below:

$$SS_{res} = SS_{pe} + SS_{lof} \quad (10)$$

When the division of the sum of the square for each source of variation (total, regression, residual, lack of fit, and pure error) is made by its respective numbers of degrees of freedom (d.f.), the

Table 1
Analysis of variance for fitted mathematical model to an experimental data set using multiple regression

Variation source	Sum of the square	Degree of freedom	Media of the square
Regression	$SS_{reg} = \sum_i^m \sum_j^{n_1} (\hat{y}_i - \bar{y})^2$	$p-1$	$MS_{reg} = \frac{SS_{reg}}{p-1}$
Residuals	$SS_{res} = \sum_i^m \sum_j^{n_1} (y_{ij} - \hat{y}_i)^2$	$n-p$	$MS_{reg} = \frac{SS_{res}}{n-p}$
Lack of fit	$SS_{lof} = \sum_i^m \sum_j^{n_1} (\hat{y}_i - \bar{y}_i)^2$	$m-p$	$MS_{lof} = \frac{SQ_{lof}}{m-p}$
Pure error	$SS_{pe} = \sum_i^m \sum_j^{n_i} (y_{ij} - \bar{y}_i)^2$	$n-m$	$MS_{pe} = \frac{SS_{pe}}{n-m}$
Total	$SS_{tot} = \sum_i^m \sum_j^{n_i} (y_{ij} - \bar{y})^2$	$n-1$	

n_i, number of observations; m, total number of levels in the design; p, number of parameter of model; $\hat{y}_i$, estimated value by the model for the level i; $\bar{y}$, overall media; y_{ij}, replicates performed in each individual levels; $\bar{y}_i$, media of replicates performed in the same set of experimental conditions.

"media of the square" (MS) are obtained. The numbers of degree of freedom for these sources of variation are calculated by the expressions presented in the third column of Table 1, where p represents the number of coefficients of the mathematical model, n represents the number of total observations, and m represents the numbers of levels used in the investigation. Equations related to the source of variations for the calculation of SSs and MSs are also presented in Table 1 [5,10].

The *significance of regression* can be evaluated by the ratio between the media of the square of regression (MS_{reg}) and the media of the square of residuals (MS_{res}) and by comparing these variation sources using the Fisher distribution (F test), taking into account its respective degrees of freedom associated to regression (ν_{reg}) and to residual (ν_{res}) variances:

$$\frac{MS_{reg}}{MS_{res}} \approx F_{\nu_{reg},\nu_{res}} \tag{11}$$

Thus, a statistically significant value for this ratio must be higher than the tabulated value for F. This is an indication that the mathematical model is well fitted to the experimental data.

Another way to evaluate the model is the *lack of fit test*. If the mathematical model is well fitted to the experimental data, MS_{lof} should reflect only the random errors inherent to the system. Additionally, MS_{pe} is also an estimate of these random errors, and it is assumed that these two values are not statistically different. This is the key idea of the lack of fit test. It is possible to use the F distribution to evaluate if there is some statistical difference between these two media, in the same way that the significance of regression was verified:

$$\frac{MS_{lof}}{MS_{pe}} \approx F_{\nu_{lof},\nu_{pe}} \tag{12}$$

where, ν_{lof} and ν_{pe} are, respectively, the degree of freedom associated with the lack of fit and the pure error variances. If this ratio is higher than the tabulated value of F, it is concluded that there is evidence of a lack of fit and that the model needs to be improved. However, if the value is lower than the tabulated value, the model fitness can be considered satisfactory. To apply a lack of fit test, the experimental design must be performed with authentic repetitions at least in its central point.

In short, a model will be well fitted to the experimental data if it presents a significant regression and a non-significant lack of fit. In other words, the major part of variation observation must be described by the equation of regression, and the remainder of the variation will certainly be due to the residuals. Most variation related to residuals is due to pure error (random fluctuation of measurements) and not to the lack of fit, which is directly related to the model quality [8,9].

The visual inspection of the residual graphs can also generate valuable information about the model suitability. Thus, if the mathematical model is well fitted, its graph of residuals presents a behavior that suggests a normal distribution. If the model generates larger residuals, it is not adequate to make precise inferences about the data behavior in the studied experimental area. Moreover, if the model needs some other term, the residual graph will present a behavior that indicates the kind of term that must be added to the model [10].

3.5. Determination of the optimal conditions

The surfaces generated by linear models can be used to indicate the direction in which the original design must be displaced in order to attain the optimal conditions. However, if the experimental region cannot be displaced due to physical or instrumental reasons, the research must find the best operational condition inside the studied experimental condition by visual inspection.

For quadratic models, the critical point can be characterized as maximum, minimum, or saddle. It is possible to calculate the coordinates of the critical point through the first derivate of the mathematical function, which describes the response surface and equates it to zero. The quadratic function obtained for two variables as described below is used to illustrate the example:

$$y = b_0 + b_1x_1 + b_2x_2 + b_{11}x_1^2 + b_{22}x_2^2 + b_{12}x_1x_2 \tag{13}$$

$$\frac{\partial y}{\partial x_1} = b_1 + 2b_{11}x_1 + b_{12}x_2 = 0 \tag{14}$$

$$\frac{\partial y}{\partial x_2} = b_2 + 2b_{22}x_2 + b_{12}x_1 = 0 \tag{15}$$

Thus, to calculate the coordinate of the critical point, it is necessary to solve the first grade system formed by Eqs. (14) and (15) and to find the x_1 and x_2 values.

The visualization of the predicted model equation can be obtained by the surface response plot. This graphical representation is an n-dimensional surface in the $(n+1)$-dimensional space. Usually, a two-dimensional representation of a three-dimensional plot can be drawn. Thus, if there are three or more variables, the plot visualization is possible only if one or more variables are set to a constant value. Fig. 1 illustrates some profile for the quadratic response surface plot in the optimization of two variables. Fig. 1(a and b) represents surfaces where the maximum point is located inside the experimental region. It is interesting to note that, in surface shown in Fig. 1(b), there is a plateau in relation to variable x_2, indicating that variation of its levels does not affect the studied system. Surface shown in Fig. 1(c) shows that the maximum point is outside the experimental region and that it is necessary to displace, if possible, the initial design to attain it. The surface shown in Fig. 1(d) presents a minimum point, and that shown in Fig. 1(e) presents a saddle point as the critical point. The saddle point is an inflexion point between a relative maximum and a relative minimum. If the purpose is to obtain a maximum or minimum response to a studied system, the saddle point coordinates do not serve as optimal values. Again, it is possible to find the optimum region through visual inspection of the surfaces.

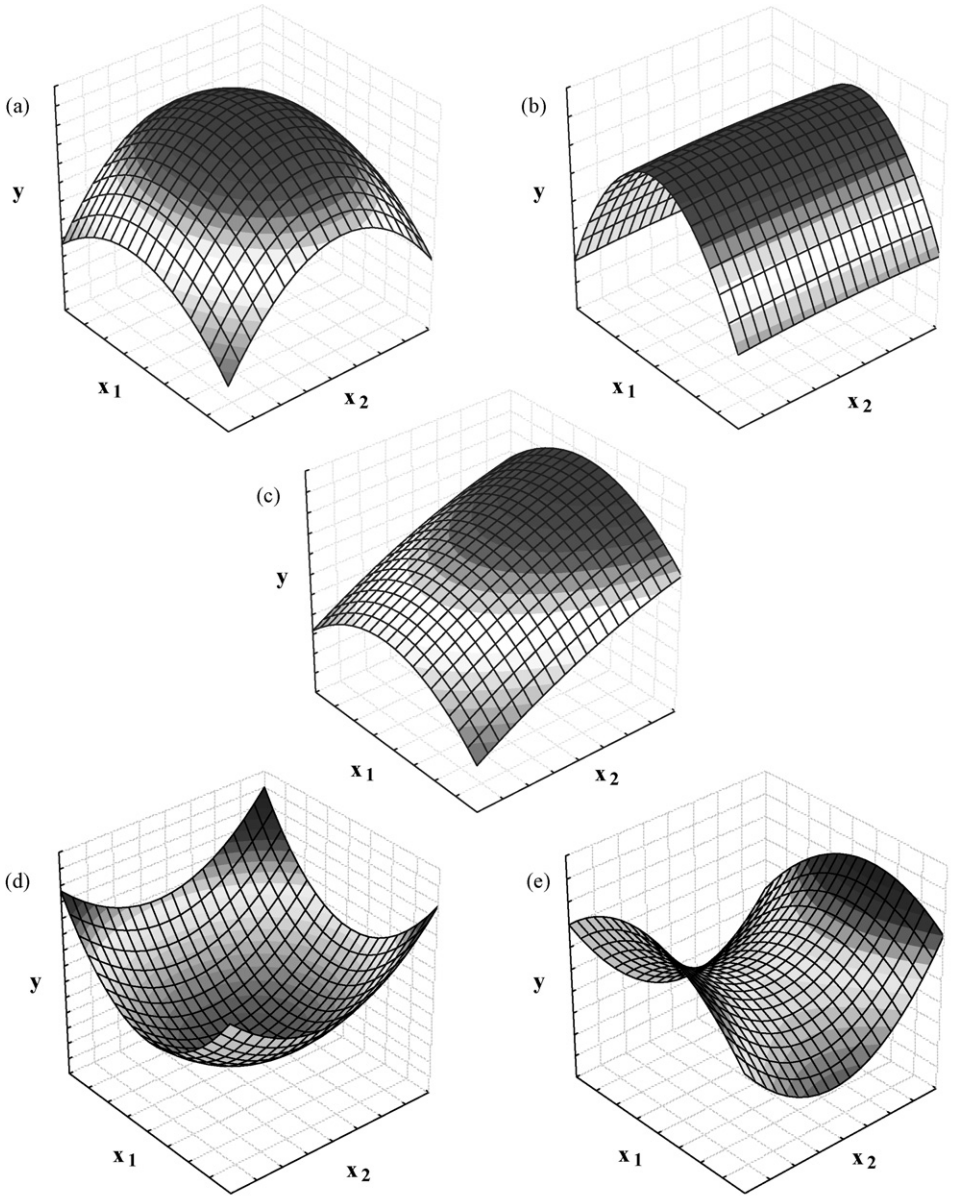

Fig. 1. Some profiles of surface response generated from a quadratic model in the optimization of two variables. (a) maximum, (b) plateau, (c) maximum outside the experimental region, (d) minimum, and (e) saddle surfaces.

4. Symmetrical second-order experimental designs and their applications in analytical chemistry

4.1. Full three-level factorial designs

Full three-level factorial design is an experimental matrix that has limited application in RSM when the factor number is higher than 2 because the number of experiments required for this design (calculated by expression $N = 3^k$, where N is experiment number and k is factor number) is very large, thereby losing its efficiency in the modeling of quadratic functions. Because a complete three-level factorial design for more than two variables requires more experimental runs than can usually be accommodated in practice, designs that present a smaller number of experimental points, such as the Box–Behnken, central composite, and Doehlert designs, are more often used [11]. However, for two variables, the efficiency is comparable with designs such as central composite [12].

Fig. 2(a and b) shows the representation of the three-level factorial designs for the optimization of two and three variables, respectively. Table 2(a) shows the experimental matrix for the optimization of two variables using this design.

The majority of applications of three-level factorial designs are in the area of chromatography. Table 3 shows some works in which this experimental design was used.

4.2. Box–Behnken designs

Box and Behnken [13] suggested how to select points from the three-level factorial arrangement, which allows the efficient estimation of the first- and second-order coefficients of the mathematical model. These designs are, in this way, more efficient and economical then their corresponding 3^k designs, mainly for a large number of variables.

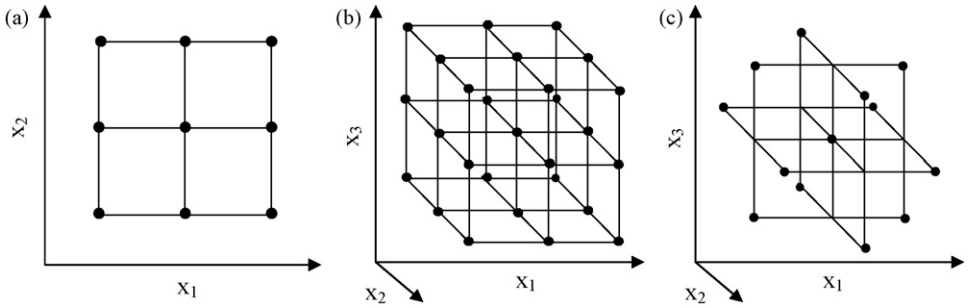

Fig. 2. Experimental designs based on the study of all variables in three levels: three-level factorial design for the optimization of (a) two variables and (b) three variables and (c) Box–Behnken design for the optimization of three variables.

Table 2
Some experimental matrices for designs based on variables study in three levels: (a) three-level factorial design for two variables and (b) Box–Behnken design for three variables matrices

(a)		(b)		
x_1	x_2	x_1	x_2	x_3
−1	−1	−1	−1	0
−1	0	1	−1	0
−1	1	−1	1	0
0	−1	1	1	0
0	0	−1	0	−1
0	1	1	0	−1
1	−1	−1	0	1
1	0	1	0	1
1	1	0	−1	−1
		0	1	−1
		0	−1	1
		0	1	1
		0	0	0

In Box–Behnken designs [14,15], the experimental points are located on a hypersphere equidistant from the central point, as exemplified for a three-factor design in Fig. 2(c). Its principal characteristics are:

(1) requires an experiment number according to $N = 2k(k-1) + c_p$, where k is the number of factors and (c_p) is the number of the central points;
(2) all factor levels have to be adjusted only at three levels (−1, 0, +1) with equally spaced intervals between these levels.

Fig. 2(c) presents the Box–Behnken design for three-variable optimization with its 13 experimental points. In comparison with the original 3^3 design with 27 experiments (Fig. 2(b)), it is noted that this design is more economical and efficient. Table 2(b) presents the coded values to the application of this design for three variables.

This experimental design has been applied for the optimization of several chemical and physical processes; however, its application in analytical chemistry is still much smaller in comparison with central composite design. Table 4 shows some applications of the Box–Behnken design in analytical chemistry.

4.3. Central composite design

The central composite design was presented by Box and Wilson [16]. This design consists of the following parts: (1) a full factorial or fractional factorial design; (2) an additional design, often a star design in which experimental points are at a distance α from its center; and (3) a central point. Fig. 3(a and b) illustrates the full central composite design for optimization of two and three variables.

Full uniformly routable central composite designs present the following characteristics:

(1) require an experiment number according to $N = k^2 + 2k + c_p$, where k is the factor number and (c_p) is the replicate number of the central point;
(2) α-values depend on the number of variables and can be calculated by $\alpha = 2^{(k-p)/4}$. For two, three, and four variables, they are, respectively, 1.41, 1.68, and 2.00;
(3) all factors are studied in five levels ($-\alpha$, −1, 0, +1, $+\alpha$).

Table 3
Some applications of three-level factorial design in analytical chemistry

Analytes	Samples	Analytical technique	Objective of study	Ref.
Caffeine, theobromine and theophylline	Coffee, tea and human urine	Reversed-phase HPLC	Improving the chromatographic resolution among these three substances	[24]
Niacin	Fresh and dry-cured pork products	Ion chromatography	Optimizing the mobile phase composition	[25]
Anionic, cationic, and neutral drugs	Pharmaceutical formulations	Electrokinetic chromatography	Stabilising the effects of the sodium dodecyl sulfate and 2-propanol concentration in the separation of these analytes	[26]
Clothiapine, clozapine, olanzapine, and quetiapine	Pharmaceutical formulations	Capillary zone electrophoresis	Development of a method for separation of these four atypical antipsychotics	[27]
Sulfonamides	Foodstuffs	HPLC	Developing a molecularly imprinted polymer for separation of the analytes	[28]
Candesartan, eprosartan, irbesartan, losartan potassium, telmisartan, and valsartan	Pharmaceutical formulations	Capillary zone electrophoresis	Optimizing the separation of these angiotensin-II-receptor antagonists	[29]
Underivatized phenol and cresols	Soil samples with a high content of carbon	GC	Optimizing the supercritical fluid extraction of these analytes	[30]
Copper	Petroleum condensate	GF AAS	Developing a method for the direct determination of analyte using detergentless microemulsions	[31]

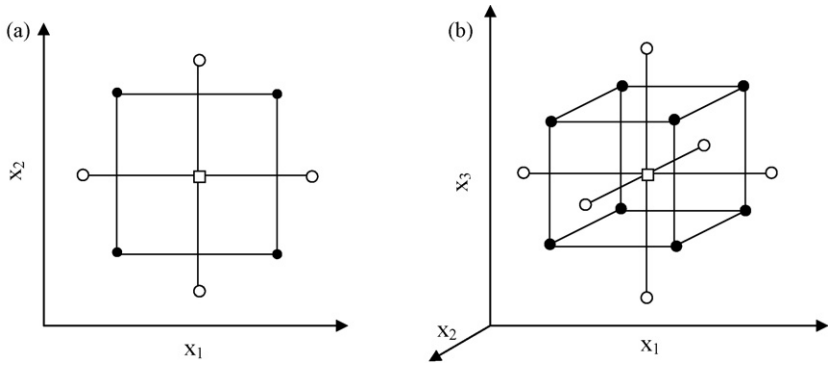

Fig. 3. Central composite designs for the optimization of: (a) two variables ($\alpha = 1.41$) and (b) three variables ($\alpha = 1.68$). (●) Points of factorial design, (○) axial points and (□) central point.

Fig. 3(a and b) shows representations of central composite designs for two- and three-variable optimization, respectively. Table 5(a and b) presents the coded values of the experimental matrices for the application of these designs.

Many applications of the central composite design in the optimization of analytical procedures can be found in the literature. Table 6 shows a limited number of applications as recent examples of the utilization of this design in some areas of analytical chemistry.

4.4. Doehlert design

Developed by Doehlert [17], the design is a practical and economical alternative in relation to other second-order experimental

Table 4
Some applications of Box–Behnken design in analytical chemistry

Analytes	Samples	Analytical technique	Objective of the study	Ref.
Aliphatic aldehydes	Potato crisps	HPLC	Establishing the optimum conditions for the derivatization reaction of the analytes with 2,4-dinitrophenylhydrazine	[32]
Alprenolol, oxprenolol, promethazine and propranolol	Human serum albumin	Affinity electrokinetic chromatography	Optimization of the chiral separation of these four drugs	[33]
Cadmium	Drinking water	FAAS	Optimizing an on-line pre-concentration system using knotted reactor	[34]
Organochlorine pesticides	Sediments	GC	Optimizing a microwave-assisted extraction method for the extraction of persistent pesticides	[35]
Neuropeptides	Biological	Capillary zone electrophoresis	Optimizing the main electrophoretic parameters involved in the analytes separation	[36]
Lead	Waters	ICP OES	Optimizing a flow injection system for the on-line pre-concentration of these metal using silica gel functionalized with methylthiosalicylate	[37]
Atenolol, sotalol, betaxolol, and metoprolol	Non-aqueous	Capillary electrophoresis	Optimizing the separation of these four beta-blocking drug substances	[38]
Captopril	Tablets of pharmaceuticals	HPLC	Optimizing the chromatographic determination of this analyte	[39]
Sulphonamides, dihydrofolate reductase inhibitors and beta-lactam antibiotics	Food products	Capillary electrophoresis	Optimizing the simultaneous separation of these substances	[40]

Table 5
Experimental matrices for central composite designs: (a) two variables and (b) three variables

(a)			(b)			
	x_1	x_2		x_1	x_2	x_3
Factorial design	−1	−1	Factorial design	−1	−1	−1
	1	−1		1	−1	−1
	−1	1		−1	1	−1
	1	1		1	1	−1
Axial points	$-\alpha$	0		−1	−1	1
	α	0		1	−1	1
	0	$-\alpha$		−1	1	1
	0	α		1	1	1
Central point	0	0	Axial points	$-\alpha$	0	0
				α	0	0
				0	$-\alpha$	0
				0	α	0
				0	0	$-\alpha$
				0	0	α
			Central point	0	0	0

Table 6
Some applications of central composite design in analytical chemistry

Analytes	Samples	Analytical technique	Objective of the study	Ref.
Chlorobenzenes	Environmental water	HPLC	Developing a headspace single-drop micro-extraction procedure using room temperature ionic liquid for determination of trace amounts of these substances	[41]
Human immunoglobulin G	Artificial mixture of proteins	Affinity HPLC	Optimizing the purification of these proteins from a mixture	[42]
Organochlorine pesticides and polychlorinated biphenyls	Human serum	GC	Developing a procedure for the determination of these substances using headspace solid-phase micro-extraction	[43]
Tetracycline, chlortetracycline, oxytetracycline and doxycycline	Pharmaceuticals	Capillary zone electrophoresis	Investigating the influence of the electrolyte composition, pH and concentration, as well as temperature and applied voltage in the separation of the analytes	[44]
Volatile compounds	Vinegar	GC	Optimizing the extraction and desorption analytical conditions of a stir bar sorptive extraction for these analytes	[45]
Polybrominated diphenyl ethers, polybrominated biphenyls and polychlorinated naphthalenes	Sediment samples	GC–MS	Optimization of the experimental conditions for a method involving microwave-assisted extraction and large-volume injection	[46]
Amlodipine, nitrendipine, felodipine, lacidipine and lercanidipine	Human plasma	HPLC	Developing a liquid–liquid extraction method using diethyl ether as organic solvent for determination of five 1,4-dihydropyridines	[47]
Nickel	Petroleum	GF AAS	Developing a procedure for the direct determination of Ni using a solid sampling strategy	[48]
Aluminum	Juices and soft drink	GF AAS	Developing a preparation method based on ultrasound-assisted pseudo-digestion	[49]
Mercury	Gasoline	CV AAS	Optimizing a method for direct aqueous $NaBH_4$ reduction of metal in microemulsion medium	[43]
As, Cd, Cu, Fe, Mg, Pb and Zn	Mussel tissues	ICP OES	Evaluation of different variables affecting the enzymatic hydrolysis of samples by five enzymes	[50]
Hydroximethylfurfural	Honey	Amperometry	Development of microbiosensors built by photolithographic techniques and based on a Pt microelectrode chip	[51]

matrices. This design describes a circular domain for two variables, spherical for three variables, and hyperspherical for more than three variables, which accents the uniformity of the studied variables in the experimental domain. Although its matrices are not routable as previous designs, it presents some advantages, such as requiring few experimental points for its application and high efficiency. Other characteristics are presented below:

(1) requires an experiment number according to $N = k^2 + k + c_p$, where k is the factor number and (c_p) is the replicate number of the central point;
(2) each variable is studied at a different number of levels, a particularly important characteristic when some variables are subject to restrictions such as cost and/or instrumental constraints or when it is interesting to study a variable at a major or minor number of levels;
(3) the intervals between its levels present a uniform distribution;
(4) displacement of the experimental matrix to another experimental region can be achieved using previous adjacent points.

For two variables, the Doehlert design is represented by a central point surrounded by six points from a regular hexagon (Fig. 4). Fig. 4 also shows some possibilities of displacement of the original experimental conditions. For three variables, this design is represented by a geometrical solid called a cuboctahedron [18], and, depending on how this solid is projected in the plane, it can generate some different experimental matrices (Fig. 5). Table 7(a) shows the experimental matrix for two variables, and Table 7(b and c) shows two experimental matrices for three-variable optimization generated by different plane projections of the cuboctahedron.

Applications of the Doehlert design in analytical chemistry are increasing in recent years, mainly because of its advantageous characteristics in relation to other designs. Some examples are shown in Table 8 to illustrate its field of application.

5. Multiple responses optimization in analytical chemistry by using RSM

It is relatively simple to find the optimal conditions for a single response using surface response designs. However, the researcher may be interested in optimizing several responses simultaneously. The simplest strategy to adopt in this case is visual inspection. If the amount of significant factors allows the graphical visualization of adjusted models, and if the numbers of response are

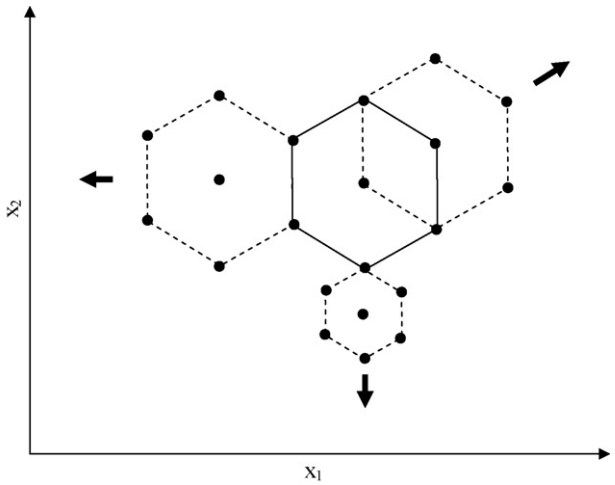

Fig. 4. Doelhert design for the optimization of two variables and some possibilities for the displacement of the initial design using previous points.

Table 7
Doehlert matrices (a) for two variables, (b) three variables for the plane projection "a" of Fig. 5 and (c) three variables for the plane projection "b" of Fig. 5

(a)		(b)			(c)		
x_1	x_2	x_1	x_2	x_3	x_1	x_2	x_3
0	0	0	0	0	0	0	0
1	0	0	−1	0	1	0	0
0.5	0.866	1	0	0	0.5	0.866	0
−1	0	0	1	0	0.5	0.289	0.817
−0.5	−0.866	−1	0	0	−1	0	0
0.5	−0.866	−0.5	−0.5	0.707	−0.5	−0.866	0
−0.5	0.866	0.5	−0.5	0.707	−0.5	−0.289	−0.817
		0.5	0.5	0.707	0.5	−0.866	0
		−0.5	0.5	0.707	0.5	−0.289	−0.817
		−0.5	−0.5	−0.707	−0.5	0.866	0
		0.5	−0.5	−0.707	0	0.577	−0.817
		0.5	0.5	−0.707	−0.5	0.289	0.817
		−0.5	0.5	−0.707	0	−0.577	0.817

not very large, the surfaces can be overlapped to enable finding the experimental region that can satisfy all the responses studied [19,10].

If the optimal values for each response are localized in different regions, it will be more difficult to find the conditions that simultaneously satisfy all responses. The level of difficulty increases as these optimum regions become more distant from each other and do not intersect. It is not rare to encounter cases where all surfaces found do not present its optimum under the same set of experimental conditions. Thus, changes in the level of a factor can improve one specific response and have a very negative effect on another.

An approach for solving the problem of the optimization of several responses is the use of a multicriteria methodology. This methodology is applied when various responses have to be considered at the same time and it is necessary to find optimal compromises between the total numbers of responses taken into account. The Derringer function or desirability function [20] is the most important and most currently used multicriteria methodology in the optimization of analytical procedures. This methodology is initially based on constructing a desirability function for each

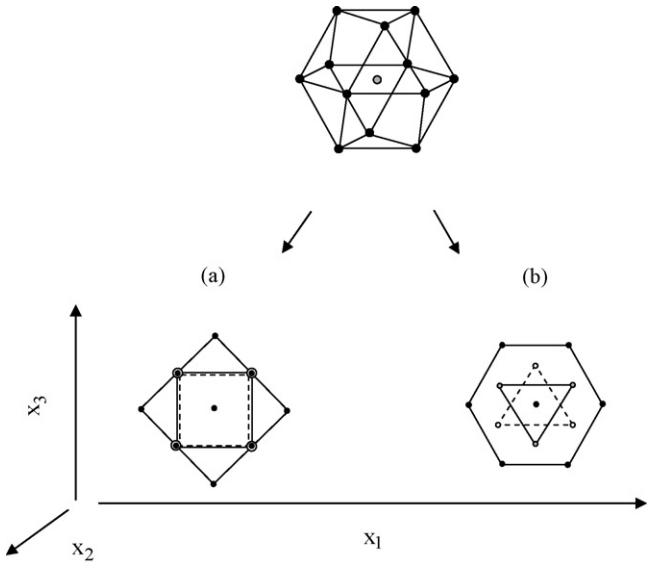

Fig. 5. Doehlert designs for the optimization of three variables originated by the two-plane projection of the cuboctahedron geometric solid.

individual response. In summary, the measured properties related to each response are transformed into a dimensionless individual desirability (d_i) scale. Through the individual functions, the analyst introduces the specifications that each response must fulfill in the measuring procedure. The scale of the individual desirability function ranges between $d = 0$, for a completely undesirable response, and $d = 1$, for a fully desired response, above which further improvements would have no importance. This transformation makes it possible to combine the results obtained for properties measured on different orders of magnitude.

With the individual desirabilities, it is then possible to obtain the overall desirability (D). The overall desirability function D is defined as the weighted geometric average of the individual desirability (d_i)

Table 8
Some applications of Doehlert design in analytical chemistry

Analytes	Samples	Analytical technique	Objective of the study	Ref.
Cd, Cr, Cu, Mn, Ni and Pb	Saline oil-refinery effluents and vegetables	ICP OES	Optimizing the cloud point extraction of these metals	[52]
Cd	Drinking water	F AAS	Optimizing a pre-concentration system that use a mini-column of polyurethane foam loaded with 4-(2-pyridylazo)-resorcinol	[53]
Uranium	Natural waters	Molecular absorption spectrometry	Developing a pre-concentration procedure using cloud point extraction	[54]
Fe, Zn and Mn	Food	F AAS	Optimizing a procedure for the food samples digestion employing a focused microwave system	[55]
Si	Naphta	GF AAS	Developing a method for direct determination of the analyte	[56]
Mn	Biological	FI ICP OES	Developing a procedure for pre-concentration of analyte using a column packed with silica gel functionalized	[57]
Catechol	Waters	Voltammetry	Optimizing variables associate to the performance of the solid-phase extraction procedure based on molecular imprinting technology	[58]
Quinolinic acid	Human plasma	Differential pulse polarography	Developing of a procedure for determining this analyte after solid-phase extraction	[59]
Chloroanisoles	Wine	GC	Optimizing the headspace solid-phase micro-extraction	[60]
Cholesterol	Milk fat, frozen diet and egg powder	GC	Modeling of the relationship analyte/internal standard to determine cholesterol	[61]
Sugars	Food	HPLC	Investigating the derived sugars with *p*-nitroaniline using microwave irradiation in a pre-column	[62]
Herbicide oxidiazin	Water and soil	GC–MS	Optimizing the chromatographic conditions to determine oxidiazin residues	[63]
Organochlorine pesticides	Water	GC	Optimizing the solid-phase micro-extraction conditions of polyacrylate-coated fiber	[64]
Tropane alkaloids	Belladonna extract	Micellar electrokinetic capillary chromatography	Optimizing the analysis of selected tropane alkaloids	[65]

according the following equation:

$$D = \sqrt[m]{d_1 d_2 \dots d_m} \tag{16}$$

where m is number of responses studied in the optimization process. Thus, the simultaneous optimization process is reduced to find the levels of factors that demonstrate the maximum overall desirability.

There are several types of transformations possible for obtaining individual desirability. Thus, if the target value (T) for the response y is a maximum, the individual desirability (d) is described by the following equation:

$$d = \begin{cases} 0 \text{ if } y < 1 \\ \left(\dfrac{y-L}{T-L}\right)^s \text{ if } L \le y \le T \\ 1 \text{ if } y > T \end{cases} \tag{17}$$

where L is the lower acceptable value to the response and s is the weight. Thus, when $s = 1$, the desirability function is linear. When $s > 1$ is chosen, a major importance is given to the points near the target value. When $s < 1$ is chosen, this last demand is of low importance.

However, if the target value for the response y is a minimum, the individual desirability (d) is given by:

$$d = \begin{cases} 1 \text{ if } T < y \\ \left(\dfrac{U-y}{U-y}\right)^t \text{ if } T \le y \le U \\ 0 \text{ if } y > U \end{cases} \tag{18}$$

where U is the upper acceptable value to the response and t is a weight. The same idea for s is applied for t to attribute levels of importance to the target value.

If the target value (T) is located between the lower limit (L) and the upper limit (U), then, a bilateral desirability function must be used. This function is expressed by the following equation:

$$d = \begin{cases} 0 \text{ if } y < L \\ \left(\dfrac{y-L}{T-L}\right) \text{ if } L \le y \le T \\ \left(\dfrac{U-y}{U-T}\right)^t \text{ if } T \le y \le U \\ 0 \text{ if } y > U \end{cases} \tag{19}$$

As demonstrated, t and s control the variation rate of the desirability functions. When these parameters are varied, it is feasible to attribute different desirability to the responses and, consequently, to increase or decrease the range of acceptable values in the optimization process.

The application of desirability functions in analytical chemistry brings advantages as efficiency, economy, and objectivity in the optimization of multiple response procedures. Despite the obvious advantages of this methodology in the optimization of analytical procedures, there are still few applications found in the literature. Derringer functions have been more applied for optimization in chromatographic and related techniques (electrochromatography and electrophoresis) principally because they can establish conditions for the best resolution among several peaks simultaneously. Table 9 shows some applications of the desirability function for the optimization of multiple responses in analytical chemistry.

6. Use of artificial neural networks in RSM

Artificial neural networks (ANNs) offer an attractive possibility for providing non-linear modeling for response surfaces and optimization in analytical chemistry.

ANNs are inspired by the arrangement of cerebral networks and consist of groups of highly interconnected processing elements called neurons. The neurons are arranged in a series of layers: one input layer with neurons representing independent variables, one output layer with neurons representing dependent variables, and several hidden layers that associate the inputs with outputs. Each neuron from one layer is connected with each neuron in the next

Table 9
Some applications of Desirability function in analytical chemistry

Analytes	Samples	Analytical technique	Objective of the study	Ref.
Organochlorines and pyrethroids	Tea	GC	Optimizing a method based on matrix solid-phase dispersion and gas chromatography for the determination of multi-residue pesticides	[66]
R-Timolol and other impurities	*S*-Timolol maleate	HPLC	Finding the optimal chromatographic condition for the simultaneous determination of analytes	[67]
Anthraquinones and bianthrones	Herbal medicine	Micellar electrokinetic chromatography	Developing a chromatography method for the analysis of anthraquinones and bianthrones in rhubarb crude drugs	[68]
Organomercury compounds and Hg(II)	Seawater	GC–MIP OES	Developing a method for determination of these species	[69]
Methyl *tert*-butyl ether, *tert*-butyl alcohol, benzene, toluene, ethylbenzene and xylene isomers	Groundwater	GC–MS	Developing a method for the simultaneous determination of these substances	[70]
Methylmercury and Hg(II)	Biological	GC	Developing a method for the extraction based microwave-assisted extraction and solid-phase micro-extraction	[71]
Methylphenobarbital enantiomers and phenobarbital	Human plasma	HPLC	Developing an automated liquid chromatographic method for the simultaneous determination of analytes	[72]
Local anesthetics	Human plasma	HPLC	Developing an automated method involving dialysis, clean-up and enrichment of the dialysate on a pre-column packed with a strong cation-exchange phase	[73]
Vitamins B_6 and B_{12}, dexamethasone and lidocaine	Pharmaceutical preparations	Capillary electrophoresis	Developing a method for the simultaneous determination of these four substances in pharmaceutical preparations	[74]
Cu, Bi and Li	Tap-water and synthetic alloys	Adsorptive stripping voltammetry	Developing a method for simultaneous determination of these metals	[75]

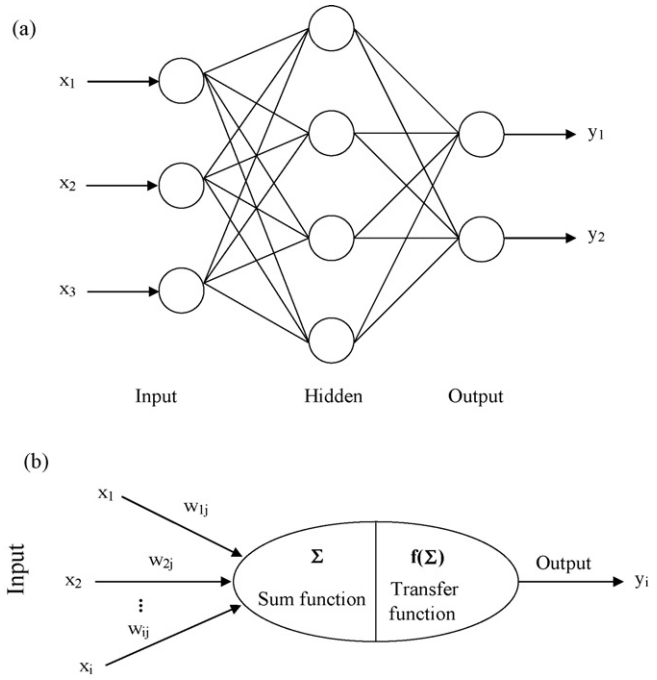

Fig. 6. Artificial neural network: (a) scheme of a three-layer network; (b) operation of a single neuron.

layer. The pattern of interconnection among the neurons is called the network "architecture", and it can be conveniently represented on a graph (Fig. 6(a)). Data generated from the experimental design can be used as relevant inputs, as well as outputs, for ANN training [21–23].

The training is carried out by adjusting the strength of connections between neurons with the aim to adapt the outputs of the entire network to be closer to the desired outputs or to minimize the sum of the training data. During the training phase, each neuron receives the input signals x_i from n neurons, aggregates them by using the weights (w_{ij}) of the synapses, and passes the result after suitable transformation as the output signal y_i (Fig. 6(b)) as a function of the sum, according to Eq. (20):

$$y_i = f\left(\sum_{i=1}^{n} x_i w_{ij}\right) \tag{20}$$

where f is the transfer function that is necessary to transform the weighted sum of all the signals connecting with a neuron. The most widely used transfer function is presented in Eq. (21):

$$f = \frac{1}{1 + e^{-cx}} \tag{21}$$

where c is a constant that determines the slope of the sigmoid function.

The training phase is finished when the square error is minimized across all training experiments. Once ANN has been trained, it has a good predictive capability and ability to accurately describe the response surface even without any knowledge about the physical and chemical background of the modeled system [14,22].

ANN offers an alternative to the polynomial regression method as a modeling tool. Classical RSM requires the specification of a polynomial function such as linear, first-order interaction, or second-order quadratic, to be regressed. Moreover, the number of terms in the polynomial is limited to the number of experimental design points, and the selection of the appropriate polynomial equation can be extremely cumbersome because each response requires its own individual polynomial equation.

The ANN methodology provides the modeling of complex relationships, especially non-linear ones, that may be investigated without complicated equations. ANN analysis is quite flexible in regards to the number and form of the experimental data, which makes it possible to use more informal experimental designs than with statistical approaches. Also, neural network models might have better predictive power than regression models. Regression analyses are dependent on predetermined statistical significance levels, and less significant terms are usually not included in the model. With the ANN method, all data are used, potentially making the models more accurate [82].

Using ANN modeling for the optimization of analytical methods has been applied mainly for the development of chromatographic methods. Table 10 shows some applications of artificial neural network modeling in analytical chemistry.

Table 10
Some applications of RSM combined with artificial neural networks in analytical chemistry

Analytes	Samples	Analytical technique	Objective of the study	Ref.
Fosinopril sodium and its degradation product fosinoprilat	Pharmaceuticals	GC–MS	Combining central composite design and ANNs in optimization of mobile phase composition for analysis	[76]
Herbicides	Waters	HPLC	Optimizing of the linear gradient separation of 10 herbicides consisting of a mixture of acids, bases and neutrals employing a single ANN for modeling the response surface	[77]
Neuroprotective peptides	Mixture of peptides	HPLC	Using experimental design conjunction with artificial neural networks for optimization of isocratic ion-pair separation of neuroprotective peptides	[22]
Huperzine A	Pharmaceutical products and biological liquids	Capillary electrophoresis	Using of the experimental design combined with the artificial neural networks for optimization of the drug separation	[78]
cis- and *trans*-resveratrol	Australians wine	Capillary zone electrophoresis	Optimizing the solid-phase extraction employing central composition design and ANN	[79]
Triazine herbicides	Waters	HPLC	Prediction of retention factors of the studied herbicides	[80]
Antimicrobial agents	Cosmetics	HPLC	Using of experimental design/ANN to correlate the retention time of each analyte (20 typical antimicrobial substances) to the variables and their interactions	[81]
Ruthenium	Refined ore	Spectrophotometry	Coupling experimental design and ANN for the optimization of an on-line microwave flow injection system	[82]
Hydrochlorothiazide and amiloride	Pharmaceuticals	HPLC	Comparing artificial neural networks for response surface modeling in HPLC with multiple regression methods	[83]

7. Conclusions

Application of response surface methodology in the optimization of analytical procedures is today largely diffused and consolidated principally because of its advantages to classical one-variable-a-time optimization, such as the generation of large amounts of information from a small number of experiments and the possibility of evaluating the interaction effect between the variables on the response.

In order to employ this methodology in experimental optimization, it is necessary to choose an experimental design, to fit an adequate mathematical function, and to evaluate the quality of the fitted model and its accuracy to make previsions in relation to the experimental data obtained.

The central composite design is still the symmetrical second-order experimental design most utilized for the development of analytical procedures. The application of three-level factorial designs is not frequent, and the use of this design has been limited to the optimization of two variables because its efficiency is very low for higher numbers of variables. However, the Box–Behnken and Doehlert designs present more efficient matrices and have increased the number of published works in recent years.

Multiple response optimization using desirability functions has until now had its utilization limited to the chromatographic field, its related techniques, and to electrochemical methods. However, its principles can be applied to the development of procedures using various analytical techniques, which demand a search for optimal conditions for a set of responses simultaneously.

Finally, as an alternative to classical modeling, an adaptive learning technique that utilizes neural networks combined with experimental design, can be employed to model a dependence relation. This approach has demonstrated a superior accuracy in data learning and prediction over the traditional RSM.

Acknowledgements

The authors acknowledge grants and fellowships from Conselho Nacional de Desenvolvimento Científico e Tecnológico (CNPq), Fundação Carlos Chagas Filho de Amparo à Pesquisa do Estado do Rio de Janeiro (FAPERJ), Coordenação de Aperfeiçoamento de Pessoal de Nível Superior (CAPES), and Pró-Reitoria de Pesquisa e Pós-Graduação (PPG) from the Universidade Estadual do Sudoeste da Bahia (UESB).

References

[1] P.W. Araújo, R.G. Brereton, Trends Anal. Chem. 15 (1996) 63.
[2] T. Lundstedt, E. Seifert, L. Abramo, B. Thelin, A. Nyström, J. Pertensen, R. Bergman, Chemometr. Intell. Lab. Syst. 42 (1998) 3.
[3] G. Hanrahan, K. Lu, Crit. Rev. Anal. Chem. 36 (2006) 141.
[4] S.G. Gilmour, Biometrics 62 (2006) 323.
[5] R.F. Teófilo, M.M.C. Ferreira, Quim. Nova 29 (2006) 338.
[6] D. Bas, I.H. Boyaci, J. Food Eng. 78 (2007) 836.
[7] S. Vieira, R. Hoffman, Estatística Experimental, Atlas, São Paulo, 1989.
[8] M.F. Pimentel, B.B. Neto, Quim. Nova 19 (1996) 268.
[9] J.A. Cornel, How to Apply Response Surface Methodology, second ed., American Society for Quality Control, 1990.
[10] R.E. Bruns, I.S. Scarminio, B.B. Neto, Statistical Design – Chemometrics, Elsevier, Amsterdam, 2006.
[11] M.D. Morris, Technometrics 42 (2000) 111.
[12] D.L. Massart, B.G.M. Vandeginste, L.M.C. Buydens, S. de Jong, P.J. Lewi, J. Smeyers-Verbeke, Handbook of Chemometrics and Qualimetrics: Part A, Elsevier, Amsterdam, 1997.
[13] G.E.P. Box, D.W. Behnken, Technometrics 2 (1960) 455.
[14] M. Otto, Chemometrics: Statistics and Computer Application in Analytical Chemistry, Wiley–VCH, Weinheim, 1999.
[15] S.L.C. Ferreira, R.E. Bruns, H.S. Ferreira, G.D. Matos, J.M. David, G.C. Brandão, E.G.P. da Silva, L.A. Portugal, P.S. dos Reis, A.S. Souza, W.N.L. dos Santos, Anal. Chim. Acta 597 (2007) 179.
[16] G.E.P. Box, K.B. Wilson, J. R. Stat. Soc. B 13 (1951) 1.
[17] D.H. Doehlert, Appl. Stat. 19 (1970) 231.
[18] A.M.G. Campaña, L.C. Rodríguez, A.L. González, F.A. Barrero, M.R. Ceba, Anal. Chim. Acta 348 (1997) 237.
[19] E. Sivertsen, F. Bjerke, T. Almoy, V. Segtnan, T. Naes, Chemom. Intell. Lab. Syst. (2007) 110.
[20] T.E. Murphy, K.L. Tsui, J.K. Allen, Res. Eng. Des. 16 (2005) 118.
[21] F. Marini, R. Bucci, A.L. Magrì, A.D. Magrì, Microchem. J. 88 (2008) 178.
[22] K. Novotná, J. Havlis, J. Havel, J. Chromatogr. A 1096 (2005) 50.
[23] H.M. Cartwright, Application of Artificial Intelligence in Chemistry, Oxford Science Publications, Oxford, 1993.
[24] N.M. Aragão, M.C.C. Veloso, M.S. Bispo, S.L.C. Ferreira, J.B. Andrade, Talanta 67 (2005) 1007.
[25] G. Saccani, E. Tanzi, S. Mallozzi, S. Cavalli, Food Chem. 92 (2005) 373.
[26] V. Harang, S.P. Jacobsson, D. Westerlund, Electrophoresis 25 (2004) 1792.
[27] S. Hilaert, L. Snoeck, W.V. Bossche, J. Chromatogr. A 1033 (2004) 357.
[28] M.P. Davies, V.D. Biasi, D. Perrett, Anal. Chim. Acta 504 (2004) 7.
[29] S. Hillaert, W.V.D. Bossche, J. Chromatogr. A 979 (2002) 323.
[30] M.P. Llompart, R.A. Lorenzo, R. Cela, J. Chromatogr. A 723 (1996) 123.
[31] W.N.L. Santos, F.S. Dias, M.S. Fernandes, M.V. Rebouças, M.G.R. Vale, B. Welz, S.L.C. Ferreira, J. Anal. At. Spectrom. 20 (2005) 127.
[32] A. Stafiej, K. Pyrzynska, A. Ranz, E. Lankmayr, J. Biochem. Biophys. Methods 69 (2006) 15.
[33] M.A.M. Gomez, R.M.V. Camanas, S. Sagrado, M.J.M. Hernandez, Electrophoresis 26 (2005) 4116.
[34] A.S. Souza, W.N.L. Santos, S.L.C. Ferreira, Spectrochim. Acta B 60 (2005) 737.
[35] M. Gfrerer, E. Lankmayr, Anal. Chim. Acta 533 (2005) 203.
[36] C.V.S. Babu, B.C. Chung, Y.S. Yoo, Anal. Lett. 37 (2004) 2485.
[37] A. Zougagh, A.G. Torres, E.V. Alonso, J.M.C. Pavon, Talanta 62 (2004) 503.
[38] A.C. Servais, M. Fillet, P. Chiap, A.M. Abushoffa, P. Hubert, J. Crommen, J. Sep. Sci. 25 (2002) 1087.
[39] T. Mirza, H.I.S. Tan, J. Pharm. Biomed. 25 (2001) 39.
[40] M.E.P. Hows, D. Perrett, J. Kay, J. Chromatogr. A 768 (1997) 97.
[41] L. Vidal, E. Psillakis, C.E. Domini, N. Grané, F. Marken, A. Canals, Anal. Chim. Acta 584 (2007) 189.
[42] P.A.J. Rosa, A.M. Azevedo, M.R. Aires-Barros, J. Chromatogr. A 1141 (2007) 50.
[43] R. López, F. Goñi, A. Etxandia, E. Millán, J. Chromatogr. B 846 (2007) 298.
[44] M.C.V. Mamani, J.A. Farfán, F.G.R. Reyes, S. Rath, Talanta 70 (2006) 236.
[45] E.D. Guerrero, R.N. Marín, R.C. Mejías, C.G. Barroso, J. Chromatogr. A 1104 (2006) 47.
[46] V. Yusà, O. Pardo, A. Pastor, M. Guardia, Anal. Chim. Acta 557 (2006) 304.
[47] A.B. Baranda, N. Etxebarria, R.M. Jiménez, R.M. Alonso, Talanta 67 (2005) 933.
[48] G.P. Brandão, R.C. Campos, E.V.R. Castro, H.C. Jesus, Anal. Bioanal. Chem. 386 (2006) 2249.
[49] N. Jalbani, T.G. Kazi, B.M. Arain, M.K. Jamali, H.I. Afridi, R.A. Sarfraz, Talanta 70 (2006) 307.
[50] C.P. Farfal, A.M. Piñeiro, A.B. Barrera, P.B. Barrera, H.P. Cancino, I.G. Henríquez, Talanta 64 (2004) 671.
[51] M.A.A. Lomillo, F.J. Campo, F.J.M. Pascual, Electroanalysis 18 (2006) 2435.
[52] M.A. Bezerra, R.E. Bruns, S.L.C. Ferreira, Anal. Chim. Acta 580 (2006) 251.
[53] W.N.L. Santos, J.L.O. Costa, R.G.O. Araújo, D.S. Jesus, A.C.S. Costa, J. Hazard. Mater. 137 (2006) 1357.
[54] H.S. Ferreira, M.A. Bezerra, S.L.C. Ferreira, Microchim. Acta 154 (2006) 163.
[55] R.E. Santelli, M.A. Bezerra, O.D. Sant'Ana, R.J. Cassella, S.L.C. Ferreira, Talanta 68 (2006) 1083.
[56] J.A.D. Amaro, S.L.C. Ferreira, J. Anal. At. Spectrom. 19 (2004) 246.
[57] M. Zougagh, A.G. Torres, J.M.C. Pavon, Anal. Lett. 36 (2003) 1115.
[58] C.R.T. Tarley, L.T. Kubota, Anal. Chim. Acta 548 (2005) 11.
[59] S. Furlanetto, S. Pinzauti, E. La Porta, A. Chiarugi, P. Mura, S. Orlandini, J. Pharm. Biomed. 17 (1998) 1015.
[60] A.M. Urunuela, J.M.G. Saiz, C. Pizarro, J. Chromatogr. A 1056 (2004) 49.
[61] P. Araujo, F. Couillard, E. Leirnes, K. Ask, A. Bøkevoll, L. Frøyland, J. Chromatogr. A 1121 (2006) 99.
[62] F. Momenbeik, J.H. Khorasani, Anal. Bioanal. Chem. 384 (2006) 844.
[63] A. Navalón, A. Prieto, L. Araújo, J.L. Vílchez, J. Chromatogr. A 946 (2002) 239.
[64] C. Aguilar, A. Peñalver, E. Pocurull, J. Ferré, F. Borrull, R.M. Marcé, J. Chromatogr. A 844 (1999) 425.
[65] L. Mateus, S. Cherkaoui, P. Christen, J.L. Veuthey, J. Chromatogr. A 829 (1998) 317.
[66] Y.Y. Hu, P. Zheng, Y.Z. He, G.P. Sheng, J. Chromatogr. A 1098 (2005) 188.
[67] R.D. Marini, P. Chiap, B. Boulanger, W. Dewe, P. Hubert, J. Crommen, J. Sep. Sci. 26 (2003) 809.
[68] C.H. Kuo, S.W. Sun, Anal. Chim. Acta 482 (2003) 47.
[69] A.M. Carro, I. Neira, R. Rodil, R.A. Lorenzo, Chromatographia 56 (2002) 733.
[70] F. Bianchi, M. Careri, E. Marengo, M. Musci, J. Chromatogr. A 975 (2002) 113.
[71] R. Rodil, A.M. Carro, R.A. Lorenzo, M. Abuín, R. Cela, J. Chromatogr. A 963 (2002) 313.
[72] A. Ceccato, B. Boulanger, P. Chiap, P. Hubert, J. Crommen, J. Chromatogr. A 819 (1998) 143.
[73] P. Chiap, B. Boulanger, L. Fotsing, P. Hubert, J. Crommen, Chromatographia 53 (2001) 678.
[74] L.V. Candioti, J.C. Robles, V.E. Mantovani, H.C. Goicoechea, Talanta 69 (2006) 140.
[75] A. Babaei, E. Shams, A. Samadzadeh, Anal. Sci. 22 (2006) 955.
[76] B. Jancić, M. Medenica, D. Ivanović, S. Janković, A. Malenović, J. Chromatogr. A 1189 (2008) 366.

[77] A.T.K. Tran, R.V. Hyne, F. Pablo, W.R. Day, P. Doble, Talanta 71 (2007) 1268.
[78] A.B. Hameda, S. Elosta, J. Havel, J. Chromatogr. A 1084 (2005) 7.
[79] M. Spanilá, J. Pazourek, M. Farková, J. Havel, J. Chromatogr. A 1084 (2005) 180.
[80] F. Ruggieri, A.A. D'Archivio, G. Carlucci, P. Mazzeo, J. Chromatogr. A 1076 (2005) 163.
[81] E. Marengo, V. Gianotti, S. Angioi, M.C. Gennaro, J. Chromatogr. A 1029 (2004) 57.
[82] H. Wang, Y. Zhou, Y. Zhao, Q. Li, X. Chen, Z. Hu, Anal. Chim. Acta 429 (2001) 207.
[83] S. Agatonovic-Kustrin, M. Zecevic, L. Zivanovic, I.G. Tucker, Anal. Chim. Acta 364 (1998) 265.

Talanta 76 (2008) 1124–1129

Contents lists available at ScienceDirect

Talanta

journal homepage: www.elsevier.com/locate/talanta

An expeditious method for the determination of organochlorine pesticides residues in estuarine sediments using microwave assisted pre-extraction and automated headspace solid-phase microextraction coupled to gas chromatography–mass spectrometry

Pedro N. Carvalho, Pedro Nuno R. Rodrigues, Filipe Alves, Rafael Evangelista, Maria Clara P. Basto, M. Teresa S.D. Vasconcelos*

CIMAR/CIIMAR – Centro Interdisciplinar de Investigação Marinha e Ambiental and Faculdade de Ciências, Universidade do Porto, R. Campo Alegre 687, Porto 4169-007, Portugal

ARTICLE INFO

Article history:
Received 17 January 2008
Received in revised form 9 May 2008
Accepted 14 May 2008
Available online 7 July 2008

Keywords:
Organochlorine pesticides
Headspace solid-phase microextraction
Microwave assisted extraction
Sediments
Gas chromatography–mass spectrometry
Gas chromatography-electron capture detector

ABSTRACT

Determination of organochlorine pesticides (OCPs) in sediments implicates extraction of these compounds from the matrix, which is difficult owing to strong interaction among OCPs and different constituents of the sediments, particularly organic content. The method here described is a combination of microwave assisted extraction (MAE), headspace solid-phase microextraction (HS-SPME) and gas chromatography–mass spectrometry (GC–MS), acting in selected-ion storage mode, or GC-electron capture detector (ECD, for routine analysis). Methanol was used as extracting solvent and aliquots of the MAE extracts (after inclusion of a step for sulfur elimination when required) were used to prepare aqueous solutions for HS-SPME. A complete automation of the SPME procedure increases the sample throughput, including standard addition for calibration purpose. The procedure has the advantage of exclude additional clean-up steps and pre-concentration before SPME. Application to reference sediments of different characteristics revealed absence of significant interferences from the matrix for α-lindane, γ-lindane, aldrin, dieldrin, endrin, 4,4′-DDT, 4,4′-DDD, 4,4′-DDE, heptachlor, heptachlor epoxide and good sensitivity. Detection limits ranged from 0.005 to 0.11 ng of OCP *per* gram of dried sediment using GC–MS and from 0.01 to 0.26 ng g^{-1} using GC-ECD. The linear response ranges embraced 5–6 orders of magnitude (up to 1000 ng g^{-1}) in GC–MS, being narrower for GC-ECD. The method was successfully applied to sandy and muddy sediments from Portuguese rivers estuaries, enabling quantification of seven OCPs. The method resulted effective, relatively simple and fast, being suitable for routine monitoring of residues of OCPs from sediments of different grain size and organic matter content, which influence concentration, mobility and availability of contaminants.

1. Introduction

Organochlorine pesticides (OCPs) integrate the semi volatile persistent organic compounds (POPs) that exhibit potentially harmful effects to the environment [1]. As most of the POPs, OCPs are lipophilic, persist in various media and some can be transported over long distances to regions where they have never been used [2]. OCPs can be introduced into the aquatic environment and accumulated in sediments by several pathways. As sediments are depositories of these toxic substances, owing to their low solubility and association with suspended particulate matter [3], levels of OCPs in sediments should be determined and controlled whenever possible.

Analysis of OCPs implicates extraction of these compounds from the sediment, which is difficult owing to strong interaction among OCPs and different constituents of the sediments, particularly organic content. Conventional techniques to extract low amounts of organic contaminants from complex solid matrix, like those of sediments, involve a long time consuming extraction/preconcentration procedure, which is often the limiting step of the overall analytical method. To overcome such constrain, new extraction procedures have been developed in the last years, namely microwave assisted extraction (MAE), pressurized fluid extraction (PFE), supercritical fluid extraction (SFE) and ultrasonic solvent extraction (USE) [4,5], all requiring shorter extraction time and small amount of solvent while sometimes gave higher recovery

* Corresponding author. Tel.: +351 220402570.
E-mail address: mtvascon@fc.up.pt (M.T.S.D. Vasconcelos).

0039-9140/$ – see front matter © 2008 Elsevier B.V. All rights reserved.
doi:10.1016/j.talanta.2008.05.035

yields of the analytes when compared with classical extraction procedures [6]. Even so, in previous cases of MAE successful application to pre-extract OCPs from soils and sediments [7–9], the obtained extracts have needed clean-up [8,9] and/or pre-concentration [7] before analysis.

Solid-phase microextraction (SPME) has been increasingly used in the analysis of trace organic compounds, having the advantage of combining extraction and concentration in a single step [10]. Headspace (HS) SPME coupled to gas chromatography (GC) with electron capture detection (ECD) has been already applied for determination of OCPs in aqueous slurries of soil and sediments [11–13]. However, in those works the possible occurrence of sulfur in sediments, which acts as an interference, has not been considered. Additionally, the use of sediment slurries for OCPs determination by means of HS-SPME requires relatively low mass of sample aliquots [13], which may not be representative of the sediment composition, unless the sample is perfectly homogeneous. This is particularly difficult to attain in sandy sediments. As sample dilution is not possible when HS-SPME is directly applied to sediment slurries, very small aliquots of sediments have to be used in case of sediments with high levels of OCPs residues, which stresses the problem of lack of sample homogeneity and representativity. Moreover, to enhance desorption efficiency of OCPs from sediment with matrices very complex and rich in organic matter, a step of pre-extraction of the analytes is required.

Therefore, a combination of MAE and HS-SPME can be much more effective than each one of these procedures acting separately, as it permits pre-concentration of analytes at the fiber and minimizes the need of a pre-clean up of the extract from MAE, since the microextraction is performed in the headspace. Even so, the complexity of the matrix in sediments makes the identification and quantification of OCPs a difficult task. Sulfur can be an important interference as it has solubility similar to OCPs and can form co-extracts with them, causing a broad overlapping peak in gas chromatography (GC) and reducing the accuracy of quantitative measurements [14]. As reported in a recent work on pesticides determination in soil [7] which has used MAE followed by HS-SPME and GC coupled to tandem mass spectrometry (MS/MS), recovery has been found to be dependent on the type of soil due to matrix effects.

To our knowledge, a combination of MAE, HS-SPME and GC–MS has never been successfully applied before to the determination of OCPs in estuarine sediments. The method here described used precisely this combination, as well as a similar one with GC-ECD for routine analysis, with complete automation of the SPME procedure (which increases the sample throughput). To minimize matrix effects, a step for elimination of sulfur interference was included when required and standard addition was used for calibration purpose. The method resulted effective, relatively simple and fast, being suitable for simultaneous monitoring of residues of ten OCPs from sediments of different grain size and organic matter content.

2. Experimental

2.1. Reagents and solutions

Solvents and reagents were analytical grade unless further information. Methanol, Chromasolv® for HPLC, was obtained from Sigma–Aldrich (Darmstadt, Germany). The water used was deionized with conductivity <0.1 $\mu S\,cm^{-1}$. Sodium sulfite (purity 98%) and copper fine powder (purity 99.7%) for sample desulfuration were obtained from Riedel-de Haën (Seelze, Germany) and Merck (Darmstadt, Germany) respectively. Sodium chloride (purity 99.5%) was also from Merck. A mixture of eighteen OCPs (HCHs, aldrin, dieldrin, endrin, endrin ketone, endrin aldehyde, endosulfan I (α), endosulfan II (β), endosulfan sulfate, 4,4′-DDT, 4,4′-DDD, 4,4′-DDE, heptachlor, heptachlor epoxide and methoxychlor) in toluene:hexane (1:1) at concentrations of 2000 $mg\,L^{-1}$, from Supelco (Bellefonte, PA, USA), was used to prepare stock standard diluted solutions in methanol and stored at 4 °C. Working solutions of pesticides were prepared daily by appropriate dilutions with water. Reference sediments Metranal™ 16 from Analytika Ltd. (Prague, Czech Republic) and CNS300-04-100 from Resource Technology Corporation (Salisbury, United Kingdom) were used in the method validation. For decontamination, all the glass and plastic ware was washed with soap, rinsed with water, soaked overnight in 20% nitric acid aqueous solutions and rinsed with water again and methanol.

2.2. Extraction conditions

MAE was carried out using a laboratory microwave system Ethos 1 Milestone (Sorisole, Italy), provided with Teflon extraction vessels, where 10 mL of methanol and a suitable mass of sediment (ranging from 0.25 to 10 g, according to OCPs concentration) were introduced. The polydimethylsiloxane SPME fibers (PDMS, 100 μm) used were purchased from Supelco (Bellefonte, PA, USA). Fibers were conditioned in the GC injector as indicated by the manufacturer before use. For the first optimization steps, spiked aqueous solutions (10 mL) were introduced in 22 mL vials, sealed with caps and septa, thermostated, and stirred using PTFE covered magnetic stirring bars. For method validation and real sediment analysis 100 μL aliquots of MAE extracts of sediment (after centrifugation) were added to the volume of water necessary to obtain 10 mL solutions contained in 20 mL sealed vials (18 mm magnetic ultraclean closers suitable for autosampler). Real estuarine sediments were previously dried at room temperature and sieved through a screen (pore size 2 mm).

In a first optimization step the fiber was manually inserted in the GC injector. In further experiments the HS-SPME was performed using an autosampler (CTC Analytics, Combi Pal model). The optimized conditions are presented in Table 1. Blanks were processed with the samples every working day for control purposes. Unless further indication, all tests were performed in triplicate.

2.3. Chromatographic conditions

GC–MS analysis were performed by using a Varian Saturn 2000 mass spectrometer (Walnut Creek, CA) coupled to a Varian 3900 gas chromatograph equipped with a split/splitless injector port, a SPME liner (0.75 mm ID), a microseal septum system (Merlin, Half Moon Bay, CA) and a CP-Sil 8CB Low Bleed/MS (Varian) column (60 m length × 0.250 mm diameter, 0.25 μm film thickness). The carrier gas was helium of high purity (99.9995% from Air Liquide). The Varian computer software MS Workstation 6.30 controlled the GC–MS.

Table 1
SPME conditions

Extraction mode	Headspace (HS)
Fiber type	100 μm film thickness PDMS
Salting out	2 g NaCl
Pre-incubation time	30 min
Pre-incubation temperature	80 °C
Pre-incubation rotation	500 rpm[a]
Extraction time	60 min
Extraction temperature	80 °C
Extraction rotation	250 rpm[a]

[a] Rotation *per* minute.

Table 2
GC operation conditions for both GC–MS and GC-ECD[a]

Injection	Splitless (7 min)
Injector temperature	250 °C
Flow	He, 1.0 mL min^{-1}
Temperature program	40 °C (5 min) +30 °C min^{-1} up to 160 °C +5 °C min^{-1} up to 275 °C +30 °C min^{-1} up to 300 °C (3 min)

[a] In GC-ECD He flow rate was 1.5 mL min^{-1}.

Table 3
Mass spectrometry operation parameters

Transfer line temperature	230 °C
Ion trap temperature	200 °C
Ionization mode	Electrical ionization/automode
SIS (selected ion storage)	

OCP	Retention time (min)	Quantification ions (m/z)
α-Lindane	20.86	109, 111, 181, 183, 217, 219
γ-Lindane	22.07	109, 111, 181, 183, 217, 219, 221
Heptachlor	24.73	100, 270, 272, 274
Aldrin	26.11	66, 79, 91, 263
Heptachlor epoxide	27.52	351, 353, 355
DDE	29.53	246, 248, 316, 318
Dieldrin	30.00	79
Endrin	30.84	67, 79, 81, 82, 261, 263, 265, 281
DDD	31.12	165, 235, 237
DDT	32.50	165, 235, 237

Analysis by GC-ECD were performed using a Varian CP-3800 gas chromatograph prepared for the simultaneous ECD and FID detection by split of the gas flux, with the same characteristics (injector, Merlin microseal and column) as the GC–MS equipment. The carrier gas, helium, was mixed with make-up gas nitrogen (99.999%) with volume mixing ratio of 1:5. The Varian computer software Star Chromatography Workstation 6.30 controlled the GC-ECD.

The optimized conditions are listed in Table 2 (GC conditions) and Table 3 (MS conditions). ECD detection was carried out with the oven at 320 °C. The mass spectrometer was operated in full scan mode for retention time determinations, using library search (m/z = 40–600) and in SIS mode for chromatographic runs. Acquisition data was chosen based on storage of the characteristic ions with relative abundance higher than 500 and ejection of interfering ions from the matrix. Analyses performed by GC-ECD were carried out after the complete optimization and validation of the GC–MS method using exactly the same conditions for comparison of the analytical results. Pesticides quantification was performed by standard addition method.

3. Results and discussion

3.1. Optimization of MAE procedure

The MAE program was developed based on the extraction application note (EX-EN-03, Milestone extraction application guide). The temperature control limit was fixed at 105 °C, which was attained within 5 min (the equipment controls the necessary power), the total duration of the program being 20 min. Selection of the solvent was carried out by comparison of efficiency of OCPs extraction from spiked real sediments using either water or methanol. Methanol was the solvent chosen because it provided much higher analytical signals (Fig. 1). The amount of solvent used was always 10 mL (minimum volume required) and the amount of sediment used depended on the OCPs concentration present (0.25 g of sediment was used for μg g^{-1} level, and 2 g were used for ng g^{-1} level).

In some cases, the characteristics of the analytical signals obtained for sediment samples in full scan chromatograms revealed the presence of interfering sulfur. Even working in SIS mode, it was observed that this interference reduced the accuracy of the analysis, so requiring a previous elimination of sulfur. Depending on the amount of sulfur in the sediment, two alternative procedures were carried out for this purpose. When sulfur content was relatively low, addition of sodium sulfite to the samples in methanol and sonication for 15 min, before MAE, was sufficient. When that procedure failed due to too high sulfur content in the sediment, an elimination process similar to that frequently

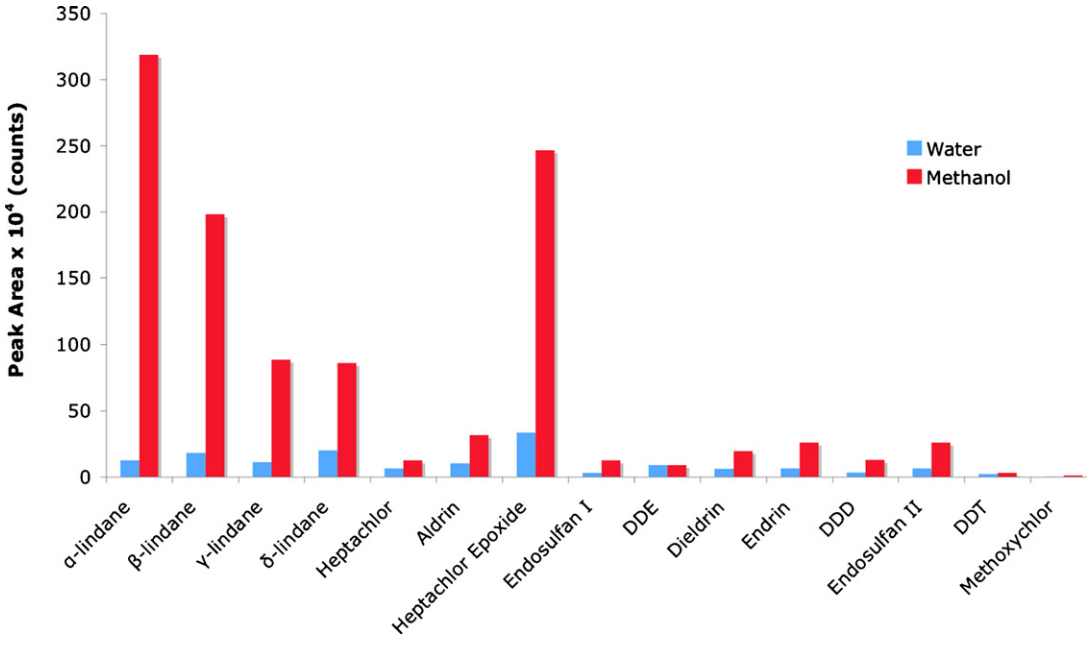

Fig. 1. Solvent influence on MAE. The analytical signals shown were obtained using MAE, HS-SPME and GC–MS.

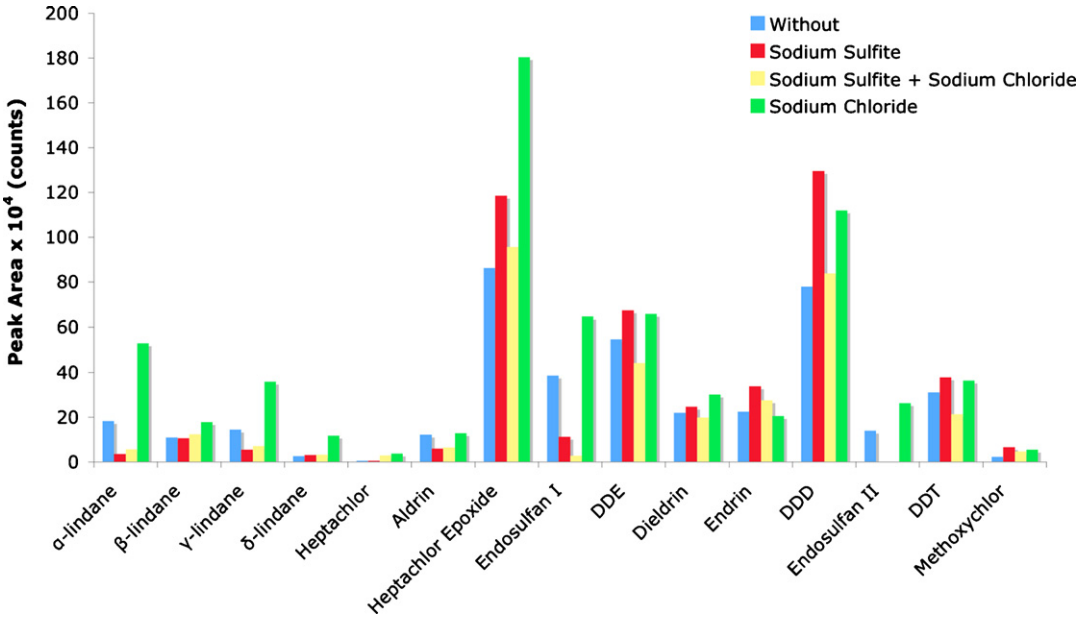

Fig. 2. Salting out effect on HS-SPME. Comparison of the signals observed (using MAE, HS-SPME, GC/MS) for sediment extract without salt addition and after addition of 1 g of Na_2SO_3 or 1 g of NaCl or 1 g of both Na_2SO_3 and NaCl.

used in the classical Soxhlet extraction [14] (addition of excess of activated copper to the sediment extract – the supernatant after MAE – and reaction for 1 h in an ultrasound bath) could solve the problem.

3.2. Optimization of the HS-SPME procedure

Polydimethylsiloxane SPME fiber (PDMS, 100 μm of coating) was chosen based on previous works [15].

Optimization of both temperature and time for HS-SPME extraction was carried out using spiked aqueous solutions.

The choice of 80 °C as extraction temperature was based on a compromise between the increase in the peak area with the temperature observed for some pesticides (*p.e.* DDT, DDE, DDD and aldrin) and the decrease of the peak areas with the temperature observed for others (*p.e.* α-lindane).

The best time for the microextraction was 60 min, similar to previous results [15,16].

The effect of salt addition is known to influence the signal intensity of several compounds including OCPs [16]. The introduction of a salt varies the ionic strength of the solution, changing the equilibrium of the pesticides between solution and headspace. Optimization of conditions for salting out effect was carried out on spiked sediment extract. Fig. 2 shows that in the presence of Na_2SO_3 (when 1 g of this salt had been added to eliminate low sulfur content in sediment), addition of 1 g of NaCl increased peak areas of lindanes, heptachlor and aldrin but decreased those for DDT's and methoxychlor (dichlorodiphenylethanes), for which the presence of only Na_2SO_3 was preferable. As salting out effect depends on the salt concentration, different amounts of NaCl were tested in the absence of Na_2SO_3 (when it was not used to eliminate sulfur). Based on the equilibrium between the increase of signals for the pesticides that presented lower peak areas and the decrease for those which presented higher peak areas, 2 g were chosen for the further experiments. A similar behavior has been previously observed [12]. In general, the results showed that the addition of only NaCl (instead a mixture of NaCl and Na_2SO_3) to the vials gave better salting out effect (higher intensity of the signals).

3.3. Characteristics of the method, validation and application to real sediments

The method (MAE, HS-SPME–GC/MS) was efficiently validated for ten OCPs: α-lindane, γ-lindane, aldrin, dieldrin, endrin, 4,4′-DDT, 4,4′-DDD, 4,4′-DDE, heptachlor and heptachlor epoxide.

Among the remaining OCPs present in the standard mixture used, endosulfan I was the only present, with a certificated value, in the reference materials used, therefore the only which was susceptible of validation. Endrin cetone, endrin aldeyde and endosulfan sulfate could not be detected either in standard solutions or in sediment extracts, probably due to their higher polarity and consequent lower affinity to the PDMS fiber used. Methoxychlor, β-lindane, δ-lindane, endosulfan I and endosulfan II could be detected in the aqueous standard solutions (LOD ≥ 10 ng L^{-1} for methoxychlor, endosulfan I, endosulfan II and LOD > 200 ng L^{-1} for β-lindane and δ-lindane). In sediment extracts too high LODs (>10 ng g^{-1} for methoxychlor; >100 ng g^{-1} for endosulfan I and II and even higher for β-lindane and δ-lindane) prevented their determination in sediments. To our knowledge these compounds have not been determined before in sediments by HS-SPME–GC/MS. A few of the non-validated OCPs have been determined by HS-SPME–GC/ECD (*e.g.* [12,13]). However ECD does not provide an unambiguous identification of the compounds in complex matrix like that of sediments.

Limit of detection (LOD) and limit of quantification (LOQ) of the overall analytical procedure were determined using extracts of samples of reference sediments, based on the concentrations which gave rise to peaks with signal-to-noise ratios of 3 and 10, respectively. LODs (Table 4) were at the ng g^{-1} level, similar or lower than those provided by previous methods using MAE combined with HS-SPME and GC–MS/MS for soils [7] or for aqueous slurries of soils [12,15] or sediments [13] using HS-SPME coupled to GC-ECD.

Linear response ranges were studied by spiking aqueous solutions and real estuarine sediment samples with increasing amounts of standard solution until linearity was lost (R^2 < 0.98). The wider ranges obtained were 0.5–1000 ng L^{-1} for OCPs in aqueous solution and 0.02–1000 ng g^{-1} of OCPs in sediment samples, depending on the OCP (Table 4). Therefore, this method provided linear range

Table 4
Characteristics of the optimized methods

OCP	GC–MS					GC-ECD				
	Linear range[a] ($R^2 \geq 0.98$)	Linear range[b] ($R^2 \geq 0.98$)	LOD (ng g^{-1})	LOQ (ng g^{-1})	RSD (%)	Linear range[a] ($R^2 \geq 0.98$)	Linear range[b] ($R^2 \geq 0.98$)	LOD (ng g^{-1})	LOQ (ng g^{-1})	RSD (%)
α-Lindane	3–800	0.15–1000	0.04	0.15	9	4–300	0.20–102	0.09	0.20	13
γ-Lindane	8–800	0.35–1000	0.11	0.35	7	1–200	0.06–255	0.05	0.06	18
Heptachlor	9–600	0.36–1000	0.11	0.36	17	10–150	0.51–255	0.26	0.51	16
Aldrin	3–1000	0.15–1000	0.05	0.15	9	2–100	0.10–55	0.04	0.10	15
Heptachlor epoxide	0.3–800	0.02–1000	0.01	0.02	12	3–100	0.15–25	0.06	0.15	6
DDE	0.5–1000	0.02–1000	0.005	0.02	8	0.7–100	0.03–28	0.02	0.03	7
Dieldrin	0.2–800	0.09–1000	0.04	0.09	14	2–100	0.12–31	0.05	0.12	11
Endrin	2–1000	0.45–1000	0.04	0.45	16	0.2–300	0.01–53	0.01	0.01	11
DDD	2–1000	0.11–1000	0.04	0.11	17	1–150	0.07–53	0.03	0.07	11
DDT	1–1000	0.06–1000	0.04	0.06	14	0.8–150	0.04–110	0.02	0.04	9

[a] In aqueous solution, as ng of OCP *per* liter of solution.
[b] In sediment, as ng of OCP *per* gram of dry sediment.

Table 5
Results obtained for certified reference materials

OCP	Metranal 16 reference values (μg g^{-1})	Metranal 16[a] (μg g^{-1}) by GC–MS	Metranal 16[a] (μg g^{-1}) by GC-ECD	CNS300-04-100 reference values (ng g^{-1})	CNS300-04-100[a] (ng g^{-1}) by GC–MS	CNS300-04-100[a] (ng g^{-1}) by GC-ECD
α-Lindane	16 ± 3	16 ± 3	17 ± 3	284 ± 70	287 ± 20	288 ± 37
γ-Lindane	44 ± 8	43 ± 3	43 ± 7	363 ± 84	315 ± 34	323 ± 57
Heptachlor		45 ± 6	39 ± 6	398 ± 107	355 ± 62	461 ± 75
Aldrin		4.0 ± 0.3	3.1 ± 0.3	125 ± 28	121 ± 11	95 ± 14
Heptachlor epoxide			11 ± 1	49 ± 15	50 ± 6	46 ± 3
DDE	39 ± 8	38 ± 7	41 ± 2	299 ± 55	312 ± 22	286 ± 20
Dieldrin	45 ± 9	46 ± 6	48 ± 7	370 ± 77	402 ± 31	361 ± 41
Endrin	19 ± 4		20 ± 3	370 ± 101	416 ± 67	395 ± 46
DDD	39 ± 8	36 ± 5	39 ± 2	287 ± 33	278 ± 102	277 ± 30
DDT	83 ± 16	72 ± 14	79 ± 10			

[a] Mean and standard deviation ($n = 6$) expressed in mass of OCP *per* gram of dry sediment.

larger than those tested previously for soils [12,15] and sediment [13] in slurries using ECD. The linear ranges in aqueous solution were narrower than those for sediments because the first ones only reflected the response of the equipment while the second ones enhanced all the experimental procedure.

Assays of repeatability and reproducibility according to IUPAC guide [17] were performed using reference sediment samples. The method presented relative standard deviation (RSD) lower than 17%, with better repeatability than reproducibility as expected.

To evaluate the accuracy of the method, commercially available reference sediments with different characteristics, Metranal™ 16 and CRM CNS300-04-100 were analyzed. For the different pesticides present in the reference sediments, Table 5 shows that concentration values were obtained inside the reference ranges.

The method was applied to analysis of OCPs in sediments from Minho and Cávado rivers estuaries, north of Portugal. Samples organic contents were of 0.6% and 6% for sandy and muddy Minho sediments, respectively, and of 11% for muddy Cávado sediment. As Table 6 shows, sandy sediments from Minho river estuary displayed measurable levels of heptachlor and aldrin, whereas muddy sediments from the same estuary displayed the same compounds but also γ-lindane, DDT and DDE. However, the concentrations were very low in both cases (≤2.7 ng of OCP *per* gram of dried sediment) the highest values being of aldrin and heptachlor. Muddy sediment from Cávado river estuary presented measurable levels of heptachlor, dieldrin, DDE, DDD and DDT, the highest value (4 ng g^{-1}) occurring for heptachlor. These results demonstrated the presence of some avoided OCPs in the tested estuarine sediments, mainly in muddy ones, though at low levels.

Therefore, the proposed method overcomes the problem of inefficient OCPs extraction from complex matrices, like those of estuarine sediments, which could difficult or even hinder direct

Table 6
Results obtained by GC–MS for real estuarine sediments

OCP	Minho river		Cávado river
	Sandy sediment[a] (ng g^{-1})	Muddy sediment[a] (ng g^{-1})	Muddy sediment[a] (ng g^{-1})
α-Lindane	<LOD	<LOD	<LOD
γ-Lindane	<LOD	1.5 ± 0.3	<LOD
Heptachlor	0.6 ± 0.2	2.6 ± 0.1	4.0 ± 0.9
Aldrin	2.7 ± 0.4	2.3 ± 0.1	<LOD
Heptachlor epoxide	<LOD	<LOD	<LOD
DDE	<LOD	0.10 ± 0.06	3 ± 1
Dieldrin	<LOD	<LOD	1.5 ± 0.8
Endrin	<LOD	<LOD	<LOD
DDD	<LOD	<LOD	1.4 ± 0.2
DDT	<LOD	0.3 ± 0.1	2.3 ± 0.5

[a] Concentration expressed in ng of OCP *per* gram of dry sediment.

application of the HS-SPME of sediment slurries, as mentioned in introduction.

In a previous work carried out only in soils [7], which has employed MAE and HS-SPME coupled to GC–MS/MS, after MAE a step of filtration of the supernatant, evaporation to dryness of the solvent extraction mixture and redissolution in a solvent suitable for HS-SPME has been required additionally. In this work, MAE combined with sulfur elimination combined with automatic HS-SPME dispensed further clean-up and pre-concentration steps, resulting in a quick and efficient procedure of sample preparation for GC–MS determination of OCPs in sediments from different origins and characteristics.

The described procedure of sample preparation was further combined with GC-ECD and applied to the same samples (either reference sediments or real estuarine sediments) for comparison purposes. For the real estuarine sediments the levels of quantified OCPs were not significantly different of those shown in Table 6. For the two tested reference sediments acceptable values were also obtained by GC-ECD (Table 5), this system providing LOD and LOQ of the same order of magnitude as those obtained with GC–MS (Table 4). However, the linear response ranges were much narrower than those provided by GC–MS, as it was expected owing to the characteristics of the two detectors.

In conclusion, the approach here described resulted in relatively fast and effective method for simultaneous determination of ten OCPs in sediments with varied characteristics (grain size and organic matter content) being suitable for routine analysis.

Acknowledgment

The authors acknowledge the Portuguese Foundation for Science and Technology for the fellowships awarded to Rafael Evangelista (Programa PRAXIS XXI, SFRH/BD/20163/2004) and equipment (CONC-REEQ/304/2001 Project).

References

[1] R. Zhou, L. Zhu, Q. Kong, Chemosphere 68 (2007) 838.
[2] Y.F. Li, R.W. Macdonald, Science of The total Environment 342 (2005) 87.
[3] D. Haynes, J.E. Johnson, Marine Pollution Bulletin 41 (2000) 267.
[4] A. Tor, M.E. Aydin, S. Özcan, Analytica Chimica Acta 559 (2006) 173.
[5] M.C. Vagi, A.S. Petsas, M.N. Kostopoulou, M.K. Karamanoli, T.D. Lekkas, Desalination 210 (2007) 146.
[6] M. Numata, T. Yarita, Y. Aoyagi, A. Takatsu, Analytical Sciences 20 (2004) 793.
[7] P. Herbert, S. Morais, P. Paíga, A. Alves, L. Santos, Analytical and Bioanalytical Chemistry 384 (2006) 810.
[8] C. Basheer, J.P. Obbard, H.K. Lee, Journal of Chromatography A 1068 (2005) 221.
[9] S. Jayaraman, R.J. Pruell, R. McKinney, Chemosphere 44 (2001) 181.
[10] G. Ouyang, J. Pawliszyn, Analytical and Bioanalytical Chemistry 386 (2006) 1059.
[11] R.-A. Doong, P.-L. Liao, Journal of Chromatography A 918 (2001) 177.
[12] R. Zhao, X. Wang, J. Yuan, T. Jiang, S. Fu, X. Xu, Analytical and Bioanalytical Chemistry 384 (2006) 1584.
[13] S.M. Chang, R.A. Doong, Chemosphere 62 (2006) 1869.
[14] B. Pan, W.X. Liu, Z. Shi, J. Cao, W.R. Shen, B.P. Qing, R. Sun, S. Tao, Journal of Environmental Science and Health. Part B. Pesticides, Food Contaminants, and Agricultural Wastes 39 (2004) 353.
[15] R.A. Doong, P.L. Liao, Journal of Chromatography A 918 (2001) 177.
[16] A.A. Boyd-Boland, S. Magdic, J.B. Pawliszyn, Analyst 121 (1996) 929.
[17] M. Thompson, S.L.R. Ellison, R. Wood, Pure and Applied Chemistry 74 (2002) 835.

Talanta 76 (2008) 1083–1087

Contents lists available at ScienceDirect

Talanta

journal homepage: www.elsevier.com/locate/talanta

Electrochemiluminescence detection of dichlorvos pesticide in luminol–CTAB medium

Xiao-mei Chen [a], Zhi-jie Lin [a], Zhi-min Cai [a], Xi Chen [a,b,*], Xiao-ru Wang [a]

[a] Department of Chemistry and Key Laboratory of Analytical Sciences of the Ministry of Education, College of Chemistry and Chemical Engineering, Xiamen University, Xiamen 361005, China
[b] State Key Laboratory of Marine Environmental Science, Xiamen University, Xiamen 361005, China

ARTICLE INFO

Article history:
Received 18 February 2008
Received in revised form 29 April 2008
Accepted 5 May 2008
Available online 16 May 2008

Keywords:
Electrochemiluminescence
Dichlorvos pesticide
Luminol
Glassy carbon electrode

ABSTRACT

A simple, novel electrochemiluminescence (ECL) method for the detection of dichlorvos pesticide (DDVP) with high sensitivity was discovered. Detection was carried out in a static ECL system, in which a glassy carbon electrode was selected as the working electrode. ECL parameters, including the concentrations of cetyrltrimethylammonium bromide and luminol, the solution pH, and the scan rate of the applied potential, were optimized. Under these optimal conditions, the linear response of ECL-emission versus DDVP concentration was valid in the range 5–8000 ng/L (r^2 = 0.9982) with a relative standard deviation of 4.3% at 2000 ng/L (n = 10), yielding a detection limit (S/N = 3) of 0.42 ng/L. The ECL emission was caused by a radical reaction process, in which the dissolved oxygen in the luminol solution reacted with the DDVP and generated free radicals. The free radicals reacted with the luminol anion and yielded the luminol radical. The approach presented was successfully applied to the determination of DDVP residues in vegetable samples.

1. Introduction

In recent years, the use of organophosphorus pesticides (OPPs) such as dichlorvos pesticide (DDVP) has become widespread because of their low persistence in the environment [1]. However, they have a highly acute toxicity since they cause protein adduction, and the lasting nature of this makes them a candidate responsible for the production of continuing ill health [2]. The dermal toxicity of DDVP is similar to its oral toxicity and dermal exposure places a premium on cancer [3]. Because of these possible health risks, efforts are continuing towards the development of rapid and accurate analytical methods for the determination of OPPs.

Several approaches have been developed for DDVP determination including gas chromatography [4–9], high performance liquid chromatography [10–12], fluorescence spectrometry [13,14] and chemiluminescence (CL) [15–17]. Generally, the above approaches are performed in centralized laboratories, requiring extensive labor and analytical resources, and often result in a lengthy turnaround time. Although several immunoassays and enzymatic methods have also been reported [18–25], the use of expensive enzymes such as acetylcholinesterase limits their application. As a result, a novel, simple, and sensitive method with a low cost is of considerable interest.

Electrogenerated chemiluminescence (ECL) is a well-known high sensitivity detection method depending on the generation of an optical signal triggered by an electrochemical reaction [26,27]. To our knowledge, there has been no report concerning the detection of DDVP using ECL. Based on our experiment results, at an applied potential of −0.38 V, the oxygen can be reduced to OOH^- on a glassy carbon (GC) working electrode [28–30], which could enhance the ECL reaction of luminol and DDVP. The concentrations of cetyrltrimethylammonium bromide (CTAB) and luminol, the solution pH and the applied potential scan rate affected the ECL intensity. The experimental results revealed that the linear response of ECL-emission versus DDVP concentration was valid in the range 5–8000 ng/L, and the detection limit (S/N = 3) was 0.42 ng/L. The ECL mechanism of DDVP in luminol solution was also discussed. The method was successfully applied to the determination of DDVP residue in vegetable samples.

2. Experimental

2.1. Chemicals and solutions

Luminol was purchased from Wake Pure Chemicals Co. Ltd. (Osaka, Japan). A 1.0×10^{-2} mol/L luminol stock solution was pre-

* Corresponding author at: Department of Chemistry and Key Laboratory of Analytical Sciences of the Ministry of Education, College of Chemistry and Chemical Engineering, Xiamen University, Xiamen, 361005, China. Tel.: +86 592 2184530; fax: +86 592 2184530.
E-mail address: xichen@xmu.edu.cn (X. Chen).

0039-9140/$ – see front matter © 2008 Elsevier B.V. All rights reserved.
doi:10.1016/j.talanta.2008.05.007

pared by dissolving luminol in 0.1 mol/L sodium hydroxide solution (NaOH) and diluted to 1.0×10^{-4} mol/L with pure water. DDVP was obtained from China Standard Technology Development Corp. (Beijing, China). The standard solution of DDVP (0.001 g/L) was prepared by diluting DDVP (0.1 g/L) with acetone. Tween-100, polyvinylol (PVA), polyvinylpyrrolidone (PVP), sodium dodecyl sulphate (SDS), cetyrltrimethylammonium chlorine (CTAC) and CTAB were obtained from Sinopharm Chemical Reagent Co. Ltd. (Guangzhou, China). The pH of the working solution was adjusted using NaOH solution. GC plates (1 cm (W) × 1 cm (L) × 0.2 cm (H)) were purchased from BAS Co. Ltd. (Japan). All other reagents were of analytical grade. The pure water for solution preparation was prepared using a Millipore Autopure WR600A (Millipore Ltd., USA).

2.2. Sample preparation

Cabbages were purchased from a local supermarket. Each cabbage was divided into three samples; each weighing 10 g. Different amounts of DDVP were spayed onto each of the three samples. All samples were processed using the following procedure: the cabbage were first placed in a ventilation cabinet for 2 h at 25 °C, then sample leaves were eluted with pure water for 15 s, and finally, the eluted solution was collected and analyzed.

2.3. Preparation of the GC electrode

For the electrochemical (EC) or ECL experiments, a GC electrode was employed as a working electrode, and was fabricated as follows: a strip of copper adhesive tape was attached to a GC plate and used as an electrical connection; a piece of a waterproof adhesive tape with a 5 mm diameter circular window was then attached to the GC plate. During electrochemical measurements, the working surface of the GC plate in contact with the solution was thus the exposed area of 19.63 mm^2.

2.4. EC and ECL measurements

Cyclic voltammetry (CV) and ECL measurements were performed using a homemade ECL/EC system, which was assembled from an electrochemical working station (CHI 660B, Chenhua Inc., China) and a model GD-1 luminometer (Ruike electronic equipment Co., China). As shown in Fig. 1, a three-electrode system employing the GC working electrode was assembled in a T-type ECL cell.

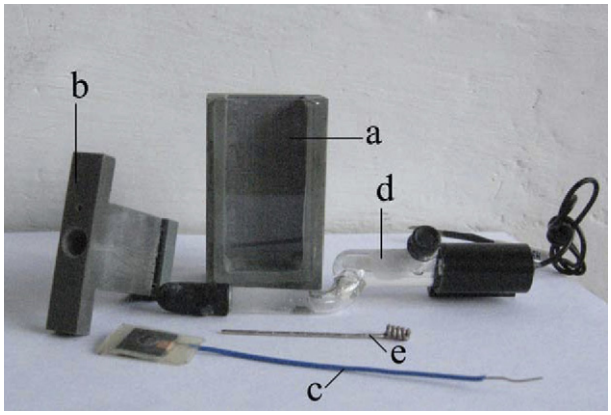

Fig. 1. Electrochemiluminescence cell assembly: (a) outer cell, (b) T-type cell body, (c) working electrode, (d) reference electrode, and (e) counter electrode.

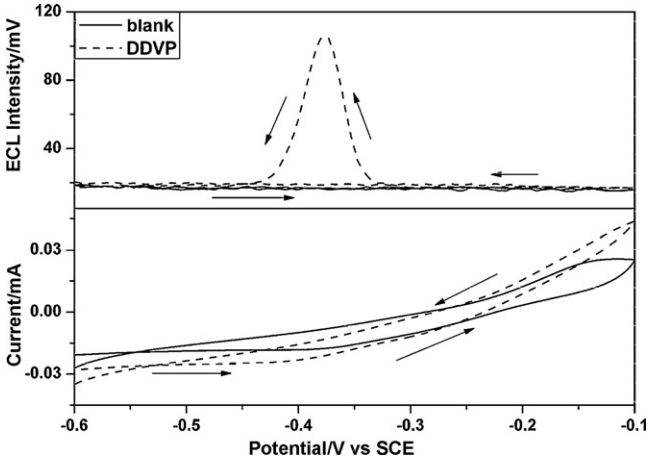

Fig. 2. I_{ECL}/E and CV curves of blank (dotted line) and DDVP solution (solid line). Experimental conditions: DDVP 2 ng/mL; CTAB 0.05 mol/L; pH 13.5, luminol 1.0 μmol/L; scan rate 20 mV/s, high voltage applied to the PMT, −800 V.

3. Results and discussion

3.1. ECL behavior

I_{ECL}/E and CV curves obtained with and without DDVP solution at pH 13.5 using the GC electrode are shown in Fig. 2. In the I_{ECL}/E curves, a CL intensity of about 20 mV was obtained from both the blank solution and the DDVP solution. Comparatively, a clear ECL signal at −0.38 V was observed in the cathodic scan when the solution contained DDVP. The results indicated that the ECL signal at −0.38 V was applicable to the detection of DDVP.

3.2. Effect of pH

The dissociation constants of luminol are pK_{a1} 6.00 and pK_{a2} 13.00, therefore, a higher pH favors the formation of the luminol anion [31]. Based on the reaction mechanism of luminol ECL ($LH^- - e^- \rightarrow LH^\bullet \rightarrow L^{\bullet -} + H^+$), a higher pH is helpful for the generation of luminol radicals. At the same time, at more basic concentrations, more hydroxide ions exist on the electrode surface, which can interfere with the adsorption of luminol. Based on these considerations, the solution pH was optimized for the best ECL response. Among several alkaline buffer solutions (sodium hydroxide, phosphate and borax), the experimental results showed that sodium hydroxide solution was the most suitable medium for ECL measurement since the higher pH (>12.0) could be achieved by diluting sodium hydroxide solution. As shown in Fig. 3, ECL intensity was increased with the increase of pH and the maximum signal

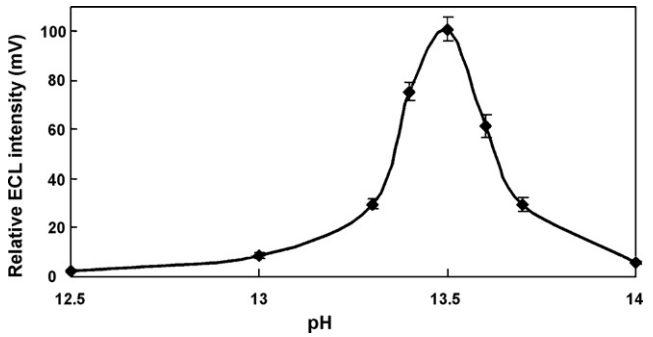

Fig. 3. Effect of solution pH on the ECL response of DDVP. Other experimental conditions were the same as in Fig. 2.

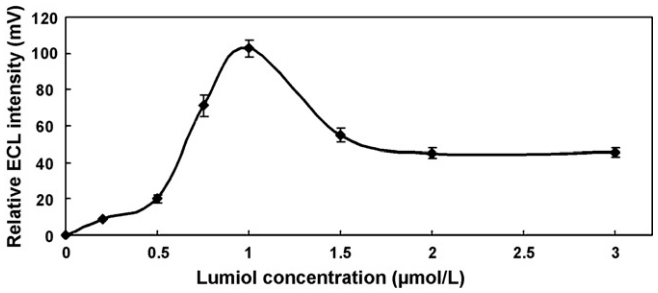

Fig. 4. ECL response of DDVP towards various concentrations of luminol. Other experimental conditions were the same as in Fig. 2.

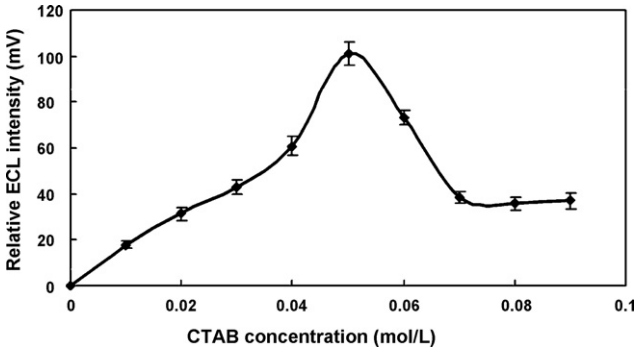

Fig. 5. Influence of CTAB concentration on the ECL response of DDVP. Experimental conditions were the same as in Fig. 2 except for the CTAB concentration.

was obtained at pH 13.5. In the following experiments, sodium hydroxide solution with pH 13.5 was selected.

3.3. Effect of the concentration of luminol

Luminol played a key role in the ECL determination of DDVP. Correspondingly, its concentration greatly affected the ECL intensity. The effect of luminol concentration (from 0 to 3.0 μmol/L) on the relative ECL intensity was studied. As can be seen from Fig. 4, the relative intensity increased with the increase of luminol concentration, whereas it was reduced at concentrations higher than 1.0 μmol/L. Based on the experimental results in the applied potential range of −0.6 to −0.1 V, higher luminescence intensity could be obtained when the luminol concentration was higher than 2.0 μmol/L, and this had an obvious effect on the ECL signal at −0.38 V. Therefore, a luminol concentration of 1.0 μmol/L was chosen.

3.4. Effect of surfactants

Experimental results indicated that the species and concentration of surfactant used affected the ECL of luminol. In the medium without any surfactant, a very weak luminol ECL signal was obtained, and when the luminol–DDVP ECL intensity was compared in media containing different surfactants such as Tween-100, PVA, PVP, CTAB, CTAC and SDS, only the cation surfactants like CTAC, CTAB could obviously enhance the ECL intensity, and CTAB was the best surfactant. This result suggested that the CTA^+ adsorbed the dissociated luminol anion and the DDV anion to form a reversed micelle microreactor, which concentrated the reactants and made them react effectively to generate ECL emission. The fact that the neutral and anionic surfactants could not enhance ECL intensity also proved this.

An optimized concentration of CTAB was selected for ECL measurement. As shown in Fig. 5, when 0.05 mol/L CTAB was employed, the brightest relative ECL intensity was obtained. In general, when the concentration of CTAB was slightly higher than its second critical micelle concentration (cmc: 2.1×10^{-2} mol/L), the clubbed micelles increased the local concentration of luminol and DDVP by the hydrophilic micelle, which protected the energy of the excited state 3-aminophthalate anion. In addition, the experimental results indicated that when the CTAB concentration exceeded 0.05 mol/L, the higher CTAB concentration caused a relative ECL intensity decrease because of CTAB crystallization. CTAB crystals blocked and reflected the light from ECL emission.

3.5. Effect of the applied potential scan rate and scan range

The applied potential scan rate affected the ECL intensity of luminol–DDVP. As shown in Fig. 6, in the scan rate range 0.01–0.05 V/s, the ECL intensity reached its highest value at the rate of 0.02 V/s and decreased drastically if the scan rate was over 0.03 V/s. The scan rate was maintained at 0.02 V/s in the following study, therefore.

The effect of the potential scan range on the ECL intensity was investigated. If the potential scan range of −1.0 to 1.0 V was selected, four peaks appeared in the ECL curve. Except for the ECL peak at −0.38 V, there was no obvious ECL difference in the solutions with and without DDVP solution. In the selected potential scan range, a bright and broad ECL emission was observed at about 0.6 V. The ECL peak had an obvious effect on the detection of DDVP at −0.38 V since the ECL peaks overlapped. Previous study suggests that oxidative species are necessary for the conversion of the luminol radical into AP^{*2-} [32]. In the negative scan direction, OOH^- was produced at a negative potential (about −0.40 V); meanwhile, no other peak could be found in the potential range from −0.6 to −0.1 V. An applied potential scan range of −0.6 to −0.1 V was helpful in avoiding the effect of the ECL peak at 0.6 V.

3.6. Calibration curve and detection limit

Under optimized conditions, ECL responses to different concentrations of DDVP solution were measured. A typical ECL response with different concentrations of DDVP solution is presented in Fig. 7. The linear range between the DDVP concentration and the ECL intensity was from 5 to 8000 ng/L, and the regression equation was $\log I = 0.3575 + 0.4838 \times \log C_{DDVP}$ (C_{DDVP}: ng/L) with a correlation coefficient of 0.9982. The relative standard deviation (R.S.D.) was 4.3% for 10 replicate analyses of 2000 ng/L DDVP. The limit of detection (S/N = 3) for DDVP was 0.42 ng/L.

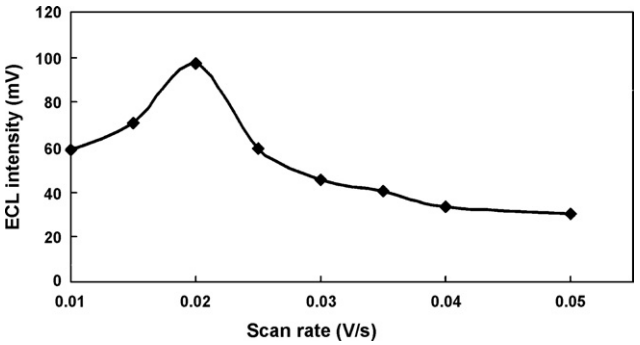

Fig. 6. Scan rate effects on ECL response of DDVP. Experimental conditions were the same with Fig. 2 without the scan rate.

Table 1
Recovery tests of DDVP for cabbage samples

Sample no.	Residue ($g\,mL^{-1}$)	Added ($\times10^{-9}\,g\,mL^{-1}$)	Found ($\times10^{-9}\,g\,mL^{-1}$)	Recovery (%)	R.S.D. (%) ($n=5$)
	–	1.00	0.94	94.00	3.29
1		3.00	2.85	95.00	2.74
		5.00	5.13	102.60	2.68
	–	1.00	0.96	96.00	4.15
2		3.00	2.83	94.33	2.93
		5.00	4.97	99.40	3.17
	–	1.00	0.95	95.00	4.89
3		3.00	2.79	93.00	3.15
		5.00	5.19	103.8	2.97

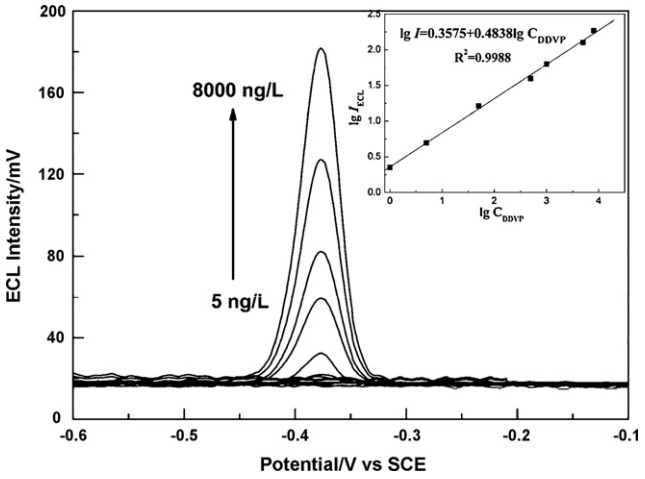

Fig. 7. Calibration curve of DDVP concentration and ECL intensity.

3.7. Interference studies

The interference of co-existing substances was taken into account for applications. In the study, 2.0 ng/mL DDVP was selected as a typical concentration. The tolerant maximum concentration of the co-existing substance was determined, in which the substance caused an ECL intensity change of approximately ±5%. Based on the experimental results, the tolerant ratio of a co-existing substance to 2.0 ng/mL DDVP was found to be 1000-fold for Ba^{2+}, K^+ and Na^+, 200-fold for Mg^{2+}, NH_4^+ and Ca^{2+}, 100-fold for Zn^{2+} and 10-fold for Fe^{3+}, glucose and fructose. We also study the effect of the inorganic anions like NO_3^-, SO_4^{2-}, Cl^-, CO_3^{2-} and PO_4^{3-}, and found that they did not affect the results. Though Co^{2+}, Cr^{3+} and Cu^{2+} cause the effect (onefold), but in the real sample, their concentrations are so low and we could eliminate them by using a cation exchange column. In our study, other organophosphorus pesticides in this optimized condition are hardly to be detected, so the method to detect DDVP is very selective.

3.8. Sample analysis

Recovery tests were performed for each sample group by adding a known amount of DDVP into the elution solution. A calibration graph as shown in Fig. 7 was applied for calculation of the DDVP concentration. As shown in Table 1, the recoveries for different DDVP concentrations varied from 93 to 103.8%, and the R.S.D. ($n=5$) ranged from 2.68 to 4.89%.

3.9. Possible ECL mechanism of luminol–DDVP

Zhang et al. [15] report the CL mechanism of the luminol and OPP. Generally, the P–O group in DDVP was oxidized by OOH^- in an alkaline solution at first, and then the superphosphate reacted with the luminol anion to generate the excited 3-aminophthalate that yielded CL emission. In this study, a possible ECL mechanism was proposed and is shown in Scheme 1. Based on the experiment results, the ECL signal only appeared in the scan direction from negative to −0.38 V. This proved that the luminescence was cause by the reaction of OOH^- but not $O_2^{\bullet-}$ (OOH^- is oxidized to $O_2^{\bullet-}$ in the positive potential direction [30]). To further support the proposed reaction mechanism, the effect of the applied potential with different scan directions was studied. The experimental results showed

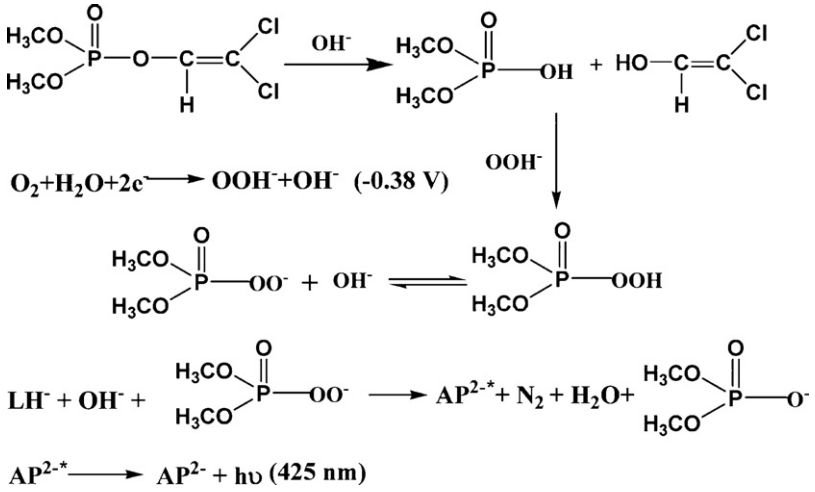

Scheme 1. Possible mechanism for the detection of DDVP using a luminol ECL system.

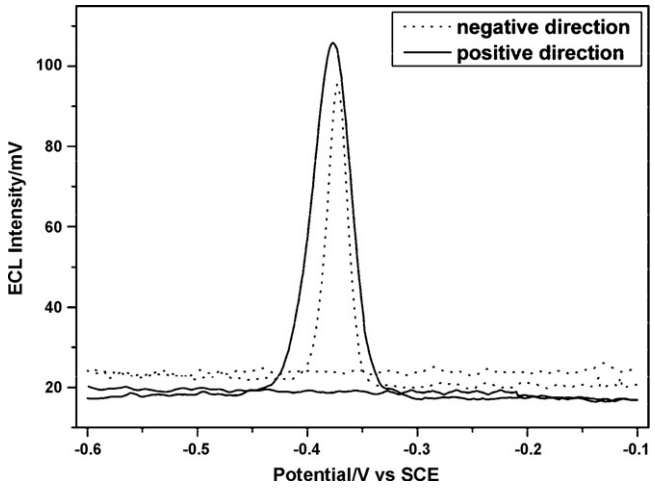

Fig. 8. I_{ECL}/E curves of DDVP solution with initial negative scan direction (dotted line) and positive scan direction (solid line).

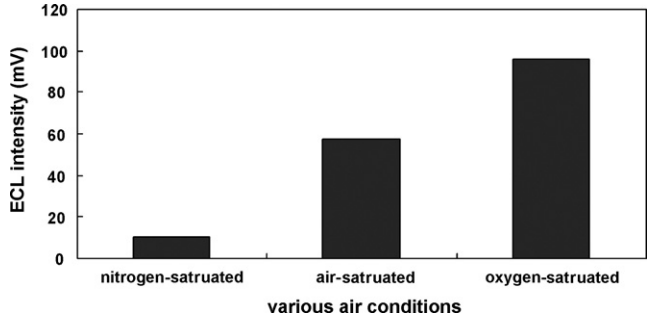

Fig. 9. ECL intensity of DDVP solution under saturated air, oxygen and nitrogen atmospheres, respectively.

that there was no obvious difference in the ECL intensity when the positive or negative direction potential scan was selected. In Fig. 8, as indicated in the solid line, the ECL signal was generated in the positive direction potential scan from −0.6 to −0.1 V and then back to the initial potential of −0.6 V. The ECL signal could be clearly observed and its intensity remained the same in the negative direction potential scan (dotted line in Fig. 8). The result indicated that the electrochemically generated products during the positive potential scan did not affect ECL generation. In addition, the difference of ECL intensities in nitrogen, air or oxygen saturated solution was compared (Fig. 9). Experimental results indicated that the concentration of oxygen in the solution greatly affected the ECL emission. The ECL intensity increased remarkably in O_2 saturated solution, but decreased in N_2 saturated solution. Obviously, higher concentration of oxygen in the solution increased the generation of OOH^- at the potential of −0.38 V, which was helpful to the generation of a bright ECL emission.

4. Conclusion

A novel ECL approach was proposed for the determination of DDVP based on its oxidation reaction with luminol and hydrogen peroxide in a CTAB alkaline medium. In addition to its simplicity, rapidity and satisfactory accuracy, the method afforded very high sensitivity in the determination of DDVP, which raises a new potential for the analytical applications of ECL detection in environmental samples and pesticide residues.

Acknowledgements

This research work was financially supported by the National Nature Scientific Foundation of China (No. 20775064), the Program for New Century Excellent Talents in University of China (NCET) and NFFTBS (No. J0630429), which are gratefully acknowledged. Furthermore, we would like to extend our thanks to Professor John Hodgkiss of The University of Hong Kong for his assistance with English.

References

[1] M. Yamashita, M. Yamashita, J. Tanaka, Y. Ando, Toxicol. Appl. 39 (1997) 84.
[2] W.G. Cater, M. Tarhoni, A.J. Rathbone, D.E. Ray, Hum. Exp. Toxicol. 26 (2007) 347.
[3] E.Y. El-Behissy, R.D. King, M.M. Ahmed, A.M. Youssef, J. Agric. Food Chem. 49 (2001) 1239.
[4] V. Kocourek, J. Hajlová, K. Holadová, J. Poustka, J. Chromatogr. A 800 (1998) 297.
[5] Q. Xiao, B. Hu, C. Yu, L. Xia, Z. Jiang, Talanta 69 (2006) 848.
[6] Y. Chen, Y. Su, J.F. Jen, J. Chromatogr. A 976 (2002) 349.
[7] N. Campillo, R. Peñalver, M. Hernández-Córdoba, Talanta 71 (2007) 1417.
[8] N. Fidalgo-Used, E. Blanco-González, A. Sanz-Medel, Talanta 70 (2006) 1057.
[9] J. Aybar-Muñoz, E. Fernández-González, L.E. García-Ayuso, A. González-Casado, L. Cuadros-Rodríguez, Talanta 60 (2003) 433.
[10] R. Carabias-Martinez, E. Rodriguez-Gonzalo, P.H. Paniagua-Marcos, J. Hernandez-Mendez, J. Chromatogr. A 869 (2000) 427.
[11] G. Huang, J. Ouyang, W.R.G. Baeyens, Y. Yang, C. Tao, Anal. Chim. Acta 474 (2002) 21.
[12] Y. Cho, N. Matsuoka, A. Kamiya, Chem. Pharm. Bull. 45 (1997) 737.
[13] P. Tavassoli, R. Snoek, M. Ray, L.G. Rao, Prostate 67 (2007) 416.
[14] S. Jin, Z. Xu, J. Chen, X. Liang, Y. Wu, X. Qian, Anal. Chim. Acta 523 (2004) 117.
[15] J. Wang, C. Zhang, H. Wang, F. Yang, X. Zhang, Talanta 54 (2001) 1185.
[16] T. Perez-Ruiz, C. Martinez-Lozano, M.D. Garcia, Anal. Chim. Acta 584 (2007) 275.
[17] B. Li, Y. He, C. Xu, Talanta 72 (2007) 223.
[18] M. Del Carlo, A. Pepe, M. De Gregorio, M. Mascini, J.L. Marty, D. Fournier, A. Visconti, D. Compagnone, J. Food Protect. 69 (2006) 1406.
[19] L. Pogacnik, M. Franko, Talanta 54 (2001) 631.
[20] A. Vakurov, C.E. Simpson, C.L. Daly, T.D. Gibson, P.A. Millner, Biosens. Bioelectron. 20 (2004) 1118.
[21] J.C. Vidal, S. Esteban, J. Gil, J.R. Castillo, Talanta 68 (2006) 791.
[22] W.R. Everett, G.A. Rechnitz, Anal. Chem. 70 (1998) 807.
[23] G. Liu, Y. Lin, Anal. Chem. 78 (2006) 835.
[24] M. Shi, J. Xu, S. Zhang, B. Liu, J. Kong, Talanta 68 (2006) 1089.
[25] G. Valdés-Ramírez, D. Fournier, M.T. Ramírez-Silva, J.L. Marty, Talanta 74 (2008) 741.
[26] B.A. Gorman, P.S. Francis, N.W. Barnett, Analyst 131 (2006) 616.
[27] N.E. Tokel, A.J. Bard, J. Am. Chem. Soc. 94 (1972) 2862.
[28] H. Cui, G.Z. Zou, X.Q. Lin, Anal. Chem. 75 (2003) 324.
[29] H. Cui, Y. Xu, Z.F. Zhang, Anal. Chem. 76 (2004) 4002.
[30] J.E. Vitt, D.C. Johnson, R.C. Engstrom, J. Electrochem. Soc. 138 (1991) 1637.
[31] S. Sakura, Anal. Chem. Acta 262 (1992) 49.
[32] K.E. Haapakka, J.J. Kankare, Anal. Chim. Acta 138 (1982) 263.

Talanta 76 (2008) 1065–1069

Contents lists available at ScienceDirect

Talanta

journal homepage: www.elsevier.com/locate/talanta

The promotion effect of titania nanoparticles on the direct electrochemistry of lactate dehydrogenase sol–gel modified gold electrode

Jiongjia Cheng[a], Junwei Di[a,b], Jianhui Hong[a], Kaian Yao[a], Yongbo Sun[a], Jingyue Zhuang[a], Quan Xu[a], Huie Zheng[a], Shuping Bi[a,*]

[a] School of Chemistry & Chemical Engineering, State Key Laboratory of Coordination Chemistry of China & Key Laboratory of MOE for Life Science, Nanjing University, Nanjing 210093, China
[b] Department of Chemistry, Suzhou University, Suzhou 215006, China

ARTICLE INFO

Article history:
Received 30 January 2008
Received in revised form 29 April 2008
Accepted 5 May 2008
Available online 13 May 2008

Keywords:
Lactate dehydrogenase (LDH)
Direct electrochemistry
Sol–Gel
Nano-TiO_2
Lactic acid

ABSTRACT

The promotion effect of titania nanoparticles (nano-TiO_2) on the direct electron transfer between lactate dehydrogenase (LDH) and the silica sol–gel modified gold electrode was investigated by adding nano-TiO_2 (50 nm) in the modification process. This nano-TiO_2–LDH electrode showed a pair of quasi-reversible cyclic voltammetry peaks with the formal potential of 70 mV (vs. SCE). Compared to the previous result of LDH modified electrode with only an irreversible cathodic peak, an anodic peak appeared and the cathodic peak potential shifted to the positive direction on this nano-TiO_2–LDH electrode, which demonstrated that the direct electrochemistry of LDH was enhanced by nano-TiO_2. We supposed that the direct electrochemistry of LDH may be due to the redox reaction of some electroactive amino acids in the LDH molecule. The surface morphologies of electrodes characterized by SEM indicated that LDH was successfully immobilized on the sol–gel matrix and also had some interactions with nano-TiO_2. This electrode can be used as a biosensor for the determination of lactic acid. The calibration range of lactic acid was from 1.0 to 20 $\mu mol\,L^{-1}$ and the detection limit was 0.4 $\mu mol\,L^{-1}$. Meanwhile, the small K_m^{app} value (2.2 $\mu mol\,L^{-1}$) suggested that LDH possessed high enzymatic activity and good affinity to lactic acid owing to the promotion effect of nano-TiO_2.

1. Introduction

The direct electrochemistry of enzymes has become a subject of extensive research owing to its great significances in the kinetic studies of biological redox process and the fabrication of third-generation biosensors [1–3]. Nowadays, more and more attentions have focused on this research [4–12]. Common enzyme contains redox center in its molecule to have the direct electrochemistry, and the redox center also acts as the active site for the catalysis on substrates [9–12]. But lactate dehydrogenase (LDH) (EC 1.1.1.27) is different from these kinds of enzyme. The conversion between pyruvate and lactate catalyzed by LDH must be added NADH (or NAD^+) as a cofactor by combining it in the modifying process or into the experimental solutions [13–16]. Considering the key role of LDH in the areas of medicine, biology and environmental assessment [17–19], the study of direct electron transfer (DET) between LDH and electrode will give a fundamental theoretical understanding of LDH and also stimulate its potential application.

However, the DET rates of enzymes are usually prohibitively slow because of the deep burying of the electroactive prosthetic groups, the adsorptive denaturation of enzymes onto electrodes, and the unfavourable orientations at the electrodes [7,8]. Great effort has been made to enhance the DET between enzymes and electrode, for example, the protein-film techniques combined with nanotechnology provide a promising access due to the high electrical conductivity, chemical stability, and significant mechanical strength of nanomaterials. Various kinds of nanomaterials, such as carbon nanotubes [20,21], gold nanoparticles [22,23], titania nanoparticles (nano-TiO_2) [24,25] and clay nanoparticles [26,27] are generally applied to promote the DET. Among these nanomaterials, the nano-TiO_2 has been widely used in solar cell, electronic devices, catalyst supports and immobilization of proteins and enzymes for bioanalytical applications because of its remarkable chemical, electronic, and optical characteristics [25,28–34]. Moreover, the investigation on nano-TiO_2 has also shown that it could be used as a good promoter for the DET of enzymes due to its good biocompatibility, specific binding with

* Corresponding author. Tel.: +86 25 86205840; fax: +86 25 83317761.
E-mail address: bisp@nju.edu.cn (S. Bi).

0039-9140/$ – see front matter © 2008 Elsevier B.V. All rights reserved.
doi:10.1016/j.talanta.2008.05.006

molecules, high loading and less denaturation of absorbed proteins [24].

In this paper, we study on the promotion effect of nanomaterial on the direct electrochemistry of LDH. Compared with our previous work about the irreversible direct electrochemistry of LDH sol–gel modified electrode [35], we found that the DET of LDH was promoted by immobilizing LDH on the gold electrode by silica sol–gel process with the addition of titania anatase nanoparticles (nano-TiO_2). A series of other promoters, such as carbon nanotubes, C_{60}, gold nanoparticles, nano-Al_2O_3 were also chosen to test their influence on the DET of LDH, but no effect of promotion was found. The surface morphology characterization, the condition optimization and the application of nano-TiO_2–LDH electrode as a lactic acid biosensor were also investigated.

2. Experimental

2.1. Reagents

L-Lactic dehydrogenase solution (from Bovine Heart, 549 Unit mg^{-1}) was purchased from Sigma (St. Louis, MO, USA). Sodium silicate ($Na_2SiO_3{\cdot}9H_2O$, Sinopharm Chemical Reagent Co., Ltd., China) was used to prepare the silica sol–gel. A 0.1% PVA stock solution was prepared by polyvinyl alcohol (Shanghai Chemical Reagent Plant imported from Japan). Nano-TiO_2 (Anatase type of titania, 50 nm, Taishan Nanomaterials Ltd., China) was used for modification as a kind of promoter. A NAD^+ solution was prepared by dissolving β-nicotinamide adenine dinucleotide (Shanghai Bio. Life Science & Technology Co., Ltd., China) in twice distilled water. L-Lactic acid stock solution was prepared by dissolving L-lactic acid (Sinopharm Chemical Reagent Co., Ltd., China) in twice distilled water. A 0.03 mol L^{-1} phosphate buffer solution (PBS) was prepared by Na_2HPO_4 and KH_2PO_4. All the chemicals were of analytical grade and were used without further purification. Water was twice distilled with a quartz apparatus.

2.2. Apparatus

BAS 100B electrochemical workstation (Bioanalytical Systems Inc., West Lafayette, IN, USA) and CHI660B Electrochemical workstation (CH Instruments Inc., USA) were employed for the electrochemical measurement. A three-electrode voltammetric system was consisted by an LDH-modified gold electrode as work electrode, a platinum counter electrode and a saturated calomel reference electrode (SCE). All the experiments were carried out at 37 °C and in pH 7.0 PBS buffers deaerated by N_2 except the especial explanations. Scanning electron microscopy (SEM) measurement was carried out by a JSM-5610LV Scanning Electron Microscope (JEOL Ltd., Japan).

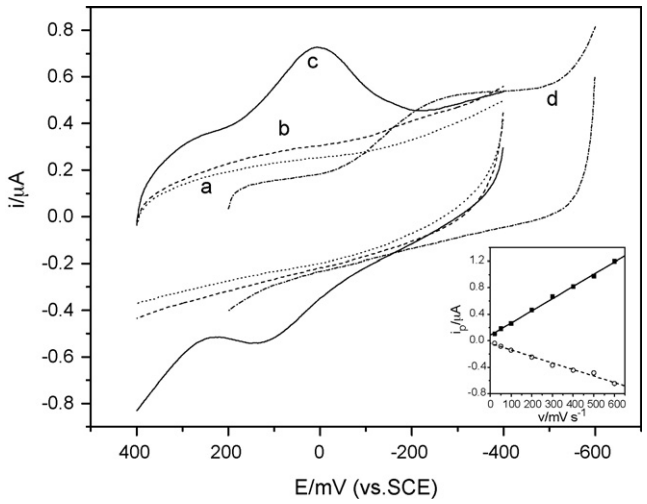

Fig. 1. Cyclic voltammograms of (a) bare Au electrode (. . .); (b) sol–gel/PVA/TiO_2/Au electrode (– – –); (c) sol–gel/PVA/TiO_2–LDH/Au electrode (—); (d) sol–gel/PVA–LDH/Au electrode (–·–·) at 100 mV s^{-1} in 0.03 mol L^{-1} Na_2HPO_4–KH_2PO_4 (pH 7.0, 37 °C). Inset: plot of peak current vs. scan rate. Scan rate (mV s^{-1}): 20, 50, 100, 200, 300, 400, 500 and 600. (■) Cathodic peak current and (○) anodic peak current.

2.3. Preparation of the nano-TiO_2–LDH electrode

The preparation of silica colloidal sol was as previously described [35–37]. The LDH modified electrode was prepared according to the steps thereinafter. The gold electrode (2 mm in diameter, CH Instruments Inc., USA) was first polished with sand paper followed by 1.0, 0.3, 0.05 μm alumina slurry, then sonicated in ethanol and twice distilled water for 15 min, respectively. The cleaned electrode was dipped into the freshly prepared *Piranha* solution (H_2SO_4:30% H_2O_2 = 3:1) for 2 min and pretreated electrochemically in 0.5 mol L^{-1} H_2SO_4 by cyclic voltammetry in the potential range of −0.4 to 1.5 V at a potential scan rate of 100 mV s^{-1} to obtain a steady state cyclic voltammogram of a clear and reproducible gold surface. The nano-TiO_2 solution used as promoters was made by dispersing the TiO_2 nanoparticles in twice distilled water in the magnetic stirrer. Then, the solution for modification was prepared by mixing nano-TiO_2 solution with silica colloidal sol, 0.1% PVA solution, LDH solution (the ratio of volume was 2:5:2:7). Finally, the gold electrode was dipped into the mixed solution for 4–7 h at 4 °C in the refrigerator, then dried by N_2 for the electrochemical measurements.

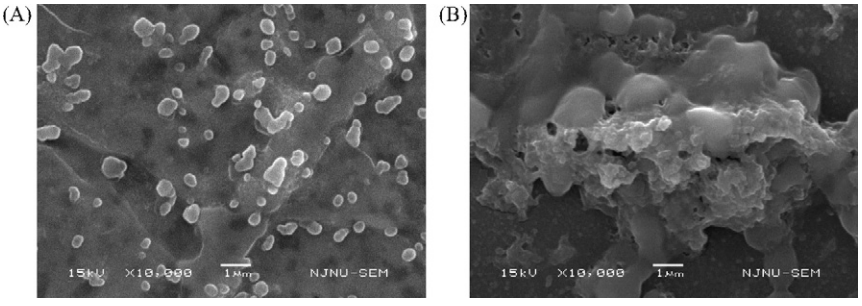

Fig. 2. SEM view with the same magnification: (A) sol–gel/PVA/TiO_2 film; (B) sol–gel/PVA/TiO_2–LDH film.

3. Results and discussion

3.1. The promotion of nano-TiO_2 on the direct electron transfer between LDH and electrode

The promotion effect of nano-TiO_2 on the direct electrochemistry of LDH sol–gel modified gold electrode can be seen in Fig. 1. There are no redox peak at the bare Au electrode and sol–gel/PVA/TiO_2/Au electrode. Meanwhile, a pair of voltammetric peaks with a formal potential ($E^{\circ\prime}$) of 70 mV (vs. SCE) is observed at the sol–gel/PVA/TiO_2–LDH/Au electrode, reflecting the direct electrochemistry of LDH (Fig. 1, curve c). The current ratio of the cathodic peak current to the anodic one (I_{pc}/I_{pc} = 1.87 at 100 mV s^{-1}) and the separation between the anodic and cathodic peak potentials (E_{pa}–E_{pc} = 160 mV at 100 mV s^{-1}) indicated that the electrode process of LDH was quasi-reversible on the gold electrode. There were several evidences that indicated the promotion effect of nano-TiO_2 on the DET between LDH and electrode (Fig. 1, curves c and d [35]): (1) the positive shift of cathodic peak potential (E_{pc} = −10 mV) compared with the result of LDH modified electrode without nano-TiO_2 (E_{pc} = −200 mV); (2) the quasi-reversible electrode process compared with the irreversible electrode process without nano-TiO_2; (3) the increased cathodic peak current (I_{pc} = 300 nA) compared with the value of 200 nA for I_{pc} without nano-TiO_2. On the other hand, the cathodic and anodic peak currents exhibited a linear relationship with the scan rate in the range of 20–600 mV s^{-1} as shown in inset of Fig. 1. This suggested that the electrochemical reaction of LDH immobilized in silica sol–gel film was typical of surface-controlled process which was in accordance with the reports on the direct electrochemistry of other enzymes [36,38,39]. The pure TiO_2 modified electrode, pure LDH modified electrode and TiO_2–LDH modified electrode are also characterized by CV and no obvious redox peaks were found (figures are not shown).

3.2. Characterization of the surface morphology of nano-TiO_2–LDH electrode

The surface morphologies of different electrodes were characterized by SEM (as shown in Fig. 2) since the morphology was also related to the performance of electrode. The top view of silica sol–gel membrane displays a three-dimensional uniform structure and the titania nanoparticles attached on the sol–gel matrix aggregate into a spherical structure, which is similar to the results of other reports [40–43] (Fig. 2A). When LDH is entrapped in the sol–gel matrix, an agglomerate crystal structure of LDH is observed from Fig. 2B. The disappearance of spherical titania nanoparticles on the sol–gel/PVA/TiO_2–LDH film suggests that there exists interaction between LDH and TiO_2. The comparison of the two films also indicated that LDH has successfully immobilized in the sol–gel matrix [44,45].

3.3. Condition optimization and stability of the nano-TiO_2–LDH electrode

The experimental conditions were optimized by investigating the cathodic current response in the cyclic voltammograms of different modified electrodes. A maximum response occurred at 37 °C and pH 7.0. The optimal concentrations of LDH and nano-TiO_2 were found to be 400–650 Unit mL^{-1} and 2–20 mg mL^{-1}, and 7 h was chosen as the modifying time (as shown in Fig. 3). The reproducibility of the nano-TiO_2–LDH electrode is good with a relative standard derivation of 5.6% (n = 8) by measuring the cathodic peak current which is similar to the results reported by other group [21,46,47].

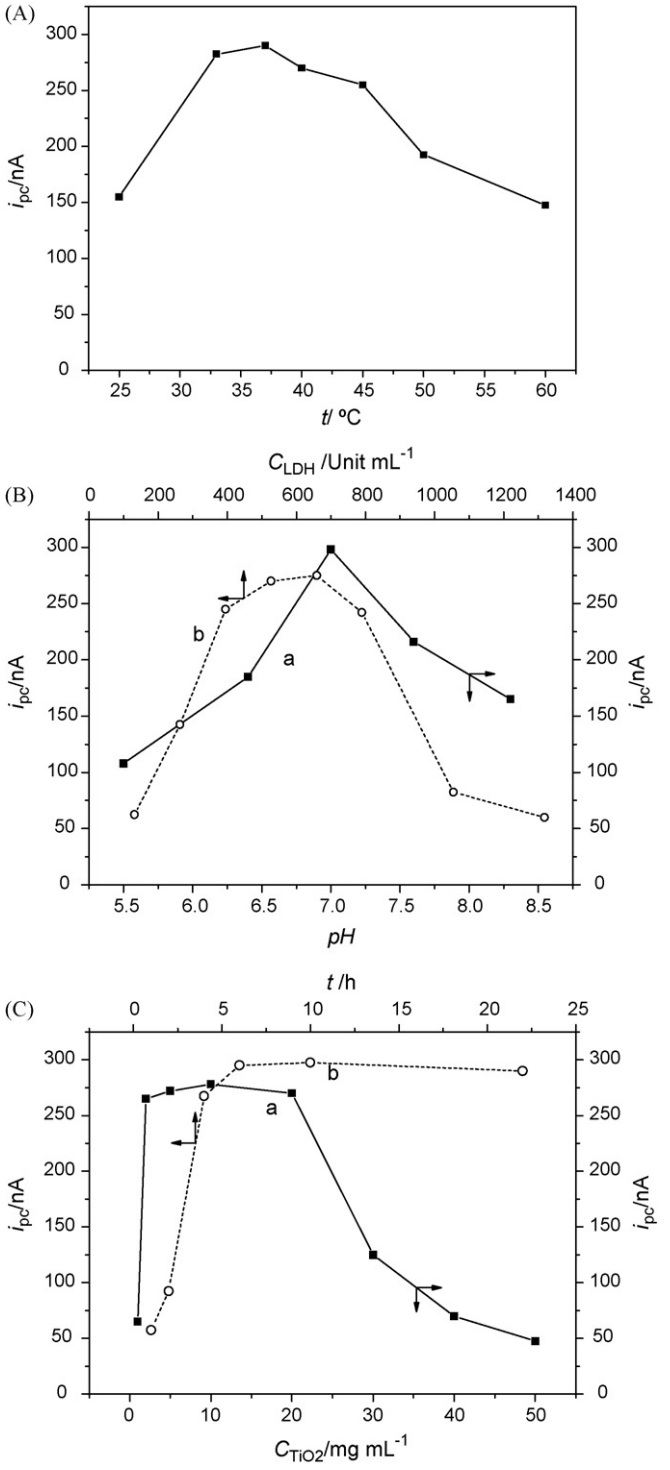

Fig. 3. Optimization of the experimental parameters for preparation of the LDH-modified electrode: (A) effect of temperature on I_{pc}; (B) effect of (a) pH (—) and (b) concentration of LDH (– – –) on I_{pc}; (C) effect of (a) concentration of TiO_2 (—) and (b) modifying time (– – –) on I_{pc}. The other conditions are the same as Fig. 1.

The storage stability of the LDH-modified electrode was also tested. When the enzyme electrode was not in use, it can be stored at 4 °C in refrigerator. The signal of the direct electrochemistry retained about 92% of its initial current response after a week and about 86% after a month.

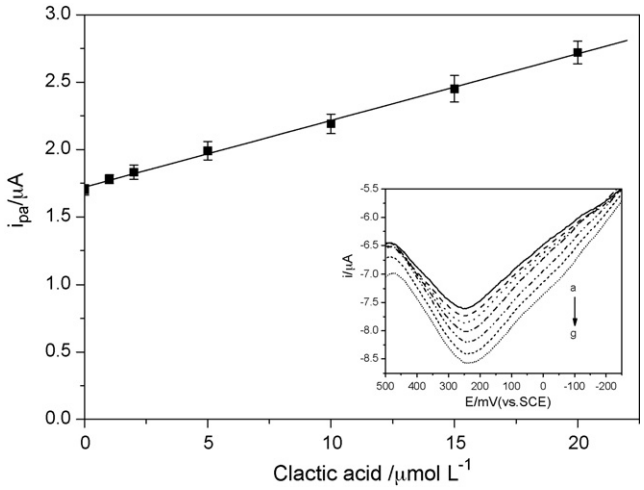

Fig. 4. The calibration curve of the biosensor for lactic acid determination. Inset: differential pulse voltammograms of sol–gel/PVA/TiO_2–LDH/Au electrode in 0.03 mol L^{-1} Na_2HPO_4–KH_2PO_4 (pH 7.0, 37 °C) in the presence of 1.0 mmol L^{-1} NAD^+ and lactic acid with different concentrations (μmol L^{-1}): (a) 0, (b) 1.0, (c) 2.0, (d) 5.0, (e) 10, (f) 15 and (g) 20. Scan rate: 100 mV s^{-1}.

3.4. Application of the nano-TiO_2–LDH electrode as a sensitive lactic acid biosensor with lower detection limit and smaller Michaelis–Menten constant

The electrocatalytic behavior of nano-TiO_2–LDH electrode for lactic acid was also tested according to the method described in previous report [35]. The changes of differential pulse voltammograms were monitored in the 1.0 mmol L^{-1} NAD^+ solution by the additions of lactic acid (inset of Fig. 4). The reaction of lactic acid catalyzed by LDH is: lactate + $NAD^+ \overset{LDH}{\rightleftharpoons}$ pyruvate + NADH + H^+. From the corresponding relationship between the regenerated NADH and the consumed lactic acid according to the reaction formula, the increased anodic current response of NADH was used to represent the increasing lactic acid concentration. The calibration range for determination of lactic acid was from 1.0 to 20 μmol L^{-1} (see Fig. 4). The linear calibration equation was I (μA) = 1.72 + 0.0493 C (μmol L^{-1}) with a correlation coefficient of 0.9988. The detection limit calculated at signal-to-noise ratio of 3 was 0.4 μmol L^{-1} which was lower than the result of 2.0 μmol L^{-1} by only immobilizing LDH on the electrode [35]. The relative standard derivation was 7.5% for five successive assays. The calibration curve also showed the characteristic of the Michaelis–Menten kinetic mechanism. The apparent Michaelis–Menten constant (K_m^{app}), can be determined from the electrochemical version of the Lineweaver–Burk equation [48]: $1/I_{ss} = 1/I_{max} + K_m^{app}/I_{max}c$, where I_{ss} is the steady-state current after the addition of substrate, c is the bulk concentration of the substrate and I_{max} is the maximum current measured under saturated substrate condition. The K_m^{app} was calculated as 2.2 μmol L^{-1} by analysis of the slope and intercept of $1/I_{ss}$ vs. $1/c$ plot. This value is lower than the result of 6.4 μmol L^{-1} without nano-TiO_2. The smaller K_m^{app} value means that the immobilized LDH in sol–gel/PVA/TiO_2 film possesses higher enzymatic activity and higher affinity to lactic acid [20,49,50] which was attributed to the addition of nano-TiO_2. The sensor retained about 85% of its initial catalytic response on lactic acid after intermittent use after 1 month.

4. Conclusion

In the current work, the nano-TiO_2–LDH electrode was prepared by immobilizing LDH on the silica sol–gel modified gold electrode with the addition of nano-TiO_2. Due to the promoting effect of nano-TiO_2, the direct electron transfer between LDH and electrode was enhanced and a quasi-reversible direct electrochemistry of LDH on the gold electrode was discovered in the optimal conditions of physiological situations (pH 7.0, 37 °C). It is difficult to conclude which group is definitely served for the redox action of LDH because of its complex structure. Considering that LDH is composed by units of the polypeptide which may have some amino acids residues, we supposed that the direct electrochemistry of nano-TiO_2–LDH electrode may be due to the redox reaction of some electroactive amino acids [51,52]. Based on this method, a new biosensor of lactic acid was constructed, which shows a stable and sensitive response of lactic acid. This nano-TiO_2–LDH electrode could also be anticipated to apply to the mechanistic studies in biological systems by constructing the small and convenient biosensors.

Acknowledgements

This project is supported by the NSFC (20575025 & NFFTBS-J0630425), NSFJ (BK2005209), grants from MOE for PhD Program (20050284030), State Key Laboratory of Electroanalytical Chemistry of China in Changchun Applied Chemistry Institution (2008008) and Analytical Center of Nanjing University.

References

[1] I. Willner, Science 298 (2002) 2407.
[2] H.A.O. Hill, J.J. Davis, Biochem. Soc. Trans. 27 (1999) 331.
[3] Y. Xiao, F. Patolsky, E. Katz, J.F. Hainfeld, I. Willner, Science 299 (2003) 1877.
[4] R. Andreu, E.E. Ferapontova, L. Gorton, J.J. Calvente, J. Phys. Chem. B 111 (2007) 469.
[5] M. Kudera, Y. Nakagawa, S. Fletcher, H.A.O. Hill, Lab Chip 1 (2001) 127.
[6] Y. Wang, W.P. Qian, Y. Tan, S.H. Ding, H.Q. Zhang, Talanata 72 (2007) 1134.
[7] E.E. Ferapontova, L. Gorton, Electrochem. Commun. 3 (2001) 767.
[8] Q. Lu, J.H. Xu, S.S. Hu, Chem. Commun. 27 (2006) 2860.
[9] Q.L. Wang, G.X. Lu, B.J. Yang, Langmuir 20 (2004) 1342.
[10] H.Y. Liu, N.F. Hu, Electroanalysis 19 (2007) 884.
[11] M.S. El-Deab, T. Ohsaka, Electrochem. Commun. 9 (2007) 651.
[12] K. Murata, N. Nakamura, H. Ohno, Electroanalysis 19 (2007) 530.
[13] S. de Marcos, J. Galban, C. Alonso, J.R. Castillo, Analyst 122 (1997) 355.
[14] J.E. Basner, S.D. Schwartz, J. Am. Chem. Soc. 127 (2005) 13822.
[15] K.A. Yao, N. Wang, J.Y. Zhuang, Z.B. Yang, H.Y. Ni, Q. Xu, C. Sun, S.P. Bi, Talanta 73 (2007) 529.
[16] O.A. Raitman, E. Katz, A.F. Buckmann, I. Willner, J. Am. Chem. Soc. 124 (2002) 6487.
[17] A.D. Ellington, J.J. Bull, Science 310 (2005) 454.
[18] S. Ferrer, I. Tunon, S. Marti, V. Moliner, M. Garcia-Viloca, A. Gonzalez-Lafont, J.M. Lluch, J. Am. Chem. Soc. 128 (2006) 16851.
[19] H.C. Shu, N.P. Wu, Talanta 54 (2001) 361.
[20] A. Salimi, A. Noorbakhsh, M. Ghadermarz, Anal. Biochem. 344 (2005) 16.
[21] J.X. Wang, M.X. Li, Z.J. Shi, N.Q. Li, Z.N. Gu, Anal. Chem. 74 (2002) 1993.
[22] J.B. Jia, B.Q. Wang, A.G. Wu, G.J. Cheng, Z. Li, S.J. Dong, Anal. Chem. 74 (2002) 2217.
[23] L. Zhang, X.E. Jiang, E.K. Wang, S.J. Dong, Biosens. Bioelectron. 21 (2005) 337.
[24] Q.W. Li, G.A. Luo, J. Feng, Electroanalysis 13 (2001) 359.
[25] A.H. Liu, M.D. Wei, I. Honma, H.S. Zhou, Anal. Chem. 77 (2005) 8068.
[26] V.V. Shumyantseva, Y.D. Ivanov, N. Bistolas, F.W. Scheller, A.I. Archakov, U. Wollenberger, Anal. Chem. 76 (2004) 6046.
[27] Y.L. Zhou, N.F. Hu, Y.H. Zeng, J.F. Rusling, Langmuir 18 (2002) 211.
[28] O. Dulub, M. Batzill, S. Solovev, E. Loginova, A. Alchagirov, T.E. Madey, U. Diebold, Science 317 (2007) 1052.
[29] M. Wagemaker, A.P.M. Kentgens, F.M. Mulder, Nature 418 (2002) 397.
[30] H.S. Zhou, D.L. Li, M. Hibino, Angew. Chem. Int. Ed. 44 (2005) 797.
[31] E. Formo, E. Lee, D. Campbell, Nano Lett. 8 (2008) 668.
[32] N. Baram, D. Starosvetsky, J. Starosvetsky, Electrochem. Commun. 9 (2007) 1684.
[33] E. Topoglidis, C.J. Campbell, A.E.G. Cass, J.R. Durrant, Langmuir 17 (2001) 7899.
[34] K.R. Meier, M. Gratzel, Chemphyschem 3 (2002) 371.
[35] J.W. Di, J.J. Cheng, Q. Xu, H.E. Zheng, J.Y. Zhuang, Y.B. Sun, K.Y. Wang, X.Y. Mo, S.P. Bi, Biosens. Bioelectron. 23 (2007) 682.
[36] J.W. Di, M. Zhang, K.A. Yao, S.P. Bi, Biosens. Bioelectron. 22 (2006) 247.
[37] J.W. Di, S.P. Bi, M. Zhang, Biosens. Bioelectron. 19 (2004) 1479.
[38] F. Yin, H.K. Shin, Y.S. Kwon, Talanta 67 (2005) 221.
[39] B.D. Fleming, Y. Tian, S.G. Bell, L.L. Wong, V. Urlacher, H.A.O. Hill, Eur. J. Biochem. 270 (2003) 4082.
[40] D.A. Gish, F. Nsiah, M.T. McDermott, M.J. Brett, Anal. Chem. 79 (2007) 4228.
[41] X.L. Luo, G.D. Vidal, A.J. Killard, A. Morrin, M.R. Smyth, Electroanalysis 19 (2007) 876.

[42] M. Chikae, K. Idegami, K. Kerman, N. Nagatani, M. Ishikawa, Y. Takamura, E. Tamiya, Electrochem. Commun. 8 (2006) 1375.
[43] S.G. Yang, X. Quan, X.Y. Li, C. Sun, Photochem. Photobiol. Sci. 5 (2006) 808.
[44] Q. Lu, S.S. Hu, D.W. Pang, Z.K. He, Chem. Commun. 20 (2005) 2584.
[45] S.A. Kumar, S.M. Chen, Talanta 72 (2007) 831.
[46] L. Wang, J.X. Wang, F.M. Zhou, Electroanalysis 16 (2004) 627.
[47] H.M. Zhang, N.Q. Li, Bioelectrochemistry 53 (2000) 97.
[48] R.A. Kamin, G.S. Wilson, Anal. Chem. 52 (1980) 1198.
[49] G.C. Zhao, Z.Z. Yin, L. Zhang, X.W. Wei, Electrochem. Commun. 7 (2005) 256.
[50] Y.X. Xu, F. Wang, X.X. Chen, S.S. Hu, Talanta 70 (2006) 651.
[51] F. Huerta, F. Morauon, F. Cases, A. Rodes, J.L. Vazquez, A. Aldaz, J. Electroanal. Chem. 421 (1997) 179.
[52] R.P. Deo, N.S. Lawrence, J. Wang, Analyst 129 (2004) 1076.

Talanta 76 (2008) 988–996

Contents lists available at ScienceDirect

Talanta

journal homepage: www.elsevier.com/locate/talanta

Review

Molecularly imprinted polymer as a solid phase extractor in flow analysis

A.C.B. Dias[a,*], E.C. Figueiredo[a], V. Grassi[b], E.A.G. Zagatto[b], M.A.Z. Arruda[a]

[a] Institute of Chemistry, University of Campinas – UNICAMP, 13083-970, Campinas, SP, Brazil
[b] Centro de Energia Nuclear na Agricultura, Universidade de São Paulo, Box 96, Piracicaba, 13400-970, Brazil

ARTICLE INFO

Article history:
Received 26 March 2008
Received in revised form 16 May 2008
Accepted 20 May 2008
Available online 3 June 2008

Keywords:
Flow analysis
Molecularly imprinted polymers
Solid phase extraction

ABSTRACT

Molecularly imprinted polymers (MIPs) are novel alternative materials for solid phase extraction. Applications in flow analysis are recent and enhanced in-line separation/concentration procedures have been proposed. Use of flow systems is very important in the context. The aim of this review is then to highlight the implementation of MIP as solid phase extractor in flow analysis, emphasizing potentialities, limitations and applications.

Contents

1. Introduction

The flow system is an important tool in the context of automated chemical analysis. Cumbersome, slow and complex analytical procedures are transformed in elegant and simple protocols. Minimal sample contamination, fast analysis, improved system ruggedness, simplicity and flexibility have been considered as the main potentialities of these systems [1,2].

Flow injection analysis [3] utilizes the insertion of a sample aliquot into an unsegmented flowing carrier stream (Fig. 1), originating a reproducible sample zone that undergoes continuous dispersion while being transported through the analytical path towards detection. Mixing of the sample with the reagents is a consequence of the continuous dispersion processduring its transport along the analytical path, where the chemical species are converted to detectable products to be monitored during sample passage through the detector. The analytical signal, ideally proportional to the analyte content in the sample, is then recorded. In this way, the flow injection system was considered as "the art of playing analytical chemistry inside narrow-bored tubing" [4], allowing the implementation of numerous analytical procedures.

The degree of automation of the flow systems has undergone amazing increase, especially after the inception of sequential injection analysis [5]. The related flow analyzer comprises a multiposition valve able to select the sample and reagent aliquots to be sequentially aspirated towards the holding coil (Fig. 1b). After flow reversal, the sample zone is directed towards detection. Other accessories and devices for sample preparation, such as thermostatic baths and separation chambers can be linked to the multi-position valve. Relevant aspects are the ease of implementation of two or more methods in a single manifold for sequential determinations [6] and the miniaturization of the manifold. The Lab-On-Valve system [7] is analogous to the sequential injection

* Corresponding author. Tel.: +55 19 35212133; fax: +55 19 35213023.
E-mail address: acbdias@gmail.com (A.C.B. Dias).

0039-9140/$ – see front matter © 2008 Elsevier B.V. All rights reserved.
doi:10.1016/j.talanta.2008.05.040

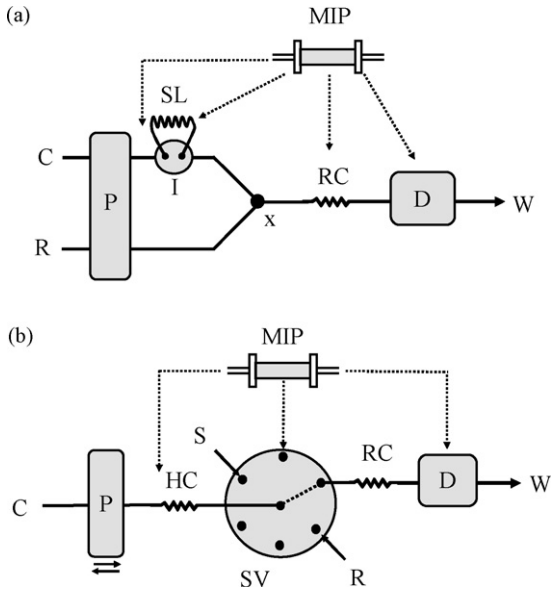

Fig. 1. Flow systems exploiting MIP for in-line SPE. (a) Flow injection system. SL = sample loop, I = injector-commuter or valve injection, P = peristaltic pump, R = reagent solution, C = carrier solution, x = confluence point, RC = reaction coil, D = detector, W = collecting flask. (b) Sequential injection systems. SV = multiport selecting valve, P = peristaltic or syringe pump, S = sample, HC = holding coil. MIP = mini-column packed with molecularly imprinted polymer.

analyzer but includes a central sample-processing unit, positioned in the selecting valve.

With the evolution of flow analysis, highly versatile manifolds have been designed with the insertion of controlled solenoid valves, syringe pumps and solenoid pumps, resulting in the inceptions of the multi-commuted [8], multi-syringe [9] and multi-pumping [10] flow systems.

As a consequence of the efficient control of sample processing, minimal sample manipulation and contamination, preservation of the matrix, high repeatability, etc. [11,12], in-line sample treatment, including analyte separation/concentration has been often implemented in flow systems [13]. Amongst the in-line sample preparation strategies, solid phase extraction (SPE) has been the most exploited one [14,15]. Depending on the involved analytical procedure and aimed flow manifold, the solid phase materials have been incorporated into mini-columns [16], membranes [17], disks [18], knotted reactors [19], renewable beads [20] or cartridges [21]. Mini-columns packed with the solid phase are by far the mostly used strategy [21,22], and the simplicity of the strategy is associated to the ease of manufacturing, manipulation and packing, as well as in the feasibility to insert the mini-column in any place of the manifold.

The main aspects related to in-line SPE are the composition of the solid material and the way it is adapted into the flow manifold. This last aspect encompasses the kind of solid phase support, flow-rate, flow pattern, automation degree, solution volumes, and system ruggedness. Limitations are usually associated to the volume of washing solution, sample dispersion inside the volume support, and composition and life-time of the solid extractor.

Constitutions of the solid phase materials are often the limitation factor in the extraction efficiency, and should be carefully selected. Ion-exchange resins [23,24] and silica-based exchangers [16,25] are mostly used in flow analysis. Alternative materials such as polyurethane foam [26], cigarette filters [27], extracting disks [18], PTFE turnings [28], grape bagasse [29], rice husks [30], fibers [31] and bio-organisms such as *Saccharomices cerevisae* [32] have been also used.

Synthetic polymers have recently been applied as selective solid phase extractors [33,34], and use of the molecularly imprinted polymers (MIPs) should be highlighted in the context. Molecular imprinting is a technique used for preparing polymers with recognition abilities resulting from the target template molecule (analyte) impression [35]. Use of MIPs for in-line SPE has been increasing mainly in relation to batch-wise analytical procedures and to liquid chromatography (LC), especially for sample clean-up and/or analyte separation/concentration. In-line procedures have been scarcely proposed and drawbacks leading to low selectivity and need for extra instrumentation have been reported [33]. Flow injection systems are then a good alternative, as simplified manifolds concerning ruggedness and flexibility of MIP as in-line solid phase extractor can be designed.

The main innovations in relation to MIP in flow systems are discussed in this review. Experimental aspects as well as potentialities, limitations and applications are described in order provide guidelines for the efficient implementation of MIPs as in-line extractors in flow analysis.

2. MIPs: general aspects

Briefly, the up-and-coming of MIPs started with the experiments carried out by the Polyakov [36] that observed the formation of selective cavities during silica preparation. The cavities, a kind of impression caused by interactions between the chemical species (template) and the silica, remained intact after the template removal, resulting in a selective solid phase extractor. The impression established in the silica was confirmed in relation to other kinds of supports such as globulins or silica gel [37–40], which were replaced by synthetic organic polymers, during the development of novel materials for polymerization and chemical interactions [41–45]. In this way, the organic polymers based on activation of functional groups in the silica became the best alternative for imprinting templates [46]. Reversible covalent bonds between template and functional monomer were the first interactions studied in the imprinting process, resulting in cavities highly selective to the template [47,48]. Non-covalent (electrostatic, hydrophobic, van der Waals) and semi-covalent interactions were also exploited in order to make the template removal easier due to the weaker bindings. Improvements in bond interactions, selectivity, molecular recognition, as well as mechanical stability have been proposed in association with the development of chemical materials, characterization and quantification techniques and analytical instrumentation [46,49–52]. After considering these features it is possible to obtain highly selective polymers in ordinary chemical laboratories in accordance to the required application [46,53].

As this review deals with the incorporation of MIPs in flow systems, a simple discussion about the imprinting process is presented.

MIPs are formed by non-covalent or covalent interactions between the functional groups of the template (analyte) and the functional monomers, being the non-covalent interactions mostly applicable in relation to in-line procedures. The strength associated with template and functional monomer is responsible for the recognition sites formed after template removal (Fig. 2). The recognition sites are cavities highly selective towards the template, and remain intact after the polymer finalization. In this way, different chemical reagents and polymerization procedures have been used for MIP synthesis depending mainly on the physical–chemistry characteristics of the template [44,46,54–60].

Regarding MIP synthesis, bulk polymerization is the most used procedure. The template and the functional monomers are added to the flask where the template molecules are bonded to the

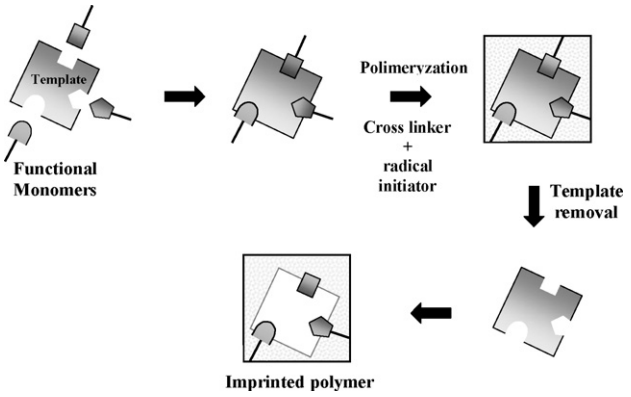

Fig. 2. Schematic representation of the molecular imprinting process.

functional monomers. Thereafter, a cross-linker reagent is added to link all functional monomers, resulting in a chain that is polymerized by adding a radical initiator. A polymer block is then generated, that should be ground with a mechanical or manual mortar, resulting in particles with desirable mesh. The template is then removed by washing the ground polymer particles with a suitable reagent and this step can be accomplished batch-wise or in-line. Microwave-assisted [61] and Soxhlet [62] extractions are good alternatives for efficient template removal. The synthesis is very simple and carried out under mild conditions (room temperature); for keeping safety, care should be taken in relation to the oxygen/air inlet, thermal stability and flask inner pressure. Limitations of this synthesis process are concerned to the heterogeneous particle size [34], to poor binding sites and to low quantity of cavities remaining after the polymer block crushing. This can be circumvented by exploiting the suspension polymerization [63], where beads with defined diameters are formed. The approach is relevant in relation to flow injection systems with in-line extraction due to the homogeneity in the mini-column packing. Other alternatives for synthesis are formation of beads by swelling [64], sol–gel synthesis [65], precipitation [66] and exploitation of monolithic columns [67].

Synthesis should be exclusive for each analyte, once the cavities generated are dependent on the three-dimensional template structure, considered the principle of molecular impression. The MIP selectivity is then dependent on the synthesis process, thus on the main parameters involved, such as template/functional monomers molar ratio, kind and volume of solvent, quantities of cross-linker and radical initiator, timing and temperature [68]. These parameters should be evaluated before designing the synthesis process of a novel MIP [55,59]. A brief comment on the parameters involved is given below, and deeper information is given elsewhere [33,34,44,46,54–60].

Template is considered as the analyte, and its chemical structure determines the functional monomer to be used in the process. The interaction between template and functional monomer is the basis of the molecular recognition. The template should be stable under the synthesis conditions (temperature or UV irradiation) and soluble in the used solvent.

Solvent is a porogen reagent, and participates of the synthesis process by dissolving all the involved substances in one phase. Its constitution, concentration and volume dictate the morphology and quantity of pores, thus the surface area [46]. Solvents such as dichloromethane, acetonitrile, toluene, dimethylsulfoxide and chloroform have been mostly used in non-covalent approaches [34]. Their volume is directly associated with the capacity of arrangement of all involved substances, therefore polymer with large pores are synthesized when higher solvent volumes are used. High solubility of the solvent leads to polymers with low pore distribution and high surface area whereas low solubility leads to large pores and low surface area [59]. This parameter plays a pronounce influence in the template-functional monomer equilibrium, which is more stable when apolar and aprotics solvents are applicable.

Functional monomers are chemical species responsible to form the binding sites imprinted in the polymer. They correspond to the template functional groups and the bonds should be strong enough to form the binding sites, yet weak enough to be further removed from the template. Generally, the amount of functional monomer is in excess relatively to the template; to ensure the equilibrium of the complex, the minimal 4:1 molar ratio is generally used [34]. Methacrylic acid and 4-vinylpiridine can be mentioned as the most frequently used acidic and basic functional monomers.

Cross-linker agent is responsible to link all the functional monomers in order to form the polymer. The most used one is the ethylene glycol dimethacrylate (EDMA) that imparts several characteristics to the MIP, such as polymeric morphology (macro or micro pores, gel), stability of the imprint interactions (template-functional monomer bonds) and mechanical stability [55].

Radical initiator yields the free radicals to initialize the polymerization. The first radicals are formed by thermal or photolytic decomposition, and start the polymerization by linking all the substances involved in the polymerization. The most frequently used reagent is the 2,2′-azo-bis-isobutyronitrile (AIBN).

For control, a non-imprinted polymer (NIP) should be prepared without the template following the same synthesis procedure as for MIP, once undesirable interactions may happen depending on the template, synthesis procedure and template removal. Low selective interactions are generally formed during the non-covalent synthesis due to the high amount of monomer used in the process. When the number of non-selective interactions is higher in relation to the selective one, a column packed with NIP could be used before the MIP column to improve selectivity [46]. The compromise between selectivity and synthesis process should be taken in account when new polymers are formed.

MIPs can be used simultaneously as sample clean-up, separation/concentration of chemical species or derivatization [22]. The search for simplified procedures, lessening of errors associated to the sample manipulation and extraction steps has lead to the increase in MIP use as in-line solid phase extraction (MISPE). Moreover, flow systems can attain efficient handling of the washing and eluent solutions, improving the polymer conditioning, resulting in faster analysis and enhanced analytical sensitivity and selectivity. Low cost, reproducible mixing of the streams, controlled dispersion, closed environment, minimal analyte losses and sample contamination, minimal waste generation and reproducible results are characteristics of the flow systems, which guarantee with success the use of MIP as in-line SPE.

3. In-line MISPE

In flow analysis, the solid phase extractor is usually accommodated in a mini-column, which can be placed before the sample injection port, at this port or in the analytical path (Fig. 1). Advantages and limitations of these different architectures are discussed elsewhere [15]. To this end, proportional injector-commuters [69], rotary injection valves [70], three-way solenoid valves [8] or multiposition valves [71] have been used. A particular situation refers to packing the extractor into the flow cell in order to behave as a sensor (Fig. 3). Although the proposal of novel approaches for SPE in flow analysis has been increasing, strategies exploiting MIP are

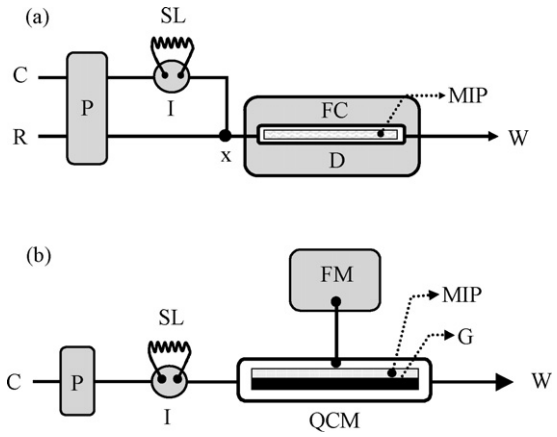

Fig. 3. Flow systems exploiting MIP as in-line sensor. (a) Photosensor. C = carrier stream, P = peristaltic or syringe pump, SL = sample loop, I = solenoid valve, valve injection or injector-commuter, R = reagent solution, FC = flow cell packed with MIP, D = detector (spectrofluorimeter, photomultiplier), W = flask collector. (b) Piezosensor. QCM = flow cell in quartz crystal microbalance, G = gold electrode; FM = frequencymeter.

scarce, probably due to the lack of the confidence in relation to the traditional SPE materials or information about potentialities and limitations in relation to flow analysis.

Flow injection analysis has been the most used flow modality in relation to in-line MISPE (Table 1). Incompatibility of organic solvents (inherent to MIP preparation) with components of the manifold as well as control of the loading, washing and conditioning steps are key issues for designing analytical systems with in-line MISPE. Implementation of MISPE in flow systems involves different aspects, ranging from the control of the synthesis process for a template to the design of a suitable flow manifold. Comments on the main aspects of polymer synthesis concerning use of MIP in flow systems are presented further.

The block resulting from the bulk polymerization is mostly used for in-line MISPE procedures and drawbacks are associated with further grinding and sieving. Depending on the architecture of the flow system, the block is not ground and is prepared as membrane or disks, as well as a micro transducer of a quartz crystal microbalance [46]. After the block formation, characteristics more closely related to the polymer synthesis such as porosity, particle size, surface area, number of effective binding sites and mechanical stability should be carefully verified, as they play a relevant role in relation to size of the mini-columns or cartridges used. Minimal amounts of polymer should be packed without holes and preferential ways for the flowing solutions. Spherical beads are the most attractive shape, but irregular particles ranging from 20 to 160 μm are often used. Sol–gel synthesis and suspension polymerization [63,65] are innovative and promising strategies for MIP fabrication aiming in-line extraction.

Another parameter regarding packed MIP is the flow-rate, which plays a similar influence as in any in-line SPE procedure. As pronounced concentration gradients are usually involved, swelling effects and high hydrodynamic pressure may interfere in the molecular recognition. Loading, washing and eluting steps are directly influenced by the flow-rate that should be adjusted as a compromise between template re-binding kinetics [72] and interference removal without bleeding of the template. Moreover, the kind of interaction between template, functional monomers and solution compositions should be taken into account.

The solvents used during the MIP synthesis are considered as the ideal washing solution after the loading step [73]. Otherwise, this solution should be selected in order to keep the target analytes strongly retained inside the binding sites of the MIP and to remove the interfering compounds retained by non-selective interactions [52]. In most applications, selectivity can be improved by using solvents diluted in water, acids or buffer solutions. Few applications involve concentrated organic solvents that are the main limitations in MISPE in flow analysis. Specific materials such as PEEK or PTFE tubing with high chemical resistance and valves, connectors, tees and flow cells made from Teflon® or thermoplastic polyetherimide resins are required when concentrated acids or organic solvents are used. In this way, solvent impregnation, corrosion and disrupter of the channels are minimized. Regarding UV–vis spectrophotometry, the Schlieren effect [74] may manifest itself due to either partial mixing of concentrated solutions or formation of fluidic optical elements. Recent investigations involving preparation of MIPs in aqueous media have been pointed out as promising, mainly for templates that are slightly soluble in the solvents [34], allowing to obtain non-covalent interactions in the presence of polar protic solvents. The approach is an alternative to sample handling under mild chemical solutions in simplified flow systems, where tubing conservation is prolonged and Schlieren effect is minimized. The flow injection and sequential injection systems involving MIPs generally use organic solvents with PTFE tubing, and the problems involving this kind of solution are not noted (see Table 1). However, if the in-line procedure is applied to large-scale analysis, this aspect should be carefully evaluated.

The main parameters involved in the conditioning (washing step, conditioning solvent), loading (sample volume, flow-rate, pH, matrix), and elution (elution mode, solvent nature, pH, flow-rate, volume) steps should be taken into account. The loading step is determined by the sample volume (enough to percolate all cavities) and flow-rate (enough to allow the interaction between analyte and MIP binding sites). The washing step is determined by flow-rate and composition of the involved solution, which should carry the matrix interferences without removing the analyte and, at the same time, improve the interactions between analyte in recognition sites. Regarding elution, the flow-rate should be compatible with the kinetics of the ruptures between analyte and binding sites. For a too low flow-rate, rebinding is noted whereas for a too high one, the analyte is partially eluted. Another aspect refers to volume of the eluent that may cause a high dispersion of the analyte inside the mini-column and flow manifold. These parameters become more important when in-line MIP is exploited to improve selectivity. Difficulties in optimization of the washing step have been often reported [75,76], and recent researches demonstrated that use of a NIP column in parallel to the MIP columns is essential to obtain selectivity [75,77]. Flow systems are suitable to implement one or more mini-columns in the manifold, changing easily the solutions and flow-rates depending on the aim, resulting in a promising alternative to improve selectivity. The flow-rate is also associated to the sampling frequency, considered the main limitation of in-line MISPE in relation to the traditional solid extractors used in-line SPE (ion-exchanger, silica cartridges, enzymes, beads). This is due to the lower flow-rate applied to sample loading, washing and elution to establish adequate template-functional monomers binding kinetics. Possibility to extract a large number of trace elements over a wide pH range, quantitative extraction (sorption and elution), kinetically faster interactions and rebinding mechanism, reusability, high retention capacity, accessibility, mechanical and chemical stability, etc. should be taken in account when exploiting MIP instead of traditional SPE [57–59]. With a proper choice of the analyte and synthesis process, MIP could satisfactorily replace other solid phase materials with additional advantages such as stability under high temperature and pressure, ease of production, lower cost, flexibility in manufacturing, mechanical resistance and simplicity in automation.

Regarding applications of MIP in flow analysis, two main objectives have been generally emphasized: (1) photochemical/piezoeletric sensor packed in the flow cell to obtain high selectivity, and (2) mini-columns for solid phase extraction before or after sample injection (analyte separation/concentration, sample clean up), as described further.

3.1. MIP as a flow through sensor

MIP has been largely used as in-line solid phase extractor packed inside a flow cell. Preparation of optical sensors for transmittance measurements is difficult due to the limitations in transparency, particle uniformity and mechanical stability required for this purpose [78]. In this way, piezoelectric or photochemical (*e.g.* chemi- and bioluminometric, fluorimetric) detection have been preferred.

Despite MIP is considered an efficient solid phase extractor, considerations about the synthesis process should be always taken into account. This is an important aspect mainly due to the formation of the particles and films packing in the mini-columns or applied in sensing techniques. Recent studies have been developed to improve the interaction of polymer–transducer resulting in better analytical signal, robustness, porosity, mechanical stability and flexibility as well as increase of binding sites in small surface areas [78,79]. The flow system promotes a better interaction between the minimal MIP sensing area and the solutions involved through variations in flow-rate and manifold geometry. Moreover, reuse of the MIP sensor is attained before next sample injection through the variation in the solution composition.

The continuous flowing stream delivered by a peristaltic pump is by far the most often exploited one, and a typical flow manifold is outlined in Fig. 3a. In general, the reagent is injected instead of the sample because of the instability and fast chemical reagents decomposition involved in the photochemical detection.

The original exploitation of MIP as a flow-trough sensor referred to fluorimetric determination of flavonol in olive oil [80]. The flow system presented one path connected to a spectrofluorimeter with a 25-μL flow cell packed with the flavonol-MIP. The sample (150 μL) was introduced into a hexane/chloroform (70:30, v:v) carrier stream and transported towards the MIP optrode where the analyte was retained and quantified. In spite of the errors inherent to the synthesis process, sensor preparation (crashing, sieving, packing, leaching), and optical measurements, the fluorimetric sensor presented suitable reproducibility demonstrating also the feasibility to determine flavonol in hydrophobic samples without any prior treatment.

Table 1
Applications of MIP for in-line SPE to real samples

Analyte	Flow system/MIP location[a]	Monomer/solvent	Eluent or reagent stream	Detection technique	Sample	Ref.
β-Estradiol	FIA/B	MAA/ACN	ACN:H_2O	Fluorescence	Natural waters[b]	[61]
Benzo[*a*]pyrene	FIA/I	MDI/THF	MeOH	Room temperature phosphorescence	Natural waters	[83]
Brucine	FIA/I	MAA/Chloroform	Potassium permanganate + sodium sulfite	Chemiluminescence	Urine	[94]
Caffeine	FIA/I	MAA/Chloroform	Caffeine in NaOH	Piezoeletric sensor	Coffee and tea leaves	[99]
Carbamate	FIA/B	MAA/Chloroform	Phosphate buffer	Potentiometry	Rat plasma	[63]
Carbaryl	FIA/B	Acrylamide/ACN	MeOH:H_2O	Luminescence	River waters[b]	[62]
Catechol	MCFS/B	4-VP/ACN	HNO_3	Spectrophotometry	Tea, guarana powder	[109]
Chloramphenicol	FIA/B	DEAEM/THF	MeOH	Square wave voltammetry	Ophthalmic solutions, milk	[111]
Chloroguaiacol	FIA/B	4-VP/ACN	MeOH:acetic acid	Amperometry	River waters	[108]
Clenbuterol	FIA/I	MAA/ACN	Formaldehyde + polyphosphate + potassium permanganate	Chemiluminescence	Animal urine	[89]
Epinephrine	FIA/I	MAA/ACN:benzoic alcohol	Luminol + $K_3Fe(CN)_6$	Chemiluminescence	Blood serum	[88]
Flavonol	FIA/I	MAA/Chloroform	Hexane:chloroform	Fluorescence	Olive oil	[80]
Fluortanthene	FIA/I	MDI/THF	ACN	Room temperature phosphorescence	River waters[b]	[82]
Hydralazine	FIA/I	MAA/Methylbenzene	Luminol + KIO_4	Chemiluminescence	Urine	[91]
Indomethacin	FIA/I	MAA/Chloroform	Mn(IV) + formaldehyde	Chemiluminescence	Urine	[93]
Isoniazid	FIA/I	MAA/ACN	Luminol + KIO_4	Chemiluminescence	Human urine	[92]
Metformin	FIA/B	MAA/ACN	Cupric polyphosphate + hydrogen peroxide	Chemiluminescence	Human serum	[105]
Nafcilin	FIA/I	TPM-sol–gel synthesis Tetramethyl orthosilicate, methyltrimethyl orthosilicate, phenyltrimethyl orthosilicate	Sodium sulphide + KI	Room temperature phosphorescence	Skimmed milk samples	[65]
Norfloxacin	FIA/I	Chloroform/N,N-dimethylformamide/	Ce(IV) + sodium sulfide	Chemiluminescence	Urine	[95]
p-Aminophenol	FIA/B	MAA/chloroform:DMSO	Tris buffer + H_2O_2	Amperometry	Natural water[b]	[113]
Pazufloxacin mesilate	FIA/B	MAA/dichloromethane	ACN:acetic acid	Chemiluminescence	Human urine	[107]
Pirimicarb	FIA/B	MAA/chloroform	MeOH:H_2O:HAc	Differential pulse voltammetry	Natural water[b]	[110]
Salbutamol	FIA/I	MAA/ACN	Luminol + $K_3Fe(CN)_6$	Chemiluminescence	Urine	[90]
Sulfamethazine	FIA/B	MAA/ACN	MeOH;Acetic acid	Square wave voltammetry	Milk	[112]
Terbutaline	μFIA/I	MAA/ACN	Luminol + $K_3Fe(CN)_6$	Chemiluminescence	Human serum	[103]
Tetracycline	FIA/B	MAA/MeOH	ACN:HNO_3	Chemiluminescence	Fish	[106]
Vanilin	FIA/I	MAA/THF	Boric acid, KCl, NaOH	Piezoelectric sensor	Vanilla sugar	[101]

MCFS: multicommuted flow system, FIA: flow injection analysis, MAA: methacrylic acid, 4-VP: 4-vinylpiridine, ACN: acetonitrile, MeOH: methanol, DMSO: dimethylsulfoxide, MDI: diphenylmethan- 4,4- diisocyanate, THF: tetrahydrofuran, DEAEM: (diethylamino)ethyl methacrylic acid.

[a] B = before detection; I = inside the detector.

[b] Spiked samples.

One of the main limitations in imprinted polymeric optrodes refers to the vacancies resulting from bad formation of binding sites during polymerization. This can be overcome by using two functional monomers (vinyl pyridine and diethyl amino ethyl methacrylate) to get better selective binding sites, as demonstrated in the fluorimetric determination of chloramphenicol [81]. A single-line manifold was used with a flow cell packed with MIP and placed outside the optical path, in order to estimate the saturation of the binding sites through the fluorescent tracer insertion. The flow-rate played a marked influence on the recognition: a high flow-rate did not allow an efficient interaction whereas a slow flow-rate impaired the analytical frequency and produced broader peaks. With a 0.25 mL min^{-1} flow-rate, a sample throughput of 5–6 samples per hour was attained.

The feasibility of using MIP in relation to room temperature phosphorescence (RTP) was demonstrated in the determination of fluoranthene in water [82]. The impression of heavy atoms allowed the induction of RTP by oxygen scavenger in the analyte recognized in the MIP sites. High selectivity was noted in relation to polycyclic aromatic hydrocarbons (PAHs), once most of these species present similar luminescence behavior [83]. The polymer particle size was a relevant parameter, resulting in a low efficiency of the polymer regeneration to the next sample and to overpressure in the flow system when smaller particles (<200 μm) were used. Metal impression could be also used for quantification of ions through ion imprinting polymers [84], with adequate selectivity, ease of preparation and versatile to the accommodation in sensors. Drawbacks were associated to poor solubility of the template in the imprinting mixture, preparation time consuming with insufficient leaching of the imprint ion and bleeding of the material [85]. Consequently, ion imprinted polymers as in-line SPE seems to be not exploited further.

A sol–gel imprinted polymer of nafcillin was synthesized and packed inside a flow cell [65] presenting low cross-reactivity of similar antibiotics, and fast and efficient interaction between the analyte and recognition sites. In relation to traditional methods, the approach was characterized by the easy and rapid use and reuse of the imprinted sol–gel polymer, mild conditions, high selectivity, high stability and adequate analytical throughput ($22\ h^{-1}$).

Chemiluminescence (CL) detection has been largely exploited for in-line MISPE through the insertion of chemical reagents inside the flow cell packed with MIP, resulting in a flow-trough sensor based on the inhibition or activation of CL by the template located inside the MIP. Initial studies about polymer preparation and its CL properties were reported by Lin and Yamada [86]. The innovation relied on the influence of dansyl amino acids and pyrene on the CL signal due to the peroxomonosulphate (HSO_5^-) decomposition in the presence of Co^{2+}. The flow cell was packed with the imprinting polymer prepared with dansyl-L-phenylalanine as template. After insertion of the reagents an intense CL signal proportional to the recognition of template was generated. With the decomposition of the analyte after the CL process, the polymeric cavities became ready for the next sample. Water was used as the washing solution (4 min) and this was an important aspect for polymer reconditioning, being easily inserted between the elution and sampling steps by a six-port injection valve.

The catalytic activity of 1,10-phenanthroline in the H_2O_2 decomposition was evaluated [87] by using a MIP formed by the 4-vynil-pyridine-Cu-phenantroline ternary complex (2:1:1) packed into a mini-column placed inside a photomultiplier detector. Studies about the molecular recognition and template decomposition were carried out, resulting in a promising alternative to MIP as flow-through sensor.

In view of some limitations originating from the MIP prepared with the CL reagents, such as incomplete decomposition of the template imprinted in the polymer and successive and laborious washing steps, other alternatives for the reaction development have been proposed. As the flow injection system presents high flexibility and a reproducible temporal window, the reaction may occur before the MIP sensor, as demonstrated in the determination of epinephrine imprinted in a non-covalent polymer packed as a mini-column placed in front of a photomultiplier detector [88]. A previously mixed luminol/potassium hexacyanoferrate (II) aliquot was inserted into the analytical path, transported towards the mini-column and allowed to react with the epinephrine bonded on the MIP. As a consequence of the favorable analytical characteristics, MIP stability, and easy operation of the flow system, analogous strategies have been developed for CL determinations [89–95]. An innovative approach was designed to enzyme-linked immunosorbent assays (ELISA) with MIP as an alternative to antibodies for molecular recognitions [96]. The 2,4-dichlorophenoxyacetic acid was imprinted into a glass capillary and implemented in the flow system in front of the photomultiplier detector. The flow injection system presented worse detection limit than the standard ELISA assay, due to the shorter time of sample contact with the MIP. Automation promoted high sample throughput and the possibility of monitoring several capillary mini-columns sequential or simultaneously.

Difficulties in preparing the imprinted polymers in small surfaces and in attaining high molecular recognition are perhaps the main reason why MIPs have been usually packed inside the flow cell as flow-trough sensor. In this context, the indirect fluorimetric determination of aluminum was possible through interaction with the Morin reagent imprinted in the MIP [97]. In order to obtain sensitivity with minimum residence time, elution and rebinding steps were adjusted in function of pH and ionic strength.

Regarding use of MIP in relation to a piezoelectric quartz crystal (Fig. 3b), advances in MIP preparation on small surfaces like the chips have been demonstrated in the flow-injection determination of caffeine [98]. After binding the MIP cavities with the analyte, a concentration-dependent change of the resonant frequency in the crystal was noted. The sensor was fabricated with a mixture of MIP, polyvinyl chloride and tetrahydrofuran, and a small aliquot (10 μL) was dropped onto the center of the electrode and spread until a film was formed. A 10-min sample stopping was needed in view of the improved sensor stability and the slow kinetics of diffusion and binding of caffeine in the MIP cavities, resulting in good measurement reproducibility and absence of interferences. Coffee and tea leaves were analyzed in a similar procedure using a modified piezoelectric sensor [99]. As the main limitation of flow-trough piezoelectric sensor refers to the MIP thin film that should be reproducible, stable and presenting a large surface area with a number of binding recognition sites, a thin film (150 nm) of MIP was synthesized on the gold electrode for separation and determination of bilirubin [100]. The analytical setup was very stable allowing fast analysis with a low sample consumption (100 μL) and simplicity in the reutilization of the MIP. Alternative synthesis processes were developed to produce MIP with better selectivity and mechanical stability on the sensor surface [79,101].

The flexibility of the polymer synthesis carried out the miniaturization of MIP in a sensor chip with minimal diameter matches the concept of micro-total analysis systems [102]. A biosensing microfluidic chip was developed to detect cholesterol, progesterone and testosterone by using the molecular imprinting technique [103]. MIPs of the analytes were synthesized as thin films inside the chip (45 mm × 45 mm) and pneumatic microvalves and micropumps were able to transport and direct a precise sample amount through multiple microchannels towards the sensing regions with

the MIP films. The detection was based on the surface plasmon resonance, where analytical signal was proportional to the number of molecules adsorbed on the MIP films. This strategy was innovative in relation to the biosensing technique allowing new applications in clinical analysis. In this way, a micro-flow sensor chip for terbutaline [104] was built with a micro flow cell (10 mm × 1 mm) packed with 2 mg MIP, presenting good quantities of recognition sites and porosity.

Most of researches carried out for improving MIP flow-trough sensors did not present problems with matrix effects, parallel interactions and low selectivity that should be deeply investigated. Indeed, most of applications presented a lower sampling rate due to kinetics of the loading, washing and reconditioning steps. This aspect becomes more pronounced when MIP is applied as in-line SPE due to the fragile interactions between analyte and polymer, strongly dependent on flow-rate. Another important feature linked to flow-rate is the stability and/or response time of the sensor that depends on the kinetics of template-polymer interaction. Sometimes, sample stopping is a suitable strategy to improve sensitivity, yet decreasing sample throughput. Anyhow, the washing step is considered as the most important parameter to obtain adequate selectivity. Application of MIP as in-line flow-trough sensor is recent and further research is needed to reach its potential in developing sensor as better alternative in relation to the sol–gel, ion exchange resin and polymeric materials used as sensing materials. Selectivity, sampling throughput and sensitivity are generally the aimed characteristics, mainly when biological processes are involved. In-line MISPE as flow through sensor is recommendable when low-cost, long-term stability and simplicity are required.

3.2. MIP as in-line solid phase extractor

Differently from the use of MIPs as flow-trough sensors performing selective interactions with the analyte and simultaneous quantification, MIP as on-line solid phase extractor acts like an adsorbent that retains the analytes or concomitants for subsequent elution and detection (Fig. 1). The species are selectively separated in the MIP packed in the mini-column and the steps of washing, elution and reconditioning are carried out. The flow injection system is a suitable analytical tool to implement these steps in a fast, rugged and efficient manner.

Generally, mini-columns are filled with an amount of MIP particles that is enough to attain adequate analytical characteristics, without vacancies that result in preferential pathways and hides for sample volume. This condition is directly associated to the particles size thus number of binding sites and surface area. Insertion of the mini-column into the flow system is considered as a simplified alternative for sample preparation to LC. Replacement of slow procedures aiming automation of the extraction processes for a single analyte or potential interfering species has been the main purpose.

A simple flow injection system for fluorimetric determination of β-estradiol after analyte concentration in a MIP capillary mini-column was developed for routine analyses [61]. The sample (500 μL) was inserted into the manifold and analyte was adsorbed on the MIP capillary (1.0 mg of 50–100 μm particles size). The eluent solution was then directed to flow through the mini-column displacing the analyte towards the fluorimeter. The approach aggregated simple and low cost instrumentation with the high selectivity of the MIP and the sensitivity of the fluorimetric technique. Lower detection limit (1.12 $\mu g\,L^{-1}$) and higher sampling throughput ($10\,h^{-1}$) in comparison with chromatographic technique were attained. A similar manifold was designed for separation and quantification of the carbaryl pesticide in river waters by exploiting fluorimetric [62] and potentiometric detection [63]. In the last application, polymeric beads packed inside a mini-column inserted between the sample injection port and the pH electrode was exploited to the molecular recognition of carbaryl in rat plasma samples.

Flow injection system is particularly attractive when a chemical reaction involving the analyte adsorbed in the MIP is required. This is usual in CL, where the analyte can be detected during or after the elution step, and the determination of metformin [105] can be selected for illustrative purposes. A versatile manifold was designed to bring together the steps of sample introduction, extraction/concentration of metformin in the MIP mini-column, elution with a mixed reagent (cupric polyphosphate plus hydrogen peroxide), and further detection. The metformin adsorbed in the MIP was oxidized by the eluent reagent, resulting in the hydroxyl radical that reacted with Rhodamine B to yield chemiluminescence. Due to the metformin decomposition during elution, it was not necessary an additional eluent or washing solution. The proposed system proved to be an excellent alternative to routine analysis, being applied to analysis of human serum.

An eight-way injection valve was used to accommodate a mini-column packed with MIP into the sampling loop for in-line separation of tetracycline (TC) [106]. After the loading step, a carrier solution (acetonitrile/HNO_3, 4:1, v/v) was used for TC elution and further reaction with Ce(IV) and Rhodamine B to generate the CL. Interferent effects were reported in relation to oxytetracycline, a structural analogous to TC, requiring an intermediate differential pulsed elution with 3% (v/v) acetic acid. Good recoveries (97–107%) were found in relation to spiked fish samples. A similar approach was reported for the determination of pazufloxacin in human urine [107], resulting in a very selective method.

MIP was implemented in a flow injection system with a manual home-made injector–commuter for separation/concentration of chloroguaiacol [108]. The MIP mini-column was inserted in the injector loop and, after analyte separation/concentration, the injector was switched for elution and further amperometric detection. The main parameters were optimized by applying fractional factorial and Doehlert design, and the system was applied to river water samples. Coupling of MIP as SPE in flow analysis was efficient presenting a concentration factor of 110.1. Washing step was not a limiting factor in sampling rate, and high selectivity and sensitivity were attained, pointing out the good perspectives of this methodology for routine analysis.

Computer operated three-way solenoid valves allow efficient insertion of the sample and reagent solutions with an increase in the automation degree of the system, as demonstrated in the spectrophotometric determination of catechol [109]. Analyte separation was performed by implementing a MIP-catechol in a multi-commuted system composed by seven solenoid valves to manage the sample insertion into MIP, the washing and elution steps, and the reaction development. Reduction of Mn(VII) to Mn(II), monitored at 528 nm, was proportional and selective to the catechol concentration after a sample clean-up in a mini-column filled with C18 and methacrylic polymer before the MIP column. Results obtained for guarana powder, mate tea and tap water were in agreement with those obtained by LC with good figures of merit, showing that a non-selective chemical reaction can be exploited together with selective adsorbents. Simplified strategies involving MIP as sample clean up and analyte concentration have been reported as in-line procedures with voltammetric detection for the determinations of pirimicarb in water [110] and chloramphenicol and sulfamethazine in milk [111,112].

A MIP synthesized with ferriprotopophyrin IX (hemin) with peroxidase-like characteristics and 4-aminophenol as template was packed into a mini-column in a flow injection system [113]. The selective amperometric determination of 4-aminophenol was

influenced by the flow and chemical parameters of the flow system that were optimized by using a fractional factorial design. Important aspects were the MIP surface area and porosity, considered more relevant than the uniformity of the packed particles. One can then infer that the irregular nature of the MIP particles becomes less relevant for polymer with larger surface areas. This corroborates with the aim of this review, where the protocols for using SPE in flow systems are very dependent on the MIP synthesis.

It is important to stress the scarce number of applications involving MIP for SPE in flow systems as an alternative to LC. In fact, even the MIP presenting suitable selectivity, molecules with similarities in chemical structure and/or functional groups are preferentially adsorbed. Deeper studies on synthesis process, binding sites and washing steps should be then carried out to attain high selective separations, *e.g.* chiral species, especially in relation to less selective detectors. On the other hand, the low cost, portability, simplicity, speed of analysis, low reagent and sample consumptions, etc. are attractive features in comparison with the traditional methods of separation.

4. Trends

Although all the in-line applications included the MIP preparation in bulk mode resulting in particles with irregular sizes, alternative synthesis such as suspension polymerization can be useful to implement MIPs in flow analysis. MIP could be easily implemented in the Lab-On-Valve system, simply by synthesizing it as beads [114,65] once that this approach demands injection of bead suspensions as sampling and extraction strategy [7].

Polymerization is considered the initial step of a successful selectivity, and capacity in monitoring the final polymer is a promising survey. Novel technologies have been developed to monitor the synthesis [115,116], where MIP is *in situ* formed assisted by a computational program exploiting combinatorial analysis. The synthesis is done by semiautomatic systems and a screening procedure is carried out in order to evaluate the most suitable polymer. Minimization of synthesis on large scale is then efficiently performed, resulting in an allied to the simplicity and low cost of the flow systems. Miniaturized systems are the most attractive form to the selective treatment of low-volume samples exploiting MIP. However, important aspects involving selectivity, conditions of percolation, washing and elution should be carefully studied in relation to the minimization of polymer mass.

5. Conclusions

After an extensive covering of the main aspects involving in-line MISPE, one can say that not all MIPs can be used in flow systems. This depends on the sample matrix, synthesis conditions, required solvents, detection systems, etc. In this way, the synthesis may offer the availability to use solvents based on water or diluted into it; or the interactions between the template and functional monomers allows the use of polar and protics solvents. It is important to emphasize that the selectivity is not an inherent MIP characteristic, but is a combination of all parameters involved during the synthesis and extraction procedures after the polymerization. Anyhow, the better way to take advantage of flow systems with MIPs as solid phase extractors is associated with the speed of the extraction steps (loading, washing, elution and reconditioning), flexibility and ruggedness regarding mechanical and chemical stability compared with other biomaterials (enzymes, imunossorbents), easy in handling solutions, simplicity in the polymer preparations and low cost. In general, all the flow parameters play a pronounced influence on the binding and rebinding in the polymer cavities, as well as particle size and packing mode. The MIP-flow analysis marriage can be considered as promising to MIP implementation in large-scale routine analyses.

Acknowledgments

The authors thank the Fundação de Amparo a Pesquisa do Estado de São Paulo (FAPESP, proc. 2005/59903-3, 2005/53767-0 and 2006/07309-3) and Conselho Nacional de Desenvolvimento Científico e Tecnológico (CNPq) for financial support and fellowships.

References

[1] Z. Fang, Anal. Chim. Acta 400 (1999) 233.
[2] V. Cerda, J.M. Estela, Int. J. Environ. Anal. Chem. 85 (2005) 231.
[3] J. Ruzicka, E.H. Hansen, Anal. Chim. Acta 78 (1975) 145.
[4] E.A.G. Zagatto, P.J. Worsfold, Flow analysis: overview, in: P.J. Worsfold, A. Townshend, C.F. Poole (Eds.), Encyclopedia of Analytical Sciences, Elsevier, Oxford, 2005, p. 24.
[5] J. Ruzicka, G.D. Marshall, Anal. Chim. Acta 237 (1990) 329.
[6] A.C.B. Dias, J.M.T. Carneiro, V. Grassi, E.A.G. Zagatto, Anal. Chim. Acta 514 (2004) 253.
[7] J. Ruzicka, Analyst 125 (2000) 1053.
[8] B.F. Reis, M.F. Gine, E.A.G. Zagatto, J.L.F.C. Lima, R.A. Lapa, Anal. Chim. Acta 293 (1994) 129.
[9] V. Cerda, J.M. Estela, R. Forteza, A. Cladera, E. Becerra, P. Altimira, P. Sitjar, Talanta 50 (1999) 695.
[10] R.A.S. Lapa, J.L.F.C. Lima, B.F. Reis, J.L.M. Santos, E.A.G. Zagatto, Anal. Chim. Acta 466 (2002) 125.
[11] J. Wang, E.H. Hansen, Trends Anal. Chem. 24 (2005) 1.
[12] A. Economou, Trends Anal. Chem. 24 (2005) 416.
[13] V. Gomez, M.P. Callao, Trends Anal. Chem. 26 (2007) 767.
[14] M. Hennion, J. Chromatogr. A 856 (1999) 3.
[15] E.A.G. Zagatto, A.C.B. Dias, In-line sample preparation in flow analysis, in: M.A.Z. Arruda (Ed.), Trends in Sample Preparation, Nova Science Pub. Inc., New York, 2007, pp. 197–232.
[16] C.F. Poole, Trends Anal. Chem. 22 (2003) 362.
[17] P.C. Hauser, J.C. Litten, Anal. Chim. Acta 294 (1994) 49.
[18] C. Pons, R. Forteza, V. Cerda, Talanta 66 (2005) 210.
[19] A.N. Anthemidis, G.A. Zachariadis, J.A. Stratis, Talanta 54 (2001) 935.
[20] Y. Wang, M.L. Chen, J.H. Wang, J. Anal. At. Spectrom. 21 (2006) 535.
[21] N. Masque, R.M. Marce, F. Borrull, Trends Anal. Chem. 20 (2001) 477.
[22] M. Miro, E.H. Hansen, Trends Anal. Chem. 25 (2006) 267.
[23] B.F. Reis, C.E.S. Miranda, N. Baccan, Quim. Nova 19 (1996) 623.
[24] V. Camel, Spectrochim. Acta B 58 (2003) 1177.
[25] Q.S. Pu, P. Liu, Q.Y. Sun, Z.X. Su, Microchim. Acta 143 (2003) 45.
[26] V.A. Lemos, A.A. Jesus, E.M. Gama, G.T. David, R.T. Yamaki, Anal. Lett. 38 (2005) 683.
[27] X.P. Yan, Y. Li, Y. Jiang, Anal. Chem. 75 (2003) 2251.
[28] G.A. Zachariadis, A.N. Anthemidis, P.G. Bettas, J.A. Stratis, Talanta 57 (2002) 919.
[29] G.D. Matos, M.A.Z. Arruda, Spectrosc. Lett. 39 (2006) 755.
[30] C.R.T. Tarley, S.L.C. Ferreira, M.A.Z. Arruda, Microchem. J. 77 (2004) 163.
[31] Z.H. Wang, Z.P. Zhang, Z.P. Wang, L.W. Liu, X.P. Yan, Anal. Chim. Acta 514 (2004) 151.
[32] H. Katsumata, A. Begum, S. Kaneco, T. Suzuki, K. Ohta, Anal. Chim. Acta 502 (2004) 167.
[33] F.G. Tamayo, E. Turiel, A. Martin-Esteban, J. Chromatogr. A 1152 (2007) 32.
[34] V. Pichon, K. Haupt, J. Liquid Chromatogr. Relat. Technol. 29 (2006) 989.
[35] C.S. Magalhaes, J.S. Garcia, A.S. Lopes, E.C. Figueiredo, M.A.Z. Arruda, Strategies for sample preparation focusing on biomolecules determination/characterization, in: M.A.Z. Arruda (Ed.), Trends in Sample Preparation, Nova Science Pub. Inc., New York, 2007, pp. 245–288.
[36] M.V. Polyakov, Zhur. Fiz. Khim. 2 (1931) 799.
[37] L. Pauling, J. Am. Chem. Soc. 62 (1940) 2463.
[38] F.H. Dickey, Proc. Natl. Acad. Sci. 35 (1949) 227.
[39] R.G. Haldeman, P.H. Emmett, J. Phys. Chem. 59 (1955) 1039.
[40] S.A. Bernhard, J. Am. Chem. Soc. 74 (1952) 4946.
[41] J. Sagiv, J. Am. Chem. Soc. 102 (1980) 92.
[42] S.R. Cohen, R. Naaman, J. Sagiv, J. Phys. Chem. 90 (1986) 3054.
[43] G. Wulff, A. Sarhan, Angew. Chem. Int. Ed. 11 (1972) 341.
[44] M. Szumski, B. Buszewski, J. Sep. Sci. 27 (2004) 837.
[45] G. Wulff, A. Sarhan, K. Zabrocki, Tetrahedron Lett. 14 (1973) 4329.
[46] C. Alexander, H.S. Andersson, L.I. Andersson, R.J. Ansell, N. Kirsch, I.A. Nicholls, J. O'Mahony, M.J. Whitcombe, J. Mol. Recognit. 19 (2006) 106.
[47] G. Wulff, Angew. Chem. Int. Ed. 34 (1995) 1812.
[48] G. Wulff, Chemtech 28 (1998) 19.
[49] L.I. Andersson, C.F. Mandenius, K. Mosbach, Tetrahedron Lett. 29 (1988) 5437.

[50] M. Glad, O. Norrlow, B. Sellergren, N. Siegbahn, K. Mosbach, J. Chromatogr. A 347 (1985) 11.
[51] I. Ferrer, D. Barcelo, Trends Anal. Chem. 18 (1999) 180.
[52] V. Pichon, J. Chromatogr. A 1152 (2007) 41.
[53] M.J. Whitcombe, E.N. Vulfson, Adv. Mater. 13 (2001) 467.
[54] P.A.G. Cormack, A.Z. Elorza, J. Chromatogr. B: Anal. Technol. Biomed. Life Sci. 804 (2004) 173.
[55] B. Sellergren, Molecularly Imprinted Polymers. Man-made Mimics of Antibodies and Their Applications in Analytical Chemistry, Elsevier, Amsterdam, 2001.
[56] L. Ye, K. Mosbach, J. Inclusion Phenom. Macrocyclic Chem. 41 (2001) 107.
[57] B. Ekberg, K. Mosbach, Trends Biotechnol. 7 (1989) 92.
[58] F.X. Qiao, H.W. Sun, H.Y. Yan, K.H. Row, Chromatographia 64 (2006) 625.
[59] D.A. Spivak, Adv. Drug Delivery Rev. 57 (2005) 1779.
[60] R.J. Ansell, J. Chromatogr. B 804 (2004) 151.
[61] J.C. Bravo, P. Fernandez, J.S. Durand, Analyst 130 (2005) 1404.
[62] I. Sanchez-Barragan, K. Karim, J.M. Costa-Fernandez, S.A. Piletsky, A. Sanz-Medel, Sens. Actuators B 123 (2007) 798.
[63] J. Hantash, A. Bartlett, P. Oldfield, G. Dénès, R. O'Rielly, F. David, Anal. Bioanal. Chem. 387 (2007) 351.
[64] J. Haginaka, C. Kagawa, J. Chromatogr. A 948 (2002) 77.
[65] L. Guardia, R. Badıa, M.E. Dıaz-Garcıa, Biosens. Bioelectron. 21 (2006) 1822.
[66] W.H. Li, H.D.H. Stover, Macromolecules 33 (2000) 4354.
[67] X.D. Huang, F. Qin, X.M. Chen, Y.Q. Liu, H.F. Zou, J. Chromatogr. A 804 (2004) 13.
[68] A. Katz, M.E. Davis, Macromolecules 32 (1999) 4113.
[69] J.R. Ferreira, E.A.G. Zagatto, M.A.Z. Arruda, S.M.B. Brienza, Analyst 115 (1990) 779.
[70] W.L. Song, Z.L. Zhi, L.S. Wang, Talanta 44 (1997) 1423.
[71] J. Ruzicka, E.H. Hansen, Flow Injection Analysis, 2nd edn., Wiley-Interscience, New York, 1988.
[72] A. Ellwanger, C. Berggren, S. Bayoudh, C. Crecenzi, L. Karlsson, P.K. Owens, K. Ensing, P. Cormack, D. Sherrington, B. Sellergren, Analyst 126 (2001) 784.
[73] D.A. Spivak, K.J. Shea, J. Am. Chem. Soc. 119 (1997) 4388.
[74] A.C.B. Dias, E.P. Borges, E.A.G. Zagatto, P.J. Worsfold, Talanta 68 (2006) 1076.
[75] E. Caro, R.M. Marce, P.A.G. Cormack, D.C. Sherrington, F. Borrull, J. Chromatogr. A 1047 (2004) 175.
[76] C.R.T. Tarley, L.T. Kubota, Anal. Chim. Acta 548 (2005) 11.
[77] F. Chapuis, V. Pichon, F. Lanza, B. Sellergren, M.C. Hennion, J. Chromatogr. B: Anal. Technol. Biomed. Life Sci. 804 (2004) 93.
[78] C.J. Stephenson, K.D. Shimizu, Polym. Int. 56 (2007) 482.
[79] O.Y.F. Henry, D.C. Cullen, S.A. Piletsky, Anal. Bioanal. Chem. 382 (2005) 947.
[80] J.L. Suárez-Rodriguez, M.E. Diaz-Garcia, Anal. Chim. Acta 405 (2000) 67.
[81] J.L. Suarez-Rodriguez, M.E. Diaz-Garcia, Biosens. Bioelectron. 16 (2001) 955.
[82] I. Sanchez-Barragan, J.M. Costa-Fernandez, R. Pereiro, A. Sanz-Medel, A. Salinas, A. Segura, A. Fernandez-Gutierrez, A. Ballesteros, J.M. Gonzalez, Anal. Chem. 77 (2005) 7005.
[83] J.M. Traviesa-Alvarez, I. Sanchez-Barragan, J.M. Costa-Fernandez, R.P.A. Sanz-Medel, Analyst 132 (2007) 218.
[84] T.P. Rao, R. Kala, S. Daniel, Anal. Chim. Acta 578 (2006) 105.
[85] T.P. Rao, S. Daniel, J.M. Gladis, Trends Anal. Chem. 23 (2004) 28.
[86] J. Lin, M. Yamada, Anal. Chem. 72 (2000) 1148.
[87] J. Lin, M. Yamada, Analyst 126 (2001) 810.
[88] J. Du, L. Shen, J. Lu, Anal. Chim. Acta 489 (2003) 183.
[89] H. Zhou, Z. Zhang, D. He, Y. Hu, Y. Huang, D. Chen, Anal. Chim. Acta 523 (2004) 237.
[90] H. Zhou, Z. Zhang, D. He, Y. Xiong, Sens. Actuators B 107 (2005) 798.
[91] Y. Xiong, H. Zhou, Z. Zhang, D. He, C. He, J. Pharm. Biomed. Anal. 41 (2006) 694.
[92] Y. Xiong, H. Zhou, Z. Zhang, D. He, C. He, Spectrochim. Acta A 66 (2007) 341.
[93] F. Nie, J. Lu, Y. He, J. Du, Talanta 66 (2005) 728.
[94] M. Liu, J. Lu, Y. He, J. Du, Anal. Chim. Acta 541 (2005) 99.
[95] Y. He, J. Lu, H. Zhang, J. Du, Microchim. Acta 149 (2005) 239.
[96] I. Surugiu, J. Svitel, L. Ye, K. Haupt, B. Danielsson, Anal. Chem. 73 (2001) 4388.
[97] S. Al-Kindy, R. Badıa, M.E. Dıaz-Garcıa, Anal. Lett. 35 (2002) 1763.
[98] B.S. Ebarvia, C.A. Binag, F. Sevilla, Anal. Bioanal. Chem. 378 (2004) 1331.
[99] M. Zougagh, A. Rıos, M. Valcarcel, Anal. Chim. Acta 539 (2005) 117.
[100] A. Wu, M. Syu, Biosens. Bioelectron. 21 (2006) 2345.
[101] M. Avila, M. Zougagh, A. Escarpa, A. Rıos, Talanta 72 (2007) 1362.
[102] Z. Zhang, D. He, W. Liu, Y. Lv, Luminescence 20 (2005) 377.
[103] S.C. Huang, G.B. Lee, F.C. Chien, S.J. Chen, W.J. Chen, M.C. Yang, J. Micromech. Microeng. 16 (2006) 1251.
[104] D. He, Z. Zhang, H. Zhou, Y. Huang, Talanta 69 (2006) 1215.
[105] C. He, Z. Zhang, D. He, Y. Xiong, Anal. Bioanal. Chem. 385 (2006) 128.
[106] Y. Xiong, H. Zhou, Z. Zhang, D. He, C. He, Analyst 131 (2006) 829.
[107] C. Yang, Z. Zhang, S. Chen, F. Yang, Microchim. Acta 159 (2007) 299.
[108] C.R.T. Tarley, M.G. Segatelli, L.T. Kubota, Talanta 69 (2006) 259.
[109] E.C. Figueiredo, C.R.T. Tarley, L.T. Kubota, S. Rath, M.A.Z. Arruda, Microchem. J. 85 (2007) 290.
[110] M.L. Mena, P. Martınez-Ruiz, A.J. Reviejo, J.M. Pingarron, Anal. Chim. Acta 451 (2002) 297.
[111] M.L. Mena, L. Agüí, P. Martinez-Ruiz, P. Yáñez-Sedeño, A.J. Reviejo, J.M. Pingarrón, Anal. Bioanal. Chem. 376 (2003) 18.
[112] A.G. Prada, P. Martınez-Ruiz, A.J. Reviejo, J.M. Pingarron, Anal. Chim. Acta 539 (2005) 125.
[113] W.J.R. Santos, P.R. Lima, C.R.T. Tarley, L.T. Kubota, Anal. Bioanal. Chem. 389 (2007) 1919.
[114] A.G. Mayes, K. Mosbach, Anal. Chem. 68 (1996) 3769.
[115] T. Takeuchi, D. Fukuma, J. Matsui, Anal. Chem. 71 (1999) 285.
[116] F.N. Villoslada, T. Takeuchi, Bull. Chem. Soc. Jpn. 78 (2005) 1354.

Talanta 76 (2008) 1252–1255

Contents lists available at ScienceDirect

Talanta

journal homepage: www.elsevier.com/locate/talanta

Short communication

Determination of Cd in urine by cloud point extraction–tungsten coil atomic absorption spectrometry

George L. Donati [a], Kathryn E. Pharr [a], Clifton P. Calloway Jr. [b], Joaquim A. Nóbrega [c], Bradley T. Jones [a,*]

[a] Department of Chemistry, Wake Forest University, Winston-Salem, NC 27109, USA
[b] Department of Chemistry, Winthrop University, Rock Hill, SC 29733, USA
[c] Departamento de Química, Universidade Federal de São Carlos, São Carlos SP, Brazil

ARTICLE INFO

Article history:
Received 21 December 2007
Received in revised form 1 May 2008
Accepted 4 May 2008
Available online 9 May 2008

Keywords:
Tungsten coil
Atomic absorption
Cloud point extraction
Cadmium
Urine

ABSTRACT

Cadmium concentrations in human urine are typically at or below the 1 μg L^{-1} level, so only a handful of techniques may be appropriate for this application. These include sophisticated methods such as graphite furnace atomic absorption spectrometry and inductively coupled plasma mass spectrometry. While tungsten coil atomic absorption spectrometry is a simpler and less expensive technique, its practical detection limits often prohibit the detection of Cd in normal urine samples. In addition, the nature of the urine matrix often necessitates accurate background correction techniques, which would add expense and complexity to the tungsten coil instrument. This manuscript describes a cloud point extraction method that reduces matrix interference while preconcentrating Cd by a factor of 15. Ammonium pyrrolidinedithiocarbamate and Triton X-114 are used as complexing agent and surfactant, respectively, in the extraction procedure. Triton X-114 forms an extractant coacervate surfactant-rich phase that is denser than water, so the aqueous supernatant is easily removed leaving the metal-containing surfactant layer intact. A 25 μL aliquot of this preconcentrated sample is placed directly onto the tungsten coil for analysis. The cloud point extraction procedure allows for simple background correction based either on the measurement of absorption at a nearby wavelength, or measurement of absorption at a time in the atomization step immediately prior to the onset of the Cd signal. Seven human urine samples are analyzed by this technique and the results are compared to those found by the inductively coupled plasma mass spectrometry analysis of the same samples performed at a different institution. The limit of detection for Cd in urine is 5 ng L^{-1} for cloud point extraction tungsten coil atomic absorption spectrometry. The accuracy of the method is determined with a standard reference material (*toxic metals in freeze-dried urine)* and the determined values agree with the reported levels at the 95% confidence level.

1. Introduction

Urinary cadmium concentration is considered the best biomarker for total body burden, past exposure, and renal accumulation [1,2]. As a result, this particular sample type has been a common target for analytical method development [3]. However, severe matrix interference and very low analyte concentration contribute to the challenging nature of this problem. The most sensitive and accurate urine-Cd analyses are therefore performed by state of the art techniques such as graphite furnace atomic absorption spectrometry (GFAAS) or inductively coupled plasma mass spectrometry (ICP-MS). Simpler, less expensive techniques such as tungsten coil atomic absorption spectrometry (WCAAS) often lack the sophistication necessary to account for the complicated background presented by the urine matrix, and this problem is exacerbated by limits of detection (LODs) that approach normal urine-Cd levels even in the absence of a complicated matrix. Previously reported Cd LODs for WCAAS devices vary from 0.04 to 3 μg L^{-1} [4–8], in relatively simple sample matrices (Table 1). Preconcentration techniques employing fullerene C-60 [9] and Chelex-100 [10] provide LODs that are lower still: 0.002 and 0.010 μg L^{-1}, respectively, when relatively simple sample matrices are analyzed. While not yet applied to WCAAS, another powerful preconcentration technique is cloud point extraction (CPE). This method has been employed for the determination of Cd in human hair by flame atomic absorption spectrometry with an LOD of 3 μg L^{-1} [11], and for the determination of Cd in blood by GFAAS with an LOD of 0.02 μg L^{-1} [12]. The work described below is the

* Corresponding author. Tel.: +1 336 758 5512; fax: +1 336 758 3889.
E-mail address: jonesbt@wfu.edu (B.T. Jones).

0039-9140/$ – see front matter © 2008 Elsevier B.V. All rights reserved.
doi:10.1016/j.talanta.2008.05.003

Table 1
Previously reported WCAAS limits of detection for cadmium

Matrix	Limit of detection ($\mu g L^{-1}$)	Reference
Water	3	[4]
Water	0.2	[5]
Water	0.1	[6]
0.2% HNO_3	0.06	[7]
Mussel acid digests	0.04	[8]
Fullerene C-60 extract from water	0.002	[9]
Chelex-100 extract from beverages	0.01	[10]

first application of a combined CPE-WCAAS method. The CPE step reduces the WCAAS LOD to the point where normal urine-Cd levels may be detected. At the same time, the urine matrix is reduced so that simple background correction techniques may be employed.

2. Experimental

2.1. Instrumental

The WCAAS system was designed and assembled in the laboratory, and is similar to those reported elsewhere [4,5,13]. The atomizer was the 10-turn tungsten filament extracted from a 150 W, 15 V commercially available slide projector light bulb (Osram Xenophot 64633 HXL, Pullach, Germany). The fused silica bulb envelope was removed, leaving the filament and bulb base intact. The bulb base was mounted in a standard ceramic two-pronged power socket. Positioning of the filament from coil to coil was highly reproducible since the bulbs were mass produced to strict optical specifications. The filament was housed inside a glass atomization cell with fused silica windows. A purge gas composed of 10% (v/v) H_2/Ar, at a 1.0 L min^{-1} flow rate, prevented coil oxidation and cooled the filament after atomization. Power was provided by a programmable, constant-current, solid-state DC power source (BatMod, Vicor, Andover, MA, USA). The output from the radiation source (10 W Cd EDL, PerkinElmer, Norwalk, CT, USA) was focused through the W-coil atomizer using a 25 mm diameter, 75 mm focal length fused silica lens. The unabsorbed radiation exiting the opposite end of the atomization cell was collected with a second identical fused silica lens, and imaged onto the entrance slit of a crossed Czerny-Turner monochromator (MonSpec 18, Scientific Measurement Systems Inc., Grand Junction, CO, USA). The monochromator was equipped with a 2400 grooves mm^{-1} grating (52 mm × 40 mm), resulting in a reciprocal linear dispersion of 2.4 nm mm^{-1} at 230 nm. The detector was a thermoelectrically cooled charge coupled device (CCD, Spec-10, Princeton Instruments, Roper Scientific, Trenton, NJ, USA) with a two-dimensional array of 1340 × 100 pixels. Each pixel was 20 μm × 20 μm in size, making the image area on the CCD camera 26.8 mm × 2 mm. Based on a slit width approximately the size of a single detector pixel (25 μm), the theoretical spectral bandpass of the system was 0.05 nm. In practice, the measured full width at half maximum (FWHM) for an emission line from the lamp was 2–3 pixels, so the practical bandpass was 0.15 nm. The spectral window covered by the CCD detector was slightly less than 65 nm, and the central wavelength was set by adjusting the monochromator wavelength dial. User selectable CCD integration times as low as 1 ms were possible, and the maximum signal to noise ratio (S/N) was observed with an integration time of 20 ms. One hundred successive spectra were recorded during the atomization step. Calibration was performed in two modes: peak height (absorbance signal measured for the single spectrum collected 500 ms after the onset of atomization) and peak area (absorbance signals summed for the 12 spectra corresponding to the period of greatest absorption, 400–620 ms after the onset of atomization).

2.2. Standards and reagents

Reference solutions were prepared by diluting a Cd stock solution (1000 mg L^{-1}, SPEX CertPrep, Metuchen, NJ, USA) with distilled-deionized water (Milli-Q, Millipore, Bedford, MA, USA). A standard reference material from the National Institute of Standards and Technology (*Toxic metals in freeze-dried urine*, normal level, SRM 2670, NIST, Gaithersburg, MD, USA) was used to check the method accuracy. Trace metal grade HNO_3 14 mol L^{-1} (Fisher Scientific, Pittsburg, PA, USA) and H_2O_2 30% (v/v) (Acros, Morris Plains, NJ, USA) were used in the microwave-assisted sample digestions. Ammonium pyrrolidinedithiocarbamate (APDC, Sigma–Aldrich, St. Louis, MO, USA) and octylphenoxypolyethoxyethanol (Triton X-114, Sigma–Aldrich) were used as complexing agent and surfactant, respectively, in the cloud point extraction. Solutions of APDC (0.5%, m/v) and TX-114 (5%, v/v) were prepared by diluting appropriate amounts of the reagents with distilled-deionized water (Millipore). All pH adjustments before the cloud point extraction were performed with trace metal grade ammonium hydroxide (Fisher).

2.3. Sample preparation

Sample aliquots of 3.0 mL urine were transferred to PTFE microwave digestion vessels. Volumes of 1.0 mL concentrated HNO_3 and 0.50 mL of H_2O_2 were added to the samples, and the solutions were submitted to a five-step heating program in the microwave oven (630 W CEM MDS 2000 closed-vessel microwave oven, CEM Corp. Matthews, NC, USA): 25% power for 2 min, 0% for 2 min, 35% for 3 min, 50% for 4.5 min, and 60% for 6 min. After cooling, the solutions were transferred to 15-mL centrifuge tubes and neutralized with NH_4OH to pH 6.0. Then, the solutions were diluted to 10 mL with distilled-deionized water, and subjected to cloud point extraction.

The CPE procedure was based on the optimal conditions suggested in the literature [14,15]. A 0.5 mL aliquot of APDC (0.5%, m/v) was added to the 10 mL diluted/digested sample volume. After 20 min, 0.5 mL of TX-114 (5%, v/v) was added, and the solution was heated in a water bath for 20 min at 45 °C. To facilitate phase separation, the solution was centrifuged at 2500 rpm (660 × *g*) for 10 min. Then, the solution was chilled in a freezer for 20 min (at 10 °C) to increase the viscosity of the lower TX-114 surfactant-rich phase, which in turn facilitated the removal of the supernatant (aqueous surfactant-poor phase) with a micropipette. Chilling for longer than 20 min risked loss of Cd, since the solution would eventually reform a one phase homogeneous mixture at temperatures below the cloud point. The final volume of the organic phase was then increased to 0.20 mL with the addition of ethanol, which served to reduce the viscosity of the surfactant phase. This step facilitated the transfer of the preconcentrated solution to the W-coil. Standard Cd solutions were treated in the same fashion. The CPE method resulted in a concentration factor of 15 (3.0 mL of urine reduced to 0.20 mL of extract).

2.4. WCAAS analysis

A 25 μL volume of the CPE preconcentrated sample (or standard) was transferred to the W-coil using a micropipette. The atomization cycle consisted of a 7-step heating program (Table 2). The first two steps accounted for gradual solvent volatilization to prevent potential sample loss. The coil reached dryness at the end of step 2, as evidenced by an increase in the applied voltage necessary to maintain a constant current during the last few seconds of this stage. Since a wet coil had a lower resistance, a dry coil reached a higher temperature at a given constant current [16]. Therefore, the ashing

Table 2
Tungsten coil heating cycle for CPE urine samples

Step	Current (A)	Temperature[a] (°C)	Time (s)
1	2.8	25–100[b]	25
2	2.3	25–100[b]	40
3	2.1	700	35
4	1.5	520	15
5	0	25	10
6[c]	10	3150	5
7	0	25	25

[a] Temperature estimated by: $T = 309A + 52$ (Ref. [16]).
[b] In steps 1 and 2, the coil is wet, so while the temperature must be below 100, it cannot be calculated using the above equation.
[c] Data was collected during this step.

stage of the cycle, steps 3 and 4, employed lower currents. Using progressively lower currents prevented the W-coil from glowing red prior to atomization, thus reducing a potential loss of analyte. A cooling period (step 5) ensured a reproducible high temperature atomization step, as the beginning temperature was always the same (near room temperature). Finally, the high current (10 A) atomization step generated the atomic cloud. This current was the maximum available from the power supply, and therefore produced the greatest possible peak heights. These peak heights also allowed for shorter detector integration times, which resulted in reduced background blackbody emission measurements from the coil. The detector was triggered at the beginning of the atomization step (step 6), and one hundred spectra were collected automatically. The final cooling step readied the W-coil for the deposition of the next sample aliquot.

2.5. ICP-MS analysis

For comparison purposes, the seven human urine samples analyzed by WCAAS were also transported (frozen) to a different laboratory for ICP-MS analysis: Research Triangle Institute, Research Triangle Park, NC. For the ICP-MS method, the urine samples were thawed and then vortexed for 15 s. Sample aliquots of 2.0 mL were transferred to digestion tubes. Volumes of 1.0 mL of concentrated HNO_3 and 0.25 mL of H_2O_2 were added to each tube. The tubes were then placed in a *Digi*PreP MS heating block (SCP Science, Champlain, NY, USA) and heated in the following stages: 60 min at 60 °C (ramp time 30 min), 60 min at 80 °C (ramp time 10 min), and 120 min at 110 °C (ramp time 20 min). After cooling, the sample solutions were diluted with distilled-deionized water to 10.0 mL and vortexed for 15 s. Finally, a 50.0 μL aliquot of a ^{89}Y internal standard solution (1 mg L^{-1} ^{89}Y solution in 2%, v/v HNO_3) was added to a 5.00 mL aliquot of the digested samples. The resulting solution was analyzed with a quadrupole ICP-MS instrument (Thermo X Series II X0637, Waltham, MA, USA).

3. Results and discussion

3.1. Background correction

Fig. 1 depicts the absorption profiles collected during the high temperature atomization step for the WCAAS analysis of a cloud point extracted urine sample. The 10 amp atomization step began at time zero, and spectra were collected at 20 ms intervals. Two emission lines from the Cd EDL were monitored simultaneously: the 228.8 nm Cd absorption line which is sensitive to both Cd and background absorption, and the 226.5 nm line which is not sensitive to Cd and thus reflects only the background absorption. The profile represented by circles is the background absorbance measured at the 226.5 nm wavelength. The profile depicted in squares represents the absorbance measured at the 228.8 nm line minus the absorbance measured at the 226.5 nm line. This profile, therefore, represents the background corrected Cd signal, assuming that the background absorbance is the same at the two wavelengths.

Notice that the background profile contains two features, a peak with maximum occurring at 480 ms and a second one with maximum at 580 ms. The first peak appears only for samples containing Triton X-114, so it may be attributed to the CPE process. The second peak occurs only for extracted urine samples, so it may be attributed to those components, other than Cd in urine, that are also concentrated by the CPE technique. Pure aqueous samples produce neither background peak, and CPE extracts of aqueous solutions produce only the first peak. These peaks are generally the same size and shape at 228.8 nm, with the Cd peak positioned in between, so that the single Cd profile in the figure results from their subtraction. This background-corrected urine-Cd signal is almost identical in time and shape to that observed for the WCAAS analysis of purely aqueous Cd standard solution. This off-line, or near-line, background correction technique has been reported previously for WCAAS determinations of Cd [5,6], and in fact tables with suggested "close lines for background correction" for many elements have been published [17].

While near-line correction has provided reasonable analytical results for simple Cd-containing samples, the complex urine matrix may affect the background spectrum such that the background absorbance measured at 226.5 nm differs from the background that might be present at 228.8 nm. While the background for the relatively clean cloud point extracts is expected to vary very little across a 2.3 nm region, the difference could become significant at low Cd concentrations. High resolution continuum source atomic absorption spectra for urine samples show that overall background absorbance levels may differ by orders of magnitude, even for samples with similar Cd levels [18]. For the high background samples reported in that work, the signal variation over a 2.3 nm range is clearly measurable. In an effort to correct for this potential error, a second background correction approach was investigated. The surfactant background peak (Fig. 1) was very reproducible, regardless of sample type or Cd level. Notice in the profile that the background absorbance measured at 460 ms, prior to the appearance of the Cd signal, closely approximates the background signal measured at 500 ms (black diamonds). This is also the case for absorption profiles measured at 228.8 nm for CPE samples containing no Cd. Therefore, the background absorbance level measured at 460 ms

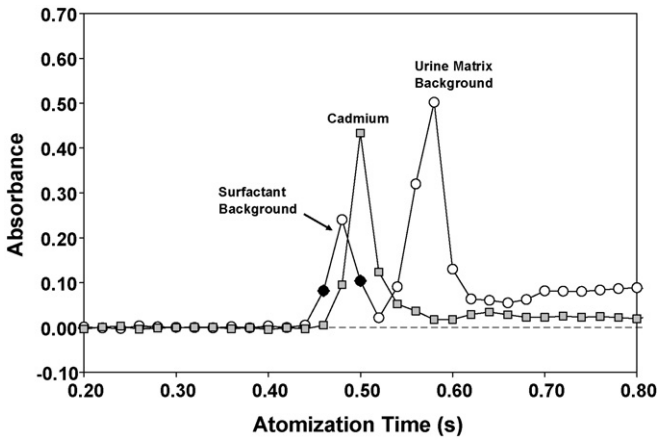

Fig. 1. Absorption profiles collected during the WCAAS analysis of a urine sample. The background profile (circles) is simply the absorbance measured at 226.5 nm. The analytical profile (squares) is the absorbance measured at 228.8 nm minus the absorbance measured at 226.5 nm.

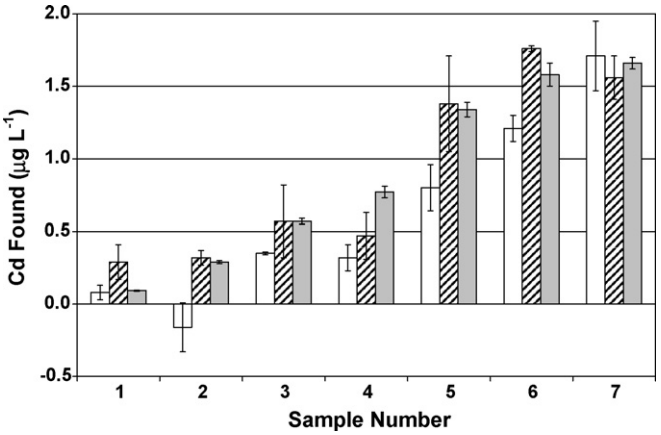

Fig. 2. Cadmium levels determined in seven urine samples by WCAAS with near-line background correction (white bars), WCAAS with temporal background correction (cross-hatched bars), and by ICP-MS (gray bars). The error bars represent ± one standard deviation ($n = 3$).

for the Cd 228.8 nm absorption line closely approximates the background level present at the time of maximum Cd signal (500 ms). Thus a "temporal" background correction may be applied using only the 228.8 nm line, by subtracting the absorbance values measured at these two times. While neither near-line nor temporal correction may be expected to match the accuracy observed for conventional background correction techniques (using the Zeeman effect or a continuum source), both can be performed without adding complexity to the WCAAS system.

Continuum source atomic absorption spectrometry has also identified structured background spectra in the vicinity of the Cd 228.8 nm line for very complex matrices like those present in solid coal samples [19]. While the molecular species giving rise to these spectra is not identified, one might speculate that similar structure in a urine spectrum may arise from the classic phosphate interference [20]. To test for the possibility of phosphate interference with the CPE-WCAAS procedure, a 5 $\mu g\,mL^{-1}$ phosphate solution was subjected to the CPE procedure described above. ICP emission analysis of the aqueous supernatant revealed that at most 20% of the phosphate was extracted into the surfactant layer. The phosphate present in a urine sample, therefore, had the potential to produce an interference. However, a 10 $\mu g\,mL^{-1}$ solution of phosphate produced no measurable absorbance at 228.8 nm by WCAAS.

3.2. Urine analyses

The CPE-WCAAS method resulted in a urine-Cd LOD (3σ) of 0.005 $\mu g\,L^{-1}$, which is in line with the other WCAAS LODs using preconcentration techniques (Table 1), and roughly a factor of 100 lower than normal urine-Cd levels. The CPE-WCAAS analysis of NIST standard reference material #2670 (*toxic metals in freeze-dried urine – normal level*) resulted in $0.38 \pm 0.03\ \mu g\,L^{-1}$ (mean ± standard deviation, $n = 3$) using the near-line correction method, and $0.36 \pm 0.05\ \mu g\,L^{-1}$ using the temporal correction method. The NIST reported Cd level for SRM #2670 is 0.40 $\mu g\,L^{-1}$.

Fig. 2 shows the urine-Cd levels measured for the seven human urine samples. The amount of Cd was determined in each sample by applying the near line correction technique (white bars) and the temporal background correction technique (cross-hatched bars). These two values were determined for exactly the same runs ($n = 3$). The ICP-MS results (gray bars) were collected at a different time using a different sample preparation technique as described above. The error bars represent the precision for each method ($\pm 1\sigma$, $n = 3$). Clearly the ICP-MS technique provides more precise results. The average standard deviation observed for the seven samples was 0.03 $\mu g\,L^{-1}$ by ICP-MS, compared to 0.12 and 0.15 $\mu g\,L^{-1}$ by CPE-WCAAS using near-line and temporal background correction respectively. Compared with ICP-MS results, the CPE-WCAAS technique with near-line correction under-reported the urine-Cd levels for the seven samples by an average of -0.28 $\mu g\,L^{-1}$. In one case (sample #2) a completely erroneous and negative urine-Cd result was reported ($-0.16\ \mu g\,L^{-1}$). Perhaps this trend can be explained by the background absorbance value at 226.5 nm being consistently higher than that measured at 228.8 nm. Such a result would not be surprising, since background absorption tends to increase with decreasing wavelength. The CPE-WCAAS technique with temporal background correction did not show a consistent systematic error. Compared to the ICP-MS results, the temporal-corrected values differed by just 0.01 $\mu g\,L^{-1}$ on average.

Acknowledgments

This material is based upon work supported by the National Science Foundation and the Department of Homeland Security through the joint "Academic Research Initiatives" program: CBET 0736214. The authors would also like to thank Keith E. Levine of the Research Triangle Institute, Research Triangle Park, North Carolina, for providing access to the ICP-MS system.

References

[1] J. Godt, F. Scheidig, C. Grosse-Siestrup, V. Esche, P. Brandenburg, A. Reich, D.A. Groneberg, J. Occup. Med. Toxicol. 1 (2006) 1–6.
[2] H. Choudhury, T. Harvey, W.C. Thayer, T.F. Lockwook, W.M. Stiteler, P.E. Goodrum, J.M. Hassett, G.L. Diamond, J. Toxicol. Environ. Health, Part A 63 (2001) 321–350.
[3] A.C. Davis, P. Wu, X. Zhang, X. Hou, B.T. Jones, Appl. Spectrosc. Rev. 41 (2006) 35–75.
[4] J.D. Batchelor, S.E. Thomas, B.T. Jones, Appl. Spectrosc. 52 (8) (1998) 1086–1091.
[5] A. Salido, B.T. Jones, Talanta 50 (1999) 649–659.
[6] K.A. Wagner, K.E. Levine, B.T. Jones, Spectrochim. Acta Part B 53 (1998) 1507–1516.
[7] C.G. Bruhn, F.E. Ambiado, H.J. Cid, R. Woerner, J. Tapia, R. Garcia, Anal. Chim. Acta 306 (1995) 183–192.
[8] C.G. Bruhn, N.A. San Francisco, J.Y. Neira, J.A. Nobrega, Talanta 50 (1999) 967–975.
[9] M.M. Silva, M.A.Z. Arruda, F.J. Krug, P.V. Oliveira, Z.F. Queiroz, M. Gallego, M. Valcarcel, Anal. Chim. Acta 368 (1998) 255–263.
[10] C.G. Bruhn, F.E. Ambiado, H.J. Cid, R. Woerner, J. Tapia, R. Garcia, Quim. Anal. 15 (1996) 191–200.
[11] J. Manzoori, A. Bavili-Tabrizi, Anal. Chim. Acta 470 (2002) 215–221.
[12] D.L.G. Boges, M.A.M.S. da Veiga, V.L.A. Frescura, B. Welz, A.J. Curtius, J. Anal. Atom. Spectrom. 18 (2003) 501–507.
[13] C.L. Sanford, S.E. Thomas, B.T. Jones, Appl. Spectrosc. 50 (1996) 174–181.
[14] P. Wu, Y. Zhang, Y. Lv, X. Hou, Spectrochim. Acta Part B 61 (2006) 1310–1314.
[15] G.L. Donati, C.C. Nascentes, A.R.A. Nogueira, M.A.Z. Arruda, J.A. Nobrega, Microchem. J. 82 (2006) 189–195.
[16] K.E. Levine, K.A. Wagner, B.T. Jones, Appl. Spectrosc. 52 (1998) 1165–1171.
[17] J. Sneddon, Spectroscopy 2 (1987) 38.
[18] R. Fernando, F.K. Ennever, B.T. Jones, Appl. Spectrosc. 47 (1993) 1696–1699.
[19] A.F. da Silva, D.L.G. Borges, F.G. Lepri, B. Welz, A.J. Curtius, U. Heitmann, Anal. Bioanal. Chem. 382 (2005) 1835–1841.
[20] K. Saeed, Y. Thomassen, Anal. Chim. Acta 130 (1981) 281–287.

Talanta 76 (2008) 1170–1176

Contents lists available at ScienceDirect

Talanta

journal homepage: www.elsevier.com/locate/talanta

Preliminary investigation of a medium power argon radiofrequency capacitively coupled plasma as atomization cell in atomic fluorescence spectrometry of cadmium

Tiberiu Frentiu[a,b,*], Eugen Darvasi[a,b], Marin Senila[a], Michaela Ponta[b], Emil Cordos[a,b]

[a] National Institute for Research and Development of Optoelectronics Bucharest – Research Institute of Analytical Instrumentation, Donath 67, 400293 Cluj-Napoca, Romania
[b] "Babes-Bolyai" University, Faculty of Chemistry and Chemical Engineering, Arany Janos 11, 400028 Cluj-Napoca, Romania

ARTICLE INFO

Article history:
Received 21 February 2008
Received in revised form 14 May 2008
Accepted 14 May 2008
Available online 21 May 2008

Keywords:
Atomic fluorescence spectrometry
Capacitively coupled plasma
Cd determination

ABSTRACT

The single ring electrode radiofrequency capacitively coupled plasma torch (SRTr.f.CCP) operated at 275 W, 27.12 MHz and Ar flow rate below 0.7 l min^{-1} was investigated for the first time as atomization cell in atomic fluorescence spectrometry (AFS) using electrodeless discharge lamps (EDL) as primary radiation source and charged coupled devices as detector. The signal to background ratio (SBR) and limit of detection for Cd determination by EDL-SRTr.f.CCP-AFS were compared to those obtained in atomic emission spectrometry using the same plasma torch. The detection limit in fluorescence was 4.3 ng ml^{-1} Cd compared to 65 ng ml^{-1} and 40 ng ml^{-1} reported in r.f.CCP-atomic emission (AES) equipped with single or double ring electrode. The lower detection limit in EDL-SRTr.f.CCP-AFS is due to a much better SBR in fluorescence. The limit of detection was also compared to those in atomic fluorescence with inductively coupled plasma (0.4 ng ml^{-1}), microwave plasma torch (0.25 ng ml^{-1}) and air–acetylene flame (8 ng ml^{-1}). The influence of light-scattering through the plasma and the secondary reflection of the primary radiation on the wall of the quartz tube on the analytical performance are discussed. The non-spectral matrix effects of Ca, Mg and easily ionized elements are much lower in EDL-SRTr.f.CCP-AFS compared to SRTr.f.CCP-AES. The new technique was applied in the determination of Cd in contaminated soils, industrial hazardous waste (0.4–370 mg kg^{-1}) and water (113 μg l^{-1}) with repeatability of 4–8% and reproducibility in the range of 5–12%, similar to those in ICP-AES. The results were checked by the analysis of a soil and water CRM with a recovery degree of 97 ± 9% and 98 ± 4%, for a confidence limit of 95%. The present EDL-SRTr.f.CCP-AFS is a promising technique for Cd determination in environmental samples.

1. Introduction

The driving forces determining the development of atomic fluorescence spectrometry (AFS) are the well-established sensitivity and selectivity, the simple and low-cost instrumentation compared to other spectrometric methods such as atomic emission and absorption spectrometry (AES and AAS) as well as the simplicity of spectra compared to those recorded in AES. Most of the reported results with applications of AFS have been obtained for volatile elements or elements converted in volatile hydrides, which can be atomized efficiently at moderate temperature [1–6]. The trends in the development of AFS regarding the atomization cells, primary radiation sources, detection devices, background correction methods and applications have been published for years as reviews [7–13]. Almost all plasma sources have been used as atomization cells for AFS, such as inductively coupled plasma (ICP-AFS) [14–17], microwave-induced plasma (MIP-AFS) [18], microwave plasma torch (MPT-AFS) [19] and direct current plasma (DCP-AFS) [20,21] with different primary radiation sources and dispersive and non-dispersive optical detection systems. Very recently a new atomizer based on atmospheric pressure non-thermal dielectric barrier discharge microplasma was designed for AFS coupled with a hydride generator (HG-DBD-AFS) [22]. The development of the new AFS instrumentation has been focused on the application of laser excited atomic/ionic fluorescence spectrometry (LEAFS and LEIFS) and the use of charge coupled detectors (CCDs). Among the laser sources, those with diode are very attractive for LEAFS due to their potential for low-cost, narrow spectral line width, compactness and ease of wavelength tunability through temperature and electrical manipulation. The applications of laser diode in atomic

* Corresponding author at: "Babes-Bolyai" University, Faculty of Chemistry and Chemical Engineering, Arany Janos 11, 400028 Cluj-Napoca, Romania.
Tel.: +40 264593833; fax: +40 264420667.
E-mail address: ftibi@chem.ubbcluj.ro (T. Frentiu).

0039-9140/$ – see front matter © 2008 Elsevier B.V. All rights reserved.
doi:10.1016/j.talanta.2008.05.020

spectrometry and their features were reviewed by Niemax and co-workers [23] and Galbacs [24]. Laser-induced fluorescence technique was used for the diagnosis of reactive capacitively coupled radiofrequency discharges operated in pure CF_4, by determining the fluorine atom number density using the loss rate constant of the CF_2 radicals in the afterglow of the plasma [25]. To date, radiofrequency capacitively coupled plasmas (r.f.CCPs) have been investigated as atomization source in AAS [26,27], excitation source in AES [27–32], and ion source in mass spectrometry (MS) [33,34], but there is no report regarding their use in analytical applications for AFS. In our laboratory an Ar r.f.CCP with a Mo tubular electrode and a single ring electrode (SRTr.f.CCP) [35–38] or a double ring electrode (DRTr.f.CCP) [35,37–42] operated at higher power (275 W, 27.12 MHz) than previously mentioned plasmas were investigated in AES for the determination of elements in liquid samples introduced by pneumatic nebulization without aerosol desolvation. Also, a very low power Ar r.f.CCP (<75 W, 13.56 MHz or 10.9 MHz) was developed in our laboratory for the direct analysis of non-conductive solid samples by r.f. sputtering [43] and pneumatically nebulized liquid samples without aerosol desolvation [44] using AES detection.

The aim of this paper is to present for the first time several figures of merit of SRTr.f.CCP as atomization cell in AFS in a particular configuration using the r.f. electrodeless discharge lamp (EDL) as primary radiation source and CCD as optical detector. The development of the plasma within a quartz tube diminishes the diffusion of N_2, O_2 and CO_2 from the air resulting in a lengthen of the plasma tail plume, most favourable for the AFS measurements. The use of a good quality quartz tube with the 160 nm cut-off limit enables the approach of the UV range useful for elements generating a high fluorescence signal in this region. Operating conditions and non-spectral matrix effects of Ca, Mg and easily ionized elements (EIE) (Li, Na and K) on Cd determination by EDL-SRTr.f.CCP-AFS were compared to SRTr.f.CCP-AES. Also a comparison of the detection limits with those obtained in SRTr.f.CCP-AES, DRTr.f.CCP-AES, EDL-ICP-AFS, HCL-MPT-AFS and flame atomic fluorescence spectrometry (FAFS) are given. The new technique was investigated for the determination of Cd in water, soil and industrial hazardous waste and checked using certified reference materials (CRMs).

2. Experimental

2.1. Instrumentation

The experimental set-up includes the SRTr.f.CCP torch (INCDO-INOE 2000 Bucharest, Research Institute for Analytical Instrumen-

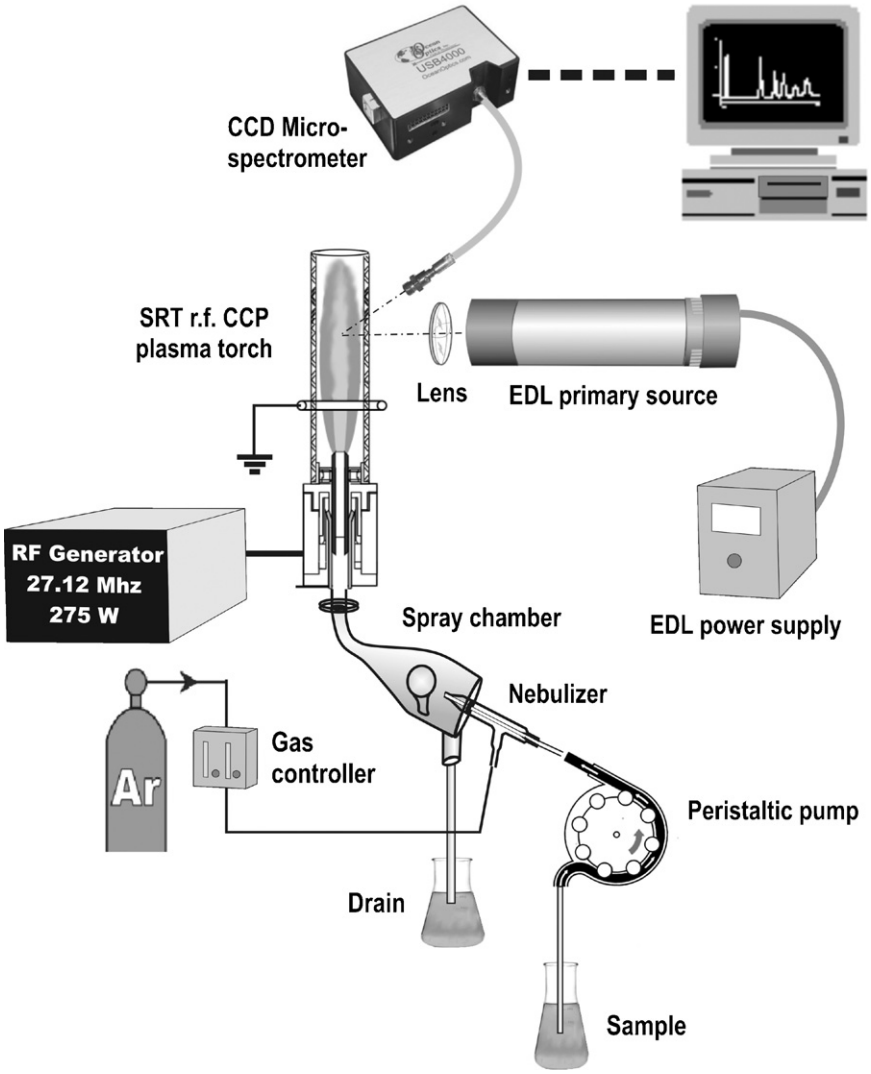

Fig. 1. Experimental set-up for EDL-SRTr.f.CCP-AFS.

Table 1
Operating parameters for the experimental EDL-SRTr.f.CCP-AFS set-up

Power supply	Free-running r.f. generator, 275 W, 27.12 MHz (INCDO-INOE 2000, Research Institute for Analytical Instrumentation, Cluj-Napoca, Romania)
Plasma torch	Capacitively coupled; coaxial geometry with molybdenum tubular electrode (inner diameter 3.5 mm) and single outer ring electrode of copper (SRTr.f.CCP) mounted at a distance of 5 mm above the tubular electrode; working gas: 5.0 quality argon (Linde gas SRL, Cluj-Napoca, Romania); argon flow rate 0.4–0.7 l min^{-1}; 16 mm i.d. quartz tube, 10 cm length, 160 nm cut-off (H. Baumbach & Co. Ltd, Ipswich Suffolk, UK).
Sample introduction system	Meinhardt pneumatic nebulizer (PerkinElmer, Norwalk, USA) equipped with a spray chamber with impactor without aerosol desolvation; aerosol intake into the plasma via the tubular electrode (0.4 ml min^{-1}, 5% nebulization efficiency)
Primary radiation source	Electrodeless discharge lamp supplied in continuum mode at 240–450 mA from a power supply model CT06859 (EDL, PerkinElmer, Norwalk, USA)
Optics	HR 4000 Microspectrometer Ocean Optics (200–420 nm, 50 μm entrance slit, 1200 groves mm^{-1} grating, Toshiba CCD with 3648 pixels, collimating system 74-UV, fibre optic QP 600 μm, 25 cm length) (Dunedin, USA)
Optical arrangement	Radial–radial and axial–radial geometry at 90°
Data acquisition	Spectrasuite soft (Ocean Optics); 10 and 30 s integration time; manually background correction

tation, Cluj-Napoca, Romania) as atomization cell, a 200–420-nm multichannel high resolution HR 4000 microspectrometer (Ocean Optics, Dunedin, USA) equipped with a 600-μm fibre optic to collect the fluorescence signal, a Meinhardt pneumatic nebulizer and a spray chamber with impactor without aerosol desolvation, an EDL as primary radiation source supplied at different currents from a power supply model CT06859 (PerkinElmer, Norwalk, USA). The schematic diagram of the new experimental EDL-SRTr.f.CCP-AFS set-up is presented in Fig. 1, while the operating parameters in Table 1.

Two optical arrangements were used to excite and measure the fluorescence signal (Fig. 2). In the radial profiling experiment (Fig. 2a) the fluorescence signal was measured in the radial direction through the quartz tube of the torch, while the primary excitation beam from EDLs was also collimated in radial direction onto the plasma. In the axial profiling (Fig. 2b), the fluorescence signal was imaged on the entrance slit of the microspectrometer using the fibre optic mounted in the radial direction related to the plasma, whereas the EDL was positioned in the axial direction. In both arrangements, the EDL, optical collimating system and fibre optic were fixed on a precision translation stage and aligned at right angle. The focusing and collimating of the EDL primary radiation onto the plasma were investigated. A silica lens (50 mm diameter and 75 mm focal length) was used to illuminate the plasma.

A mortar grinder Retsch RM 100 and a sieve shaker Retsch AS200 (Haan, Germany), an overhead shaker REAX20/8 Heidolph (Kelheim, Germany) and a closed-vessel microwave system Berghof MWS-3+ with temperature control mode (Eningen, Germany), and a Sartorius vacuum filter equipment (Goettingen, Germany) were used during sample preparation. Results found by EDL-SRTr.f.CCP-AFS were compared to those obtained by AES using the ICP multichannel spectrometer SPECTRO CIROS^{CCD} (Spectro Analytical Instruments, Kleve, Germany).

2.2. Reagents, standard solutions and CRMs

Stock solutions of 1000 μg ml^{-1} of Cd, Li, Na, K, Ca and Mg purchased from Merck (Darmstadt, Germany) were used in this study. A solution of 400 ng ml^{-1} Cd was used to determine the optimum operating conditions of EDL-SRTr.f.CCP-AFS. Solutions of 400 ng ml^{-1} Cd in the presence of 1–500 μg ml^{-1} Li, Na, K, Ca and Mg were used in the study of the non-spectral interferences on the Cd fluorescence and emission. All dilutions were made with 1% HNO_3 (v/v). Hydrochloric acid 37% and nitric acid 69% (GR for analysis ACS) purchased from Merck were used for digestion of samples. The soil CRM 025-050 RTC-Laramie (New York, USA) and the water from LGC Proficiency Testing, Aquacheck Scheme (distribution 331, group 17C)—LGC Promochem GmbH (Wesel, Germany) were used in the internal quality control of Cd determination. Argon (5.0 qual-

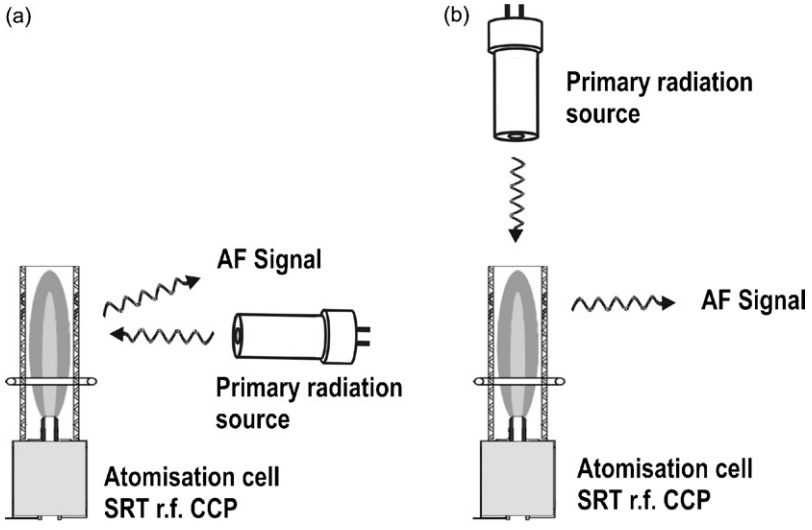

Fig. 2. Optical arrangement for radial–radial (a) and axial–radial (b) geometry.

Table 2
Operating conditions for the microwave digestion system

	Stage			
	1	2	3	4
Temperature (°C)	180	100	100	100
Ramp time (min)	5	1	1	1
Hold time (min)	25	10	1	1
Power (%)[a]	60	20	10	10

[a] 100% power corresponds to 1450 W.

ity) from Linde Gas SRL Cluj-Napoca, Romania was used as working gas.

2.3. Sample preparation

Ten replicate amounts of 1.000 g of CRM 025-050 or contaminated soil were digested with 10 ml aqua regia in closed PTFE containers of the microwave system according to the digestion program presented in Table 2. The procedure and settings were those recommended by the equipment producer for this type of samples. Ten replicate amounts of 175 g industrial hazardous waste were leached with distilled water (<10 μS cm^{-1}) at 2:1 liquid to solid ratio at 20 ± 2° C for 24 ± 0.5 h (SR EN 12457/1:2003) with the Heidolph shaker at 16 rpm. Cadmium was determined in the filtered solutions and in water CRM by EDL-SRTr.r.CCP-AFS and ICP-AES after calibration on the range of 20–400 ng ml^{-1} Cd at 228.812 nm.

3. Results and discussions

3.1. Optimization of operating parameters

The operation of EDL-SRTr.f.CCP-AFS was optimized with respect to the Ar flow rate, observation height, lamp current and non-spectral interferences of Ca, Mg and EIE on Cd.

3.2. Influence of Ar flow rate and observation height

A single Ar stream was used as plasma support gas and sample carrier. The effect of Ar flow rate on 400 ng ml^{-1} Cd fluorescence signal in EDL-SRTr.f.CCP-AFS with radial–radial arrangement is shown in Fig. 3.

The measurements were performed at different observation heights above the tubular electrode for gas flow rates in the range of 0.4–0.7 l min^{-1}. Although a single gas flow is used, two factors control the Cd fluorescence signal: efficiency of the pneumatic nebulizer and the cooling of the discharge occurring at higher gas flow rates, which is favourable in fluorescence measurement. It can be seen that the maximum of the fluorescence signal is reached at higher heights in the plasma tail, where the temperature and the background of the discharge are lower. Therefore for a flow rate of 0.7 l min^{-1} Ar considered as optimum for both nebulizer operation and plasma development, the maximum fluorescence signal occurs at 72 mm above the tubular electrode.

Unlike fluorescence, the maximum of the Cd signal in SRTr.f.CCP-AES is reached at lower observation height (16 mm). The emission signal decreases as the Ar flow rate increases and the optimum value is considered to be 0.4 l min^{-1}. The results are similar to those obtained in ICP-AES and ICP-AFS [45]. Whereas the maximum of emission in ICP-AES occurs at lower heights (15–20 mm), the fluorescence signal for most metals in ICP-AFS is maximum in the tail plasma zone. Also, in ICP-AFS an increase of the injector gas flow to 1.5–2 l min^{-1} is required compared to 1.0 l min^{-1} in ICP-AES.

The dependence of the signal to background ratio (SBR) for 400 ng ml^{-1} Cd on the observation height in the axial–radial geometry of EDL-SRTr.f.CCP-AFS (0.7 l min^{-1} Ar) and SRTr.f.CCP-AES (0.4 l min^{-1} Ar) is presented in Figs. 4 and 5, respectively. The axial–radial arrangement of the AFS set-up was chosen for comparison with AES as in this geometry the interference caused by the secondary reflection of the EDL primary radiation at 228.812 nm could be avoided unlike to the radial–radial geometry where this undesirable phenomenon limited the fluorescence sensitivity. Therefore the integration time was increased to 30 s in the axial–radial arrangement, which improved the fluorescence signal of 1.7 times.

As shown in Figs. 4 and 5 the maximum SBR of Cd in fluorescence and emission occurs at 72 mm and 16 mm height, respectively. The SBR decreases in fluorescence at lower heights as a result of the diminished primary radiation due to the prefilter phenomenon and increase of background. Although the background decreases over 72 mm, SBR decreases due mainly to air diffusion into the plasma and quenching of the Cd fluorescence as well as increase of the light-scattering interference through the cool reactive oxidant environment. Since the SBR in fluorescence is 15 times higher that in

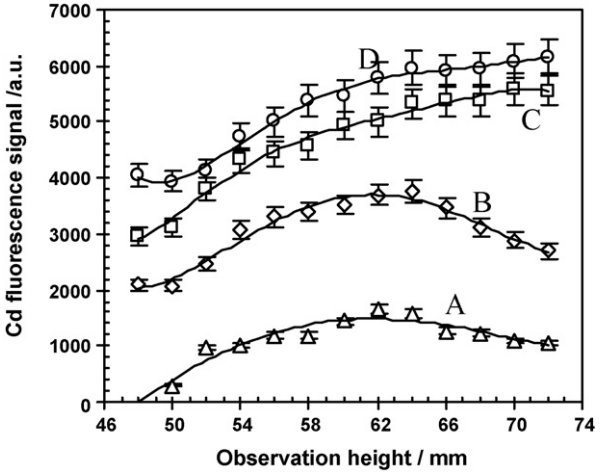

Fig. 3. Effect of Ar flow rate on Cd fluorescence signal at 228.812 nm (400 ng ml^{-1}) for different observation heights in EDL-SRTr.f.CCP-AFS with radial–radial arrangement. Ar flow rate: (A) 0.4 l min^{-1}; (B) 0.5 l min^{-1}; (C) 0.6 l min^{-1}; (D) 0.7 l min^{-1}. Experimental conditions: 275 W power level; 350 mA lamp current; 10 s integration time; collimated primary radiation.

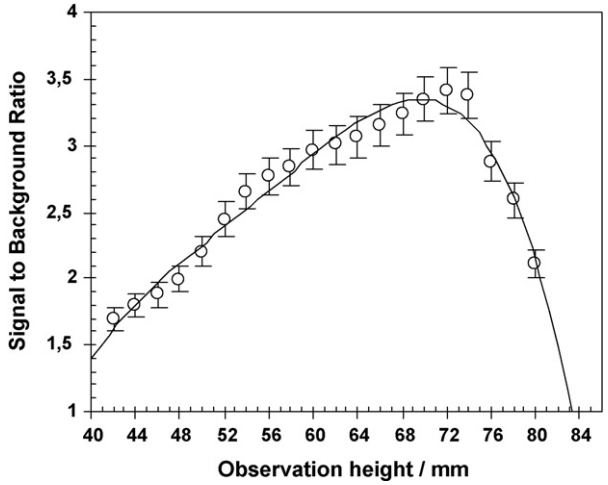

Fig. 4. Dependence of signal to background ratio for Cd at 228.812 nm on the observation height in the axial–radial arrangement of EDL-SRTr.f.CCP-AFS. Experimental conditions: Cd concentration 400 ng ml^{-1}; 275 W power level; 0.7 l min^{-1} Ar flow rate; 350 mA lamp current; collimated primary radiation; 30 s integration time.

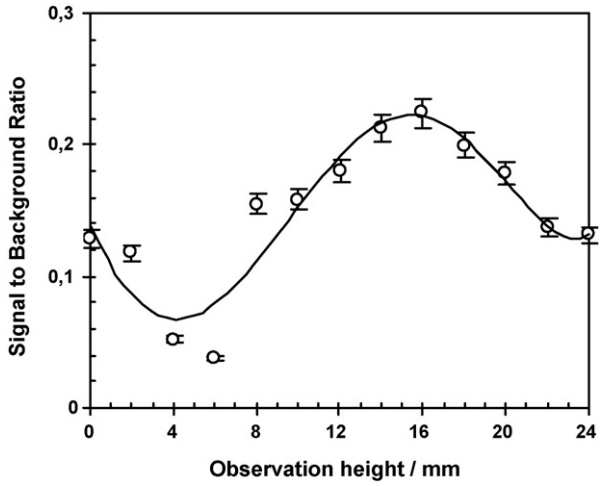

Fig. 5. Dependence of signal to background ratio for Cd at 228.812 nm in SRT r.f.CCP-AES on the observation height. Experimental conditions: Cd concentration 400 ng ml^{-1}; 275 W power level; 0.4 l min^{-1} Ar flow rate; 30 s integration time.

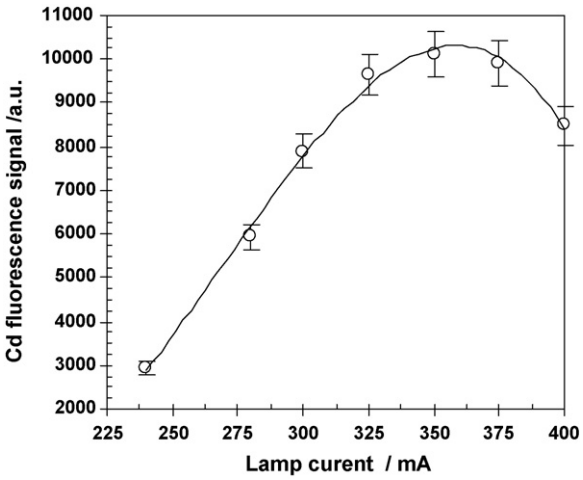

Fig. 6. Dependence of the Cd signal at 228.812 nm on lamp current in EDL-SRTr.f.CCP-AFS with axial–radial arrangement. Experimental conditions: Cd concentration 400 ng ml^{-1}; 275 W power level; 0.7 l min^{-1} Ar flow rate; collimated primary radiation; 30 s integration time.

emission the SRTr.f.CCP is more suitable for atomization than for excitation.

3.3. Operating current for EDL

The optimum operating condition of Cd EDL was established by measuring the fluorescence signal for a concentration of 400 ng ml^{-1} Cd at different input currents. The dependence curve obtained for EDL-SRTr.f.CCP-AFS in the axial–radial arrangement for an observation height of 72 mm is illustrated in Fig. 6.

The fluorescence signal is linearly proportional to the operating current up to 325 mA, which means that the de-excitation rate of the Cd atoms is faster than the excitation rate. The limitation of the fluorescence signal at the operation current of 350 mA is a consequence of the beginning self-reversal of the EDL. It should be noted that the fluctuation of the EDL primary radiation is not strongly reflected in the fluorescence signal at this current as the curve slope in this point is the lowest. Consequently the 350 mA operation current was considered as optimum.

3.4. Non-spectral matrix effects of EIE, Ca and Mg in EDL-SRTr.f.CCP-AFS and SRTr.f.CCP-AES

The non-spectral matrix effects of Li, Na, K, Ca and Mg in concentrations up to 500 μg ml^{-1} on the fluorescence signal of 400 ng ml^{-1} Cd in EDL-SRTr.f.CCP-AFS in the radial–radial and axial–radial arrangements for the optimum observation height (72 mm) are presented in Fig. 7a and b, while in SRTr.f.CCP-AES at an observation height of 16 mm in Fig. 8. The non-spectral matrix effect (%) was calculated according to the equation:

$$\mathrm{ME} = \frac{S - S_0}{S_0} \times 100$$

where S and S_0 are the Cd signal in the presence and absence of a particular concomitant, respectively.

The non-spectral matrix effects of Ca, Mg, Li, Na and K are similar in both arrangements used in the study of fluorescence and much smaller compared to emission. Thus, the influence of the Ca, Mg and Na matrices are usually in the range ±10% up to a concentration of 500 μg ml^{-1} concomitant. The results show that

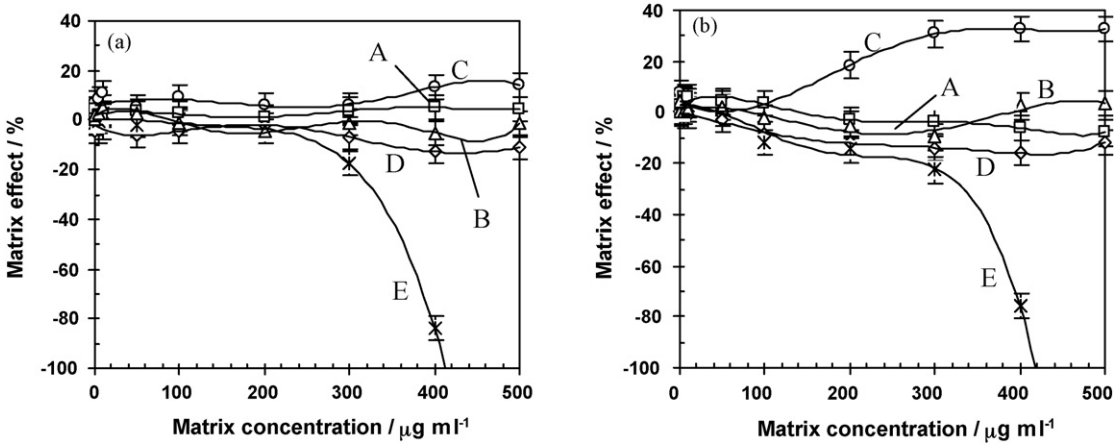

Fig. 7. Non-spectral matrix effects of Ca (A), Mg (B), Li (C), Na (D) and K (E) in the range 0–500 μg ml^{-1} on the fluorescence of Cd (400 ng ml^{-1}) at 228.812 nm in EDL-SRTr.f.CCP-AFS with radial–radial (a) and axial–radial (b) arrangement. Experimental conditions: 275 W power level; 0.7 l min^{-1} Ar flow rate; 72 mm observation height; 350 mA lamp current.

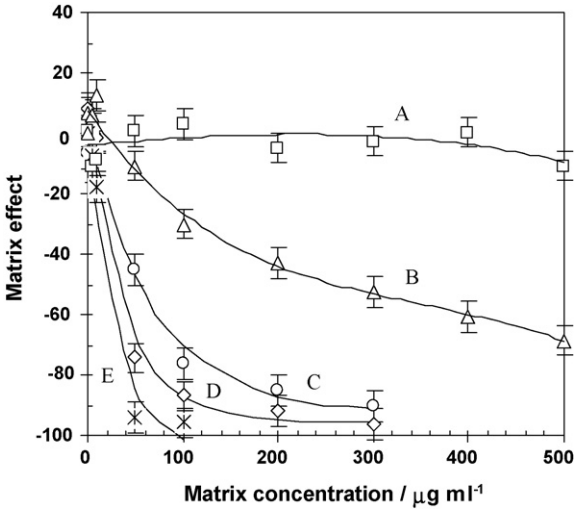

Fig. 8. Non-spectral matrix effects of Ca (A), Mg (B), Li (C), Na (D) and K (E) in the range 0–500 μg ml^{-1} on the emission of Cd (400 ng ml^{-1}) at 228.812 nm in SRTr.f.CCP-AES. Experimental conditions: 275 W power level; 0.4 l min^{-1} Ar flow rate; 16 mm observation height.

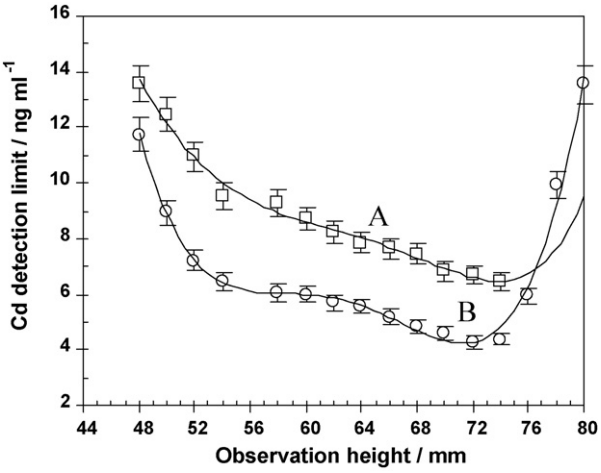

Fig. 9. Detection limit of Cd at 228.812 nm for EDL-SRTr.f.CCP-AFS in radial–radial (A) and axial–radial (B) arrangement as a function of observation height. Experimental conditions: 275 W power level; 0.7 l min^{-1} Ar flow rate; collimated primary radiation; 10 s integration time for radial–radial arrangement and 30 s for axial–radial arrangement.

less the volatility of the matrix and higher the ionization energy of the concomitant, smaller the non-spectral matrix effects. The vaporization–atomization interferences of the refractory elements (Ca, Mg) in EDL-SRTr.f.CCP-AFS are fewer and smaller than in flames and furnaces, and are comparable to those reported in ICP-AFS [45].

Unlike fluorescence, in emission the non-spectral matrix effects on Cd are slightly depressive in the case of Ca and very depressive in the case of Mg, Li, Na and K. The decrease of Cd emission signal in the presence of these concomitants follows the order: Ca < Mg < Li < Na < K. The higher depressive interference in emission compared to that observed in fluorescence is the result of easily liberated electrons by EIE, which affect the equilibrium balance between atoms and ions with the consequent alteration of the energy-transfer pathway for excitation in the plasma. In short, SRTr.f.CCP is suitable as atomization cell in AFS in the presence of complex matrices.

3.5. Limits of detection

Detection limit was calculated using the 3σ criteria. In this method the SBR was determined for a concentration of 200 ng ml^{-1} Cd, while the relative standard deviation of the background (RSDB) was calculated from 10 successive measurements of the background signal in the proximity of the Cd 228.812 nm line.

The dependence of the detection limit for Cd on the observation height for EDL-SRTr.f.CCP-AFS in radial–radial (A) and axial–radial (B) arrangement is presented in Fig. 9. Table 3 gives a comparison of detection limits for Cd in EDL-SRTr.f.CCP-AFS, SRTr.f.CCP-AES, DRTr.f.CCP-AES, as well as in AFS using other atomization cells. According to Fig. 9, the lowest detection limit in EDL-SRTr.f.CCP-AFS for both arrangements is obtained at 72 mm observation height, where SBR is maximum.

As shown in Table 3, the Cd detection limits in EDL-SRTr.f.CCP-AFS with radial–radial and axial–radial arrangement using pneumatic nebulization, without aerosol desolvation are 6.4 ng ml^{-1} and 4.3 ng ml^{-1}, respectively. The improvement of the detection limit by a factor of 1.5 in the axial–radial arrangement is the result of a diminished interference caused by the secondary reflection on the quartz tube of the primary radiation onto the lens of the fibre optic. The Cd detection limit in EDL-SRTr.f.CCP-AFS was about 10–15 folds lower compared to SRTr.f.CCP-AES and 6.3–9.3 folds compared to DRTr.f.CCP-AES.

The comparison with the other AFS systems is difficult because of significant differences in their experimental set-up. Several comments could be made. The limit of detection in EDL-SRTr.f.CCP-AFS is lower than that obtained in LEAFS using an air–acetylene flame, where the background signal is higher. Although the detection limits obtained in EDL-SRTr.f.CCP-AFS are higher than in EDL-ICP-AFS, the advantages of our atomization cell are lower background, low operation power and total Ar consumption, resulting in low-cost

Table 3
Detection limits (3σ criteria) for Cd determination by EDL-SRTr.f.CCP-AFS in radial–radial and axial–radial arrangement, SRTr.f.CCP-AES, DRTr.f.CCP-AES, EDL-ICP-AFS, HCL-MPT-AFS and LEAFS

Method	LOD (ng ml^{-1})	Operating conditions	Reference
EDL-SRTr.f.CCP-AFS radial–radial arrangement	6.4	275 W; 0.7 l min^{-1} Ar; 72 mm observation height; 10 s integration time; CCD	This paper
EDL-SRTr.f.CCP-AFS axial–radial arrangement	4.3	275 W; 0.7 l min^{-1} Ar; 72 mm observation height; 30 s integration time; CCD	This paper
EDL-ICP-AFS	0.4	EDL and solar-blind photomultiplier tube	[14]
HCL-MPT-AFS	0.25	80 W; dry aerosol; boosted HCL; solar-blind photomultiplier tube	[19]
SRTr.f.CCP-AES	65	275 W; 0.4 l min^{-1} Ar; 16 mm observation height	[35]
DRTr.f.CCP-AES	40	275 W; 0.4 l min^{-1} Ar; 12 mm observation height	[35,39]
LEAFS[a]	8	Air–acetylene flame; laser excitation	[46]

[a] LEAFS—laser flame atomic fluorescence spectrometry.

Table 4
Analytical determination of Cd in reference materials

Sample	Measure units	Certified content	Found content	
			EDL-SRTr.f.CCP-AFS	ICP-AES
LGC—aquacheck scheme water	$\mu g\,l^{-1}$	113 ± 7	111 ± 4	117 ± 4
CRM 025-050 soil	$mg\,kg^{-1}$	369 ± 41	358 ± 31	365 ± 19

Values are reported with 95% confidence limit ($n = 10$).

Table 5
Cadmium content in soil leached in aqua regia and industrial hazardous waste leached in water obtained by EDL-SRTr.f.CCP-AFS compared to ICP-AES

Sample	Found content, $mg\,kg^{-1}$	
	EDL-SRTr.f.CCP-AFS	ICP-AES
Contaminated soil	16 ± 1	19 ± 1
Contaminated soil	51 ± 2	52 ± 1
Industrial hazardous waste	0.40 ± 0.02	0.38 ± 0.02

Values are reported with 95% confidence limit ($n = 10$).

operation. The poor limits of detection compared to HCL-MPT-AFS are due to the use of CCD detector in our configuration compared to the solar-blind photomultiplier tube with higher sensitivity used in the method of comparison. The difference in the detection limits is also the result of sample introduction as wet aerosol in our approach.

3.6. Analytical determination

Statistical data of the calibration curve $y = (51 \pm 106) + (26 \pm 1)C$ ($n = 5$, 95% confidence limit) over the concentration range of 20–400 $ng\,ml^{-1}$ Cd (correlation coefficient 0.9999) obtained by EDL-SRTr.f.CCP-AFS in the axial–radial set-up show the lack of systematic errors. Standard deviation of reproducibility (s_R) and accuracy in the internal quality control were assessed on the basis of two CRMs with different Cd content. The found results compared to the reference values are given in Table 4. The standard deviation of reproducibility in EDL-SRTr.f.CCP-AFS was 5.0% and 12.0% for Cd determination in water and soil, at recovery degrees of 98 ± 4% and 97 ± 9% (95% confidence limit), comparable with ICP-AES. Repeatability in EDL-SRTr.f.CCP-AFS was checked by carrying out 10 replicates on separate soil and industrial hazardous waste subsamples and compared with the standardized ICP-AES method. The data in Table 5 show a precision range of 4–8% in both methods.

4. Conclusions

The figures of merit of a new atomization cell in AFS for pneumatic nebulization of aqueous samples without desolvation using EDL as primary excitation source and CCD for detection were evaluated. The advantages of the r.f.CCP as atomization cell in AFS include low-cost as instrumentation and maintenance, excellent discharge stability and high tolerance to complex matrix as well as a good capability for sample dissociation and atomization. Non-spectral matrix effects were much lower than those observed in SRTr.f.CCP-AES. The method exhibits a detection limit of Cd 10 times better than in DRTr.f.CCP-AES due to an improved signal-to-background ratio.

Acknowledgment

The present investigations are supported by the Romanian Ministry of Education and Research, PNCDI II Program (Project FLUOROSPEC no. 71019/2007).

References

[1] S. Jianbo, T. Zhiyong, T. Chunchua, C. Quan, J. Zrxiang, Talanta 56 (2002) 711–716.
[2] M.M. Gomez, M. Kovecs, M.A. Palacios, I. Pizarro, C. Camara, Microchim. Acta 150 (2005) 9–14.
[3] R. Wietecha, P. Koscelniak, T. Lech, T. Kielar, Microchim. Acta 149 (2005) 137–144.
[4] Z. Li, Y. Guo, Talanta 65 (2005) 1318–1325.
[5] Z. Li, X. Yang, Y. Guo, H. Li, Y. Feng, Talanta 74 (2008) 915–921.
[6] P. Wu, X. Wen, L. He, Y. He, M. Chen, X. Hou, Talanta 74 (2008) 505–511.
[7] P. Stchur, K.X. Yang, X. Hou, T. Sun, R.G. Michel, Spectrochim. Acta 56B (2001) 1565–1592.
[8] N.H. Bings, A. Bogaerts, J.A.C. Broekaert, Anal. Chem. 76 (2004) 3313–3336.
[9] A.A. Bol'shakov, A.A. Ganeev, V.M. Nemets, Russ. Chem. Rev. 75 (2006) 289–302.
[10] D.J. Butcher, Appl. Spectrosc. Rev. 41 (2006) 15–34.
[11] O.T. Butler, J.N. Cook, C.F. Harrington, S.J. Hill, J. Rieuwerts, D.L. Miles, J. Anal. Atom. Spectrom. 21 (2006) 217–243.
[12] O.T. Butler, J.N. Cook, C.F. Harrington, S.J. Hill, J. Rieuwerts, D.L. Miles, J. Anal. Atom. Spectrom. 22 (2007) 187–221.
[13] E.H. Evans, J.A. Day, C. Palmer, W.J. Price, C.M.M. Smith, J.F. Tyson, J. Anal. Atom. Spectrom. 22 (2007) 663–696.
[14] A. Montaser, V.A. Fassel, Anal. Chem. 48 (1976) 1490–1499.
[15] A. Young, L. Pitts, S.W. Greenfield, M. Foulkes, J. Anal. Atom. Spectrom. 18 (2003) 44–48.
[16] G. Galbacs, Z. Galbacs, O. Axner, Z. Geretovszky, Spectrochim. Acta 60B (2005) 299–306.
[17] S.Y. Zhand, Z.B. Gong, B.L. Hung, Spectrosc. Spectral. Anal. 26 (2006) 331–335.
[18] Y. Oki, E. Tashiro, M. Maeda, C. Honda, Y. Hasegawa, H. Futami, J. Izumi, K. Matsuda, Anal. Chem. 65 (1993) 2096–2101.
[19] Z. Duan, X. Du, Z. Li, Q. Jin, Appl. Spectrosc. 49 (1995) 1079–1081.
[20] M.S. Hendrick, M.D. Selzer, R.G. Michel, Spectrochim. Acta 46B (1986) 335–348.
[21] C. LeBlanc, M.W. Blades, J. Anal. Atom. Spectrom. 5 (1990) 99–107.
[22] Z. Zhu, J. Liu, S. Zhang, X. Na, X. Zhang, Anal. Chim. Acta 607 (2008) 136–141.
[23] K. Niemax, A. Zybin, D. Eger, Anal. Chem. 73 (2001) 134A–139A.
[24] G. Galbacs, Appl. Spectrosc. Rev. 41 (2006) 259–303.
[25] G. Cunge, P. Chabert, J.P. Booth, J. Appl. Phys. 89 (2001) 7750–7755.
[26] D.C. Liang, M.W. Blades, Anal. Chem. 60 (1988) 27–31.
[27] M.W. Blades, Spectrochim. Acta 49B (1994) 47–57.
[28] G.F.R. Gilchirst, P.M. Celliers, H. Yang, C. Yu, D.C. Liang, J. Anal. Atom. Spectrom. 8 (1993) 809–814.
[29] M.M. Rahman, M.W. Blades, Spectrochim. Acta 55B (2000) 327–338.
[30] S. Luge, J.A.C. Broekaert, A. Schalk, H. Zach, Spectrochim. Acta 50B (1995) 441–452.
[31] S. Luge, J.A.C. Broekaert, Anal. Chim. Acta 332 (1996) 193–199.
[32] F. Herwig, J.A.C. Broekaert, Microchim. Acta 134 (2000) 51–56.
[33] M.M. Rahman, M.W. Blades, J. Anal. Atom. Spectrom. 15 (2000) 1313–1319.
[34] S.Y. Lu, C.W. LeBlanc, M.W. Blades, J. Anal. Atom. Spectrom. 16 (2001) 256–262.
[35] E.A. Cordos, T. Frentiu, A.M. Rusu, S.D. Anghel, A. Fodor, M. Ponta, Talanta 48 (1999) 827–837.
[36] T. Frentiu, A.M. Rusu, S.D. Anghel, S. Negoescu, A. Popescu, A. Simon, E.A. Cordos, ACH Models Chem. 136 (1999) 119–129.
[37] T. Frentiu, E. Darvasi, S.D. Anghel, A. Simon, M. Ponta, E.A. Cordos, Chem. Anal. (Warsaw) 47 (2002) 725–736.
[38] T. Frentiu, S.D. Anghel, M. Nicola, E. Darvasi, A. Simon, E.A. Cordos, Croat. Chem. Acta 72 (1999) 763–778.
[39] T. Frentiu, M. Ponta, A.M. Rusu, S.D. Anghel, A. Simon, E.A. Cordos, Anal. Lett. 33 (2000) 323–335.
[40] T. Frentiu, M. Ponta, S.D. Anghel, A. Simon, I. Marginean, E.A. Cordos, Microchim. Acta 143 (2003) 245–254.
[41] T. Frentiu, M. Ponta, S.D. Anghel, A. Simon, A.M. Incze, E.A. Cordos, Microchim. Acta 147 (2004) 93–103.
[42] A. Simon, T. Frentiu, S.D. Anghel, S. Simon, J. Anal. Atom. Spectrom. 20 (2005) 956–965.
[43] S.D. Anghel, T. Frentiu, E.A. Cordos, A. Simon, A. Popescu, J. Anal. Atom. Spectrom. 14 (1999) 541–545.
[44] S.D. Anghel, A. Simon, T. Frentiu, J. Anal. Atom. Spectrom. 20 (2005) 966–973.
[45] A. Montaser, D.W. Golightly, Inductively Coupled Plasmas in Analytical Atomic Spectrometry, 2nd ed., VCH Publishers, New York, 1992, ISBN 1-56081-514-0, pp. 519–550.
[46] S.J. Weeks, H. Haraguchi, J.D. Winefordner, Anal. Chem. 50 (1978) 360–368.

Talanta 76 (2008) 1035–1040

Contents lists available at ScienceDirect

Talanta

journal homepage: www.elsevier.com/locate/talanta

Evaluation of Co-Polyaniline nanocomposite thin films as humidity sensor

Madhavi V. Fuke[a,*], Anu Vijayan[a], Milind Kulkarni[b], Ranjit Hawaldar[b], R.C. Aiyer[a]

[a] Center for Sensor Studies, Department of Physics, University of Pune, Pune 411007, India
[b] Center for Materials for Electronics Technology, Pashan, Pune 411008, India

ARTICLE INFO

Article history:
Received 4 February 2008
Received in revised form 29 April 2008
Accepted 30 April 2008
Available online 14 May 2008

Keywords:
Composites
Polymers
Nanostructures
Optical properties

ABSTRACT

Spin coated films of Co-Polyaniline nanocomposite are evaluated for their transmission properties using He–Ne laser for humidity sensing. The thickness (17–29 μm) of the films is varied by multiple deposition of Co-Polyaniline nanocomposite on a glass substrate. The samples exhibit typically two to three regions in their sensitivity curve when tested in the relative humidity (RH) range of 20–95%. The sensitivity ranges from 0.1 mV/%RH to 12.26 mV/%RH for lower to higher thickness. The sensors show quick response of 8 s (20–95%RH), and a recovery time of 1 min (95–20%RH) with good repeatability, reproducibility and low hysteresis effect. The sensitivity of the sensor increases with humidity and thickness. Material characterization is done by X-ray diffraction (XRD), scanning electron micrograph (SEM) and Fourier transform infra-red spectroscopy (FTIR).

1. Introduction

Measurement of humidity is required in numerous applications including the meteorological services, chemical and food industry, civil engineering, air conditioning, agriculture and electronic processing. Humidity sensors are of increasing interest in electronic control systems [1–7]. Therefore, the relative humidity measurements have been extensively studied and a remarkable progress has been made [8]. Based on the changes in electrical or optical properties, different humidity sensors are popularly studied. Different types of polymers play an important role in optical sensors categorized as inorganic and organic [9] e.g. poly(vinyl chloride) (PVC), poly(tetrafluoro ethylene) (PTFE), nafion, nylon, agarose, sol–gels, etc.

Recent studies on conducting polymers have increased the range of applications in optoelectronics and microelectronics. Polyaniline is unique among the known conducting polymers because its conductivity is controlled by the doping levels of oxidation and protons. Oxidation states of polyaniline, whose electrical properties are sensitive to water, provide a basis for potential applications in sensors for humidity control. The aqueous environment changes the conductivity due to two reasons:

1. Adsorbed water molecules dissociate at imine nitrogen centers.
2. Positive charge migrates through the polymer.

Thus, most of the imine units in bulk polyaniline are enveloped in the polymetric network and only the imine units on the surface have a chance of coming in contact with water, affecting its sensitivity to humidity [2].

The paper reports an evaluation of Co-Polyaniline films as a simple humidity sensor for a broad range of relative humidity ranging from 20%RH to 95%RH.

2. Experimentation

The experimentation is divided into four parts: (a) synthesis of Co nanoparticle, (b) synthesis of Co-Polyaniline nanocomposite, (c) deposition of films and (d) their evaluation as humidity sensor.

The cobalt nanoparticles were synthesized as reported by Shao et al. [10]. The cobalt acetate from Aldrich Chemical (0.354 g (0.06 M)) was dissolved in 2-pyrrolidinone (bp: 245 °C, Aldrich) as a precursor. Then this solution was mixed together with a combination of trioctylphosphine (TOP), oleylamine and oleic acid and added into 35 ml trioctylamine (bp: 365–367 °C)). The prepared mixture was placed in a 250 ml three-neck distillation flask and heated up to 260 °C for 90 min. To avoid oxidation, the flask was flushed with high-purity N_2 gas during the synthesis process. To precipitate cobalt nanoparticles, ethanol was introduced. The precipitated cobalt nanoparticles were washed several times with ethanol and vacuum dried. Spherical Co nanoparticles of average size 30–50 nm are thus synthesized.

For synthesizing Co-Polyaniline nanocomposite, 50 wt.% of Co was diluted with 100 ml of toluene. This was added to 0.265 ml of aniline. The polymerization of monomer was initiated by a drop

* Corresponding author. Tel.: +91 20 2569 2678; fax: +91 20 2569 1684.
E-mail address: mfuke@physics.unipune.ernet.in (M.V. Fuke).

0039-9140/$ – see front matter © 2008 Elsevier B.V. All rights reserved.
doi:10.1016/j.talanta.2008.04.064

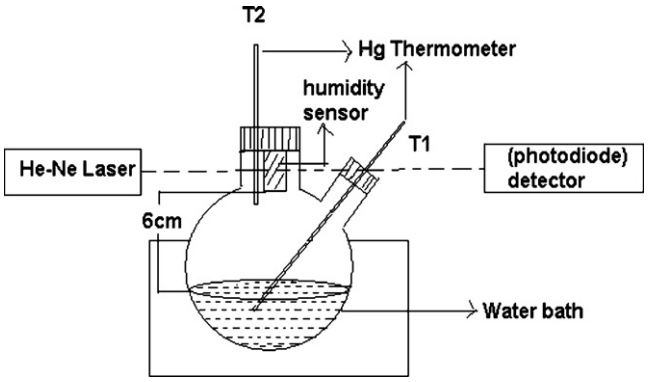

Fig. 1. Experimental set-up for the measurement of relative humidity (two-temperature method).

wise addition of oxidizing agent (0.63 g of ammonium persulfate in 2 ml water with 48 ml of methanol) in an acidic solution of aniline containing 1.26 g of *Para*-toluene sulfonic acid (PTSA), under constant stirring at low temperature between 0 and 5 °C. After complete addition of the oxidizing agent the reaction mixture was kept under constant stirring for 24 h. A solution of Co-Polyaniline nanocomposite was obtained.

To form a film of Co-Polyaniline, 0.1 cm^3 of the above solution was spin coated on to a glass substrate on a fixed area of 5 mm × 5 mm at an optimized spinning speed to get uniform films. To get films of various thicknesses, i.e. from 17 μm to 29 μm (measured using a Light Section Microscope (BK 70 × 50, VEB Carl Zeisco Jena, Germany)), the films were deposited layer-by-layer (0.1 cm^3 solution/layer was kept constant).

The prepared films were examined for their sensitivity towards humidity as measured by the standard two-temperature method. For testing the humidity response of the films, a closed humidity system similar to that of Ansari et al. [3] was used (Fig. 1). It consists of a closed flask, with two necks for inserting thermometers (range −10 to 60 °C with an accuracy of 0.5 °C), half-filled with water (total volume 500 ml). The flask is kept in a container filled with ice to the equal level of water in the flask. The temperature of the system is adjusted by mixing ice and water as required. Thus, the water inside the flask can be kept at the required temperature (T_1). The sensor is mounted inside the flask at a height of 6 cm from the level of water and the temperature of the sample (T_2) is measured with a thermometer placed at the height of the sample under study. It is to be noted that the temperature of the sample changes by 3–6 °C during the experiment.

The relative humidity inside the chamber is calculated by the equation given below. The RH of the air in the system is given by

$$\%\mathrm{RH} = E_W \frac{(T_1)}{E_W}(T_2) \times 100$$

where, $E_W(T_1)$ is the saturated vapor pressure at the temperature of the water bath (T_1) and $E_w(T_2)$ is the saturated vapor pressure at the temperature of the sample element (T_2). The values of the saturated vapor pressure are obtained from CRC [11] manual of chemistry. The ranges of RH values are obtained by adjusting the temperature of the water inside the flask, with ice and water mixture from room temperature to 0 °C.

A He–Ne laser beam, incident perpendicular to the plane of the film, is allowed to pass through the sample (films) and the transmitted output is measured using a simple photovoltaic detector. Normalized output with respect to the lowest humidity is plotted with respect to the relative humidity. The sensitivity is defined as the change in transmitted output (mV) per unit change in RH%, i.e. δ (mV)/δ (RH%) [1]. Thickness of the films, for getting highest sensitivity, was optimized. Film of neat polyaniline of the optimized thickness was deposited to compare their performance.

Time required for getting stable output for a direct transition from air ambient (i.e. ≈55%RH) to higher %RH (i.e. 95%RH) is measured as the response time. The response time is observed for the direct transition from 20%RH to air ambient (55%RH). The time is measured after exposing the sensor directly to the air ambient from 95%RH by removing the sample from the test chamber, till the sensor regains the original output value, as the recovery time. The recovery time is also observed for direct transition from 95%RH to 55%RH.

For measuring hysteresis of the sensor, first the humidity of the chamber is reduced to 20%RH and then was increased to 80%RH. The humidity was then reduced to 20%RH. The maximum difference in the output of the two cycles at any particular RH is measured as a hysteresis. Five cycles are performed on a sample to study the reliability of the sensor. Similarly five samples of each thickness were characterized to check the sensor repeatability.

3. Material characterization

Philips X-ray diffractometer with Cu Kα is used for X-ray diffraction (XRD). A JOEL JSM 6360A Analytical scanning electron microscope (SEM) was used to investigate the surface morphology of the composite films. The Fourier transform Infrared (FTIR) spectra of the samples were recorded on a Perkin Elmer-Spectrum 2000 spectrophotometer operated between 400 and 4000 cm^{-1} in a KBr medium.

4. Results and discussion

The XRD pattern of Co-Polyaniline is as shown in Fig. 2. The characteristic peaks of Polyaniline are found to be in the lower diffraction angle range. The partial crystalline nature of the polymer is indicated by the presence of peaks for 2θ values lying between 10° and 30°. The peaks for Polyaniline are observed at 15.11°, 19° and 24.52°. The characteristic peak of Co_2O_3 at 2θ values of 31.23°, due to (0 0 2) plane; Co at 2θ values of 44.75°, due to (1 1 1) plane; Co_3O_4 at 2θ values of 36.73° are seen in the pattern. Co_xO_y phases clearly show oxidation of Co on dispersion in Polyaniline due to the addition of ammonium persulphate which is a strong oxidizing agent.

SEM for thickness variation of films from 17 μm to 29 μm are as shown in Fig. 3(a–e), respectively. The grains as well as flower-like structures are observed in Fig. 3(a) for lowest film thickness

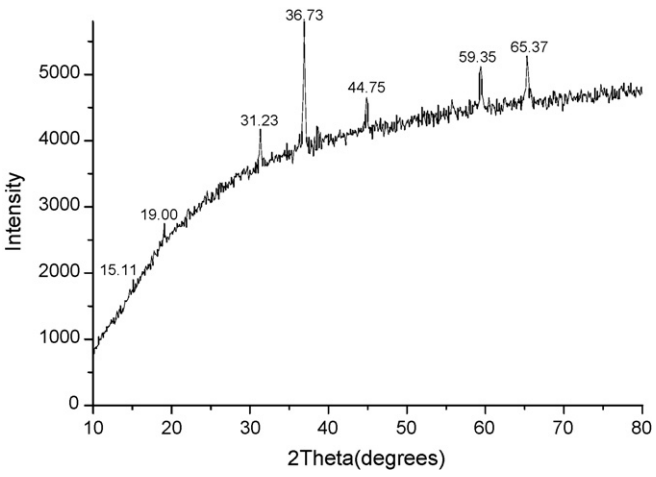

Fig. 2. XRD spectra of Co nanocomposite dispersed in Polyaniline.

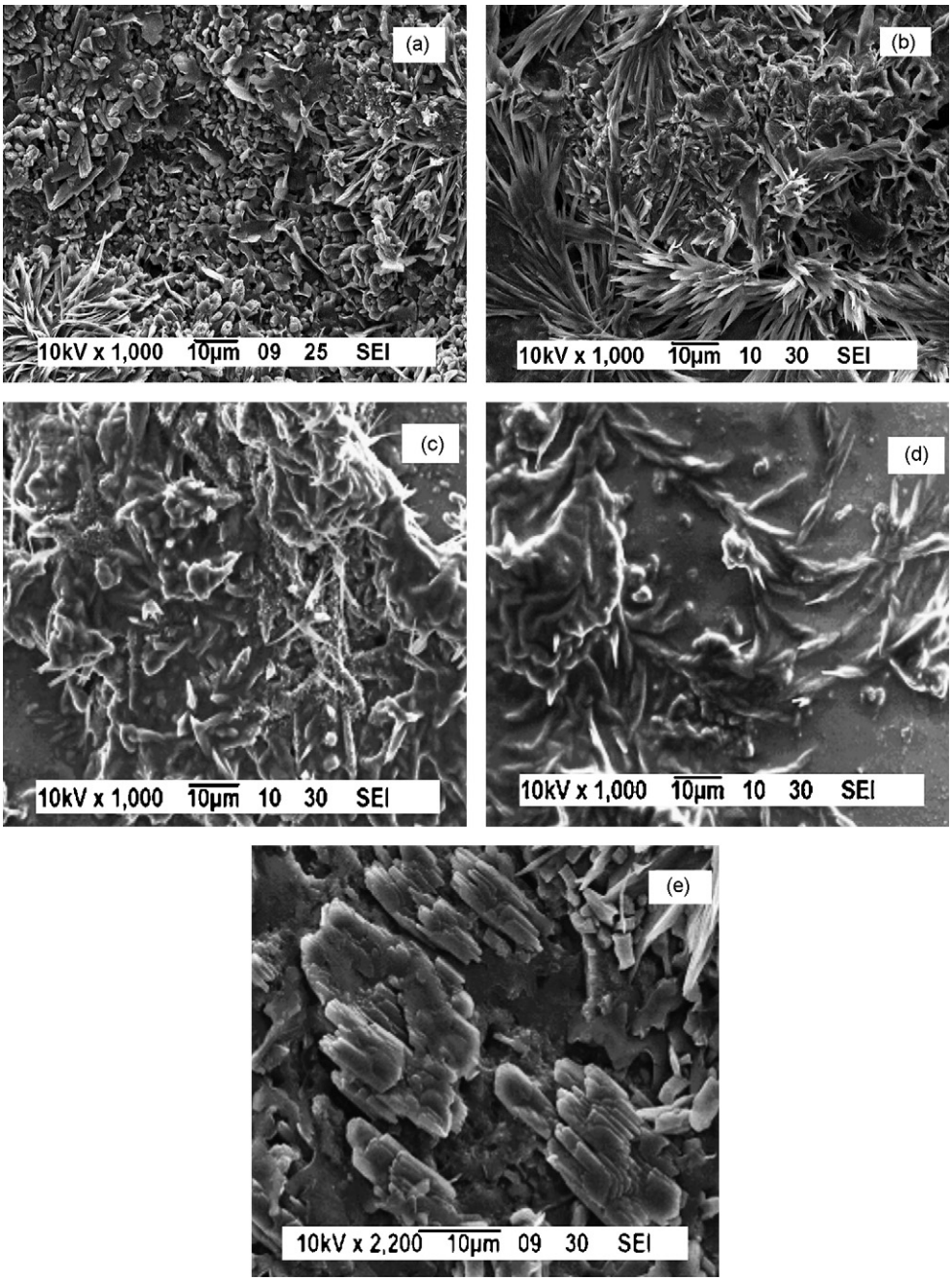

Fig. 3. Scanning electron micrograph (SEM) of Co-Polyaniline nanocomposite films for different thicknesses (a) 17.26 μm, (b) 20.08 μm, (c) 23.57 μm, (d) 26.03 μm and (e) 28.81 μm.

of 17 μm. A globular-like aspect consistent with the instantaneous nucleation of the nanocomposite is observed at higher magnification Fig. 3(e) for highest film thickness of 29 μm. Flower-like structure appears more frequently (Fig. 3(b)) whereas in Fig. 3(c) wire-like structures are observed. Fig. 3(d) shows branching to the formed wires. The films show changes in morphology with increasing thickness. The composite shows agglomeration of polymer for higher thicknesses and porosity is seen for lower thicknesses. The pores facilitate adsorption of water vapours in such composites. Rods and spherical shaped Co is seen in lower thicknesses, later on formed bigger rods and then looked like wires, which changed to platelets. Fig. 3(e) shows rod-like structure. Polyaniline agglomerates and also forms rods, chains and then platelet-like structures with increasing thicknesses.

The FTIR spectra of Co-Polyaniline nanocomposite is demonstrated in Fig. 4. The peak at 814.41 cm^{-1}, is the characteristic of paradistributed aromatic rings indicating polymer formation. C–H in plane and C–H out of plane, bending vibrations appear at 1126.8 and 685.34 cm^{-1}, respectively. Aromatic C–N stretching indicates appearance of the secondary aromatic amine group at 1303.29 cm^{-1}. The bands in the vicinity of 1459.19 and 1601.84 cm^{-1} corresponding to the benzoid ring and quinoid ring modes respectively are of particular interest. The presence of these bands clearly gives composition of insulating and conducting phase of the polymer. Band at 3409.59 cm^{-1} is assigned to N–H stretching vibrations. Presence of these characteristics bands confirms the presence of conducting ES phase in the polymer. The metal oxygen stretching frequency of Co–O is at 568 cm^{-1} [4].

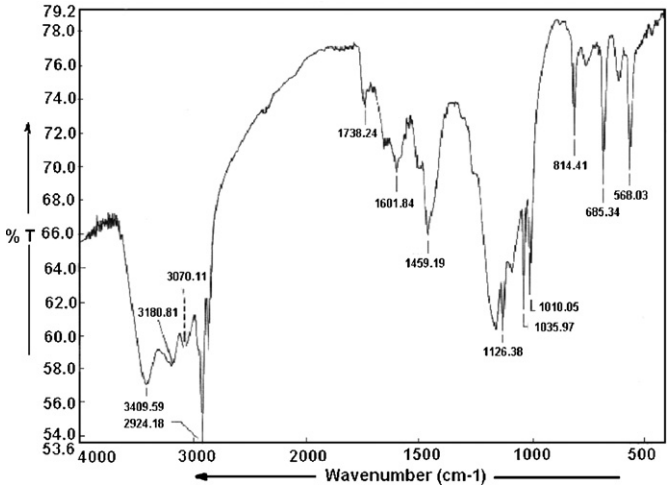

Fig. 4. FTIR spectra of Co nanocomposite dispersed in Polyaniline.

The characteristic response of Co-Polyaniline nanocomposite as a function of relative humidity is revealed in Fig. 5. All the sensors roughly exhibit three regions of sensitivity with very low sensitivity at low humidity levels, increased sensitivity at medium humidity levels and high sensitivity at the high humidity levels. At the thickness of 23.57 μm the maximum sensitivity is seen. As the relative humidity increases the output voltage decreases. At a lower humidity (20 to 40 RH%) the layer of hydroxyl groups is formed [4]. The water vapor molecules are chemisorbed through a dissociative mechanism by which two surface hydroxyl groups per water molecule are formed. This does not change the transmission of light through the film. Therefore at lower relative humidity the sensor response is poor. At a higher humidity (60 to 80 RH%) the water molecules get adsorbed on the wall of the pores. The light through the film gets absorbed in proportion to the deposition of water molecules on the pore walls, in turn the output voltage decreases. For all the samples at higher humidity, around 80%RH, switching behavior is exhibited because of formation of water meniscus on the film, which absorbs the incident light making transmitted intensity to be small.

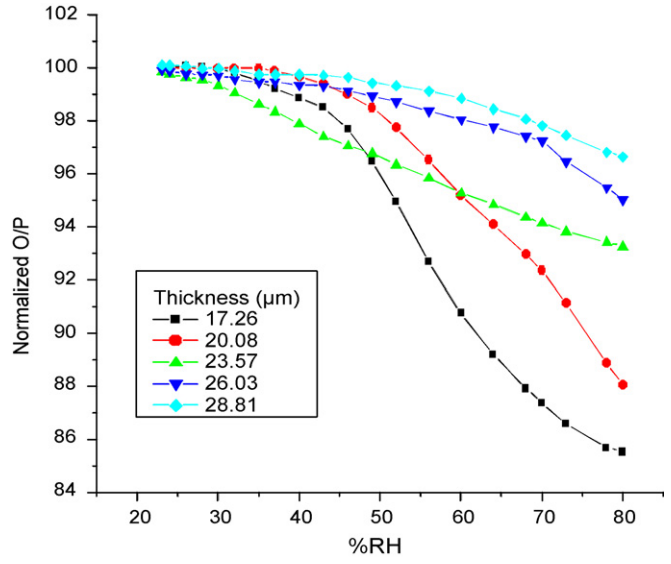

Fig. 5. Variation of the normalized output with respect to the humidity for different thicknesses.

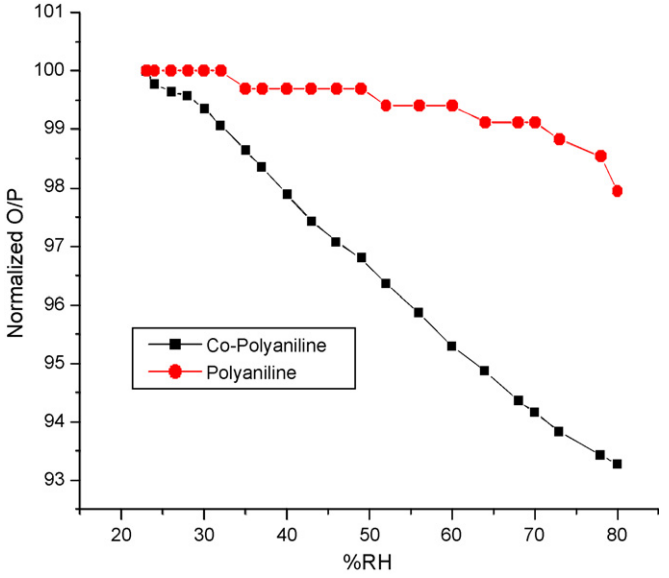

Fig. 6. Comparative study of humidity response for Polyaniline and Co-Polyaniline.

Though the thickness of the casted films is increased by adding the solution layer-by-layer the transmitted intensity either at higher or lower humidity is not affected. As layer-by-layer deposition of film of Co-Polyaniline nanocomposite is done, with drying of films after each deposition may also be responsible for the morphology. The decrease in the output voltage with increase in the relative humidity can also be attributed to the mobility of Co ions which are loosely attached to the polymer by weak Van der Waals' forces of attraction. At low humidity, the mobility of Co is restricted because under the dry conditions the polymer chains would tend to curl up into a compact coil form. On the other hand, when water molecules get absorbed, uncurling of compact foils into a straight chain occurs. This changes the transmission properties of the film through the effective refractive index of the film which increases with the increase in thickness giving less transmitted intensity of light. With increase in thickness, the surface morphology of the films is changing. The changes in surface morphology are creating more pores/channels for absorption of water. At higher thickness more water is absorbed which also absorbs the incident light. This situation favors the output voltage to decrease [12].

Fig. 5 shows typical responses, i.e. the change in transmitted light with RH% for various thicknesses. It is observed that the transmission decreases with increase in RH%. From SEM, it is clear that lower thicknesses have higher porosity and hence gives higher sensitivity. It is seen from Fig. 5 that the humidity response of the sensor shows two or three different sensitivity regions. Above 80%RH, there is a switching behavior. The abrupt change in the output is attributed to the absorption/scattering of light because of formation of water meniscus on the film. With the increasing thickness from 17 μm to 29 μm, the refractive index increases from 1.35 to 1.47 decreasing transmission of light through the films (measured by Able's method). The sensitivity increases with increasing humidity upto a thickness of 23 μm and decreases with further increase in thicknesses. The thickness of 23 μm gives a maximum sensitivity (3.35 mV/%RH) having a fairly linear response, over the range of 20–80%RH. It is seen from Fig. 6 that the Co-Polyaniline nanocomposite is more sensitive to humidity in comparison to Polyaniline alone. This clearly shows that Co nanoparticles play an important role in enhancing the humidity sensing.

The mechanism of oxidation and reduction is crucial in deciding the increase or decrease in the output. The mechanism is explained

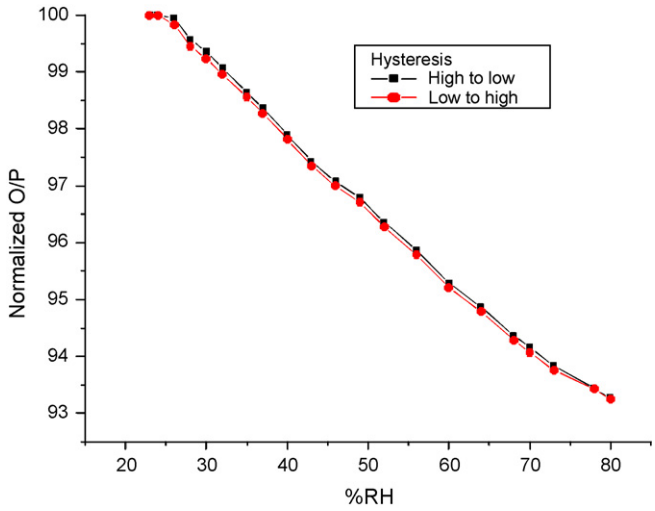

Fig. 7. Hysteresis result for 23.57 μm thickness for the best linear fit having film area 25 mm^2.

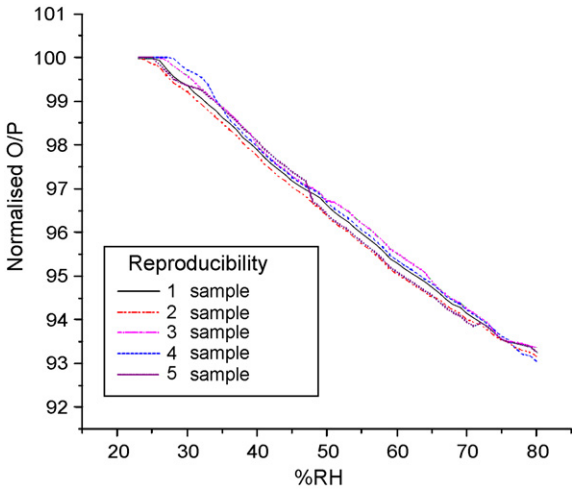

Fig. 9. Reproducibility result for 23.57 μm thicknesses for the best linear fit having film area 25 mm^2.

by Jain et al. [13]. The transformation of one state to the other state occurs due to the oxidation–reduction process. It has been evidenced from NMR studies that such a proton transfer from a polymer can take place in presence of water molecule. This transfer can be described by the following acid–base reaction:

$$NH_2^+ + H_2O \rightarrow NH + H_3O^+$$

The role of water thus appears crucial for this mechanism. The redox reactions in presence of humidity are therefore expected to result in the variation of output of Co-Polyaniline nanocomposite.

The fast response of the sensors can be attributed to the fast penetration of water molecules into the film. The slow recovery in the response is a result of the slow desorption process and capillary forces [1]. The maximum response is evidenced for thickness of 23.57 μm which gives the maximum output voltage at the highest humidity.

Hysteresis defined as the maximum difference in the two outputs (increasing and decreasing cycle) at the same RH level is observed to be nearly 1% for all of the thicknesses. The hysteresis in the response at lower RH is a result of slow desorption of the water from the pores of the capillary. At higher humidity, the capillary condensation occurs and forms a meniscus over the capillaries of the film, which attributes to hysteresis and nonlinearity in the response. Here, hysteresis for 23.57 μm thickness is shown in Fig. 7 which is 1%.

The response and recovery time of the sensor is given as 8 s and 1 min, respectively. The sensing response time of layer-by-layer (LbL) nano-assembly for deposition of ultrathin poly(anilinesulfonic acid) (SPANI) films as reported by Nohria et al. [14] was 15 s. In this case the response is quite fast and the recovery is slow.

The repeatability and the reproducibility of the optical humidity sensor using Co-Polyaniline nanocomposite was found to be very encouraging for all the concentrations for 23.57 μm thickness is shown in Figs. 8 and 9, respectively. About 1% uncertainty from cycle to cycle and uncertainty of about 2% from sample to sample is observed Figs. 8 and 9 indicate better repeatability and reproducibility.

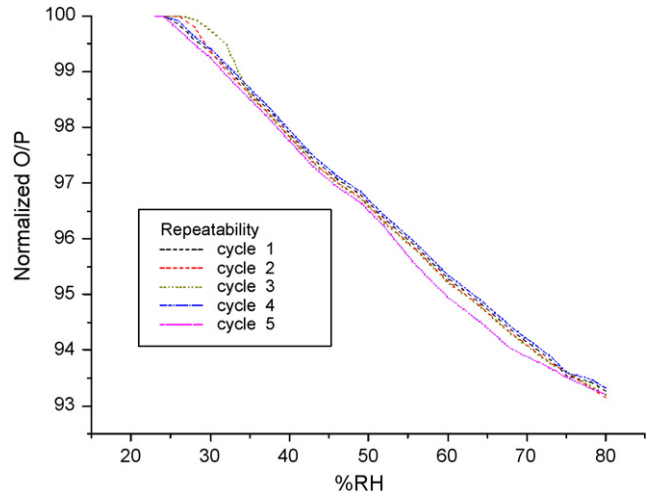

Fig. 8. Repeatability result for 23.57 μm thickness for the best linear fit having film area 25 mm^2.

5. Conclusion

A simple humidity sensor based on Co nanoparticles dispersed in polyaniline in Toluene medium for various thicknesses is reported. The sensor exhibits a fast response time (8 s) and recovery time (60 s) with good repeatability, reproducibility and low hysteresis effect. The humidity range covered is 20–95%RH using two-temperature method. The laser light can be replaced by a simple LED with appropriate optics and electronics.

References

[1] Z.A. Ansari, R.N. Karekar, R.C. Aiyer, Thin Solid Films 305 (1997) 330.
[2] N. Li, X. Li, W. Geng, T. Zhang, Y. Zuo, S. Qiu, J. Appl. Polym. Sci. 93 (4) (2004) 1597.
[3] S.G. Ansari, Z.A. Ansari, M.R. Kadam, R.N. Karekar, R.C. Aiyer, Sens. Actuators B 21 (1994) 159.
[4] N. Parvatikar, S. Jain, S.V. Bhoraskar, M.V.N. Ambika Prasad, J. Appl. Polym. Sci. 102 (6) (2006) 5533.
[5] M.V. Kulkarni, A.K. Viswanath, R.C. Aiyer, P.K. Khanna, J. Polym. Sci., Part B, Polym. Phys. 43 (16) (2005) 2161.
[6] P.R. Somani, A.K. Viswanath, R.C. Aiyer, S. Radhakrishanan, Sens. Actuators B 4054 (2001) 1.
[7] B. Kulwicki, J. Am. Ceram. Soc. 74 (1991) 697.
[8] S.K. Khijwania, K.L. Srinivasan, J.P. Singh, Sens. Actuators B 104 (2005) 217.
[9] T.E. Brook, R. Narayanaswamy, Sens. Actuators B 51 (1998) 77.
[10] H.C. Shao, Y. Huang, H. Lee, Y.J. Suh, C.O. Kim, J. Magn. Magn. Mater. 304 (2006) e28.

[11] R.C. Weast (Ed.), CRC Handbook of Chemistry and Physics, 56th edition, CRC Press, Ohio, 1975–1976.
[12] N. Parvatikar, S. Jain, C.M. Kanamadi, B.K. Chougule, S.V. Bhoraskar, M.V.N. Ambika Prasad, J. Appl. Polym. Sci. 103 (2) (2007) 653.
[13] S. Jain, S. Chakane, A.B. Samui, V.N. Krishnamurthy, S.V. Bhoraskar, Sens. Actuators B: Chem. 96 (2003) 124.
[14] R. Nohria, R.K. Khillan, Y. Su, R. Dikshit, Y. Lvov, K. Varahramyan, Sens. Actuators B: Chem. 114 (1 30 March) (2006) 218.

Talanta 76 (2008) 1130–1135

Contents lists available at ScienceDirect

Talanta

journal homepage: www.elsevier.com/locate/talanta

Detection and quantification of additives (urea, biuret and poultry litter) in alfalfas by nir spectroscopy with fibre-optic probe

Inmaculada González-Martín*, José Miguel Hernández-Hierro

Departamento de Química Analítica, Nutrición y Bromatología, Facultad de CC, Químicas, Universidad de Salamanca, C/Plaza de la Merced s/n, 37008 Salamanca, Spain

ARTICLE INFO

Article history:
Received 31 January 2008
Received in revised form 9 May 2008
Accepted 14 May 2008
Available online 21 May 2008

Keywords:
Additives
Urea
Biuret
Poultry litter
Detection
Quantification
Near infrared spectroscopy
Fibre-optic probe
Alfalfa

ABSTRACT

The additives (urea, biuret and poultry litter) present in alfalfa, which contribute non-proteic nitrogen, were analysed using near infrared spectroscopy (NIRS) technology together with a remote reflectance fibre-optic probe. We used 75 samples of known alfalfa without additives and 75 samples with each of the additives, urea (0.01–10%), biuret (0.01–10%) and poultry litter (1–25%). Using the discriminant partial least squares (DPLS) algorithm, the presence or absence of the additives urea, biuret and poultry litter is classified and predicted with a high prediction rate of 96.9%, 100% and 100%, obtaining the equations of discrimination for each additive. The regression method employed for the quantification was modified partial least squares (MPLS). The equations were developed using the fibre-optic probe to determine the content of urea, biuret and poultry litter with multiple correlation coefficients (RSQ) and prediction corrected standard errors (SEP (C)) of 0.990, 0.28% for urea, 0.991, 0.29% for biuret and 0.925, 2.08% for poultry litter. The work permits the instantaneous and simultaneous prediction and determination of urea, biuret and poultry litter in alfalfas, applying the fibre-optic directly on the ground samples of alfalfa.

1. Introduction

Alfalfa (*Medicago sativa*) is one of the main forages produced in the Mediterranean area. The alfalfas, especially the alfalfa hay, require systematic quality control, because their nutritive value varies in relation to the quality of the initial raw material, conservation, storage (fermentation, bacterial and fungal contamination) and adulteration with ingredients such as urea, biuret and poultry litter among others [1], which are used as sources of nitrogen.

The legislation of the EU (Regulation CE, no. 1831/2003, 22 September 2003) [2] regulates the feed for cattle and the procedures of feeding safety, which must be fulfilled; this legislation controls the maximum content of urea and its derivatives considered as "nutritional" additives for animal feed and which are intentionally added to fodder. The compounds which contribute non-proteic nitrogen (NNP), such as ammoniac, urea, biuret and poultry litter, can be used in forage in a certain quantity as a substitute for protein, both in the fattening of bovines to produce meat and in the feeding of dairy cows and other animals. In the systems of animal production, urea [3,4] is the best known exponent of NNP and is widely used due to its easy obtainment and low cost; it is a compound with an approximate content of 46% nitrogen. It is recommended that not more than 1% of urea should be included in the ration of ruminants in order to prevent the intoxication due to excess ammoniac in the rumen [5]; however, levels of incorporation of 3% have been reported, with no signs of toxicity [6,7]; the urea is added to the alfalfa in silo storage. To this end, between 5 and 6 kg of urea can be added per ton of material (i.e. 0.5–0.6% bulk weight) at the time of filling the silo; this procedure is also employed with the rest of the additives. Biuret is produced from urea by heating and contains 41% nitrogen. However, it is more expensive than urea and the animals require an adaptation period of between 2 weeks and 2 months [8–11]. The poultry litter, avian residue, adequately treated can be utilised as a source of nutrients (proteins, fats, minerals, etc.) in animal feeding. In the case of alfalfas, added as dry excreta, the risks of possible contamination with bacteria and/or fungi and the excess of minerals, such as copper, convert the use of poultry litter into an extensive task for it to be trustworthy [12]. Poultry litter contains total N (depending on the food ingested by the birds) with a mean value of 19.3 mg/g dry weight and is used as a protein supplement in forages like alfalfa for ruminants [13–15] and for the content in P as a mineral source [16].

The former bibliographical antecedents [3,5,10] describe the effects on animals and the determination of the contents of N, P,

* Corresponding author. Tel.: +34 23 294483; fax: +34 23 294483.
E-mail address: inmaglez@usal.es (I. González-Martín).

0039-9140/$ – see front matter © 2008 Elsevier B.V. All rights reserved.
doi:10.1016/j.talanta.2008.05.013

fibre, dry material, metabolizable energy, by wet chemical methods of reference when the additives that contribute non-proteic nitrogen are added to forages including alfalfa.

The methods used for determining parameters of interest in alfalfa, such as total protein and the content in different minerals, are tedious, slow and not very economically viable for application in routine analyses [17,18]. The use of near infrared spectroscopy (NIRS) allows analytes to be determined with little or no sample preparation. This technique has been used in forages such as alfalfa to determine their quality [19,20], fibre and crude protein contents [21], digestibility [22], the changes that occur during silo storage [23], and after they have been subjected to a drying process [24]. It has also been used to determine the different nitrogen fractions [25] and mineral contents [26,27]. More recently NIRS technology with fibre-optic probe has been used [28,29], which permits the determination of vitamins, proteins, fat, humidity and mineralogical elements in alfalfa. Works that use NIRS technology to quantify the presence of additives, such as urea, biuret and poultry litter in alfalfas have not been found.

The objective of this work is the use of NIRS technology with fibre-optic probe of remote reflectance for the detection and quantification of the additives urea, biuret and poultry litter in alfalfas.

2. Material and methods

2.1. Samples

A set of 75 alfalfa samples were collected during 2004–2006. Their composition in protein varied from 13.06% and 21.04%, with a mean and standard deviation of 18.84% and 1.50%, respectively. The 75 samples of alfalfa of known origin were ground (grinder KNIFETEC 1095, FOSS Tecator, Höganäs, Sweden). An aliquot of each of the 75 original alfalfa samples was spiked with the urea, biuret and poultry litter additives, such that for the experiments, we had 75 unspiked samples, 75 spiked with urea, 75 with biuret and 75 with poultry litter. In the case of urea and biuret, the levels of enrichment employed were 0.01, 0.1, 0.2, 0.5, 1.0, 2.0, 3.0, 4.0, 5.0, 5.5, 7.0, 8.5, 10 in percentage (weight/weight), with a minimum of five samples for each enrichment level. In the case of poultry litter, a single origin was used and the level of enrichment was between 1 and 25% by weight, with levels of 1.0, 5.0, 10.0, 15.0, 20.0, 25.0%, with a minimum of 12 samples for each level (Table 1). The urea and biuret are solids (Scharlau; Reactive degree ACS) and are mixed directly with the ground alfalfa. In the case of the poultry litter, it is ground previously and later mixed with the alfalfa. The poultry litter samples were not used as reference material; they came from a farm. The prepared samples, to the human eye, do not present any anomaly, which permits the detection of the presence of any of the additives.

2.2. NIR spectroscopy

A Foss NIR System 5000 with a standard 1.5-m, 210/7210 bundle fibre-optic probe, Ref no. R6539-A, was used. The probe employs a remote reflectance system and uses a ceramic plate as reference. The window is of quartz with a 5 cm × 5 cm surface area, measuring reflectance in the IR zone close to 1100–2000 nm. The spectra were recorded at intervals of 2 nm, performing 32 scans for both the reference and samples. To minimise sampling error, all the samples were analysed in triplicate. The software used was Win ISI 1.50.

Table 1
Grouping of training and calibration samples

Components	*N*	Minimum	Maximum	Mean	S.D.
Urea	65	0.01	10.00	3.39	3.12
Biuret	65	0.01	10.00	3.39	3.12
Poultry litter	65	1.00	25.00	12.63	8.42

Percentage of additives added to the samples of alfalfa.

2.3. Chemometric techniques

For the qualitative analysis, a model of groups is developed and the equations of discrimination by the algorithm discriminate partial least squares (DPLS). The quantification is performed by the method of lineal multivariate lineal calibration, modified partial least squares (MPLS). For the qualitative analysis, supervised pattern recognition refers to techniques in which *a priori* knowledge about the category membership of samples is used for classification. Within the supervised methods, discriminatory analysis is based on the concept that a discriminatory function finds explicit frontiers between classes and in this way the space is divided into regions for each of the classes. It consists of two stages, the construction of the discriminatory functions and determination of the rules of classification.

To obtain the equations of discrimination, the algorithm discriminate partial least squares (DPLS) [30] was used, which is a lineal, parametric, discriminate method and permits the modelling of classes (modelling classes); it has the advantage of being able to handle collinear X-variables, missing data and noisy variables and can deal with overlapped classes. The calibration method applied to this procedure is PLS [31]. In this study for DPLS, PLS 2 was used in all cases. The PLS 2 was applied to the dummy variables (as many classes) with a value of 1 if an object was a member of a class and 0 if otherwise. To evaluate the model of discrimination, it was performed by cross-validation; this method was conducted as in normal PLS to test the accuracy of the discrimination [32,33]. The predicted values of dummy variables were transformed in the other scale, in this way; a limit to belong in a class was 1.5 as cut-off value. If the highest number is associated with the wrong group, the result is a miss. The studies using DPLS for classification are few for NIRS [34].

The quantification of the additives is performed by the modified partial least squares (MPLS) regression method. This was used to obtain the NIR equations for all the parameters studied. Partial least squares (PLS) regression is similar to principal component regression (PCR), but uses both reference data (chemical, physical, etc.) and spectral information to form the factors useful for fitting purposes [35]. MPLS is often more stable and accurate than the standard PLS algorithm. In MPLS, the NIR residuals at each wavelength, obtained after each factor has been calculated, are standardised (dividing by the standard deviations of the residuals at each wavelength) before calculating the next factor. When developing MPLS equations, cross-validation is recommended in order to select the optimal number of factors and to avoid overfitting [36]. For cross-validation, the calibration set is divided into several groups; each group is then validated using a calibration developed on the other samples. Finally, validation errors are combined into a standard error of cross-validation (SECV) [37]. It has been reported that the SECV is the best single estimate for the prediction capability of the equation, and that this statistic is similar to the average standard error of prediction (SEP) from 10 randomly chosen prediction sets [38]. The cross-validation groups used were six for urea, biuret and poultry litter. The effects of scattering were removed using multiplicative scatter correction (MSC), standard normal variate (SNV), DeTrend (DT) or SNV–DT [39,40]. Moreover, the mathematical treatments were tested in the development of the NIRS calibrations, 2,4,4,1, where the first digit is the number of the derivative, the second is the gap over which the derivative

is calculated, the third is the number of data points in a running average or smoothing, and the fourth is the second smoothing [41]. The statistics used to select the best equations were RSQ (multiple correlation coefficients) and the standard error of cross-validation (SECV). Of the total of samples available in each case, 65 constitute the training or calibration group (depending on whether classification or quantification is the objective) and 10 samples are left to externally validate the models.

3. Results and discussion

3.1. Spectral information

The NIR spectra were recorded applying the fibre-optic probe directly to the samples of ground alfalfa, with and without residues. In Fig. 1, the NIR spectra of the alfalfa are compared with those of the additives urea, biuret and poultry litter, and the spectra of the alfalfa with and without the presence of the additives. The NIR spectra reflect the variability of the additives and their proportion, which permits their detection and quantification.

3.2. Qualitative analysis

3.2.1. Classificatory analysis

Firstly the modelling of the groups was carried out using the NIR spectral data and the discriminate analysis; thus the explicit algebraic models denominated DPLS were constructed. The training samples are constituted by the alfalfa samples with and without additives, as indicated in Table 1. The results of the modelling of classes of the groups considered are presented in Table 2; we can conclude that by the NIR spectral information and the DPLS analysis we can classify and predict the presence or absence of the additives urea, biuret and poultry litter individually or as a whole (some of the three additives simultaneously) with a high degree of efficacy.

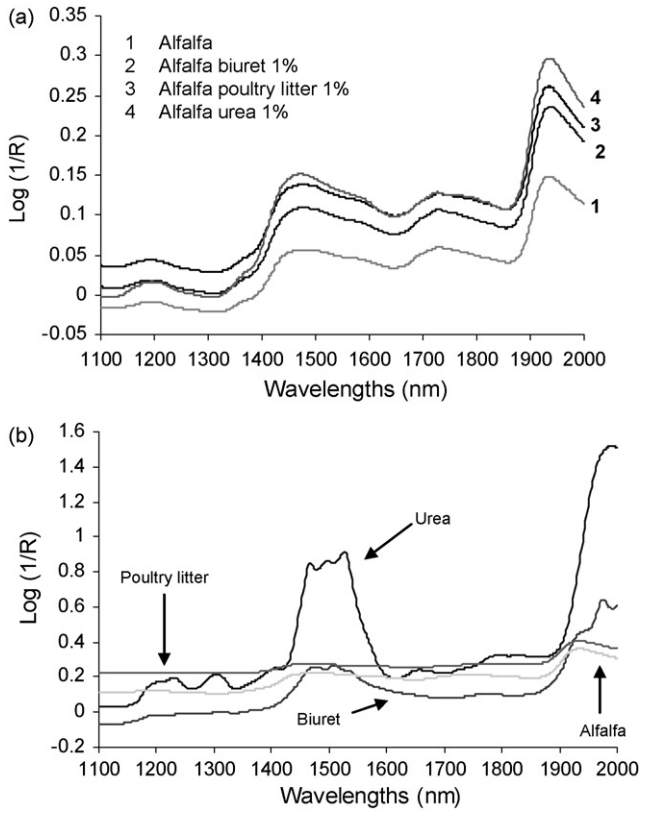

Fig. 1. (a) Spectra of the alfalfa with and without the presence of additives. (b) NIR spectra of the alfalfa with those of the additives urea, biuret and poultry litter.

In the models separated by each additive in internal validation, a prediction rate is obtained (mean of 98.7% and in external validation 93.3%). When all the models are used together, that is, they are classified globally, the three additives simultaneously, the prediction rate is 96.9% in internal validation and 92.5% in external validation. The poorly classified samples of the individual components are as follows: Always in the presence in internal validation, two samples with urea additive with an enrichment of 1%. In external validation: one sample with 0.1% urea additive. In the global analysis: two samples with 1% urea additive (the sample coincides with a poorly classified sample in the internal validation, individual constituent) and two urea samples enriched at 0.5%; in external validation one sample with 0.5% urea enrichment.

Therefore, it can be concluded that the DPLS method can perform the classification and predict the three additives in alfalfa (urea, biuret and poultry litter) with high prediction rates of 96.9%, 100% and 100%, indicating that it is an appropriate method of classification of additives in alfalfa with the spectral data. This demonstrates that NIR spectroscopy and discriminate DPLS analysis permit a clear differentiation between the samples with and without additives.

The use of these discriminate models can be carried out in two ways, systematically, applying it to all the samples before the quantification of protein, developed in an earlier work [29], or if in the determination of protein the values of this parameter surpass the habitual margins or the sample is eliminated because of spectral criteria, $H > 3$, the discriminate analysis is used to classify and predict the presence or absence of some of the additives and later quantify them.

3.2.2. Equations of discrimination

The equations of discrimination are obtained by the algorithm discriminant partial least squares (DPLS) for each constituent, urea, biuret and poultry litter (with 130 samples) and the global equation (with 260 samples) for the three samples simultaneously.

In Table 3 the number of samples of each group, the interval of application in the equation of discrimination and the statistics, RSQ, SEC and SECV are presented, like the groups of cross-validation and the factors PLS (this number is greater in this method compared with normal PLS). The data are obtained without any mathematical treatment of the NIR spectra or scattering. The results obtained indicate that the discriminate functions are capable of predicting the pertinence of an object to one category or another, quantitatively, with the statistics RSQ and SECV, are good in a regression and the percentage of samples are correctly classified.

3.3. Quantitative analysis: calibration equations

A PCA analysis was carried out with the 65 samples of each group of additives (urea, biuret and poultry litter). The risk of mistakes in the equations under practical conditions is very low or almost nil when using the standardised H-statistic (Mahalanobis distance) during routine analysis of unknown samples; zero samples were removed for urea, two for biuret and two for poultry litter. In all cases, the spectral variability explained was 99%, in each case taking the following principal components as 6 for urea and biuret and 5 for poultry litter.

Calibrations were performed by modified partial least squares regression (MPLS). Using the $T \geq 2.5$ criterion, samples that were different from the population owing to chemical criteria were removed from the set. According to this chemical criterion, seven

Table 2
Classificatory analysis: samples correctly classified (%)

Constituent	Internal validation			External validation		
	Presence		Absence	Presence		Absence
Urea	96.9		95.4	90.0		80.0
Biuret	100		100	100		90.0
Poultry litter	100		100	100		100
	Urea	93.8		Urea	90.0	
All the additives	Biuret	100	93.8	Biuret	100	80.0
	Poultry litter	100		Poultry litter	100	

samples were removed from the calibration set in the case of urea, five for biuret and four in the case of poultry litter.

The statistical parameters of the calibration equations for each additive in the alfalfa are shown in Table 4 where *N*, the number of samples used to obtain the calibration equation, is presented after removing the samples for spectral (H criterion) or for chemical reasons (T criterion). The best of the different mathematical treatments, concentration range, and standard deviations for the presence of urea, biuret and poultry litter in alfalfa are also shown. The results obtained indicate that it is possible to determine these parameters in alfalfa with broad applicability.

3.4. Validation

3.4.1. Internal validation (prediction)

Model evaluation was performed by cross-validation. In this method, the set of calibration samples is divided into a series of subsets. In all cases, cross-validation was performed by splitting the population into six groups. Of these, five were taken for the calibration set and one for the prediction set. The process is repeated as many times as there are sets, so that all pass through the calibration set and the prediction set. Using this process, we validated the model used and checked its prediction capacity. Fig. 2 shows the correlations of the values obtained at the laboratory with respect to those predicted by NIR with a fibre-optic probe for urea, biuret and poultry litter in the alfalfa samples.

3.4.2. Prediction capacity of the model

The prediction capacity of the model was assessed using the RPD (ratio performance deviation) parameter [42], defined as the relationship between the standard deviation of the chemical method (S.D. ref) and that of prediction in the NIR model (SEP). If the RPD value is greater than 2.5, it is assumed that the calibration model is adequate. The RPD values obtained in ground samples for urea, biuret and poultry litter (11.0, 11.1, 4.0) show that the NIR equations obtained can be applied to unknown samples.

From these data, it may be deduced that the NIRS technique, using a fibre-optic probe, is a good alternative for the determination of the additives urea, biuret and poultry litter in alfalfa samples.

3.4.3. External validation

We checked the robustness of the method by applying NIRS technology to 10 new samples that did not belong to the calibration group. The procedure was as follows: Spectra were recorded in triplicate and the spectral mean was taken. Then, the calibration equations obtained during the work were applied and the predicted values were compared with the data on enrichment (%) of the spiked alfalfa samples**.** The NIRS and chemical methodologies were compared for the three additives using the Student's *t*-test for paired values with these samples. The levels of significance were found to be 0.42 for urea, 0.66 for biuret and 0.33 for poultry litter. The level of significance for all constituents was higher than

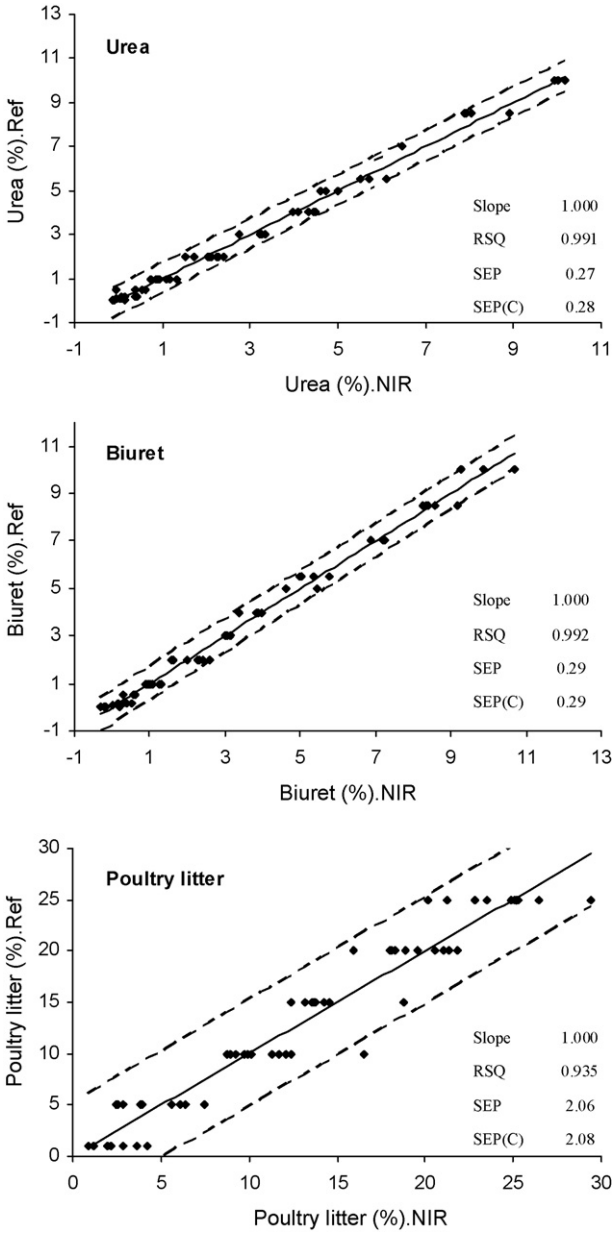

Fig. 2. Comparison of reference values with the values predicted by the calibration equations for additives urea, biuret and poultry litter in alfalfa. RSQ, multiple correlation coefficients; SEP, standard prediction error; SEP(C), standard prediction error corrected by the bias.

Table 3
Presence of additives in alfalfa: equations of discrimination

Components	*N*	S.D.	Estimate	RSQ	SEC	SECV	Cross-validation group	No. of fac PLS
Urea	130	0.5	0.0–1.5	0.755	0.247	0.326	6	17
Biuret	130	0.5	0.0–1.5	0.953	0.108	0.179	6	22
Poultry litter	130	0.5	0.0–1.5	0.934	0.128	0.202	6	19
Global	260	0.43	0.0–1.3	0.793	0.197	0.235	4	25

N, number of samples; S.D., standard deviation; RSQ, multiple correlation coefficients; SEC, standard error of calibration; SECV, standard error of cross-validation; PLS, partial least squares.

Table 4
Determination of additives in alfalfa: calibration statistical descriptors for the NIR

Components	*N*	Mathematical treatment	S.D.	Estimate	RSQ	SEC	SECV	No. of fac PLS	Cross-validation group	RPD
Urea	58	SNV 2,4,4,1	2.97	0.00–11.90	0.990	0.29	0.59	7	6	11.0
Biuret	58	None 2,8,6,1	3.22	0.00–12.99	0.991	0.31	0.45	8	6	11.1
Poultry litter	59	Detrend 1,4,4,1	8.19	0.00–38.08	0.925	2.24	3.21	6	6	4.0

N, number of samples; SNV, standard normal variate; S.D., standard deviation; RSQ, multiple correlation coefficients; SEC, standard error of calibration; SECV, standard error of cross-validation; PLS, partial least squares; RPD, ratio performance deviation.

Table 5
Determination of additives in alfalfa: external validation of the calibration model (10 samples)

Components	*P* (level of significance)	Residual mean	RMSE
Urea	0.42	0.78	1.17
Biuret	0.65	0.54	0.76
Poultry litter	0.33	4.64	6.31

RMSE, root mean standard error.

0.05 (chosen as the minimum); i.e., there were no differences between the results obtained; thus it may be concluded that the method provides significantly equal data to the starting reference data. Table 5 shows the results obtained in the external validation, the means of the residuals, and the root mean standard error (RMSE) values. Our findings show that the analytical method discussed – employing a fibre-optic probe and measuring the samples by direct application of the probe – is rapid, does not require sample treatment and can be used to monitor the urea, biuret and poultry litter parameters in alfalfas.

4. Conclusions

The results show that the analytical method discussed, employing a fibre-optic probe with which NIR spectra were measured by applying the fibre-optic probe directly on ground samples, in direct contact with the sample, is rapid and non-contaminant. This method can be used for monitoring alfalfa quality. In summary, it may be concluded that the NIRS technique with a fibre-optic probe is suitable for detection and quantification of additives (urea, biuret and poultry litter) in alfalfa samples, with limits of detection (the minimum amount that can be classified as positive by DPLS) of 0.01% for urea, 0.01% for biuret and 1% for poultry litter.

The work permits the instantaneous and simultaneous determination of urea, biuret and poultry litter in alfalfas, applying the fibre-optic probe directly to the samples, thereby affording faster analysis times because sample preparation is minimal or unnecessary.

References

[1] C. de Blas, G.G. Mateos, P.G. Rebollar, FEDNA. Tablas FEDNA de composición y valor nutritivo de alimentos para la formulación de los piensos compuestos, 2nd ed., Fundación española para el desarrollo de la nutrición animal, Madrid, España, 2003, p. 423.
[2] Regulation (EC) No. 1831/2003 of the European Parliament and of the Council of 22 September 2003 on additives for use in animal nutrition, Official Journal of the European Union L 268 (2003) 29.
[3] Agricultural Research and Food Council, Protein Nutr. Abstr. Rev. Ser. B 62 (1992) 787–835.
[4] Institut de la Recherche Agronomique, Alimentation des Bovins, Ovins, et Caprins, R. Jarrige, Institut National de la Recherche Agronomique, Paris, 1988.
[5] A.D. Adamu, J.R. Russell, M.C. Gilliard, A. Trenkle, Anim. Feed Sci. Technol. 22 (1989) 227.
[6] L. Lines, W. Weiss, J. Dairy Sci. 79 (1996) 1992.
[7] G.A. Broderick, W.M. Craig, D.B. Ricker, J. Dairy Sci. 76 (1993) 2266.
[8] National Academy Press, Nutrient Requirements of Beef Cattle, 7th rev. edition, National Academy Press, Washington, DC, 1996.
[9] G.A. Broderick, J.H. Kang, J. Dairy Sci. 63 (1980) 64–75.
[10] C.A. Löest, E.C. Titgemeyer, J.S. Drouillard, B.D. Lambert, A.M. Trater, Anim. Sci. Technol. 94 (2001) 115.
[11] E.S. Vanzant, R.C. Cochran, J. Anim. Sci. 72 (1994) 1059.
[12] K.E. Webb, J.P. Fontenot, J. Anim. Sci. 41 (1975) 1212.
[13] J.P. Fontenot, K.E. Webb Jr., Am. Soc. Exp. Biol. 33 (1976) 1936.
[14] National Research Council, Nutrient Requirements of Domestic Animals. Nutrient Requirements of Beef Cattle, 7th ed., National Academy of Sciences, Washington, DC, 1996.
[15] S. Thakur, J.P. Srivastava, A.K. Verma, B.S. Gupta, J. Anim. Sci. 52 (1982) 1260.
[16] G.M. Barnett, Bioresource Technol. 49 (1994) 139.
[17] S. Kume, T. Toharmat, K. Nonaka, T. Oshita, T. Nakui, J.H. Ternouth, Anim. Feed Sci. Technol. 93 (2001) 157.
[18] I. Murray, in: P. Garnsworthy (Ed.), Recent Advances in Animal Nutrition, University of Nottingham Press, UK, 1996.
[19] K.H. Norris, R.F. Barnes, J.E. Moore, J.S. Shenk, J. Anim. Sci. 43 (1976) 889.
[20] J.S. Shenk, M.O. Westerhaus, Forage Quality Evaluation and Utilization, A.S.A., C.S.S.A., S.S.S.A., Madison, WI, 1995.
[21] F.E. Barton, W.R. Windham, J. Assoc. Off. Anal. Chem. 71 (1988) 1162.
[22] F.J. Gordon, K.M. Cooper, R.S. Park, R.W. Steen, Anim. Feed Sci. Technol. 70 (1998) 339.
[23] E.R. Deaville, D.I. Givens, Anim. Feed Sci. Technol. 72 (1998) 41.
[24] D. Alomar, R. Fuchslocher, J. Stockebrands, Anim. Feed Sci. Technol. 80 (1999) 309.
[25] C. Valdes, S. Andres, F.J. Giráldez, R. Garcia, A. Calleja, J. Agric. Food Chem. 86 (2006) 308.
[26] J.L. Halgerson, C.C. Sheaffer, N.P. Martin, P.R. Peterson, S.J. Weston, Agron. J. 96 (2004) 344.
[27] D.H. Clark, H.F. Mayland, R.C. Lamb, Agron. J. 79 (1987) 485.
[28] I. González-Martín, J.M. Hernández-Hierro, M. Bustamante-Rangel, N. Barros-Ferreiro, Anal. Bioanal. Chem. 386 (2006) 1553.
[29] I. González-Martín, J.M. Hernández Hierro, J.M. González Cabrera, Anal. Bioanal. Chem. 387 (2007) 2199.
[30] L. Stahle, S. Wold, J. Chemometr. 1 (1987) 185.
[31] G. Vandeginste, D. Massart, L. Buydens, S. De Jong, P. Lewi, J. Smeyers-Verbeke, Handbook of Chemometrics and Qualimetrics, Elsevier, NY, 1988, p. 207.
[32] M. Sharaf, D. Illman, B. Kowalski, Chemometrics, Wiley/Interscience, NY, 1986, p. 228.
[33] M. Tenenhaus, La Regression PLS, Technip, Paris, 1998.
[34] L. Xie, Y. Ying, T. Ying, J. Kell, J. Food Eng. (2007) 395.
[35] H. Martens, T. Naes, Multivariate Calibration, Wiley, Chichester, 2001, p. 116.
[36] J.S. Shenk, M.O. Westerhaus, Analysis of Agriculture and Food Products by Near Infrared Reflectance Spectroscopy, NIR Systems, 1995.

[37] A.M.C. Davies, P. Williams (Eds.), Proceedings of the Seventh International Conference on Near Infrared Spectroscopy, NIR Publications, Chichester, West Sussex, UK, 1996.
[38] P.C. Williams, K. Norris, Near Infrared Technology in the Agricultural and Food Industries, American Association of Cereal Chemists, Inc., St. Paul, MN, USA, 1997.
[39] P. Geladi, D. Mac Dougall, H. Martens, Appl. Spectrosc. 39 (1985) 491.
[40] M.S. Dhanoa, S.J. Lister, R.J. Barnes, Appl. Spectrosc. 49 (1995) 765.
[41] J.S. Shenk, M.O. Westerhaus, Routine Operation, Calibration, Development and Network System Management Manual, NIR Systems, Silver Spring, MD, USA, 1995.
[42] P.C. Williams, D.C. Sobering, Near Infrared Spectr. 1 (1993) 25.

Talanta 76 (2008) 1261–1264

Contents lists available at ScienceDirect

Talanta

journal homepage: www.elsevier.com/locate/talanta

Short communication

A novel chiral column for the HPLC separation of a series of dansyl amino and arylalkanoic acids

Yves-Claude Guillaume, Claire André*

Equipe des Sciences Séparatives et Biopharmaceutiques (2SB)-EA 3924, Laboratoire de Chimie Analytique, Faculté de Médecine Pharmacie, Place Saint Jacques, 25030 Besançon Cedex, France

ARTICLE INFO

Article history:
Received 29 October 2007
Received in revised form 12 May 2008
Accepted 14 May 2008
Available online 21 May 2008

Keywords:
Separation
CLHP
Cyclic hexapeptide

ABSTRACT

In a previous paper [C. Andre, M. Thomassin, A. Umrayami, L. Ismaili, B. Refouvelet, Y.C. Guillaume, Talanta 71 (2007) 1817] a novel cyclic hexapeptide molecule dissolved in the mobile phase was evaluated as a chiral selector (CS) for the enantiomer separation of a series of dansyl amino and arylalkanoic acids using high performance liquid chromatography (HPLC). In this paper, this CS was immobilized to the surface of a monolithic support and the enantioselectivity and the performance of this novel column are discussed.

1. Introduction

The separation and analysis of chiral compounds is an area of increasing interest and high performance liquid chromatography columns containing immobilized chiral selector (CS) [1] have a great potential for optical resolution of such compounds. The chiral selector commonly used include amino acids [2,3], proteins [4–7], crown ethers [8–9], oligo and polysacharides [10–12] or macrocyclic antibiotics [13–15]. In a previous paper, a novel macrocyclic chiral selector synthesized in our laboratory was dissolved in the mobile phase [1]. This CS demonstrated to be effective in the separation of a great number of enantiomer pairs [1]. In this paper, this novel CS was immobilised on a monolithic support and the enantioselective properties of the resulting material was investigated using D,L-dansyl amino and arylalkanoic acids as model compounds.

2. Materials and methods

2.1. Apparatus

The HPLC system for these measurements consisted of a Merck Hitachi pump L7100 (Nogent sur Marne, France), an Interchim Rheodyne injection valve model 7125 (Montluçon, France) fitted with a 20 μL sample loop injection, and a Merck L4500 diode array detector. The column used was an Interchim C1 monolithic (100 mm × 4.6 mm i.d.) under controlled temperature conditions (25 °C) in an interchim TM 701 oven (Montluçon, France). The detection wavelength was fixed at 254 nm.

2.2. Solvents and samples

Water was obtained from an Elgastat option I water purification system (Odil, Talant, France) fitted with a reverse osmosis cartridge. Methanol, analytical grade, was provided by Prolabo (Paris, France). Sodium hydrogen phosphate and potassium dihydrogen phosphate were obtained from prolabo (Paris, France) and the mobile phase consisted of a phosphate buffer (at pH 5.60). This phosphate buffer was prepared by mixing 10 mL of sodium hydrogen phosphate (0.06 M) and 190 mL of potassium dihydrogen phosphate. The chiral selector was synthesized as described in a previous paper [1]. Sodium nitrate was used as a dead time marker (Merck, Saint Quentin Fallavier, France). Dansyl amino acids (i.e., dansyl-alanine (dan-ala), dansyl-valine (dan-val), dansyl-norvaline (dan-nor), dansyl-leucine (dan-leu), dansyl-phenylalanine (dan-phe), dansyl-tryptophane (dan-try)) and arylalkanoic acids, i.e., etodolac (eto), flobuphen (flo), ibuprofen (ibu), flurbiprophen (flu), naproxen (nap), sulindac (sul), racemic standard compounds and *D*-enantiomers were purchased from Sigma–Aldrich (Saint Louis, MO, USA). The molecular structure of the arylalkanoic acids is given in Fig. 1. Sample solutions were separately prepared at concentrations of 5 mM in the phosphate buffer. All samples and mobile phases

* Corresponding author. Tel.: +33 3 81 66 55 44; fax: +33 3 81 66 56 55.
E-mail address: yves.guillaume@univ-fcomte.fr (Y.-C. Guillaume).

0039-9140/$ – see front matter © 2008 Elsevier B.V. All rights reserved.
doi:10.1016/j.talanta.2008.05.014

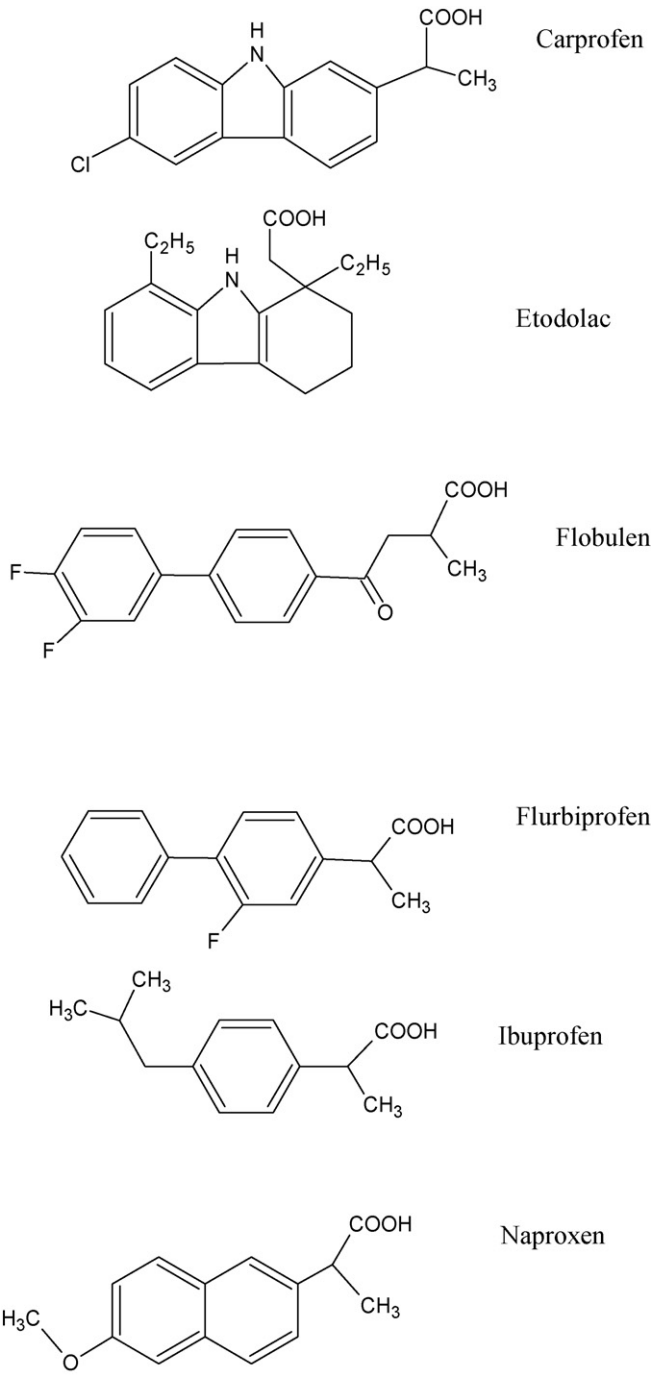

Fig. 1. Arylalkanoic acid molecular structure.

were filtered with 0.45 μM syringe filter discs (Whatman, Clifton, NJ, USA) and degassed by sonification. Twenty microliters of each sample were injected in triplicate and the retention times were measured.

2.3. Chiral selector immobilisation via physical absorption

The in situ process, which consists of the attachment of the chiral selector (CS) directly in pre-packed columns, was used to immobilize the CS to create the chiral column. The physical absorption was carried out on the C1 stationary phase by hydrophobic interaction. The immobilisation was carried out at a pH 5.60. At room temperature, the interchim C1 monolithic stationary phase (100 mm × 4.6 mm i.d.) was connected to the HPLC system. The chiral selector solution (2 g/L) in (M/15) phosphate buffer (pH 5.60) containing 0.5 M of sodium chloride was recycled through the column at a flow rate of 0.5 mL/min until saturation. Thereafter, the column was washed with (M/15) phosphate buffer (pH 5.60). The amount of CS bound to the column was determined from the HPLC analysis of the fractions collected at the column outlet during the percolation of the CS and the washing steps.

Table 1
Retention factor, k, of the *D*-enantiomer, and enantioselectivity α for the compound analysed in this study

Compound	k	α
dan-ala	4.71	1.32
dan-val	5.04	1.31
dan-nor	8.24	1.34
dan-leu	7.00	1.33
dan-phe	7.95	1.20
dan-try	6.10	1.18
Eto	4.01	≈0
Flo	13.10	1.44
Flu	14.89	1.41
Ibu	12.50	1.43
Nap	10.20	1.54
Sul	6.58	≈0

Mobile phase: phosphate buffer (pH 5.60, M/15), T = 25 °C, mobile phase flow-rate 1 mL/min.

3. Results and discussion

From the retention time obtained, the retention factor (k) of all the enantiomers were determined for a phosphate buffer pH 5.6 (0.06 M). All the experiments were repeated three times. The precisions of retention times of each enantiomer was characterised by relative standard deviation (R.S.D.) values comprised between 0.10 and 0.30%. The variation coefficients of the k values were less than 1% in most cases, indicating a high reproducibility and good stability for the chromatographic system. The stability was tested by comparing the D-naproxen retention factor during the study and then after more than 4 months under the same conditions. The maximum relative difference between retention time of this compound was never more than 0.6% proving the stability of the column during an extended period of time. The chromatographic parameters – retention factor (k) selectivity (α) – of the racemic mixtures tested are presented in Table 1. The chromatograms of dan-nor, dan-tryp, flu and nap are depicted in Fig. 2. For each solute molecule the *L*-enantiomer was more retained than the *D*-enantiomer. For the dansyl amino acid series, and for each enantiomer (*D* or *L*) the retention factor increased in the order: dan-ala < dan-val < dan-try < dan-leu < dan-phe < dan-nor.

For the arylalkanoic acids, and for each enantiomer (*D* or *L*), the retention order increased in the order: eto < sul < nap < ibu < flo < flu.

Table 2
Chromatographic parameters of naproxen (D-naproxen retention factor (k), enantioselectivity, (α) asymmetry factor (A_s)) on the chiral column at different flow-rate

Flow-rate (mL/min)	k	α	A_s
0.5	10.19	1.54	1.20
0.8	10.21	1.53	1.19
1.0	10.22	1.55	1.22
1.2	10.20	1.56	1.21
1.5	10.21	1.53	1.20
2.0	10.23	1.53	1.19

Mobile phase: phosphate buffer (pH 5.60, M/15), T = 25 °C.

Table 3
Retention factor, k, of D-naproxen and enantioselectivity factor, α, for the naproxen molecule on the chiral column at different methanol fraction (v/v) in the mobile phase (phosphate buffer (pH 5.60, M/15)) and with different injection number, $T = 25\,^{\circ}C$

Injection number	0.10 (v/v)		0.15 (v/v)		0.20 (v/v)		0.25 (v/v)		0.30 (v/v)		0.40 (v/v)	
	k	α	k	α	k	α	k	α	k	α	k	α
100	8.52	1.43	7.21	1.34	6.12	1.20	5.09	1.15	4.10	1.10	3.22	1.03
200	8.52	1.43	7.22	1.35	6.11	1.21	5.09	1.14	4.09	1.09	3.22	1.02
300	8.53	1.41	7.21	1.33	6.12	1.22	5.08	1.15	4.07	1.08	3.21	1.00
400	8.53	1.42	7.23	1.35	6.10	1.20	5.07	1.14	4.05	1.09	3.18	1.00
500	8.52	1.43	7.21	1.34	6.12	1.21	5.06	1.13	4.04	1.08	3.15	1.00
600	8.53	1.42	7.22	1.33	6.11	1.20	5.06	1.12	3.98	1.09	3.00	1.00
700	8.54	1.41	7.21	1.35	6.12	1.22	5.05	1.11	3.97	1.07	2.95	1.00
800	8.52	1.42	7.22	1.34	6.12	1.21	5.04	1.13	3.89	1.07	2.90	1.00
900	8.54	1.41	7.21	1.35	6.11	1.22	5.05	1.14	3.87	1.07	2.92	1.00
1000	8.52	1.40	7.22	1.34	6.12	1.21	5.03	1.11	3.86	1.06	2.93	1.00

Mobile phase flow-rate 1 mL/min.

These results were in accordance with those obtained in a previous paper [1]. Indeed, the overall association of the enantiomer-CS depended, at least in part, on the overall hydrophobic interaction between the enantiomer and the methyl group of the chiral selector. In addition, the shape of the side chain R for the dansyl amino acid series for example participated in the overall association mechanism [1]. From a chiral discrimination point of view, for the aliphatic amino acids dan-ala, dan-val, dan-nor, dan-leu) the enantioselectivity remained relatively constant around 1.31. As it was observed previously when the CS was dissolved in the mobile phase [1], for the aromatic dansyl amino acids (dan-phe, dan-try) a decrease of the enantioselectivity was observed (around 1.20). For the arylalkanoic acid derivatives, the nap molecule presented the highest separation (1.54). flo, flu and ibu presented an intermediate separation around 1.40. No separation of sul and eto enantiomers was observed in accordance with previous results obtained when the CS was dissolved in the bulk solvent [1]. An important feature of monolithic supports is their ability to operate at high flow-rate regardless of column back pressure, this is intrinsically not possible with particulate columns because by operating at flow-rate higher than 1.0 mL/min a high column back pressure would result. Focus was therefore given to the evaluation of this column with respect to speed of eluent flow. D-naproxen was used as a probe to demonstrate that this novel chiral column can operate at high flow rate without a significant loss in enantioselectivity Table 2. A decrease in retention and enantioselectivity was observed, for all solutes, when the methanol fraction increased in the bulk solvent. An example was given in Table 3. This behaviour suggested that both retention and enantioselectivity mechanisms were depended on hydrophobic effects and confirmed a competition effect for the binding with the chiral selector between the enantiomer and methanol added in the mobile phase. In addition, Table 3 showed the stability of the column when the methanol fraction in the mobile phase was lower than 0.25 (v/v). Over a methanol fraction in the mobile phase equal to 0.25 (v/v) the retention decreased when near 400 injections were made. This behaviour can be explained by a possible desorption of the CS on the chromatographic support for a methanol fraction >0.25 (v/v). These results indicated that a mobile phase containing a methanol fraction lower than 0.25 (v/v) guaranteed a long lifetime and correct peak shape.

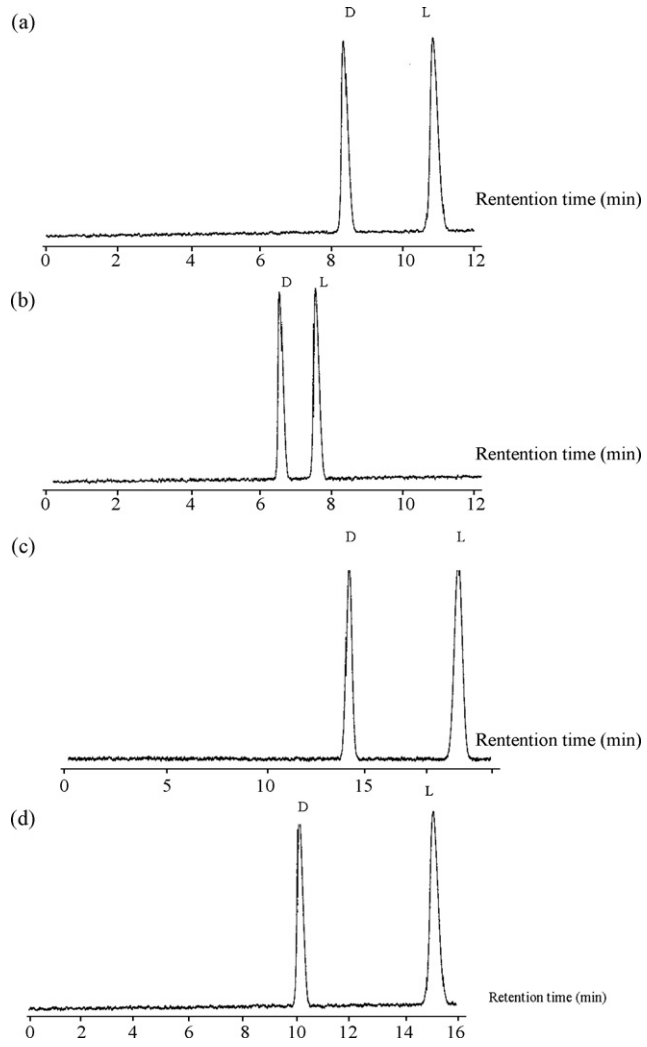

Fig. 2. Chromatographic enantioseparation of (a) dan-nor; (b) dan-tryp; (c) flu; (d) nap. Mobile phase: phosphate buffer (M/15) (pH 5.6); flow rate 1 mL/min; $T = 25\,^{\circ}C$.

4. Conclusion

This newly developed chiral stationary phase was successfully used for enantioseparations combining the chiral recognition properties of the cyclic hexapeptide molecule and the unique properties concerning the flow behaviour of silica monoliths. This work demonstrated that this CS monolithic column can operate at high flow rate without a significant loss of enantioselectivity. Consequently, faster enantioseparations can be achieved making the prepared supports of interest for high-throughput separations.

References

[1] C. Andre, M. Thomassin, A. Umrayami, L. Ismaili, B. Refouvelet, Y.C. Guillaume, Talanta 71 (2007) 1817.

[2] F. Gasparrini, D. Misiti, W. Still, C. Villani, H. Vennemers, J. Org. Chem. 62 (1997) 8221.
[3] (a) W.H. Pirkle, T.C. Pachapsky, J. Am. Chem. Soc. 108 (1986) 352;
(b) W.H. Pirkle, J.M. Finn, J. Org. Chem. 46 (1981) 2936.
[4] D.S. Hage, J. Chromatogr. 3 (2002) 768.
[5] T. Fornstedt, G. Gotmar, M. Andersson, G. Guiochon, J. Am. Chem. Soc. 121 (1999) 1164.
[6] S.C. Jacobson, S. Golshan-Shirazi, G. Guiochon, J. Am. Chem. Soc. 112 (1990) 6492.
[7] J. Hermansson, J. Chromatogr. 325 (1985) 379.
[8] M. Hilton, D.W. Armstrong, J. Liq. Chromatogr. 14 (1991) 3673.
[9] G. Dotsevi, Y. Sogaah, D.J. Gram, J. Am. Chem. Soc. 97 (1975) 1259.
[10] T. Kubota, C. Yamamoto, Y. Okamoto, J. Am. Chem. Soc. 122 (2000) 4056.
[11] K.B. Lipkowitz, G. Pearl, B. Coner, M.A. Peterson, J. Am. Chem. Soc. 119 (1997) 600.
[12] A. Berthod, S.C. Chang, D.W. Armstrong, Anal. Chem. 64 (1992) 395.
[13] A. Peter, G. Torok, D.W. Armstrong, G. Toth, D. Tourvé, J. Chromatogr. A 828 (1998) 177.
[14] D.W. Armstrong, Y. Liu, K.H. Ekborg-Ott, Chirality 7 (1995) 474.
[15] D.W. Armstrong, S. Chen, Y. Zhou, C. Bagwill, J.R. Chen, Anal. Chem. 66 (1994) 1473.

Talanta 76 (2008) 1159–1164

Contents lists available at ScienceDirect

Talanta

journal homepage: www.elsevier.com/locate/talanta

Activity of lactoperoxidase when adsorbed on protein layers

Karolina Haberska[a,b,*], Olof Svensson[a], Sergey Shleev[a], Liselott Lindh[c], Thomas Arnebrant[a], Tautgirdas Ruzgas[a]

[a] Biomedical Laboratory Science and Technology, Faculty of Health and Society, Malmö University, SE-205 06 Malmö, Sweden
[b] Department of Analytical Chemistry, Lund University, P.O. Box 124, SE-221 00 Lund, Sweden
[c] Prosthetic Dentistry, Faculty of Odontology, Malmö University, SE-205 06 Malmö, Sweden

ARTICLE INFO

Article history:
Received 17 January 2008
Received in revised form 8 May 2008
Accepted 14 May 2008
Available online 21 May 2008

Keywords:
Lactoperoxidase
BSM
BSA
MUC5B
Ellipsometry
Gold electrode

ABSTRACT

Lactoperoxidase (LPO) is an enzyme, which is used as an antimicrobial agent in a number of applications, e.g., food technology. In the majority of applications LPO is added to a homogeneous product phase or immobilised on product surface. In the latter case, however, the measurements of LPO activity are seldom reported. In this paper we have assessed LPO enzymatic activity on bare and protein modified gold surfaces by means of electrochemistry. It was found that LPO rapidly adsorbs to bare gold surfaces resulting in an amount of LPO adsorbed of 2.9 mg/m^2. A lower amount of adsorbed LPO is obtained if the gold surface is exposed to bovine serum albumin, bovine or human mucin prior to LPO adsorption. The enzymatic activity of the adsorbed enzyme is in general preserved at the experimental conditions and varies only moderately when comparing bare gold and gold surface pretreated with the selected proteins. The measurement of LPO specific activity, however, indicate that it is about 1.5 times higher if LPO is adsorbed on gold surfaces containing a small amount of preadsorbed mucin in comparison to the LPO directly adsorbed on bare gold.

1. Introduction

Lactoperoxidase (LPO) is an enzyme, which has been recognised as one of the innate antimicrobial proteins in addition to lectins, lysozyme, lactoferrin and secretory peroxidases. LPO from bovine milk is a medium size heme-containing protein comprising a single polypeptide chain of 612 amino acids. The molecular mass of the enzyme ranges from 74.5 to 79.2 kDa depending on the degree of glycosylation, which might span from 6.4 to 11.5% of the total mass [1]. At neutral pH LPO is positively charged due to a p*I* ranging from 8.5 to 9.3. The catalytic reaction of LPO can be described by conventional peroxidase reaction Eqs. (1–3), where Compound-I and Compound-II are two- and one-electron oxidised forms of LPO, respectively. AH* represents a one-electron oxidised reducing agent. The catalytic mechanism of the enzyme is, however, much more complicated. LPO shows, e.g., catalase activity [2]. One of the not well-understood phenomena is the relatively low stability of LPO already at low (μM) concentrations of peroxide, whereas the enzyme has been found to be structurally stable at room temperatures [3].

$$\text{LPO}(\text{Fe}^{3+}) + \text{H}_2\text{O}_2 \rightarrow \text{Compound-I} + \text{H}_2\text{O} \quad (1)$$

$$\text{Compound-I} + \text{AH}_2 \rightarrow \text{Compound-II} + \text{AH}^* \quad (2)$$

$$\text{Compound-II} + \text{AH}_2 \rightarrow \text{LPO}(\text{Fe}^{3+}) + \text{AH}^* + \text{H}_2\text{O} \quad (3)$$

Despite the relatively low stability of LPO, the enzyme is of high interest for its involvement in the mammalian defence system. The basic antimicrobial principle of action is due to LPO assisted generation of halogens (e.g., I_2) and pseudohalogens (e.g., $(SCN)_2$), which react with and inactivate the proteins of bacterial cells. The bacteriostatic or bactericidal effects of LPO-H_2O_2-SCN^- and LPO-H_2O_2-I^-, respectively, have been demonstrated [4]. Following the current understanding of how LPO acts as antimicrobial agent a number of LPO applications have been proposed in biotechnology, food technology and biomedical technology (e.g., oral hygiene products and salivary substitutes) [5,6]. The majority of the applications rely on the addition of LPO to a homogeneous product phase or immobilisation of LPO on the surface, e.g., of a packaging material [7] or dental (titanium) implants [8]. The development of new methods on how LPO could be introduced into different products is continuously evaluated; one of the recently demonstrated examples describes a possibility of a multilayer assembly of LPO

Abbreviations: LPO, lactoperoxidase; BSM, bovine submaxillary mucin; BSA, albumin bovine serum; MUC5B, human salivary high molecular weight mucin; ABTS, 2,2-azinobis-(3-ethylbenzthiazoline-6-sulfonate).

* Corresponding author at: Biomedical Laboratory Science and Technology, Faculty of Health and Society, Malmö University, SE-205 06 Malmö, Sweden.
Tel.: +46 76 828 3664; fax: +46 46 222 4544.
E-mail address: karolina.haberska@mah.se (K. Haberska).

0039-9140/$ – see front matter © 2008 Elsevier B.V. All rights reserved.
doi:10.1016/j.talanta.2008.05.017

in combination with other proteins using layer-by-layer deposition [9]. In this and other applications, where LPO is adsorbed on a surface, the measurements of the enzymatic activity would be of the high interest. Within the present article we describe electrochemical LPO-activity measurements on gold surfaces. The ability of the enzyme to oxidise phenolic compounds, specifically catechol, is exploited for the enzyme activity measurements. The activity of LPO adsorbed on gold is compared to LPO co-adsorbed with other proteins.

2. Experimental

2.1. Chemicals

Na_2HPO_4, NaH_2PO_4, $CaCl_2$, NaCl, H_2O_2, H_2SO_4, $K_4[Fe(CN)_6]$, 2,2-azinobis-(3-ethylbenzthiazoline-6-sulfonate) (ABTS), catechol, hydroquinone, phenol, *p*-cresol, and hexaammineruthenium(II) chloride of analytical or higher grade were obtained from Sigma–Aldrich Sweden AB (Stockholm, Sweden). Deionized water (18 MΩ) used for preparation of all solutions was purified with a PURELAB™ UHQ system (ELGA LabWater, UK).

2.2. Proteins

Bovine lactoperoxidase (LPO) (L8257, from bovine milk), bovine mucin (BSM) (M3895, from bovine submaxillary glands, Type I-S), and bovine albumin (BSA) (A8531, from bovine serum) were purchased from Sigma–Aldrich. Human salivary high molecular weight mucin (MUC5B) was purified from collected saliva according to Wickstrom et al. [10] and dialyzed using a Spectra/Por® Dialysis Membrane, MWCO: 6–8000 from Spectrum Europe (Breda, The Netherlands) according to Lindh et al. [11]. All protein solutions were prepared freshly before each experiment.

The specific activity of lactoperoxidase in homogeneous solutions towards different substrates was determined spectrophotometrically in 10 mM phosphate buffer, pH 7.0 containing 100 mM NaCl using a Ultrospec II Biochrom "LKB" (Bromma, Sweden) spectrophotometer. The absorbance change at different wavelengths was measured at 25 °C for 60 s, *viz.* ABTS ($\lambda = 420$ nm, $\varepsilon = 36000\ M^{-1}\ cm^{-1}$) and $K_4[Fe(CN)_6]$ ($\lambda = 420$ nm, $\varepsilon = 1040\ M^{-1}\ cm^{-1}$). One unit of activity is defined as the amount of lactoperoxidase oxidising 1 μmol of substrate per min at room temperature (approximately 21 °C). Specific activities are expressed as units of activity per mg of protein.

2.3. Gold surfaces

The gold substrates were manufactured in a Balzers UMS 500 P system by electron-beam deposition of 2000 Å of gold onto silicon (1 0 0) wafers, precoated with a 25-Å-thick titanium adhesion layer (Laboratory of Applied Physics, Linköping University, Sweden). Prior to each experiment the gold surface was cleaned electrochemically in 0.5 M H_2SO_4 by means of cyclic voltammetry.

2.4. Ellipsometry measurements

The adsorption of proteins on to gold surfaces was studied with *in situ* ellipsometry using a Rudolph thin film automated ellipsometer (type 43063-200E, Rudolph Research, Fairfield, NJ, USA) equipped with a xenon lamp. With a fixed angle of incidence (67.8°) the light was detected at 442.9 nm employing an interference filter with ultraviolet and infrared blocking (Melles Griot, Netherlands). The gold surface was vertically mounted into a glass trapezoid cuvette (Hellma, Germany) containing 5 mL of solution, which was thermostated at 25 °C and stirred using magnetic stirrer with rotation speed of 325 rotations per minute. In order to determine the refractive index of the surface, prior to each measurement, a two-zone surface characterization in buffer solution was carried out. After a stable baseline was acquired, protein stock solutions were added to the cuvette containing 10 mM phosphate buffer with 100 mM NaCl and 1 mM $CaCl_2$, pH 7.0 and formation of the adsorbed protein film was monitored. In the case of LPO the adsorption was carried out for 60 min from a 10 μg/mL enzyme solution, which corresponds to the concentration presents in human saliva [4]. Combined protein layers with lactoperoxidase were realised by 60 min preadsorption from solutions containing 50 μg/mL of BSM, BSA or MUC5B, respectively. In addition, a lower concentration of MUC5B (0.5 μg/mL) was also investigated. Each protein adsorption was followed by 5 min cuvette rinsing with phosphate buffer at a continuous flow of 18 mL/min and monitoring for 15 min before the LPO addition. After LPO adsorption the cuvette was rinsed for 5 min and monitored for 30 min. From ellipsometric data the thickness and the adsorbed amount was calculated using the value of 0.18 mL/g [12] as a refractive index increment (dn/dc) with protein concentration. All ellipsometry experiments were performed at least in duplicate.

2.5. Electrochemical studies

2.5.1. Cyclic voltammetry

Electrochemical cleaning of the gold surfaces was carried out in 0.5 M H_2SO_4 by means of cyclic voltammetry, i.e., by sweeping the applied potential between 0 and 1.9 V *vs.* NHE with scan rate of 100 mV/s for 30 min. A three-electrode potentiostat (AMEL Instruments, Model 2059, Milano, Italy) with a SCE as a reference and platinum as a auxiliary electrode was used. An electroactive area of gold electrodes was determined electrochemically *via* analysis of the current peak that was due to the electrochemical reduction of surface bound gold oxide. The method is based on the assumption that a monolayer of oxygen is chemisorbed onto the gold film in a relation of 1:1 with the surface gold atoms. Thus integration of the area of the reduction peak from a current–potential plot provided the charge passed during the gold oxide reduction. The value was related to the theoretical value (390 ± 10 μC) required for the coverage of 1 cm^2 of polycrystalline gold with oxide film [13].

2.5.2. Amperometry

In all experiments, a one-compartment electrochemical cell (volume of 10 mL) was used. The equilibrium current values were registered under aerobic conditions at room temperature. A two-electrode system with the enzyme-modified electrode as a working electrode and a silver wire as a combined reference and counter electrode was connected to a potentiostat (ZPta Elektronik, Höör, Sweden). The current responses were recorded on a strip chart recorder (Kipp & Zonen, Delft, The Netherlands). The applied potential was −50 mV in the supporting electrolyte: 10 mM phosphate buffer, pH 7.0 with 100 mM NaCl and 1 mM $CaCl_2$. The error bars presented on figures correspond to the highest and the lowest measured values, whereas each data point represents the average of three independent measurements.

3. Results and discussion

3.1. Adsorption of lactoperoxidase on bare gold surfaces

Previous investigations on lactoperoxidase adsorption on hydrophilic and hydrophobic silica have shown very high LPO surface affinity and formation of a monolayer at low (0.5 μg/mL) enzyme concentrations [14]. Higher adsorbed masses, up to

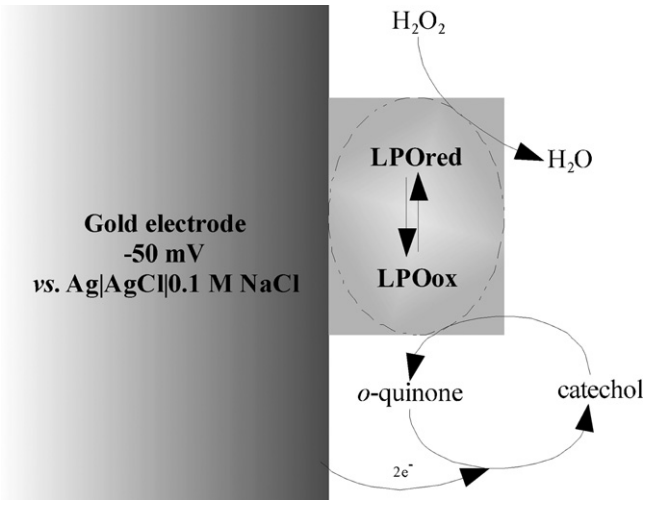

Fig. 1. Schematic representation of electroreduction of LPO-produced *o*-quinone at a gold electrode.

3.2 mg/m^2 of LPO depending on enzyme concentration in solution, were obtained on hydrophilic surfaces [15]. One problem with silica surfaces is that it is difficult to measure the activity of the adsorbed enzyme, which is of obvious importance for the development of antimicrobial surfaces. In this work LPO adsorption was studied on gold substrates which due to the electrical conductivity provide possibilities to measure the activity of surface bound LPO by electrochemical means, as illustrated by Fig. 1 (described in Section 3.3), based on our earlier electrochemical studies of peroxidases [16,17].

LPO is an asymmetric, oval molecule of dimensions 55 Å × 81 Å × 78 Å and a partial specific volume of 0.721 mL/g [14]. Keeping in mind these geometric characteristics of the enzyme Mårtensson et al. [14] have proposed two models for molecular organization of LPO on hydrophilic and hydrophobic silicon dioxide surfaces, i.e., "side-on" and "end-on" orientation. An average thickness of 33 Å of a lactoperoxidase layer on gold was estimated from our ellipsometric measurements, Fig. 2. The final value of the adsorbed amount of 2.9 mg/m^2 corresponds to 4466 Å^2 per LPO molecule, which is practically the same as the area occupied by the "end-on" adsorbed enzyme molecule, 55 Å × 81 Å = 4455 Å^2. Data in Fig. 2 show that adsorption of LPO on gold is a rapid process and is finished within 10–15 min. The apparent lack of adsorption reversibility and very small desorption of the protein from the surface can also be observed, Fig. 2.

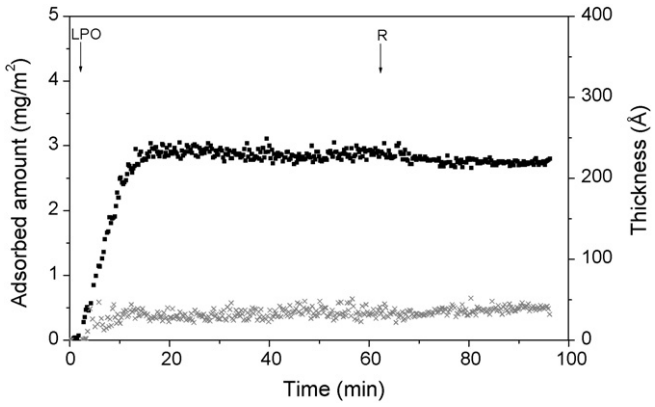

Fig. 2. Adsorbed amount (■) and thickness (×) versus time of adsorption of LPO on a gold electrode surface. Arrows indicate protein addition or rinsing with phosphate buffer (R).

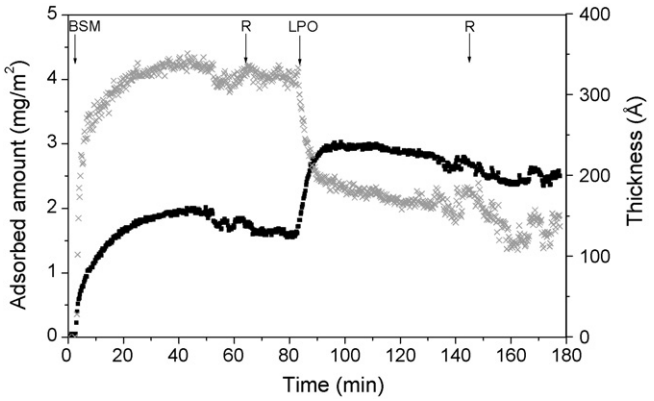

Fig. 3. Adsorbed amount (■) and thickness (×) versus time of adsorption for sequential adsorption of BSM and LPO on a gold electrode surface. Arrows indicate protein addition or rinsing with phosphate buffer (R).

3.2. LPO adsorption on gold surface with other pre-adsorbed proteins

The gold surface was modified with other proteins (BSM, BSA or MUC5B) and the subsequent adsorption of lactoperoxidase was studied. The most important question was to understand if the BSM-LPO, BSA-LPO, or MUC5B-LPO layers will show substantial differences in the specific activity or stability of the peroxidase as compared to LPO adsorbed directly on gold.

3.2.1. LPO adsorption on Au-BSM surface

Bovine mucin from the submaxillary glands exhibits structural properties similar to some salivary mucins, e.g., MUC7 (MG2). It is known that from synergistic interactions BSM can form complexes with other proteins [18,19]. Castillo et al. [20] have proposed the three-layer model for the *in vitro* bovine mucin adsorption on the surface of a contact lens with the top layer consisting of BSM gel layers capable of desorption. The proposed model confirmed previous *in situ* studies on the adsorption of BSM at solid/liquid interfaces showing the presence of a loosely bound mucin layer in addition to irreversibly bound BSM [21]. In general, a surface bound BSM layer is considered to be much softer than a rigid layer of surface bound BSA [19].

In the present investigation it has been observed, that after BSM adsorption on gold, the amount as well as the thickness of adsorbed bovine mucin decreased slightly with time (Fig. 3.), achieving an approximate surface concentration of 1.6 mg/m^2 after rinsing with phosphate buffer. The decrease of initially adsorbed amount of BSM probably indicates that the thick layer of BSM is composed of both strongly and weakly bound glycoprotein molecules where the latter are removed upon protein rearrangement at the surface. Subsequent addition of lactoperoxidase to the mucin layer resulted in an increase in the total adsorbed amount on the gold surface. However, LPO adsorption simultaneously leads to a reduction of the thickness of the film. A noticeable compaction of the protein bi-layer may be expected by the incorporation of LPO molecules into the mucin layer. Similar compaction behaviour of a surface bound BSM layer was previously observed upon subsequent addition of BSA [19] or chitosan [22]. The adsorption conditions might be of high importance in determining the interactions between biopolymers at surfaces since a swelling of an adsorbed BSM layer upon subsequent adsorption of chitosan has been also reported [23,24]. The structural changes of the BSM layer upon LPO adsorption might be a consequence of electrostatic interactions between the oppositely charged bovine mucin and the bovine LPO.

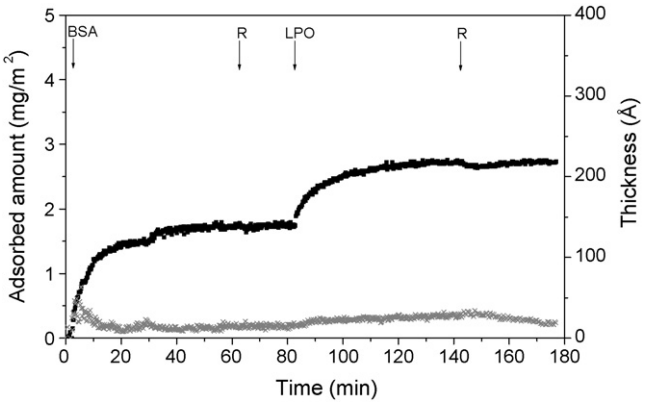

Fig. 4. Adsorbed amount (■) and thickness (×) for sequential adsorption of BSA and LPO on a gold electrode surface. Arrows indicate protein addition or rinsing with phosphate buffer (R).

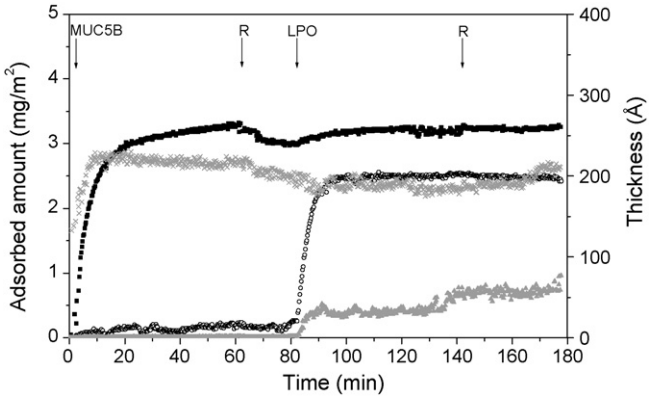

Fig. 5. Comparison of the adsorption behaviour upon sequential adsorption of human mucin (MUC5B) and LPO on gold surfaces at two (■, ×: 50 μg/mL and ○, ▲ : 0.5 μg/mL) concentrations of MUC5B (adsorbed amount (■, ○) and thickness (×, ▲) versus time). Arrows indicate protein addition or rinsing with phosphate buffer (R).

3.2.2. LPO adsorption on Au-BSA surface

Bovine serum albumin was used as a control as it is used in surface preparations or as a "blocking agent" in ELISA methods or biosensor applications. Earlier studies of the adsorption of BSA on gold and stainless steel have shown that albumin adsorbs strongly on metals [25]. The adsorption profile of BSA on the gold surface and sequential LPO adsorption is presented in Fig. 4. A thin albumin layer remained on the surface despite buffer rinsing and an increase of adsorbed amount and of the film thickness was observed after LPO adsorption. A substantial difference between LPO adsorption on Au-BSA (Fig. 4) can be seen compared to LPO adsorption on Au-BSM surfaces (Fig. 3).

3.2.3. LPO adsorption on Au-MUC5B surface

Iontcheva et al. [26] have shown that human salivary mucin MG1 (MUC5B) selectively forms hetero-complexes with amylase, proline-rich proteins, statherin, and histatins. Further molecular mapping of statherin- and histatin-binding domains in human salivary mucin MG1 by the yeast two-hybrid system has been studied [27]. Wickstrom et al. [28] demonstrated macromolecular organization of saliva and identification of "insoluble" MUC5B assemblies and non-mucin proteins in the gel phase. It has earlier been reported that MUC5B and lactoperoxidase can be used to build multilayers on hydrophobic and hydrophilic silica surfaces [9]. In our studies human salivary mucin (MUC5B) adsorption on a gold surface has been investigated (Fig. 5). Two different mucin concentrations in the reaction solution: 50 μg/mL and 0.5 μg/mL have been tested. For the higher MUC5B concentration, amounts adsorbed of over 3 mg/m^2 have been obtained, which can be compared to 2.5 mg/m^2 previously observed at hydrophobized silica [11]. However, a small decrease in this value and in layer thickness can be seen after buffer rinsing. Sequential addition of LPO did not significantly change the ellipsometric parameters of the film indicating no or minor LPO adsorption. Therefore, adsorption from a 100 times lower concentration of MUC5B solution was used to modify the gold surface. A much lower MUC5B adsorption was observed, which was followed by the highest adsorbed amount of LPO recorded in the present study, in fact the amount of LPO adsorbed is close to the value recorded for pure gold which might be expected due to the small amounts of MUC5B adsorbed.

3.3. Activity measurements of immobilised lactoperoxidase

The enzymatic activity of surface bound LPO was evaluated from measurements of the current generated by electrochemical reduction of the enzymatically oxidised electron donor as shown in Fig. 1. The feasibility of current measurements has been tested with electron donors (called electron transfer mediators) such as ABTS, $K_4[Fe(CN)_6]$, hydroquinone, phenol, *p*-cresol, hexaaminеruthenium(II) chloride, and catechol. The highest current response has been achieved with catechol. Therefore the activity of LPO adsorbed on various surfaces was monitored electrochemically using catechol. From Fig. 6 significant differences in current responses (presented as current densities) can be observed at different electrodes. The current response varied between 0.2 and 5.5 μA/cm^2, being the highest from LPO adsorbed on gold, modified with a low amount of MUC5B. The current response is proportional to the activity of the enzyme and to the amount of the adsorbed enzyme (Table 1). Since the amount of the enzyme can be estimated from ellipsometric measurements, the specific activity of LPO on different surfaces was calculated.

The fact, that the current densities (Fig. 6) are about one order of magnitude below what could be expected from diffusion-controlled currents, allows us to consider the responses as being kinetically limited. Thus, electrochemical current measurements can be used to estimate the specific activity of adsorbed LPO accord-

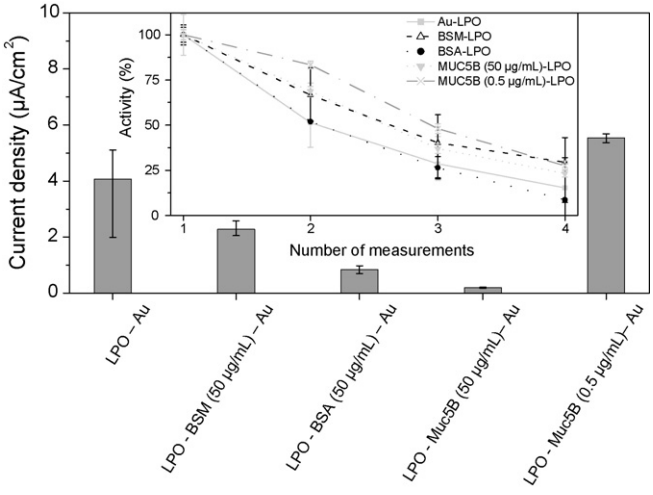

Fig. 6. Current density of LPO adsorbed on bare gold and gold with preadsorbed proteins immediately after ellipsometric measurements; 10 mM phosphate buffer, pH 7.0, 100 mM NaCl, 1 mM $CaCl_2$, 0.1 mM catechol, applied potential: −50 mV *vs.* Ag|AgCl|0.1 M NaCl. Insert: operation stability of LPO adsorbed on bare gold and on protein-modified gold electrodes for four subsequent activity measurements.

Table 1
Adsorbed amounts of LPO on bare gold and on gold with preadsorbed protein layers after buffer rinsing

Surface	Concentration of the surface modifier in the stock solution (μg/mL)	Adsorbed amount of LPO (mg/m^2)
Au	0	2.93 ± 0.24
Au-BSM	50.0	1.01 ± 0.17
Au-BSA	50.0	0.74 ± 0.24
Au-MUC5B	50.0	0.22 ± 0.15
Au-MUC5B	0.5	2.41 ± 0.22

Note: LPO concentration in the stock solution used for surface modification was 10.0 μg/mL.

ing to a simple equation (Eq. (4)):

$$\text{LPO activity (U/mg)} = \frac{\text{Current density } (\mu\text{A/cm}^2) \times 60\ \text{s}}{\text{Amount of LPO } (\text{mg/cm}^2) \times n \times F} \quad (4)$$

where $n = 2$ is a number of electrons by which catechol is enzymatically oxidised, F is the Faraday constant. In Fig. 7 the estimates for the specific activities of LPO are shown for all surfaces studied. It can be seen that the specific activity varied from 2.7 up to 7.9 U/mg. The simple conclusion that can be made is that the specific activity of the enzyme is relatively well preserved on all surfaces, i.e., varies less than a factor of three. The highest estimated specific LPO activity was found on gold surfaces pretreated with BSM or low amounts of MUC5B. It is important to note that at these surfaces the specific activity is higher than that found for LPO adsorbed on bare surfaces. The specific activities estimated on gold electrodes pretreated with BSA and high concentrations of MUC5B were the lowest. It is not straightforward to interpret these results. One should keep in mind that the amounts of adsorbed LPO used in the estimation of the specific activity are subject to some uncertainty. First, we might expect that some of the initially adsorbed protein, i.e., BSA, BSM or MUC5B, could be exchanged by LPO. Not accounting for this would lead to an overestimation of the specific enzymatic activity rather than an underestimation. Second, the amounts were based on assumption of the same dn/dc for all proteins. For example, the dn/dc for mucin has been reported to 0.16 mL/g [9], resulting in a possible underestimation of the amount of mucin of about 10% but provided that no exchange takes place this does not affect the activity data. In the case of MUC5B adsorption at the low concentration (0.5 μg/mL), however, the small amount of adsorbed (exchangeable) MUC5B will make the possible error small.

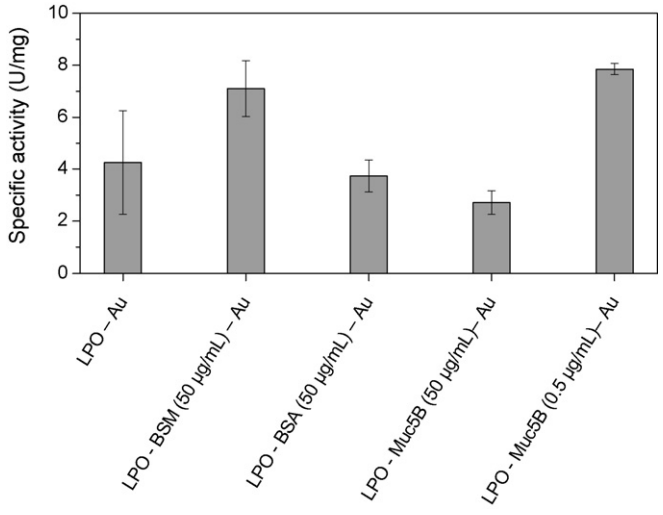

Fig. 7. Specific activity of LPO adsorbed on bare gold and on protein-modified gold electrodes.

In summary, the specific activities of bovine LPO on bare Au and protein modified Au surfaces are comparable (Fig. 7). The stability of adsorbed LPO was found to be almost independent of surface modification (Fig. 6, insert) and relatively poor as such. On average about 25% of the activity is lost after each electrochemical enzyme activity assay.

4. Conclusions

In this paper we demonstrate that LPO adsorbs on bare gold and gold surfaces pre-treated with other proteins such as BSA, BSM and MUC5B. The amount of adsorbed LPO on gold is close to a monolayer. LPO adsorption on a BSM layer imposes substantial compaction of the protein bi-layer indicating strong (possibly electrostatic) interactions between LPO and bovine BSM or substantial exchange of BSM by LPO.

Specific activities of LPO on different surfaces were determined using hydrogen peroxide as oxidant and catechol as electron donor. On all surfaces studied the specific activity was found to be in the range of 2.7–7.9 U/mg. The LPO activity was about 1.5 times higher on gold surfaces carrying a small amount of preadsorbed human mucin (MUC5B) in comparison to LPO directly adsorbed on bare gold. The observed activity variations are too low to prove any beneficial interaction between LPO and studied salivary proteins in terms of lactoperoxidase activity or stability.

Acknowledgements

The work was financially supported by Marie Curie "BIONEL" project (ref. no.: 373–4515/2004), the Knowledge Foundation (KK-stiftelsen, Biofilms—Research Centre for Biointerfaces), and Malmö University.

References

[1] S.M. Wolf, R.P. Ferrari, S. Traversa, K. Biemann, J. Mass Spectrom. 35 (2000) 210.
[2] E. Ghibaudi, E. Laurenti, Eur. J. Biochem. 270 (2003) 4403.
[3] B. Boscolo, S.S. Leal, E.M. Ghibaudi, C.M. Gomes, Biochim. Biophys. Acta: Proteins Proteom. 1774 (2007) 1164.
[4] K.M. Pruitt, J.O. Tenovuo, The Lactoperoxidase System: Chemistry and Biological Significance., in: Immunology Series, vol. 27, 1985.
[5] E. Seifu, E.M. Buys, E.F. Donkin, Trends Food Sci. Technol. 16 (2005) 137.
[6] J.W. Boots, R. Floris, Int. Dairy J. 16 (2006) 1272.
[7] R.D. Joerger, Pack. Technol. Sci. 20 (2007) 231.
[8] M. Ahariz, J. Mouhyi, P. Louette, J. Van Reck, C. Malevez, P. Courtois, J. Biomed. Mater. Res. 52 (2000) 567.
[9] L. Lindh, I.E. Svendsen, O. Svensson, M. Cardenas, T. Arnebrant, J. Colloid Interface Sci. 310 (2007) 74.
[10] C. Wickstrom, J.R. Davies, G.V. Eriksen, E.C.I. Veerman, I. Carlstedt, Biochem. J. 334 (1998) 685.
[11] L. Lindh, P.-O. Glantz, I. Carlstedt, C. Wickstrom, T. Arnebrant, Colloids Surf. B 25 (2002) 139.
[12] J.A. De Feijter, J. Benjamins, F.A. Veer, Biopolymers 17 (1978) 1759.
[13] S. Trasatti, O.A. Petrii, Pure Appl. Chem. 63 (1991) 711.
[14] J. Mårtensson, H. Arwin, I. Lundström, T. Ericson, J. Colloid Interface Sci. 155 (1993) 30.
[15] I.E. Svendsen, L. Lindh, T. Arnebrant, Colloids Surf. B 53 (2006) 157.
[16] T. Ruzgas, L. Gorton, J. Emneus, G. Markovarga, J. Electroanal. Chem. 391 (1995) 41.
[17] L. Gorton, A. Lindgren, T. Larsson, F.D. Munteanu, T. Ruzgas, I. Gazaryan, Anal. Chim. Acta 400 (1999) 91.
[18] W.-K. Park, J.-W. Chung, Y.-K. Kim, S.-C. Chung, H.-S. Kho, Arch. Oral Biol. 51 (2006) 861.
[19] A.A. Feiler, A. Sahlholm, T. Sandberg, K.D. Caldwell, J. Colloid Interface Sci. 315 (2007) 475.
[20] E.J. Castillo, J.L. Koenig, J.M. Anderson, N. Jentoft, Biomaterials 7 (1986) 9.
[21] J.E. Proust, A. Baszkin, E. Perez, M.M. Boissonnade, Colloids Surf. 10 (1984) 43.
[22] A. Dedinaite, M. Lundin, L. Macakova, T. Auletta, Langmuir 21 (2005) 9502.

[23] O. Svensson, L. Lindh, M. Cardenas, T. Arnebrant, J. Colloid Interface Sci. 299 (2006) 608.
[24] O. Svensson, Interaction of mucins with biopolymers and drug delivery particles, Health and Society Dissertations, 2008, Malmö University, Malmö.
[25] D. Beaglehole, B. Webster, S. Werner, J. Colloid Interface Sci. 202 (1998) 541.
[26] I. Iontcheva, F.G. Oppenheim, R.F. Troxler, J. Dent. Res. 76 (1997) 734.
[27] I. Iontcheva, F.G. Oppenheim, G.D. Offner, R.F. Troxler, J. Dent. Res. 79 (2000) 732.
[28] C. Wickstrom, C. Christersson, J.R. Davies, I. Carlstedt, Biochem. J. 351 (2000) 421.

Talanta 76 (2008) 1256–1260

Contents lists available at ScienceDirect

Talanta

journal homepage: www.elsevier.com/locate/talanta

Short communication

Synthesis of chitosan-based resins modified with tris(2-aminoethyl)amine moiety and its application to collection/concentration and determination of trace mercury by inductively coupled plasma atomic emission spectrometry

Lukman Hakim, Akhmad Sabarudin, Koji Oshita, Mitsuko Oshima, Shoji Motomizu*

Department of Chemistry, Faculty of Science, Okayama University, 3-1-1 Tsushimanaka, Okayama 700-8530, Japan

ARTICLE INFO

Article history:
Received 7 April 2008
Received in revised form 7 May 2008
Accepted 7 May 2008
Available online 23 May 2008

Keywords:
Resin
Chitosan
Tris(2-aminoethyl)amine moiety
Mercury
On-line pretreatment
Computer control
Inductively coupled plasma-atomic emission spectrometry

ABSTRACT

A novel chitosan-based chelating resin modified with tris(2-aminoethyl)amine moiety (CCTS-TAA) was synthesized, and its characteristics in the collection/concentration of mercury was examined. The synthesized resin showed good adsorption toward mercury in a wide pH range, and the adsorbed mercury can be easily eluted by using 2 M HNO_3 without any addition of complexing agent. The resin was then packed in a mini-column and the mini-column was installed on a computer-controlled automated-pretreatment (Auto-Pret) system coupled with inductively coupled plasma-atomic emission spectroscopy (ICP-AES) for on-line mercury collection and determination at trace level.

1. Introduction

Mercury (Hg) is one of the most toxic heavy metals commonly found in the global environment layer [1]. Mercury represents a serious environmental problem because it is widely used in many industries to produce various kinds of products [2]. The toxicity of mercury even at very low levels has led to its stringent control with a maximum contaminant level of 2 ng mL^{-1}, which has been set by the US Environmental Protection Agency [3]. This regulated value is even lower in Japan, as it was set to 0.5 ng mL^{-1} by Japan Ministry of Environment [4]. The regulated value and the concentration of mercury in natural waters are very low; hence, powerful techniques to monitor mercury in natural water are required. In order to achieve accurate, reliable and sensitive results, the separation and preconcentration step for mercury is necessary prior to its measurement.

In recent years, solid phase extraction (SPE) method has received considerable interest for the enrichment of metal ions for their accurate determination at trace levels. The importance of separation and concentration technique involving chelating sorbent in trace analysis has risen substantially because it can increase analyte concentration to a detectable level, while at the same time it can eliminate matrix effects [5].

In general, mercury ion interacts strongly with ligands containing nitrogen and sulfur atoms [6]. Several sorbent containing nitrogen and/or sulfur ligands have been proposed for mercury enrichment [7–11]. Tris(3-aminoethyl)amine, which possesses several amine groups, was expected to have a potential to form chelate with mercury ion.

Recently, much attention has been paid to the adsorption of metal ions on various kinds of biomass. Among those biomass, chitosan has been proved to be an extremely promising material due to its high chelating ability, higher hydrophilicity, environmentally safe, and abundant base material. Chitosan also has been proposed as biopolymers for mercury removal [12–14]. However, the application of chitosan to Hg determination has been hardly reported.

Although the sample pretreatment with solid phase extraction method has a potential to improve the sensitivity of trace metals analysis, the operation of the pretreatment procedures may become tedious and time-consuming if it is carried out in a manual batch-wise procedure where stringent control of the laboratory environment is required to avoid sample contamination, especially when the determination of trace levels of analytes is attempted. Such drawback can be overcome by utilizing an automated

* Corresponding author. Tel.: +81 86 251 7846; fax: +81 86 251 7846.
E-mail address: motomizu@cc.okayama-u.ac.jp (S. Motomizu).

0039-9140/$ – see front matter © 2008 Elsevier B.V. All rights reserved.
doi:10.1016/j.talanta.2008.05.025

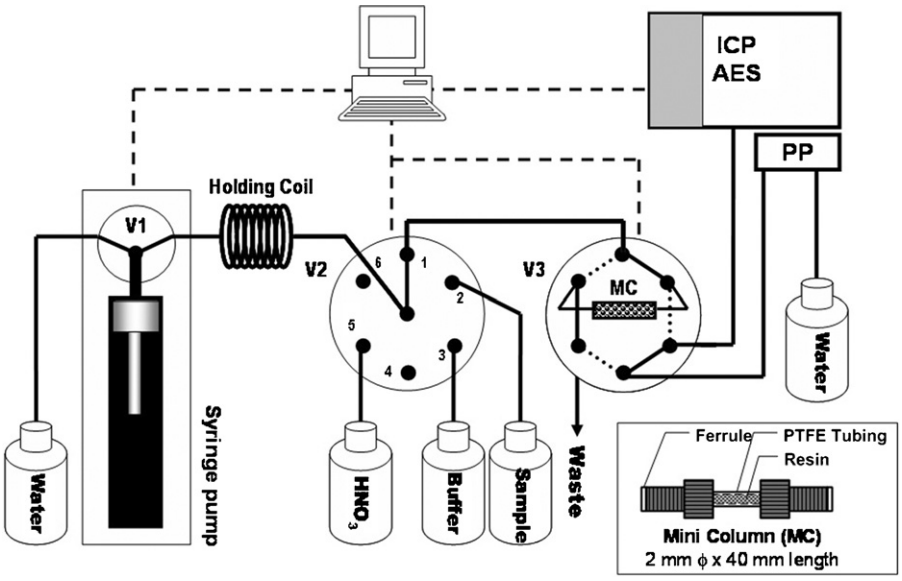

Fig. 1. Manifold of Auto-Pret AES System. MC: mini-column; PP: ICP-AES peristaltic pump; V1: syringe valve; V2: 6-ports selection valve; V3: 6-way switching valve. Solid-line shows the load (pretreatment) position, and dotted-line shows inject (elution) position.

on-line preconcentration procedure, where less contamination, less reagent consumption, and less waste-generation can be achieved [15–21].

In this work, the cross-linked chitosan (CCTS) functionalized with tris(2-aminoethyl)amine (TAA) moiety was synthesized to improve chitosan capability and selectivity for Hg adsorption from aqueous solution. The potential of the synthesized resin to be applied to Hg determination was also demonstrated. This work was a fundamental study and dedicated to explore the potential of the synthesized resin to concentrate inorganic Hg(II) as well as the possibility of this resin to be utilized in an automated-pretreatment system (Auto-Pret) prior to its application to determine mercury in environmental samples.

2. Experimental

2.1. Instruments

An inductively coupled plasma mass spectrometer (ICP-MS) SPQ8000H System Seiko Instruments (Chiba, Japan) was used for investigating the adsorption behavior of various elements on CCTS-TAA. Infrared spectra (4000–400 cm^{-1}) were recorded by using Jasco FT/IR-4100 Jasco International Co. Ltd. (Tokyo, Japan) for characterization of the synthesized-resin. A modular digital syringe pump Cavro (San Jose, CA, USA), a selection valve and a switching valve Hamilton (Reno, NV, USA) were used as a part of Auto-Pret system. This Auto-Pret system was coupled with ICP-AES Vistapro Seiko Instruments (Chiba, Japan) to demonstrate the potential of the synthesized resin to be applied to the determination of mercury in aqueous solution.

2.2. Reagents

Chitosan, flake type with 80% deacetylation degree, and tris(2-aminoethyl)amine were purchased from Tokyo Kasei Co. Ltd. (Tokyo, Japan). All other reagents used for the synthesis of CCTS-TAA were of analytical reagent grade.

Multi-element standard solutions were prepared from several kinds of single element standard solution for atomic absorption (1000 $\mu g\,mL^{-1}$) purchased from Wako Pure Chemicals (Osaka, Japan). Two multi-element stock solutions for ICP-MS, XSTC-13 and XSTC-1, provided by Spex CertiPrep Inc. Metuchen (New Jersey, USA) were mixed with the single element solutions to give a multi-element standard solution containing 63 elements. Accurate dilution of the standard solutions was carried out by weight.

Ultrapure grade nitric acid (60%, density 1.38 $g\,mL^{-1}$) purchased from Kanto Chemicals (Tokyo, Japan) was diluted with ultrapure water to give 1 M nitric acid. Acetic acid (minimum 96%) and ammonia water (29%), which were used for preparing ammonium acetate solutions, were electronic industrial reagent grade purchased from Kanto Chemicals (Tokyo, Japan). Ultrapure water (18.3 $M\Omega\,cm^{-1}$ resistance) prepared by Elix 3/Milli-Q Element system Nihon Millipore (Tokyo, Japan) was used for diluting standard solution.

2.3. Synthesis of CCTS-TAA resin

The CCTS-TAA resin was synthesized in two major steps (Scheme 1): (1) The synthesis of cross-linked chitosan, and (2) introduction of tris(2-aminoethyl)amine moiety into cross-linked chitosan.

Chitosan dissolves in acidic medium and this characteristic is considered to be a serious disadvantage from the view-point of metal collection based on solid phase extraction method. Therefore, in order to improve the mechanical and chemical durability of chitosan in acidic medium, a cross-linked structure of chitosan was synthesized with ethyleneglycoldiglycidylether (EGDE) as the cross-linker. Among two reactive groups in chitosan, the hydroxyl group was used as a terminal for the cross-link structure, while the reactive amino group was preserved for further derivatization. The detail of synthesis procedure of EGDE cross-linked chitosan had been reported by Motomizu and co-workers [13].

In the second step, EGDE cross-linked chitosan (5 g) was reacted with epibromohydrin (30 g) in order to introduce an extension arm of epibromohydrin into CCTS, giving CCTS-epibromohydrin. With bromo functional-group on its terminal which serve as a leaving group, this extension arm can facilitate the introduction of the tris(2-aminoethyl)amine moiety. The CCTS-epibromohydrin was then mixed with TAA (10 g) in dioxane (100 mL), and the mixture

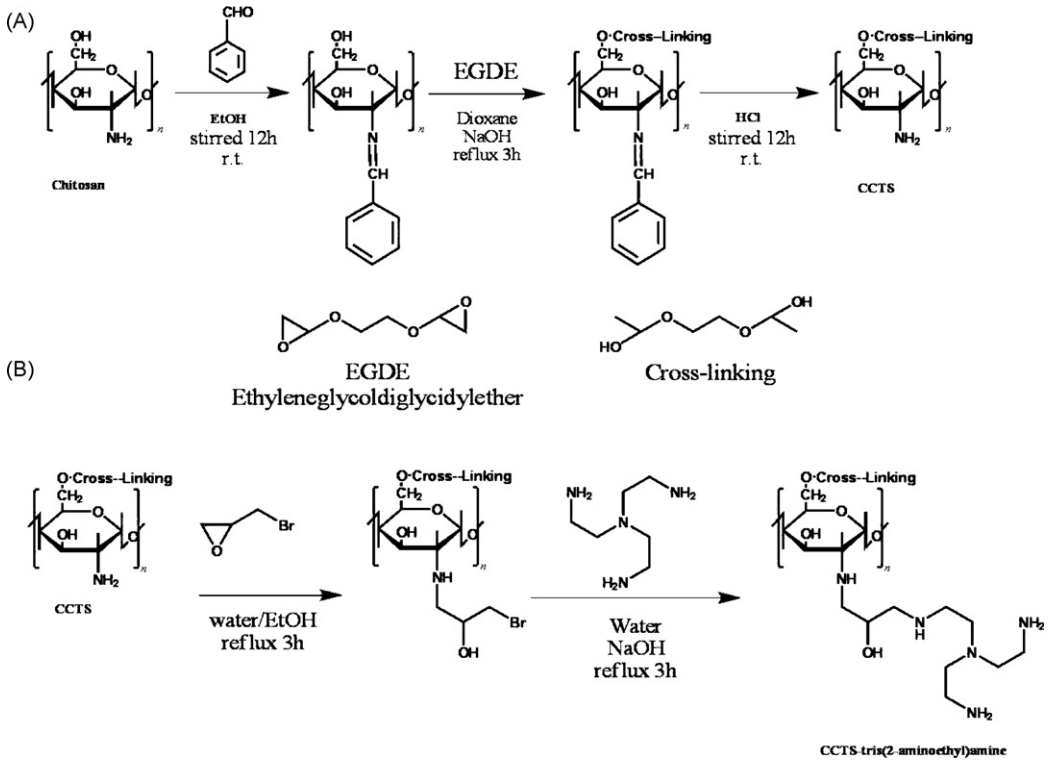

Scheme 1. Synthesis of CCTS-TAA.

was refluxed for 3-h. Tertiary amine possesses higher nucleophilicity compared to primary amine because the central nitrogen atom was surrounded by alkyl group which act as an electron donating group. However, in aqueous solution, the stabilization role is mainly played by the solvation which involves hydrogen bonding. In this situation, primary amine has a higher nucleophilicity because it can form hydrogen bonding with the presence of N–H, thus the coupling was likely to take place through primary amine group.

2.4. On-line metal collection and determination procedure

The manifold of Auto-Pret AES system for on-line Hg collection/concentration and determination is shown in Fig. 1. CCTS-TAA resin was packed in a polytetrafluoroethylene (PTFE) column (2 mm i.d. × 4 cm), and the column was installed on switching valve (SWV) at the position shown in Fig. 1. PTFE tubing with 0.8 mm of inner diameter was used for all connecting lines, except for holding coil where PTFE tubing with 2 mm of inner diameter was used. The on-line pretreatment procedure was carried out in four major steps: *column conditioning*, *preconcentration*, *washing*, and *elution*.

2.4.1. Column conditioning step

One milliliter of 0.5 M ammonium acetate solution of appropriate pH was aspirated at flow rate of 400 $\mu L\,s^{-1}$ into holding coil through the port 3 of selection valve (SLV). While the SWV was kept in load position, the solution in the holding coil was propelled at flow rate of 40 $\mu L\,s^{-1}$ into the column in order to adjust the pH of the resin.

2.4.2. Preconcentration step

Five milliliters of sample was aspirated at flow rate of 400 $\mu L\,s^{-1}$ into the holding coil through the port 2 of SLV. The aspirated sample was then propelled into the column at flow rate of 30 $\mu L\,s^{-1}$ for the metal collection on the resin and the removal of the matrices.

2.4.3. Washing step

One milliliter of ultrapure water was aspirated at flow rate of 400 $\mu L\,s^{-1}$ into the syringe pump, and then the ultrapure water was propelled into the column at flow rate of 40 $\mu L\,s^{-1}$. This process will force the remaining sample in the connecting-line to pass through the column, and at the same time this process will remove matrices and the un-adsorbed elements.

2.4.4. Elution step

0.5 mL of 2 M nitric acid was aspirated into the holding coil at flow rate of 400 $\mu L\,s^{-1}$ from the port 5 of SLV, and then the position of syringe pump was set to 2.5 mL by aspirating ultrapure water into the syringe pump. The position of SWV was turned to inject-position, and the eluent was propelled into the column at flow rate of 30 $\mu L\,s^{-1}$; the effluent zone moved to the ICP-AES for the metal measurement.

The entire sequence described above was automatically controlled with a home-made software developed by the authors, using Microsoft Visual Basic 6.

2.5. On-line metal collection procedure for CCTS-TAA adsorption behavior study

The adsorption behavior of CCTS-TAA resin was investigated by using on-line mini-column procedure, where CCTS-TAA was packed in a small PTFE column (2 mm i.d. × 40 mm) and the column was installed on Auto-Pret AES System. The on-line procedure of this work is similar to that described in Section 2.4, except for 2.5 mL of sample was used in preconcentration step, 2.5 mL of eluent was used in elution step, and the effluent obtained from this procedure was transferred into a polypropylene test tube and then analyzed with ICP-MS.

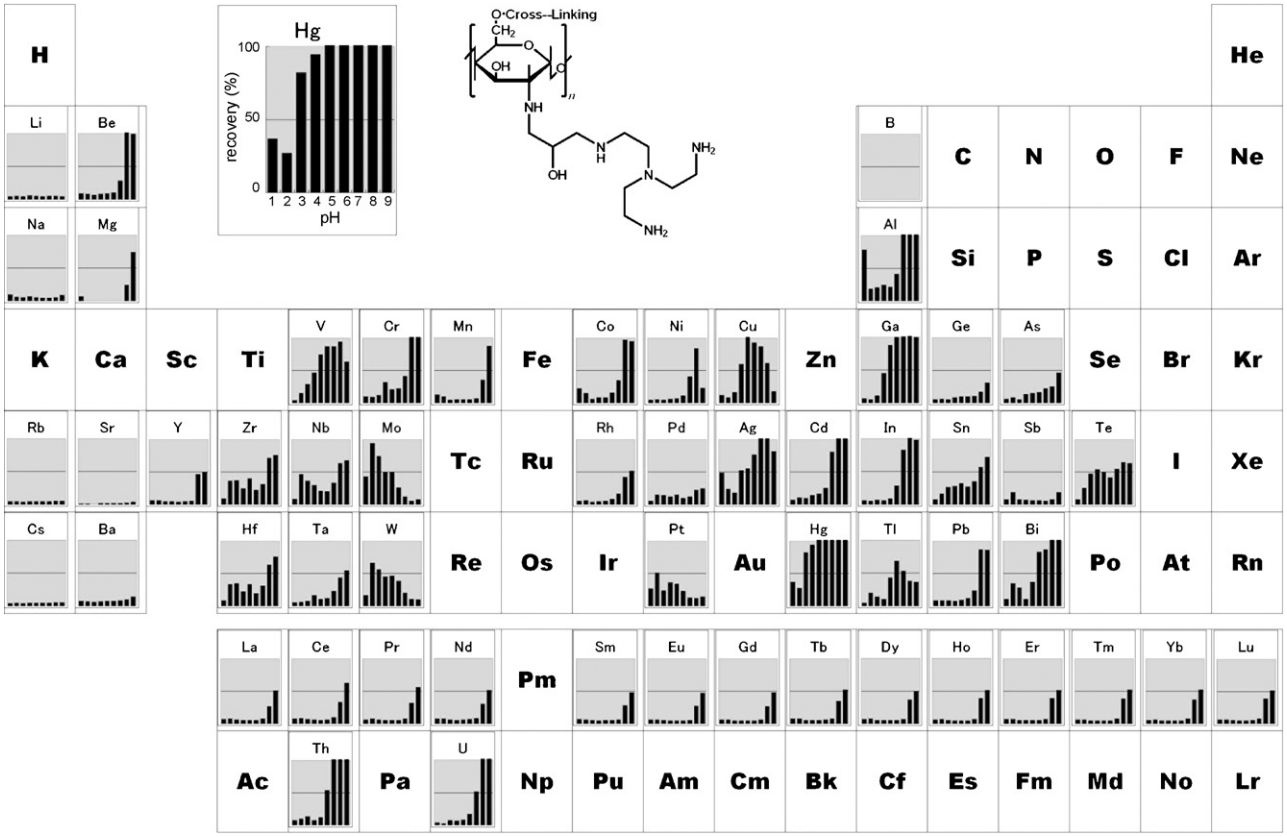

Fig. 2. Adsorption of various elements on CCTS-TAA. Sample: 2.5 mL of solution containing 10 ppb of various elements; Elution: 2.5 mL of 2 M HNO_3.

3. Results and discussion

3.1. Characteristics of CCTS-TAA

The products obtained from each synthesis step were characterized by measuring their IR spectra. The peak at 894 cm^{-1} in the spectrum of cross-linked chitosan confirms the N–H wagging of the amino group. This band intensity was decreased when the extension arm of epibromohydrin was attached through the amino group. In CCTS-epibromohydrin, the peak C–Br can be clearly observed in 500–600 cm^{-1}. The intensity of this peak was decreased in the spectra of final product which indicate that the substitution of bromo group by tris(2-aminoethyl)amine was occurred in the reaction.

3.2. Adsorption of metal ions on CCTS-TAA

The result of CCTS-TAA adsorption behavior study is summarized in Fig. 2, expressed as the recovery of each 10 $\mu g\,L^{-1}$ of 57 elements when the adsorption was carried out in various pH.

CCTS-TAA has a good affinity toward Cr, Co, Cu, Ag, Al, Ga, In, Bi, and Hg, of which Co, Cu, Ag, and Hg can be expected due to the presence of amine group. The affinity toward Cr, Al, Ga, In, and Bi is extraordinary from the view-point of chelating mechanism. One possibility for such affinity is considered from the ion exchange mechanism, in which anionic species can be trapped on the positively charged amino groups: Cr species, as well as Al, Ga, In, and Bi are possibly present as an anionic species in alkaline solution.

It is well known that N and S ligands possess affinity to adsorb Hg^{2+} which belongs to group III "soft" cation. Although S ligand possess better affinity to bind soft cation compared to N, usually the retention of soft cation on S ligand is so strong that a complexing agent is necessary for elution [22]. The CCTS-TAA possesses tertiary amine and primary amine which can serve as a ligand for Hg complexation under moderate affinity. Compared to primary amine, tertiary amine has a higher affinity and selectivity for Hg(II) in aqueous solution [6]. The proposed chelation structure of Hg by CCTS-TAA is shown in Fig. 3.

The adsorption of Hg on CCTS-TAA can be carried out in wide pH range ($pH \geq 3$) with excellent recovery value when 2 M nitric acid was used as the eluent. Although CCTS itself was reported to have a good adsorption toward mercury, the adsorption only takes place when sample was prepared in HCl solution [13]. In that case, Hg forms stable complex with Cl^-, and the adsorption occurs through ion exchange mechanism. Moreover, the adsorbed Hg on CCTS could not be removed with nitric acid, and thus the addition of thiourea into the eluent was necessary [13]. Another work on mercury preconcentration by using YPA_4 chelating resin

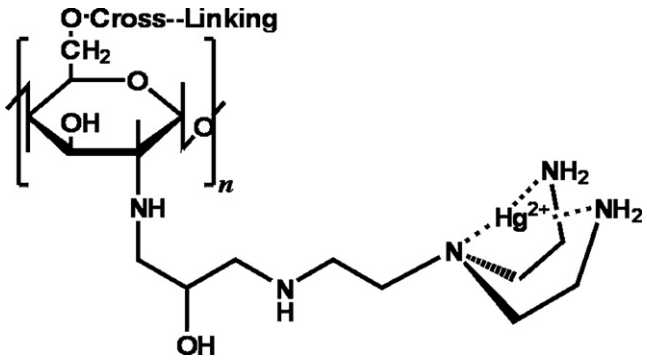

Fig. 3. Proposed structure of Hg chelation on CCTS-TAA.

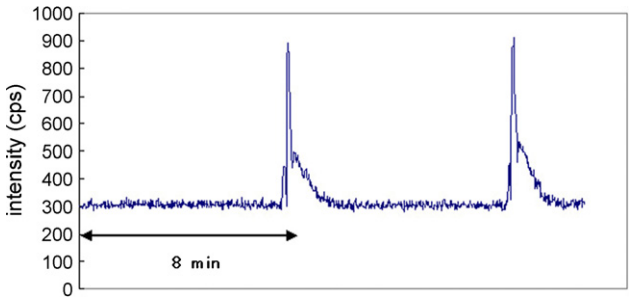

Fig. 4. Peak profile of 5 ng mL^{-1} Hg obtained by using Auto-Pret AES system with CCTS-TAA. Sample: 5 mL; Eluent: 0.5 mL of 2 M HNO_3; Sample flow rate: 30 μL s^{-1}; Eluent flow rate: 30 μL s^{-1}.

was also reported to require thiourea addition into the eluent [23]. In CCTS-TAA, it was found that the elution of adsorbed Hg can be easily carried out by using 2 M nitric acid without any addition of complexing agent. The resin cannot adsorb Hg at pH lower than 3, which indicates that Hg could be easily desorbed by using strong acid.

3.3. On-line collection/concentration and determination of Hg with CCTS-TAA and Auto-Pret AES system

The possibility for applying CCTS-TAA to Hg collection/concentration and determination using Auto-Pret AES system was investigated. The result showed that a good peak profile was observed when a solution containing 5 ng mL^{-1} Hg was used as a sample, as shown in Fig. 4. The tailing signal, which appeared after the sharp peak, was a result from the common memory effect of Hg on ICP-AES. However, the signal reproducibility is enough for reproducible measurement of Hg and the signal rapidly went down to baseline during the process of preconcentration of the next sample, and thus the next measurement sequence should not be affected by such drawback.

The limit of detection (LOD) corresponding to S/N = 3 for Hg measurement was found to be 0.1 ng mL^{-1} for 5 mL of sample, and lower LOD can be expected when larger volume of sample is used. This LOD is lower compared to another work which utilize Hg-imprinted thiol functional sorbent with the same detector [8]. Another work on sequential cloud-point extraction method by using the same detector was reported to have lower LOD, but the extraction procedure was tend to be laborious and more time-consuming [24,25].

4. Conclusion

A novel chitosan resin functionalized with tris(2-aminoethyl) amine moiety was synthesized, and its ability to adsorb Hg at various pH was examined. The synthesized resin showed good adsorption toward Hg in wide pH range (pH ≥ 3) with excellent recovery value when 2 M of HNO_3 was used as the eluent. Compared to Hg adsorption on CCTS, the adsorbed Hg on CCTS-TAA can be easily eluted by using HNO_3 without any addition of complexing agent. The proposed method has showed that CCTS-TAA which was packed in a mini-column and then installed on Auto-Pret AES system can be applied to the on-line collection/concentration and determination of trace amounts of Hg.

Acknowledgement

This work was supported partially by the Grant-in-Aid for Scientific Research (B) (No. 19350038) from Japan Society for the Promotion of Science (JSPS).

References

[1] L. Zhang, M.H. Wong, Environ. Int. 33 (2007) 108.
[2] A. Lezzi, S. Cobianco, A. Roggero, J. Polym. Sci. A 32 (1994) 1877.
[3] http://www.epa.gov/safewater/contaminants/dw_contamfs/mercury.html (January 2007).
[4] http://www.env.go.jp/en/water/wq/wp.html (January 2007).
[5] D. Bilba, D. Bejan, L. Tovan, Croat. Chem. Acta 71 (1998) 155.
[6] X. Zhu, S.D. Alexandratos, Ind. Eng. Chem. Res. 44 (2005) 7490.
[7] A.A. Atia, A.M. Donia, K.Z. Elwakeel, React. Func. Polym. 65 (2005) 267.
[8] Z. Fan, Talanta 70 (2006) 1164.
[9] G. Wu, Z. Wang, J. Wang, C. Hea, Anal. Chim. Acta 582 (2007) 204.
[10] N.L.D. Filho, D.R. Carmo, A.H. Rosa, Electrochim. Acta 52 (2006) 965.
[11] Y. Baba, K. Ohe, Y. Kawasaki, S.D. Kolev, React. Func. Polym. 66 (2006) 1158.
[12] R.S. Vieira, M.M. Beppu, Water Res. 40 (2006) 1726.
[13] K. Oshita, Y. Gao, M. Oshima, S. Motomizu, Anal. Sci. 17 (2001) 317.
[14] K. Oshita, M. Oshima, Y. Gao, K.H. Lee, S. Motomizu, Anal. Sci. 18 (2002) 1121.
[15] C. Hang, B. Hu, Z. Jiang, N. Zhang, Talanta 71 (2007) 1239.
[16] A. Ali, Y. Ye, G. Xu, X. Yin, T. Zhang, Microchem. J. 63 (1999) 365.
[17] V.A. Lemos, J.S. Santos, L.S. Nunes, M.B. Carvalho, P.X. Baliza, R.T. Yamaki, Anal. Chim. Acta 494 (2003) 87.
[18] X.Z. Wu, P. Liu, Q.S. Pu, Q.Y. Sun, Z.X. Su, Talanta 62 (2004) 918.
[19] M.S. Jimenez, R. Velarte, J.R. Castillo, Spectrochim. Acta: Part B 57 (2002) 391.
[20] L. Hakim, A. Sabarudin, M. Oshima, S. Motomizu, Anal. Chim. Acta 588 (2007) 73.
[21] L. Hakim, A. Sabarudin, M. Oshima, S. Motomizu, Talanta 74 (2008) 977.
[22] T. Ninomiya, K. Oshita, M. Oshima, S. Motomizu, Bunseki Kagaku 52 (2003) 811.
[23] H. Jiang, B. Hu, Z. Jiang, Y. Qin, Talanta 70 (2006) 7.
[24] Y. Li, B. Hu, Spectrochim. Acta: Part B 62 (2007) 1153.
[25] J.C.A. Wuilloud, R.G. Wuilloud, M.F. Silva, R.A. Olsina, L.D. Martinez, Spectrochim. Acta: Part B 57 (2002) 365.

Talanta 76 (2008) 1199–1206

Contents lists available at ScienceDirect

Talanta

journal homepage: www.elsevier.com/locate/talanta

FSiNPs mediated improved double immunofluorescence staining for gastric cancer cells imaging

Xiaoxiao He[a,b], Jia Ge[a,b], Keming Wang[a,b,*], Weihong Tan[a,b], Hui Shi[a,b], Chunmei He[a,b]

[a] Biomedical Engineering Center, State Key Laboratory of Chemo/Biosensing and Chemometrics, College of Chemistry and Chemical Engineering, Changsha 410082, China
[b] Key Laboratory for Bio-Nanotechnology and Molecule Engineering of Hunan Province, Changsha 410082, China

ARTICLE INFO

Article history:
Received 28 February 2008
Received in revised form 12 May 2008
Accepted 18 May 2008
Available online 28 May 2008

Keywords:
Double immunofluorescence staining
RuBPY doped silica nanoparticles (RFSiNPs)
FITC doped silica nanoparticles (FFSiNPs)
Gastric cancer cells
Confocal laser scanning microscopy (CLSM) imaging

ABSTRACT

A fluorescent silica nanoparticles (FSiNPs) mediated double immunofluorescence staining technique has been proposed for MGC-803 gastric cancer cells imaging by confocal laser scanning microscopy. Anti-CEA antibody and anti-CK19 antibody which can be both bonded to MGC-803 gastric cancer cells were first conjugated to fluorescein isothiocyanate (FITC) doped fluorescent silica nanoparticles (FFSiNPs) and RuBPY doped fluorescent silica nanoparticles (RFSiNPs), respectively. The MGC-803 gastric cancer cells were incubated with the mixture of anti-CEA antibody-conjugated FFSiNPs and anti-CK19 antibody-conjugated RFSiNPs, and subsequently imaged using confocal laser scanning microscopy. With this method, the in vitro cultured MGC-803 gastric cancer cells lines were successfully doubled labeled and distinguished through antigen–antibody recognition, together with the green and red signal of FFSiNPs and RFSiNPs simultaneously obtained without crossreactivity by confocal laser scanning microscopy imaging. By comparison with the conventional double immunofluorescence staining using green-emitting and red-emitting dyes, the photostability of this proposed method for confocal laser scanning microscopy imaging has been greatly improved. Furthermore, the ex vivo imaging of primary MGC-803 gastric cancer cells samples came from the tumor tissues of mice bearing the MGC gastric cancer tumor xenografts by this method have also been explored. The results demonstrate that the method offers potential advantage of photostability for the confocal laser scanning microscopy imaging of MGC-803 gastric cancer cells, and is applicable to the imaging of primary MGC-803 gastric cancer cells from the tumor tissues.

1. Introduction

The detection and imaging of gastric cancer cells is of great clinical significance for effectively preventing and treating gastric cancer because a few cells escape from the original focus and disseminated into other organs are the common reasons leading to death of gastric cancer patients [1–3]. Up to now, the primary techniques used for gastric cancer cells recognition mainly include morphological analysis and biochemical analysis [4–15]. The morphological analysis takes advantage of small difference in normal gastric cells and gastric cancer cells by using hematoxylin and eosin (H&E) staining [7–10]. But some minor changes of the cells are difficult to be easily distinguished by H&E staining morphological analysis. Biochemical analysis has shown its uniqueness on gastric cancer cells detection, which relies on the biochemical characteristics of the cell membrane or inside the cells, mainly including reverse-transcription polymerase chain reaction (RT-PCR), immunolabeling staining and so on [4–6,11–13]. The molecular biological protocol using RT-PCR targeting some marks appears to be an attractive method for gastric cancer cells detection with high objectivity and sensitivity, especially the recent real-time quantitative reverse transcription polymerase chain reaction (RQ-PCR) [6]. While false positive or false negative results would occur when the related organisms sharing similar genetic sequences with target organisms or inhibitors that inactivate the DNA polymerase. The immunolabeling staining, especially the immunofluorescence staining, possesses its advantages in simple manipulation, intuitionistic results and is popular for diagnosis and micrometastases detection of gastric cancer. However, photobleaching and sensitivity of fluorochromes used in the immunofluorescence staining are still regarded problem. There is a great need to develop suitable immunofluorescence staining to avoid the difficulties for detecting gastric cancer cells, especially multi-antibody combined immunolabeling staining. Because many markers have been used for detection gastric cancer using immunolabeling staining, such as carcino-embryonic antigen (CEA), cytokeratin (CK), epithelia

* Corresponding author at: Biomedical Engineering Center, State Key Laboratory of Chemo/Biosensing and Chemometrics, College of Chemistry and Chemical Engineering, Changsha 410082, China. Tel.: +86 731 8821566; fax: +86 731 8821566.
E-mail address: kmwang@hnu.cn (K. Wang).

0039-9140/$ – see front matter © 2008 Elsevier B.V. All rights reserved.
doi:10.1016/j.talanta.2008.05.029

membrane antigen (EMA) and so on [15], there is difference in affinity between gastric cancer cells and different markers. The immunolabeling staining marked different antibodies may improve the veracity in gastric cancer cells detection.

Recently, the development of luminescent nanoparticles has helped improve bioimaging, including semiconductor quantum dots, Au nanoparticles, fluorescent silica nanoparticles and so on [16–25]. Among the nanoparticles, fluorescent silica nanoparticles have shown to display good dispersibility in an aqueous environment, good photostability, strong fluorescence and low toxicity, which make them excellent candidates for use in biological markers [21–25]. Moreover, thousands of dye molecules are encapsulated in a single nanoparticle and many biomolecules can be modified on the surface of nanoparticles due to their high surface-to-volume ratio, so the detection sensitivity can be greatly increased compared with the direct fluorochromes labeling [26]. These properties have opened new possibilities for advanced molecular and cellular imaging as well as for ultrasensitive bioassays and diagnosis by using of fluorescent silica nanoparticles. Up to now, various kinds of fluorochromes doped silica nanoparticles with different emission have been developed in our group and well used in bioimaging [25–29].

Herein, a fluorescence dye doped silica nanoparticles (FSiNPs) mediated double immunofluorescence staining has been developed for gastric cancer cells confocal laser scanning microscopy imaging by taking luminescent and photostable RuBPY doped silica nanoparticles (RFSiNPs) and fluorescein isothiocyanate (FITC) doped silica nanoparticles (FFSiNPs) as fluorescence labels simultaneously. The microgastric cancer (MGC) cells line (MGC-803 cells) was selected as the target cells because MGC is one kind of early gastric cancer [30,31]. Anti-CEA antibody and anti-CK19 antibody were first conjugated to FFSiNPs and RFSiNPs, respectively. The MGC-803 cells were incubated with the mixture of anti-CEA antibody-conjugated FFSiNPs and anti-CK19 antibody-conjugated RFSiNPs. Then the detection of MGC-803 cells was performed on confocal laser scanning microscopy (CLSM) for obtaining high-resolution optical images. The bioconjugated FFSiNPs and RFSiNPs mediated double immunofluorescence staining has been used to image the in vitro cultured MGC-803 cells line, ex vivo primary MGC-803 cells from tumor tissues. The photostability of the bioconjugated FFSiNPs and RFSiNPs mediated double immunofluorescence staining has also been investigated by comparison with the conventional double immunofluorescence staining using green-emitting and red-emitting dyes.

2. Experimental details

2.1. Reagents and materials

Tris(2,2-bipyridyl)dichlororuthenium(II) hexahydrate (RuBPY), Triton X-100, fluorescein isothiocyanate (FITC), tetramethyl rhodamine isothiocyanate (TRITC) and anti-CEA antibody were purchased from Sigma–Aldrich. Anti-CK19 antibody was purchased from Jingmei Company. Cell medium RPMI 1640 was obtained from Clontech. Cyanogen bromide (CNBr) was from J&K CHEMICAL. FACSTM lysing solution was obtained from BD Biosciences (USA). Phosphate-buffered saline (PBS) solutions at pH 7.4 were prepared from PBS tablets (Amresco). Other chemicals if not specified were all commercially available and used as received. All aqueous solutions were prepared exclusively in deionized distilled water (Barnstead Co., USA). MGC-803 cells, COS-7 cells, Hela cells and 1E8 cells were provided by Cell Center in our lab. Balb/c and athymic nude mice were obtained from Beijing Vital River Laboratory Animal Co., Ltd. (Balb/c). Mice were used at ages from 6 to 12 weeks. All operations on mice were in accord with institutional animal use and care regulations.

2.2. Instruments

A Hitachi JEM-1230 transmission electron microscope was used for analyzing the shape and size of the nanoparticles. Fluorescence spectra of the fluoresecent nanoparticles were measured on a PerkinElmer LS-55 spectrofluorometer. The cell imaging was carried out with an Olympus FV-500 laser confocal scanning microscope.

2.3. Experimental details

2.3.1. Preparation of bioconjugated FSiNPs

Previously published procedures [24–26] were first used to synthesize FSiNPs, including RFSiNPs and FFSiNPs. Briefly, a solution containing 7.5 ml cyclohexane, 1.77 ml Triton X-100, 1.8 ml *n*-hexanol was mixed with 400 μL water and 100 μL 0.1 mol/L aqueous RuBPY dye or FITC-IgG solutions as the core material. After stirred for 1 h, 200 μL of TEOS was then added as a precursor for silica formation, followed by the addition of 100 μL NH_4OH to initiate the polymerization process. The reaction was allowed to continue for 24 h to produce FFSiNPs and RFSiNPs, respectively. When it was completed, the FSiNPs were isolated.

The well prepared and isolated FSiNPs were then bioconjugated with antibody by using the followed CNBr method as previous reported [26]. The dried FSiNPs were suspended in 2 ml 2 mol L^{-1} sodium carbonate solutions and ultrasonicated for 10 min. Solution of CNBr in acetonitrile (1.0 g of CNBr dissolved in 0.5 ml of acetonitrile) was then added drop-wise to the FSiNPs suspensions under stirring for 10–15 min at room temperature. The CNBr activated FSiNPs were washed twice successively with ice-cold water and PBS buffer (pH 7.4), followed by resuspension in 500 μL PBS buffer (pH 7.4). Subsequently, 40 μL (1 mg ml^{-1}) antibody diluted in PBS buffer was added into the activated FSiNPs suspension, and stirring was continued for 24 h at 4 °C. Antibody-conjugated FSiNPs were then treated with 10 ml of 0.03 M glycine solution overnight at 4 °C. Finally, antibody-conjugated FSiNPs were washed, resuspended in PBS buffer (pH 7.4), and stored at 4 °C for future usage. Anti-CEA antibody and anti-CK19 antibody were successfully conjugated to FFSiNPs and RFSiNPs, respectively, by using the above-mentioned method.

2.3.2. Characterization of bioconjugated FSiNPs

The samples for transmission electron microscopy (TEM) were prepared respectively by placing a few drops of FFSiNPs, RFSiNPs, anti-CEA antibody-conjugated FFSiNPs and anti-CK19 antibody-conjugated RFSiNPs on carbon-coated copper grids. After evaporation of the solvent, the particles were observed by a JEM-1230 transmission electron microscope. To investigate whether the FFSiNPs and RFSiNPs were fit to be used as a double fluorescence labeling for CLSM imaging, the spectrum of FFSiNPs (9.5 mg/ml), RFSiNPs (9.5 mg/ml) and mixture of FFSiNPs (9.5 mg/ml) and RFSiNPs (9.5 mg/ml) at the volume ratio of 1:1 were carried out respectively on a PerkinElmer LS-55 spectrofluorometer.

2.3.3. In vitro imaging of MGC-803 cells by bioconjugated FSiNPs mediated double immunofluorescence staining

In vitro cultured MGC-803 cells were first used to evaluate the feasibility of the double immunofluorescence confocal imaging using FSiNPs labeling. The MGC-803 cells was seeded at 1×10^6 cells/well in 6-well plates (Invitrogen, CA) and incubated (37 °C, 5% CO_2) in an RPMI 1640 medium supplemented with 10%

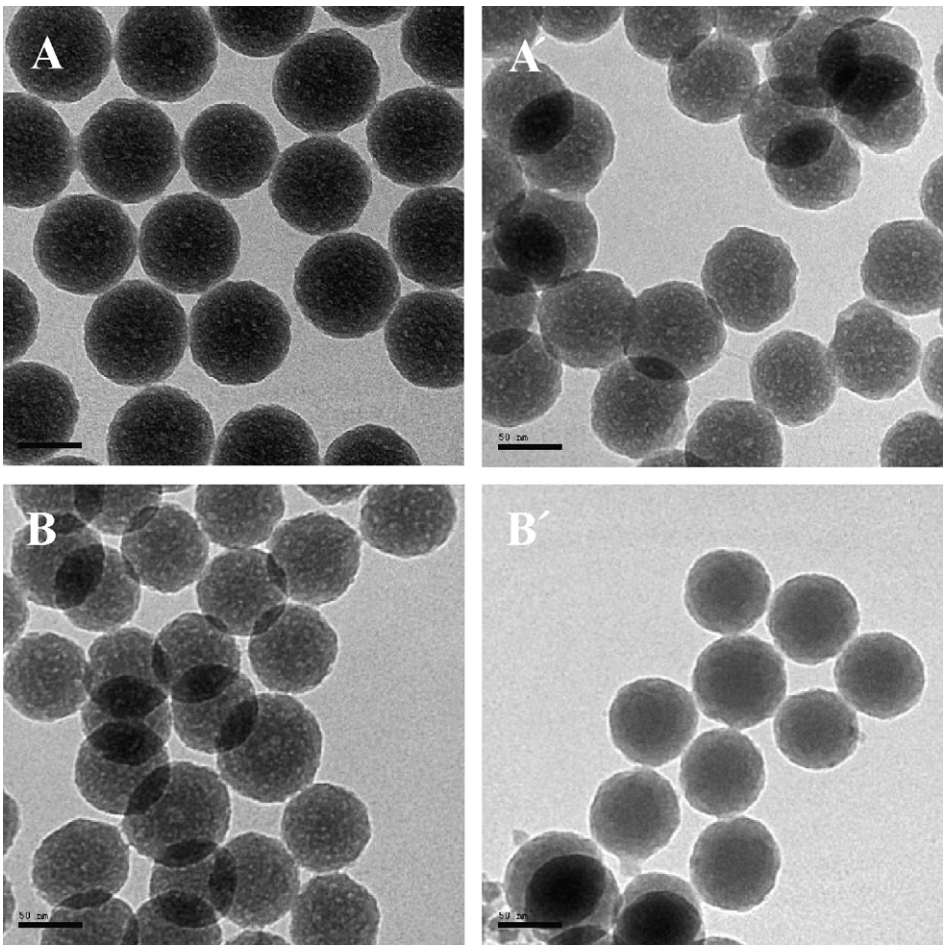

Fig. 1. TEM images of FSiNPs and bioconjugated FSiNPs. (A) FFSiNPs; (A′) anti-CEA antibody-conjugated FFSiNPs; (B) RFSiNPs; (B′) anti-CK19 antibody-conjugated RFSiNPs. Scar bar 50 nm.

fetal bovine serum, 100 μg/ml of streptomycin and 100 IU/ml penicillin for 24 h. The medium in the six-well plate was removed after the cells were cultured until the cover rate on the glass slide reached 70–90%. The glass slide with cells was washed thrice with PBS buffer, and then fixed with 4% paraformaldehyde solution for 10 min at 37 °C, followed by washing with pH 7.4 PBS buffer for three times. The cells were divided into three groups. One part of the cells was incubated for 30 min at 37 °C in the presence of mixture of anti-CEA antibody-conjugated FFSiNPs (9.5 mg/ml) and anti-CK19 antibody-conjugated RFSiNPs (9.5 mg/ml) at the volume ratio of 1:1. The other two parts of cells were respectively incubated with anti-CEA antibody-conjugated FFSiNPs or anti-CK19 antibody-conjugated RFSiNPs suspension for 30 min at 37 °C. The all incubated cells were then washed several times with PBS to discard bioconjugated FSiNPs that were not attached to cells. Fluorescence imaging of MGC-803 cells was visualized using CLSM (FV 500-IX700, Olympus, excitation: 488 nm). Controls included MGC-803 cells incubated with pure FFSiNPs and RFSiNPs, respectively, COS-7 cells, Hela cells, 1E8 cells incubated with mixture of anti-CEA antibody-conjugated FFSiNPs and anti-CK19 antibody-conjugated RFSiNPs.

2.3.4. Ex vivo imaging of MGC-803 cells by bioconjugated FSiNPs mediated double immunofluorescence staining

Ex vivo MGC-803 cells were derived from the primary tissue explants as the followed procedure. 2×10^6 MGC-803 cells in 200 ml PBS was implanted subcutaneously into Balb/c and athymic nude mouse on the quadriceps. Tumor growth was monitored daily until it reached 2–3 mm in diameter. The tumors tissue was gotten out from the mice under a sterile condition. Place the isolated tissue in a sterile bottle containing hanks balanced salt solution with penicillin/streptomycin added. The whole tissue was cut into slices as small pieces as possible. Then the slices were put into a culture flask containing a glass slide, and then cultured in the RPMI 1640 medium with 10% heat-inactivated fetal calf serum, 100 mg/ml streptomycin and 100 IU/ml penicillin (37 °C, 5% CO_2). Remove medium from culture flask and wash cells in a balanced salt solution when adherent cells from the primary tissue explants became semi-confluent. The cells were harvested with 0.5% trypsin and were allowed to grow (37 °C, 5% CO_2) in the 6-well culture dishes to a confluent state in an RPMI 1640 medium supplemented with 10% fetal bovine serum, 100 μg/ml streptomycin and 100 IU/ml penicillin. Then the primary MGC-803 cells was harvested and incubated with mixture of anti-CEA antibody-conjugated FFSiNPs and anti-CK19 antibody-conjugated RFSiNPs for 30 min at 37 °C. The incubated cells were washed several times with PBS to discard bioconjugated FSiNPs that were not attached to the cells and then analyzed with CLSM.

3. Results and discussion

3.1. Characterization of bioconjugated FSiNPs

The size and shape of FSiNPs and bioconjugated FSiNPs were characterized with transmission electron microscope. FFSiNPs and

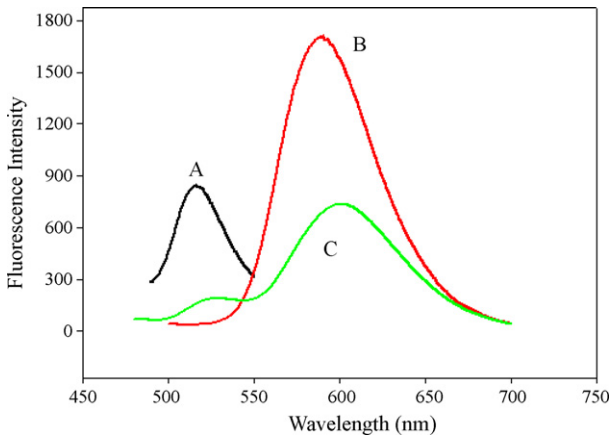

Fig. 2. Fluorescence emission spectra of FFSiNPs (A), RFSiNPs (B) and mixture of FFSiNPs and RFSiNPs (C) when they were excited at 488 nm.

RFSiNPs were spherical in shape and have an average diameter of 76 ± 4 nm and 70 ± 5 nm, respectively (Fig. 1A and B). When the FSiNPs were conjugated with antibody, the size of the anti-CEA antibody-conjugated FFSiNPs and anti-CK19 antibody-conjugated RFSiNPs was not changed obviously by comparison with that of FFSiNPs and RFSiNPs, having diameter of 75 ± 5 nm and 70 ± 3 nm, respectively (Fig. 1A′ and B′).

In addition, reliable separation of the signals generated by the fluorochromes is critical to double immunofluorescence staining in CLSM imaging [32]. In order to demonstrate whether the FFSiNPs and RFSiNPs were suit for double labeling in CLSM imaging, the spectrum of FFSiNPs, RFSiNPs and mixture of FFSiNPs and RFSiNPs have been first detected using fluorescence spectrophotometer. As shown in Fig. 2, the FFSiNPs and RFSiNPs showed maximum emissions at 516 nm and 590 nm, respectively when they were excited at 488 nm, which represented the maximum emission of FITC and RuBPY, respectively. And it can be seen that the mixture of FFSiNPs and RFSiNPs has two maximum emissions at 529 nm and 601 nm when they were excited at 488 nm, which only display red shift with 13 nm and 11 nm, respectively, than that of FFSiNPs and RFSiNPs. The emission spectra results demonstrated that there was no obvious fluorescence resonance energy transfer (FRET) between FFSiNPs and RFSiNPs, and the overlap between the emission spectra of FFSiNPs and RFSiNPs is about at 550 nm. Therefore, the FFSiNPs and RFSiNPs can be used as double labeling for CLSM imaging, the green-emitting and red-emitting can be visualized by CLSM when excited with the 488-nm line of an argon ion laser and detected using 505–525 nm bandpass and 560 nm longpass filters.

3.2. MGC-803 cells imaging by FSiNPs mediated double immunofluorescence staining

3.2.1. The principle of MGC-803 cells imaging using FSiNPs mediated double immunofluorescence staining

Cytokeratin is a component of cell skeleton and distributes in cells deriving from ectoderm. CK19, a member of this family has been found to be good candidate for detecting disseminated gastric cancer cells using RQ-PCR or immunohistochemical staining. CEA is a type of protein molecule that can be found in many different cells of the body, but is typically associated with certain tumors. Many immunohistochemistry staining works reported both CEA and CK19 proteins were expressed in gastric cancer [6,12]. Therefore, CEA and CK19 were selected as the markers, a method of FSiNPs mediated double immunofluorescence staining was developed for the CLSM imaging of MGC-803 cells. The principle for this method was illustrated in Fig. 3. In this scheme, anti-CEA antibody-conjugated FFSiNPs and anti-CK19 antibody-conjugated RFSiNPs were first mixed with volume ratio of 1:1, and then the MGC-803 cells were incubated with the mixture of anti-CEA antibody-conjugated FFSiNPs and anti-CK19 antibody-conjugated RFSiNPs. After washing with PBS to discard unbounded bioconjugated FFSiNPs and RFSiNPs, the confocal microscopy imaging of the incubated MGC-803 cells was performed on a CLSM (FV 500-IX700, Olympus) with an argon laser emitting at 488 nm to excite both RFSiNPs and FFSiNPs fluorescence simultaneously. We used a dichroic beam splitter (DCB) around 560 nm, together with a 560-nm longpass (LP) filter for RFSiNPs signal and a 505–525-nm bandpass filter for FFSiNPs signal. Two channels were available for simultaneous data acquisition: channel 1 (displayed as green) includes emission from 505–525 nm, while channel 2 (displayed as red) includes emission from 560 nm. Because CEA and CK19 were both expressed in MGC-803 cells, the cells can bind both anti-CEA antibody-conjugated FFSiNPs and anti-CK19 antibody-conjugated RFSiNPs and were double labeled. The confocal image of the labeled MGC-803 cells demonstrated the green signal in channel 1 and red signal in channel 2. The merged image of the MGC-803 cells would appear green, red, and yellow. In the control experiments, the cells are only visualized one signal of FFSiNPs or RFSiNPs if the cells only expressed CEA or CK19. Moreover, the cells cannot be visualized if none of CEA and CK19 is expressed in cells.

3.2.2. In vitro imaging of MGC-803 cells

Before applying bioconjugated FSiNPs mediated double immunofluorescence staining for in vitro cultured MGC-803 cells imaging, anti-CEA antibody-conjugated FFSiNPs and anti-CK19 antibody-conjugated RFSiNPs were first respectively incubated with different well-grown MGC-803 cells group to ensure the binding of bioconjugated FSiNPs with the antigen in the MGC-803 cells, the absence of crossreactivity and non-specific binding of FSiNPs with MGC-803 cells. As demonstrated in Fig. 4, with this arrangement, MGC-803 cells were respectively stained with anti-CEA antibody-conjugated FFSiNPs and anti-CK19 antibody-conjugated RFSiNPs as a result of the specific antigen–antibody binding, and the staining pattern were green and red fluorescent signal, respectively. There was no detectable crosstalk in either direction between the non-co-localizing signals from CEA staining and CK19 staining. It was also observed that there were no obvious green or red fluorescence signals in the cells when the MGC-803 cells were incubated with pure FFSiNPs or RFSiNPs, which was consisted with our previous reported cells imaging using single functionalized nanopaticles [26–29] (not shown).

Therefore, we used bioconjugated FSiNPs mediated double immunofluorescence staining for the MGC-803 cells imaging. The well-grown MGC-803 cells group was incubated with mixture of anti-CEA antibody-conjugated FFSiNPs and anti-CK19 antibody-conjugated RFSiNPs. Using appropriate settings for PMT gain, co-localization staining for MGC-803 cells imaging was shown in Fig. 5A, stained for antigens of CEA and CK19. Green signal was obvious visualized in MGC-803 cells with the PMT gain for the green signal in channel 1 and red signal in channel 2. The results indicated the green signal, red signal and merged images of green and red shown as yellow were all demonstrated in MGC-803 cells by simultaneous acquisition of data in both channels. To further confirm the veracity of this method for recognition of MGC-803 cells, the COS-7 cells without expression of CEA and Ck 19, Hela cells with expression of CEA, and 1E8 cells with expression of CK19 were designed as the contrast groups [33,34]. The three kinds of cell lines were all incubated with mixture of anti-CEA antibody-conjugated FFSiNPs and anti-CK19 antibody-conjugated RFSiNPs, respectively.

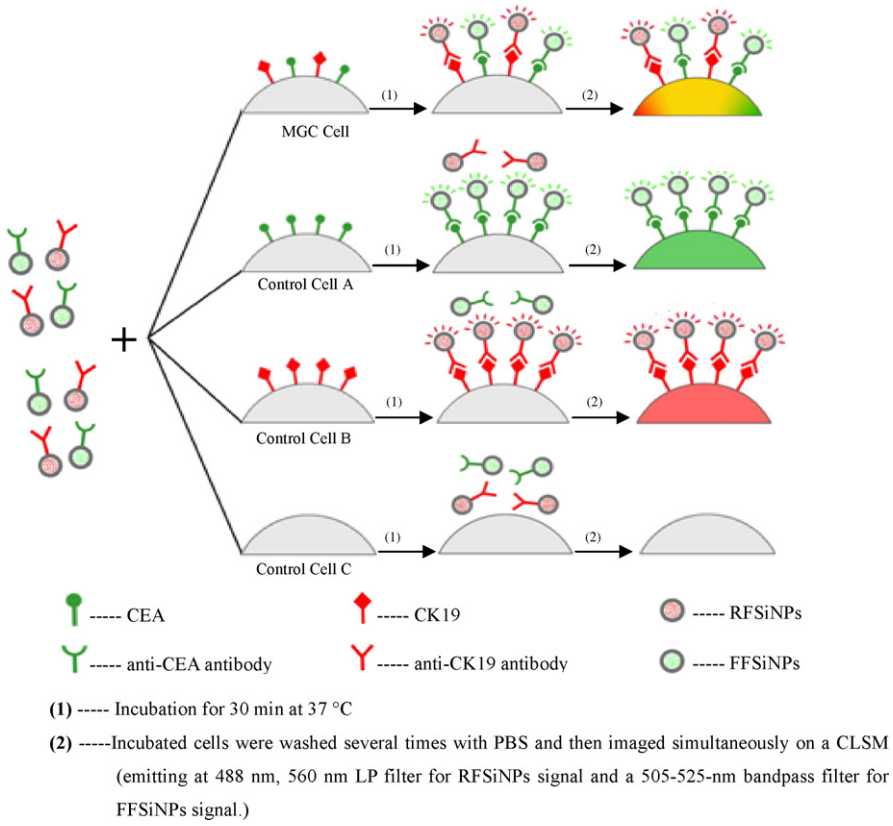

Fig. 3. Schematic illustrations of MGC-803 cells CLSM imaging using bioconjugated FSiNPs mediated double immunofluorescence staining.

The treated cells were visualized with the same PMT gain for simultaneous acquisition of data in channel 1 and channel 2. The Hela cells and 1E8 cells were both demonstrated only one fluorescence emission with green emission and red emission respectively after simultaneous acquisition of data in channel 1 and channel 2 (Fig. 5B and C). While the COS-7 cells did not show any signal for detection of green emission and red emission in the two channels (Fig. 5D). Such observations clearly suggested that the bioconjugated FSiNPs mediated double immunofluorescence staining could be reliably used for the MGC-803 cells imaging.

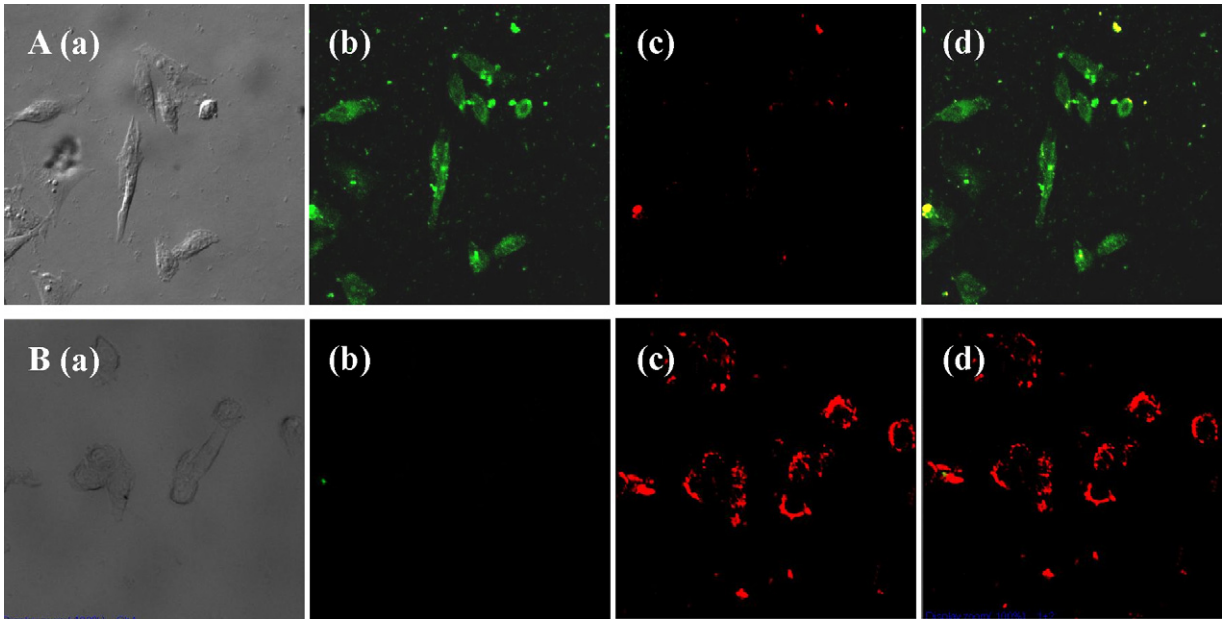

Fig. 4. CLSM images of (A) MGC-803 cells incubated with anti-CEA antibody-conjugated FFSiNPs and (B) MGC-803 cells incubated with anti-CK19 antibody-conjugated RFSiNPs. a, b, c, and d were represented the images acquired in bright-field, channel 1 (green signal), channel 2 (red signal) and merged images of the green channel and the red channel (channel 1: PMT 750 V; laser intensity 10.0, gain power 1.7. Channel 2: PMT 650 V; laser intensity 10.0, gain power 1.7).

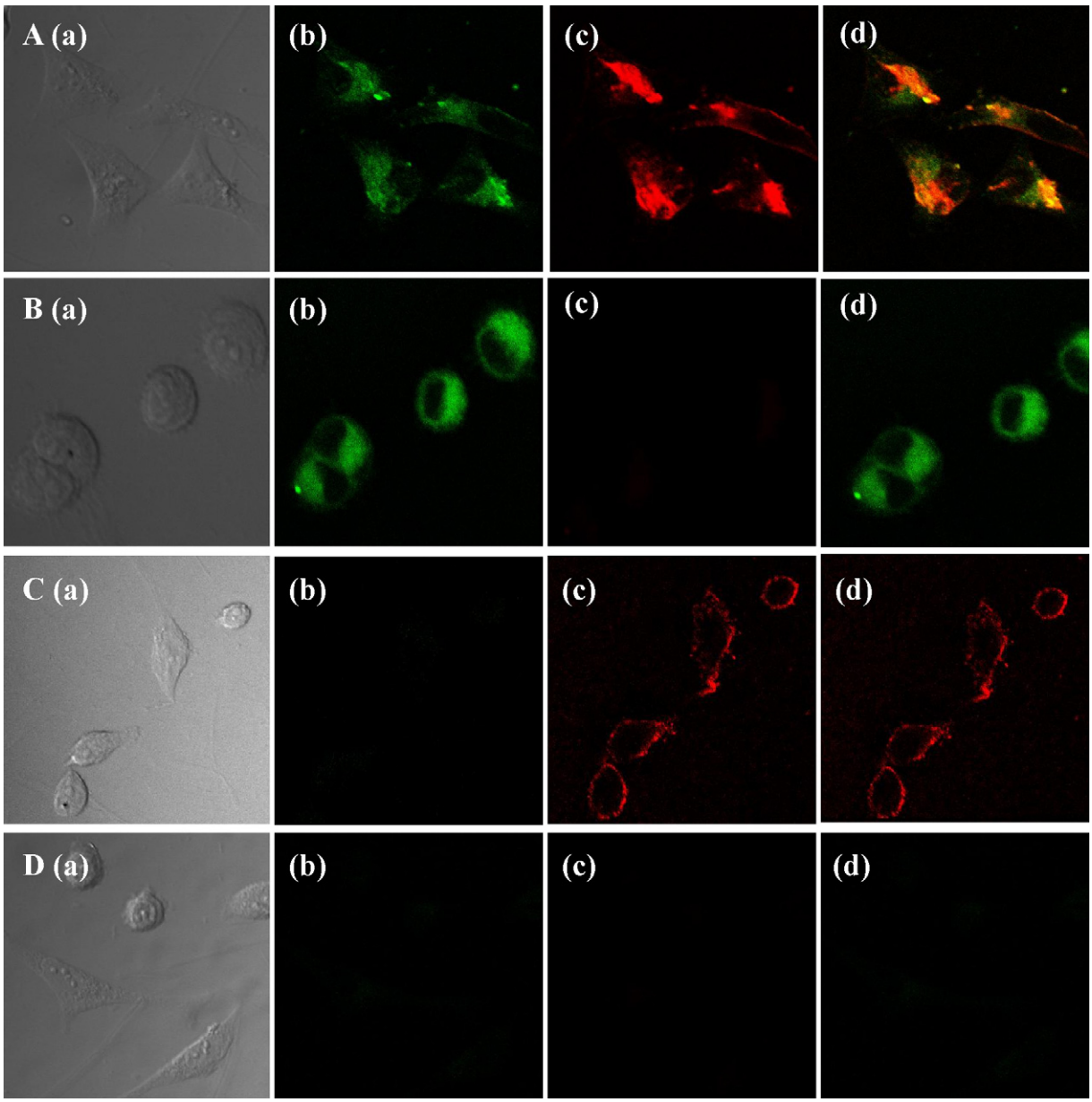

Fig. 5. Bioconjugated FSiNPs mediated double immunofluorescence images by CLSM of the cells that were incubated with mixture of anti-CEA antibody-conjugated FFSiNPs and anti-CK19 antibody-conjugated RFSiNPs. A, B, C and D were represented MGC-803 cells, Hela cells, 1E8 cells and COS-7 cells, respectively. a, b, c, and d were represented the images acquired in bright-field, channel 1 (green signal), channel 2 (red signal) and merged images of the green channel and the red channel (channel 1: PMT 750 V; laser intensity 10.0, gain power 1.7. Channel 2: PMT 650 V; laser intensity 10.0, gain power 1.7).

3.2.3. Photostability of FSiNPs mediated double immunofluorescence staining

Photostability of fluorochromes is a major issue for CLSM imaging, particularly for multi-labeling reconstruction of images. As we known, green-emitting fluorescein (FITC) is a recognized problem in the cells imaging. Although our previous studies have shown FSiNPs-based single labeling method was more photostable than the pure fluorochrome for cells imaging with fluorescence microscopy or CLSM [26–29], the FSiNPs-based double immunofluorescence staining was commonly visualized using CLSM with relative intensive irradiation. The photostability of FSiNPs-based double immunofluorescence staining has been investigated. The imaged MGC-803 cells were excited for 10 min by successive argon laser irradiation at 488 nm, and fluorescent images in channel 1 and channel 2 were acquired every few minutes. And the relative intensity of staining mean pixel intensity of the first 16-scan image of each series for the region was first determined using the Image/Histogrammenu option in Adobe Photoshop software (AdobeSystems; San Jose, CA). To quantify photodegradation, the intensity expressed as a percentage of the initial value for that series. We found that the fluorescence intensity of the MGC-803 cells imaged by the bioconjugated FSiNPs double immunofluorescence staining decreased slowly, and both of the green signals and red signals were still clearly distinguishable after 10 min continuous irradiation. The relative intensity of FFSiNPs and RFSiNPs still kept about more than 80% of their initial value. These findings were confirmed by the fluorescence image and photodegradation analysis (Fig. 6). In contrast, substantial fading was clearly observed in the imaged MGC-803 cells using FITC and TRITC as double immunoflu-

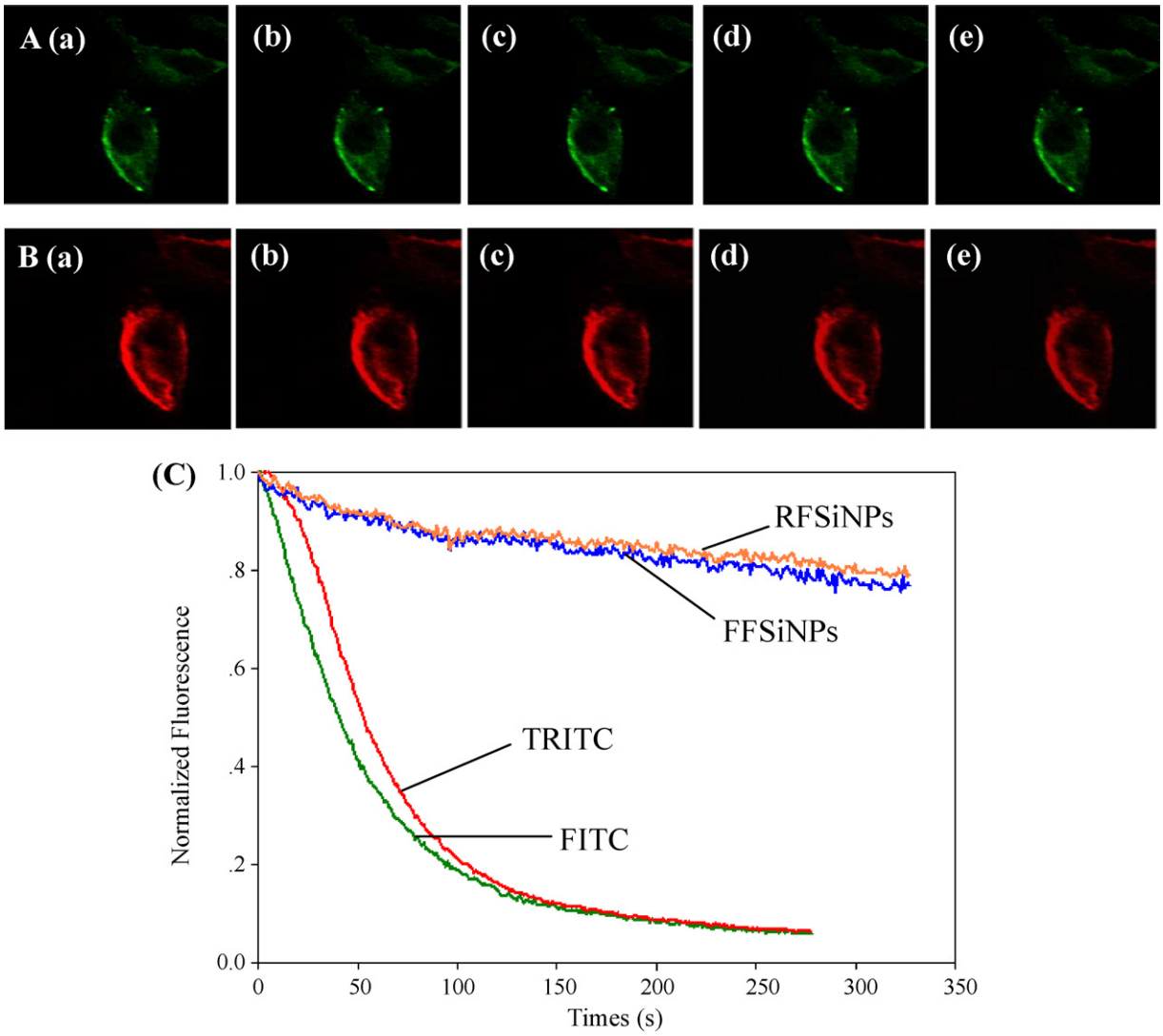

Fig. 6. Photostability of imaged MGC-803 cells using the bioconjugated FSiNPs-based double immunofluorescence staining. (A) Imaged MGC-803 cells in channel 1. (B) Imaged MGC-803 cells in channel 2. a, b, c, d, and e were taken 0 min, 1 min, 2 min, 5 min, and 10 min of continually intense excitation, respectively. (C) Photodegradation comparison of FSiNPs-based (FFSiNPs and RFSiNPs) double immunofluorescence staining and fluorochromes-based (FITC and TRITC) double immunofluorescence staining (channel 1: PMT 750 V; laser intensity 10.0, gain power 1.7. Channel 2: PMT 650 V; laser intensity 10.0, gain power 1.7).

orescence staining under the same experiment condition. It demonstrated that the bioconjugated FFSiNPs and RFSiNPs-based double immunofluorescence staining also possessed much better photostability.

3.2.4. Ex vivo imaging of MGC-803 cells

After successfully imaging the MGC-803 cells in vitro using anti-CEA antibody-conjugated FFSiNPs and anti-CK19 antibody-conjugated RFSiNPs-based double immunofluorescence staining,

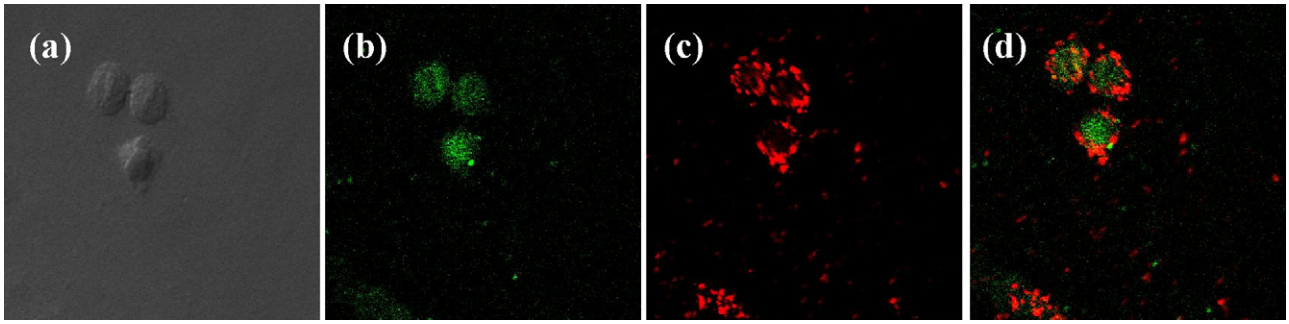

Fig. 7. Bioconjugated FSiNPs mediated double immunofluorescence images by CLSM of ex vivo primary MGC-803 gastric cancer cells samples came from the tumor tissues of mice bearing the MGC gastric cancer tumor xenografts. a, b, c, and d were represented the images acquired in bright-field, channel 1 (green signal), channel 2 (red signal) and merged images of the green channel and the red channel (channel 1: PMT 750 V; laser intensity 10.0, gain power 1.7. Channel 2: PMT 650 V; laser intensity 10.0, gain power 1.7).

we then did ex vivo MGC-803 cells imaging using the FFSiNPs and RFSiNPs-based double immunofluorescence staining. Firstly, ex vivo MGC-803 cells gained from the tumor tissues of mice bearing the MGC gastric cancer tumor xenografts were cultured to a confluent state and followed by incubation with mixture of anti-CEA antibody-conjugated FFSiNPs and anti-CK19 antibody-conjugated RFSiNP as the same procedure of in vitro cultured MGC-803 cells treatment. Then the incubated ex vivo MGC-803 cells were imaged by CLSM with the same arrangement of PMT gain and filter for signals collection. As demonstrated in Fig. 7, green fluorescence signal and red fluorescence signal were, respectively, visualized in channel 1 and channel 2. Some co-localization shown as yellow was obtained by simultaneous acquisition of data in both channels. It was proposed that the ex vivo primary MGC-803 cells gained from the tumor tissues of mice bearing the MGC gastric cancer tumor xenografts could still be successfully imaged using labeling in this fashion of anti-CEA antibody-conjugated FFSiNPs and anti-CK19 antibody-conjugated RFSiNPs double immunofluorescence staining, which maybe applicable for MGC gastric cancer tumor imaging in vivo.

4. Conclusions

In summary, an improved double immunofluorescence staining based on FFSiNPs and RFSiNPs has been developed for imaging of target cells. Because there was no obvious FRET between FFSiNPs and RFSiNPs, successful visualization of dual staining without crosstalk under the simultaneous excitation with the 488-nm line of an argon ion laser by CLSM can be obtained by use of appropriate settings for PMT gain and emission filter of 505–525-nm bandpass and 560-nm longpass. In this study, the in vitro imaging of MGC-803 cells has been successfully realized by using of the bioconjugated FSiNPs mediated double immunofluorescence staining. This relies on the use of antigen–antibody recognition of CEA and CK19 in the MGC-803 cells with the anti-CEA antibody and anti-CK19 antibody on FFSiNPs and RFSiNPs, respectively, together with the green and red signal during the double immunofluorescence staining procedure. Other control cells groups, including COS-7 cells, Hela cells, and 1E8 cells did not obtained the same imaging results. Moreover, the bioconjugated FSiNPs mediated double immunofluorescence staining was superior to the conventional double immunofluorescence staining using green-emitting and red-emitting dyes in photostability. The further demonstration of imaging of MGC-803 cells from tumor tissues of mice bearing the MGC gastric cancer tumor xenografts confirmed this new bioconjugated FSiNPs mediated double immunofluorescence staining was reliable to effectively imaging interested cells. The bioconjugated FSiNPs mediated double immunofluorescence staining will be promising approach in bioimaging for early diagnosis of disease, cancer metastasis and so on.

Acknowledgements

This work was partially supported by the National Key Basic Research Program (2002CB513100-10), Key Technologies Research and Development Programme (2003 BA310A16), Program for New Century Excellent Talents in University (NCET-06-0697), National Science Foundation of P.R. China (90606003, 20405005, 20775021) and Outstanding Youth Foundation of Hunan Province (06JJ10004).

References

[1] J.R. Kelley, J.M. Duggan, J. Clin. Epidemiol. 56 (2003) 1.
[2] M.S. Karpeh, D.P. Kelsen, J.E. Tepper, in: V.T. DeVita, S. Hellman, S.A. Rosenberg (Eds.), Cancer: principles and practice of oncology, 6th ed., Lippincott Williams & Wilkins, Philadelphia, 2001.
[3] J.C. Layke, P.P. Lopez, Am. Fam. Physician 69 (2004) 1133.
[4] S. Nishida, D. Ichikawa, D. Ichikawa, Anticancer Res. 20 (2000) 2155.
[5] E. Oki, Y. Maehara, E. Tokunaga, K. Shibahara, S. Hasuda, Y. Kakeji, K. Sugimachi, Cancer Lett. 188 (2002) 191.
[6] Y. Fujita, M. Terashima, Y. Hoshino, S. Ohtani, S. Kashimura, N. Kanzaki, F. Osuka, M. Kogure, M. Gotoh, Gastric Cancer 9 (2006) 308.
[7] X.B. Liao, W.P. Tang, Q.M. Zhang, Z.G. Fu, Y.H. Zhao, China Natl. J. New Gastroenterol. 3 (1997) 90.
[8] M. Ishikawa, J. Kitayama, S. Kazama, H. Nagawa, World J. Surg. Oncol. 3 (2005) 1.
[9] X.Y. Meng, W.J. Lu, H. Zhang, W.Q. Wang, X.X. Lv, Pract. J. Cancer 8 (2003) 68.
[10] B.K. Zehentner, Expert Rev. Mol. Diagn. 2 (2002) 89.
[11] M. Fukunaga, T. Monden, H. Nakanishi, M. Ohue, K. Fukuda, N. Tomita, T. Shimano, T. Mori, Am. J. Clin. Pathol. 101 (1994) 177.
[12] M. Hara, H. Nakanishi, Q. Jun, Y. Kanemitsu, S. Ito, Y. Mochizuki, Y. Yamamura, Y. Kodera, M. Tatematsu, T. Hirai, Clin. Exp. Metastasis 3 (2007) 179.
[13] J.H. Shin, H.O. Kim, Aliment Pharmacol. Ther. 2 (2002) 137.
[14] M.F. McCarty, J. Wey, O. Stoeltzing, W.B. Liu, F. Fan, C. Bucana, P.F. Mansfield, A.J. Ryan, L.M. Ellis, Mol. Cancer Ther. 3 (2004) 1041.
[15] G.Y. Wang, S.J. Wang, Y. Li, L.L. Wang, X.L. Wang, Z.Q. Song, L.Q. Fan, Chin. J. Cancer 5 (2004) 559.
[16] W.C.W. Chan, S.M. Nie, Science 281 (1998) 2016.
[17] J.M. Bruchez, M. Moronne, P. Gin, S. Weiss, A.P. Alivisatos, Science 281 (1998) 2013.
[18] S.L. Gac, I. Vermes, A. Berg, Nano Lett. 6 (2006) 1863.
[19] S.Z. Wang, B.R. Jarrett, S.M. Kauzlarich, A.Y. Louie, J. Am. Chem. Soc. 129 (2007) 3848.
[20] T. Powell, J.Y. Yoon, Biotechnol. Prog. 22 (2006) 106.
[21] H. Ow, D.R. Larson, M. Srivastava, B.A. Baird, W.W. Webb, U. Wiesner, Nano Lett. 5 (2005) 113.
[22] M. Nakamura, M. Shono, K. Ishimura, Anal. Chem. 79 (2007) 6507.
[23] Z. Ye, M. Tan, G. Wang, J. Yuan, Anal. Chem. 76 (2004) 513.
[24] X.J. Zhao, L.R. Hilliard, S.J. Mechery, Y. Wang, R.P. Bagwe, S. Jin, W.H. Tan, Proc. Natl. Acad. Sci. U.S.A. 101 (2004) 15027.
[25] W.H. Tan, K.M. Wang, X.X. He, X.J. Zhao, T. Drake, L. Wang, R.P. Bagwe, Med. Res. Rev. 24 (2004) 621.
[26] X.X. He, K.M. Wang, W.H. Tan, J. Li, S.S. Huang, Y.C. Xia, X.H. Yang, D. Li, J. Nanosci. Nanotechnol. 2 (2002) 317.
[27] X.X. He, J.H. Duan, K.M. Wang, W.H. Tan, X. Lin, C.M. He, J. Nanosci. Nanotechnol. 4 (2004) 585.
[28] X.X. He, J.Y. Chen, K.M. Wang, D.L. Qin, W.H. Tan, Talanta 72 (2007) 1519.
[29] H. Shi, X.X. He, K.M. Wang, Y. Yuan, K. Deng, J.Y. Chen, W.H. Tan, Nanomed. Nanotechnol. Biol. Med. 3 (2007) 266.
[30] G.W. Zhang, Chin. Med. J. 99 (1986) 835.
[31] S. Shimada, Y. Yagi, K. Shiomori, U. Honmyo, N. Hayashi, A. Matsuo, T. Marutsuka, M. Ogawa, Surgery 129 (2001) 714.
[32] R.K. Kumar, C.C. Chapple, N. Hunter, J. Histochem. Cytochem. 47 (1999) 1213.
[33] L.J.F. Hefta, M. Neumaier, J.E. Shively, Immunotechnology 4 (1998) 49.
[34] M.T. Machado, F. Fonseca, A.P. Fantinato, I. Bendit, M.L. Wroclawski, E. Wroclawski, A. Giglio, Tumori 91 (2005) 248.

Talanta 76 (2008) 1189–1193

Contents lists available at ScienceDirect

Talanta

journal homepage: www.elsevier.com/locate/talanta

Direct determination of ammoniacal nitrogen in water samples using corona discharge ion mobility spectrometry

M.T. Jafari, T. Khayamian*

Department of Chemistry, Isfahan University of Technology, Isfahan 84156-83111, Iran

ARTICLE INFO

Article history:
Received 6 April 2008
Received in revised form 12 May 2008
Accepted 15 May 2008
Available online 28 May 2008

Keywords:
Ammoniacal nitrogen
Water
Corona discharge
Ion mobility spectrometry

ABSTRACT

In this study, direct determination of ammoniacal nitrogen residues in water samples using corona discharge ion mobility spectrometry (CD-IMS) was investigated. Pyridine was used as an alternate reagent gas to enhance selectivity and sensitivity of the method. The results indicate that the limit of detection (LOD) was about 9.2×10^{-3} μg mL^{-1} and the linear dynamic range was obtained from 0.03 to 2.00 μg mL^{-1}. The relative standard deviation was about 11%. Furthermore, this method was successfully applied to the direct determination of ammoniacal nitrogen in river and tap water samples and the results were compared with the Nessler method. The comparison of the results validates the potential of the proposed method as an alternative technique for the analysis of the ammoniacal nitrogen in water samples.

1. Introduction

The analysis of ammoniacal nitrogen, which represents the sum of the ammonia and ammonium compounds, is especially important in water samples. The microbial degradation of nitrogenous organic material is one of the most important sources for producing of ammoniacal nitrogen in a river [1]. These compounds are transferred into the environment through the different sources such as cattle excrement, waste incineration, sewage treatment, and car exhausts [2]. In addition, ammoniacal nitrogen is originated by releasing of fertilizers, industrial emissions, and volcanic activity. Ammoniacal nitrogen has been known to be responsible for hygienic problems in environmental waters as well as reduction of growth for farmed animals. The monitoring of aqueous ammonia provides important information about water quality in various samples such as drinking, river, and waste waters. The aqueous ammonia concentration above 0.2 mg L^{-1} may be hazardous to many aquatic organisms [1]. Therefore, the sensitive and selective method is required for the determination of ammonia/ammonium in the aquatic ecosystems. Two major factors that influence selection of the method to determine ammonia are concentration and presence of interferences [3].

Ammoniacal nitrogen has been determined using various methods including classical and instrumental methods. The standard methods such as the Nessler reaction, the Indophenol Blue method, and the Kjeldahl method were recommended for the examination of water and wastewater for ammoniacal nitrogen [4–7]. However, there is a possibility of interferences from amines or other organic chemicals in these methods. Traditional instrumental methods such as: potentiometric [8], conductometric [9], fluorometric [10,11], reflectance spectroscopy [12], flow injection [13,14], liquid chromatography [15,16], and ion mobility spectrometry [1,17,18] have also been used for analysis of ammoniacal nitrogen. The measurement of ammoniacal nitrogen by UV spectrophotometry is useful only in clean water due to interferences from turbidity and from both inorganic and organic compounds. Colorimetric methods suffer from serious interferences, poor reproducibility and sensitivity, or tedious procedures and undesirable reagents [19,20]. The ammonia electrode is extremely sensitive to temperature changes and there is a problem of losing possibility of ammoniacal nitrogen in alkaline solution due to temperature changes [21].

Ion mobility spectrometry (IMS) is another alternative technique for determination of ammoniacal nitrogen. The IMS is a sensitive, simple, fast, and portable analytical technique for the detection of volatile organic compounds (VOCs) at low concentration. It plays an important role in practical application such as industrial and environmental monitoring and, drug and explosives detection [22]. The IMS works in positive and negative modes. In the positive mode of IMS, the analyte is ionized in ion-molecular exchange reactions with reactant ions, which are commonly hydrated protons. Ionization source is one of the key parts of the instrument and ^{63}Ni is a common ionization source for IMS, Przybylko et al. [1] determined the aqueous ammonia using

* Corresponding author. Tel.: +98 311 391 2351; fax: +98 311 391 2350.
E-mail address: taghi@cc.iut.ac.ir (T. Khayamian).

0039-9140/$ – see front matter © 2008 Elsevier B.V. All rights reserved.
doi:10.1016/j.talanta.2008.05.028

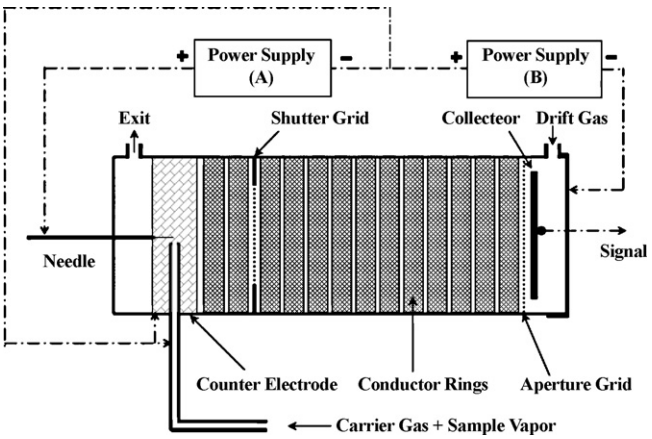

Fig. 1. Schematic diagram of the corona discharge ion mobility spectrometer (CD-IMS) used in this work.

^{63}Ni-IMS technique by thermally extracting the ammonia through a silicon membrane and passing the vapors into the instrument. Their data have indicated the detection limit of 1.2 mg L^{-1}, although, they noted lower concentrations were attainable. In this decade, we have investigated the capability of continuous corona discharge as an ionization source for IMS in both positive [23] and negative modes [24]. The advantage of corona discharge as an ionization source over ^{63}Ni is a higher total ion current by about an order of magnitude. This, results a better sensitivity, a higher signal-to-noise and a wider dynamic range.

Due to the low limits of detection (LODs) of IMS and its response to the numerous organic functionalities, the ion mobility spectra are complicated by matrix effects if the analyte is in real sample [25]. In order to remove background interferences and to enhance sensitivity, reagent gases may be used to create alternate reactant ions that provide additional selectivity in the response. Ammonium, acetone, and halide ions were used as alternate reagent ions to improve the selectivity of some compounds under the positive and negative operation modes [18,26–28]. The subject of alternate reagent ion chemistry in IMS has been an interesting research topic [29].

The objective of this study is to evaluate the potential use of CD-IMS for direct quantitative analysis of ammoniacal nitrogen in various water samples. Pyridine has also been used as the alternate reagent ions to improve the selectivity of the proposed method.

2. Experimental

2.1. Apparatus

The IMS apparatus with corona discharge as the ionization source in the positive mode has been described previously [23]. All the parts of the IMS utilized in this work are the same as previously described except sample introduction system. The schematic diagram of the cell and the sample introduction system are shown in Fig. 1. In summary, the glass tube (i.d. 4 cm and 9 cm long) mounted with 20 stainless steel guard rings, located 1 mm from each other, was used as the IMS cell. The guard rings are connected by a series of resistors to form the electric field. The corona electrode is a sharp needle, made of stainless steel that is fixed at one end of the cell. In the positive mode of IMS, the analyte is ionized in ion-molecular exchange reactions with reactant ions. These ions are injected electronically from the ion source region into the drift region by means of ion gate. In the drift region, ions are separated based on their mobility. A brass tube (i.d. 3 mm and o.d. 6 mm), located orthogonally with respect to the corona needle, and was used to carry out the sample to the cell. The vapor of pyridine was injected to the carrier gas by a syringe pump to provide a certain concentration of sample which could be varied by adjusting of the pump speed. The optimum experimental conditions for obtaining the ion mobility spectra of the compounds are given in Table 1.

Table 1
IMS operation parameters

Parameter	Setting
Corona voltage	2.00 kV
Drift field	530 V cm^{-1}
Drift gas flow (N_2)	500 mL min^{-1}
Carrier gas flow (air)	250 mL min^{-1}
Drift tube temperature	150 °C
Inlet temperature	150 °C
Drift tube length	11 cm
Reagent gas	Pyridine
Shutter grid pulse	100 μs

2.2. Sample introduction system

The sample introduction system which is based on purging method was selected for injection of the analyte to the IMS. This separation technique removes the volatile compounds from a liquid by diffusion of these materials into a stream of gas bubbles passing through it [30]. In this work, the sample introduction system consisted of a gas washing bottle (150 mL), a rotameter for measuring the gas flow rate and Teflon tubing for connections. Each aqueous standard solution of ammonia was transferred into the washing bottle. A sodium hydroxide pellet was then added to the solution to raise the pH of the sample 2–3 units above the pK_a value of NH_4^+. The pH was checked using a pH meter (Corning M140, England). Then, the pure nitrogen with a flow rate of 50 mL min^{-1} was bubbled through the solution. The outlet of the washing bottle was connected to the IMS cell by Teflon tube and the analyte was transferred by nitrogen into the IMS cell.

2.3. Chemicals and solutions

Ammonia solution (25%) and hydrochloric acid were purchased from Merck. Sodium carbonate (analytical grade) for standardizing of hydrochloric acid and sodium hydroxide were also prepared from Merck. Stock standard solution (20 mg L^{-1} ammonia equivalent at elevated pH), was prepared by dissolving 0.047 g of ammonium nitrate (Riedel-deHaen) in triply-distilled water and making up to 500 mL. Working solutions were prepared by successive dilution of the stock solutions for these compounds. Since ammonia concentration in water samples easily varies with time during the storage of samples, fresh samples should be analyzed immediately after sample collection for most reliable results.

3. Results and discussion

In this work, the selectivity to ammonia was achieved by doping the carrier gas with low levels of pyridine, delivered by a syringe pump. In the presence of triply-distilled water as the blank, pyridine produces a dominant reactant ion species believed to be a hydrated protonated pyridine, as shown in Fig. 2. This figure shows the ion mobility spectra of background before and after the doping of pyridine at the optimized conditions of IMS. The ion mobility spectrum of background before doping of pyridine shows two peaks labeled RIP_1 and A, with reduced mobility values of 2.33 and 2.77 cm^2 V^{-1} s^{-1}, respectively. The comparison of the recorded mobility values with the reduced motilities of $H^+(H_2O)_n$

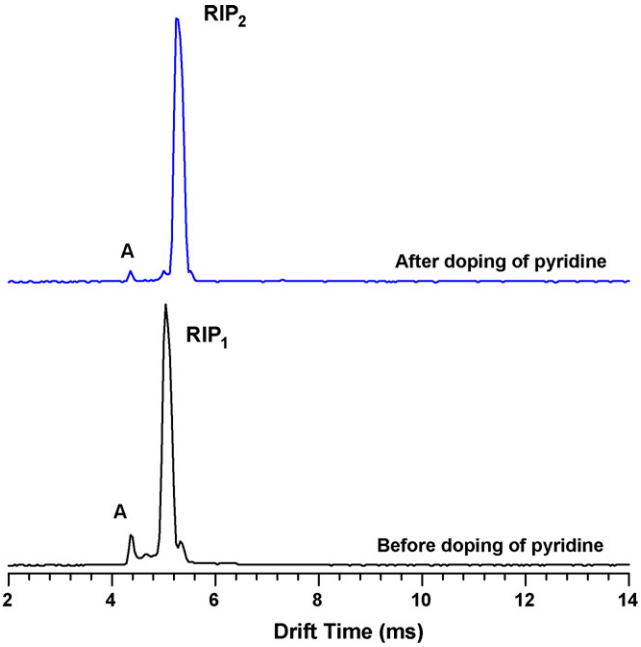

Fig. 2. The ion mobility spectra of the background before and after the doping of pyridine at the optimized conditions of IMS.

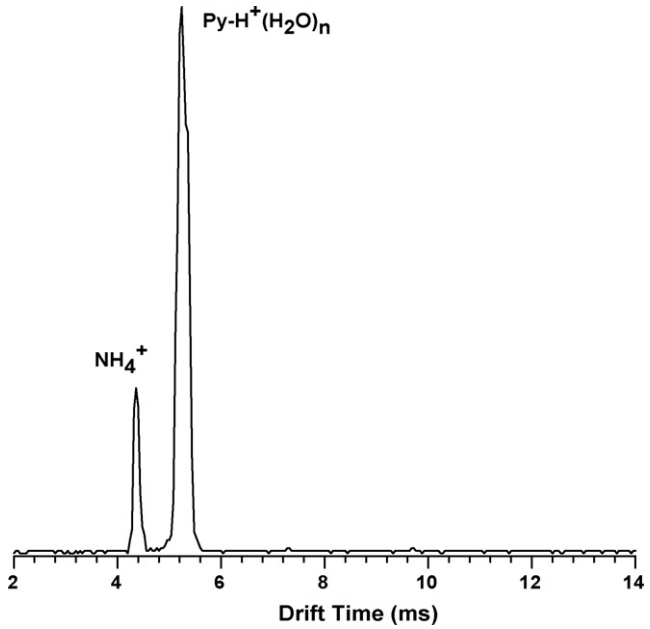

Fig. 3. The ion mobility spectrum of the standard solution of ammoniacal nitrogen (0.1 μg L^{-1}).

(2.32 $cm^2\ V^{-1}\ s^{-1}$) and NH_4^+ (3.00 $cm^2\ V^{-1}\ s^{-1}$) reported by Carroll et al. [31] at 160 °C confirms that the peaks of RIP_1 and A belong to $H^+(H_2O)_n$ and NH_4^+, respectively. Although, the major reactant ions produced in corona discharge are protonated water clusters, but trace impurity of ammonia in the ionization region also gives rise to production of hydrated NH_4^+ [32]. When pyridine was doped into the carrier gas, the ion peak of hydrated protonated pyridine (RIP_2) is raised and the height of $H^+(H_2O)_n$ and NH_4^+ are decreased. As a result, the major reactant ion in ion mobility spectrum of background, after doping of pyridine, is RIP_2. The reduced mobility of RIP_2 is 2.24 $cm^2\ V^{-1}\ s^{-1}$ that is much closed to 2.21 $cm^2\ V^{-1}\ s^{-1}$ reported by Karpas [33] for protonated pyridine. When the blank solution was replaced with the standard solution of ammonia, the height of NH_4^+ peak was increased. This increasing is proportional to ammonia concentration in aqueous solution. The ion mobility spectrum obtained after passing the purging gas through the ammonia solution (0.1 μg L^{-1}) is shown in Fig. 3. The reduced mobility and their corresponding standard deviations for all the ions in the ion mobility spectra of background are listed in Table 2.

3.1. Response of the analyte

Solvated ammonia partitions between the gas and aqueous phases and aqueous ammonia exists in equilibria with ammonium ions according to the equation of:

$$NH_3 + H_2O \rightleftharpoons NH_4^+ + OH^-$$

Therefore, raising the pH above $pK_a + 1$, converts almost all the ammonium ions to aqueous ammonia. At that pH, the measurement of the aqueous ammonia will present the ammoniacal nitrogen.

In this work, after raising the pH of the solution to about 12, the aqueous ammonia was introduced into the IMS cell. The selected

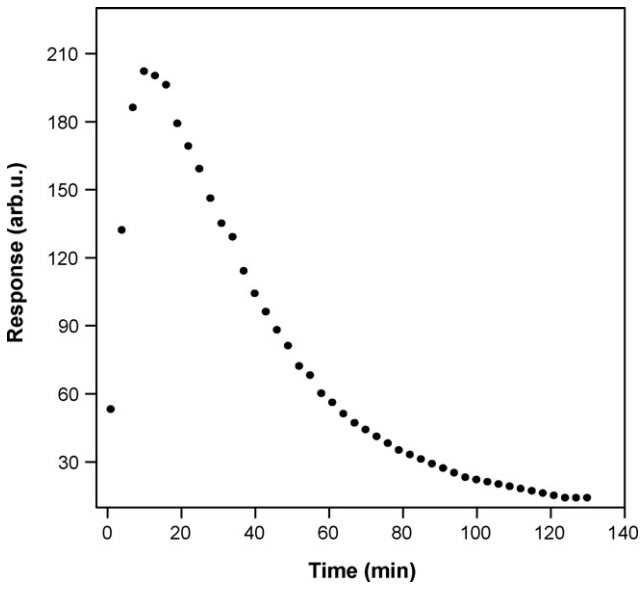

Fig. 4. Plot of ammoniacal nitrogen signal versus dilution time obtained by purging of aqueous solution (0.2 μg mL^{-1}).

Table 2
Characteristic ions for blank (before and after pyridine doping) and ammonia ion mobility spectra

Peak	Reduced mobility, K_0 ($cm^2\ V^{-1}\ s^{-1}$)	Drift time, t (ms)
RIP_1 ($H^+(H_2O)_n$)	2.33 ± 0.08	5.04
RIP_2 ($Py\text{-}H^+(H_2O)_n$)	2.24 ± 0.06	5.24
NH_4^+	2.76 ± 0.12	4.26

Table 3
Analytical parameters for determination of ammonia nitrogen using CD-IMS

Parameter	Value
Linear range (μg mL^{-1})	0.03–2.00
Correlation coefficient	0.9914
Limit of detection, LOD (μg L^{-1})	9.2
Relative standard deviation, %RSD (n = 3, 200 μg L^{-1})	10.8

Table 4
Statistical results for comparison of CD-IMS and nesslerization methods in ammoniacal nitrogen analysis

Water sample	NH_3-N found ($\mu g\,L^{-1}$)		$F_{exp.}$	$F_{tab.(0.05);2,2}$	S_{pooled}	$t_{exp.}$	$t_{tab.\,(98\%)}$
	CD-IMS	Nesslerization					
Ground water (IUT university)	<30	<40[a]	–	–	–	–	–
Tap water (Isfahan city)	<30	<40	–	–	–	–	–
Zayanderood river (Dorche)	68.3 ± 7.9	85.3 ± 6.5	1.5	19.0	7.2	2.9	3.8
Zayanderood river (Isfahanak)	107.3 ± 22.0	132.3 ± 20.8	1.1	19.0	21.4	1.4	3.8

[a] Limit of quantification (LOQ) of nesslerization method.

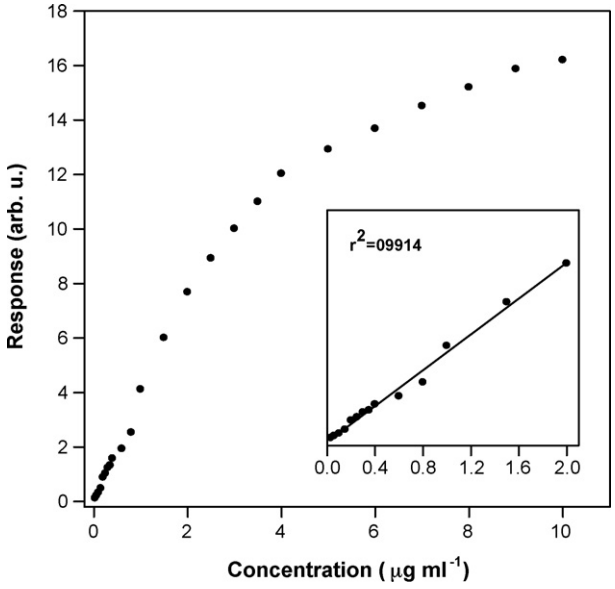

Fig. 5. Plots of IMS response against the concentration of ammoniacal nitrogen, the plot shown as onset of this graph shows the linear section of the calibration curve.

sample introduction system has a characteristic, which the amount of the analyte in the purging gas decreases during the dilution time. This phenomenon is shown for a solution of ammonia ($0.2\ \mu g\ mL^{-1}$) in Fig. 4. According to this figure, when the purged analyte injected into the carrier gas, the peak of the compound appears after a short time, reaches a maximum and decays almost exponentially. This figure shows that the height of the ammonia signal is dependent on the purging time and it decreases with time. The response of all analytes was measured after 10 min from beginning of the purging. In the proposed method, there is no difference between using air and nitrogen as the purging gas. However, using air is suitable for portable IMS in field screening.

3.2. Calibration curves

The calibration curve for the ammoniacal nitrogen was plotted and it is shown in Fig. 5. The linear range was from 30 to 2000 $\mu g\,L^{-1}$ and the correlation coefficient (R^2) was 0.9914. The working range is about three orders of magnitude for the compound. Limit of detection (LOD) of this method for determination of ammonia was $9.2\ \mu g\,L^{-1}$. The detection limit and dynamic range of the proposed method is superior to the previous reported values using ^{63}Ni-IMS. The limit of detection of $1200\ \mu g\,L^{-1}$ and a linear range of one order of magnitude for ammoniacal nitrogen have been reported [1]. In addition, ammonia in ethylene was also determined using ^{63}Ni-IMS with the detection limit of $25\ \mu g\,L^{-1}$ and a linear range of one order of magnitude [17]. The advantage of corona discharge as an ionization source over the conventional ^{63}Ni is an order of magnitude higher ion current [23]. The higher current also allows using narrower ion pulse widths, which might be improved the resolving power. According to previous results [23], we have shown the peak height is more than 2 nA, and the signal-to-noise ratio is clearly much higher than that of the ^{63}Ni ionization source for a single run spectrum. Therefore, the CD-IMS technique has a better sensitivity and a wider working range with respect to ^{63}Ni-IMS. The relative standard deviation percentage (RSD%) was found to be typically below 11% for ammoniacal nitrogen. The analytical parameters of the CD-IMS method for determination of ammoniacal nitrogen are given in Table 3.

3.3. Analysis of ammoniacal nitrogen in water samples

The proposed method was employed for analysis of the ammoniacal nitrogen in some environmental waters such as: Zayanderood river water at two different positions of Dorche and Isfahanak, the tap water of Isfahan city, and the ground water at Isfahan University of Technology (IUT). 100 mL of the water samples were transferred into the gas purging bottle and the nitrogen gas was passed through the samples at the elevated pH. In this method, pyridine was used as the reagent gas for enhancing the selectivity. According to the proton affinity values [22], the proton affinity differences between pyridine and many of organic compounds are very high. Therefore, there will not be any significant limitation caused by these compounds in the analysis of ammonia. The samples were also analyzed with a conventional spectrometric method using Nessler reagent according to standard methods committee [3]. The results of both methods are listed in Table 4 and the statistical results show that there is a good agreement between the results of two methods for analysis of ammoniacal nitrogen in these samples. The higher concentration in the Zayanderood water in Isfahanak position with respect to the Dorche position seems to be caused by sewage discharged from the houses. The results in Table 4 reveal the capability of the CD-IMS as an easy and rapid method for direct analysis of ammoniacal nitrogen in these samples.

4. Conclusions

Corona discharge ion mobility spectrometry (CD-IMS) was successfully applied for the determination of ammoniacal nitrogen in aqueous samples. This methodology is simple, fast and has the low detection limits, which reveal the capability of the method. Additionally, the analysis of the river and tap waters by CD-IMS yields good agreement with the Nessler method, thereby reinforcing the applicability of this technique as an alternative method for routine analysis.

Acknowledgements

The authors acknowledge to the Research Council of Isfahan University of Technology and Center of Excellency in Chemistry of Isfahan University of Technology for the support of this work.

References

[1] A.R.M. Przybylko, C.L.P. Thomas, P.J. Anstice, P.R. Fielden, J. Brokenshire, F. Irons, Anal. Chim. Acta 311 (1995) 77.
[2] A. Mirmohseni, A. Oladegaragoze, Sens. Actuators B 89 (2003) 164.
[3] A.E. Greenberg, L.S. Clesceri, A.D. Eaton, Standard Methods for the Examination of Water and Wastewater, 18th ed., EPS Group, Inc., Hanover, Maryland, 1992.
[4] M.J. Taras, A.E. Greenberg, R.D. Hoak, M.C. Rand, Standard Methods for the Examination of Water and Wastewater, 13th ed., American Public Health Association, Washington, DC, 1971.
[5] D. Scheiner, Water Res. 10 (1976) 31.
[6] H. Verdouw, C.J.A. Van Echteld, E.M.J. Dekkers, Water Res. 12 (1978) 399.
[7] B.M. Stewart, Water Res. 19 (1985) 1443.
[8] U. Fritsche, M. Gernert, Anal. Chim. Acta 244 (2003) 179.
[9] J.M.G. Laranjeira, W.M. Deazevedo, M.C.U. Dearaujo, Anal. Lett. 30 (1997) 2189.
[10] H. Mana, U. Spohn, J. Fresenius Anal. Chem. 366 (2000) 825.
[11] S. Meseguer Lloret, J. Verdú Andrés, C. Molins Legua, P. Campíns Falcó, Talanta 65 (2005) 869.
[12] Y. Moliner-Martínez, R. Herráez-Hernández, P. Campíns-Falcó, Anal. Chim. Acta 534 (2005) 327.
[13] Y.Y. Luo, R. Alothman, G.D. Christian, J. Ruzicka, Talanta 42 (1995) 1545.
[14] H. Shen, T.J. Cardwell, R.W. Cattrall, Anal. Chim. Acta 367 (1998) 193.
[15] B. Sahasrabuddhey, A. Jain, K.K. Verma, Analyst 124 (1999) 1017.
[16] M. Kaminski, D. Jastrzebski, A. Przyjazny, R. Kartanowicz, J. Chromatogr. A 947 (2002) 217.
[17] J.H. Cross, T.F. Limero, J.L. Lane, F. Wang, Talanta 45 (1997) 19.
[18] G.A. Eiceman, M.R. Salazar, M.R. Rodriguez, T.F. Limero, S.W. Beck, J.H. Cross, R. Young, J.T. James, Anal. Chem. 65 (1993) 1696.
[19] D. Jenkins, Prog. Water Technol. 8 (1977) 31.
[20] P.J. Rennie, A.M. Sumner, Analyst 104 (1979) 837.
[21] R.S. Siegel, Soil Sci. Am. J. 44 (1980) 943–947.
[22] G.A. Eiceman, Z. Karpas, Ion Mobility Spectrometry, 2nd ed., CRC Press, Boca Raton, 2005.
[23] M. Tabrizchi, T. Khayamian, N. Taj, Rev. Sci. Instrum. 71 (2000) 2321.
[24] M. Tabrizchi, A. Abedi, Int. J. Mass Spectrom. 218 (2002) 75.
[25] T. Khayamian, M. Tabrizchi, M.T. Jafari, Talanta 69 (2006) 795.
[26] S.H. Kim, F.W. Karasek, S. Rokushika, Anal. Chem. 50 (1978) 152.
[27] C.J. Proctor, J.F.J. Todd, Anal. Chem. 56 (1984) 1794.
[28] G.A. Eiceman, Y.F. Wang, G.G. Lizbeth, C.S. Harden, D.B. Shoff, Anal. Chim. Acta 306 (1995) 21.
[29] Y.T. Long, Y. Guo, M.Q. Lu, Anal. Chem. 70 (1998) 347.
[30] T. Khayamian, M. Tabrizchi, E. Jabarootian, Int. J. Ion Mobility Spectrom. 6 (2003) 1.
[31] D.I. Carroll, I. Dzidic, R.N. Stillwell, E.C. Horning, Anal. Chem. 47 (1975) 1956.
[32] M.M. Shahin, J. Chem. Phys. 45 (1966) 2600.
[33] Z. Karpas, Anal. Chem. 61 (1989) 684.

Talanta 76 (2008) 1246–1251

Contents lists available at ScienceDirect

Talanta

journal homepage: www.elsevier.com/locate/talanta

Simultaneous determination of trace amounts of borate, chloride and fluoride in nuclear fuels employing ion chromatography (IC) after their extraction by pyrohydrolysis

S. Jeyakumar, Vaibhavi V. Raut, K.L. Ramakumar*

Radioanalytical Chemistry Division, Bhabha Atomic Research Centre, Mumbai 400085, India

ARTICLE INFO

Article history:
Received 7 April 2008
Received in revised form 26 May 2008
Accepted 27 May 2008
Available online 3 June 2008

Keywords:
Borate
Chloride
Fluoride
Nuclear fuels
Pyrohydrolysis
Mannitol

ABSTRACT

An accurate and sensitive method based on the combination of pyrohydrolysis-ion chromatography (PH-IC) is proposed for the simultaneous separation and determination of boron as borate, chloride and fluoride in nuclear fuels such as U_3O_8, (Pu,U)C and Pu-alloys. The determination is based on the initial pyrohydrolytic extraction of B, Cl and F from the samples as boric acid, HCl and HF, respectively, which are subsequently separated by ion chromatography (IC). The proposed method significantly improves the existing analytical methodology as it combines the determination of boron, a critical trace constituent in nuclear materials, along with F^- and Cl^- for chemical quality control measurements. Various experimental parameters were optimized to achieve maximum recoveries of the analytes during the pyrohydrolysis and to get better ion chromatographic (IC) separation of borate, F^- and Cl^- along with other anions such as CH_3COO^-, NO_2^-, NO_3^-, Br^-, PO_4^{3-} and SO_4^{2-}. Recoveries of more than 93% could be obtained for all the analytes in the sample (0.5–1.5 g) at 1200 ± 25 K and distilled with pre-heated steam at the flow rate of 0.3 mL/min. An isocratic elution with a mobile phase of 0.56 M D-mannitol in 6.5 mM $NaHCO_3$ was used for the IC separation. The detection limits for B (as borate), F^- and Cl^- were 24, 13 and 25 $\mu g\,L^{-1}$, respectively. Precision of about 5% was achieved for determination of boron, Cl^- and F^- in the samples containing 1–5 ppm_w of boron, and 10–25 ppm_w of Cl and F. The method was validated with reference materials and successfully applied to the nuclear fuels. The methodology is easy to adapt on routine basis.

1. Introduction

Analytical methods have been playing a vital role in the quality control aspects of nuclear fuels. Some of the elements, when present even at trace or ultra trace level cause detrimental effects on the performance of the fuel and hence required to be determined accurately. For example, presence of F^- and Cl^- even at trace level can cause local depassivation of the oxide film on the surface of the clad leading to corrosion and eventual failure of the cladding [1]. Similarly, due to high thermal neutron absorption cross-section, boron can act as a neutron poison. Therefore, depending upon the type of the fuel, specification limits have been laid down for B, Cl and F. Hence, precise determination of these elements forms an indispensable part of the chemical quality control of nuclear fuels [2,3]. For this purpose, new analytical methodologies, which are simple, fast, require small sample size (safe handling of radioactive materials and minimum exposure to radiation), generate minimum waste and offer better precision and accuracy, are being developed. Though many techniques are available for analyzing boron at trace levels [4–8], spectrophotometry is widely used for its determination in various uranium based nuclear fuels and reactor grade materials [9,10]. In case of plutonium bearing materials ICP-AES [11] or ICP-MS [5,12] is widely employed. Boron is separated from the matrix prior to its determination employing solvent extraction [13,14], ion exchange [15,16], or methyl borate distillation [17,18]. It is well known that during the dissolution, separation and other stages of sample preparation, there exits possibility of boron loss causing erroneous results [19–21]. Pyrohydrolysis, a simple reagent-free separation technique, has been reported for the separation of boron in the fairly volatile boric acid form from metal borides at 1450–1475 K [22,8,23]. Also in nuclear industry, pyrohydrolysis is a well recognized separation method for the separation of F^- and Cl^- from various nuclear materials [3,24,25]. However, simultaneous extraction of boron along with F^- and Cl^- from these matrices has not been explored. Present investigation therefore explores the feasibility of separating B, Cl and F together in their acid form, employing pyrohydrolysis technique by optimizing its various parameters.

* Corresponding author. Tel.: +91 22 2559 3747; fax: +91 22 25505151.
E-mail address: klram@barc.gov.in (K.L. Ramakumar).

0039-9140/$ – see front matter © 2008 Elsevier B.V. All rights reserved.
doi:10.1016/j.talanta.2008.05.039

Ion chromatography (IC) coupled with conductivity detector is a powerful analytical technique for the simultaneous separation and quantification of anions or cations, preferably present in a clean matrix solution (like water) [26]. Pyrohydrolysis combined with IC is widely employed for the individual separation and determination of $F^-$and Cl^- in nuclear fuel materials [3,27] since the distillate obtained is as clear as water. Unlike the halides, direct IC of borate or boric acid is not possible because boric acid is a weak acid (pK_{a1} = 9.1). Separation of borate or boric acid on an anion exchanger is feasible only after converting the borate into a strong borate-polyol anion complex by the addition of mannitol, sorbitol or glycerol [28]. The possibility of analyzing borate, F^- and Cl^- in a single IC run has been explored by the addition of either mannitol or sorbitol in hydroxide eluent and the same has been extended to the water samples of pharmaceutical interest, where the separation was limited up to the elution of Cl^- only [29]. This procedure, however, could not be extended to the simultaneous determination of borate, F^- and Cl^- in pyrohydrolysed distillates obtained from the nuclear fuel materials mainly because the Cl^- peak could not be resolved from other anions due to poor selectivity.

The aim of the present work was therefore to propose a pyrohydrolysis-ion chromatography (PH-IC) combined method for standardizing a simultaneous separation and determination methodology for boron as borate-mannitol anion complex, F^- and Cl^- in presence of other common anions in nuclear fuel materials. Since pyrohydrolysis converts the non metallic impurities into their corresponding acids and thereby produces the acid radicals such as borate, F^-, Cl^-, NO_2^-, NO_3^-, PO_4^{3-}, SO_4^{2-} etc., there is a need for an IC methodology, which is capable of separating borate, $F^-$and Cl^- with desired resolutions and eluting the other anions for better column performance.

For meeting this purpose, two different types of anion exchange separator columns with OH^- and HCO_3^- mobile phases were examined in the present study which is discussed in two parts. The first part deals with the development of an IC procedure for the simultaneous separation and determination of borate, F^- and Cl^- in presence of other anions and the second part focuses on the optimization of pyrohydrolysis conditions to obtain maximum recoveries of the analytes in the distillate. The proposed methodology was validated with standard reference materials and successfully applied to (Pu,U)C, Pu-alloy and U_3O_8 samples.

2. Experimental

2.1. Instrumentation

The IC system used in the present study was DX500 (Dionex CA, USA) consisting of an isocratic solvent delivery pump (IP-20), a conductivity detector (ED 50A) and an Anion Self-Regenerant Suppressor (ASRS-II). The samples were injected through a 100 μL loop fitted to a Rheodyne six port injector. The separator columns used were IonPac AS4A-SC, 250 mm × 4.6 mm with its guard column AG4 (Dionex CA, USA) and IC-Pak A (Waters, Japan), 50 mm × 4.6 mm, with its anion guard insert. Part of the equipment consisting of injector, column(s), suppressor, conductivity cell of the detector and waste collection bottle was set inside an active fume hood for the safe handling and analyses of the active sample solutions. Pyrohydrolysis of samples was performed in an all Quartz apparatus installed in a radioactive glove box. The details of the apparatus including the modifications incorporated in the system for the pyrohydrolysis of radioactive materials and to minimize the activity in the distillate were described elsewhere [30]. All pH measurements were made on a CL-5 pH meter (Toshniwal, India).

2.2. Reagents and solutions

Analytical grade (AR) reagents were used. Standard stock solutions having 1000 mg L^{-1} of chloride, fluoride, bromide, nitrite, nitrate, phosphate and sulphate were prepared by dissolving calculated amount of their corresponding sodium salts of 99.9% purity (Merck, Germany). Standard boron solution of similar concentration was prepared by dissolving known amount of boric acid (GR-ACS, Merck, Germany). High purity deionised water having 18.2 MΩ specific resistance was obtained from a Milli Q water system (Millipore, USA) and used for preparation of all the solutions. The eluents were prepared with NaOH, D-mannitol (GR-ACS, Merck, Germany) and $NaHCO_3$ (AR grade, Thomas Baker, India) and filtered through nylon membrane filters (0.45 μm) before use.

3. Results and discussion

3.1. Ion chromatography separation

Since for the IC separation of boric acid or borate anion on an anion exchanger, conversion to borate-polyol anionic form is a prerequisite due to the very weak dissociation of boric acid K_a is 6×10^{-10} (pK_a 9.1) [31]. In the present study, D-mannitol was chosen as complexing polyol because the formation and stability of borate-mannitol complexes were well studied [32–34]. Among the various complexes formed, from the IC separation point of view, the complex $B(H_2L)_2^-$ is useful as it is the most abundant anion when the pH of the medium is above 4.1 [29]. Further, the same study explored the possibility of analyzing the borate, F^- and Cl^- ions in a single run by using IonPac AS4A-SC column and an eluent of 0.8 M D-mannitol in 5 mM NaOH, where the eluent composition was arrived at considering the available thermodynamic data [32] for the formation of $B(H_2L)_2^-$ and the weak elution strength of NaOH, which can separate the weakly retained ions like $B(H_2L)_2^-$, F^- and acetate. However, the study did not include those anions exhibiting stronger retention than Cl^-. During our preliminary investigations, the same procedure was followed with a view to analyzing the distillates obtained from the pyrohydrolysis of nuclear fuels for borate, F^- and Cl^- along with other common anions (e.g. NO_2^-, NO_3^- etc.). We used an Anion Self-Regenerant Suppressor (Dionex-ASRS) to lower the background conductivity in place of an Anion Micro Membrane Suppressor (Dionex-AMMS-1). A standard solution containing mixture of boric acid, F^-, Cl^-, NO_2^-, Br^-, NO_3^-, PO_4^{3-} and SO_4^{2-} was injected and the following were observed.

(i) The eluent could separate the $B(H_2L)_2^-$ from F^- but it could not separate the Cl^- peak from NO_2^-, which showed very similar retention behaviour as that of Cl^-.
(ii) The ions that have retentions more than Cl^- got eluted very slowly and ultimately produced a bulk unresolved peak which continued for 45 min and this impaired base line stability and the separation quality in the subsequent injections. The difficulty of eluting these strongly retained peaks may be circumvented by employing a gradient elution with NaOH, however, it could not be resorted as the IC system available was configured with isocratic solvent delivery pump.
(iii) A negative peak (dip) appeared between $B(H_2L)_2^-$ and F^- peaks, due to which proper fixing of the base line for both the peaks was not possible making precise determination of both borate and F^- difficult. This was the case even when standard solutions were injected in eluent.

The above limitations necessitated for another separator column which could provide better selectivity for these ions.

3.2. Selection of separation column

The IonPac AS4A-SC (capacity: 20 μeq. per column; working pH range: 0–14) used in the above studies is packed with ethyl vinyl benzene cross linked with 55% of divinyl benzene having alkanol quaternary ammonium functional group and was designed to bring fast separation among the common anions using CO_3^{2-}/HCO_3^- buffer eluents. With low strength NaOH, it is unable to elute the strongly retained anions, though it exhibits good selectivity for the weak anions. Hence, a separator column that exhibits good selectivity for both weak and strong anions is required for the isocratic separation. In general, methacrylate polymer based strong anion exchangers with quaternary ammonium functional group show more hydrophilic behaviour and good selectivity than the vinyl benzene polymer based columns for majority of the common anions including the weakly retained ions. In view of this, IC-Pak A, a short length methacrylate polymer based column (50 mm × 4.6 mm; capacity: 30 μeq. per column; working pH range: 2–12) was chosen and separations were performed on this column with the same eluent composition as in the case of IonPac AS4A-SC. The column showed good selectivity for $B(H_2L)_2^-$, which got eluted after 4 min and the Cl^- was well separated from its neighboring nitrite. However, the other anions were not eluted from the column due to low concentration of NaOH. In order to elute the strongly retained ions, the strength of NaOH eluent could not be increased because such increase would have raised the pH of the eluent, which is detrimental to the column integrity and performance. So, under such condition, there is a need for an alternate eluent, which can circumvent these limitations.

3.3. Selection of mobile phase

The selection of a mobile phase for the isocratic separation and determination of borate along with other common anions depends on four important factors:

(i) the eluent should separate both weakly and strongly retained anions with appreciable resolution between them.
(ii) The pH of the modified eluent after addition of D-mannitol should be more than 8 (for facilitating the formation of the $B(H_2L)_2^-$ complex kinetically faster).
(iii) The eluent should be compatible with the ASRS suppressor and amenable to ion suppression.
(iv) The resultant pH of the eluent after suppression and before detection should be more than 4.1 for the stability of the $B(H_2L)_2^-$ complex.

Therefore, in suppressed IC, the choice of mobile phase is limited to OH^-, HCO_3^- and CO_3^{2-} in direct or modified forms. Sodium hydrogen carbonate (HCO_3^-) was chosen as its elution strength lies in between the weaker OH^- and stronger CO_3^{2-}. The pH of 2 to 10 mM HCO_3^- solutions having 0.8 M D-mannitol was found to be between 8.8 and 9.2. At the suppressor the HCO_3^- gets converted into H_2CO_3 (weak acid) resulting in drastic reduction in the pH which could be calculated from the K_{a1} value (4.5×10^{-7}) of H_2CO_3 [35]. The values obtained were between 4.2 and 4.3 and this was also confirmed experimentally by measuring the pH of the suppressed eluents collected at the suppressor outlet. This pH range is suffice for the stability of $B(H_2L)_2^-$. The deprotonation of D-mannitol (pK_{a1} = 13.1, pK_{a2} = 13.8) [36] had negligible contribution in changing the eluent-pH due to its very high pK_a values. However, during the suppression, the protonation of $B(H_2L)_2^-$ occurs, which can cause variation in the eluent-pH and the degree of variation depends on the amount of boron present in the sample. In the present case, the variation is negligible as the methodology deals with boron in μM concentration. Therefore, by considering the formation, stability aspects of $B(H_2L)_2^-$s and amenability towards ion suppression for better detection, HCO_3^- eluent was chosen for further investigation.

3.4. Optimization of mobile phase conditions

(i) Effect of concentration of HCO_3^-

To study the elution behaviour of eight anions such as $B(H_2L)_2^-$, F^-, Cl^-, Br^-, NO_2^-, NO_3^-, HPO_4^{2-} and SO_4^{2-} with eluents of varying concentrations of HCO_3^- in 0.8 M D-mannitol, for each eluent composition, the total time of separation, resolution between adjacent peaks and peak symmetry were examined. Since, in general, the acetate and F^- have close retentions on an anion exchanger, the standard solution was spiked with acetate and the separations were carried out. In Fig. 1, the log(retention factors) as a function of log [HCO_3^-] are presented for all the ions under investigation and the plots resulted linearity with negative slopes, which suggests that the modified hydrogen carbonate eluent follows anion exchange mechanism for separation. When the HCO_3^- concentration was more than 8 mM, the resolution between the peaks of NO_3^- and HPO_4^{2-} became poor and at 10 mM, they got merged as an unresolved singlet peak, where the $B(H_2L)_2^-$ peak eluted along with the excluded water peak. Based on these results, an eluent composition 0.8 M D-mannitol in 6.5 mM HCO_3^- was found to be the optimum to realise all the chromatographic parameters in the acceptable range. Fig. 2 shows a typical chromatogram obtained under the optimized condition for a standard solution containing mixture of nine anions. The earliest eluted anion $B(H_2L)_2^-$ was well resolved from both F^- and the excluded water dip and an insert in Fig. 2 exhibits the same.

(ii) Effect of concentration of D-mannitol

Though 0.8 M D-mannitol in 6.5 mM HCO_3^- eluent brought out the desired separation, the use of mannitol at such high concentration caused certain serious practical difficulties. The 0.8 M D-mannitol solution behaves like a saturated solution and it resulted in undesirable deposition of mannitol on the flow lines of the IC system. With respect to the suppressor, both ASRS and AMMS are membrane based and can tolerate a maximum flow pressure of 100 psi only. The slow deposition of mannitol occurring at the membrane surface increases the suppressor

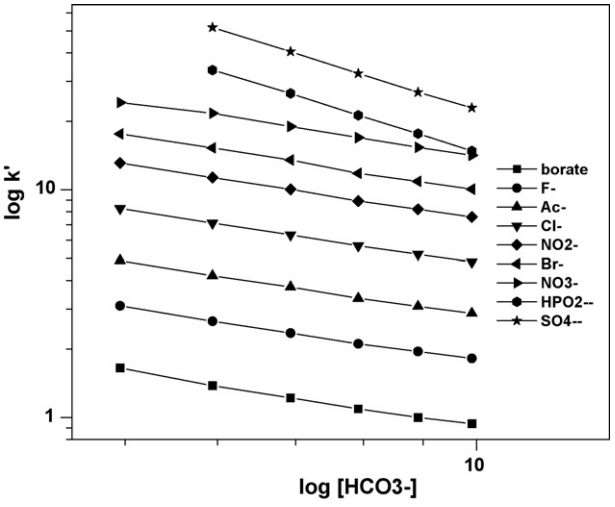

Fig. 1. Dependence of logarithms of retention factors on logarithms of concentration of eluting anion (HCO_3^-). Column: Waters IC-Pak A, 50 × 4.6 mm. Mobile phases: 5–10 mM HCO_3^- + 0.8 M mannitol.

pressure which not only deteriorates the suppression process but also leads to permanent damage to the suppressor. This necessitates cleaning of the suppressor after every two or three sample runs, which is practically difficult. The deposition of dissolved mannitol on the membrane surface is not expected one as the cation exchange membrane of the suppressor will not have any affinity for the neutral organic mannitol. However, this deposition might be resulting because the mannitol solution is exposed to relatively larger surface of the membrane from the narrow flow tubing. In order to circumvent this problem, the mannitol concentration in the eluent needs to be reduced and such a reduction should not effect a change in the formation of $B(H_2L)_2^-$ complex and other optimized chromatographic parameters. From the chromatographic point of view, the effect of mannitol concentration on the complex formation with boric acid was not investigated earlier and such an investigation is essential to know if any significant changes would occur in the elution of $B(H_2L)_2^-$ including the sensitivity of its measurement. Therefore, the retention behaviour of all ions under investigation was examined by eluting them with varying mannitol concentration from 0.24 to 0.72 M in 6.5 mM HCO_3^- which was compared with the retention behaviour when no mannitol was added in the eluent. The following were observed.

(a) The retention behaviour of ions did not change due to change in the mannitol concentration, however, a little difference in the retention time (not significant) was observed when the elution was carried out without mannitol. Fig. 3 shows the comparison of chromatograms obtained for a standard mixture with and without mannitol in the eluent. It implies that the mannitol played an important role in the formation of $B(H_2L)_2^-$ complex and it has no influence on the retentions of other ions.

(b) Another interesting observation was while increasing the concentration of D-mannitol in the eluents, the detector response for $B(H_2L)_2^-$ peak also increased. This indicates that the concentration of the $B(H_2L)_2^-$complex increases while increasing the mannitol concentration.

Further a plot of concentration of mannitol against detector response (conductivity) in the form of peak area/peak height of the $B(H_2L)_2^-$ peak was constructed and shown in Fig. 4. The detector response increased steeply up to 0.56 M and thereafter small increase was observed and hence, the concentration of mannitol was changed from 0.8 to 0.56 M. Standard boron solutions were injected under the changed condition and the peak areas thus obtained for the standards were proportional to their concentrations. Based on these, the eluent composition was re-optimized as 0.56 M D-mannitol in 6.5 mM HCO_3^-, which brought down the amount of mannitol per litre of the mobile phase from 146 to 102 g. This has minimized the formation of mannitol deposit on the suppressor and thereby decreased the suppressor working pressure.

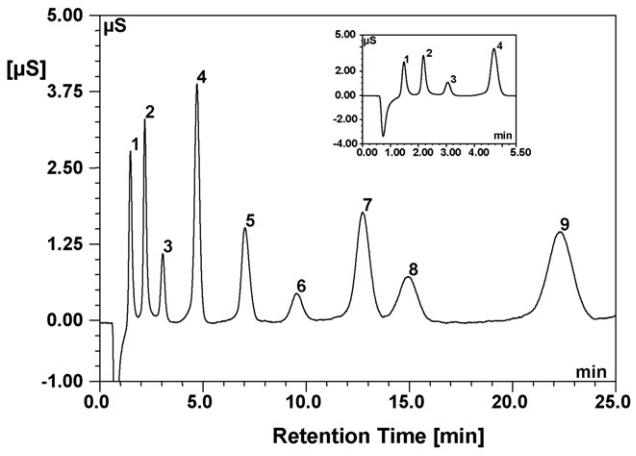

Fig. 2. Separation of standard mixture of anions. Column: Waters IC Pak A, Mobile phase: 0.8 M mannitol + 6.5 mM $NaHCO_3$, Flow rate: 1 mL/min. Detection: suppressed conductivity. Peaks: 1 = borate-mannitol anion (1.4 ppm of B), 2 = F^- (0.5 ppm), 3 = $CH_3CO_2^-$ (0.8 ppm), 4 = Cl^- (1 ppm), 5 = NO_2^- (2 ppm), 6 = Br^- (1.7 ppm), 7 = NO_3^- (2 ppm), 8 = HPO_4^{2-} (7.4 ppm) and 9 = SO_4^{2-} (7 ppm). Insert exhibits part of the chromatogram to show the borate peak resolved from the excluded negative peak.

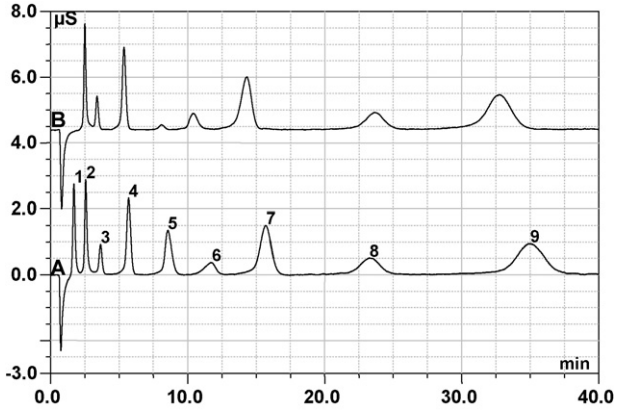

Fig. 3. Comparison of two chromatograms obtained for studying the effect of mannitol on the retention of all common ions by eluting them with 5 mM $NaHCO_3$. (A) Presence of 0.8 M mannitol (B) absence of mannitol. In the absence of mannitol the borate peak was appeared and other peaks were shifted little extent (within 5%). Peak labels are as in Fig. 2.

3.5. Calibration curve

The method has been calibrated with standard solutions of all the analytes. Limits of Detection (LOD), linear concentration range and coefficients of determination (R^2) are shown in Table 1.

3.6. Optimization of the pyrohydrolysis conditions and validation of the method

For the separation of borate, F^- and Cl^- from the sample matrix, pyrohydrolysis was opted for because IC requires a clean sample

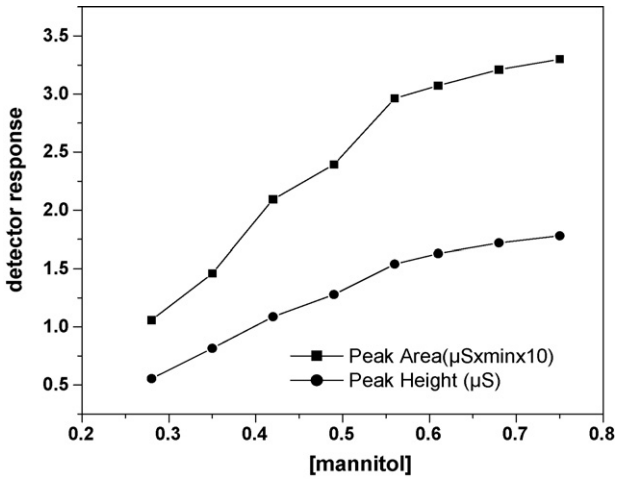

Fig. 4. Detector response measured as peak height and peak area for 1.4 mg of B L^{-1} under varying concentrations of D-mannitol in 6.5 mM HCO_3^-.

Table 1
Calibration parameters and Limit of Detection (LOD)

Analyte	Range (mg L^{-1})	Linearity (R^2)	LOD[a] (mg L^{-1})
B	0.05–5.0	0.9995	0.015
F^-	0.03–5.0	0.9999	0.005
Cl^-	0.05–10.0	0.9996	0.01
NO_2^-	0.20–10.0	0.9995	0.04
Br^-	0.30–10.0	0.9983	0.85
NO_3^-	0.35–10.0	0.9997	0.05
PO_4^{3}	0.50–25.0	0.9991	0.2
SO_4^{2-}	0.50–25.0	0.9994	0.09

[a] Calculated on the basis of S/N = 3.

solution which is free from bulk ions of any form. Though separations of F^- and Cl^- in various nuclear materials have been investigated in our laboratory and the pyrohydrolysis conditions were well optimized [27], separating boron in boric acid form along with the F^- and Cl^- requires optimization of pyrohydrolysis conditions. For this purpose, generally the certified reference materials are subjected to different pyrohydrolysis conditions and the recoveries of borate, the F^- and Cl^- are calculated for each condition. Since commercially available CRMs were not accessible to us, for boron we used two certified reference materials (U_3O_8–CRM-ILCE-IV and V), which were prepared by the Department of Atomic Energy (DAE), India in 2002 and characterized employing ICP-AES, DC-Arc-AES, Flame-AAS and ICP-MS techniques during the inter-laboratory inter-comparison experiments (ILCE) conducted among nine different laboratories [37]. Since these two standards are not certified for F^- and Cl^- contents, we used an in-house standard material (UO_2), which was prepared and characterized employing spectrophotometry and ion selective electrode methods [30].

Pyrohydrolytic separation mainly depends on (i) temperature, (ii) carrier gas flow rate (which controls the rate of distillate collection), (iii) mass of sample, and (iv) time (duration of pyrohydrolysis). Since pyrohydrolysis is decomposition of materials by the combined action of heat and water vapour, the pyrohydrolysis of metal halides is expressed as

$$MX_{2n} + nH_2O \rightarrow MO_n + 2nHX$$

This reaction is known to occur at about 1000–1200 K [38] and during pyrohydrolysis the F^- and Cl^- present in the sample are converted into HF and HCl, respectively. In case of actinide borides, it is necessary to ensure the feasibility of converting borides into boric acid in the above temperature range. The actinide borides normally exist in the form of MB_4 (UB_4, PuB_4) and the possible pyrohydrolysis reaction of MB_4 is

$$MB_4 + 14H_2O \rightarrow MO_2 + 4H_3BO_3 + 8H_2$$

Gibbs free energy changes for the conversion of UB_4 into H_3OB_3 at reaction temperatures 1100, 1200, 1300 and 1400 K were calculated by using Fact Sage software version 5.31 and it suggested that the reaction is thermodynamically more prominent in the temperature range 1100–1200 K. However, previous studies on the pyrohydrolysis of some ceramic materials showed that the recovery of boron (boric acid) was faster at temperatures above 1650 K [39,40]. The all quartz pyrohydrolysis apparatus used in the present study can reach a maximum temperature of 1225 K only and due to this limitation, the temperature of pyrohydrolysis was fixed as 1175 K, which is the maximum safe operational temperature. To find out the recovery of boron, U_3O_8–CRM-ILCE-IV (sample mass of 1.5 g) was subjected to pyrohydrolysis for different time durations and the distillates were collected in cleaned polyvinyl chloride (PVC) make bottles each containing 5 ml of 5 mM $NaHCO_3$ solution. The carrier gas flow rate was adjusted to get a flow rate of

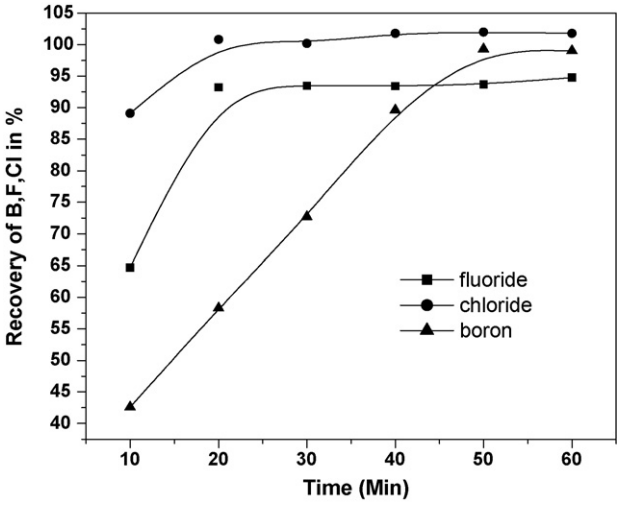

Fig. 5. Pyrohydrolytic borate, chloride and fluoride recovery as function of time (furnace temperature was 1175–1225 K).

steam (as liquid) as 0.3 mL/min. Prior to the IC analysis, the distillates were not diluted and they were analyzed by weight basis for the sake of getting appreciable concentration of boron in the distillate for accurate measurement. Similar exercises were performed with the in-house UO_2 standard (sample mass 0.5 g) to check the recovery of F^- and CL^-. The relation between the pyrohydrolysis time against the recoveries of B, F and Cl is shown in Fig. 5. The plot shows that at 1175 K, maximum F^- and CL^- could be recovered in 30 min and in case of boron the same could be achieved only after 50 min. Based on the results, the pyrohydrolysis conditions were optimized and listed in Table 2. Prior to the sample pyrohydrolysis, blanks were obtained by following the same procedure.As the work was carried out inside a radioactive glove box, necessary radioactive handling safety procedures were followed and further IC analyses were performed inside an active Fume-hood. Under the optimized conditions, both CRMs (U_3O_8) for boron and in-house UO_2 standard for F^- and Cl^- were subjected to pyrohydrolysis repeatedly and the recoveries of all the analytes were calculated by employing the optimized IC procedure and the values obtained are shown in Table 3.

3.7. Sample analysis

Accurately weighed quantities of (Pu,U)C (fuel for Indian Fast Breeder Test Reactor) and Pu-alloy samples (sample mass range 0.5–1.5 g) were subjected to pyrohydrolysis. Fig. 6 shows a typical chromatogram obtained for a sample and the results are given in Table 4.

Table 2
Pyrohydrolysis conditions for the complete extraction of borate, F^- and Cl^- from nuclear fuel materials

Parameters	Optimum condition
Sample mass (g)	0.5–1.5
Pyrohydrolysis temperature (K)	1175–1225
Rate of flow of the steam (as liquid) (mL/min)[a]	0.3
Extraction time (min)	60
Volume of the condensed distillate (mL)[b]	15–20

[a] Controlled by adjusting the carrier gas flow rate.
[b] Collected in pre-weighed PVC bottles containing 5 mM HCO_3^-.

Table 3
Results obtained for standard materials

Analyte	Standard	Certified ($\mu g\,g^{-1}$)	Obtained ($\mu g\,g^{-1}$)	Deviation	% of recovery[a]
Boron	ILCE-IV[b]	1.1	1.08 ± 0.09	−0.02	98.2
	ILCE-V[b]	0.77	0.72 ± 0.06	−0.05	93.5
Fluorine	UO_2-std[c]	12.6	11.88 ± 0.21	−0.72	94.3
Chlorine	UO_2-std[c]	16.4	16.47 ± 0.24	+0.07	100.4

[a] Mean of six replicate analysis.
[b] Certified reference materials prepared by the Department of Atomic Energy India and characterized by employing ICP-AES and ICP-MS techniques in nine different laboratories.
[c] In-house standards whose fluoride and chloride contents were arrived by replicate analyses carried out by employing ion selective electrode and spectrophotometric methods.

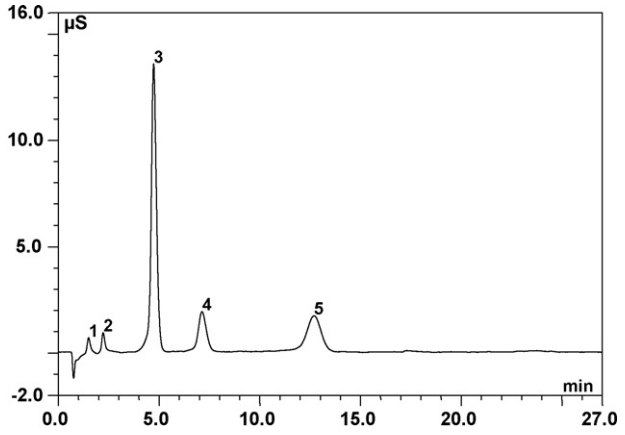

Fig. 6. Typical chromatogram obtained for a sample. Eluent: 0.56 M D-mannitol in 8 mM $NaHCO_3$. Other conditions are as in Fig. 2. Peaks: 1 = borate-mannitol anion, 2 = F^-, 3 = Cl^-, 4 = NO_2^-, 5 = NO_3^-.

Table 4
Results obtained for the samples

Sample	Boron ($\mu g\,g^{-1}$)	Fluoride ($\mu g\,g^{-1}$)	Chloride ($\mu g\,g^{-1}$)
UPuC-1	3.91 ± 0.20	0.56 ± 0.03	4.67 ± 0.23
UPuC-2	1.69 ± 0.08	0.54 ± 0.03	3.86 ± 0.19
UPuC-3	1.94 ± 0.10	3.10 ± 0.16	7.59 ± 0.38
UPuC-4	1.58 ± 0.08	0.45 ± 0.02	10.6 ± 0.53
UPuC-5	2.30 ± 0.12	0.72 ± 0.04	13.2 ± 0.66
UPuC-6	0.32 ± 0.02	0.62 ± 0.03	21.9 ± 1.1
UPuC-7	2.61 ± 0.13	0.85 ± 0.04	17.3 ± 0.87
Pu-A-1	4.84 ± 0.30	2.48 ± 0.12	47.2 ± 2.80
Pu-A-2	3.95 ± 0.22	1.42 ± 0.09	68.2 ± 3.50
U_3O_8-1	0.24 ± 0.01	0.38 ± 0.02	6.10 ± 0.31
U_3O_8-2	0.28 ± 0.01	0.80 ± 0.04	7.21 ± 0.36

3.8. Conclusions

The proposed pyrohydrolysis-ion chromatography combined methodology is sensitive, accurate and rapid for the simultaneous determination of F^-, Cl^- and borate (boron) in Pu bearing nuclear materials. Pyrohydrolysis separation enables safety in handling radioactive materials and provides clean sample solution (without producing the undesirable active liquid waste) suitable for the trouble free IC separation. Since the IC separation and detection were resorted with isocratic elution with conductivity detection, it is simple and versatile compared to other spectroscopic techniques. Boron, Cl and F at sub-ppm levels, can be determined by the proposed methodology with a reproducibility better than 5% in U and Pu based nuclear fuel materials.

Acknowledgements

Authors thank Dr. V. Venugopal, Director, RC&IG, BARC for his keen interest and kind support. They are also thankful to their colleagues Dr. R.M. Sawant and Mr. M.A. Mahajan for their kind support in carrying out the pyrohydrolysis.

References

[1] J.R. Theakar, R. Choubey, G.D. Moan, S.A. Alridge, L. Davis, R.A. Graham, C.E. Colemah, Tenth International Symposium on Zirconium in the Nuclear Industry, ASTM-STP-1245, 1994, p. 221.
[2] M.V. Ramaniah, Pure Appl. Chem. 54 (4) (1982) 889.
[3] W. Dams, E. Bauer, S. Baumann, R. Krause, J. Nucl. Mater. 153 (1988) 108.
[4] R.N. Sah, P.H. Brown, Microchem. J. 56 (1997) 285.
[5] Z. Kopajtic, S. Rollin, B. Wernli, C. Hochstrasser, G. Ledergerber, J. Anal. At. Spectrom. 10 (1995) 947.
[6] G.J. Hill, R.P. Lash, Anal. Chem. 52 (1980) 24.
[7] D.Y. Sarica, N. Ertas, Turk. J. Chem. 25 (2001) 305.
[8] R.M. Hamner, L.A. De'Aeth, Talanta 27 (1980) 535.
[9] P.S. Ramajaneyulu, Y.S. Sayi, V.A. Raman, K.L. Ramakumar, J. Radioanal. Nucl. Chem. 274 (2007) 109.
[10] P. Palkans, Metallurgia Metal Forming 39 (1972) 308.
[11] M. Gopalakrishnan, K. Radhakrishnan, P.S. Dhami, V.T. Kulkarni, M.V. Joshi, A.B. Patwardhan, A. Ramanujam, J.N. Mathur, Talanta 44 (1997) 169.
[12] S. Vijayalakshmi, R. Krishna Prabhu, T.R. Mahalingam, C.K. Mathews, At. Spectrosc. 13 (1992) 61.
[13] G. Troll, A. Sauever, Analyst 110 (1985) 283.
[14] K.R. Betty, G.T. Day, Analyst 111 (1986) 455.
[15] J. Aznarez, A. Ferrer, J.M. Rabadan, L. Marco, Talanta 32 (1985) 1156.
[16] M.P. Semov, Zh. Anal. Khim. 23 (1968) 245.
[17] Chang J. Parg, S. Song, J. Anal. At./Spectrom. 18 (2003) 1248.
[18] J.R. Castillo, J.M. Mir, C. Martinez, C. Bendicho, Analyst 110 (1985) 1435.
[19] T. Ishikawa, E. Nakamura, Anal. Chem. 62 (1990) 2612.
[20] W.P. Leelan, R.D. Vocke Jr., E.S. Beary, P.J. Paulsen, Geoshim. Cosmochim. Acta 55 (1991) 3901.
[21] Y.K. Xiao, R.D. Vocke Jr., G.H. Swihart, Y. Xiao, Anal. Chem. 69 (1997) 5203.
[22] T. Yoshimori, T. Miwa, T. Takeuchi, Talanta 11 (1964) 993.
[23] V.R. Wiederkehr, G.W. Goward, Anal. Chem. 12 (1959) 2102.
[24] T.I. Evseeva, I.L. Poletaeva, N.A. Zemlyanukhina, I.V. Pavlova, A.M. Rybin, M.Yu. Malykh, L.A. Fedorova, Radiokhimiya 31 (1989) 125.
[25] C. Ganguly, R.N. Jayaraj, Characterisation and Quality Control of Nuclear Fuels, Allied Publications, New Delhi, 2004, p.616.
[26] C. Sarzanini, J. Chromatogr. A 956 (2002) 3.
[27] R.M. Sawant, M.A. Mahajan, P. Verma, D. Saha, U.K. Thakur, K.L. Ramakumar, V. Venugopal, Radiochim. Acta 95 (2007) 585.
[28] E.M. Oliveira, G.A. Finazzi, I.A. Carlos, Surf. Coat. Technol. 200 (2006) 5978.
[29] A. Tapparo, P. Pastore, G. Giorgio Bombi, Analyst 123 (1998) 1771.
[30] M.A. Mahajan, M.V.R. Prasad, H.R. Mhatre, R.M. Sawant, R.K. Rastogi, G.H. Rizvi, N.K. Chadhuri, J. Radioanal. Nucl. Chem. Art. 148 (1991) 93.
[31] P.P. Power, W.G. Woods, Plant Soil 193 (1997) 1.
[32] J.J. Kankare, Anal. Chem. 45 (1973) 2050.
[33] G.W. Campbell, J. Inorg. Nucl. Chem. 31 (1969) 2625.
[34] L.B. Magrusson, J. Inorg. Nucl. Chem. 33 (1971) 3602.
[35] Ju. Lurie, Hand book of Analytical Chemistry, Mir Publications, Moscow, 1975, p. 275.
[36] E. Gaidamauskas, E. Norkus, J. Vaiciuniene, D.C. Crans, T. Vuotinen, J. Jaciauskiene, G. Baltrunas, Carbohydr. Res. 340 (2005) 1553.
[37] DAE-Interlaboratory comparison experiment (ILCE) for trace metal assay of uranium – Phase 2, Document, BARC, India, 2002.
[38] V.L. Dressler, D. Pozebon, E.L.M. Flores, J.N.G. Paniz, E.M.M. Flores, Anal. Chim. Acta 466 (2002) 117.
[39] J.P. Williams, E.E. Campbell, Anal. Chem. 31 (1959) 1561.
[40] V.R. Wiederkehr, G.W. Goward, Anal. Chem. 31 (1959) 2103.

Talanta 76 (2008) 1053–1057

Contents lists available at ScienceDirect

Talanta

journal homepage: www.elsevier.com/locate/talanta

The application of CdTe@SiO_2 particles in immunoassay

Li Jin [a], Dong-Dong Yu [c], Yan Liu [a], Xiao-Li Zhao [a], Jian-Guang Zhou [a,b,*]

[a] Department of Analytical Chemistry, College of Chemistry, Jilin University, Jiefang Road 2519, Changchun 130023, China
[b] Research Center for Analytical Instrumentation, Zhejiang University, China
[c] Department of Infectious Diseases, the First Hospital, Jilin University, Changchun 130021, China

ARTICLE INFO

Article history:
Received 23 November 2007
Received in revised form 28 April 2008
Accepted 5 May 2008
Available online 9 May 2008

Keywords:
CdTe@SiO_2 fluorescent particles
Water-in-oil (W/O) emulsion
Fluoroimmunoassay

ABSTRACT

CdTe@SiO_2 fluorescent particles were synthesized via hydrolysis and condensation of tetraethyl orthosilicate (TEOS) in water-in-oil (W/O) emulsion. Uniform luminophore-doped silica nanoparticles with 100 nm in diameter were obtained using microemulsion method and characterized by SEM. Antibody proteins were successfully conjugated to the fluorescent particles by the reaction of avidin and biotin, which were confirmed by fluorescence spectra. CdTe@SiO_2 fluorescent particles were potentially useful for the applications in biolabeling and imaging.

1. Introduction

Semiconductor nanoparticles made a significant impact on biotechnological and bioanalytical research [1–3], due to its advantages of desirable fluorescent properties, such as tunable emission spectra, high photostability, resistance to photobleaching, controllable surface characteristics, etc. [4–6].

The first milestone application of Quantum dots (QDs) as luminescence labels in bioimaging was reported by Alivisatos' group, and the multicolor labeling of fixed mouse 3T3 fibroblasts was demonstrated [7]. To be used in bioconjugation, a silica shell was intentionally coated onto the nanocrystals (NCs), followed by coupling of ligands to the silica. Biotinylated QDs with red photoluminescence selectively stained cytoskeletal filaments modified with streptavidin. Green-emitting QDs with trimethoxysilylpropyl urea and acetate groups showed high affinity to the cell nucleus. Constant excitation of bioactive QDs over 4 h with an Ar^+ laser resulted in constant emission with little decay. Almost at the same time, Chan and Nie prepared water soluble CdSe QDs by surface exchange of the organic ligands for mercaptoacetic acid, which could offer pendant carboxylic acid groups for further coupling [8]. CdSe QDs that were labeled with the protein transferrin underwent receptor-mediated endocytosis in cultured HeLa cells, and those QDs that were labeled with immunomolecules recognized specific antibodies or antigens. These two papers reported in 1998 laid the foundation of QDs as biolabels and opened the door to biological applications of semiconductor nanoparticles (NPs).

Quantum dots, however, have characteristics that limit their effectiveness for such applications. These limitations include particle growth, photoinduced decomposition, and conjugate aggregation [7]. Especially, they are rapidly photobleached in the presence of oxygen. It is a major problem in their use of bioanalytical application, such as biosensor and real-time imaging applications. Amorphous silica shells show some prime advantages necessary for bioconjugation of QDs. The silica shell prevents flocculation of particles and species from adsorbing onto the surface, and help to maintain the photoluminescence. In previous work [9,10], the development of organic-dye-doped silica NPs have been reported, but the fluorescence intensity of organic-dye-doped silica NPs was limited due to the relative low quantum yield of organic dyes, these NPs were unsuitable for bioanalysis because of their high hydrophobicity and poor dispersibility in water [11,12].

In order to solve this problem, coating inorganic nanoparticles with silica has been widely investigated. Using the well-known StÖber method, Liz-Marzán and his co-workers succeeded in coating aqueous CdS NCs stabilized by sodium citrate and obtained CdS@SiO_2 particles with core-shell structure [13]. Nann and Mulvaney further demonstrated that the silica coating on organic-soluble NCs by the StÖber process could also lead to well-defined structures [14]. Under optimized conditions, they successfully obtained silica spheres with 30–120 nm in diameter and single-quantum-dot cores. Murase and his co-workers reported the preparation of fluorescent CdTe-silica particles by the reverse microemulsion method. It emerged that the CdTe NCs were only

* Corresponding author at: Department of Analytical Chemistry, College of Chemistry, Jilin University, Jiefang Road 2519, Changchun 130023, China.
Tel.: +86 431 88498099; fax: +86 431 88499976.
E-mail address: JGzhou70@126.com (J.-G. Zhou).

0039-9140/$ – see front matter © 2008 Elsevier B.V. All rights reserved.
doi:10.1016/j.talanta.2008.05.002

situated on the surface of the resultant silica particles [15]. Kirchner et al. reported high cell viability of various cell lines including MDA-MB-435S breast cancer and NRK cell lines when ingested and adsorbed with silica-coated CdSe/ZnS nanoparticles, silica coated QDs showed there were no cytotoxic effects in the cell lines investigated with concentrations as high as 30 μM [16].

In this work, we developed a method for producing "biofriendly," spherical, stable, easily preserved, and monodisperse silica nanoparticles. Silica was used as a matrix in this work because it has been one of the most commonly used matrices for making nanoparticles for in vivo applications, and it has several superior properties. Silicate glass is a porous, high-purity, optically transparent and homogeneous material [17], so these make it an ideal choice as a matrix for the encapsulation of optically active reagents. Also, the preparation of silica particles is technically simple, and tailoring their physicochemical properties, i.e., pore size or innersurface hydrophobicity, could be achieved easily by varying the processing conditions and the concentration or type of reactants used [18]. Furthermore, the silica matrix made it possible to retain to a much larger extent compared to organic polymers, the specificity and reactivity of biologic molecules (i.e., proteins) in the solid state and provides morphologic and structural control, but that is not available when the biologic molecules are simply dissolved in aqueous media [19].

As it is well known that CdTe nanoparticles lose their highly fluorescent properties in the presence of common buffers such as phosphate-buffered saline (PBS), the growth of a silica shell has been found to significantly enhance the photoluminescence stability of CdTe QDs in buffer solution, provided a versatile platform for decoration with any number of functional groups and for successful conjugation to IgG proteins, which confirmed both bioactivity and binding specificity. Also it is common knowledge that Cd is highly toxic, and this could be a major concern for its vivo applications. The surface oxidation of the core QDs can be reduced by using silica based shell layers, which could create a barrier for oxygen diffusion. Remarkably, Kirchner et al. [16] reported that silanized CdSe did not elicit genes related to exposure to heavy metals. Silanization of various metal and semiconductor nanoparticle systems have shown great success in protecting their surface characteristics. This indicates that silica is an outstanding biocompatible protective layer and may hold the best promise for non-cytotoxic bioimaging and site-directed surgeries.

To further expand the usefulness of silica nanoparticles, a variety of surface modification and immobilization procedures are utilized and can be developed to couple the nanoparticles to various biomolecule targets. For example, oligonucleotides, enzymes, antibodies, and other proteins have been used for bioanalytical detection after the nanoparticles are linked to probe biomolecules. The silica surface can be modified to contain avidin, sulfide, amine, or carboxylate groups [20]. Avidin can be passively adsorbed on the silica surface followed by glutaraldehyde cross-linking. The resulting avidin-coated nanoparticles can then be conjugated with biotinylated molecules based on the strong avidin–biotin affinity. The capacity of silica to bind with avidin will allow the use of the nanoparticles to assays requiring commonly used and widely available biotinylated compounds.

In this paper, the CdTe@SiO_2 fluorescent particles were synthesized via hydrolysis and condensation of tetraethyl orthosilicate (TEOS) in water-in-oil (W/O) emulsions. CdTe nanocrystals were stabilized by 3-mercaptopropyl acid (MPA). Under optimized conditions, highly fluorescent SiO_2 spherical particles with CdTe nanocrystal cores were obtained, and terminated with an outermost layer of avidin. The optical investigation showed that the avidin-bound CdTe–silica particles retain bioactivity and had specific biorecognition ability, a fluoroimmunoassay employing bioconjugation of antibody and antigens was carried out in this experiment. The avidin-bound CdTe-silica particles were treated in biotinylated goat-anti-rabbit IgG solution to form new outermost layer through the strong affinity between avidin and biotin, the antibody (biotinylated goat-anti-rabbit IgG) could combine to biospecific antigen (FITC-rabbit-anti-goat IgG) to form a typical immunoreaction on the surface of CdTe-silica particles. The inclusion of nanoparticles into the silica matrix was demonstrated and discussed briefly. Also given were specific protein-binding studies that relate to the biocompatibility of the silica nanoparticles.

2. Materials and methods

2.1. Materials and reagents

All chemicals used in this experiment were of analytical reagent grade without further purification. Triton X-100, 3-mercaptopropyl acid (99+%), tellurium powder (~200 mesh, 99.8%), $CdCl_2$ (99+%), $NaBH_4$ (99%) were purchased from Aldrich Chemical Co. The following biochemicals were used: avidin (10 mg, Rockland), biotinylated goat-anti-rabbit IgG (1.0 mg/mL, Beijing Dingguo Biotechnology Ltd. China), FITC-rabbit-anti-goat IgG (1.5 mg/mL, Beijing Dingguo Biotechnology Ltd. China); BSA (5 g, Beijing Dingguo Biotechnology Ltd. China). BSA and avidin powder were dissolved in a 2 mmol/L phosphate buffered saline solution (PBS, pH 7.4) to obtain 1 mg/mL solution and all the solutions were stored at 0–4 °C, diluted only prior to immediate use. Water used throughout was doubly distilled water (>18 MΩ cm).

2.2. Instrument and spectrometry

Fluorescence spectra were recorded by a Shimadzu RF-5301 PC spectrofluorophotometer. UV–vis absorption spectra were obtained using a Varian GBC Cintra 10e UV–vis spectrometer. In both experiments, a 1-cm path-length quartz cuvette was used to measure the absorption or fluorescence spectrum. All pH values were measured with a PHS-3C pH meter (Hangzhou, China). A bath ultrasonic cleaner (Autoscience AS 3120, Tianjin, China) was used to disperse the microspheres. All optical measurements were carried out at room temperature under ambient conditions.

2.3. Synthesis of aqueous-compatible CdTe quantum dots

Stable water-compatible CdTe quantum dots were prepared by derivatizing nanocrystal surfaces with MPA as described in previous papers [21,22]. In brief, freshly prepared oxygen-free NaHTe solution was added to nitrogen-saturated 1.25×10^{-3} M $CdCl_2$ aqueous solution at pH 11.4 in the presence of MPA as a stabilizing agent. NaHTe was produced in an aqueous solution by reaction of $NaBH_4$ with tellurium powder at a molar ratio of 2:1. The molar ratio of Cd^{2+}:MPA:HTe^- was fixed at 1:2.4:0.5. The resulting mixture was then subjected to refluxing to control the size of the CdTe nanocrystals. Finally, QDs with different sizes were synthesized under different refluxing conditions respectively. The final clean and stable aqueous QDs were well-dispersed in basic solutions (pH > 6), and the luminescence quantum yield of 25% was obtained for the CdTe nanoparticles at room temperature compared with the fluorescent emission of Rhodaminutese 6G [23]. Stable water-compatible MPA-capped CdTe QDs with emission maximum at 610 nm were used in this study.

2.4. Preparation of biofunctional CdTe@SiO_2 particles

CdTe@SiO_2 particles were prepared as follows: typically, 7.5 mL cyclohexane, 1.77 mL Triton X-100, 1.8 mL *n*-hexanol, 48 μL aque-

ous solution of as prepared CdTe NCs, 60 μL ammonia aqueous solution (25 wt.%), and 0.1 mL tetraethyl orthosilicate (TEOS) were added to a flask with stirring. Normally 24 h were required to obtain CdTe@SiO_2 particles. The CdTe@SiO_2 particles were washed with ethanol and water, alternately, followed by centrifugation (3000 rpm, 10 min) with sonication (1 min). Finally the particles were sonicated and resuspended in 1 mL PBS.

The final deposited layer was avidin, the biofunctional CdTe@SiO_2 particles were obtained by electrostatic reaction, through incubating CdTe@SiO_2 particles with avidin for 30 min.

2.5. Formation of the immunoreaction system of biofunctional CdTe@SiO_2 particles/biotinylated goat-anti-rabbit IgG/FITC-rabbit-anti-goat IgG

The formation of immunoreaction system of CdTe@SiO_2 particles/biotinylated goat-anti-rabbit IgG/FITC-rabbit-anti-goat IgG was obtained by incubating the biofunctional CdTe@SiO_2 particles in biotinylated goat-anti-rabbit IgG solution at 37 °C for 30 min (BSA was added to avoid non-specific binding), followed by FITC-rabbit-anti-goat IgG solution added, incubating for another 30 min. A followed wash step was carried out after incubating, The CdTe@SiO_2 particles were washed three times with 200 μL PBS by centrifugation (3000 rpm, 10 min) and sonication (1 min) between each wash step. Then the particles were sonicated and resuspended in 1 mL PBS.

3. Results and discussion

3.1. Characterization of nanoparticles

Microemulsion method yielded uniform luminophore-doped silica nanoparticles with 100 nm in diameter (Fig. 1), and characterized by SEM. The low polarity of the microemulsion water pool allows quantum dots to aggregate while the silica network would be formed. In the current reverse-microemulsion system, cyclohexane was served as a continuous phase, in which TEOS was dissolved. Microscale water pools containing fluorescent CdTe nanocrystals were stabilized by Triton X-100 and *n*-hexanol. The formation of silica shell was initiated by hydrolyzing TEOS at the oil/water interface, catalyzed by ammonia. The possibility for the formation of CdTe@SiO_2 core-shell structures was that the hydrolyzed silica species formed in the initial stage of the reaction are bound onto the surfaces of the CdTe nanocrystals and form a silica monolayer. Then the silica layer grows up in situ by adsorbing the subsequently hydrolyzed TEOS [24].

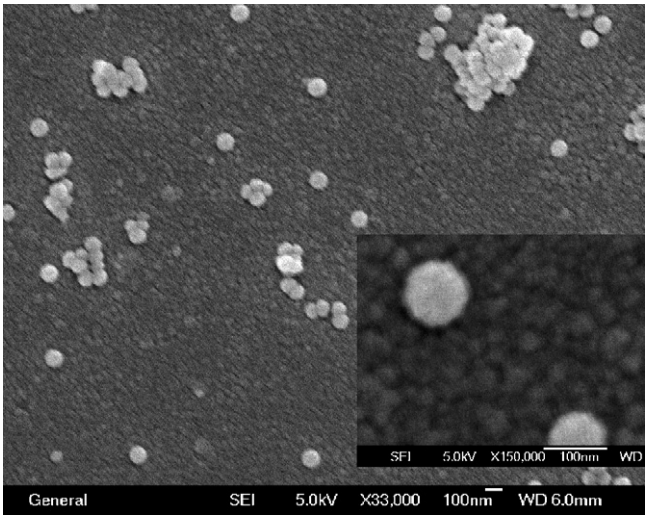

Fig. 1. SEM image of silica nanoparticles at 33,000× magnification.

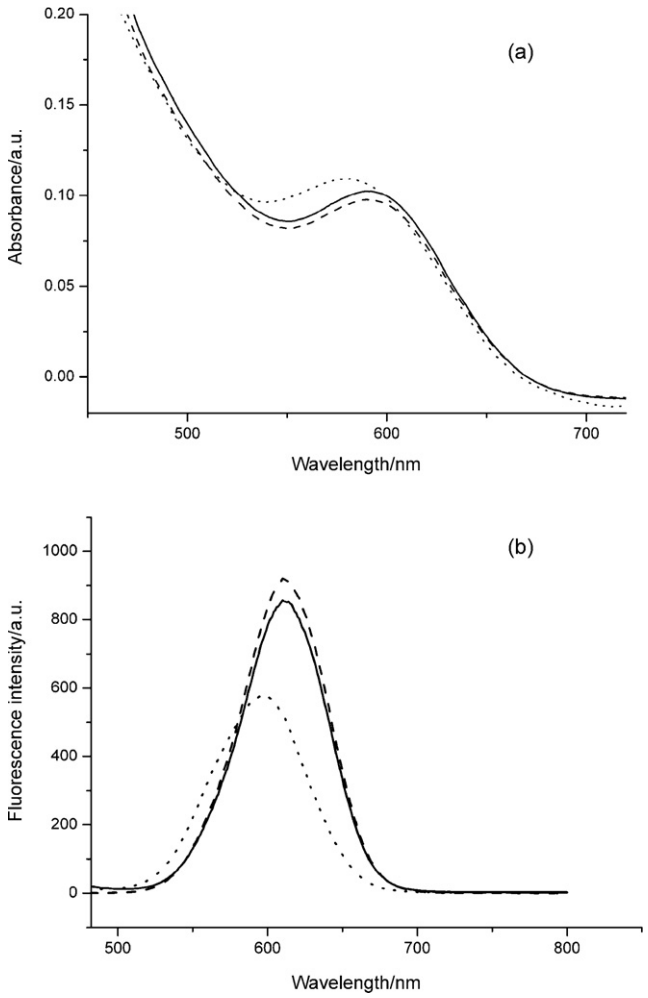

Fig. 2. Absorption (a) and fluorescence (b) spectra of unmodified CdTe nanocrystals (solid lines), unmodified CdTe nanocrystals mixed with silicate (dashed lines) and composite CdTe@SiO_2 spheres formed after silicate addition (dotted lines).

These nanoparticles were characterized with some spectroscopic methods. Fig. 2 shows the absorption and fluorescence spectra of selected samples of CdTe nanocrystals in aqueous solutions as prepared and of the same crude nanoparticles mixed with silicate. Almost no change was observed in the absorption spectra of crude CdTe nanoparticles after mixing with silica, but the fluorescence intensity decreased a little. After the formation of the CdTe@SiO_2 particles, the maximum absorption spectrum of the particles became broader, and the fluorescence spectra was blue-shifts and became broader, with fluorescence intensity decreases strongly, compared with crude nanocrystals. Such decreasing was also observed in refs [25] for either CdTe, or CdSe, or CdSe/CdS nanocrystals. The silica shell noticeably altered the optical properties of the nanoparticles due to (1) the change of the refraction index of the media, (2) the inhomogeneous broadening of the electronic transitions affected by the local morphology of the silica shell, and (3) the chemical reactions at the semiconductor/silica interface. The blue shift of the spectral features indicated the reduction of the particle size during the ripening of the silica layer.

The CdTe@SiO_2 materials appeared to be fairly stable over time, when exposed to air for more than a week, the fluorescence

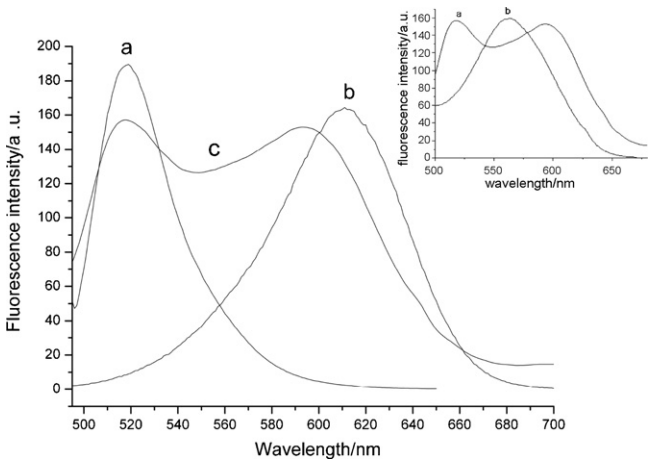

Fig. 3. Fluorescence emission spectra of (a) FITC-rabbit-anti-goat IgG solution, (b) CdTe@SiO_2 particles and (c) immunocomplex of FITC-rabbit-anti-goat IgG solution and CdTe@SiO_2/biotinylated goat-anti-rabbit IgG (FITC-rabbit-anti-goat IgG solution/biotinylated goat-anti-rabbit IgG/CdTe@SiO_2 particles). (Figure of inset (a) FITC-rabbit-anti-goat IgG solution/biotinylated goat-anti-rabbit IgG/CdTe@SiO_2 particles, (b) CdTe@SiO_2 particles immunocomplex absence of avidin in the coating). An excitation wavelength of 480 nm was used for all samples.

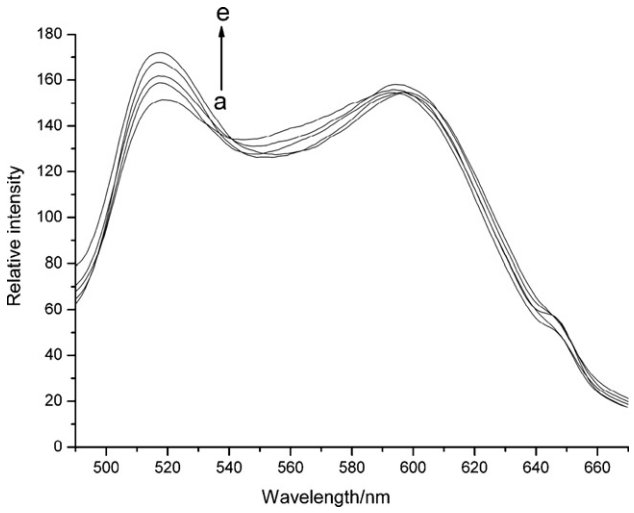

Fig. 4. The fluorescence emission spectra of immunoreaction system of CdTe@SiO_2 particles/biotinylated goat-anti-rabbit IgG/FITC-rabbit-anti-goat IgG with a series of different concentration of biotinylated goat-anti-rabbit IgG added: (a) 0.8 mg/L, (b) 1.6 mg/L, (c) 2.4 mg/L, (d) 3.2 mg/L, and (e) 4.0 mg/L biotinylated goat-anti-rabbit IgG. All solutions were prepared in 2 mmol/L PBS buffer (pH 7.4). An excitation wavelength of 480 nm was used for all samples.

intensity remained unchanged. Also the fluorescence intensity of solutions of CdTe@SiO_2 after silanization was measured in PBS buffers (2 mM), but no significant fluorescent quenching was observed during 2 h. It is worth noting here that the silica shell had dramatic effect on the stabilility of the luminescent properties compared to those of crude CdTe. Although the fluorescence intensity of the materials showed significantly degradation after 3 weeks, it showed improved resistance to air oxidation compared to crude CdTe. It is suggested that the silicon nanoparticles are protected in two ways. The first is the existence of Si–H sites, which are significantly less reactive to oxidation due to hydrogen termination of dangling silicon bonds, and the second is inhibited diffusion of oxygen and water into the mesopores, reducing the rate of oxidation of the silicon. Practically, the enhanced chemical stability to oxidation of the nanocomposite material is a major advantage in terms of developing a practical silicon-nanocluster-based LED [26]. UV–vis absorption spectrum confirm that the nanocrystals is still displaying normal exitonic behavior (Fig. 2), which also confirm that interactions between particles is mediated by the shell; the silica shell prevent flocculation and keep the structural integrity of the CdTe cores and is sufficient for fluorescent stability.

3.2. Fluorescence spectra of the immunocomplex

To demonstrate the use of CdTe@SiO_2 for biochemical assays, FITC-rabbit-anti-goat IgG was used as an antigen and red CdTe@SiO_2 with emission wavelengths at 610 nm were used to evaluate the binding property of the CdTe@SiO_2. The fluorescent emission spectra of the CdTe@SiO_2 were measured before and after conjugation with FITC-rabbit-anti-goat IgG, and the results are shown in Fig. 3.

From Fig. 3, it can be seen that the fluorescence spectra changed obviously when CdTe@SiO_2 was conjugated with FITC-rabbit-anti-goat IgG. There are two emission peaks in the fluorescence spectrum, one is at 520 nm, and the other one is at 596 nm, corresponding to the FITC-rabbit-anti-goat IgG and the CdTe@SiO_2 particles, respectively. Also, a single luminescence peak was observed, corresponding to the CdTe@SiO_2 particles immunocomplex absence of avidin in the coating (insert of Fig. 3). Obviously, without the coating of avidin, CdTe@SiO_2 particles can not be conjugated to IgG. It could also be observed that there is a blue shift in the peak emission of CdTe@SiO_2 particles (596 nm) immunocomplexes compared with that free CdTe nanoparticles (610 nm), which clearly shows that the CdTe@SiO_2 particles could bind with avidin to form the biofunctional fluorescent particles, and was also the evidence for the formation of CdTe@SiO_2/IgG immunocomplexes. It could be seen from Fig. 3 that the peak width increase by conjugating the CdTe quantum dots with FITC-rabbit-anti-goat IgG; this may be caused by surface charge neutralization that occurs concomitant with conjugate formation.

3.3. Immunoreaction between biotinylated goat-anti-rabbit IgG and FITC-rabbit-anti-goat IgG

The bioactivity of CdTe@SiO_2 was investigated through selective reaction between antibody and antigen in this study. For this purpose, CdTe@SiO_2/biotinylated goat-anti-rabbit IgG conjugate was formed using the same method as CdTe@SiO_2/FITC-rabbit-anti-goat IgG conjugate. A series of different concentrations of biotinylated goat-anti-rabbit IgG was added in the incubating step to study the effect of the concentration of biotinylated goat-anti-rabbit IgG, while the concentration of FITC-rabbit-anti-goat IgG was constant. Fig. 4 demonstrates the change of fluorescence spectra of CdTe@SiO_2/biotinylated goat-anti-rabbit IgG/FITC-rabbit-anti-goat IgG immunocomplexes, corresponding to gradually increasing quantity of biotinylated goat-anti-rabbit IgG. From Fig. 4, it can be seen that the fluorescent intensity at 520 nm increases with the concentration of biotinylated goat-anti-rabbit IgG increasing, while the fluorescence intensity at 596 nm corresponding to the emission of CdTe QDs was unvaried.

The effect of the concentration of FITC-rabbit-anti-goat IgG was also studied in the same way as above. From Fig. 5, fluorescence intensity of FITC-rabbit-anti-goat IgG (520 nm) is increased obviously when the concentration of biotinylated goat-anti-rabbit is fixed. It can be seen that the fluorescence emission intensity at 520 nm increase corresponding to the increasing of the concentration of FITC-rabbit-anti-goat IgG in the range from 0.8 to 4 mg/L.

As expected, both Figs. 4 and 5 demonstrate the immunoreaction between biotinylated goat-anti-rabbit IgG (antibody) and FITC-rabbit-anti-goat IgG (antigen). The result also proves the com-

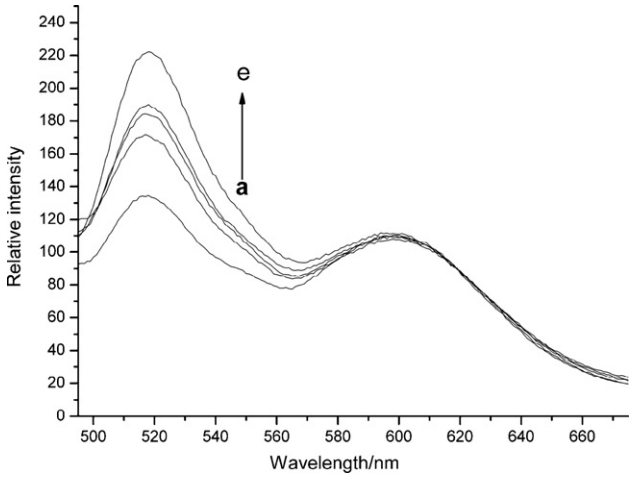

Fig. 5. The fluorescence emission spectra of immunoreaction system of CdTe@SiO_2 particles/biotinylated goat-anti-rabbit IgG/FITC-rabbit-anti-goat IgG with a series of different concentration of FITC-rabbit-anti-goat IgG added: (a) 0.50 mg/L, (b) 0.90 mg/L, (c) 1.20 mg/L, (d) 1.30 mg/L, and (e) 1.60 mg/L FITC-rabbit-anti-goat IgG. An excitation wavelength of 480 nm was used for all samples.

bination between biotinylated goat-anti-rabbit IgG and avidin on the surface of the biofunctional fluorescent microspheres.

4. Conclusions

In conclusion, uniform biocompatible CdTe@SiO_2 nanoparticles were obtained using a reverse microemulsion. A controlled hydrolysis of tetraethyl orthosilicate in W/O microemulsion led to the formation of monodisperse CdTe@SiO_2 nanoparticles. The nanoparticles had a uniform size of ~100 nm. The particles were protected from the environmental oxygen, as they were doped inside the silica network of the nanoparticles. Therefore, it was reasonable to infer that the silica shell could also prevent the diffusion of Cd^{2+} ions release upon the photooxidation of CdTe NCs, and could consequently reduce the cytotoxicity of those NCs in biological applications [27]. The avidin-bound fluorescent nanoparticles were treated in biotinylated goat-anti-rabbit IgG solution to form new outermost layer through a strong affinity between avidin and biotin, which could be used for a variety of biomolecules. This simple bioconjugation method will promote the application of luminophores in biochemical analysis and biomolecular interaction studies.

References

[1] W.C.W. Chan, S.M. Nie, Science 281 (1998) 2016.
[2] S.R. Emory, S. Nie, J. Phys. Chem. B 102 (1998) 493.
[3] M. Han, X. Cao, J.Z. Su, S. Nie, Nat. Biotechnol. 9 (2001) 631.
[4] C.B. Murray, D.J. Norris, M.G. Bawendi, J. Am. Chem. Soc. 115 (1993) 8706.
[5] D. Gerion, F. Pinaud, S.C. Williams, W.J. Parak, D. Zanchet, S. Weiss, A.P. Alivisatos, J. Phys. Chem. B 105 (2001) 8861.
[6] N. Gaponik, D.V. Talapin, A.L. Rogach, K. Hoppe, E.V. Shevchenko, A. Kornowski, A. Eychmuller, H. Weller, J. Phys. Chem. B 106 (2002) 7177.
[7] N.N. Mamedova, N.A. Kotov, A.L. Rogach, J.A. Studer, Nano Lett. 1 (2001) 281.
[8] M. Bruchez, J.M. Moronne, P. Gin, S. Weiss, A.P. Alivisatos, Science 281 (1998) 2013.
[9] S. Santra, P. Zhang, K. Wang, R. Tapec, W. Tan, Anal. Chem. 73 (2001) 4988.
[10] X. Zhao, R. Tapec-Dytioco, W. Tan, J. Am. Chem. Soc. 125 (2003) 11474.
[11] C. Zhou, Y. Zhao, T.C. Jao, M.A. Winnik, C. Wu, J. Phys. Chem. B 106 (2002) 1889.
[12] S.S. Kwon, Y.S. Nam, J.S. Lee, B.S. Ku, S.H. Han, J.Y. Lee, I.S. Chang, Colloid Surf. A 210 (2002) 95.
[13] M.A. Correa-Duarte, M. Giersig, L.M. Liz-Marzán, Chem. Phys. Lett. 286 (1998) 497.
[14] T. Nann, P. Mulvancy, Angew. Chem. 116 (2004) 5511;
T. Nann, P. Mulvaney, Angew. Chem. Int. Ed. 43 (2004) 5393.
[15] S.Y. Chang, L. Liu, S.A. Asher, J. Am. Chem. Soc. 116 (1994) 6739.
[16] C. Kirchner, T. Liedl, S. Kudera, T. Pellegrino, A.M. Javier, H.E. Gaub, S. Stolzle, N. Fertig, W.J. Parak, Nano. Lett. 5 (2005) 331.
[17] D.R. Uhlmann, G. Teowee, J. Boulton, J. Sol–Gel. Sci. Technol. 8 (1997) 1083.
[18] H. Xu, F. Yan, E.E. Monson, R. Kopelman, J. Biomed. Mater. Res. A 66 (2003) 870.
[19] B.C. Dave, B. Dunn, J.S. Valentine, J.I. Zink, Anal. Chem. 66 (1994) 1120A.
[20] W.H. Tan, K.M. Wang, X.X. He, X.J. Zhao, T. Drake, L. Wang, R.P. Bagwe, ChemInform 42 (2004) 621.
[21] M. Gao, A.L. Rogach, A. Kornowski, S. Kirstein, A. Eychmuller, H. Mohwald, H. Weller, J. Phys. Chem. B 102 (1998) 8360.
[22] H. Zhang, Z. Zhou, B. Yang, M. Gao, J. Phys. Chem. B 107 (2003) 8.
[23] J. Georges, N. Arnaud, L. Parise, Appl. Spectrosc. 50 (1996) 1505.
[24] Y. Yang, M.Y. Gao, Adv. Mater. 17 (2005) 2354.
[25] A.L. Rogach, D. Nagesha, J.W. Ostrander, et al., Chem. Mater. 12 (2000) 2676.
[26] Y. Cohen, K. Landskron, N. Tetreault, G.A. Ozin, Adv. Mater. 15 (2005) 593.
[27] A.M. Derfus, W.C.W. Chan, S.N. Bhatia, Nano Lett. 4 (2004) 11.

Talanta 76 (2008) 1029–1034

Contents lists available at ScienceDirect

Talanta

journal homepage: www.elsevier.com/locate/talanta

Brewster angle microscopic study of mixed lipid–protein monolayer at the air–water interface and its application in biosensing

A.K.M. Kafi*, Young-Soo Kwon**

Department of Electrical Engineering & NTRC, Dong-A University, 840 Hadan-2dong, Saha-gu, Busan 604-714, Republic of Korea

ARTICLE INFO

Article history:
Received 20 February 2008
Received in revised form 28 April 2008
Accepted 30 April 2008
Available online 8 May 2008

Keywords:
BAM
Protein
Lipid
Biosensor

ABSTRACT

This study investigated lipid–protein LB film formation with Brewster angle microscopy. Our experimental results show that hemoglobin (Hb) molecules can enter the lipid layer and remain for an extended time. We investigated the KCl effect on the LB monolayer of lipid–protein. The lipid–Hb monolayer was transferred from the air–water interface to a QCM gold electrode. UV–vis spectra showed that Hb retained its natural structure in the lipid layer. Cyclic voltammetric (CV) and amperometric systems were applied in this study in order to confirm the remaining bioactivity and sensitivity of Hb to hydrogen peroxide (H_2O_2). Lipid–Hb-modified electrodes showed well-defined redox peaks, indicating that the direct electron transfer between Hb and the electrode was enhanced by Hb incorporated in lipid layer. Based on this phenomenon, a novel biosensor for H_2O_2 was designed. Experimental conditions influencing the biosensor performance such as pH, and potential were optimized and assessed. The levels of the R.S.D.'s (<5%) for the entire analyses reflected the highly reproducible sensor performance. Using optimized conditions the linear range for the detection of H_2O_2 was observed from 1×10^{-6} to 1.00×10^{-4} mol L^{-1} with a detection limit of 4.00×10^{-7} mol L^{-1} (based on the S/N = 3).

1. Introduction

The behavior of protein adsorption on different matrices and the interaction and direct electron transfer between proteins and the electrode surfaces are of great importance in electrocatalytic biosensing [1]. Langmuir–Blodgett (LB) technique offers the possibility of developing an ultra-thin film with well-organized structure on the molecular scale [2]. As well, this technique is considered as a suitable immobilization method for biosensor manufacture given its applicability to creating uniform, well-ordered thin films with the amount of biocomponents controlled by varying the number of deposited layers. LB technique has previously been used to immobilize various biomolecules [3–7]. One of the emerging fields of application of LB film is the development of organized protein or enzyme layers for biosensors and for various analytical techniques [8]. The potentiality of two-dimensional LB monolayer of lipid molecules, which have been extensively used as a part of designing sensitive biosensor [9,10]. It is very important for the electroactivity of a protein or enzyme to be conserved on the solid surface. Normally proteins or enzymes have high molecular weight, large relative size, and a very flexible structure that can change conformation according to the experimental and immobilization conditions. A number of methods have been used to form protein/enzyme monolayers to protect the denaturization of its activity during the fabrication of biologically active films [8,11,12].

As part of the research interests of our lab, we already report the formation of protein layers by various matrix preparations, including LB technique, all applied to direct electron transfer processes [9,10,13]. It is noteworthy that the conventional method for forming lipid–protein film is to first dissolve proteins in subphase firstly, then dispersing lipid onto the subphase surface. There are problems associated with this system such as the unwanted formation of a passive layer prior to film deposition which can impact the electron transfer activity of protein. To solve this problem, we already have reported a new method of forming lipid–protein film [9,10].

In the present study, the above-mentioned method was applied to the formation of Hb–lipid monolayer at the water–air surface and deposition onto the solid substrate. A number of biosensors have been designed based on Hb in various configurations [14–18]. The redox centre of Hb is electrically insulated by a relatively thick protein shell, hindering its direct electrical communication with an electrode, yet it is very important for this molecule to maintain its electroactivity on the electrode surface [19]. We seek to overcome this problem by using LB technique [9,10,20]. The approach

* Corresponding author. Current address: Department of Chemistry, Lakehead University, Thunder Bay, Ontario P7B 5E1, Canada. Tel.: +1 807 343 850; fax: +1 807 346 7775.
** Corresponding author.
E-mail addresses: akafi@lakeheadu.ca (A.K.M. Kafi), yskwon@dau.ac.kr (Y.-S. Kwon).

0039-9140/$ – see front matter © 2008 Elsevier B.V. All rights reserved.
doi:10.1016/j.talanta.2008.04.061

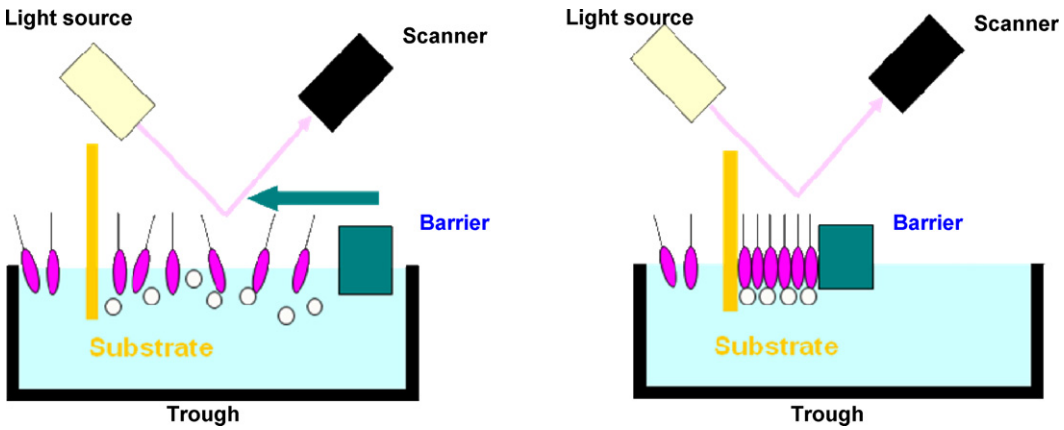

Fig. 1. The schematic figure of BAM image during Hb–LA LB film formation at air–water interface.

we propose for making Hb–lipid LB film was expected to enhance performance of Hb electron transfer activity at the electrode. Finally this Hb–lipid film was applied as a biosensor for detecting H_2O_2.

Hemoglobin is a promising biomaterial for the study of electron transfer reactions of proteins and for designing biosensors [13,16–18]. Reports have been published on the incorporation of Hb in different membranes or microenvironments [21–23], but the study of Hb with lipid film at the air–water interface has received scant attention. Lipid monolayers have been used as an adsorption layer for deposition of nanoparticles [24,25], salts [26], clay [27], or enzymes [28] from the aqueous phase. The performances of protein adsorbed onto the matrix monolayer at the air–water interface has been observed using fluorescence spectra, ellipsometry, surface plasmon resonance, etc. [29]. In this regards, Brewster angle microscopy (BAM) was first used to study monolayer in the early 1990s [30]. With the implementation of BAM for monolayer characterization, it has become possible to visualize the inner structure of different stages of lipid–protein LB film at the air–water interface without the requirement of added probes [1]. It is noteworthy that the conventional method for forming lipid–protein film is to dissolve proteins in subphase first, proceeded by dispersion of lipid onto the surface of subphase. There are problems associated with this system that affect the electron transfer activity of protein such as the creation of a passive layer before film deposition. To solve this problem, we already have reported a new method of forming lipid–protein film [9,10].

Reported for the first time in this paper are the formation of Hemoglobin (Hb)–lauric acid (LA) LB films characterized with BAM study. Specifically the formation of Hb–LA film has been observed using BAM. After depositing this film onto the Au surface, electrochemical properties were investigated. Our experimental data showed that this type of highly uniform film has good potential as a recognition layer for biosensing. As an extension of this the film possessed good electrocatalytic properties towards H_2O_2.

2. Experimental

2.1. Reagents

Hemoglobin was purchased from Sigma and used as received. Lauric acid (LA) was obtained from Aldrich. Stock solutions of H_2O_2 were diluted from 30% solution. All other reagents were of analytical grade and were used as supplied. The experimental solutions were freshly prepared each day by appropriate dilution of the stock solutions. Stock solutions were stored at a temperature of 4 °C. All stock solutions were made using freshly double distilled water. Water (18 MΩ cm) was purified using the Nanopure water system and was used to prepare all solutions. All experiments were performed in 0.1 M phosphate buffer solution (PBS) prepared from K_2HPO_4 and KH_2PO_4 then adjusted to desired pH by adding HCl.

2.2. LB film formation and BAM investigation

Fig. 1 shows a schematic BAM image taken of Hb–LA LB film forming at the air–water interface. LA (chloroform solution, 1 mg/ml) was spread onto the interface of subphase containing 1.0 M KCl and 0.001 mM PBS in a Langmuir–Blodgett through together with Multiskop (Optrel, German). The surface pressure was measured using a Wilhelmy balance equipped with a strip of chromatography paper suspending at the air–water interface. Surface pressure data along with trough and molecular areas are fed and recorded directly into a computer. After LA solution was spread onto the subphase interface for a minimum of 10 min, Hb solution (0.5 mg/ml, pH 7.0 phosphate buffer) was spread carefully onto the subphase, covered with a layer of LA. A pressure–surface area (π–A) curve was immediately recorded to evaluate the state of Hb/LA layer. BAM images were also concurrently recorded. The mixed Hb–LA layer was deposited from LB trough to a 9 MHz AT-cut PQC with gold electrode substrate. The monolayer of Hb–LA on substrate surface was obtained under controlled surface pressures using vertical withdrawal method, keeping 5 mm min^{-1} as the withdrawal speed. Prior to electrochemical measurements, Hb–LA-modified gold electrode was thoroughly washed with ultra-pure water. The modified electrode was kept at 4 °C when not in use. Only LA-modified gold electrode was fabricated in the same way. The electrodes will be referred to from this point on as Au–Hb–LA and Au–LA electrode, respectively.

2.3. Instrumentation and electrochemical measurements

The UV–vis spectrum was measured using a PerkinElmer UV–vis spectrometer. Cyclic voltammetry and amperometry were carried out with the CHI630 (B) workstation. A three-electrode system was employed in these experiments. A quartz crystal microbalance gold electrode was used as the mass loading substrate and working electrode following cleaning with a piranha solution. Cyclic voltammetry (CV) experiments were carried out in 0.1 M PBS by applying 0.3–−0.7 V vs. Ag/AgCl sweep range in the negative scanning direction. Amperometric measurements were carried out in a stirred cell by applying a potential of −500 mV to the working electrode. Prior to each experiment, the electrolyte solution was purged with high purity nitrogen for a minimum of

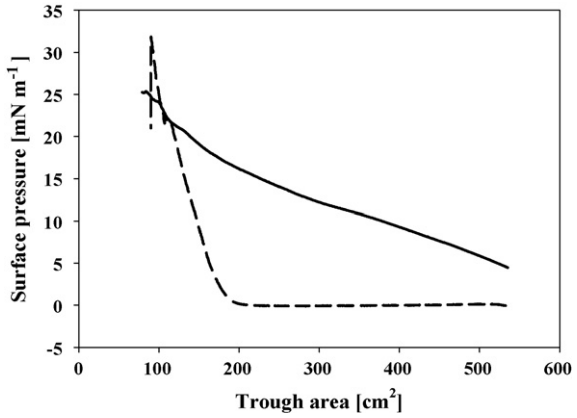

Fig. 2. π–A isotherm of lipid-only (LA) (dashed line) and lipid–Hb film (solid line) on subphase.

30 min. An inert environment was maintained during electrochemical measurements by allowing a gentle flow of nitrogen through the cell. A magnetic stirrer was employed during amperometry experiments. All measurements were performed at room temperature.

3. Results and discussion

3.1. LB film formation and BAM

Fig. 2 shows the typical pressure–area (π–A) isotherm of lipid and lipid–Hb Langmuir film onto a subphase of KCl solution in pure water. As can be seen in this figure, after spreading Hb molecule onto the subphase surface covered with lauric acid, the initial surface pressure increased immediately. This would indicate that already some Hb molecules have entered the lipid layer. We have investigated the effect of KCl concentration on the formation of lipid–Hb LB monolayer. Maximum increase of initial surface occurred at a 1.0 M KCl concentration. It is at this point that the maximum amounts of Hb molecules enter into the lipid layer. For this reason 1.0 M concentration of KCl was chosen as the optimal condition for forming lipid–Hb LB film.

Fig. 3 shows the BAM images along with π–A isotherm of lipid-only LB monolayer in the different states. Fig. 3(a) shows the BAM image of only lipid layer after solvent evaporation (chloroform) just prior to the start of barrier compression. In this image are visible clear white dots predicted to be lipid molecule. Fig. 3(b) shows a BAM image of same lipid film when surface pressure of the monolayer was approx. 15 mN/m. In this figure the white dots are seen to be approaching each other forming a colony type of film. Finally, in Fig. 3(c), we can observe the highly organized monolayer of LB–lipid film. This BAM image was taken at a surface pressure of approx. 25 mN/m. From this we can ascertain that the lipid will form a well packed LB film monolayer when the surface pressure reaches approx. 25 mN/m. Fig. 4 shows BAM images of lipid–Hb monolayer along with π–A isotherm obtained when Hb was spread onto lipid covered subphase. Fig. 4(a) shows the BAM image of lipid–Hb monolayer just after spreading Hb molecules onto the lipid film. The surface pressure was approx. 4 mN/m. In this figure can be discerned bright dots along with patch-like black spots. In Fig. 4(b) the black spots are more clearly visible and presumed to be Hb molecules. Fig. 4(c) shows the same lipid–Hb LB film at a surface pressure of approx. 25 mN/m. It is of interest to note that the black spots are more clearly observed in this picture. In contrast the white dots are less aggregated than in the lipid-only film of Fig. 3(b) at identical surface pressures. From this set of observations we can characterize the black patch-like spots as being Hb molecule. Thus, it can be concluded that Hb molecule entered the lipid layer and formed a well-defined lipid–Hb layer. We observed similar images after 2 h resting time suggesting that the lipid–Hb LB film has long time stability.

3.2. UV study of the LB film

For this experiment, the lipid–Hb film was transferred onto quartz at a surface pressure of 20 mN/m controlled by maintaining a withdrawal speed of 5 mm min^{-1}. Only lipid film was also deposited onto the quartz under same conditions. After depositing this film quartz, the UV–vis properties were investigated. To characterize the native structure of Hb in lipid film we investigated the UV–vis spectra. According to Fig. 5, UV–vis spectra of mixed Hb–lipid showed almost identical absorption pattern as Hb alone in solution (maximum absorption was at approx. 428 nm). The results illustrate that Hb keeps its native structure in LA film.

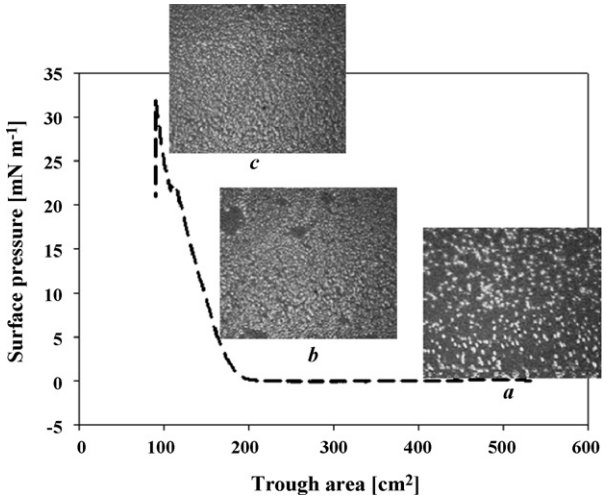

Fig. 3. BAM image of lipid-only LB film at different surface pressures: (a) surface pressure is 0 mN/m, (b) surface pressure is 15 mN/m and (c) surface pressure is 25 mN/m.

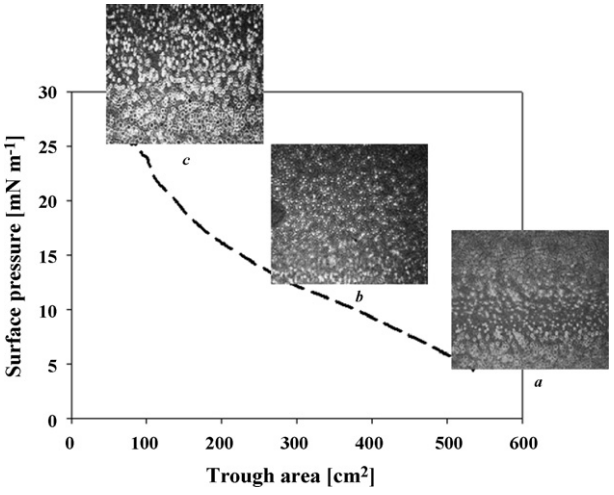

Fig. 4. BAM image of lipid–Hb LB film at different surface pressures: (a) surface pressure is 0 mN/m, (b) surface pressure is 15 mN/m and (c) surface pressure is 25 mN/m.

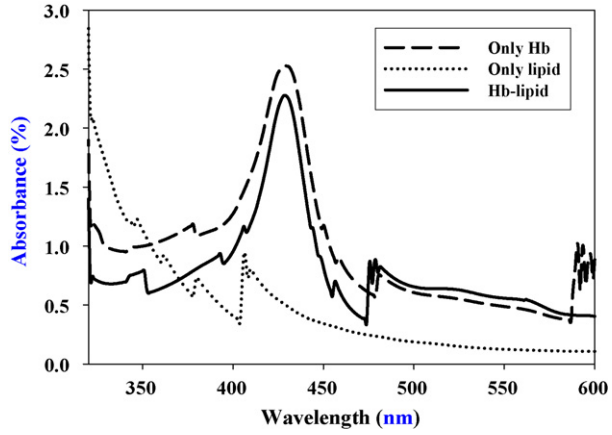

Fig. 5. UV of LA-only (dotted line), Hb-only (dashed) and LA–Hb-modified gold electrode.

3.3. Electrochemistry of LB film

Fig. 6 compares the cyclic voltammograms of the Au–Hb–LA and Au–LA electrode. It can be observed that there is a pair of well-defined redox peaks (solid line) at the Au–Hb–LA-modified electrode in 0.1 PBS (7.0). In contrast, no peak was observed at the Au–LA (dashed line) electrode under same experimental conditions. This comparison verifies that the redox peak arises from the electrochemical reaction of Hb. The result also establishes that direct electron transfer between Hb and the electrodes has occurred. The anodic and cathodic peak potentials for Hb are located at approx. −260 and −40 mV. The formal potential, E_0, was calculated to be −150 mV. Normally, Hb does not show electroactivity at the bare electrode [22]. Therefore, it can be established that Au–Hb–LA electrode plays an important role in enhancing electron transfer rate between the Au electrode and Hb. From this it can also be gathered that lipid layer provides a good matrix for Hb immobilization and biosensor fabrication. Fig. 7 shows the effect of scanning rate on the Au–Hb–LA electrode response. It was found that with an increase of scan rate from 50 to 200 mV/s the redox peak currents of Hb increased linearly. It should also be noted that peak-to-peak separation increased with increasing scan rates. The experimental data proves that this is a quite quasi-reversible and surface-controlled redox process [13].

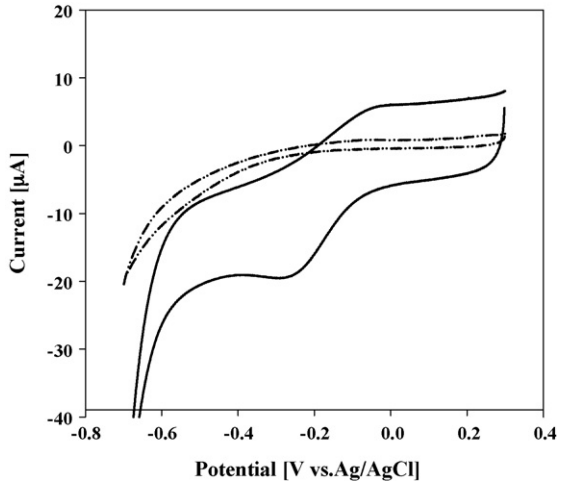

Fig. 6. CV graphs of LA-only (dashed line) and LA–Hb-modified gold electrode (solid line) (scan rate was 100 mV/s).

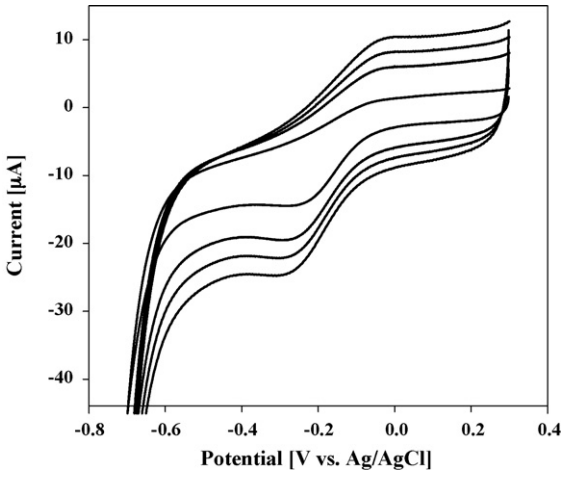

Fig. 7. CV graphs of LA–Hb-modified gold electrode (with different scan rate).

3.4. Electrocatalytic activity towards H_2O_2

Fig. 8 shows typical cyclic voltammograms (CVs) of the Au–Hb–LA electrode in the absence of and in the presence of 1.0×10^{-4} mol L^{-1} H_2O_2 in 0.1 M PBS at pH 7.0. As shown in Fig. 8 when 1.0×10^{-4} mol L^{-1} H_2O_2 is added to PBS, a marked increase in peak reduction current was observed accompanied by a decrease in the oxidation peak, providing an indication of the electrocatalytic properties of the modified electrode. It can be confidently stated that the catalytic reduction of H_2O_2 is due to hemoglobin immobilized in lipid film. We suggest that this type of lipid–Hb film can be used for biosensor fabrication. The generic reaction occurring at the electrode is given by the following equation [16]:

$$Hb(Fe^{III}) + H^+ + e^- \; Hb(Fe^{II}) \quad (1)$$

3.5. Optimization of experimental parameters

The effect of applied potential on the amperometric response of the biosensor is an important parameter. We investigated the influence of applied potential on the current response of the Au–Hb–LA electrode surface to H_2O_2. Fig. 9(A) shows the current response at different applied potentials in the presence of 2.0×10^{-5} mol L^{-1} H_2O_2 in a pH 7.0 PBS. This data reveals that the steady-state reduction current increases gradually as the voltage decreases from

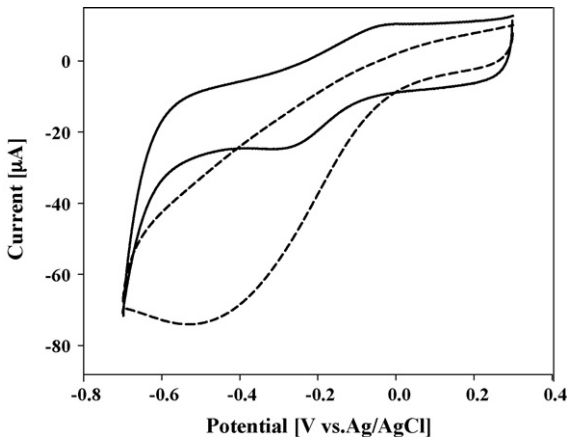

Fig. 8. CV graphs of the LA–Hb-modified gold electrode in the presence of 1.0×10^{-4} mol L^{-1} H_2O_2 in 0.1 M PBS at pH 7.0 (solid line) and the absence (dashed line) of H_2O_2 (scan rate was 100 mV/s).

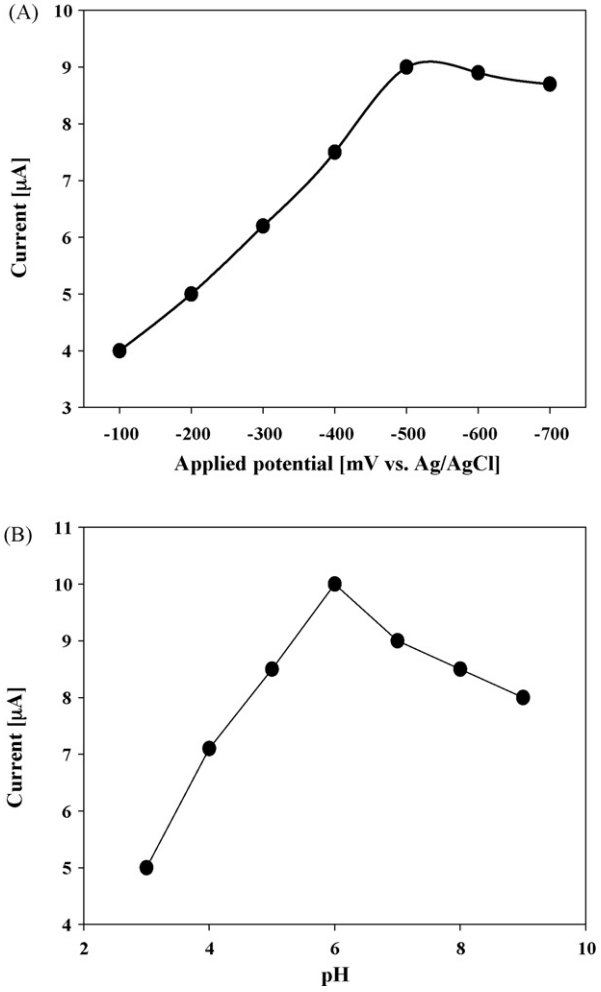

Fig. 9. (A) Dependence of biosensor catalytic current on applied potentials in the presence of 2.0×10^{-5} mol L^{-1} H_2O_2 in a pH 7.0 PBS. (B) Influence of pH on biosensor catalytic current in the presence of 2.0×10^{-5} mol L^{-1} H_2O_2 at a potential of −500 mV.

−100 to −500 mV. The maximum reduction current was achieved at −500 mV. At more negative potential risk of interference from other electroactive species may be involved. With this in mind we chose a working potential of −500 mV for this biosensor, where the background current is minimized and any unforseen interference reactions of other electroactive species can be effectively avoided.

The influence of pH value is another important factor on the response of electrolytic H_2O_2 biosensors. The effect of pH on biosensor response in the presence of H_2O_2 was investigated for the electrodes in question. Fig. 9(B) shows the amperometric current response of the Au–Hb–LA-electrode at different pH in the presence of 2.0×10^{-5} mol L^{-1} H_2O_2. An increase in amperometric current corresponded to an increase in pH from 3.0 to 6.0; however, the amperometric response decreased when pH was further increased from 7.0 to 9.0. In lower pH values (<4.0) the current response is very low. At these pH values the low response may be due to denaturation of the biomolecule [31]. As the maximum response current in this experiment was observed at pH 6.0, this pH was chosen as a working pH for the following experiment.

3.6. Amperometric response of the biosensor

Investigation of the amperometric response of the Au–Hb–LA-electrode was performed in a stirred cell containing 0.1 M PBS (pH 6.0) at an operating potential of −500 mV. Fig. 10 shows the typical current-response at Au–Hb–LA-electrode for successive addition of H_2O_2. Observe that as soon as H_2O_2 was added, the background current changed and the reduction current rose steeply to reach maximum value. The response of the fabricated biosensor to H_2O_2 is very quick; over 95% of the steady-state current was achieved within 5 s. Increasing the H_2O_2 concentration resulted in a proportional increase of the amperometric response.

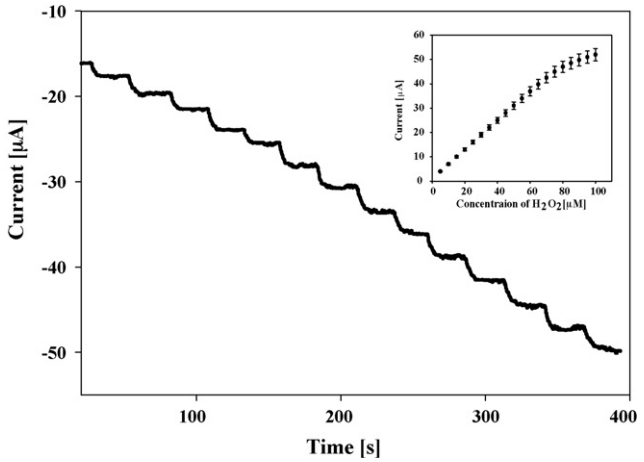

Fig. 10. Typical current–time response of LA–Hb-modified gold electrode with total additions of 1×10^{-4} mol L^{-1} H_2O_2 in 0.1 M PBS (pH 6.0) at an operating potential of −500 mV (inset, the calibration plot of the biosensor based on Fig. 10).

Fig. 10 (inset) shows the calibration plots obtained for the Au–Hb–LA-electrode electrode using optimum experimental conditions. Under optimal conditions, the proposed biosensor displays a linear range for H_2O_2 determination from 1×10^{-6} to 1.00×10^{-4} mol L^{-1} with a correlation coefficient of 0.996 ($n = 14$). The detection limit of the proposed biosensor was estimated to through the S/N = 3 is 4×10^{-7} mol L^{-1}.

3.7. Selectivity and stability of the biosensor

We also investigated the effect of a select number of substances that interfere with the response of the proposed biosensor. Analytes were added to the PBS containing 0.2 mM H_2O_2. The current inhibition was obtained for each interfering substance present at a concentration of 0.2 mM. Glucose, acetic acid, ethanol, and citric acid caused no observable interference. In the case of ascorbic acid, the initial value of current response decreased by 20%. This effect was presumably due to the consumption of H_2O_2 through oxidation of ascorbic acid [32]. The long-term stability of this biosensor was also investigated. The Au–Hb–LA-electrode was stored in PBS (pH 7.0) at 4 °C when not in use. It retained 85% of its initial current response after being stored for 35 days. The repeatability of the sensor's current response was also examined. It was found that the relative standard deviation (R.S.D.) was 4.75% for ten successive measurements at a H_2O_2 concentration of 2×10^{-5} μM.

4. Conclusion

We have observed the Brewster angle microscopic image of hemoglobin in lipid film at the air–water interface. The BAM results illustrate that hemoglobin molecules can enter lipid film and remain for an extended time. Cyclic voltammetric results showed there is a well-defined redox peak attributed to the redox heme centre of Hb. UV–vis spectra showed that Hb keeps its native structure in lipid layer following deposition to the electrode surface. In addition, this kind of film is promising for biosensor design. Based

on LA–Hb film, a hydrogen peroxide biosensor was designed. Our experimental data showed that this LB film could be employed as a functional H_2O_2 detector. As a biosensor it shows long linear range and low detection limit. The combination of low detection limit, long linear range and high stability are obvious advantages of this biosensor. This present work will further guide us towards an understanding of the redox characteristics of enzymes in lipid matrix at the air–water interface.

Acknowledgment

This work was supported by the Korean Science and Engineering Foundation (KOSEF) grant funded by the Korean government (MOST) (No. R01-2006-000-11120-0).

References

[1] Z. Zhang, R.S. Magliozzo, J.F. Rusling, Anal. Chem. 74 (2002) 163.
[2] G.G. Roberts, Langmuir Blodgett Films, Plenum, New York, 1990.
[3] J.M. Chovelon, M. Provence, N. Jaffrezic-Renault, N.V. Derue, D. Lair, S. Alexandre, J.M. Valleton, J. Biol. Phys. Chem. 1 (2001) 68.
[4] J.M. Chovelon, M. Provence, N. Jaffrezic-Renault, Langmuir 16 (2000) 6228.
[5] A. Zhang, A. Jafferezic-Renault, J. Wan, Y. Hou, J.M. Chovelon, Mater. Sci. Eng. 21 (2002) 91.
[6] G.K. Chudinova, A.V. Chudinov, V.V. Savransky, A.M. Prokhorov, Thin Solid Films 307 (1997) 294.
[7] A. Barraud, H. Perrot, V. Billard, C. Martelet, J. Therasse, Biosens. Bioelectron. 8 (1993) 39.
[8] M. Aizawa, K. Owaku, M. Matsuzawa, H. Shinorhara, Y. Ikariama, Thin Solid Films 180 (1989) 227.
[9] F. Yin, H.-K. Shin, Y.-S. Kwon, Talanta 67 (2005) 221.
[10] F. Yin, A.K.M. Kafi, H.-K. Shin, Y.-S. Kwon, Thin Solid Films 488 (2005) 223.
[11] Y. Okahata, T. Tsuruta, K. Ijiro, K. Ariga, Thin Solid Films 180 (1989) 65.
[12] S.Y. Zaitsev, Colloid Surf. 75 (1993) 211.
[13] A.K.M. Kafi, D.-Y. Lee, S.-H. Park, Y.-S. Kwon, J. Nanosci. Nanotechnol. 6 (2006) 3539.
[14] H. Hang, R. Guan, C. Fan, D. Zhu, G. Li, Sens. Actuators B 84 (2002) 214.
[15] F. Zhao, X. Wu, M. Wang, Y. Liu, L. Gao, S. Dong, Anal. Chem. 76 (2004) 4960.
[16] S. Liu, Z. Dai, H. Chen, H. Ju, Biosens. Bioelectron. 19 (2004) 963.
[17] Y.D. Zhao, Y.H. Bi, W.D. Zhang, Q.M. Luo, Talanta 65 (2005) 489.
[18] Y. Wang, W. Qian, Y. Tan, S. Ding, H. Zhang, Talanta 72 (2007) 1134.
[19] B.Q. Wang, J.Z. Zhang, G.J. Cheng, S.J. Dong, Anal. Chim. Acta 407 (2000) 111.
[20] K. Wan, J.M. Chovelon, N.J. Renault, Talanta 52 (2000) 663.
[21] J.H. Sun, N.F. Hu, H.Y. Ma, Electroanalysis 12 (2002) 1064.
[22] A.-E.F. Nassar, J.F. Rusling, J. Am. Chem. Soc. 118 (1996) 3043.
[23] Q.D. Huang, Z.Q. Lu, J.F. Rusling, Langmuir 12 (1996) 5472.
[24] K. Muramatsu, M. Takahashi, K. Tajima, K. Kobayashi, J. Colloid Interf. Sci. 242 (2001) 127.
[25] H. Du, Y.B. Bai, Z. Hui, L.S. Li, Y.M. Chen, X.Y. Tang, T.J. Li, Langmuir 13 (1997) 2538.
[26] P. Ganguly, D. Paranjape, V. Sastry, Langmuir 9 (1993) 574.
[27] R.H.A. Ras, C.T. Johnston, E.I. Franses, R. Ramaekers, G. Maes, P. Foubert, F.C. De Schryver, R.A. Schoonheydt, Langmuir 19 (2003) 4295.
[28] J. Jin, L.S. Li, X. Wang, Y. Li, Y.J. Zhang, T.J. Li, Langmuir 15 (1999) 6969.
[29] T. Kondo, T. Kakiuchi, M. Shimomura, Thin Solid Films 244 (1994) 887.
[30] S. Henon, J. Meunier, Rev. Sci. Instrum. 62 (1991) 936.
[31] X. Chen, N. Hu, Y. Zeng, J.F. Rusling, J. Yang, Langmuir 15 (1999) 7022.
[32] A.K.M. Kafi, D.-Y. Lee, S.-H. Park, Y.-S. Kwon, Microchem. J. 85 (2007) 308.

Talanta 76 (2008) 1070–1076

Contents lists available at ScienceDirect

Talanta

journal homepage: www.elsevier.com/locate/talanta

Encapsulation of tris(4,7-diphenyl-1,10-phenanthroline)ruthenium(II) complex linked with dendrons in sol–gels: Stable optical sensing membranes for dissolved oxygen

Hyung Jin Kim*, Yong Chae Jeong, Jong Il Rhee

Center for Functional Nano Fine Chemicals, School of Applied Chemical Engineering, Chonnam National University, Gwangju 500-757, Republic of Korea

ARTICLE INFO

Article history:
Received 5 March 2008
Received in revised form 1 May 2008
Accepted 4 May 2008
Available online 9 May 2008

Keywords:
Ru(II) complex
Optical oxygen sensor
Encapsulation
Leaching
Covalent incorporation of dendron

ABSTRACT

To circumvent the leaching problem of optical sensing membranes used for dissolved oxygen (DO) measurements, the encapsulation of Ru(II) complexes linked with bulky dendron(s) in a sol–gel matrix was investigated. A dendron, readily formed via chemical transformations such as amidation and catalytic reduction, was covalently incorporated into tris(4,7-diphenyl-1,10-phenanthroline)ruthenium(II) complex, leading to an increase in the size and lipophilicity of dye molecules. Sol–gel-based sensing membranes encapsulating these Ru(II) complexes displayed a strong luminescence emission at 590 nm induced by radiation at 480 nm, and showed excellent DO sensing properties and stability for repeated measurements in aqueous solution. The encapsulation of the dendron-incorporated Ru(II) complexes in sol–gels prevented the dyes from leaching out of the membranes.

1. Introduction

Dissolved oxygen (DO) measurements in an aqueous environment are widely applied to the biological [1], environmental [2,3], and industrial [4–6] areas. The most popular detection method for DO is the electrochemical method using an oxygen electrode (Clark electrode). This type of electrode, however, is not suitable for long-term operation, because it is easily poisoned and consumes oxygen by an electrochemical reduction reaction [7].

Recently, much effort has been made to develop optical DO sensors based on the oxygen quenching effect of the luminescence emitted from dye molecules because, compared to conventional electrochemical methods, optical sensing methods offer many advantages such as a faster response time, no poisoning, no oxygen consumption and no requirement for a reference electrode [7–14].

The performance of optical oxygen sensors generally relies on the ability of the polymer matrix to immobilize the oxygen-sensitive luminophore while allowing for oxygen diffusion and permeability through the matrix. Consequently, various polymer matrices have been explored including ethyl cellulose [15], fluoropolymers [16], ion-exchange polymers [17], poly(methyl methacrylate) [18], poly(styrene) [19], poly(vinyl chloride) [20], silicone rubber [21,14], and sol–gel matrices [8]. Among these materials, sol–gel matrices are increasingly utilized as a host material for optical sensing membranes, due to their superior chemical stability, mechanical strength, optical transparency and high porosity [22].

Sol–gels, glass-like membranes or thin films, are readily manufactured by the hydrolysis and subsequent polycondensation reactions of silicon alkoxide precursors at room temperature. To make good sol–gel-based optical sensors, the control of the porous structure of the sol–gel membrane and a suitable immobilization method of the dye molecules are crucial. The pore size can be controlled within the range from several angstroms to several nanometers by varying the sol–gel process conditions, including the type of silicate precursors, pH, ratio of alcohol/water/alkoxide, and aging time [23,24]. Immobilization methods of dyes in sol–gels are generally categorized into either the encapsulation or covalent binding methods. Of these, the encapsulation method is more often utilized, because it is accomplished simply by the addition of dyes to the silicate precursor solution prior to gel formation. However, the encapsulation method could cause the leaching of small dye molecules from the matrix into the analyte solution during liquid-phasing sensing, thereby reducing the sensor lifetime. The adjustment of the sol–gel process conditions to decrease the pore size could reduce the extent of dye leaching, but this option may increase the sensor response time, due to the reduced

* Corresponding author. Tel.: +82 62 530 1893; fax: +82 62 530 1909.
E-mail address: hyungkim@chonnam.ac.kr (H.J. Kim).

0039-9140/$ – see front matter © 2008 Elsevier B.V. All rights reserved.
doi:10.1016/j.talanta.2008.05.004

oxygen permeability of the sol–gel membrane. An alternative method would be the attachment of the dye molecules to an inert macromolecule for the purpose of increasing their size [25–28]. By means of this strategy, Senarath-Yapa and Saavedra [28] recently were able to prevent the leaching of the dye by its attachment to a PAMAM dendrimer having a molecular weight of 14,215.

Tris(4,7-diphenyl-1,10-phenanthroline)ruthenium(II) complex [$Ru(dpp)_3$] is one of the well-known luminescence dyes used in luminescence-based oxygen sensors, because of its high photochemical stability, high molar absorptivity, long lifetime derived from its metal to ligand charge transfer (MLCT) excited states, and large Stokes shift [9,14,29–32]. In recent years, the immobilization of such Ru(II) luminophores in sol–gels has been intensively investigated for the purpose of developing optical oxygen sensors [8,33–35,40]. However, sensing membranes prepared by the encapsulation of Ru(II) luminophores in sol–gels still have the problem of dye leaching when used for DO sensing in an aqueous environment, although the use of a covalent immobilization method provides another solution [40].

In this study, to realize the stable encapsulation of $Ru(dpp)_3$ in sol–gels without the leaching problem, we designed bulky dendrons, which are covalently incorporated onto $Ru(dpp)_3$ to increase the size and lipophilicity of the Ru(II) luminophore. This paper reports the preparation of Ru(II) complexes linked with specially designed dendrons, and the sensing properties and stability of the sol–gel membranes immobilizing these Ru(II) luminophores.

2. Experimental

2.1. Reagents and instrumentation

All reagents were purchased from Aldrich Chemical Co. and used without further purification. Solvents were purchased and dried by the standard method. 4-(2-carboxyethyl)-4-nitroheptanedioic acid (**1**), 4-[4-(7-phenyl-1,10-phenantrolin-4-yl)phenyl]butyric acid (**7**) and Ru(II) complex (**6**, Fig. 1) were prepared according to the methods described in the literature [36,37].

The ^1H and ^{13}C NMR spectra were recorded at 300 and 71 MHz, respectively, on a Bruker ARX-R300 spectrometer and were obtained in $CDCl_3$, unless otherwise stated. The mass spectral data were obtained on either a Jeol JMS-HX110 high resolution tandem mass spectrometer (ESI-MS) or a Voyager DE-STR proteomics analyzer (MALDI-TOF). The luminescence measurements were performed with a Hitachi F-4500 fluorescence spectrophotometer.

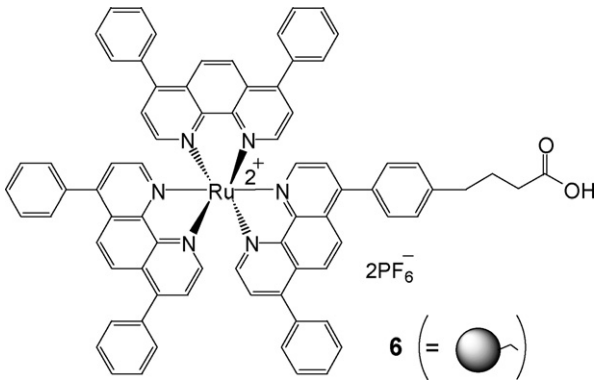

Fig. 1. Structure of $Ru(dpp)_3$ possessing a linker arm (**6**).

2.2. Syntheses

2.2.1. 4-(2-Hexylcarbamoylethyl)-4-nitroheptanedioic acid bishexylamide (*2*)

DCC (4.71 g, 22.9 mmol) and 1-HOBT (3.09 g, 22.9 mmol) were added to a stirred solution of 4-(2-carboxyethyl)-4-nitroheptanedioic acid (**1**; 1.63 g, 5.88 mmol) in dried DMF (50 mL) at 25 °C. After 30 min, hexyl amine (2.14 g, 22.15 mmol) was added. After stirring for 24 h at 25 °C, the mixture was filtered and the filtrate was concentrated in vacuo to give the crude product, which was column chromatographed (SiO_2) by eluting with a mixture of *n*-hexane/EtOAc (1:1) to afford the amide **2** (2.41 g, 78%). ^1H NMR ($CDCl_3$): δ 6.28 (br t, 3H, N*H*), 3.18 (m, 6H, NHCH_2), 2.22 (t, 7.2 Hz, 6H, CH_2CH$_2$CONH), 2.21 (t, 7.2 Hz, 6H, CH$_2$CH_2CONH), 1.47 (m, 6H, CH_2CH$_2$NH) 1.31 (m, 12H, CH$_2$CH_2CH_2CH$_3$) 0.87 (t, J = 7.0 Hz, 9H, CH_3). ^{13}C NMR ($CDCl_3$): δ 171.3 (*C*ONH), 93.5 (*C*NO$_2$), 39.8 (NHCH_2), 31.5, 30.9, 30.8, 29.4, 26.6, 22.57 (CH_2), 14.0 (CH_3). ESI-MS for $C_{28}H_{54}N_4O_5$: calcd 526.41, found 527.4 $(M+H)^+$.

2.2.2. 4-Amino-4-(2-hexylcarbamoylethyl)heptanedioic acid bishexylamide (*3*)

Raney-Ni (8 g) was added to a solution of the amide **2** (2.41 g, 4.58 mmol) in absolute EtOH (30 mL), and then the mixture was stirred under 90 psi of H_2 for 12 h at 25 °C. The catalyst was carefully filtered, and the filtrate was concentrated in vacuo to afford the amine **3** (2.23 g, 98%). ^1H NMR ($CDCl_3$): δ 6.62 (br t, 3H, N*H*), 3.16 (m, 6H, NHCH_2), 2.5 (br s, 2H, NH_2), 2.23 (t, J = 7.2 Hz, 6H, CH_2CH$_2$CONH), 1.63 (t, J = 7.2 Hz, 6H, CH$_2$CH_2CONH), 1.45 (m, 6H, CH_2CH$_2$NH) 1.25 (m, 12H, CH$_2$CH_2CH_2CH$_3$) 0.86 (t, J = 8.9 Hz, 9H, CH_3). ^{13}C NMR ($CDCl_3$): δ 173.3 (CONH), 58.0 (*C*NH$_2$), 39.6 (NHCH_2), 34.6, 31.4, 30.9, 29.4, 26.6, 22.5 (CH_2), 13.9 (CH_3). ESI-MS for $C_{28}H_{56}N_4O_3$: calcd 496.44, found 497.4 $(M+H)^+$.

2.2.3. Nitro-substituted dendron (*4*)

DCC (739 mg, 3.58 mmol) and 1-HOBT (484 mg, 3.58 mmol) were added to a stirred solution of the acid **1** (225 mg, 0.92 mmol) in dried DMF (30 mL) at 25 °C. After 30 min, the amine **3** (1.78 g, 3.58 mmol) was added. After stirring for 24 h at 25 °C, the mixture was filtered and the filtrate was concentrated in vacuo to give the crude product, which was column chromatographed (SiO_2) by eluting with a mixture of MeOH/EtOAc (1:20) solution to afford the amide **4** (1.13 g, 72%). ^1H NMR ($CDCl_3$): δ 3.15 (m, 18H, NHCH_2), 2.22 (m, 18H, CH_2CH$_2$CONH), 2.20 (m, 30H, NO$_2$CCH_2, NO$_2$CCH$_2$CH_2, CH$_2$CH_2CONH), 1.46 (m, 18H, CH_2CH$_2$NH) 1.23 (m, 54H, CH$_2$CH_2CH_2CH_2CH$_3$) 0.89 (t, J = 6.9 Hz, 27H, CH_3). ^{13}C NMR ($CDCl_3$): δ 173.7 (CONHCH$_2$), 171.1 (*C*ONHC), 91.5 (*C*NO$_2$), 58.3 (NHCH_2), 39.8 (NHC), 31.5, 31.1, 30.7, 29.4, 26.7, 22.5 (CH_2CH$_3$), 14.0 (CH_3). ESI-MS for $C_{94}H_{177}N_{13}O_{14}$: calcd 1712.35, found 1713.3 $(M+H)^+$.

2.2.4. Amine dendron (*5*)

The nitro compound **4** (842 mg, 0.49 mmol) was hydrogenated with Raney-Ni (2.5 g) in absolute EtOH (20 mL) at 90 psi for 12 h. The reaction mixture was filtered through Celite and the solvent was evaporated in vacuo to give the amine **5** (794 mg, 96%). ^1H NMR ($CDCl_3$): δ 3.13 (m, 18H, NHCH_2), 2.22 (m, 18H, CH_2CH$_2$CONH), 2.20 (m, 30H, NO$_2$CCH_2, NO$_2$CCH$_2$CH_2, CH$_2$CH_2CONH), 1.44 (m, 18H, CH_2CH$_2$NH) 1.21 (m, 54H, CH$_2$CH_2CH_2CH_2CH$_3$) 0.87 (t, J = 6.9 Hz, 27H, CH_3). ^{13}C NMR ($CDCl_3$): δ 173.6 (CONHCH$_2$), 171.0 (*C*ONHC), 58.2 (NHCH_2), 49.0 (*C*NH$_2$), 39.7 (NHC), 31.5, 31.3, 30.8, 29.4, 26.7, 22.5 (CH_2), 14.0 (CH_3). ESI-MS for $C_{94}H_{179}N_{13}O_{12}$: calcd 1682.38, found 1683.3 $(M+H)^+$.

*2.2.5. Bis{4-[4-(7-phenyl-1,10-phenanthrolin-4-yl)-phenyl]butyric acid}ruthenium(II) dichloride (**8**)*

A mixture of 4-[4-(7-phenyl-1,10-phenanthrolin-4-yl)phenyl]-butyric acid (**7**) (200 mg, 0.48 mmol) and $RuCl_3{\cdot}3H_2O$ (62.5 mg, 0.24 mmol) dissolved in DMF (5 mL) was refluxed for 2 h under an N_2 atmosphere. After cooling to 25 °C, the reaction mixture was concentrated in vacuo until the volume became ca. 2 mL and the residue was dissolved in water (5 mL). The resulting mixture was treated with a 30% LiCl solution. The precipitate was collected by filtration, washed several times with cold water, and dried under vacuum to afford **8** (193 mg, 80%), as a dark violet microcrystalline solid. The material was used directly without further purification in the next step.

*2.2.6. Tris{4-[4-(7-phenyl-1,10-phenanthrolin-4-yl)-phenyl]butyric acid}ruthenium(II) hexafluorophosphate (**9**)*

A solution of the complex **8** (100 mg, 0.1 mmol) and 4-[4-(7-phenyl-1,10-phenanthrolin-4-yl)phenyl]butyric acid (**7**) (54 mg, 0.12 mmol) in EtOH (10 mL) was refluxed for 3 h under an N_2 atmosphere. After cooling to 25 °C, the reaction mixture was concentrated in vacuo to give the crude product, which was column chromatographed (SiO_2) by eluting with a mixture of CH_3CN/saturated KNO_3/H_2O (10:1:1). After being concentrated in vacuo, the residual material was dissolved in MeOH (2 mL) and treated with a saturated aqueous NH_4PF_6 solution. The precipitate was filtered, washed with several portions of cold ethanol and dried to afford **9** (115 mg, 70%). ^{1}H NMR (DMSO-D_6): δ 8.33–8.24 (m, 12H, Ar), 7.83 (m, 6H, Ar), 7.83–7.46 (m, 27H, Ar), 4.38 (bs, 1H), 2.71 (t, J = 7.2 Hz, 2H, CH_2CH$_2$CH$_2$CO$_2$H), 2.26 (t, J = 7.2 Hz, 2H, CH_2CO$_2$H), 1.86 (m, 2H, CH$_2$CH$_2$CO$_2$H). ^{13}C NMR (DMSO-D_6): δ 174.8 (*C*O$_2$H), 152.6, 148.4, 148.31, 148.36, 143.9, 135.7, 133.3, 130.3, 130.2, 130.0, 129.52, 129.51, 128.55, 128.52, 126.88, 126.80, 126.5, 126.3 (Ar), 34.5 (*C*H$_2$CO$_2$H), 33.6 (*C*H$_2$CH$_2$CH$_2$CO$_2$H), 26.4 (*C*H$_2$CH$_2$CO$_2$H). MALDI-TOF for $C_{75}H_{54}N_8O_7Ru$: calcd 1646.34, found 1357.41 $(M-2PF_6)^{2+}$.

*2.2.7. Ruthenium(II) complex possessing mono-dendron (**10**)*

DCC (9 mg, 0.042 mmol) and 1-HOBT (6 mg, 0.042 mmol) were added to a solution of **6** (44 mg, 0.03 mmol) in DMF (3 mL) at 25 °C. After stirring for 30 min, dendron **5** (66 mg, 0.039 mmol) was added and the mixture maintained for 24 h at 25 °C. After filtration, the filtrate was concentrated in vacuo to give the crude product, which was column chromatographed (SiO_2) by eluting with a mixture of CH_3CN/saturated KNO_3/H_2O (10:1:1), and then treated with saturated NH_4PF_6 solution to afford the complex **10** (75 mg, 80%). ^{1}H NMR ($CDCl_3$): δ 8.41 (bd, 6H, Ar), 8.33 (s, 6H, Ar), 7.80–7.54 (m, 35H, Ar), 3.16–2.85 (m, 20H, NHCH_2), 2.43–2.10 (m, 50H, CH_2), 1.47 (m, 18H, CH_2CH$_2$NH) 1.23 (m, 54H, CH$_2$CH_2CH_2CH_2CH$_3$) 0.89 (t, J = 6.9 Hz, 27H, CH_3). ^{13}C NMR: δ 173.1, 171.8, 170.6, 152.9, 150.0, 149.5, 145.3, 136.6, 130.8, 130.7, 130.5, 130.2, 130.1, 129.9, 126.9, 58.3, 49.0, 39.9, 36.4, 31.4, 30.86, 30.83, 28.9, 26.6, 22.4, 13.9. MALDI-TOF MS for $C_{170}H_{231}F_{12}N_{19}O_{13}P_2Ru$: calcd 3138.63, found 2848.7 $(M-2PF_6)^{2+}$.

*2.2.8. Ruthenium(II) complex possessing tri-dendron (**11**)*

DCC (21 mg, 0.1 mmol) and 1-HOBT (14 mg, 0.1 mmol) were added to a solution of **9** (40 mg, 0.024 mmol) in DMF (3 mL) at 25 °C. After stirring for 30 min, a solution of dendron **5** (160 mg, 0.095 mmol) in DMF (2 mL) was added and the mixture stirred for a further 24 h at 25 °C. After filtration, the filtrate was concentrated in vacuo to give the crude product, which was column chromatographed (SiO_2) by eluting with a mixture of CH_3CN/saturated KNO_3/H_2O (10:1:1), and then treated with saturated NH_4PF_6 solution to afford the complex **11** (97 mg, 61%). ^{1}H NMR ($CDCl_3$): δ 8.33–8.24 (m, 12H, Ar), 7.83 (m, 6H, Ar), 7.83–7.46 (m, 27H, Ar), 3.13–2.82 (m, 60H, NHCH_2), 2.3–2.1 (m, 150H, CH_2CH$_2$CONH), 1.8–1.5 (m, 60H, CH_2) 1.20–1.18 (m, 162H, CH_2) 0.85 (t, J = 7.0 Hz, 81H, CH_3). ^{13}C NMR ($CDCl_3$): δ 173.6, 173.3, 170.6, 152.6, 148.4, 148.31, 148.36, 143.9, 135.7, 133.3, 130.3, 130.2, 130.0, 129.52, 129.51, 128.55, 128.52, 126.88, 126.80, 126.5, 126.3, 58.3, 48.9, 39.9, 36.4, 31.4, 30.9, 30.8, 28.9, 26.7, 22.5, 14.1. MALDI-TOF MS for $C_{366}H_{597}F_{12}N_{45}O_{39}P_2Ru$: calcd 6639.44, found 6349.5 $(M-2PF_6)^{2+}$.

2.3. Preparation of sensing membranes (M-RuD$_1$, M-RuD$_3$ and M-Ru)

Microscopic slides were used as solid supports onto which the sol–gel was cast by a manual pipetting technique. Prior to their use, the surface of the microscope slides was activated by treating it with 1N HF solution for ca. 2 min, followed by washing with distilled water and MeOH, and then dried at 25 °C. A sol–gel solution was prepared by mixing tetraethyl orthosilicate (TEOS) (0.67 mL, 3 mmol), ethanol (340 μL, 6 mmol), water (108 μL, 6 mmol) and 0.1 *M* HCl solution (3 μL, 0.3 μmol).

For the preparation of the sensing membrane (M-RuD$_1$, the membrane encapsulating Ru complex linked with one dendron) containing the Ru(II) complex **10**, the latter (4.3 mg, 1.37 μmol) was added to the above sol–gel solution and the mixture was stirred for 4 h at 25 °C. The resulting mixture was spread on the microscope slide and dried at 25 °C for 24 h, after which a glassy membrane was formed, and it was finally dried at 80 °C for 12 h.

For the preparation of the sensing membrane (M-RuD$_3$, the membrane encapsulating Ru complex linked with three dendrons) containing the Ru(II) complex **11**, the latter (9.1 mg, 1.37 μmol) was added to the above sol–gel solution and the mixture was stirred for 4 h at 25 °C. The resulting mixture was spread on the microscope slide and dried at 25 °C for 24 h, and finally dried at 80 °C for 12 h.

For comparison, a sol–gel membrane (M-Ru) doped with $Ru(dpp)_3$ was prepared from a mixture of $Ru(dpp)_3{\cdot}2PF_6^-$ (1.9 mg, 137 μmol) and the above sol–gel solution.

2.4. Measurement of fluorescence intensity

The luminescence spectra and quenching response data of the sensing membranes were obtained with a 2D fluorescence spectrophotometer (Model F-4500, Hitachi, Japan). The 2D fluorescence spectrophotometer was connected by a 2 m bifurcated liquid light conductor (Lumatec GmbH, Germany) to a dye-immobilized sensing membrane on a glass slide placed in the port of a 10 mL stainless steel gas flow chamber. Thus, there was no interference from light outside the chamber. The measurement conditions of the spectrophotometer were as follows: scanning speed, 30,000 nm min^{-1}; PMT voltage, 950 V; excitation wavelength range, 250–650 nm; emission wavelength range 250–650 nm; excitation and emission slits, 10 nm. The desired concentrations of oxygen in water were obtained by passing pure N_2 and O_2 gas through the chamber using computer-controlled mass flow controllers (Model GFC171, Aalborg, USA) with a constant flow rate of 1 L min^{-1}.

2.5. Leaching experiments

After aging, each sensing membrane on a glass slide was washed several times with $CHCl_3$, and immersed in 100 mL of distilled water in a leaching vessel continuously shaken at room temperature. The membranes were periodically withdrawn, placed into the flow chamber, and their luminescence intensities measured. The membranes were then returned to the leaching vessel containing fresh distilled water. The extent of dye leaching was determined by calculating the relative decrease in the luminescence intensity of each sensing membrane compared with the initial value.

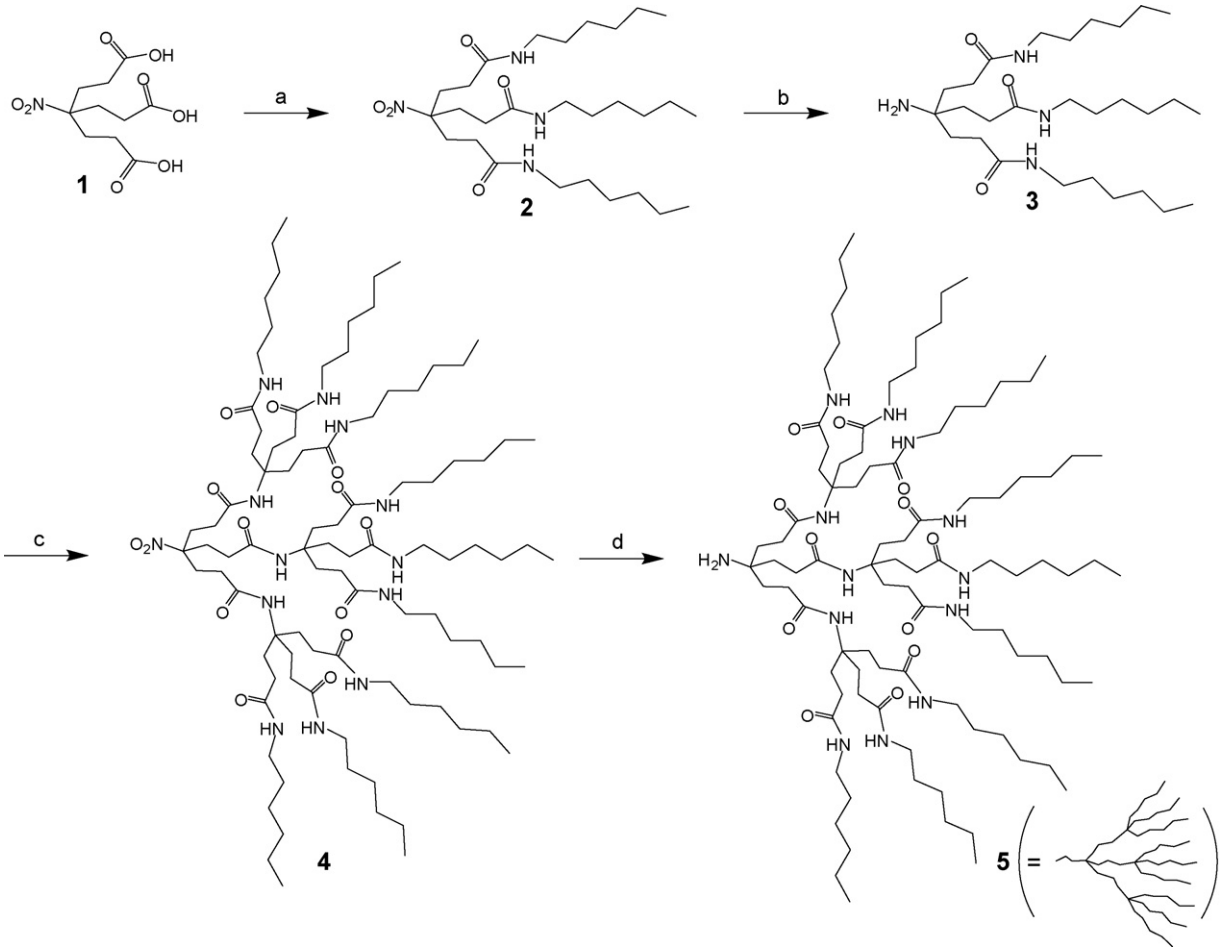

Scheme 1. Synthesis of dendron: (a) hexyl amine, DCC, HOBT, DMF, 25 °C, 24 h; (b) Raney-Ni, absolute EtOH, 90 psi H_2, 25 °C; (c) triacid **1** (1/3 eq.), DCC, HOBT, DMF, 25 °C, 24 h; (d) Raney-Ni, absolute EtOH, 90 psi H_2, 25 °C.

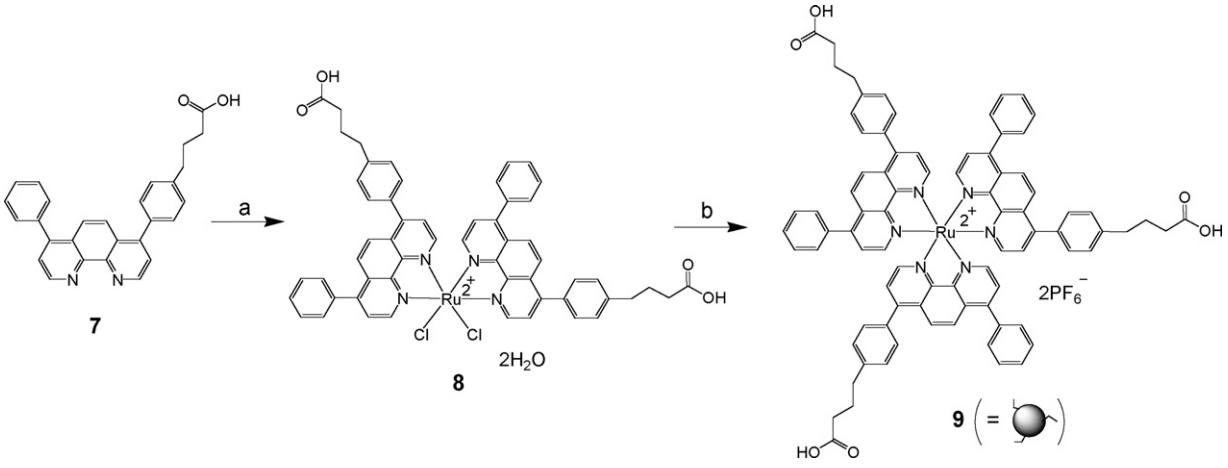

Scheme 2. Synthesis of Ru(II) complex possessing linker arms: (a) $RuCl_3 \cdot H_2O$ (0.5 eq.), DMF, reflux 3 h; (b) **7**, EtOH, reflux 3 h.

3. Results and discussion

3.1. Syntheses

Considering the bond formation with the Ru(II) complex as well as the steric effect of the dye molecule, the second-generation dendron **5** possessing both an amine moiety and nine C_6-hydrocarbon chains was devised, although numerous choices could be envisioned (Scheme 1). Therefore, the triacid **1** [36] was reacted with *n*-hexyl amine under a standard peptide coupling condition [38] to afford (78%) the amide **2**, whose formation was confirmed by its NMR spectra and the ESI-MS peak at *m*/*z* 527.4 $(M+H)^+$. The reduction of the nitro group in **2** was accomplished (98%) by means of a Raney-Ni catalyst under 90 psi of hydrogen in EtOH at 25 °C to

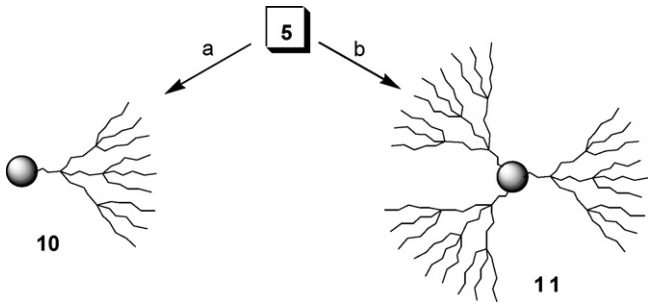

Scheme 3. Synthesis of Ru(II) complex linked with dendron(s): (a) complex **6**, DCC, HOBT, DMF, 25 °C, 24 h; (b) complex **9**, DCC, HOBT, DMF, 25 °C, 24 h.

afford the corresponding amine **3**, whose structure was confirmed by the chemical shift (^{13}C NMR) from 93.5 (CNO_2) to 58.0 ppm (CNH_2) and the molecular ion peak (ESI-MS) at m/z 1713.3 $(M+H)^+$. To obtain the desired dendron **5**, the same synthetic strategy as that used in the preparation of **2** was employed. Thus, the resulting amine **3** was reacted again with the triacid **1** to give (72%) the nitro compound **4**, which was then reduced (96%) to the corresponding amine dendron **5**. The structural confirmation of **5** was provided by the appropriate chemical shift (^{13}C NMR) from 91.5 ppm (O_2NC) to 49.0 ppm (H_2NC), as well as the peak for the molecular ion (ESI-MS) at m/z 1683.3 $(M+H)^+$.

The Ru(II) complex **9**, possessing three carboxylic acid moieties available for the formation of bonds with the amine dendron, was prepared as depicted in Scheme 2. The phenanthroline derivative **7**, which had previously been synthesized [37], was treated with a half equivalent of $RuCl_3$ in DMF under reflux to give (80%) the complex **8**, which was then reacted with an equivalent of **7** in refluxing ethanol. The chromatographic purification of the crude product afforded (70%) the desired ruthenium complex **9**, whose structure was confirmed by the presence of the appropriate peaks (^{13}C NMR) as well as the observed mass peak (MALDI-TOF) at m/z 1357.41 $(M-2PF_6)^{2+}$.

The attachment of the dendron **5** to Ru(II) the complex **6** was achieved through the use of the traditional peptide coupling condition to give (80%) the Ru(II) complex **10** linked with one dendron (Scheme 3). The structural confirmation of the product included the appearance of appropriate ^{13}C NMR peaks and MALDI-TOF MS peak at m/z 6349.5 $(M-2PF_6)^{2+}$. Similarly, the Ru(II) complex **11** linked with three dendrons was successfully prepared (61%) by the reaction of the complex **9** with three equivalents of the dendron **5** under DCC-promoted coupling conditions. The structure of **11** was identified by the presence of a newly appeared peak (^{13}C NMR) at 173.3 ppm corresponding to the *C*ONH bond and the complete disappearance of the CO_2H peak at 174.8 ppm, as well as the MALDI-TOF MS peak at m/z 6349.5 $(M-2PF_6)^{2+}$.

3.2. Spectral and DO sensing properties of optical sensing membranes

The Ru(II) complexes linked with dendron(s) **10** and **11** have molecular weights of 3140 and 6643, respectively. Unlike $Ru(dpp)_3$, the Ru(II) complexes **10** and **11** are quite soluble in volatile organic solvents, such as $CHCl_3$, CH_3CN and MeOH, so that these materials are well dissolved in the sol–gel solution, which enables these dye molecules to be rather evenly distributed in the membrane.

We prepared sol–gel-based sensing membranes (M-RuD_1 and M-RuD_3) by encapsulating these Ru(II) complexes (**10** and **11**) in gels derived from the sol solution containing TEOS and studied their spectral and DO sensing properties.

The 2D luminescence spectra of the sensing membranes, M-RuD_1 and M-RuD_3, are shown in Fig. 2 Similarly to $Ru(dpp)_3$ [39], both membranes M-RuD_1 and M-RuD_3 exhibit a strong luminescence emission at 590 nm when excited by radiation at 480 nm in de-aerated water. It is evident that the covalent incorporation of the dendrons into $Ru(dpp)_3$ does not cause any significant change in its absorption and emission spectra.

The test for the quenching responses of the sensing membranes was performed by continuously exposing them to a mixture of dissolved O_2 and N_2 obtained by bubbling the two gases. As shown in Fig. 3, the sensing membranes (M-RuD_1, M-RuD_3) showed typical quenching responses in that their luminescence emission intensities were decreased by the quenching process when they were exposed to an aqueous solution saturated with O_2 gas. The membranes are also regenerated by flushing with N_2 gas, and there was no drift in any of the signal changes, indicating that the membranes M-RuD_1 and M-RuD_3 can be used for repeated measurements.

3.3. Stability of sensing membranes

We compared the extent of dye leaching from the various sensing membranes in order to evaluate their long-term operation in aqueous solution. The sensing membranes, M-RuD_1, M-RuD_3 and M-Ru, were soaked separately in distilled water for 40 days. The membranes were periodically withdrawn from the water and their

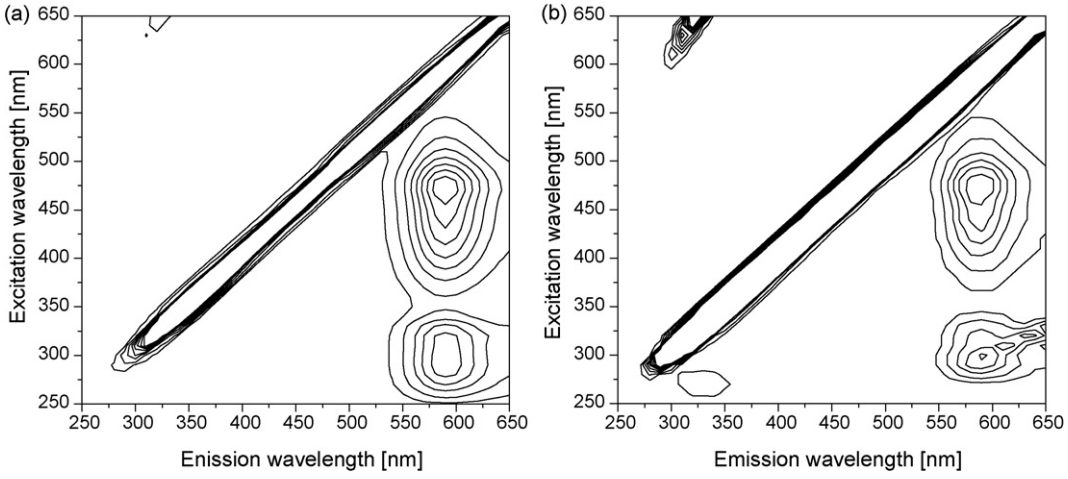

Fig. 2. 2D luminescence spectra of the sensing membranes M-RuD_1 (a) and M-RuD_3 (b) in de-aerated water.

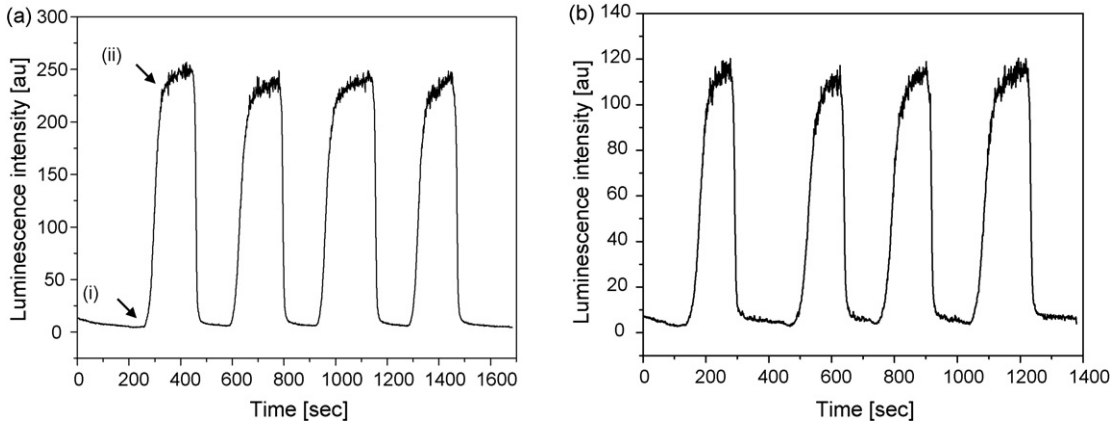

Fig. 3. Quenching response of the sensing membranes M-RuD_1 (a) and M-RuD_3 (b) to DO when the solution is saturated with O_2 (i) and N_2 (ii).

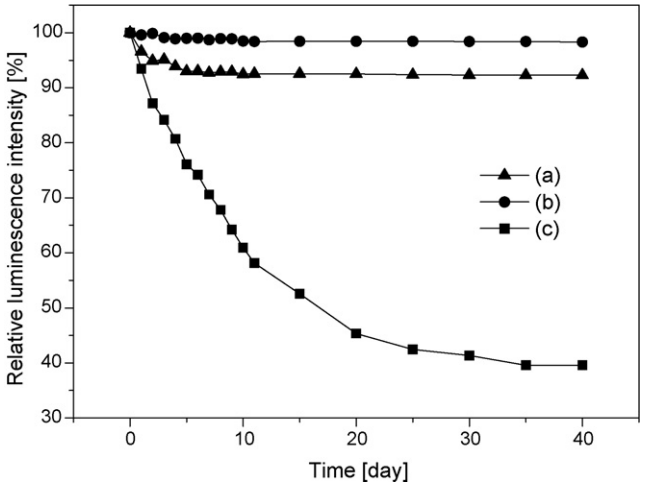

Fig. 4. Leaching of the dye molecules from the membranes M-RuD_1 (a), M-RuD_3 (b) and M-Ru (c) in water.

luminescence intensities were measured at 590 nm with an excitation wavelength of 480 nm. As depicted in Fig. 4, the luminescence intensity of the membrane M-Ru gradually decreased, which indicates that Ru(dpp)$_3$ leached out of the membrane and only about 40% of the Ru(dpp)$_3$ originally present in the gels was retained after 40 days [40]. In contrast, in the case of the membrane M-RuD_3, the Ru(II) complexes did not leach out of the membrane during the same time period. In the case of the membrane M-RuD_1, a slight decrease of the emission intensity was observed during the initial stage of the experiment, but about 92% of the dye was retained in the gels. These results demonstrate that the encapsulation of the dyes **10** and **11** in gels prevents them from leaching out of the matrix. The initial decrease in the luminescence intensity of the membrane M-RuD_1 is probably due to the smaller size of the dye molecule **10** as compared to the complex **11**, causing it to be loosely retained underneath the membrane surface, so that it slightly leaches from the gels in the initial stage of the experiment.

4. Conclusion

In order to prevent the leaching of small dye molecules from a sol–gel-based optical sensing membrane by increasing the size and lipophilicity of the dye molecules, a bulky dendron (**5**) possessing an amino group, which is readily prepared by chemical transformations such as amidation and catalytic reduction, was designed and covalently attached through the amide bond formation to Ru(dpp)$_3$ possessing carboxylic groups. As a result of these manipulations, the molecular weights of the Ru(II) complex (**10**) linked with one dendron and the Ru(II) complex (**11**) linked with three dendrons became 3140 and 6643, respectively. Optical sensing membranes (M-RuD_1, M-RuD_3) were prepared by the encapsulation of these Ru(II) complexes (**10**, **11**) in a TEOS derived sol–gel matrix. These Ru(II) complexes linked with dendron(s) are quite soluble in sol–gel solution to provide a rather even distribution of dyes in the membrane.

The sensing membranes (M-RuD_1 and M-RuD_3) displayed good DO sensing properties equal to those of the membrane (M-Ru) doped with Ru(dpp)$_3$, and showed excellent stability in aqueous solution. The membrane M-RuD_3 was superior to M-RuD_1 with respect to the inhibition of dye leaching. Therefore, this approach to link a sensing moiety to bulky dendritic side-chains can be a useful means to prevent dye leaching from porous matrices.

In addition, the Ru(II) complexes, **10** and **11**, are quite soluble in most volatile organic solvents such as $CHCl_3$, CH_3CN, EtOAc and MeOH, so that they are promising dyes for developing optical sensing membranes based on various polymer matrices soluble in organic solvents, such as silicone rubber, poly(ester), poly(styrene), etc.

Acknowledgement

This work was supported by grant no. RTI04-03-03 from the Regional Technology Innovation Program of the Ministry of Commerce, Industry and Energy (MOCIE).

References

[1] C.K. Sen, G.L. Semenza, Oxygen Sensing, Methods in Enzymology, vol. 381, Elsevier Academic Press, San Diego, 2004.
[2] R.E. Sojka, D.M. Oosterhuis, H.D. Scott, in: M. Pessarakli (Ed.), Handbook of Photosynthesis, second ed., CRC Press, Boca Raton, FL, 2005, pp. 299–314.
[3] L.A. Taylor, B. Cooper, D.S. McKay, R.O. Colson, Miner. Metal. Proc. 10 (1993) 43.
[4] V.S. Whiffin, M.J. Cooney, R. Cord-Ruwisch, Biotechnol. Bioeng. 85 (2004) 422.
[5] P.L. Kebabian, R.R. Romano, A. Freedman, Meas. Sci. Technol. 14 (2003) 983.
[6] M. Fitzgerald, D.B. Papkovsky, M. Smiddy, J.P. Kerry, C.K. O'Sullivan, D.J. Buckley, G.G. Guilbault, J. Food Sci. 66 (2001) 105.
[7] L.C. Clark, Trans. Am. Artif. Organs 2 (1956) 41.
[8] C. McDonagh, B.D. MacCraith, A.K. McEvoy, Anal. Chem. 70 (1998) 45.
[9] J.N. Demas, B.A. DeGraff, Anal. Chem. 63 (1991) 829A.
[10] Z. Osenzweig, R. Kopelman, Anal. Chem. 67 (1995) 2650.
[11] Z. Osenzweig, R. Kopelman, Sens. Actuators B 36 (1996) 475.
[12] S.K. Lee, I. Okura, Anal. Chim. Acta 342 (1997) 181.
[13] P.K. McNamara, X. Li, A.D. Stull, Z. Rosenweig, Anal. Chim. Acta 361 (1998) 73.
[14] J.R. Bacon, J.N. Demas, Anal. Chem. 59 (1987) 2780.
[15] P. Douglas, K. Eaton, Sens. Actuators B 82 (2002) 200.
[16] Y. Amao, Y. Ishikawa, I. Okura, Anal. Chim. Acta 445 (2001) 177.

[17] V.V. Vasil'ev, S.M. Borisov, Sens. Actuators B 82 (2002) 272.
[18] A. Mills, M. Thomas, Analyst 122 (1997) 63.
[19] P. Hartmann, M.J.P. Leiner, M.E. Lippitsch, Anal. Chem. 67 (1995) 88.
[20] P. Hartmann, W. Trettnak, Anal. Chem. 68 (1996) 2615.
[21] X.M. Li, F.C. Ruan, K.Y. Wong, Analyst 118 (1993) 289.
[22] B.D. Mac Craith, C. McDonagh, A.K. McEvoy, T. Butler, G. O'Keeffe, V. Murphy, J. Sol–Gel Sci. Tech. 8 (1997) 1053.
[23] C. McDonagh, P. Bowe, K. Mongey, B.D. MacCrath, J. Non-Cryst. Solids 306 (2002) 138.
[24] J. Estella, J.C. Echeverria, M. Laguna, J.J. Garrido, J. Non-Cryst. Solids 353 (2007) 286.
[25] M.J. Plaschke, R. Czolk, J. Reichert, H.J. Ache, Thin Solid Films 279 (1996) 233.
[26] P.J. Skrdla, S.S. Saavedra, N.R. Armstrong, Appl. Spectrosc. 53 (1999) 785.
[27] G.A. Baker, A.N. Watkins, S. Pandey, F.V. Bright, Analyst 124 (1999) 373.
[28] M.D. Senarath-Yapa, S.S. Saavedra, Anal. Chim. Acta 432 (2001) 89.
[29] E.R. Carraway, J.N. Demas, B.A. DeGraff, J.R. Bacon, Anal. Chem. 63 (1991) 337.
[30] X.-M. Li, F.-C. Ruan, W.-Y. Ng, K.-Y. Wong, Sens. Actuators B 21 (1994) 143.
[31] P. Hartmann, M.J.P. Leiner, Anal. Chem. 67 (1995) 88.
[32] B.D. MacCrath, C.M. McDonagh, G.E. O'Keeffe, T. Keyes, J.G. Vos, B. O'Kelly, J.F. McGilp, Analyst 118 (1993) 385.
[33] B.D. MacCraith, G. O'Keeffe, C. McDonagh, A.K. McEvoy, Electron. Lett. 30 (1994) 888.
[34] M. Krihak, M.R. Shahriari, Electron. Lett. 27 (1996) 12.
[35] M. Murtagh, D. Ackley, M.R. Shahriari, Electron. Lett. 32 (1996) 477.
[36] G.R. Newkome, C.N. Moorefield, K.J. Theriot, J. Org. Chem. 53 (1988) 5552.
[37] H.J. Kim, Y.C. Jeong, J.I. Rhee, T.H. Kim, Bull. Korean Chem. Soc. 27 (2006) 1.
[38] Y.S. Klausner, M. Bodansky, Synthesis (1972) 453.
[39] R.J. Watts, G.A. Crosby, J. Am. Chem. Soc. 93 (1971) 3184.
[40] Y.C. Jeong, O.-J. Sohn, J.I. Rhee, S. Lee, H.J. Kim, Bull. Korean Chem. Soc. 28 (2007) 883.

Talanta 76 (2008) 1136–1140

Contents lists available at ScienceDirect

Talanta

journal homepage: www.elsevier.com/locate/talanta

Functional group analysis on oxidized surfaces of synthetic textile polymers

Dierk Knittel*, Eckhard Schollmeyer

Deutsches Textilforschungszentrum Nord-West e.V. (DTNW), Adlerstrasse 1, D-47798 Krefeld, Germany

ARTICLE INFO

Article history:
Received 25 October 2007
Received in revised form 13 May 2008
Accepted 14 May 2008
Available online 7 July 2008

Keywords:
Polymer surface analysis
Functional groups
Wet-chemical analysis
Advanced oxidation process
Synthetic textiles

ABSTRACT

A comprehensive collection of wet-chemical analyses of functional groups on oxidatively treated surfaces of hydrophobic polymers like poly(ethylene terephthalate) or polyolefine is presented. New methods are introduced. Textiles and foils have been subjected to advanced oxidation processes and the different oxygen functions have been quantified. Analysis of surface functional groups includes radical site determination with radical scavengers like diphenylpicrylhydrazyl, reduction of peroxides determined iodometrically, cationic dyestuff adsorption, carbonyl binding to Girard reagent P and surface hydroxyl group determination by surface nitrosation and subsequent azo-dye formation photometrically determinable. Use of potential surface swelling agents has been excluded except for addition of wetting agent. Wet-chemical analyses on textile surfaces bear the benefit of integrating over (relatively) large sample areas, a point which is interesting when regarding inhomogenities of textile or other surface constructions. In addition examples for visualisation for the existence of surface groups are described.

1. Introduction

During the course of a research project on the influence of ozone treatment (or ozone and UV-irradiation treatment, advanced oxidation process—AOP) on fibre surfaces of textile materials the importance of a quick analysis of surface oxidized functionalities posed an urgent demand [1].

In the literature AOP-treatment of plastics for surface functionalization has been reported frequently. Thereby mainly hydroxyl radicals and peroxy radicals are involved attacking the polymer. Some of the primarily formed species on the surface are rather long-lived other rearrange to stable functions. Quite often the oxygenated surface functions decline on storage ('hydrophobic recovery') due to polymer segment diffusion into the bulk polymer (especially with polymers of low glass transition temperature). In most of the papers XPS-spectroscopy was used in order to assess chemical groups on the surface [2–5,8,9]. Some chemical analysis methods for selected groups were mentioned too. These include the determination of peroxides, of carboxyl groups and of radicals [6–12]. An interesting chemical approach mainly for fluorescent derivatization on PE surfaces was given by Holländer in 2004 but requires rather uncomfortable calibration [13] and still introducing organic solvents.

Regarding drawbacks of XPS-analyses for quantitative determination on textile constructions (curvature of filaments, extremely small area accessible compared to practical production widths of >1.5 m, cost of equipment) it was felt necessary to establish wet-chemical analytics for the determination of oxygen containing functions on common, originally hydrophobic textile polymers exposed to advanced oxidation processes. For this aim some of the methods cited have been adopted and modified for easy analysis, also some new methods have been developed. The paper presented compiles the methods introduced.

Only methods were chosen which can be applied from almost pure aqueous solutions. Thus it should be possible to minimise swelling effects of surface layers of synthetic polymers like poly(ethylene terephthalate) (PETP), polypropylene (PP) or similar polymers when working with organically soluble reagents thus keeping the (chemical) information depth as close to the surface as possible. Some of the methods established were tested too and described as qualitative spray-test method for visualisation of AOP-treatments.

2. Experimental

2.1. Materials used

Poly(ethylene terephthalate) foil, thickness 190 μm, 274 g/m^2 (Cadillac Plastics), polypropylene foil, 75 μm, 68 g/m^2 (Leco); poly(ethylene terephthalate) (PETP) fabric, pleine weave,

* Corresponding author. Tel.: +49 2151 843 165; fax: +49 2151 843 143.
E-mail addresses: knittel@dtnw.de, info@dtnw.de (D. Knittel).

0039-9140/$ – see front matter © 2008 Elsevier B.V. All rights reserved.
doi:10.1016/j.talanta.2008.05.036

129 g/m^2, warp 24.8 cts/cm, weft 21.2 cts/cm (Testex); polyethylene fabric (PE), 104 g/m^2, warp 6.6 cts/cm, weft 6.2 cts/cm (Leco); polypropylene fabric (PP), pleine weave, 196 g/m^2, warp 22.5 cts/cm, weft 15.3 cts/cm (C.C. Cramer); poly(butylene terephthalate) (PBT) non-woven, 51.8 g/m^2; thickness 390 μm (Freudenberg).

All materials have been extracted in a Soxhlet-apparatus prior to AOP with methanol/water (1:1). Advanced oxidation of textile samples (ozone, ozone + UV) has been done as described in [1], i.e. samples of textiles (30 cm × 15 cm) were treated with ozone (68–74 and 190–185 g/N m^3, respectively) in a cell equipped with a quartz window. Treatment time usually was 10–30 min. Some samples too were simultaneously irradiated with a mercury UV-lamp for AOP.

2.2. Apparatus used

UV–VIS Diode Array Spectrophotometer HP 8452 A (Hewlett-Packard) with cuvettes of 1 cm optical path length and analyte volume of about 80–100 μl (Brand) was used for measurements of dyes. A spectrophotometer Datamaster Type DC 3880 (Datacolor) was used for remission measurements.

2.3. Chemicals used

Methylene blue for microscopy (Merck).
Ethyl red 97% (lithium-salt) (prepared from sodium salt, Aldrich).
Intracronred® BF-3RM 150%, reactive dyestuff (Yorkshire).
Nonionic wetting agent Marlipal® O13/80 (Sasol) and SDS (Aldrich).
H-acid (4-amino-5-hydroxynaphthaline-2,7-disulfonic acid disodium salt hydrate 85%) (Aldrich or Hoechst).
Sulfanilic acid (Fluka).
Girard reagent P (*N*-acetylhydrazinopyridinium chloride) (Aldrich).
2,2-Diphenyl-1-picrylhydrazyl (DPPH) (Aldrich).
Other reagents were of analytical grade.

2.4. Radical determination on surfaces

The wet-chemical test is oriented on methods of MacManus et al. [11]. A DPPH-solution (2 mg/20 ml MeOH) is prepared and applied to (as-received and after surface oxidation) textile samples of about 120 mg in brown flasks. After shaking for several hours (up to 3 days) at room temperature the supernatant solution is quantified by photometry at 516 nm. From the decrease of DPPH-absorbance the amount of radicals reacted can be determined.

This test can be modified for visualisation by simultaneous addition of an acid dye like the lithium salt of ethyl red. The dye anion binds to the C-cation of the surface.

2.5. Determination and visualisation of peroxidic groups on oxidized polymer surfaces

Reaction vessels given in Fig. 3 are used for quantification (details in [1]). Briefly, they enable the treatment of small samples of fabric to be analysed with heating under inert atmosphere in presence of reaction partner. Additionally, titration of reagents formed may be done using microsyringes. These vessels may be used too for grafting reactions (occurrence of radicals or peroxides).

For visualisation of the existence of peroxidic groups on oxidized polymer a graft polymerization of acrylic acid monomer may be induced by heating under inert atmosphere. After removal of homopolymers formed by alkaline washing staining is done with cationic dyestuff methylene blue.

2.6. Determination of hydroxyl containing surfaces: visualisation of surface hydroxyl groups

A known amount of sample (0.1–0.2 g) is treated with 2.5 ml of 1 mol/l HCl and 1 ml of 15% Na-nitrite solution. After 10 min the textile sample is removed and rinsed intensively with 10 ml $NaHCO_3$-solution (1%, containing 0.5% Na-dodecylsulfate for wetting). After neutralisation (about 3 times with 20 ml dist. water) the sample is transferred to a 25 ml measuring flask and 1 ml of freshly prepared solution of sulfanilic acid (1%) is added. After 9 min of shaking 1 ml of H-acid (0.5% fresh solution) is added and shaken in the dark for 1.5 h. The resulting red solution can be analysed at 510 nm. Water introduced by the sample is corrected by weighing. Calibration is done simply by the use of a nitrite solution for the sulfanilic acid/H-acid procedure.

This reaction sequence can be used for visualisation as spraying test sequence on the oxidized fabric: the sample is dried following the nitrite treatment and sprayed with sulfanilic acid followed by H-acid. Photographs can be taken after 1.5 h storage in the dark. Alternatively a surface oxidized sample may be stained by conventional reactive dyeing procedures and resulting colouration may be determined in reflectance measurements.

2.7. Determination of carbonyl groups on oxidized polymer surfaces

0.5 g of sample is shaken with 2.7 g of Girard P solution (1.11 g/l). After addition of 0.3 g acetic acid the vessel is stirred in a closed vessel (see Fig. 3) for 30 min at 90 °C. After cooling the solution is transferred into a 100-ml flask. The decrease of reagent concentration due to binding of reagent to surface carbonyls is analysed photometrically at 260 nm.

2.8. Determination of carboxylic groups on surfaces of partially oxidized surfaces of hydrophobic polymers

Samples (0.1–0.5 g) are treated at room temperature with a 0.05% solution of methylene blue in Britton–Robinson buffer (pH 7.1–7.4). The bluish samples are rinsed thoroughly and dried in air. For quantitative determination the sample is exposed to 20 ml of 84% aqueous acetic acid and shaken for 1 h. Photometric analysis is done at 650 nm.

3. Strategies for wet-chemical analysis

The analytical methods elaborated enables the quantification of surface functional groups on synthetic polymers. The methods too can be used as a qualitative quick-test and for visualisation of surface effects obtained by AOP-treatment. In the following the scheme of analyses and chemical basics are described.

3.1. Radicals on surfaces of hydrophobic textile surfaces

For the determination of surface radicals on PP or PETP the following reactions have been used (according to [12]) (Fig. 1) and widened for visualisation purposes by dye binding. First step after radical formation is an electron transfer to DPPH followed by irreversible protonation to diphenylpicryl hydrazine and a surface cation. The decay of the violet colour of DPPH can be followed pho-

tometrically. The surface cation can be trapped by adding an acid dye.

3.2. Wet-chemical detection and determination of hydroxyl groups on oxidized polymers

For quantification of hydroxyl group contents of oxidized surfaces the esterification by aqueous nitrous acid has been chosen. This reagent has been known for the use in homogeneous reactions for detection of alcohols [14]. It proved to be suitable even in heterogeneous application and one may expect no interference from possibly coexisting amino groups since $-NH_2$ groups will be destroyed by HONO.

Fig. 2 shows the reaction sequence used. In concentrated solutions of nitrous acid hydroxyl groups on the polymer surface are esterified. Those surface nitrous acid esters are stable against washing but can be cleaved afterwards by dilute acid. Cleavage is done on the washed surface in solutions capably of trapping HONO. The newly formed nitrous acid immediately is transformed to a diazonium salt, which can be used for formation of an azo-dye, i.e. with H-acid or similar.

This reaction sequence can be used too for visualisation on the textile as a spray-test application.

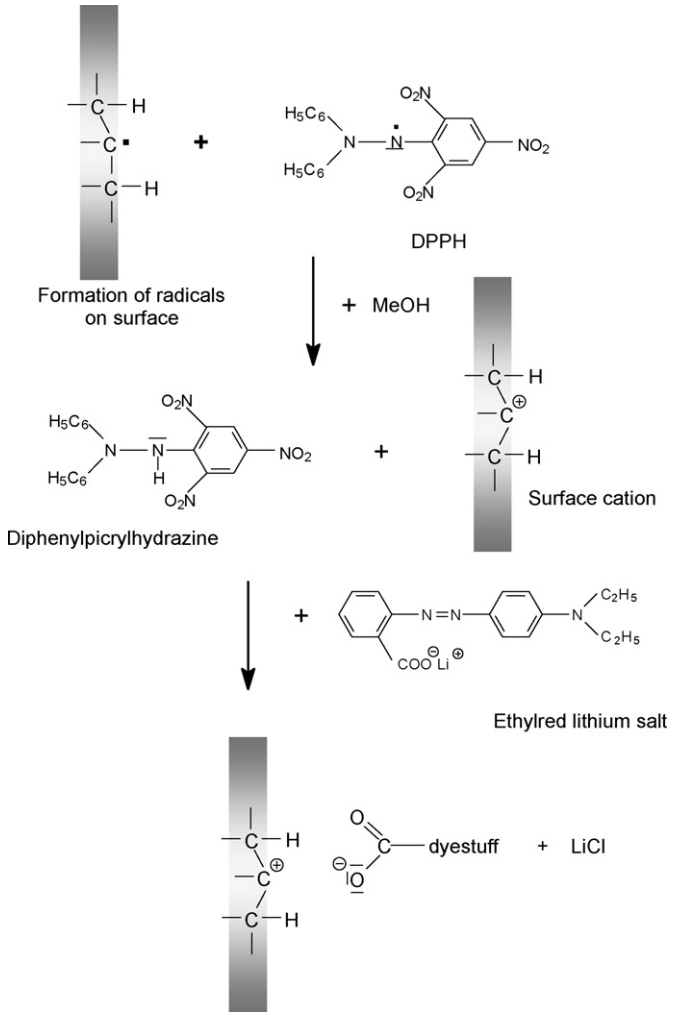

Fig. 1. Detection of radical functions on oxidized polymers by reaction with diphenyl-picrylhydrazyl, followed by formation of dyestuff binding for visualisation.

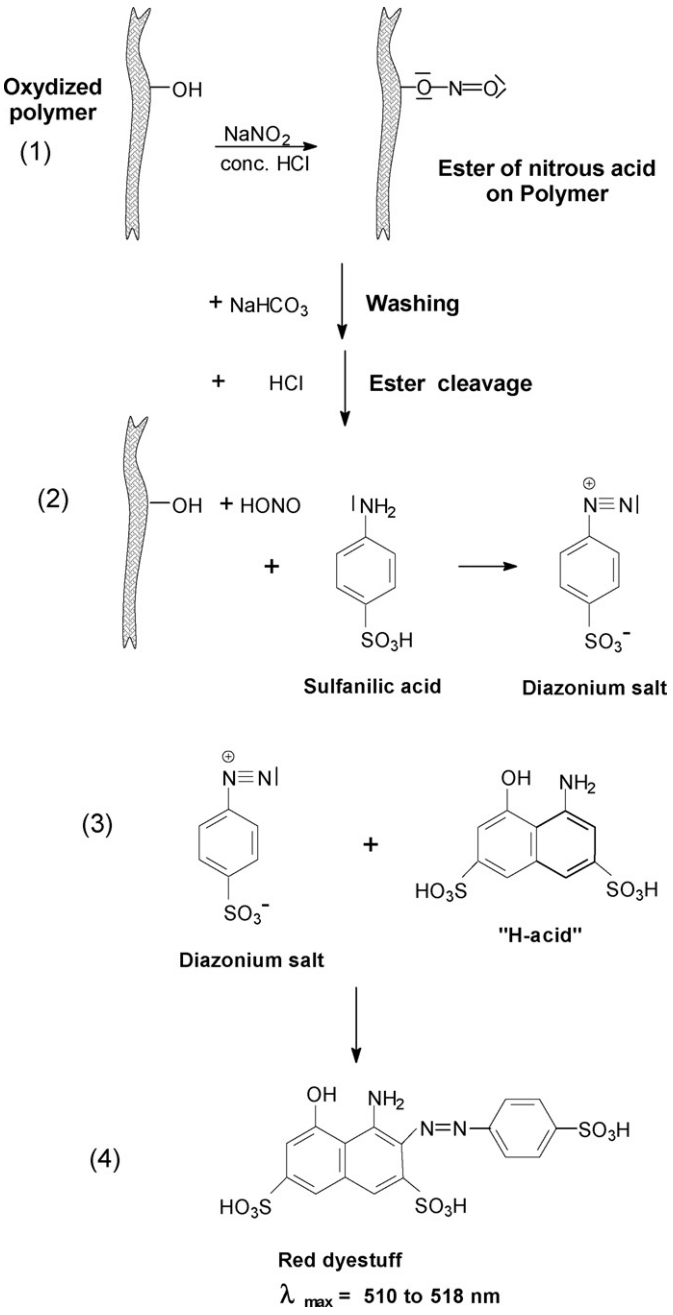

Fig. 2. Scheme for quantification of hydroxyl groups on surfaces of oxidized polymers.

3.3. Wet-chemical detection and determination of peroxidic groups on oxidized polymers

The presence of peroxidic groups on oxidized polymer surfaces (ozone treatment) can be determined using potassium iodide (cf. [12]). There is no discrimination between hydroperoxides or dialkylperoxides. Using apparatuses as described in Fig. 3, a simple titrimetric analysis can be performed.

This reaction vessel can be used too for other analyses on oxidized samples.

In addition to titration peroxidic structures on surfaces may be used for inducing grafting reactions on the surface with acrylic monomers (cf. [4,15–18]). A successful grafting reaction, e.g. with acrylic or methacrylic acid can be visualised after-

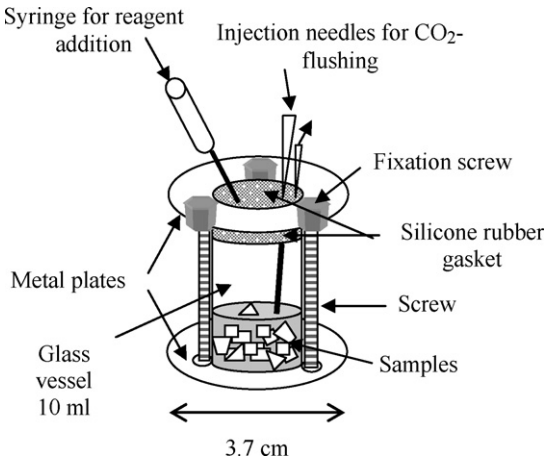

Fig. 3. Testing equipment for radical-, peroxide-, carbonyl- and grafting-analysis.

wards by using a cationic dyestuff as described in Section 2.4 (cf. [16,17]).

3.4. Wet-chemical detection and determination of carbonyl groups on oxidized polymers

There are numerous reaction for the determination of carbonyl groups in solution. An important one for the purpose of surface analysis lies in the use of a water soluble Girard reagent (Girard P). Qualitative analysis using such a reagent can be done by reflectance measurements on oxidatively treated polymer surfaces after exposure to Girard P solutions.

Performing this analysis on oxidized textiles with minimal volumes of reagent (i.e. almost not more than textile wet pick up) the decrease of Girard-concentration in the treating solution can be monitored and quantified by photometric analysis within cuvettes of about 100 μl working volume.

3.5. Wet-chemical detection and determination of carboxyl groups on oxidized polymers

Detection and determination of carboxylic groups on oxidized polymer surfaces follows well known strategies, i.e. binding of cationic dyestuffs on carboxylate functions, visualisation for documentation and then detachment of the cationic dyestuff by acid treatment and photometric analysis of the solutions obtained (cf. [6]). Preferable for this determination is the use of highly pure cationic dyestuff as used for microscopy (i.e. methylene blue).

4. Results on AOP-treated samples obtained by wet-chemical analyses

4.1. Results on AOP-treated polymers

To illustrate the versatility of the analytical methods described some examples are given in Table 1 for surface group analysis on AOP-treated foils and Table 2 for textiles (details see [1]). Samples are analysed immediately after preparation.

Analysis for radicals on treated PE-fabric showed 0.012 μmol/g fabric just after AOP-treatment, decreasing to about 0.006 μmol/g on storage for 6 days, traces are still detectable even after 22 days. As known from the literature, all the samples showed hydrophobic recovery on storage for several days. Thus the chemical surface analysis proves to be a rather quick and sensitive and inexpensive tool.

4.2. Visualisations of functional groups on surfaces of synthetic material

Visualisation of hydroxyl groups can be done as test on the fabric or on the foil by spraying the reagents (nitrite/-HCl/sulfanilic acid/H-acid) onto the sample.

Other examples of various staining reactions on oxidized polymer surfaces, differently treated with ozone and analysed for visualisation of carboxylic and peroxidic groups and radical centers, respectively are presented in Fig. 4. Radical detection on oxidatively treated polyesters and on polyolefins combines the reaction with DPPH resulting in a surface cation which is trapped by use of an anionic dyestuff like salts of ethyl red giving rise to visible staining.

5. Discussion

In this work it could be shown that almost all relevant oxygenated functions on polymer surfaces can be quantitatively assessed by wet-chemical analysis on textile constructions. Wet-chemical analyses on textile surfaces bear the benefit of integrating

Table 1
Wet-chemical analysis of oxygen functionalities before and after ozone treatment of polymer foils (30 min O_3) (sum of both sides)

Sample	Total –COOH (μmol/cm²)	Total –C=O ($\times 10^{-2}$ μmol/cm²)	Total –OH ($\times 10^{-2}$ μmol/cm²)
PETP-original	$(2.0 \pm 0.1) \times 10^{-4}$	(2.7 ± 0.04)	(1.4 ± 0.3)
O_3-treated	$(4.2 \pm 0.2) \times 10^{-2}$	(2.7 ± 0.04)	(80 ± 17.6)
PP-original	$(7.0 \pm 0.5) \times 10^{-4}$	(1.22 ± 0.015)	(5.0 ± 1.1)
O_3-treated	$(1.7 \pm 0.13) \times 10^{-2}$	(1.77 ± 0.02)	(24 ± 5.3)

Table 2
Oxygen containing groups of AOP-treated fabrics

Sample code	Total –COOH (μmol/g)	Total –C=O (μmol/g)	Total –OH (μmol/g)	Total peroxides (μmol/g)
PETP-original	0.11 ± 0.006	0.17 ± 0.03	3.4 ± 0.75	0
PETP, 30 min O_3	0.48 ± 0.03	5.4 ± 0.03	~29 ± 6.3	6.6 ± 0.12
PBTP-original	0.37 ± 0.007	n.d.	15 ± 3.3	n.d.
PBTP, 30 min O_3	0.39 ± 0.007	n.d.	8.4 ± 2.85	n.d.
PBTP, 30 min O_3 with UV-irradiation	1.62 ± 0.03	n.d.	3.5 ± 0.8	n.d.
PP-original	0.04 ± 0.003	0.6 ± 0.02	0.4 ± 0.09	0
30 min O_3	0.07	2.4	7.7 ± 1.7	2.04

n.d., not determined.

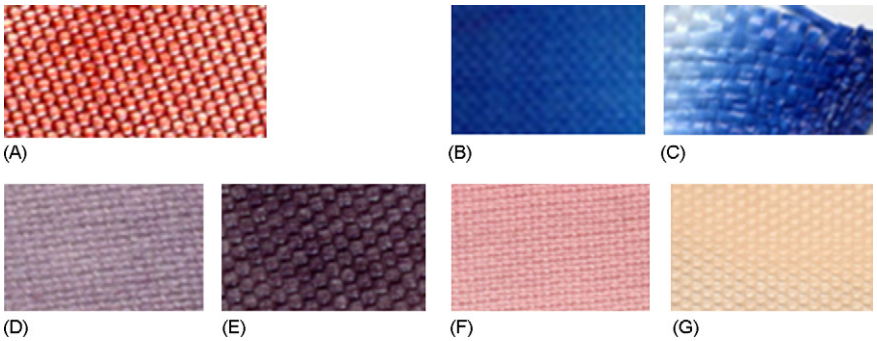

Fig. 4. (A) Spray test on AOP-treated PP-fabric for visualisation of the existence of hydroxyl groups (nitrite/sulfanilic acid/H-acid). (B) Methylene blue staining of AOP-treated PET. (C) Same on PE. (D) Visualisation of peroxides on PET by KI/starch solutions. (E) Same for PP. (F) Visualisation of radical formation on AOP-treated synthetic polymers by simultaneous application of DPPH in the presence of an acid dye for marking the cationic centres formed. (G) Same for PE.

over (relatively) large sample areas, a point which is interesting when regarding inhomogenities of textile or other surface constructions. In addition, the wet-chemical analysis – being rather quick – avoids problems due to changes during sample storage.

Especially important are the possibilities to characterize partially oxidized surfaces of rather large size. Obviously wet-chemical analysis includes surfaces of cracks or other morphological irregularities thus giving higher analytical values than an XPS-sampling. At present a preliminary comparison of values for carboxylic groups on surface indicates about 20-fold higher values for wet-chemical analysis on PETP-fabric than as detected by XPS. This higher value may be due sampling over large fabric areas including fibre irregularities like cracks.

XPS-sampling is methodically restricted to specimen of some micrometer dimensions, often randomly taken for measurements. More comparative investigations on oxygenated films (wet-chemical vs. XPS-analysis) will be systematically done in future with synchronously performed analysis. This has to be done because it is known that surface functionalities disappear often rather quickly (hydrophobic recovery) and to correlate information depth obtained. Problems in detectability of functional groups on surfaces may arise when dealing with compact and smooth surfaces because of sensitivity of analytical methods introduced.

In addition the methods presented in this work uses inexpensive equipment and can be done quickly in a normal lab even as process control.

Acknowledgements

We would like to thank the Forschungskuratorium Textil e.V. for funding this research project (AiF-No. 13924N). This project was funded with financial resources of the Bundesministerium für Wirtschaft und Technologie (BMWi) with a grant from the Arbeitsgemeinschaft industrieller Forschungsvereinigungen "Otto-von-Guericke" e.V., AiF). The final report is available from: Deutsches Textilforschungszentrum Nord-West e.V., Adlerstrasse 1, D-47798 Krefeld, FRG.

References

[1] Research project of DTNW, Federal Ministry for economics and technology, FRG, grant no. AiF 13924N, 2004–2006;
D. Knittel, E. Schollmeyer, DTNW-Mitt, vol. 56, 2007, ISSN 1430-1954.
[2] K.L. Mittal (Ed.), Polymer Surface Modification: Relevance to Adhesion, VSP BV, Utrecht, NL, 1996, ISBN 90-6764-201-0.
[3] M.J. Walzak, F. Flynn, R. Foerch, J.M. Hill, E. Karbashewski, A. Lin, M. Strobel, in: K.L. Mittal (Ed.), Polymer Surface Modification: Relevance to Adhesion, VSP BV, Utrecht, NL, 1996, ISBN 90-6764-201-0, pp. 253–272.
[4] O.D. Greenwood, B.J. Hopkins, J.P.S. Baydal, in: K.L. Mittal (Ed.), Polymer Surface Modification: Relevance to Adhesion, VSP BV, Utrecht, NL, 1996, ISBN 90-6764-201-0, pp. 17–32.
[5] J.F. Friedrich, W. Unger, A. Lippitz, T. Gross, P. Rohrer, W. Saur, J. Erdmann, H.J. Gorsler, in: K.L. Mittal (Ed.), Polymer Surface Modification: Relevance to Adhesion, VSP BV, Utrecht, NL, 1996, ISBN 90-6764-201-0, pp. 49–72.
[6] D. Praschak, T. Textor, T. Bahners, E. Schollmeyer, Technol. Text. 41 (1998) 136–138.
[7] P. Hedenberg, P. Gatenholm, J. Appl. Polym. Sci. 60 (1996) 2377–2385.
[8] M. Strobel, M.J. Walzak, J.M. Hill, A. Lin, E. Karbashewski, C.S. Lyons, in: K.L. Mittal (Ed.), Polymer Surface Modification: Relevance to Adhesion, VSP BV, Utrecht, NL, 1996, ISBN 90-6764-201-0, pp. 239–251.
[9] A. Hartwig, K. Albinsky, FhG Fertigungstechnik und Angewandte Materialforschung, Bremen, AiF-Researchproj. 10900N/1, 1999.
[10] S. Dasgupta, J. Appl. Polym. Sci. 41 (1990) 233–248.
[11] L.F. MacManus, M.J. Walzak, N.S. McItyre, J. Polym. Sci. A: Polym. Chem. 37 (1999) 2489–2501.
[12] P. DeAntonio, W.J. Bertrand, S.L. Coulter, K.G. Mayhan, J. Am. Chem. Soc., Polym. Preprints 31 (1990) 448–449.
[13] A. Holländer, Surf. Interface Anal. 36 (2004) 1023–1028.
[14] B. Kakác, Z.J. Vejdelek, Handbuch der Photometrischen Analysen Organischer Verbindungen, VCH, Weinheim, 1974.
[15] D.J. Carlsson, D.M. Wiles, Macromolecules 2 (1969) 597–606.
[16] K. Fujimoto, Y. Takebayashi, H. Inoue, Y. Ikada, J. Appl. Poly. Sci. A: Polym. Chem. 31 (1993) 1035–1043.
[17] M. Suzuki, A. Kishida, H. Iwata, Y. Ikada, Macromolecules 19 (1984) 1804–1808.
[18] C.I. Simionescu, S. Oprea, J. Polym. Sci. C 37 (1972) 251–263.

Talanta 76 (2008) 1147–1152

Contents lists available at ScienceDirect

Talanta

journal homepage: www.elsevier.com/locate/talanta

An amperometric biosensor based on multiwalled carbon nanotube-poly(pyrrole)-horseradish peroxidase nanobiocomposite film for determination of phenol derivatives

Seyda Korkut, Bulent Keskinler, Elif Erhan*

Department of Environmental Engineering, Gebze Institute of Technology, 41400 Cayirova, Kocaeli, Turkey

ARTICLE INFO

Article history:
Received 6 December 2007
Received in revised form 12 May 2008
Accepted 14 May 2008
Available online 21 May 2008

Keywords:
Immobilized horseradish peroxidase
Carbon nanotube
Phenol derivatives
Amperometric biosensor
Polypyrrole

ABSTRACT

An amperometric biosensor based on horseradish peroxidase (HRP) and carbon nanotube (CNT)/polypyrrole (PPy) nanobiocomposite film on a gold surface has been developed. The HRP was incorporated into the CNT/PPy nanocomposite matrix in one-step electropolymerization process without the aid of cross-linking agent. Amperometric response was measured as a function of concentration of phenol derivatives, at a fixed bias voltage of −50 mV. Optimization of the experimental parameters was performed with regard to pH and concentration of hydrogen peroxide. The linear range, sensitivity and detection limit of the biosensor were investigated for eighteen phenol derivatives. The sensitivity in the linear range increased in this order: 4-methoxyphenol > 2-aminophenol > guaiacol = *m*-cresol > 2-chlorophenol = 4-chlorophenol = hydroquinone = pyrocatechol > 2,6-dimethoxyphenol > 3-chlorophenol > *p*-cresol > *p*-benzoquinone = 4-acetamidophenol > catechol > phenol = pyrogallol = 2,4-dimethylphenol. CNTs was shown to enhance the electron transfer as a mediator and capable to carry higher bioactivity owing to its intensified surface area. The biosensor exhibited low detection limits with a short response time (2 s) for the tested phenolics compared to the reported working electrodes. It retained 70% of its initial activity after using for 700 measurements in 1 month.

1. Introduction

The determination of phenol and its derivative compounds is of the environmental importance, since these species are toxic and evolved in many industrial processes. They are present in many wastewater streams of the oil, paint, polymer and pharmaceutical industries [1]. Electrochemical methods have been widely used for measuring these compounds due to their advantages such as good selectivity in the presence of phenol oxidases, relatively low cost of realization and storage and the potential for miniaturization and automation [2–4]. Regarding the amperometric enzyme biosensors, tyrosinase has been the most currently used enzyme for the detection of phenolic compounds [5–9]. However, these tyrosinase biosensors are restricted to the monitoring of phenolic compounds having at least one *ortho*-position free [10]. On the other hand, laccase biosensors give response to phenolic compounds with free *para*- and *meta*-position with a complicated catalytic cycle [11]. HRP having less selectivity to phenolics is capable of giving response to a large number of phenol derivatives [12], and shows a high stability and efficiency for different biosensor designs [3,13].

The selectivity and sensitivity of the modified electrodes depends on the stability of the phenoxy radicals produced in the enzyme reaction, electrode material, immobilization method, and the magnitude of the applied potential [11]. In addition to this, the performance of biosensor is mainly affected by the electrocatalytic activity of modified electrode material and composites. CNTs have emerged as a new class nanomaterials that are receiving considerable interest owing to their ability to promote electron transfer reactions with enzymes [14,15]. The high conductivity of this carbon material leading to level of $10^2\ \Omega^{-1}\,cm^{-1}$ improves electrochemical signal transduction, while its nano-architecture imposes the electron contact between the redox centres, deeply inlaided in enzyme structure, and the smooth surface of the electrode [16]. Sotiropoulou et al. reported that CNTs have a metallic character in the range of potentials between −1.5 and +1.5 V, since there are no apparent oxidation or reduction peaks. Based on this, CNTs can donate and accept electrons in a wide range of potentials, and could therefore be used as mediators in biosensor systems [17]. A key barrier for developing CNT-based biosensors is the insolubility of CNTs in most solvents [18]. Functionalization of CNTs has been achieved by an oxidation process, which involves extensive

* Corresponding author. Tel.: +90 262 6053217; fax: +90 262 6053205.
E-mail address: e.erhan@gyte.edu.tr (E. Erhan).

0039-9140/$ – see front matter © 2008 Elsevier B.V. All rights reserved.
doi:10.1016/j.talanta.2008.05.016

ultrasonic treatment in a mixture of concentrated hydrogen peroxide and sulfuric acid [19]. The ends and sidewalls of the treated CNTs are mainly decorated with carboxyl groups. CNTs functionalized in this manner obtain good solubility in water and retain their pristine electronic and mechanical properties [20]. Recently, there has been growing interest in using CNT-based electrode configurations with tyrosinase and laccase polyphenol oxidases for detection of phenolics [21,22]. However, the use of HRP, alternative polyphenol oxidase, in modified CNT electrodes has been less reported for the measurement of phenol derivatives.

The aim of this study is to develop a CNT/PPy/HRP nanobiocomposite film for the bioanalytical applications. The working electrode was constructed in one-step by the electropolymerization process of multiwalled CNT, pyrrole and HRP. The parameters such as operating potential, pH level and concentration of hydrogen peroxide were investigated and were tested using a large set of eighteen phenol derivatives.

2. Experimental

2.1. Reagents

Horseradish peroxidase (E.C.1.11.1.7) with an activity of 10,000 U/vial (according to pyrogallol method performed by the supplier), aqueous solution of hydrogen peroxide (30%), lithium chloride, di-potassium hydrogen phosphate, citric acid, tri-sodium citrate, acetic acid (96%), sodium acetate tri-hydrate and potassium di-hydrogen phosphate were purchased from Merck. Phenol, ρ-benzoquinone, hydroquinone, 2,6-dimethoxyphenol, 2-chlorophenol, 3-chlorophenol, 4-chlorophenol, 2-aminophenol, 4-methoxyphenol, pyrocatechol, guaiacol, *m*-cresol, *o*-cresol, *p*-cresol, catechol, 4-acetamidophenol, pyrogallol, 2,4-dimethylphenol, pyrrole (99%), CHES buffer and sodium dodecyl sulfate (SDS) were obtained from Sigma. The phenol reagents were used as purchased without any further pre-treatment. Stock solutions of various phenols were daily prepared in 0.1 M phosphate buffer solution (pH 7.0). Multiwalled CNTs were obtained from Nanocs, Inc., NY, USA.

2.2. Apparatus

Electrochemical experiments were performed by using a CHI Model 800B electrochemical analyzer. A gold working electrode (2 mm diameter), a Platinum wire counter electrode, an Ag/AgCl (3 M NaCl) reference electrode, and a conventional three-electrode electrochemical cell were obtained from CH Instruments.

2.3. Preparation of CNT/PPy/HRP nanobiocomposite film coated gold electrode

Gold electrode was polished with slurries of fine alumina powders (0.3 and 0.05 mm) on a polishing microcloth pad. The electrode was then rinsed with distilled water. The facile routine for preparation of water-soluble CNTs was a modification of the acid oxidative method developed by Smalley's group [23]. Firstly, 14 mg of multiwalled CNTs were added into 5 mL of a 9:1 concentrated H_2SO_4/H_2O_2 (30%) aqueous solution and the mixture was stirred for 30 min for CNTs oxidation. After the reaction, 15 mL of the 9:1 concentrated H_2SO_4/H_2O_2 (30%) aqueous solution was added into the mixture. The mixture was placed in an ultrasonic bath (Elma 460-H) and sonicated for 5 min. Resulting CNTs dispersion was diluted using 1 L of distilled water, then was filtered through a 0.45 μM cellulose membrane. After, the filtrate was washed with 10 mM NaOH solution and distilled water till the pH level reaching to 7, the filtrate was separated from the membrane and dispersed in distilled water (0.03 mg/L). The resulting CNTs solution was sonicated for 2 min to obtain a homogeneous CNTs solution [19].

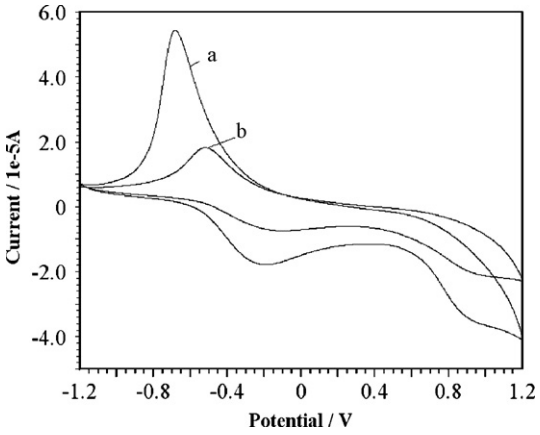

Fig. 1. Multiscan cyclic voltametric curves for CNT/PPy/HRP nanobiocomposite film (a), CNT/PPy film (b) in 0.1 M phosphate buffer (pH 7.0). Potential was scanned between −1.2 and +1.2 V at the scan rate of 100 mV s^{-1}.

CNT/PPy/HRP nanobiocomposite film was coated onto the surface of the gold working electrode by electrochemical polymerization in a three-electrode cell. The polymerization medium contained 5 mL of oxidized CNTs solution, 5 mL of 50 mM pH 6.5 citrate buffer including 0.01 M pyrrole, 0.6 mg/mL SDS and 0.3 mg/mL. HRP used in this study is a water-soluble enzyme. SDS is one of the best supporting electrolyte for electropolymerization of pyrrole in aqueous medium [24]. Since the anion of the SDS represents the dopant ions that stabilize the cationic sites in the polypyrrole, it might have a certain effect on the amount of the immobilized enzymes as well as its activity. Cyclic voltammogram of the nanobiocomposite film was scanned between 0 and 1.2 V for 4 min.

2.4. Electrochemical measurements

Electrochemical batch measurements were carried out in a 0.1 M phosphate buffer solution (pH 7.0) in the presence of 0.7 mg/mL lithium chloride with an applied working potential of −50 mV and a continuous stirring at 600 rpm in three-electrode cell mentioned in Section 2.2. Various phenol derivatives were tested to produce *i*–*t* curves of chronoamperometric measurements.

3. Results and discussion

3.1. Characterization of the CNT/PPy/HRP nanobiocomposite film

Fig. 1 shows the CV of the CNT/PPy film and CNT/PPy/HRP nanobiocomposite film in 0.1 M phosphate buffer (pH 7.0) at the scan rate of 100 mV s^{-1}. The peak current increased by the introduction of HRP into the film, indicating the synergy effect between HRP and CNT similar to the previous study [25]. In addition to this, the electrocatalytic sites placed in the active centre of HRP would join into the CNT/PPy nanobiocomposite film. There was virtually no change in the shape or peak potentials of the CV suggests that there was no hindrance for electron transfer process between electrode and HRP. The well-defined peaks indicate that films are highly homogeneous.

3.2. Effect of applied potential and pH on biosensor response

The response of the peroxidase biosensors to phenolic compounds is based on the so-called double displacement or

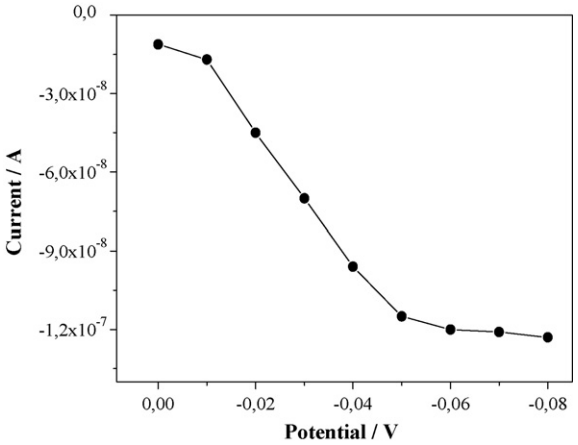

Fig. 2. Influence of applied potential on amperometric response of the biosensor to 16 μM hydroquinone in 0.1 M, pH 7.0 phosphate buffer.

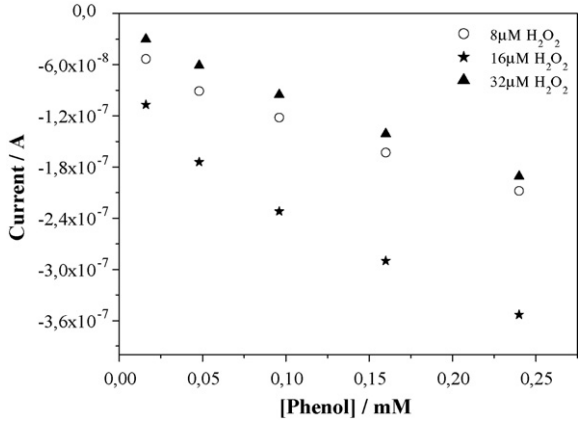

Fig. 4. The dependence of the biosensor response for phenol concentration in the presence of different hydrogen peroxide concentrations in 0.1 M, pH 7.0 potassium phosphate buffer solution. Applied potential −50 mV vs. Ag/AgCl, 3 M NaCl.

"ping-pong" mechanism in which two substrates, a peroxide and the given phenolic compound are involved [26,27]. At the surface of an electrode, where resting state and oxidized state of enzyme can be electrochemically reduced directly, the use of a second substrate such as a phenolic compound gives rise to a much faster process [12]. The monitoring of the enzymatic reaction is carried out by the electrode reduction of the phenoxy radicals. The reduction current is proportional to the concentration of phenolic compound in the medium, if adequate concentration of hydrogen peroxide is present. The dependence of CNT/PPy/HRP nanobiocomposite film electrode response on applied potential is shown in Fig. 2. The reduction peak tends to increase with the additions of hydroquinone. Hydroquinone is already reduced around 0 mV, and the reduction current increases rapidly as the applied potential moves negatively from 0 to −50 mV, which is due to the increased driving force for the fast reduction of hydroquinone at low potential. The current change approaches a plateau at −50 mV, thus this value is selected as the working potential. Same results were obtained for the other phenol deriatives tested (*not shown*).

The influence of pH on the response of CNT/PPy/HRP nanobiocomposite film electrode was investigated to optimize the reaction conditions. The change of chronoamperometric current between the pH level of 5–9 at a constant *p*-benzoquinone concentration (0.1 μM) is shown in Fig. 3. As seen in Fig. 3 the maximum response was obtained at pH 7.0 which is very similar to those observed for the soluble enzyme [28]. The optimized pH level of 7.0 was then used through further experiments.

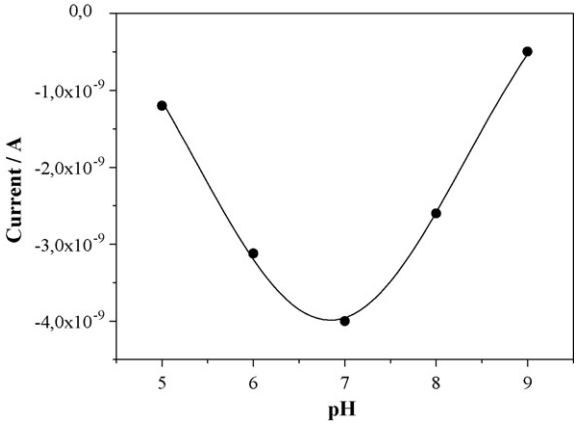

Fig. 3. Dependence of the current response of CNT/PPy/HRP nanobiocomposite film electrode to 0.1 μM *p*-benzoquinone on the pH of buffer solutions at an applied potential of −50 mV vs. Ag/AgCl, 3 M NaCl.

3.3. Determination of optimum hydrogen peroxide concentration

The peroxide concentration is very important in HRP reactions to produce good sensitivity and avoid the inactivation of the enzyme due to high concentration of peroxide [29]. Fig. 4 shows dependence of the hydrogen peroxide concentration of CNT/PPy/HRP nanobiocomposite film electrode response for phenol concentrations in the range of 16–240 μM. The analytical curve obtained for phenol at various hydrogen peroxide concentrations of 8, 16, and 32 μM, showed a linear response ranging from 16 to 48 μM with a correlation coefficient (r) of 0.98 and a sensitivity of 0.7 nA/μM, 16 to 144 μM with a r value of 0.99 and a sensitivity of 1 nA/μM, and 16 to 48 μM with a r value of 0.98 and a sensitivity of 0.65 nA/μM, respectively. Thus, 16 μM of hydrogen peroxide was used for further experiments due to its maximum sensitivity and the widest linear range with an excellent correlation coefficient.

3.4. Response of the CNT/PPy/HRP nanobiocomposite film electrode to eighteen phenol derivatives

Eighteen phenolic compounds (phenol, catechol, *p*-benzoquinone, *m*-cresol, *o*-cresol, *p*-cresol, guaiacol, 2,4-dimethylphenol, 2,6-dimethoxyphenol, 2-chlorophenol, 3-chlorophenol, 4-chlorophenol, hydroquinone, 4-acetamidophenol, pyrogallol, 4-methoxyphenol, pyrocatechol, 2-aminophenol) were detected by CNT/PPy/HRP nanobiocomposite film electrode in 0.1 M phosphate buffer solution (pH 7.0) at a working potential of −50 mV (vs. Ag/AgCl). Fig. 5 (*not included all the phenolics tested*) illustrates typical amperometric responses for the CNT/PPy/HRP working electrode after the addition of successive aliquots of phenolic compounds under continuous stirring. Table 1 summarizes the characteristics of the calibration plots obtained for the phenol derivatives, as well as the corresponding limits of detection calculated according to the $3s_b/m$ criteria in Ref. [30], where m is the slope of the linear range of the respective calibration plot, and s_b is estimated as the standard deviation of the signals from different solutions of the phenolics at the concentration level corresponding to the lowest concentration of the calibration plot. The lowest detection limit was found to be 0.027 μM ($S/N = 3$) for *p*-benzoquinone and the highest detection limit was found to be 27.9 μM ($S/N = 3$) for 2,4-dimethylphenol among the tested derivatives. Detection limit ranges between 0.00003 and 346 μM

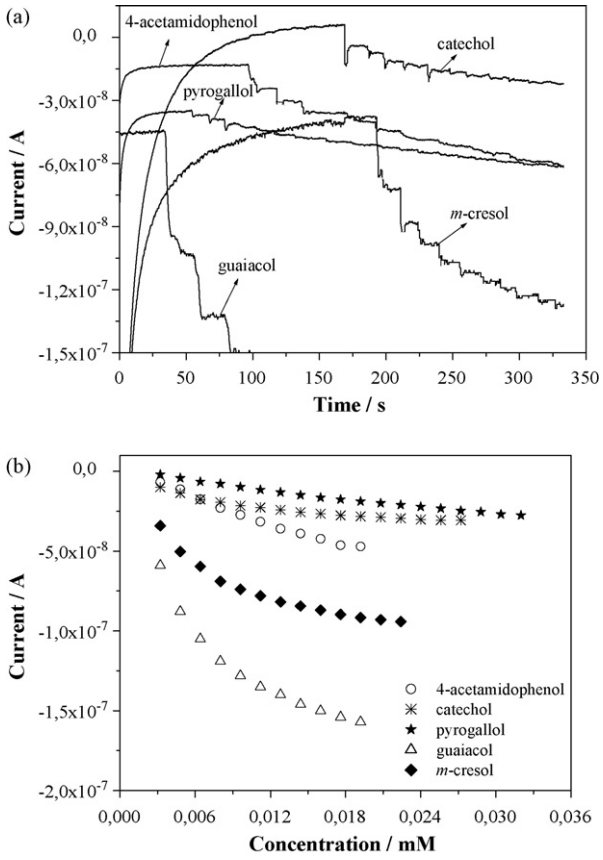

Fig. 5. (a) Current–time recordings and (b) calibration curve of the CNT/PPy/HRP nanobiocomposite film electrode to increasing 4-acetamidophenol, catechol, pyrogallol, guaiacol and *m*-cresol concentrations (initial phenolic concentration is 1.6 μM). Applied potential: −50 mV vs. Ag/AgCl, 3 M NaCl.

(S/*N* = 3) for various phenol derivatives with different phenol oxidases in recently reported biosensors [31–44].

The sensitivity of HRP-based biosensor depended on the stability of the phenoxy radicals produced in the enzyme reaction, electrode material, HRP immobilization method and the magnitude of the applied potential [11]. For the detection of different phenolic compounds, the trend of the sensitivity was consistent with the ability of the substituents for forming electron-donor conjugation. Usually, stronger ability of electron-donor conjugation resulted in higher sensitivity for the detection. According to Wilkolazka et al. [31], the enzymatic oxidation products of the *ortho*-substituted phenols are more rapidly produced showing an increase in the amplification reaction cycle. In this study, 2-aminophenol and guaiacol showed the higher sensitivity among the *ortho*-substituted phenols tested. For 2-aminophenol, the corresponding conjugation structure could be easily formed because of strong ability of electron-donor conjugation of the substituent. Kane et al. [45] reported that the phenol compounds with electron-donor substituents in an *ortho*-position gave no response. CNT/PPy/HRP nanobiocomposite film electrode did not give any response to *o*-cresol. The sensitivity was calculated from the slope of the calibration curves. The sensitivity in the linear range increase in this order: 4-methoxyphenol > 2-aminophenol > guaiacol = *m*-cresol > 2-chlorophenol = 4-chlorophenol = hydroquinone = pyrocatechol > 2,6-dimethoxyphenol > 3-chlorophenol > *p*-cresol > *p*-benzoquinone = 4-acetamidophenol > catechol > phenol = pyrogallol = 2,4-dimethylphenol (Table 1). It can be deduced that there is obvious difference among the phenol derivatives with regard to sensitivity. The different sensitivities observed can be attributed to the formation of *o*-quinones during the enzymatic reaction for each phenolic compounds [32]. The highest sensitivity was obtained from the calibration of 4-methoxyphenol. The presence of $-OCH_3$ group of 4-methoxyphenol allows HRP to oxidize more efficiently. A lower sensitivity was observed for 2,4-dimethylphenol, as expected, for the one having the *ortho*-position occupied by a methyl group. The sensitivity ranges between 1 and 50 nA/μM for the phenolics tested (Table 1). It is reported in the range between 0.011 and 746 nA/μM for various phenol derivatives at recent studies of phenoloxidases [31–44].

According to Koile and Johnson, a lose in linearity at higher concentration of phenolic compounds is attributed to slow surface fouling by the reaction products [46]. CNTs-based electrode was reported to increase electrocatalytic activity and to minimize surface fouling [32]. In this study, wide linear range with high *r*-value (0.99) was obtained for each phenolic tested. This result can be attributed to the nanobiocomposite structure based on CNTs.

Fig. 6 shows the comparison of the produced responses to the successive additions of 16 μM hydroquinone for CNT/PPy/HRP and PPy/HRP working electrodes in 0.1 M phosphate buffer (pH 7.0) at the potential of −50 mV (vs. Ag/AgCl). PPy/HRP biocomposite film electrode showed no reproducible signals to the hydroquinone

Table 1
Calibration plot parameters and analytical characteristics for various phenolic compounds at CNT/PPy/HRP nanobiocomposite film electrode

Compound	*r*	Sensitivity (nA/μM)	Lineer range (μM)	LOD (μM)	Response time (*s*)	%RSD
Phenol	0.99	1	16–44	3.52	2	2.89
p-Benzoquinone	0.99	3	0.02–0.16	0.027	2	4.43
Hydroquinone	0.99	8	16–240	6.42	2	6.5
2,6-Dimethoxyphenol	0.99	7	1.6–9.2	0.29	2	1.8
2-Chlorophenol	0.99	8	1.6–8	0.26	2	1.7
3-Chlorophenol	0.99	6	1.6–12.8	0.2	2	1.1
4-Chlorophenol	0.99	8	1.6–14.4	0.3	2	1.87
2-Aminophenol	0.99	40	8–60.8	1.53	2	5.4
4-Methoxyphenol	0.99	50	1.6–81.6	1.06	2	2.8
Pyrocatechol	0.99	8	1.6–446.4	6.27	2	6.7
Guaiacol	0.98	9	1.6–9.6	0.3	2	1.92
m-Cresol	0.99	9	8–20.8	1.5	2	2.84
o-Cresol			no response			
p-Cresol	0.98	5	128–832	24	2	2.5
Catechol	0.98	2	1.6–8	0.93	2	3.8
4-Acetamidophenol	0.99	3	1.6–16	1.11	2	2.57
Pyrogallol	0.98	1	1.6–22.4	1.24	2	1.2
2,4-Dimethylphenol	0.98	1	64–240	27.9	2	2.2

Applied potential; −50 mV, 0.1 M phosphate buffer (pH 7.0) containing 16 μM H_2O_2.

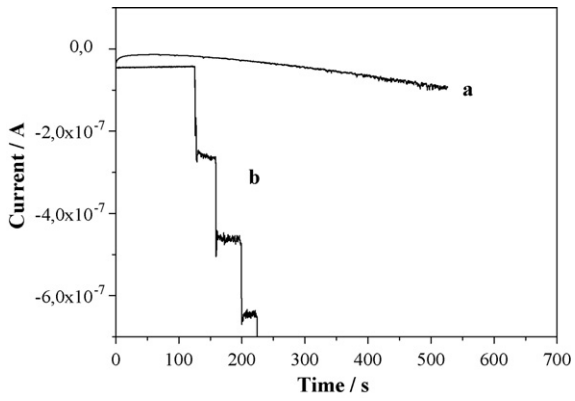

Fig. 6. Steady-state current–time responses to the successive additions of hydroquinone (16 μM) at PPy/HRP working electrode (a), at CNT/PPy/HRP working electrode (b). Applied potential: −50 mV vs. Ag/AgCl, 3 M NaCl.

additions. Nevertheless, CNT/PPy/HRP nanobiocomposite film electrode achieved to produce measurable responses by the regular growth of reduction currents. CNTs were thought to impose the electron transfer of the mediated reaction. It was previously reported that peroxidases were able to do direct electron transfer between enzyme molecules and electrode thus they did not need electron mediators for electron transfer [47]. However, in this study, the available responses could only be obtained by CNTs-based electrode. Furthermore, the amount of active immobilized enzyme in CNT/PPy/HRP nanobiocomposite film and PPy/HRP biocomposite film was found to be 6.1 and 2.7 μg, respectively. The immobilized enzyme quantity was measured by using the enzyme activity assay according to the procedure performed by Vojinovic et al. [48]. Nanobiocomposite film, involving CNTs, attached higher amount of enzyme than the composite film without CNTs due to their unique structure having activated large surface area. The nanostructure of the biocomposite could intensify the surface for higher biocatalytic activity. The sensitivity value of CNT/PPy/HRP nanobiocomposite film electrode was calculated as 8 nA/μM in the concentration range of 16–240 μM hydroquinone.

Time to allow the system to come to equilibrium is defined as "response time". The response of CNT/PPy/HRP nanobiocomposite film electrode was rapidly reached to steady-state current in about 2 s for all phenolics tested. This value is obviously shorter than most of the previously reported biosensors where the response time is ranged between 5 and 35 s for various phenolic compounds [32,38,41,44].

3.5. Stability of the CNT/PPy/HRP nanobiocomposite film electrode

The stability of the CNT/PPy/HRP nanobiocomposite film electrode was monitored by the measurement of the response for a series of 50 successive additions of a 1.6 μM phenolic to 0.1 M phosphate buffer (pH 7.0) at the potential of −50 mV (vs. Ag/AgCl). Well-defined reduction responses were obtained for all phenolics with relative standard deviations (RSD) range between 1.1% and 6.7% (Table 1). The biosensor response lost 30% of its initial value at the end of 1 month after 700 measurements. Relatively high stability can be attributed to the mild enzyme immobilization condition. Since, the acid treatment of CNTs attaches various oxygen groups (mainly carbonyl groups) to the sidewalls and ends of multiwalled CNT [49], large amount of HRP can be immobilized on the activated surfaces of CNTs. Therefore, nanostructure of CNT can provide favorable architecture for retaining the bioactivity of the enzyme and contribute to the stability of the working electrode.

4. Conclusions

The relative response of the CNT/PPy/HRP nanobiocomposite film electrode was investigated for eighteen phenol derivatives. Due to the relatively low oxidation potential of the pyrrole monomer, the immobilization of enzyme in a CNT/PPy nanocomposite film through electropolymerization enables films to be grown in aqueous solution that are compatible with most of the biological elements. The properties of good compatibility and film-forming ability make CNT/PPy nanocomposite film electrode suitable and robust matrix to incorporate enzyme in a one-step without using any cross-linking reagents. CNTs was shown to enhance the electron transfer as a mediator and capable to carry higher bioactivity owing to its intensified surface area. In conclusion, the fabricated biosensor can easily detect various phenolics in a wide range of linearity. The developed biosensor exhibited available sensitivity and low detection limit for the most of phenolics comparable to other polyphenol oxidase based electrodes. The response time of the biosensor for all phenol derivatives was very short, reaching 99% of its maximum response in about 2 s. The biosensor subjected to at least 700 measurements showed 70% of its initial activity after 1-month storage at 4 °C in the dark.

Acknowledgements

The authors are grateful to "The Scientific & Technological Research Council of Turkey" (TUBITAK) for financial support of this project.

References

[1] F. Ortega, E. Dominguez, E. Burestedt, J. Emneus, L. Gorton, G. Marko-Varga, J. Chromatogr. 675 (1994) 65.
[2] C. Nistor, J. Emneus, L. Gorton, A. Ciucu, Anal. Chim. Acta 387 (1999) 309.
[3] G. Marko-Varga, J. Emneus, L. Gorton, T. Ruzgas, Trends Anal. Chem. 14 (1996) 319.
[4] E.S. Forzani, V.M. Solis, E.J. Calvo, Anal. Chem. 72 (2000) 5300.
[5] M. Hedenmo, A. Narvaez, E. Dominguez, I. Katakis, J. Electroanal. Chem. 425 (1997) 1.
[6] S. Cosnier, A. Lepellec, B. Guidetti, I. Rico-Lattes, J. Electroanal. Chem. 449 (1998) 165.
[7] B. Wang, J. Zhang, S. Dong, Biosens. Bioelectron. 15 (2000) 397.
[8] B. Wang, S. Dong, J. Electroanal. Chem. 487 (2000) 45.
[9] A.G. Rivas, V.M. Solis, Electroanalysis 6 (1994) 1136.
[10] B. Serra, B. Benito, L. Agui, A.J. Reviejo, J.M. Pingarron, Electroanalysis 13 (2001) 693.
[11] S. Yang, Y. Li, X. Jiang, Z. Chen, X. Lin, Sens. Actuators B: Chem. 114 (2006) 774.
[12] T. Ruzgas, E. Csöregi, J. Emneus, L. Gorton, G. Marko-Varga, Anal. Chim. Acta 330 (1996) 123.
[13] M.A. del Cerro, G. Cayuela, A.J. Reviejo, J.M. Pingarron, J. Wang, Electroanalysis 9 (1997) 1113.
[14] J. Li, E.K. Jessica, M.C. Alan, C. Hua, N. Hou Tee, Y. Qi, F. Wendy, H. Jie, M. Meyyapan, Electroanalysis 17 (2005) 15.
[15] Y. Zang, J. Li, Y. Shen, M. Wang, J. Li, J. Phys. Chem. B 108 (2004) 1543.
[16] J.H.T. Luong, S. Hrapovic, D. Wang, F. Bensebaa, B. Simard, Electroanalysis 16 (2004) 132.
[17] S. Sotiropoulou, V. Gavalas, V. Vamvakaki, N.A. Chaniotakis, Biosens. Bioelectron. 18 (2003) 211.
[18] X. Chu, D. Duan, G. Shen, R. Yu, Talanta 71 (2007) 2040.
[19] W. Zhao, C. Song, P.E. Pehrsson, J. Am. Chem. Soc. 124 (2002) 12418.
[20] J. Zhang, H. Zou, Q. Qing, Y. Yang, Q. Li, Z. Liu, X. Guo, Z. Du, J. Phys. Chem. B 107 (2003) 3712.
[21] Y.C. Tsai, C.C. Chiu, Sens. Actuators B: Chem. 125 (2007) 10.
[22] D. Vega, L. Agui, A. Gonzales-Cortes, P. Yanez-Sedeno, J.M. Pingarron, Talanta 71 (2007) 1031.
[23] J. Liu, A.G. Rinzler, H. Dai, J.H. Hafner, R.K. Bradley, P.J. Boul, A. Lu, Science 280 (1998) 1253.
[24] S. Alkan, L. Toppare, Y. Yagci, Y. Hepuzer, J. Biomater. Sci. 10 (1999) 1223.
[25] Y.C. Tsai, S.C. Li, J.M. Chen, Langmuir 21 (2005) 3653.
[26] H. Anni, T. Yonetani, Metal Ions in Biological Systems, Marcel Dekker, New York, 1992.
[27] O. Ryan, M.R. Smyth, C. O'Fagain, Essay in Biochemistry 28 (1994) 129.
[28] A.C. Maehly, in: S.P. Colowick, N.O. Kaplan (Eds.), Plant Peroxidase Methods in Enzymology, 2, Academic Press, New York, 1995, p. 807.
[29] S.S. Rosatto, L.T. Kubota, G. de Oliveira Neto, Anal. Chim. Acta 390 (1999) 65.

[30] K. Hasebe, J. Osteryoung, Anal. Chem. 47 (1975) 2412.
[31] A.J. Wilkolazka, T. Ruzgas, L. Gorton, Talanta 66 (2005) 1219.
[32] Y.C. Tsai, C. Cheng-Chiu, Sens. Actuators B: Chem. 125 (2007) 10.
[33] M.A. Kim, W.Y. Lee, Anal. Chim. Acta 479 (2003) 143.
[34] F. Vianello, S. Ragusa, M.T. Cambria, A. Rigo, Biosens. Bioelectron. 21 (2006) 2155.
[35] Y.F. Li, Z.M. Liu, Y.L. Liu, Y.H. Yang, G.L. Shen, R.Q. Yu, Anal. Biochem. 349 (2006) 33.
[36] S.C. Chang, K. Rawson, C.J. McNeil, Biosens. Bioelectron. 17 (2002) 1015.
[37] S. Tembe, S. Inamdar, S. Haram, M. Karve, S.F. D'Souza, J. Biotech. 128 (2007) 80.
[38] Q. Fan, D. Shan, H. Xue, Y. He, S. Cosnier, Biosens. Bioelectron. 22 (2007) 816.
[39] D. Shan, M. Zhu, E. Han, H. Xue, S. Cosnier, Biosens. Bioelectron., in press.
[40] V. Carrelero, M.L. Mena, A. Gonzales-Cortes, P. Yanez-Sedeno, J.M. Pingarron, Biosens. Bioelectron. 22 (2006) 730.
[41] Rajesh K. Kaneto, Curr. Appl. Phys. 5 (2005) 178.
[42] Y. Liu, X. Qu, H. Guo, H. Chen, B. Liu, S. Dong, Biosens. Bioelectron. 21 (2006) 2195.
[43] Y.L. Zhou, R.H. Tian, J.F. Zhi, Biosens. Bioelectron. 22 (2007) 822.
[44] J. Yu, S. Liu, H. Ju, Biosens. Bioelectron. 19 (2003) 509.
[45] S.A. Kane, E.I. Iwuoha, M.R. Smyth, Analyst 123 (1998) 2001.
[46] R.C. Koile, D.C. Johnson, Anal. Chem. 51 (1979) 741.
[47] L. Gorton, G. Jönsson-Petersson, E. Csöregi, K. Johansson, E. Dominguez, G. Marko-Varga, Analyst 117 (1992) 1235.
[48] V. Vojinovic, A.M. Azevedo, V.C.B. Martins, J.M.S. Cabral, T.D. Gibson, L.P. Fonseca, J. Mol. Catal. B: Enzyme 28 (2004) 129.
[49] Y.C. Tsai, S.C. Li, S.W. Liao, Biosens. Bioelectron. 22 (2006) 495.

Talanta 76 (2008) 997–1005

Contents lists available at ScienceDirect

Talanta

journal homepage: www.elsevier.com/locate/talanta

Electroanalytical determination of acetaminophen using nano-TiO_2/polymer coated electrode in the presence of dopamine

S. Ashok Kumar, Chun-Fang Tang, Shen-Ming Chen *

Department of Chemical Engineering and Biotechnology, National Taipei University of Technology, No. 1, Section 3, Chung-Hsiao East Road, Taipei 106, Taiwan, ROC

ARTICLE INFO

Article history:
Received 28 March 2008
Accepted 25 April 2008
Available online 4 May 2008

Keywords:
Detection of acetaminophen
Dopamine
Modified electrodes
Electrocatalysis
Sensors

ABSTRACT

We report a new method for selective determination of acetaminophen (AP) in physiological condition. A new hybrid film modified electrode was fabricated using inorganic semiconducting nano-TiO_2 particles and redox active polymer. Redox polymer, poly(acid yellow 9) (PAY) was electrochemically deposited onto nano-TiO_2 coated glassy carbon (GC) electrode. Surface characterizations of modified electrode were investigated by using atomic force microscope and scanning electron microscope. The PAY/nano-TiO_2/GC hybrid electrode shows stable redox response in the pH range 1–12 and exhibited excellent electrocatalytic activities towards AP in 0.1 M phosphate buffer solution (pH 7.0). Consequently, a simple and sensitive electroanalytical method was developed for the determination of AP. The oxidation peak current was proportional to the concentration of acetaminophen from 1.2×10^{-5} to 1.20×10^{-4} M and the detection limit was found to be 2.0×10^{-6} M (S/N = 3). Possible interferences were tested and evaluated that it could be possible to selective detection of AP in the presences of dopamine, nicotinamide adenine dinucleotide (NADH), ascorbic acid and uric acid. The proposed method was used to detect acetaminophen in commercial drugs and the obtained results are satisfactory.

1. Introduction

Nanomaterials have received much interest by virtue of their excellent properties suited for applications in various fields such as electronic, pharmaceutical, biomedical, cosmetic, energy, and catalysis [1–6]. The nano-TiO_2 films and membranes had good structural and catalytic properties, including homogeneity without cracks and pinholes, high surface area and porosity, narrow pore size distribution, small crystallite size, high crystallinity, and active anatase phase [1]. Devices containing functional molecules anchored to nanocrystalline TiO_2 electrodes have attracted a significant amount of attention [2–6]. Nanocrystalline TiO_2 electrodes coated with light-absorbing dyes are fundamental components of dye-sensitized solar cells [7] and a number of display devices utilizing TiO_2 electrodes with adsorbed electrochromic compounds have been reported [8]. In each case, the redox chemistry of the bound molecular species is intimately involved with the device performance. Nano-TiO_2, known as their biocompatible and environmentally benign properties, have been proposed as a potential interface for the immobilization of biomolecules and applied in photochemistry [9,10] and electrochemistry [11–13] tentatively.

A wide range of polymer and inorganic mesoporous metal oxide have been combined to form nanocomposite materials with unique mechanical, electrical, magnetic and adhesive properties [1,14]. Inorganic nanoparticles of different nature and size can be combined with the conducting polymers, giving rise to a host of nanocomposites with interesting physical properties and important applications [14,15]. This is related to some distinctive properties of nanoparticles and anomalous cooperative properties of systems and it has several advantages than its individuals.

Dopamine (3,4-dihydroxyphenylethylamine) is an important neurotransmitter of the catecholamine group that exists in the mammalian central nervous system and is well characterized by its electrochemical activity [16]. In recent years, there has been considerable interest in developing new methods to measure this neurotransmitter in biological samples [17]. Identification and determination of DA with electrochemical techniques are more promising approach. However, DA oxidation required high overpotential at bare electrodes and its oxidation products were strongly adsorbed onto bare electrode surface results electrode fouling and unstable analytical signal [16,18]. Ascorbic acid (AA), uric acid (UA) and reduced form of nicotinamide adenine dinucleotide (NADH) are the important biomolecules often coexist with DA. Electrochemical oxidation of AA, UA and NADH at bare electrode results highly

* Corresponding author. Tel.: +886 2 27017147; fax: +886 2 27025238.
E-mail addresses: sakumar80@gmail.com (S.A. Kumar), smchen78@ms15.hinet.net (S.-M. Chen).

0039-9140/$ – see front matter © 2008 Elsevier B.V. All rights reserved.
doi:10.1016/j.talanta.2008.04.057

overlapped peak which lead poor selectivity and reproducibility of the electrode. To determine these biomolecules selectively in the presence of each other has been a major goal of electroanalytical research [19] and several methods mainly based on the chemical modification of traditional electrode materials, have been developed to resolve the problem [20–38].

Recently, selective electrochemical determination of DA in the presence of ascorbic acid using sodium dodecyl sulfate micelles as masking agent [39], poly-chromotrope 2B modified GC electrode [40], poly(4-amino-1-1′-azobenzene-3, 4′-disulfonic acid) coated electrode [41], poly(*p*-nitrobenzenazo resorcinol) modified GC electrode [42], nano-Au self-assembly GC electrode [43], Nafion/carbon-coated iron nanoparticles–chitosan composite film modified electrode [44] and PtAu hybrid film modified electrode [45] were reported.

Acetaminophen (*N*-acetyl-*p*-aminophenol or paracetamol) has been used widely all over the world as a pharmaceutical analgesic and antipyretic agent. It is suitable for patients who are sensitive to aspirin and safe up to therapeutic doses [46]. So it is necessary to develop a rapid, precise, simple and reliable method for the determination of acetaminophen. Recently, L-cysteine film modified GC electrode [47], carbon-coated nickel magnetic nanoparticles modified GC electrodes [48], and 4-amino-2-mercaptopyrimidine self-assembled monolayer modified gold electrode [49] has been fabricated and they were applied to the electrochemical determination of acetaminophen.

Catecholamines are small molecules made by nerve tissue (including the brain) and the adrenal gland. The major catecholamine is dopamine. This substance breaks down into other compounds, which leave our body through our urine. A urine test can be done to measure the level of catecholamine in our body. The important drugs such as acetaminophen will interfere with the catecholamine measurements in biological samples [50]. So, it is very important to measure the concentration of acetaminophen in the presence of dopamine. For the first time, in this paper, we report a new method for electrochemical determination of acetaminophen in the presence of dopamine using poly(acid yellow 9)/nano-TiO_2 modified glassy carbon electrode. The electrochemical properties of the poly(AY) coated nano-TiO_2 modified GC electrodes and the valuable applications of this electrode in the fabrication of stable and high sensitive electrochemical sensor for AP was developed. Surface characterization of PAY/nano-TiO_2 and nano-TiO_2 coated electrodes were investigated using scanning electron microscope (SEM) and atomic force microscope (AFM).

2. Experimental

2.1. Reagents and instruments

All chemicals and reagents used in this work were of analytical grade and used as received without further purification. These were 4-amino-1-1′-azobenzene-3,4′-disulfonic acid (AY, dye content about 95%), reduced form of β-NADH, dopamine hydrochloride and uric acid were purchased from Sigma–Aldrich (St. Louis, MO, USA). *p*-Acetaminophen, sulfuric acid (H_2SO_4) and sodium hydroxide (NaOH) were purchased from Wako pure chemicals (Osaka, Japan). Ascorbic acid, sodium acetate (CH_3COONa) and sodium dihydrogen phosphate (NaH_2PO_4) were received from E-Merck (Darmstadt, Germany). Nano-TiO_2 suspension was purchased from Ever-light Chemical Industrial Co., Ltd., Taiwan. Supporting electrolytes were prepared by using doubly distilled deionized water and before each experiment the solutions were deoxygenated by purging with pre-purified nitrogen gas for 10 min.

Electrochemical measurements were performed with CH Instruments (TX, USA) Model-400 potentiostat with a conventional three-electrode cell. A BAS glassy carbon and platinum wire are used as the working electrode and counter electrode, respectively. All the cell potentials were measured with respect to an Ag/AgCl [KCl (sat)] reference electrode. Hitachi scientific instruments (London, UK) Model S-3000H Scanning Electron Microscope was used for surface image measurements. The AFM images were recorded with a Multimode Scanning Probe Microscope System operated in tapping mode using model CSPM4000 Being Nano-Instruments (Beijing, China). All experiments were carried out at room temperature.

2.2. Modification of the electrodes

Prior to electrode modification, the GC electrode was mechanically polished with alumina powder (Al_2O_3, 0.05 μm) up to a mirror finish and ultrasonicated in distilled water for 5 min. Then GC electrode was electrochemically activated by using 20-times cyclic potential sweeps in the range of −0.5 to 2.0 V in 0.1 M H_2SO_4 solution at a scan rate of 100 mV/s. Indium tin oxide (ITO) coated glass substrates were cleaned by using detergent, diluted hydrochloric acid and then finally rinsed with distilled water.

5 mg nano-TiO_2 particles suspension was added into 10 mL double-distilled water and then ultrasonicated for 10 min to create a suspension with a concentration of 0.5 mg mL^{-1}. The mixture of 10 μL nano-TiO_2 suspension was spread evenly onto the surface of the GC electrode which was left to evaporate the solvent under ambient conditions in the absence of light. The PAY/nano-TiO_2/GC electrode and alone PAY/GC coated electrode were fabricated in 0.5 mM AY monomer solution under the same conditions as those in the electrode activation procedure using nano-TiO_2/GC or GC electrodes. The as-prepared dark blue colored films were obtained and strongly adherent to the substrates. Subsequently, the modified electrodes were rinsed thoroughly with distilled water and then they were dried in air and used in electrochemical experiments.

3. Results and discussion

3.1. Electrochemical modification of electrode

The electrochemical polymerization was carried out onto nano-TiO_2 modified GC electrode as said condition in Section 2.2. Fig. 1

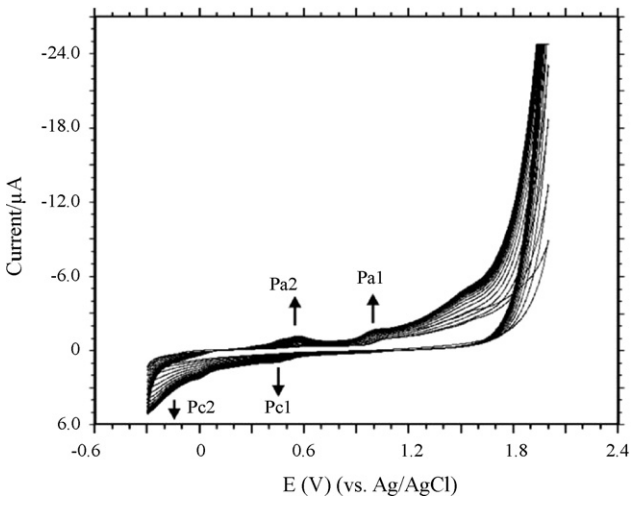

Fig. 1. CVs of the poly(AY) film growth on nano-TiO_2 coated GC electrode from electrolyte 0.1 M H_2SO_4 solution containing 0.5 mM AY monomers. Scan rate = 0.1 V/s.

shows the consecutive cyclic voltammograms (CVs) of polymer growth on the electrode surface. First scan started at −0.30 V, during the first scan an anodic peak observed at +1.0 V (P_{a1}), this peak ascribed to oxidation of $-NH_2$ group of acid yellow 9 (AY) monomer [41,51,52]. Upon continuous cycling, a new cathodic peak (at +0.41 V, P_{c1}) and a new anodic peak (at +0.56 V, P_{a2}) were developed which is indicated that the growth of the polymer film on nano-TiO_2/GC electrode. The polymerization mechanism may be described as follows AY was first oxidized to free radical (P_{a1}); the free radical combined together rapidly to hydrazobenzene sulfonic acid; then hydrazobenzene sulfonic acid was oxidized to azobenzene sulfonic acid (P_{a2}), and azobenzene sulfonic acid reduced to hydrazobenzene sulfonic acid (P_{c1}) (Scheme 1). After polymerization started, a broad cathodic peak (P_{c2}) centered at −0.24 V was developed. It may due to the insertion of anions (for example SO_4^{2-}) accompanied by the hydrogenation of polymer site and similar kinds of observations were reported for some azo and sulfonated aniline compounds at solid electrodes [41,53–56].

3.2. Electrochemical properties and surface characterizations

Typical CVs of PAY/nano-TiO_2/GC electrode in pH 1.5 H_2SO_4 solutions at different scan rates are shown in Fig. 2A. A pair of redox peak was obtained in each of the CVs at $E^{0\prime}$ +0.31 V and the peak currents of the PAY/nano-TiO_2/GC electrode are proportional to the scan rates up to 1000 mV/s, indicating the surface confined electrochemical redox process [57]. The anodic peak currents (I_{pa}) were linearly dependent of scan rate with the linear equation:

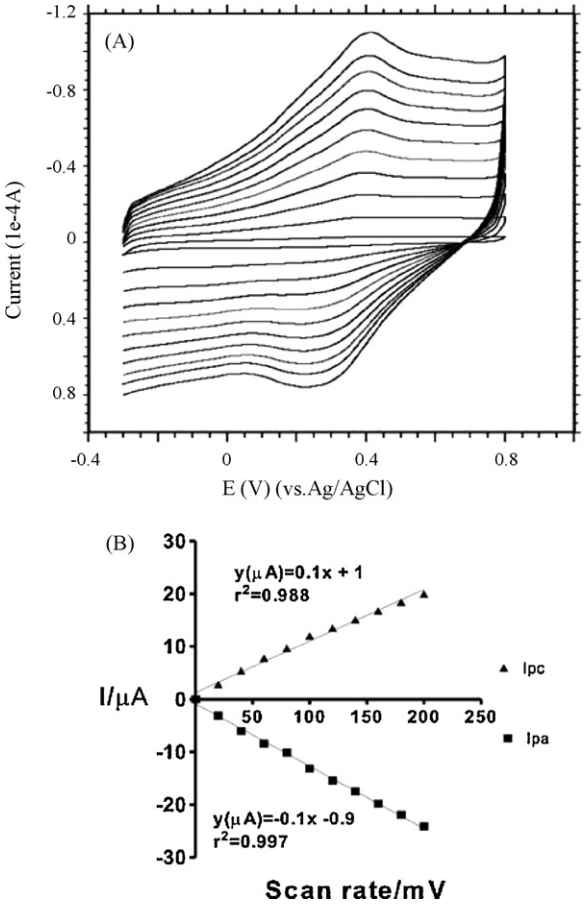

Fig. 2. (A) CVs of PAY/nano-TiO_2/GC modified electrode in pH 1.5 acidic solutions at different scan rates. The scan rates from inner to outer are 0.02, 0.1, 0.2, 0.3, 0.4, 0.5, 0.6, 0.7, 0.8, 0.9 and 1.0 V/s, respectively. (B) Plot of I_{pa} and I_{pc} vs. scan rate.

I_p (μA) = −0.1x − 0.9 (r^2 = 0.997), and the ratio of anodic peak current to cathodic peak current (I_{pa}/I_{pc}) was almost equal to unity (Fig. 2B). The peak to peak separation ($\Delta E_p = E_{pa} - E_{pc}$) was 75 mV at low scan rate (5–20 mV/s). According to the following equations

$$I_p = \frac{n^2F^2\Gamma\upsilon A}{4RT} \quad (1)$$

$$Q_\Gamma = nFA\Gamma \quad (2)$$

where n is the number of electrons, A is the working electrode area (0.0707 cm^2), υ scan rate (20 mV/s) and other parameters are usual meanings [57–59], the electron transfer number and the surface coverage were calculated to be 2.10 and 3.7×10^{-10} mol/cm^2, respectively. The cyclic voltammograms of PAY/nano-TiO_2/GC electrode was strongly affected by the solution pH (Fig. S1). An increase of solution pH caused a negative shift in $E^{0\prime}$ value with slopes of −58 mV/pH which is close to the expected value of −59 mV/pH for involving same number of electron and proton coupled electron transfer process (Scheme 1) [41].

The surface characterizations of the TiO_2 and PAY/nano-TiO_2 coated electrodes were performed using SEM (a and b) and AFM (c and d) as shown in Fig. 3. The average particle size of the TiO_2 particles was found to be in the range of 100 ± 20 nm. SEM and AFM images of poly(AY) coated electrode confirmed that the polymer thin film deposition on electrode surface. The average roughness values found to be 17.7 and 171 nm for nano-TiO_2 and PAY/nano-TiO_2 coated electrode, respectively. It is confirmed that the poly(AY)/nano-TiO_2 hybrid films on the electrode surface. Thickness of the nano-TiO_2 and poly(AY)/nano-TiO_2 hybrid films were found to be 200 and 1391 nm, respectively. Film thickness and roughness values are higher for hybrid film modified electrodes; the high conductivity of nano-TiO_2 in the composite film increases the electrical properties of the redox processes of polymer and also provides a large surface area available for polymer intercalation.

3.3. Electrocatalysis

The electrocatalytic ability of the PAY/nano-TiO_2/GC electrode towards DA was investigated. In order to assess the electrocatalytic activity of PAY/nano-TiO_2/GC electrode, its response to the oxidation of DA was studied. When 120 μM DA was added to a pH 7.0 buffer solution, an increase in the oxidation peak at about 0.21 V could be seen with cathodic peak at 0.18 V(Fig. 4A, curve b). This new anodic peak results from DA oxidized to dopamine-*o*-quinone (DOQ), cathodic peak results from DOQ reduced to DA (Scheme 2, Eq. (4)) at PAY/nano-TiO_2/GC electrode. However, direct oxidation of DA on bare GC electrode results a highly ill-defined anodic peak potential at 0.23 V and a reduction peak potential at 0.16 V (curve c). For the oxidation of DA at PAY/nano-TiO_2/GC electrode, the separation of peak potentials (ΔE_p) was 30 mV, which was on accordance with a near Nernst reversible behavior and identified that the number of electrons involved in the reaction was about equal to 2. Intensive increase in DA peak current was also observed due to the improvement in the reversibility of electron transfer process on the larger surface area of the PAY/nano-TiO_2/GC electrode. All the above results suggested that an efficient oxidation reaction of DA at the PAY/nano-TiO_2/GC electrode.

3.4. Effect of scan rate and pH on DA oxidation

The effect of the scan rate on peak current of DA was investigated in pH 7.0 buffer solution containing 120 μM DA. The anodic and cathodic peaks current were proportional to the scan rate over the range 10–100 mV/s. The linear regression equations were i_{pa} (μA) = −0.249x − 0.612 and i_{pc} (μA) = 0.174x − 0.42, with the

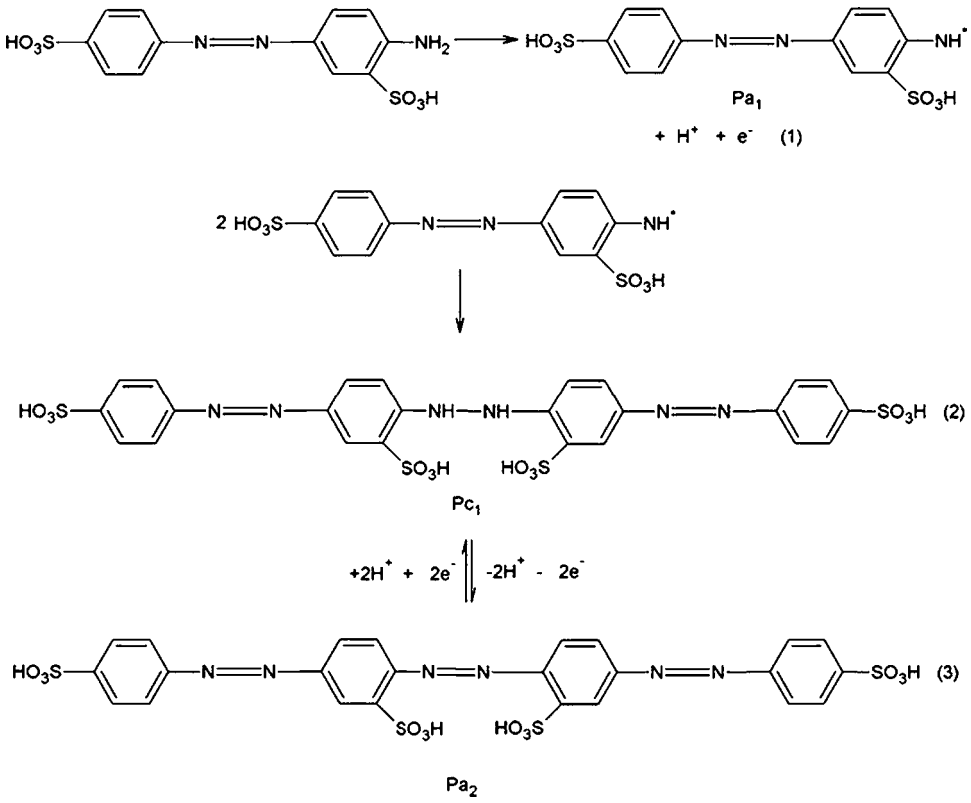

Scheme 1. Electrochemical polymerization mechanism of AY.

correlation coefficient, 0.999 and 0.999, respectively. Therefore, the electrochemical reaction of DA was surface confined electrode process. CVs were recorded in the presence of 120 μM DA in various pH supporting electrolyte solutions. The $E^{0\prime}$ of DA redox peak was shifted negatively with a slope of −60 mV/pH, it was indicated that same number of electrons and protons involved in the redox reaction of DA. In addition, we found that the maximum catalytic current was obtained for DA oxidation at PAY/nano-TiO_2/GC electrode in neutral buffer solutions (Fig. S2). Reasons for this phenomenon could be partly explained on the basis of the dissociation ability of $-SO_3^-$ (H) group of poly(AY) film in different pH environments. When the solution pH was neutral, the $-SO_3H$ group of poly(AY) film could dissociate favorably into a negative charge group $-SO_3^-$. Under this condition, the $-NH_2$ group of DA molecules (pK_a 8.9) [41,54] could obtain a proton and form the positive ion of DA. Therefore, the negative charge group $-SO_3^-$ on the surface of poly(AY) modified electrode had a well affinity to the DA positive ions and could catalyze and promote the oxidation of DA efficiently. Based on the above results the electrochemical oxidation reactions of DA is described in Scheme 3.

3.5. DA oxidation at PAY/GC and PAY/nano-TiO_2/GC modified electrodes

Fig. 4B shows the CVs of 120 μM DA oxidation by using PAY/GC (curve a) and PAY/nano-TiO_2/GC (curve b) modified electrodes. The I_{pa} of DA oxidation almost no change but a new hump is observed about −0.22 V at PAY/GC electrode. This is indicating that the oxidation product of DA was adsorbed on the electrode surface (curve a) [60,61]. By contrast this behavior is not observed in nano-TiO_2 coated electrode (curve b). Poly(AY) is negatively charged polymer, however, it has more affinity for positively charged species like DA (pK_a 8.9). As discussed in Section 3.4, poly(AY) coated electrode had potent electrocatalytic properties towards DA. However, our experimental results suggested that alone poly(AY) coated electrode get adsorbed by DA molecules after continuous measurements or dipping of poly(AY) electrode in pH 7 buffer solution containing 100 μM DA for an hour (Fig. 4C, curve a). This may be a usual behavior for opposite charged species but it is a limitation of modified electrodes. By contrast to PAY/GC modified electrode, PAY/nano-TiO_2/GC modified electrode was also immersed in 100 μM DA solution for an hour, thereafter, CVs were recorded, and the same voltammograms were observed before and after immersion. This result suggested that DA molecules were not adsorbed on the nano-TiO_2 incorporated electrode (Fig. 4C, curve b). This study clearly suggested that an application of nano-TiO_2 particles in this hybrid film modified electrode. In addition, after 50 measurements of 100 μM DA in pH 7.0 buffer solution using PAY/nano-TiO_2/GC modified electrode, there is no change in CVs before and after measurements which is indicated that nano-particles improved antifouling properties of electrode surface. For these reasons, we fabricated nano-TiO_2 coated polymer modified electrode and used in further studies throughout this work.

3.6. Electrocatalysis of AP

Cyclic voltammetry (CV) was used to investigate the electrochemical behavior of AP at the PAY/nano-TiO_2/GC coated electrode in 0.1 M PBS. As shown in Fig. 5, a reversible peak is observed at the PAY/nano-TiO_2/GC electrode. After addition of 120 μM AP, the PAY/nano-TiO_2/GC modified electrode gave a highly enhanced

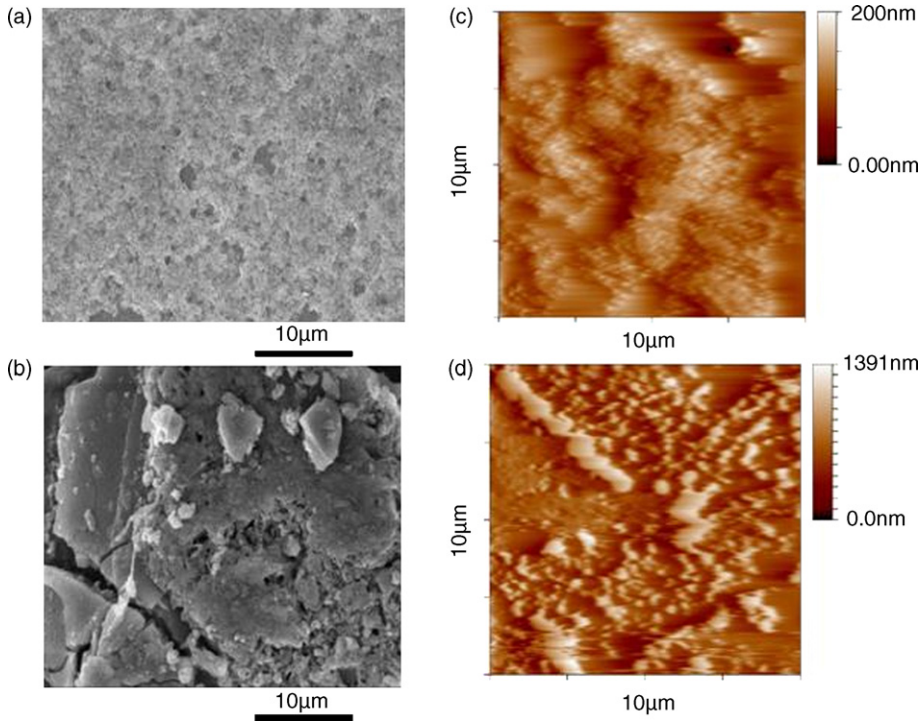

Fig. 3. SEM (a and b) and AFM (c and d) images of (a and c) Nano-TiO_2 film, (b and d) PAY/nano-TiO_2 hybrid film.

peak current and a more reversible electron transfer process to AP. A well-defined and stable redox wave of AP was observed with the anodic and cathodic peak potentials at 0.397 and 0.37 V, respectively (curve f). The separation of peak potentials at the PAY/nano-TiO_2/GC film modified electrode, ΔE_p was 27 mV, which was on accordance with a near Nernst reversible behavior and identified that the number of electrons involved in the reaction was about equal to 2.

The CV of 120 μM AP at the bare GC electrode under identical conditions is given for comparison. As shown in Fig. 5, curve a′, a highly irreversible oxidation peak is obtained at about 0.5 V, and no reduction peak appears in the reversal scan. The comparison of curves f and a′ shows that the PAY/nano-TiO_2/GC film enhances the oxidation/reduction peak currents of acetaminophen remarkably and the electrode process turns more reversible, suggesting that PAY/nano-TiO_2/GC film can accelerate the electron transfer of AP and overpotential required for AP oxidation is reduced about 100 mV and increases I_{pa} four times higher than bare GC electrode.

Electrochemical oxidation of AP at PAY/nano-TiO_2/GC electrode is two-electron transfer reaction, AP is oxidized to *N*-acetyl-*p*-benzoquinone imine (NAPQI) (Eq. (5) and Scheme 3) [62–64]. Further Fig. 5 (curve a–f) shows the voltammetric responses of the PAY/nano-TiO_2/GC modified electrode to the various concentrations of AP in pH 7.0 PBS. Distinct voltammetric peaks were obtained for concentrations as low as 20 μM AP. The peak current values showed a strong linear correlation with AP concentration, I_p (μA) = −0.06x − 0.5, displaying an r^2 value of 0.994. The calibration curve exhibited a linear range up to 120 μM, with a limit of detection (S/N = 3) for AP was 2 μM.

3.7. Effect of interferences

In biological samples, ascorbic acid (AA), uric acid (UA) and reduced form of NADH are the most important interferences. Moreover, at bare electrodes, the oxidation of these molecules takes place at a potential close to that of DA and AP [29,37,38]. The voltam-

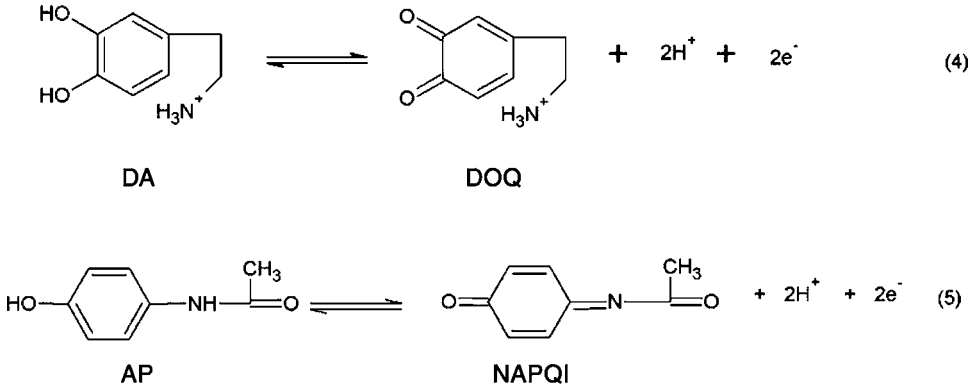

Scheme 2. Electrochemical oxidation of DA and AP.

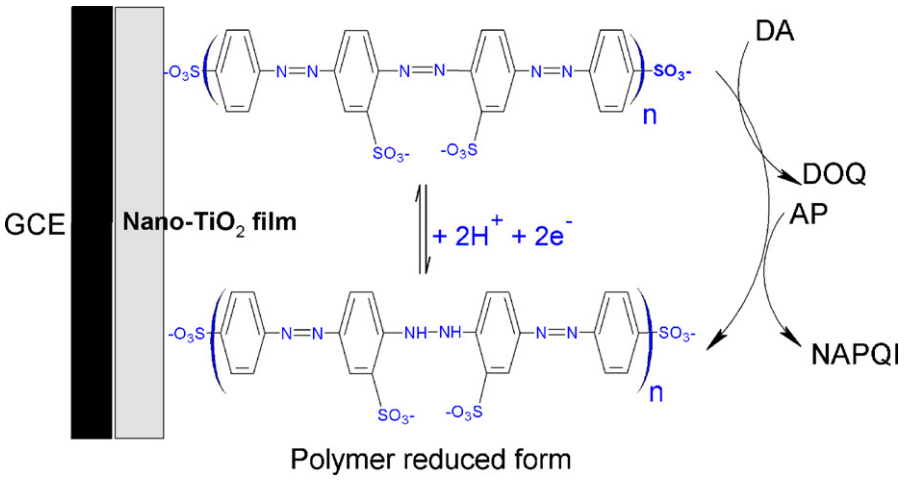

Scheme 3. Electrochemical oxidation of DA and AP on nano-TiO_2/poly(AY) film.

metric responses were recorded by using PAY/nano-TiO_2/GC coated electrode in 0.1 M PBS before (curve a) and after successive additions of 10mM AA, 10mM UA and 15mM NADH (Fig. 6A curves b–d). There is no any change in anodic or cathodic peak currents of redox polymer due to above biomolecules oxidation reactions under the potential range used. It was concluded that these biomolecules are not interferences at this modified electrode. This behavior could be partly explained on the basis of the dissociation ability of $-SO_3Na$ (H) group of poly(AY) film in different pH environments, in pH 7.0 PBS SO_3^- groups are negatively charged and this properties makes polymer backbone to repel the negatively charged species, since AA, UA and NADH are negatively charged at pH 7 [16,18–22]. We concluded that, the PAY/nano-TiO_2/GC coated electrode can be applied for determination of DA and AP in the presences of AA, UA and NADH.

3.8. Simultaneous detection of DA and AP

The next attempt was taken to detect DA and AP simultaneously by using the PAY/nano-TiO_2/GC. The linear sweep voltammetry (LSV) results show that the simultaneous determination of DA and AP with well-distinguished two anodic peaks corresponding to their oxidation could be possible at the PAY/nano-TiO_2/GC. Fig. 6B shows the LSVs obtained at the modified electrode when the concentrations of DA and AP were simultaneously changed. The presence of PAY/nano-TiO_2/GC film resolved the mixed voltammetric response into two well-defined voltammetric peaks at potentials 0.202 and 0.39 V, corresponding to the oxidation of DA and AP, respectively. The separation between the two peak potentials is sufficient enough for the simultaneous determination of DA and AP. In addition, a substantial increase in peak currents was also observed due to the improvements in the reversibility of the electron transfer processes. LSV results show that the calibration curves for DA and AP were linear for the whole concentrations range investigated (12–120 μM for DA and 12–120 μM for AP) with good correlation coefficients. The linear regression equations for DA and AP were $I_p\,(\mu A) = -0.04x - 0.006$ ($r^2 = 0.963$) and $I_p\,(\mu A) = -0.05x + 0.09$ ($r^2 = 0.992$), respectively. Experimental results showed that the detection limit was 1.0 μM for DA and 2.0 μM for AP (S/N = 3). We have tested the linear detection of DA using PAY/nano-TiO_2/GC electrode as shown in Fig. 7. PAY/nano-TiO_2/GC electrode responds with the concentration of added amount of DA. The perfect linear regression equation ($y = -x$) was found with correlation coefficient value of $r^2 = 1$. This r^2 value is very good than other electroanalytical methods reported for detection of DA [39–45]. We believe our proposed modified electrode can be applied for selective detection of DA too.

3.9. Stability, reproducibility and repeatability of the modified electrode

Stability test for PAY/nano-TiO_2/GC electrode was tested by keeping the electrode in pH 7 buffer solutions about 1 month, after a month the CVs were recorded and compared with CVs obtained before immersion, the results indicated that 2% peak current was decreased for PAY/nano-TiO_2/GC electrode. It was concluded that PAY/nano-TiO_2/GC electrode have good stability and higher shelf-life. Good stability of the PAY/nano-TiO_2/GC electrode can be attributed to the irreversible deposition and the strong adherent of poly(AY) onto nano-TiO_2 modified GC electrodes.

A relative standard deviation (R.S.D.) of 2.3% for nine measurements of 120 μM AP ($n = 9$) suggested that the PAY/nano-TiO_2/GC electrode have good reproducibility. Six hybrid film electrodes fabricated independently, were used to determine 120 μM AP, and the R.S.D. was 3.9%, revealing an excellent repeatability of the electrode preparation procedure. The R.S.D. of 15 successive detections of 100 μM DA using a same PAY/nano-TiO_2/GC modified electrode was 1.2%, and the R.S.D. of 8 different modified electrodes based on the same fabrication procedure and determination was 2.34%. These results indicated that the PAY/nano-TiO_2/GC electrode has good reproducibility. To ascertain the repeatability of the electrode, measurement of 100 μM AP were done using the same modified electrode for 21 times at the intervals of 2 h. The R.S.D. value was found to be 2.8% which is indicated that PAY/nano-TiO_2/GC electrode has good repeatability.

3.10. Determination of AP in real samples

To ascertain the applicability of the method presented above was applied to the determination of AP in PACIN^{TM} 650 tablets (John-

Table 1
Determination of AP in tablets

Samples	Labeled (mg/tablet)	Found[a] (mg/tablet)	R.S.D. (%)	Recovery (%)
Tablet-1	650	656.83	3.84	101.05
Tablet-2	650	662.00	2.33	101.85
Tablet-3	650	666.33	1.52	102.51

[a] Average value of three measurements.

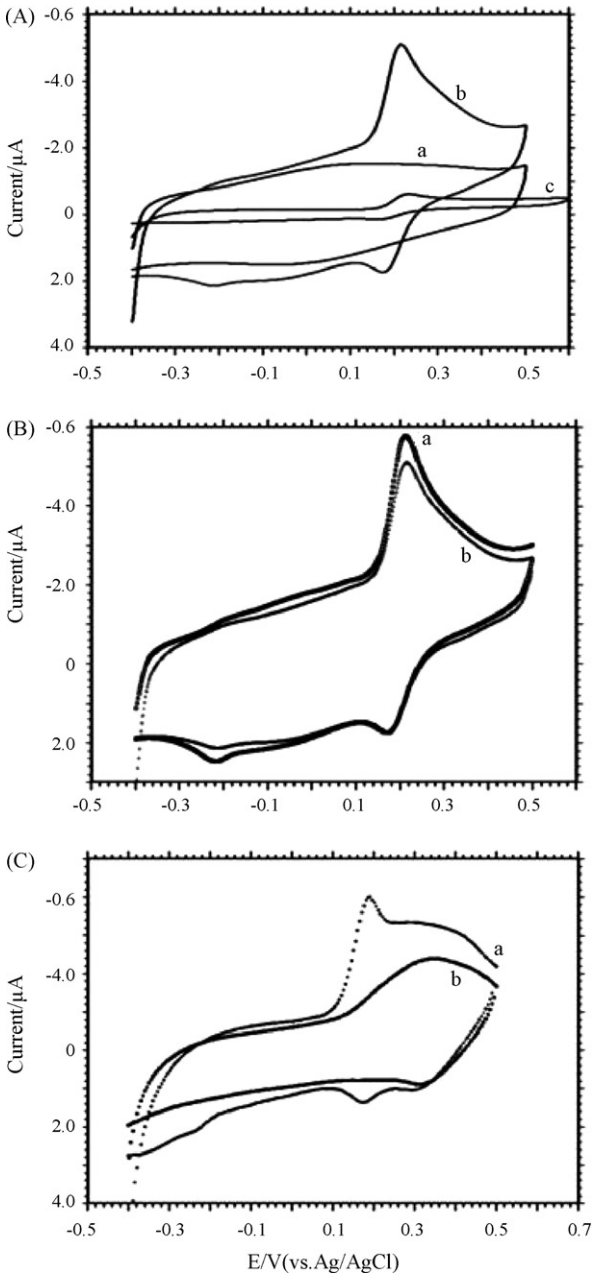

Fig. 4. (A) CVs recorded using PAY/nano-TiO_2/GC modified electrode in pH 7.0 buffer solutions in the presences of (a) 0.0 μm DA, (b) 120 μM DA and (c) at bare GC electrode. (B) CVs recorded using (a) PAY/GC and (b) PAY/nano-TiO_2/GC modified electrode in pH 7.0 buffer solutions containing 120 μM DA. (C) CVs were recorded in pH 7.0 PBS after immersion of (a) PAY/GC and (b) PAY/nano-TiO_2/GC modified electrode in 0.5 mM DA solution for an hour.

son & Smith Co., Bangalore, India). The results obtained are listed in Table 1. In our experiments, the concentration of AP was calculated using standard additions method. The R.S.D. of each sample for three time's parallel detections is less than 3.84%. In addition, the recovered ratio on the basis of this method was investigated and the value is between 102.51 and 101.05%. The recovered ratio indicates that the determination of AP using PAY/nano-TiO_2/GC electrode is effective and can be applied for detection of AP in real samples.

The linear range, detection limit, oxidation potential and pH used for detection of AP were compared with the earlier reports in Table 2. From the data's shown in Table 2, this new method could be

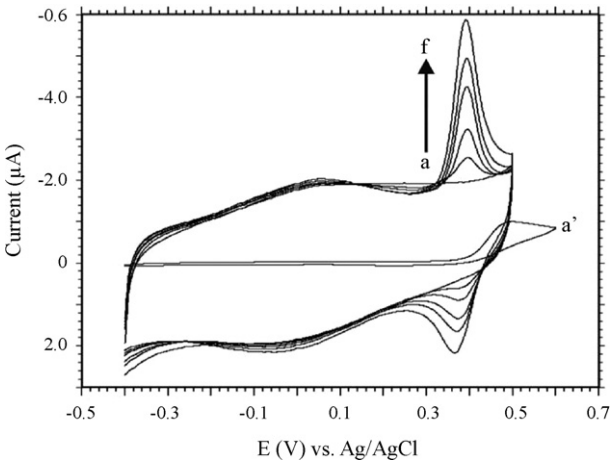

Fig. 5. CVs recorded in pH 7 PBS after each addition of acetaminophen using PAY/nano-TiO_2/GC modified electrode, (a) 0.0 μM, (b) 20 μM, (c) 40 μM, (d) 60 μM, (e) 80 μM, (f) 120μM and (a') bare GC electrode with 120 μM AP.

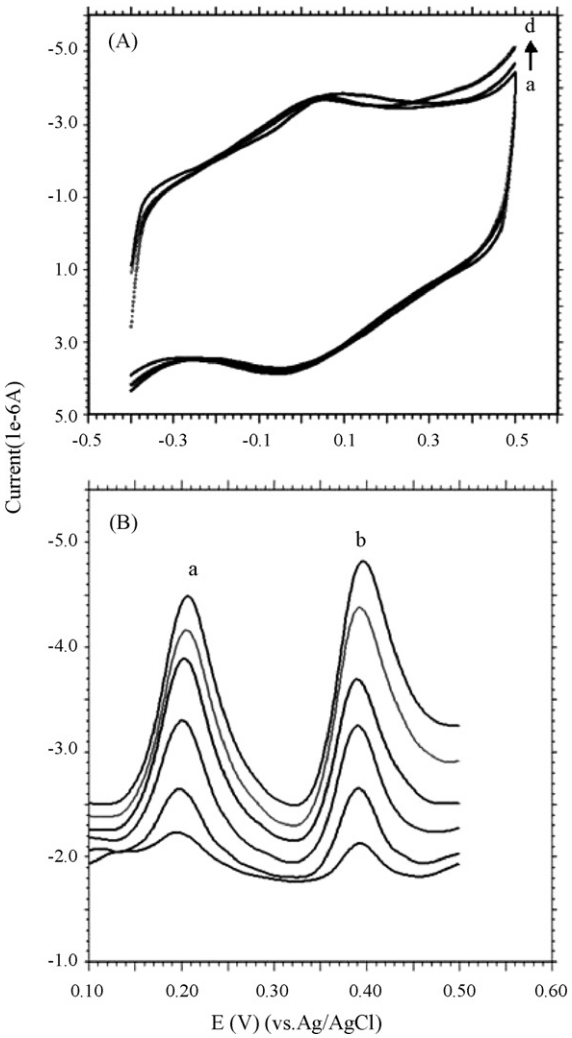

Fig. 6. (A) Typical CVs obtained with a PAY/nano-TiO_2/GC modified electrode in 0.1 M PBS (pH 7.0) with successive additions of (a) blank, (b) 10 mM ascorbic acid, (c) 10mM uric acid and (d) 15 mM NADH solutions. (B) LSVs of simultaneous detection of DA and AP at PAY/nano-TiO_2/GC modified electrode (each additions increased 20 μM).

Table 2
Comparisons of various electroanalytical methods proposed for detection of acetaminophen

Modified electrodes	pH used	Linear range	Detection limit	Oxidation potential (V)	References
(PANI–MWCNTs) composite modified electrode	5.5	1.0×10^{-6} to 1.0×10^{-4} mol/L	2.5×10^{-7} mol/L	0.436	[64]
Tetra (*p*-aminophenyl)porphyrin nickel film electrode	Basic medium (0.5 M NaOH)	1×10^{-6} to 2×10^{-4} M	–	0.43	[62]
Multi-wall carbon nano-tube composite film modified glassy carbon electrode	5.0	5.0×10^{-7} to 1.0×10^{-4} mol/L	5.0×10^{-8} mol/L	0.4	[63]
Cu(II)-conducting polymer complex modified electrode	7.0	2.0×10^{-5} and 5.0×10^{-3} M	5.0×10^{-6} M	–	[65]
PAY/nano-TiO_2/GC electrode	7.0	1.2×10^{-5} to 1.2×10^{-4} M	2.0×10^{-6} M	0.397	Proposed method

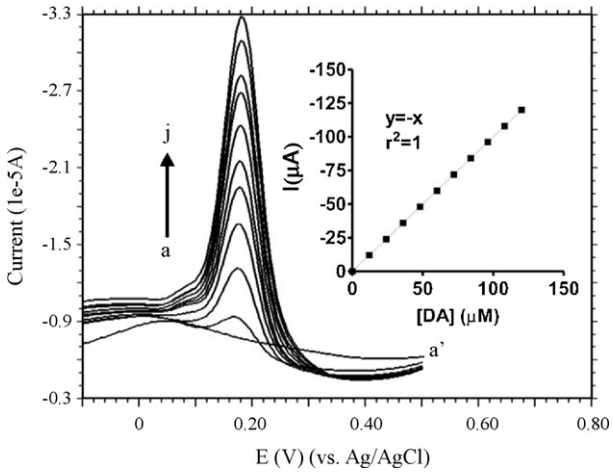

Fig. 7. Differential pulse voltammograms recorded in 0.1 M PBS at different concentration of DA using PAY/nano-TiO_2/GC modified electrode, (a′) 0.0 μM, (a) 12 μM, (b) 24 μM, (c) 36 μM, (d) 48 μM, (e) 60 μM, (f) 72 μM, (g) 84 μM, (h) 96 μM, (i) 108 μM and (j) 120 μM DA.

applied for detection of AP in neutral buffer solution (pH 7) at lower oxidation potential. For the first time we demonstrated simultaneous detection of dopamine and acetaminophen in neutral solution. The major biological compounds ascorbic acid, NADH and uric acid are not interferences at this method. From our experimental data's we conclude that our proposed method can be applied for selective detection AP in the presence of DA, ascorbic acid, NADH and uric acid.

4. Conclusions

Herein, we reported a new PAY/nano-TiO_2/GC hybrid film modified GC electrode fabrication, characterizations and its applications for detection of DA and AP by cyclic voltammetry and LSV. It was found that the peak current responses of DA and AP were improved significantly and the oxidation peak shifted towards more negative potential in the presence of PAY/nano-TiO_2 hybrid film. The results indicated that the hybrid film provided a good platform for determination of DA and AP. The enhanced electrocatalytic activity of PAY/nano-TiO_2/GC towards DA and AP mainly came from the combined properties of organic polymer/inorganic nano-TiO_2 particles such as strong adsorptive ability, larger specific area. Finally, the hybrid film electrode was successfully employed for the voltammetric determination of DA and AP in neutral buffer solution. We also demonstrated that the application of PAY/nano-TiO_2/GC for detection of AP in commercial tablets with satisfactory results.

Acknowledgements

This research work was supported by the Ministry of Education and the National Science Council of Taiwan, ROC.

Appendix A. Supplementary data

Supplementary data associated with this article can be found, in the online version, at doi:10.1016/j.talanta.2008.04.057.

References

[1] P.C. Chiang, W.T. Whang, Polymer 44 (2003) 2249.
[2] A.L. Linsebigler, G.Q. Lu, J.T. Yates, Chem. Rev. 95 (1995) 735.
[3] A. Hagfeldt, M. Graetzel, Chem. Rev. 95 (1995) 49.
[4] R. Argazzi, N.Y.M. Iha, H. Zabri, F. Odobel, C.A. Bignozzi, Coord. Chem. Rev. 248 (2004) 1299.
[5] H. Tributsch, Coord. Chem. Rev. 248 (2004) 1511.
[6] M. Valden, X. Lai, D.W. Goodman, Science 281 (1998) 1647.
[7] E. Topoglidis, A.E.G. Cass, G. Gilardi, S. Sadeghi, N. Beaumont, J.R. Durrant, Anal. Chem. 70 (1998) 5111.
[8] U. Diebold, Surf. Sci. Rep. 48 (2003) 53.
[9] Q. Li, G. Luo, J. Feng, Electroanalysis 13 (2001) 359.
[10] M. Koelsch, S. Cassaignon, J.F. Guillemoles, J.P. Jolivet, Thin Solid Films 312 (2002) 403.
[11] M.K. Nazeeruddin, M. Graetzel, Compr. Coord. Chem. II 9 (2004) 719.
[12] F. Campus, P. Bonhôte, M. Grätzel, S. Heinen, L. Walder, Solar Energy Mater. Solar Cells 56 (1999) 281.
[13] S. Yuan, S. Hu, Electrochim. Acta 49 (2004) 4287.
[14] R. Gangopadhyay, A. De, Chem. Mater. 12 (2000) 608.
[15] S.A. Kumar, S.M. Chen, Anal. Chim. Acta 592 (2007) 36.
[16] R.N. Adams, Anal. Chem. 48 (1976) 1126A.
[17] R.A. de Toledo, A.M.C. Santos, A.E.T.G. Cavalheiro, L.H. Mazo, Anal. Bioanal. Chem. 381 (2005) 1161.
[18] M.A. Kutnink, W.C. Hawkes, E.E. Schaus, S.T. Omaye, Anal. Biochem. 166 (1987) 424.
[19] J.A. Stamford, J.B. Justice Jr., Anal. Chem. 68 (1996) 359a.
[20] S.A. Wring, J.P. Hart, B.J. Birch, Anal. Chim. Acta 229 (1990) 63.
[21] M.E.G. Lyons, W. Breen, J. Cassidy, J. Chem. Soc., Faraday Trans. 87 (1991) 115.
[22] J.M. Leal, P.L. Domingo, B. Garcia, S. Ibeas, J. Chem. Soc., Faraday Trans. 89 (1993) 3571.
[23] H. Mao, P.G. Pickup, J. Electroanal. Chem. 265 (1989) 127.
[24] L. Zhang, X. Lin, Y. Sun, Analyst 126 (2001) 1760.
[25] A. Fragoso, E. Almirall, R. Cao, L. Echegoyen, R. González-Jonte, Chem. Commun. (2004) 2230.
[26] H. Olivia, B.V. Sarada, D. Shin, T.N. Rao, A. Fujishima, Analyst 127 (2002) 1572.
[27] W. Chen, X. Lin, L. Huang, H. Luo, Microchim. Acta 151 (2005) 101.
[28] H. Zhao, Y. Zhang, Z. Yuan, Analyst 126 (2001) 358.
[29] T. Selvaraju, R. Ramaraj, Electrochem. Commun. 5 (2003) 667.
[30] G. Jin, Y. Zhang, W. Cheng, Sens. Actuators B 107 (2005) 528.
[31] G. Milczarek, A. Ciszewski, Electroanalysis 16 (2004) 1977.
[32] P.R. Roy, T. Okajima, T. Ohsaka, Bioelectrochemistry 59 (2003) 11.
[33] A.M. Yu, H.Y. Chen, Anal. Chim. Acta 344 (1997) 181.
[34] F. Xu, M.N. Gao, L. Wang, G. Shi, W. Zhang, L. Jin, J. Jin, Talanta 55 (2001) 329.
[35] X. Lin, Y. Zhang, W. Chen, P. Wu, Sens. Actuators B 122 (2007) 309.

[36] Z. Wang, J. Liu, Q. Liang, Y. Wang, G. Luo, Analyst 127 (2002) 653.
[37] S.M. Chen, W.Y. Chzo, J. Electroanal. Chem. 587 (2006) 226.
[38] H.R. Zare, N. Nasirizadeh, M. Mazloum Ardakani, J. Electroanal. Chem. 577 (2005) 25.
[39] G. Alarcĭon-Angeles, S. Corona-Avendaño, M. Palomar-Pardavĭe, A. Rojas-Hernĭandez, M. Romero-Romo, M.T. Ramĭırez-Silva, Electrochim. Acta 53 (2008) 3013.
[40] X. Lin, Q. Zhuang, J. Chena, S. Zhanga, Y. Zheng, Sens. Actuators B 125 (2007) 240.
[41] S. Ashok Kumar, C.-F. Tang, S.-M. Chen, Talanta 74 (2008) 860.
[42] X. Lin, Y. Zhang, W. Chena, P. Wu, Sens. Actuators B 122 (2007) 309.
[43] G.Z. Hu, D.P. Zhang, W.L. Wu, Z.S. Yang, Colloids Surf. B: Biointerfaces 62 (2008) 199.
[44] G.S. Lai, H.L. Zhang, D.Y. Han, Microchim. Acta 160 (2008) 233.
[45] S. Thiagarajan, S.M. Chen, Talanta 74 (2007) 212.
[46] A. Wade, Martindale the Extra Pharmacopia, 27th ed., The Pharmaceutical Press, London, 1979.
[47] C. Wang, C. Li, F. Wang, C. Wang, Microchim. Acta 155 (2006) 365.
[48] S.F. Wang, F. Xie, R.F. Hu, Sens. Actuators B 123 (2007) 495.
[49] L. Jia, X.-H. Zhang, Q. Li, S.-F. Wang, J. Anal. Chem. 62 (2007) 266.
[50] S.P. Wilson, D.L. Kamin, J.M. Feldman, Clin. Chem. 31 (1985) 1093.
[51] H.H. Rehan, J. Appl. Electrochem. 30 (2000) 945.
[52] X.-G. Li, M.-R. Huang, W. Duan, Y.-L. Yang, Chem. Rev. 102 (2002) 2925.
[53] A. Eriksson, L. Nyholm, Electrochim. Acta 44 (1999) 4029.
[54] H. Yao, Y. Sun, X. Lin, Y. Tang, L. Huang, Electrochim. Acta 52 (2007) 6165.
[55] S.A. Kumar, S.M. Chen, Sens. Actuators B 123 (2007) 964.
[56] J. Yue, A.J. Epstein, J. Am. Chem. Soc. 112 (1990) 2800.
[57] A.P. Brown, F.C. Anson, Anal. Chem. 49 (1977) 1589.
[58] M. Sharp, M. Petersson, K. Edstrom, J. Electroanal. Chem. 95 (1979) 123.
[59] A.J. Bard, L.R. Faulkner, Electrochemical Methods Fundamentals and Applications, Wiley, New York, 1980, pp. 521–525.
[60] E. Winter, R.M. de Carvalho, L.T. Kubota, S. Rath, J. Braz. Chem. Soc. 14 (2003) 564.
[61] E. Winter, L. Codognoto, S. Rath, Electrochim. Acta 51 (2006) 1282.
[62] S.-S. Huang, H. Tang, B.-F. Li, Mikrochim. Acta 128 (1998) 37.
[63] C. Li, G. Zhan, Q. Yang, J. Lu, Bull. Korean Chem. Soc. 27 (2006) 1854.
[64] M. Li, L. Jing, Electrochim. Acta 52 (2007) 3250.
[65] M. Boopathi, M.-S. Won, Y.-B. Shim, Anal. Chim. Acta 512 (2004) 191.

Talanta 76 (2008) 1097–1104

Contents lists available at ScienceDirect

Talanta

journal homepage: www.elsevier.com/locate/talanta

Electrocatalysis of reduced L-glutathione oxidation by iron(III) tetra-(*N*-methyl-4-pyridyl)-porphyrin (FeT4MPyP) adsorbed on multi-walled carbon nanotubes

Rita C.S. Luz [a,*], Flavio S. Damos [b], Auro A. Tanaka [c], Lauro T. Kubota [a], Yoshitaka Gushikem [a]

[a] *Institute of Chemistry, UNICAMP, P.O. Box 6154, 13084-971 Campinas, SP, Brazil*
[b] *Department of Chemistry, UFVJM, Rua da Glória, 187, 39100-000 Diamantina, MG, Brazil*
[c] *Department of Chemistry, UFMA, Avenida dos Portugueses s/n, 65085-580 São Luís, MA, Brazil*

ARTICLE INFO

Article history:
Received 16 February 2008
Received in revised form 6 May 2008
Accepted 9 May 2008
Available online 17 May 2008

Keywords:
Reduced L-glutathione
Iron(III)
tetra-(*N*-methyl-4-pyridyl)-porphyrin
Carbon nanotubes
Erythrocyte

ABSTRACT

The development of a highly sensitive voltammetric sensor for reduced L-glutathione (GSH) using a basal plane pyrolytic graphite (BPPG) electrode modified with iron(III) tetra-(*N*-methyl-4-pyridyl)-porphyrin (FeT4MPyP) adsorbed on multi-walled carbon nanotubes (MWCNT) is described. Scanning electron microscopy (SEM) and energy dispersive X-ray spectroscopy (EDS) were used to verify the morphologies and composition of the MWCNT after modification with the FeT4MPyP complex. The modified electrode showed very efficient electrocatalytic activity for L-glutathione oxidation, substantially decreasing the oxidation peak to −0.025 V vs Ag/AgCl. A linear response range from 5 μmol L^{-1} to 5 mmol L^{-1} was obtained with a sensitivity of 703.41 μA L $mmol^{-1}$. The detection limit for GSH determination was 0.5 μmol L^{-1} and the relative standard deviation (R.S.D.) for 10 determinations of 250 μmol L^{-1} GSH was 1.4%. The modified electrode was applied for GSH determination in erythrocyte samples and the results were in agreement to those obtained by a comparative method described in the literature.

1. Introduction

Carbon nanotubes (CNT) have attracted enormous interest in recent years due to their exceptional electrical, chemical and mechanical properties, which make them attractive candidates for many applications [1,2], particularly in the area of chemical sensors with electrochemical detections [3,4], once CNTs can be functionalized with organic compounds without destroying their electrical and chemical properties [5–10]. In this context, studies of catalytic activity of modified multi-walled carbon nanotubes (MWCNT) electrodes with several electrocatalysts have been performed.

The choice of a metalloporphyrin molecule was based on the fact that porphyrins play an important role in several biochemical processes [11] and the observed electrochemical reversibility of iron-porphyrin derivatives on several electrode materials, which make them perfectly suitable electron transfer mediators in preparing chemically modified electrodes. Iron-porphyrins are also well known for their excellent electrocatalytic properties toward the detection of many important analytes, such as nitric oxide [12], neurotransmitters [13], oxygen [14], hydrogen peroxide [15], nitrite [16], superoxide [17], sulfur oxyanions [18] and tryptophan and its derivatives [19]. Unfortunately, most of the modified electrodes based on iron-porphyrin derivatives have shown poor stability and selectivity, and some of the methods that have been employed for surface modifications are laborious and expensive.

In addition, given the widespread involvement of thiols and the corresponding disulfides in many essential biological functions, much effort has been made to develop sensitive and selective methods for the detection of such compounds. Specifically, L-glutathione (Fig. 1a) can exist in oxidized (GSSG) or reduced (GSH) forms and it is an essential compound in many biological processes such as catabolism and transportation [20]. The reduced form of L-glutathione (GSH) is required to maintain the iron(II) form of hemoglobin in its reduced state and for maintaining the structure of red blood cells [21,22]. Although many studies on GSH electrochemical oxidation using various modified electrodes have been reported, to our best knowledge, there is no report about the use of a basal plane pyrolytic graphite (BPPG) electrode with FeT4MPyP (Fig. 1b) complex and MWCNT. In this sense, a simple one-step procedure was used for modification of a BPPG electrode with Fe(III)T4MPyP and MWCNT by non-covalent (–(stacking, aiming at designing a new special nanostructured interface to improve the electron transfer.

* Corresponding author. Tel.: +55 19 3521 3053; fax: +55 19 3521 3023.
E-mail address: rcsluz@iqm.unicamp.br (R.C.S. Luz).

0039-9140/$ – see front matter © 2008 Elsevier B.V. All rights reserved.
doi:10.1016/j.talanta.2008.05.009

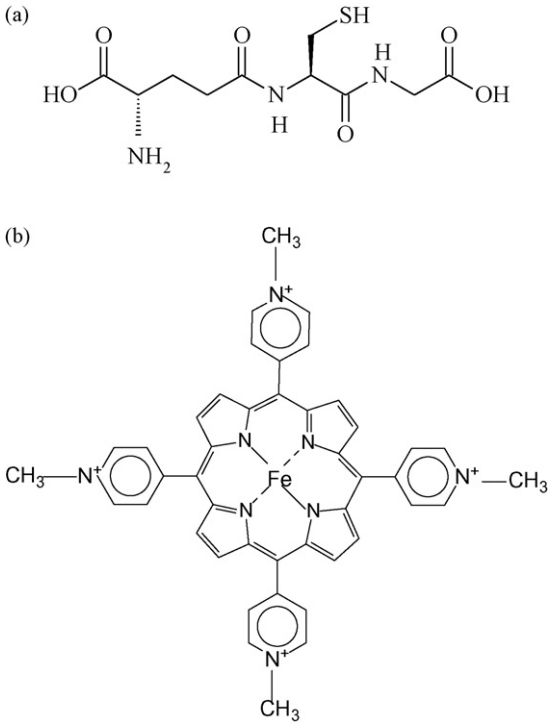

Fig. 1. Chemical structures of (a) L-glutathione and (b) iron(III) tetra-(*N*-methyl-4-pyridyl)-porphyrin.

2. Experimental

2.1. Reagents and solutions

All used chemicals were of analytical grade. The multi-walled carbon nanotubes (>95% purity, 10–30 nm diameter, 5–20 μm length), reduced L-glutathione (γ-L-glutamyl-L-cysteinyl-glycine, GSH), 5,5′-dithio-bis(2-nitrobenzoic acid), L(+)-cysteine, L(+)-ascorbic acid, L(+)-glutamic acid, D(+)-glucose and glycine were acquired from Sigma, St. Louis, USA; disodium and monosodium phosphates (Na_2HPO_4 and NaH_2PO_4) and $Na_2H_2EDTA{\cdot}2H_2O$ from Synth, São Paulo, Brazil; and iron(III) tetra-(*N*-methyl-4-pyridyl)-porphyrin (FeT4MPyP) from Porphyrin Products Inc., UT, USA. *N*,*N*′-dimethylformamide (DMF) was purchased from Merck, Rio de Janeiro, Brazil. Ellman's reagent, 5,5′-dithio-bis(2-nitrobenzoic acid) (DTNB), utilized in the reference method for GSH determination, was prepared at a concentration of 3 mmol L^{-1} in 0.1 mol L^{-1} phosphate buffer containing 0.5 mmol L^{-1} Na_2H_2-EDTA. Working standard solutions were daily prepared with appropriate dilution of the stock solutions with deionized water.

FeT4MPyP solution was prepared in DMF and the other solutions were prepared with water purified in a Milli-Q Millipore system. The actual pH of the buffer solutions was determined with a Corning pH/Ion Analyzer 350 model. Phosphate buffer solutions (0.1 mol L^{-1}) were prepared from 0.1 mol L^{-1} H_3PO_4–NaH_2PO_4, and the pH was adjusted with 0.1 mol L^{-1} H_3PO_4 or 2.0 mol L^{-1} NaOH.

2.2. Microscopy and electrochemical measurements

Scanning electron micrographs were obtained using a JEOL JSM-5610LV scanning electron microscope (SEM). MWCNT and FeT4MPyP/MWCNT elemental compositions were determined by energy dispersive X-ray spectroscopy (EDS) using a Noran Vantage 4105 spectrometer.

Electrochemical measurements were performed with an Autolab PGSTAT 10 potentiostat/galvanostat from Eco Chemie (Utrecht, Netherlands) coupled to a microcomputer with GPES 4.9 software. A three electrode electrochemical cell was employed for all electrochemical measurements. The working electrode was a basal plane pyrolytic graphite (BPPG) disk, with a geometrical area of *ca*. 0.35 cm^2, mounted in Teflon®. The counter and reference electrodes were a platinum electrode and Ag/AgCl (sat.), containing KCl (3 mol L^{-1}), respectively.

2.3. Preparation of the FeT4MPyP/MWCNT/BPPG modified electrode

Prior to the electrode modification, the BPPG surface was polished with emery paper and then cleaned by sonication to remove any adhesive [23]. Right after, a dispersion of 1.2 mg MWCNT in 1 mL of a solution of 1.5 mmol L^{-1} FeT4MPyP in DMF was prepared with the aid of sonication and 30 μL of the dispersion was placed directly onto the BPPG electrode surface. The electrode was let dry at 80 °C during 10 min to form the FeT4MPyP/MWCNT composite on the BPPG surface. Finally, the modified electrode was thoroughly rinsed with distilled water and placed in the electrochemical cell.

The effective area of the FeT4MPyP/MWCNT/BPPG electrode was estimated as described by Siswana et al. [24] and using the $Fe[(CN)_6]^{3-/4-}$ redox couple and the Randles–Sevcik equation [25]. The effective area determined was approximately 0.42 cm^2.

2.4. Sample preparation and spectrophotometric measurements

Blood samples of 10 mL were collected from six volunteers (between 24 and 32 years old) in tubes containing heparin. The samples were treated according to the literature [26]. The blood was centrifuged at 1000 × *g* for 15 min at 4 °C and the plasma was discarded. The erythrocytes were washed three times with phosphate buffer solution (0.2 mol L^{-1}, 0.9% NaCl, pH 7.4) and aliquots of the erythrocytes were hemolysed (1:1, v/v) in 1 mmol L^{-1} Na_2H_2EDTA solution. After preparing the hemolysed erythrocytes, 10% (w/v) 5-sulfosalicylic acid was added, followed by vigorous shaking and centrifugation at 1000 × *g* for 10 min at 4 °C. The supernatant was collected for the GSH determinations.

For the amperometric measurements, 50 μL of the hemolysate sample was diluted in 5 mL of 0.1 mol L^{-1} phosphate buffer (pH 7.4), while for spectrophotometric method the procedure described by Griffith [27], which is based on the reaction of GSH and DTNB (Ellman's reagent), was followed. DTNB reacts specifically with the analyte, forming 2-nitro-5-mercapto-benzoic acid, which is monitored spectrophotometrically at 412 nm. A Beckman DU 640 spectrophotometer and a cell with 1.0 cm optical path were employed in the optical measurements.

3. Results and discussion

3.1. Characterization of the MWCNT and of the FeT4MPyP/MWCNT composite

The SEM images of the unmodified (Fig. 2a) and the FeT4MPyP modified MWCNT (Fig. 2b) show that FeT4MPyP molecules are distributed on the MWCNT surface without any detectable large-scale aggregation of the porphyrin molecules [28,29], indicating a good dispersion onto the surface.

Energy dispersive X-ray spectroscopy measurements of the MWCNT surface showed two peaks, at 0.280 and 0.527 keV, corresponding to the C and O atoms (Fig. 2c). A Fe peak was observed at 6.37 keV, due to impurities present in the carbon nanotubes. In addition to theses peaks, the MWCNT surfaces coated with the

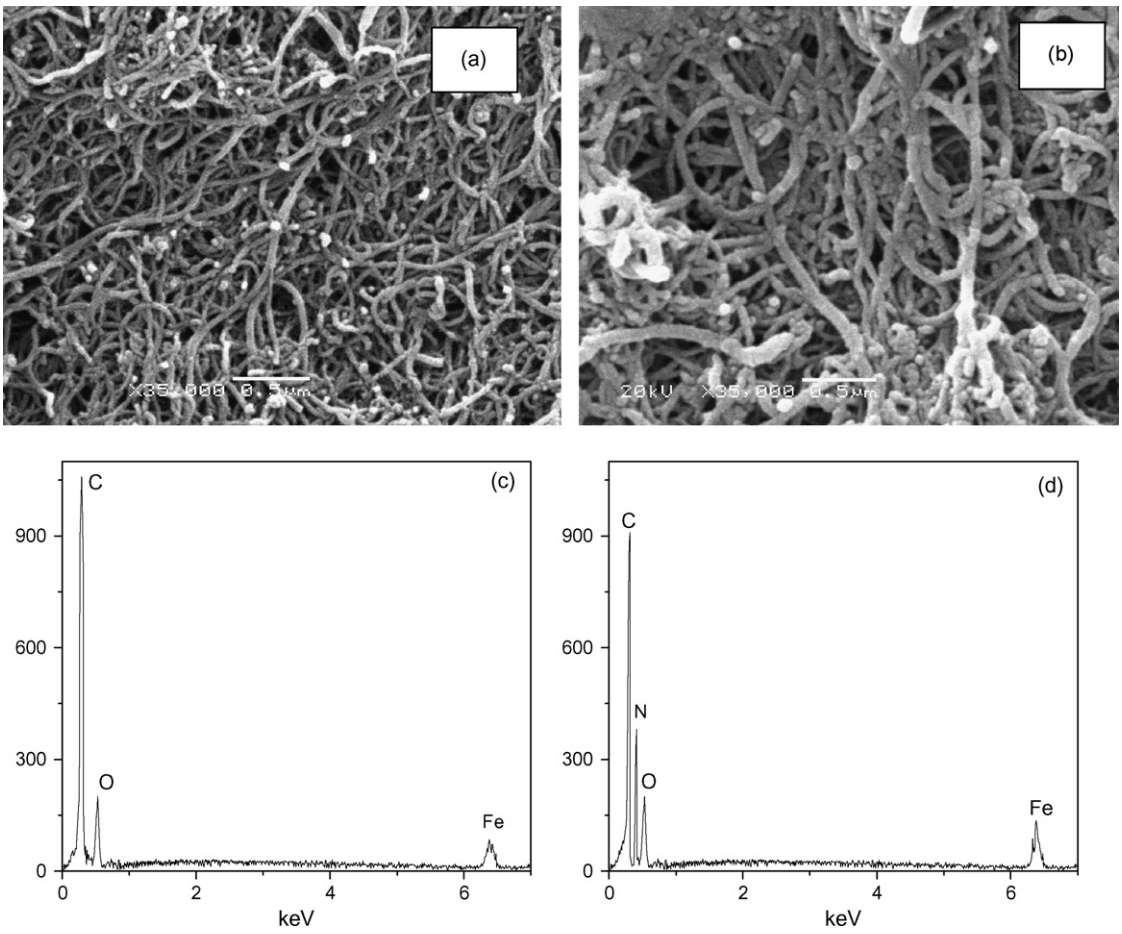

Fig. 2. SEM images of (a) MWCNT and (b) FeT4MPyP/MWCNT and the corresponding EDS spectra of (c) MWCNT and (d) FeT4MPyP/MWCNT.

porphyrin complex (Fig. 2d) presented a peak at 0.413 keV, which corresponds to the N atom of the porphyrin complex. Furthermore, the presence of the iron in the porphyrin ring intensified the peak at 6.37 keV. It is important to stress that the characteristic line for each element is in agreement with that reported in the literature [30].

3.2. Electrocatalytic oxidation of GSH on the FeT4MPyP/MWCNT/BPPG electrode

Fig. 3a shows cyclic voltammograms obtained with the bare BPPG electrode in the absence (curve 1) and the presence (curve 2) of 5 mmol L^{-1} GSH and the cyclic voltammograms of the FeT4MPyP/MWCNT/BPPG electrode in the absence (curve 3) and the presence (curve 4) of 5 mmol L^{-1} GSH. After co-immobilizations of iron-porphyrin and MWCNT on the BPPG electrode surface, a redox couple with anodic and cathodic peak potentials at −0.095 and −0.145 V vs Ag/AgCl, respectively, was verified (Fig. 3a, curve 3). This redox couple can be associated to the reactions of the immobilized $[Fe(II)T4MPyP]^{3+}$ into $[Fe(III)T4MPyP]^{4+}$ species on the carbon nanotubes. Upon addition of 5.0 mmol L^{-1} GSH, there is a significant enhancement of the anodic peak current while the cathodic peak current disappears (Fig. 3a, curve 4), which characterizes an electrocatalytic oxidation process [31]. The anodic peak potential for oxidation of GSH on the FeT4MPyP/MWCNT/BPPG electrode is about 0.0 V, whereas in an unmodified BPPG electrode the GSH is not oxidized until 0.7 V (Fig. 3a, curve 2). Thus, a decrease in overpotential and an enhancement in the peak current are achieved with the FeT4MPyP/MWCNT/BPPG electrode.

Fig. 3b shows the cyclic voltammograms of the MWCNT/BPPG electrode in the absence (Fig. 3b, curve 1) and the presence (Fig. 3b, curve 2) of 5.0 mmol L^{-1} GSH. In the absence of GSH no redox peaks were observed (Fig. 3b, curve 1). Upon addition of 5.0 mmol L^{-1} GSH (Fig. 3b, curve 2), there is a poor enhancement of the anodic peak current when compared to the FeT4MPyP/MWCNT/BPPG electrode (Fig. 3a, curve 4). Indeed, the peak potential for GSH oxidation on the MWCNT/BPPG electrode was observed at 0.45 V (Fig. 3b, curve 2), which is located at much more positive potential when compared to the FeT4MPyP/MWCNT/BPPG electrode.

Fig. 3c shows the cyclic voltammograms of a FeT4MPyP/BPPG electrode in the absence (Fig. 3c, curve 1) and the presence (Fig. 3c, curve 2) of 5 mmol L^{-1} GSH. The FeT4MPyP modified BPPG, in the absence of MWCNT, presented poor response for GSH oxidation. These results show that the presence of the complex and of the carbon nanotubes is of fundamental importance to get high electrocatalytic activity toward gluthatione oxidation. The high activity of the FeT4MPyP/MWCNT/BPPG electrode for the oxidation of GSH in aqueous solutions can be associated with the low charge transfer resistance of the FeT4MPyP/MWCNT system as well as to the better catalyst dispersion on MWCNT.

3.3. Effect of the amount of FeT4MPyP and MWCNT on the response of the modified electrode

The FeT4MPyP and MWCNT concentrations used in the composite preparation were investigated. Firstly, the electrode response dependence on the FeT4MPyP amount for 250 μmol L^{-1} GSH was investigated by using different amounts of FeT4MPyP (0.1, 0.5, 1.5,

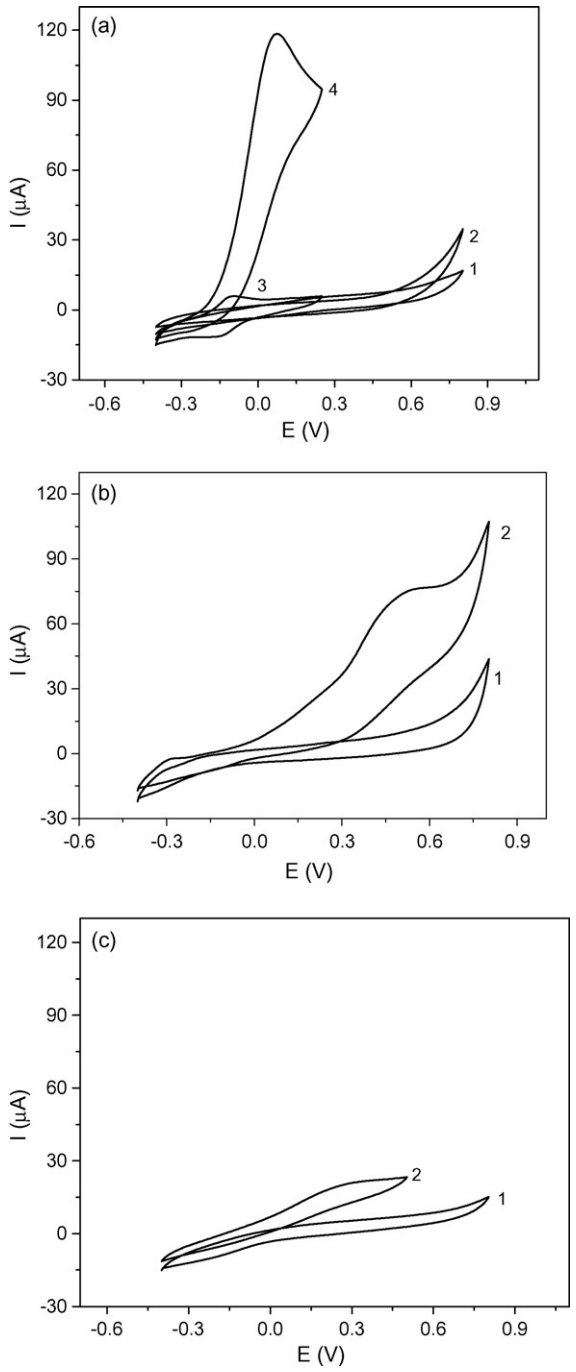

Fig. 3. Cyclic voltammograms for: (a) the unmodified electrode in the absence (curve 1) and the presence (curve 2) of 5 mmol L^{-1} GSH; the FeT4MPyP/MWCNT/BPPG electrode in the absence (curve 3) and the presence (curve 4) of 5 mmol L^{-1} GSH; (b) the MWCNT/BPPG electrode in the absence (curve 1) and the presence (curve 2) of 5 mmol L^{-1} GSH; (c) the FeT4MPyP/BPPG electrode in the absence (curve 1) and the presence (curve 2) of 5 mmol L^{-1} GSH. Potential scan rate: 0.01 V s^{-1}.

2.0 and 2.5 mmol L^{-1}) and maintaining the MWCNT concentration at 1.0 mg mL^{-1} (Table 1). The best responses were obtained for the 1.5 mmol L^{-1} FeT4MPyP solution. The use of FeT4MPyP concentrations lower than 1.5 mmol L^{-1} resulted in low responses, probably due to the small amount of porphyrin complex on the electrode surface. On the other hand, the use of FeT4MPyP concentrations higher than 1.5 mmol L^{-1} did not promote an increase of the oxidation peak current, which can be associated to a maximum

Table 1
Influence of the FeT4MPyP concentration on the peak current obtained with the sensor for 250 (mol L^{-1} GSH in phosphate buffer solution at pH 7.4

[FeT4MPyP] (mmol L^{-1})	I_p (A)
0.1	5.75 (±0.03)
0.5	6.02 (±0.02)
1.5	7.10 (±0.02)
2.0	7.05 (±0.01)
2.5	7.08 (±0.03)

Experiments carried out using 1.0 mg mL^{-1} MWCNT. Potential scan rate: 0.01 V s^{-1}.

Table 2
Influence of the MWCNT concentration on the peak current obtained with the sensor for 250 (mol L^{-1} GSH in phosphate buffer solution at pH 7.4

Concentration of MWCNT (mg mL^{-1})	I_p (μA)
0.3	2.05 (±0.22)
0.5	5.38 (±0.15)
1.0	7.10 (±0.13)
1.2	10.09 (±0.20)
1.5	10.34 (±0.10)
2.0	10.80 (±0.12)

Experiments carried out using 1.5 mol L^{-1} FeT4MPyP. Potential scan rate: 0.01 V s^{-1}.

capability of the MWCNT for the complex sorption. Based on these aspects, a 1.5 mmol L^{-1} concentration was chosen to prepare the FeT4MPyP/MWCNT/BPPG electrodes.

The response of the FeT4MPyP/MWCNT/BPPG electrode is also affected by the MWCNT amount on the surface. This amount was controlled by using the same volume of suspension with different concentrations of MWCNT (0.3, 0.5, 1.0, 1.2, 1.5 and 2.0 mg mL^{-1}). As can be seen in Table 2, an increase of the MWCNT concentration significantly increases the current response up to a MWCNT concentration of 1.2 mg mL^{-1}.

3.4. Influences of pH, buffer solution and buffer concentration

The influence of the solution pH on the GSH electrochemical oxidation was investigated in 0.1 mol L^{-1} phosphate buffer solutions with pH 6.0, 6.4, 7.0, 7.4, 8.0 and 8.4. This study showed that the electrocatalytic peak current was not significantly affected by the solution pH in the investigated range. Thus, the optimum pH for further studies was set at 7.4, which is similar to the physiological pH. On the other hand, it was observed that the peak potential depended on the solution pH (Fig. 4). A linear correla-

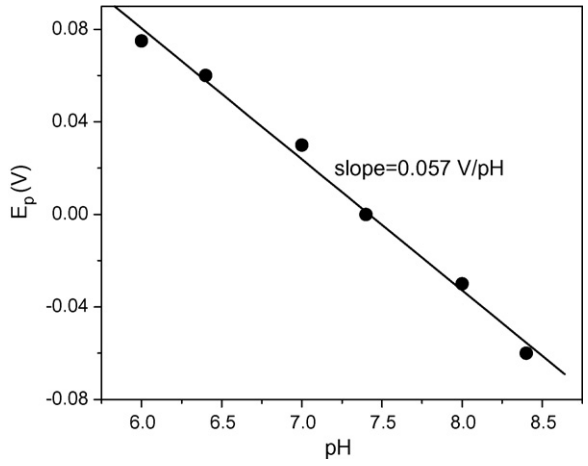

Fig. 4. Influence of the solution pH on the peak potential for 250 μmol L^{-1} GSH. Measurements carried out in 0.1 mol L^{-1} phosphate buffer solution. Potential scan rate: 0.01 V s^{-1}.

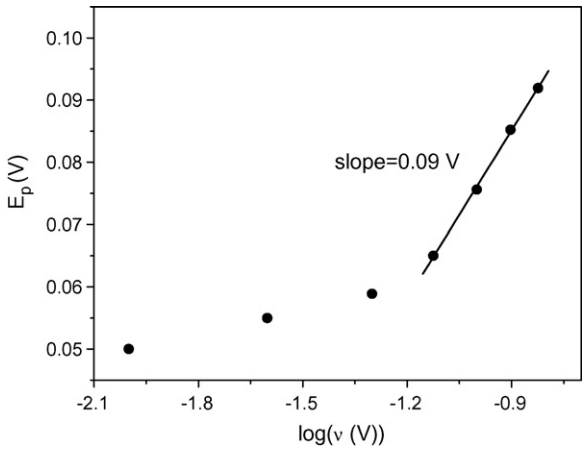

Fig. 5. Plot of E_p vs log v for GSH at the modified electrode. All measurements were performed in 0.1 mol L^{-1} phosphate buffer at pH 7.4.

tion was obtained from pH 6.0 to 8.4 for the E_p vs pH curve with a slope of 0.057 V/pH. This slope is close to a Nernst system, which is 0.059 V/pH at 25 °C, where n_p (number of protons) = n_e (number of electrons) [32].

The influence of the buffer solution type on the sensor response was tested with three different buffer solutions (phosphate, Pipes and HEPES), at concentrations of 0.1 mol L^{-1}, and indicated that phosphate buffer solution at pH 7.4 gives the best response. Finally, the measurements carried out in different concentrations of phosphate varying from 0.1 to 0.25 mol L^{-1} presented almost constant current. Thus, a 0.1 mol L^{-1} phosphate buffer solution at pH 7.4 was chosen for further experiments.

3.5. Kinetic studies of GSH oxidation on the FeT4MPyP/MWCNT/BPPG electrode

According to Andrieux and Saveant [33], the catalytic current I_p depends on the potential scan rate v (Fig. 5) for the case of slow scan rates and large catalytic rate constants as follows:

$$I_p = 0.496nFAC_0D_0^{1/2}v^{1/2}\left(\frac{nF}{RT}\right)^{1/2} \quad (1)$$

where D_0 and C_0 are the diffusion coefficient ($cm^2\,s^{-1}$) and the bulk concentration ($mol\,cm^{-3}$) of the substrate, respectively, and the other symbols have their usual meanings.

The value of $I_p/\left[nFAD_0^{1/2}v^{1/2}C_0(nF/RT)^{1/2}\right]$ was calculated from the corresponding cyclic voltammograms for the FeT4MPyP/MWCNT/BPPG electrode in the presence of GSH. Then the value of $\log[k_{obs}\Gamma/D^{1/2}v^{1/2}C_0(nF/RT)^{1/2}]$ was graphically determined from Fig. 1(b) in the article of Andrieux and Saveant [33] and according to the procedure described by Florou et al. [34], where k_{obs} and Γ are the rate constant and the amount of the active catalyst on the electrode surface (coverage), respectively. Γ can be estimated from the relation $\Gamma = Q/nFA$, where Q is the charge obtained by integration the anodic peak of the modified electrode in the absence of GSH and the other symbols have their usual meanings. In the present case, the value of Γ was determined as 4.5×10^{-10} mol cm^{-2}.

By using a GSH concentration of 5 mmol L^{-1} at pH 7.4, a value of 5.0×10^{-6} $cm^2\,s^{-1}$ for the diffusion coefficient [35], a rate constant of 5.19×10^5 $mol^{-1}\,L\,s^{-1}$ was calculated for the FeT4MPyP/MWCNT/BPPG electrode with a coverage of 4.5×10^{-10} mol cm^{-2} and an effective area (A) of 0.42 cm^2.

3.6. Chronoamperometric measurements

Chronoamperometry was used to investigate the electrode process of GSH on the FeT4MPyP/MWCNT/BPPG electrode as well as to corroborate the diffusion coefficient of the GSH molecules in solution. Under diffusion control, the observed currents are function of the time t according to the Cottrell's equation [36]:

$$I = nFAD_0^{1/2}C_0\pi^{-1/2}t^{-1/2} \quad (2)$$

Based on Eq. (2), a plots of I vs $t^{-1/2}$ was constructed and resulted in a straight line with correlation coefficient of 0.999, for experimental times between 0.6 and 2 s, GSH concentrations between 10.0 and 50.1 μmol L^{-1}, and considering that GSH is oxidized to GSSG (n = 2). The average value estimated for the GSH diffusion coefficient was 5.76×10^{-6} $cm^2\,s^{-1}$, which is close to the value found in the literature [35].

3.7. Rotating disk electrode (RDE) experiments

Analyses of the rotating disk electrode polarization curves recorded at different electrode rotation rates ω (s^{-1}) showed deviations from linearity in the Levich plots (Fig. 6a), suggesting kinetic limitations when rotating rates were used. Under these conditions, to determine the number of electrons n of total electrons transferred to the electrode during the oxidation of GSH and the heterogeneous rate constant k_{obs} ($mol^{-1}\,L\,s^{-1}$), the

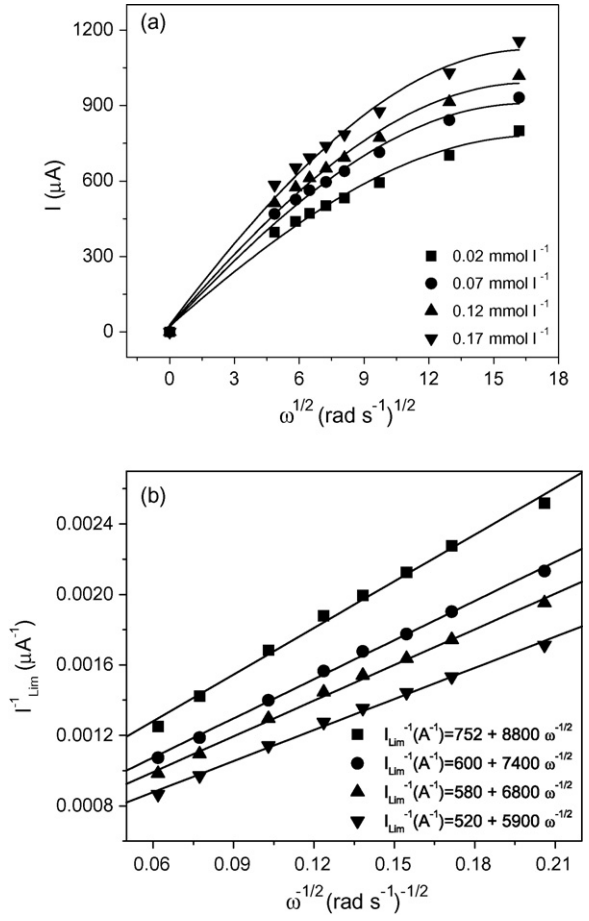

Fig. 6. (a) Levich and (b) Koutecky–Levich plots constructed from RDE data recorded on FeT4MPyP/WMCNT/BPPG electrode at different rotation rate (225, 325, 400, 500, 625, 900, 1600 and 2000 rpm) in (1) 0.02, (2) 0.07, (3) 0.12 and (4) 0.17 mmol L^{-1} GSH solutions in 0.1 mol L^{-1} phosphate buffer (pH 7.4). Potential scan rate of 0.005 V s^{-1}.

Table 3
Summary of the oxidation potentials, sensitivities and detection limits for L-glutathione determination on various modified electrodes

Electrode	Potential (V)	Dynamic range (μmol L^{-1})	Limit of detection (μmol L^{-1})	Sensitivity (μA cm^{-2} μmol)
CoTsPc/PLL [26]	0.2	0.05–2.16	0.015	1.5
Glassy carbon electrode modified with MWCNT [37]	0.3	5–100	3.3	0.097
Well-aligned CNT array electrode [41]	0.52	0.4–16.4	0.2	0.25
Renewable sol–gel carbon ceramic electrodes modified with a Ru-complex [22]	0.8	5–700	1	0.25
PQQ/PPy[42]	0.5	–	13.2	0.0003
CNT–epoxy composite [43]	0.8	5–50	2.9	0.18
Ceramic–CNT nanocomposite [44]	0.45	–	20	0.07
L-Glutathione peroxidase [45]	0.65	19–140	–	0.22
TTF-TCNQ [46]	0.2	5–340	0.3	0.09
FeT4MPyP/MWCNT immobilized on basal plane pyrolytic graphite electrode (this work)	−0.025	5–5000	0.5	1.67

Koutecky–Levich equation [36] was used:

$$\frac{1}{I_{\text{lim}}} = \frac{1}{0.62nFAD^{2/3}\nu^{-1/6}\omega^{1/2}C_0} + \frac{1}{nFAC_0k_{\text{obs}}\Gamma} \quad (3)$$

where D (cm^2 s^{-1}) and ν (0.01 cm^2 s^{-1}) are the diffusion coefficient and the kinematic viscosity of the aqueous solution, respectively, and C_0 (mol cm^{-3}), k_{obs} (mol^{-1} L s^{-1}) and Γ (mol cm^{-2}) represent the bulk concentration of the reactant in the solution, the heterogeneous rate constant for the reaction between the catalyst and the GSH molecule and the amount of the active catalyst on the electrode surface, respectively. All other parameters have their usual meanings.

According to Eq. (3), at a given potential, a plot of I^{-1} vs $\omega^{-1/2}$ should be linear, as shown in Fig. 6b. In addition, the rate constant k_{obs} can be calculated from the intercept of such plot. The values of k_{obs} decreased from 7.65×10^5 to 1.65×10^5 mol^{-1} L s^{-1} as the GSH bulk concentration increased from 0.02 to 0.17 mmol L^{-1}. The average calculated value of 4.65×10^5 mol^{-1} L s^{-1}, which is close to that determined by cyclic voltammetric measurements. However, such k_{obs} value is higher than those reported previously for electrocatalytic oxidation of thiols, including L-glutathione, on other electrode materials [22,37–39].

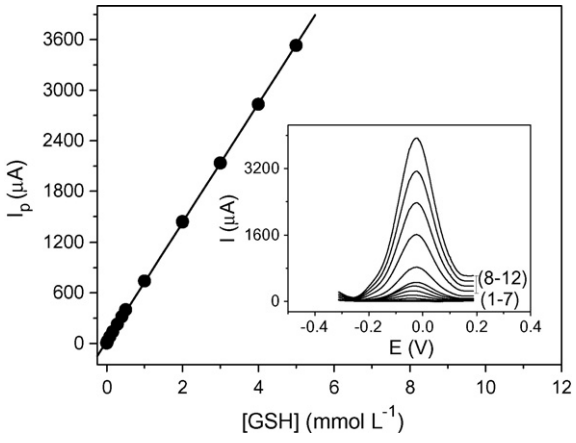

Fig. 7. Analytical curve for the electro-oxidation of GSH in phosphate buffer solution at pH 7.4 in the concentrations: (1) 5, (2) 20, (3) 85, (4) 160, (5) 280, (6) 400 and (7) 500 μmol L^{-1}, (8) 1, (9) 2, (10) 3, (11) 4 and (12) 5 mmol L^{-1}. Step potential (ΔE) = 0.002 V, frequence (f) = 80 Hz and amplitude (a) = 0.03 V (insert: the square wave voltammograms of the analytical curve).

Table 4
Effects of some possible interfering compounds on GSH determinations on FeT4MPyP/MWCNT/BPPG electrodes with SWV technique under optimized conditions

Interfering compound	Relative response (%)
L(+)-Ascorbic acid	103.5 (±0.3)
L(+)-Cysteine	102.7 (±0.2)
L(+)-Glutamic acid	100.8 (±0.6)
D(+)-Glucose	99.3 (±0.4)
Glycine	100.5 (±0.6)

[Interfering compound added] = 10 μmol L^{-1}, [GSH] = 50 μmol L^{-1}. ΔE = 0.002 V, f = 80 Hz, a = 0.03 V.

3.8. Analytical characterization

The proposed sensor showed a large GSH linear response range from 1.5 μmol L^{-1} to 5 mmol L^{-1} (Fig. 7), which can be expressed according to the following equation:

$$I_p\ (\mu\text{A}) = 24.34(\pm 4.98) + 703.41(\pm 2.41)[\text{GSH}]\ (\text{mmol L}^{-1}) \quad (4)$$

with a correlation coefficient of 0.999 (for n = 12). A detection limit of 0.5 μmol L^{-1} was determined using the 3σ/slope ratio and the quantification limit was estimated as 1.65 μmol L^{-1} using the 10σ/slope ratio, where σ is the standard deviation calculated from 10 background current values (blank measurements) and according to the IUPAC recommendations [40].

Table 3 shows that FeT4MPyP/MWCNT/BPPG electrodes presents a lower oxidation potential, higher sensitivity and lower detection limit for L-glutathione than those reported in the literature using other modifiers [22,26,37,41–46]. The good sensitivity can be attributed to the efficiency of the electron transfer between the modified BPPG electrode and GSH due to the good catalytic effect of the FeT4MPyP/MWCNT system.

The stability of the FeT4MPyP/MWCNT/BPPG electrode was checked by performing 200 successive square wave voltammetric measurements in presence of 250 μmol L^{-1} GSH in a 0.1 mol L^{-1}

Table 5
L-Glutathione determination in six human erythrocyte samples (n = 3)

Samples	Proposed method (mmol L^{-1})	Spectrophotometric method [27] (mmol L^{-1})
1	1.13 (±0.02)	1.00 (±0.03)
2	1.00 (±0.01)	0.98 (±0.03)
3	1.91 (±0.01)	1.85 (±0.04)
4	1.25 (±0.02)	1.19 (±0.03)
5	1.02 (±0.01)	0.99 (±0.02)
6	1.88 (±0.01)	1.85 (±0.05)

Table 6
Recovery values of L-glutathione obtained for six erythrocyte samples ($n = 3$)

Samples	GSH added (mmol L^{-1})	GSH expected (mmol L^{-1})	GSH found (mmol L^{-1})	Recovery (%)
1	0.0	–	1.13 (±0.01)[a]	–
	0.2	1.33	1.32 (±0.03)	99.25 (±0.10)
2	0.0	–	1.0 (±0.01)[a]	–
	0.2	1.20	1.21 (±0.02)	100.83 (±0.21)
3	0.0	–	1.91 (±0.02)[a]	–
	0.2	2.11	2.10 (±0.03)	99.53 (±0.22)
4	0.0	–	1.25 (±0.01)[a]	–
	0.2	1.45	1.43 (±0.01)	98.62 (±0.18)
5	0.0	–	1.02 (±0.02)[a]	–
	0.2	1.22	1.21 (±0.03)	99.18 (±0.24)
6	0.0	–	1.88 (±0.01)[a]	
	0.2	2.08	2.09 (±0.02)	100.48 (±0.15)

[a] Standard addition method.

phosphate buffer solution (pH 7.4) and no change was observed in the response of the modified electrode. Even when stored at room temperature, no significant change in the response was observed for at least two months.

The modified electrode presented good repeatability for the GSH determination. The relative standard deviation (R.S.D.) for 10 determinations of 250 μmol L^{-1} GSH was 1.4%. Additionally, a series of 10 sensors were prepared in the same manner and tested in phosphate buffer (pH 7.4) containing 250 μmol L^{-1} GSH, and responses with a relative standard deviation of 4.5% were observed. These results indicate that the FeT4MPyP/MWCNT/BPPG electrode has good stability and repeatability, probably due to the ability of MWCNT to fix the FeT4MPyP complex on the electrode surface in a stable and reproducible way.

3.9. Interference study

The influence of some GSH metabolites and structurally related substances of common blood components on the assay were also examined, since this electrode is to be applied in erythrocyte samples. 50 μmol L^{-1} solutions of these compounds were freshly prepared in the same conditions as for GSH (0.1 mol L^{-1} phosphate buffer, pH 7.4) and the sensor response was monitored and compared with the signal obtained with and without the presence of interferences by SWV (Table 4). The results showed that L-ascorbic acid produced a slight increase in the sensor response and this behavior can be attributed to the high reactivity of this antioxidant agent. A slight interference from cysteine was also observed, due to the structural similarity between this compound and the GSH molecule. Although both L-ascorbic acid and cysteine showed slight interferences, they are normally not present at a significant levels (as 10 μmol L^{-1} used in this work) in erythrocyte samples [46]. The other interfering compounds (glutamic acid, glucose and glycine) did not show significant interferences on the sensor response.

3.10. Application to biological samples and recovery tests

The proposed method was applied for GSH determination in six erythrocyte samples, each determined in triplicate and using the standard addition method. For comparison, the concentrations of GSH in the erythrocyte samples were also determined by the spectrophotometric method [27]. The results are presented in Table 5 and show that the relative standard deviations of the proposed method were lower than those obtained by the comparative method. In addition, applying a paired Student's t-test [47], it was possible to conclude that, at 95% confidence level, there was no statistical difference between the methods.

For an additional check on the accuracy of the developed method and the possibility of matrix interferences, analytical recovery experiments were performed by adding known amounts of GSH to six samples of human erythrocytes. The percentage recovery values were calculated by comparing the concentration obtained from the samples with actual and added concentrations. The recovery results for the samples are shown in Table 6 and it can be clearly observed that there is no influence of the matrix on the proposed sensor for the evaluated samples.

4. Conclusions

This work shows that a BPPG electrode modified with FeT4MPyP adsorbed onto MWCNT is a feasible alternative for the analytical determination of GSH in hemolysed erythrocytes. The modified electrode exhibited a good response for GSH probably due to low resistance to charge transfer and an electrocatalytic effect. Optimization of the experimental conditions yielded a detection limit and sensitivity for GSH similar or better than those described in the literature. This sensor showed good repeatability for both the measurements and electrode preparation, evaluated in terms of relative standard deviations of 1.5% and 4.5%, respectively. The proposed sensor was applied to biological samples and the results were in agreement with those obtained by a reference method described in the literature. Therefore, it can be concluded that the FeT4MPyP/MWCNT/BPPG electrode is a sensitive, robust and stable sensor for GSH determination in biological samples.

Acknowledgements

The authors are grateful to CNPq and FAPESP (Research Grant 00/11103-5), for financial support. R.C.S.L. (Grant: 06/05185-5) is indebted to FAPESP for postdoctoral fellowships. Professor C.H. Collins is also acknowledged for manuscript revision.

References

[1] J. Wang, G. Liu, M.R. Jan, J. Am. Chem. Soc. 126 (2004) 3010.
[2] J.N. Wohlstadter, J.L. Wilbur, G.B. Sigal, H.A. Biebuyck, Adv. Mater. 15 (2003) 1184.
[3] J.J. Gooding, Electrochim. Acta 50 (2005) 3049.
[4] Y.H. Lin, W. Yantasee, J. Wang, Front. Biosci. 10 (2005) 492.
[5] E.V. Basiuk, E.V. Rybak-Akimova, V.A. Basiuk, D. Acosta-Najarro, J.M. Saniger, Nano Lett. 2 (2002) 1249.
[6] A. Star, T. Han, J.P. Gabriel, Nano Lett. 3 (2003) 1421.
[7] D. Sun, L. Zhu, H. Huang, G. Zhu, J. Electroanal. Chem. 597 (2006) 39.

[8] K. Zhao, H. Song, S. Zhung, L. Dai, P. He, Y. Fang, Electrochem. Commun. 9 (2007) 65.
[9] Z. Li, J. Chen, D. Pan, W. Tao, L. Nie, S. Yao, Electrochim. Acta 51 (2006) 4255.
[10] J. Wang, Electroanalysis 17 (2005) 7.
[11] B. Alberts, D. Gray, J. Lewis, M. Raff, K. Roberts, J.D. Watson, Molecular Biology of the Cell, 3rd ed., Garland, New York, 1994.
[12] Y. Chi, J. Chen, M. Miyake, Electrochem. Commun. 7 (2005) 1205.
[13] B. Duong, R. Arechabaleta, N.J. Tao, J. Electroanal. Chem. 447 (1998) 63.
[14] N. Zheng, Y. Zeng, P.G. Osborne, Y. Li, W. Chang, Z. Wang, J. Appl. Electrochem. 32 (2002) 129.
[15] Y.L. Zhang, C.X. Zhang, H.X. Shen, Electroanalysis 13 (2001) 1431.
[16] W.J.R. Santos, A.L. Sousa, R.C.S. Luz, F.S. Damos, L.T. Kubota, A.A. Tanaka, S.M.C.N. Tanaka, Talanta 70 (2006) 588.
[17] J. Chen, U. Wollenberger, F. Lisdat, B. Ge, F.W. Scheller, Sens. Actuators B 70 (2000) 15.
[18] S.M. Chen, Inorg. Chim. Acta 244 (1996) 155.
[19] C.G. Nan, Z.Z. Fena, W.X. Li, D.J. Ping, C.H. Qin, Anal. Chim. Acta 45 (2002) 245.
[20] M. Black, Ann. Rev. Med. 35 (1984) 577.
[21] J.D. Rawn, Biochemistry, Harper & Row, New York, 1983, p657.
[22] J. Chen, Z. He, H. Liu, C. Cha, J. Electroanal. Chem. 588 (2006) 324.
[23] J. Pillay, K.I. Ozoemena, Electrochem. Comm. 9 (2007) 1816.
[24] M.P. Siswana, K.I. Ozoemena, T. Nyokong, Electrochim. Acta 52 (2006) 114.
[25] J. Wang, Analytical Electrochemistry, VCH Publishers, New York, 1994.
[26] R.C.S. Luz, F.S. Damos, P.G. Gandra, D.V. Macedo, A.A. Tanaka, L.T. Kubota, Anal. Bioanal. Chem 387 (2007) 1891.
[27] O.W. Griffith, Anal. Biochem. 106 (1980) 207.
[28] A.V. Udal'tsov, L.A. Kazarin, A.A. Sweshnikov, J. Mol. Struct. 562 (2001) 227.
[29] A.V. Udal'tsov, M. Tosaka, G. Kaupp, J. Mol. Struct. 660 (2003) 15.
[30] P.J. Goodhey, F.J. Humpheys, Electron Microscopy Analysis, 2nd ed., Taylor and Francis, London, 1992.
[31] A. Salimi, S. Pourbeyram, Talanta 60 (2003) 205.
[32] L. Papouchado, R.W. Sandford, G. Petrie, R.N. Adams, J. Electroanal. Chem. 65 (1975) 275.
[33] C.P. Andrieux, J.M. Saveant, J. Electroanal. Chem. 93 (1978) 163.
[34] A.B. Florou, M.I. Prodromidis, M.I. Karayannis, S.M. Tzouwara-Karayanni, Anal. Chim. Acta 409 (2000) 113.
[35] W.R. Jin, H.F. Chen, Chromatographia 52 (2000) 17.
[36] A.J. Bard, L.R. Faulkner, Electrochemical Methods: Fundamentals and Applications, 2nd ed., John Wiley & Sons, Hoboken, NJ, 2001.
[37] A. Salimi, R. Hallaj, Talanta 66 (2005) 967.
[38] A.A. Ensafi, S. Behyan, Sens. Actuators B 122 (2007) 282.
[39] Z.N. Gao, J. Zhang, W.Y. Liu, J. Electroanal. Chem. 580 (2005) 9.
[40] Analytical Methods Commitee, Analyst 112 (1987) 199.
[41] H. Tang, J. Chen, L. Nie, S. Yao, Y. Kuang, Electrochim. Acta 51 (2006) 3046.
[42] T. Inoue, J.R. Kirchhoff, Anal. Chem. 72 (2000) 5755.
[43] G. Chen, L.Y. Zhang, J. Wang, Talanta 64 (2004) 1018.
[44] K.P. Gong, M.N. Zhang, Y.M. Yan, L. Su, L.Q. Mao, S.X. Xiong, Y. Chen, Anal. Chem. 76 (2004) 6500.
[45] L. Rover Jr., L.T. Kubota, N.F. Höehr, Clin. Chim. Acta 308 (2001) 55.
[46] P. Calvo-Marzal, K.Y. Chumbimuni-Torres, N.F. Hoehr, L.T. Kubota, Clin. Chim. Acta 371 (2006) 152.
[47] J.C. Miller, J.N. Miller, Statistics for Analytical Chemistry, Ellis Horwood, New York, 1993.

Talanta 76 (2008) 1006–1014

Contents lists available at ScienceDirect

Talanta

journal homepage: www.elsevier.com/locate/talanta

Use of experimental design and effective mobility calculations to develop a method for the determination of antimicrobials by capillary electrophoresis

Mónica Cecília Vargas Mamani[a], Jaime Amaya-Farfan[b], Felix Guillermo Reyes Reyes[c], José Alberto Fracassi da Silva[a], Susanne Rath[a,*]

[a] Institute of Chemistry, Department of Analytical Chemistry, University of Campinas (UNICAMP), P.O. Box 6154, 13084–971 Campinas, SP, Brazil
[b] Department of Food & Nutrition, University of Campinas (UNICAMP), P.O. Box 6121, 13083–862 Campinas, SP, Brazil
[c] Department of Food Science, University of Campinas (UNICAMP), P.O. Box 6121, 13083–862 Campinas, SP, Brazil

ARTICLE INFO

Article history:
Received 24 April 2008
Accepted 25 April 2008
Available online 13 May 2008

Keywords:
Chloramphenicol
Fluoroquinolones
Sulfonamides
Capillary zone electrophoresis
Experimental design
Effective mobilities

ABSTRACT

A capillary zone electrophoresis (CZE) method for the determination of chloramphenicol (CLP), danofloxacin (DANO), ciprofloxacin (CIPRO), enrofloxacin (ENRO), sulfamethazine (SMZ), sulfaquinoxaline (SQX) and sulfamethoxazole (SMX) is described. For the development, the effective mobilities were estimated and a central composite design was performed. The method was in-house validated for CLP, CIPRO, ENRO and SMX determination in pharmaceuticals. In comparison with the HPLC method recommended by the United States Pharmacopoeia, this CZE method exhibited the same performance, with the advantage that seven different antimicrobials in pharmaceutical formulations could be simultaneously determined.

1. Introduction

Sulfonamides (sulfamethoxazole (SMX), sulfamethazine (SMZ), sulfaquinoxaline (SQX)) and fluoroquinolones (enrofloxacin (ENRO), danofloxacin (DANO) and ciprofloxacin (CIPRO)) are antimicrobials widely used to treat a variety of infections in both human and veterinary medicine [1–4]. Chloramphenicol (CLP) is a broad-spectrum antibiotic not approved for use in animals for food production in several countries, including the European Union, the USA and Brazil [5]. The use of this drug in humans is reserved for certain patients with serious infections, such as meningitis, typhus, and typhoid fever, who cannot take safer alternatives because of resistance or allergies [2]. The chemical structures of these antimicrobials are shown in Fig. 1.

In recent years, methods have been published using capillary zone electrophoresis (CZE) for the determination of fluoroquinolones [6–9], chloramphenicol [10–11] and sulfonamides [12–17]. Several approaches have also been followed for the determination of CLP, CIPRO and SMX by the United States Pharmacopoeia (USP) using high performance liquid chromatography (HPLC) for quality control of these antimicrobials [18]. However, the physicochemical properties of CLP, the fluoroquinolones and the sulfonamides, their ionic natures, multiple ionization sites and different water solubilities, make these compounds more suitable for electrophoretic analysis. CZE continues to grow rapidly as an analytical technique for a wide range of applications, including the analysis of pharmaceuticals. CZE is also advantageous because lower volumes of fluids and samples are employed, in comparison with HPLC [19].

The official monographs of the United States Pharmacopoeia describe different HPLC methods for CLP, CIPRO and SMX. The stationary phases employed for CLP, CIPRO and SMX determination are octadecylsilane columns, whereas the mobile phases comprise a mixture of water, methanol and glacial acetic acid for CLP; phosphoric acid, adjusted to pH 3 with triethylamine plus acetonitrile for CIPRO, and water, acetonitrile and triethylamine at pH 6.0 for, SMX.

Nevertheless, several separation methods for the determination of antimicrobials are presented in the literature most of them focusing on the quantitation of antimicrobials of the same group. Only a few papers describe the simultaneous determination of antimicrobials of different groups, among which, β-lactam antibiotics,

* Corresponding author. Tel.: +55 19 35213084; fax: +55 19 35213023.
E-mail address: raths@iqm.unicamp.br (S. Rath).

0039-9140/$ – see front matter © 2008 Elsevier B.V. All rights reserved.
doi:10.1016/j.talanta.2008.04.062

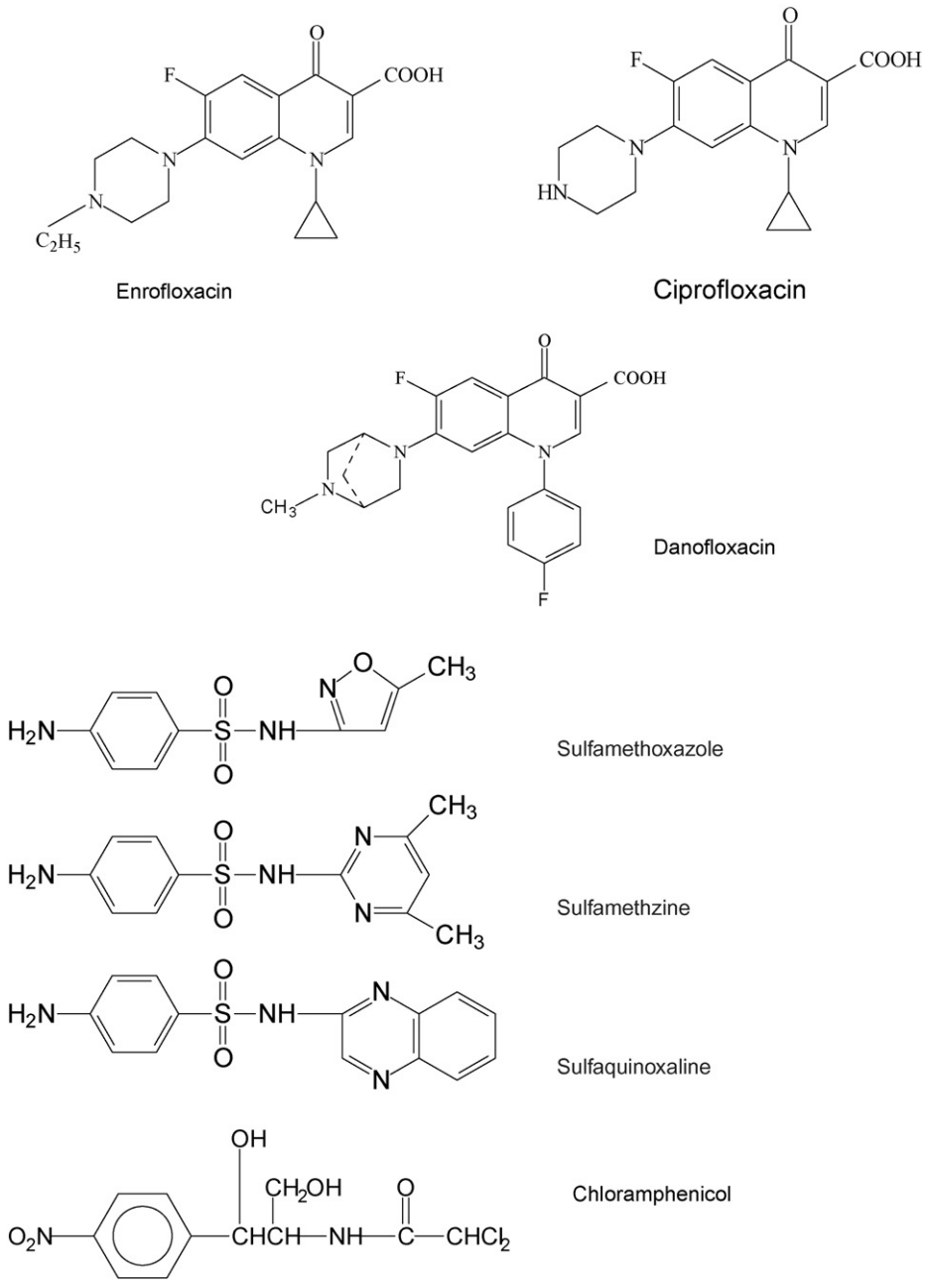

Fig. 1. Structure of fluoroquinolones, sulfonamides and chloramphenicol.

tetracyclines and chloramphenicol in milk [20] and streptomycin and oxytetracycline in agricultural antimicrobials [21]. A review about other applications has been written by Garcia-Ruiz and Marina [22].

There is an advantage in the quality control to use the same method for the determination of several kinds of compounds, without the need to change solvents, analytical columns and procedures.

Due to the different physicochemical properties of fluoroquinolones, sulfonamides and chloramphenicol, the optimization of separation with CZE is complex and difficult, because a high number of parameters (temperature, pH, voltage, buffer composition) will affect the separation. Rather than following the conventional monovariate approach used to adjust the parameters, thus involving a large number of independent analyses, one could advantageously replace the procedure by statistically designed experimental protocols, in which several factors are simultaneously varied. The use of an experimental design can be extremely beneficial in developing capillary electrophoretic methods.

This paper describes the development of a simple and comprehensive CZE method for the simultaneous determination of CLP, DANO, CIPRO, ENRO, SMZ, SQX and SMX in pharmaceutical formulations, using effective mobility calculation and experimental planning. The method was validated for CLP, CIPRO, ENRO and SMX and its performance was compared with that of the official HPLC methods described in the United States Pharmacopoeia. Since there is no Pharmacopoeia method available for ENRO, this fluoroquinolone was treated in a similar manner as CIPRO for validation purposes.

2. Experimental

2.1. Instrumental and operating conditions

The capillary electrophoresis was performed on a Hewlett Packard 3D Capillary Electrophoresis system (Waldbronn, Germany), equipped with a DAD detector. CLP and fluoroquinolones were detected at 270 nm and sulfonamides at 203 nm. Data were collected using the HP 3D Chemstation software from Hewlett-Packard. The separations were carried out in fused silica capillaries (50 μm I.D.), with effective (l) and total (L) lengths of 60.0 and 68.3 cm, respectively. Injection was done hydrodynamically for 20 s at 20 mbar. Measurements of pH were made with a DM-20 pH-meter from Digimed (São Paulo, Brazil), using a combined glass electrode. When necessary, the electrolyte pH was adjusted using 0.1 mol L^{-1} NaOH or 0.1 mol L^{-1} phosphoric acid before making up to volume.

The high performance liquid chromatographic analyses were performed using a Waters chromatographic system (Milford, USA), composed of a binary pumping system, model 1525, a diode array detector (DAD) model 2996 and a Rheodyne 7725 injector, with a sample loop of 50 μL.

Chromatographic separation was achieved using a LiChrosphere C_{18} column (125 mm × 4.6 mm, 5 μm) with a C_{18} guard-column (4.0 mm × 4.0 mm, 5 μm), purchased from Merck (Darmstadt, Germany). The mobile phase for CLP consisted of a mixture of water, methanol, and glacial acetic acid (55:45:0.1, v/v/v). The mobile phase for CIPRO was a mixture of 0.025 mol L^{-1} phosphoric acid, previously adjusted with triethylamine to pH 3, and acetonitrile (87:13, v/v). For SMZ, the mobile phase was obtained by mixing 1400 mL of water, 400 mL of acetonitrile and 2 mL of triethylamine and bringing the volume to 2000 mL with water. Remaining HPLC conditions were as described in the United States Pharmacopoeia [18].

2.2. Standards and reagents

Standards of SMZ, SQX and SMX were purchased from Sigma (St. Louis, USA), while CLP was from ICN Biomedical Inc. (Cleveland, USA). CIPRO and ENRO were from Fluka Biochemicals (Steinheim, Switzerland) and danofloxacin mesylate, from Pfizer (Guarulhos, Brazil).

Analytical grade disodium hydrogenphosphate, sodium tetraborate, sodium hydroxide, sodium carbonate, phosphoric acid, sodium ethylenediaminetetraacetate (EDTA) and phosphoric acid were purchased from Merck (Darmstadt, Germany). Methanol and dimethylformamide, HPLC-grade solvents, were purchased from Tedia (Fairfield, USA).

Throughout the study, water was obtained from a Milli-Q system from Millipore (Bedford, USA). Before analysis, all the solutions were filtered through 0.22 μm nylon filters from Millipore (São Paulo, Brazil).

2.3. Samples

The commercial samples of pharmaceutical formulations like ophthalmic solutions containing CLP, tablets containing CIPRO, injections containing ENRO and tablets and oral suspensions containing SMX from different batches were purchased at local drugstores in Campinas, SP, Brazil.

2.4. Standard solutions

Standard stock solutions of CLP, DANO, CIPRO, ENRO, SMZ, SQX and SMX were prepared by dilution of appropriate volumes of the standards in methanol to a final concentration of 2 mg mL^{-1}. These solutions were stored at −18 °C for up to 1 month. Working solutions in the concentration range of 50–250 μg mL^{-1} were prepared daily by dilution of the standard stock solutions in water.

2.5. CZE procedures

Before daily use, the capillary was sequentially washed with water (10 min), 1 mol L^{-1} NaOH (2 min), 0.1 mol L^{-1} NaOH (3 min) and background electrolyte (5 min). After each determination, the capillary was sequentially washed with water (2 min), 1 mol L^{-1} NaOH (1 min), 0.1 mol L^{-1} NaOH (1 min) and background electrolyte (2 min).

The separation conditions for the determination of the seven antimicrobials were 60 mmol L^{-1} sodium phosphate plus 20 mmol L^{-1} sodium tetraborate, pH 8.5; voltage, 24 kV and temperature, 26 °C.

2.6. HPLC procedure

The HPLC determinations of CLP, CIPRO, ENRO and SMZ in the samples followed the official monograph of the United States Pharmacopoeia [18], without modification.

2.7. Experimental design

Preliminary analytical trials were carried out to identify the significant parameters. The results of this analysis showed the temperature and voltage to be significant. Therefore, these parameters were used to plan a subsequent higher order 2^2 design, with central composite. The variables evaluated were temperature (19–27 °C) and voltage (16–24 kV) (Table 1). All statistical calculations were developed with the software Statistic Statsoft, Inc., v. 5.5 (Tulsa, USA).

2.8. Method validation

The method was in-house validated using the following performance criteria: linearity and linear range, sensitivity, selectivity, intra-assay and inter-assay precision, detectability, accuracy and ruggedness. The linearity, linear range, sensitivity and detectability were established through the analytical curve obtained by triplicate analysis of CLP, DANO, CIPRO, ENRO, SMZ, SQX, SMX at five concentration levels 50, 100, 150, 200 and 250 μg mL^{-1}. The sensitivity is the slope of the analytical curve.

The detectability for each antimicrobial was calculated according to Miller and Miller [23], using the following expression: detectability = $k\, s_{y/x}/m$, where $k = 3$, $s_{y/x}$ is the standard deviation of the residuals and m, the slope of the analytical curve.

The intra-assay precision of the method, expressed as the relative standard deviation of peak area measurements ($n = 5$), was evaluated through the results obtained with the method operating over 1 day, under the same conditions, using solutions of each analyte at a single concentration level, 50 μg mL^{-1}. The inter-assay precision was determined for two concentration levels, 50 and 100 μg mL^{-1}, and the analyses were performed for 5 days.

Table 1
Nominal values corresponding to −1, 0, +1, −1.41 and 1.41 in the first experimental design

Variables	−1.41	−1	0	+1	1.41
A—Temperature (°C)	19	20	23	26	27
B—Voltage (kV)	16	17	20	23	24

Table 2
Nominal values corresponding to −1, 0, +1, −1.68 and 1.68 in the second experimental design

Variables	−1.68	−1	0	+1	1.68
A—pH	8.3	8.4	8.5	8.6	8.7
B—Phosphate concentration (mmol L^{-1})	58	59	60	61	62
C—Temperature (°C)	24.3	25	26	27	27.7

The selectivity of the method was evaluated by exposing CLP, DANO, CIPRO, ENRO, SMZ, SQX, SMX, at the concentration of 50 μg mL^{-1}, to the following stress conditions for 1 h: 0.1 mol L^{-1} HCl, 0.1 mol L^{-1} NaOH, 3% (v/v) H_2O_2 or temperature (55 °C). The solutions were analyzed considering the resolution between the analytes and the possible presence of other substances formed during the experiment and the analytical signal before and after the exposure of the analyte to the stress conditions, expressed as recovery.

The accuracy of the method was evaluated through analyses of samples of pharmaceutical formulations containing the CLP, CIPRO, ENRO, SMX by the proposed CZE method, using the procedure described below, and by HPLC according to the method described in the United States Pharmacopoeia [18].

The susceptibility of the developed analytical method to changes was tested in order to evaluate the ruggedness of the method. For this purpose a 2^3 experimental design was employed (Table 2), where the following variables were tested: pH (8.3–8.7), phosphate concentration (58–62 mmol L^{-1}) and temperature (24.3–27.7 °C).

2.9. Sample analysis

The content of three samples of each commercial formulation from the same batch containing either: CLP, CIPRO, ENRO or SMX, was used. In the case of CLP, an ophthalmic solution was used. An accurately measured volume, equivalent to about 150 μg mL^{-1} was transferred, diluted with water and mixed.

In the case of CIPRO, tablets were analyzed. An accurately weighed quantity of the freshly mixed powder, equivalent to about 100 mg of ciprofloxacin hydrochloride, was transferred to a 50 mL volumetric flask, added with 2 mL of glacial acetic acid and 25 mL of water. The mixture was sonicated for about 10 min, allowed to cool, diluted to volume with water and filtered through a 0.22 μm membrane filter. A volume of 150 μL of this solution was diluted to 10 mL with water in a volumetric flask (150 μg mL^{-1}).

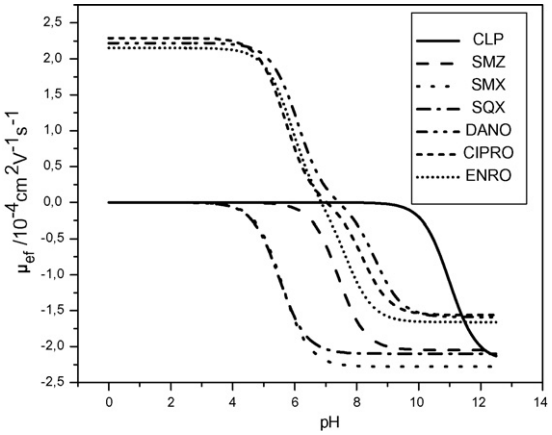

Fig. 2. Simulated electrophoretic mobilities of sulfonamides, chloramphenicol and fluoroquinolones as a function of pH in the range 0.0–14.0 in CZE. Electrolyte: 60 mmol L^{-1} sodium phosphate plus 20 mmol L^{-1} sodium tetraborate, 24 kV, 26 °C.

In the case of ENRO, injections for animal use were analyzed. Aliquots of 300 μL were transferred to a 100 mL volumetric flask (150 μg mL^{-1}) and diluted with water.

The last antibacterial, SMX, was determined in two pharmaceutical formulations: tablets and an oral suspension. For tablets, an accurately weighed quantity of the freshly mixed powder (about 100 mg SMX) was transferred to a 50 mL volumetric flask and 15 mL of methanol were added, followed by 25 mL of water. The mixture was sonicated for about 10 min, allowed to cool to room temperature, diluted to volume with water and filtered through a 0.22 μm membrane filter. A volume of 750 μL of this solution was diluted to 10 mL with water in a volumetric flask (150 μg mL^{-1}). Oral suspensions were diluted as in the procedure for the tablets and processed in an identical manner. All samples were analyzed in quintuplicate.

The analyses by CZE were carried out as described in Section 2.5 and quantitation was accomplished through an external analytical curve with five concentration levels in the range of 50–250 μg mL^{-1}. The samples were also analyzed by HPLC using the methods described in the United States Pharmacopoeia [18].

3. Results and discussion

3.1. Eletrophoretic mobilities

The composition of the background electrolyte has great influence on its separation ability for the antimicrobials under study. Principally, the pH of the electrolyte influences the effective mobilities of the analytes. In order to assess the best pH-value of the background electrolyte for the separation of all antimicrobials under study, the effective mobilities (μ_{ef}) for each compound were calculated using Eq. (1) [24] and a plot of μ_{ef} versus pH was constructed. This characterization of the electrophoretic behavior is suitable to indicate the pH regions where the solute mobilities differ and separation of the analytes would be possible.

$$\mu_{ef} = \sum_{j=1}^{n} \mu_j \alpha_j \quad (1)$$

In Eq. (1), μ_j is the absolute electrophoretic mobility and α_j is the distribution function of species j. The distribution functions are related to the pH and to the acid–base equilibrium constants.

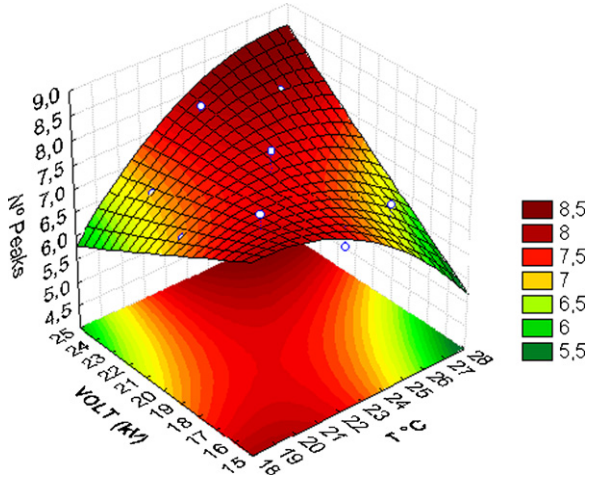

Fig. 3. Response surface for CLP, DANO, CIPRO, ENRO, SMZ, SQX and SMX showing the number of separated compounds as a function of significant separation parameters using temperature and voltage, obtained using a 2^2 factorial design with the central composite design.

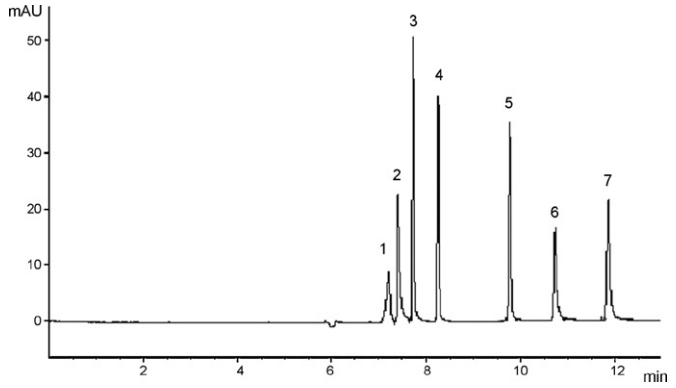

Fig. 4. A typical electropherogram of 100 μg mL^{-1} of (1) CLP, (2) DANO, (3) CIPRO, (4) ENRO, (5) SMZ, (6) SQX and (7) SMX (t_{m1} 7.2 min, t_{m2} 7.4 min, t_{m3} 7.7 min, t_{m4} 8.3 min, t_{m5} 9.8 min, t_{m6} 10.7 min, and t_{m7} 11.9 min, respectively). Capillary: uncoated fused silica; background electrolyte, a solution of 60 mmol L^{-1} sodium phosphate plus 20 mmol L^{-1} sodium tetraborate, pH 8.5; temperature, 26 °C; applied voltage, 24 kV; detection wavelength, 270 nm for CLP and fluoroquinolones and 203 nm for sulfonamides.

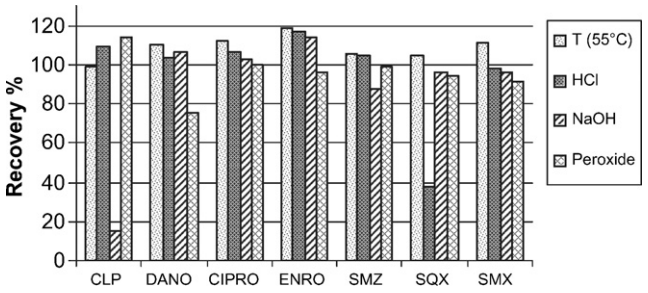

Fig. 5. Recovery (%) of CLP, fluoroquinolones and sulfonamides after exposure of standard solutions (50 μg mL^{-1}) to temperature (55 °C), 0.1 mol L^{-1} HCl, 0.1 mol L^{-1} NaOH or 3% (v/v) H_2O_2.

For the fluoroquinolones (FQ) two acid–base equilibria must be considered. The first one involves the cation form H_2FQ^+ and the neutral HFQ (K_{a1}), while the second equilibrium involves the neutral HFQ and anionic FQ^- forms (K_{a2}).

For the sulfonamides and chloramphenicol, just one acid–base equilibrium between the neutral form and the unprotonated anion was considered. Using Eq. (1), the pK_a values and the eletrophoretic mobilities [10,25–27], it was possible to calculate the μ_{ef} for each antimicrobial as a function of pH, using the software Microsoft Excel, Microsoft Corporation (USA). Fig. 2 shows the calculated effective mobilities in which the effects of ionic strength were not taken into account. The results indicate that the separation of all the antimicrobials can be performed in the pH range of 7.5–9, with all the analytes having a negative charge.

Consequently, the CZE method was developed using the high pH background electrolyte, normal polarity, and cathodic EOF. Under these conditions, the antimicrobials migrate against the EOF and that having the smallest μ_{ef} would reach the detector first. Thus, the predicted migration order becomes: CLP, DANO, CIPRO, ENRO, SMZ, SQX, and SMX.

3.2. CZE method development

In view of reports on the influence of the electrolyte on selectivity [15], it was deemed mandatory first to compare the performance of different types of background electrolytes for the separation of the antimicrobials. Different electrolytes at pH 8.5 were evaluated: sodium phosphate, Tris, sodium carbonate and sodium tetraborate. The electrolytes were prepared in the concentration range of 20–140 mmol L^{-1} with uniform steps of 40 mmol L^{-1}.

Considering the resolution of the analytes and the analysis time, the best conditions for the simultaneous separation of CLP, fluoroquinolones and sulfonamides were achieved with the sodium phosphate plus sodium tetraborate electrolyte (40–100 mmol L^{-1}). Subsequently, it was necessary to optimize the electrolyte concentration, pH, temperature and voltage. An initial set of trials was made using a monovariate approach, as was done with the electrolyte concentration. The optimum concentration was 60 mmol L^{-1}. Concentrations below and above 60 mmol L^{-1} resulted in increased migration times and in higher currents, respectively. The effect of the pH was evaluated in the interval 6.8–10.2, permitting the best separation for all compounds at 8.5, confirming the pH-value previously established through the evaluation of the effective eletrophoretic mobilities. The optimum temperature and voltage conditions were selected through the response surfaces obtained by a 2^2 chemometric experimental design (11 tests). This procedure offers an efficient route for determining the best resolution from a selected number of conditions. Moreover, by using experimental design it is possible to evaluate the interaction of factors that have a significant effect on the separation using a small number of experiments.

The experimental design was thus constructed by the use of a full 2^2 experimental design, including three central and four axial points. The conditions are presented in Table 1.

Fig. 3 depicts the response surface, showing that the separation of the seven antimicrobials (CLP, DANO, CIPRO, ENRO, SMZ, SQX and SMX) under study could be achieved, for example, at 24 kV and 26 °C, when using 60 mmol L^{-1} sodium phosphate plus 20 mmol L^{-1} sodium tetraborate, pH 8.5 as background electrolyte.

Since the analytes migrate toward the detector pulled by the electroosmotic flow (EOF), shorter analysis times can be obtained by raising the pH of the background electrolyte, but incomplete separations were obtained at pH values higher than 8.5.

A typical electropherogram of CLP, DANO, CIPRO, ENRO, SMZ, SQX and SMX at the optimized conditions established through the experimental design is shown in Fig. 4.

Table 3
Quantitative features for CLP, CIPRO, ENRO, SMZ and SMX

Parameter	CLP	CIPRO/DANO	ENRO/DANO	SMZ/SQX	SMX/SQX
Linear range (μg mL^{-1})	50–250	50–250	50–250	50–250	50–250
Sensitivity (aU μg mL^{-1}) ($P<0.05$)	0.0083 ± 0.0001	0.0070 ± 0.0001	0.0070 ± 0.0001	0.0050 ± 0.0001	0.0050 ± 0.0001
Linearity (r)	0.999	0.998	0.998	0.999	0.997
Intercept ($P<0.05$)	0.02 ± 0.04	−0.02 ± −0.04	−0.02 ± −0.05	−0.07 ± 0.02	−0.02 ± −0.04
Intra-assay precision, 50 μg mL^{-1}, $n=5$ (R.S.D.%)	1.48	2.11	1.39	1.19	1.40
Inter-assay precision, 50 μg mL^{-1}, $n=5$ (R.S.D.%)	1.31	2.29	2.13	1.01	1.69
Inter-assay precision, 100 μg mL^{-1}, $n=5$ (R.S.D.%)	1.60	1.01	1.50	2.52	1.98
Detectability (μg mL^{-1})	10	12	15	10	17

R.S.D.: relative standard deviation.

3.3. Method validation

The results of the CZE method in-house validation for the determination of CLP, CIPRO, ENRO, SMZ and SMX are summarized in Table 3. The accuracy was evaluated by comparing the results obtained from the analysis of pharmaceutical formulations by the proposed CZE method with those obtained using the recommended HPLC method described in the United States Pharmacopoeia [18].

The linearity, linear range and sensitivity were obtained from analytical curves using external standard ization for CLP and an internal standard (DANO) for CIPRO and ENRO, and SQX as internal standard for SMZ and SMX, at five concentration levels for each antimicrobial under study, with triplicate analyses. The linearity was tested using a pure error lack of fit test with simple regression, which was not significant at the 5% level.

The selectivity of the method indicates the ability to accurately measure the analyte response in the presence of potentially interfering sample components or degradation products. In this study, the selectivity was evaluated by exposing the analyte to stress conditions, such as acid (0.1 mol L^{-1} HCl), base (0.1 mol L^{-1} NaOH) and an oxidant (3%, v/v H_2O_2). The solutions were analyzed considering the resolution between the analyte and other substances formed during the experiment, and the analytical signal before and after exposure of the analyte to the stress conditions. The results (Fig. 5) showed that the stabilities of the antimicrobials to the three stressing conditions depend on the chemical structure. CLP is the least stable compound to the alkaline conditions and CLP degraded almost completely in 0.1 mol L^{-1} NaOH, while CIPRO, ENRO, SMZ, SMX and TC were stable to alkaline, acid, temperature, and peroxide stress. SQX was sensitive to the acid treatment. DANO was less stable under peroxide stress. The degradation products of CLP formed under the stressing conditions migrated in shorter times (approx. 6 min) than the other compounds. Antimicrobials like DANO, ENRO and SMX generated degradation products at 6–7 min. DANO had another degradation product evident at 8.9 min, but since no other compound appears at or about this time, the selectivity of the method can be confirmed. Co-migration of any degradation products with the authentic standards did not occur as evidenced by the perfect overlay of the absorption spectra of the pure standards with those of the peaks obtained after degradation.

Table 4
CLP content per mL of solution, determined in commercial ophthalmic samples by CZE and HPLC

	Sample 1		Sample 2		Sample 3	
	CZE	HPLC	CZE	HPLC	CZE	HPLC
Average content (mg mL^{-1})	4.48	3.60	4.43	3.59	4.23	3.64
s (mg mL^{-1})	0.05	0.02	0.06	0.03	0.07	0.08
R.S.D. (%)	1.1	0.58	1.6	0.93	2.4	2.2

$n = 5$; s, estimate of the standard deviation (mg mL^{-1}); R.S.D., relative standard deviation.

The precision of the method for CLP, CIPRO, ENRO, SMZ and SMX was evaluated using the results obtained over 1 day of operation under the same conditions (intra-assay precision) and for 5 days (inter-assay precision). The intra- and inter-assay precisions were determined at 100% of the target concentration from 5 determinations. The results were expressed as relative standard deviations (R.S.D.) and were lower than 2.1 and 2.3% for intra- and inter-assay, respectively (Table 3). Considering that regulatory agencies [18] recommend that the precision should be lower than 2%, the values obtained by the CZE method are acceptable.

The established detectability represents the lowest concentration of an analyte in sample solutions to be introduced in the CE equipment that can be detected. The detection and the quantitation limits of the method are not presented, due to the fact that the active compound is the major constituent of the formulation and this parameter is not required for method validation for the quality control of pharmaceutical products. Furthermore, these limits would depend on sample dilution before analysis.

The accuracy of the method was assessed for CLP, CIPRO, ENRO and SMX by analyzing commercial formulations by the CZE method and the recommended United States Pharmacopoeia methods. The mean values obtained using the proposed method and the reference method (Tables 4–6), for all the samples, do not differ significantly ($P = 0.05$).

Finally, the ruggedness of the method was assessed by introducing small changes to the procedure and examining the effect on the results (analytical signal). For this purpose, the temperature (26.0 ± 0.8 °C), pH (8.5 ± 0.2) and electrolyte concentration (60 ± 2 mmol L^{-1}) were changed simultaneously using a 2^3 factorial design (17 tests). The response graphs can be seen in Figs. 6

Table 5
CIPRO and ENRO content per tablet and per mL of solution, determined in commercial samples by CZE and HPLC

	Sample CIPRO		Sample ENRO 1		Sample ENRO 2		Sample ENRO 3	
	CZE	HPLC	CZE	HPLC	CZE	HPLC	CZE	HPLC
Average content (mg/tablet)[a] or (mg mL^{-1})[b]	501	450	47	52	48	52	49	52
s (mg/tablet)[a] or (mg mL^{-1})[b]	1.2	0.2	0.9	0.6	0.9	0.2	0.4	0.4
R.S.D.	2.5	0.04	1.8	1.24	1.8	0.40	0.78	0.84

$n = 5$; s, estimate of the standard deviation (mg mL^{-1}); R.S.D., relative standard deviation.
[a] Units for CIPRO.
[b] Units for ENRO.

Table 6
SMX content per tablet and per mL of solution, determined in commercial samples by CZE and HPLC

	Sample 1[t]		Sample 2[t]		Sample 3[s]	
	CZE	HPLC	CZE	HPLC	CZE	HPLC
Average content (mg/tablet)[a] or (mg mL^{-1})[b]	411	409	435	382	39	36
s (mg/tablet)[a] or (mg mL^{-1})[b]	7	4.7	7.6	7	0.7	0.65
R.S.D.	1.72	1.14	1.75	1.79	1.67	1.8

$n = 5$; s, estimate of the standard deviation (mg mL^{-1}); R.S.D., relative standard deviation.
[a] Units for tablet.
[b] Units for oral suspension.

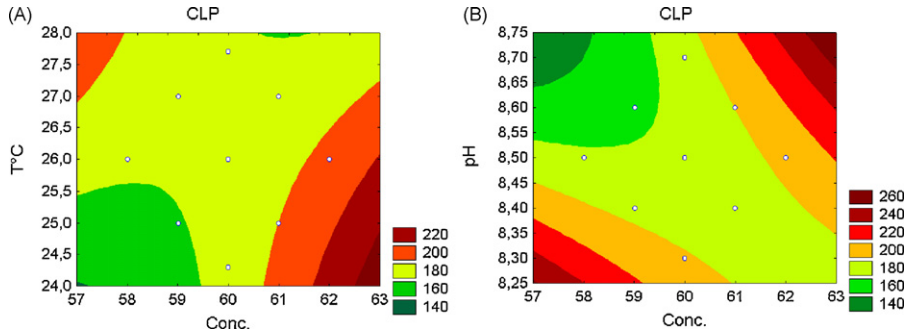

Fig. 6. Contour plots used to evaluate the ruggedness of the method selected by the 2^3 experimental design. (A) CLP (temperature vs. electrolyte concentration); (B) CLP (pH vs. electrolyte concentration).

(CLP), 7 (DANO, CIPRO, ENRO) and 8 (SMZ, SMX, and SQX). The analytical signal of CLP, DANO, CIPRO and ENRO were less influenced by small variations in temperature in relation to the other parameters, while SMZ and SQX were less affected by small variations in the electrolyte concentration. In turn, SMX was most affected by small variations in temperature, and pH. Considering that the same method should be applicable to all seven antimicrobials, it is important that the range of each variable that produces acceptable results be incorporated in the analytical procedure in order to guarantee consistency of the results. The results obtained in this study allowed establishing the following parameters: 60 ± 1 mmol L^{-1} sodium phosphate, pH 8.5 ± 0.1 and 26.0 ± 0.5 °C.

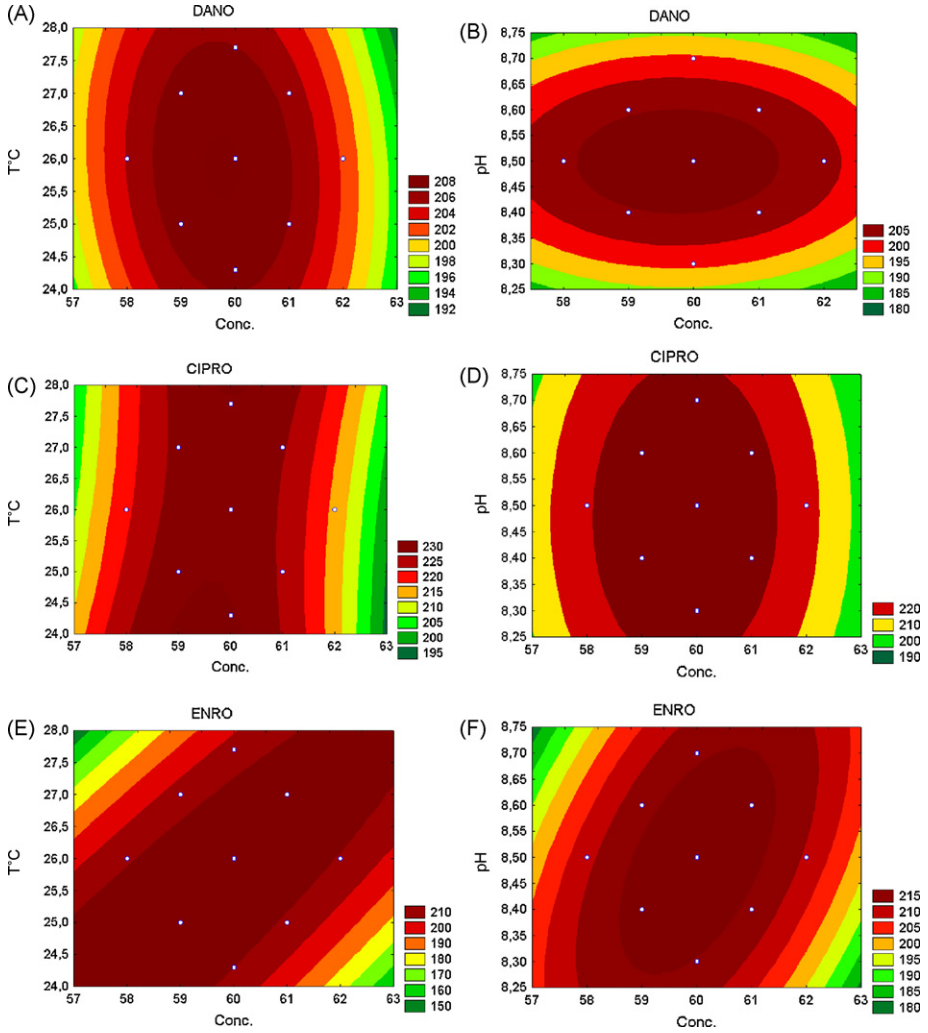

Fig. 7. Contour plots used to evaluate the ruggedness of the method selected by the 2^3 experimental design. (A) DANO (temperature vs. electrolyte concentration); (B) DANO (pH vs. electrolyte concentration); (C) CIPRO (temperature vs. electrolyte concentration); (D) CIPRO (pH vs. electrolyte concentration); (E) ENRO (temperature vs. electrolyte concentration); (F) ENRO (pH vs. electrolyte concentration).

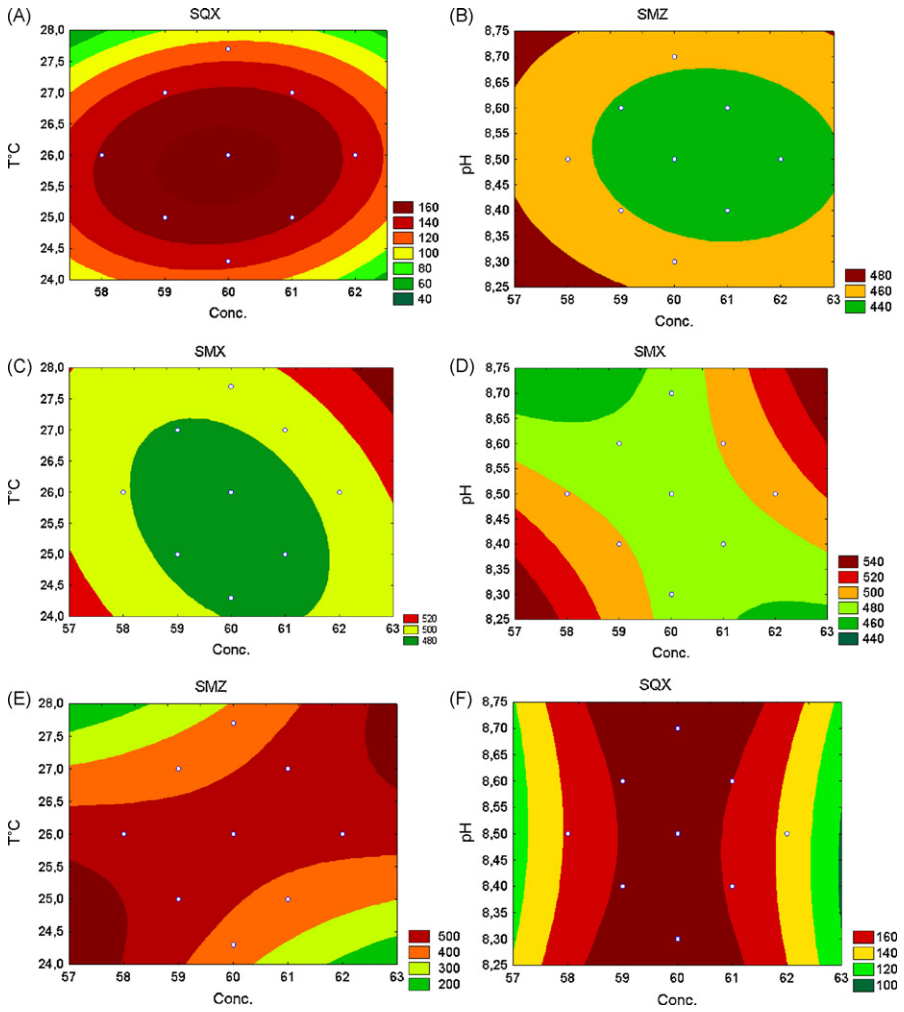

Fig. 8. Contour plots used to evaluate the ruggedness of the method selected by the 2^3 experimental design. (A) SQX (temperature vs. electrolyte concentration); (B) SQX (pH vs. electrolyte concentration); (C) SMX (temperature vs. electrolyte concentration); (D) SMX (pH vs. electrolyte concentration; (E) SMZ (temperature vs. electrolyte concentration); (F) SMZ (pH vs. electrolyte concentration).

3.4. Analysis of commercial samples

After validation, the CZE method was applied to assay three different commercial samples labeled to contain 4 mg mL^{-1} of CLP, 500 mg of CIPRO, 50 mg mL^{-1} of ENRO, 400 mg of SMX in tablet form and 40 mg mL^{-1} of SMX in oral suspension. Three of the samples were analyzed by HPLC. The average concentrations determined in the samples were 4.2–4.5 mg mL^{-1} of CLP (Table 4), 501 mg/tablet of CIPRO, 47–49 mg mL^{-1} of ENRO (Table 5), 411–435 mg for SMX tablets and 39 mg mL^{-1} for the SMX oral suspension. Considering that the active ingredient needs to be in the range of 90–110% for nearly all the compounds and between 93 and 107% for the SMX tablets (Table 6), all of the samples analyzed were in accordance with their specifications and also agreed with the results of the HPLC assay.

4. Conclusions

Most of the methods for the determination of antimicrobials described in Pharmacopoeias recommend analysis by HPLC. Nevertheless, these methods require the use of relatively large volumes of HPLC-grade solvents. Recently, many CZE methods have been developed. However, in spite of their advantages, such as analytical efficiency and cost, most of them continue to be considered as alternative methods in the quality control of pharmaceuticals.

By combining the calculation of effective mobilities and the use of experimental design it was possible to arrive at optimal separation conditions for the simultaneous determination of seven antimicrobials of rather different nature, from a relatively small number of experiments.

The results obtained in this work confirm that the CZE method, when properly optimized and validated, fulfills all the pre-established requirements based on international regulations and is adequate to be used in the quality control of pharmaceuticals. This validated electrophoretic method could be advantageous because it does not require the usual frequent changes of operating analytical conditions, besides reducing the cost of mobile phases and saving time of analysis in research and quality control of pharmaceutical formulations.

Acknowledgements

The authors gratefully acknowledge the financial support from CNPq and FAPESP (01/14072-6, 04/07312-9) and thank Professor C.H. Collins for language assistance.

References

[1] A. Anadón, M.R. Martinez-Larranaga, Livestock Prod. Sci. 59 (1999) 183.
[2] L.S. Goodman, A.G. Gilman (Eds.), The Pharmacological Basis of Therapeutics, 9th ed., McGraw-Hill, New York, 1996, pp. 1131–1135.
[3] M.D. Marzuela, M.C. Moreno-Bondi, J. Chromatogr. A 1034 (2004) 25.
[4] J.A. Van Rhijn, J.J.P. Lasaroms, B.J.A. Berendsen, U.A.Th. Brinkman, J. Chromatogr. A 960 (2002) 121.
[5] E. Gikas, P. Kormall, D. Tsipi, A. Tsarbopoulos, J. Agric. Food Chem. 52 (2004) 1025.
[6] P.H. Schmitt-Kopplin, J. Burhenne, D. Freitag, M. Spiteller, A. Kettrup, J. Chromatogr. A 837 (1999) 253.
[7] K. Michalska, G. Pajchel, S. Tyski, J. Chromatogr. A 1051 (2004) 267.
[8] D. Barrón, J. Jiménez-Lozano, J. Barbosa, J. Chromatogr. B 759 (2001) 73.
[9] C. Lin, Y. Deng, W. Liao, S. Sun, W. Lin, C. Chen, J. Chromatogr. A 1051 (2004) 283.
[10] M.R. Gomez, R.A. Olsina, L.D. Martinez, M.F. Silva, Talanta 61 (2003) 233.
[11] A. Wang, L. Zhang, Y. Fang, Anal. Chim. Acta 394 (1999) 309.
[12] C. Lin, C. Chang, W. Lin, J. Chromatogr. A 768 (1997) 105.
[13] M.E.P. Hows, D. Perrett, J. Kay, J. Chromatogr. A 768 (1997) 97.
[14] L.Y. Fan, H.L. Chen, X.G. Chen, Z. De Hu, J. Sep. Sci. 26 (2003) 1376.
[15] M.S. Fuh, S. Chu, Anal. Chim. Acta 499 (2003) 215.
[16] S. Lamba, K.S. Sunil, A. Asthana, M. Shelke, Anal. Chim. Acta 552 (2005) 110.
[17] B. Santos, A. Lista, B.M. Simonet, A. Rios, M. Valcarcel, Electrophoresis 26 (2005) 1567.
[18] The United States Pharmacopoeia, The National Formulary, 28th ed., United States Pharmacopoeia Convention, Rockville, 2005, pp. 1886–1887.
[19] A. Weston, P.R. Brown (Eds.), LC and CZE Principles and Practice, Academic Press, San Diego, 1997, p. 279.
[20] S.M. Santos, M. Henriques, A.C. Duarte, V.I. Esteves, Talanta 71 (2007) 731.
[21] P.P. Maia, J.A. Farfan, S. Rath, F.G.R. Reyes, J. Pharm. Biomed. Anal. 43 (2007) 450.
[22] C. García-Ruiz, M.L. Marina, Electrophoresis 27 (2006) 266.
[23] J.C. Miller, J.N. Miller (Eds.), Statistics for Analytical Chemistry, 3rd ed., Ellis Horwood, New York, 1993, p. 233.
[24] R. Kuhn, S. Hoffstetter-Kuhn, Capillary Electrophoresis: Principles and Practice, Springer-Verlag, Berlin, 1993, pp. 74–80.
[25] C. Lin, W. Lin, Y.C.S. Wang, J. Chromatogr. A 792 (1997) 37.
[26] M.F.M. Tavares, V.L. Guffin, J. Chromatogr. A 686 (1994) 129.
[27] D. Barrón, J. Jiménez-Lozano, J. Barbosa, J. Chromatogr. A 919 (2001) 395.

Talanta 76 (2008) 1022–1028

Contents lists available at ScienceDirect

Talanta

journal homepage: www.elsevier.com/locate/talanta

Electroanalysis of some common pesticides using conducting polymer/multiwalled carbon nanotubes modified glassy carbon electrode

P. Manisankar*, PL. Abirama Sundari, R. Sasikumar, SP. Palaniappan

Department of Industrial Chemistry, Alagappa University, Karaikudi-630003, Tamil Nadu, India

ARTICLE INFO

Article history:
Received 6 March 2008
Received in revised form 25 April 2008
Accepted 28 April 2008
Available online 4 May 2008

Keywords:
Pesticide analysis
Multiwalled carbon nanotubes (MWCNTs)
Differential pulse stripping voltammetry
Surface morphology
Polymer modified electrodes

ABSTRACT

The cyclic voltammetric behaviour of three common pesticides such as isoproturon (ISO), voltage (VOL) and dicofol (DCF) was investigated at glassy carbon electrode (GCE), multiwalled carbon nanotubes modified GCE (MWCNTs/GCE), polyaniline (PANI) and polypyrrole (PPY) deposited MWCNT/GCE. The modified electrode film was characterized by scanning electron microscopy (SEM) and X-ray diffraction analysis (XRD). The electroactive behaviour of the pesticides was realized from the cyclic voltammetric studies. The differential pulse voltammetric principle was used to analyze the above-mentioned pesticides using MWCNT/GCE, PANI/MWCNT/GCE and PPY/MWCNT/GCE. Effects of accumulation potential, accumulation time, Initial scan potential, amplitude and pulse width were examined for the optimization of stripping conditions. The PANI/MWCNT/GCE performed well among the three electrode systems and the determination range obtained was 0.01–100 mg L^{-1} for ISO, VOL and DCF respectively. The limit of detection (LOD) was 0.1 μg L^{-1} for ISO, 0.01 μg L^{-1} for VOL and 0.05 μg L^{-1} for DCF on PANI/MWCNT/GCE modified system. It is significant to note that the PANI/MWCNT/GCE modified system results in the lowest LOD in comparison with the earlier reports. Suitability of this method for the trace determination of pesticide in spiked samples was also realized.

1. Introduction

Carbon nanotubes (CNTs) have been the subject of numerous investigations in chemical, physical and material science research areas since their discovery in 1991 [1], due to novel structural, mechanical, electronic and chemical properties [2,3]. It is of two types namely single walled (SWCNT) and multiwalled carbon nanotubes (MWCNTs) [4]. Depending on their atomic structure, CNTs behave electrically as a metal or as a semiconductor [4,5]. CNTs are attractive materials for the development of electrochemical sensors because of their capability to provide strong electrocatalytic activity and minimize surface fouling of the sensors. Carbon nanotubes display excellent chemical stability, good mechanical strength and electrical conductivity [2]. The electrocatalytic and adsorption properties lead to the development of many electrochemical sensors [6–8]. Joseph Wang et al. reported the utilization of CNTs for voltammetric sensing of some organic compounds of biomedical and environmental importance [9]. In this study, they have chosen 2,4,6-trinitrotoluene and dopamine as potentially interesting model compounds. A dramatically improved electrochemical behaviour has been reported for cytochrome *c* [10], NADH [11,12], hydrogen peroxide [13] and hydrazine compounds [14]. Simultaneous determination of hydroquinone and catechol at a glassy carbon modified with MWCNTs has also been reported [15]. Enhanced oxidation of simvastatin molecule at MWCNTs-Dihexadecyl hydrogen phosphate composite modified GCE has been studied [16]. Comparison of the electrochemical reactivity of electrodes modified with CNT from different sources has been made by Nathan et al. [17]. A disposable biosensor for organophosphate nerve agents based on CNTs modified thick film strip electrode has been reported [18]. Adsorptive stripping voltammetric determination of amitrole at a MWCNTs paste electrode has been studied in detail by Moreno et al. [19]. These studies open a new way for a widespread use of MWCNTs as a modifier for electrochemical sensing of organic compounds polluting the environment. Pesticides are highly toxic chemicals because of their bioaccumulation properties. Trace contamination of these toxic organic compounds present in the natural aquatic systems creates a lot of pollution problem. The presence of pesticides in water, soil and air has raised concerns for the protection of the environment. Techniques such as TLC, HPLC/UV, GC/MS, UV and colorimetry have been used for the determination of residues of pesticides [20–28]. HPLC, at its current stage

* Corresponding author. Tel.: +91 4565228836; fax: +91 4565225202.
E-mail addresses: pms11@rediffmail.com, cvedhi@rediffmail.com (P. Manisankar).

0039-9140/$ – see front matter © 2008 Elsevier B.V. All rights reserved.
doi:10.1016/j.talanta.2008.04.056

Table 1
Structure and physical status of the selected pesticides

Compound	Structure	Class and physical nature
ISOPROTURON [3-(4-isopropylphenyl)-1,1-dimethylurea]	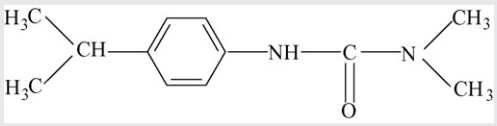	Herbicide colourless, crystalline solid M.pt. 155–156 °C
VOLTAGE (RS)-[O-1-(4-chlorophenyl)pyrazol-4-yl O-ethyl S-propyl phosphorothioate]	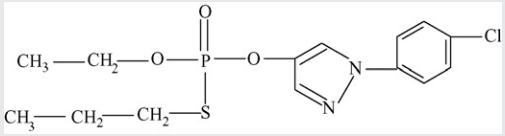	Insecticide pale yellowish oily liquid B.pt. 164 °C
DICOFOL [2,2,2-trichloro-1,1-bis(4-chlorophenylethanol]	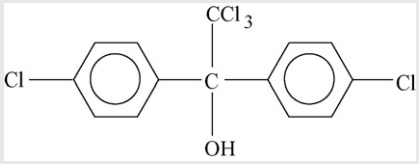	Acaricide, white solid, mp 78.5–79.5 °C

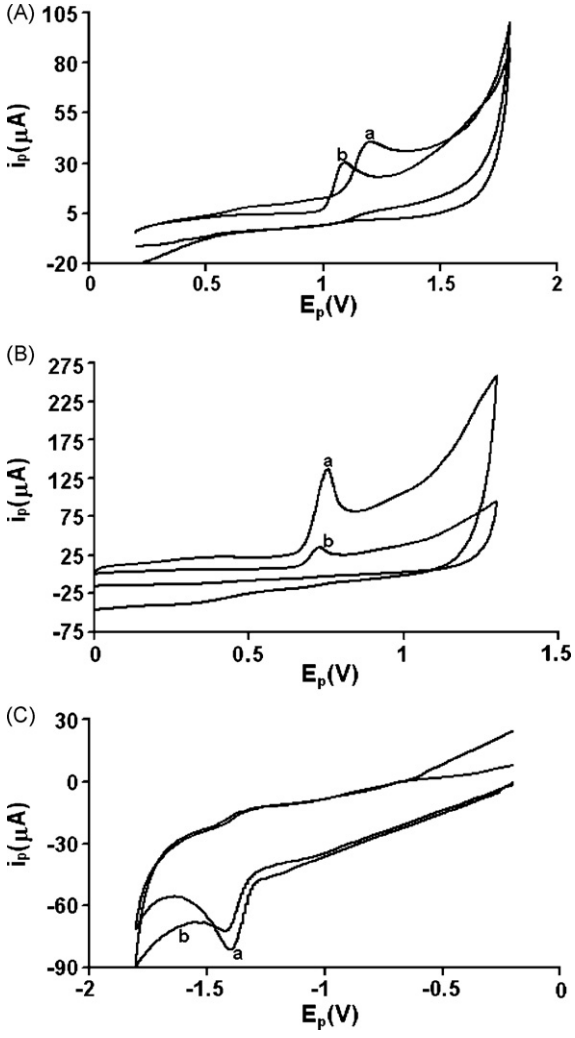

Fig. 1. (A) Cyclic voltammogram of ISO; (B) cyclic voltammogram of VOL; (C) cyclic voltammogram of DCF; (a) PANI/MWCNT/GCE, (b) PPY/MWCNT/GCE (scan rate = 0.100 V s^{-1}; concentration = 0.99 mmol L^{-1}).

of development, is clearly not a method for analytical problems with a high repetition rate because the receptive condition of the system requires 24–36 h [29]. On the other hand, electroanalysis is a manageable method, which is suitable for various problems [30]. Electroanalytical techniques represent the most effective answer to the increasing worldwide demand of reliable and rapid determinations of the widest variety of analytes in complex matrices. In recent years, new sensors have been developed, based on modified electrodes for the voltammetric determination of both electroactive and non-electroactive analytes. Nowadays, many research articles are being published to propose methods for the determination of pesticides using different modified electrodes like CNT [31], clay [32,33] and ploy ethylenedioxythiophene [34]. Since MWCNTs exhibit excellent electrocatalytic and adsorption properties [2] and conducting polymers exhibit preferential accumulation of analytes on bound surface functionalities [34], the selectivity and sensitivity of trace determinations are expected to improve sufficiently and the determination limit will go down to $\mu g\,L^{-1}$ (ppb) level. Such improvements in the trace analysis of pesticides become necessary nowadays and assume importance. This paper deals with the development of stripping voltammetric procedures for the determination of pesticides such as isoproturon (ISO), voltage (VOL) and dicofol (DCF) using GCE, MWCNT modified GCE, PANI/MWCNT/GCE and PPY/MWCNT/GCE.

2. Experimental

2.1. Reagents

Multiwalled CNTs (I.D. × length 2–15 nm × 1–10 μm) produced by arc method was purchased from Sigma–Aldrich. AR sodium dodecyl sulphate (SDS) from Merck. Pyrrole (AR-Merck), Aniline (AR-Merck) and Lithium perchlorate (Sigma–Aldrich) were used for electropolymerization. Technical grade of all the pesticides were obtained from the Bureau of Indian Standards. 0.1 M stock solution was made up in ethanol for all the three pesticides. For studies in aqueous media, 0.1 M H_2SO_4 (for pH 1), Britton Robinson Buffers (for pH 4, 7, and 9.2), 0.1 M NaOH (for pH 13), in 50% aqueous alcohol were used. Table 1 represents the pesticides used in this study, their structures and physical properties.

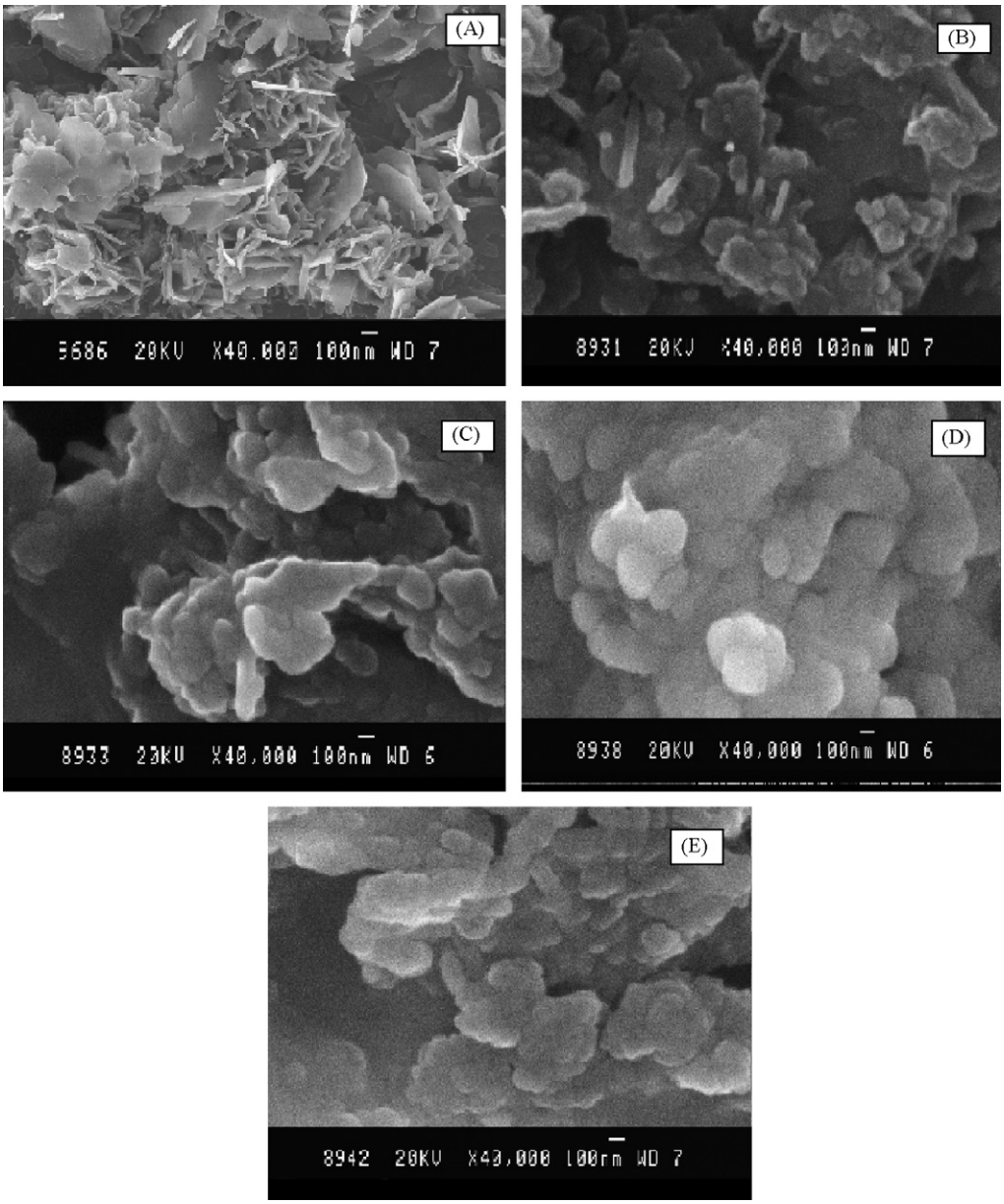

Fig. 2. SEM photograph of (A) MWCNTs deposited on GCE; (B) PANI/MWCNT/GCE; (C) ISO adsorbed on PANI/MWCNT/GCE; (D) VOL adsorbed on PANI/MWCNT/GCE; (E) DCF adsorbed on PANI/MWCNT/GCE.

2.2. Apparatus

All the electrochemical studies were performed with a CHI 760C electrochemical workstation (CH Instruments, USA). The modified GCE was used as a working electrode. Area of working electrode is 0.0707 cm^2. Platinum wire and Ag/AgCl were employed as an auxiliary and reference electrode respectively.

2.3. Electrode pretreatment

To get reproducible results, great care was taken in the electrode pretreatment. The GCE was pretreated in two ways: (i) mechanical polishing over a velvet micro-cloth with 0.3 and 0.05 μm alumina slurry (CH instrument, Inc.) and (ii) electrochemical treatment by applying a potential of +1.5 V for 2 s. The electrochemical pretreatment was done in the same supporting electrolyte solution in which the measurement was carried out. Background currents for each supporting electrolyte solutions were recorded and later corrected with the current values obtained with analytes. The reproducibility of the result was often verified by voltammogram under identical conditions at various time intervals.

2.4. Preparation of MWCNT modified GCE

1 mg MWCNT was dispersed in 1 mL of 0.1 M sodium dodecyl sulphate using an ultrasonicator to give black suspensions. Cast films were prepared by placing 5 μL of the MWCNT/surfactant suspensions on GCE and then evaporating it in an oven at 50 °C.

2.5. Preparation of PANI/MWCNT/GCE and PPY/MWCNT/GCE

MWCNT film coated GCE was prepared as before. Polyaniline was deposited by electrooxidation of 0.1 M aniline, in

presence of 1 M sulphuric acid as a supporting electrolyte by applying a potential between −0.2 and 0.8 V. Polypyrrole film was deposited by the electrooxidation of 0.1 M pyrrole in acetonitrile containing 0.1 M lithium perchlorate as a supporting electrolyte by applying a potential between 0 and 1 V.

3. Results and discussion

3.1. Cyclic voltammetric (CV) studies

Cyclic voltammetric studies of 0.99 mmol L^{-1} of ISO, VOL and DCF at 0.100 V s^{-1}, revealed the presence of one well defined peak at different pHs in the range 1.0–13.0 on plain GCE, MWCNT/GCE, PPY/MWCNT/GCE and PANI/MWCNT/GCE systems. Peak with lowest potential and maximum current was observed only at pH 1 for ISO and VOL, revealing easy oxidation due to prior protonation of nitrogen in the substrate, which facilitated oxidative cleavage. Thus pH 1 was selected as the suitable medium for the electrochemical studies of ISO and VOL. One well defined oxidation peak each at 1.094 V (2.614 μA), 1.090 V (25.25 μA), 1.2 V (28.41 μA) and 1.085 V (25.26 μA) for ISO and 0.810 V, (11.37 μA), 0.725 V, (12.34 μA), 0.752 V (114.1 μA) and 0.814 V, (29.01 μA) for VOL on plain GCE, MWCNT/GCE, PPY/MWCNT/GCE and PANI/MWCNT/GCE systems was observed at pH 1.0. There was no cathodic response in the reverse scan indicating the irreversible electron transfer process. Fig. 1A(a and b) and B(a and b) showed cyclic voltammograms of ISO and VOL respectively on PANI (polyaniline)/MWCNT/GCE and PPY (polypyrrole)/MWCNT/GCE at pH 1. Cyclic voltammetric studies of DCF at various pHs showed very good cathodic response at pH 13.0 compared to other pHs. DCF exhibited one well defined reduction peak at a potential (peak current) of −1.390 V (19.18 μA), −1.398 V, (23.71 μA), −1.360 V (34.68 μA) and −1.419 V (26.44 μA) on four electrode systems respectively. There was no anodic response observed in the reverse scan suggesting irreversibility. Fig. 1C(a and b) exhibited cyclic voltammograms of DCF on PANI/MWCNT/GCE and PPY/MWCNT/GCE at pH 13. From analytical point of view, of all the modified systems, PANI/MWCNT/GCE responded well and peak current increases to 14 times for ISO, 10 times for VOL and approximately 2 times for DCF respectively when compared to that of bare GCE.

Various cyclic voltammograms of 0.99 mmol L^{-1} of ISO, VOL and DCF were run at various sweep rates from 0.025 to 0.500 V s^{-1} at all electrode systems. The peak current increases linearly with ν up to $\nu < 0.1$ V s^{-1}, while at the higher scan rates a linear dependence of peak currents on $\nu^{1/2}$ is observed. This agrees with the cyclic voltammetric behaviour expected for an electroactive species incorporated within the polymeric layer of coated electrode. The film thickness is smaller than the diffusion layer at low scan rates; hence the surface confined electrolysis of all the preconcentrated analyte is possible. On the contrary, the diffusion layer is smaller than the film thickness at high scan rates and diffusion-controlled behaviour is observed. The plot of i_p versus $\nu^{1/2}$ led to straight lines and slopes of these straight lines (Table 2) suggest diffusion-controlled adsorption reaction of all pesticides at all electrode systems. The peak potentials (E_p) are correlated with logarithm of sweep rate ($\log \nu$). Straight lines with good correlation were obtained and the results of correlations are presented in Table 2. From the slope of these plots, (0.47–0.68) the transfer coefficient (αn) was calculated and these results ascertain the fact that all the reported pesticides underwent irreversible electron transfer process at all electrode systems.

Table 2
Cyclic voltammetric correlation plots of ISO, VOL and DCF on different electrode systems

Insecticides		Plain GCE	MWCNT/GCE	PANI/MWCNT/GCE	PPY/MWCNT/GCE
ISO	Plot of i_p vs. ν	$i_p = 0.1936\nu + 4.85$ $R^2 = 0.9885$	$i_p = 0.1779\nu + 0.7043$ $R^2 = 0.999$	$i_p = 0.1888\nu + 2.4$ $R^2 = 0.997$	$i_p = 0.0352\nu + 0.34$ $R^2 = 0.995$
	Plot of i_p vs. $\nu^{1/2}$	$i_p = 2.4267\nu^{1/2} - 0.5572$ $R^2 = 0.997$	$i_p = 2.117\nu^{1/2} - 3.2257$ $R^2 = 0.986$	$i_p = 2.6807\nu^{1/2} - 6.1458$ $R^2 = 0.991$	$i_p = 0.435\nu^{1/2} - 0.4712$ $R^2 = 0.981$
	Plot of $\log i_p$ vs. $\log \nu$	$\log i_p = 0.5687 \log \nu + 0.2114$ $R^2 = 0.989$	$\log i_p = 0.5075 \log \nu + 0.2608$ $R^2 = 0.997$	$\log i_p = 0.4945 \log \nu + 0.3531$ $R^2 = 0.997$	$\log i_p = 0.4752 \log \nu - 0.354$ $R^2 = 0.997$
	αn	0.62	0.55	0.57	0.58
VOL	Plot of i_p vs. ν	$i_p = 0.1128\nu + 2.5$ $R^2 = 0.991$	$i_p = 0.1684\nu + 4.05$ $R^2 = 0.991$	$i_p = 0.0665\nu + 3.47$ $R^2 = 0.998$	$i_p = 0.0833\nu + 1.945$ $R^2 = 0.995$
	Plot of i_p vs. $\nu^{1/2}$	$i_p = 1.5538\nu^{1/2} - 2.0338$ $R^2 = 0.9768$	$i_p = 2.0221\nu^{1/2} + 1.0225$ $R^2 = 0.989$	$i_p = 0.9787\nu^{1/2} - 0.0074$ $R^2 = 0.983$	$i_p = 1.12\nu^{1/2} - 1.4153$ $R^2 = 0.982$
	Plot of $\log i_p$ vs. $\log \nu$	$\log i_p = 0.6045 \log \nu - 0.1004$ $R^2 = 0.989$	$\log i_p = 0.5811 \log \nu + 0.1235$ $R^2 = 0.988$	$\log i_p = 0.4899 \log \nu + 0.0135$ $R^2 = 0.995$	$\log i_p = 0.5833 \log \nu - 0.1906$ $R^2 = 0.993$
	αn	0.86	0.47	0.56	0.58
DCF	Plot of i_p vs. ν	$i_p = 0.1544\nu + 2.6$ $R^2 = 0.994$	$i_p = 0.2044\nu + 2.6$ $R^2 = 0.992$	$i_p = 0.1556\nu + 0.45$ $R^2 = 0.999$	$i_p = 0.144\nu - 2.35$ $R^2 = 0.998$
	Plot of i_p vs. $\nu^{1/2}$	$i_p = 2.1894\nu^{1/2} - 4.2152$ $R^2 = 0.984$	$i_p = 2.7813\nu^{1/2} - 6.2397$ $R^2 = 0.988$	$i_p = 1.36\nu^{1/2} + 2.4345$ $R^2 = 0.985$	$i_p = 1.8874\nu^{1/2} - 2.923$ $R^2 = 0.978$
	Plot of $\log i_p$ vs. $\log \nu$	$\log i_p = 0.6493 \log \nu - 0.0777$ $R^2 = 0.992$	$\log i_p = 0.658 \log \nu - 0.0037$ $R^2 = 0.988$	$\log i_p = 0.498 \log \nu + 0.1819$ $R^2 = 0.999$	$\log i_p = 0.6234 \log \nu - 0.068$ $R^2 = 0.989$
	αn	0.48	0.54	0.50	0.56

Where i_p, peak current (μA); ν, scan rate (V s^{-1}).

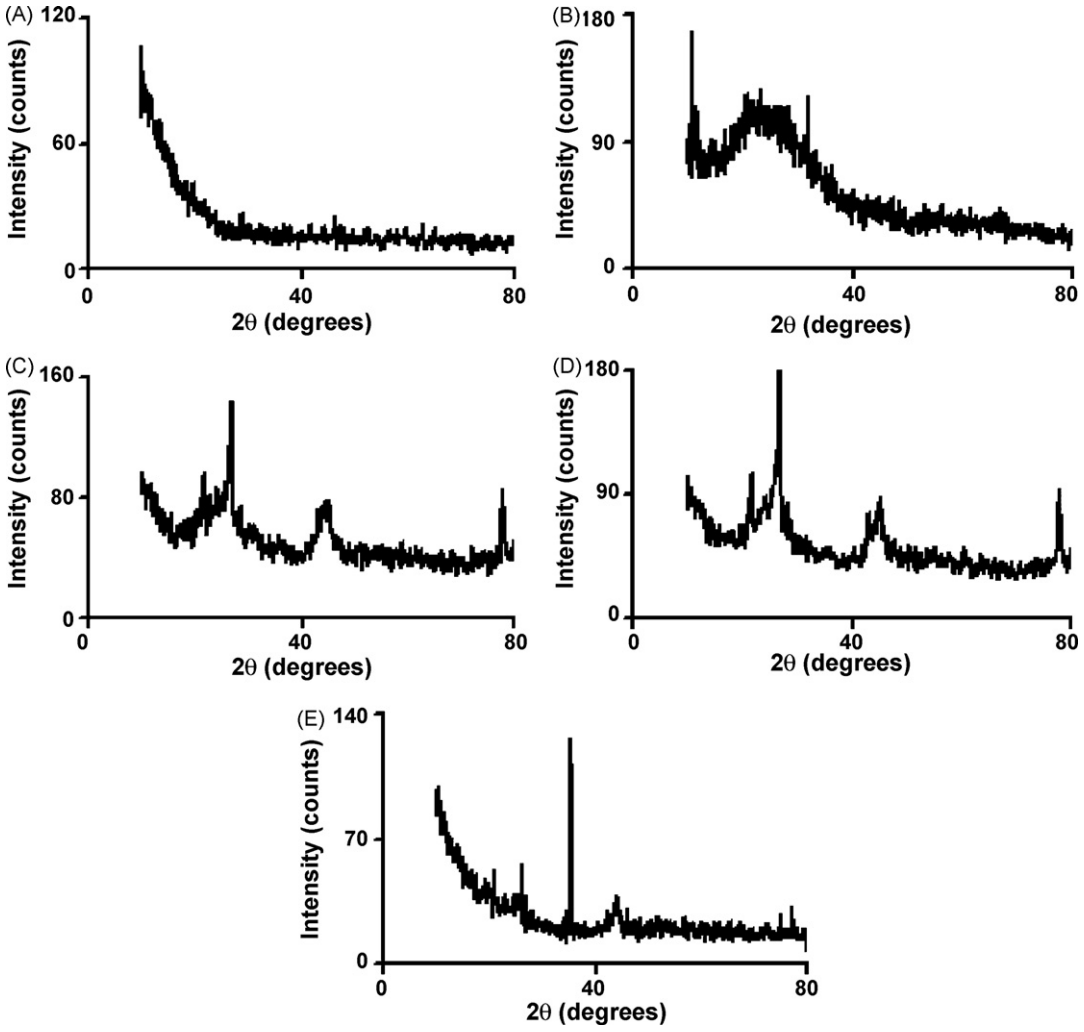

Fig. 3. XRD behaviour of (A) MWCNTs deposited on GCE, (B) PANI/MWCNT/GCE; (C) ISO adsorbed on PANI/MWCNT/GCE; (D) VOL adsorbed on PANI/MWCNT/GCE; (E) DCF adsorbed on PANI/MWCNT/GCE.

3.2. Surface morphology of MWCNT film and adsorption studies

MWCNT dispersed in SDS was coated on the GCE surface. Fig. 2A shows the SEM photograph of the working electrode surface. The stem like structure of the coating confirmed the presence of MWCNTs on GCE. The average tube size of the material is 50 nm. The X-ray diffraction profile (Fig. 3A) indicates substantial amorphous nature of MWCNT. The crystallite size was determined as 84 nm by employing XRD results and Scherrer's formula [35].

CV studies ascertained that all the reported pesticides undergo diffusion-controlled adsorption. Hence it was thought to study the surface morphological change of adsorbed pesticides on the suitable modified system which resulted in good analytical signal. Higher peak current was observed at PANI/MWCNT/GCE sys-

Table 3
DPSV results and pesticides percentage recovery from soil samples on different modified systems

Insecticides	Modified systems	LOD ($\mu g\,L^{-1}$)	Calibration equation results			Recovery from spiked sample ± R.S.D.	
			$^{*}i_p$ (μA), $^{\#}c$ ($mg\,L^{-1}$)	R^2	R.S.D.%	Pure compound	Agro chemical product
ISO	MWCNT/GCE	10	$i_p = 0.8297c - 0.1784$, $0.1 < c > 100$	0.999	2.6	88.6 ± 3.2	85.5 ± 4.2
	PANI/MWCNT/GCE	0.1	$i_p = 1.066c + 1.0258$ $0.01 < c > 100$	0.999	3.2	93.5 ± 2.6	90.6 ± 3.1
	PPY/MWCNT/GCE	5	$i_p = 0.8943c + 0.3398$ $0.05 < c > 100$	0.999	2.8	91.7 ± 2.2	89.7 ± 5.2
VOL	MWCNT/GCE	1	$i_p = 0.8959c - 0.319$, $0.1 < c > 100$	0.996	3.5	89.3 ± 2.1	87.6 ± 2.8
	PANI/MWCNT/GCE	0.01	$i_p = 1.1384c + 0.4488$ $0.01 < c > 100$	0.999	1.9	94.1 ± 3.4	91.0 ± 4.3
	PPY/MWCNT/GCE	0.05	$i_p = 0.9912c + 0.2351$ $0.05 < c > 100$	0.999	2.2	93.4 ± 3.4	89.5 ± 2.6
DCF	MWCNT/GCE	1	$i_p = 0.2871c + 0.1022$, $0.1 < c > 100$	0.999	1.8	89.8 ± 4.3	86.3 ± 3.1
	PANI/MWCNT/GCE	0.05	$i_p = 0.3288c + 0.068$ $0.01 < c > 100$	0.999	2.6	94.8 ± 5.0	88.7 ± 4.5
	PPY/MWCNT/GCE	0.1	$i_p = 0.30762c - 0.0174$ $0.05 < c > 100$	0.999	3.4	92.3 ± 2.6	87.3 ± 3.2

* Peak current (μA).
$^{\#}$ Concentration of the pesticide used ($mg\,L^{-1}$).

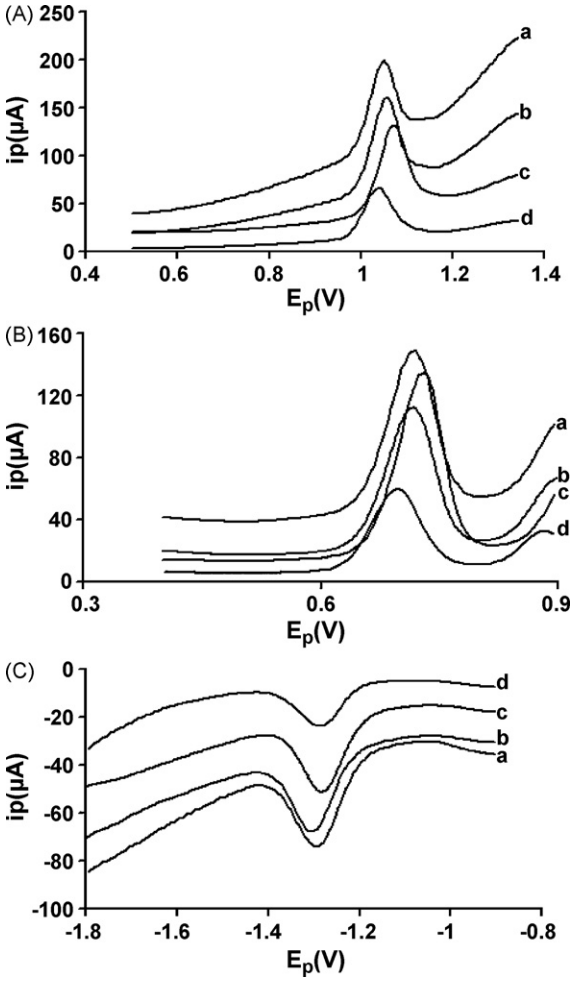

Fig. 4. (A) DPSV of ISO; (B) DPSV of VOL; (C) DPSV of DCF for 100 mg L^{-1} at optimum experimental conditions in (a) PANI/MWCNT/GCE; (b) PPY/MWCNT/GCE; c) MWCNT/GCE; (d) real sample.

tem, because of the availability of electroactive surface capable of accommodating the insecticide molecules. Hence adsorption studies were carried out in the above said system alone. Stripping voltammetric experiments were carried out to ascertain the best conditions for the adsorption process. Many preconcentration stripping experiments were studied for accumulation potentials (E_{acc}) of −0.5 to 0.5 V. Maximum peak current was observed for an accumulation potential of 0 V for ISO and DCF and −0.5 V for VOL respectively. The accumulation potentials observed reveals that the accumulation step does not involve any redox reaction or electron transfer and the accumulation is by physical adsorption of pesticides. After fixing the accumulation potential, accumulation time was varied between 5 and 25 s. Maximum peak current was observed at 10 s for ISO and VOL, 5 s for DCF. The decreased current above the maximum current signal condition might be due to saturation of the electrode surface and blocking of the products formed on the surface. Under the optimum conditions of accumulation potential and time, accumulation of the pesticide on the modified system was done and the surface characterizations were studied. The SEM photograph of PANI/MWCNT/GCE (Fig. 2B) showed leaf like structure which was different from that of MWCNT/GCE (Fig. 2A) and the average grain size was found to be 100 nm. From the SEM analysis the surface morphology of PANI/MWCNT/GCE and the adherence of PANI on MWCNT/GCE were understood. Fig. 2C–E are the SEM photographs of adsorbed pesticides. This surface morphology is unquestionably distinct from that of MWCNT/GCE and PANI/MWCNT/GCE morphology. This confirms the adsorption process. The average grain size of the pesticide adsorbed composite surface is 100 nm. Fig. 3B showed XRD behaviour of PPY/MWCNT/GCE. Fig. 3C–E represent the XRD behaviour of adsorbed surface. Using Scherrer's formula, the crystallite size was found to be 57, 24, 38 and 46 nm for PANI/MWCNT/GCE, adsorbed ISO, adsorbed VOL and adsorbed DCF respectively. The size of crystallite becomes small compared to PANI surface because of complete adsorption of nanometer size pesticides on the PANI surface.

3.3. Differential pulse stripping

After surface preparation and accumulation for maximum peak current, stripping was carried out at modified systems since we got poor response in plain GCE. Initial scan potential (E_{is}) is an important parameter in controlling the peak characteristics. It was varied between −0.25 and 0.75 V and an initial scan potential of 0.400 V was chosen for stripping voltammetric studies of ISO because of maximum current signals. In a similar manner, 0.500 and −0.900 V were found out for VOL and DCF respectively. Stripping peak current increased with an increase in amplitude from 0.025 to 0.075 V and decreased above 0.075 V. However amplitude of 0.075 V was selected for all pesticides owing to maximum current response. Stripping peak current decreased with an increase in pulse width from 0.005 to 0.075 s and pulse width of 0.005 s was chosen for ISO and VOL respectively. Whereas pulse width of 0.025 s was chosen for DCF because of high current response. After applying each pulse, a quite time of 0.020 s is given before measuring the response. These optimum parameters were used to study the effect of concentration.

3.4. Analytical characteristics

Differential pulse stripping voltammograms at different concentrations of ISO, VOL and DCF were recorded using their maximum signal conditions and the curves are given in Fig. 4. The peak current increased linearly with an increase in concentration. The calibration plots of i_p versus concentration lead to good linear correlation at PANI/MWCNT/GCE (Table 3). In a similar manner the DPSV studies at other two modified systems were carried out and the results were compared (Table 3). The limit of detection (LOD) was determined as 0.1, 0.01 and 0.05 μg L^{-1} for ISO, VOL and DCF on PANI/MWCNT/GCE respectively. Among the three modified systems, lowest LOD was achieved in PANI/MWCNT/GCE. Five replicates were analyzed at the insecticide concentration of 10 μg L^{-1} and standard deviations were calculated and the results are presented in Table 3.

3.5. Determination of pesticides in soil samples

The soil sample analyzed was collected from a paddy field in Karaikudi and was washed repeatedly with water and exposed to the atmosphere. Approximately 50 g of the sieved soil was spiked with 25 mL of 1 mmol L^{-1} ISO solution by shaking in a closed bottle for about 30 min. ISO was extracted using dichloromethane. The extract was filtered and evaporated to dryness by gentle heating on a water bath. The residue was transferred into a 250 mL calibrated flask, dissolved in ethanol and made up to the mark. A 10 mL portion of this solution was transferred into a 50 mL calibrated flask and 0.1 mmol L^{-1} H_2SO_4 containing 50% aqueous ethanol was used to dilute the contents of the flask to the required volume. The standard addition method was used. 0.05 mL aliquot of the 1 mmol L^{-1} ISO stock standard solution was added to the solution prepared

as above. Differential pulse stripping voltammetric studies under the optimum experimental conditions were carried out to determine ISO in the soil sample. Similar soil samples analysis was done for VOL and DCF. The stripping voltammograms thus obtained are given in Fig. 4A(d)–C(d) at PANI/MWCNT/GCE. Similar studies were carried out at other two modified systems also. Ten identical measurements were made and the relative standard deviations of all the three pesticides are given in Table 3.

4. Conclusions

In this paper a simple method for the preparation of MWCNT/GCE, PANI/MWCNT/GCE and PPY/MWCNT/GCE is described. Electrochemical behaviour of three pesticides was investigated by cyclic voltammetry and differential pulse stripping voltammetry. Based on this, a convenient procedure for the determination of above said pollutants using stripping voltammetric techniques is proposed. The PANI/MWCNT/GCE modified electrode gave good response and it was applied for the determination of above said pesticides in spiked soil samples with good result. This method of analytical determination of pesticides is simple, fast and it has sufficient precision and accuracy.

Acknowledgement

The financial support for this work by DST, New Delhi, India is gratefully acknowledged.

References

[1] S. Iijima, Nature 354 (1991) 56.
[2] P.M. Ajayan, Chem. Rev. 99 (1999) 1787.
[3] T.W. Odom, J.L. Haung, P. Kim, C.M. Lieber, Nature 391 (1998) 62.
[4] J.W. Jang, D.K. Lee, C.E. Lee, T.J. Lee, C.J. Lee, S.J. Noth, Solid State Commun. 122 (2002) 619.
[5] D. Tekleab, R. Czerw, D.L. Carroll, P.M. Ajayan, Appl. Phys. Lett. 76 (2000) 3594.
[6] R. Andrews, M.C. Weisenberger, Curr. Opin. Solid State Mater. Sci. 8 (2004) 31.
[7] S. Sotiropoulou, N.A. Chaniotakis, Anal. Bioanal. Chem. 375 (2003) 103.
[8] Y. Tu, Y. Lin, W. Yantasee, Z. Ren, Electroanalysis 17 (2005) 79.
[9] J. Wang, S.B. Hocevar, B. Ogorevc, Electrochem. Commun. 6 (2004) 176.
[10] X. Qu, Z. Peng, Y. Wang, S. Dong, Electroanalysis 17 (2005) 3.
[11] J. Wang, Analyst 130 (2005) 421.
[12] Y. Lin, W. Yantasee, J. Wang, Front. Biosci. 10 (2005) 492.
[13] F. Valentini, S. Orlanducci, M.L. Terranova, A. Amine, G. Palleschi, Sensors Actuators B: Chem. 100 (1–2) (2004) 117.
[14] Y.D. Zhao, W.D. Zhang, H. Chen, Q.M. Luo, Talanta (2002) 529.
[15] Q. Honglan, Z. Chengxiao, Electroanalysis 17 (10) (2005) 823.
[16] H. Zhang, C. Hu, S. Wu, S. Hu, Electroanalysis 17 (2005) 749.
[17] S.L. Nathan, P.D. Randhir, Joseph Wang, Electroanalysis 17 (1) (2005) 65.
[18] K.A. Joshi, J. Tang, R. Haddon, J. Wang, W. Chen, A. Mulchandani, Electroanalysis 17 (2005) 54.
[19] M. Moreno, M. Chicharro, E. Bermejo, A. Sanchez, A. Zapardiel, G.A. Rivas, Electroanalysis 17 (5–6) (2005) 476.
[20] E. Hogendoorn, P. van Zoonen, J. Chromatogr. A 892 (2000) 435.
[21] G.R. van der Hoff, P. van Zoonen, J. Chromatogr. A 843 (1999) 301.
[22] A. Amirav, H. Jing, J. Chromatogr. A 814 (1998) 133.
[23] F.O. Akbal, N. Akdemir, A. Nur Onar, Talanta 53 (2000) 131.
[24] S. Jayaramareddy, M. Hermes, F. Schulz, Electroanalysis 8 (1996) 955.
[25] E. Mallat, D. Barcelo, Trends Anal. Chem. 20 (2001) 124.
[26] Y.S. Fung, J.L.L. Mak, Electrochim. Acta 44 (1999) 3855.
[27] P. Manisankar, A. Sarpudeen, S. Viswanathan, J. Pharm. Biomed. Anal. 26 (2001) 873.
[28] R. Kalvoda, R. Parsons, Electrochemistry in Research and Development, Plenum Press, New York, 1985, p. 164.
[29] M.C. Gennaro, E. Marengo, V. Gianotti, V. Maurino, J. Chromatogr. A 910 (2001) 79.
[30] E. Mallat, C. Barzen, R. Abuknesha, G. Gauglitz, D. Barcelo, Anal. Chim. Acta 426 (2000) 209.
[31] R.P. Deo, J. Wang, I. Block, A. Mulchandani, K.A. Joshi, M. Trojanowicz, F. Scholz, W. Chen, Y. Line, Anal. Chim. Acta 530 (2005) 185.
[32] P. Manisankar, G. Selvanathan, C. Vedhi, Appl. Clay Sci. 29 (2005) 249.
[33] P. Manisankar, G. Selvanathan, C. Vedhi, Talanta 68 (2006) 686.
[34] P. Manisankar, S. Viswanathan, A. Mercy Pusphalatha, C. Rani, Anal. Chim. Acta 528 (2005) 157.
[35] P. Manisankar, C. Vedhi, G. Selvanathan, H. Gurumallesh Prabu, Electrochim. Acta 52 (2006) 831.

Talanta 76 (2008) 1224–1232

Contents lists available at ScienceDirect

Talanta

journal homepage: www.elsevier.com/locate/talanta

Optimisation of sensitivity in the multi-elemental determination of 83 isotopes by ICP-MS as a function of 21 instrumental operative conditions by modified simplex, principal component analysis and partial least squares

Emilio Marengo*, Maurizio Aceto, Elisa Robotti, Matteo Oddone, Marco Bobba

Department of Environmental and Life Sciences, University of Eastern Piedmont, Via Bellini 25/G, 15100 Alessandria, Italy

ARTICLE INFO

Article history:
Received 11 January 2008
Received in revised form 16 May 2008
Accepted 21 May 2008
Available online 8 June 2008

Keywords:
ICP-MS
Modified simplex optimisation
Multivariate ranking methods
Principal component analysis
Partial least squares

ABSTRACT

The optimisation of the sensitivity in the ICP-MS determination of 83 isotopes, as a function of 21 operative parameters was performed by generating an initial experimental design that was used to define, by principal component analysis, the multi-criteria target function. The first PC, which contained an overall evaluation of the signal intensity of all isotopes, was used to rank the experiments. The modified simplex optimisation technique was then applied on the ranked experiments. The increase in signal intensity was, on the average, 3.9 times for the isotopes considered for the simplex procedure. When finally convergence was achieved, a PLS regression model calculated on the available experiments allowed to investigate the effect played by each factor on the experimental response. Simplex and PCA proved to be extremely effective to obtain the optimisation and to generate the multi-criteria target function: they can be suggested as an automatic method to perform the optimisation of the instrumental operative conditions.

1. Introduction

Inductively Coupled Plasma-Mass Spectrometry (ICP-MS) is becoming one of the most widely used techniques for the determination of elements at trace and ultra-trace level (ppb, ppt). The ICP-MS instruments are characterised by a large set of operative parameters which can exhibit various effects on the analytical results by influencing the interference pattern, the sensitivity of the determination, the time of analysis, etc. These parameters setting must be optimised as a function of the specific analysis. As a rule of thumb, all instruments do present an auto-tuning procedure, usually based on the One-Variable-At-a-Time (OVAT) approach, to search for the optimal setting of the operative parameters. The OVAT approach consists in the optimisation of each instrumental parameter independently, to obtain the maximum signal of a selected isotope: this approach therefore does not take into consideration the interactions that often exist between the operative parameters.

Several papers appeared in the nineties about the optimisation of ICP-MS instrumental conditions. Among them, the paper from Ford et al. [1] reports the multi-elemental optimisation of plasma parameters and ion optics in ICP-MS. The simplex procedure was applied to the optimization of plasma and ion optics parameters. Optimisation was successfully performed on the S/N ratios of 10 elements.

Another paper from van Veen et al. [2] reports the optimisation of ICP-MS conditions with respect to short- and long-term precision. The authors derived an expression of the precision as a function of the mass intensity in terms of the source flicker and shot noise contributions.

More recently, some more dedicated papers have appeared dealing with the optimisation of the instrumental parameters in ICP-MS by experimental design techniques [1–11]. Brennetot et al. [3] applied experimental designs to the optimisation of 10 operating conditions of a Multiple-collector inductively coupled plasma mass spectrometry (MC–ICP-MS) for the isotopic analysis of gadolinium. Ingle et al. [4] applied a multivariate approach to characterise and optimise the dominant H-2-based chemistries in a hexapole collision cell used in ICP-MS: in this case the target function for the optimisation was the S/N ratio. Recently, Gomez-Ariza et al. [5] optimised a two-dimensional on-line coupling for the determination of anisoles in wine using an electron capture detector (ECD) and ICP-MS after solid phase micro-extraction – gas-chromatographic (SPME-GC) separation, by a chemometric approach: different ICP-MS conditions (forward power, carrier gas flow and the addition of small percentages of alternate gases) have been optimised. Other

* Corresponding author. Tel.: +39 0131 360272; fax: +39 0131 360250.
E-mail address: marengoe@tin.it (E. Marengo).

0039-9140/$ – see front matter © 2008 Elsevier B.V. All rights reserved.
doi:10.1016/j.talanta.2008.05.052

applications of experimental designs to the optimisation of ICP-MS analysis are by Gomez-Ariza et al. [5], Darrouzes et al. [6] and Martos et al. [7]. In the paper from Darrouzes the optimisation of ICP-MS equipped with collision/reaction cell (C/RC) technology for the determination of selenium at ultra-trace level. Several parameters were optimised: gas flow rates for helium and hydrogen and the voltage of the different ionic lenses disposed around the C/RC (quadrupole bias, octopole bias, cell entrance, cell exit, plate bias). The paper from Martos et al. is focused instead on the pre-concentration and determination of Pt; various parameters and chemical variables affecting the preconcentration and determination of this metal by ICP-AES were evaluated. Five variables (sample flow rate, eluent flow rate, nebulizer flow rate, buffer concentration and mixing coil length) were considered as factors in the optimisation process. Interactions between analytical factors, and their optimal levels were investigated using two level factorial and central composite designs. The optimum conditions established were applied to the determination of platinum by flow injection inductively coupled plasma atomic emission spectrometry (FI-ICP-AES).

Optimisation procedures are usually applied to ICP-MS analysis focusing on a restricted number of instrumental parameters or of elements, according to the scientists' particular interests; it is important to point out however that one of the potentials of ICP-MS analysis is the possibility of determining a great number of elements contemporarily: this is particularly interesting for routine analyses. From this starting consideration, we focused our attention on the contemporary determination of 83 isotopes, in order to obtain experimental conditions representing the best compromise for the identification of all these isotopes in routine analyses. Due to the large number of isotopes to be determined, an exhaustive study of all the instrumental parameters involved is necessary, in order to achieve the best experimental settings. 21 parameters, described in detail in the experimental section, were thus involved in the study. The modified simplex procedure [12–15] was selected to perform the optimisation of the 21 parameters. Simplex represents in this case the best choice in order to limit the number of experiments needed to accomplish optimisation: due to the large number of factors studied, full factorial designs cannot be applied, while fractional factorial designs generate complex confounding structures and, furthermore, complex variables effects and interactions are possibly expected. The simplex iterative procedure represents thus a good alternative.

The large number of experimental signals to be maximised (the 83 isotopes), requires the definition of an effective and suitable multi-criteria target function. Usually the target function adopted is the sum of all the signals. In this case, the multi-criteria target function, representing the signal of almost all the isotopes simultaneously, was generated by Principal Component Analysis (PCA) [16,17]. The initial simplex (22 starting experiments) was used to generate the multi-criteria target function: PCA was carried out on the signals recorded for the 83 isotopes for the initial pool of 22 experiments. This procedure represents a valid alternative due to the robustness of PCA: considering only the first relevant principal components (PCs), random variations due to experimental noise can be eliminated. Once defined the multi-criteria function, the iterative modified simplex method was applied. At each iteration each new experiment is projected on the space given by the relevant PCs previously calculated in order to evaluate the final multivariate experimental response. The iterative simplex allows to obtain new best settings with respect to the OVAT approach. The results obtained by the Simplex procedure were compared to those obtained from the OVAT approach, representing the default settings.

Simplex optimisation, however, provides no model relating the instrumental parameters and the target function. Therefore, a Partial Least Squares (PLS) [16,17] regression model was built based on the overall set of experiments performed, to shed light on the effect of each experimental factor on the final response. This model can be used to identify which experimental factors are more important and the relationships existing among them.

From an operative point of view, the contemporary optimisation of all the instrumental parameters to obtain the best conditions for the determination of all the detectable elements represents an important application in routine analyses and could represent a valid alternative for default instrumental settings optimisation. Here, the attention is focussed on the proposal of a multivariate procedure for the automatic optimisation of the instrumental settings in ICP-MS.

The present approach represents a valid procedure due to the coupling of simplex optimisation to the establishment of a target function based on principal component analysis: this allows to take into consideration the relationships and the interactions among the variables that cannot be taken into account in standard OVAT procedures where each variable is optimised independently from the others. Moreover, even if the Simplex procedure is stopped before achieving convergence, it can provide experimental settings that are better with respect to the initial ones, due to the iterative method applied. This is important when optimisation has to be undertaken with constraints on the maximum time available to perform the optimisation itself.

2. Theory

2.1. The proposed procedure

The optimisation of the signals of 83 isotopes as function of 21 operative parameters in ICP-MS is carried out here by the application of a procedure consisting in four main steps:

- *Identification of the initial simplex*. The initial set of experiments to be performed was determined by the simplex procedure [12–15]. In the present case 21 operative parameters were studied, thus providing an initial set of 22 experiments ($p+1$ initial experiments, where p is the number of factors to be investigated), called *simplex*. The default settings provided by the proprietary software present on the instrument, were selected as starting conditions for the initial simplex. The initial Simplex establishes a starting pool of experiments where the parameters are varied one-at-a-time.
- *Identification of a multivariate target function by Principal Component Analysis*. For each experiment of the initial simplex the signal of the 83 isotopes was recorded. A multivariate target function was then identified by applying Principal Component Analysis (PCA) [16,17] on the data recorded from the initial simplex. As commonly acknowledged, PCA is a pattern recognition method representing objects in a new reference system characterised by variables called Principal Components (PCs). PCs are orthogonal to each other and are computed hierarchically (the information accounted for by successive PCs is decreasing): in this way they account for independent sources of information and experimental noise and random variations are contained in the last PCs (they contain the least possible information). The optimisation of the instrumental parameters with respect to the simultaneous maximisation of the signal of all the isotopes (expressed as number of counts for each isotope) requires the use of a multi-criteria ranking method: PCA can then be effectively used to this purpose. PCA is then performed on the dataset consisting in the experimental responses of the initial pool of experiments and the final target function can be selected by the identification of the PC mostly related to the overall signal increase. This represents a valid alter-

native to the use of the total sum of the signals of all the isotopes of interest since PCA can effectively separate experimental noise from actual systematic information. The optimisation can be performed in this case on a more robust target function that takes into account the relationship between the signal of different isotopes.
- *Application of the modified simplex optimisation procedure*. Once the target function is established, the modified simples optimisation procedure can be applied. In the present research we used the modified simplex [14] version, in which, during the search for the optimum, the simplex changes its shape, assuring a more rapid convergence. It is important to point out that Simplex, being an iterative procedure, does not guarantees to achieve the global optimum but it may converge on local optimal conditions. This procedure is however suitable in the present case characterised by a large number of parameters to be investigated. At each iteration, the experimental responses of the 83 isotopes are projected on the space given by the PCs selected as multivariate target function and the final multivariate response is then calculated. On this multivariate response the simplex optimisation procedure is carried out. After convergence is achieved, LOD and LOQ are calculated using the optimised instrumental conditions and compared to those calculated using the default settings.
- *Final refinement by Partial Least Squares regression*. The overall dataset consisting in the whole set of experiments performed (initial simplex plus the experiments carried out to accomplish optimisation) can be used to build a PLS model [16,17] relating the 21 operative parameters (*X*-variables) and the signal of the 83 isotopes detected (*Y*-variables). Since in this case several *Y*-variables are present, the PLS2 algorithm was used [16,17]. This model can be used for understanding the effect played by each instrumental parameter on the signal of each isotope, thus providing information about their effect on different masses.

The procedure adopted represents a interesting method for online optimisation of ICP-MS experimental conditions since it can be completely automated. Moreover, it can be easily implemented in the instrument software and causes no further time consumption with respect to the OVAT approach. Finally, it can also be accomplished by imposing a limiting time consumption: the procedure can be stopped at every iteration providing in each step better experimental setting with respect to the default ones even if final convergence is not achieved. It must also be considered that the simplex optimisation procedure coupled to PCA for providing an adequate multivariate target function takes into consideration the relationships existing between the variables and among the experimental responses, that is impossible by the use of the OVAT approach, where correlations are neglected.

3. Experimental

3.1. ICP-MS analysis

An X5 ICP-MS instrument (Thermo Elemental, Winsford, UK), equipped with an ASX-500 autosampler (CETAC, Omaha, USA) was used for elemental analysis. Data acquisition and processing were performed using the PlasmaLab 2.3 software (Thermo Elemental, Winsford, UK). The instrumental configuration was varied according to Simplex and PLS experiments. The instrument was tuned daily with a solution containing 10 $\mu g L^{-1}$ of Li, Y, Ce and Tl.

All the reagents used were of analytical purity. Nitric acid used to acidify the samples before analysis was further purified by sub-boiling distillation in a quartz apparatus. Water was purified in a Milli-Q system, resulting in water with a resistivity of 18 MΩ.

ICP-MS optimisation through the simplex procedure was performed on standard metal solutions (i.e. no matrix effects nor polyatomic interferences were analysed in this first study). Standard metal solutions were prepared from 10 $mg L^{-1}$ multi-element stock solutions (Analab, Hoerdt, France). The solution used for Simplex procedure was at concentration of 10 $\mu g L^{-1}$ for all isotopes. To calculate limits of detection (LOD) and limits of quantification (LOQ) we used 40, 75, 100, 200 and 400 $ng L^{-1}$ solutions. LOD and LOQ were calculated by keeping in due consideration the calibration curves and the signal due to blanks and standards [16–19].

3.2. Software

PCA, PLS and graphical representations were performed by dedicated software packages: Unscrambler 9.5 (CAMO, Norway), Statistica 7.5 (Statsoft Inc, USA), Excel 2000 (Microsoft Corporation, USA).

3.3. Dataset

The optimisation procedure was applied to 21 instrumental parameters, divided into four main groups with respect to their purpose: torch-box parameters, related to the position of the torch in the torch-box (*Horizontal*, *Vertical* and *Sampling depth*); gas-flow parameters (*Nebuliser*, *Cool and Auxiliary*); quadrupole and acquisition parameters (*Pole bias*, *Forward power*, *Standard resolution*, *Dwell time*, *Sweeps*, *Channel*); focusing parameters. This last group consists in 9 parameters related to the position of lenses and deflectors of the ion flow. *Extraction* is related to the first lens, located in the "ion transfer system", which avoids dispersion of ions into the vacuum chamber and speeds them up towards the system. *Lens* 1, 2 and 3 retain negative ions or neutral species. *D1*, *D2*, *DA* act as deflectors of the ionic flow retaining photons generated from plasma from reaching the detector (thus increasing the baseline noise). *Focus* acts on particle dispersion into the "ion transfer system". *Hexapole bias* acts on the reduction of the interferences due to polyatomic species.

4. Results and discussion

4.1. Initial simplex and multi-criteria target function

The simplex procedure was applied to the optimisation of the 21 instrumental parameters previously described. The default settings (selected according to an OVAT approach), provided by the proprietary software present on the instrument, were selected as starting conditions for the simplex procedure. The default settings and the variations applied to each factor are reported in Table 1, while the initial 22 experiments are listed in Table 2. As just pointed out, the initial Simplex establishes a starting pool of experiments where the parameters are varied one-at-a-time. The initial simplex has the double purpose of identifying a suitable multivariate target function (by the application of PCA) and providing the starting point for the subsequent optimisation procedure by the modified simplex algorithm.

In order to establish an appropriate target function, PCA was performed on the dataset constituted by the initial simplex, after autoscaling. The dataset thus consists in 22 experiments described by the 83 signals of the isotopes detected. From an operative point of view, the choice of a target function based on the overall signals of the isotopes could not be the best alternative since the optimisation of signals due to interferences is simultaneously considered. This choice was justified in our case, since the large number of isotopes to be monitored did not allow the simultaneous monitoring of all interfering species together in a reasonable time of analysis.

Table 1
Default settings (selected as starting conditions for the simplex procedure), the variations applied to each factor and the optimal settings obtained from the simplex procedure (corresponding to exp. 119)

	Default	Variation	Simplex optimal settings
Sweeps	25	50	37
Dwell time	10	50	39
Channels	3	2	1
Standard res	125	25	111
Extraction	−200	50	−240
Lens 1	−2.3	20	−14.0
Lens 2	−57.2	40	−45.2
Lens 3	−112.9	20	−106.2
Focus	28.1	5	23.6
Horizontal	45	15	57
Vertical	425	80	340
Sampling depth	90	60	66
Nebuliser	0.92	0.05	0.92
D1	−26.6	10	−27.2
D2	−145	40	−127.5
DA	−146.6	20	−146.9
Pole bias	6.5	2	1.7
Hexapole bias	−4.9	1	−4.8
Cool	13.1	0.5	13.1
Auxiliary	0.9	0.05	0.9
Forward power	1310	80	1349

Moreover, the increase of the signal recorded setting up experimental parameters cannot reasonably be completely ascribed to an increase of the interferences: isotopic signals will be increased as well. This compromise can be acceptable if interferences are kept in due consideration in a subsequent step, once a restricted pool of target isotopes, to be detected in a particular sample, are identified. A valid alternative should be the used of S/N ratios but the choice adopted in the present case does not invalidate the overall proce-

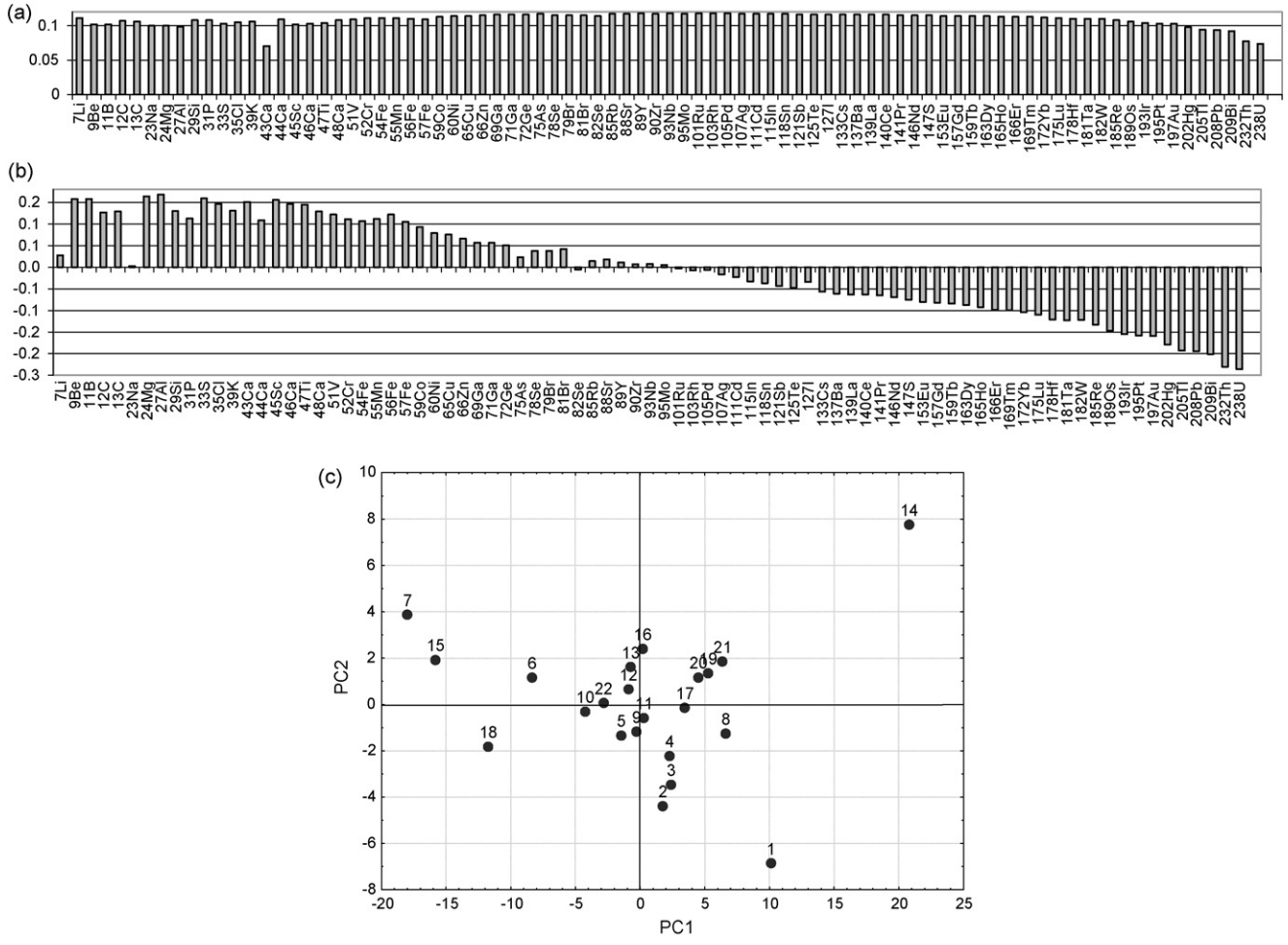

Fig. 1. Results of PCA performed on the initial simplex: loading plot of PC_1 (a) and PC_2 (b) and score plot (c) for the first two PCs.

dure since the a posteriori calculation of LODs and LOQs states that an overall improvement is achieved, as will be widely documented afterwards.

The first two PCs calculated were then retained as significant, since they account for more than 97% of the total variance (86% PC_1, 11% PC_2). The score plot and loading plot of the first two PCs are represented in Fig. 1. The loadings of PC_1 and PC_2 are represented separately as bar diagrams, reporting the variables on the *x*-axis and the loadings on the *y*-axis.

Looking at the loading plot (Fig. 1(a) and (b)), the first component shows positive loadings for all the isotopes. However, isotopes with intermediate mass values show the largest positive loadings and lay along the first component, while isotopes characterised by small and large masses have, respectively, large positive and large negative loadings on the second component. For what regards PC_1, an anomalous weight can be detected for ^{43}Ca, showing a value smaller than that of near isotopes. An anomalous behaviour can be detected for ^{7}Li and ^{23}Na as well, on the second PC: ^{7}Li shows a smaller weight on PC_2 with respect to that of the isotopes with a similar mass, while ^{23}Na shows a weight around 0, where a positive value is expected. On the whole, PC_1 mainly accounts for the overall signal intensity, since all variables present positive loadings on this PC. This behaviour is possible even if data are autoscaled, since the first PC accounts for the overall signal increase. The second PC is instead responsible for the information about the elemental mass: large negative loadings for isotopes with large masses, large positive loadings for isotopes with small masses. For the optimisation of the instrumental settings, a target function related to the overall increasing instrumental signal was needed, the choice was therefore the first PC: large PC_1 values will then be searched for, corresponding to large overall signals.

Looking at the corresponding score plot (Fig. 1(c)), experiments at positive values on PC_1 correspond to experiments showing an increase of all the signals simultaneously, while experiments at negative values present a decrease of all the isotopes signal. Moving along the first PC towards more positive values therefore means moving towards higher instrumental signals; this is particularly true for the isotopes showing intermediate masses (larger positive loading), rather than for isotopes with low or high masses (smaller positive loadings).

Table 2
The initial Simplex experimental conditions

No.	Sweeps 1	Dwell time 2	Channels 3	Std Res 4	Extraction 5	Lens 1 6	Lens 2 7	Lens 3 8	Focus 9	Horizontal 10
1	25	10	3	125	−200	−2.3	−57.2	−112.9	28.1	45
2	67	16	3	128	−194	0.2	−52.2	−110.4	28.7	47
3	31	52	3	128	−194	0.2	−52.2	−110.4	28.7	47
4	31	16	5	128	−194	0.2	−52.2	−110.4	28.7	47
5	31	16	3	146	−194	0.2	−52.2	−110.4	28.7	47
6	31	16	3	128	−158	0.2	−52.2	−110.4	28.7	47
7	31	16	3	128	−194	14.3	−52.2	−110.4	28.7	47
8	31	16	3	128	−194	0.2	−23.9	−110.4	28.7	47
9	31	16	3	128	−194	0.2	−52.2	−96.3	28.7	47
10	31	16	3	128	−194	0.2	−52.2	−110.4	32.3	47
11	31	16	3	128	−194	0.2	−52.2	−110.4	28.7	57
12	31	16	3	128	−194	0.2	−52.2	−110.4	28.7	47
13	31	16	3	128	−194	0.2	−52.2	−110.4	28.7	47
14	31	16	3	128	−194	0.2	−52.2	−110.4	28.7	47
15	31	16	3	128	−194	0.2	−52.2	−110.4	28.7	47
16	31	16	3	128	−194	0.2	−52.2	−110.4	28.7	47
17	31	16	3	128	−194	0.2	−52.2	−110.4	28.7	47
18	31	16	3	128	−194	0.2	−52.2	−110.4	28.7	47
19	31	16	3	128	−194	0.2	−52.2	−110.4	28.7	47
20	31	16	3	128	−194	0.2	−52.2	−110.4	28.7	47
21	31	16	3	128	−194	0.2	−52.2	−110.4	28.7	47
22	31	16	3	128	−194	0.2	−52.2	−110.4	28.7	47

No.	Vertical 11	Sampling depth 12	Nebuliser 13	D1 14	D2 15	DA 16	Pole bias 17	Hexapole bias 18	Cool 19	Auxiliary 20	Forward power 21
1	425	90	0.92	−26.6	−145	−146.6	6.5	−4.9	13.1	0.90	1310
2	435	97	0.93	−25.4	−140	−144.1	6.7	−4.8	13.2	0.91	1320
3	435	97	0.93	−25.4	−140	−144.1	6.7	−4.8	13.2	0.91	1320
4	435	97	0.93	−25.4	−140	−144.1	6.7	−4.8	13.2	0.91	1320
5	435	97	0.93	−25.4	−140	−144.1	6.7	−4.8	13.2	0.91	1320
6	435	97	0.93	−25.4	−140	−144.1	6.7	−4.8	13.2	0.91	1320
7	435	97	0.93	−25.4	−140	−144.1	6.7	−4.8	13.2	0.91	1320
8	435	97	0.93	−25.4	−140	−144.1	6.7	−4.8	13.2	0.91	1320
9	435	97	0.93	−25.4	−140	−144.1	6.7	−4.8	13.2	0.91	1320
10	435	97	0.93	−25.4	−140	−144.1	6.7	−4.8	13.2	0.91	1320
11	435	97	0.93	−25.4	−140	−144.1	6.7	−4.8	13.2	0.91	1320
12	492	97	0.93	−25.4	−140	−144.1	6.7	−4.8	13.2	0.91	1320
13	435	140	0.93	−25.4	−140	−144.1	6.7	−4.8	13.2	0.91	1320
14	435	97	0.96	−25.4	−140	−144.1	6.7	−4.8	13.2	0.91	1320
15	435	97	0.93	−18.3	−140	−144.1	6.7	−4.8	13.2	0.91	1320
16	435	97	0.93	−25.4	−112	−144.1	6.7	−4.8	13.2	0.91	1320
17	435	97	0.93	−25.4	−140	−130.0	6.7	−4.8	13.2	0.91	1320
18	435	97	0.93	−25.4	−140	−144.1	8.2	−4.8	13.2	0.91	1320
19	435	97	0.93	−25.4	−140	−144.1	6.7	−4.1	13.2	0.91	1320
20	435	97	0.93	−25.4	−140	−144.1	6.7	−4.8	13.5	0.91	1320
21	435	97	0.93	−25.4	−140	−144.1	6.7	−4.8	13.2	0.94	1320
22	435	97	0.93	−25.4	−140	−144.1	6.7	−4.8	13.2	0.91	1377

Experiment 1, corresponding to the default settings (Table 2), shows quite good instrumental conditions (large value on PC_1) but it performs better for large mass isotopes (large negative value on PC_2). Experiment 14 is the best one, since it shows the largest positive score on PC_1 but it shows a larger signal for small masses than for large ones; it corresponds to an increase of all the parameters with respect to the default settings, with particular regard to the variable "*nebuliser*". The position of Experiment 14 in the score plot suggests a quite different behaviour from the other samples: however, this was not detected as an outlier and it was retained in PCA calculation.

From the point of view of the multivariate target function identified as the first PC, the worst experiment is experiment number 7, showing the smallest score on PC_1: this experiment will be the first to be re-projected during the optimisation procedure.

4.2. Simplex procedure

Once obtained the multi-criteria target function necessary to accomplish the optimisation procedure, a modified simplex procedure [14] was applied for the optimisation of the 21 experimental factors. Convergence was achieved after 128 iterations, leading to a total of 150 experiments. At each iteration, the worst sample (the one showing the largest negative score on PC_1) is selected and re-projected with respect to the centroid of the others. The new experiment is projected on the space given by the first two PCs previously calculated to provide the final multivariate experimental response in terms of the score of the experiment on PC_1. The new experiment replaces the selected one in the experimental plan if it shows a better result (a less negative score on PC_1).

The 150 experiments performed are represented in the space of the first two PCs in Fig. 2: the experiments belonging to the original simplex are represented as squares (they are contained in the ellipse drawn in the figure), while the new projections are represented as triangles. As expected, the new experiments move towards larger positive values on PC_1, but in the meantime, larger positive values on PC_2 are reached. So, the new experiments show a larger signal for all isotopes but in particular for those with small mass values. This is probably due to a major removal of polyatomic interferences for small mass isotopes.

The experimental settings corresponding to the best conditions obtained by the Simplex procedure are reported in Table 1 (corresponding to experiment no. 119). Table 3 reports the signals obtained for some of the selected isotopes expressed as number of counts: the signal registered after the simplex procedure improved on the average 3.9 times with respect to the default settings; as expected, the improvements were recorded for small mass isotopes.

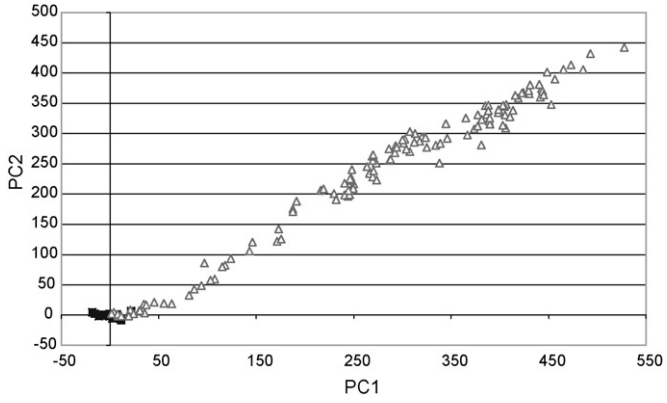

Fig. 2. Representation of the 150 experiments performed on the space of the first two PCs.

The improvements by far the largest were obtained for ^{51}V and ^{52}Cr. For what regards precision (standard deviation calculated from 5 genuine replicates of a standard solution at 100 ng L^{-1}), with the default settings the average precision is 10%, while it improves to about 5% with the simplex optimised conditions. Good linearity was achieved for all the revealed isotopes.

Table 3 reports also the LOD and LOQ values calculated by the use of the calibration curve for some of the considered isotopes, selecting the instrumental tuning according to experiment no. 119. Values inferior to 1 indicate that the corresponding optimisation procedure produced a worse result with respect to the default settings. After performing the Simplex procedure, the sensitivity improvement was, on the average, 2 times. The best LOD and LOQ improvements were obtained, as expected, with light isotopes (5.97 times for arsenic, 5.15 times for cobalt).

The experimental conditions obtained for experiment no. 119 are thus the best settings achieved through the simplex procedure. It is important to point out that the presence of the variable *dwell time* in the group of variables to be tuned could be a problem if the target function is based on the overall number of counts, in fact obviously increasing *dwell time* corresponds to an increase of the number of counts; however, the best settings obtained prove that this variable is not so driving since it is settled at intermediate values.

4.3. Partial least squares

PLS can be used in this case to provide a model relating the 21 experimental parameters (*X*-variables) to the 83 experimental responses (*Y*-variables). This analysis, rather than providing a quantitative predictive model, is used here to sum up the effect played by each experimental factor on the signals of the selected isotopes. The complete experimental matrix, consisting of 150 rows (the experiments) and 104 columns (83 columns representing the signal of each isotopes and further 21 columns representing the experimental settings of each parameter) was used to calculate a PLS model. This model was calculated to obtain a quantitative relationship between the 21 instrumental settings (*X*-variables) and the 83 experimental responses (*Y*-variables). Since our aim was the achievement of a unique model relating the signal of all the isotopes together to the experimental settings, the PLS2 method [16,17] was selected. Data were autoscaled before performing PLS.

The first two latent variables account for about 50% and 81% of the total variance contained in the *X*- and *Y*-variables, respectively, and they were considered as significant in the successive analysis.

The regression coefficients of the PLS2 model, built with the first two latent variables on both *X*- and *Y*-variables, are represented in Fig. 3. The graphical representation reports the instrumental parameters on the *y*-axis and the isotopes on the *x*-axis; the regression coefficients for each parameter for each isotope are represented on a colour scale from blue to red: increasing blue tones correspond to increasing negative coefficients, while increasing red tones correspond to increasing positive coefficients. Coefficients represented as white tones are characterised by values around zero, which do not play a relevant role on modelling the experimental responses. This representation allows a clearer identification of the parameters which have to be increased or decreased in order to optimise the signal of isotopes of interest. The parameters can be divided in three main groups according to the behaviour of their coefficients towards small or large isotopic masses: positive coefficients for all isotopic masses (Fig. 3, first five parameters), negative coefficients for all isotopic masses (Fig. 3, from *focus* to *auxiliary*), different positive/negative coefficients for small/large

Table 3
Signal intensities of some of the selected isotopes obtained for the standard 100 ng L^{-1}, corresponding LOD and LOQ values expressed as ng L^{-1} and signal and LOD improvements with the default and the simplex optimised experimental conditions

	Default				Simplex				Signal improvement[a]	LOD improvement[b]
	Mean signal	Dev. std	LOD	LOQ	Mean signal	Dev. std	LOD	LOQ		
^{51}V	45.33	8.33	78.90	118.35	429.44	8.03	19.48	29.21	9.47	4.05
^{52}Cr	75.11	10.69	46.42	69.62	913.65	6.40	30.38	45.57	12.16	1.53
^{55}Mn	104.00	5.33	55.78	83.67	833.03	18.02	26.44	39.66	8.01	2.11
^{59}Co	50.22	3.85	65.51	98.26	343.27	20.75	12.72	19.08	6.84	5.15
^{69}Ga	61.33	7.42	40.85	61.28	305.16	2.62	13.12	19.68	4.98	3.11
^{72}Ge	19.11	1.54	48.50	72.75	117.12	17.92	47.70	71.55	6.13	1.02
^{75}As	39.56	14.13	321.07	481.60	149.00	12.84	53.79	80.68	3.77	5.97
^{85}Rb	103.56	7.70	30.96	46.44	683.56	10.38	24.52	36.79	6.60	1.26
^{88}Sr	280.45	21.72	70.92	106.38	1201.74	32.77	41.66	62.49	4.29	1.70
^{89}Y	141.78	3.36	30.24	45.36	589.76	11.58	16.93	25.39	4.16	1.79
^{90}Zr	78.67	12.22	58.43	87.65	384.62	18.18	33.14	49.72	4.89	1.76
^{93}Nb	121.33	6.93	47.04	70.55	517.46	20.73	15.12	22.68	4.26	3.11
^{95}Mo	29.33	4.00	77.34	116.01	94.48	6.21	44.29	66.43	3.22	1.75
^{101}Ru	32.00	4.81	102.37	153.56	101.41	12.40	22.62	33.93	3.17	4.53
^{103}Rh	1905.09	106.02	16.97	25.46	7217.23	168.74	8.19	12.28	3.79	2.07
^{105}Pd	42.67	8.33	67.25	100.88	145.07	15.44	27.21	40.82	3.40	2.47
^{107}Ag	68.89	0.77	59.21	88.82	268.89	26.54	57.50	86.24	3.90	1.03
^{111}Cd	20.44	2.04	54.95	82.42	78.54	15.72	37.44	56.16	3.84	1.47
^{118}Sn	59.11	7.34	61.92	92.88	219.68	5.23	25.91	38.87	3.72	2.39
^{121}Sb	79.11	4.68	63.79	95.69	289.22	7.47	14.54	21.80	3.66	4.39
^{125}Te	1.78	0.77	157.73	236.60	15.71	2.23	103.00	154.50	8.84	1.53
^{133}Cs	141.33	10.91	27.47	41.20	676.16	10.05	16.93	25.40	4.78	1.62
^{137}Ba	92.45	1.54	262.34	393.50	326.18	19.43	248.89	373.34	3.53	1.05
^{139}La	210.67	26.23	37.24	55.86	783.82	28.89	17.20	25.81	3.72	2.16
^{140}Ce	324.01	24.33	75.57	113.36	1103.79	30.51	54.20	81.30	3.41	1.39
^{141}Pr	266.23	30.71	18.91	28.36	943.45	12.79	14.12	21.18	3.54	1.34
^{146}Nd	56.89	10.78	54.94	82.41	172.33	10.10	21.37	32.06	3.03	2.57
^{147}Sm	52.44	6.71	49.46	74.19	152.46	5.00	29.01	43.51	2.91	1.71
^{153}Eu	201.34	22.19	20.34	30.50	582.60	35.62	11.61	17.42	2.89	1.75
^{157}Gd	60.89	10.36	40.86	61.29	174.87	17.43	23.29	34.93	2.87	1.75
^{159}Tb	422.68	8.74	12.53	18.80	1195.97	23.65	14.97	22.45	2.83	0.84
^{163}Dy	98.67	10.07	22.48	33.72	313.93	12.26	18.18	27.27	3.18	1.24
^{165}Ho	448.01	7.42	15.38	23.08	1190.19	16.29	16.04	24.06	2.66	0.96
^{166}Er	143.56	6.71	24.20	36.30	403.57	14.04	13.96	20.95	2.81	1.73
^{169}Tm	471.12	34.11	13.67	20.50	1220.92	58.02	17.63	26.44	2.59	0.78
^{172}Yb	105.78	7.70	40.21	60.31	280.44	3.82	31.93	47.90	2.65	1.26
^{175}Lu	541.35	30.14	11.94	17.91	1322.34	22.81	14.22	21.32	2.44	0.84
^{178}Hf	132.89	4.07	30.40	45.60	336.11	29.95	31.79	47.69	2.53	0.96
^{181}Ta	623.13	28.01	22.10	33.14	1443.64	46.62	17.96	26.95	2.32	1.23
^{182}W	154.22	7.58	32.80	49.21	367.07	20.89	22.73	34.09	2.38	1.44
^{185}Re	159.56	16.07	37.77	56.65	424.59	13.01	18.51	27.77	2.66	2.04
^{193}Ir	288.89	23.41	24.73	37.10	627.42	15.95	16.17	24.25	2.17	1.53
^{195}Pt	98.22	7.34	41.72	62.58	215.06	6.59	16.88	25.32	2.19	2.47
^{205}Tl	321.34	15.38	28.15	42.23	718.44	11.81	9.65	14.48	2.24	2.92
^{208}Pb	327.12	17.91	14.44	21.66	792.83	11.15	14.69	22.03	2.42	0.98
^{209}Bi	606.69	35.51	67.63	101.45	1192.04	30.30	31.75	47.62	1.96	2.13
^{232}Th	716.92	58.43	36.01	54.02	1445.48	34.21	13.23	19.84	2.02	2.72
^{238}U	553.35	23.10	13.80	20.70	1143.52	46.09	16.61	24.91	2.07	0.83

[a] As calculated from ratio $Mean_{Simplex}/Mean_{Default}$.
[b] As calculated from ratio $LOD_{Default}/LOD_{Simplex}$ or $LOQ_{Default}/LOQ_{Simplex}$.

mass elements (last four parameters). Looking at Fig. 3, the first four parameters show positive or almost null coefficients for all the isotopic masses: an increase of these parameters increases the signal of the investigated isotopes. In particular, an increase of *D2* and *dwell time* increases prevalently the signal of small masses while an increase of *forward power* and *nebuliser* improves the signal of large masses.

For what regards negative coefficients, the first six parameters (from *focus* to *standard resolution*) provide an increase of the overall signals when they are decreased. *DA*, *lens 3* and *cool* act prevalently on large mass isotopes (they have to be decreased to record a larger signal), while *lens 1*, *sweeps* and *auxiliary* act on small mass isotopes (they have to be decreased to record a larger signal). The last four parameters show a different behaviour with respect to their effect on the signal of small and large mass isotopes: *channels* and *D1* show positive coefficients for large masses and negative ones for small masses (they have to be increased to improve large masses and decreased to improve small masses); *lens 2* and *hexapole bias* show an opposite behaviour, so they have to be increased to improve small masses and decreased to improve large masses. However, *Channels* and *hexapole bias* show the smallest coefficients and are not particularly relevant to the regression model built.

Fig. 3 thus allows to sum up the effects played by each instrumental parameter on the signal recorded for the investigated isotopes: looking at this representation it is therefore possible to obtain different optimal experimental conditions according to the elements of interest. In fact, it allows the definition of a quantitative mathematical model relating the signal of each isotope to the experimental settings.

The effects played by each factor on the final experimental response pointed out so far are obviously characteristic for this specific case. However, some of the parameters analysed are of

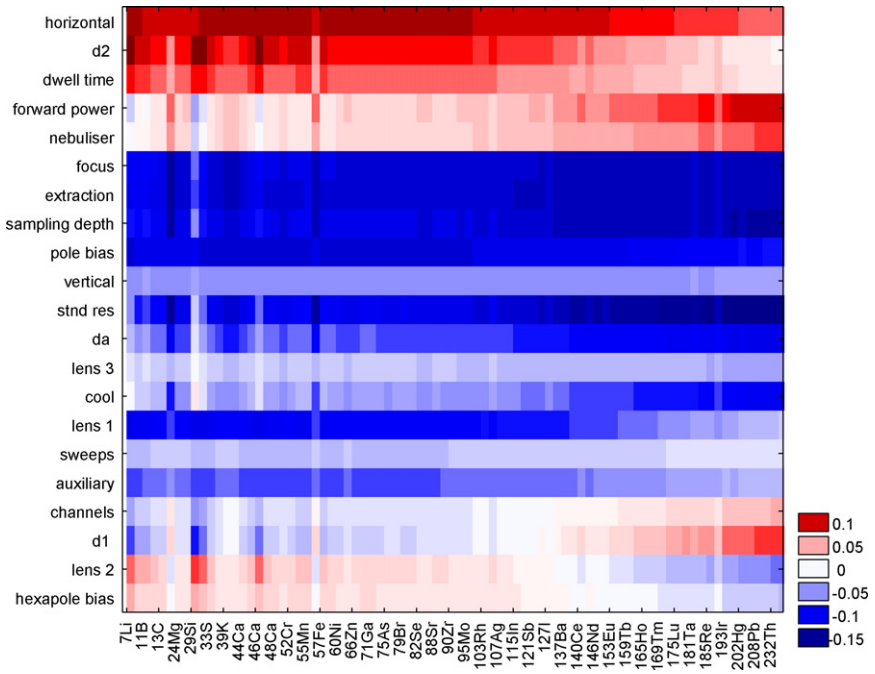

Fig. 3. Regression coefficients of the PLS2 model built with the first two latent variables on both x- and y-variables. The instrumental parameters and the isotopes are represented on the y- and x-axes respectively.

general interest in ICP-MS optimisation, since they are universally important in ICP-MS determinations (e.g. gas flow, torch position, channels, resolution, etc.). Anyway, the present application does not focus on the identification of the particular role played by each factor on the selected isotopic masses but on the potential of multivariate optimisation tools for the achievement of optimal experimental settings in cases where a large number of parameters and experimental responses have to be taken into account. From this point of view, this application proves that multivariate tools, as Simplex coupled to PCA to identify a suitable target function, perform well in the identification of optimal settings providing larger number of counts and better LOD and LOQ values with respect to common optimisation tools based on the OVAT procedure generally present in software packages. This procedure could thus represent a valid alternative for routine analyses.

5. Conclusions

21 experimental parameters were optimised with respect to the increasing sensitivity of the ICP-MS determination of 83 isotopes. The innovation of the proposed approach is represented by the contemporary optimisation of the 21 instrumental parameters to obtain the best settings for the determination of all the detectable isotopes together. The procedure is interesting for routine analyses where a great number of elements have to be determined, but it can be also exploited by companies as a valid alternative to the OVAT approach, for proposing default optimal instrumental settings. In particular, the simplex procedure, coupled to the use of a multivariate target function selected by PCA, is particularly effective since it takes into consideration the relationships and interactions among the experimental parameters and the experimental responses: this is impossible exploiting an OVAT approach where each variable is considered separately. Moreover, the simplex procedure can be applied to achieve convergence but it can also be applied considering a limited time consumption: after a selected time period dedicated to optimisation the procedure can be stopped and the final best settings can be used as optimised conditions providing in any case an improvement of the final response. The applied procedure can be easily implemented in the instrument software, thus providing a completely automated procedure for optimisation.

For what regards the present application, an initial set of 22 experiments was performed according to a starting simplex involving the variation of one parameter at a time (Table 2). Due to the large number of signal intensities to be maximised (for the overall 83 isotopes), the set of 22 experiments was used to choose a suitable multi-criteria target function, accounting for the overall signal intensity of all the isotopes to be determined. The best target function was selected as the first PC calculated performing a PCA on the dataset given by the first 22 experiments. The subsequent modified simplex optimisation procedure was then carried out maximising the target function (i.e. the positive score of the experiments on the first PC) and it reached convergence after 128 iterations (150 total experiments).

The best experimental conditions obtained by this procedure were further investigated through a PLS2 model, relating the signal of the 83 isotopes to the experimental settings.

The increase in signal intensity was on average 3.9 times. LOD and LOQ were calculated for the default settings and for the optimal settings obtained by the Simplex procedure: the increase in sensitivity obtained from the simplex optimised conditions was, on the average, 2 times, with a maximum of 5.97 times for arsenic.

The final PLS also allows to obtain a mathematical model relating the instrumental parameters to the experimental responses, thus allowing to sum up the information about the role played by each parameter in influencing the isotopes number of counts.

References

[1] M.J. Ford, L. Ebdon, R.C. Hutton, S.J. Hi, Anal. Chim. Acta 285 (1994) 23–31.
[2] E.H. van Veen, S. Bosch, M.T.C. de Loos-Vollebregt, Spectrochim. Acta B 51 (1996) 591–608.
[3] R. Brennetot, A.L. Becquet, H. Isnard, C. Caussignac, D. Vailhen, F. Chartier, J. Anal. Atom. Spectrom. 20 (6) (2005) 500–507.
[4] C.P. Ingle, P.K. Appelblad, M.A. Dexter, E.J. Reid, B.L. Sharp, J. Anal. Atom. Spectrom. 16 (9) (2001) 1076–1084.

[5] J.L. Gomez-Ariza, T. Garcia-Barrera, F. Lorenzo, J. Anal. Atom. Spectrom. 20 (9) (2005) 883–888.
[6] J. Darrouzes, M. Bueno, G. Lespes, M. Potin-Gautier, J. Anal. Atom. Spectrom. 20 (2) (2005) 88–94.
[7] N.R. Martos, P.C. Rudner, A.G. de Torres, J.M.C. Pavon, Microchim. Acta 148 (1–2) (2004) 35–42.
[8] F. Seby, M. Gagean, H. Garraud, A. Castetbon, O.F.X. Donare, Anal. Bioanal. Chem. 377 (4) (2003) 685–694.
[9] F. Vanhaecke, G. Stevens, G. De Wannemacker, L. Moens, Can. J. Anal. Sci. Spect. 48 (2003) 251–257.
[10] G. De Wannemacker, A. Ronderos, L. Moens, F. Vanhaecke, M.J.C. Bijvelds, Z.I. Kolar, J. Anal. Atom. Spectrom. 16 (6) (2001) 581–586.
[11] B.T. Sturman, P.S. Doidge, J. Anal. Atom. Spectrom. 13 (1) (1998) 69–74.
[12] E. Marengo, M.C. Gennaro, V. Gianotti, J. Chromatogr. A 39 (8) (2001) 339–344.
[13] J.A. Nelder, R. Mead, Comput. J. 7 (1964) 308.
[14] R. Carlson, L. Hansson, T. Lundstedt, Acta Chem. Scand. B 40 (1986) 444.
[15] R. Carlson, Design and Optimisation in Organic Synthesis, Elsevier, Amsterdam, 1992.
[16] D.L. Massart, B.G.M. Vanderginste, S.M. Deming, Y. Michotte, L. Kaufman, Chemometrics: A Textbook, Elsevier, Amsterdam, 1988.
[17] B.G.M. Vanderginste, D.L. Massart, L.M.C. Buydens, S. De Jong, P.J. Lewi, J. Smeyers-Verbeke, Handbook of Chemometrics and Qualimetrics: Part A, Elsevier, Amsterdam, 1998.
[18] L.E. Vanatta, D.E. Coleman, J. Chromatogr. A 770 (1–2) (1997) 105–114.
[19] D. Coleman, J. Auses, N. Grams, Chemometr. Intell. Lab. 37 (1) (1997) 71–80.

Talanta 76 (2008) 1077–1082

Contents lists available at ScienceDirect

Talanta

journal homepage: www.elsevier.com/locate/talanta

Immuno-column for on-line quantification of human serum IgG antibodies to *Helicobacter pylori* in human serum samples

Luis Molina, Germán A. Messina, Patrícia W. Stege, Eloy Salinas, Julio Raba*

INQUISAL, Department of Chemistry, National University of San Luis, CONICET, Chacabuco y Pedernera, D5700BWS, San Luis, Argentina

ARTICLE INFO

Article history:
Received 24 January 2008
Received in revised form 4 May 2008
Accepted 4 May 2008
Available online 9 May 2008

Keywords:
Helicobacter pylori
Alkaline phosphatase
P-Aminophenyl phosphate
Immuno-column
FIA

ABSTRACT

This study report an human serum IgG antibodies to *Helicobacter pylori* quantitation procedure based on the multiple use of an immobilized *H. pylori* antigen on an immuno-column incorporated into an a flow-injection (FI) analytical system. The immuno-adsorbent column was prepared by packing 3-aminopropyl-modified controlled-pore glass (APCPG) covalently linking *H. pylori* antigens in a 3-cm of Teflon tubing (0.5 i.d.). Antibodies in the serum sample are allowed to react immunologically with the immobilized *H. pylori* antigen, and the bound antibodies are quantified by alkaline phosphatase (AP) enzyme-labeled second antibodies specific to human IgG. *p*-Aminophenyl phosphate (*p*APP) was converted to *p*-aminophenol (*p*AP) by AP and an electroactive product was quantified on glassy carbon electrode (GCE) modified with multiwall carbon nanotubes (MWCNT) (GCE-CNTs) at 0.30 V. The total assay time was 25 min. The calculated detection limits for amperometric detection and the ELISA procedure are 0.62 and 1.8 U mL^{-1}, respectively. Reproducibility assays were made using repetitive standards of *H. pylori*-specific antibody and the intra- and inter-assay coefficients of variation were below 5%. The immuno-affinity method showed higher sensitivity and lower time-consumed, demonstrate its potential usefulness for early assessment of human serum immunoglobulin G (IgG) antibodies to *H. pylori*.

1. Introduction

The incidental discovery, in 1983, of a gastric bacterium led to a dramatic change in the field of gastroenterology [1]. *Helicobacter pylori* infects more than half the global population, causing peptic ulcer disease and chronic gastritis; it is also strongly associated with gastric malignancies. Indeed, it has been classified as a class I carcinogen [2]. The disease can be cured by eradication of *H. pylori* through the triple therapies based on a proton pump inhibitor with two antibiotics (clarithromycin and metronidazole or amoxicillin) [3]. In the absence of therapeutic intervention, infection by *H. pylori* lasts for the life of the host [4]. To prevent the indiscriminate use of multiple antibiotics, an accurate diagnosis for the presence of *H. pylori* infection becomes crucial.

H. pylori infection can be diagnosed by invasive techniques (endoscopy with biopsies for histology, culture and a rapid urease test) and non-invasive techniques (e.g. serology, the 13C-urea breath test and the stool antigen test) [5]. The availability of culture and PCR may be limited because they require highly experienced laboratory personnel. The EIA (enzyme immunoassay) and immunochromatographic method are more convenient, and can be interpreted either spectrophotometrically or visually and has good accuracy [6,7]. Some non-invasive tests are based on serological procedures that detect immunoglobulin G (IgG) against *H. pylori* in human serum. Circulating anti-*H. pylori* IgG antibody has proved to be of considerable value in the diagnosis of active infection due to the reliable correlation between the presence of the antibody and gastric mucosal colonization [8,9].

Different immunological procedures have been described for the determination of *H. pylori* in different samples: immunochromatographic, microplate enzyme-immunoassay, electrochemical and piezoelectric biosensors [10–15]. Common serum IgG measurements are carried out using enzyme-linked immunosorbent assay (ELISA) [16]. ELISA for serum IgG against *H. pylori* are based on measuring the quantity of IgG bound onto *H. pylori* antigens immobilized on the solid-phase. In all instances, the immobilized antigens are discarded after only one use.

An ideal diagnostic test should be easy to perform, fast, involve a few steps, and have high sensitivity and specificity. Conventional tests are time-consuming and include several steps, which increase the likelihood of errors by the operator [17]. ELISA is amenable for automation, but at an increased cost that cannot usually be afforded by most laboratories in underdeveloped countries.

* Corresponding author. Departamento de Química, Facultad de Química, Bioquímica y Farmacia, Universidad Nacional de San Luis, Chacabuco y Pedernera, 5700 San Luis, Argentina. Tel.: +54 2652 42 5385; fax: +54 2652 43 0224.
E-mail address: jraba@unsl.edu.ar (J. Raba).

0039-9140/$ – see front matter © 2008 Elsevier B.V. All rights reserved.
doi:10.1016/j.talanta.2008.05.005

In general, enzyme immunoassays combine the specificity of the antigen–antibody reaction with the sensitivity and signal amplification of enzyme-catalyzed reaction. Alkaline phosphatase (AP) is widely employed for this purpose since its reactions are basically free of interferences, it is highly stable, and it has a high turnover, low cost, and broad substrate specificity [18].

Carbon nanotubes (CNTs) are a novel type of carbon material and can be considered as the result of folding graphite layers into carbon cylinders. The CNTs have generated great interest in future applications based on their field emission and electronic transport properties [19], their high mechanical strength and their chemical properties [20]. The research has been focused on their electrocatalytic behaviours toward the oxidation of biomolecules and their performance has been found to be much superior to those of other carbon electrodes in terms of reaction rate, reversibility and detection limit [21]. The uses of CNTs for preparation of immunosensors based on CNT-modified electrodes have been reported previously [22–26].

Heterogeneous enzyme immunoassays, coupled with flow injection (FI) system and electrochemical detection, represent a powerful analytical tool for the determination of low levels of many analytes such as antibodies, hormones, drugs, tumor markers, and microorganism [27]. Electrochemical methods typically have the advantage of being highly sensitive, rapid, and inexpensive [28].

Here, we report an human serum IgG antibodies to *H. pylori* quantification procedure based on the multiple use of an immobilized *H. pylori* antigen on a immuno-column incorporated into an a flow-injection analytical system. Antibodies in the serum sample are allowed to react immunologically with the immobilized *H. pylori* antigen, and the bound antibodies are quantified by AP enzyme-labeled second antibodies specific to human IgG. *p*-Aminophenyl phosphate (*p*APP) was converted to *p*-aminophenol (*p*AP) by AP and an electroactive product was quantified on GCE-CNTs at 0.30 V. The current obtained from the oxidation of the product of enzymatic reaction is proportional to the activity of the enzyme and, consequently, to the amount of antibodies bound to the immuno-column. This method allows for a rapid determination of anti-*H. pylori* IgG and minimizes the wastage of expensive antigens and other reagents and does not require highly skilled technicians or expensive and dedicated equipment.

2. Materials and methods

2.1. Reagents and solutions

All reagents used were of analytical reagent grade. AP enzyme-labeled second antibodies specific to human γ-chain was purchased from Sigma Chemical (St. Louis, MO, USA). 4-Nitrophenyl phosphate disodium salt hexahydrate (pNPP) were purchased from Fluka Chemie (Steinheim, Switzerland). All other reagents employed were of analytical grade and used without further purifications. Aqueous solutions were prepared using purified water from a Milli-Q system.

The ELISA test kit for the quantitative determination of *H. pylori*-specific IgG class antibodies was purchased from EQUIPAR Diagnostici (Rome, Italy) and was used in accordance with the manufacturer's instructions [29].

2.2. The flow-injection manifold

The immuno-column was prepared by packing varying lengths of Teflon tubing with 3-aminopropyl-modified controlled-pore glass (AP-CPG) bound *H. pylori* antigens. Both ends of the tubing were blocked with glass fiber. A pump (Wilson Minipuls 3 peristaltic pump, Gilson Electronics, Middleton, WI, USA) was used for pumping, introducing the sample. Fig. 1 illustrates schematically the components of the single-line continuous-flow setup. The body of the amperometric detector was made of Teflon (Fig. 2). The GCE-CNTs are on the top of the amperometric detector micro-flow cell. The potential applied to the working electrode was 0.30 V versus Ag wire (pseudoreference electrode) and a Pt wire was used as counter electrode. At this potential, a catalytic current was well established. The pump tubing was Tygon (Fisher Accu Rated, 0.4 mm i.d., Fisher Scientific, Pittsburgh, PA, USA), and the remaining tubing used was Teflon (0.8 mm i.d. from Cole–Parmer, Chicago, IL, USA).

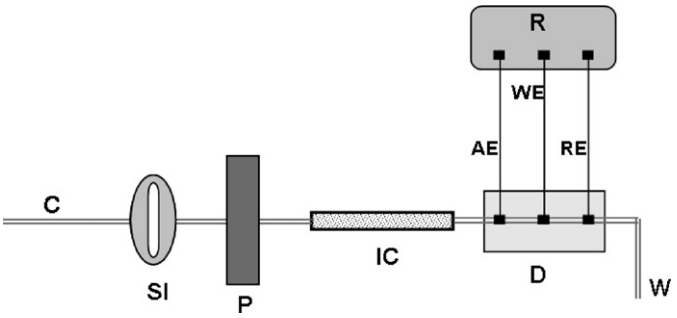

Fig. 1. Block diagram of the continuous-flow system and detection arrangement. P: pump (Gilson Minipuls 3 peristaltic pump, Gilson Electronics Inc., Middleton, WI); C: carrier buffer line; SI: sample injection; W: waste line; IC: immuno-column; D: BAS LC-4C (Bioanalytical System, West Lafayette, IN); R: recorder.

Amperometric detection was performed using the BAS LC-4C and the BAS 100 B (electrochemical analyzer Bioanalytical System, West Lafayette, IN) was used for cyclic voltammetric analysis.

The absorbancies were detected by Bio-Rad Benchmark microplate readers (Japan) and a Beckman DU 520 general UV–vis spectrophotometer (Fullerton, CA, USA). The *H. pylori* antigens were sonicated by a Sonics Vibra Cell ultrasonic processor (Sonics & Materials, Newtown, CT, USA).

2.3. Preparation of the CNTs-modified GCE

Prior to the modification, the glassy carbon electrode surface was polished with 0.3 μm alumina slurries, rinsed thoroughly with

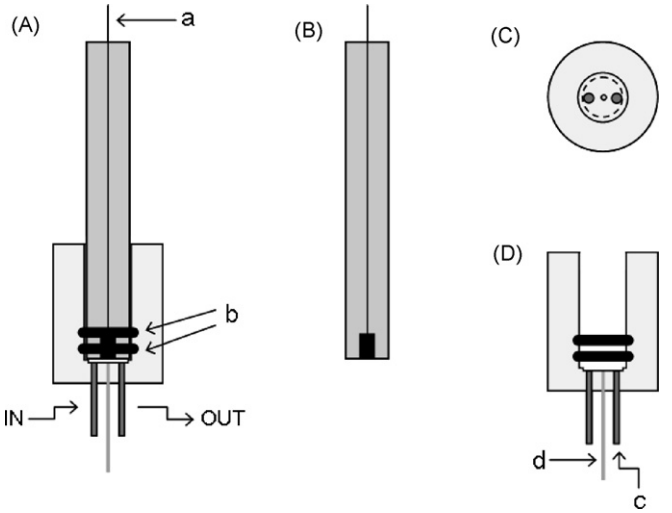

Fig. 2. Schematic representation of components in the amperometric flow cell. A: Assembled detector; B: GCE-CNTs working electrode; C: top-view of lower cell body; D: lower cell body. a: Electrical connection; b: O-ring; c: auxiliary electrode; d: pseudoreference electrode.

purified water, sonicated 30 s into water and 30 s into acetone, and dried in air. One milligram of CNTs was dispersed with the aid of ultrasonic stirring for 45 min in methanol/water (50:50, v/v) in an aqueous 0.1% Nafion solution. A 20-μL aliquot of this dispersion was dropped on the GC electrode surface and then the solvent was evaporated under an infrared heat lamp [30].

2.4. H. pylori-specific IgG antibody immunoassay

A series of standards that covered the clinically relevant range (0–100 U mL^{-1}) was supplied with the ELISA test kit. A standard curve for the spectrophotometric procedure was produced by following the manufacturer's protocol. Concentrations of *H. pylori*-specific IgG antibody were detected spectrophotometrically by measuring absorbance changes at 450 nm.

2.5. Preparation of the H. pylori antigens

The antigens was prepared from a sonicate *H. pylori* culture strain. The *H. pylori* were grown on blood agar plates at 37 °C for 3 days and then harvested, washed, and resuspended in 0.01 M phosphate-buffered saline (PBS, pH 7.2). This preparation was subjected to sonication. The sonic amplitude level was set at 20% and the machine was operated using four cycles of 60 s regulated alternatively. The sonicated preparation was centrifuged at 1000 × *g* for 10 min, and the supernatant was stored in the 0.01 M PBS (pH 7.2), at −20 °C between uses.

2.6. H. pylori antigens immobilization

The immuno-column was prepared by packing varying lengths of Teflon tubing with 3-aminopropyl-modified controlled-pore glass (APCPG) and was allowed to react with an aqueous solution of 5%, w/w glutaraldehyde at pH 10.00 (0.20 M carbonate) for 2 h at room temperature. After washing with purified water and 0.10 M phosphate buffer of pH 7.00, 0.5 mL of antigens preparation (100 μg mL^{-1} 0.01 M PBS, pH 7.2) was coupled to the residual aldehyde groups overnight at 5 °C. The immobilized antigens preparation was finally washed with phosphate buffer (pH 7.00) and stored in the same buffer at 5 °C between uses. The immobilized *H. pylori* antigens preparations were perfectly stable for at least 1 month.

2.7. Procedure for the immuno-column

This method was applied in the determination of IgG antibodies to *H. pylori* in 40 human serum samples. Prior to the analysis of each serum sample, the immuno-column was conditioned by flowing through 500 μL of desorption buffer (0.1 M glycine–HCl, pH 2) and then washed with 500 μL of 0.01 M PBS (pH 7.2). These solutions were pumped at a flow rate of 0.4 mL min^{-1}. The unspecific binding was blocked by flowing through 500 μL of 3% descremate milk in a 0.01-M PBS (pH 7.2). The serum samples were first diluted 50-fold with 0.01 M PBS (pH 7.2) and then 200 μL was injected into the PBS carrier stream at a flow rate of 0.15 mL min^{-1}. The immuno-column was washed with 0.01 M PBS (pH 7.2) at a flow rate of 0.4 mL min^{-1}. 200 μL of anti-human IgG AP enzyme-labeled second antibodies (dilution of 1/2000 in 0.01 M PBS, pH 7.2) was then injected into the 0.01 M PBS (pH 7.2) carrier stream at a flow rate of 0.15 mL min^{-1}.

The immuno-column was then washed free of any traces of unbound enzyme conjugate with 0.01 M PBS (pH 7.2). DEA buffer (100 mM diethanolamine, 50 mM KCl, 1 mM $MgCl_2$, pH 9.6) was used to prepare the *p*APP solution. 200 μL of substrate solution (2.7 mM *p*APP in a DEA buffer, pH 9.6) was injected into the carrier stream a flow rate of 0.15 mL min^{-1} and the enzymatic product (*p*AP) was measured on the surface of a GCE-CNTs coupled to a micro-flow cell. For the next analysis, the immuno-column was conditioned by flowing 500 μL of desorption buffer (0.1 M glycine–HCl, pH 2) and then washed with 500 μL of 0.01 M in PBS (pH 7.2) at a flow rate of 0.4 mL min^{-1}. A 10-port injector valve, with two different size loops, was used to inject the reagents.

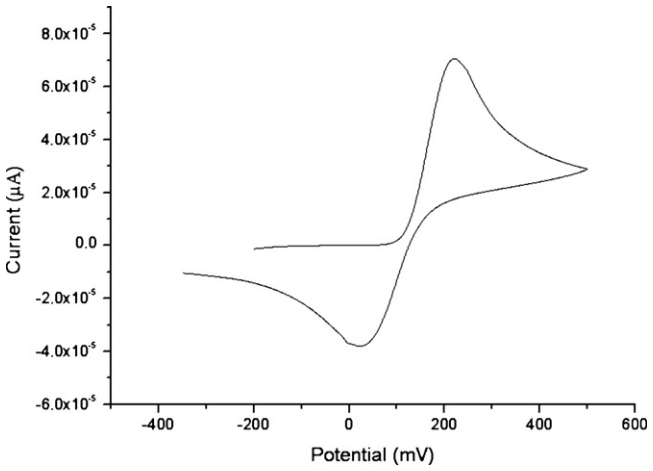

Fig. 3. Electrochemical study of *p*AP with the GCE-CNTs. Cyclic voltammogram in aqueous solution of *p*AP 5 mM in DEA buffer (pH 9.6). Scan rate: 100 mV s^{-1}.

A standard curve for the immuno-column procedure was produced by following our protocol with a series of standards that covered the clinically relevant range (0–100 U mL^{-1}) supplied with the ELISA test kit. When not in use, the immuno-column was stored in 0.01 M PBS (pH 7.2) containing sodium azide (0.01%) at 4 °C. The stock solution of *p*APP was prepared freshly before the experiment and stored under the exclusion of light for the duration of the experiment.

3. Results and discussion

3.1. Electrochemical study of p-AP with the GCE-CNTs

The electrochemical behaviour of the hydrolysis products (*p*AP) of the enzyme substrates *p*APP, was examined by cyclic voltammetry at GCE-CNTs. A cyclic voltammetric study of 5 mM of *p*AP in DEA buffer (pH 9.6), was performed by scanning the potential from −300 to 500 mV versus Ag/AgCl. CV showed well-defined anodic and corresponding cathodic peak, which corresponds to the transformation of *p*AP to *p*-benzoquinoneimine (QI) and vice versa within a quasireversible two-electron process (Fig. 3). A peak current ratio (I_{C1}/I_{A1}) of nearly unity, particularly during the recycling of potential, can be considered as criteria for the stability of QI produced at the surface of electrode under the experimental conditions.

3.2. Effect of continuous-flow operation

The immuno-column was prepared and incorporated into a FI manifold as illustrated in Fig. 1. To optimise the proposed method is necessary to have an understanding of the effect of the parameters governing the system. It has been shown that the theoretical framework developed for static ELISA system cannot be applied to describe the kinetics of antibody–antigen interactions occurring in a continues flow immunoassay [31]. Several parameters differ significantly. The buffer flow reduces the limitations of diffusion as observed in static ELISA systems [32]. Furthermore, the surface density of immobilized antigens in the flow immunoassay

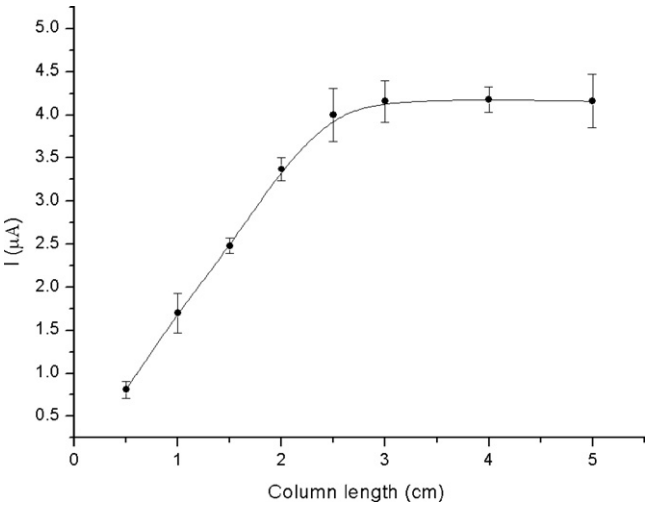

Fig. 4. Relationship between immuno-column length and its antibody binding capacity.

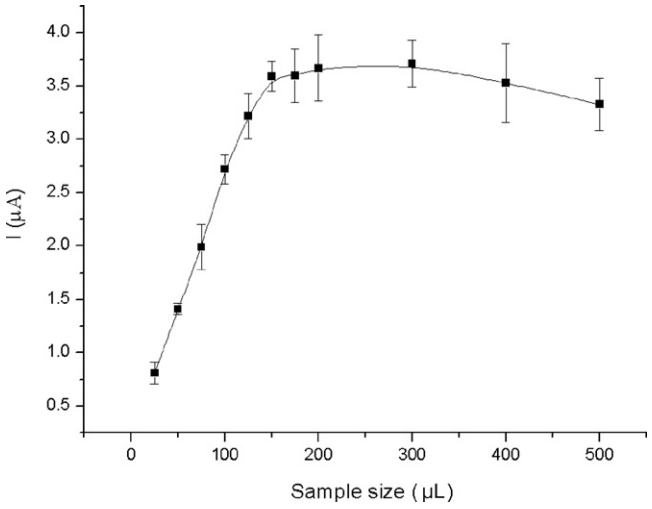

Fig. 5. Effect of sample size. Each value of *i* (μA) based on five determinations.

is at least three orders of magnitude higher than in static ELISA systems, because the controlled-pore glass increase the area for immobilization, about three orders of magnitude [33], and a high sensitivity can be attained by a rotating bioreactor and continuous-flow/stopped-flow/continuous-flow processing [34].

The proposed method manifolds follow the ELISA principles, but instead of using a microtiter plate, the reagents and washing buffers were pumped consecutively through the column containing immobilized antigen, coupled to amperometric detection for the determination of human antibody. AP enzyme-labeled second antibodies specific to human γ-chain was used as conjugate and the product of the enzymatic indicator reaction was measured at 0.30 V.

The implementation of continuous-flow permits: (a) utilization of relatively low immunoreactants loading conditions, (b) instantaneous operation under high initial rate conditions, (c) easy detection of accumulated products, and (d) reduction of apparent Michaelis–Menten constant, K'_M. The main advantages of this system are its simplicity, and the easy with which it can be applied to the determination of specific IgG antibodies to *H. pylori* in serum samples.

The response obtained from the enzymatic reaction oxidation is proportional to the activity of the enzyme conjugated and consequently, to the amount of specific antibodies of serum samples bound to the immuno-column with *H. pylori* antigens immobilized.

3.3. Optimum conditions for the determination of the enzymatic products

Various column lengths (1–5 cm) were prepared and incorporated into the FI manifold and the current noted when a 100-U mL^{-1} *H. pylori* specific antibodies control sera was injected and analyzed. The results as summarized in Fig. 4 show that immuno-columns longer than 3 cm would contain sufficient immobilized antigen to complex with antibodies to *H. pylori* of the range of patient sera investigated. An immuno-column of 3 cm long was adopted for further studies.

The sample size was studied in the range 50–500 μL and shows a maximum rate of response at 150 μL. For convenience a sample size of 200 μL was used to evaluate other parameters (Fig. 5).

The rate of enzymatic response under flow conditions was studied in the pH range 8–10 and shows a maximum value of activity at pH 9.6 (Fig. 6). The pH value used was 9.6 in DEA buffer. The effect of varying *p*APP concentration from 0.1 to 5 mM on the enzymatic response was evaluated. The optimum *p*APP concentration found was 2.7 mM. That concentration was then used.

3.4. Quantitative test for the detection of H. pylori-specific IgG antibody

Under the selected conditions described above, the absorbance of the enzymatic product is proportional to the concentration of *H. pylori*-specific IgG antibody in the serum. A linear calibration curve for the detection of *H. pylori*-specific IgG antibody in serum was produced over the range of 0–100 U mL^{-1}. The linear regression equation was $i = 0.0125 + 0.031$ CHp, with the linear relation coefficient $r = 0.998$. The coefficient of variation (CV) for the determination of *H. pylori*-specific antibody was 3.2% (six replicates). The ELISA procedure was also carried out as described, absorbance changes were plotted against the corresponding *H. pylori*-specific IgG antibody concentration and a calibration curve was constructed. The linear regression equation was $A = 0.031 + 0.029$ CHp, with the linear relation coefficient $r = 0.996$,

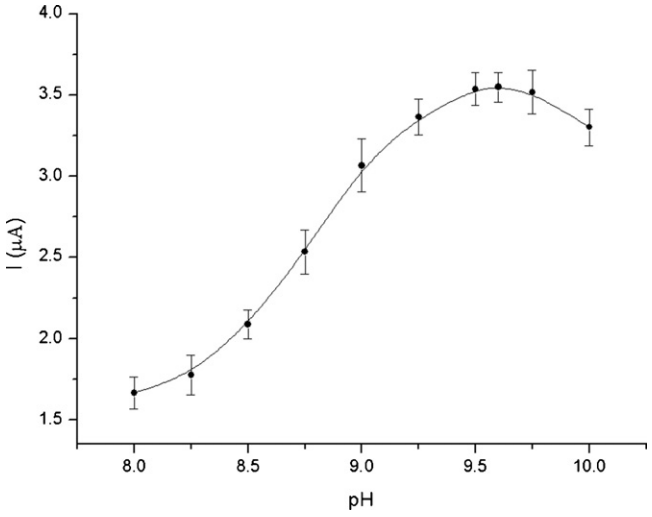

Fig. 6. Effect of pH on the rate of enzymatic response. Flow rate 150 μL min^{-1}. DEA buffer in the pH range 8–10 was used to prepare the 2.7 mM of *p*APP solution and 200 μL of each solution was injected in the system.

Table 1
Within-assay precision (five measurements in the same run for each control serum) and between-assay precision (five measurements for each control serum, repeated for 3 consecutive days)

Control sera[a] (U mL^{-1})	Within-assay		Between-assay	
	Mean	CV %	Mean	CV %
20	20.21	1.90	20.94	4.68
50	50.20	3.14	49.46	3.75
100	99.52	2.38	98.82	4.16

[a] U mL^{-1} *H. pylori*-specific antibodies.

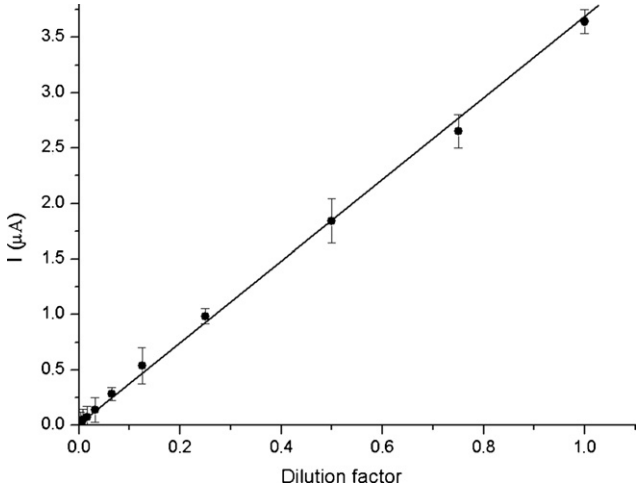

Fig. 7. Dilution test results for 100 U mL^{-1} *H. pylori*-specific antibodies. Each value of *i* (μA) is based on five determinations.

the CV for the determination of 20 U mL^{-1} *H. pylori*-specific antibodies was 4.7% (six replicates).

Taking the detection limit to be the concentration that gives a signal three times the standard deviation (S.D.) of the blank; for electrochemical detection and ELISA procedure was 0.62 and 1.8 U mL^{-1}, respectively. This result shows that electrochemical detection was more sensitive than spectrophotometric method.

The sensitivity (*S*) is defined as the slope of the regression line signal versus concentration, *S* for electrochemical detection and ELISA procedure was 0.031 and 0.029 Abs/U mL^{-1}, respectively.

The precision of the assay was checked with control serum at 20, 50 and 100 U mL^{-1} *H. pylori*-specific antibody concentrations. The within-assay precision was tested with five measurements in the same run for each serum. These series of analyses were repeated for 3 consecutive days in order to estimate the between-assay precision. The results obtained are presented in Table 1. The *H. pylori* assay showed good precision; the CV within-assay values were below 3.2% and the between-assay values were below 5%.

Table 2
Reproducibility assays using repetitive standards ($n = 6$) of 20 U mL^{-1} *H. pylori*-specific antibody

Standards of 20 U mL^{-1} *H. pylori*-specific antibody	Proposed method (U mL^{-1})	ELIZA (U mL^{-1})
1	20.20	19.31
2	19.87	19.53
3	20.54	20.29
4	20.09	20.89
5	19.72	19.05
6	19.94	19.39
$X \pm$ S.D.[a]	20.06 ± 0.288	19.74 ± 0.70

[a] (U mL^{-1}), mean ± S.D., standard deviation.

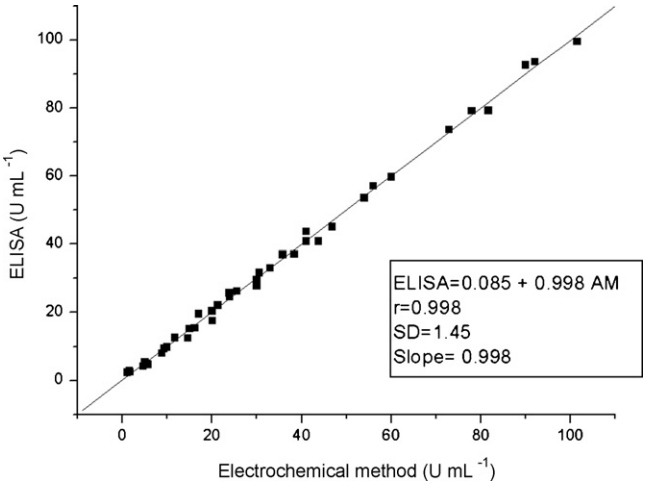

Fig. 8. Correlation between proposed method and commercial photometric assays.

The accuracy was tested with dilution and recovery tests. A dilution test was performed with 100 U mL^{-1} *H. pylori*-specific antibodies control sera with 0.01 M PBS, pH 7.2 (Fig. 7).

Reproducibility assays were made using a repetitive standard ($n = 6$) of 20 U mL^{-1} *H. pylori*-specific antibody; the percentage standard error was less than 3.2% (Table 2). When stored in PBS containing sodium azide (0.01%), the immunoreactor was found to retain 90% of its antibody binding property over a 1-month period.

The immuno-column was compared with a commercial spectrophotometric system for the quantification of *H. pylori*-specific antibodies in 40 serum samples. The slopes obtained were reasonably close to 1, indicating a good correspondence between the two methods (Fig. 8). These results suggest that the detectable concentration of *H. pylori*-specific antibodies in this system has been already at the levels of clinical analysis, and the sensitivity has reached to the levels to meet the determination of *H. pylori*-specific antibodies in serum even in light infected degree serum.

4. Conclusions

In this work, a immuno-column coupled with flow injection system for rapid sensitive and selective quantification of specific antibodies against *H. pylori* in human serum sample was developed.

The overall assay time (25 min) was shorter than the time reported for ELISA commercially test kits (160 min), this may be possible without reduce the selectivity. Also minimizes the waste of expensive antigens and other reagents; shows physical and chemical stability, and accuracy.

In conclusion, we took advantage of the simplicity of the ELISA system to develop a immuno-column that was capable of measuring the same levels of specific antibodies against *H. pylori* in human serum sample as detected by the conventional methods while having the advantages of speed and simplicity. Analytical results of clinical samples show the developed immunoassay has a promising alternative approach for detecting specific antibodies against *H. pylori* in human serum sample in the clinical diagnosis.

Acknowledgements

The authors wish to thank the financial support from the Universidad Nacional de San Luis and the Consejo Nacional de Investigaciones Científicas y Técnicas (CONICET).

References

[1] J.R. Warren, B.J. Marshall, Lancet I (1983) 1273.
[2] International Agency for Research on Cancer, World Health Organization, Schistosomes, Liver Flukes and *Helicobacter pylori*, IARC, Lyon, 1994, p. 177.
[3] W.A. de Boer, G.N.J. Tytgar, Br. Med. J. 320 (2000) 31.
[4] W. Rahna, R.W. Redlineb, T.G. Blancharda, Vaccine 23 (2004) 807.
[5] D. Vaira, N. Vakil, Gut 48 (2001) 287.
[6] O.J. Van Doorn, D.K. Bosman, B.W. Van't Hoff, J.A. Taminiau, F.J. Ten Kate, A. Van der Ende, Eur. J. Gastroenterol. Hepatol. 13 (2001) 1061.
[7] F.J. Yu, D.C. Wu, C.H. Kuo, C.Y. Lu, Y.C. Su, Y.C. Lee, S.R. Lin, C.S. Liu, C.M. Jan, W.M. Wang, J. Med. Sci. 17 (2001) 344.
[8] A.A. Van Zwet, J.C. Thijs, R. Roosendaal, E.J. Kuipers, S. Pena, J. de Graa, Eur. J. Gastroenterol. Hepatol. 8 (1996) 501.
[9] G.I. Perez-Perez, W.R. Brown, T.L. Cover, B.E. Dunn, P. Cao, M.J. Blaser, Clin. Diagn. Lab. Immunol. 1 (1994) 325.
[10] H.M. Hu, C.H. Kuo, Y.C. Lo, M.T. Wu, I.C. Wu, C.Y. Lu, Y.C. Su, F.J. Yu, Y.C. Lee, S.R. Lin, C.S. Liu, C.M. Jan, W.M. Wang, D.C. Wu, Hepatogastroenterology 54 (2007) 119.
[11] J. Richter, M. Grimmova, I. Stiborova, V. Kral, D. Jilek, Cas Lek Cesk 142 (2003) 665.
[12] D. Vaira, P. Malfertheiner, F. Mègraud, A. Axon, M. Deltenre, A.M. Hirschl, G. Gasbarrini, C. O'Morain, J.M. Pajares, M. Quina, G.N.J. Tytgat, Lancet 354 (1999) 30.
[13] G.A. Messina, A. Torriero, I.E. De Vito, R.A. Olsina, J. Raba, Anal. Biochem. 337 (2005) 195.
[14] G.A. Messina, I.E. De Vito, J. Raba, Sens. Actuator B 128 (2007) 23.
[15] X. Su, S.F.Y. Li, Anal. Chim. Acta 429 (2001) 27.
[16] A.R. Stacy, G.D. Bell, D.G. Newell, in: G. Gasbarrini, S. Petrolani (Eds.), Basic and Clinical Aspects of *H. pylori* Infection, Springer, Berlin, 1998, p. 159.
[17] A.O. Luquetti, A. Rassi, in: Z. Brener, Z.A.A. Andrade, M. Barral-Neto (Eds.), Trypanosoma cruzi e doencia de Chagas, 2nd ed., Rio de Janeiro, Guanabara-Koogan, 1999, p. 344.
[18] C. Ruan, Y. Li, Talanta 54 (2001) 1095.
[19] H. Murakami, M. Hirakawa, C. Tanaka, H. Yamakawa, Appl. Phys. Lett. 76 (2000) 1776.
[20] M.M. Treachy, T.W. Ebbesen, J.M. Gibson, Nature (Lond.) 381 (1996) 678.
[21] G. Li, J.M. Liao, G.Q. Hu, N.Z. Ma, P.J. Wu, Biosens. Bioelectron. 20 (2005) 2140.
[22] X. Yu, S.N. Kim, F. Papadimitrakopoulos, J.F. Rusling, Mol. Biosyst. 1 (2005) 70.
[23] X. Yu, B. Munge, V. Patel, G. Jensen, A. Bhirde, J.D. Gong, S.N. Kim, J. Gillespie, J.S. Gutkind, F. Papadimitrakopoulos, J.F. Rusling, J. Am. Chem. Soc. 128 (2006) 11199.
[24] J. Okuno, K. Maehashi, K. Kerman, Y. Takamura, K. Matsumoto, E. Tamiya, Biosens. Bioelectron. 22 (2006) 2377.
[25] L. Wu, F. Yan, H. Ju, J. Immunol. Methods 322 (2007) 12.
[26] N.V. Panini, G.A. Messina, E. Salinas, H. Fernández, J. Raba, Biosens. Bioelectron. 23 (2008) 1145.
[27] G. Gübitz, C. Shellum, Anal. Chim. Acta 283 (1993) 421.
[28] A.G. Gehring, C.G. Crawford, R.S. Mazenko, L.J. Van Houten, J.D. Brewster, J. Immunol. Methods 195 (1996) 15.
[29] EQUIPAR Diagnostici, Enzyme Immunoassay for the Quantitative Determination of IgG Class Antibodies to *Helicobacter pylori* (instruction manual), EQUIPAR Diagnostici, Rome, Italy, 2003.
[30] D.S. Vega, L. Agüí, A. González-Cortés, P. Yáñez-Sedeño, J.M. Pingarrón, Talanta 71 (2007) 1031.
[31] G.A. Wemhoff, S.Y. Rabbany, A.W. Kusterbeck, R.A. Ogert, R. Bredehorst, F.S. Ligter, J. Immunol. Methods 156 (1992) 223.
[32] E. Salinas, J. Torriero, F. Battaglini, M.I. Sanz, R.A. Olsina, J. Raba, Biosens. Bioelectron. 21 (2005) 313.
[33] M.C. Gosnell, R.E. Snelling, H.A. Mottola, Anal. Chem. 58 (1986) 1585.
[34] A. Lapierre, F. Battaglini, J. Raba, Anal. Chim. Acta 443 (2001) 17.

Talanta 76 (2008) 1265–1268

Contents lists available at ScienceDirect

Talanta

journal homepage: www.elsevier.com/locate/talanta

Short communication

Leaf anatomy affects the extraction of photosynthetic pigments by DMSO

Dimosthenis Nikolopoulos, Christina Korgiopoulou, Kyriakos Mavropoulos, Georgios Liakopoulos, George Karabourniotis*

Laboratory of Plant Physiology, Department of Agricultural Biotechnology, Agricultural University of Athens, Iera Odos 75, 11855 Botanicos, Athens, Greece

ARTICLE INFO

Article history:
Received 14 November 2007
Received in revised form 16 May 2008
Accepted 21 May 2008
Available online 3 June 2008

Keywords:
Chlorophyll extraction
Dimethylsulfoxide
DMSO
Heterobaric leaves
Leaf anatomy
Sclerophylls

ABSTRACT

Dimethylsulfoxide (DMSO) is a widely used solvent for the extraction of chlorophylls (Chls) from leaves of higher plants. The method is preferred because the time-consuming steps of grinding and centrifuging are not required and the extracts are stable for a long time period. However, the extraction efficiency of this solvent is not comparable among plant species, whereas the particular leaf anatomical characteristics responsible for this unevenness remain unknown. In order to examine the influence of leaf anatomy on the extraction efficiency of DMSO (i.e. the concentration of Chls extracted with DMSO as % of the concentration of Chls extracted with 80% acetone), leaves of 19 plant species with different anatomical characteristics were incubated for 40 min in DMSO at 65 °C. Under these conditions, heterobaric leaves, which are characterized by the occurrence of bundle sheath extensions in the mesophyll, showed lower extraction efficiency of DMSO compared to homobaric leaves and conifer needles. Microscopical observations of DMSO incubated leaf tissues showed that bundle sheath extensions behave as anatomical barriers which prevent the diffusion of DMSO within heterobaric leaves, even after prolonged incubation with the solvent. The effect was stronger in heterobaric leaves possessing thick bundle sheath extensions. The extraction efficiency of DMSO in these leaves was improved by vacuum infiltration of the samples in the presence of warm (65 °C) solvent.

1. Introduction

Dimethylsulfoxide (DMSO), an aprotic solvent with amphiphilic properties [1] has been successfully used for the extraction of chlorophylls from algae [2,3], lichens [4,5], sediments [6] and leaves of higher plants [5,7–9]. The use of DMSO instead of other solvents (methanol, ethanol, and acetone) has two advantages: (A) extraction is easy and fast because grinding and centrifuging is not required. Thus this method is suitable under field conditions [9] and allows the preparation and analysis of a large number of samples in a relatively short time periods. (B) The stability of Chl extracts in DMSO is better than that of acetonic extracts [7,5]. However the DMSO method appears to have an inherent disadvantage. The extraction of Chls is based on the diffusivity of DMSO within the particular tissue, because mechanical disruption of the cells does not take place. Thus the incubation time is not constant and it depends on 'the degree of cutinization and thickness of the leaf' [7,5]. This practically means that the samples are incubated in DMSO until all Chl is visibly removed from plant tissues. In some cases, exhaustive Chls extraction with DMSO requires several hours of incubation and may also require mechanical disruption of the cells [10].

In order to investigate the above-mentioned methodological problems, leaf samples of different plant species were extracted by DMSO under constant extraction conditions. The extraction efficiency was investigated versus specific anatomical parameters in order to identify which character is responsible for the low solvent efficiency observed in some plant species. Some modifications of the existing protocol are proposed in order to increase the efficiency of the DMSO extraction.

2. Materials and methods

Mature leaves were collected from plant species grown under field conditions at the experimental plantation of the Agricultural University of Athens (*Ligustrum japonicum*, *Eruca sativa*, *Amaranthus* sp., *Morus alba*, *Malva sylvestris*, *Arundo plinii*, *Avena sativa*, *Cercis siliquastrum*, *Sinarundinaria murialea* and *Magnolia grandiflorum*; 37°58′N, 23°42′E, 37 m a.s.l.), the mount Parnis (*Juniperus oxycedrus*, *Abies cefallonica*, *Pinus halepensis*, *Quercus coccifera* and *Nerium oleander*; 38°08′N, 23°43′E, 500–800 m a.s.l.), or a local

Abbreviations: BSE, bundle sheath extension; Chl, chlorophyll; DMSO, dimethylsulfoxide; SLA, specific leaf area; TLA, transparent leaf area.

* Corresponding author. Fax: +30 2105294286.
E-mail address: karab@aua.gr (G. Karabourniotis).

0039-9140/$ – see front matter © 2008 Elsevier B.V. All rights reserved.
doi:10.1016/j.talanta.2008.05.037

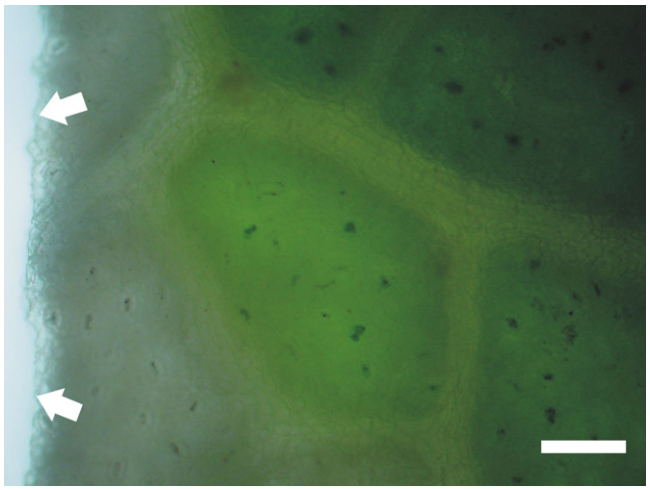

Fig. 1. Portion of a *Quercus coccifera* leaf cutting after incubation with DMSO at 65 °C for 40 min without vacuum infiltration. The leaf piece was photographed under low magnification using transmitted light. The extraction of Chls from the areoles neighbouring the cut edge of the lamina appears complete, but areoles possessing intact bundle sheath extensions preserve the green colour. The areole at the centre of the picture shows a light-green colour, that indicates partial extraction of the pigments. Scale bar 100 μm. (For interpretation of the references to color in this figure legend, the reader is referred to the web version of the article.)

market (*Lactuca sativa*, *Spinacia olearacea* and *Beta vulgaris*) during summer.

For extraction of chlorophylls, the original method of Hiscox and Israelstam [7] was used. Leaf samples of each species were cut into small (1–4 mm^2) pieces and placed in vials containing DMSO. Samples were incubated in a water-bath at 65 °C for 40 min. In parallel, a similar series of samples were vacuum pre-treated at −1000 mbar for 10 min and afterwards were incubated as above. To compare the extracting efficiency of DMSO, leaf samples from all plant species were also extracted with a mortar and pestle using fine sand and 80% acetone at 4 °C according to Arnon's method [11]. After centrifugation the extracts were adjusted to a final volume, transferred to a cuvette and the absorbances were recorded using a UV 160A spectrophotometer (Shimadzu Co., Tokyo, Japan). Concentrations of chlorophylls were calculated according to Lichtenthaler and Wellburn [12] for acetone extracts and according to Wellburn [13] for DMSO extracts.

In heterobaric leaves a significant portion of the leaf surface does not correspond to photosynthetic tissue, but to transparent regions of the bundle sheath extensions (see Fig. 1). The percentage of transparent leaf area (% TLA) was calculated by the method described in Nikolopoulos et al. [14]. Briefly, fresh leaf disks were fixed between two microscopic slides and viewed using transmitted light under the microscope. Digital images were recorded using the above equipment and saved as 8-bit gray-scale files. Digital images were processed using a custom program developed under Matlab (version 6.0.0.88, Mathworks Inc., Natick, MA, USA). The processing consisted of the following steps: (a) a filter was applied to correct non-uniform illumination of the microscopic image; (b) a threshold level was chosen by the program using an appropriate algorithm; (c) using the threshold value, the images were converted to binary mode (the white areas corresponded to the BSEs while the black pixels corresponded to the mesophyll); (d) the area occupied by the white pixels (TLA %) was calculated and expressed as percent (%) of the image area.

Comparison of means was performed using Microsoft Excel 2003 (Microsoft Corporation, Redmond, CA, USA). Regression statistics were performed using MedCalc v. 9.5.2.0 (MedCalc Software, Mariakerke, Belgium).

3. Results

In order to examine the influence of leaf anatomy on the extraction efficiency of DMSO (i.e. the concentration of Chls extracted with DMSO as % of the concentration of Chls extracted with 80% acetone), leaves of 19 plant species with different anatomical characteristics (sclerophylous or malacophylous, homobaric or heterobaric leaves and conifer needles) were incubated with DMSO under the same conditions (40 min at 65 °C). We tested if specific anatomical parameters, i.e. specific leaf mass (SLA), leaf density (LD) and leaf thickness (LT), affect the extraction efficiency of DMSO. In all cases, the linear correlation between each parameter and the extraction efficiency of the solvent was poor ($r^2 = 0.35$ for SLA, $r^2 = 0.44$ for LD and $r^2 = 0.28$ for LT, data not shown). We observed, however, that species bearing homobaric leaves or conifer needles exhibited high extraction efficiencies of DMSO extraction (>78%, mean yield 99%, Table 1). The majority of plant species of this group showed DMSO extraction efficiencies comparable to those obtained using the customary method of acetone extraction (Table 1). On the other hand, species bearing heterobaric leaves showed significantly lower concentration of Chls when extracted with DMSO compared to 80% acetone (except for leaves of *S. murialea* and *M. grandiflorum* which showed lower but non-significant differences compared to the Chls concentration of acetone extracts, Table 1). For heterobaric leaves, DMSO extraction efficiency was <72% (mean DMSO yield 61%). Microscopical observations of DMSO incubated leaf tissues showed that bundle sheath extensions of the heterobaric leaves behave as anatomical barriers which prevent the entrance of the solvent within photosynthetic tissues, even after prolonged incubation times (Fig. 1). Moreover, it was found that the extraction efficiency of DMSO was negatively correlated with the transparent leaf area (TLA) of the heterobaric leaves (Fig. 2). TLA is a parameter representing the leaf area occupied by bundle sheath extensions and is therefore indicative of the thickness and density of these structures [14]. Due to the occurrence of these anatomical barriers, it was hypothesized that vacuum infiltration of the leaf tissues in the presence of DMSO would accelerate the entrance of the solvent and, therefore, increase the extraction efficiency. Additionally, increased incubation temperatures would reduce the viscosity and correspondingly

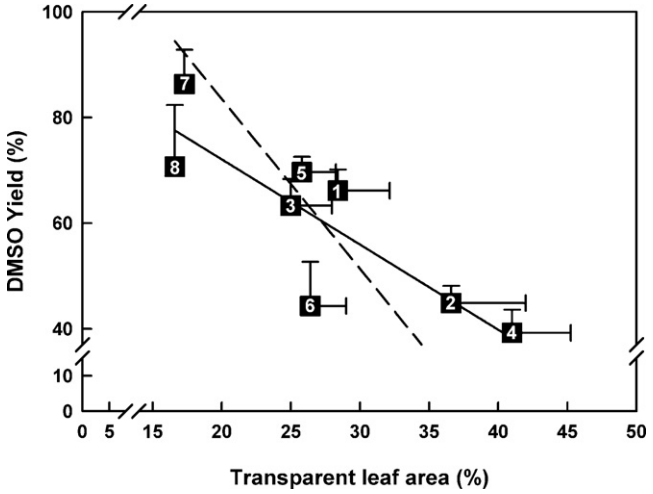

Fig. 2. Linear regression between TLA and DMSO yield. Each point represents different plant species possessing heterobaric leaves (numbers in data points correspond to plant species shown in Table 1). Data are means of five observations ± standard error of the mean. Solid line shows linear regression ($r^2 = 0.70$; $P = 0.001$; [DMSOYield] = 104.3–1.62 TLA). Dashed line shows Deming regression ($r = -0.84$; [DMSOYield] = 147.8–3.21 TLA).

Table 1
Concentration of chlorophylls in 80% acetonic leaf extracts and efficiency of DMSO extraction (as % yield of the corresponding acetonic extracts) with or without vacuum incubation pre-treatment

Plant species (# in Fig. 2)	Acetone 80% Chl conc. ($\mu g\,cm^{-2}$)	DMSO yield (%) (0 mbar)	DMSO yield (%) (−1000 mbar)
Homobaric leaves			
Ligustrum japonicum	4.56 ± 0.08	79 ± 1**	
Lactuca sativa	2.41 ± 0.09	106 ± 4	
Spinacia oleracea	3.63 ± 0.12	108 ± 2	
Beta vulgaris	3.42 ± 0.08	92 ± 1*	
Ilex aqualiforium	5.44 ± 0.26	95 ± 3	
Eruca sativa	1.86 ± 0.08	131 ± 7	
Amaranthus sp.	3.39 ± 0.51	96 ± 10	
Juniperus oxycedrus[a]	0.80 ± 0.05	108 ± 3	
Abies cefallonica[a]	0.47 ± 0.01	79 ± 13	
Pinus halepensis[a]	0.88 ± 0.05	97 ± 2	
Mean yield		99	
Heterobaric leaves			
Morus alba (1)	3.68 ± 0.05	66 ± 4**	82 ± 8
Arundo plinii (2)	7.07 ± 0.08	45 ± 3**	64 ± 5**
Avena sativa (3)	4.06 ± 0.18	63 ± 5**	90 ± 2
Quercus coccifera (4)	5.97 ± 0.24	39 ± 4**	82 ± 3*
Nerium oleander (5)	5.28 ± 0.18	70 ± 3**	76 ± 7**
Cercis siliquastrum (6)	4.17 ± 0.26	44 ± 8**	106 ± 17
Sinarundinaria murialea (7)	2.07 ± 0.27	86 ± 6	113 ± 3
Magnolia grandiflorum (8)	4.44 ± 0.81	71 ± 12	79 ± 3
Mean yield		61	87

Values are means of three to five observations ± standard error of the mean. Significant differences denoted in the table are always between values of chlorophylls concentration of the acetonic and the corresponding values of chlorophylls concentrations of the DMSO extracts (data not shown), according to the Student's *t*-test.
[a] In conifers (*J. oxycedrus*, *A. cefallonica* and *P. halepensis*) Chls concentration values are expressed as $\mu g\,g^{-1}$ fresh mass.

increase the diffusivity of DMSO, also contributing to the increase of the extraction efficiency. Indeed, the extraction efficiency of DMSO increased considerably by applying vacuum infiltration of leaf tissues in the presence of warm (65 °C) DMSO during incubation (Table 1). Under the above conditions, all samples exhibited DMSO extraction efficiencies higher than 75% (mean DMSO yield 87%, Table 1).

4. Discussion

Hiscox and Israelstam [7] and Barnes et al. [5] pointed out that the extraction of Chls from leaf tissues with DMSO requires incubation 'for various times, depending on the degree of cutinization and thickness of the leaf'. No attempt, however, was made to determine the influence of the particular anatomical factors on the extracting efficiency of the solvent. We observed that specific anatomical parameters such as SLA, LD and LT did not strongly affect the extraction efficiency of DMSO. It was found however that according to the extracting efficiency of the solvent, plant species could be divided in two major groups. The first group (exhibiting high DMSO efficiencies) was populated by species possessing homobaric leaves or needles, whereas the second one (exhibiting low DMSO efficiencies) was populated by species possessing heterobaric leaves (Table 1). Heterobaric leaves, contrary to homobaric leaves and needles, are characterized by the occurrence of BSEs formed by parenchyma or sclerenchyma cells which project as ribs on both surfaces of the lamina [15,16]. BSEs are reported to play important water conducting, light transferring, mechanical and protecting roles [14,17–21]. BSEs, which are relatively free of intercellular spaces and pigments, create an anatomical barrier which separates the photosynthetic cells in a series of compartments, called "aeroles" or "BSE compartments". This anatomical barrier probably prevents the entrance of DMSO within aeroles located in the interior of the leaf cuttings (Fig. 1). Moreover, the extraction efficiency of DMSO in heterobaric leaves was dependant on the thickness of the anatomical barrier, as it is described by the TLA parameter (Fig. 2). In homobaric leaves and conifer needles, lacking these structures, unhampered diffusion of the solvent was evident judging from the high DMSO extracting efficiency. High extraction efficiency of DMSO in conifer needles has also been reported by Barnes et al. [5]. In the present study, the extraction efficiency of DMSO in the heterobaric leaves was improved by vacuum infiltration which enhanced the entrance of the solvent within all aeroles of the leaf cuttings indicating that BSEs indeed behave as barriers against the diffusion of DMSO. Under field conditions, where laboratory means are limited, the DMSO method of Chls extraction is a simpler alternative to the acetone method [9]. The application of the DMSO method under such conditions could be enhanced by applying of vacuum with the help of a common syringe before storing the leaf disks into the DMSO. This simple treatment will facilitate solvent infiltration and avoid pigment degradation. Furthermore, incubation of samples at 65 °C can follow under laboratory conditions.

In conclusion, we recommend the following protocol for the extraction of photosynthetic pigments by DMSO from leaves of higher plants. Upon collection, leaf samples should be observed under a low magnification microscope under transmitted light or with the help of a magnifying glass against a light source so as to distinguish the homobaric leaves from the heterobaric ones. In the case of heterobaric leaves, vacuum infiltration prior incubation with DMSO is recommended to improve the extraction efficiency. In all cases, an examination of the leaf cutting is needed to ensure satisfactory pigment extraction at the end of the incubation period.

References

[1] R. Notman, M. Noro, B.O. Malley, J. Anwar, J. Am. Chem. Soc. 128 (2006) 13982–13983.
[2] W.T. Shoaf, B.W. Lium, Limnol. Oceanogr. 21 (1976) 926–928.
[3] B.K. Burnison, Can. J. Fish. Aquat. Sci. 37 (1980) 729–732.
[4] R. Ronen, M. Galun, Environ. Exp. Bot. 24 (1984) 239–245.
[5] J.D. Barnes, L. Balaguer, E. Manrique, S. Elvira, A.W. Davison, Environ. Exp. Bot. 32 (1992) 85–100.
[6] R. Devesa, A. Moldes, F. Dıaz-Fierros, M.T. Barral, Talanta 72 (2007) 1546–1551.

[7] J.D. Hiscox, G.F. Israelstam, Can. J. Bot. 57 (1979) 1332–1334.
[8] A.D. Richardson, S.P. Duigan, G.P. Berlyn, New Phytol. 153 (2002) 185–194.
[9] M.A. Tait, D.S. Hik, Photosynth. Res. 78 (2003) 87–91.
[10] T. Shinano, T.T. Lai, T. Kawamukai, M.T. Inoue, T. Koike, T. Tadano, Photosynthetica 32 (1996) 409–415.
[11] D.I. Arnon, Plant Physiol. 24 (1949) 1–15.
[12] H.K. Lichtenthaler, A.R. Wellburn, Biochem. Soc. Trans. 11 (1983) 591–592.
[13] A.R. Wellburn, J. Plant Physiol. 144 (1994) 307–313.
[14] D. Nikolopoulos, G. Liakopoulos, I. Drossopoulos, G. Karabourniotis, Plant Physiol. 129 (2002) 235–243.
[15] R.B. Wylie, Am. J. Bot. 38 (1951) 355–361.
[16] K. Esau, Anatomy of Seed Plants, John Wiley & Sons, New York, 1977, p. 767.
[17] T.D. Pizzolato, J.L. Burbano, J.D. Berlin, P.R. Morey, R.W. Pease, J. Exp. Bot. 27 (1976) 145–161.
[18] P.W. Lucas, M.F. Choong, H.T.W. Tan, I.M. Turner, A.J. Berrick, Phil. Trans. R. Soc. Lond. B 334 (1991) 95–106.
[19] R.B. Wylie, Am. J. Bot. 30 (1943) 273–280.
[20] A. Roth-Nebelsick, D. Uhl, V. Mosbrugger, H. Kerp, Ann. Bot. 87 (2001) 553–566.
[21] G. Karabourniotis, J.F. Bornman, D. Nikolopoulos, Plant Cell Environ. 23 (2000) 423–430.

Talanta 76 (2008) 1153–1158

Contents lists available at ScienceDirect

Talanta

journal homepage: www.elsevier.com/locate/talanta

Optimization of serotonin imprinted polymers and recognition study from platelet rich plasma

Burcu Okutucu*, Azmi Telefoncu

Ege University, Faculty of Science, Biochemistry Department, 35100 Bornova-Izmir, Turkey

ARTICLE INFO

Article history:
Received 11 December 2007
Received in revised form 5 May 2008
Accepted 14 May 2008
Available online 7 July 2008

Keywords:
Molecular imprinting
Serotonin
Rebinding characteristics
Molecular recognition

ABSTRACT

Molecularly imprinted polymers using serotonin as the template molecule was prepared for selective recognition from platelet rich plasma by non-covalent imprinting approach. Four different monomers (methacrylic acid, acrylamide, 4-vinylpyridine and 2-acrylamido-2-methylpropane sulfonic acid) and acetonitrile and DMSO as porogen were investigated for the first time by bulk polymerization. The molecularly imprinted polymer which was prepared by acrylamide/methacrylic acid had the largest imprinting factor for serotonin. The affinity and specificity of these polymers were evaluated by equilibrium binding experiments. The effect of polarity of the solvents was examined by polymers binding capacity and imprinting factor. According to the Scatchard analysis the K_d and Q_{max} values were calculated as 1.95 μmol l^{-1} and 19.129 μmol g^{-1}, respectively. The polymer was tested to evaluate serotonin from platelet rich plasma and 70% serotonin recovery was found.

1. Introduction

The topic about biomimic recognition has been an active field for biochemistry and bioorganic research. The development of synthetic receptors capable of encapsulating target analytes with high affinity is therefore in demand, especially if natural receptors are not available, or laborious and expensive to isolate. Development and application of molecularly imprinted polymers (MIPs) has matured over the past couple of decades, and is nowadays considered a straightforward and versatile technique for the generation of synthetic receptors for small organic constituents, and is increasingly adopted for large biological macromolecules. The principle of the molecular imprinting is: a target molecule (template) and functional monomers are polymerized with a cross-linking reagent. After removal of the template, the functional groups in the resulting binding sites should be arranged in positions suitable for interaction with the template molecule [1]. MIPs have been employed in a wide area, such as liquid chromatography, solid-phase extraction, membranes, sensors, artificial antibodies, catalysis, biotransformation process and diagnostic tools for drug assays [2–8]. Two main approaches to molecular imprinting have emerged to date, however, with a wide variety of modifications and combinations published: (i) the covalent approach pioneered by Wulff [9], and the non-covalent approach initially developed by Arshady and Mosbach [10].

Serotonin (5-hydroxytryptamine, 5-HT) is a heterocyclic amine that was found in enterochromaffin cells originating from the gastric and mucosa. It was found in gastric and serotonergic neurones of the brain, pineal gland and platelets. Abnormalities of serotonin-related processes give rise to various pathological conditions. Aberrations involved in anorexia, anxiety, depression and schizophrenia, whereas degeneration of serotonergic neurones has been noted in Alzheimer's and Parkinson's diseases. Peripheral aberrations in serotonin-related processes have been implicated in drug-induced emesis, hypertension, and migraine, genesis of cardiac arrhythmias, Raynaud's disease, fibrotic syndromes and some symptoms of the carcinoid syndrome. Plasma free 5-HT can also be taken up by circulating platelets and nearly all 5-HT in the blood (>99%) is found stored within the platelet, with the typical blood concentration being approximately 150 ng/ml (~600 ng/109 platelets, ~3.5 nmol/109 platelets). Levels of free plasma 5-HT in the general circulation appear to be quite low (<300 pg/ml). A wide variety of analytical methods has been used for the qualitative and quantitative determination of serotonin in blood such as fluorimetric methods [11–13], HPLC EC detection [14–17] and fluorimetric detection [18–21], GC-MS [22,23], thin layer chromatography [24,25] and enzyme immunoassay [26,27]. All these techniques are time-consuming and expensive.

Comparing to other methods, analysis of serotonin from blood takes short time by serotonin-imprinted polymer. The aim of preparing serotonin-imprinted polymer was to distinguish

* Corresponding author. Tel.: +90 232 3438624; fax: +90 232 3438624.
E-mail address: burcu.okutucu@ege.edu.tr (B. Okutucu).

0039-9140/$ – see front matter © 2008 Elsevier B.V. All rights reserved.
doi:10.1016/j.talanta.2008.05.033

serotonin from similar compounds that was present in platelet. By using this polymer many extraction steps would be eliminated and removing these interferences any HPLC conditions could be used without using any expensive and specific chemicals. In this paper, we have prepared a series of MIPs by bulk polymerization using serotonin as template. In order to find out the suitable functional monomer and to get a MIP which has specific affinity for the serotonin, polymers were prepared using different monomers and porogens. We examined binding characteristics under varying polymerization conditions such as different functional monomers, porogens, and different rebinding conditions. So we are be able to evaluate these parameters which were important in determining the ability of MIPs to recognize serotonin. The quantity of binding sites of the MIP was examined by using Scatchard analysis. Also molecularly imprinted polymer was tested to recognize serotonin in platelet rich plasma (PRP). For this aim the molecularly imprinted polymer was used as a solid phase extraction sorbent to distinguish serotonin from its similar compounds in platelets. The results of molecularly imprinted polymer solid phase extraction (MISPE) were showed that it can be an alternative sorbent for evaluating serotonin from PRP.

2. Experimental

2.1. Materials

Serotonin (Ser), acrylamide (AA), methacrylic acid (MAA), 4-vinylpyridine (4-VPy), 2-acrylamido-2-methylpropane sulfonic acid (AMPSA), dimethylsulfoxide (DMSO), acetonitrile (ACN), methanol (MeOH), chloroform (CHL), tetrahydrofuran (THF), acetone (ACE), acetic acid (AcA) and ethylene glycol dimethacrylate (EGDMA) were obtained from Sigma (St. Louis, MO, USA). 2,2′-Azobisisobutyronitrile (AIBN) was purchased from the Wako Pure Chemical Ind. (Osaka, Japan). Other chemicals were analytical grade.

2.2. Preparation of the serotonin-imprinted polymer

The synthetic procedure for the preparation of the standard polymer as follows: 1 mmol serotonin and 4 mmol functional monomer(s) (molar ratio of functional monomers, 2:2) were dissolved in the porogen (5 ml) in 25 ml glass vial. Into the mixture, the cross linker EGDMA (20 mmol) and initiator AIBN (20 mg) were added. The solution was degassed in a sonicating bath and deoxygenated with a stream of nitrogen for 10 min. The polymerization was allowed to carry out in a constant water bath at 50 °C for 20 h. The chemical compositions of MIPs were given in Table 1. The molar ratio of cross linker, functional monomer(s) and the template was 20:4:1. The resultant rigid polymers were ground to pass through a 35–42 μm sieve. The polymers were washed with three rounds of methanol/acetic acid (4:1, v/v) followed by two rounds of methanol to remove residual acetic acid and dried to constant weight under vacuum at 50 °C (washing steps were continued till no serotonin was found in supernatant). A reference non-imprinted polymers (NIPs) were prepared using the same recipe without addition of the template and worked up by the same washing procedure.

Table 1
Polymer compositions

MIP	Functional monomer(s)	Porogen
P1	MAA/AA	THF/ACN[a]
P2	MAA/AA	ACE/ACN[a]
P3	MAA/AA	CHL/ACN[a]
P4	MAA/AA	DMSO/ACN[a]
P5	MAA/AA	DMSO[b]
P6	4-VPy/MAA	DMSO[b]
P7	4-VPy/AMPSA	DMSO[b]
P8	AA/4-VPy	DMSO[b]
P9	AA/AMPSA	DMSO[b]
P10	AA	DMSO[b]
P11	MAA	DMSO[b]

[a] 500 μl (DMSO; THF; ACE; CHL)–4500 μl ACN as porogen.
[b] 5 ml DMSO as porogen.

2.3. Instrumentation

Solid polymer was crushed and ground using MM200 ground and sieved with an AS200 control "g" siever Retsch GmbH Co. (Haan, KG, Germany). Stuart linear shaker water bath and Jasco V-530 was used as a spectrophotometer. The chromatographic evaluations were performed by Agilent 1100 HPLC system. The analysis was performed on a column packed with Kromasil ODS (150 mm × 4.6 mm, 5 μm).

2.4. Rebinding experiments

In order to investigate the binding property of the imprinted polymer, rebinding experiments and Scatchard analysis were employed. The sized and washed MIP particles (10 mg) were suspended in different solvents (methanol; methanol:acetic acid; DMSO; DMSO:acetic acid; methanol:water). From this stock (10 mg/ml), a series of suspensions ranging in concentration from 0.1 to 4 mg ml^{-1} were prepared and serotonin (0.5 mmol ml^{-1}) was added to each tube (final volume 1 ml). The tubes were shaken 4 h at room temperature and then centrifuged for 5 min, and the concentration of the unbinding substrate in the solutions was determined by using a spectrophotometry (absorbance was measured at 320 nm) [28]. The amount of substrates bound to the polymer as known binding capacity (Q) was calculated according to the equation:

$$Q\,(\mu\text{mol}) = V(C_i - C_s)$$

where V, C_i and C_s represent the volume of the solution (ml), initial solution concentration (μmol l^{-1}) and the solution concentration after adsorption (μmol ml^{-1}), respectively.

The maximum binding capacity and dissociation constant were employed to evaluate the binding properties of the MIP. The data of static absorption experiments were processed with Scatchard equation as was follows

$$\frac{Q}{C_{free}} = \frac{Q_{max} - Q}{K_d}.$$

Q is the amount of serotonin bounded to MIP, C_{free} the free analyte concentration of serotonin at equilibrium (mmol l^{-1}), Q_{max} the maximum apparent binding capacity and K_d is the dissociation constant at binding site.

2.5. Chromatographic conditions

Serotonin was isolated from PRP as follows: venous blood was collected into a blood tube containing EDTA and centrifuged at room temperature for 10 min at 200 × g. The resulting PRP was collected (supernatant). For deprotenization before HPLC: 875 μl of 0.4 M $HClO_4$ ($HClO_4$ was used denaturing the enzymes thus preventing any further metabolism or auto oxidation of serotonin) were added to PRP solutions after vortexed the tubes, they were maintained for 1 h at 4 °C, then centrifuged at 1000 × g for 2 min at 4 °C [29]. Twenty microliter of each samples were applied to HPLC Agilent 1100 System. All analyses were performed by Kromasil ODS

column (150 mm × 4.6 mm, 5 μm, USA) at 37 °C. The mobile phase consisted of 25% acetonitrile and 5% MeOH in 0.1 M NaH_2PO_4 (pH 3.8) using an isocratic elution at 7 min. The flow rate was 1 ml/min and detection wavelength set at 220 nm [30].

2.6. Selectivity of serotonin from platelet rich plasma by serotonin-imprinted polymer (MISPE)

Hundred milligram of MIP and NIP (MAA/AA-based) polymers were conditioned with methanol (5 ml). After 1 h, 250 μl platelet samples (spiked with 15 ng/ml pure serotonin) were dissolved in DMSO (1 ml) and loaded to serotonin imprinted and non-imprinted polymer. Polymers were stirred on orbital shaker for 4 h at 500 speed/min and then centrifuged at 10,000 rpm for 5 min. Polymers were washed with MeOH:AcA (4:1) to eliminate non-specific interactions and for the elution of extracts they were washed with MeOH. All fractions (NIP and MIP applied) were collected and analyzed by HPLC. The procedure was done triplicate.

3. Results and discussion

3.1. Influence of functional monomers on adsorption properties of MIP

The nature of the template and monomers and the polymerization reaction itself determine the quality and performance of the polymer product. Moreover, the quantity and quality of the molecularly imprinted polymer recognition sites is a direct function of the mechanisms and extent the monomer–template interactions present in the pre-polymerization mixture [31]. To further testify the influence of interaction strength between the template and functional monomers on imprinting effect, the MIPs using MAA, AA, AMPSA and 4-VPy as the functional monomers were synthesized. All polymers (MIPs and NIPs) were analyzed for binding template using equilibrium binding experiments. The binding data of MIPs compared to the corresponding NIPs are given in Fig. 1. It can be seen that among the MIPs prepared using the three different types of functional monomers, only AA/MAA-based polymers show higher binding affinity for the template. The MIPs prepared with MAA, AMPSA or 4-VPy as functional monomers exhibited low binding for the template due to the absence of significant interaction between these functional monomers and the template molecules.

In general methacrylic acid was used for the preparation of synthetic imprinted polymers [32,33]. Nevertheless, excess of carboxylic groups often remain on the polymer the carboxyl group is the most commonly used hydrogen-bonding functional group in molecular imprinting. Although it can form strong ionic interactions with basic functional groups, the hydrogen-bonding ability of this functional group is not very strong in polar solvents. MIPs made in a polar solvent using carboxyl functional monomers and print molecules which could only form hydrogen bond interactions have often exhibited weak recognition so that MAA polymer has a low affinity for serotonin (polar molecule). For templates having hydrogen bonding and OH-functional groups, the combination of methacrylic acid and a basic functional monomer vinylpyridine has previously been shown to give MIPs with improved good selectivity [34]. The problem of 4-VPy/MAA polymer was the ionic interaction between these two functional monomers will compete with their interactions with serotonin and may decrease the imprinting efficiency [35,36].

AMPSA has a strong ionizing sulfonic acid group so it can be a good monomer because of the hydrophobic moiety. However, the polymer has been hydrolysed due to the presence of strong sulfonic acid. Also some coloration of the polymers was observed as a consequence of possible template oxidation [37,38]. Hence the AMPSA-based polymers did not show good affinity because of serotonin oxidation during polymerization because of AMPSA.

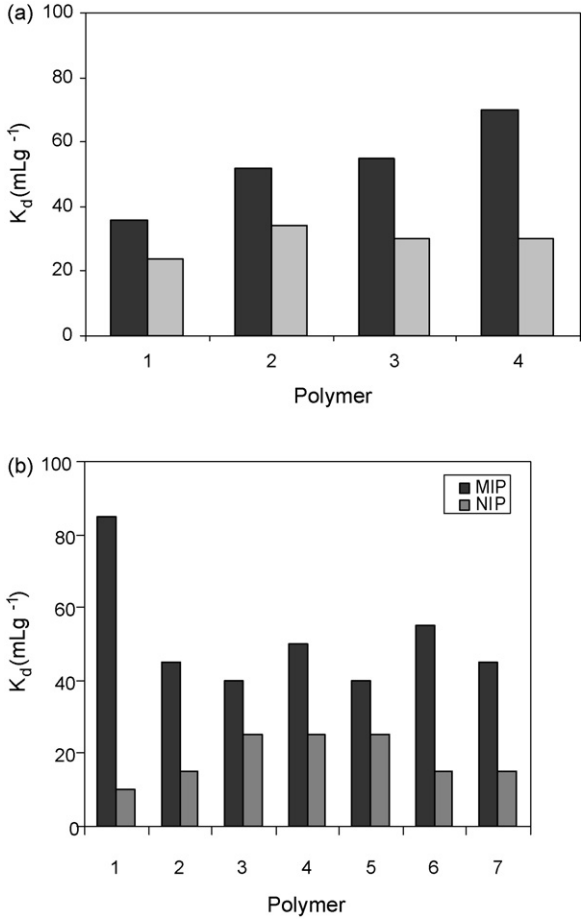

Fig. 1. K_d of serotonin on MIPs and NIPs prepared with different functional monomers under equilibrium conditions—initial concentration of serotonin: 0.5 mmol^{-1}; volume: 1 ml; adsorption time: 4 h. (a) 1: MAA/AA(THF/ACN)-P1; 2: MAA/AA(ACE/ACN)-P2; 3: MAA/AA(CHL/ACN)-P3; 4: MAA/AA(DMSO/ACN)-P4. (b) 1: AA/MAA(DMSO)-P5; 2: 4-VPy/MAA-P6; 3: 4-VPy/AMPSA-P7; 4: AA/4-VPy-P8; 5: AA/AMPSA-P9; 6: AA-P10; 7: MAA-P11.

The hydrogen bonding functional monomer acrylamide, is better than both the acidic and the basic functional monomers. It also shows that the recognition of the amide MIP is comparable with the MIP made of methacrylic acid and vinylpyridine. When only hydrogen-bonding interactions are used, amide MIPs prepared in DMSO generally have much better recognition properties than the corresponding MIPs prepared using methacrylic acid [39]. It can be concluded that AA-based polymer has showed very low affinity to the serotonin.

Methacrylic acid and acrylamide MIPs prepared by polymerizing in a relatively nonpolar organic solvent exhibit better recognition properties than a polar organic solvent. Because of this reason, the hydrogen bonding strength is very much modulated by the medium, and the functional group of the monomer associates more weakly with the template molecules in a polar solvent [40]. Whereas, the single interaction between MAA or AA was weak to form stable serotonin MAA or AA complex. Therefore, MAA/AA-based MIPs showed good recognition effect together. MAA/AA MIPs which has prepared in DMSO was the most selective polymer for serotonin. AA can made hydrogen bond and MAA can made ionic bonds with serotonin. So that in our study ACM/MAA couple was

selected as the most suitable monomers for serotonin imprinted polymer.

3.2. Influence of porogen on adsorption capacity of AA/MAA-based MIP

For non-covalent imprinting approach, the selectivity and affinity of MIPs are closely related with the polarity of the porogens used in polymerization and rebinding conditions. The affinity and selectivity of MIP was usually influenced by solvent in two aspects. On one hand, the interaction between the template and the functional monomer was influenced by porogens with different dielectric constants and hydrogen bonding capacities, leading to the different affinities and selectivities of resultant MIPs [41,42]. To evaluate the main interaction between serotonin and monomers (MAA/AA), we prepared polymers with 500 μl portions of different solvents (ACE, CHL, THF, DMSO)(according to different dielectric constant and hydrogen bonding capacity) while preparing polymer in ACN as porogen (4.5 ml) and tested the polymers binding capacity in MeOH:AcA (1%) according to imprinting factor (Table 2).

The imprinting factor was used as a measure of the strength of interaction between the template and its corresponding functional monomer and was calculated according to the following equation:

$$\text{Imprinting factor (IF)} = \frac{\text{Binding capacity on MIP}}{\text{Binding capacity on NIP}}$$

We discovered that the hydrogen-bonding capacity of the solvent is the most important factor in MAA/AA-based serotonin MIP. The interaction in DMSO probably induced the formation of selective binding sites. On the other hand, CHL, ACE and THF interacted with the amide and carboxyl groups by hydrogen bonding, and interfered with the interaction between the amide groups and the carboxyl group. As a result, it also interfered with formation of the binding sites. So that the polymers except DMSO/ACN exhibited very low affinity to serotonin.

3.3. Rebinding experiments in different solvents

The polarity of solvent influences the binding properties of polymer-based MAA/AA monomers (P5). A solvent with higher polarity competes more efficiently with the sample molecules for binding of the functional groups of the recognition sites and thus weakens the specific interaction. To distinguish from the influence of different solvents on specific and non-specific interaction during rebinding, serotonin imprinted and non-imprinted polymers were dissolved in methanol; methanol:acetic acid (1%); DMSO; DMSO:acetic acid (1%); methanol:water (9:1). The imprinting factor of MIP and NIP in different solvents was given at Table 3. As known, water has strong hydrogen binding ability and may interfere with this bonding formation of serotonin and binding sites, which leads the binding amounts of polymer to decrease. So that the lowest imprinting effect was found in methanol:water. It was previously reported that the best imprinting effect can be found in the solvent which was the polymer was prepared. Nevertheless, DMSO had a swelling effect on the polymer during rebinding experiment time may be DMSO could be deformed in pore structure so that rebinding capacity was lower than MeOH:AcA (1%) [43]. In methanol:acetic acid (1%) the best imprinting factor was taken because acetic acid reduced non-specific bindings for NIP and MIP and methanol did not interfere rebinding process.

Table 2
Binding amounts and imprinting factors of MAA/AA-based MIP toward serotonin in different solvents

Solvent	Q_{MIP}	Q_{NIP}	Imprinting factor[a]
Acetone	74.5	43.2	1.72
Choloroform	68.88	38.45	1.79
Tetrahydrofuran	40	24.0	1.66
Dimethylsulfoxide	88.94	48	1.85

[a] Imprinting factor: Q_{MIP}/Q_{NIP}; Q_{NIP} and Q_{MIP} are the amounts of serotonin at saturation binding to imprinted and non-imprinted polymer (MAA/AA), respectively (monomers, serotonin, crosslinker and initiator were dissolved in 500 μl (DMSO; THF; ACE; CHL)–4500 μl ACN was used as porogen and polymers were get by thermal polymerization. Rebinding experiments were done in MeOH:AcA (1%)).

Table 3
Binding amounts and imprinting factors of MAA/AA-based MIP toward serotonin in different rebinding solvents

Solvent	Q_{MIP}	Q_{NIP}	Imprinting factor[a]
Methanol	85.7	35.6	2.40
Methanol:acetic acid (1%)	92.4	30.4	3.03
DMSO	80.5	48	1.68
DMSO:acetic acid (1%)	76.4	44.2	1.72
Methanol:water	42.8	26.8	1.59

[a] Imprinting factor: Q_{MIP}/Q_{NIP}; Q_{NIP} and Q_{MIP} are the amounts of serotonin at saturation binding to MAA/AA (DMSO)-based serotonin imprinted and non-imprinted polymer, respectively. MAA/AA-based polymers (10 mg) were dissolved in different solvents (1 ml) methanol; methanol:acetic acid (1%); DMSO; DMSO:acetic acid (1%); methanol:water and stirred 4 h (constant serotonin concentration). After centrifugation supernatants were analyzed for finding the imprinting factor.

3.4. Scatchard analysis of AA/MAA-based serotonin MIP

The binding parameters of MIPs are mainly estimated by Scatchard analysis [44,45]. The Scatchard plot is the easiest way to see multiple classes of binding sites. The equilibrium binding experiments were carried out by varying the concentration of serotonin from 0 to 2 mmol l^{-1} in methanol:acetic acid (1%) in the presence of MAA/AA-based polymer. The obtained data were plotted according to the Scatchard model. As shown in Fig. 2 linear relationship was obtained between Q/C and Q. According to Scatchard equation K_d and Q_{max} values are 1.95 μmol l^{-1} and 19.129 μmol g^{-1}, respectively (from the graph). As a result homogenous binding sites were existed for serotonin in polymer.

3.5. Chromatographic analyses

The polymers (MIP and NIP) which were prepared with MAA/AA monomers were used for recognition of serotonin from platelets. The DMSO utilized in the loading step in order to prevent the dissolution problem of serotonin in other organic solvents. All

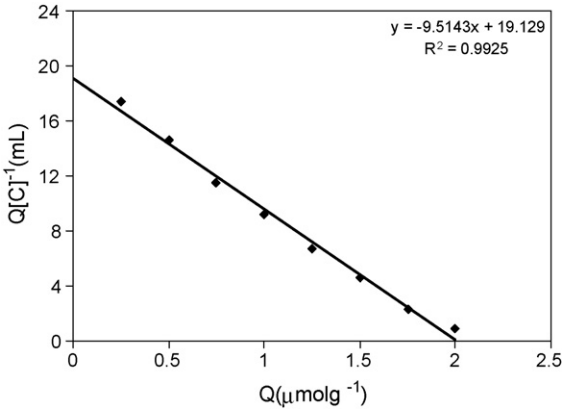

Fig. 2. Scatchard plot analysis of the binding of serotonin to imprinted polymer. Q is the amount of serotonin bound to 10 mg of MAA/AA.

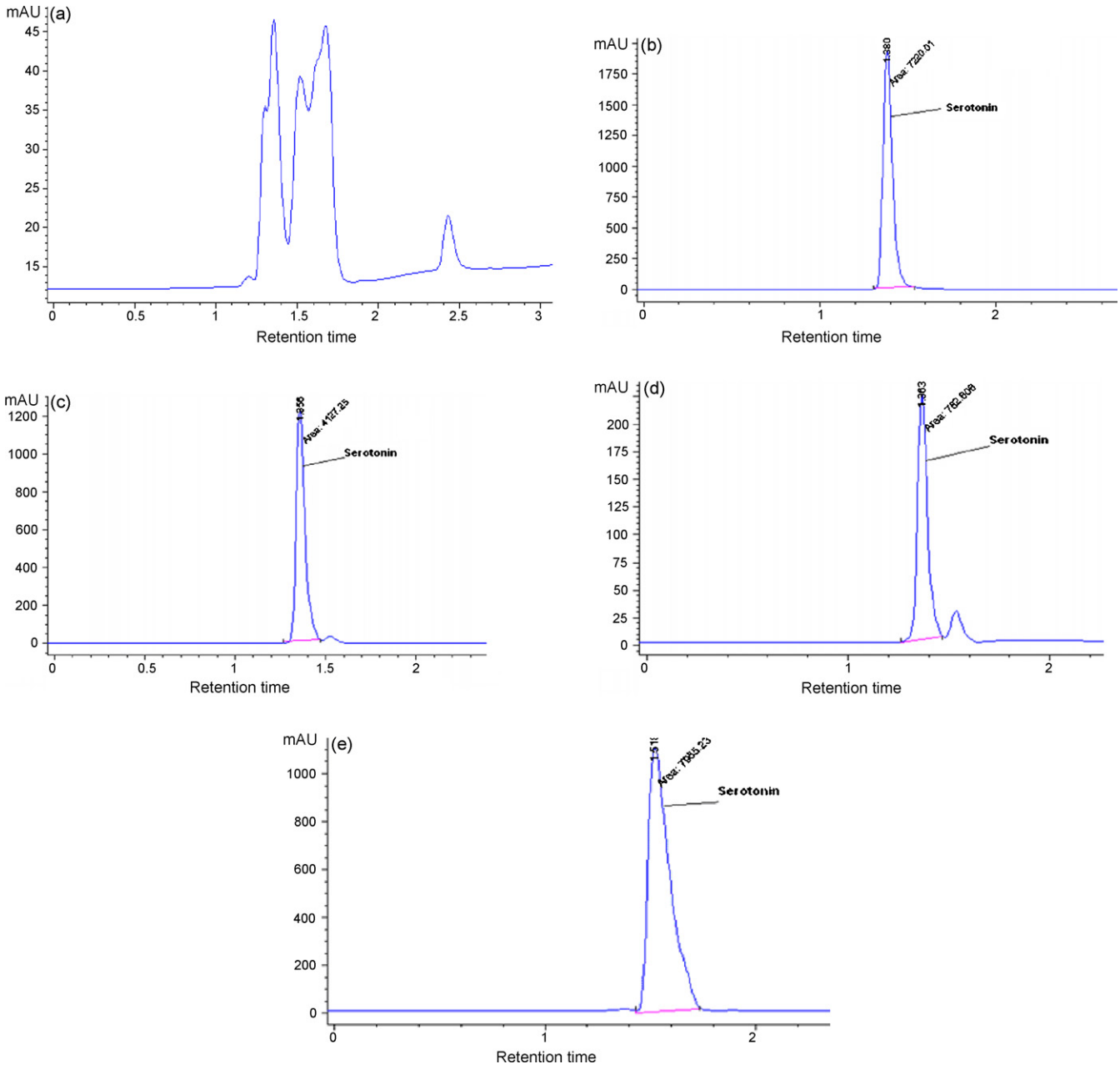

Fig. 3. Chromatograms of serotonin from the MIP and NIP: (a) direct platelet rich plasma; (b) serotonin added platelet rich plasma sample; (c) eluent of sample after NIP; (d) eluent of sample after serotonin imprinted polymer; (e) eluent after MeOH:AcA washing of MIP.

serotonin samples were retained at serotonin imprinted polymer (MIP) when using DMSO. Fifteen percent of serotonin was retained on the surface of NIP because of non-specific bindings so that optimization of the washing procedure becomes critical at that time. After testing some solutions with different polarity MeOH:AcA (4:1) was chosen (data not shown). In order to investigate the potential of MIP for the selective entrapment of target analyte from human platelet rich plasma, samples were applied to AA/MAA MIP under optimal MISPE conditions and extraction of samples were performed by MeOH:AcA (4:1). The recovery of serotonin was 70% in eluting solutions according to chromatograms (Fig. 3). The calculated responses were in agreement with the three experimental mean values. NIP and MIP was tested five times for pure serotonin 20% leakage of recognition capacity was observed.

4. Conclusion

As our knowledge, it was the first time serotonin imprinted polymer was prepared. Suedee et al. was prepared temperature sensitive DOPA imprinted polymer and was used it also for recognition of serotonin [46]. Hence this polymer's selectivity depended on temperature and pH. Our serotonin imprinted polymer can recognize serotonin without relatively to temperature or pH. By examining binding characteristics of serotonin MIPs prepared different functional monomers, porogens and changing rebinding conditions, we expected not only to understand their underlying origin of recognition properties, but also to be able to evaluate these parameters which were important in determining the ability of MIPs to recognize serotonin can be concluded that to decide on the proper polymer was important because it will be influential on non-

covalent interactions between serotonin and monomers. Another important result was to find out rebinding conditions (MeOH:AcA (1%)). The homogenous binding sites were found in polymer according to Scatchard model and the K_d and Q_{max} values are 1.95 μmol l^{-1} and 19.129 μmol g^{-1}, respectively. This study may be of instructive significance and provide a comprehensive conception for the preparation of high selective MIP for serotonin. The synthesized MAA/AA-based MIP will hopefully further make a potential use for analytical purposes, such as preparative affinity separation, solid-phase extraction. The results of platelet rich plasma applications was showed that serotonin imprinted polymer can be used as a sorbent because it can be used several times and no need any special storage conditions.

Acknowledgement

This work was supported by Ege University Research Foundation 2003FEN024.

References

[1] S. Wei, B. Mizaikoff, J. Sep. Sci. 30 (2007) 1794.
[2] G. Macsi, F. Aulenta, V. Crescenzi, J. Appl. Polym. Sci. 83 (2002) 2660.
[3] S.A. Piletsky, T.L. Panasyuk, E.V. Piletskaya, I.A. Nicholls, M. Ulbricht, J. Membr. Sci. 157 (1999) 263.
[4] D. Stevenson, Trends Anal. Chem. 18 (1999) 154.
[5] K. Haupt, K. Mosbach, Chem. Rev. 100 (2000) 2495.
[6] G. Wulff, Chem. Rev. 102 (2002) 1.
[7] C.C. Hwang, W.C. Lee, J. Chromatogr. B. 765 (2001) 45.
[8] P.T. Vallano, V.T. Remcho, J. Chromatogr. A. 887 (2000) 125.
[9] G. Wulff, Pure Appl. Chem. 54 (1982) 2093.
[10] R. Arshady, K. Mosbach, Macromol. Chem. Phys. 182 (1981) 687.
[11] K.M.A. Welch, J.S. Meyer, S. Kwant, J. Neurochem. 19 (1972) 1079.
[12] G.M. Anderson, J.G. Young, Life Sci. 28 (1981) 507.
[13] G.M. Anderson, Adv. Exp. Med. Biol. 294 (1991) 51.
[14] I.P. Kema, E.G.E. de Vries, F.A.J. Muskiet, J. Chromatogr. B. 747 (2000) 33.
[15] B.A. Patel, M. Arundell, K.H. Parker, M.S. Yeoman, D. O'Hare, J. Chromatogr. B. 818 (2005) 269.
[16] T. Sasaki, T. Fukushima, M. Ohishi, T. Toyo'oka, Biomed. Chromatogr. 22 (2008) 888.
[17] S. Parrot, L. Lambes-Senas, S. Sentenac, L. Denoray, B. Renaud, J. Chromatogr. B. 850 (2007) 303.
[18] T. Yoshitake, K. Fujino, J. Kehr, J. Ishida, H. Nohta, M. Yamaguchi, Anal. Biochem. 312 (2003) 125.
[19] K. Takezawa, M. Tsumada, N. Wtanobe, K. Imai, Anal. Chem. 72 (2000) 4009.
[20] S. Umeda, G.W. Staglino, M.R. Borenstein, R.B. Raffa, J. Pharmacol. Toxicol. Meth. 51 (2005) 73.
[21] P. Lemaine, R.K. Adosraku, Phytochem. Anal. 13 (2002) 333.
[22] R. Meatherall, P. Sharma, J. Anal. Toxicol. 27 (2003) 313.
[23] S.D. Brandt, S. Freeman, I.A. Fleet, P. Mcgagh, J.F. Alder, Analyst 130 (2005) 330.
[24] P. Baumann, N. Morasimhachari, J. Chromatogr. 86 (1973) 269.
[25] N. Kato, T. Kojima, S. Yoshiyagawa, H. Ohta, A. Tariba, H. Nishimura, K. Hayakawa, J. Chromatogr. A. 1145 (2007) 229.
[26] S.D. Paredes, M.P. Terron, J. Cubero, V. Valero, C. Barriga, R.J. Reiter, A.B. Rodriques, Chronobiol. Int. 23 (2006) 779.
[27] M. Fouassier, E. Bourqerette, F. Libert, C. Poupland, A. Marquez-Verdier, J. Thromb. Haemost 4 (2006) 1136.
[28] A. Chattopedhyay, R. Rukmini, S. Mukherjee, Biophys. J. 71 (1996) 1952.
[29] M.T. Morgadinho, C.A.F. Ribeiro, T.R.A. Macedo, Biomed. Chromatogr. 18 (2004) 739.
[30] R. Xiao, O. Beck, P. Hjemdahl, Scand. J. Clin. Lab. Invest. 58 (1998) 505.
[31] K. Karim, F. Breton, R. Rouillon, E.V. Piletska, A. Guerreiro, I. Chianella, S.A. Piletsky, Adv. Drug Del. Rev. 57 (2005) 1795.
[32] A. Kugimiya, H. Takei, Anal. Chim. Acta 564 (2006) 179.
[33] Z. Shi-an, H. Kelong, L. Qifu, X. Haiyan, J. Central South Uni. Technol. 12 (2005) 102.
[34] C. Baggiani, L. Anfossi, C. Giovannoli, C. Tozzi, Talanta 62 (2004) 1029.
[35] R. Hsieh, H. Tsai, M. Syu, Biomaterials 27 (2006) 2083.
[36] S.A. Piletsky, H.S. Andersson, I.A. Nicholls, J. Mol. Recogn. 11 (1998) 94.
[37] E. Piletska, S. Piletsky, K. Karim, E. Terpetschnig, A. Turner, Anal. Chim. Acta 504 (2004) 179.
[38] H.S. Andersson, O. Ramstrom, J. Mol. Recogn. 11 (1998) 103.
[39] C. Yu, K. Mosbach, J. Mol. Recogn. 11 (1998) 69.
[40] C. Yu, K. Mosbach, J. Org. Chem. 62 (1997) 4057.
[41] J. Wang, R. Guo, J. Chen, Q. Zhang, X. Liang, Anal. Chim. Acta 540 (2005) 307.
[42] L. Wu, K. Zhu, M. Zhao, Y. Li, Anal. Chim. Acta 549 (2005) 39.
[43] Y. Lv, Z. Lin, W. Feng, T. Tan, Chromatographia 66 (2007) 339.
[44] E. Caroa, R.M. Marce, P.A.G. Cormack, D.C. Sherrington, F. Borrulla, J. Chromatogr. B. 813 (2004) 137.
[45] J.A. García-Calzón, M.E. Díaz-García, Sens. Actuat. B: Chem. 123 (2007) 1180.
[46] R. Suedee, V. Seechamnanturakit, B. Canyuk, C. Ovatlarnporn, G.P. Martin, J. Chromatogr. A. 1114 (2006) 239.

Talanta 76 (2008) 978–987

Contents lists available at ScienceDirect

Talanta

journal homepage: www.elsevier.com/locate/talanta

Review

Ion mobility spectrometers with doped gases

Jarosław Puton*, Marjaana Nousiainen, Mika Sillanpää

Laboratory of Applied Environmental Chemistry, Department of Environmental Sciences, University of Kuopio, Patteristonkatu 1, FI-50100 Mikkeli, Finland

ARTICLE INFO

Article history:
Received 25 February 2008
Received in revised form 15 May 2008
Accepted 21 May 2008
Available online 29 May 2008

Keywords:
Ion–molecule reactions
Ion mobility spectrometry
Alternate reactant ions
Detection of hazardous materials

ABSTRACT

Ion mobility spectrometry (IMS) is an instrumental technique used successfully for the detection of wide range of organic compounds in the gas phase. In this paper, advances in using special substances called dopants for gases flowing through IMS detectors are reviewed. These substances influence the ion–molecule chemistry in sample ionisation region as well as change conditions for the drift of ions. Improved selectivity and sensitivity of detection can be obtained by the use of dopants. In some cases, especially when measurements are conducted in the presence of different substances disturbing detection, the use of dopants is indispensable.

The theory of the function of dopants is based on the knowledge of ion–molecule reactions. Fundamental information about these reactions is presented here. Mechanisms of changing the composition of ions produced in reactant section of IMS detector are explained on this basis.

The most commonly used dopants are acetone and ammonia for positive mode and chloride for negative mode IMS. Other substances, such as higher ketones, organophosphorous compounds or methyl salicylate are used for special purposes and are selected for given analytical problem. Particular examples for the application of these substances are described.

Contents

* Corresponding author. Tel.: +358 15 3556236; fax: +358 15 3556513.
E-mail address: jaroslaw.puton@uku.fi (J. Puton).

0039-9140/$ – see front matter © 2008 Elsevier B.V. All rights reserved.
doi:10.1016/j.talanta.2008.05.031

1. Introduction

Ion mobility spectrometry (IMS) is an instrumental technique for chemical analysis, an object of many research works for almost 40 years and a method that has been systematically used in practice for 20 years. With regard to the physical phenomena taking place in IMS instruments, these devices can be classified to the group of ionisation detectors working under ambient pressure. As distinct from other instruments in this group, IMS detectors make the identification of the analyte possible. Different substances in IMS are distinguished on the basis of differences in the velocity of ions, which are created by different compounds and are moving in electric field in the gas [1]. This velocity is proportional to the mobility coefficient which depends on the mass, shape and dimensions of ions.

The principle of operation of IMS detector is similar to that of time of flight mass spectrometer. The main difference between these measurement techniques is that in mass spectrometry ions are moving in the vacuum and in IMS in the gas. In the classic IMS detector (Fig. 1) one can see two parts, which fulfil different functions. The first part is the reactant section in which, as a result of complicated and diverse processes, ions are produced. Small portions of ions are periodically introduced to the drift section, which constitutes the second part of the detector. In the drift section, the separation of ionic products occurs. Ions with greater mobility reach the collector electrode earlier than heavier ions having lower mobility. The current induced in the ion collector is an output signal from IMS detector. Its time dependence is called drift time spectrum. With regard to electric field direction it is possible to measure spectra of positive or negative ions. In this connection, positive and negative modes of IMS detector operation are distinguished. Numerous different constructions of IMS detectors are known. In Fig. 1, IMS detector with bidirectional gas flow is shown, but in many detectors gas flow is unidirectional, i.e., ions are moving in opposite direction to gas flow in reactant and drift sections. Detailed description of the principle of operation and the analysis of phenomena occurring in detectors can be found in new [1] and older [2] monographs on IMS as well as in review articles [3,4]. The practical applications of IMS are inseparably connected with the detection of hazardous materials and chapters about IMS can be also found in books devoted to related analytical techniques [5,6].

The quality of information obtained from drift time spectrum depends on constructional features of the detector and on working parameters like temperature, gas flows, values of potentials and electric fields [7,8]. All these parameters can be optimised for obtaining high sensitivity and good selectivity of the measurements. However, effective detection depends always on ion production processes, i.e., ion–molecule reactions taking place in the reactant section of IMS detector. These processes can be controlled in some degree by selecting the suitable temperature, but much greater possibilities to influence the reaction course is to intentionally select reaction components by introducing suitable substances to streams of gas flowing through the detector. These substances are commonly named dopants and can be added to the carrier gas only or also to the drift gas.

If no sample is introduced to the reactant section of spectrometer, the so-called reactant ions are produced as a result of primary ionisation and some ion–molecule reactions. They are characteristic for given carrier gas. The reactant ions constitute the "reservoir" of electric charge, which can be transferred for ionisation of analyte molecules. When carrier gas contains the dopant, the reactant ions are built from dopant molecules or their fragments. They are different from ions existing in clean carrier gas. Such ions are named alternative reactant ions or have the names of specific ion products, for example acetone or chlorine reactant ions. The importance of using the alternative reactant ions lies in the fact that they interact with analyte and interfering substances different from "normal" reactant ions. Three important reasons for using dopants are:

- It is possible that alternative reactant ions can interact with analyte but not with interfering substances. As a result of such situation, molecules of interfering substance do not create ions and their peaks do not appear in drift time spectrum.
- Drift times for ions observed in gas in the presence of dopant are different in comparison with drift times for clean carrier gas. This effect can be used for peak shifting and for avoiding the overlap of peaks.
- Ion products created with alternative ions can be more stable. The drift time spectra are more readable and contain more analytically useful information.

2. Sample ionisation in IMS detectors

The processes of creation of sample ions in the reaction section of IMS detectors consist of complex and diverse cycles of ion–molecule reactions. Very frequently, exact course of these reactions is unknown. In particular, there are no precise data concerning kinetics and thermodynamics of ion creation processes. The course of ionisation processes can also depend on the kind of ionisation method used in IMS detector. Compositions of ions produced in reactant section are different for radioionisation, photoionisation and corona discharge sources.

In this chapter, only the most important theoretical and experimental results will be presented, which allow the understanding of basic qualitative and quantitative aspects of using dopants. The production of positive and negative sample ions takes place in different processes and for this reason, phenomena occurring during creation of ions of both polarities will be discussed separately.

2.1. Ionisation of chemical compounds in positive mode

In the air or nitrogen containing small admixture of water vapour, hydronium ions $H^+(H_2O)_n$, named also hydrated protons or protonated water, are dominant reactant ions [1]. The processes of formation of these ions are very fast. Therefore the most probable way to ionise the analyte or other molecules is through interactions with such reactant ions. If compound A, which molecules have ability for attachment of proton, is introduced to the gas containing such ions, the following ion–molecule reaction is possible:

$$\begin{aligned} &H^+(H_2O)_n + A \leftrightarrow AH^+(H_2O)_n^* \\ &AH^+(H_2O)_n^* + Z \leftrightarrow AH^+(H_2O)_{n-1} + H_2O + Z \end{aligned} \quad (1)$$

Reaction described by Eq. (1) is classified as proton transfer reaction though, as one can see from this notation, hydrated proton or ligand is transferred. As a result of reaction, more than one water molecule can be detached from ion. Substance A in Eq. (1) can be an analyte which is to be detected, intentionally introduced admixture or interfering compound which may make the detection process difficult. Directly after the attachment of molecule A, ionic product in excited state is created. Excitation energy is transferred to the third body Z, which most often is a neutral molecule of the gas.

The characteristic feature of the ion–molecule reactions leading to the production of positive ions is that the final product of reaction, here protonated molecule A, can participate in next reaction with neutral molecule of the same or another substance:

$$AH^+(H_2O)_n + B \leftrightarrow ABH^+(H_2O)_{n-1} + H_2O \quad (2)$$

If in the above equation A = B, the reaction taking place is dimerisation, and its final product is symmetrical dimer $A_2H^+(H_2O)_m$.

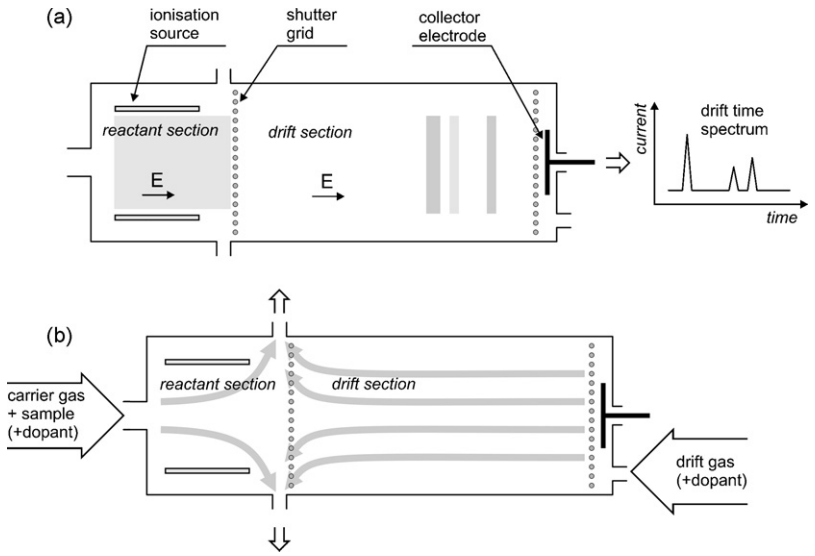

Fig. 1. Schematic of the IMS detector. (a) Principle of operation. (b) Gas flows in the detector.

Otherwise final product is specified as proton bound cluster. Very comprehensible description of kinetics and thermodynamics of proton transfer reactions is presented in the work by Stone [9], and analysis of processes connected with creation and disintegration of complexes with proton binding is described in the article by Ewing et al. [10].

Reaction (1) determines transformation efficiency of molecules of a given compound into ionic products. The parameter, which defines the probability of reaction, is proton affinity (PA). This parameter is related to energetic effect of proton transfer reaction. The experiments carried out in order to study chemical ionisation under atmospheric pressure (APCI) [11–13] indicated that two basic groups of compounds participating in reaction (1) exist. The first one consists of compounds with higher PA. Typical members of first group are ammonia, amines and organophosphorous compounds (OPCs). For these substances reaction (1) takes place practically only in forward direction. The yield of reaction is described by so-called collision rate constant. Its value is in the order of 10^{-9} cm^3/s, and the produced ions are relatively stable. The concentration of reaction product depends on kinetics of the process. It means that all analyte molecules, which have possibility for effective interaction with reactant ions, will be transformed into ionic form. A good description for this case is the statement that quantity of product is "kinetically controlled" [12]. The second group of substances are compounds with lower PA. The compounds, which belong to second group, are ketones, alcohols and many other organic compounds. For these compounds, the reversal of the reaction of proton attachment is significant. The reaction equilibrium constant defines the concentration of ionic reaction products and processes of ion production are "thermodynamically controlled". The dependence of efficiency of chemical ionisation on PA is schematically presented in Fig. 2.

Despite the fact that above description is very simplified, it can be stated that in IMS reactions are conducted by kinetic and thermodynamic mechanisms. The main factor, which complicates the course of reactions, is the hydration of ions. This phenomenon has two characteristics. The first one is the dependence between equilibrium number of water molecules in ionic cluster and PA of protonated molecule. As a rule, the number of water molecules is lower for a molecule of higher PA [9]. The second feature of hydration is that ions having greater degree of hydration participate in proton transfer reactions not as readily as ions surrounded by small number of water molecules. Number of water molecules participating in creation of clusters depends on humidity of the gas and therefore sensitivity of detection is often lower for wet gases.

The presence of two substances (A and B) with different PA values in the carrier gas does not mean that only ions of substance with higher PA give contribution for drift time spectrum. If PA differences are not very significant, the proton transfer reactions can take place in accordance with the following equation:

$$AH^+ + B \leftrightarrow BH^+ + A \quad (3)$$

The concentrations of ion products AH^+ and BH^+ can be determined in this case on the basis of equilibrium constant [14].

Besides proton transfer reactions the complexation plays great role in positive ion formation. This creation mechanism of ions is particularly important when differences in PA between reaction partners are not too high. Other important processes observed in positive mode of IMS are charge transfer or fragmentation of ionic products.

2.2. Production of the negative ions

Ionisation processes of chemical substances in negative mode are far less systematically investigated than in positive mode IMS although there are various classes of chemicals that favour forma-

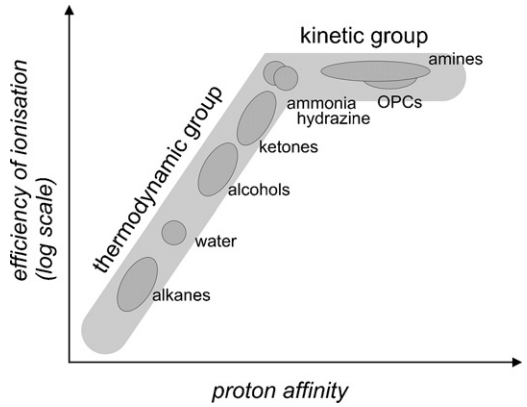

Fig. 2. Schematic relationship between proton affinity and efficiency of ionisation (based on [11]).

Table 1
Dopants used in IMS

Dopant (IMS mode)	Mechanism of dopant's interaction with sample	Detected analytes	References
Acetone (positive)	Control of proton transfer	Organophosphorous compounds (OPCs)	[24–28]
Dimethyl sulfoxide (positive)	Control of proton transfer	OPCs	[25,26]
Nonylamine (positive)	Control of proton transfer	Biogenic amines	[29,30]
Nicotine amide (positive)	Control of proton transfer	Narcotics	[31–33]
Ammonia (positive)	Control of proton transfer, clusterisation	OPCs, narcotics, pyridine, formaldehyde, dinitroalkanes	[34–44]
OPCs (positive)	Control of proton transfer, clusterisation	Ammonia	[46–49]
Higher ketones (positive)	Clusterisation, control of proton transfer	Hydrazines, ammonia, alkanoamines	[34,51,52]
Halogens (negative)	Production of stable adducts	Explosives	[53–60]
Methyl salicylate (negative)	Selective creation of clusters	Acid gases	[63,64]
Naphthalene (positive)	Charge exchange after selective photoionisation	Narcotics	[40]
(*S*)-(+)-2-Butanol (positive)	Changing of collision cross-section for ions moving in drift section	Stereoisomers	[66]

tion of negative ions and are therefore best to be detected on the basis of drift time spectrum of negative ions. The creation of negative ions differs considerably from positive ions production. For clean carrier gases, nitrogen or air, the dominant positive reactant ions are, as it was mentioned above, hydrated protons. On the contrary in negative mode, the formation of reactant ions is much more complicated. If the carrier gas is pure nitrogen, the carriers of negative charge are electrons. They can ionise different chemical compounds with appropriately high electron affinity. The probability of such reactions is usually highest for thermal electrons and depends on electron energy. In air, very diverse reactant ions are produced. In the classic work by Spangler and Collins [15], the reactant ions in air were identified mainly as O_2^- and $(H_2O)O_2^-$. In addition, an occurrence of Cl^-, $(H_2O)OH^-$ and NO_2^- was stated. Very detailed results of investigation of ion composition were presented by Hayhurst et al. [16] and Watts [17]. Also in these studies, hydrated oxygen ions O_2^- and $O_2^-{\cdot}O_2$ were found to be the most abundant ionic species. Moreover, significant quantities of CO_3^- and $O_2^-{\cdot}CO_2$ ions and trace amount of NO_2^- were observed. These latter ions have low reactivity because of high electron affinity of nitrous oxide. It causes serious problems especially when corona discharge is used as ionisation method since it produces nitrogen oxides [18].

When air is used as carrier gas, the ionisation of neutral molecules takes place through reactions with the oxygen ions via charge transfer (4), adduct formation (5), or proton abstraction (6)

$$O_2^-(H_2O)_n + A \leftrightarrow A^- + nH_2O + O_2 \quad (4)$$

$$O_2^-(H_2O)_n + A \leftrightarrow AO_2^- + nH_2O \quad (5)$$

$$O_2^-(H_2O)_n + A \leftrightarrow (A-H)^- + \text{neutrals} \quad (6)$$

that are often followed by the formation of hydrated product ions by clusterisation with water molecules, resulting mainly $A^-(H_2O)_n$ and $(A-1)^-(H_2O)_n$ [1,3]. In reactions with electrons in pure nitrogen, the most common processes are dissociative (7) and associative (8) attachments [2]:

$$e^- + A \rightarrow (A_1) + (A_2)^- \quad (7)$$

$$e^- + A \rightarrow A^- \quad (8)$$

Reaction product type depends not only on properties of analyte molecule but also on the nature of negative charge carrier. A well-known example illustrating this phenomenon is ionisation of trinitrotoluene (TNT). If free thermal electrons are the source of the charge, the reaction follows Eq. (8) and reaction products are TNT^- ions [19]. By contrast the reaction between TNT molecules and oxygen ions creates the short living intermediate product $(TNT{\cdot}O_2)^-$, which easily dissociates producing $(TNT-H)^-$ ions as in Eq. (6) [20].

3. Applications of dopants

Chemical compounds added to the carrier and sometimes also to the drift gas in IMS should be selected according to the polarity of detected ions, specific properties of analyte molecules and other components of sample and, in some cases, method of gas ionisation. In positive mode, the most often used dopants are acetone and ammonia whereas for the detection in negative mode the most popular ones are halogens. Examples of using dopants are presented in this chapter.

Dopants can be classified according to different criteria. From theoretical point of view, the most important criterion is mechanism of ion molecule reactions that take place when sample ions are produced. There are two problems in classifying dopants in this way. The first one is that often two different phenomena determine the final composition of ions produced in doped gases. The second difficulty lies in lack of full data about mechanism of interactions between dopant, reactant ions and sample molecules. In many cases we can only guess how ionisation processes are proceeding. Distinguishing of dopants according to their effect is often also ambiguous. Properly chosen dopant can, for example, cut off competition from potential interfering substances and simultaneously shift analyte peak to the position where it does not overlap with reactant ion or another peak, which is normally present in the spectrum. For these reasons, description of the use of dopant was divided here only to three subchapters, i.e., to problems of doping in positive and negative mode as well as to specific applications. Shortened information about all discussed dopants is included in Table 1.

3.1. Dopants for positive mode of IMS operation

The most common phenomenon utilized in detection with dopants in positive IMS mode is dependence between PA and probability of sample ionisation. The explanation of mechanism of selectivity improvement with dopant requires examination of ion–molecule reactions in which analyte, dopant and at least one interfering substance participate. All these components can take part in the simple proton transfer reaction (1) as well as in reaction (2), where creation of dimers and asymmetric complexes is possible. Because of the complexity of reactions in the gas phase in IMS detector, their modelling and theoretical estimation of detection sensitivity is very difficult. The most common way to explain the importance of using dopants is that ionisation of a given chemical compound is possible in practice only when PA of this compound is greater than PA of the molecule creating reactant ion. Thus if reactant ion is formed from molecule with relatively high PA, only compounds with greater PA will be ionised by it via proton transfer reactions. Potential interfering substances with lower PA would not participate in the creation of drift time spectrum. The mecha-

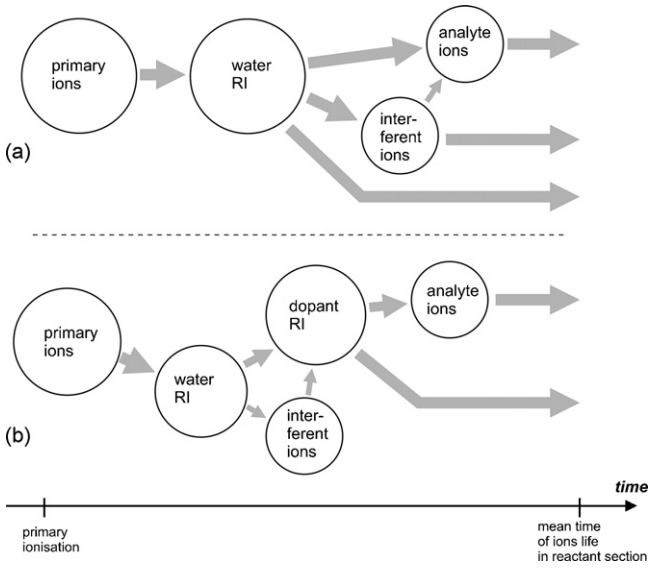

Fig. 3. Processes of charge transfer during ionisation in positive mode without (a) and with (b) dopant.

nism of ionisation in the gas containing an analyte and interfering substance hampering detection is shown in Fig. 3. Typical history of electric charge is presented here from the moment of primary ionisation to the end of "ions' life" in reactant section of IMS detector. In the case when dopant is not present in the carrier gas, the charge is distributed between analyte and interfering substance ions (Fig. 3a). Typically for practical application the interferent has PA lower than analyte. It can mean that the concentration of interferent ions is determined by thermodynamics of the reaction and the concentration of analyte ions by kinetics of the reaction. Due to the difference in proton affinities, proton transfer reactions from interferent ions to analyte can also take place. The presence of admixture of dopant in the carrier gas effects in creation of dopant ions. If concentration of dopant is relatively high and its PA is greater than that of interferent but smaller than that of analyte, ionisation can take place according to Fig. 3b. If the concentration of dopant is much higher than the concentration of water, ionisation mechanisms of dopant without participation of hydronium may also be possible. The ionised dopant molecule cannot ionise the interferent but is capable to ionise the analyte. For this reason we usually observe ions of both analyte and dopant in the drift time spectrum. The dopant ions could be considered as new reagent ions. Since the ions of interfering substance do not participate in the creation of drift time spectrum, an improvement of the selectivity of detection can be achieved.

PA of compounds participating in ionisation processes in positive mode is always very important parameter but in many cases structure of sample ions are defined by complexation. This way of ionisation is quite popular and also useful in practice.

3.1.1. Acetone

Using acetone as a dopant for gases in IMS detectors is connected with applying these instruments for detection of OPCs with high PA. Acetone belongs to the group of compounds with medium PA (194 kcal/mol [21]) and therefore it can be used for the elimination of interferences from such organic substances as hydrocarbons, alcohols, esters and other which can often be found in atmosphere. As a result of reactions of acetone with hydronium ions at medium temperatures, monomer and dimer acetone ions are formed. The characteristic feature of these ionic species is that monomer ions are hydrated and, in practice, dimers are devoid of water molecules [22]. Nitrogen molecules can also be present in acetone ionic clusters. In ppm range of acetone concentration, only symmetric dimer ions $(CH_3COCH_3)_2H^+$ can be found. Further increase of acetone concentration effects on production of ionic clusters having greater masses and dimensions [23].

When acetone dimer collides with analyte molecule A having high PA, exchange of one acetone molecule in dimer by an analyte molecule occurs and an asymmetric complex is created [24]:

$$(CH_3COCH_3)_2H^+ + A \rightarrow (CH_3COCH_3)AH^+ + CH_3COCH_3 \quad (9)$$

This reaction can be followed by collision of complex ion with analyte molecule leading to the production of dimer A_2H^+. The product of reaction (9) as well as dimer A_2H^+ can be further hydrated. The following course of ionisation results in drift time spectrum where one can observe acetone dimer $(CH_3COCH_3)_2H^+$, which can be treated as reactant ion, asymmetric complex $(CH_3COCH_3)AH^+$ and analyte dimer A_2H^+. In the spectra obtained with acetone reactant ions the first two peaks are shifted to greater drift times when compared to the spectra measured with air or nitrogen reactant gas. The drift time of the analyte dimer does not change.

Full evaluation of doping efficiency is possible when one or more substances interfering detection are present in the sample, which is introduced into the spectrometer. Acetone was used in such experiments and its effectiveness was compared with that of other compounds applied as dopants. Results of comparative measurements were presented in the work by Eiceman et al., who investigated the influence of dopants on the detection of mixture containing 19 different OPCs [25]. A large number of substances (45 compounds) belonging to the group of volatile organic compounds (VOCs) was chosen as the set of interfering agents. Dopants used in the measurements were acetone and dimethyl sulfoxide (DMSO). It was clearly shown that the use of alternative reactant ions significantly improves selectivity of detection. Also an example of quantitative results was presented. Calibration dependences, i.e., relations between mass of sample and spectrometer's signal, were nearly the same for hydronium reactant ions and DMSO dopant.

Very interesting comparative investigations were carried out for a set of three ion mobility spectrometers working with different reagent gases [26]. In the first spectrometer clean air was used as carrier and drift gas, in the second acetone was the dopant and in the third alternative reactant ions were created on the basis of DMSO. The tests were performed in the laboratory where students were working with organic compounds. The results of tests were very convincing. Applying the dopant with suitable PA made it possible to reduce intensity of the signal originating from compounds with low affinity nearly to zero.

Investigations of a wide group of dopants, including also acetone, were performed in order to optimise conditions for the detection of organophosphorus pesticide (dimethioate) in the presence of interfering ethane and three aromatic hydrocarbons [27,28]. Beside acetone the compounds used for creating reactant ions were ammonia, ethanol, methanol and ether. It was found that good detection results can be achieved when two dopants, for example ammonia and acetone, are used simultaneously. Quantitative aspects of detection carried out with doped gases were also subjects of investigation. It was shown that optimal level of dopant concentration exists for which the analyte peak is the most intense. The dependence of peak amplitude on dopant concentration is rather strong. From the presented data one can see that the peak amplitude obtained with optimal concentration is several times (5–10) greater than that with commonly used excessive amount of dopant [27]. This concentration dependence was explained to result from complicated sample ionisation processes.

3.1.2. Nonylamine and nicotinamide

High PA of amines makes it possible to apply IMS detectors for investigation of some biological samples. Amines, which are products of microbiological or enzymatic processes, can be indicators of freshness of food and also human diseases. The composition of biological material is complex and therefore dopants are very useful in detection of specific gaseous substances emitted by samples. *n*-Nonylamine was found as an effective compound for creating reagent ions for biogenic amines detection. This dopant was added to carrier gas with concentration in the ppm range in the method proposed by Karpas et al. for the diagnosis of vaginal infections on the basis of biogenic amines detection [29]. *n*-Nonylamine is characterised by very high PA (219 kcal/mol) and therefore only strong bases (like other amines) can form ions when this dopant is present in the carrier gas. Mobility of reactant ions produced by *n*-nonylamine is considerably lower than the mobility of biogenic amines and problems of peak overlapping can be eliminated. The method, which is dedicated here for medical purposes, can be applied also in the determination of meat freshness [30].

An effective dopant used for the detection of narcotics is nicotinamide [31]. A research carried out for the set of narcotics have shown that for hydronium reactant ions drift time spectra contain many peaks originating from the fragmentation of analyte molecules. Introduction of nicotinamide to carrier gas reduces the number of peaks and only ions produced by large drug molecules are observed [32]. Nicotinamide dopant is used in commercial instruments designated not only for drug analysis but also for the detection of chemical warfare agents and toxic industrial chemicals [33].

3.1.3. Ammonia

Ammonia is very often used dopant in IMS studies. Its PA (204 kcal/mol) is greater than that of acetone and therefore it can be used for blocking the ionisation of most organic compounds. The peak of positive ammonia ions is normally observed in the drift time spectra in "clean" air or nitrogen. The mobility of these ions at 100 °C is about 20% greater than the mobility of hydronium. Ammonia ions, named often ammonium, are created in the process of proton transfer from hydronium to ammonia molecule [34]:

$$(H_2O)_nH^+ + NH_3 \rightarrow (H_2O)_{n-x}NH_4{}^+ + xH_2O \quad (10)$$

Small concentration of ammonia existing naturally in the air or nitrogen is sufficient for producing ammonium ions whose peak in drift time spectrum is few times smaller than the main peak of hydronium ions. In increased concentrations of ammonia, the amplitude of ammonium peak will increase at the cost of hydronium peak. When concentration of ammonia is high enough, dimerisation process occurs:

$$(H_2O)_nNH_4{}^+ + NH_3 \rightarrow (H_2O)_{n-y}(NH_4{}^+)_2 + yH_2O \quad (11)$$

In measurements carried out with simple ion mobility spectrometers one peak created by ammonium monomer as well as dimer ions is observed. If resolving power of the spectrometer is appropriately high (in order of 50 or higher), two separate peaks exist in the drift time spectrum [35]. The unique feature of such spectrum is that dimer ions are "faster" than monomer because monomer creates clusters with higher number of water molecules than dimer.

Ammonia dimers were confirmed by IMS coupled with MS in the study of ions that were produced in ammonia-doped air [36]. It was also shown that for some compounds ion clusters with structure $[A_2NH_4]^+$are created. These complex ions are named ammonium bound dimers [37]. Creation of $[A_2NH_4]^+$ ions does not occur by proton transfer reaction but as a result of cluster formation.

The effectiveness of doping with ammonia was shown for the first time in the work by Kim et al. [38]. They investigated the possibility of detection of pyridine in the presence of different solvents. It was evidenced that the used IMS system was insensitive to benzene, hexane, cyclohexane and pentane when ammonia was added to carrier gas. The presence of these solvents did not disturb the process of pyridine detection. This work is most probably the oldest published article concerning the intentional doping of gases in IMS.

An important group of compounds, which can be detected with IMS with gases doped by ammonia, are narcotics. The studies on morphine and noscapine showed that their detection limits can be achieved at the level of 0.1 ng [39]. The method was demonstrated to be applicable also for the simultaneous quantitative analysis of morphine and noscapine. Ions A^+ and $[A-(H_2O)]^+$ were suggested to be the product ions of morphine. However, these suppositions were not confirmed by IMS–MS experiments. Very high efficiency of ammonia as dopant in the detection of cocaine has also been shown [40]. The measurements were conducted in the presence of few interfering substances. Though the concentrations of interferences were up to thousand times greater than the concentration of analyte, it was possible to observe the characteristic cocaine peak in the drift time spectra.

Ammonia is successfully used as a dopant in commercial instruments for detection of chemical warfare agents [41]. Besides their high sensitivity, an important precondition for such instruments is possibility to eliminate the risk of false alarms, which can be triggered by different chemicals present in air. Most important potential interferents are solvents, components of fuels or products of burning. The use of ammonia as dopant prevents in significant degree a signal generation by compounds of lower PA than an analyte.

In addition to using ammonia as dopant for elimination of the peaks created by compounds with lower PA, it is also possible to use it for shifting the analyte and reactant ion peaks in drift time spectrum. Such procedure was applied to optimise conditions for the detection of formaldehyde [42]. When clean air was used as carrier gas, peaks corresponding to formaldehyde overlapped those of reactant ions in IMS spectra. For ammonia-doped carrier gas, reactant ions peak was placed for shorter drift time. Simultaneously in the presence of dopant, the ion complexes created by ammonia and formaldehyde had greater drift times than protonated formaldehyde observed in air.

The use of ammonia as dopant can lead to simplification of drift time spectrum through elimination of particular ions in the gas phase. Such phenomenon was observed during investigations of the detection of dinitroalkanes [43,44]. When the ionisation was based on water reactant ion chemistry, the ionisation products were unstable and dissociated after ionisation. In the spectra obtained for ammonium reagent ions, dissociation products were not observed.

3.1.4. Organophosphorous dopants for ammonia detection

High PA of ammonia makes it possible to detect and quantitatively analyse traces of ammonia in air with high sensitivity by IMS technology. Estimation of ammonia concentration can be performed by measuring the amplitude or determining the area of peaks corresponding to ammonia which are fastest positive ions when nitrogen or air is used as carrier gas [35,45]. This method is, however, connected with the risk of disturbances caused by some chemical compounds present in the air. For example, the presence of hydrocarbons can influence the intensity of ammonium peaks. This kind of interferences can be eliminated by using suitable doping, for example with OPCs that have high PA values [46]. One can say that in comparison with applications described previously, the roles of analyte and dopant were exchanged here. In the proposed

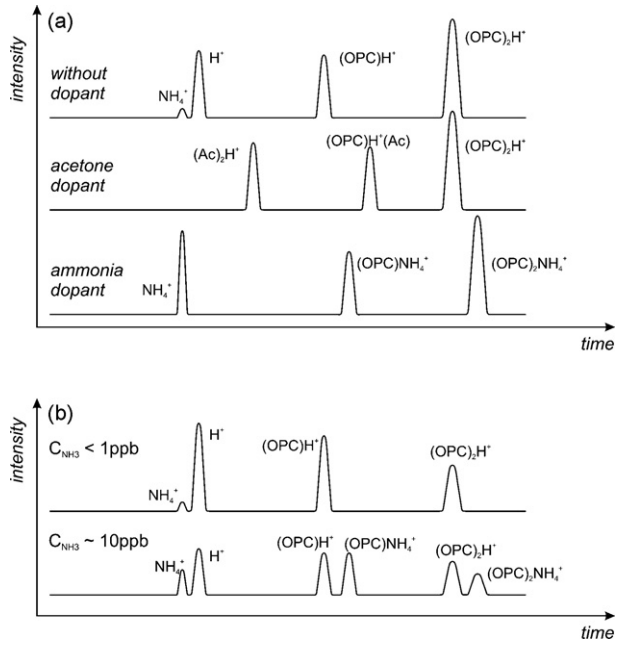

Fig. 4. Schematic of drift time spectra. (a) Detection of organophosphorous compound without dopant and in the presence of acetone and ammonia dopants. (b) Detection of ammonia in spectrometer with carrier gas doped by OPC.

method dopant has greater PA than analyte. It should be noted that in the detection of OPC ammonia concentration should be high. On the contrary, in the detection of ammonia the concentration of organophosphorous dopant should be sufficiently high and stable. For such conditions hydronium reactant ions $H^+(H_2O)_k$ as well as monomer $(OPC)H^+(H_2O)_m$ and dimer $(OPC)_2H^+(H_2O)_n$ dopant ions are observed in the drift time spectrum. Introduction of ammonia results usually in three additional peaks. The first one is the "fast" peak of $NH_3(H_2O)_n$ ions and two next peaks correspond to complex ions with drift times greater than monomer and dimer of dopant [47]. The quantitative measurements are based on the analysis of complex ions peaks.

Typical configurations of the peaks in drift time spectra in the schematic form are shown in Fig. 4. These spectra illustrate three different cases. In Fig. 4a, the detection of OPC is presented in the absence and presence of two most important dopants, i.e., acetone and ammonia. Second graph (Fig. 4b) illustrates detection of ammonia when OPC is used as dopant. Graphs were prepared on the basis of our own measurement results and other data [35,46,47].

Ion mobility spectrometer with dimethyl methanphosphonate dopant was used for environmental measurements of ammonia concentration in air in Florida [48]. The instrument had measurement range from 0 to 100 ppb and detection limit equal to 0.1 ppb. Values of measured ammonia concentration were in the range of few ppb. It is possible also to measure the concentration of ammonia in water. In the method, which was used in practice [49], an analyte was introduced to reactant section of IMS through silicone membrane. External side of this membrane was in contact with the stream of water containing ammonia. The analyte passing through the membrane by diffusion was brought into reactant section by carrier gas. The detection limit for this method was determined to be 1.2 mg/l. The dopant used in this work was not specified but was defined to belong to organophosphonates [49]. The trial of using ketones as dopants for the detection of ammonia in the presence of propylene was also carried out [50]. This procedure appeared ineffective because of low sensitivity. Obtained detection limit was only in the order of 1 ppm and the measurements were finally conducted by using traditional method based on the intensity determination of the main peak of ammonia ions in the air.

3.1.5. Higher ketons

Hydrazine and its derivatives are substances with high PA and therefore they can successfully be detected with IMS. These compounds are used as main components of rocket fuel. Simultaneously, they are strong oxidants and constitute serious threat for human health. In the beginning of 1990s, studies were carried out in order to find a method for the monitoring of hydrazine concentration levels on the board of space shuttle. The use of IMS with air as carrier and drift gas was impossible because of too high risk of disturbances in the presence of VOCs in atmosphere inside the shuttle. Extensive investigations for selecting dopant for this analytical problem were conducted [51]. It turned out that acetone is unsuitable dopant because ion complexes created with hydrazine and also ions produced by many potential interfering substances have mobilities very close to acetone dimer. Finally, 5-nonanone was selected as optimal dopant which, at appropriate concentration, creates proton bound dimers $(5\text{-non})_2H^+$. As a result of interaction of such ions with analyte, complex ions $(5\text{-non})AH^+$ and $(5\text{-non})_2AH^+$ where A is the molecule of ammonia, hydrazine or monomethylhydrazine, were created.

The detection of hydrazine and its derivatives was carried out in measurement conditions where both carrier and drift gases were doped. It was found that drift times for particular ions strongly depend on the concentration of dopant. This dependence was explained as the result of multiple changes of the number of ketone molecules attached to nitrogen base during the movement of ions along the drift section [51]. Very detailed investigations of the formation processes of complex ions in the mixtures containing ammonia or hydrazines and ketons were recently described by Bollan et al. [34]. One of the most interesting results in this work is that when 5-nonanone is used as dopant, the drift times of ammonia, hydrazine, monomethylhydrazine and unsymmetrical dimethylhydrazine increase with decreasing mass of molecule that had created the core of the ion. Bollan et al. have shown that this relationship results from the number of ketone molecules, which can be attached to the protonated nitrogen in the core of the complex ion. This number is equal to the number of hydrogen atoms bound to protonated nitrogen. In the case of ammonia, the number of bound ketones is highest (equal to 4) whereas in the case of unsymmetrical dimethylhydrazine only 1 ketone was observed to be bound in the complex. Therefore complexes built on the basis of smaller core ions have greater dimensions and masses than those consisting of larger core ions.

Another group of compounds which can be detected by IMS with doped gases are alkanoamines. They are used as absorbers for removing carbon dioxide from the air in closed rooms and are characterised by high reactivity and toxicity as hydrazines. The detection of alkanoamines with ketone-doped gases by IMS has been studied by Gan and Corino [52]. Clear separation of peaks corresponding to analyte ions and interference substances was not achieved when acetone was used as dopant. In this analytical problem, 4-heptanone was found to be an effective dopant for improvement of detection effectiveness. However, as in the case of hydrazines, complex reaction products containing protonated bases and ketones were unstable. The investigations of stability of ionic complexes were carried out with collision-induced dissociation (CID) method. It was shown that stabilities of particular ionic alkanoamine products increased in the following order:

$$(4-\text{hept})_2AH^+ \ll (4-\text{hept})AH^+ < A_2H^+ < AH^+ \quad (12)$$

It should be mentioned, however, that the content of given product depends on the concentrations of analyte and dopant. When

dopant is added into carrier and drift gases, three most stable products create the characteristic peak of analyte.

Generally, the structure of product ions is much more complicated when doping with higher ketones is applied in comparison with the use of acetone reactant ions. Higher ketones have also greater PA than acetone, which makes possible larger variety of different interactions between analyte and dopant. Particularly favoured process is clusterisation. Products of such reactions are less stable than products generated when acetone dopant is used.

3.2. Dopants for negative mode of IMS operation

3.2.1. Halide reactant ions

The most often detected group of compounds with IMS instruments in negative mode are explosives. The main problem in the detection of different explosives is that they easily dissociate during the ionisation process (see Eq. (7)). As result of this process, NO_2^- or NO_3^- are typically created. They do not produce peaks specific to given chemical compound in drift time spectrum, and their drift times are similar to normal reactant ions existing for negative mode in air. The molecular ions of explosive material can be created as adducts of explosive molecules and NO_2^- or NO_3^- ions. Produced clusters are relatively instable and disintegrate during the drift of ions. In many cases the stability can be improved by doping with halogens, particularly with chloride [53,54].

Halide ions can be generated via dissociative electron capture from halogenated organic compounds [55]. Electron capture reaction produces monoatomic halide ions, which can be hydrated. When carrier gas introduced to the reactant section of IMS detector contains admixture of molecular chloride, generation of molecular ions Cl_2^- and also more complicated complexes is possible [56].

The detection of ethylene glycol dinitrate (EGDN), one of the main components of dynamite, using IMS and dichloromethane-doped carrier gas was described in the often quoted article of Proctor and Todd [57]. Drift time spectra presented in this work made it evident that doping improves detection specificity. This results from the fact that the stability of $(EDGN)Cl^-$ ions is higher than that of $(EDGN)NO_3^-$. The detection of EDGN has been also described as an example of situation where dopant increases sensitivity of detection [1]. There are two possible reasons, which can cause the raise of signal generated by characteristic ions due to dopant introduction. The first one is connected with mechanism of ionisation. When air is used as carrier gas, creation of characteristic ions takes place in two-stage process. As it was mentioned above, firstly NO_3^- ions are produced by means of charge transfer connected with dissociation. These ions play a role of reactant ions in the formation of $(EDGN)NO_3^-$ adducts. The efficiency of adduct production is determined by concentration of NO_3^- ions. If the analyte concentration is not very high the concentration of NO_3^- ions is low, too. On the contrary, when air is doped with chlorinated hydrocarbon, the concentration of reactant ions (Cl^-) is high and the production of characteristic molecular ion, in this case $(EDGN)Cl^-$, is more effective. The second reason for the increase in the detection sensitivity is greater stability of product ions in the presence of dopant. The consequence of this fact is greater quantity of characteristic ions reaching the collector electrode of IMS detector. This leads to an increase of the amplitude of characteristic peak of molecular ion, i.e., rise of detection sensitivity. The course of sample ionisation processes without and with chlorine dopant is schematically illustrated in Fig. 5.

More detailed results of EGDN detection are described by Lawrence and Neudorfl [58]. It was shown that the detection of EGDN at a concentration level as low as 10 ppt is possible when chloride is used as dopant. Unfortunately, the measurements cannot be carried out at higher temperatures because of fast disin-

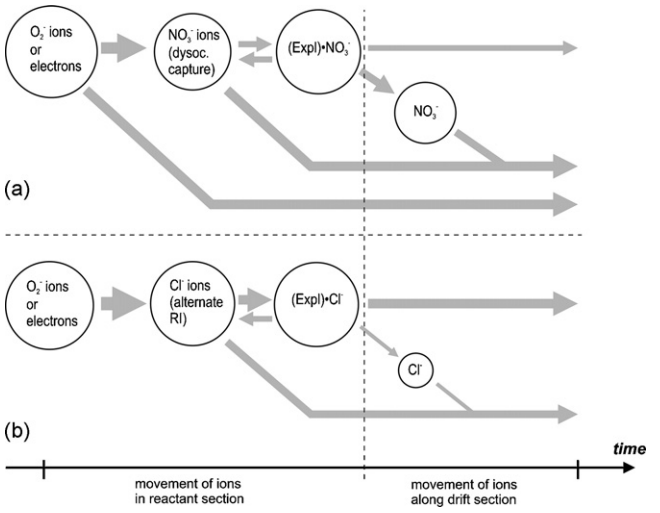

Fig. 5. Processes of explosive sample ionisation in negative mode without dopant (a) and using chlorine reagent gas (b).

tegration of $(EDGN)Cl^-$ complexes above 100 °C. It is very similar when nitroglycerine (NG) is detected in the presence of chloride dopant. The $(NG)NO_2^-$ ions were shown to be the most abundant product ions at low dopant concentrations whereas $(NG)Cl^-$ are the major sample ions when quantity of dopant introduced to the sample is high [58]. The stability of ion complexes consisting of chlorine ion and nitrocompound molecule was investigated for dinitroalkanes [59]. It was stated, that the structure of nitrocompound plays an important role in improving the stability of the complex. The stability depends on $C–NO_2$ dipoles alignment and the number of hydrogen atoms connected to carbon atoms for which nitro groups are bonded.

The ionisation of analyte with halogen reactant ions has also interesting quantitative aspects. If the carrier gas is nitrogen and halogenated hydrocarbon is used as dopant, the creation of halogen ions occurs via dissociative electron capture. The rate of such reaction is defined by electron attachment constant, which depends on the type of chemical compound used as dopant and on the average electron energy. In conditions existing in the reactant region of IMS detector, electron attachment constants for different halogenated compounds differ as much as 8 orders of magnitude [60]. Consequently, it is necessary to use different amount of particular halogenated compound for obtaining the same quantity of halogen reactant ions. Efficiency of sample ionisation is proportional to this quantity.

Chlorine ions are not the only possible alternative reactant ions in the detection of explosives. It was shown [61] that it is possible to carry out the detection of explosives using oxygen, chloride or bromide reactant ions. There is no universal dopant optimal for all analytical situations. This statement is in agreement with the results of Klassen et al. [62]. Besides halide reactant ions, they also investigated the possibility of using admixtures of SO_2 and NO_2. It was demonstrated that these substances are good dopants for detection of TNT in wet air.

3.2.2. Methyl salicylate

Another important group of compounds which can be analysed in negative mode of IMS are acid and halogen gases, i.e., hydrogen fluoride, hydrogen chloride, chlorine, chlorine dioxide and some other. These compounds posses high electron affinity and create negative ions but the mobilities of ions are very close to normal negative reactant ions present in the air. The method of acid gases measurement consists in the use of methyl salicylate (MS) as

dopant. Adducts $(MS)O_2^-$ have lower mobility than ions produced by simple acid gases. Concentration of dopant is so high that in the absence of analytes only the peak originating from $(MS)O_2^-$ ions peak can be observed in the drift time spectrum. Introduction of acid gas to reactant region of IMS causes appearance of peak for shorter drift time [63,64].

3.3. Special applications of dopants

Doping of gases in IMS detectors effects significantly on the shape of drift time spectrum. The presence and position of particular peaks in the spectrum depend on the type of dopant. The quantity of analytically useful information can be increased by measurements in the presence of dopant and with pure carrier gas. Baim and Hill demonstrated such approach with halogenated compounds in negative mode [65]. The measurements were performed using pure nitrogen and nitrogen with small addition of oxygen as carrier gas. In the presence of pure nitrogen, the ionisation took place through dissociative electron capture. By contrast in the presence of small concentration of oxygen the analyte was ionised by dissociative charge transfer. The efficiency of ionisation was shown to depend on chemical properties of analyte and the method of ionisation and therefore it is possible to select optimal condition for the detection of a given group of compounds. The idea of using two sample ionisation methods was described by Kunz et al. [40]. They proposed parallel detection using two different IMS instruments. The first IMS system uses a typical radioactive isotope 63-Ni as ionisation source and carrier gas doped by ammonia. The second detector works with multiphoton ionisation of reactant ions followed by charge exchange (MPI-CE). In this method, UV radiation is used for the ionisation of chemical compounds, which are introduced into carrier gas as dopants. Naphthalene is particularly useful for this purpose because of its small ionisation potential (IP) as well as low PA. Ionised naphthalene molecules are reactant ions, which can interact with analyte molecules via charge exchange. Sample ionisation methods in both detectors are different. In the detector doped with ammonia, the possibility of ionisation is defined by PA whereas in the detector doped with naphthalene the critical parameter is IP. There is no correlation between the PA and IP values and therefore the data obtained from both detectors contained independent information.

One of the most interesting examples of using admixtures to gases in IMS is chiral ion separation [66]. This method makes it possible to distinguish enantiomers by means of chiral modifier in the drift gas. Enantiomers (stereoisomers) are nonsuperimposable isomers, which are mirror images of each other. The drift of enantiomeric ions of the same chemical compound occurs without any differences in "normal" drift gas. However, if a chiral dopant is added to the drift gas, its interaction with isomers differs influencing on the product ion drift time. Investigations carried out for 10 pairs of enantiomers for drift gas doped with (*S*)-(+)-2-butanol showed that in some cases separation of isomers is possible but the obtained differences between reduced mobility coefficients for both enantiomers are very small.

4. Conclusions

Analytical performances of ion mobility spectrometers are determined by the phenomena occurring in the receptor part of IMS detector, i.e., in the reactant section. Both sensitivity and selectivity of measurements depend on the processes taking place mostly in this space. Traditionally used carrier gases, nitrogen and air do not allow any significant effect on the course of sample ionisation. Addition of suitable chemical compound into carrier gas enables optimisation of detection. Such method is particularly effective when IMS instrument is used for environmental measurements or monitoring technological processes where analyte is in the complex mixture of different compounds, i.e., potential interferences.

In detection performed in positive mode, the role of dopants usually consists of fixing the reference level, which is equivalent to the PA of chemical compounds creating alternative reactant ions. The most common way to explain the sample ionisation mechanism is based on the assumption that proton transfer reaction proceeds towards increasing PA of molecules, which are charge carriers in ionic form. Certainly, such mechanism is useful to effectively prevent ionisation of interferences. However, both in positive and negative mode, the creation of clusters and adducts is quite often a determining step in ionisation in the presence of dopant. The stability of such complexes, depending on the type of analyte and dopant, is often not high. Therefore the quality of spectrum can be improved by adding dopant admixture not only for carrier but also for drift gas.

The availability of information on doping for IMS is limited. Especially there is lack of data concerning quantitative aspects of doping. With small exceptions, the experimental data in hitherto published reports do not give answers to questions on the influence of dopant on detection sensitivity and optimal concentration of dopant. There is also lack of works concerning mathematical modelling of complicated sample ionisation processes and the estimation of dependence between concentrations of sample components and signal. The subsequent studies will provide theoretical analysis of selected problems of dopant usage as well as experimental material for verification of theoretical models.

Acknowledgements

This work has been supported by a Marie Curie Transfer of Knowledge Fellowship of the European Communitýs Sixth Framework Program under contract number MTKD-CT-2006-042637. MN also acknowledges the financial support of The Academy of Finland. The authors thank Anshy Plamthottathill Oonittan for language revision.

References

[1] G.A. Eiceman, Z. Karpas, Ion Mobility Spectrometry, 2nd ed., CRC Press/Taylor & Francis, Boca Raton, FL, 2005.
[2] T.W. Carr, Plasma Chromatography, Plenum Press, New York, 1984.
[3] H. Borsdorf, G.A. Eiceman, Appl. Spectrosc. Rev. 41 (2006) 323.
[4] J. Stach, J.I. Baumbach, Int. J. Ion Mobility Spectrom. 5 (2002) 1.
[5] Y. Sun, K.Y. Ong, Detection Technologies for Chemical Warfare Agents and Toxic Vapors, CRC Press LLC, Boca Raton, FL, 2005.
[6] R.W. Woodfin, Trace Chemical Sensing of Explosives, John Wiley & Sons, Inc., Hoboken, NJ, 2007.
[7] C. Wu, W.E. Steiner, P.S. Tornatore, L.M. Matz, W.F. Siems, D.A. Atkinson, H.H. Hill Jr., Talanta 57 (2002) 123.
[8] G.A. Eiceman, E.G. Nazarov, J.E. Rodriguez, J.A. Stone, Rev. Sci. Instrum. 72 (2001) 3610.
[9] J.A. Stone, Int. J. Ion Mobility Spectrom. 5 (2002) 19.
[10] R.G. Ewing, G.A. Eiceman, J.A. Stone, Int. J. Mass Spectrom. 193 (1999) 57.
[11] J. Sunner, G. Nicol, P. Kebarle, Anal. Chem. 60 (1988) 1300.
[12] J. Sunner, M.G. Ikonomou, P. Kebarle, Anal. Chem. 60 (1988) 1308.
[13] G. Nicol, J. Sunner, P. Kebarle, Int. J. Mass Spectrom. Ion Proc. 84 (1988) 135.
[14] M. Tabrizchi, S. Shooshtari, J. Chem. Thermodyn. 35 (2003) 863.
[15] G.E. Spangler, C.I. Collins, Anal. Chem. 47 (1975) 393.
[16] C.J. Hayhurst, P. Watts, A. Wilders, Int. J. Mass Spectrom. Ion Proc. 121 (1992) 127.
[17] P. Watts, Int. J. Mass Spectrom. Ion Proc. 121 (1992) 141.
[18] M. Tabrizchi, T. Khayamian, N. Taj, Rev. Sci. Instrum. 71 (2000) 2321.
[19] G.E. Spangler, P.A. Lawless, Anal. Chem. 50 (1978) 884.
[20] K.A. Daum, D.A. Atkinson, R.G. Ewing, Int. J. Mass Spectrom. 214 (2002) 257.
[21] E.P.L. Hunter, S.G. Lias, J. Phys. Chem. Ref. Data 27 (1998) 413.
[22] P. Watts, Anal. Proc. 28 (1991) 328.
[23] J.M. Mäkelä, V. Jokinen, T. Mattila, A. Ukkonen, J. Keskinen, J. Aerosol Sci. 27 (1996) 175.
[24] G.A. Eiceman, J.A. Stone, Anal. Chem. 76 (2004) 392A.

[25] G.A. Eiceman, Y.-F. Wang, L. Garcia-Gonzalez, C.S. Harden, D.B. Shoff, Anal. Chim. Acta 306 (1995) 21.
[26] Q. Meng, Z. Karpas, G.A. Eiceman, Int. J. Environ. Anal. Chem. 61 (1995) 81.
[27] Y.T. Long, Y. Guo, M.Q. Lu, Anal. Chem. 70 (1998) 347.
[28] Y.T. Long, Y. Guo, M.Q. Lu, Rev. Anal. Chem. 19 (2000) 179.
[29] Z. Karpas, W. Chaim, R. Gdalevsky, B. Tilman, A. Lorber, Anal. Chim. Acta 474 (2002) 115.
[30] Z. Karpas, B. Tilman, R. Gdalevsky, A. Lorber, Anal. Chim. Acta 463 (2002) 155.
[31] A. Miki, M. Katagi, H. Tsuchihashi, J. Health Sci. 49 (2003) 325.
[32] J.E. Parmeter, G.A. Eiceman, J.E. Rodriguez, Trace detection of narcotics using a preconcentrator/ion mobility spectrometer system, U.S. Department of Justice, NIJ Report 602-00, April 2001.
[33] IMS and FTIR for gas detection and identification, Application Brief AB-071, Smith Detection, 2004.
[34] H.R. Bollan, J.A. Stone, J.L. Brokenshire, J.E. Rodriguez, G.A. Eiceman, J. Am. Soc. Mass Spectrom. 18 (2007) 940.
[35] J.W. Leonhardt, S. Bockisch, H. Miessner, Drift time spectra of ammonia, IUT GmbH, Berlin, 2007, unpublished results.
[36] C.A. Hill, C.L.P. Thomas, Analyst 128 (2003) 55.
[37] C.A. Hill, C.L.P. Thomas, Analyst 130 (2005) 1155.
[38] S.H. Kim, F.W. Karasek, S. Rokushika, Anal. Chem. 50 (1978) 152.
[39] T. Khayamian, M. Tabrizchi, M.T. Jafari, Talanta 69 (2006) 795.
[40] R.R. Kunz, W.F. Dinatale, P. Becotte-Haigh, Int. J. Mass Spectrom. 226 (2003) 379.
[41] T. Arthen-Engeland, S. Meyer-Plath, Proceedings of the Ninth International Chemical Weapons Demilitarization Conference, Luneburg, Germany, 2006.
[42] J.W. Leonhardt, J. Radioanal. Nucl. Chem. 257 (2003) 133.
[43] W.A. Munro, C.L.P. Thomas, M.L. Langford, Anal. Chim. Acta 374 (1998) 253.
[44] W.A. Munro, C.L.P. Thomas, M.L. Langford, Anal. Chim. Acta 375 (1998) 49.
[45] A.-K. Viitanen, E. Saukko, H. Junninen, S. Rantanen, J.M. Mäkelä, P. Keronen, H.-C. Hansson, K. Rosma, M. Marjamäki, M. Kulmala, J. Keskinen, In 16th International Conference on Ion Mobility Spectrometry, Mikkeli, Finland, 2007.
[46] A.T. Bacon, US Patent 5,234,838 (1993).
[47] H. Bensch, J. Leonhardt, R. Rudolph, In 13th International Conference on Ion Mobility Spectrometry, Gatlinburg, TN, 2004.
[48] L. Myles, T.P. Meyers, L. Robinson, Atmos. Environ. 40 (2006) 5745.
[49] A.R.M. Przybylko, C.L.P. Thomas, P.J. Anstice, P.R. Fielden, J. Bronkenshire, F. Irons, Anal. Chim. Acta 331 (1995) 77.
[50] J.H. Cross, T.F. Limero, J.L. Lane, F. Wang, Talanta 45 (1997) 19.
[51] G.A. Eiceman, M.R. Salazar, M.R. Rodriguez, T.F. Limero, S.W. Beck, J.H. Cross, R. Young, J.T. James, Anal. Chem. 65 (1995) 1090.
[52] T.H. Gan, G. Corino, Anal. Chem. 72 (2000) 807.
[53] G.E. Spangler, J.P. Carrico, D.N. Campbell, J. Test. Eval. 13 (1985) 234.
[54] R.G. Ewing, D.A. Atkinson, G.A. Eiceman, G.J. Ewing, Talanta 54 (2001) 515.
[55] F.W. Karasek, O.S. Tatone, D.W. Denney, J. Chromatogr. 87 (1973) 137.
[56] V. Bocos-Bintintan, A. Brittain, C.L.P. Thomas, Analyst 126 (2001) 1539.
[57] C.J. Proctor, J.F.J. Todd, Anal. Chem. 56 (1984) 1794.
[58] A.H. Lawrence, P. Neudorfl, Anal. Chem. 60 (1988) 104.
[59] A.H. Lawrence, P. Neudorfl, J.A. Stone, Int. J. Mass Spectrom. 209 (2001) 185.
[60] K.A. Daum, D.A. Atkinson, R.G. Ewing, Talanta 55 (2001) 491.
[61] K.A. Daum, D.A. Atkinson, R.G. Ewing, W.B. Knighton, E.P. Grimsrud, Talanta 54 (2001) 299.
[62] S.E. Klassen, P. Rodacy, R. Silva, Sandia Report SAND97-2165, Sandia National Laboratories, Albuquerque, NM, 1997.
[63] A.T. Bacon, J. Reategui, R.C. Getz, US Patent 5,032,721 (1991).
[64] T. Bacon, K. Webber, Acid and Halogen Gas Monitoring Utilizing Ion Mobility Spectroscopy (IMS), Technical Note, Molecular Analytics, 2005.
[65] M.A. Baim, H.H. Hill Jr., J. High Res. Chromatogr. Chromatogr. Commun. 6 (1983) 4.
[66] P. Dwivedi, C. Wu, L.M. Matz, B.H. Clowers, W.F. Siems, H.H. Hill Jr., Anal. Chem. 78 (2006) 8200.

Talanta 76 (2008) 1119–1123

Contents lists available at ScienceDirect

Talanta

journal homepage: www.elsevier.com/locate/talanta

Analysis of recognition of fructose by imprinted polymers

Rajagopal Rajkumar[a,b], Axel Warsinke[a], Helmuth Möhwald[c], Frieder W. Scheller[a,b], Martin Katterle[b,*]

[a] Analytical Biochemistry, Potsdam University, D-14476 Potsdam-Golm, Germany
[b] Fraunhofer Institute for Biomedical Engineering (IBMT), D-14476 Potsdam-Golm, Germany
[c] Max Planck Institute of Colloids and Interfaces, D-14476 Potsdam-Golm, Germany

ARTICLE INFO

Article history:
Received 10 January 2008
Received in revised form 12 May 2008
Accepted 14 May 2008
Available online 23 May 2008

Keywords:
MIP sensor
Thermistor
Covalent imprinting
Fructose
Cross-reactivity
TRIM

ABSTRACT

Binding of fructose to the fructose imprinted polymer (MIP(Frc)) and pinacol imprinted polymer (control) were studied both in batch and a flow through mode. The influence of the cross-linkers ethylene glycol dimethacrylate (EDMA) and trimethylolpropane trimethacrylate (TRIM) on the binding characteristics was analysed. TRIM cross-linked MIPs showed a lower (unspecific) binding for the control polymer (pinacol imprinted) and higher binding of fructose as compared with the EDMA-MIPs. Furthermore interactions of a TRIM cross-linked molecularly imprinted polymer against fructose and its corresponding template were studied using a thermistor. Label-free detection of fructose was realised in the range of 0.5–10 mM. The difference in enthalpy changes between specific binding of fructose to boronic acid moieties of the MIP and non-specific binding to the matrix leads to an 18-fold higher apparent imprinting factor than batch binding studies. Cross-reactivity studies using MIP sensor indicate that the interaction of fructose to MIP generates higher signal than disaccharides. The studies described in this paper demonstrate the potential of direct characterisation of molecular binding events.

1. Introduction

Molecular imprinting is a method for preparing polymers possessing microcavities having a predetermined selectivity for an analyte of interest. Based on template–monomer interactions MIPs have been synthesised using covalent, non-covalent and semi-covalent approaches [1–5].

MIPs towards carbohydrates and their derivatives were synthesised making use of hydrogen or covalent bonds between functional monomers and templates. These MIPs were found to be suitable for chromatography and sensing. Aromatic boronic acids have the unique property of forming reversible complexes with *cis*-diols, e.g., in sugars. The resulting cyclic diesters can be prepared either in organic solvents or in aqueous alkaline media. Apart from aryl boronic acids, metal complexes and non-covalent interactions were successfully used for preparing MIPs targeting carbohydrates and their derivatives [6,7].

In this paper the covalent approach was employed to prepare a MIP against fructose. Since typically 80–90% of the MIP matrix consists of cross-linker and the template–monomer content is usually between 5 and 10% the cross-linking agent will have an influence on the binding properties of the polymers [8–10]. For this reason we compared MIPs prepared by using two different cross-linkers.

As MIPs are robust and can be re-used, their application in sensing is promising and they are used as recognition elements with transducers like Quartz crystal microbalance, field effect transistors, surface plasmon resonance, and calorimeters [11–37]. MIP based fructose sensors use fluorescence or electrochemical methods for signal generation [38,39]. In this paper, we investigate the MIP–analyte interactions by using a flow calorimeter whereby label-free detection of fructose is demonstrated. Further the cross-reactivity was evaluated using the MIP thermistor.

2. Experimental

2.1. Chemicals and reagents

D-Fructose was purchased from Merck, Germany. D-Sucrose, D-maltose was obtained from Serva Feinbiochemica, Germany. Nitrobenzene, trimethylolpropane trimethacrylate (TRIM) and 4-vinylphenyl boronic acid were purchased from Aldrich, Germany. Anthrone, 2,2′-azobisisobutyronitrile (AIBN), dioxane and ethylene glycol dimethacrylate (EDMA) were obtained from Fluka, HPLC grade methanol (MeOH) was purchased from Carl Roth, Germany.

* Corresponding author. Tel.: +49 331 58187 503; fax: +49 331 58187 299.
E-mail address: Martin.Katterle@ibmt.fraunhofer.de (M. Katterle).

0039-9140/$ – see front matter © 2008 Elsevier B.V. All rights reserved.
doi:10.1016/j.talanta.2008.05.022

2.2. MIP synthesis

MIPs were synthesised according to Wulff's covalent approach described earlier [40]. To prepare the MIP(Frc) 1 g of β-D-fructopyranose 2,3;4,5-bis-*O*-((4-vinylphenyl)boronate), 1 ml of toluene:acetonitrile (1:1), 26.5 mmol TRIM or 45.3 mmol of EDMA and 3.98 mmol of AIBN were added, mixed well and purged with nitrogen for 10 min. Free radical polymerisation was initiated and carried out at 65 °C for 48 h. Temperature was increased to 95 °C and kept constant for the next 24 h for the final curing of polymer. In analogy the control polymer (pinacol as template) and the MIP(Fru-Val) were prepared by applying 1 g of the respective 4-vinylphenyl boronate esters. Therefore the control polymer contains almost 70% more and the MIP(Fru-Val) has 20% less binding sites as fructose imprinted polymer. The polymer monoliths obtained were crushed, ground in a ball mill (Retsch type S 100, Germany) for 10 min at 400 rpm and wet sieved (mesh 25 μm) using acetone to remove the fines. For template removal polymer particles were washed with 500 ml of water/methanol (1:1, v/v) and the final washing was done with 100 ml methanol.

2.3. Batch experiments

To 10 mg of polymer 1 ml of fructose (0.1–5 mM) in 100 mM sodium carbonate buffer containing 10% MeOH (pH 11.4) was added and incubated at 26 °C. After 12 h the MIP suspension was centrifuged at 13,000 rpm for 10 min and the supernatant was used to determine the concentration of unbound fructose. Two hundred microliters of supernatant and 1800 μl of anthrone tryptophan reagent was added, mixed well and incubated for 1 h at 65 °C. The absorbance was measured at 540 nm with a Shimadzu 160-A UV–vis spectrophotometer. The fructose concentrations in the supernatants were calculated using a fructose calibration curve [41]. All measurements were performed as triplicates and the error bars indicate the derived standard deviation.

2.4. Thermometric measurements

Thermometric measurements were carried out in an enzyme thermistor developed by Mosbach and Danielsson [42]. Hundred milligrams of the imprinted or control polymer was packed in a 500 μl plastic column. The MIP column was placed in an insulated thermistor block. Analyte solution was pumped into the thermistor block using a peristaltic pump for 10 min followed by neat buffer (100 mM sodium carbonate pH 11.4, 10% MeOH) for the next 10 min. A constant flow rate of 1 ml/min was used in all experiments. All measurements were performed as triplicates and the error bars indicate the derived standard deviation. Thermometric experiments with control polymer was done in the same way as described for imprinted polymer. All analytes (fructose and disaccharides) were dissolved in 100 mM carbonate buffer, pH 11.4, 10% MeOH before the start of the experiments and used immediately.

3. Results and discussion

3.1. Batch binding studies

Batch binding studies were carried out for different time intervals by incubating the MIP suspension with 0.1 mM fructose in 100 mM carbonate buffer/pH 11.4 containing 10% methanol to determine the time to reach the equilibrium. Fig. 1 shows that the equilibrium was reached after 2 h. For further binding studies an incubation period of 2 h was therefore considered as sufficient.

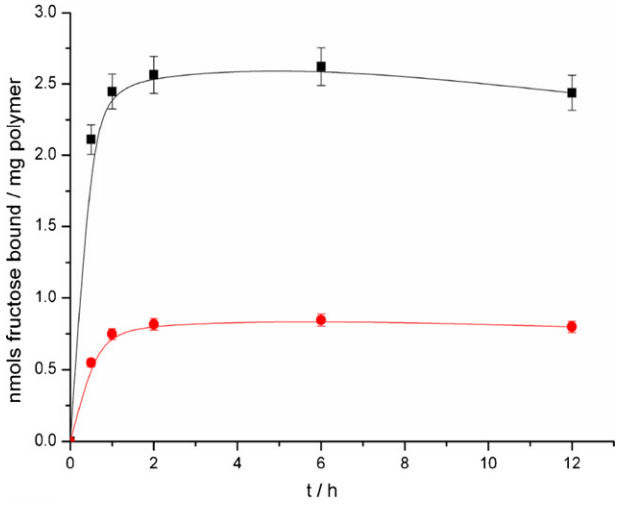

Fig. 1. Time dependence for fructose binding to fructose imprinted (squares) and pinacol imprinted (circles) polymers. Ten milligrams of TRIM cross-linked polymer + 1 ml of 0.1 mM fructose in 100 mM sodium carbonate buffer containing 10% methanol, pH 11.4; 0–12 h; 26 °C.

3.2. Influence of cross-linker on molecular recognition

Polymers prepared in parallel with EDMA and TRIM were compared to study the influence of the cross-linker.

Since the selectivity of MIPs might not only be determined by the print molecule but also by the nature of the cross-linker used for polymerisation, binding of fructose to MIPs prepared by EDMA and TRIM, respectively, against fructose MIP(Frc), fructosyl valine MIP(Fru-Val) and pinacol (control polymer) were compared in batch studies (Table 1).

At equilibrium TRIM cross-linked MIP(Frc) binds 3.6-fold more fructose than control polymer and 1.4-fold more fructose than MIP(Fru-Val). On the other hand, the EDMA cross-linked MIP(Frc) binds only 2.5-fold more fructose than the control polymer, and almost the same amount is bound to the MIP(Fru-Val). In general the TRIM cross-linked polymers showed lower unspecific binding compared with EDMA cross-linked polymers. These results indicate that better complementarity to the template is obtained with TRIM cross-linked materials than using EDMA, making TRIM a better cross-linker for fructose imprinting.

TRIM is a trimethacryl ester and it has been shown to be an ideal cross-linker in comparison with DVB and EDMA for imprinting penicillin [43], R-phenylbutyric acid [44] and protected dipeptides [8]. Wulff has shown that the enantiomeric selectivity of covalent MIPs is strongly dependent on the nature and amount of cross-linker [9]. When divinylbenzene was used as a cross-linker the stiffness and hyrdophobicities of the polymer increased severely thereby reducing the accessibility of cavities as shown by smaller percentage of templates that can be removed. However when using

Table 1
Influence of cross-linkers TRIM and EDMA on fructose binding to MIP and control polymer

	TRIM as cross-linker (nmol fructose/mg)	EDMA as cross-linker (nmol fructose/mg)
MIP(Frc)	2.5	2.3
MIP(Fru-Val)	1.7	2.2
Control	0.7	0.9

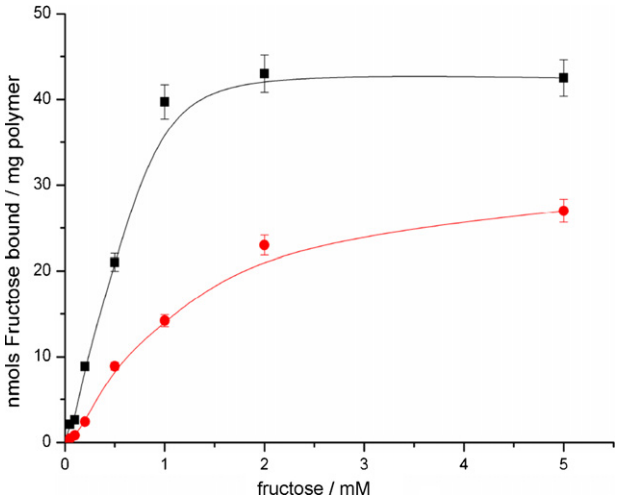

Fig. 2. Concentration dependency for fructose binding to fructose imprinted (black squares) and pinacol imprinted (red circles) polymers. Ten milligrams TRIM cross-linked polymer + 1 ml of 0–5 mM fructose in 100 mM sodium carbonate buffer containing 10% methanol, pH 11.4; 12 h; 26 °C. (For interpretation of the references to colour in this figure legend, the reader is referred to the web version of the article.)

EDMA as cross-linker an improved selectivity was obtained and the polymers were found to have high thermal and mechanical stability. The finding that the TRIM cross-linked MIPs exhibit better selectivities than EDMA cross-linked polymers is in accordance to our earlier report on fructosyl valine MIPs [45]. These results show that the cross-linker is not merely an inert compound but plays a role in promoting interactions with the template to afford molecular recognition.

3.3. Concentration dependency

Fig. 2 shows the concentration dependence of fructose binding to the MIP(Frc) and the control polymer. At saturating fructose concentrations MIP(Frc) has a fructose binding capacity of about 40 nmol/mg MIP. The theoretical capacity of the polymer would be 300 nmol/mg by taking into consideration that all the template molecules during the polymerisation process would result in an

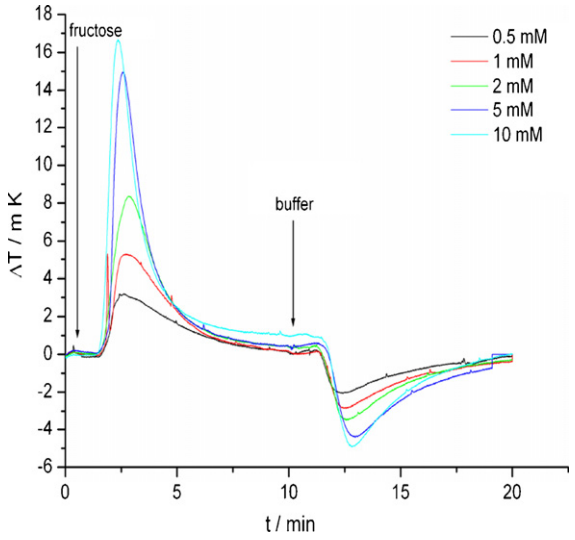

Fig. 3. Thermogram representing the interaction of fructose with the MIP in a thermistor. Fructose flow at 0 min and start of washing at 10 min with 100 mM sodium carbonate (pH 11.4)/10% methanol.

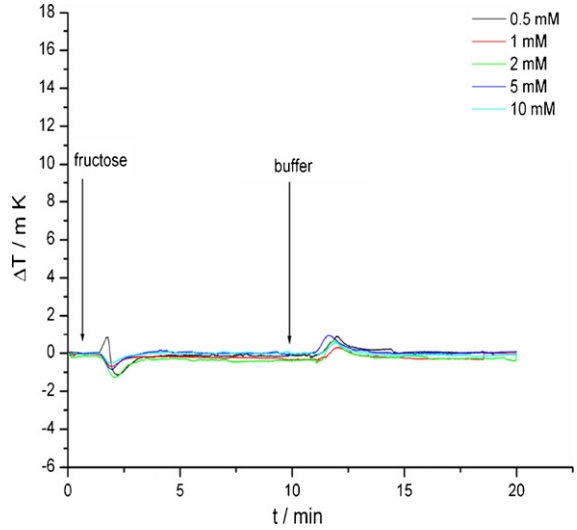

Fig. 4. Thermogram representing the interaction of fructose with the control polymer in a thermistor. Fructose flow at 0 min and start of washing at 10 min with 100 mM sodium carbonate (pH 11.4)/10% methanol.

effective binding pocket. The difference in the experimental and theoretical capacities may be attributed to the fact that not all template molecules resulted in the formation of accessible binding pockets. At 0.2 mM fructose the ratio of binding to the MIP(Frc) and to the control polymer, i.e. the "imprinting factor" (IF), was ~3.8, whereas this ratio was reduced to ~1.5 at saturation concentrations. Taking into consideration the higher number of potential binding sites in the control polymer (Section 2.2) the difference in the binding of fructose is even more pronounced. Evaluation of batch binding studies reveals the half-saturation concentrations for fructose at 0.5 mM for MIP(Frc) and 1 mM for the control polymer.

3.4. MIP sensor for studying fructose interactions with imprinted and control polymers

Injection of fructose which leads to formation of reversible covalent linkages with the boronic acids within the micro cavities of

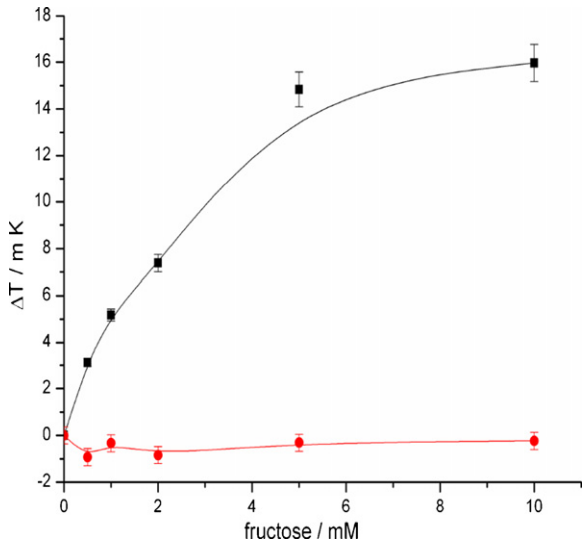

Fig. 5. Temperature changes at peak position (2.5 min) for different fructose concentration for MIP (black squares) and control polymer (red circles). (For interpretation of the references to colour in this figure legend, the reader is referred to the web version of the article.)

the MIP(Frc) generates an exothermic peak signal and the signal decrease down to the baseline within 5 min (Fig. 3). Contrary to the behaviour with fructosyl valine binding to the MIP(Fru-Val) [46] for fresh fructose no long-term exothermic steady state signal is found. When the flow was changed from the analyte (fructose) containing buffer to the neat buffer (after 10 min of analyte flow) an endothermic peak was seen which indicated the desorption of bound fructose from the boronic acids. On the other hand, the interaction of fructose with the control polymer generated considerably smaller endothermic adsorption and exothermic desorption heat signals (Fig. 4).

3.5. Concentration dependency in thermistor studies

The height (2.5 min) of adsorption peak plotted against the fructose concentration generates a binding curve for the interaction of fructose to the MIP and control polymer, respectively (Fig. 5). For the MIP the signal rises up to 5 mM fructose and half-saturation is reached at 1.8 mM. Binding to the control polymer results in a considerably smaller temperature increase. Thus a very clear difference in binding behaviour between the polymers is seen.

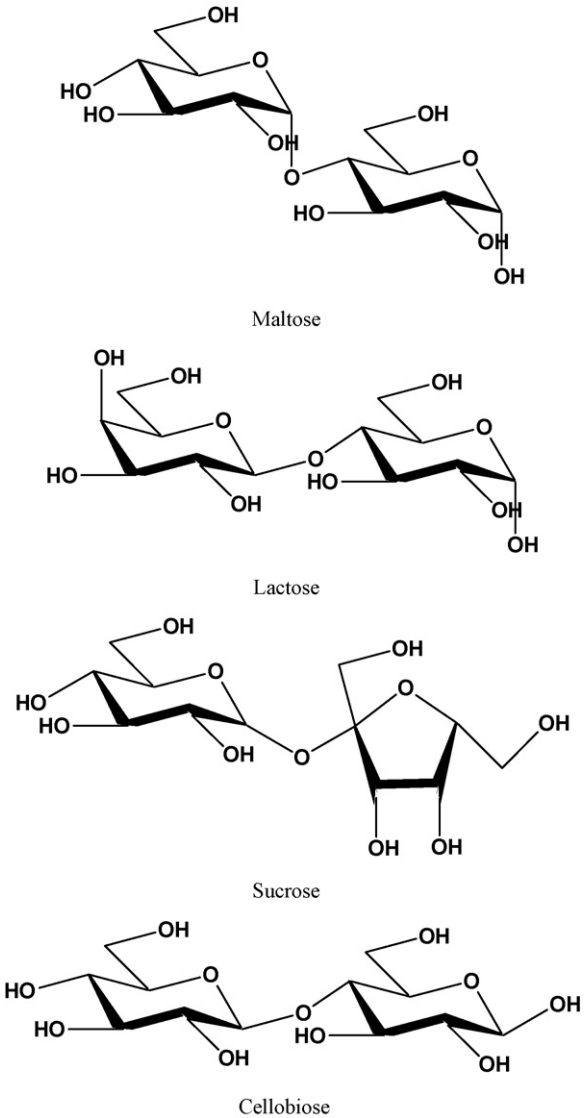

Fig. 6. Structure of disaccharides used to evaluate MIP cross-reactivity.

Table 2
Characterisation of MIP cross-reactivity expressed by the height of the adsorption peak

Analyte	MIP ΔT (mK)
5 mM Fructose	14.8
5 mM Sucrose	0.1
5 mM Maltose	2.8
5 mM Cellobiose	2.2
5 mM Lactose	1.4

A ratio of heat generation by MIP and the control polymer, i.e. an "apparent imprinting factor" of 28 is found at saturation conditions which exceeds the respective value of batch binding studies by a factor of 18. The flow experiments mostly reflect high affinity binding sites because the binding does not reach equilibrium within 10 min. On the other hand, the batch measurements cover all binding sites since the equilibrium is established.

3.6. Evaluation of disaccharide cross-reactivity using MIP sensor

MIPs generally show a remarkable cross-reactivity with the molecules analogous to the imprinted template. To evaluate the cross-reactivity, the interaction of MIP(Frc) with disaccharides were compared. The structures of the compounds used to evaluate the cross-reactivity are given in Fig. 6.

Interaction of sucrose with MIP(Frc) caused a negligible heat change in the order of 0.1 mK. Maltose and cellobiose generate a five- and sixfold smaller signal in comparison with fructose. Table 2 shows the heat values obtained for the interaction of different saccharides with imprinted polymer.

The reason for the lower signal is due to the 'shape selectivity' of the MIP(Frc) and the decreased affinity of disaccharides to the boronic acid residues. At pH 7.4 phenyl boronic acid in solution was found to have lower association constants for disaccharides (maltose 2.5 M^{-1}; lactose 1.6 M^{-1}; sucrose 0.67 M^{-1}) as compared with fructose (160 M^{-1}) [47].

4. Conclusions

Fructose imprinted polymer has been integrated in a thermistor for the label-free online detection of fructose in a range of 0.5–10 mM. MIP/fructose interaction studies in a thermistor leads to an apparent imprinting factor of 28 which exceeds the batch binding studies by a factor of 18. The large difference between fructose binding to the MIP(Frc) and the control polymer is based on the assumption of several factors:

- complementarity of the binding pockets to fructose in the MIP(Frc) in comparison to "mis-match" with the shape of "pinacol pockets" in the control polymer;
- formation of two boronic acid esters per fructose molecule as compared with only one for the pinacol imprinted control polymer;
- predominance of heat generation by the esterification of vicinal diols as compared with the non-specific adsorption to the bulk polymer.

Acknowledgements

Prof. Günter Wulff, Heinrich-Heine University Düsseldorf is greatfully acknowledged for scientific discussions. We would like to thank the IMPRS on Biomimetic Systems and the BMBF (InnoRegio 03i1314 and BioHySys 0311993) for financial support.

References

[1] G. Wulff, Angew Chem., Int. Ed. Engl. 34 (1995) 1812.
[2] K. Mosbach, Trends Biochem. Sci. 19 (1994) 9.
[3] D. Batra, K.J. Shea, Curr. Opin. Chem. Biol. 7 (2003) 434.
[4] B. Sellergren, TrAC-Trends Anal. Chem. 16 (1997) 310.
[5] M.J. Whitcombe, M.E. Rodriguez, P. Villar, E.N. Vulfson, J. Am. Chem. Soc. 117 (1995) 7105.
[6] A.G. Mayes, L.I. Andersson, K. Mosbach, Anal. Biochem. 222 (1994) 483.
[7] S. Striegler, Bioseparation 10 (2001) 307.
[8] M. Kempe, Anal. Chem. 68 (1996) 1948.
[9] G. Wulff, J. Vietmeier, H.G. Poll, Makromol. Chem. Macromol. Chem. Phys. 188 (1987) 731.
[10] D. Spivak, M.A. Gilmore, K.J. Shea, J. Am. Chem. Soc. 119 (1997) 4388.
[11] C. Alexander, H.S. Andersson, L.I. Andersson, R.J. Ansell, N. Kirsch, I.A. Nicholls, J. O'Mahony, M.J. Whitcombe, J. Mol. Recogn. 19 (2006) 106.
[12] L.I. Andersson, J. Chromatogr. B: Anal. Technol. Biomed. Life Sci. 745 (2000) 3.
[13] R.J. Ansell, D. Kriz, K. Mosbach, Curr. Opin. Biotechnol. 7 (1996) 89.
[14] G.H. Chen, Z.B. Guan, C.T. Chen, L.T. Fu, V. Sundaresan, F.H. Arnold, Nat. Biotechnol. 15 (1997) 354.
[15] F.L. Dickert, M. Tortschanoff, W.E. Bulst, G. Fischerauer, Anal. Chem. 71 (1999) 4559.
[16] F.L. Dickert, O. Hayden, TrAC-Trends Anal. Chem. 18 (1999) 192.
[17] N.T. Greene, S.L. Morgan, K.D. Shimizu, Chem. Commun. 10 (2004) 1172.
[18] K. Haupt, K. Mosbach, Chem. Rev. 100 (2000) 2495.
[19] A.L. Hillberg, K.R. Brain, C.J. Allender, Adv. Drug Deliver. Rev. 57 (2005) 1875.
[20] A.L. Jenkins, O.M. Uy, G.M. Murray, Anal. Chem. 71 (1999) 373.
[21] R. Kirchner, J. Seidel, G. Wolf, G. Wulff, J. Inclusion Phenom. 43 (2002) 279.
[22] D. Kriz, M. Kempe, K. Mosbach, Sensors Actuat. B: Chem. 33 (1996) 178.
[23] A.G. Mayes, K. Mosbach, TrAC-Trends Anal. Chem. 16 (1997) 321.
[24] S.A. Piletsky, E.V. Piletskaya, T.L. Panasyuk, A.V. El'skaya, R. Levi, I. Karube, G. Wulff, Macromolecules 31 (1998) 2137.
[25] N. Sallacan, M. Zayats, T. Bourenko, A.B. Kharitonov, I. Willner, Anal. Chem. 74 (2002) 702.
[26] T. Takeuchi, J. Haginaka, J. Chromatogr. B: Anal. Technol. Biomed. Life Sci. 728 (1999) 1.
[27] P. Turkewitsch, B. Wandelt, G.D. Darling, W.S. Powell, Anal. Chem. 70 (1998) 2025.
[28] A. Weber, M. Dettling, H. Brunner, G.E.M. Tovar, Macromol. Rapid Commun. 23 (2002) 824.
[29] K. Yano, I. Karube, TrAC-Trends Anal. Chem. 18 (1999) 199.
[30] I. Surugiu, J. Svitel, L. Ye, K. Haupt, B. Danielsson, Anal. Chem. 73 (2001) 4388.
[31] K. Sode, S. Ohta, Y. Yanai, T. Yamazaki, Biosens. Bioelectron. 18 (2003) 1485.
[32] D. Nopper, O. Lammershop, G. Wulff, G. Gauglitz, Anal. Bioanal. Chem. 377 (2003) 608.
[33] J.H.G. Steinke, I.R. Dunkin, D.C. Sherrington, Macromolecules 29 (1996) 407.
[34] K. Lettau, A. Warsinke, M. Katterle, B. Danielsson, F.W. Scheller, Angew Chem., Int. Ed. Engl. 45 (2006) 6986.
[35] K. Sreenivasan, Talanta 68 (2006) 1037.
[36] Y. Tan, Z. Zhou, P. Wang, L. Nie, S. Yao, Talanta 55 (2001) 337.
[37] R. Suedee, W. Intakong, F.L. Dickert, Talanta 70 (2006) 194.
[38] S. Gao, W. Wang, B. Wang, Bioorg. Chem. 29 (2001) 308.
[39] B. Deore, M.S. Freund, Analyst 128 (2003) 803.
[40] G. Wulff, S. Schauhoff, J. Org. Chem. 56 (1991) 395.
[41] B.L. Somani, J. Khanade, R. Sinha, Anal. Biochem. 167 (1987) 327.
[42] K. Mosbach, B. Danielsson, Anal. Chem. 53 (1981).
[43] J. Cederfur, Y. Pei, M. Zihui, M. Kempe, J. Comb. Chem. 5 (2003) 67.
[44] F.A. El-Toufaili, A. Visnjevski, O. Bruggemann, J. Chromatogr. B Analyt. Technol. Biomed. Life. Sci. 804 (2004) 135.
[45] R. Rajkumar, A. Warsinke, H. Mohwald, F.W. Scheller, M. Katterle, Biosens. Bioelectron. 22 (2007) 3318.
[46] R. Rajkumar, A. Warsinke, M. Katterle, H. Mohwald, F. Scheller, Biosens. Bioelectron. 23 (2008) 1195.
[47] G. Springsteen, B.H. Wang, Tetrahedron 58 (2002) 5291.

Talanta 76 (2008) 1041–1046

Contents lists available at ScienceDirect

Talanta

journal homepage: www.elsevier.com/locate/talanta

Sorption profile and chromatographic separation of uranium (VI) ions from aqueous solutions onto date pits solid sorbent

E.M. Saad [a], R.A. Mansour [b], A. El-Asmy [b], M.S. El-Shahawi [c,*]

[a] Chemistry Department, Faculty of Education at Suez, Suez Canal University, Egypt
[b] Chemistry Department, Faculty of Science, Mansoura University, Mansoura, Egypt
[c] Chemistry Department, Faculty of Science, King Abdulaziz University, Jeddah, P.O. Box 80203, Jeddah 21589, Saudi Arabia

ARTICLE INFO

Article history:
Received 15 January 2008
Received in revised form 30 April 2008
Accepted 30 April 2008
Available online 15 May 2008

Keywords:
Uranium (VI)
Retention
Date pits
Separation
Wastewater

ABSTRACT

The retention profile of uranium (VI) as uranyl ions (UO_2^{2+}) from the aqueous media onto the solid sorbent date pits has been investigated. The sorption of UO_2^{2+} ions onto the date pits was achieved quantitatively ($98 \pm 3.4\%$, $n = 5$) after 15 min of shaking at pH 6–7. The sorption of UO_2^{2+} onto the used sorbent was found fast, followed by a first order rate equation with an overall rate constant, k of $4.8 \pm 0.05\ s^{-1}$. The sorption data were explained in a manner consistent with a "solvent extraction" mechanism. The sorption data were also subjected to Freundlich isotherm model over a wide range of equilibrium concentration ($1–20\ \mu g\ mL^{-1}$) of UO_2^{2+}. The results revealed that, a "dual-mode" of sorption mechanism involving absorption related to "solvent extraction" and an added component for "surface adsorption" is most likely operated simultaneously for uranyl ions uptaking the solid sorbent. The thermodynamic parameters ($-\Delta H$, ΔS and ΔG) of the uranyl ions uptake onto the date pits indicated that, the process is endothermic and proceeds spontaneously. The interference of some diverse ions on the sorption UO_2^{2+} from the aqueous media onto the date pits packed column was critically investigated and the data revealed quantitative collection of UO_2^{2+} at 5 mL min^{-1} flow rate. The retained UO_2^{2+} was recovered quantitatively with HCl (3.0 mol L^{-1}) from the column at 5 mL min^{-1} flow rate. The mode of binding of the date pits with UO_2^{2+} was determined from the IR spectral date bits before and after extraction of uranium (VI). The height equivalent (HETP) and the number (N) of theoretical plates of the date pits packed column were determined from the chromatograms. Complete retention and recovery of UO_2^{2+} spiked to wastewater samples by the date pits packed column was successfully achieved. The capacity of the used sorbent towards retention of uranium (VI) from aqueous solutions was much better than the most common sorbents.

1. Introduction

During the last decade, considerable effort has being directed towards the development of low cost extractive chromatographic resins applicable for the separation and pre-concentration of actinide ions and selected fission products from biodegradable, environmental and nuclear waste samples for subsequent determination [1,2]. Pollution with radioactive elements has been a matter of great concern for the last decades for human health and animals [3–7]. Uranium is one of the most radioactive elements affecting the environment. Therefore, recent years have seen an upsurge of interest in controlling environmental pollution from radioactive elements [3,4]. Low cost and effective biological materials as algae have been also used for the removal of heavy metals in different matrices [8–13].

Solid phase extraction (SPE) has been increasingly used for pre-concentration/separation of trace and ultra trace amounts of inorganic and organic species from complex matrices as seen from recent reviews [14–16]. Various researchers have highlighted the advantages of SPE over liquid–liquid extraction most, e.g. AmberliteXAD [14–17], silica [18], octadecyl silica membrane discs [19,20], activated silica gel [21], controlled pore glass [22], polyurethane foam [5–7,23] and cationic or anionic exchange resins [24–31] have been used in batch and flow modes of SPE for the enrichment of UO_2^{2+} from wastewaters and dilute solutions prior determination.

A potential usefulness of date pits as an inexpensive solid sorbent for a number of metal ions has been demonstrated earlier [32]. The uranyl (II) ions are able to form stable complexes with amino acids, hydroxyl and carboxyl groups available in the date

* Corresponding author. Permanent address: Department of Chemistry, Faculty of Science at Damietta, Mansoura University, Mansoura, Egypt.
E-mail addresses: mohammad_el_shahawi@yahoo.co.uk, mohammad_el_shahawi@hotmail.com (M.S. El-Shahawi).

0039-9140/$ – see front matter.
doi:10.1016/j.talanta.2008.04.065

pits [31–38]. Therefore, the present paper reports the salient features of our findings regarding the available function groups, e.g. amino, hydroxyl and carboxyl groups on the date pits and the retention profile of UO_2^{2+} onto this solid sorbent as an effective and low cost solid extractor for the removal and/or minimization of uranyl (II) species from aqueous and wastewater samples. The kinetics, isotherm and thermodynamic characteristics of uranyl ions sorption from the aqueous media onto the date pits will be discussed. Moreover, the most probable retention mechanism of UO_2^{2+} retention onto the used date pits will also be discussed.

2. Experimental

2.1. Apparatus

The electronic spectra and the absorbance measurements of the uranyl ions with arsenazo III [39] were recorded using computer-controlled double beam UV–vis spectrophotometer UV-2401 PC (Shimadzu, Japan) with quartz cell (10 mm). The IR spectra were recorded using Mattson (model 5000, MA, USA) FTIR infrared spectrophotometer. The pH values were measured using a pH-meter (Hanna-Instruments 8519, Italy) calibrated against standard buffer solutions (pH 4.0 and 9.2) with absolute accuracy limits at the pH measurements being defined by NIST buffers. Glass columns (18 cm × 15 mm i.d.) and a variable mechanical Shaker (Corporation Precision Scientific, Chicago, USA) with a shaking rate in the range of 10–250 rpm were used for the retention experiments of uranium (VI) species at different pH.

2.2. Reagents and materials

The date palm cultivars grown in El-Qassim region, Saudi Arabia, were collected and washed with distilled water to be completely free from dirt and inherent pulp, dried in at 150 °C for 3 h and finally crushed to give a dark brown powder (mesh, 5 mm). The chemical analyses of the date palm cultivars used in this investigation are summarized in Table 1.

Analytical reagent grade chemicals of metal ions as chlorides and/or nitrates and solvents (BDH, USA) were used. A stock solution of UO_2^{2+} (1000 μg mL^{-1}) was prepared by dissolving an appropriate amount of uranyl acetate dehydrate (Fluka Chemie AG, Buchs, Switzerland) in double-distilled water. Stock solutions (1000 μg mL^{-1}) of the metal ions (as chloride or nitrate salts) were prepared in double-distilled water. Arsenazo III (0.1%, w/v) (Fluka Chemie AG) was prepared in ethanol and completed with water. A series of Britton–Robinson buffer solutions of pH 1.8–12.2 were prepared by mixing equimolar concentrations (0.4 mol L^{-1}) of the acid mixture: boric, acetic and phosphoric acids in double-distilled water and adjusting the pH of the solution to the required value with NaOH [40]. The other reagents used were of analytical reagent grade.

Table 1
Chemical analysis of date pits from three different locations in Saudi Arabia

Analysis	Component (%)		
	Fard	Khalas	Lulu
Moisture	10.3	7.1	9.9
Crude fat	9.9	13.2	10.5
Crude protein	5.7	6.0	5.2
Ash	1.4	1.8	1.0
Acid detergent fiber	45.6	50.6	49.3
Natural detergent fiber	61.5	64.5	68.8

2.3. Recommended batch procedures

In a low density polyethylene (LDPE) sample bottles, an accurate weight (0.2 ± 0.002 g) of the date pits solid sorbent was shaken with an aqueous solution (50 mL) at different pH (1.8–12.6) containing uranium (VI) at concentration level of 10 μg mL^{-1} UO_2^{2+} for 15 min at 25 ± 1 °C. After equilibrium, the amount of UO_2^{2+} ions retained on the solid sorbent was determined from the difference between the absorbance of the uranyl (II) ions–arsenazo III complex before (C_0) and after (C_a) shaking with the date pits sorbent. The sorption percentage (%E) and the distribution ratio (D) were then determined employing the equations: thermostat mechanical shaker,

$$\%E = \left[(C_b - C_a)/C_b\right].100 \quad (1)$$

$$D(\text{mL g}^{-1}) = \frac{\%E}{100 - \%E}\frac{V}{W} \quad (2)$$

where V and W are the sample volume (mL) and weight of the dried date pits in grams. Following these procedures, the effect of different parameters, e.g. shaking time, temperature (5–60 °C), sorbent doze and UO_2^{2+} concentration on the retention of UO_2^{2+} was carried out. The data are the average of three independent measurements and the precision in most cases was ±2%.

2.4. Column experiment

An aqueous solution of wastewater sample (100 mL) spiked with UO_2^{2+} ions (10 μg mL^{-1}) was percolated through the date pits (2.0 g) packed column at a flow rate of 2 mL min^{-1}. Under the same conditions, a blank experiment was also carried out in the absence of UO_2^{2+} ions. Sorption of UO_2^{2+} on the date pits took place as proved from the analysis of uranyl ion in the effluent solution. Elution of the uranyl ion from the date pits packed column was then achieved quantitatively by passing 20 mL of HCl (3.0 mol L^{-1}) at 2 mL min^{-1} flow rate. Equal fractions of the eluate were collected and analyzed spectrophotometrically for uranyl (II) ions. The same procedures were also applied in the blank experiment. The HETP, N and breakthrough capacity were then calculated from the output of the chromatograms.

2.5. Separation and recovery of uranyl ions from various water samples

An aqueous solution of tap or industrial wastewater samples (0.1 L) spiked with uranyl ions at a total concentration ≤10 μg mL^{-1} was first filtered through 0.45 μm cellulose membrane filters and stored in LDPE sample bottles (200 mL). The test solution at the optimum experimental conditions of uranyl ions sorption described above was percolated through the date pits (1.0 ± 0.01 g) packed columns at 5 mL min^{-1} flow rate using the vacuum method of foam packing [41]. Complete sorption of uranyl ions was achieved quantitatively as indicated from the analysis of uranium (VI) in the effluent solution by the method reported earlier [39]. Complete recovery of the retained uranyl ions was achieved by percolation on aqueous solution of HCl (20 mL, 3.0 mol L^{-1}) at 5 mL min^{-1} flow rate.

3. Results and discussion

3.1. Retention profile of UO_2^{2+} sorption

The pH medium is one of the most important factors that commonly controls and strongly influence the retention of the metal ions by the solid sorbent. The data of the UO_2^{2+} sorption by the date pits from the aqueous solution at different pH are summarized in

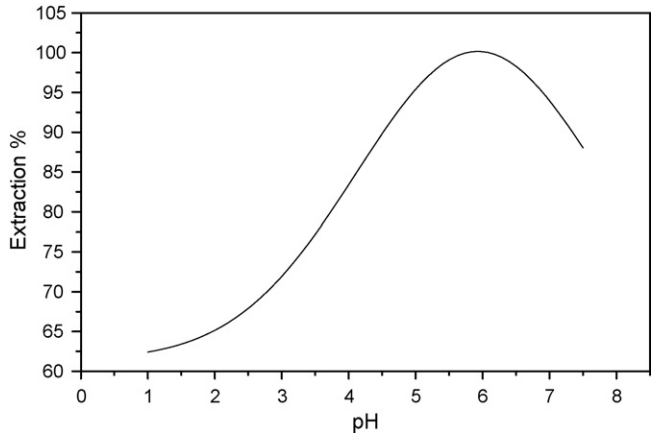

Fig. 1. Influence of the pH of aqueous solution on the uptake (%) of UO_2^{2+} from the aqueous solutions onto the date pits solid sorbent.

Fig. 1. The data revealed that, the uptake of uranyl (II) ions is low at acidic pH ≤ 5. The protonation of the available active sites (amino acids, hydroxyl and carboxyl groups) in the date pits most likely inhibit their binding towards the uranyl (II) ions as reported earlier by El-Shahawi et al. [5–7] for the solid sorbent polyurethane foams thus lowering the UO_2^{2+} ions uptake from the aqueous media. The pK_a values of the protonation of the available active sites in the date pits [42,43] may account for the observed trend (Fig. 1). At pH 5.5–6.5 range (Fig. 1), the sorption performance of the date pits towards uranyl (II) ions reached maximum (99.7%) and leveled off at pH higher than pH 7.5 (Fig. 1). This behavior is most likely attributed to the instability of the uranyl (II) complexes with the active sites of the date pits sorbent and/or hydrolysis of the produced uranyl (II) complexes with the active sites of the date pits. The diffusion of the uranyl (II) ions through the date pits film is most likely consistent with its solubility in the solid sorbent as reported earlier [32]. Therefore, in the subsequent work, the sorption experiments of uranyl (II) ions by the date pits sorbent were carried out at pH 5.5–6.5.

The influence of shaking times on the extraction percentage of UO_2^{2+} ions from the aqueous solution of pH 5.5–7 by the date pits was critically studied. The extraction was fast and the equilibrium reached maximum within 15 min of shaking time (Fig. 2) and remains constant. The half-life ($t_{1/2}$) time of the equilibrium sorption of uranyl (II) ions onto the solid sorbent was fast. The value of $t_{1/2}$ calculated from the plots of $-\log(A_b - A_a)/A_b$ was found to be 1.71 ± 0.02 min, respectively. Thus, gel diffusion is not the rate-controlling step for the solid sorbent as in the case of common ion exchange resins [5,6]. Thus, a 15-min shaking time was adopted in the subsequent experiments.

The effect of the sorbent doze (0.05–0.50 g) on the sorption of UO_2^{2+} at pH 6.5 was examined. The uranyl (II) ions sorption increased on increasing the sorbent doze and maximum sorption was achieved at sorbent doze 0.1–0.3 g. Therefore, in the subsequent work, a 0.2-g of the solid sorbent was employed. The sorption percentage of uranyl (II) onto the date pits sorbent decreased up to 60 ± 3.5% on increasing the sample volume to 200.0 mL.

3.2. Kinetics of UO_2^{2+} uptake onto date pit

The kinetics of UO_2^{2+} sorption onto the date pits was subjected to Lagergren model [43]. The rate constant for the retention step was evaluated in the light of the Lagergren rate equation [43]:

$$\log(q_e - q_t) = \log q_e - \left(\frac{kt}{2.303}\right) \quad (3)$$

where q_e and q_t are the sorbed concentration of UO_2^{2+} onto date pits at equilibrium and at time t, respectively and k is the overall rate constant. The plot of $\log(q_e - q_t)$ versus time was found linear (Fig. 3) with an overall rate constant of 4.8 ± 0.05 s^{-1}. The value of k confirmed a first order kinetics for the uranyl (II) ions retention towards the used sorbent. The influence of different sorbent doze and adsorbate concentration was investigated. The results also indicate that, the value of k increases on increasing the sorbent doze and adsorbate concentration confirming the formation of monolayer of uranyl (II) species onto the surface of the used adsorbent as well as the first order kinetic nature of the process.

The retention of uranyl (II) ions sorption onto the date pits depends on film diffusion and intraparticle diffusion, and the more rapid one will control the overall rate of transport. Thus, the concentration of the sorbed UO_2^{2+}, q_t (mg g^{-1}) was plotted against time applying the Weber–Morris equation [44]:

$$q_t = R_d(t)^{1/2} \quad (4)$$

where R_d is the rate constant of intraparticle transport in mg g^{-1} $min^{1/2}$. The diffusion rate was found high in the initial stages and decreased on passage of time up to 18 min, indicating that the rate of the retention step is film diffusion at the early stage

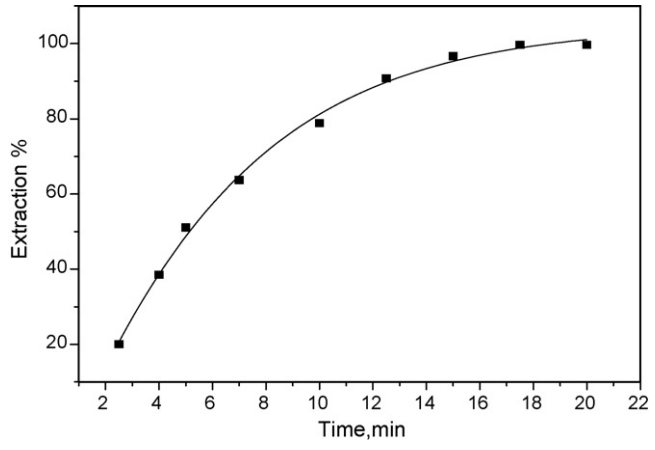

Fig. 2. Effect of shaking time on the retention (%) of UO_2^{2+} from the aqueous solution of pH 6–7 onto the date pits.

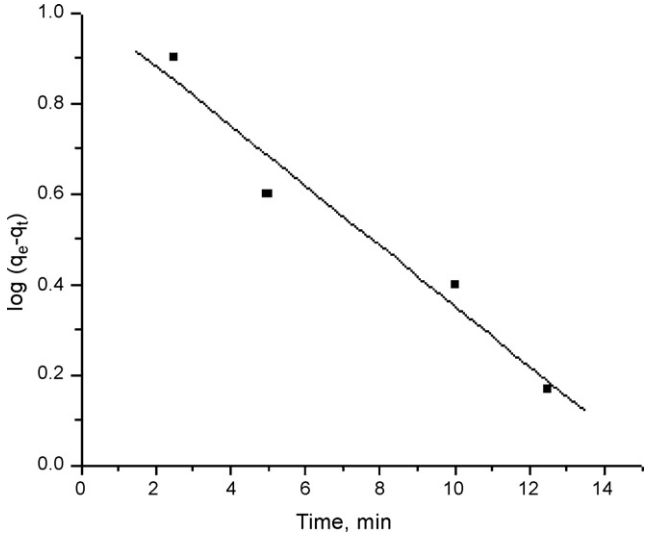

Fig. 3. Plot of $\log(q_e - q_t)$ versus time (min) for the sorbed UO_2^{2+} from the aqueous solution of pH 6–7 onto the date pits at room temperature.

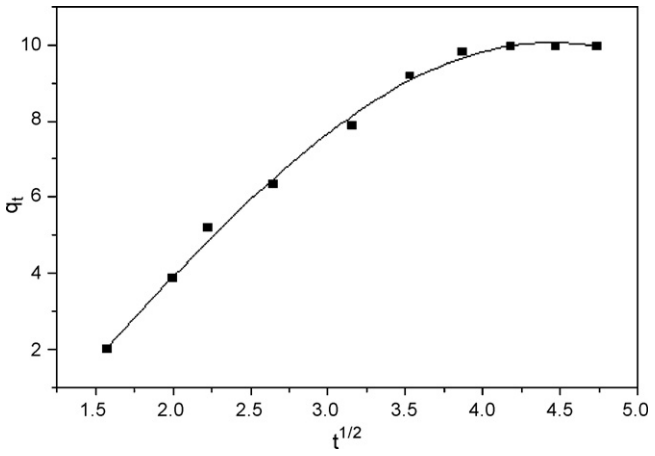

Fig. 4. Weber–Morris plot of sorbed concentration of UO_2^{2+} at 5.0 μg mL^{-1} from the aqueous solution of pH 6–7 versus square root of time onto date pits at room temperature.

of extraction. The value of R_d calculated from the slope of the linear plot of q_t versus square root of time (Fig. 4) was found to be 3.8 mg g^{-1} min$^{1/2}$. The values of R_d indicated that intraparticle diffusion step could be a rate-controlling step. The change in the slope may be due to the existence of different pore size [45]. This behavior was also confirmed from the linear plot of Bt versus time employing Reichenburg equation [46]:

$$\mathrm{Bt} = -0.4977 - 2.303 \log(1 - F) \quad (5)$$

where Bt is a mathematical function (F) of q_t/q_e. The plot was linear up to 12.5 min and does not pass through the origin.

3.3. Thermodynamic studies

The influence of temperature on the UO_2^{2+} retention onto the date pits was investigated in the temperature range of 5–60 °C at pH 6–7 and shaking time of 15 min. The uptake of UO_2^{2+} ions by the date pits increases on raising the temperature up to 25 °C and remains more or less constant confirming the endothermic nature of the retention step. A clear pronounced thermal stability of UO_2^{2+} uptake was also noticed at temperature higher than 25 °C. Thus, in the subsequent work, all experiments were carried out at room temperature. At this temperature, the thermodynamic parameters (ΔH, ΔS, and ΔG) of the uranyl (II) ions sorption from the aqueous media at pH 6–7 onto the date pits were calculated employing the equations:

$$\log K_c = -\frac{\Delta H}{2.303RT} + \frac{\Delta S}{2.303R} \quad (6)$$

$$\Delta G = -RT \log K_c \quad (7)$$

$$\Delta G = \Delta H - T\,\Delta S \quad (8)$$

The plot of K_c versus $1/T$ (Fig. 5) was linear over the temperature range of 278–293 K. The values of ΔH, ΔS, and ΔG calculated from the slope and intercept of Fig. 6 were found equal to −63.18 J, 27.43 J mol^{-1} K^{-1} and −3.43 kJ mol^{-1}, respectively. The value of ΔH confirms the exothermic nature of the uranyl uptake. The increase of ΔG with temperature is attributed to the spontaneous nature of the absorption process which is more favorable at low temperature. The data confirm that the compound associate attains the equilibrium within short time suggesting the possible application of the date pits in column operations for the enrichment and separation of UO_2^{2+} species from large sample volume of industrial waste water.

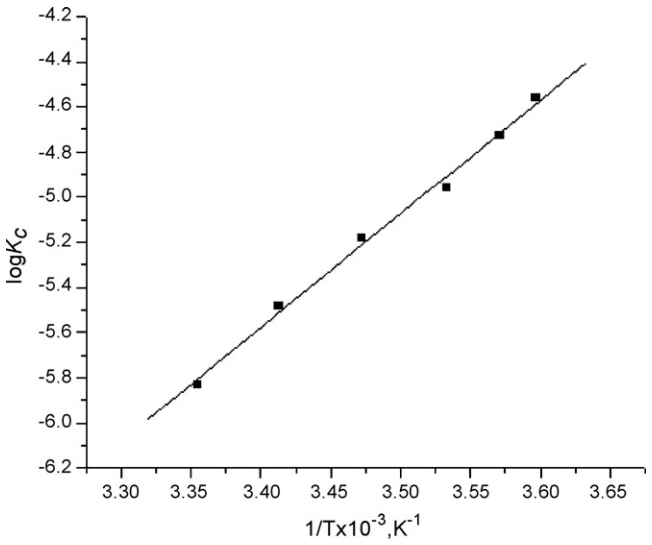

Fig. 5. The plot of equilibrium constant ($\log K_c$) versus $1/T$ of uranyl (II) retention onto the date pits from aqueous solutions of pH 6–7 and 15 min shaking time.

3.4. Sorption isotherms

The uptake of UO_2^{2+} ions from the bulk aqueous solutions at pH 6.5, 15 min shaking time and at room temperature onto the date pits was dependent on the initial UO_2^{2+} concentration. Therefore, the sorption profile of UO_2^{2+} was determined over a wide range of equilibrium concentration (1–20 μg mL^{-1}). At low and moderate UO_2^{2+} concentrations, the amount of UO_2^{2+} retained onto the solid sorbent varied linearly with that remained in the aqueous solution. Thus, the data was subjected to Freundlich isotherm model [47] over a wide range of equilibrium concentrations. The familiar form of Freundlich [47] isotherm model is expressed in the following linear form:

$$\log C_{ads} = \log A + \frac{1}{n} \log C_e \quad (9)$$

where A and $1/n$ are Freundlich parameters related to the maximum sorption capacity of solute (mg g^{-1}), C_{ads} is the concentration of the retained uranyl (II) ions onto the date pits per unit mass (mg g^{-1}) at

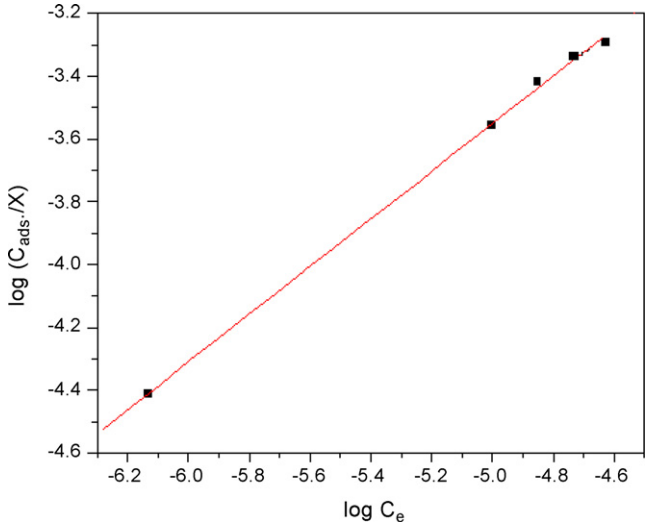

Fig. 6. Freundlich sorption isotherm of uranyl (II) sorption from the aqueous solutions of pH 6–7 onto the date pits at pH 6–7 at room temperature after 15 min shaking time.

equilibrium and C_e is the concentration of UO_2^{2+} left in the aqueous solution (mg L^{-1}). The plot of log C_{ads} versus log C_e (Fig. 6) was found linear (R^2 = 0.96–0.97) over the entire concentration range of uranyl ions indicating a better fit for the experimental data. The values of the Freundlich constants A and $1/n$ computed from the intercepts and slopes of the plots of uranyl (II) ions sorption onto the date pits were found to be 0.6 ± 0.07 mg g^{-1} and 0.31 ± 0.01, respectively. The values of $1/n < 1$ indicated that, the favorable sorption of uranyl ions from the aqueous onto the tested solid sorbent. The value of $1/n$ (<1) revealed that, the retention capacity is slightly reduced at lower equilibrium concentration and the isotherm does not predict any saturation of the solid surface of the sorbent by the sorbate. Thus, infinite surface coverage is predicted mathematically and physic sorption on the surface is expected [37]. The retention capacity of the date pits towards uranyl (II) ions from the aqueous solution was found equal to 10 mg g^{-1}.

3.5. Effect of foreign ions

The influence of a relatively high excess (1 mg) of some diverse ions relevant to waste water, e.g. alkali and alkaline earth metals Cu^{2+}, Hg^{2+}, Pb^{2+}, Bi^{3+}, Co^{2+}, Zn^{2+}, Mn^{2+}, Na^{+}, K^{+}, Cl^{-}, SO_4^{2-}, AsO_2^{2-}, SO_4^{2-}, and PO_4^{3-} ions on the pre-concentration of uranyl ions at 5 μg mL^{-1} uranium (VI) concentration level from the aqueous (50 mL) at pH 5–6 by developed date pits was investigated. The tolerance limits (w/w) less than ±3% change in the percentage uptake of uranyl ions was taken as free from interference. The data revealed that, the presence of large amounts of foreign ions in the sample has no significant effect on the pre-concentration of analyte (>98 ± 2%). Thorium (IV) interfered seriously even at 1:1 molar ratio and the uptake of UO_2^{2+} (5 μg mL^{-1}) by date pits decreased to 88–90%.

3.6. IR spectral studies

The IR spectrum of the UO_2^{2+} sorbed species was compared with the IR spectrum of date pits alone. The observed shift of some bands in the IR spectra to lower and/or higher wave numbers as well as the appearance of new bands in the low frequency region (600–200 cm^{-1}) are most likely corresponding to the participation of the oxygen and/or nitrogen of the amino acids of the date pits in the complex formation with the uranyl (II) ions [48]. The observed strong band at 935–940 cm^{-1} and the medium intensity band at 6830–835 cm^{-1} are most likely assigned to ν_{as} (O=U=O) and ν_s (O=U=O) [48], respectively.

3.7. Chromatographic behavior of uranyl ion on date pits

The kinetics and the sorption data and the available active sites of the date pits towards uranyl (II) in aqueous solution suggested the use of the sorbent in flow mode. Percolation of an aqueous solution (0.1 L) of de-ionized water contained uranyl (II) ions at concentration ≤10 μg Au mL^{-1} at 2 mL min^{-1} flow rate. Analysis of uranyl (II) species in the effluent solution against the reagent blank under the same experimental conditions revealed complete sorption of UO_2^{2+} by the date pits packed columns. A series of eluting agents, e.g. $HClO_4$ (1.0 mol L^{-1}), H_2SO_4 (1.0 mol L^{-1}) and HCl (1.0 mol L^{-1}) was investigated to recover uranyl (II) species from the date pits packed column. Among these reagents, HCl (1 mol L^{-1}) was found the most suitable eluting agent. Therefore, the influence of HCl concentration (0.5–5.0 mol L^{-1}) on the recovery of uranyl (II) ions from the date pits packed column was critically investigated at 2–3.0 mL min^{-1}. The results revealed that, the use of HCl at 3.0 mol L^{-1} concentrations or higher are suitable as proper eluting agent for complete recovery (97–101 ± 2%) of uranyl (II) ions from the date pits at 2–3 mL min^{-1}.

Good recovery of uranyl (II) ions was achieved employing HCl. The retained species were recovered quantitatively (97–101%) employing HCl as indicated from the analysis of uranium (VI) in the eluate [31]. The performance of the date pits packed column is generally described quantitatively by the number (N) and the height equivalent to the theoretical plates (HETP). The chromatogram of the plot of the volume of the HCl (1.0 mol L^{-1}) as eluting agent (12 mL, 6× 2 mL) at 2 mL min^{-1} versus the percent uranyl (II) recovered was used to calculate the column performance employing the Glueckauf equation [4,5]:

$$N = \frac{8V_{max}^2}{W^2} = \frac{L}{\text{HETP}} \quad (10)$$

where N is the number of theoretical plates, V_{max} is the volume of eluate to peak maximum, W is the width of the peak at $1/e$ times the maximum solute concentration and L is the length of the date pits bed column in mm. The values of HETP and N were 0.84 mm/plate and 71.1 ± 5, respectively confirming the good performance of the date pits packed column. The utility of the date pits packed column for the recovery of uranyl (II) ions spiked at 5.0 μg mL^{-1} to wastewater samples (100 mL) was also investigated at 5 mL min^{-1} flow rate. Complete sorption of uranyl (II) ions took place and the retained uranyl (II) species in the column were then recovered quantitatively (97–102%) with HCl (25 mL, 1.0 mol L^{-1}) at 5 mL min^{-1} flow rate. The results confirmed the good performance of the proposed date pits solid sorbent in flow mode for the separation of uranyl (II) ions in complicated matrices.

3.8. Analytical performance and application of the proposed method

The validation of the developed method was successfully assessed by comparing the capacity of the used sorbent with the most of other sorbents DCQ-naphthalene [26], PAN-benzophenone [27], Q-AmberliteXAD-4 [28], azo-oxime ion exchanger [29] and DAB–AC [37] towards uranium (VI) uptake. The results are summarized in Table 2. The capacity of the used date pits sorbent (10 ± 0.02 mg g^{-1}) towards uranium (VI) is much better than the first four solid sorbent and lower than the solid sorbent DAB–AC (18.35 ± 0.2 mg g^{-1}). The developed date pits packed column was successfully used for the removal of uranium (VI) spiked to wastewater samples at a total concentration in the range of 6–10 μg mL^{-1} levels as follows: the water samples were first acidified with nitric acid (1.0 mol L^{-1}) and filtered through a 0.45-μm cellulose membrane filter. The sample solutions were percolated through the date pits packed columns at 5 mL min^{-1} flow rate. Complete retention of uranium (VI) was achieved. The retained uranium (VI) species was then recovered quantitatively from the date pits packed column with HCl (3.0 mol L^{-1}) at flow rate of 5 mL min^{-1}. A satisfactory recovery percentage (95.8 ± 2.1) of uranium (VI) was achieved con-

Table 2
Retention capacities of the investigated date pits and other solid sorbents towards uranyl (II) ions from aqueous media by batch mode*

SPE material	Retention/binding capacity (mg g^{-1}) of SPE	Reference
DCQ-naphthalene	1.88 ± 0.02	[26]
PAN-benzophenone	2.34 ± 0.01	[27]
Q-AmberliteXAD-4	2.74 ± 0.02	[28]
Azo-oxime ion exchanger	7.14 ± 0.01	[29]
DAB–AC	18.35 ± 0.2	[37]
Date pits	10 ± 0.02	Present work

* Average of five measurements ± standard deviation.

firming the good performance of the developed procedures and its independence from matrix effects.

4. Conclusions

The date pits solid sorbent offers unique advantage in rapid preconcentration and recovery of UO_2^{2+} in dilute aqueous solution at pH 6–7.5 by flow mode of separation. The interaction between date pits and UO_2^{2+} followed the Freundlich adsorption isotherm models. The dual-mode mechanism involving "complex formation of uranyl (II) ions with the active sites of the sorbent" and an added component for "surface adsorption" of uranyl (II) ions retention offers an excellent description of the observed trend. However, work is still continuing for the chemical separation and recovery of UO_2^{2+} in real samples by on line solid phase spectrophotometry in water.

References

[1] E.P. Horwitz, R. Chiarizia, M.L. Dietz, Solvent Extr. Ion Exch. 10 (1992) 313.
[2] E.P. Horwiz, R. Chiarizia, M.L. Dietz, React. Funct. Polym. 33 (1997) 25.
[3] X. Yang, Y. Feng, Z. He, P.J. Stoffella, J. Trace Elem. Med. Biol. 18 (2005) 339.
[4] T.R. Dulsk, Trace Elemental Analysis of Metals, Methods and Techniques, Marcel Dekker Inc., 1999.
[5] M.M. Abou-Mesalam, I.M. El-Naggar, M.S. Abdel-Hai, M.S. El-Shahawi, J. Radioanal. Nucl. Chem. 258 (2003) 619.
[6] M.S. El-Shahawi, M.A. Othman, M.A. Abdel-Fadeel, Anal. Chim. Acta 546 (2005) 221.
[7] M.S. El-Shahawi, M.A. Othman, H.M. Nassef, M.A. Abdel-Fadeel, Anal. Chim. Acta 536 (2005) 227.
[8] B. Volesky, Z.R. Holan, Biotechnol. Prog. 11 (1995) 235.
[9] J. Matheickal, Q. Yu, G. Woodburn, Water Res. 33 (1999) 335.
[10] P. Vasudevan, V. Padmavathy, N. Tewari, S.J. Dtingra, Sci. Ind. Res. 60 (2001) 112.
[11] Y. Ho, J. Porter, G. Mckay, Water Air Soil Pollut. 141 (2002) 1.
[12] P. Kaewsarn, S.P. Padina, Chemosphere 47 (2002) 1081.
[13] T.P. Rao, J.M. Gladis, Rev. Anal. Chem. 20 (2001) 145.
[14] T.P. Rao, C.R. Precetha, Sep. Purif. Rev. 32 (2003) 1.
[15] P. Metilda, K. Sanghamitra, J.M. Gladis, G.R.K. Naidu, T.P. Rao, Talanta 65 (2005) 192, and references cited in.
[16] F.A. Aydin, M. Soylak, Talanta 72 (2007) 187.
[17] M.S. Carvalho, M.F. Domingues, J.L. Mantovano, E.Q.S. Filho, Spectrochim. Acta B 53 (1998) 1945.
[18] M.L. Dietz, E.P. Horwitz, L.R. Sajdak, R. Chiarizia, Talanta 54 (2001) 1173.
[19] N.L. Misra, S. Dhara, K.D.S. Mudher, Spectrochim. Acta B 61 (2006) 1169.
[20] M. Merdivan, M.Z. Duz, C. Hamamci, Talanta 55 (2001) 639.
[21] J.M. Gladis, T.P. Rao, Anal. Bioanal. Chem. 373 (2002) 867.
[22] S. Hirata, Y. Ishida, M. Aihara, K. Honda, O. Shikino, Anal. Chim. Acta 438 (2001) 205.
[23] M. Shamsipur, Y. Yamini, P. Shtari, A. Khanchi, M. Ghannadi, Sep. Sci. Technol. 35 (2002) 1011.
[24] M. Shamsipur, A.R. Ghiasvand, Y. Yamini, Anal. Chem. 71 (1999) 4892.
[25] T.P. Rao, P. Metilda, J.M. Gladis, Talanta 68 (2006) 1047, and references cited in.
[26] S.M. Nnelms, G.M. Greenway, D. Koller, J. Anal. Atom. Spectrom. 11 (1996) 907.
[27] S. Katragadda, H.D. Gesser, A. Chow, Talanta 44 (1997) 1865.
[28] C.H. Lee, M.Y. Suh, K.S. Joe, T.Y. Eom, W. Lee, Anal. Chim. Acta 351 (1997) 57.
[29] C.H. Lee, M.Y. Suh, J.S. Joe, D.Y. Kim, W.H. Kim, Anal. Chim. Acta 382 (1999) 199.
[30] M.E. Khalifa, Sep. Sci. Technol. 33 (1998) 2123.
[31] M. Merdivan, M.R. Buchmeiser, G. Bonn, Anal. Chim. Acta 402 (1991) 91.
[32] S.Y. Bae, G.L. Southard, G.M. Murray, Anal. Chim. Acta 397 (1999) 173.
[33] J.M. Gladis, T.P. Rao, Anal. Lett. 35 (2002) 501.
[34] C.R. Preetla, T.P. Rao, Radiochim. Acta 91 (2002) 247.
[35] J.M. Gladies, T. Prasada Rao, Anal. Lett. 36 (2003) 2107.
[36] J.S. Hamada, I.B. Hashim, F.A. Sherif, Food Chem. 76 (2002) 136.
[37] A. Sergeev, G.M. Karshunov, Koord. Khim. 1 (1975) 1654.
[38] M. Cefola, R.C. Taylor, A.V. Philip, S. Gantile, J. Phys. Chem. 66 (1962) 790.
[39] Z. Marczenko, Spectrophotometric Determination of Elements, 3rd ed., Ellis Horwood Chichester, UK, 1986, and references cited in Chapter 23.
[40] H.T.S. Britton, Hydrogen Ions, 4th ed., Chapman & Hall, 1952.
[41] T. Braun, J.D. Navratil, A.B. Farag, Polyurethane Foam Sorbents in Separation Science, CRC Press Inc., Boca Raton, FL, USA, 1985.
[42] H.D. Gesser, G.A. Horsfall, J. Chim. Phys. 74 (1977) 1072.
[43] S. Lagergren, B.K. Sven, Hand 1 (1898) 24.
[44] W.J. Weber Jr., J.C. Morris, J. Sanit. Eng. Div. Am. Soc. Civ. Eng. 90 (SA3) (1964) 70.
[45] S.L.C. Ferreira, H.C. dos Santos, M.S. Fernandes, J. Anal. Atom. Spectrom. 17 (2002) 115.
[46] D. Reichenburg, J. Am. Chem. Soc. 75 (1972) 589.
[47] G.A. Somorja, Introduction of Surface Chemistry and Catalysis, Wiley, New York, 1994.
[48] K. Nakamoto, Infrared and Raman Spectra of Inorganic and Coordination Compounds, 3rd ed., Wiley, New York, 1978, p. 305.

Talanta 76 (2008) 1113–1118

Contents lists available at ScienceDirect

Talanta

journal homepage: www.elsevier.com/locate/talanta

Direct determination of Cd, Cu and Pb in wines and grape juices by thermospray flame furnace atomic absorption spectrometry

Daniela Schiavo [a], José Y. Neira [b], Joaquim A. Nóbrega [a,*]

[a] Grupo de Análise Instrumental Aplicada, Departamento de Química, Universidade Federal de São Carlos, P.O. Box 676, 13560-970 São Carlos, SP, Brazil
[b] Departamento de Análisis Instrumental, Facultad de Farmacia, Universidad de Concepción, Casilla 237, Concepción, Chile

ARTICLE INFO

Article history:
Received 5 February 2008
Received in revised form 10 May 2008
Accepted 12 May 2008
Available online 18 May 2008

Keywords:
Thermospray
FAAS
Copper
Cadmium
Lead
Wine
Grape juice

ABSTRACT

The applicability of thermospray flame furnace atomic absorption spectrometry (TS-FF-AAS) was evaluated for direct determination of Cu, Cd and Pb in wines and grape juices. The developed procedure does not require preliminary acid digestion of the samples. The optimum conditions for determination of Cu, Cd and Pb in wines were studied and the performance was compared to those typically obtained by flame atomic absorption spectrometry (FAAS). A sample volume of 150 μL was introduced into a heated nickel tube at a flow rate of 0.54 mL min^{-1} and 0.14 mol L^{-1} HNO_3 was used as sample carrier flowing at 2.5 mL min^{-1} for determining all analytes. The effect of ethanol concentrations on Cu, Cd and Pb absorbance signals were studied. All determinations were carried out by adopting optimized conditions and quantification was based on the standard additions method. Limits of detection (LOD) of 12.9, 1.8 and 5.3 μg L^{-1} ($n = 14$) for Cu, Cd and Pb, respectively, were obtained for wine samples ($3\sigma_{blank}$/slope, $n = 14$). Relative standard deviations (R.S.D., %) of 2.7, 2.1 and 2.6 for Cu, Cd and Pb, were obtained ($n = 6$) for wine samples. The values determined for grape juice samples were similar to these ones. The analytical throughput was 45 determinations h^{-1} and accuracy was checked by addition-recovery experiments.

1. Introduction

Trace metals play an important effect in the quality of wine. They promote specific redox processes during maturing that give a good appearance to the wines. However, high concentrations of Cu, Fe, Mn and Zn may cause instability and turbidity [1]. Other metals, such as As, Cd and Pb, are toxic [2].

The current legislation in Brazil demands a strict control of the levels of contamination for metals in beverages [3]. Wine and grape juices are widely consumed beverages and they can contain metals added to remove sulfur oxides and from other sources. The control of Cu concentration is important because high amounts can cause oxidative spoilage of the wine leading to lightening of red wine and darkening of white wine [4,5]. The total copper concentration in red and white wines must be 0.3 and 0.5 mg L^{-1}. In wines, the main sources of copper are equipments used in the wine production, additions of copper salts ($CuSO_4$) and pesticides employed during growth. The maximum allowed level of copper in wine is 1.0 mg L^{-1} [3,6].

A significant amount of Cd may be present in wines due to residues of agrochemical products used such as insecticides and fungicides and also by contact with equipments employed for wine production. The consumption of large quantities of wine can imply in accumulation of Cd in the organism [5]. The maximum allowed concentration of Cd in wine is 10 μg L^{-1} [6–8]. On the other hand, the maximum allowed amount of Pb in wine established by the Office International de la Vigne et du Vin (OIV) is 200 μg L^{-1} [6] and according to the Brazilian legislation is 300 μg L^{-1} [3]. The source of Pb contamination in alcoholic beverages may be either raw material or technological processes, for instance, corks are covered by a film made of plastic, by a foil made of Pb or by an alloy containing Al [9]. The intoxication caused by intake of foods containing Pb can cause severe damages to health such as encephalic alterations, headache, cardiovascular and hepatic problems [10].

Several techniques have been described to determine metals in wines such as atomic spectrometry (FAAS, electrothermal atomization AAS, inductively coupled plasma optical emission spectrometry) [11,12] and electroanalytical techniques [4,13,14]. An official method for trace metal determination in wine is provided by AOAC (Official Methods of Analysis of AOAC International) which does not consider previous acid digestion and recommend sample dilution [15]. The typical sensitivity reached by FAAS does not allow the adoption of this strategy when Cu, Cd and Pb concentrations are at μg L^{-1} levels.

A recent work has shown the advantage of thermospray flame furnace atomic absorption spectrometry (TS-FF-AAS) for direct

* Corresponding author. Tel.: +55 16 3351 8088; fax: +55 16 3351 8350.
E-mail address: djan@ufscar.br (J.A. Nóbrega).

0039-9140/$ – see front matter © 2008 Elsevier B.V. All rights reserved.
doi:10.1016/j.talanta.2008.05.010

determination of Cu, Mn, Pb and Zn in commercial beer at $\mu g\,L^{-1}$ [16]. The TS-FF-AAS technique is relatively recent and few applications for determination of metals in beverages were described in the literature. A previous work has demonstrated its applicability for determining Cu and Zn in fruit juices and bovine milk [17]. The main advantage of TS-FF-AAS is the significant increment of sensitivity by adapting a simple and low cost Ni tube to the flame. This simple device associated to a ceramic capillary allows the total introduction of the sample and increases the residence time of the atomic cloud in the atomizer. Both effects help to improve the formation of analyte atoms and, consequently, the sensitivity.

The aim of this work was to develop a procedure for direct determination of Cu, Cd and Pb in wines and grape juices by TS-FF-AAS. Since these elements are usually present at low levels in wine and grape juices, sensitive analytical techniques are required. TS-FF-AAS was employed due to its simplicity, suitable sensitivity, low cost and rapidity when compared to electrothermal atomization in a graphite furnace AAS. The effective dilution factor was chosen based on ethanol effects on sensitivity. The system was optimized and the standard additions method (SAM) was employed for Cu, Cd and Pb determination in wine and grape juice samples.

2. Experimental

2.1. Instruments and accessories

All experiments were carried out in a Varian SpectraAA-640 flame atomic absorption spectrometer (Varian, Mulgrave, Australia) equipped with a deuterium lamp background corrector. The instrument parameters for determination of Cu, Cd and Pb by TS-FF-AAS are shown in Table 1. Hollow cathode lamps of Cu, Cd and Pb (Varian) were employed. All data acquisition was carried out in peak area mode.

2.2. Arrangement of the TS-FF-AAS

The TS-FF-AAS system consists of a peristaltic pump with 8 channels (Ismatec, Labortechnik Analytik, Glattbrugg-Zürich, Switzerland) furnished with Tygon® propulsion tube (i.d. = 0.89 mm), Teflon® extension tube (i.d. = 0.8 mm), a lab-made acrylic commutator injector was utilized for sample introduction, a lab-made thermospray flame furnace unit, including a ceramic capillary (Friatec, Mannhein, Germany, i.d./o.d. 0.5 mm/2.0 mm, and 100 mm of length) and nickel tubes. The tube employed contains 99.7% of Ni and it has the following specifications: 10 cm of length, 1 cm of i.d and 1.2 cm of o.d. One of the tubes employed has six holes of 2 mm in its bottom for increasing the temperature inside of the tube. The second tube does not have any hole in its bottom. Both Ni tubes have a central hole with 2 mm of diameter. This central hole is perpendicular to the bottom holes and it is used for introduction of the ceramic capillary tube. The Ni tube was positioned on a lab-made stainless steel support with four ceramic pins on the flame burner. The thermospray was generated by contact between the nickel tube on the flame and the heated ceramic capillary. Samples were introduced inside of the heated tube without the need of a nebulizer and losses of sensitivity caused by the poor nebulization efficiency were totally circumvented.

Table 1
Instrument parameters for determination of Cu, Cd and Pb by TS-FF-AAS

Variables	Cu	Cd	Pb
Flow rate ($mL\,min^{-1}$)	0.54	0.54	0.54
Sample volume (μL)	150	150	150
Air flow rate ($L\,min^{-1}$)	13.5	13.5	13.5
Acetylene flow rate ($L\,min^{-1}$)	2.0	2.0	2.0
Measurement time (s)	80	80	80
Spectral resolution (nm)	0.5	0.5	0.5
Lamp current (mA)	4.0	4.0	10.0
Wavelength (nm)	327.4	228.8	283.3
Height of the Ni tube (cm)	1.5	0.3	0.3
Carrier	HNO_3 1% (v/v)	HNO_3 1% (v/v)	HNO_3 1% (v/v)

2.3. Reagents

All solutions were prepared using analytical-grade reagents. Water was distilled and deionized (Milli-Q, Millipore Corp., Bedford, MA, USA). All glassware and polypropylene flasks were washed with soap, soaked in 10% (v/v) nitric acid and rinsed with deionized water prior use.

Standard stock solutions of Cu, Cd and Pb containing $1000\,mg\,L^{-1}$ (Tec-Lab, Hexis, São Paulo, Brazil) were used for application of the SAM and reference solutions of Cu, Cd and Pb were prepared by diluting the stock solution. Solutions containing 2–30% (v/v) of ethanol were prepared by diluting ethanol absolute anhydrous 99.7% (v/v) (Mallinckrodt-Baker, Xalostoc, Mexico).

A $0.14\,mol\,L^{-1}$ HNO_3 solution was prepared by diluting concentrated HNO_3 (Merck, Darmstadt, Germany).

2.4. Influence of solution medium on Cu, Cd and Pb absorbance signals

Solutions containing $1.0\,mg\,L^{-1}$ of Cu in 2.0, 5.0, 8.0, 11, 15, 20, 30% (v/v) ethanol medium were evaluated by FAAS and TS-FF-AAS with both Ni tubes. This same study was carried out for solutions containing 25 and 500 $\mu g\,L^{-1}$ of Cd and Pb, respectively, in the same media. In this case, measurements were only performed using the Ni tube with six holes.

The influence of each medium, i.e. water, nitric acid and ethanol, on the transport and atomization processes of the sample was also evaluated. Solutions containing $1.0\,mg\,L^{-1}$ of Cu, 25 and 500 $\mu g\,L^{-1}$ of Cd and Pb, respectively, were prepared in different media: (a) water; (b) $0.14\,mol\,L^{-1}$ HNO_3; (c) 2% (v/v) ethanol; (d) $0.14\,mol\,L^{-1}$ HNO_3 plus 2% (v/v) ethanol.

2.5. Optimization of sample flow rate, sample volume, and measurement time

The experiments here described were carried out using a solution containing $1.0\,mg\,L^{-1}$ of Cu in 2% (v/v) ethanol. All measurements were performed using the Ni tube with six holes.

The effect of the carrier flow rate on Cu absorbance signals was evaluated for 0.46, 0.54, 0.57 and $0.85\,mL\,min^{-1}$. The volume of the sample loop was kept in 150 μL.

The carrier flow rate was kept in $0.54\,mL\,min^{-1}$ and the effect of the sample volume on the absorbance signals was studied for 150, 300 and 450 μL sampling loops.

Afterwards, the acquisition of the transient signals was made in 80 s because this period of time was sufficient to measure transient signals when injecting a sample volume of 150 μL without compromising the analytical throughput.

2.6. Sample preparation

Wine samples were analyzed without any step of sample digestion. A simple 1:6 v/v dilution with $0.14\,mol\,L^{-1}$ HNO_3 was performed to reach an ethanol concentration around 2% (v/v). This ethanol concentration provided maximum sensitivity.

For determination of the metals in grape juices, samples were analyzed directly. The obstruction of the ceramic capillary tube

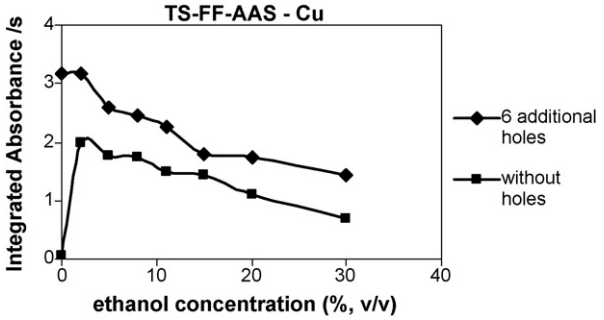

Fig. 1. Effect of ethanol concentration on Cu absorbance signals by TS-FF-AAS (Ni tubes without holes and with six additional holes).

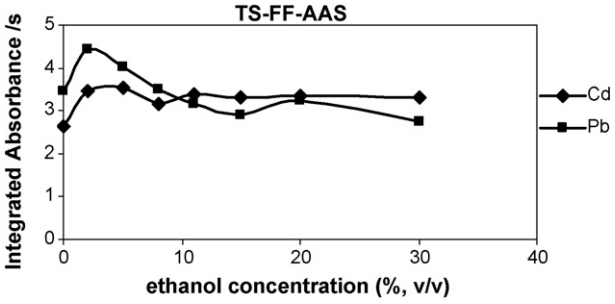

Fig. 3. Effect of ethanol concentration on Pb and Cd absorbance signals by TS-FF-AAS (Ni tube with six additional holes).

was avoided by adding a 1% (v/v) H_2O_2 solution after each measurement. The direct analysis avoids contamination and losses of volatile elements during the sample preparation, decreases the consumption of reagents and consequently the amount of residues.

Different commercial wines were bought in local markets and represent two types of grapes: Merlot (C) and Cabernet Sauvignon (A–G) from Chile (A–C, F and G) and Brazil (D and E). The ethanol concentration in wines is around 12% (v/v). Grape juice samples in different packages (cartons, plastic and glass bottles) also were bought in a local store. Samples in different packages were evaluated to check if there is any influence of the material in the contents of the analytes.

2.7. Comparison between TS-FF-AAS and FAAS

Solutions containing 1.5, 3.0, 4.5, 6.0, and 7.5 mg L^{-1} of Cu in 2% (v/v) ethanol were analyzed according the optimized conditions for conventional FAAS and TS-FF-AAS.

3. Results and discussions

3.1. Effect of ethanol concentration on the Cu, Cd and Pb absorbance signals

It can be seen in Fig. 1 that the utilization of a tube with six holes in its bottom provided better sensitivity than the tube without holes. The Ni tube with six holes allowed the partial penetration of the flame, causing an increase of the temperature of the tube and improving the atomization process of the analyte.

The relatively low sensitivity of FAAS (Fig. 2) can be attributed to the physical properties of the solutions such as surface tension and viscosity that affect the aspiration rate of the sample and the nebulization process [18]. Maximum sensitivity for Cu, Cd and Pb was reached for a solution containing 2.0% (v/v) ethanol (Figs. 1 and 3). Solutions containing greater ethanol concentrations shown a decrease in Cu and Pb absorbance signals, while those for Cd remained practically constant (Fig. 3). These last results are also in agreement with those obtained by conventional FAAS and also with Pb or Cd determinations in methanol by using hydraulic high pressure nebulization-beam injection flame furnace atomic spectrometry [19]. Ethanol exerts significant influence in the volatilization and atomization processes of the analytes. It is a volatile solvent and presents low surface tension, thus originates aerosols with smaller particles and improves the dissociation and atomization of the analyte.

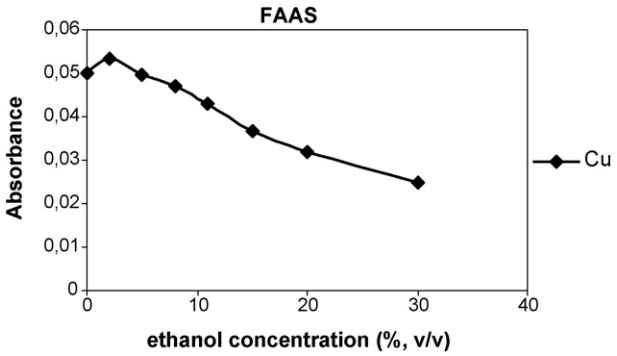

Fig. 2. Effect of ethanol concentration on Cu absorbance signals by FAAS.

3.2. Influence of the medium on Cu, Cd and Pb absorbance signals

The effect of solution medium on sensitivity was studied. Results are presented in Fig. 4 and the medium containing water-ethanol-nitric acid provided a better atomization for Cu (a) and Pb (b), while for Cd (c) the best sensitivity was obtained in nitric acid medium. Although nitric acid solution was the best medium to improve sensitivity for Cd, all further studies were carried out in ethanol plus nitric acid medium to simulate the alcohol concentration typically found in wine samples. In TS-FF-AAS the use of ethanol instead of water can increase the temperature inside the tube due to the combustion heat of the organic solvent.

3.3. Optimization of TS-FF-AAS parameters

Instrumental parameters such as flow rate, sample volume and measurement time were evaluated in order to find ideal conditions to reach maximum sensitivity in ethanol medium. The influence of the flow rate employed to transport the solution into the heated Ni tube was studied from of 0.46–0.85 mL min^{-1}. The use of flow rates higher than 0.67 mL min^{-1} was not suitable because of the residence time of the flowing liquid in the heated tip of the capillary was too short for formation of the thermospray [16,20]. A higher flow rate leads to intense cooling of the inner atmosphere of the flame furnace and also of the capillary tip causing an irregular aerosol formation and consequently affecting negatively the atomization. Higher flow rates neither improve the repeatability nor increase the sensitivity. According to Pereira-Filho et al. [21] the use of lower flow rates in TS-FF-AAS provide higher sensitivity due to the increase of the residence time of the analyte, but the disadvantage of lower flow rates is the reduction of the analytical throughput due to the longer measurement time. A flow rate of 0.54 mL min^{-1} was chosen as a compromise between sensitivity and repeatability.

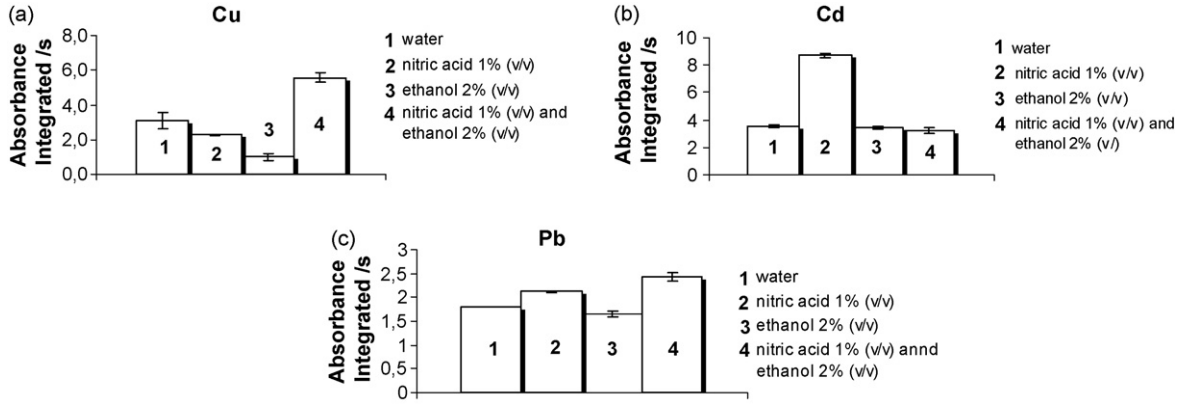

Fig. 4. Influence of the medium on Cu, Cd and Pb absorbance signals. (a) Copper; (b) cadmium; and (c) lead.

Table 2
Analytical figures of merit for Cu, Cd and Pb determinations by TS-FF-AAS in wine samples

Figures of merit	TS-FF-AAS		
	Cu	Cd	Pb
LOD[a] ($\mu g\,L^{-1}$)	12.9	1.8	5.3
LOQ[b] ($\mu g\,L^{-1}$)	43	5.8	17.5
R.S.D.%[c]	2.7	2.1	2.6
Linear range ($\mu g\,L^{-1}$)	43.0–200	5.8–200	17.7–200
Regression equation	$y = 0.00130x + 0.0498$	$y = 0.0877x + 0.0503$	$y = 0.0082x + 0.0534$
Reading time (s)	80	80	80
Sample volume (μL)	150	150	150
Coefficient of determination (R^2)	0.9999	0.9992	1.0000
Analytical throughput[d] (h^{-1})	45	45	45

[a] LOD: limit of detection ($3\sigma_{blank}$/slope, $n = 14$).
[b] LOQ: limit of quantification ($10\sigma_{blank}$/slope, $n = 14$).
[c] R.S.D.(%): relative standard deviation, $n = 6$.
[d] Estimated for 1 h working session.

The sample volume was varied from 150 to 450 μL. All further measurements were made using a sample volume of 150 μL and signal acquisition was carried out in peak area mode. As expected the sensitivity was proportional to the sample volume. However, a decrease of the analytical throughput occurs due to the need of a long time for signal returning to the baseline.

The acquisition of the transient signals for all analytes was made in 80 s for wine and grape juices samples. Memory effects for samples were avoided by inserting a 1% (v/v) H_2O_2 solution after each measurement.

3.4. Figures of merit for determination of Cu, Cd and Pb in wine and grape juice samples

Based on the optimized instrument parameters for each analyte, the accuracy, limits of detection and quantification and linear equation of the calibration curve were determined. Precision was expressed as relative standard additions (R.S.D., %) obtained for 6 measurements of Cu (1 $mg\,L^{-1}$), Cd (25 $\mu g\,L^{-1}$) and Pb (500 $\mu g\,L^{-1}$) by TS-FF-AAS. The limits of detection (LOD) were defined as the concentration corresponding to 3-fold the standard deviation of 14 measurements of the blank divided by the slope of the analyt-

Table 3
Analytical figures of merit for Cu, Cd and Pb determinations by TS-FF-AAS in grape juice samples

Figures of merit	TS-FF-AAS		
	Cu	Cd	Pb
LOD[a] ($\mu g\,L^{-1}$)	13.7	0.90	5.6
LOQ[b] ($\mu g\,L^{-1}$)	45.6	3.0	18.5
R.S.D.%[c]	3.3	2.0	2.3
Linear range ($\mu g\,L^{-1}$)	45.6–200	3.0–50	18.3–100
Regression equation	$y = 0.0045x + 1.552$	$y = 0.186x + 0.435$	$y = 0.0069x + 0.2301$
Reading time (s)	80	80	80
Sample volume (μL)	150	150	150
Coefficient of determination (R^2)	0.9992	1.0000	0.9999
Analytical throughput[d] (h^{-1})	45	45	45

[a] LOD: limit of detection ($3\sigma_{blank}$/slope, $n = 14$).
[b] LOQ: limit of quantification ($10\sigma_{blank}$/slope, $n = 14$).
[c] R.S.D. (%): relative standard deviation, $n = 6$.
[d] Estimated for 1 h working session.

Table 4
Analytical figures of merit for TS-FF-AAS and FAAS determination of Cu using 2% (v/v) ethanol plus 0.14 mol L^{-1} HNO_3

Figures of merit	Cu TS-FF-AAS		Cu FAAS
	Six additional holes	Without holes	
LOD[a] ($\mu g\,L^{-1}$)	20	63	160
LOQ[b] ($\mu g\,L^{-1}$)	66	210	528
R.S.D.%[c]	3.0	4.5	8.0
Linear range ($\mu g\,L^{-1}$)	66–7500	210–6000	533–6000
Regression equation	$y = 1.203x + 0.158$	$y = 0.869x + 0.1371$	$y = 0.028x + 0.002$
Reading time (s)	80	80	20
Sample volume (μL)	150	150	1000
Coefficient of determination (R^2)	0.9986	0.9968	0.9983
Analytical throughput[d] (h^{-1})	45	45	180

[a] LOD: limit of detection ($3\sigma_{blank}$/slope, $n = 14$).
[b] LOQ: limit of quantification ($10\sigma_{blank}$/slope, $n = 14$).
[c] R.S.D. (%): relative standard deviation, $n = 6$.
[d] Estimated for 1 h working session.

Table 5
Analytical figures of merit for Cd and Pb using the standard additions method

Figures of merit	Cd	Pb
Linear range ($\mu g\,L^{-1}$)	5.8–200	17.7–200
Regression equation	$y = 0.1751x + 0.0134$	$y = 0.0082x + 0.0534$
Reading time (s)	80	80
Sample volume (μL)	150	150
Coefficient of determination (R^2)	0.9996	1.0000
Analytical throughput[a] (h^{-1})	45	45

[a] Estimated for 1 h working session.

ical curve and the limit of quantification as 10-fold the standard deviation of 14 measurements of the blank divided by the slope of the analytical curve. Figures of merit for Cu, Cd and Pb determination by TS-FF-AAS in wine and grape juices samples are shown in Tables 2 and 3.

3.5. Comparison between FAAS and TS-FF-AAS

A comparison was carried out among the figures of merit obtained for TS-FF-AAS using Ni tubes with and without holes, and FAAS. Table 4 presents the results for Cu determination employing 2.0% (v/v) ethanol plus 0.14 mol L^{-1} HNO_3.

Best results for Cu were obtained using a Ni tube with six additional holes. The 8-fold improvement of the LOD is consequence of factors such as total sample introduction into the absorption volume while in conventional pneumatic nebulizers only 5–10% of the primary aerosol reaches the flame and also because of the increased residence time of the sample in the optical path for occurrence of the dissociation and atomization processes. The average residence time of the atoms in the observation zone is around 200 ms, which is more than an order of magnitude longer than the typical residence time of the analyte in FAAS [22].

3.6. Evaluation of the calibration strategy

The SAM is frequently used when the composition of the sample is unknown and interferences caused by concomitants can occur. Figures of merit are presented in Table 5 adopting this strategy for calibration. The slope for Cd analytical curve obtained by the SAM was around 2.8-fold greater than those observed in either 1% (v/v) HNO_3 or 2% (v/v) ethanol. Similar effect was observed for Pb, but for this element the slope variation was around 2.1-fold. It means that interferences are present and consequently the SAM must be adopted for calibration. On the other hand, wine samples contain different alcohol and sugar concentrations and this strategy was

Table 6
Direct determination of Cu, Cd and Pb in wine samples and addition-recovery experiments ($n = 3$)

Sample	Cu ($\mu g\,L^{-1}$)	Cd ($\mu g\,L^{-1}$)	Pb ($\mu g\,L^{-1}$)	Cu ($\mu g\,L^{-1}$)		Recovered (%) Cu	Cd ($\mu g\,L^{-1}$)		Recovered (%) Cd	Pb ($\mu g\,L^{-1}$)		Recovered (%) Pb
				Added	Found		Added	Found		Added	Found	
A	216.0 ± 0.01	2.4 ± 0.07	25.6 ± 0.05	100	323.0	107.0	10	12.2	97.5	100	123.4	97.8
B	232.2 ± 0.04	5.4 ± 0.03	40.4 ± 0.06	100	332.0	99.8	10	16.5	110.0	100	140.2	90.7
C	764.4 ± 0.03	1.7 ± 0.03	70.2 ± 0.04	100	868.1	103.7	10	11.9	102.8	100	171.3	101.1
D	189.6 ± 0.01	3.4 ± 0.04	100.3 ± 0.09	100	298.7	109.1	10	13.4	95.3	100	209.4	100.2
E	148.2 ± 0.01	5.8 ± 0.03	39.1 ± 0.01	100	260.9	112.7	10	15.6	98.3	100	138.4	99.3
F	77.6 ± 0.04	7.7 ± 0.04	84.6 ± 0.04	100	189.8	112.1	10	16.5	117.8	100	182.0	87.8
G	56.2 ± 0.02	8.6 ± 0.03	17.3 ± 0.11	100	158.7	102.5	10	19.5	108.5	100	42.6	101.3
A				200	408.0	96.0	20	22.7	101.4	200	229.6	102.0
B				200	427.5	97.7	20	25.1	98.1	200	243.7	101.7
C				200	949.2	97.4	20	21.7	99.9	200	268.6	99.2
D				200	393.9	102.1	20	23.4	99.6	200	301.6	99.9
E				200	343.4	97.6	20	26.9	105.6	200	239.4	100.2
F				200	270.0	96.2	20	28.3	96.2	200	285.7	103.0
G				200	262.2	103.1	20	28.3	98.5	200	67.9	101.4

Table 7
Direct determination of Cu, Cd and Pb in grape juice samples and addition-recovery experiments ($n = 3$)

Sample	Cu ($\mu g\,L^{-1}$)	Cd ($\mu g\,L^{-1}$)	Pb ($\mu g\,L^{-1}$)	Cu ($\mu g\,L^{-1}$)		Recovered (%) Cu	Cd ($\mu g\,L^{-1}$)		Recovered (%) Cd	Pb ($\mu g\,L^{-1}$)		Recovered (%) Pb
				Added	Found		Added	Found		Added	Found	
A*	31.1 ± 0.02	3.0 ± 0.08	16.5 ± 0.08	100	121.1	90.1	25	40.9	97.3	25	29.9	107.3
B*	344.9 ± 0.08	3.7 ± 0.03	79.3 ± 0.12	100	450.8	105.9	50	125.9	93.1	25	28.5	98.8
C**	239.8 ± 0.01	3.1 ± 0.13	26.1 ± 0.06	100	337.6	97.7	50	82.6	112.8	25	27.4	97.1
D**	105.5 ± 0.09	4.5 ± 0.04	75.9 ± 0.08	100	204.5	98.9	50	126.1	100.4	25	31.8	109.0
E***	1463.6 ± 0.07	2.3 ± 0.06	171.8 ± 0.11	100	1569.3	105.7	50	227.5	111.2	25	27.1	99.2
F***	3431.1 ± 0.04	2.2 ± 0.05	25.0 ± 0.09	100	3537.9	106.9	50	72.5	95.0	25	27.7	102.0
A*				200	235.1	102.0	50	74.5	115.9	50	52.1	98.2
B*				200	534.7	94.9	100	182.2	103.0	50	53.9	100.2
C**				200	441.5	100.5	100	129.2	103.0	50	53.5	100.7
D**				200	301.0	98.2	100	175.6	99.7	50	53.5	97.7
E***				200	1662.4	99.4	100	267.5	95.7	50	52.4	100.2
F***				200	3625.3	97.2	100	126.3	101.3	50	52.1	99.5
A*				100	121.1	90.1	25	40.9	97.3	25	29.9	107.3
B*				100	450.8	105.9	50	125.9	93.1	25	28.5	98.8

* Cartons.
** Plastic bottles.
*** Glass bottles.

adopted to minimize matrix effects due to the complexity of the sample matrixes.

3.7. Determination of Cu, Cd and Pb in wine and grape juice samples by TS-FF-AAS

Tables 6 and 7 contain results for determination of Cu, Cd and Pb in wine and grape juices samples. Wine samples were measured after simple dilution and grape juice samples were analyzed without any treatment. An appreciable variation of the concentrations of Cu, Cd and Pb in wines can be seen. All concentrations of Cu, Cd and Pb are below the maximum levels allowed by legislation [3,6]. Tables 6 and 7 indicate the accuracy of the developed procedure applying addition-recovery experiments for determination of low concentrations of these metals in wine samples. Recoveries ranged between 90.1 and 112.7% for Cu, 93.1 and 117.8% for Cd, and 87.8 and 109% for Pb. Standard deviation values can be considered appropriate. For Cd, accuracy was also verified by using GFAAS and all results were in agreement at a 95% confidence level.

The maximum allowed levels of metals in grape juices are $1.0\,mg\,L^{-1}$ for Cu, $10\,\mu g\,L^{-1}$ for Cd and $300\,\mu g\,L^{-1}$ for Pb [3,6]. In grape juice samples, the concentrations of metals ranged from 31.1 to 3431.1 $\mu g\,L^{-1}$ for Cu, 16.5 to 171.8 $\mu g\,L^{-1}$ for Pb and 2.2 to 4.5 $\mu g\,L^{-1}$ for Cd. Thus, samples E and F presented concentrations higher than the maximum allowed levels for Cu and none sample contained Cd an Pb concentrations above the legislation limits.

It is important to emphasize that two grape juice samples contained Cu and Cd concentrations between the LOD's and the LOQ's. This is not a suitable region to obtain quantitative data, however due to the low standard deviation of the measurements and adequate recoveries they can be considered reliable.

4. Conclusions

Thermospray flame furnace atomic absorption spectrometry (TS-FF-AAS) has demonstrated the possibility of the direct determination of Cu, Cd and Pb at $\mu g\,L^{-1}$ levels in wines and grape juices without any critical sample preparation step, but calibration must be performed using the SAM. Due to the efficiency on the sample introduction and atomization processes, the limits of detection obtained are much better than those usually established in FAAS.

Acknowledgements

The authors are grateful to the Fundação de Amparo à Pesquisa do Estado de São Paulo by financial support (FAPESP, Grants 02/12127-5 and 03/00326-1) and are also thankful to the Coordenação de Aperfeiçoamento de Pessoal de Nível Superior (CAPES) by research funds. J.A.N. is thankful to Conselho Nacional de Desenvolvimento Científico e Tecnológico by his research fellowship. We also are thankful to Dr. Harald Berndt (ISAS, Germany) for kindly supplying ceramic capillary tubes.

References

[1] Z.N. Lishkovskii, I.M. Skurikhin, Chemistry of Wine, Pischevaya Promyshlennost, Moscou, 1976, p. 312.
[2] K.Z. Brainina, N.Y. Stozhko, G.M. Belysheva, O.V. Inzhevatova, L.I. Kolyadina, C. Cremisini, M. Galletti, Anal. Chim. Acta 514 (2004) 227.
[3] ANVISA. http://e-legis.anvisa.gov.br/leisref/public/showAct.php?id=90, accessed in September, 12, 2007, Decree number 685, August, 27, 1998.
[4] A.C. Clark, G.R. Scollary, Anal. Chim. Acta 413 (2000) 25.
[5] R. Lara, S. Cerutti, J.A. Salonia, R.A. Olsina, L.D. Martinez, Food Chem. Toxicol. 43 (2005) 293.
[6] www.oiv.org.br, accessed in October, 23, 2006.
[7] B.W. Zoecklein, K.C. Fugelsang, B.H. Gump, O.S. Nury, Wine Analysis and Production, Chapman & Hall, New York, 1994, p. 644.
[8] J. Cvetkovic, S. Arpadjan, I. Karadjova, T. Stafilov, Acta Pharm. 56 (2006) 69.
[9] J.M. Concon, Food Toxicology, Marcel Dekker, New York, 1998.
[10] E.S. Bordeu, J.B.B. Scarpa, Análisis Químico del Vino, Textos Universitários, Ediciones Universidad Católica de Chile, 1998.
[11] M. Llobat-Estellés, A.R. Mauri-Aucejo, R. Marin-Saez, Talanta 68 (2006) 1640.
[12] M. Aceto, O. Abollino, M.C. Bruzzoniti, E. Mentasti, C. Sarzanini, M. Melandrino, Food Addit. Contam. 19 (2002) 126.
[13] M.A. Baldo, C. Bragato, S. Daniele, Analyst 122 (1997) 1.
[14] A.M. Gree, A.C. Clark, G.R. Scollary, Fresenius J. Anal. Chem. 358 (1997) 711.
[15] Official Methods of Analysis of AOAC International, 16th Edition, vol. II, 1998.
[16] C.C. Nascentes, M.Y. Kamogawa, K.G. Fernandes, M.A.Z. Arruda, A.R.A. Nogueira, J.A. Nóbrega, Spectrochim. Acta Part B 60 (2005) 749.
[17] C.C. Nascentes, M.A.Z. Arruda, A.R.A. Nogueira, J.A. Nóbrega, Talanta 64 (2004) 912.
[18] F.R.P. Rocha, J.A. Nóbrega, J. Chem. Educ. 73 (1996) 982.
[19] J.Y. Neira, E. González, R. Ahumada, V. Medina, U. González, Quím. Nova 27 (2004) 873.
[20] A. Gaspar, H. Berndt, Spectrochim. Acta Part B 55 (2000) 587.
[21] E.R. Pereira-Filho, H. Berndt, M.A.Z. Arruda, J. Anal. At. Spectrom. 17 (2002) 1308.
[22] J. Davies, H. Berndt, Anal. Chim. Acta 479 (2003) 215.

Talanta 76 (2008) 1233–1240

Contents lists available at ScienceDirect

Talanta

journal homepage: www.elsevier.com/locate/talanta

A systematic study on extraction of total arsenic from down-scaled sample sizes of plant tissues and implications for arsenic species analysis

Anne-Christine Schmidt*, Nora Haufe, Matthias Otto

TU Bergakademie Freiberg, Faculty of Chemistry and Physics, Institute of Analytical Chemistry, Leipziger Str. 29, D-09596 Freiberg, Germany

ARTICLE INFO

Article history:
Received 15 February 2008
Received in revised form 19 May 2008
Accepted 21 May 2008
Available online 29 May 2008

Keywords:
Extraction
Arsenic speciation
Reduction of sample size
Inductively coupled plasma atomic emission spectroscopy
Tropaeolum majus

ABSTRACT

An easily feasible, species-conserving and inexpensive protocol for the extraction of total arsenic and arsenic species from terrestrial plants was designed and applied to the investigation of accumulation and metabolization of arsenite (As(III)), arsenate (As(V)), monomethylarsonate (MMA(V)), and dimethylarsinate (DMA(V)) by the model plant *Tropaeolum majus*. In contrast to existing extraction methods hazardous additives and elaborate procedures to enhance the extraction yields were omitted. The proposed protocol is suited to down-scale the sample sizes used for the extractions and to promote a compartmentally resolved analysis of the arsenic distribution within individual leaves, leaf stalks, and stems instead of the conventional extraction of pooled samples. In a two-step extraction, the high extraction efficiencies (85–92%) for arsenic achieved by phosphate buffer from larger amounts (200 mg) of homogenized leaf material in a one-step extraction, could be enhanced to 94–100% in a second extraction step. A strong dependence of the arsenic extractability on the type of arsenic species accumulated in the tissue as well as on the type of the tissue (leaf, leaf stalk, stem) was found. For the extraction of 5 mm long segments cut from individual leaves without previous homogenization of the plant parts yields between 75 and 93% depending on arsenic species prevailing in the cells were obtained using 1 or 10 mM phosphate buffer. The total extraction and analysis protocol was validated using a standard reference material as well as by spiking experiments. The arsenic species analysis by IC/ICPMS revealed a number of nine unidentified metabolites in the plant extracts in addition to the species MMA(V), DMA(V), As(III), and As(V) that were provided to the plants during their growth phase.

1. Introduction

Many studies deal with the analysis of arsenic species in various kinds of samples as comprehensively reviewed in [1] and [2]. Qualitative and quantitative determinations of arsenic species are mainly based on chromatographic separations combined with elemental or molecular mass spectrometric detection. For the extraction process no uniform procedure exists and several variants were proposed throughout the literature (see references in [1] and [2]). Because the success of the extraction is also dependent both on the constitution of the matrix and on the kind of species and their concentrations, the development of a generally valid procedure is difficult. Most commonly, methanol, water and mixtures of them were used as extracting agents for arsenic species from biological materials. Thereby, increasing methanol contents often result in diminished extraction efficiencies in comparison to water extraction in case of plant material [3–5], whereas methanol proved to be suitably to extract arsenic from marine animals. Several additives such as strong inorganic acids [4,6] or enzymes [7,8] and additional steps such as the supply of microwave energy or of ultrasound [7,9] were included in the extraction process in order to improve the extraction efficiency and the reproducibility of the results. A focused supply of ultrasound by a special probe for sample treatment proved to be a powerful tool to improve extraction efficiency and to reduce extraction time significantly. This kind of sample preparation was successfully employed for the extraction of total arsenic and arsenic species from different sample types, mainly rice grains, chicken, fish and soil providing extraction yields between 85 and 100% depending on sample type in a few minutes [10,11]. For different algae samples extraction efficiencies of 64–69% were obtained using focused ultrasound energy within 30 s comprising a slight improvement compared to magnetic stirring (59–64% extraction efficiency achieved in 30 min) [12]. Higher plants of aquatic as well as of terrestrial origin remain a complicated subject for extraction of arsenic compounds. In the majority of cases high extraction yields are difficult to attain. Even with the employment of a focused ultrasonic probe only 26–53% of total arsenic

* Corresponding author. Tel.: +49 3731 393255; fax: +49 3731 393666.
E-mail address: Anne-Christine.Schmidt@chemie.tu-freiberg.de (A.-C. Schmidt).

0039-9140/$ – see front matter © 2008 Elsevier B.V. All rights reserved.
doi:10.1016/j.talanta.2008.05.032

could be extracted from different plant species [13]. In a current study dealing with arsenic speciation in plants from contaminated sites low and varying extraction efficiencies (3–41%) resulted from several plant samples using a water–methanol mixture by shaking for 16 h [14]. Pressurized liquid extraction (PLE) of different plant parts offered high extraction yields using water as solvent [15,16].

In the majority of studies dealing with arsenic species analysis the sample preparation was focused on the maximization of extraction efficiency without regard to binding and localization of the species inside different tissues. Typically, for the extraction of algae and terrestrial plants portions in the range of 0.1–1.0 g dry mass corresponding to about 1–10 g fresh mass were amended with 10–30 mL of the extracting agent [3,7,17,18]. Still larger amounts of solvents are required for soxhlet extractions, e.g. 70 mL [4]. The analysis of larger sample amounts provides informations about the general metalloid accumulation of organisms but no conclusions can be drawn concerning the sites of storage and binding within the tissues. A fractionated extraction scheme was proposed for the analysis of arsenic species in an acid-soluble non-protein fraction, in a water-soluble protein fraction, and in the fraction of insoluble structure components of plant cells [19].

In order to enable a compartmentally resolved arsenic species analysis for the elucidation of the arsenic distribution within plant tissues the reduction of the sample size as a first step towards a miniaturized extraction scheme is promoted in the current study. The aim was to evaluate the suitability of different extracting agents under varied conditions for the extraction of total arsenic and arsenic species from reduced sample amounts of different tissues of plants contaminated with methylated and inorganic arsenic compounds which are the prevalent arsenic species found in terrestrial plants [18,20]. To preserve the native arsenic species composition, gentle extraction conditions should be preferred. For this reason, aggressive extractants such as strong and oxidizing acids were omitted in the current study. The potential of the extraction method for miniaturized extractions was studied regarding both extraction efficiency, species integrity and compatibility with the ion chromatographic separation used for arsenic species analysis. This is to our knowledge the first approach for a minimization of sample sizes in extraction methods preceding arsenic species analysis. Since most of the conventional techniques used for extraction of arsenic species are not appropriate for simultaneous extraction of proteins, the extractants deionized water, a biologically compatible buffer system and a cellulose-digesting enzyme were explored that can potentially solve proteins from the plant matrix [21].

2. Experimental

2.1. Plant cultivation and arsenic exposure

The plant material for the extraction experiments was obtained from *Tropeaolum majus* cultivated under arsenic exposure during 8 weeks after an initial arsenic-free germination and growth phase of 4 weeks. Four different arsenic species, dimethylarsinate (DMA(V)), monomethylarsonate (MMA(V)), arsenite (As(III)), and arsenate (As(V)), were applied to the soil used for plant cultivation twice per week in 100 mL portions containing 5 mg arsenic. The applied arsenic solution was not in contact with the above-ground plant parts ensuring an arsenic uptake solely through the roots. DMA(V) was obtained as sodium cacodylate trihydrate (purity grade ≥98%) from Sigma–Aldrich, Steinheim, Germany, As(III) as 0.05 M sodium arsenite solution, and As(V) as disodium hydrogen arsenate heptahydrate (purity grade ≥98%) from Sigma–Aldrich as well, whereas MMA(V) was purchased in the form of monosodium acid methane arsonate sesquihydrate from Chem Service, West Chester, PA, USA. The plants were harvested and divided into stems, leaves, and leaf stalks, and stored frozen.

2.2. Extraction experiments for total arsenic and arsenic species from plant tissue

The extracting agent was varied between deionized water, aqueous buffer solutions containing Na_2HPO_4 in different concentrations (1, 5, 10, 100 mM) adjusted to pH 7.0 with 1 M H_3PO_4, and different amounts of cellulase (0.1, 0.5, 1.0, 2.0 and 4.0 g L^{-1}) in this phosphate buffer system. The solid buffer substance sodium phosphate dibasic (puriss). p.a. and cellulase powder (from *Aspergillus niger*, 1.92 units/mg solid) were purchased from Sigma–Aldrich, Seelze and Steinheim, Germany. Fresh leaves of *Tropaeolum majus* were homogenized under liquid nitrogen using mortar and pestle. Aliquots of varied fresh mass (10–200 mg) of this leaf material were weighed either in 15 mL or in 2 mL polypropylene tubes and mixed with varying volumes of the extracting agent by vortexing. Alternatively, small pieces of 5 mm length characterized by a fresh mass of 5–30 mg were cut from intact leaves, leaf stalks, and stems without prior homogenization of the tissues. The extraction was carried out for 4 or 16 h at room temperature and completed with 15 min ultrasonication. For extractant volumes >2 mL the extracts were filtered through 0.45 μm cellulose acetate membrane filters (Whatman, Schleicher & Schuell, Dassel, Germany). The extraction residue was collected on the filter and rinsed with 2 mL of the extractant. For extractant volumes <2 mL the filtration was displaced by centrifugation (10,000 × g, 10 min) of the extract and the extraction residue was washed with 1 mL of the extractant under short vortexing. In case of two-step extractions the extraction residues were subjected to a repeated extraction and filtration or centrifugation. In the filtrated or centrifuged extracts the concentrations of total arsenic as well as of individual arsenic species were measured using atomic emission spectroscopy (ICPAES, Section 2.4.) and ion chromatography coupled to inductively coupled plasma mass spectrometry (IC/ICPMS, Section 2.5.), respectively. The extraction residues were digested in a microwave device (Section 2.3) prior to total arsenic determination by ICPAES.

The standard reference material BCR-CRM 060 (aquatic plant, *Lagarosiphon major*) provided by the Institute for Reference Materials and Measurements, Joint Research Centre of the European Commission (EC-JRC-IRMM), Geel, Belgium, was used for a validation of the extraction procedure.

2.3. Microwave digestion of extraction residues

The remaining washing residues of all extraction experiments described in Section 2.2 were transferred into 6 mL microwave-transparent teflon digestion vessels. 2 mL 65% HNO_3 and 0.5 mL 30% H_2O_2 (both in suprapur quality from Merck, Darmstadt, Germany) were added to each sample, and three of the prepared 6 mL vessels were placed in the inset of a 100 mL digestion vessel filled with 8 mL deionized water and 2 mL 30% H_2O_2. A four-step digestion was programmed on the microwave device (Microwave system Start 1500, MLS, Leutkirch, Germany) comprising of an initial heating to 85 °C in 3 min and then to 145 °C in 5 min providing a power of 700 W for both heating steps followed by an increased power of 1000 W for step 3 and 4 in which the temperature was increased in 3 min to 210 °C and then hold for 15 min. The clear digests obtained from this procedure were filled in 15 mL polypropylene tubes and diluted to 5 mL with deionized water for ICPAES analysis. The averaged arsenic content of five blank digests was subtracted from all

sample arsenic contents. These blanks contained same volumes of both digestion chemicals HNO_3 and H_2O_2 and of deionized water as the plant samples.

2.4. ICPAES for determination of total element concentrations

The total arsenic concentrations in the extracts as well as in the microwave digests of the extraction residues were determined using an atomic emission spectrometer with an inductively coupled plasma as excitation source (ICPAES, iCAP 6500, Thermo Electron, Dreieich, Germany). The sample was infused at a flow rate of 2 mL min^{-1} into a parallel path nebulizer (Mira Mist) associated to a glass cyclone spray chamber. The emission of As was measured axially in the argon plasma torch at the wavelengths of 189.0, 193.7, and 228.8 nm. In addition to As, in samples originating from the standard reference material, the atomic emission of copper, zinc, and cadmium was measured at 324, 213, and 226 nm, respectively.

2.5. IC/ICPMS for determination of arsenic species

The arsenic species in the various plant extracts were separated and detected using a coupling of ion chromatography with inductively coupled plasma mass spectrometry (IC/ICPMS). An anion exchange column (IonPac AS7, 4 mm × 250 mm, Dionex, Sunnyvale, USA) with a guard column (IonPac AG7, 4 mm × 50 mm) was employed for the separation of arsenic species. A HPLC 1100 series system consisting of a degasser, thermostated autosampler and quarternary pump was coupled with PEEK capillaries to the ICPMS VG PQ ExCell (ThermoElemental) via a microconcentric nebulizer (MicroMist, GE, Australia) and a cyclon spray chamber. The separation was performed with a gradient elution based on 0.04 mM HNO_3 and 50 mM HNO_3 with 0.05 mM benzene-1,3-disulfonic acid (BDSA) as ion pairing reagent and was previously described [16,22]. The eluent flow rate was set to 1 mL min^{-1} and 50 μL of sample were injected. The m/z ratio of 75 (As) was detected with a dwell time of 1 s under following operation conditions of the ICPMS: rf-power 1350 W; cool gas flow 13 L min^{-1}; auxiliary gas flow 1 L min^{-1}; nebulizer gas flow 0.9 L min^{-1}.

2.6. Statistical test for extraction efficiencies

The total arsenic concentrations in the different extracts and in the corresponding extraction residues determined by ICPAES were used for calculation of the extraction efficiencies achieved under different extraction conditions. The extraction efficiency is defined as ratio of the arsenic concentration in the extract to the total arsenic content.

The extraction efficiencies of different samples were compared regarding statistically significant differences using one-way analysis of variance (ANOVA) for a level of significance of $\alpha = 0.05$ corresponding to a probability value of 95%.

3. Results and discussion

3.1. Variation of the extraction medium for larger sample sizes

3.1.1. Evaluation of extraction efficiencies for total arsenic

The extraction capabilities achieved by pure water, 100 mM phosphate buffer, pH 7, and by a solution of cellulase, which cleaves the β-1,4-glycosidic linkages of the cell wall component cellulose, are compared in Table 1. High and reproducible extraction efficiencies were achieved that varied between 80 and 92% depending on the extraction medium and on the arsenic species application. A pairwise comparison between the extraction efficiencies achieved by the buffer and by the enzyme in this buffer offered no significant differences including all four arsenic species applications. For this behaviour different explanations can be supposed: either no additional arsenic species were extracted from the tissue by the degradation of macromolecular components if the cells are broken up previously by grinding under liquid nitrogen or the enzyme did not work efficiently under the influence of proteases released from the broken cells. Neither an elevation of the enzyme concentration in the extraction medium from 1 to 2 or 4 g L^{-1} nor the use of other enzymes such as amylase, protease or trypsin did improve the extraction yield (data not shown).

However, comparing the extraction efficiencies obtained by deionized water with those obtained by the buffer and the enzyme solution, a significant higher extraction yield resulted from the use of both extraction media containing the buffer. Significant differences were further ascertained for the extraction efficiencies of the four different arsenic species applications for a comparison of all extraction media listed in Table 1. At a level of significance of $\alpha = 0.05$ the yields of arsenic extraction were significantly different for As(V)- and DMA(V)-application, for As(III)- and MMA(V)-application, and for MMA(V)- and DMA(V)-application. This means that the extractability of arsenic depends on the arsenic species exposure. The highest extractability occurred in case of DMA application (90.6 ± 1.8%) followed by As(III) application (87.7 ± 3.7%) and As(V) application (85.9 ± 4.9%). The leaf tissue of MMA application was characterized by the lowest extractability (84.6 ± 3.7%).

3.1.2. Influence of the extraction medium on arsenic species analysis

The applied arsenic species did not correspond in each case to the species dominating in the plant cells as can be seen from the arsenic species analysis (Fig. 1a–d). Plants grown under As(III) or As(V) application are characterized by a similar arsenic species distribution in their leaves that showed a high As(III) level (Fig. 1a and b). The extraction yields achieved for the As(III) and As(V) plants were also similar (see Section 3.1.1). The unknown metabolite X1 was found in leaf extracts when plants are exposed to As(III) in considerably higher amounts than in extracts of the As(V) application. In aqueous and buffer extracts of leaves from plants exposed to DMA this species appeared as the main arsenic species. Peak X3 and X7–X9 could represent metabolization

Table 1
Comparison of the yields of total arsenic extraction from 200 mg homogenized leaf tissue achieved by 7 mL of the extraction media deionized water, phosphate buffer, and cellulase in phosphate buffer in an extraction time of 4.25 h

Arsenic species application	Extraction efficiency [%] achieved by different extraction media		
	Deionized water	100 mM phosphate buffer, pH 7	1 g L^{-1} cellulase in 100 mM phosphate buffer, pH 7
As(III)	83 ± 3	90 ± 2	90 ± 1
As(V)	80 ± 1	88 ± 1	89 ± 1
MMA(V)	81 ± 7	85 ± 2	88 ± 0.1
DMA(V)	89 ± 2	92 ± 2	91 ± 3

Average values with standard deviations from five replicates are given.

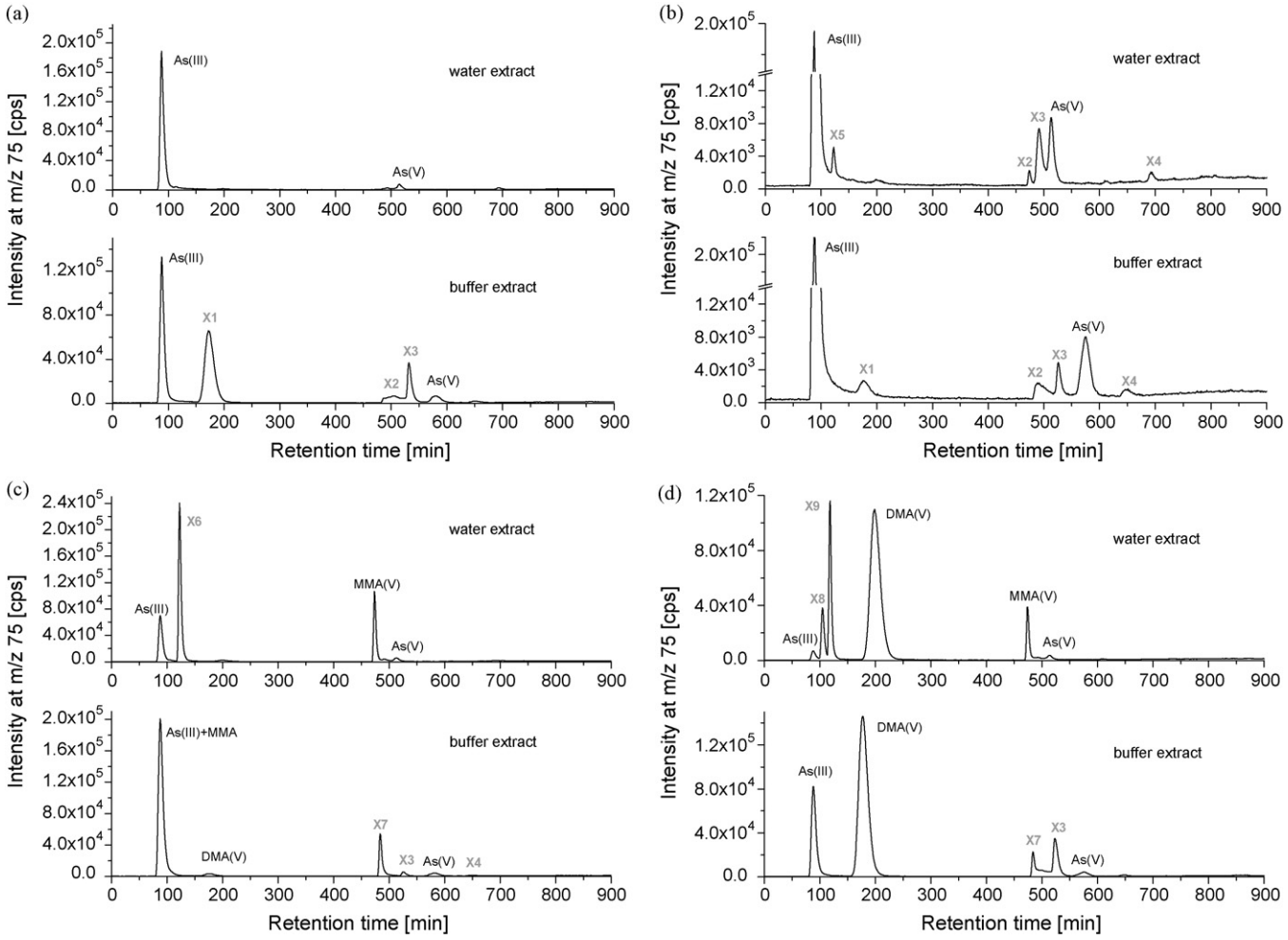

Fig. 1. Effect of the extraction medium on the IC/ICPMS chromatograms for arsenic species analysis in different leaf extracts of *T. majus*. The extraction media were deionized water and 100 mM phosphate buffer, pH 7. Unidentified arsenic species are marked by "X". (a) As(III) application; (b) As(V) application; (c) MMA(V) application; (d) DMA(V) application.

products. A demethylation of DMA to As(III) by terrestrial plants was reported previously [23]. The identification of arsenic species solely by means of their retention times is questionable [24] and an additional structure elucidation by MS or NMR would be necessary.

If the extraction was performed with 100 mM phosphate buffer, some additional arsenic species were found in the leaf extracts that did not appear using pure water as extraction medium. In this context, the peak marked with X1 in Fig. 1a and b occurred in case of As(III) and As(V) application whereas the peak X7 and X3 were detected in case of the methylarsenic applications. Otherwise, some peaks that were remarkable in the water extracts, disappeared in the chromatograms after enzymatic or buffer extraction especially in case of the methylarsenic applications (peak X6, X8, X9). This fact can be ascribed to a dislocation of the retention times due to the buffer component (Fig. 2). In standard solutions containing the phosphate buffer the As(V) peak shifted to higher retention time if the buffer concentration increased whereas the DMA(V) peak eluted earlier from the IC column. The most rigorous effect of an increasing phosphate buffer concentration was observed for MMA(V) which co-eluted with As(III) at phosphate concentrations $\geq$50 mM. Therefore, MMA and As(III) cannot be differentiated in the leaf extracts since they contained a buffer concentration of 100 mM. Only at the low buffer concentration of 1 mM the retention times of all four species did not change compared to a standard solution in deionized water. Within water or buffer extracts the reproducibility of the retention times in the plant samples was very high (R.S.D. 0.4–1.8% for $n = 10$). A possible explanation for the changing elution order could be ascribed to the high ionic strength provided by the phosphate and sodium ions of the buffer [25]. Otherwise, the neutral pH conditions of the phosphate buffered solutions disagree with the pH of the non-buffered aqueous extracts.

In summary, the distribution of arsenic species in the chromatograms was similar for buffer extracts and enzymatic extracts containing the same buffer concentration as matrix for the enzyme independently on the enzyme concentration (1, 2, or 4 g L^{-1}, data not shown). This means that the 0.1 M phosphate buffer mainly affects both kind and quantity of arsenic species recorded in the plant extracts compared to pure water extraction and not the enzyme even if its concentration is increased.

3.2. Two-step extraction versus one-step extraction

The first extraction step was performed with deionized water in order to receive the part of arsenic accumulated in the plant that is characterized by a high mobility and water solubility. In the second extraction step, the extracting agents, deionized water and an aqueous cellulase solution were compared regarding the extraction yield achieved (Table 2). The main part of arsenic was extracted from the

Table 2
Arsenic species extracted in the 2nd step of a two-step extraction of 200 mg homogenized leaves of *T. majus* treated with As(III), As(V), MMA(V), and DMA(V) using 5 mL deionized water[a] or 1 g L^{-1} cellulase in 100 mM phosphate buffer, pH 7[b]

Arsenic application	Extraction medium	Arsenic species concentrations in the extract (IC/ICPMS) [μg L^{-1}] obtained in the 2nd extraction step							Total arsenic conc. (ICPAES) [μg L^{-1}]	Extraction efficiency [%]	
		As(III)	X1	X2	X3	As(V)	X4	Sum		1st step	2nd step
As(III)	Water[a]	2.9	1.2	0.3	0.1	4.6	2.6	11.7	10.0	81.9	91.0
	Buffer[b]	8.2	4.2	1.8	0.7	2.2	1.0	18.2	16.0		95.7
As(V)	Water	20.4	–	1.7	1.8	3.1	1.1	28.0	25.0	80.6	91.5
	Buffer	41.5	–	3.5	2.1	6.5	1.4	55.0	43.0		93.6
		As(III)	DMA	MMA	X7	X3	As(V)				
MMA(V)	Water	14.2	2.6	2.5	0.7	1.0	1.1	22.1	25.0	80.2	87.5
	Buffer	36.2	1.2	–	2.4	–	1.2	41.0	40.0		100
		As(III)	DMA		X7	X3	As(V)				
DMA(V)	Water	6.4	21.2		1.1	–	3.1	31.8	26.0	87.5	96.9
	Buffer	1.0	34.5		0.9	1.2	2.2	40.3	48.0		97.9

Comparison of the sum of arsenic species concentrations detected by means of IC/ICPMS with the total arsenic concentrations measured by ICPAES and extraction yields achieved by 1st and 2nd extraction step. The 1st step was performed with 7 mL deionized water. X1–X7: unidentified arsenic-containing metabolites.

plant tissue in the first step using water (80–88%). A subsequent repeated extraction with water led to an additional extraction of 7–11% of the arsenic totally present in the tissue but an increase of 10–20% of the extraction yield in the second step was observed caused by the enzyme-buffer solution. This enhanced extraction in the second step is consistent with the higher extraction yields attained by buffer and enzyme in buffer compared to deionized water in the one-step extractions (see Table 1). After completing both extraction steps, nearly 100% of the arsenic was solved from the leaf matrix.

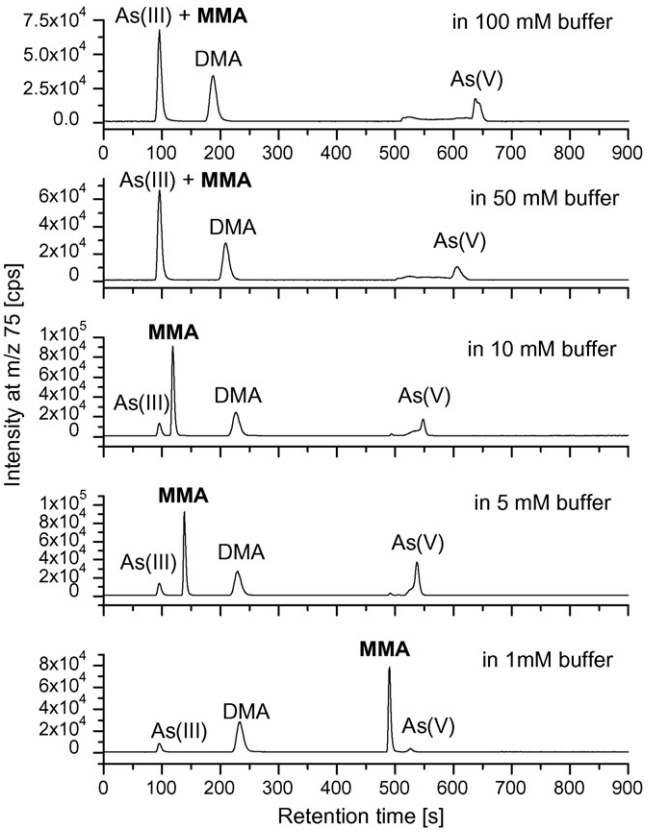

Fig. 2. Influence of the phosphate buffer concentration (pH 7) in the standard solution containing As(III), As(V), MMA(V), and DMA(V) on the ion chromatographic separation of these four arsenic species. ICPMS detection at *m/z* 75 for As^+. Concentration of 25 μg As L^{-1} for inorganic and 50 μg As L^{-1} for methylated species.

3.3. Reduction of sample size

In order to study the extraction behaviour in dependence on the sample size, the initial leaf weight was systematically reduced starting from such large amounts as 400 mg and preliminary ending at 10 mg over five intermediate steps. The individual samples were taken from a larger homogenized pool of ground fresh leaf material. According to the diminished amounts of leaf mass the volume of the extracting agent was reduced from 8 mL down to 200 μL thereby maintaining a phase ratio between the volume of extractant and the leaf mass of 0.02 mL mg^{-1}. Whereas the high extraction yield remained unaltered in the mass range 400–125 mg, it declined continuously with further decreasing sample size (Fig. 3). A slight raise of the phase ratio for smaller initial leaf weights prevented the declining of the extraction yield that occurred in case of a constant phase ratio. According to a theory formulated for the extraction process of arsenic species from algae [11] the highest extraction yields may be expected at large *V*/*m* ratios.

Subsequently, the reduction of sample sizes was further promoted in terms of cutting up small pieces of approximately 5 mm in length from an undestroyed leaf, leaf stalk or stem instead of the homogenization of different leaves. In these experiments, the buffer concentration was decreased because a higher phosphate molarity as used before caused a serious modification of the ion chromatographic arsenic species separation (see Fig. 2). Concerning the concentration of cellulase used for the extractions (0.1–4 g L^{-1}), no influence on the yield was observed for slices of leaves, leaf stalks and stems from all arsenic species applications suggesting that the

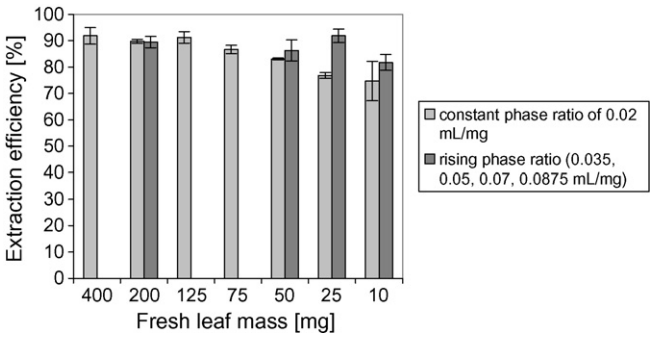

Fig. 3. Extraction efficiencies achieved under a constant and a rising phase ratio for arsenic from continuously reduced sample sizes of leaves from *T. majus* cultivated under As(V) exposure. The extraction was performed with 100 mM phosphate buffer, pH 7. Standard deviations from three parallel extractions are indicated.

primary extraction effect is caused by the buffer component as it has been proven before for the homogenized leaf samples. The effects of the other varied parameters on the extraction efficiency are compared in Table 3. No significant differences were obtained from ANOVA tests for both phosphate buffer concentrations 1 and 10 mM regarding the yield of arsenic extraction from leaf, leaf stalk, and stem tissue. Likewise, for leaf tissue from plants exposed to DMA(V) during growing an elevation of the extraction time from 4 h up to 16 h did not improve the yield. Such high portions as 78% up to 93% of the total arsenic accumulated in the leaf were extracted during 4 or 16 h. However, for leaf slices from plants of the As(V) application for which lower extraction yields were obtained (63–77%), a prolonged extraction time resulted in increased arsenic concentrations in the extracts. A significant higher extraction yield could be achieved for leaves from DMA application compared to leaves from As(V) application in case of both extraction times and buffer concentrations. These findings confirm the dependence of the extraction efficiency on the kind of arsenic species prevailing in the plants (see Section 3.1.1). For leaf stalks from DMA(V) and As(V) application no significant difference was observed concerning the extractability whereas for stems the extraction efficiency was significantly higher for As(V) application. This converse behaviour related to the leaves suggests a different kind of interaction for the arsenic species with components of leaf and stem cells. Within each arsenic application (DMA or As(V)), extraction yields gained for different kind of tissue (leaf, leaf stalk, and stem segments) were highly divergent as it is reflected by significant differences resulting from ANOVA tests. Equally, for non-miniaturized samples a varying extraction efficiency was noticed for different plant parts such as roots, stems, leaves, and fruits of *Capsicum annuum* [2].

If all extracts are considered that were produced from reduced sample sizes, the extraction of small pieces of intact leaves revealed nearly the same efficiency ($87.3 \pm 8.2\%$ for $n = 12$) as it resulted from miniaturized portions of homogenized leaf material ($87.4 \pm 5.3\%$ for $n = 13$) in case of plants that mainly contained DMA. No significant difference arised from that comparison. In contrast, the homogenization of leaves treated with As(V) and mainly containing As(III) improved the extraction yield ($87.8 \pm 4.6\%$ for $n = 12$) opposite to pieces of intact leaves ($71.0 \pm 9.5\%$ for $n = 14$). In this case, the ANOVA offered a significant difference.

If a second extraction step was performed using deionized water as extracting agent for 2 h after a 4 h incubation of small slices (5 mm long) of intact leaves with buffer solutions containing cellulase, an enhancement of $5.8 \pm 3.1\%$ ($n = 6$, plants exposed to DMA(V) during growth) and $7.2 \pm 2.8\%$ ($n = 6$, plants exposed to As(V)) of the extraction efficiency was attained. This additional extraction yield is characterized by the same order of magnitude as in case of the 2nd extraction step of homogenized leaf material with deionized water as extracting agent (compare Table 2).

3.4. Figures of merit for the arsenic species and total arsenic determinations

A detection limit of $0.7\ \mu g\ L^{-1}$ was achieved for total arsenic by ICPAES. For the individual arsenic species the following detection limits resulted from IC/ICPMS: 0.2, 0.3, 0.2, and 0.5 μg/L for As(III), MMA(V), DMA(V), and As(V), respectively. Calibration curves were received in the range between 10 and 200 $\mu g\ As\ L^{-1}$ over five single concentrations with R^2 values >0.99. The precision for the peak areas of arsenic species in aqueous standard solutions (from five independent measurements) was assessed to 1.9, 0.02, 0.7, and 1.3% for As(III), DMA(V), MMA(V), and As(V), respectively, at a concentration level of 10 $\mu g\ As\ L^{-1}$ for each species and to 1.8, 0.2, 0.1, and 0.4% for As(III), DMA(V), MMA(V), and

Table 3
Comparison of extraction efficiencies for arsenic from plant material achieved under varied parameters for extraction

Varied parameters				Extraction efficiency (%) (average ± s.d., $n = 4$)	Significance from ANOVA[a] ($n = 3$–6)			
Buffer concentration (mM)[b]	Extraction time (h)	Applied arsenic species	Plant tissue		Buffer concentration	Extraction time	DMA(V)/As(V) application	Leaf/leaf stalk, leaf/stem, leaf stalk/stem
1	4	DMA(V)	Leaf	78 ± 11	(–)			
10	4	DMA(V)	Leaf	91 ± 3				Leaf/leaf stalk: (++) for DMA(V), (++) for As(V)
1	16	DMA(V)	Leaf	88 ± 4	(–)	DMA(V): (–)		
10	16	DMA(V)	Leaf	93 ± 2			Leaf: (++) for 4 h, (++) for 16 h	
1	4	As(V)	Leaf	68 ± 6	(–)			
10	4	As(V)	Leaf	63 ± 16		As(V): (++)		Leaf/stem: (++) for DMA(V), (++) for As(V)
1	16	As(V)	Leaf	75 ± 1	(–)			
10	16	As(V)	Leaf	77 ± 4				
1	16	DMA(V)	Leaf stalk	50 ± 9	(–)			
10	16	DMA(V)	Leaf stalk	46 ± 11			Leaf stalk: (–)	
1	16	As(V)	Leaf stalk	55 ± 16	(–)			
10	16	As(V)	Leaf stalk	49 ± 18				Leaf stalk/stem: (++) for DMA(V), (++) for As(V)
1	16	DMA(V)	Stem	75 ± 5	(–)			
10	16	DMA(V)	Stem	66 ± 4			Stem: (++)	
1	16	As(V)	Stem	83 ± 7	(–)			
10	16	As(V)	Stem	96 ± 6				

Approximately 5 mm long segments (5–30 mg fresh mass) of intact leaves, leaf stalks, and stems were cut and extracted with 2 mL extractant.
[a] ANOVA test for estimate of significant differences in extraction efficiency; significance level $\alpha = 0.05$; (++), the difference is significant; (–), the difference is not significant.
[b] Na_2HPO_4 adjusted with H_3PO_4 to pH 7.0.

Table 4
Validation of arsenic species determination using IC/ICPMS in 0.1 M phosphate buffer extracts from arsenic treated plants

Arsenic species application	Arsenic species measured by IC/ICPMS	Relative peak area deviation (%), $n = 5$	Relative retention time deviation (%), $n = 5$
As(III)	As(III)	11.5	0.4
	X1	22.2	5.8
	X2	13.4	1.4
	X3	48.1	1.8
	As(V)	13.1	1.1
	X4	6.7	0.7
As(V)	As(III)	15.3	0.3
	X1	12.0	3.1
	X2	6.5	0.7
	X3	9.3	0.4
	As(V)	11.8	0.6
	X4	11.1	0.2
MMA(V)	As(III)+MMA	13.4	0.1
	DMA(V)	10.4	2.2
	X7	16.4	0.4
	X3	5.3	1.1
	As(V)	11.1	0.6
	X4	5.2	0.4
DMA(V)	As(III)	10.9	1.1
	DMA(V)	20.6	1.5
	X7	25.1	1.0
	X3	23.7	1.3
	As(V)	11.4	0.8
	X4	5.9	0.3
	X8	8.1	0.2

The relative standard deviations are calculated for peak areas normalized to 200 mg leaf mass and for retention times of five parallel prepared extracts.

As(V), respectively, at a concentration level of 50 μg As L^{-1} for each species.

In order to validate the full procedure for arsenic species determination in the plant extracts including extraction and IC/ICPMS analysis, the relative standard deviations both of the peak areas and of the retention times of the individual arsenic species in five parallel prepared extracts are calculated (Table 4). The retention times show a high reproducibility, whereas the peak areas are characterized by a larger variability attributed to the biological variation rather than to the chromatography because in standard solutions the relative peak area deviations listed above were considerably smaller. The biological variation is also reflected by the relative standard deviations of the total arsenic concentrations (see below, Table 5).

The accuracy of the determination of arsenic species concentrations in the various types of extracts was validated by comparison with the total arsenic concentrations in the same extracts measured using a different analytical method (ICPAES) which should be not effected by the sample matrix. The values listed in Table 2 show a good agreement of both methods for all types of extracts indicating a sufficient reliability of the arsenic species concentrations obtained by means of IC/ICPMS. For this reason, a loss of some arsenic species prior to ICPMS detection due to strong retention onto the ion exchange column can be widely excluded.

3.5. Validation of the digestion and extraction procedures for reduced sample sizes

3.5.1. Total concentrations of four different elements in a standard reference material

A standard reference material was chosen, which shows similar matrix properties and arsenic concentration level as in the *T. majus* plants investigated in the current study. Unfortunately, no appropriate terrestrial plant was available as reference material for arsenic. Therefore, a higher aquatic plant, the aquatic moss *L. major*, BCR-CRM 060, was used for the validation experiments.

The microwave digestion procedure without prior extraction was validated by comparison of the total concentrations measured by ICPAES for four different elements (Cu, Zn, As, Cd) which are present in BCR-CRM 060 at different concentration levels with the certified contents. From five parallel digestions of 10 mg of the aquatic moss the following values arose (certified values in parentheses): 50.8 ± 10.2 (51.2 ± 1.9) mg kg^{-1} for Cu, 2.1 ± 0.4 (2.2 ± 0.1) mg kg^{-1} for Cd, 325.6 ± 67.1 (313 ± 8) mg kg^{-1} for Zn. Due to the reduced mass of the aliquots the standard deviations are higher but the average values agree with the certified contents. The arsenic content of the reference material is not certified but a value of 8 mg kg^{-1} is given which is obtained from neutron activation analysis from one laboratory. Our analysis revealed a value of

Table 5
Total arsenic concentrations in different parts of *T. majus* after application of As(III), As(V), MMA(V), and DMA(V) (column 2–4) and biological variation within individual leaves (column 5–7)

Arsenic species application	Arsenic concentration (mg kg^{-1} f.m.) (average ± s.d., $n = 6$)[a]			R.S.D. for miniaturized extraction of 5 mm segments ($n = 18$–30)[b]		
	Leaf	Leaf stalk	Stem	Leaf	Leaf stalk	Stem
As(III)	15 ± 5	2 ± 0.4	1 ± 0.1	38	50	45
As(V)	16 ± 3	2 ± 0.2	1 ± 0.3	54	56	60
MMA(V)	21 ± 4	6 ± 1	4 ± 1	19	41	30
DMA(V)	25 ± 3	9 ± 1	4 ± 0.4	17	45	26

[a] Extraction of 150–200 mg fresh mass and microwave digestion of the extraction residue.
[b] Extraction of 5–30 mg fresh mass and microwave digestion of the extraction residue.

$4.1 \pm 0.9\ mg\ kg^{-1}$ which has been approved in the following extraction experiments (see below).

In order to verify the recoveries for the extraction step with subsequent microwave digestion of the extraction residue collected on a cellulose acetate filter, the sum of the element fraction of BCR-CRM 060 extracted with 0.1 M phosphate buffer, pH 7, and the fraction remaining in the extraction residue was likewise compared with the certified contents. For an initial weight of 10 mg BCR-CRM 060 and a volume of extractant of 600 μL, sum concentrations of 57.3 ± 2.9, 2.1 ± 0.1, 333.7 ± 10.6, and $4.8 \pm 1.1\ mg\ kg^{-1}$ ($n = 5$) were obtained for Cu, Cd, Zn, and As, respectively. For 25 mg reference material extracted with 1.5 mL the following sum concentrations resulted: $53.6 \pm 6.9\ mg\ kg^{-1}$ Cu, $1.9 \pm 0.2\ mg\ kg^{-1}$ Cd, $302.2 \pm 40.3\ mg\ kg^{-1}$ Zn, and $4.7 \pm 0.3\ mg\ kg^{-1}$ As ($n = 5$ parallel extractions). The comparison of these results with the certified values listed above suggests a high recovery (86–112%) for the extraction combined with the digestion procedure and rather an overestimation in case of small sample sizes.

3.5.2. Spiking of T. majus homogenate with arsenic species

The recovery of arsenic during the extraction process was evaluated in an additional series using 200 mg of homogenized leaf material from uncontaminated *T. majus* that was spiked with two arsenic species (As(V) and DMA(V)) at three concentration levels (40, 400, and 4000 $\mu g\ As\ L^{-1}$ in 7 mL extract solution). The same procedure as for the arsenic-treated plants was carried out, that means the extraction was performed with 0.1 M phosphate buffer and the extract was separated from the residue by filtration. For the whole sample treatment process including extraction and microwave digestion of the extraction residues, high recoveries of the spiked arsenic species could be demonstrated: in case of DMA(V) addition $100.0 \pm 4.4\%$, $98.7 \pm 1.3\%$, and $88.1 \pm 2.7\%$ ($n = 4$) of the spiked amounts were found for spiking levels of 40, 400, and 4000 $\mu g\ As\ L^{-1}$, respectively. In case of As(V) addition slightly lower arsenic concentrations were detected in the extracts and corresponding residues, $86.1 \pm 9.0\%$ and $93.1 \pm 7.1\%$ ($n = 4$) of the original amounts 40 and 400 $\mu g\ As\ L^{-1}$, respectively. The added arsenic species were mainly present in the resulting extracts, whereas a considerably lower part (0.1–1.3%) was found in the filtration residues after microwave digestion possibly due to adsorption on the leaf material during extraction.

In addition to this determination of total arsenic by ICPAES, the arsenic species concentrations in the spiked extracts were ascertained by IC/ICPMS. For a spiking level of 40 $\mu g\ As\ L^{-1}$ in the leaf extracts $37.3 \pm 4.4\ \mu g\ As\ L^{-1}$ and $41.1 \pm 3.3\ \mu g\ As\ L^{-1}$ ($n = 4$) were recovered from the IC column in case of As(V) and DMA(V) addition, respectively. Whereas DMA(V) was detected as the only species in the extracts after DMA(V) addition, $15.4 \pm 2.0\%$ ($n = 7$) of the added As(V) was converted to As(III) by reducing components released from leaf cells.

3.6. Total arsenic concentration in plants and locally resolved biological variation

Despite of the application of the same total arsenic amount during the growth period the total arsenic concentrations accumulated in the plants differed in dependence on the kind of arsenic species provided for the expositions. The mean accumulation capacity deduced from larger sample amounts was higher for the methylated forms than for the inorganic ones (Table 5) and the arsenic taken up from soil is mainly deposited in the leaves. A high biological variation was observed between different segments of individual leaves, leaf stalks and stems as indicated in column 5–7 of Table 5.

4. Conclusion

The proposed extraction protocol provides high yields for arsenic extraction from plant tissues and offers the possibility to resolve the arsenic distribution within compartments of a single leaf, leaf stalk, or stem. The sample sizes could be minimized up to 5 mm long slices of tissue corresponding to a minimal fresh mass of 5 mg. The method is characterized by an uncomplicated feasibility, a minimal consumption of extractant volumes, and a compatibility with the arsenic species analysis if low buffer concentrations are used. In the future, the biological variation within individual plant parts should be elucidated more systematically. To reduce the extraction time, the applicability of focused ultrasound should be tested. Furthermore, not only the free arsenic species should be analyzed in the extracts but rather their possible binding to biomolecules because the extracting agents used are compatible with the extraction of proteins.

Acknowledgements

We thank Björn Knauthe from the Institute of Analytical Chemistry of the TU Freiberg for the ICPAES measurements and Dr. Jürgen Mattusch from the Helmholtz Centre for Environmental Research Leipzig for providing the IC/ICPMS method. The investigations were supported by the German Research Foundation (Deutsche Forschungsgemeinschaft, DFG).

References

[1] K.A. Francesconi, D. Kuehnelt, Analyst 129 (2004) 373.
[2] C. Dietz, J. Sanz, E. Sanz, R. Muñoz-Olivas, C. Cámara, J. Chromatogr. A 1153 (2007) 114.
[3] J. Száková, P. Tlustoš, W. Goessler, D. Pavlíková, J. Balík, Appl. Organometal. Chem. 19 (2005) 308.
[4] K.A. Mir, A. Rutter, I. Koch, P. Smith, K.J. Reimer, J.S. Poland, Talanta 72 (2007) 1507.
[5] A.C. Schmidt, W. Reisser, J. Mattusch, P. Popp, R. Wennrich, J. Chromatogr. A 889 (2000) 83.
[6] S. Foster, W. Maher, F. Krikowa, S. Apte, Talanta 71 (2007) 537.
[7] J.A. Caruso, D.T. Heitkemper, C. B'Hymer, Analyst 126 (2001) 136.
[8] A.H. Ackerman, P.A. Creed, A.N. Parks, M.W. Fricke, C.A. Schwegel, J.T. Creed, D.T. Heitkemper, N.P. Vela, Environ. Sci. Technol. 39 (2005) 5241.
[9] M. Quaghebeur, Z. Rengel, M. Smirk, J. Anal. At. Spectrom. 18 (2003) 128.
[10] E. Sanz, R. Muñoz-Olivas, C. Cámara, J. Chromatogr. A 1097 (2005) 1.
[11] E. Sanz, R. Muñoz-Olivas, C. Cámara, Anal. Chim. Acta 535 (2005) 227.
[12] S.G. Salgado, M.A.Q. Nieto, M.M.B. Simón, Talanta 68 (2006) 1522.
[13] R. Schaeffer, K.A. Francesconi, C. Kienzl, P. Soeroes, L. Fodor, L. Váradi, R. Raml, W. Goessler, D. Kuehnelt, Talanta 69 (2006) 856.
[14] M.J. Ruiz-Chancho, J.F. López-Sánchez, E. Schmeisser, W. Goessler, K.A. Francesconi, R. Rubio, Chemosphere 71 (2008) 1522.
[15] A.C. Schmidt, J. Mattusch, W. Reisser, R. Wennrich, Appl. Organometal. Chem. 19 (2005) 590.
[16] A.C. Schmidt, W. Reisser, J. Mattusch, R. Wennrich, K. Jung, J. Anal. At. Spectrom. 19 (2004) 172.
[17] J.T. van Elteren, Z. Slejkovec, M. Kahn, W. Goessler, Anal. Chim. Acta 585 (2007) 24.
[18] A. Geiszinger, W. Goessler, W. Kosmus, Appl. Organometal. Chem. 16 (2002) 473.
[19] A.C. Schmidt, J. Mattusch, R. Wennrich, Microchim. Acta 151 (2005) 167.
[20] J. Mattusch, R. Wennrich, A.C. Schmidt, W. Reisser, Fresenius J. Anal. Chem. 366 (2000) 200.
[21] C. Schmidt de Magalhães, M.A.Z. Arruda, Talanta 71 (2007) 1958.
[22] S. Londesborough, J. Mattusch, R. Wennrich, Fresenius J. Anal. Chem. 363 (1999) 577.
[23] A.C. Schmidt, J. Mattusch, W. Reisser, R. Wennrich, Chemosphere 56 (2004) 305.
[24] H.R. Hansen, A. Raab, M. Jaspars, B.F. Milne, J. Feldmann, Chem. Res. Toxicol. 17 (2004) 1086.
[25] J. Mattusch, M. M. Cimpean, R. Wennrich, Int. J. Environ. Anal. Chem. 86 (2006) 629.

Talanta 76 (2008) 1194–1198

Contents lists available at ScienceDirect

Talanta

journal homepage: www.elsevier.com/locate/talanta

Rapid analysis of clenbuterol, salbutamol, procaterol, and fenoterol in pharmaceuticals and human urine by capillary electrophoresis

Somsak Sirichai [a,*], Proespichaya Khanatharana [b]

[a] Department of Chemistry, Faculty of Science, Burapha University, Bangsaen, Chonburi 20131, Thailand
[b] Department of Chemistry, Faculty of Science, Prince of Songkla University, Hat Yai, Songkla 90110, Thailand

ARTICLE INFO

Article history:
Received 26 February 2008
Received in revised form 15 May 2008
Accepted 16 May 2008
Available online 27 May 2008

Keywords:
Capillary electrophoresis
Clenbuterol
Salbutamol
Procaterol
Fenoterol

ABSTRACT

Capillary electrophoresis (CE) with UV detection for the simultaneous and short-time analysis of clenbuterol, salbutamol, procaterol, fenoterol is described and validated. Optimized conditions were found to be a 10 mmol l^{-1} borate buffer (pH 10.0), an separation voltage of 19 kV, and a separation temperature of 32 °C. Detection was set at 205 nm. Under the optimized conditions, analyses of the four analytes in pharmaceutical and human urine samples were carried out in approximately 1 min. The interference of the sample matrix was not observed. The LOD (limits of detection) defined at S/N of 3:1 was found between 0.5 and 2.0 mg l^{-1} for the analytes. The linearity of the detector response was within the range from 2.0 to 30 mg l^{-1} with correlation coefficient >0.996.

1. Introduction

β_2-Agonists such as clenbuterol, salbutamol, procaterol, and fenoterol have long been used for the treatment of acute asthma symptoms in both adults and children, and also in the prevention of exercise-induced asthma [1–3]. They are administrated as an aerosol, injection fluid, mixtures, and tablets. There are concerns regarding the possible contribution of β_2-agonists in asthmatic deaths [4]. This may because excessive use of β_2-agonists inhalants during asthma attacks leading to cardiac arrhythmia. Furthermore, β_2-agonists at higher dose levels may also be illegally used as repartitioning agents in meat-producing animals. Residues of these compounds could present a potential risk for health of individuals consuming illegally treated animals [5]. Consequently, it is necessary to develop rapid and simple methods for analysis of β_2-agonists in both pharmaceuticals and biological fluids.

Numerous analytical methods for determination of β_2-agonists in pharmaceuticals and biological fluids have been reported. These include gas chromatography–mass spectrometry (GC–MS) [6–10], high-performance liquid chromatography (HPLC) [11–15], ion chromatography [16], ELISA [17], and recently flow injection analysis coupled with electrogenerated chemiluminescence (FIA–ECL) [18]. All these methods have their own disadvantages. Although GC–MS is a common method to detect these compounds, a derivatisation step is required prior to injection. However, derivatisation procedure is time-consuming, laborious, complicated, and requires large volume of organic solvents. HPLC and LC–MS provide many advantages over GC for the analysis of β_2-agonists. However, LC–MS instrument is expensive, and does not belong to the facilities of average investigator.

Capillary electrophoresis (CE) is an attractive method for the analysis of both neutral and charged species. It provides high separation efficiency, rapidity of separation, and small sample and reagent volume required, leading to lower cost. Several reports on the determination of β_2-agonists have been published [19,20].

Although a variety of methods have been proposed to separate β_2-agonists. One that is simple, rapid, inexpensive, and reliable and allows a simultaneous routine determination of these compounds is needed. Consequently, we presented a rapid and simple CE method using a UV detector that could be used to monitor the amount of clenbuterol, salbutamol, procaterol, and fenoterol in pharmaceutical and human urine samples. CE separation of this combination has not been reported. The molecular structures of the investigated analytes are shown in Fig. 1. The determination of clenbuterol and salbutamol compounds using the developed method is 8 times faster than the reported method [19].

* Corresponding author. Tel.: +66 3810 3114; fax: +66 3839 3494.
E-mail address: sirichai@buu.ac.th (S. Sirichai).

0039-9140/$ – see front matter © 2008 Elsevier B.V. All rights reserved.
doi:10.1016/j.talanta.2008.05.026

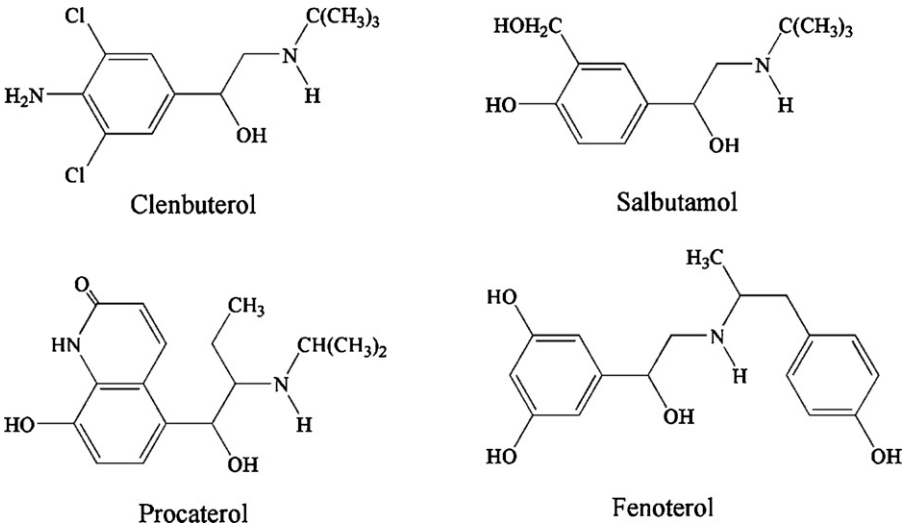

Fig. 1. Chemical structures of clenbuterol, salbutamol, procaterol, and fenoterol.

2. Experimental

2.1. Chemicals

All chemicals were of analytical grade, prepared using high resistivity (18 MΩ), deionised water, and filtered using 0.45 μm filter. Clenbuterol, Salbutamol, Procaterol, and Fenoterol were purchased from Sigma–Aldrich (St. Louis, MO, USA). Sodium hydroxide and methanol were supplied by Merck (Darmstat, Germany). Sodium tetraborate anhydrous were obtained from Fluka (Buchs, Switzerland). Pharmaceutical samples were purchased in a drugstore.

2.2. Instrumentation and software

A Hewlett-Packard Model G1600A ^{3D}CE system (Waldbronn, Germany) coupled with a diode-array detector was used throughout all experiments. A ^{3D}CE Chemstation software equipped with a HP Vectra VL5, 166 MHz personal computer was employed for controlling the CE system, data acquisition, and data analysis. All electrophoretic separations were carried out in 32 cm × 50 μm i.d. extended light path fused-silica capillary (Agilent, Germany). The effective length of the capillary was 23.5 cm. The sample solutions were hydrodynamically injected at the anodic end of the capillary by using a pressure of 50.0 mbar for 1 s. The detection wavelength was set at 205 nm. At each sequence experiment, the capillary was conditioned with 0.1 mol l^{-1} sodium hydroxide for 3 min, and separation buffer for 3 min. A Beckman pH meter (Beckmann Instrument, USA) equipped with a combined glass-Ag/AgCl electrode was used for pH measurement.

2.3. Preparation of standard solutions

Stock standard solutions (500 mg l^{-1}) of compounds: clenbuterol, salbutamol, procaterol, and fenoterol were prepared in methanol, and the working solutions at various concentrations were prepared by appropriate dilution from the stock standard solution when needed. The stock solutions were stored in a refrigerator at 4 °C for 1 week. Buffer solution was prepared by dissolving the proper amount of sodium tetraborate in deionised water, and the pH of the buffer solution was adjusted by the addition of sodium hydroxide.

2.4. Preparation of samples

Salbutamol and procaterol tablets containing 2 mg and 50 μg, respectively, and fenoterol solutions containing 1.25 mg/4 ml were obtained from a local drug store. Each tablet was ground and dissolved in deionised water, sonicated, filtered, and diluted with deionised water. Human urine samples were collected from a healthy drug-free male, filtered through a membrane filter, and diluted with deionised water before analysis.

3. Results and discussion

3.1. Effect of buffer pH and buffer concentration

In theory, the pH of running buffer would affect the ionization of the acidic silanols of the inner wall of the capillary, and the degree of dissociation of analytes. To investigate the influence of running buffer pH on the migration time and resolution of the analytes, four different buffer pH values, namely 9.3, 9.5, 9.8, and 10.0, were studied. High pH values was chosen as preliminary experiments because the use of buffer with high pH value offered decreasing the residence time due to a relatively high electroosmotic flow. The results obtained are shown in Fig. 2a. It can be seen that when the pH value of the running buffer was changed, the migration time and resolution were affected. At buffer pH 9.3, procaterol and fenoterol could not be resolved. By increasing the pH value of the running buffer, the resolution of the analytes was increased, and the baseline separation could be achieved at pH 10.0. Consequently, buffer pH 10.0 in the subsequent experiments was chosen.

The ionic strength of buffer affecting on solute mobilities and separation efficiency was investigated. This effect was studied by varying the borate buffer concentration from 5 to 15 mmol l^{-1}. The results obtained are shown in Fig. 2b. It was found that the migration times of four analytes, and electrophoresis current were increased with increase in buffer concentration. A 10 mmol l^{-1} borate buffer developing current of 16.6 μA was adopted as a compromise between peak shape and current generated in the capillary.

3.2. Effect of separation voltage

The effect of separation voltage, ranging from 12 to 19 kV on migration time of the compounds is shown in Fig. 3. While the migration times were decreased with increasing the separation

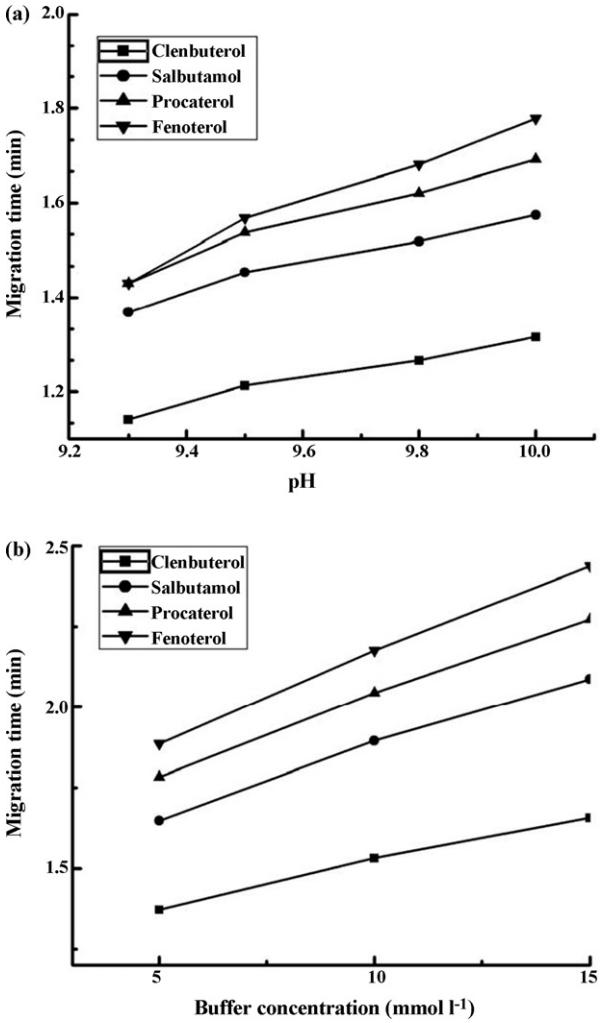

Fig. 2. (a) Effect of buffer pH on migration times of clenbuterol, salbutamol, procaterol, and fenoterol. Conditions: Capillary: extended fused silica (32/23.5 cm eff., 50 μm i.d., 360 μm o.d.); buffer: 5 mmol l^{-1} borate, pH value from 9.3 to 10.0; temperature: 25 °C; voltage: 15 kV; injection: 50 mbar for 1 s; detection: 205 nm; sample: 10 mg l^{-1} for clenbuterol, salbutamol, and fenoterol, and 20 mg l^{-1} for procaterol. (b) Effect of buffer concentration on migration times of clenbuterol, salbutamol, procaterol, and fenoterol. Conditions: Capillary: extended fused silica (32/23.5 cm eff., 50 μm i.d., 360 μm o.d.); buffer: 5–15 mmol l^{-1} borate, pH 10.0; temperature: 25 °C; voltage: 15 kV; injection: 50 mbar for 1 s; detection: 205 nm; sample: 10 mg l^{-1} for clenbuterol, salbutamol, and fenoterol, and 20 mg l^{-1} for procaterol.

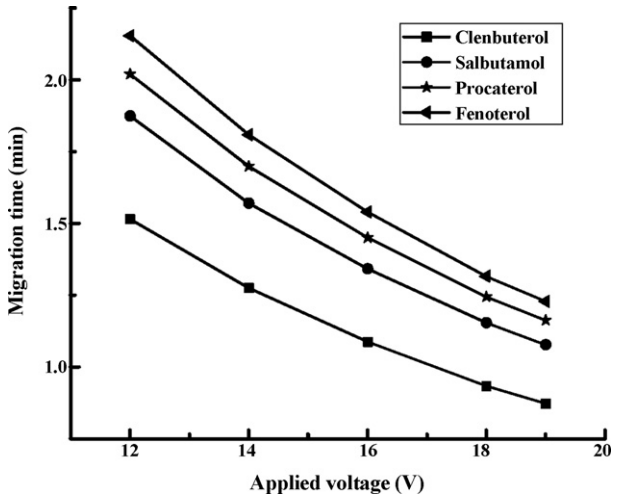

Fig. 3. Effect of separation voltage on migration times of clenbuterol, salbutamol, procaterol, and fenoterol. Conditions: Capillary: extended fused silica (32/23.5 cm eff., 50 μm i.d., 360 μm o.d.); buffer: 10 mmol l^{-1} borate, pH 10.0; temperature: 25 °C; voltage: 12 to 19 kV; injection: 50 mbar for 1 s; detection: 205 nm; sample: 10 mg l^{-1} for clenbuterol, salbutamol, and fenoterol, and 20 mg l^{-1} for procaterol.

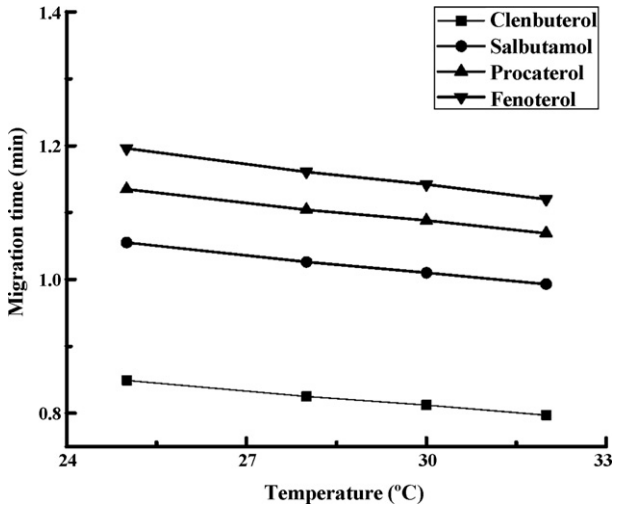

Fig. 4. Effect of separation temperature on migration times of clenbuterol, salbutamol, procaterol, and fenoterol. Conditions: Capillary: extended fused silica (32/23.5 cm eff., 50 μm i.d., 360 μm o.d.); buffer: 10 mmol l^{-1} borate, pH 10.0; temperature: 25 to 32 °C; voltage: 19 kV; injection: 50 mbar for 1 s; detection: 205 nm; sample: 10 mg l^{-1} for clenbuterol, salbutamol, and fenoterol, and 20 mg l^{-1} for procaterol.

voltage, the analysis time became shorter. This resulted in an increase of electroosmotic flow in the capillary. A separation voltage of 19 kV provided the best compromise in terms of analysis time, electrophoresis current, and resolution. This separation voltage was selected for subsequent stages of the method optimization.

3.3. Effect of separation temperature

Separation temperature studies from 25 to 32 °C were performed to determine the optimized capillary temperature for separation. Fig. 4 shows the effect of the temperature on the migration time. As expected, an increase in the temperature results in a decrease of migration times. This is because the buffer viscosity decreased with increase of capillary temperature. A temperature of 32 °C was chosen for the optimized condition regarding to migration time, and resolution. Fig. 5 shows the typical separation of analyte standards at the optimized conditions.

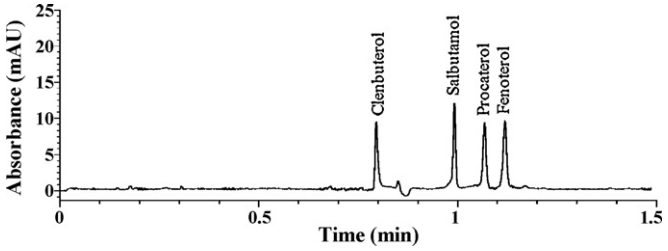

Fig. 5. Electropherogram of the four analytes under the optimized conditions. Conditions: Capillary: extended fused silica (32/23.5 cm eff., 50 μm i.d., 360 μm o.d.); buffer: 10 mmol l^{-1} borate, pH 10.0; temperature: 32 °C; voltage: 19 kV; injection: 50 mbar for 1 s; detection: 205 nm; sample: 10 mg l^{-1} for clenbuterol, salbutamol, and fenoterol, and 20 mg l^{-1} for procaterol.

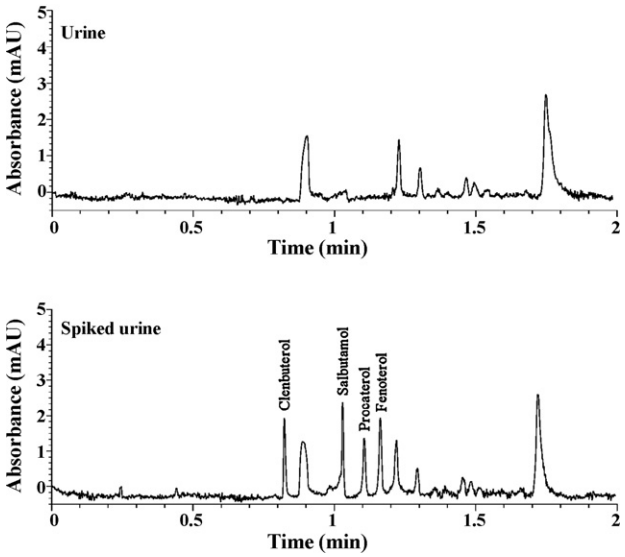

Fig. 6. Electropherogram of a blank urine sample and a urine sample spiked with a mixture of 3 mg l^{-1} each of clenbuterol, salbutamol, procaterol, and fenoterol. Conditions: Capillary: extended fused silica (32/23.5 cm eff., 50 μm i.d., 360 μm o.d.); buffer: 10 mmol l^{-1} borate, pH 10.0; temperature: 32 °C; voltage: 19 kV; injection: 50 mbar for 1 s; detection: 205 nm.

3.4. Method performances

For validation of the CE methods using the optimized conditions (a running buffer of 10 mmol l^{-1} borate buffer at pH 10.0, an applied voltage of 19 kV, a temperature of 32 °C, and hydrodynamic injection of 1 s at 50 mbar), linearity, limits of detection (LOD), limits of quantification (LOQ), precision, accuracy, and specificity were investigated according the ICH Harmonised Tripartite Guideline [21] under the optimized conditions. Fig. 6 shows the electropherogram of a blank urine sample, and a spiked urine sample.

3.4.1. Linearity, LOD and LOQ

A series of mixed standard solutions including clenbuterol, salbutamol, procaterol, and fenoterol with different concentrations were prepared to the linearity. Determination of LOD and LOQ were calculated based on signal-to-noise ratio of 3 and 10, respectively. Table 1 shows linearity, LOD and LOQ of the optimized CE method.

3.4.2. Precision

The precision of a method is defined as the closeness of agreement between independent test results obtaining under conditions. For repeatability precision, five replicate experiments were performed on the same day. For intermediate precision, five replicate experiments were performed on each of 5 days. The results of precision expressed as the %R.S.D. shown in Table 2 indicate that the proposed method is reliable.

Table 2
Method repeatability and intermediate precision for proposed method ($n = 5$)

Analyte	Concentration (mg l^{-1})		
	10	30	50
Intraday %R.S.D.			
Clenbuterol	1.2	2.1	1.3
Salbutamol	1.5	1.9	1.7
Procaterol	1.3	1.1	1.2
Fenoterol	1.6	1.4	2.5
Interday %R.S.D.			
Clenbuterol	2.8	2.4	3.5
Salbutamol	3.5	3.1	3.8
Procaterol	3.0	2.9	3.2
Fenoterol	3.3	3.1	4.2

Table 3
Accuracy of the proposed method ($n = 5$)

Analyte	% Recovery		
	2.0 mg l^{-1}	4.0 mg l^{-1}	5.0 mg l^{-1}
Clenbuterol	98.7	100.2	99.8
Salbutamol	97.8	99.8	100.8
Procaterol	98.8	99.0	99.9
Fenoterol	98.8	100.5	99.8

3.4.3. Accuracy

In order to establish the feasibility of the method developed, a blank urine and urine spiked with standard mixture were chosen as the test samples. To evaluate the recovery of the method, recovery experiments were performed. The spiked urine samples were prepared by adding the analytes into the diluted blank urine sample to obtain the three different concentration levels of clenbuterol, salbutamol, procaterol, and fenoterol in each urine sample 2.0, 4.0, and 5.0 mg l^{-1}. The results of recoveries are given in Table 3.

3.4.4. Specificity

An investigation of specificity can be carried out by measurement of the peak purity to ensure that no comigrating impurity contributes to peak's response. In this work, evaluating peak purity was assessed on test sample solutions by using Agilent ^{3D}CE ChemStation software. Five spectra (two spectra on each of the up and down slopes and one at the apex) per peak were used to assess purity. The five spectra were averaged and compared spectra from 200 to 400 nm. An absorbance threshold was set to 1 mAU to ensure that the spectra at the edges of the peak are included in the purity check. A smooth factor of seven and spline factor of five were chosen for spectra processing. Noise threshold was determined automatically, using the standard deviation of 14 pure noise spectra at the beginning of a run (0 min). The display of peak purity was the purity ratio. For a spectrally pure peak, the ratio values are below 1, and for spectrally impure peaks, the values are above 1 [22]. The ratios were found 0.305 for clenbuterol, 0.439 for salbutamol, 0.278 for procaterol, and 0.354 for fenoterol. The results showed that there were no other hidden components in analysis of clenbuterol, salbutamol, procaterol, and feneterol.

Table 1
Linearity, LOD and LOQ obtained in method validation

β_2-Agonists	Regression equation	Correlation coefficient	LOD (mg l^{-1})	LOQ (mg l^{-1})	%R.S.D_t ($n = 5$)	%R.S.D_a ($n = 5$)
Clenbuterol	$y = 0.4807x + 0.4824$	0.9987	0.5	2.0	1.1	3.1
Salbutamol	$y = 0.4430x + 0.6180$	0.9979	0.5	2.0	1.3	2.5
Procaterol	$y = 0.3411x + 0.1524$	0.9968	2.0	3.0	1.2	2.2
Fenoterol	$y = 0.6370x - 0.1380$	0.9965	0.5	2.5	1.2	2.7

R.S.D_t = R.S.D. of the migration times.
R.S.D_a = R.S.D. of the peak areas.

Table 4
Results for determination of salbutamol, procaterol, and fenoterol in pharmaceutical formulations

β_2-Agonists	Manufacturer's value	Average found ($n = 5$)
Salbutamol tablets	2 mg/tablet	1.93 ± 0.16
Procaterol tablets	50 μg/tablet	48.78 ± 0.27
Fenoterol solutions	1.25 mg/4 ml	1.21 ± 0.11

3.5. Analysis of pharmaceutical formulations

The optimized proposed CE method was applied to the determination of salbutamol, procaterol, and fenoterol in pharmaceutical formulations. The amounts of analytes were calculated using calibration curve. The results are shown in Table 4.

4. Conclusion

This work presented the simultaneous, simple, and rapid determination of clenbuterol, salbutamol, procaterol, and fenoterol by capillary electrophoresis. The results showed that this proposed method is the relatively short analysis time (about 1 min), easily usable for routine analysis, and less costly. In addition, the method can be used for clinical and medical researchers interested monitoring these compounds in human urine. However, the determination of these compound residues in the illegally treated animals using UV detection in the proposed method could not provide LOD. Sample preconcentration techniques are needed.

Acknowledgements

The authors would like to gratefully acknowledge the Thailand Research Fund (TRG4580008) and the Center for Innovations in Chemistry: Postgraduate Education and Research Program in Chemistry (PERCH-CIC), Commission on Higher Education, Ministry of Education for their financial support of this work.

References

[1] A.R. Martin, in: J.N. Delgado, W.A. Remers (Eds.), Textbook of Organic Medicinal and Pharmaceutical Chemistry, Lippincott, Philadelphia, PA, 1991, p. 155.
[2] H.S. Nelson, N. Engl. J. Med. 333 (1995) 499.
[3] M. Nishikawa, J.C.W. Mak, P.J. Barnes, Eur. J. Pharmacol. 318 (1996) 123.
[4] N.A. Molfino, L.J. Nannini, A.N. Martelli, A.S. Slutsky, A. Engl. J. Med. 324 (1991) 285.
[5] C.A. Ricks, R.H. Dalrympale, P.K. Baker, D.L. Ingle, J. Anim. Sci. 59 (1984) 1247.
[6] F. Ramos, A. Cristino, P. Carrola, T. Eloy, J.M. Silva, M. da, C. Castilho, M.I.N. da Silveira, Anal. Chim. Acta 483 (2003) 207.
[7] F. Ramos, C. Santos, A. Silva, M.I.N. Silveira, J. Chromatogr. B 716 (1998) 366.
[8] G. van Vyncht, S. Preece, P. Gaspar, G. Maghuin-Rogister, E. DePauw, J. Chromatogr. A 750 (1996) 43.
[9] H. Hooijerink, R. Schilt, E.O. van Bennekom, F.A. Huf, J. Chromatogr. B 660 (1994) 303.
[10] M.C. Dumasia, E. Houghton, J. Chromatogr. 564 (1991) 503.
[11] L. Mälkki, S. Tammilehto, J. Pharm. Biomed. Anal. 11 (1993) 79.
[12] A. Polettini, M. Montagna, E.A. Hogendoorn, E. Dijkman, P. van Zoonen, L.A. van Ginkel, J. Chromatogr. A 695 (1995) 19.
[13] A. Koole, J. Bosman, J.P. Franke, R.A. de Zeeuw, J. Chromatogr. B 726 (1999) 149.
[14] D. Boyd, M. O'Keeffe, M.R. Smyth, Analyst 121 (1996) 1R.
[15] K.D. Wasch, H.D. Brabander, D. Courtheyn, Analyst 123 (1998) 2701.
[16] S. Shen, J. Ouyang, W.R.G. Raeyens, J.R. Delanghe, Y. Yang, J. Pharm. Biomed. Anal. 38 (2005) 166.
[17] R. Ventura, G. González, M.T. Smeyers, R. de la Torre, J. Segura, J. Anal. Toxicol. 22 (1998) 127.
[18] C.A. Lindino, L.O.S. Bulhões, Talanta 72 (2007) 1746.
[19] Y. Shi, Y. Huang, J. Duan, H. Chen, G. Chen, J. Chromatogr. A 1125 (2006) 124.
[20] C.N. Carducci, S.E. Lucangioli, V.G. Rodríguez, J. Chromatogr. A 730 (1996) 313.
[21] ICH Harmonised Tripartite Guideline Q28, Validation of Analytical Procedures: Text and Methodology Q2(R1), November 2005.
[22] Agilent Technologies, Understanding Your Spectra Module, Waldbronn, 2007.

Talanta 76 (2008) 1141–1146

Contents lists available at ScienceDirect

Talanta

journal homepage: www.elsevier.com/locate/talanta

HPLC determination of sulfamethazine in milk using surface-imprinted silica synthesized with iniferter technique

Shufang Su, Min Zhang, Baoli Li, Haiyan Zhang, Xiangchao Dong*

College of Chemistry, Nankai University, Tianjin 300071, China

ARTICLE INFO

Article history:
Received 2 December 2007
Received in revised form 9 May 2008
Accepted 14 May 2008
Available online 21 May 2008

Keywords:
Iniferter
Surface grafted
Molecularly imprinted polymer
Sulfamethazine
Milk

ABSTRACT

A new method for the synthesis of sulfamethazine-imprinted polymer on the surface of silica *via* quasi-living radical polymerization and the application of the resulting polymer in determination of the SMZ in milk is developed. In the synthesis, initiator-transfer agent-terminator (iniferter) was immobilized on the silica surface using chemical reagents with good availability. The imprinting polymerization was initialized by the silica-supported iniferter under the UV radiation. The molecularly imprinted polymer (MIP) layer grafted on the silica surface was constructed by using sulfamethazine (SMZ) as the template, methacrylic acid (MAA) as the functional monomer and ethylene dimethacrylate (EDMA) as cross-linker. The resulting MIP-silica has good selectivity for SMZ and high column efficiency in the HPLC analysis. The result demonstrated that the SMZ-imprinted polymer was grafted on the silica surface successfully. Under the optimized HPLC condition, the MIP-silica has been used for the determination of SMZ in milk. The method was linear over the concentration range of 0.1–50 μg mL^{-1} with correlation coefficient $R > 0.999$. The detection limit for SMZ was 25 ng mL^{-1}. The recoveries were above 78% at the spiked concentration of 0.024, 0.24 and 0.48 μg mL^{-1}.

1. Introduction

Sulfamethazine (SMZ) is one kind of antibiotic medicine used in veterinary for livestock diseases such as gastrointestinal and respiratory tract infections. In the dairy industry, SMZ is also selected as the feed additive for the prevention of the mastitis with low cost and high cure efficiency. The inappropriate use in food can cause the undesirable residues in edible foodstuffs and it is suspected to be carcinogenic [1]. For food safety, the European Community adopted a maximum residue level (MRL) of 100 ng mL^{-1} for sulfonamides in foodstuffs of animal origin including milk [2]. HPLC is a common method for drug residue analysis in milk [3,4]. However, in order to remove the matrix components, multiple sample clean-up processes are generally used which have lower efficiency and result in lower recovery. Thus finding an efficient method for the sulfamethazine residue determination in milk is necessary.

Molecularly imprinted polymers (MIPs) are artificial materials synthesized by polymerization of functional and cross-linking monomers in the presence of target molecule (template). With high selectivity and advantages such as easy preparation, chemical and thermal stability and low cost, MIPs have been used in many fields such as chemical sensing [5,6], catalysis [7], solid phase extraction [8–10] and HPLC separations [11–13].

In the MIP preparation, different methods have been employed to obtain MIP particles for the chromatographic column packing. One way is the bulk polymerization followed by grinding and sieving processes [14,15]. This method has simple synthetic procedure but contains inherent drawbacks such as time-consuming and sample-wasting. Moreover, particles obtained in this method always have irregular shape and provide poorer column efficiency. To obtain spherical particles, suspension and multi-swelling polymerization were introduced into the MIP preparation [16]. The limitation of these methods is that water is often used in the polymerization system, which may affect the formation of the hydrogen bond between the template and the functional monomer. Another approach for making spherical MIP is the precipitation polymerization [17,18]. This method generally produces particles with diameter less than 2 μm, which may not be suitable for the application of the ordinary HPLC analysis. To solve these problems, surface-imprinting technique [19,20] emerged. Using this approach, MIP can be grafted on the surface of substrate with suitable particle diameter and narrow size distribution. This kind of sorbent provides better chromatographic efficiency mainly due to the lower mass transfer resistance of the thin MIP layers [21]. Hence, surface imprinting is a promising way for the MIP stationary phase preparation.

* Corresponding author at: College of Chemistry, Nankai University, 94 Weijin Road, Tianjin 300071, China. Tel.: +86 22 23504694.
E-mail address: xcdong@nankai.edu.cn (X. Dong).

0039-9140/$ – see front matter © 2008 Elsevier B.V. All rights reserved.
doi:10.1016/j.talanta.2008.05.015

In this study, the surface-imprinted stationary phase was synthesized *via* initiator-transfer agent-terminator (iniferter) technique [22] for HPLC analysis of sulfamethazine. Benzyl *N*,*N*-diethyldithiocarbamate (BDC), a typical iniferter was used in the study. Under the UV irradiation, BDC dissociated into a benzyl radical and a dithiocarbamyl (DC) radical [22–24]. The benzyl radical is reactive and initiates radical polymerization. While the DC radical is relatively stable and mainly reacts with growing radicals to form a "dormant species", which reduces the concentration of the free radicals to some extent [22–24]. Compared with the conventional radical polymerization, the polymerization process can be well controlled by iniferter due to the avoidance of the adverse reactions such as radical coupling or disproportionation action [25]. In 2002, Sellergren and co-workers [26] reported their work of using iniferter to make the MIP-grafted materials. Because the polymerization was initiated by the benzyl radical which was attached on the substrate, the MIP can be covalently bound on the substrate with "graft from" procedure.

To make further development for the MIP surface grafting technique, SMZ-imprinted polymer grafted on the silica support was synthesized by the quasi-living radical polymerization using a new iniferter grafting procedure. Low-cost materials were used in the process. The application of the surface-imprinted stationary phase for sulfamethazine residue analysis in milk was developed. The research work is presented in this paper.

2. Experimental

2.1. Chemicals

Silica gel (average particle size: 10 μm, specific surface area 380 $m^2\,g^{-1}$) was purchased from Tianjin No. 2 Reagent Company (Tianjin, China). 2-Chloroethanol and sodium *N*,*N*-diethyldithiocarbamate trihydrate were from Guangfu Plant (Tianjin, China). 4-(Chloromethyl)benzoyl chloride was obtained from Haiqu Chemical Factory (Shanghai, China). MAA was purchased from Damao Chemical Plant (Tianjin, China). All liquid reagents mentioned above were purified by distillation before use. EDMA was from Yunkai Chemical Factory (Yantai, China) and washed with 10% NaOH aqueous to remove inhibitor. Sulfamethazine (SMZ) was from Second Pharma Co. Ltd. (Zhejiang, China). Sulfamethoxazole (SMO) was kindly provided by Xi'nan Hecheng Pharma Co. Ltd. Other solvents were all analytical grade and used as received.

2.2. Preparation of silica-supported iniferter

The silica gel was rehydroxylated with hydrochloric acid–H_2O (1:1) under reflux for 4 h. After being washed with deionized water and acetone, the silica was dried under vacuum at 120 °C for 12 h.

The procedure for the preparation of silica-supported iniferter involved the following four reaction steps (Scheme 1). Firstly, in a 100 mL flask, 1.63 g of freshly cut sodium pieces was added into anhydrous methanol (50 mL) to form the sodium methoxide. The silica gel was added into the solution. The mixture was stirred for 4 h at ambient temperature under nitrogen to form Si–ONa groups on the surface of the silica. The product was denoted as Si-i in this presentation. In the second step, the silica (Si-i) was mixed with 60 mL of 2-chloroethanol. The reaction was allowed to proceed for 8 h at 50 °C under stirring and nitrogen protection. The resulting particles (Si-ii) with $-(CH_2)_2OH$ groups were isolated and were reacted with 4-(chloromethyl)benzoyl chloride (6.63 g) in chlorobenzene (60 mL). Pyridine (2 mL) was used to scavenge the acid produced during the reaction. The reaction was performed at 70 °C for 8 h with stirring and nitrogen protection. The product (Si-iii) was washed with anhydrous ethanol and dried at 50 °C under vacuum.

In the forth step, Si-iii particles (2.65 g) was added into 20 mL of absolute ethanol. Ethanol solution (12 mL) containing sodium *N*,*N*-diethyldithiocarbamate trihydrate (1.10 g) was added dropwise under stirring. The mixture was continually stirred for 12 h at room temperature and then filtered. The iniferter-modified silica (Si-I) produced were washed with distilled water and ethanol, respectively, then was dried at 50 °C under vacuum for 4 h.

2.3. Photo-grafting of the SMZ-imprinted polymer on the iniferter-bonded silica

The SMZ-imprinted polymer layer was synthesized using SMZ as the template, MAA as the functional monomer and EDMA as the cross-linker. The molar ratio of SMZ/MAA/EDMA was 1:8:40. In the photo-grafting reaction, Si-I (2.50 g) was added into a quartz flask containing SMZ (0.28 g, 1 mmol), MAA (0.69 g, 8 mmol), EDMA (7.93 g, 40 mmol) in acetonitrile (40 mL). After deaerated with nitrogen, the flask was sealed and was rotated in a rotary mixer at a speed of 90 rpm. Polymerization was initiated by the UV light from a high-pressure mercury lamp (Yingze Scientific Technology, Tianjin, China, 400 W) at the distance of 15 cm from the flask. The temperature was controlled at about 10 °C. After the reaction, the MIP-silica particles were Soxhlet-extracted using CH_3OH/HOAC (90:10) and then with CH_3OH to remove the template and unreacted monomer. Non-imprinted polymer-modified silica (NIP-silica) was synthesized in the same way as the corresponding MIP-silica except no addition of the template in the polymerization.

The thickness of the imprinted polymer layer on the silica support was estimated with the following equation [27]:

$$d = \frac{n_p \times M_p}{DS} \times 10^3 \quad (1)$$

and

$$n_p = \frac{m_c}{M_c}, \qquad m_c = (C_p - C_I) \times 1\,g$$

In the equations, d is the thickness of the polymer layer. n_p is the number of polymer units in 1 g of MIP-silica. M_p is the molar mass of one repeating unit of polymer assuming the polymer was composed by stoichiometric incorporation of MAA and EDMA. D is the weighted average density of the monomers. S is the specific surface area of the bare silica measured by N_2 adsorption method by Tristar 3000 instrument (Micromeritics, USA). M_c is the mass of total carbon in one polymer unit. The m_c is the weight of carbon in the MIP polymer layer in 1 g of MIP-silica. C_p and C_I are the carbon content obtained by elemental analysis in the MIP-silica and Si-I, respectively.

2.4. Chromatographic evaluation

A Shimadzu HPLC instrument equipped with a LC-20 AD pump, an SPD-20A UV detector and a manual injector with a 20 μL loop was employed for the chromatographic analysis. The polymer-grafted silica was slurry packed into stainless steel columns (150 mm × 4.6 mm), which then was connected to the HPLC instrument. Acetonitrile at flow rate of 0.5 mL min^{-1} was used as the mobile phase. The detection wavelength was 268 nm. The sample concentration was 0.05 mg mL^{-1} for each component. The retention factor (k) was determined by $k = (t_R - t_0)/t_0$. In the equation, t_R is the retention time of the analyte and t_0 is the void time measured by potassium dichromate using acetonitrile–H_2O (90:10, v/v) as a mobile phase. Separation factor (α) was calcu-

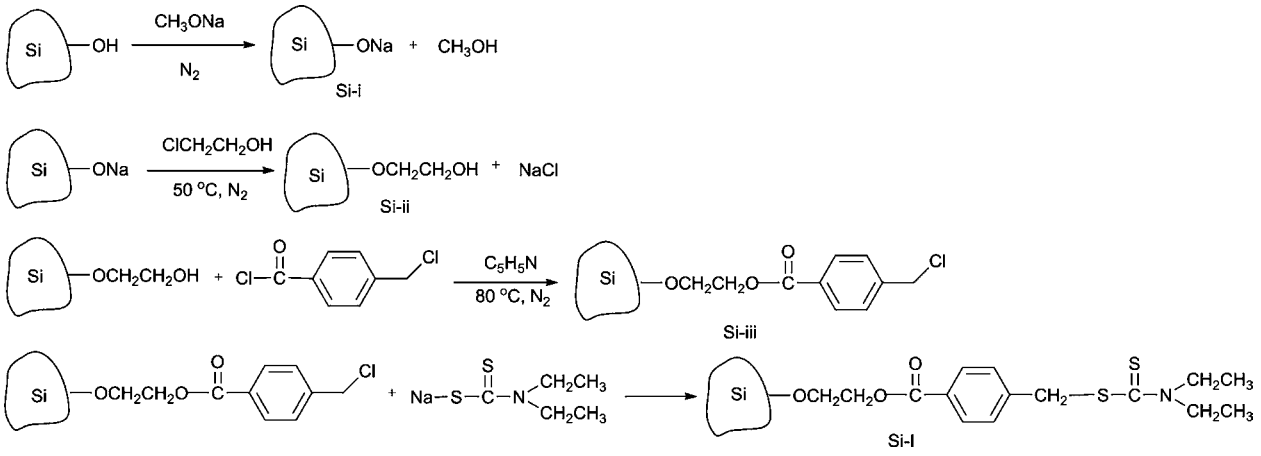

Scheme 1. Synthesis of the silica-supported iniferter.

lated by $\alpha = k_{SMZ}/k_{SMO}$, where k_{SMZ} and k_{SMO} are retention factors of SMZ and SMO, respectively. Column efficiency was evaluated by the number of theoretical plates (N) according to the equation: $N = 5.54(t_R/W_{1/2})^2$, where t_R is the retention time of SMZ and $W_{1/2}$ is the peak width at half-peak height. Imprinting factor (IF) was determined by $IF = k_{MIP}/k_{NIP.}$, where k_{MIP} and k_{NIP} are the retention factors of the template (SMZ) on the MIP-silica and NIP-silica, respectively.

2.5. HPLC determination of SMZ in milk using the MIP-silica stationary phase

The milk was purchased from local food market. In the sample pretreatment, milk (10 mL) was mixed with 20 mL of acetonitrile for protein precipitation and then centrifuged at 10,000 rpm. The supernatant was withdrawn. The precipitant was extracted with 2 mL of acetonitrile and centrifuged. The supernatant was combined and brought to dryness at 45 °C with rotary evaporator. Acetonitrile (1.0 mL) was added into the residue and sonicated. After being filtered through a 0.45 μm membrane filter, the sample was analyzed with the MIP-silica packed HPLC column (150 mm × 4.6 mm). Acetonitrile–water (25:75, v/v) was used as mobile phase at flow rate of 1.0 mL min^{-1}. The detection wavelength was 268 nm. External standard method was used for quantification.

The milk samples with spiked SMZ concentration of 0.024, 0.24 and 0.48 μg mL^{-1} were prepared by addition of 0.5 mL of SMZ in acetonitrile with different concentration into 10.0 mL of milk.

3. Results and discussion

3.1. Immobilization of iniferter on the surface of silica

In the research, four simple reactions were employed to produce iniferter groups on the surface of silica with no requirement for harsh conditions. In each step the amount of reactants added was generally excessive to the reaction sites on the silica in order to have a higher reaction yield. The redundant substance was removed

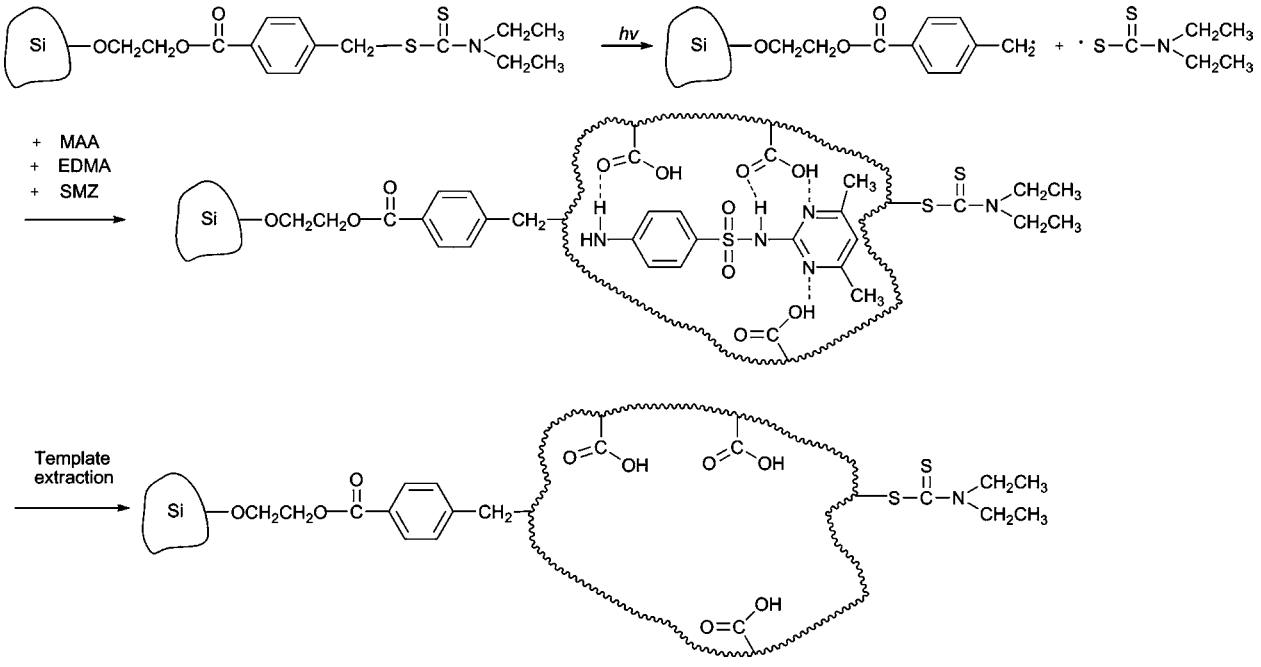

Scheme 2. SMZ-imprinted polymerization *via* iniferter on the surface of silica.

simply by filtration after each reaction. Different methods were utilized to characterize the functional groups bound on the silica surface. The amount of $-(CH_2)_2OH$ groups in the Si-ii was 0.83 mmol g^{-1} derived from the carbon content in the material by the elemental analysis. The content of $-CH_2Cl$ group in Si-iii was 0.21 mmol g^{-1} and iniferter in the Si-I was 15.30 μmol g^{-1} determined by oxygen flask-ion chromatography analysis [28]. The experimental results showed that the amount of iniferter able to be immobilized on the surface of silica was affected by the pore size of the substrate. Under the same reaction condition, higher iniferter density (1.99 μmol m^{-2}) was obtained in the silica with larger pore size (average pore size 1700 Å), while lower iniferter density (0.04 μmol m^{-2}) was obtained when the silica with 100 Å pore size was used as the substrate. The structural hindrance of the pores for the BDC could be the reason for this situation.

3.2. Photo-initiated polymerization of SMZ-imprinted polymer on the surface of silica

The reaction of grafting MIP on the silica-support *via* iniferter was illustrated in Scheme 2. In the process, the immobilized iniferter was radiated by the UV light to produce active radicals and dormant species. The active radical was able to initiate the imprinting polymerization on the surface of silica. The amount of polymer that can be grafted on the silica is the function of the reaction rate and time of polymerization. The reaction rate was influenced by the concentration of initiator, light intensity and concentration of monomer. The experimental result showed higher iniferter density resulted in faster polymerization rate (data omitted). In the photo-initiated polymerization, the light intensity can be adjusted by the distance between the lamp and reaction vessel. When flask–lamp distance was 10 cm, undesired solution polymerization happened easily. The possible reason is that with the higher light intensity, the monomers can be initiated directly leading to fast chain propagation in the solution. Furthermore, reaction temperature could not be well controlled due to the proximity of the UV lamp, which is not benefit for self-assembly between monomers and the template. When the irradiation distance was changed to 15 cm, no solution polymerization was found during the 3 h irradiation process. Another factor which influenced the light intensity was the material of the reaction vessel. Glass and quartz flasks have different UV transmission ability. The MIP-sil-G (obtained in glass flask) and MIP-sil-Q (obtained in quartz flask) were characterized, respectively. The thickness of the MIP layer in MIP-sil-G is thinner than that in MIP-sil-Q (Table 1). Slower reaction speed due to the less UV light through the glass may be the reason for this situation. When packed in the column, the MIP-sil-Q has higher retention for the template and better separation ability than the MIP-sil-G material.

Table 1
Characteristics of the MIP-silica materials obtained in glass and quartz vessels, respectively

MIP-silica	C (%)[a]	d[b] (nm)	k_{SMO}	k_{SMZ}	α	R_s
MIP-sil-G	6.07	0.12	0.6	0.9	1.5	1.06
MIP-sil-Q	11.48	0.35	0.7	1.2	1.7	1.62

The reaction time is 3 h and irradiation distance was 15 cm.
[a] Carbon content from the elemental analysis.
[b] Thickness of the polymer layer was calculated by Eq. (1).

To find out the relation between the reaction time and the properties of the MIP-silica, different polymerization period was employed in the MIP grafting process (Table 2). 2h-MIP-sil and 3h-MIP-sil were products of the reaction performed for 2 and 3 h, respectively, in the quartz flask. The MIP-silica was characterized with nitrogen adsorption, elemental and chromatographic analysis. The results indicated that the grafted polymer layer became thicker with increasing of the irradiation time. Also, a smaller specific surface area and pore volume of the 3h-MIP-sil than the 2h-MIP-sil was found which can be attributed to the partially filling of the pores on the silica by the polymer. Chromatographic analysis showed that the 3h-MIP-sil with thicker polymer layers has higher retention and better selectivity for the template molecule. Since solution polymerization was observed when the reaction time was 4 h, 3 h is considered as the proper reaction time in the study.

3.3. Evaluation of the selectivity of the MIP-silica

Using MIP-silica and NIP-silica as stationary phase, separation of SMZ and SMO was performed to evaluate the selectivity and imprinting effect of the MIP-silica in the HPLC study. The structures of SMZ and SMO are shown in Fig. 1. SMZ and SMO have the same aminobenzene sulfonamide moiety but different substituting groups in their structures. Although SMO has smaller molecular size than SMZ, it has less retention on the MIP-silica. This observation indicated that the pyrimidine group in the SMZ structure plays a role in binding with the imprinted polymer.

Table 2
Characteristics of silica-grafted molecular imprinted polymers

MIP-silica	C (%)[a]	S[b] (m^2 g^{-1})	V_p[c] (mL g^{-1})	d[d] (nm)	k_{SMO}	k_{SMZ}	α	R_s	N[e]
2h-MIP-sil	7.04	352	0.97	0.16	0.6	0.9	1.5	1.04	3833
3h-MIP-sil	11.48	333	0.82	0.35	0.7	1.2	1.7	1.62	3583

[a] Carbon content from the elemental analysis.
[b] BET-specific surface area.
[c] Pore volumes were measured by nitrogen absorption.
[d] Thickness of the polymer layer was calculated by Eq. (1).
[e] Number of theoretical plates per meter evaluated from the SMZ elution profile.

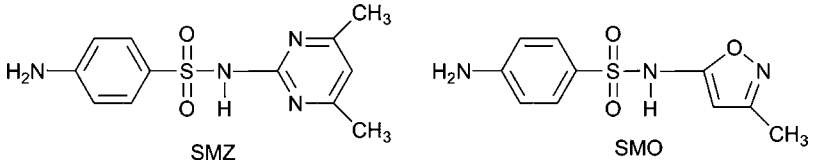

Fig. 1. The structures of SMZ and SMO.

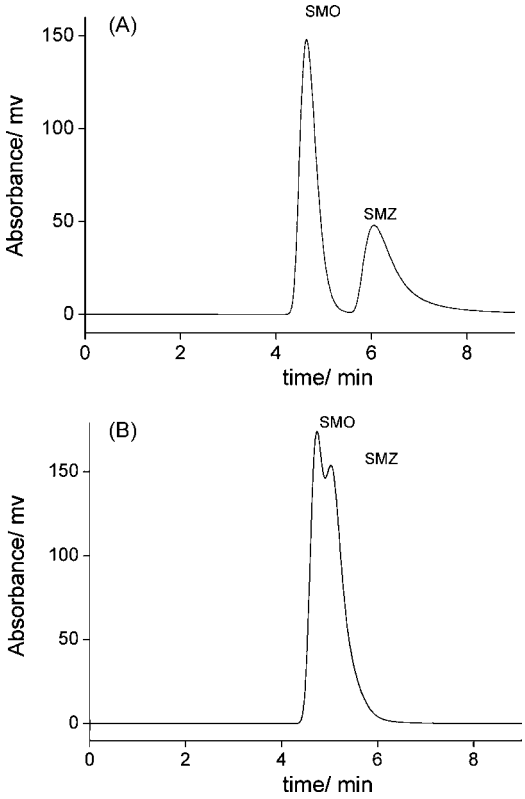

Fig. 2. Chromatograms of SMZ and SMO on the MIP-silica column (A) and NIP-silica column (B). HPLC separation was performed with a stainless steel column (150 mm × 4.6 mm) packed with MIP-silica (A) or NIP-silica (B). Acetonitrile was used as mobile phase at the flow rate of 0.5 mL min^{-1}. The detection wavelength was 268 nm. Injection volume was 20 μL.

Fig. 2 shows the liquid chromatograms using MIP-silica (3h-MIP-Sil) and its non-imprinted polymer-grafted silica (NIP-silica) as the stationary phases. Baseline separation was achieved on the MIP-silica column. The selectivity of the MIP-silica is much better (α = 1.7, Table 2) than that of the NIP-silica (α = 1.1). Moreover, the longer retention of SMZ on the MIP-silica while the retention of SMO on both columns were the same also demonstrated that specific binding sites for the SMZ molecules were formed in the MIP-modified silica. The imprinting factor was 1.56. Also, column efficiency evaluated by the number of theoretical plates was higher than the other MIP columns packed with the bulk polymers due to the narrow particle diameter and the fast mass transfer of the surface-grafted MIPs.

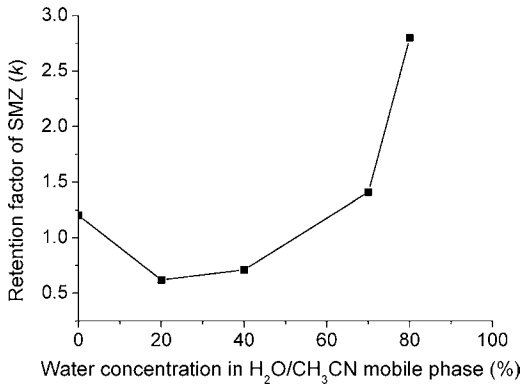

Fig. 3. Influence of the water concentration in the mobile phase on the retention factor of SMZ on the MIP-silica stationary phase.

Table 3
Accuracy and precision of HPLC analysis of SMZ for the spiked milk samples (n = 5)

Spiking level[a] (μg mL^{-1})	Concentration of spiked SMZ in milk (μg mL^{-1})	Average recovery % (R.S.D, %)
0.5	0.024	79.3 (11.9)
5.0	0.24	78.2 (2.4)
10.0	0.48	87.4 (7.8)

[a] Spiking level was the concentration of SMZ in the spiking solution.

3.4. Influence of mobile phase for the retention of SMZ on the imprinted silica stationary phase

To find a suitable mobile phase for the SMZ analysis, different ratios of H_2O/CH_3CN were used to study the effect of the water concentration on the retention of SMZ. As depicted in Fig. 3, when the water concentration was below 20%, the retention factor (k) of SMZ decreased with the increase of water content. Whereas when water concentration was higher than 20%, a reversed correlation was observed. It can be explained as following: at the lower content of water, the hydrogen bonding plays an important role for the binding between the template and the imprinted sites in the stationary phase. The binding interaction was weakened by the addition of water, which enhanced the polarity of the mobile phase. When the water content was higher than 40%, hydrophobic interaction in addition to shape recognition are the dominant effects. Longer retention was observed with higher ratio of water in the mobile phase. The same phenomenon was also reported by Zhao and co-workers [29]. Though a little peek tailing was observed, higher content of water in the mobile phase will prevent the possible rudimental protein from precipitation in the milk analysis. Therefore, the acetonitrile–water (25:75, v/v) was selected as the optimum elution solvent for further studies.

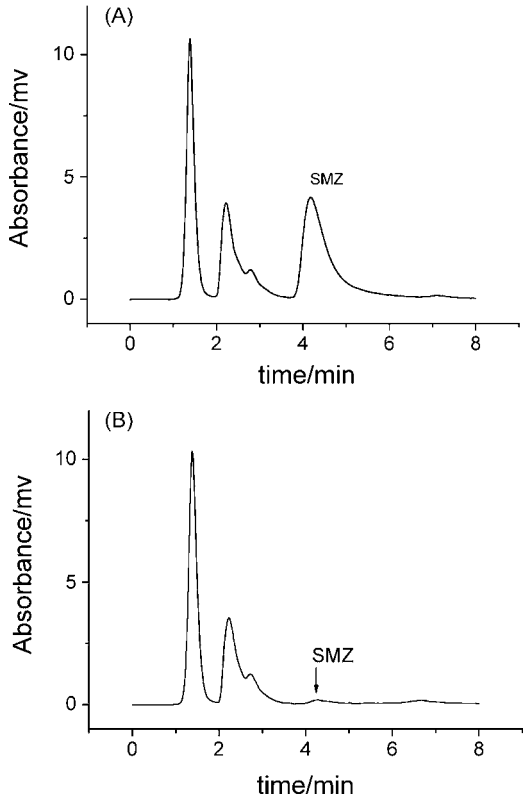

Fig. 4. HPLC profiles of the SMZ (0.24 μg mL^{-1}) spiked milk (A) and the original milk (B). The HPLC condition was described in Section 2.5.

3.5. Determination of SMZ in milk

SMZ in milk was analyzed on the MIP-silica stationary phase under the optimized HPLC conditions. The calibration plot was drawn in the range of 0.1–50 $\mu g\,mL^{-1}$ with good linearity ($R = 0.9999$). The limit of detection in the HPLC was 25 $ng\,mL^{-1}$ defined as three times of the noise. The limit of quantification of SMZ in milk was 7.9 $ng\,mL^{-1}$ calculated by 10 times of the noise. The average recoveries for the milk samples at different spiking levels (0.5, 5.0 and 10.0 $\mu g\,mL^{-1}$) and the relative standard deviations (R.S.D.) are shown in Table 3. The chromatograms of the blank and the spiked milk samples on the imprinted column are displayed in Fig. 4. The analytical results showed that the residue content of SMZ in milk from the market was about 0.007 $\mu g\,mL^{-1}$, which does not exceed the maximum residue level (MRL) [2].

4. Conclusions

The photo-active iniferter was synthesized on the surface of silica in a procedure containing four reactions using the inexpensive materials. The SMZ-imprinted polymer was immobilized on the silica *via* living radical polymerization. Chromatographic results demonstrated that MIP-grafted silica has good selectivity to the template. Better column efficiency and low backpressure were also observed in the analysis which indicated that surface grafting method based on iniferter is a promising choice for the MIP stationary phase synthesis. Furthermore, The SMZ-imprinted silica was used successfully for the determination of SMZ in milk with HPLC. It demonstrated that the silica-supported imprinted polymer can be used as a stationary phase allowing the analysis of complex samples pretreated by a simple cleaning-up step. The MIP-grafted silica exhibits an application potential in drug residue analysis for complex samples with high selectivity and better column efficiency.

Acknowledgement

This research was supported by the National Natural Science Foundation of China (Grant No. 20575030).

References

[1] N.A. Littlefield, W.G. Sheldon, R. Allen, D.W. Gaylor, Food Chem. Toxicol. 28 (1990) 157.
[2] C. Hartig, T. Storm, M. Jekel, J. Chromatogr. A 854 (1999) 163.
[3] F. de Zayas-Blanco, M.S. García-Falcón, J. Simal-Gándara, Food Control 15 (2004) 375.
[4] K. Kishida, N. Furusawa, J. Chromatogr. A 1028 (2004) 175.
[5] D. Kriz, O. Ramstroem, A. Svensson, K. Mosbach, Anal. Chem. 67 (1995) 2142.
[6] Y. Fu, H.O. Finklea, Anal. Chem. 75 (2003) 5387.
[7] G. Wulff, Chem. Rev. 102 (2002) 1.
[8] M.T. Muldoon, L.H. Stanker, Anal. Chem. 69 (1997) 803.
[9] A. Molinelli, R. Weiss, B. Mizaikoff, J. Agric. Food Chem. 50 (2002) 1804.
[10] C. Baggiani, L. Anfossi, C. Giovannoli, Anal. Chim. Acta 591 (2007) 29.
[11] M. Kempe, K. Mosbach, J. Chromatogr. A 691 (1995) 317.
[12] N. Zheng, Y.Z. Li, M.J. Wen, J. Chromatogr. A 1033 (2004) 179.
[13] T. Kubo, M. Nomachi, K. Nemoto, T. Sano, K. Hosoya, N. Tanaka, K. Kaya, Anal. Chim. Acta 577 (2006) 1.
[14] X.C. Dong, H. Sun, X.Y. Lü, H.B. Wang, S.X. Liu, N. Wang, Analyst 127 (2002) 1427.
[15] M.L. Mena, L. Agüí, P. Martinez-Ruiz, P. Yáñez-Sedeño, A.J. Reviejo, J.M. Pingarrón, Anal. Biochem. 376 (2003) 18.
[16] J. Haginaka, C. Kagawa, J. Chromatogr. A 948 (2002) 77.
[17] J. Wang, P.A.G. Cormack, D.C. Sherrington, E. Khoshdel, Angew. Chem. 115 (2003) 5494.
[18] L. Ye, P.A.G. Cormack, K. Mosbach, Anal. Chim. Acta 435 (2001) 187.
[19] F.G. Tamayo, M.M. Titirici, A. Martin-Esteban, B. Sellergren, Anal. Chim. Acta 542 (2005) 38.
[20] C.H. Lu, W.H. Zhou, B. Han, H.H. Yang, X. Chen, X.R. Wang, Anal. Chem. 79 (2007) 5457.
[21] T.A. Sergeyeva, H. Matuschewski, S.A. Piletsky, J. Bendig, U. Schedler, M. Ulbricht, J. Chromatogr. A 907 (2001) 89.
[22] T. Otsu, M.M. Yoshida, Chem. Rapid Commun. 3 (1982) 127.
[23] T. Otsu, T. Matsunaga, T. Doi, A. Matsumoto, Eur. Polym. J. 31 (1995) 67.
[24] T. Otsu, A. Kuriyama, Polym. Bull. 11 (1984) 135.
[25] Y. Nakayama, T. Matsuda, Langmuir 15 (1999) 5560.
[26] B. Rückert, A.J. Hall, B. Sellergren, J. Mater. Chem. 12 (2002) 2275.
[27] M.M. Titirici, B. Sellergren, Chem. Mater. 18 (2006) 1773.
[28] Q. Wang, B.W. Zhi, Y. Xia, Ion Exch. Adsorpt. 19 (2003) 468.
[29] Z.Y. Chen, R. Zhao, D.H. Shangguan, G.Q. Liu, Biomed. Chromatogr. 19 (2005) 533.

Talanta 76 (2008) 1047–1052

Contents lists available at ScienceDirect

Talanta

journal homepage: www.elsevier.com/locate/talanta

Ag island film-enhanced rare earth co-luminescence effect of Tb–Gd–protein–sodium dodecyl benzene sulfonate system and sensitive detection of protein

Chang Xia Sun[a,1], Xia Wu[a,*], Hai Ping Zhou[a], Fei Wang[b], Hong Hong Ding[a], Liang Liang Zhao[a], Jing He Yang[a,*]

[a] *Key Laboratory of Colloid and Interface Chemistry (Shandong University), Ministry of Education, School of Chemistry and Chemical Engineering, Shandong University, Jinan 250100, PR China*
[b] *China National Analytical Center, Guangzhou 510070, PR China*

ARTICLE INFO

Article history:
Received 14 January 2008
Received in revised form 30 April 2008
Accepted 5 May 2008
Available online 9 May 2008

Keywords:
Metal nanoparticle-enhanced fluorescence
Rare earth co-luminescence effect
Determination of proteins
Fluorescence resonance energy transfer

ABSTRACT

This paper reported the coupling technique of Ag island film-enhanced fluorescence with rare earth co-luminescence effect of Tb–Gd–sodium dodecyl benzene sulfonate (SDBS)–protein system. While the collagen is used as the separator between Ag island film and the fluorophore because it not only can decrease the fluorescence of the blank, but also can promote the adsorption of other proteins and change the conformation of the protein. The effects of Ag island film on both the fluorescence and resonance energy transfer process of Tb–Gd–SDBS–protein system are studied, finding that Ag island film can enhance the energy transfer efficiency of this system, resulting in fluorescence enhancement about ten-fold compared with this system without Ag island film. Therefore, this technique is used for the detection of proteins as low as 0.72 ng/mL for BSA and 1.3 ng/mL for HSA. In addition, Ag island film can also change the energy transfer process of Tb–SDBS–protein system.

1. Introduction

The detection and quantification of proteins at or below the ng/mL concentration range are of critical importance for biochemical studies, biological techniques, clinical diagnosis and analysis of food nutrition. This has been achieved by the development of high sensitivity detection methods based on the fluorescence probes of proteins [1–3].

As rare earth ions have luminescence characteristics such as narrow spectral width, long luminescence lifetime, large Stokes shift and strong binding with biological molecules, they are used as fluorescence probes to study nucleic acids [4,5], proteins [6,7] and drugs [8–10]. Rare earth co-luminescence effect is a fluorescence enhancement effect that is first found and studied by our research group in 1986 [11]. While studying the Eu^{3+} multi-complex system, a significant fluorescence enhancement phenomenon is found when Gd^{3+}, La^{3+}, Lu^{3+}, Tb^{3+} and Y^{3+} are added. This rare earth co-luminescence effect-induced increase fluorescence sensitivity has been applied on rare earth ion assays during the past decades [12–14]. Recently, this effect was also observed in the presence of biological molecule systems, and new detection methods had been established for the nucleic acid [15,16] and protein [17,18].

In recent year, the favorable effects of silver nanoparticles on fluorophores near the metallic surface have been reported [19–22]. These effects include decreasing the lifetime, increasing photostability and quantum yield of fluorophores, particularly those with low quantum yields, which are known as metal-enhanced fluorescence (MEF) or surface-enhanced fluorescence (SEF). The effects of silver nanoparticles on the fluorescence of fluorophores were studied experimentally and theoretically, it is considered that above effects are due to the interaction of the excited state fluorophores with the surface plasmon resonance on the surface of silver nanoparticles. The combination of increased brightness, short lifetime and better photo-stability makes MEF become a potential tool for the DNA hydridization [23], but the real application for the detection of biological molecules has not been reported.

In present report, we combine MEF with rare earth co-luminescence effect of Tb–Gd–SDBS–protein system [17], to establish a simple and sensitive approach to detection protein using common spectrofluorimeter. In addition, the luminescence mechanism, especially the change in energy transfer process of Tb–Gd–SDBS–protein system is discussed.

* Corresponding authors. Tel.: +86 531 88365459; fax: +86 531 88564464.
E-mail addresses: wux@sdu.edu.cn (X. Wu), yjh@sdu.edu.cn (J.H. Yang).
[1] Current address: The Texas A&M Health Science Center College Station, TX 77843, USA.

0039-9140/$ – see front matter © 2008 Elsevier B.V. All rights reserved.
doi:10.1016/j.talanta.2008.05.001

2. Experimental

2.1. Materials

Unless otherwise noted, all reagents and solvents used in this study were analytical grade. Proteins (BSA, HSA and Collagen) were purchased from Sigma Chemical Co., USA without further purification. The rare earth oxides (99.9%) are obtained from Yuelong Chemical Co., Shanghai. Stock standard solutions (0.01 mol/L) of rare earth ions are prepared by dissolving the corresponding oxides in hydrochloric acid and diluting with deionized water. A 0.05 mol/L Tris–HCl buffer solution was prepared by dissolving 3.03 g of Tris in 500 mL deionized water, and adjusting the pH to 7.0 with HCl using a Delta 320-S acidity meter (Mettler Toledo, Shanghai). A stock solution of SBDS purchased from Chemical Co. of China, Shanghai was prepared (1.00×10^{-2} mol/L) with deionized water.

2.2. Methods

2.2.1. Treatment of the quartz slides

The quartz slides used for silver deposition were first cleaned overnight according to the reported method [19–23] by soaking in the mixture of H_2SO_4 (95–98%) and H_2O_2 (30%). After washing with ultrapure water, the quartz surface was coated with amino groups by dipping the slides in a 1% aqueous solution of 3-aminopropyltriethoxysilane (APS) for 30 min in room temperature. The slides were washed extensively with water and air-dried.

2.2.2. Preparation of Ag island film

Ag island film (AIF) deposition was accomplished as described previously [24,25]. To a fast stirring silver nitrate solution (0.22 g in 26 mL of Millipore water), eight drops of fresh 5% NaOH solution were added. Dark-brownish precipitates formed immediately. Less than 1 mL of ammonium hydroxide was then added drop by drop to redissolve the precipitates. The clear solution was cooled to 5 °C by placing the beaker in an ice bath, followed by soaking the cleaned and dried quartz slides in the solution. At 5 °C, a fresh solution of D-glucose (0.35 g in 4 mL of water) was added. The mixture was stirred for 2 min at that temperature. Subsequently, the beaker was removed from the ice bath. The temperature of the mixture was allowed to warm up to 30 °C. As the color of the mixture turning from yellow green to yellowish brown, the color of the slides become greenish; the slides were removed and washed with water. After being rinsed with water several times, the slides were stored in water for several hours prior to the experiments. The SEM image of Ag island film is displayed in Fig. 1. It can be seen that the size of nanoparticles in Ag island film is well distributed.

All of the quartz slides are only half coated with Ag island film. Its UV absorption spectrum of is reported, the result indicated that Ag island film have the plasmon resonance absorption bands at about 417 nm, meaning that the nanometer structure is achieved in the preparation.

2.2.3. The adsorption of the collagen on the surfaces of quartz slides

The adsorption of the collagen on the surfaces of quartz slides was accomplished by soaking the Ag nanoparticle-coated slides in 6.0×10^{-2} mol/L collagen solution overnight, followed by rinsing with water to remove the unbound material.

2.2.4. Fluorescence measurement

The co-luminescence effect of Tb–Gd–SDBS–protein system has been studied by us [17]. Here, we choose this system to investigate its fluorescence properties near the Ag nanoparticle. The experimental conditions are Tb^{3+}: 1.0×10^{-5} mol/L; Gd^{3+}: 1.0×10^{-4} mol/L; BSA: 1.0×10^{-6} g/mL; SDBS: 1.5×10^{-3} mol/L; Tris–HCl: 5.0×10^{-3} mol/L, pH 8.50.

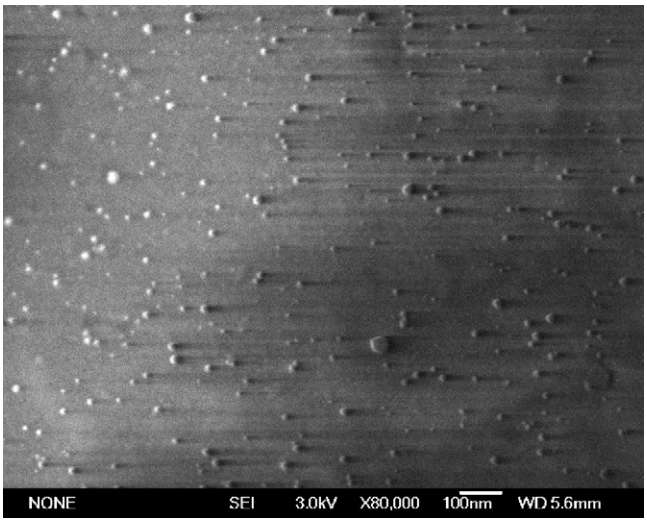

Fig. 1. SEM image of Ag island film.

Experimental setup used in fluorescence measurements is shown in Scheme 1, where the quartz slides or nano-Ag surfaces were examined in a sandwich configuration in which two coated surfaces faced inward toward an approximate 1 μm thick aqueous sample [26]. The incident angle of excitation light is about 65°. Steady state emission spectra were recorded using a LS 55 spectrofluorometer (PE, USA) with excitation at 290 nm after the solution of Tb–Gd–SDBS–protein was filled in the space between the two quartz slides.

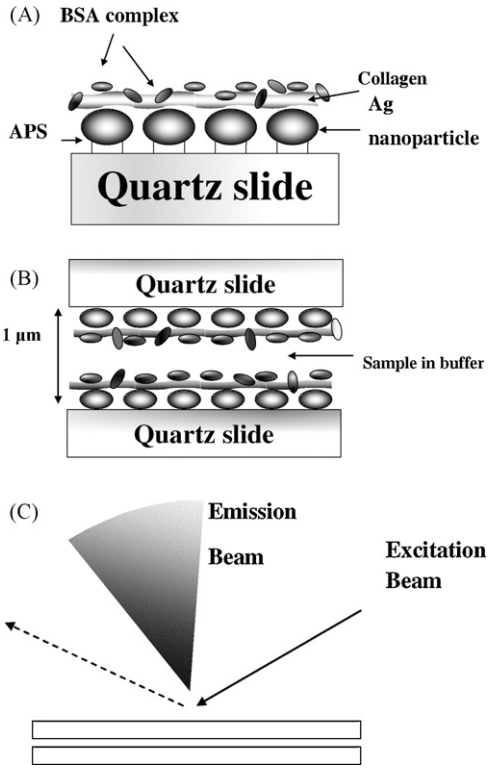

Scheme 1. (A) Glass (quartz) surface geometry. APS is used to functionalize the surface of glass with amine groups that readily bind silver nanoparticle; (B) the sample geometry; (C) experimental geometry.

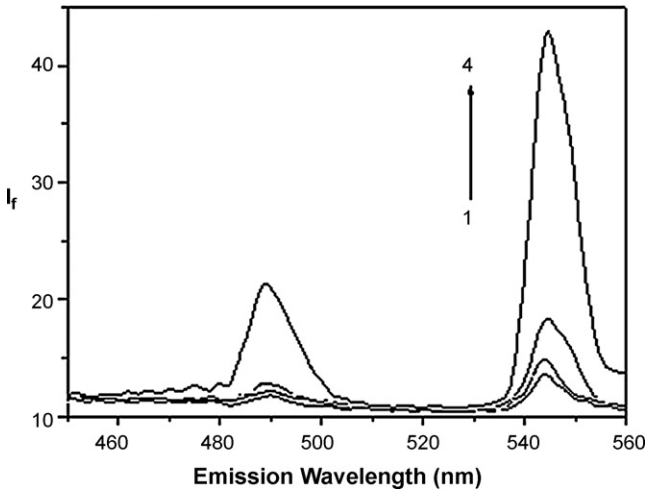

Fig. 2. Emission spectra of the systems at the excitation wavelength of 290 nm. (1) Tb–Gd–SDBS–BSA system without Ag island film; the systems with Ag island film. (2) Tb–BSA system. (3) Tb–SDBS–BSA system. (4) Tb–Gd–SDBS–BSA system. *Conditions*: Tb^3: 1.0×10^{-5} mol/L; Gd^{3+}: 1.0×10^{-4} mol/L; BSA: 1.0×10^{-6} g/mL; SDBS: 1.5×10^{-3} mol/L; Tris–HCl: 5.0×10^{-3} mol/L, pH 8.50.

3. Results and discussion

3.1. Choice of the spacer between Ag island film and the fluorophore

The metal-enhanced fluorescence effect requires a suitable space distance between fluorophore and metal nanoparticle. Generally, HSA and BSA were chosen as the spacer in literatures reported [19–22]. However, the aim of our research is to detect the protein. HSA and BSA acted as spacer must interfere with the measurement because of their native fluorescence. Here, we choose collagen as spacer because that there are no tryptophan residues in its molecule to overcome the interference of native fluorescence. In addition, it is considered that there is strong interaction between collagen and other proteins through the hydrophobic force, which can promote the adsorption of BSA on the surface of Ag island film.

3.2. The fluorescence spectra

The emission spectra of Tb–BSA, Tb–SDBS–BSA and Tb–Gd–SDBS–BSA systems are shown in Fig. 2. It can be seen that the fluorescence intensity of Tb–Gd–SDBS–BSA system is greatly enhanced by nearby Ag island film.

3.3. Analytical application

Interference of various ions was tested and shown in Table 1. It is found that the foreign ions tested have little effect on the determination of 1.0×10^{-6} g/mL BSA within the permissible ±5% error. Under the optimum conditions defined, the calibration graphs for BSA and HSA are obtained and show that there is a linear relationship between the fluorescence intensity of the system and the concentration of proteins (shown in Table 2). The limit of detection (S/N = 3) is 0.72 ng/mL for BSA and 1.30 ng/mL for HSA, which are much lower than those without Ag nanoparticles (8 ng/mL for BSA and 20 ng/mL for HSA).

Table 1
Interference from foreign substances (1.0×10^{-6} g/mL BSA)

Foreign substance	Highest permissible concentration ($\times 10^{-4}$ mol/L)
Mg^{2+}, SO_4^{2-}	5.3
Al^{3+}, NO_3^-	2.4
K^+, Cl^-	200.0
Mn^{2+}, SO_4^{2-}	30.0
Na^+, SO_4^{2-}	192.0
Ba^{2+}, Cl^-	30.2
Al^{3+}, Cl^-	25.0
Fe^{3+}, Cl^-	5.2
Na^+, Cl^-	263.0
Na^+, CO_3^{2-}	6.2
Zn^{2+}, Cl^-	15.3
Ca^{2+}, Cl^-	9.4
L-Ala	3.1
L-Asp	8.2
L-Arg	7.4
L-Tyr	5.7
L-Phe	2.2
L-His	3.0
L-Cys	4.1

Subsequently, an actual sample of human blood serum was tested by the standard addition method. This sample was obtained from The Hospital of Shandong University and diluted to satisfy the requirements of linear range. For comparison with our proposed method, we used other two methods to test the total serum protein concentration in human blood sample. The UV spectrophotometry was based on the absorption of protein at 280 nm [27]. And co-luminescence method was performed in the same system (Tb–Gd–SDBS) but in solution which was described in detail in our previous published paper [17]. The results are shown in Table 3, it can be seen that this method is satisfactory.

3.4. Enhanced fluorescence for adsorbed luminescent molecules

From Fig. 3, it can be seen that the fluorescence intensity of BSA near the surface of Ag island film is about 20 times stronger than that without Ag island film. In general, the fluorescence of native BSA is mainly attributed to the tryptophan residue for its higher quantum yield, whereas the contribution of tyrosine residue is very low for its lower quantum yield [24]. Fig. 4 is the synchronous fluorescence spectra of BSA with $\Delta\lambda$ of 30 and 60 nm, which can characterize the fluorescence of tyrosine and tryptophan residues, respectively. It can be seen that in the presence of Ag island film, the fluorescence of tyrosine residue is increased and its contribution for the intrinsic fluorescence of BSA is similar to that of tryptophan residues. This increased fluorescence of the molecule with lower quantum yield is consistent with the MEF theory which is explained to be the results of an enhanced electric field, and larger quantum yields due to increased rates of radiative decay [23]. In addition, we consider that the enhancement is also related to the adsorption of BSA on the surface of Ag island film, while collagen not only can

Table 2
Analytical parameters

	Protein	Linear range (g/mL)	Correlation coefficient	Limit of detection (ng/mL)
With Ag island film	BSA	6.0×10^{-8}–3.0×10^{-5}	0.9990	0.72
	HSA	3.0×10^{-7}–9×10^{-5}	0.9986	1.3
Without Ag island film	BSA	7.0×10^{-7}–5.0×10^{-5}	0.9995	8.0
	HSA	1.0×10^{-7}–8.0×10^{-5}	0.9991	40

Table 3
Determinations of the total protein from actual human blood serum

	Protein found (mg/mL)	Average (mg/mL)	S.D. (%)
The proposed method	65.3, 65.4, 65.9, 65.1, 65.7	65.5	0.32
The ultraviolet spectrophotometry	67.2, 70.1, 66.4, 68.3, 65.4	67.5	1.8
This co-luminescence in solution	65.7, 65.2, 66.0, 65.1, 65.4	65.5	0.37

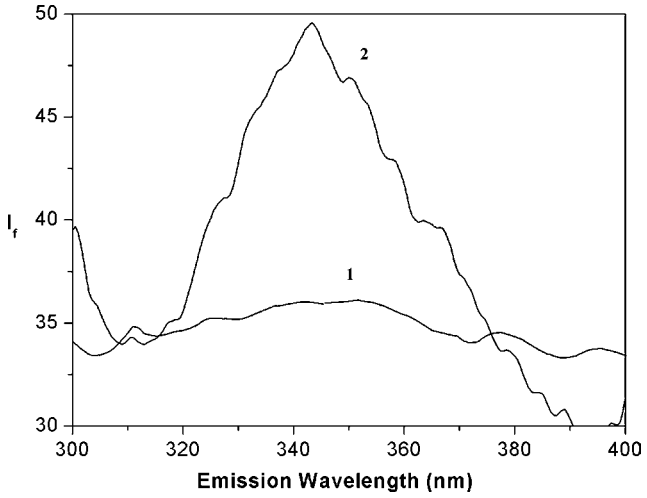

Fig. 3. Emission spectrum of BSA under the excitation of 290 nm. (1) BSA without Ag island film; (2) BSA with Ag island film.

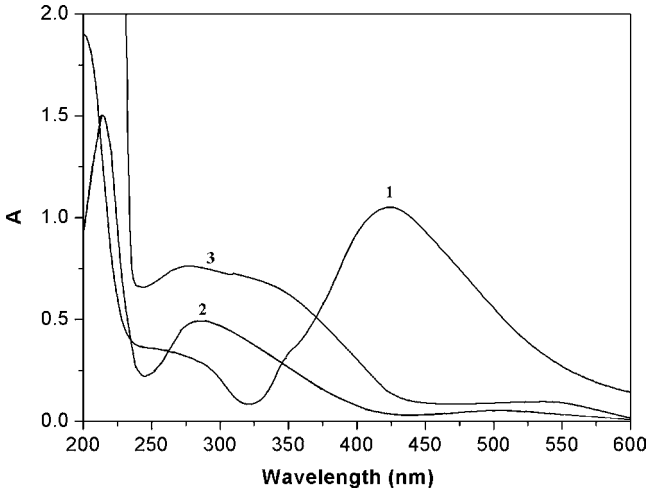

Fig. 5. Overlap of absorption spectra of Ag island film, SDBS and BSA. (1) Ag island film; (2) BSA; (3) SDBS.

decrease the fluorescence of the blank, but also can promote the adsorption of BSA and change its conformation, resulting in strong interaction between BSA and Ag island film.

In fact, not only the fluorescence of BSA, but also the fluorescence of other fluorophores such as Tb^{3+}, SDBS and their complexes (not shown in this paper) are also enhanced by the surface of collagen–Ag island film. This enhancement is believed to be the results of their interaction with Ag nanoparticles. The experiment shows that the plasmon resonance absorption of Ag island film is decreased in the presence of fluorophores, indicating the strong interaction between them. In addition, we find that there are the overlap between the absorption spectra of these fluorophores and the plasmon resonance absorption spectrum of Ag island film (Fig. 5), indicating that it is possible for the fluorophore to form the complex of ground state induced by the metal nanoparticle at appropriate distance, which prevents the dissociating of the adsorbed monolayer, resulting in the enhancement of incident field [24]. Above all, the plamson resonance of Ag island film increases the incident field and modifies the radiative rate of fluorophores, resulting in the enhancement of their fluorescence intensities.

3.5. *Effects of Ag island film on the fluorescence resonance energy transfer in co-luminescence system*

From the fluorescence spectra in Fig. 6, it can be seen that the fluorescence resonance energy transfer of this co-luminescence system in the presence of Ag island film is similar to that in the common solution system in the absence of Ag island film which has been studied in details in our previous paper [17], that is, a efficient

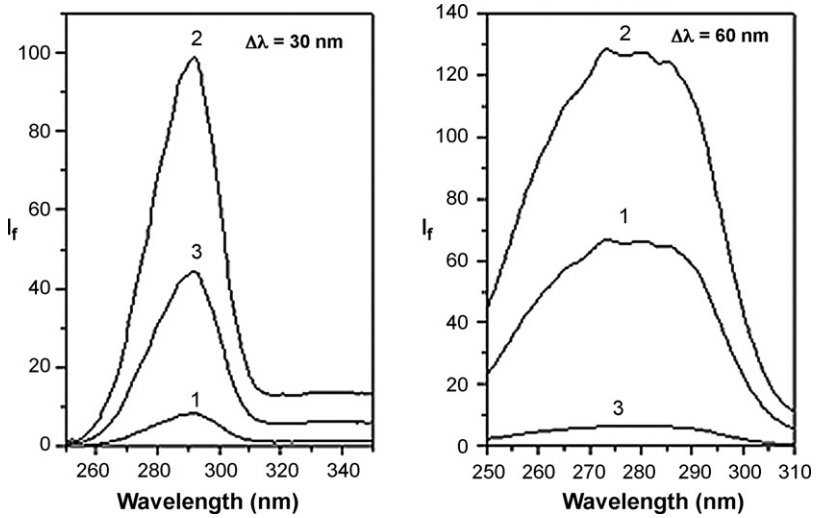

Fig. 4. Fluorescence synchronous spectra. (1) BSA in solution; (2) BSA on the surface of Ag island film; (3) BSA–SDBS-on the surface of Ag-island film.

Table 4
The energy transfer efficiency (E_a) and the critical transfer radius (R_0)

System		Donor	Acceptor	E_a	R_0 (Å)
With Ag island film	SDBS–BSA	BSA	SDBS	0.65	10.1
	Tb–BSA	BSA	Tb	0.05	11.0
	Tb–SDBS	SDBS	Tb	0.10	9.1
	Tb–SDBS–BSA	BSA	SDBS	0.92	8.9
		SDBS	Tb	0.21	7.3
		BSA	Tb	0.19	13.0
	Tb–Gd–SDBS–BSA	Gd–SDBS–BSA	Tb	0.61	
		BSA	Tb	0.95	
Without Ag island film[17]	SDBS–BSA	BSA	SDBS	0.59	9.3
	Tb–BSA	BSA	Tb	0.03	10.6
	Tb–SDBS	SDBS	Tb	0.07	8.4
	Tb–SDBS–BSA	BSA	SDBS	0.83	8.1
		SDBS	Tb	0.18	6.9
		BSA	Tb	0.15	12.8
	Tb–Gd–SDBS–BSA	Gd–SDBS–BSA	Tb	0.50	
		BSA	Tb	0.89	

intramolecular fluorescent energy transfer occurs from unfolded protein to rare earth ions through SDBS acting as a "transfer bridge" to enhance the emission fluorescence of Tb^{3+} in this ternary complex of Tb–SDBS–BSA. Cooperating with the intramolecular energy transfer above is the intermolecular energy transfer between the simultaneous existing complexes of both Tb^{3+} and Gd^{3+}. Herein, the research on the difference in the whole energy transfer channel is emphasized. From Figs. 4 and 6, it can also be seen that when BSA and SDBS are mixed in solution, the fluorescence of BSA is quenched. At the same time, the fluorescent intensities of SDBS are enhanced. It indicates that there is energy transfer between them. SDBS has two fluorescent peaks: the peak at 355 nm is attributed to the fluorescence of individual monomer and the peak at 410 nm is attributed to the fluorescence of SDBS excimer [28]. In the BSA–SDBS system with Ag island film, the fluorescence intensities of tryptophan and tyrosine residues are quenched (Fig. 4), whereas two fluorescence peaks of SDBS are enhanced (Fig. 6). It indicates that in the presence of Ag island film, the energy of tryptophan and tyrosine residues of BSA can be transferred to monomer and excimer of SDBS, which is different with them in the solution without Ag island film that the dominant energy transfer occurs only between monomers of SDBS and tryptophan residues of BSA [17]. It is considered that there are two reasons for this difference: (1) the energy of SDBS excimer also matches the plasmon absorption energy of Ag island film to promote the energy transfer between BSA and SDBS; (2) collagen can promote the adsorption of BSA and change its conformation, resulting in strong interaction between BSA and Ag island film.

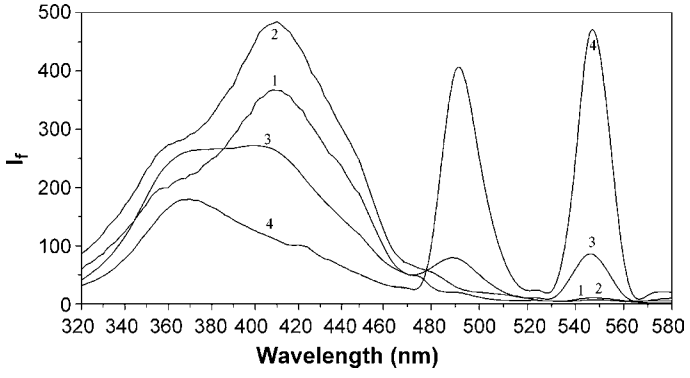

Fig. 6. Fluorescence energy transfer of the systems with Ag island film. (1) SDBS; (2) BSA–SDBS; (3) BSA–SDBS–Tb; (4) BSA–SDBS–Tb–Gd. *Conditions*: Tb^{3+}: 1.0×10^{-5} mol/L; Gd^{3+}: 1.0×10^{-4} mol/L; BSA: 1.0×10^{-6} g/mL; SDBS: 1.5×10^{-3} mol/L; Tris–HCl: 5.0×10^{-3} mol/L, pH 8.50.

Ag island film can also affect the energy transfer from SDBS to Tb^{3+} as shown in Fig. 6. After addition of Tb^{3+}, the fluorescence of SDBS, especially the peak at 410 nm, is quenched, indicating that the dominant energy transfer is happened between the excimer of SDBS and Tb^{3+}. When Gd^{3+} is added in the above system, the fluorescence intensities of both excimer and monomer of SDBS are greatly quenched, and the more energy can be transferred from SDBS to Tb^{3+}.

The effect of Ag island film on the energy transfer in the co-luminescence system is evaluated according to Förster theory, mainly including two parameters: the energy transfer efficiency E_a and the critical transfer radius R_0. The results are listed in Table 4. It can be seen that Ag island film can increase the efficiencies of intramolecular and intermolecular energy transfers in Tb–SDBS–BSA system, which is consistent with the results of energy transfer immunoassays [29]. In a word, Ag island film not only can enhance the efficiency of the energy transfer in rare earth co-luminescence effect, but also can change the energy transfer process of Tb–SDBS–BSA system, that is, the process in the presence of Ag island film is mainly BSA (tryptophan and tyrosine residues) → SDBS (excimer) → Tb^{3+}, which is different from that in the absence of Ag island film (BSA (tryptophan residue) → SDBS (monomer) → Tb^{3+}. The mechanism is under study in order to thoroughly understand the energy transfer process.

In conclusion, based on the combination of Ag island film-enhanced fluorescence with rare earth co-luminescence effect of Tb–Gd–SDBS–protein system, a new protein detection method has been reported in this paper. This method shows the potential application in clinic test by its advantages including the high sensitivity, fast assay process and small amount loading of protein sample. The mechanism studies on the fluorescence enhancement of the co-luminescence effect near Ag island film are helpful for us to understand the energy transfer of biological molecules near metal nanoparticles.

Acknowledgments

The Natural Science Foundations of China (20575035) and Shandong Province (Y2003B02) supported this work.

References

[1] P.R. Banks, Trends Anal. Chem. 17 (1998) 612.
[2] C.K. Larive, S.M. Lunte, M. Zhong, M.D. Perkins, G.S. Wilson, G. Gokalvangan, T. Williams, F. Afroz, C. Schoneich, T.S. Derick, C.R. Middaugh, S. Bodanowich-Knipp, Anal. Chem. 71 (1999) 389R.
[3] C.X. Sun, J.H. Yang, L. Li, X. Wu, Y. Liu, S.F. Liu, J. Chromatogr. B 803 (2004) 173.

[4] J.H. Yang, C.L. Tong, N.Q. Jie, H.Y. Gong, Chinese Biochem. J. 12 (1996) 143.
[5] C.G. Lin, J.H. Yang, G.L. Zhang, R.T. Liu, R.J. Han, Anal. Chim. Acta 403 (2000) 219.
[6] J. Bruno Jr., W.D. Horrocks, R.J. Zauhar, Biochemistry 31 (1992) 249.
[7] T.M. Corneillie, P.A. Whetstone, A.J. Fisher, C.F. Meares, J. Am. Chem. Soc. 125 (2003) 3436.
[8] C.L. Tong, G.H. Xiang, J. Fluoresc. 16 (2006) 831.
[9] C.L. Tong, G.H. Xiang, D.J. Huang, W.P. Liu, Chinese J. Anal. Chem. 32 (2004) 619.
[10] C.L. Tong, G.H. Xiang, W.P. Liu, Spectrosc. Spect. Anal. 25 (2005) 2061.
[11] J.H. Yang, G.Y.J. Zhu, J. Shandong Univ. (Nat. Sci.) 21 (1986) 133.
[12] J.H. Yang, G.Y. Zhu, B. Wu, Anal. Chim. Acta 198 (1987) 287.
[13] Y.X. Ci, Z.H. Lan, Anal. Chem. 61 (1989) 1063.
[14] J.H. Yang, H.M. Ge, N.Q. Jie, X.Z. Ren, C.L. Tong, J.Z. Wang, Analyst 120 (1995) 1705.
[15] C.G. Lin, J.H. Yang, X. Wu, G.L. Zhang, R.T. Liu, R.J. Han, Anal. Chim. Acta 403 (2000) 219.
[16] L. Li, J.H. Yang, X. Wu, C.X. Sun, G.J. Zhou, Talanta 59 (2003) 81.
[17] C.X. Sun, J.H. Yang, X. Wu, B.Y. Su, S.F. Liu, Biochimie 86 (2004) 569.
[18] C.X. Sun, J.H. Yang, X. Wu, B.Y. Su, S.F. Liu, Chem. Phys. Lett. 398 (2004) 343.
[19] A. Parfenov, I. Gryczynski, J. Malicka, C.D. Geddes, J.R. Lakowicz, J. Phys. Chem. B 107 (2003) 8829.
[20] J. Malicka, I. Gryczynski, J.R. Lakowicz, Biochem. Biophys. Res. Commun. 306 (2003) 213.
[21] C.D. Geddes, J.R. Lakowicz, J. Fluoresc. 12 (2002) 212.
[22] J. Malicka, I. Gryczynski, J.Y. Fang, J. Kusba, J.R. Lakowicz, J. Fluoresc. 12 (2002) 439.
[23] C.D. Geddes, A. Parfenov, I. Gryczynski, J.R. Lakowicz, J. Phys. Chem., B 107 (2003) 9989.
[24] J.R. Lakowicz, Y. Shen, S. D'Auria, J. Malicka, J. Fang, Z. Gryczynski, I. Gryczynski, Anal. Biochem. 301 (2002) 261.
[25] J.R. Lakowicz, Y. Shen, Z. Gryczynski, S. D'Auria, I. Gryczynaltered, Biochem. Biophys. Res. Commun. 286 (2001) 875.
[26] C.D. Geddes, H. Cao, I. Gryczynski, Z. Gryczynski, J.R. Lakowicz, J. Phys. Chem., A 107 (2003) 3443.
[27] A.M. Glass, A. Wokaun, J.P. Heritage, J.G. Bergman, P.F. Liao, D.H. Olson, Phys. Rev. B 24 (1981) 4906.
[28] M. Aoudia, M.A.J. Rodgers, W.H. Wade, J. Phys. Chem. 88 (1984) 5008.
[29] J.R. Lakowicz, Anal. Biochem. 298 (2001) 1.

Talanta 76 (2008) 1058–1064

Contents lists available at ScienceDirect

Talanta

journal homepage: www.elsevier.com/locate/talanta

Facile synthesis of hollow Co_3O_4 microspheres and its use as a rapid responsive CL sensor of combustible gases

Fei Teng[a,b,*], Wenqing Yao[b], Youfei Zheng[a], Yutao Ma[c], Tongguang Xu[b], Guizhi Gao[a], Shuhui Liang[b], Yang Teng[d], Yongfa Zhu[b,*]

[a] Department of Chemistry, Nanjing University of Information Science & Technology, Nanjing 210044, PR China
[b] Department of Chemistry, Tsinghua University, Beijing 100084, PR China
[c] School of Science, Beijing Jiaotong University, Beijing 100044, PR China
[d] Department of Information Science, Suzhou Institute of Trade & Commerce, PR China

ARTICLE INFO

Article history:
Received 3 February 2008
Received in revised form 27 April 2008
Accepted 5 May 2008
Available online 18 May 2008

Keywords:
Hollow Co_3O_4 microspheres
Chemiluminescence
CO oxidation
Gas sensor

ABSTRACT

The hollow Co_3O_4 microspheres (HCMs) were prepared by the carbonaceous templates, which did not need the surface pretreatment. The chemiluminescence (CL) and catalytic properties for CO oxidation over these hollow samples were evaluated. The samples were characterized by scanning electron microscopy (SEM), energy disperse spectra (EDS), transmission electron microscopy (TEM), selected area electron diffraction (ED), X-ray diffraction (XRD), temperature-programmed desorption (TPD) and N_2 adsorption. The influences of filter' band length, flow rate of gas, test temperature, and particle structure on CL intensities were mainly investigated. It was found that compared with the solid Co_3O_4 particles (SCPs), HCMs had a stronger CL intensity, which was ascribed to its hollow structure; and that CL properties of the catalysts were well correlated with their reaction activities. Moreover, HCMs were used to fabricate a highly sensitive gas detector, which is a rapid and effective method for the selection of catalysts or the detection of environmental deleterious gases.

1. Introduction

In 1976, Breysse et al. [1] first reported chemiluminescence (CL) phenomenon. They observed that a weak catalytic luminescence phenomenon occurred while CO was catalytically oxidized on the ThO_2 surface. This luminescence mode was defined as "cataluminescence". Since the 1990s, micro- and nano-particles have been widely applied in various fields of catalysis [2], chemical and biochemical sensing [3], and biological imaging [4]. Many investigations have indicated that CL property of nanoparticles would be promising for new applications [5]. Recently, Zhu et al. [6] investigated CL of organic vapor over different nanoparticles, including MgO, TiO_2, Al_2O_3, Y_2O_3, $LaCoO_3$:Sr^{2+} and $SrCO_3$. Rakow and Suslick [7] reported that the nanoparticles are potentially suitable for processing as a chip-mounted sensor array. Nakagawa et al. [8] have manufactured a γ-Al_2O_3 sensor to detect ethanol, acetone and butyric acid, which utilize the combustibility of these chemicals on this solid. Okabayashi et al. [9] have also manufactured a Dy-doped γ-Al_2O_3 sensor used for hydrocarbon gases. Zhang and co-workers [10–12] have designed the highly selective CL sensors for ammonia, hydrogen sulfide and acetone. They reported that ZrO_2 nanoparticles-based sensor for ethanol has no response to hexane, cyclohexane, ethylene, hydrogen, ammonia and nitrogen oxides. While Tb was doped, the sensibility of Tb–ZrO_2 sensor can be enhanced as high two level as that of the undoped one. A lot of researches about CL properties of micro- or nano-particles have focused on CL applications in analysis [13]. Nevertheless, the highly sensitive CL sensors are still challenged by the structure properties of materials. It is well known that the properties of materials are strongly dependent on the morphology and structure of the particles. Compared with solid particles, the hollow structures generally have a higher surface area and a lighter weight. Hollow structures with nano- to micro-meters dimensions are an important class of materials, which are widely used in various fields, such as drug delivery carriers, light-weight structural materials, microreactors. Generally, the hollow particles are prepared by the templated methods. In order to form the coating, the surface modification of the templates is usually needed beforehand [14]. It is needed to develop a simple templated method to prepare the hollow spheres.

The spinel Co_3O_4 has great application potential in heterogeneous catalysts, anode materials in Li ion rechargeable batteries, solid-state sensors, solar energy absorbers, and so on. CO oxidation

* Corresponding author at: Department of Chemistry, Nanjing University of Information Science & Technology, Nanjing 210044, PR China; Department of Chemistry, Tsinghua University, Beijing 100084, PR China. Tel.:/Fax: +86 10 6278 7601.
E-mail addresses: tfwd@163.com (F. Teng), zhuyf@mail.tsinghua.edu.cn (Y. Zhu).

0039-9140/$ – see front matter © 2008 Elsevier B.V. All rights reserved.
doi:10.1016/j.talanta.2008.05.011

of Co_3O_4 has been extensively researched. Recently, hollow Co_3O_4 have been reported by the researcher [15,16]. To the best of our knowledge, nevertheless, fewer researches have reported the CL properties of gases over hollow Co_3O_4 and the essence correlations between CL process and catalytic reaction [17].

Herein, carbonaceous microspheres (CMs) were synthesized by a hydrothermal method; and hollow Co_3O_4 microspheres (HCMs) were prepared by the impregnation and annealing. The carbonaceous templates can be directly used to accept the foreign species to form a coating without surface modification. The CL and catalytic properties for CO oxidation over HCMs were evaluated, and the correlation between them was revealed. Most importantly, a highly sensitive CL sensor was fabricated by HCMs.

2. Experimental

2.1. Synthesis of the samples

All chemicals used in this experiment were analytical grade (Beijing Chemical Reagent Factory), and used as purchased.

2.1.1. Synthesis of carbonaceous microspheres

The carbonaceous templates were prepared by a hydrothermal method [18]. Typically, 5 g of glucose was dissolved in water (40 mL). The mixture was continuously sonicated for 5 min until a clear solution was formed. The solution was then transferred to a Teflon-lined stainless-steel autoclave with 50 mL capacity, and kept at 170 °C for 12 h. The black products were recovered by centrifugation. The solid was washed by water and alcohol at least four cycles of centrifugation/washing/redispersion, respectively. Finally, the product was dried at 80 °C overnight in an oven.

2.1.2. Synthesis of hollow Co_3O_4 microspheres

The hollow microspheres were prepared by impregnating the CMs with nitrate solution. Typically, 0.5 g of CMs was dispersed in 100 mL 1.0 M $Co(NO_3)_2$ solution under sonification. The mixture was continuously sonicated for 30 min at room temperature, and then magnetically stirred for 24 h, so that Co ions entered the surface layers of CMs; the solids were separated by centrifugation, and washed with water once; then the sample were dried in an oven at 80 °C overnight. To remove the carbonaceous templates, the sample was calcined at 450 °C for 2 h at a rate of 1 °C min^{-1} under flowing air.

2.1.3. Synthesis of the solid Co_3O_4 particles (SCPs)

The solid Co_3O_4 particles were obtained by a solid-state decomposition reaction of cobalt nitrate. The cobalt nitrate solids were ground homogeneously in mortar, and then calcined at 700 °C for 2 h in air.

2.2. Characterization

The samples were characterized by X-ray diffraction (XRD) on a Rigaku D/MAX-RB X-ray powder diffractometer, using graphite monochromatized Cu Kα radiation ($\lambda = 0.154$ nm), operating at 40 kV and 50 mA. The patterns were scanned from 10° to 70° (2θ) at a scanning rate of 5° min^{-1}. The morphology, surface microstructure and compositional distribution of the sample were determined by a JEOL JSM 6400 scanning electron microscope (SEM) equipped with a Link ISIS energy disperse spectra analyzer (EDS). The same instrument was involved in the recording of X-ray maps. The acceleration voltage in all cases was 15 keV and the current was 1.2 nA. In the recording of X-ray maps the current of 6.7 nA was used. The morphology and microstructure of the sample were also characterized with a transmission electron microscopy (TEM) (JEOL 200CX) with the accelerating voltage of 200 kV. The powders were dispersed in ethanol ultrasonically, and then the samples were deposited on a thin amorphous carbon film supported by copper grids. A nitrogen adsorption isotherm was performed at 77 K on a Micromeritics ASAP 2010 gas adsorption analyzer. Surface areas were calculated by the BET method. The sample was degassed at 250 °C for 3 h before the measurement.

2.3. Evaluation of chemiluminescence properties

The CL detection system employed in this work is shown in literature [6]. The detect system consists of a CL-based sensor, a digital programmable temperature controller of the sensor, and an optical detector. The CL sensor was made by sintering a 0.2-mm-thick layer of the catalyst powder on a cylindrical ceramic heater of 5 mm in diameter. Typically, 0.02 g of Co_3O_4 powders were mixed with absolute ethanol to prepare a paste, and the paste was coated on the surface of heating tube; and then, it was dried in an oven at 110 °C for 24 h and heated at 450 °C for 1 h in air to form a film. In order to accurately control the thickness, the same procedure was repeated for two times. The obtained sensor was set in a quartz tube of 12-mm (i.d.) through which an air at atmospheric pressure flows at a constant rate. A certain volume pulse of CO was injected into the airflow. The sample gas can flow only through the outside of the ceramic heater because this ceramic tube is solid. The temperature of the sensor was controlled by a digital temperature controller. The CL intensity at a certain wavelength was measured by a photon-counting method with a BPCL ultraweak chemiluminescence analyzer (BPCL, Chemiluminescence analyzer made by Biophysics Institute of the Chinese Academy of Science). In the experiment, the optical filter with the wavelength of 640 nm was used. Before each test, the catalyst sensor was heated at 450 °C for 1 h in air to avoid the influence of previous absorbates.

2.4. Evaluation of catalytic activity

The oxidation of CO was carried out in a conventional flow system at atmospheric pressure. 0.1 g of Co_3O_4 powders were loaded in a quartz reactor (inner diameter: 5 mm), with quartz beads packed at both ends of the catalyst bed. The thermal couple was placed in the catalyst bed to monitor the reaction temperature since CO oxidation is an exothermic reaction. Before each run, the catalyst was flushed with air (200 mL min^{-1}) at 450 °C for 1 h in order to remove the previous absorbates from the catalyst surface, and then cooled to 30 °C. A gas mixture of 1 vol.% CO and 99 vol.% air was fed to the catalyst bed at a certain flowing rate of 200 mL min^{-1}. The inlet and outlet gas compositions were analyzed by an on-line gas chromatograph with a GDX-403 GC-column (1.5 m × 4 mm) at 100 °C and a hydrogen flame ionization detector (FID).

3. Results and discussion

3.1. Formation of carbonaceous microspheres and hollow Co_3O_4 microspheres

Fig. 1 shows SEM and TEM images of CMs. It can be observed that CMs have uniformed size of about 5 μm. It seems that their surfaces are smooth (Fig. 1a); but the TEM image reveals that the surfaces of CMs are not smooth but coarse, and there exist surface layer (Fig. 1b). This can be ascribed to the removal of residual organic compounds (i.e. oligosaccharides). The surfaces of CMs became coarse due to the removal of these chemicals from the surface layer while CMs were washed with water and alcohol. Li and co-worker [18] have reported that there are some nanopores in the surface layer while they synthesized carbonaceous spheres. The existence

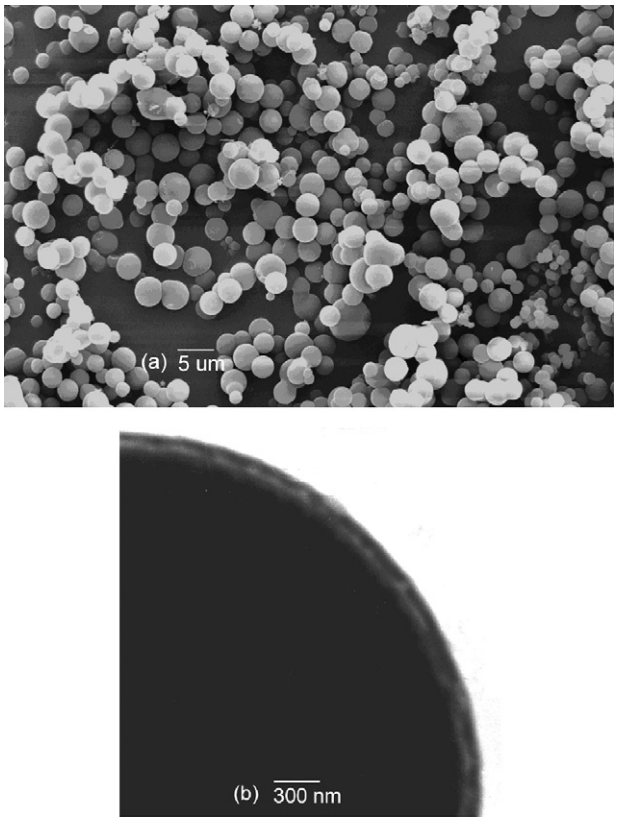

Fig. 1. SEM (a) and TEM micrographs (b) of carbonaceous microspheres (CMs).

of nanopores in surface layer is very important, which can not only increase the surface area, but also favor for the accommodation of foreign species.

Carbonaceous microspheres are formed by dehydration of saccharide under hydrothermal conditions [18–20]. It has been reported that under hydrothermal conditions, a variety of chemical reactions for glucose could take place, which resulted in a complex mixture of organic compounds. As a result, it is difficult to determine exactly the chemical reactions in the sealed autoclave. In the experiment, after hydrothermal treatment, the appearance of black solids and the increased viscosity of the resulting solution indicated that the aromatic compounds and oligosaccharides may have formed, which has been denoted a "polymerization" process [18–20]. The carbonization step may arise from the cross-linking process of oligosaccharides or other macromolecules. The formation of CMs seems to conform to the LaMer model [21]. While the solution reached a critical supersaturation, a short burst of nucleation occurred. The resulting nuclei then grew uniformly through the diffusion of solutes toward the nuclei surfaces until the final size was attained. Importantly, in comparison to the synthesis of polymer spheres, the adopted approach has two outstanding features: (i) the synthetic approach is very simple since no intricate operations are involved; (ii) the approach is environmentally friendly, since no toxic reagents were used. For preparation of polymer microspheres, however, toxic reagents (organic solvents, initiators or/and surfactants) are commonly used.

The surfaces of CMs are hydrophilic due to the functional groups (OH, C=O) [18–20] and the surface layer contains the nanopores [22]. This means that the templates can be directly used without needing surface treatment. We assumed that the surface layers of CMs could adsorb or accommodate cobalt ions. This may be through electrostatic or chelating interactions between foreign metal ions and surface functional groups (OH, C=O) [18–20]. Upon subsequent drying, a sol–gel process may be involved in the formation of cobalt oxide due to the formation of chelate compouds [23]. Further, the annealing treatment in air can not only remove the carbonaceous templates, but also give rise to the self-supporting cobalt oxide nanocrystals. Fig. 2(a and b) presents the typical SEM micrographs of HCMs. The sizes of HCMs are 2–3 μm, which are much smaller than those (5 μm) of the templates. It is obvious that HCMs retained the morphological characteristics of the original templates except for shrinkage in size (about 40%). It is easily understood that upon annealing, the dehydration and dehydroxylation may lead to the contraction of the sample. As a result, the rough surface coatings were constructed by randomly aggregated Co_3O_4 nanocrystals. Further, the surface microstructure of individual HCM was scanned by high-magnification SEM (Fig. 2c). HCMs have the hollow interiors of about 2.6 μm in size and the shells of about 200 nm in thickness. The HCMs have a coarse surface structure, which is different from that of CMs. In the process of annealing in air, the formation of Co_3O_4 and the combustion of templates occurred simultaneously. Co_3O_4 nanocrystals were formed and trapped within the carbonaceous networks; therefore, the nanocrystals could be effectively protected from growth or agglomeration. When the templates were removed, the Co_3O_4 nanocrystals formed the shells. The EDS spectra (Fig. S1 of supporting material) of HCMs firmly demonstrate that the sample consist of cobalt. HCMs were further characterized by TEM. As shown in Fig. 3(a and b), the clear–obscure contrast between the inner and the outer regions of the particles can be observed clearly, revealing the presence of hollow interior. electron diffraction (ED) patterns (Fig. 3c) of the sample further demonstrate that the shells consist of Co_3O_4 polycrystals. Fig. S2 (see supporting material) gives the TEM images of SCPs, which were prepared by decomposition of nitrate. The solid particles have the diameters of 100–200 nm and they agglomerated severely.

XRD patterns were performed to determine the structure of the samples. After being annealed at 450 °C, the sample was composed of Co_3O_4 nanocrystals (Fig. 4a). Co_3O_4 nanocrystals show a spinel structure with the lattice constants $a_0 = 0.8084$ nm (JCPDS file no. 43-1003: space group of Co_3O_4: $Fd3m$). Fig. 4b shows the XRD patterns of carbonaceous templates. The broad peak with low peak intensity centered at about $2\theta = 23.5°$ can be indexed as [0 0 2] diffraction peak of turbostratic and polyaromatic carbon. The broadening of the "graphite" peaks actually indicates the highly disordered structures [19]. While the sample was calcined in a muffle at 450 °C under flowing air, carbonaceous chemicals combusted to form CO_2. In this process, a significant amount of heat would be released. The local temperatures of the sample may be higher than 450 °C. Co (II) was partly oxidized to form Co (III). On the other hand, the functional groups (OH) can impart the reduction ability to Co (III), which can reduce metal ions into lower valence ion. Such reduction ability has been reported in literatures [24,25]. As a result, Co_3O_4 was formed. The XRD patterns of SCPs by decomposition of nitrate were also shown in Fig. S2 (supporting material). Calculated by Scherrer equation, the average crystal size is about 32.2 nm, which is larger than that (25.5 nm) of HCMs.

3.2. The CL properties over the samples

We have researched the effects of the filter's band length and flow rate of gas on CL intensity. These research results are given in Figs. S4 and S5 (supporting material). The result showed that the highest CL intensity was obtained with 640-nm filter (Fig. S4). The CL intensity increases with an increase of the flow rate and it saturates above a flow rate ($F = 200\ \mathrm{mL\,min^{-1}}$) (Fig. S5). This may mean that the whole reaction is mainly controlled by a diffusion process at $F \leq 200\ \mathrm{mL\,min^{-1}}$. At $F \geq 200\ \mathrm{mL\,min^{-1}}$, the whole

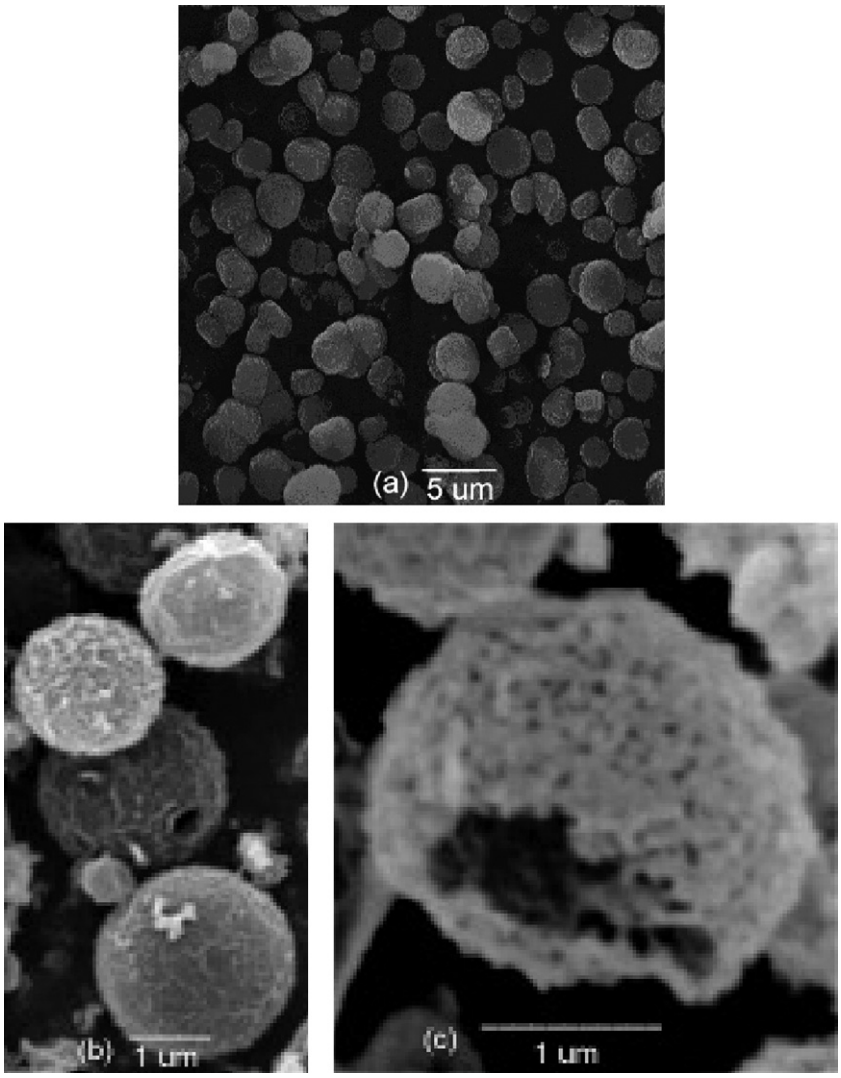

Fig. 2. SEM micrographs of hollow Co_3O_4 microspheres (HCMs): (a) low magnification images of HCMs; (b) broken HCMs; (c and d) high-resolution images of HCMs surface.

reaction is mainly controlled by a surface reaction. Therefore, the CL spectra were determined at $F = 200\,mL\,min^{-1}$ with the 640-nm filter in the latter experiments. Typically, Fig. 5 shows the effect of test temperature on the CL intensity of HCMs. The CL intensities increased from 6×10^3 to 7×10^4 a.u. while the temperature increased from 160 to 300 °C. It is clear that the test temperature has a significant influence on CL intensity. This is because CO conversion increased with the temperature. More CO molecules were oxidized into CO_2 molecules at high temperatures. It is important for CL determination to maintain a constant test temperature. The influence of CO concentration (C) on CL intensity of HCMs is shown in Fig. 6 and Table 1. A good linear correlation between CL intensity and CO concentration can be observed in the concentration range ($5.0–300.0\,\mu g\,mL^{-1}$), and the relative coefficient is 0.995. The detection limit of CL sensor for CO has been determined as low as $0.23\,\mu g\,mL^{-1}$. This means that CL properties of the catalyst should be determined at a constant concentration of CO.

Many researchers have proposed that the CL luminescence results from the excited species produced in catalytic oxidation [26,27]. The exothermal chemical reaction produces energy enough to induce the transition of an electron from its ground state to an excited electronic state. This electronic transition is often accompanied by vibrational and rotational changes in the molecule. CL is observed when the electronically excited product relaxes to its ground state with emission of photons [28]. CL reaction can be represented with the following formula:

$$CO_2(\text{ads.}) + \text{Energy} \rightarrow {}^*CO_2(\text{ads.}) \rightarrow CO_2 + h\nu \quad (1)$$

It is accepted that CO_2 was the luminescence species. While CO molecules were oxidized on the catalyst surface, an amount of energy was released, which would be absorbed by CO_2 molecules. As a result, CO_2 molecules would jump from ground state up to electronic excited state ($^*CO_2$). While the electronic excited $^*CO_2$ molecules decayed to the ground state, a CL was generated. CL spectra are closely correlated with the catalytic reaction, in which the conversion of CO into CO_2 is directly related to the catalytic properties of the catalysts. The easier the catalytic reaction was, the

Table 1
Analytical characteristics of CL determination for CO of hollow Co_3O_4 microspheres (HCMs)

Linear range, C ($\mu g\,mL^{-1}$)	5.0–320.0
Regression equation	$I^a = 67.8C + 55.2$
Relative coefficient	0.995
Detection limit ($\mu g\,mL^{-1}$)	0.23

[a] I, CL intensity; C, CO concentration.

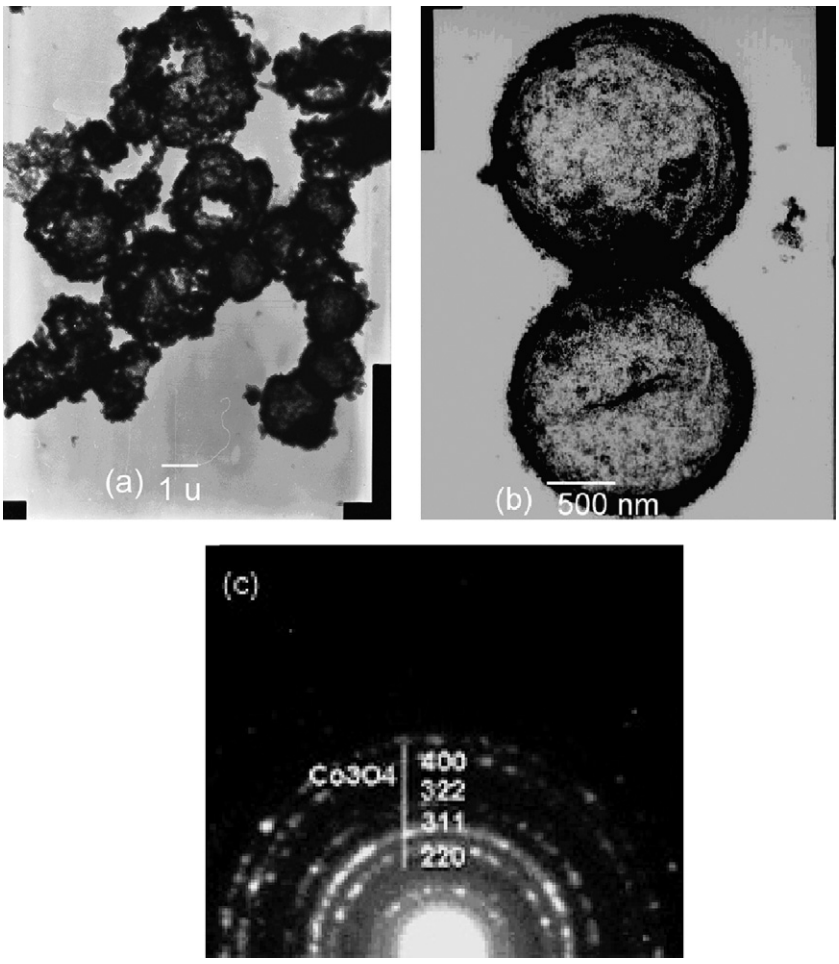

Fig. 3. TEM micrographs and electron diffraction (ED) patterns of hollow Co_3O_4 microspheres (HCMs): (a) low resolution; (b) high resolution; (c) ED.

more CO_2 molecules were formed. As a result, the CL intensity is stronger. The activity and CL represent the same process. It is reasonable that CL spectra can be used to quantitatively evaluate a given catalytic reaction. Fig. 7 shows the CL spectra of HCMs and SCPs. The CL intensity of HCMs is higher than that of SCPs (7×10^4 vs. 4.5×10^4), indicating that more CO molecules were oxidized into CO_2 molecules. The results may mean that HCMs had a higher catalytic activity for CO oxidation than SCPs. The catalytic activity for CO oxidation over the sample was further evaluated.

3.3. The reaction activity for CO oxidation over the catalysts

Fig. 8 shows the activities for CO oxidation over the samples. T_{10}, T_{50}, and T_{90} of HCMs were 135, 175 and 230 °C, respectively.

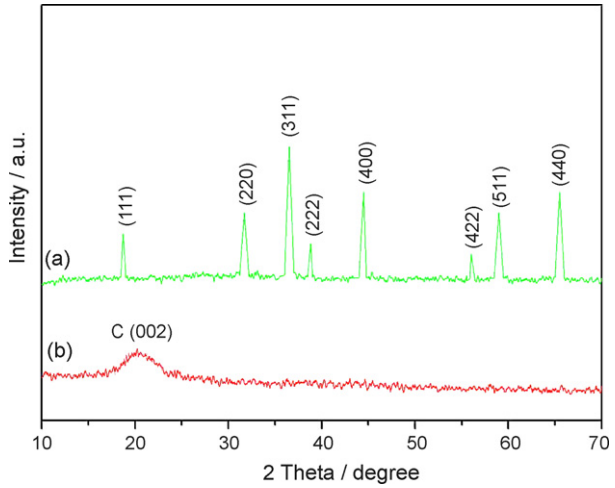

Fig. 4. XRD patterns of the samples: (a) carbonaceous microspheres (CMs); (b) hollow Co_3O_4 microspheres (HCMs).

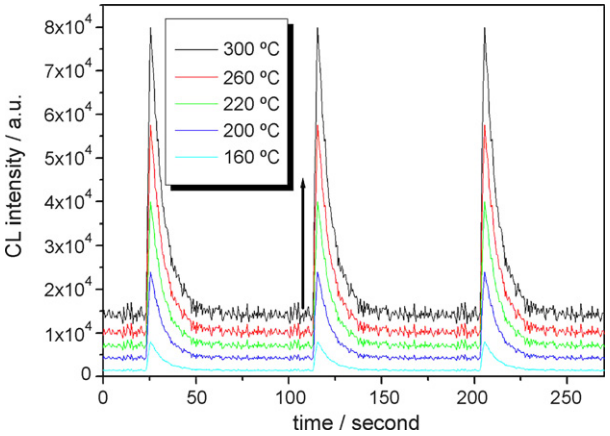

Fig. 5. The temperature dependent CL intensity of HCMs: T = 300 °C, F (flowing rate of gas) = 200 mL min^{-1}; C (CO concentration) = 200 μg mL^{-1}, λ_{filter} (wave number of filter) = 640 nm.

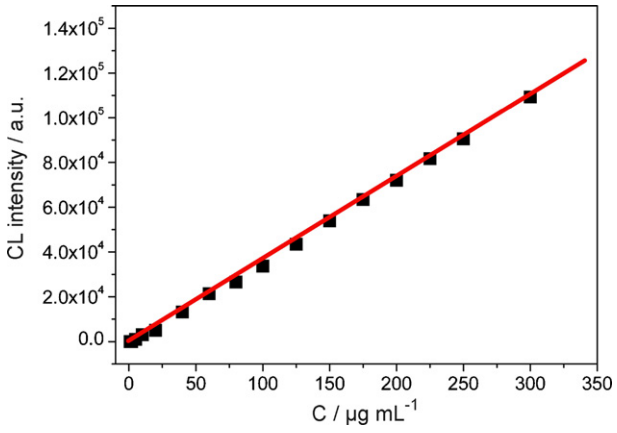

Fig. 6. The CO concentration (C)-dependent CL intensity of hollow Co_3O_4 microspheres (HCMs): T = 300 °C, F = 200 mL min^{-1}, λ_{filter} = 640 nm.

HCMs had a higher activity than the SCPs (T_{10}, T_{50} and T_{90}: 155, 200 and 270 °C), which is well consistent with their CL order. The textural properties of HCMs were characterized by N_2 adsorption isotherm (Table 2). The BET surface areas of HCMs and SCPs are 30.7 and 17.5 m^2 g^{-1}, respectively. The high BET area of HCMs is beneficial to adsorb molecules. Fig. S3 (see supporting material) shows CO-temperature-programmed desorption (TPD) profiles on

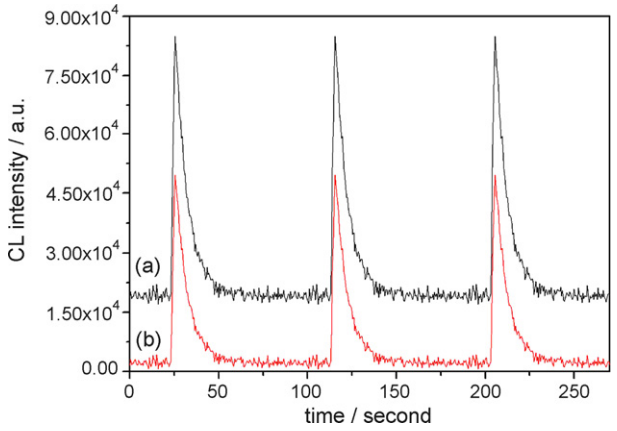

Fig. 7. The CL spectra of CO over (a) HCMs and (b) SCPs: T = 300 °C, F = 200 mL min^{-1}, λ_{filter} = 640 nm, C = 200 μg mL^{-1}.

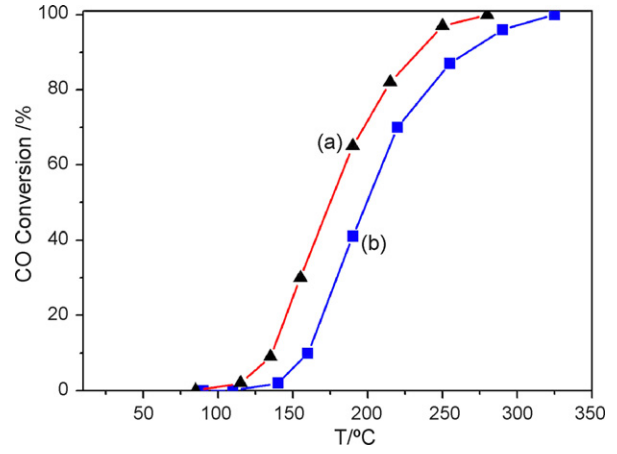

Fig. 8. The activities of CO oxidation over (a) hollow Co_3O_4 microspheres (HCMs) and (b) SCPs: 1 vol.% CO; 99 vol.% air, gas hourly space velocity (GHSV) = 12,000 h^{-1}.

Table 2
Surface areas, particle sizes and crystal sizes of hollow Co_3O_4 microspheres (HCMs) and solid Co_3O_4 particles (SCPs)

Sample	HCMs	SCPs
SA[a] (m^2 g^{-1})	30.7	17.5
Crystal[b] size (nm)	25.5	32.2
T_{10}[c] (°C)	135	155
T_{50}[c] (°C)	175	200
T_{90}[c] (°C)	230	270

[a] Surface area calculated by the BET method.
[b] Average crystal size calculated by Scherrer equation.
[c] T_{10}, T_{50}, and T_{90}, the temperatures at 10, 50 and 90% CO conversions, respectively.

the samples. In the range of 100–600 °C, 3 desorption peaks of CO can be observed over HCMs and SCPs. The adsorbed amounts of CO over both samples are significantly different (Table S1). The adsorbed amount on HCMs is higher than that on the latter.

The BET difference may be closely related to their different microstructures [29]. The BET surface area (30.7 m^2 g^{-1}) of HCMs is significantly larger than that (ca. 1.5 m^2 g^{-1}) of the hollow microspheres with an outer diameter of 5 μm and an inner diameter of 4.5 μm. The surface area of the latter is calculated on base of idea hollow microspheres (the theoretical density of Co_3O_4 is 6.056 g cm^{-3}). The calculation result further confirms that the increased surface area (29.2 m^2 g^{-1}) of HCMs may result from the pores in shells. The porous surface structures of the carbonaceous templates were passed onto the resultant shells after the removal of the templates. The increase of surface areas supports the formation of the porous shells, which resulted from the closely packing of Co_3O_4 nanocrystals. The high BET area of HCMs is beneficial to adsorb molecules, while the pores in the shells of the HCMs benefit the reactant molecules to get to the reactive sites of the catalysts. The chemical reactions can occur more easily, when the transport paths through which reactant molecules move in or out of the materials are included as an integral part of the porous structures.

3.4. Potential use of CL sensor for environmental combustible gases

Most importantly, the activity order of the catalysts is well consistent with that of CL intensity. This may indicate that CL mode can be an effective means to judge the catalyst activity, because the determination of CL spectra can be fulfilled within a few minutes. We have found that luminescent efficiencies and spectral shapes of the CL are dependent on the kinds of reactants and catalysts (Table S2, Figs. S6 and S7 of supporting material). Even if the same luminescent species could be produced from the different combustible gases on a given catalyst, the amounts of the generated luminescent species by different combustible gases are different. Therefore, the same nanomaterial exhibits different intensities of CL upon exposure to different gases. This enables us to discriminate the kind of combustible gas. The compounds within a given chemical class can be still discriminated effectively, because the mechanisms and rates of catalytic reactions are dependent on temperature, which leads to different luminescence efficiencies and spectral shapes [30]. Even if similar shape were recorded with the sensor for two gases at one temperature, they may be differentiated by different CL intensities at another temperature. We have fabricated a CL sensor (Fig. S8 of supporting material). The CL sensor system may be useful for analyzing various environmental toxic gases because of the linear characteristics of CL intensity as a function of gas concentration [29].

The CL properties on catalytic materials provide abundant optical information which motivates the fabrication of chemical sensor arrays. An intensive effort is currently devoted toward the develop-

ment of high-throughput screening approaches. The CL reaction is of practical importance for detecting environmental pollutants or selecting catalysts. The extensive researches are ongoing.

4. Conclusions

Compared with the SCPs, the HCMs showed a stronger CL intensity and a higher catalytic activity for CO oxidation, which was attributed to the hollow microstructure. The good correlation between CL and activity indicates that the CL mode is a facile and rapid means for the detection of environmentally deleterious gases and the selection of excellent catalysts from thousands of materials.

Acknowledgements

The authors gratefully acknowledge the research funding supported by National Basic Research Program of China (2007CB613303) and Chinese Postdoctoral Science Foundation (No. 20060390057).

Appendix A. Supplementary data

Supplementary data associated with this article can be found, in the online version at doi:10.1016/j.talanta.2008.05.011.

References

[1] M. Breysse, B. Claudel, L. Faure, M. Guenin, R.J.J. Williams, T.J. Wolkenstein, J. Catal. 45 (1976) 137.
[2] M.C. Daniel, D. Astruc, Chem. Rev. 104 (2004) 293.
[3] R. Elghanian, J.J. Storhoff, R.C. Mucic, R.L. Letsinger, C.A. Mirkin, Science 277 (1997) 1078.
[4] I.H. El-Sayed, X. Huang, M.A. El-Sayed, Nano Lett. 5 (2005) 829.
[5] A.M. Powe, K.A. Fletcher, N.N. St. Luce, M. Lowry, S. Neal, M.E. McCarroll, P.B. Oldham, L.B. McGown, I.M. Warner, Anal. Chem. 76 (2004) 4614.
[6] Y.F. Zhu, J. Shi, Z. Zhang, C. Zhang, X.R. Zhang, Anal. Chem. 74 (2002) 120.
[7] N.A. Rakow, K.S. Suslick, Nature 406 (2000) 710.
[8] M. Nakagawa, T. Okabayashi, T. Fujimoto, K. Utsunomiya, I. Yamamoto, T. Wada, Y. Yamashita, N. Yamashita, Sens. Actuators B 51 (1998) 159.
[9] T. Okabayashi, T. Fujimoto, I. Yamamoto, K. Utsunomiya, T. Wada, Y. Yamashita, N. Yamashita, M. Nakagawa, Sens. Actuators B 64 (2000) 54.
[10] Z.Y. Zhang, C. Zhang, X.R. Zhang, Analyst 127 (2002) 792.
[11] J.J. Shi, J.J. Li, Y.F. Zhu, W. Fan, X.R. Zhang, Anal. Chim. Acta 466 (2002) 69.
[12] Z.M. Rao, J.J. Shi, X.R. Zhang, Acta Chim. Sin. 60 (2002) 1668.
[13] T. Corralles, C. Peinado, N.S. Allen, M. Edge, G. Sandoval, F.J. Catalina, Photochem. Photobiol. A 156 (2003) 151.
[14] F. Caruso, R.A. Caruso, Science 282 (1998) 1111.
[15] T. He, D. Chen, X. Jiao, Y. Xu, Y. Gu, Langmuir 20 (2004) 8404.
[16] B. Liu, H. Zeng, Small 1 (2005) 566.
[17] Q. Ye, Q. Gao, X.R. Zhang, B.Q. Xu, Acta Chim. Sin. 64 (2006) 751.
[18] X. Sun, J. Liu, Y. Li, Chem. Eur. J. 12 (2006) 2039.
[19] Y.F. Shen, P.R. Zerger, N.R. DeGuzman, L.S. Suib, L. McCurdy, I.D. Potter, C.L. O'Young, Science 260 (1993) 511.
[20] X. Sun, Y. Li, Angew. Chem. Int. Ed. 43 (2004) 597.
[21] V.K. Lamer, Ind. Eng. Chem. 44 (1952) 1270.
[22] H. Qian, G. Lin, Y. Zhang, P. Gunawan, R. Xu, Nanotechnol. 18 (2007) 355602.
[23] J. Huang, T. Kunitake, J. Am. Chem. Soc. 125 (2003) 11834.
[24] S. Chen, H. Zeng, Carbon 41 (2003) 1265.
[25] R. Fu, H. Zeng, Y. Lu, Carbon 31 (1993) 1089.
[26] M. Nakagawa, N. Yamashita, Springer Ser. Chem. Sens. Biosens. 3 (2005) 93.
[27] X. Wang, N. Na, S. Zhang, Y. Wu, X. Zhang, J. Am. Chem. Soc. 129 (2007) 6062.
[28] X.Y. Huang, J.C. Ren, Trends Anal. Chem. 25 (2006) 155.
[29] G.S. Chai, S.B. Yoon, J. Ho Kim, J.S. Yu, Chem. Commun. 11 (2004) 2766.
[30] N. Na, S. Zhang, S. Wang, X. Zhang, J. Am. Chem. Soc. 128 (2006) 14420.

Talanta 76 (2008) 1212–1217

Contents lists available at ScienceDirect

Talanta

journal homepage: www.elsevier.com/locate/talanta

Application of a wool column for flow injection online preconcentration of inorganic mercury(II) and methyl mercury species prior to atomic fluorescence measurement

V. Nüket Tirtom, Şahande Goulding, Emur Henden*

Department of Chemistry, Faculty of Science, Ege University, Bornova, Izmir, Turkey

ARTICLE INFO

Article history:
Received 11 December 2007
Received in revised form 15 May 2008
Accepted 21 May 2008
Available online 3 June 2008

Keywords:
Mercury
Methyl mercury
Preconcentration
Wool
Atomic fluorescence spectrometry
Flow injection

ABSTRACT

The use of an unmodified native sheep wool packed minicolumn for the online preconcentration of Hg(II) and methyl mercury species prior to the determination of mercury by atomic fluorescence spectrometry was investigated. Experimental conditions, such as pH, desorbing agents, volume of solution were optimized. 0.5 M thioglycolic acid was found to be a successful eluting agent for both mercury species. Breakthrough and total capacities were determined. The method is simple and rapidly applicable for the determination of Hg(II) and methyl mercury in tap water. The accuracy of the method was examined by the analysis of a peach leaves standard reference material. Recoveries of spiked mercury species in tap water were 105.8% for Hg(II) and 98.8% for methyl mercury.

1. Introduction

Mercury is one of the most toxic elements and its toxicity to human has been well established. The environmental behaviour of mercury is interesting and differs from those of other toxic elements. Both inorganic and organic mercury compounds (i.e. methylmercury chloride [MeHg(I)], ethylmercury chloride, dimethylmercury and phenylmercury chloride) are toxic substances. MeHg(I) is the most toxic mercury species [1]. Various analytical techniques have been used for the determination of mercury at low concentrations, but the most commonly used ones are the cold-vapour technique coupled with atomic absorption (CV-AAS) [2,3], atomic fluorescence(CV-AFS) [4,5] and inductively coupled plasma emission (CV-ICP-AES) [6,7] spectrofotometry and inductively coupled plasma mass spectrometry (ICP-MS) [8]. Although, CV-AAS is the most used technique in the determination of traces of mercury, atomic fluorescence spectrometry (AFS) allows a more sensitive determination of mercury than AAS [5].

Several authors have applied flow injection analysis (FIA) methodology to the determination of mercury using the cold-vapour technique in order to combine a high analysis rate with both sensitivity and selectivity of the method itself [9]. FIA systems allow inexpensive automation of chemical analysis [10]. Moreover, it works in a closed system with a significant reduction of airborne contamination and a fairly high sampling frequency [6].

Since the toxicities and the behaviour of inorganic and organic mercury species are different and all are highly toxic, determination of each species of mercury at trace level is of great importance. Preconcentration techiques are usually required in order to determine such low levels of mercury. Several online preconcentration methods have been reported. These include liquid–liquid [2] and liquid–solid [11] extraction processes which have been performed in the presence of various complexing agents. This is usually carried out with FIA of mercury using a minicolumn. Solid phase extraction has several advantages over other techniques such as; it is rapid, reproducible, high preconcentration factors can be attained and it requires only small volumes of solvents [12,13]. The typical sorbents are obtained by immobilization of suitable organic agents through physical or chemical binding to different solid surfaces such as organic polymeric resins [3,6,12,14–18], inorganic silica gel [19,20] and modified silica C18 [11,21]. The capabilities of three solid chelating reagents; 7-(4-ethyl-1-methyloctyl)-8-hydroxiquinoline (Kelex 100) adsorbed on Bondapack C18 (Kelex-100/C18), 8-hydroxiquinoline immobilized on vinyl co-polymer Toyopearl gel and the commercial polystyrene/DVB ion exchange resin with paired iminodiacetate groups (Chelex-100) were compared for the

* Corresponding author. Fax: +90 232 3888264.
E-mail address: emur.henden@ege.edu.tr (E. Henden).

0039-9140/$ – see front matter © 2008 Elsevier B.V. All rights reserved.
doi:10.1016/j.talanta.2008.05.038

Table 1
Limits of detection of various preconcentration techniques

Preconcentration sorbent	Instrument	LOD	Reference
SPE, 2-mercaptobenzothiazole loaded Bio-Beads SM-7 resin	CV-AAS	10 ng l^{-1}	[3]
SPE, polystyrene-divinylbenzene with 6-mercaptopurine	CV-AAS	20 ng l^{-1}	[12]
Chemically modified chloromethylated polystyrene-PAN (ion-exchanger)	CV-AAS	2 ng l^{-1}	[15]
Resin functionalized with a 1,2-bis(*o*-aminophenylthio)ethane moiety	CV-AAS	90 ng l^{-1}	[16]
2-(Methylthio)aniline-functionalized XAD-2	FAAS	28 ng l^{-1}	[17]
Silica gel immobilized aliphatic amines 2-thiophenecarboxaldehydde Schiff's bases	AAS	4.75 ng l^{-1}	[19]
Silica gel-2-mercaptobenzimidzol sorbent	CV-AFS	0.07 ng l^{-1}	[20]
Silica C_{18} modified	CV-AAS	0.25 ng l^{-1}	[21]
7-(4-Ethyl-1-methyloctyl)-8-hydroxiqinoline adsorbed on Bodapack C18	AAS	0.23 μg l^{-1}	[22]
YPA_4 chelating resin	GFAAS	2 ng l^{-1}	[23]
Hg(II)-imprinted thiol functionalized mesoporous sorbent	CV-ICP-OES	0.39 ng ml^{-1}	[24]

preconcentration of lead and mercury [22]. Dimethyl sulfoxide immobilized on alumina packed in a minicolumn was reported to be highly efficient for mercury preconcentration [13].

A minicolumn packed with aminoisopropylmercaptan type chelating resin as solid phase-extractor was used for the separation and preconcentration of trace mercury prior to its measurement by GFAAS with palladium as a permanent modifier by Jiang et al. [23]. The solid phase extraction of Hg(II) and MeHg(I) using a chelating resin containing nitrogen and sulphur donor sites of the 1,2-bis(*o*-aminophenylthio)ethane moiety that is selective for mercury has been reported for preconcentration of mercury at ng ml^{-1} level [16].

A new method using a minicolumn packed with Hg(II)-imprinted thiol-functionalized mesoporous sorbent has been developed for the preconcentration of trace mercury prior to its determination using CV-ICP-OES by Zhefeng Fan [24].The limits of detection reported using various preconcentation methods are listed in Table 1.

A method for the rapid sequential determination of Hg(II) and MeHg(I) in natural waters at the ng l^{-1} level has been described by Jian and McLeod [4]. Trace enrichment and separation of mercury species were achieved using a minicolumn of sulphydryl cotton which has a relatively high affinity for MeHg(I).

Maclaren and Milligan reported the use of wool and polymer/wool grafts as sorbents to remove heavy metal pollutants from industrial effluents and to purify contaminated water supplies [25]. Removal of some metal ions (Ni^{2+}, Cu^{2+}, Zn^{2+}, Hg^{2+}, Pb^{2+}) from water using native wool was studied by Balköse and Baltacioğlu [26].

Wool has many functional groups (such as carboxylate, amine, amide, disulfide and thiol) which are potential binding sites for metal cations [27]. Plowman reviewed the identification of wool components and characterizations of wool keratin proteins by using modern proteomic techniques [28].

Goulding and Henden in a preliminary study showed that ship wool could be used for the preconcentration of mercury species [29], the basic problem was that it was not possible to recover the sorbed mercury quantitatively from wool using usual eluting agents such as EDTA, HCl and HNO_3 solutions. However, thioglycolic acid (TGA) solution was shown to be effective to recover mercury from the wool column.

Although several compounds of mercury exist in water and food, the dominant species are the Hg(II) ions and MeHg(I). Both mercury species show adsorption affinity for the potential binding sites in wool. Therefore, in this study, it was aimed to investigate the optimum conditions for the preconcentration of Hg(II) and MeHg(I) using unmodified native wool and apply it to the determination of both these mercury species using a flow injection online preconcentration system coupled with AFS.

Table 2
Fluorescence measurement conditions

Delay time	5–10 s
Rise time	25 s
Analysis time	0.5 min
Memory time	40 s
Carrier gas (argon)	0.55 l min^{-1}
Shield gas (argon)	0.1 l min^{-1}
Dryer gas (argon)	1.5 l min^{-1}
Blank and sample solution	7 ml min^{-1}
$SnCl_2$ solution (3%)	3 ml min^{-1}

2. Experimental

2.1. Apparatus and operating conditions

The measuring apparatus was a PSA 10.004 atomic fluorescence spectrometer with a continuous-flow vapour generator. In flow injection studies, a sample injection valve (Omnifit) was connected to the sample line. In breakthrough studies, a variable speed peristaltic pump (Eyela Tokyo Rikakikai Co. MP-3) was connected to the sample line. The sample loop was 130 μl. The fluorescence measurement conditions are listed in Table 2.

A domestic microwave oven (Vestel Model 550 W power) with a 45 ml microwave acid digestion bomb with PTFE sample cups (Parr Instrument company No. 4782) was used for sample decomposition.

2.2. Reagents

All reagents used were of analytical-reagent grade (from Merck). Quartz distilled water was used in the preparation of solutions and as the carrier solution. As reducing agent, 3% (w/v) stannous chloride was prepared daily by dissolving 7.5 g of $SnCl_2{\cdot}2H_2O$ in 37.5 ml of concentrated hydrochloric acid and finally diluting to 250 ml with distilled water. Sulphamic acid (100 g l^{-1}) solution was prepared in water. Hg(II) solution (1000 mg l^{-1}) was prepared by dissolving 1.00 g of analytical-reagent grade mercury in 10 ml concentrated nitric acid. 0.3 ml of 5% $K_2Cr_2O_7$ solution was added to prevent adsorption on the glassware. Finally nitric acid was added as the final solution to be 10% in HNO_3 and diluted to 1 l with distilled water. A stock solution of MeHg(I) (1000 mg l^{-1} mercury) was obtained from Alfa Inorganics. All of the more dilute mercury standard solutions were prepared by dilution with water and the final solutions contained 0.04 M HNO_3. 0.5 M thioglycolic acid (from Merck) (TGA), EDTA (from Merck), thiourea (from BDH) were prepared and used as eluting solutions. As oxidant bromide/bromate solution (0.5% KBr + 0.14% $KBrO_3$ w/v) was prepared by dissolving potassium bromide and potassium bromate in distilled water. All glasswares were soaked in 10% nitric acid for at least 24 h prior to use to remove any mer-

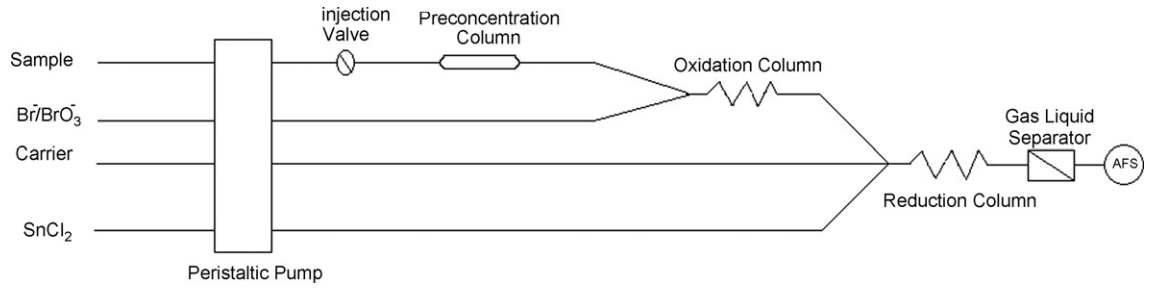

Fig. 1. Scheme of online preconcentration flow injection system.

cury and stop cross contamination and then rinsed with distilled water.

2.3. Flow injection system descriptions

The flow injection system used is shown in Fig. 1. The system consists of a 4-line peristaltic pump of the measuring apparatus, eluent injection valve, wool packed minicolumn, oxidation and reduction coils and gas–liquid separator. The connection tubing was 1.5 mm i.d. PTFE. The preconcentration minicolumn was a PTFE tubing, 5 cm × 3 mm i.d. packed with wool. The oxidation and reduction coils were 1.5 mm i.d. PTFE tubing, the lengths were 60 cm and 25 cm, respectively. The flow rates of $SnCl_2$ and Br^-/BrO_3^- solutions were 3 ml min^{-1}. Sample and carrier solutions flow rates were 7 ml min^{-1} if not otherwise mentioned.

2.4. Preparation of wool column

In this study unmodified native sheep wool was used. After washing with Triton X-100, the wool was extracted with *n*-hexane under reflux for 8 h to remove oil contamination. Then, it was rinsed with distilled water and dried at 60 °C in an oven. It was cut into small pieces of about 1–2 mm length and then 0.050 g wool was filled into a minicolumn (PTFE tubing, 5 cm × 3 mm i.d., wool packing length 1 cm) between two glasswool plugs using a plastic forceps for trace enrichment of mercury. Glasswool showed no adsorptive property for the mercury species used.

2.5. Procedure for the determination of Hg(II) and MeHg(I)

For the determination of mercury(II) Br^-/BrO_3^- oxidizing reagent line in Fig. 1 was removed and the preconcentration column was directly connected to the reduction column. A known volume of sample or standard solution was passed through the wool packed minicolumn at 7 ml min^{-1} rate. 130 μl 0.5 M TGA as eluent was then injected using the injection valve to elute the Hg(II) from the column. The carrier and reductant ($SnCl_2$) streams were passed at 3 ml min^{-1} rate into the reduction coil for mixing with the sample solution. Here, the mercury(II) was reduced to the elemental state and separated from the solution in the gas–liquid separator and swept into the atomic fluorescence detector with argon gas. The peak height of the fluorescence signal was monitored.

Organic mercury cannot be measured directly so the organic mercury was first oxidized by bromide/bromate solution (3 ml min^{-1}) in the oxidation coil as shown in Fig. 1 and the mercury(II) ions formed were then reduced to the elemental state as described for Hg(II) in the reduction coil and measured.

2.6. Procedure for the determination of mercury in peach leaves

0.200 g peach leaves sample was placed into the PTFE cups (45 ml) of the microwave closed vessel sample decomposition bomb. 3 ml of concentrated HNO_3 and 1 ml of 35% H_2O_2 were added and the PTFE cups were closed. Decomposition was carried out in the microwave oven using 40% power for 8 min, 60% power for 8 min and 80% power for 4 min. After cooling the cups the solutions were transferred into 50 ml beakers. 1 ml of 100 g l^{-1} sulphamic acid solution was added on to each solution and the solutions were heated at 50 °C for 30 min. 1 ml of 5% $K_2Cr_2O_7$ was added on to the each solution after cooling. The solutions were quantitatively transferred to 25 ml volumetric flasks and diluted to volume with water for analysis. Alternatively, the peach leaves samples were decomposed in the same way, but addition of sulphamic acid was omitted. Each decomposition was repeated three times.

3. Results and discussion

In the initial studies native wool was used only after washing with Triton X-100. However, a very high blank signal was obtained by AAS and AFS measurements. Thus, the refluxing step with *n*-hexane was included as described above. In this way, native wool was cleaned up from all dirt, grease and contamination. Wool structure is not affected in hot hydrocarbons [25] and does not change by heating at temperatures below 150 °C [30]. Wools of the Merino and Daglic sheeps were compared as mercury adsorbent. No significant difference was found in their adsorption efficiencies. White colour Daglıc sheep wool was used in all studies.

Elution curves obtained with the flow injection systems by separate measurements for 28 ng Hg(II) and mercury as MeHg(I) are shown in Fig. 2. Since the pump of the AFS used had a constant speed of 7 ml min^{-1}, the effect of the solution flow rate at the sorption and elution peaks was not studied.

No significant difference was observed for the Hg(II) and MeHg(I) in single standards and in admixtures. Therefore, for the optimization and analytical performance studies for Hg(II) the oxidation coil line was dismantled for saving purposes.

3.1. Effect of eluent type and concentration on the desorption of mercury from the wool column

In this study, the effect of eluent composition on the recovery of mercury from the wool column was investigated. In order to obtain a calibration graph, 10–40 ng ml^{-1} mercury standard solutions were injected into the empty minicolumn (without wool) using the sample injection valve. A calibration graph was obtained by measuring the fluorescence signals. Then, the wool column was connected to the system and 30 ng ml^{-1} mercury solution was injected using the same injection valve. The mercury collected in the wool column was then eluted by injecting one of the eluent in

Table 3
Desorption of Hg(II) and MeHg(I) by different eluents from the wool column

Eluent		Recovery (%)	
		Hg(II)	MeHg(I)
EDTA	0.01 M	31.0	40.3
HCl	1 M	19.1	20.0
	2 M	30.6	35.2
	4 M[a]	24.7	20.5
HNO_3	2 M	24.0	27.4
	4 M[a]	10.1	12.1
Thiourea	10% (m/v)	15.8	9.5
Thiourea (in 1 M HCl)	5% (m/v)	17.9	12.0
	10% (m/v)	19.4	15.2
TGA	0.05 M	64.0	37.1
	0.1 M	81.8	88.3
	0.5 M	100.1	99.5

[a] 4 M HCl and 4 M HNO_3 caused denaturation of wool [29].

Table 3. The signal was measured and the recoveries were calculated using the calibration graph.

Sorption of both mercury species on wool was found to be quantitative and fast. However, elutions with various reagents such as EDTA, thiourea, HCl and HNO_3 were not complete. 4 M HCl and 4 M HNO_3 caused denaturation of the wool. The results are shown in Table 3. Similar results were also reported earlier by Goulding and Henden [29].

If wool is to be used as a sorbent for mercury preconcentration in flow injection studies, rapid quantitative desorption of the sorbed mercury should be possible. However, only elution with TGA was found to be quantitative and rapid.

Effect of the TGA concentration on elution was, therefore, optimized. It was found that 0.5 M TGA was optimal for elution of both Hg(II) and MeHg(I) from the wool column at the experimental conditions used and, therefore, was used in the following experiments as eluent.

In order to check the recovery (sorption efficiency × elution efficiency) 25 ml of 4.0 ng ml^{-1} Hg(II) was passed through the wool column. The end of the sorption column was then directed to a 25 ml volumetric flask and the mercury sorbed on the wool column was eluted by injecting 0.5 M TGA using the injecting valve. The solution was diluted to 25 ml with water and the mercury content of the solution was measured using AFS without flow injection system. It was found that the recovery was 100.1%. The same experiment was repeated for MeHg(I) with inclusion of $KBrO_3$/KBr oxidation step and the total recovery was found to be 99.8%.

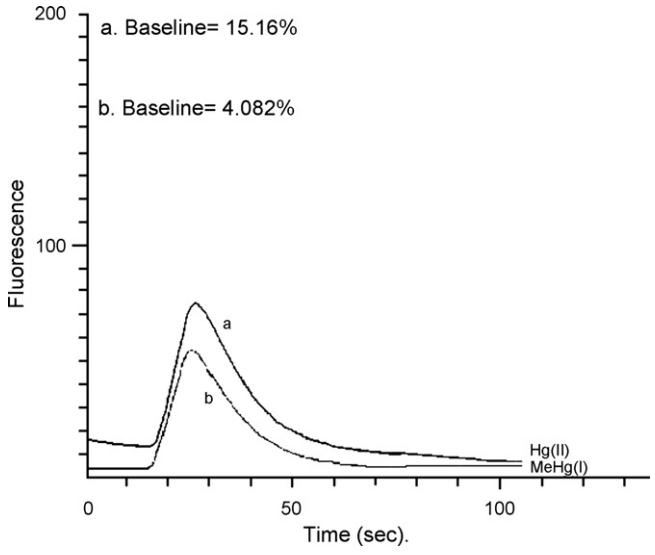

Fig. 2. Elution peaks of mercury(II) and methyl mercury.

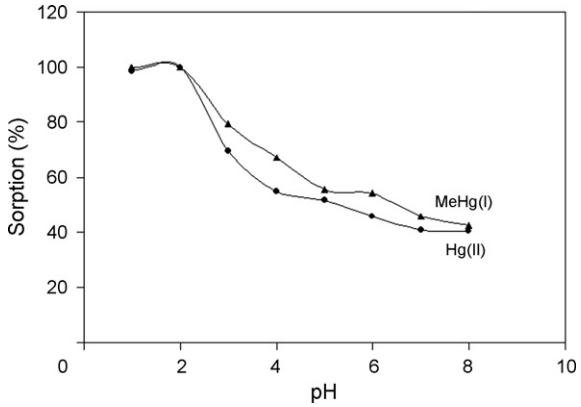

Fig. 3. Effect of pH on sorption of 4.0 ng ml^{-1} Hg(II) (●) and 4.0 ng ml^{-1} MeHg(I) (▲); collection time 1 min, sample flow rate 7.0 ml min^{-1}, elution 130 μl of 0.5 M TGA.

3.2. Effect of acid concentration on the sorption for Hg(II) and MeHg(I)

4.0 ng ml^{-1} Hg(II) and 4.0 ng ml^{-1} MeHg(I) solutions were prepared in 0.005–0.1 M HCl. Mercury in each solution was collected for 1 min at a rate of 7 ml min^{-1}. Signal intensity in the 0.01–0.10 M HCl range did not change significantly. HCl concentration of 0.05 M was selected for the following experiments.

The effect of HNO_3 concentration on the signal intensity was also studied in the same acid concentration range. The results showed that the signal intensity did not change significantly in the nitric acid concentration range of 0.01–0.10 M.

3.3. Effect of pH on the sorption for Hg(II) and MeHg(I)

4.0 ng ml^{-1} Hg(II) and 4.0 ng ml^{-1} MeHg(I) solutions in the pH range 1–8 were prepared. After collecting mercury on the wool column, the sorbed mercury was eluted and measured. The pHs of the solutions were adjusted in the pH range 1–3 using dilute HCl, 3–6 using 0.1 M acetic acid/acetate buffers, and 6–8 using 0.1 M sodium dihydrogen phosphate/disodium hydrogen phosphate buffers.

The results are shown in Fig. 3, which indicated that sorption of Hg(II) and MeHg(I) on wool decreased above pH 2. It was observed from the graph of the variation of the concentrations of the mercury(II) species with pH obtained using the visual Minteq program [31] (Fig. 4) that after pH 2 species Hg(II) decreases while $Hg(OH)^+$ and $Hg(OH)_2$ increasing, which explains the weak sorption after pH 2 in Fig. 3.

3.4. Effect of volume

7–56 ml solutions containing 28 ng Hg as Hg(II) or MeHg(I) were passed through the wool column at 7 ml min^{-1} flow rate and then the sorbed mercury was eluted with TGA and determined by measuring the fluorescence signal. The results showed that the volume of the solution in the range used had no significant effect on the mercury signal.

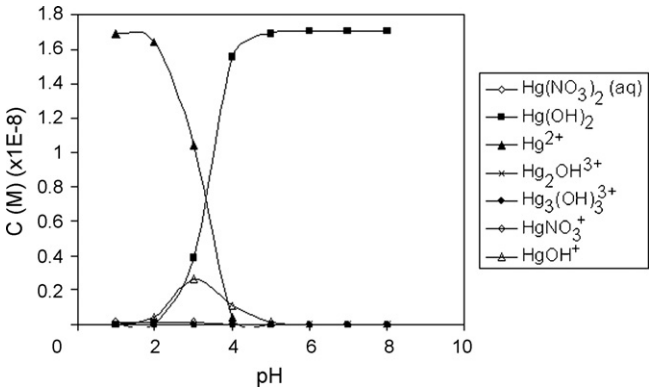

Fig. 4. The graph obtained by using the visual Minteq programme for 4 ng ml^{-1} mercury (II) species in the pH range 1–8.

3.5. Breakthrough and total capacities for Hg(II) and MeHg(I)

Breakthrough capacity studies were carried out by using the present pump with a speed of 7 ml min^{-1} and also in order to see the effect of flow rate on the capacity using a lower speed peristaltic pump (2 ml min^{-1}).

10 ng ml^{-1} mercury as Hg(II) or MeHg(I) solutions were allowed to pass through a column containing 0.0502 g wool for Hg(II) and 0.0514 g wool for MeHg(I) adsorption at a flow rate of 2.0 ml min^{-1}. Mercury was measured in every 2 ml portion of the eluate. No mercury was detected in the effluents until 40.5 ml of the Hg(II) solution as shown in Fig. 5. The breakthrough capacity was calculated as 8.07 μg g^{-1} Hg(II). The breakthrough capacity curve for MeHg(I) is also shown in Fig. 5. The MeHg(I) breakthrough volume was 38 ml. The breakthrough capacity was calculated to be 7.39 μg g^{-1} mercury as MeHg(I). Similar breakthrough capacities for Hg(II) and MeHg(I) species were obtained using an AFS pump with a flow rate of 7 ml min^{-1}. Therefore, this pump was used in the following studies.

The breakthrough capacity of the wool column did not change significantly by the amount of wool packing. When 0.080 g wool was used in the column the breakthrough capacity was found as 8.14 μg g^{-1} Hg(II).

In order to determine the total capacity of wool a batch method was applied. Each two series of 50 ml of 10 μg ml^{-1} mercury as Hg(II) or MeHg(I) solutions in 0.05 M HNO_3 were placed in 100 ml beakers containing 0.045 g wool. In order to correct sorption losses of mercury by the beaker walls parallel experiments were carried out without using wool. All solutions were kept for 12 h while slowly mixing with a magnetic stirrer. The concentrations of mercury in all solutions were measured. Any loss of mercury in the solutions without wool was deducted from the sorbed mercury amount by the wool in the capacity calculations. Total capacities were found to be 5.69 mg g^{-1} for Hg(II) and 5.28 mg g^{-1} mercury as MeHg(I) for batch method.

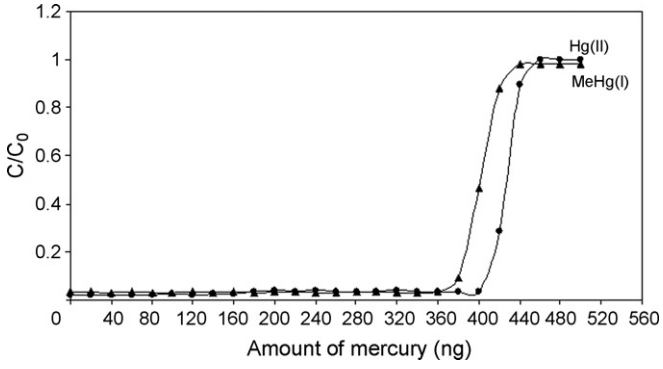

Fig. 5. Breakthrough curve of the wool packed column for Hg(II) (●) and MeHg(I) (▲). Flow rate, 2 ml min^{-1}. 0.0502 g wool for Hg(II) and 0.0514 g wool for MeHg(I).

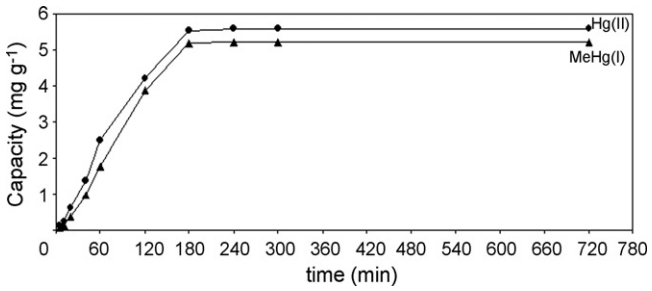

Fig. 6. Effect of sorption time on wool capacity for Hg(II) (●) and MeHg(I) (▲) for batch studies. 0.045 g wool was kept in 50 ml of 10 μg ml^{-1} mercury containing solutions in 0.05 M HNO_3.

The effect of time on the wool capacity was studied under the conditions used above for the total capacity determination and capacity measurements were repeated with time. The results plotted in Fig. 6 show that maximum sorption of the both mercury species is reached in 3 h.

The capacities of the wool did not change significantly in 3 months time of use, approximately after 600 experiments.

Breakthrough capacities in the column studies were found to be about 1000 times lower than the total capacities found by the batch method. This may be because wool contains several functional groups as potential binding sites for mercury, and possibly surface thiol groups which are known to show a very high affinity to mercury species are the main effective binding sites in column studies. Because the sorption time in the column studies are very short (about 2 s with 2 ml min^{-1} flow rate).

3.6. Analytical performance

The analytical performance parameters were evaluated under the optimal experimental conditions. The calibration graph obtained using AFS without wool column was linear in the range used, 0.05–50.0 ng ml^{-1} Hg(II). The calibration graphs obtained using FIA system by collecting mercury in the wool column for 1 min (7 ml solution) were linear in the range studied, 0.05–10 ng ml^{-1} Hg(II) and MeHg(I). The equations were $y = 99.315x + 0.924$ ($R^2 = 0.9944$) for Hg(II) and $y = 97.84x + 0.908$ ($R^2 = 0.999$) for mercury as MeHg(I). The relative standard deviation for six replicate measurements of 4.0 ng ml^{-1} mercury was 2.9% for Hg(II) and 3.1% for MeHg(I). The limit of detection (3σ above blank) was 0.01 ng ml^{-1} mercury for Hg(II) or MeHg(I) under the experimental conditions use. If the sorption time was increased to 8 min (56 ml solution) 0.0014 ng ml^{-1} mercury could be detected.

3.7. Accuracy studies

The method for the determination of mercury was applied to tap water samples with a hardness value of 300 mg l^{-1} $CaCO_3$. The samples were spiked with standard mercury solutions. The recovery values obtained were 105.8% for Hg(II) and 98.8% for MeHg(I) as shown in Table 4.

For the accuracy control of the method, NIST Standard Reference Material No. 1547 peach leaves, was also analyzed for total mercury. Peach leaves samples were decomposed using a microwave oven acid digestion bomb. The obtained results were in good agree-

Table 4
Recoveries of added Hg(II) and methyl mercury from tap water with a hardness of 300 mg l^{-1} $CaCO_3$

Hg(II)			MeHg(I)		
Added	Found	Recovery (%)	Added	Found	Recovery (%)
Mercury concentration (ng ml^{-1}) (n = 3)					
0.00	1.04 ± 0.05	–	0.00	0.27 ± 0.02	–
4.00	5.27 ± 0.01	105.8	4.00	4.22 ± 0.02	98.8

Table 5
Analysis of standard reference material, Peach Leaves NIST 1547

Sample	Method	Found (μg g^{-1})
Peach Leaves	Microwave oven digestion with[a]	0.033 ± 0.005
Peach Leaves	Microwave oven digestion with[b]	0.040 ± 0.008

Certified value 0.031 ± 0.007 (μg g^{-1}).
[a] Sulphamic acid was used.
[b] Sulphamic acid was not used.

ment with the certified values when sulphamic acid was used (Table 5).

3.8. Effect of diverse ions on mercury measurements

Interferences of various cations on the preconcentration and determination of mercury were examined by comparing the signal intensities of mercury in the presence and absence of interfering ions.

For this purpose 4.0 ng ml^{-1} Hg(II) and 4.0 ng ml^{-1} mercury as MeHg(I) solutions with and without interfering ions (400 ng ml^{-1}) were passed at 7.0 ml min^{-1} rate for 1 min through the wool column and then the collected mercury was eluted by injecting 0.5 M TGA. The effects of the diverse ions are shown in Table 6. The results show that the ions at the level studied did not affect significantly the mercury signal.

TGA and EDTA as complexing agents were used to elute mercury from the wool column. Recovery of the elution with EDTA was only 40.3% (Table 3). In order to understand whether the low recovery was due to uncompleted reduction of mercury in Hg-EDTA complex by $SnCl_2$, direct AFS measurements of the mercury in the presence of 0.1 M EDTA was realized without using wool column. The similar experiments were repeated in order to determine any possible effect of TGA, which is used as eluent, on mercury signal. The signal intensities of 4.0 ng ml^{-1} mercury as Hg(II) or MeHg(I) were compared in the presence and absence of these complexing agents. The signal intensities of mercury in the presence of EDTA and TGA were 98.9% and 99.5% for Hg(II), and 98.5% and 99.4% for MeHg(I), respectively compared to the signals obtained in the absence of EDTA or TGA. Therefore, the effect of TGA and EDTA on the mercury signals were not significant.

Table 6
Interference effects of diverse ions (400 ng ml^{-1}) on the preconcentration and determination of Hg(II) and MeHg(I) (4.00 ng ml^{-1})

Interfering ion	Recovery (%)	
	Hg(II)	MeHg(I)
Zn^{2+}	99.6	98.2
Ni^{2+}	98.6	98.6
Cu^{2+}	98.8	98.9
Fe^{3+}	97.6	98.4
Pb^{2+}	99.4	99.4
Na^{+}	100.2	99.9
Ca^{2+}	98.8	98.7
Mg^{2+}	98.9	99.6

4. Conclusion

Use of wool as a preconcentration adsorbent has several advantages, it is easily found and can be used at least for 3 months for about 600 experiments without any significant change in its capacity and sorption efficiency. The method described was successfully used for the preconcentration and determination of Hg(II) and MeHg(I) species. The elution rate of mercury species from the wool column with TGA is fast, which makes the wool column appropriate for online studies. Quantitatively elution of mercury was not possible with the other usually used reagents. We would suggest the use of TGA to solve the elution problem of mercury from also the other sorbents. This is the first paper suggesting the use of TGA for mercury elution.

Acknowledgements

The authors thank TUBİTAK, The Scientific and Technological Research Council of Turkey and Ege University Research Fund for financial support during this study.

References

[1] F.A. Patty, in: S. Clayton, F. Clayton (Eds.), Patty's Industrial Hygiene and Toxicology, vol. 2A, John Wiley & Sons, New York, 1981.
[2] Z. Fang, Z. Zhu, S. Zhang, S. Xu, L. Guo, L. Sun, Anal. Chim. Acta 214 (1988) 41.
[3] J. Chwastowska, A. Rogowska, E. Sterliska, J. Dudek, Talanta 49 (1999) 837.
[4] W. Jian, C.W. McLeod, Talanta 39 (1992) 1537.
[5] G. Vermeir, C. Vandecasteele, R. Dams, Anal. Chim. Acta 242 (1991) 203.
[6] P.C. Rudner, A.G. Torres, J.M.C. Pavoin, F.S. Rojas, Talanta 46 (1998) 1095.
[7] J.C.A. Wuilloud, R.G. Wuilloud, M.F. Silva, R.A. Olsina, L.D. Martinez, Spectrochim. Acta 57B (2002) 365.
[8] L. Jian, W. Goessler, K.J. Irgolic, Fresenius J. Anal. Chem. 366 (2000) 48.
[9] L.O. Leal, O. Elsholz, R. Dams, Anal. Chim. Acta 573–574 (2006) 399.
[10] J. Ruzicka, E.H. Hansen, Flow Injection Analysis, second ed., Wiley, New York, 1988.
[11] M.F. Garcia, R.P. Garcia, N.B. Garcia, A. Sanz-Medel, Talanta 41 (1994) 1833.
[12] B.C. Mondal, D. Das, A.K. Das, Anal. Chim. Acta 450 (2001) 223.
[13] E.M. Soliman, M.B. Saleh, S. Ahmed, Talanta 69 (2006) 55.
[14] K. Minagawa, Y. Takizawa, I. Kifune, Anal. Chim. Acta 115 (1980) 103.
[15] M.A.H. Hafez, I.M.M. Kenawey, M.A. Akl, R.R. Lashein, Talanta 53 (2001) 749.
[16] B.C. Mondal, A.K. Das, Anal. Chim. Acta 477 (2003) 73.
[17] Y. Guo, B. Din, Y. Liu, X. Chang, S. Meng, M. Tian, Anal. Chim. Acta 504 (2004) 319.
[18] S.D. Çekiç, H. Filik, R. Apak, Anal. Chim. Acta 505 (2004) 15.
[19] E.M. Soliman, M.B. Saleh, S. Ahmed, Anal. Chim. Acta 523 (2004) 133.
[20] H. Bagheri, A. Gholami, Talanta 55 (2001) 1141.
[21] S.R. Segade, J.F. Tyson, Talanta 71 (2007) 1696.
[22] L.R. Bravo-Sanchez, B.S.V. Riva, J.M. Costa-Fernandez, R. Pereiro, A. Sanz-Medel, Talanta 55 (2001) 1071.
[23] H. Jiang, B. Hu, Z. Jiang, Y. Qin, Talanta 70 (2006) 7.
[24] Z. Fan, Talanta 70 (2006) 1164.
[25] J.A. Maclaren, B. Milligan, Wool Science: The Chemical Reactivity of Wool Fiber, Science Press, Australia, 1981.
[26] D. Balköse, H. Baltacioğlu, J. Chem. Tech. Biotechnol. 54 (1992) 393.
[27] M.S. Masri, M. Friedman, in: M. Friedman (Ed.), Protein Metal Interactions, Plenum Press, New York, 1974, pp. 551–588.
[28] J.E. Plowman, J. Chromatogr. B 787 (2003) 63.
[29] Ş. Goulding, E. Henden, Ultratrace determination of mercury by cold vapour generation atomic fluorescence spectrometry, in: 35th IUPAC Congress, İstanbul, 14–19 August, 1995.
[30] W. Xu, W. Guo, W. Li, J. Appl. Polym. Sci. 87 (2003) 2372.
[31] P.J. Gustafsson, Visual Minteq, ver. 2.32. KTH Dept. of Land and Water Resources Engineering, Stockholm, Sweden, 2005, p. 7.

Talanta 76 (2008) 1088–1096

Contents lists available at ScienceDirect

Talanta

journal homepage: www.elsevier.com/locate/talanta

Analysis of natural and synthetic estrogenic endocrine disruptors in environmental waters using online preconcentration coupled with LC-APPI-MS/MS

L. Viglino[a,b], K. Aboulfadl[a,b], M. Prévost[b], S. Sauvé[a,*]

[a] Département de chimie, Université de Montréal, Montréal, QC, Canada
[b] Chaire CRSNG en Eau Potable, Département des génies civil, géologique et des mines, École Polytechnique de Montréal, Canada

ARTICLE INFO

Article history:
Received 21 January 2008
Received in revised form 7 May 2008
Accepted 8 May 2008
Available online 17 May 2008

Keywords:
Estrogens
Progestagens
Automated online extraction
Wastewater
Surface water
APPI

ABSTRACT

This paper describes a fully automated online method for solid-phase extraction coupled with liquid chromatography and tandem mass spectrometry using atmospheric pressure ionization (LC-LC-APPI-MS/MS) to simultaneously detect selected dissolved natural and synthetic hormones at concentrations as low as 5 ng/L from aqueous matrices. The method shows excellent performance for the direct analysis of water and wastewater with respect to calibration curve linearity, analytic specificity, sensitivity, and carryover, as well as overall method accuracy and precision. With a runtime of 15 min, a minimum of 200 samples were analyzed using a single online solid-phase extraction (SPE) column without noticeable differences in system performance. Because of the ruggedness and simplicity of this system, generic methods can be easily developed and applied for the high-throughput analysis of a wide variety of compounds without the need to resort to laborious offline SPE sample preparation.

1. Introduction

Among the group of endocrine disrupting compounds, natural and synthetic estrogens are considered the most potent estrogenic compounds [1]. Even at concentrations as low as 1 ng/L, steroidal hormones can have endocrine-disrupting effects on aquatic organisms, such as decreased fertility, feminization, and hermaphroditism [2–4]. Other recent studies have shown the influence of these substances on the reproductive and immune systems of humans [5,6]. Special attention has been given to the natural estrogens, estradiol and estrone, as well as to the synthetic estrogen 17-alpha-ethinylestradiol, because of the strong endocrine-disrupting potency of these molecules (they are actually designed to be strongly estrogenic). There is no information available in the literature on the potential adverse environmental effects of the synthetic progestins (levonorgestrel, medroxyprogesterone, and norethindrone) used in various hormone therapies (contraception, the treatment of endometriosis and infertility, and hormone replacement therapy (HRT)) [7]. Drug consumption compilations estimate that 128 million birth control pills and 107 million hormone replacement therapy doses are consumed in the province of Quebec (7.7 million people) each year [8].

Human and animal excretion is considered the main source of estrogen and progestogen (natural and synthetic) occurrence in aquatic ecosystems [9,10]. Steroids, which are continually being discharged into the environment, are also present at concentrations of toxicological concern, and have now been shown to reach drinking water sources [11–19].

The potential effects to human health and the ecological impacts of these natural and synthetic hormones are a growing concern, and have recently become the focus of scientific research [20–26]. It is crucial to be able to understand and predict the fate of these substances in environmental ecosystems, and consequently to optimize wastewater and drinking water processes, by establishing their occurrence using sensitive and reliable methods. However, because of the low limits of detection (around 1 ng/L) corresponding to the concentrations of these compounds known to affect living organisms, analyzing them remains a significant challenge, and labor-intensive analytical procedures (sample preparation and solid-phase extraction) are usually needed to accurately measure their occurrence.

Several analytical methods have been developed for the detection and quantification of estrogens in environmental samples, all of which use essentially the same extraction and clean-up methods,

* Corresponding author at: Département de chimie, Université de Montréal, CP 6128 Centre-ville, Montréal, QC, Canada H3C 3J7. Tel.: +1 514 343 6749; fax: +1 514 343 7586.
E-mail address: sebastien.sauve@umontreal.ca (S. Sauvé).

0039-9140/$ – see front matter © 2008 Elsevier B.V. All rights reserved.
doi:10.1016/j.talanta.2008.05.008

but different detection techniques (see reviews by [2,6]). A preconcentration step in the extraction protocol is needed to reach the required detection limits (LDs) for these analytes. Large sample volumes (several liters) are required for offline solid-phase extraction (SPE), followed by solvent evaporation, the traditional sample preparation method. Most of these procedures are time-consuming and error-prone, given the number of sample manipulations involved.

To reduce sample preparation time and to analyze the samples at the required concentration levels, there is considerable interest in developing an online sample preparation procedure to overcome the need for the time-consuming evaporation and reconstitution steps typically used in offline sample preparation [27,28]. Online SPE methods preceding liquid chromatography have been proposed to detect selected endocrine disruptors [29,30]. However, the duration of the extraction under these protocols is incompatible with routine analysis, as they greatly limit sample throughput. More recently, an online SPE-LC application with derivatization for the analysis of three estrogens (estrone, estradiol, and ethylestradiol) has been proposed using injection volumes which are more suitable for high sample throughput and at the same time applicable to routine analysis [31]. Environmental monitoring would benefit from further developments aimed at the simultaneous detection of different classes of steroids, or other emerging contaminants, using a combination of online solid-phase extraction and tandem MS with high sample throughput.

The focus of the present work was to develop a method for the simultaneous determination of selected dissolved natural hormones and related synthetic compounds from aqueous matrices based on online SPE coupled with tandem mass spectrometry

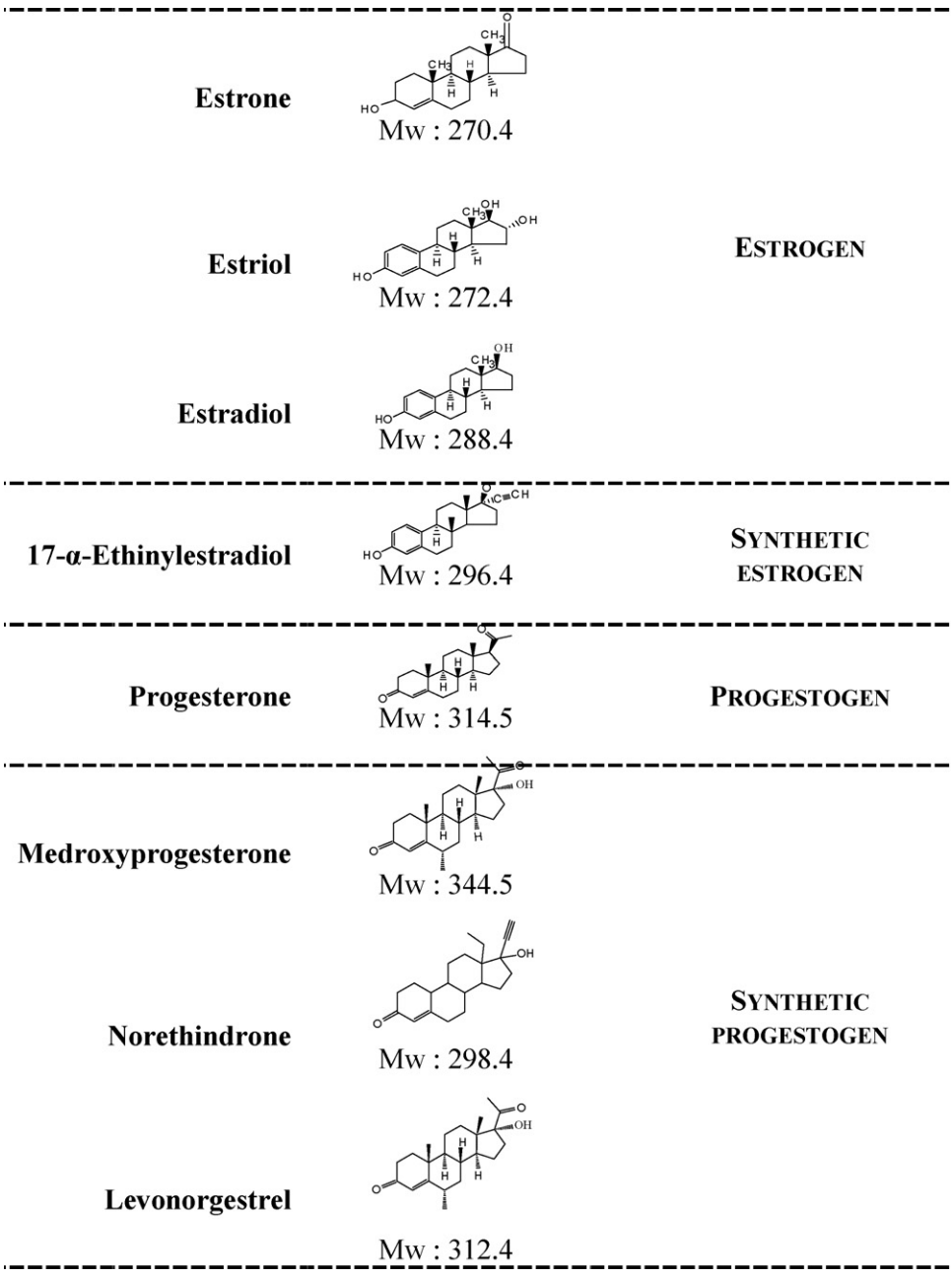

Fig. 1. Molecular structures of selected natural and synthetic estrogens and progestagens.

without resorting to derivatization. The features of the proposed method are: (1) to use a sample volume of 1 mL; (2) to fully automate the procedure by column-switching, thereby minimizing sample preparation and operator interaction (i.e. washing, conditioning, enrichment); (3) to process at least 200 samples without altering the performance of the preconcentration column (which would be impossible using standard online SPE with large sample volumes); and (4) to apply atmospheric pressure photoionization as the ionization source for steroid detection with the LC-MS/MS system to reduce background signals and provide high sensitivity for steroids (bypassing the need for derivatization).

The eight compounds, representing the three different classes of steroids that were investigated are shown in Fig. 1. The method was validated in two types of water: surface water containing low concentrations of hormones in a diluted organic matrix, and wastewater containing higher concentrations of hormones in a more complex matrix which can influence the performance of the analytical method [32,33]. Performance was evaluated by estimating linearity, accuracy, precision, and DL. Finally, results on environmental samples from drinking water intakes and wastewater plants are presented to illustrate the strengths and limitations of the proposed method.

2. Experimental

2.1. Chemicals

All natural and synthetic estrogen and progestogen standards were obtained from Sigma–Aldrich (St. Louis, MO, USA). The internal standard [$^{13}C_2$]-estradiol was obtained from ACP Chemical Inc. (Montreal, QC, Canada). Individual stock solutions of 500 μg/mL for all compounds were prepared in HPLC-grade methanol and kept at −20 °C. Standard solutions containing all compounds were mixed and diluted with methanol, and working solutions of all compounds and calibration concentrations were prepared by appropriate dilution of the stock solutions in the waters studied.

All the solvents (trace analysis grade), as well as the 0.1% formic acid water and the LC-grade water were purchased from Baker (QC, Canada).

2.2. Sampling

Sampling was undertaken in the Montreal (QC) area in October 2007. Water samples were collected in precleaned 250-mL glass bottles and stored at 4 °C immediately after sampling. Raw sewage and treated wastewater effluent were collected at the Montreal

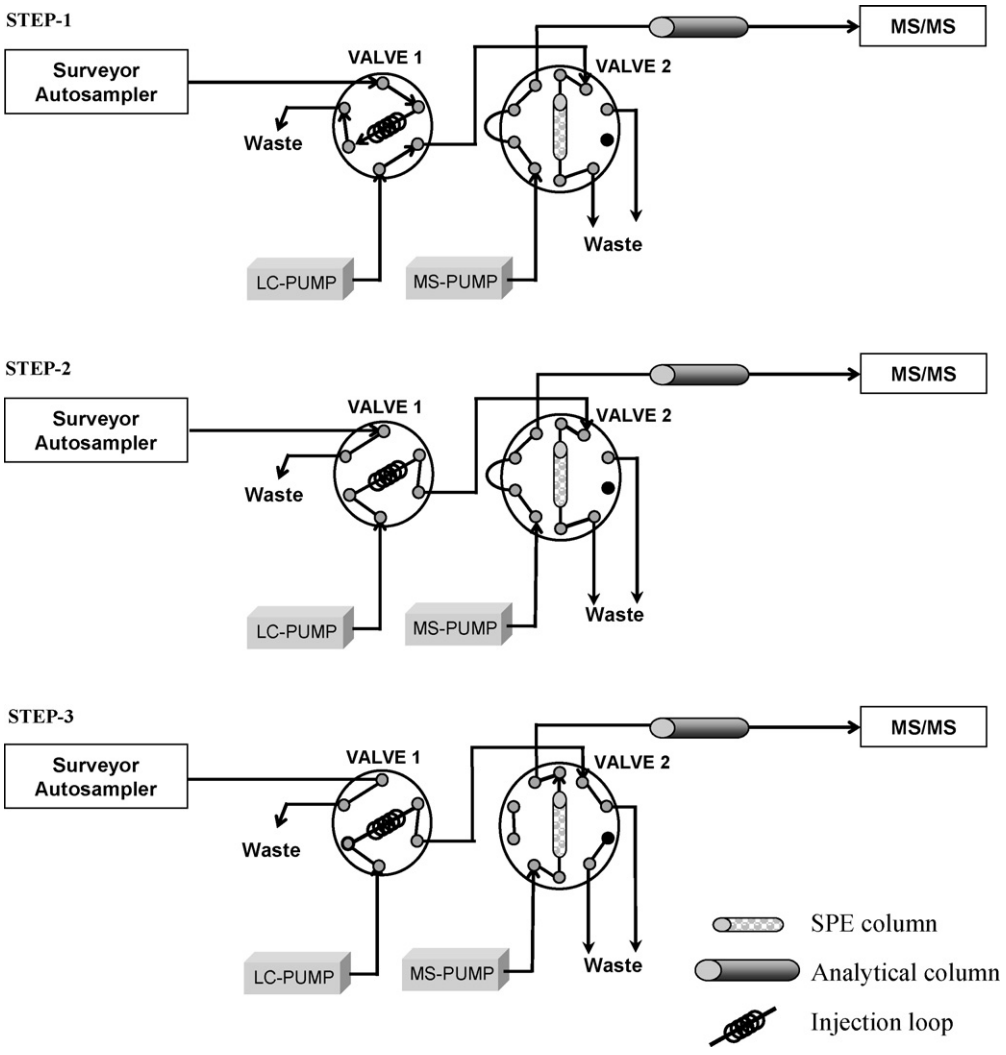

Fig. 2. Schematic diagram of the tandem LC-MS/MS system.

Urban Community sewage treatment plant which represents the largest primary physico-chemical treatment plant of the Americas (nominal capacity of 2,500,000 m^3/day). Treatment processes at this primary plant include grit removal, screening, and chemically assisted settling [34]. Samples from drinking water intakes located in the Mille-Iles and St. Lawrence Rivers were also analyzed. These two waters vary widely in terms of chemistry and potential contamination by wastewater and combined sewer overflow discharges.

2.3. Sample preparation

Prior to analysis, water samples were filtered using 0.45-μm pore size, mixed cellulose membranes (Millipore, MA, USA) and then acidified with a 1% formic acid solution to pH 2.4 to achieve compatibility with the initial mobile phase conditions. Analysis was carried out within 24 h of sampling in order to avoid the need to add chemical preservatives and to minimize potential degradation and transformation of the analytes.

2.4. Instrumentation

The system consisting of tandem liquid chromatography coupled with tandem mass spectrometry (LC/LC-MS/MS) was made up of a Thermo HPLC system (a high-flow Surveyor LC Pump Plus, a low-flow Surveyor MS Pump, a thermostated column compartment, two 6-port switching valves (Rheodyne LLC, Rohnert Park, CA, USA), a Surveyor autosampler (Thermo Fisher Scientific, Waltham, MA, USA), and a TSQ Quantum Ultra AM Mass Spectrometer (Thermo Fisher Scientific, Waltham, MA, USA) with an API source. A schematic diagram of the tandem setup is shown in Fig. 2.

2.5. Online procedure

The online procedure consists of a divert valve on the mass spectrometer which is programmed by the data system to control the loading and elution of the two LC columns. In the load position (STEP 1), 1 mL of the acidified water sample was injected into a 1-mL loop using a Surveyor autosampler modified to use a 1000-μL Peek loop (Upchurch Scientific Inc., Oak Harbor, WA, USA), and then the sample was loaded onto the trapping column a Hypersil GOLD™ C18 online SPE cartridge 12 μm, 20 mm × 2.1 mm i.d. (Thermo Fisher Scientific, Waltham, MA, USA) by the Surveyor LC-Pump (STEP 2). The columns were preconditioned using water acidified with 0.1% formic acid and delivered by the LC pump, which loads the sample and simultaneously directs to waste the matrix that is not retained during the extraction process. After 2.4 min (STEP 3), the valve is switched to the inject position and the analytes are then backflushed onto a 3-μm Hypersil GOLD column, 50 mm × 2.1 mm i.d. (Thermo Fisher Scientific, Waltham, MA, USA) preceded by a guard column (5 μm, 2 mm × 2 mm i.d.) of the same packing material from the same manufacturer. A binary gradient consisting of 0.1% formic acid (v/v) in water (A) and 100% methanol (B) at a flow rate of 200 μl/min was provided by a Surveyor™ MS Pump Plus (Thermo Fisher Scientific, Waltham, MA, USA) to separate the analytes (Table 1). The analytical column was kept at 40 °C. After 11 min, the switching valve was returned to the loading position 100% methanol being used for a thorough cleanup of the extraction and analytical columns to reduce analyte carryover and potential interference. Before processing the next sample, the cartridge was reconditioned with water acidified with 0.1% formic acid. The total cycle time was 15 min.

Table 1
MS gradient for hormone separation at 200 μl/min.

STEP	Total time (min)	*A* (%)	*B* (%)	Valve 2 position
0	2.4	60	40	Load
1	3.0	60	40	Inject
2	4.4	0	100	Inject
3	1.2	0	100	Load
4	4.0	60	40	Load

2.6. Mass spectrometry

Mass spectrometry was performed using a TSQ Quantum Ultra AM Mass Spectrometer (Thermo Fisher Scientific, Waltham, MA, USA). Techniques used for the optimization of the mass spectrometer parameters occurred in three separate steps: (1) determination of the best ionization source and polarity; (2) optimization of the compound-dependent parameters; and (3) optimization of the source-dependent parameters. To determine the best ionization for each hormone, all compounds were tested using electrospray ionization (ESI), atmospheric pressure chemical ionization (APCI), and atmospheric pressure photoionization (APPI) using flow injection with a carrier stream of 0.1% formic acid/MeOH (50:50, v/v). The full-scan mass spectra and the MS–MS spectra of the selected compounds were obtained from the infusion of 5 μg/mL standards of each compound at a flow-rate of 200 μL/min using both negative and positive ion polarity for ESI. For the APCI and APPI sources, each analyte was prepared at a concentration of 10 μg/mL in methanol and infused at 20 μl/min into a flow of 500 μL/min for APCI and 200 μL/min for APPI (various fluxes were tested). In the APPI experiment, the photoionization lamp was a Cathodeon Ltd. 10 eV krypton discharge lamp model PKS 100 (Thermo Fisher Scientific, Waltham, MA, USA). The highest intensity was selected for further study. Optimization of the compound-dependent parameters, such as the collision energy and tube lens for individual analytes, was adjusted by syringe pump infusion, as described above. Mass spectrometer parameters were also optimized by continuous infusion of standards in order to find the best method for detecting all compounds with the best possible signal for the compounds of interest. Quantitative analysis was performed using selected reaction-monitoring mode (SRM) for the detection of transitions at their respective m/z ratios. Instrument control and data acquisition were performed with the Xcalibur software (rev. 2.0 SP2, Thermo Fisher Scientific).

2.7. Evaluation of the matrix effect

The matrix effect was evaluated because MS signal suppression or enhancement effects have been widely reported in the literature when complex matrices are analyzed [35]. The MS/MS response obtained from standard solutions in Milli-Q water (Milli-Q) was compared to those measured in surface water (SW) or sewage treatment plant (STP) samples with the same analyte concentrations (SW or STP). The absolute matrix effect is the ratio SW/MilliQ × 100. A value of 100% indicates that there is no absolute matrix effect. There is signal enhancement if the value is greater than 100% and signal suppression if the value is less than 100%. Matrix effects were evaluated at 20, 50, and 100 ng/L in surface water and wastewater effluents in quadruplicate ($n = 4$).

2.8. Extraction recovery

Method recoveries were evaluated in the online SPE extraction and analysis of 1 mL of spiked (20, 50, and 100 ng/L) surface water samples. The extraction efficiencies were calculated from the peak areas obtained from the online analysis ($n = 5$) of the water samples

as percentages of the peak areas obtained from the direct injection (25 μL) without the enrichment column of equivalent amounts of the standard mixtures. For estriol, the extraction efficiencies at 20 and 50 ng/L levels were not measured due to its method DL of 50 ng/L (see MDL section).

2.9. Linearity and precision of the method

To test the linearity of the calibration curve of each compound, a five-point calibration ($n = 3$) was performed with concentrations ranging between the DL and 100 ng/L, using the online analysis of investigated water samples spiked with a standard mixture of the analytes and using a linear regression analysis.

Repeatability (intra-day precision expressed as a % relative standard deviation) was evaluated by injecting the same spiked river water (Mille-Iles River) at 100 ng/L, once in every workday. Reproducibility (inter-day precision) was calculated by extracting a river sample (Mille Iles River) spiked at 100 ng/L freshly prepared every day for 4 days.

2.10. Method detection limit

The DL of the method (MDL) was determined as suggested by [32]. Seven replicate solutions of all compounds, with concentrations ranging from two to five times the estimated DL, were subjected to the analytical protocol. Standard deviations (S.D.s) were calculated from the replicates, and the DL from the equation: DL = 3.707 S.D.

2.11. Quantification and quality assurance

For quantification, the internal standard was added (50 ng/L for surface water and 70 ng/L for waste water) and standard addition calibration was constructed on the basis of five points from limit of detection (DL) to 100 ng/L for surface waters, and from the DL to 300 ng/L for the sewage treatment plant samples. Calibration curves were built with the response ratio (area of the analyte standard divided by area of the internal standard) as a function of the analyte concentration.

Environmental samples were analyzed in triplicate. Thus, the values shown in the results and discussion section represent the mean of the triplicate measurements (mean ± S.D.). Quality assurance was performed by measuring an extracted calibration curve at the beginning and the end of every sequence, and quantifying the same fortified sample (200 ng/L) in every sequence.

3. Results and discussion

3.1. Mass spectrometry optimization

Preliminary experiments were performed with the three API sources under the conditions described earlier in order to detect all hormones with the SRM mode and with the most sensitivity. Preliminary results showed a good sensitivity for all hormones, using both APCI and APPI, but with a higher signal response with the APPI source. Consequently, APPI was preferred. Moreover, as mentioned by other authors, for some estrogens [36] the signal-to-noise ratio detected with the APPI source in our experiments was better than that found using the APCI source for all hormones. Also, the intensity of the second or third transitions is higher with the APPI source than with the APCI source (i.e. estrone, transitions #1, #2, and #3 were 8.55, 4.97, and 4.74E+06 in APCI and 3.43, 2.24, and 1.83E+07 in APPI, respectively), which eased the confirmation step for the ultra-trace analysis of those hormones.

Although some workers have demonstrated that the addition of a dopant (toluene or acetone) can greatly increase the ionization yield of the target compound [37,38], in our setup, the APPI experiments with a dopant (toluene and acetone) showed no improvement of sensitivity for the selected hormones. As a result, we decided to use direct APPI without any dopant.

Under the APPI positive mode condition, progesterone and estrone were seen as proton adducts $[M+H]^+$, whereas estradiol, estriol, and 17-alpha-ethinylestradiol as the dehydrated fragment ions $[M+H-H_2O]^+$. These results are in agreement with other published studies [38]. Norethindrone, medroxyprogesterone, and levonorgestrel were also detected as proton adducts $[M+H]^+$, and these were the most sensitive transitions. To the best of our knowledge, this is the first report on the environmental analysis of such synthetic progestogens with the APPI source, apart from one report on levonorgestrel [39].

The source-dependent parameters were as follows: vaporizer temperature (450 °C); sheath gas pressure (35 arbitrary units); auxiliary gas pressure (15 arbitrary units); skimmer offset (6 V); capillary temperature (350 °C); collision pressure (1.5 mtorr); and scan time of 0.1 s scan^{-1}; and the compound-dependent parameters presented in Table 2. The 15-min run time for the analysis was divided into three segments, during which only a select group of compounds was monitored to obtain the best sensitivity for each compound included in one segment [33].

In order to use this method to identify the analyte in aqueous samples, two transitions providing the best sensitivity were selected for the combination of precursor and product ions in the SRM mode study (Table 2). The first is used to quantify the analyte and the second for validation [40]. Identification of the analytes was also confirmed by the LC retention time, which should agree with the retention time (±2%) for a reference standard of the same compound analyzed under the same conditions [41].

3.2. Online procedure optimization

The optimization of some parameters is essential in the development of an online procedure: sample volume, cartridge sorbent, and loading flow rate. In this work, given that the online setup was configured to allow the injection of 1 mL, tests to determine the best online method were performed with a sample volume fixed at 1 mL. Two flow rates (0.5 and 1 mL/min) were investigated, and the results showed no statistical difference between the two responses ($p < 0.05$; one-way ANOVA with SPSS 13 software (SPSS Inc., Chicago, IL)); a 1 mL/min rate was selected for further study. Another adjusted parameter for online extraction is the type of sorbent used for binding the selected analytes. One limitation of an online enrichment SPE-LC system is that the precolumn contains a small amount of sorbent, and therefore the retention capacity could possibly be exceeded by non-selective materials, including the alkyl-bonded silica and apolar copolymers already used for online enrichment [42,43]. To test for the sorption and elution of the nonpolar or low-polar compounds, such as the selected hormones, two suitable materials for hormone extraction were tested: (1) alkyl-bonded silica, Hypersyl Gold C18 (12 μm, 20 mm × 2.1 mm i.d.; Thermo Fisher Scientific, Waltham, MA, USA) and copolymers (2) STRATA-X cartridges (surface-modified styrene divinylbenzene polymer; 25 μm, 20 mm × 2.0 mm i.d., Phenomenex, Torrance, CA, USA). STRATA-X has already been used in many offline SPE applications for a large range of substances [44]. However, during the optimization experiments, the elution of the selected hormones with the STRATA-X cartridge was difficult, suggesting that the hormones were strongly retained in the cartridge, especially the less polar ones (i.e. progesterone, medroxyprogesterone). When loading the doped sample (100 ng/L), chromatograms with low peak

Table 2
Mass spectrometry optimized parameters for all selected compounds

Compound	Retention time (min)	Precursor ion (*m*/*z*)	Product ion (*m*/*z*)	CE (V)	Product ion (*m*/*z*)	CE (V)	Tube lens
Segment-1							
Estriol	6.42	271.15	253.2	11	133.06	22	72
Segment-2							
Estradiol	7.55	255.17	159.2	18	133.09	15	74
17-α-Ethinylestradiol	7.56	279.15	133.2	21	159.05	20	76
Estrone	7.61	271.16	253.2	11	159.06	21	72
Norethindrone	7.61	299.16	109.08	25	91.08	41	71
Levonorgestrel	7.89	313.18	245.16	22	91.10	44	77
Segment-3							
Medroxyprogesterone	8.01	345.21	123.06	24	97.09	23	82
Progesterone	8.18	315.2	109.2	26	97.09	22	85

areas for progesterone and medroxyprogesterone were observed. After loading, the analytical column was analyzed for residual matrix or selected compounds (carryover investigations) using the same gradient method with a blank sample. The chromatogram showed evidence of carryover, and even peaks, for both hormones, indicating a strong sorption of hormones onto the STRATA-X column. The differences observed may be attributed to differences in the retention mechanisms. STRATA-X has a higher surface area (800 m^2/g), which allows for more π–π interactions. This increases the need for a stronger solvent than methanol to elute the analytes. It also translates into a longer desorption time (>30 min) under isocratic conditions (100% MeOH), which is not compatible with high sample throughput. HypersilGold was also tested with the same experiments, showing a balance between the sorption and desorption of the investigated compounds. Thus, HypersilGold was selected to be the most appropriate for our purposes here and all further studies were based on the use of this sorbent.

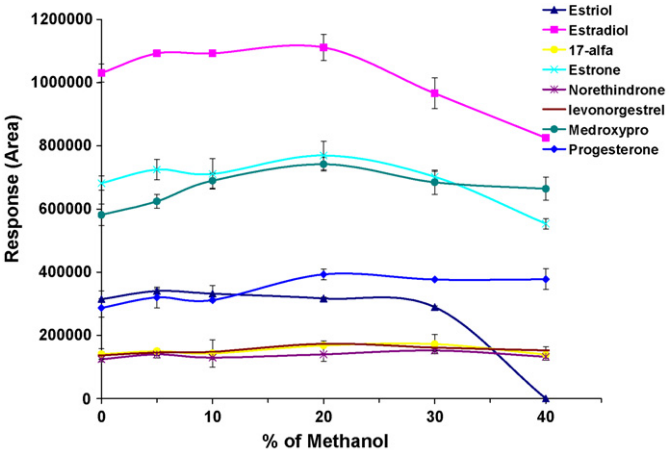

Fig. 3. Influence of the methanol percentage in the washing step on analyte response ratios (mean ± S.D.). Error bar lengths represent the standard deviations of triplicate measurements.

3.3. Sample cleanup procedure

The presence of organic substances in the environmental water samples may cause some interference and complicate quantification. A preconcentration of the matrix components for online extraction is an important factor [45]. A washing step is often required after sample loading in order to remove impurities [46]. In this study, the presence of a large peak due to the interference compounds located prior to the estriol and estrone peaks were observed, and made the quantification of these hormones difficult, and even impossible. Various tests showed that this interference was nearly eliminated when the precolumn was washed with the organic phase MeOH after sample loading. However, excessive washing with a high percentage of organic solvent could lead to analyte losses. In order to reduce or eliminate these impurities without decreasing the signal for the hormones, several washing conditions were investigated. The impact of increasing concentrations of organic phase MeOH were investigated on surface water, and on raw sewage samples spiked at 100 ng/L with selected hormones ($n = 3$). Results (mean ± S.D.) showed that the addition of 20% methanol improves the response of selected hormones (Fig. 3). Consequently, a washing step with 20% MeOH was included in the final online procedure.

3.4. Matrix effect evaluation

APPI is not generally considered to be susceptible to matrix suppression when compared to other ionization sources (ESI, APCI). However, it has been demonstrated that the occurrence of ion suppression might differ between ionization techniques (ESI, APC, APPI), ionization mode (positive, negative), or different source designs for the equipment [35,47,48]. Thus, this phenomenon was investigated in light of the interference observed during method development (sample cleanup procedures). Results (mean ± R.S.D.)

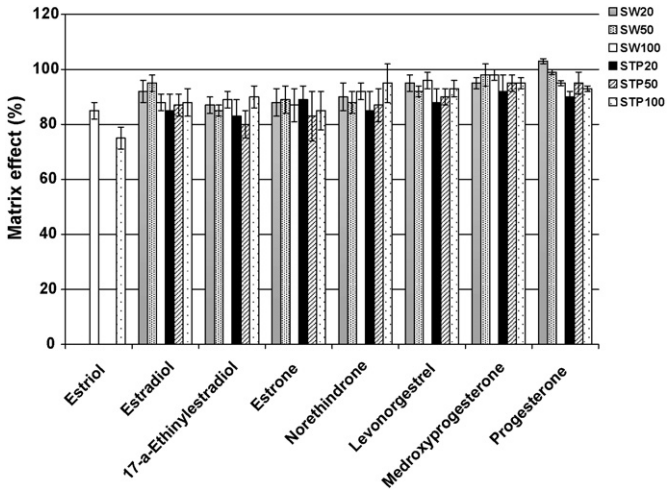

Fig. 4. Matrix effect for all hormones in surface and wastewater samples at 20 ng/L (SW20 and STP20), 50 ng/L (SW50 and STP50), and 100 ng/L (SW100 and STP100). The results are the mean of quadruplicate spikes, and the error bar lengths represent the relative standard deviations.

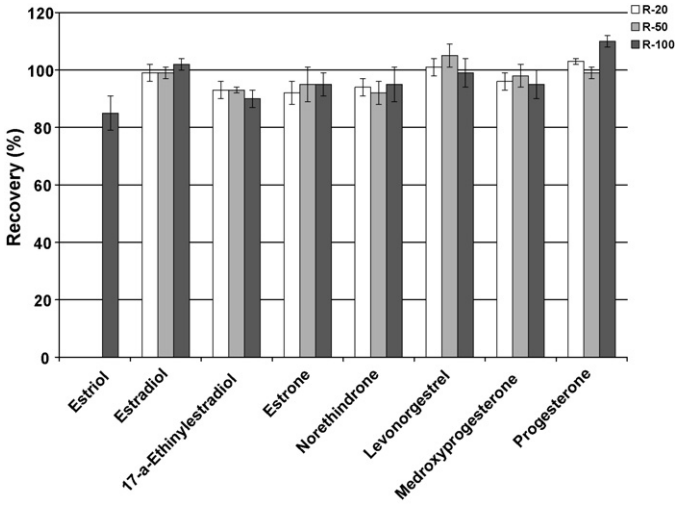

Fig. 5. Recovery percentages obtained for the various target hormones in the replicate ($n = 5$) online SPE-LC-MSMS analysis of spiked (20, 50, 100 ng/L) surface water (R20, R50 and R100). The results constitute the mean of five replicate spikes, and the error bar lengths represent the relative standard deviations.

show values ranging from 85 to 103% in surface water, and from 75 to 95% in sewage water samples (Fig. 4). Signal suppression has been defined as $(100 - (SW/MilliQ \times 100))$ and represents loss of signal due to ion suppression [49]. In this study, signal suppression remained below 25% (100% – 75% = 25%). Hence, 25% of the expected signal will be lost due to ion suppression, confirming that the cleanup procedure is essential and effective for the detection of the selected hormones. Moreover, in order to take into account matrix effects in the analyte quantification, the standard addition calibration was used [33].

3.5. Extraction recovery, linearity and precision of the method

As shown in Fig. 5, good recoveries (mean ± R.S.D.) were obtained, and ranged from 92 to 110%, except for estriol at 85%. These results indicate an efficient retention for all selected hormones.

The calibration curve showed good linearity with correlation coefficients (r^2) above 0.990, except for estrone, with a slightly lower value (mean ± S.D.) at 0.985 (Table 3). Good linearity was also observed for wastewater samples, with values similar to those found in surface water samples (data not shown). Moreover, reproducibility ranged from 2 to 9% and 4 to 11% for intra- and inter-precisions respectively (% R.S.D.), indicating a good precision of the method (Table 3).

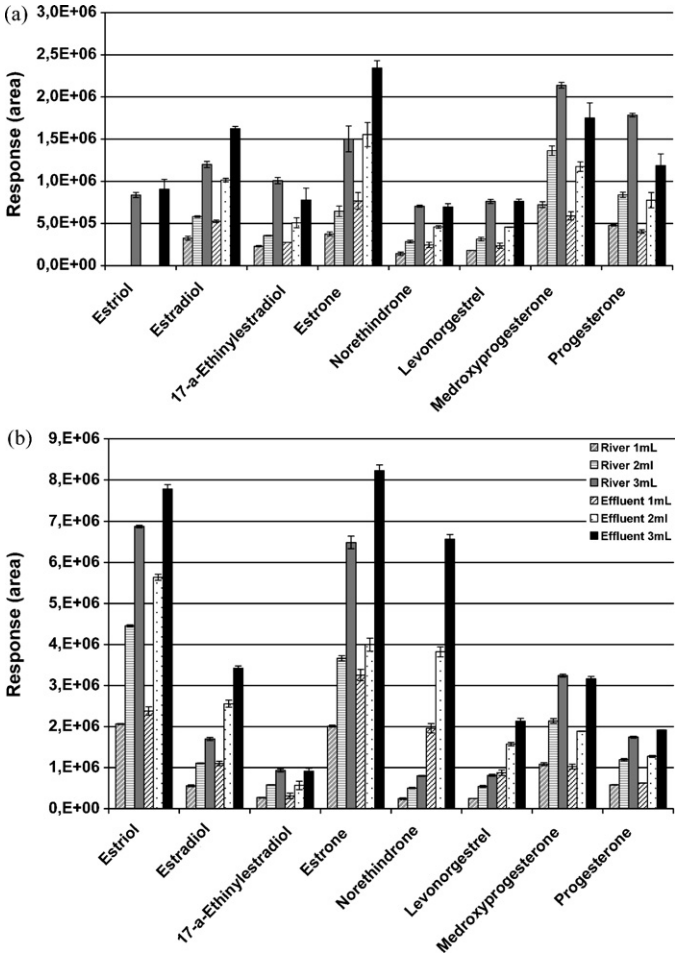

Fig. 6. Injection of three sample volumes (1, 2, and 3 mL) using surface and wastewater samples spiked at: (a) 10 ng/L and (b) 50 ng/L, with target analytes ($n = 4$). Bars represent the mean of quadruplicate measurements and the length of the error bars the standard deviations.

3.6. Method Detection Limit (MDL)

The detection limit of the method (MDL) was also determined. As shown in Table 3, the MDL range varies between 2 and 10 ng/L, except for estriol (50 ng/L) (Table 3).

As mentioned earlier, one of the analytical challenges in quantifying hormones in environmental samples is their very low levels. In our study here, the current online SPE setup allows the injection of a maximum sample volume of 1 mL. Although the objective of this study was to develop a suitable online method for high sam-

Table 3
Validation parameters including linearity (R^2), repeatability, reproducibility, and method detection limit (MDL, ng/L) for volume injections of 1 and 3 mL

Compound	Surface water (Milles Iles River)				
	R^2	Repeatability (%)	Reproducibility (%)	MDL (ng/L)	MDL[a]$_{3mL}$ (ng/L)
Estriol	0.991	5	9	50	25
Estradiol	0.994	3	8	3	0.9
17-Alfa-Ethinylestradiol	0.989	5	11	7	2.7
Estrone	0.985	9	10	10	3.2
Northindrone	0.989	4	8	7	2.7
Levonorgestrel	0.990	2	7	5	1.8
Medroxyprogesterone	0.992	3	4	2	0.6
Progesterone	0.991	6	6	3	1.0

[a] MDL_{3mL}: method detection limit for a volume injection of 3 mL.

Table 4
Occurrence of the selected compounds in surface waters (Mille Iles and St. Lawrence Rivers), raw sewage (north and south collectors) and wastewater treatment plant effluent from the Montreal STP

	River		Montreal STP		
Compound (ng/L)	Mille Iles	St Lawrence	North collector	South collector	Effluent
Estriol	n.d.	n.d.	243 ± 24	230 ± 13	Trace
Estradiol	9 ± 3	8 ± 4	125 ± 4	120 ± 6	90 ± 4
17-α-ethinylestradiol	n.d.	n.d.	75 ± 3	90 ± 4	n.d.
Estrone	n.d.	n.d.	Trace	Trace	n.d.
Norethindrone	n.d.	n.d.	205 ± 3	70 ± 4	53 ± 3
Levonorgestrel	n.d.	n.d.	150 ± 7	170 ± 4	30 ± 6
Medroxyprogesterone	Trace	n.d.	5 ± 3	n.d.	n.d.
Progesterone	3	n.d.	Trace	n.d.	n.d.

n.d. stands for not detected; trace refers to cases where a peak was observed, but it was close to the MDL.

ple throughput in routine analysis with a sample volume fixed at 1 mL, this volume could easily be increased by repeating the loading injections. In this context, three sample volumes (1, 2, and 3 mL) were tested using surface and wastewater samples spiked at 10 and 50 ng/L ($n = 4$). Fig. 6a and b show a linear response of all selected hormone signals to increasing injection volumes, suggesting the possibility of improving the DLs for applications where detection levels are low (i.e. surface or drinking water). Thus, the MDL was also determined for an injection volume of 3 mL, as with the previous procedure. Table 3 presents the MDL for an injection volume of 3 mL. This also confirms that the maximum retention capacity of the loading column was not reached under the proposed setup.

3.6.1. Environmental applications

The proposed method was then applied to the detection of the selected hormones in several water samples. All hormones were detected in the raw sewage of the MUC wastewater treatment plant (North and South sewer collectors), whereas only estradiol, norethindrone, and levonorgestrel were detected in the corresponding effluents at quantifiable concentrations (90 ± 4, 53 ± 3, and 30 ± 6 ng/L) and estriol at trace levels (Table 4). For natural estrogens and progesterone, no differences in composition and concentrations were observed between the two collectors. The highest values were found for estriol and estradiol, with concentrations ranging from 120 ± 6 to 243 ± 24 ng/L (Table 4), while estrone and progesterone were detected at trace levels. Synthetic hormones were present at similar levels in the raw sewage from both collectors, except for norethindrone since concentrations were 205 ± 3 and 70 ± 4 ng/L in the North and South sewage collectors respectively (Table 4). Levonorgestrel levels reached concentrations of up to 100 ng/L, whereas medroxyprogesterone was detected at trace levels and even below our DLs in the South collector (Table 4). Levels found in this study are in agreement with those published by other authors regarding the presence of both natural and synthetic estrogens and progestogens in wastewater treatment plants in Canada in the nanogram per liter range [13,27,50]. Temporal variability of estrogenic compounds in effluents and surface waters has been observed; suggesting that the actual maximum concentrations in the waste water and source waters tested could be higher than those displayed in Table 4 [51]. In addition, other studies have shown that estrone concentrations may be higher than estradiol concentrations, reflecting the oxidation of 17β-estradiol to estrone that may occur during collection and sewage treatment [50,52]. In this study, almost no estrone was detected, either in the raw or the treated wastewater samples. The absence of oxidation of 17β-estradiol to estrone in the collectors probably reflects the relatively short residence time at the plant (<2 h) and the wastewater temperature (~16 °C) which is not conducive to biodegradation. Grab samples were timed to correspond approximately to the peak morning urine flow reaching the wastewater treatment plant. The absence of transformation into estrone by primary treatment is not surprising in the absence of a biological process, minimal solids retention times, and low temperature. However, the observed removals of estriol by the plant exceed those reported usually for primary treatment [50].

According to [53], hormone levels found in the effluent samples are sufficient to induce an estrogenic activity, suggesting a potential concern for the aquatic ecosystem receiving this effluent. The concentrations of the various hormones will depend on consumption rates [8] and transformations rates, which will be compound-specific.

Only estradiol was detected at quantifiable concentrations in both source waters, whereas progesterone and medroxyprogesterone were found at trace levels in the Mille Iles River (Table 4). Estradiol concentrations observed in this study in surface water are of potential concern because they are close to the range where some studies have shown disruption of the sexual characteristics of wild fish populations [54]. For example, at concentrations of ≥1 ng/L, sperm fertility was significantly reduced in male rainbow trout (*Oncorhynchus mykiss*) after an exposure time of 50 days. Also, the exposure of fathead minnows (*Pimephales promelas*) to 0.1 ng/L of estradiol induced vitellogenesis after an exposure time of 3 weeks. This led to a concentration-dependent increase in the mean number of spawned eggs at 0.1–1 ng/L, while at higher concentrations it decreased the number of spawned eggs [55].

4. Conclusion

This proposed method for online SPE and LC combined with the APPI-MS/MS method seems to be suitable for the rapid screening of some natural and synthetic hormones in both surface water and wastewater samples with DLs in the low ng/L range. The low injection volume (1 mL) used in this method makes it easy to automate, and considerably reduces its total run time (15 min., including preconcentration, clean up, elution, and detection). However, this volume could be easily increased to reach the better DLs that might be needed to preclude the adverse endocrine-disrupting effects of many of those hormones, giving the method flexibility. The reproducibility and repeatability of the method are improved by automation, thereby minimizing human errors during sample preparation and transfer.

The relative estrogenicity of synthetic progestagens is not well established [33], but, given that 30 to 50 ng/L of levonogestrel and norethindrone were found in the WWTP effluents, the potential impact of their presence will need to be better evaluated.

Acknowledgments

The authors thank the technical teams of the Industrial Chair on Drinking Water and the MUC Treatment Plant for their assistance

with sample collection. Funding for this study was provided by the Canadian Foundation for Innovation, the NSERC and the NSERC Industrial Chair on Drinking Water at the École Polytechnique de Montréal and its partners (City of Montréal, Ville de Laval and John Meunier Inc.).

References

[1] D. Bila, A.F. Montalvão, D. de, A. Azevedo, M. Dezotti, Chemosphere 69 (2007) 736.
[2] S. Jobling, M. Nolan, C.R. Tyler, G. Brichty, J.-P. Sumpter, Environ. Sci. Technol. 32 (1998) 2498.
[3] E.M. Santos, G.C. Paull, K.J.W. Van Look, V.L. Workman, W.V. Holt, R. van Aerle, P. Kille, C.R. Tyler, Aquat. Toxicol. 3 (2007) 134.
[4] R.J. Williams, A.C. Johnson, J.J.L. Smith, R. Kanda, Environ. Sci. Technol. 37 (2003) 1744.
[5] A. Bouman, M.J. Heineman, M.M. Faas, Hum. Repr. Update 11 (2005) 411.
[6] K.A. Kidd, P.J. Blanchfield, K.H. Mills, V.P. Palace, R.E. Evans, J.M. Lazorchak, R.W. Flick, Proc. Natl. Acad. Sci. 104 (2007) 8897.
[7] D. Koubovec, K. Ronacher, E. Stubsrud, A. Louw, J.P. Hapgood, Mol. Cell. Endocrinol. 242 (2005) 23.
[8] IMS Health Canada, Canadian CompuScript, Montréal, QC, 2007.
[9] A.M. Andersson, N.E. Skakkebaek, Eur. J. Endocrinol. 140 (1999) 477.
[10] J.A. Beardmore, G.C. Mair, R.I. Lewis, Aquaculture 197 (2001) 283.
[11] J.E. Harries, A. Janbakhsh, S. Jobling, P. Matthiessen, J.P. Sumpter, C.R. Tyler, Environ. Toxicol. Chem. 18 (1999) 932.
[12] K.M. Nichols, S.R. Miles-Richardson, E.M. Snyder, J.P. Giesy, Environ. Toxicol. Chem. 18 (1999) 2001.
[13] M.P. Fernandez, M.G. Ikonomou, I. Buchanan, Sci. Total Environ. 373 (2007) 250.
[14] H. Noppe, T. Verslycke, E. De Wulf, K. Verheyden, E. Monteyne, P. Van Caeter, C.R. Janssen, H.F. De Brabander, Ecotox. Environ. Saf. 66 (2007) 1.
[15] A.D. Vethaak, J. Lahr, S.M. Schrap, A.C. Belfroid, G.B.J. Rijs, A. Gerritsen, et al., Chemosphere 59 (2005) 511.
[16] A. Joss, E. Keller, A.C. Alder, A. Göbel, C.S. McArdell, T. Ternes, H. Siegrist, Water Res. 39 (2005) 3139.
[17] L.S. Shore, M. Shemesh, Pure Appl. Chem. 75 (2003) 1859.
[18] J.E. Drewes, L.S. Shore, in: C.G. Daughton, T. Jones-Lepp (Eds.), Pharmaceuticals and Personal care Products in the Environment: Scientific and Regulatory Issues, Symposium Series 791, American Chemical Society, Washington, DC, 2001.
[19] D.W. Kolpin, E.T. Furlong, M.T. Meyer, E.M. Thurman, S.D. Zaugg, L.B. Barber, H.T. Buxton, Environ. Sci. Technol. 36 (2002) 1202.
[20] C.G. Daughton, T.A. Ternes, Environ. Health Perspect. 107 (1999) 907.
[21] P.-D. Hansen, H. Dizer, B. Hock, A. Marx, J. Sherry, M. McMaster, C. Blaise, Trends Anal. Chem. 17 (1998) 448.
[22] M.J. Giorgino, R.B. Rasmussen, C.M. Pfeifle, Geological Survey Scientific Investigations Report 2007-5054, 28 p., available at http://pubs.water.usgs.gov/sir2007-5054.
[23] C.E. Purdom, P.A. Hardiman, V.V.J. Bye, N.C. Eno, C.R. Tyler, J.P. Sumpter, Chem. Ecol. 8 (1994) 275.
[24] S.A. Snyder, P. Westerhoff, Y.P. Yoon, D.L.Y. Sedlak, Environ. Eng. Sci. 5 (2003) 449.
[25] G.F. Warren, Can. J. Public Health 89 (1998) 41.
[26] M.S. Díaz-Cruz, M.J.L. de Alda, R. López, D. Barceló, J. Mass Spectrom. 38 (2003) 917.
[27] F. Hernández, J.V. Sancho, O. Pozo, A. Lara, E. Pitarch, J. Chromatogr. A 939 (2001) 1.
[28] J.M. Marín, J.V. Sancho, O.J. Pozo, F.J. López, F. Hernández, J. Chromatogr. A 1133 (2006) 204.
[29] M.J. López de Alda, D. Barceló, J. Chromatogr. A 911 (2001) 203.
[30] S. Rodriguez-Mozaz, M.J. Lopez de Alda, D. Barceló, Anal. Chem. 76 (2004) 6998.
[31] A. Salvador, C. Moretton, A. Piram, R. Faure, J. Chromatogr. A 1145 (2007) 102.
[32] J.A. Glaser, D.L. Foerst, G.D. McKee, S. Quave, W.L. Budde, Environ. Sci. Technol. 15 (1981) 1426.
[33] T. Reemtsa, Trends Anal. Chem. 20 (2001) 533.
[34] Communauté urbaine de Montréal, Treatment Process: Wastewater Treatment Plant, 1999, http://services.ville.montreal.qc.ca/station/an/pdf/process.pdf.
[35] J.P. Antignac, K. de Wasch, F. Monteau, H. de Brabander, F. Andre, B. le Bizec, Anal. Chim. Acta 529 (2005) 129.
[36] J.F. Alary, Proceedings of the 49th ASMS Conference on Mass Spectrometry and Allied Topics, American Society for Mass Spectrometry, Chicago, Ill, 2001 (book on CD-ROM).
[37] M. Takino, S. Daishima, T. Nakahara, Rapid Commun. Mass Spectrom. 17 (2003) 1965.
[38] A. Yamoto, N. Kakutani, K. Yamamoto, T. Kamiura, H. Miyakoda, Environ. Sci. Technol. 40 (2006) 4132.
[39] H.B. Theron, C. Coetzee, F.C.W. Sutherland, J.L. Wiesner, K.J. Swart, J. Chromatogr. B 813 (2004) 331.
[40] M.P. Schlüsener, K. Bester, Rapid Commun. Mass Spectrom. 19 (2005) 3269.
[41] L.Y.T. Li, D.A. Campbell, P.K. Bennett, J.D. Henion, Anal. Chem. 68 (1996) 3397.
[42] D. Barceló, M.-C. Hennion, Trace Determination of Pesticides and their Degradation Products in Water, Techniques and Instrumentation in Analytical Chemistry, vol. 19, Elsevier, Amsterdam, 1997, pp. 357–423 (Chapter 5).
[43] K. Stoob, H.P. Singer, C.W. Goetz, M. Ruff, S.R. Mueller, J. Chromatogr. A 1097 (2005) 138.
[44] P.H. Roberts, P. Bersuder, J. Chromatogr. A 1134 (2006) 143.
[45] E.A. Hogendoorn, E. Dijkman, B. Baumann, C. Hidalgo, J.V. Sancho, F. Hernandez, Anal. Chem. 71 (1999) 1111.
[46] J. Bones, K. Thomas, P.N. Nesterenko, B. Paull, Talanta 70 (2006) 1117.
[47] K.A. Hanold, S.M. Fisher, P.H. Cormia, C.E. Miller, J.A. Syage, Anal. Chem. 76 (2004) 2842.
[48] L.C. Short, S.-S. Cai, J.A. Syage, J. Am. Soc. Mass Spectrom. 18 (2007) 589.
[49] D.L. Buhrman, P.I. Price, P.J. Rudewicz, J. Am. Soc. Mass Spectrom. 7 (1996) 1099.
[50] M.R. Servos, D.T. Bennie, B.K. Burnison, A. Jurkovic, R. McInnis, T. Neheli, A. Schnell, P. Seto, S.A. Smyth, T.A. Ternes, Sci. Total Environ. 336 (2005) 155–170, ISSN: 0048–9697.
[51] T.P. Rodgers-Gray, S. Jobling, S. Morris, C. Kelly, S. Kirby, A. Janbakhsh, et al., Environ. Sci. Technol. 34 (2000) 1521.
[52] T.A. Ternes, J. Kreckel, J. Mueller, Sci. Total Environ. 225 (1999) 91.
[53] L. Salste, P. Leskinen, M. Virta, L. Kronberg, Sci. Total Environ. 378 (2007) 343.
[54] F. Lahnsteiner, B. Berger, M. Kletzl, T. Weismann, Aquat. Toxicol. 79 (2006) 124.
[55] S. Jobling, D. Casey, T. Rodgers-Gray, J. Oehlmann, U. Schulte-Oehlmann, S. Pawlowski, T. Baunbeck, A.P. Turner, C.R. Tyler, Aquat. Toxicol. 65 (2003) 205.

Talanta 76 (2008) 1218–1223

Contents lists available at ScienceDirect

Talanta

journal homepage: www.elsevier.com/locate/talanta

Adjusting mobility scales of ion mobility spectrometers using 2, 6-D*t*BP as a reference compound

A.-K. Viitanen[a,*], T. Mauriala[b], T. Mattila[c], A. Adamov[b,d], C.S. Pedersen[e], J.M. Mäkelä[a], M. Marjamäki[a], A. Sysoev[f], J. Keskinen[a], T. Kotiaho[b,d]

[a] *Aerosol Physics Laboratory, Department of Physics, Tampere University of Technology, P.O. Box 692, FI-33101 Tampere, Finland*
[b] *Laboratory of Analytical Chemistry, Department of Chemistry, University of Helsinki, P.O. Box 55, FI-00014 University of Helsinki, Finland*
[c] *Environics Oy, P.O. Box 1199, FI-70211 Kuopio, Finland*
[d] *Division of Pharmaceutical Chemistry, Faculty of Pharmacy, University of Helsinki, P.O. Box 56, FI-00014 University of Helsinki, Finland*
[e] *Department of Chemistry, University of Copenhagen, Universitetsparken 5, DK-2100 Copenhagen Ø, Denmark*
[f] *Moscow Engineering Physics Institute (State University), Kashirskoe sh. 31, 115409 Moscow, Russia*

ARTICLE INFO

Article history:
Received 8 January 2008
Received in revised form 16 May 2008
Accepted 21 May 2008
Available online 29 May 2008

Keywords:
IMS
Time-of-flight
2,6-D*t*BP
Reference compound
Instrument comparison

ABSTRACT

Performance of several time-of-flight (TOF) type ion mobility spectrometers (IMS) was compared in a joint measurement campaign and their mobility scales were adjusted based on the measurements. A standard reference compound 2,6-di-*tert* butylpyridine (2,6-D*t*BP) was used to create a single peak ion mobility distribution with a known mobility value. The effective length of the drift tube of each device, considered here as an instrument constant, was determined based on the measurements. Sequentially, two multi-peaked test compounds, DMMP and DIMP, were used to verify the performance of the adjustment procedure in a wider mobility scale. By determining the effective drift tube lengths using 2,6-D*t*BP, agreement between the devices was achieved. The determination of effective drift tube lengths according to standard reference compound was found to be a good method for instrument inter-comparison. The comparison procedure, its benefits and shortcomings as well as dependency on accuracy of literature value are discussed along with the results.

1. Introduction

Ion mobility spectrometry (IMS) is a rapid analytical technique to detect and identify gas phase compounds [1]. IMS was developed in 1970s [2] and since then, the most widespread applications based on ion mobility have been the chemical warfare detectors and airport security [1,3]. A number of other applications have been published, e.g. from the field of atmospheric studies [4,5], environmental analysis [6] and health care [7]. The IMS-device construction can be divided into two major categories. Aspiration condensers [8–11] sample the ions and separate them by mobility in an electric field perpendicular to the gas flow, by practical configuration of electrometer strips or sampling slits on the side wall of the mobility analyzer. Usually a term DMA (differential mobility analyzer) is used in this context (e.g. [12–14]). However, most of the instruments rely on the time-of-flight (TOF) method [1–7,15,16].

In the TOF-method the drift time of an ion swarm under influence of weak electric field is measured and the mobility of an ion can be determined according to

$$K = \frac{l}{E t_d}, \quad (1)$$

where K is the electrical mobility of an ion, E is the electric field, l is the length of the drift region and t_d is the drift time of the ion. The mobility K is commonly normalized to standard conditions to facilitate comparison between different measurements according to

$$K_0 = K \frac{T_0}{T} \frac{p}{p_0}, \quad (2)$$

where T is the gas temperature and p is the pressure.

Normalization of the mobility value removes the effect of pressure and reduces the effect of temperature on the ion mobility. The normalization procedure, however, does not remove the effect of cluster formation nor does it remove the effects of internal parameters such as changes in the drift tube length caused by heat expansion, or inhomogeneities of the electric field [15,16]. Conditions, for one, affect on the nature of ions and hence the

* Corresponding author. Tel.: +358 3 31152133; fax: +358 3 31152600.
E-mail address: anna-kaisa.viitanen@tut.fi (A.-K. Viitanen).

0039-9140/$ – see front matter © 2008 Elsevier B.V. All rights reserved.
doi:10.1016/j.talanta.2008.05.030

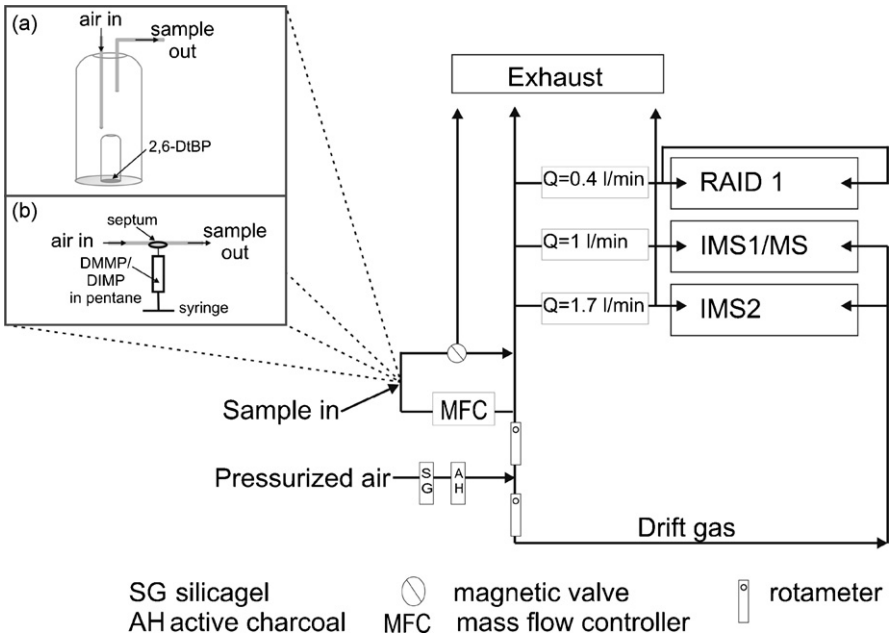

Fig. 1. The measurement setup. Sample introduction is implemented using either diffusion method (a) or injection method (b).

ion mobility. With decreasing temperature larger clusters are being formed (e.g. [17,18]). The degree of hydration depends on temperature and prevailing moisture concentration (e.g. [17]). Furthermore there are other kinds of defects that arise from real effects in the non-ideal instruments, e.g. diffusion of the ions in the drift chamber and electronic response time of the detector, which usually tend to skew the instrument function and lower the instrument resolution. One fundamental issue is the determination of the zero point of the time-of-flight discussed by Spangler [19].

Instrument testing, comparison measurements, etc. require an efficient method to be utilized to obtain reliable results on the performance of the device. In IMS, either internal or external references can be used. In the case of an internal reference, a known gaseous compound, forming well-defined ions, is injected together with the sample ions. External reference, on the contrary, is measured independently. Sample introduction in IMS applications can be implemented by ionizing evaporated compounds or using electrospray. Electrospray technique is used, e.g. in the case of non-volatile compounds such as tetraheptyl ammonium bromide (THABr) [12] and other tetra-alkyl halides [12,20], PAMAM-dendrimers [21] or large protein molecules [22]. The technique utilizing non-volatile liquid compounds in an ESI-source is actually widely used for aspiration type of IMS-instruments, reaching down to mobility values such as 0.1 cm^2/Vs, or even 0.01 cm^2/Vs, but non-volatile compounds from electrospray may also be analyzed in the high mobility range of 1.0–2.5 cm^2/Vs, conventionally covered in gas phase IMS studies (e.g. [20]).

All in all, a good reference compound, resulting in known ions either from an ionized gaseous compound or from an ESI-unit, should satisfy a variety of properties such as minor dependency on temperature and humidity, minor tendency to form clusters and strong ion signal close to the mobility values of the compounds of interest [15,23]. Compared to other IMS techniques, due to good resolution of TOF the spectrum formed by the reference peak can be verified with high accuracy. For commercial IMS-devices based on time-of-flight technique the resolving power is in the scale of 20–60 [24]. However, even higher values have been obtained with custom-made devices (e.g. [25]).

Some of the chemicals suggested as standards for positive ion mode ion mobility spectrometry were reviewed by Eiceman et al. [15], who concluded the 2,6-di-*tert* butylpyridine (2,6-D*t*BP) to be the best candidate, and, instead of using Eqs. (1) and (2) to determine the reduced mobility, they calculated the mobility values with the help of reference compound based only on time-of-flight of a compound under interest according to

$$\frac{K(\text{unknown})}{K(\text{standard})} = \frac{K_0(\text{unknown})}{K_0(\text{standard})} = \frac{t_d(\text{standard})}{t_d(\text{unknown})} \quad (3)$$

As a parallel method for the use of Eq. (3) in instrument comparison, the reference compound can also be used to adjust the mobility scale of the test instrument by determining a crucial parameter for it, such as 'effective drift tube length' or some another related quantity.

The aim of this study is to explore a suitable procedure to adjust the mobility scales and to perform inter-comparison between different IMS-devices. For this a standard reference compound 2,6-di-*tert* butylpyridine discussed earlier is used. This gaseous compound is assumed to produce well defined ions with known reduced mobility value of 1.42 cm^2/Vs, which is an estimation from the Fig. 4 in Eiceman et al. [15]. To further test the different procedures in inter-comparison of different devices, two different compounds, dimethylmethylphosphonate (DMMP) and di-iso-propyl methyl phosphonate (DIMP) are chosen as test compounds. The chosen compounds provide relatively wide coverage of mobilities.

2. Experimental

2.1. Chemicals and sample introduction

Chemicals used in this study were 2,6-di-*tert* butylpyridine (Sigma–Aldrich, Steinheim, Germany), dimethylmethylphosphonate (Fluka, Switzerland) and di-iso-propyl methyl phosphonate (Alfa-Aesar Johnson Matthey Company, Germany). Pentane (Labscan, Ireland) was used for dilution.

The diffusion tube method was used for 2,6-D*t*BP and the injection method for DMMP and DIMP. In the diffusion tube method a

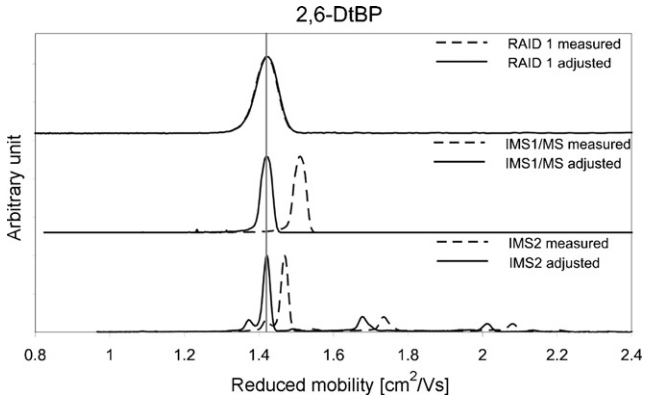

Fig. 2. Reduced mobility spectra of 2,6-D*t*BP for all three instruments in the comparison, derived by the nominal tube length (dashed line) and by the effective drift tube length (solid line). In the case of RAID 1 the effective drift tube length given by the manufacturer is used as a nominal drift tube length. The literature value for 2,6-D*t*BP (1.42 cm^2/Vs) is marked with gray vertical line. The *y*-axis is normalized to highest signal value.

small amount of liquid sample compound was placed into a container. This container was placed into a gas washing bottle. When the sample flow was guided through the gas washing bottle, a steady concentration was achieved. In the injection method, the glass syringe was filled with the liquid phase sample. The sample was then injected through a septum into the sample flow. In cases of DMMP and DIMP the dilution of 0.1% in pentane was used and the injection was performed using 100 μl syringe (Hamilton Bonaduz AG, Switzerland) operated with syringe pump (Cole-Parmer Instrument Company, Vernon Hills, USA). The sample introduction methods are illustrated in Fig. 1. The concentration was adjusted so that both protonated monomer and proton bound dimer peaks were possible to identify from the measurement spectra, and kept constant through out the measurements.

2.2. Ion mobility spectrometers

For the measurements, three different IMS-devices all based on time-of-flight method were used. One of the devices was a commercial ion mobility spectrometer (RAID 1, Brüker Daltonics GmbH) and two were custom-made IMS-devices, available at University of Helsinki, developed in cooperation with Moscow Engineering Physics Institute (State University). The first one of those (IMS1/MS), was mounted in front of a commercial API 300 triple quadrupole mass spectrometer (Sciex Applied Biosystems, Canada). Mass spectrometer was operated in selected ion monitoring (SIM) mode (*m*/*z* 192 for 2,6-D*t*BP, *m*/*z* 125 and 249 for DMMP, *m*/*z* 181 and 361 for DIMP). The voltages in IMS1/MS were supplied by self-made power source which was connected to the PC through a serial COM port. The IMS1/MS instrument has been described with details by Sysoev et al. [26]. The second device, an identical ion mobility spectrometer (IMS2) equipped with Faraday cup detector operated as a stand-alone unit. The resolving power of the RAID 1 was in the range of 20–30, while for the custom-made instruments (IMS1/MS and IMS2) it was in the range of 50–70 for all compounds measured in this study.

For data acquisition of RAID 1 a Brüker IMS NT 3.0 software was used. A spectrum was obtained every 5 s after accumulation of four individual spectra (approximately 30 ms each). In data processing a median of six sequential spectra was formed to produce a final spectrum to be used in results. The IMS1/MS was operated in a dual-gate mode [26]. Delay time was scanned in 50 μs increments with the dwell time of 1 s. Maximum separation time was 50 ms. Gate opening times for both gates were 0.3 ms. The data was collected by Analyst 1.4.2 software (Sciex Applied Biosystems, Canada) and

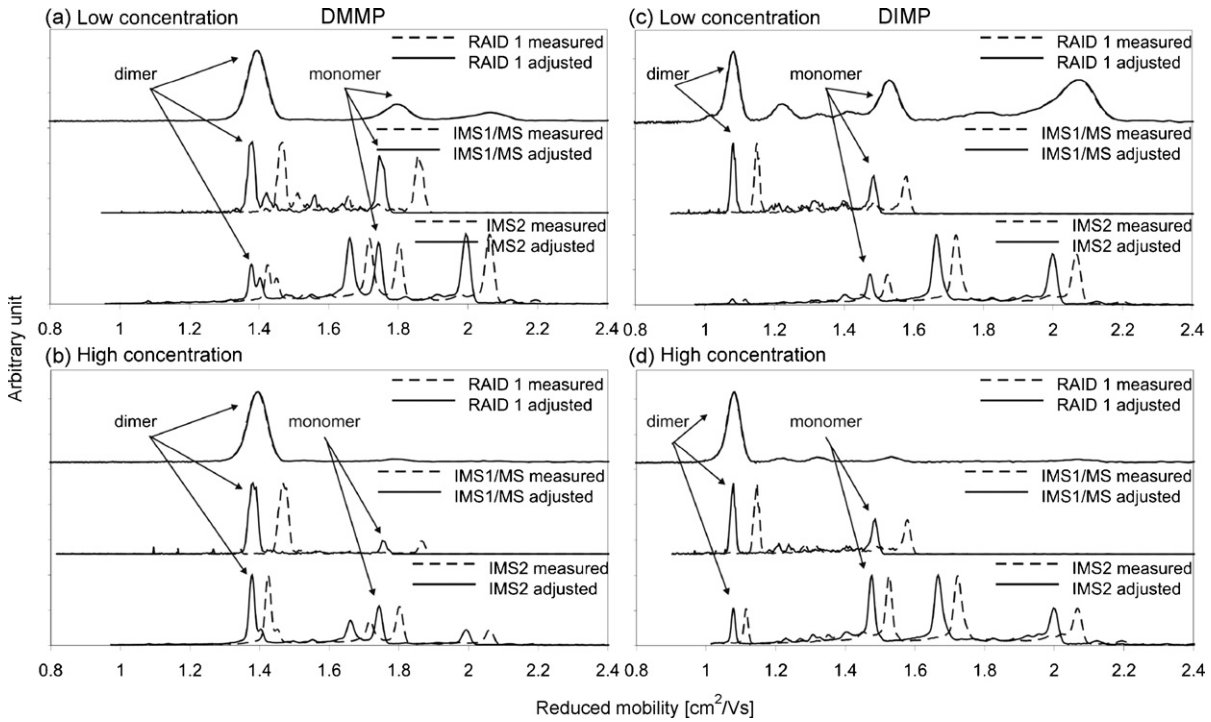

Fig. 3. Mobility spectra of DMMP (a–b) and DIMP (c–d). Measurements with low vapor concentration above and with high vapor concentration below. Mobility distributions have been calculated using the nominal drift tube length (dashed lines) and the effective drift tube length corresponding to the reference value 1.42 cm^2/Vs for 2,6-D*t*BP (solid lines). In the case of RAID 1 the effective drift tube length given by the manufacturer is used as a nominal drift tube length. The *y*-axis is normalized to highest signal value.

Table 1
Operation parameters of RAID 1, IMS1/MS and IMS2 during the measurements

	RAID 1	IMS1/MS	IMS2
Drift gas	Air	Air	Air
Gas flow	0.4 l/min	1 l/min	1.7 l/min
Pressure	Ambient	Ambient	Ambient
Ionization method	^{63}Ni (15 mCi)	Corona	Corona
Drift voltage	1465.4 V	3508 V	3517 V
Drift tube length	5.76 cm[a]	13.3 cm	13.85 cm
Electric field	254 V/cm	264 V/cm	254 V/cm
Pulse width	0.3 ms	0.3 ms	0.3 ms

[a] Effective drift tube length given by the manufacturer.

treated in MS Excel. The IMS1 was controlled by self-made software designed in LabVIEW (National Instruments, Austin, US). The IMS2 was operated in single gate mode [25]. The first gate opening time was 0.3 ms. The second ion gate was kept open at all times. Mobility distributions were recorded for 50 ms with repetition rate of 20 Hz. A 2000 transients were combined to obtain the analytical signal. With the IMS2 data collection and treatment was done using a self-made LabVIEW program. The operation parameters of the devices are listed in the Table 1.

2.3. Measurement setup

The measurement setup is presented in Fig. 1. In order to exclude all the external parameters possibly effecting on the measurements and the actual comparison of the devices, the measurements were performed in a joint campaign at a same laboratory. To synchronize the operating conditions, all the devices sampled from the same gas line simultaneously. The electric field strength of all three devices was adjusted to be close to each other. Ion pulse width of 0.3 ms was used in every device. The measurements were carried out in open cell conditions thus, the membrane normally used in the sample introduction system of RAID 1, was removed. In order to allow close electric fields in all three TOF-instruments, both IMS1/MS and IMS2 operated at reduced drift voltages (3508 V for IMS1/MS, and 3517 V for IMS2 instead normal operating drift voltage of 5040 V), though decrease of drift voltage resulted on significant decrease of resolving power reaching 100 at normal operation conditions for both instruments.

Purified and dried (RH <1%) pressurized air was used as a carrier and drift gas. The carrier gas was divided into a sample and dilution flows. Gas flows were controlled with mass flow controller (Teledyne Hastings Instruments, Hampton, US) and rotameters (Kytölä Instruments, Muurame, Finland). Teflon tubing was used to connect the parts.

The instruments were not heated. The laboratory room was air conditioned, so that the temperature during measurements was constant ~25 °C. This temperature was used when calculating reduced mobilities for IMS1/MS and IMS2. Both of these devices are constructed so that the electronics will not heat up the drift tube substantially. Additionally, during the measurements, the temperature of in- and outgoing gas lines were measured and verified to be in line with the room temperature. For RAID 1, temperature was controlled using internal thermo sensor inside the drift tube wall.

Pressure was monitored at the SMEAR III station of University of Helsinki, 51 m above sea level. The pressure varied between 1001 and 1012 mbar during the measurements. Pressure values used in calculations were obtained by determining the mean pressure value from the time period of the measurements. This value was used for calculating the reduced mobility of IMS1/MS and IMS2 measurements. For RAID 1 a pressure value measured by the device automatically was used.

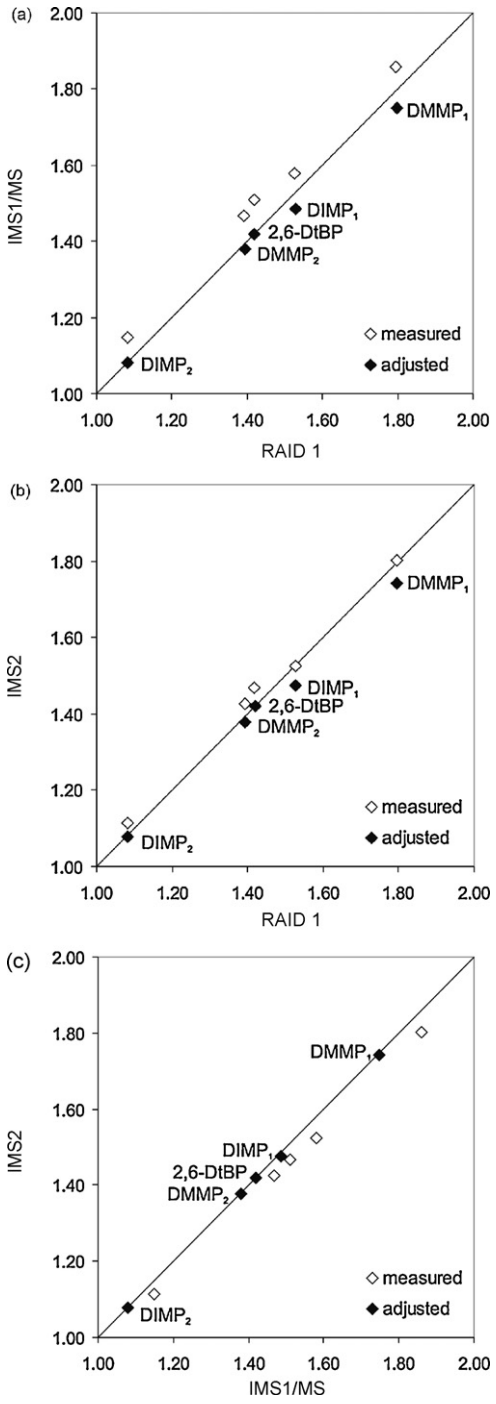

Fig. 4. (a–c) Comparisons of measured and adjusted mobility values of 2,6-D*t*BP, DMMP and DIMP measured by each instrument pair (a) RAID 1-IMS1/MS; (b) RAID 1-IMS2; (c) IMS1/MS-IMS2. White diamonds have been derived using nominal values for drift tube length and the black diamonds have been obtained using effective tube length that corresponds the 2,6-D*t*BP mobility 1.42 cm^2/Vs.

3. Results and discussion

In principle, the reduced mobility values for this study could be calculated using three different procedures. In traditional method, a reduced mobility value for each compound is calculated from the original measured value using Eqs. (1) and (2) and physical parameters for each instrument, listed in Table 1. This procedure will give a straightforward result for the ion mobilities measured. In the second procedure, suggested by Eiceman et al. [15], Eq. (3) is used.

There, the mobility value for a reference compound is used to obtain mobilites for the test compounds, and only the drift times of the reference and the test compounds in the same conditions are needed. This method gives straightforward values for reduced mobilities but does not provide any additional information about the actual instrument. The third method is to use also the known reduced mobility value for a reference compound, but tune the instrument parameters such as those presented in Table 1 according to that. In practice, this method assumes that some of the values in Table 1 may not actually be the real effective parameters of the device, but rather parameters based on the physical construction of the device. For instance, the electric field may not be fully homogeneous throughout the whole drift tube, and so the field strength derived from measured voltage and measured drift tube length, may not give a fully correct result. Therefore it is more practical to come up with an 'effective' value either for the field strength or the drift tube length. A feasible value for drift tube length is needed, e.g. in aerosol measurements, where the mobility distribution is derived from time-of-flight spectrum by help of instrument functions (e.g. [14]).

Here, the effective drift tube length to be used as an instrument constant of each device is determined. First, the actual mobility value in measurement conditions is calculated and reduced to normal conditions according to Eqs. (1) and (2). This reduced mobility is then compared with the literature value thus, the effective drift tube length can be determined. Then, the effective drift tube length is used as a solid parameter to derive the mobilities for the test compound ions. From this analysis we obtain both an effective drift tube length for each instrument in the inter-comparison, plus the mobility values for the test compounds. This method is dependent only on the value used as a reduced mobility of the reference compound and therefore it should be known with great accuracy. Here, the reduced mobility of 2,6-D*t*BP (1.42 cm^2/Vs) given by Eiceman et al. [15] is used. The derived effective drift tube length values for RAID 1, IMS1/MS and IMS2 are 5.764, 12.900 and 13.621 cm, respectively. In the case of commercial RAID 1, though, one should recognize that the value for the drift tube length in Table 1 is the one given by the manufacturer. The actual physical drift tube length of RAID 1 was not available.

In Fig. 2 in addition to the actual measured mobility distributions, also the adjusted distributions are shown as solid lines. Thus, Fig. 2 illustrates the shifting of the mobility distribution when the nominal drift tube length is replaced with effective drift tube length in case of reference compound 2,6-di-*tert* butylpyridine. For RAID 1 these two distributions are in practice the same, while the calibration had to be made based on the effective drift tube length given by the manufacturer instead of actual physical length of the drift tube. In the case of IMS1/MS and IMS2 the results of the calibration is more clearly seen. The further measurement spectra of the test compounds are shown in Fig. 3(a–d). From the measurement results it can be seen, how adjustment procedure works in practice. The reduced mobility of the proton bound dimer peaks for both test compounds were in extremely good agreement between all the three devices after the adjustment. The peak formed by protonated monomers, however, showed some variation between the devices.

The final comparisons of the reduced mobility values for the test compounds, obtained by each instrument using their effective drift tube lengths, are shown in Fig. 4(a–c). These figures illustrate that consistence between the instruments can be achieved when the adjustment procedure is used. When RAID 1 is compared to IMS1/MS and IMS2, indeed the strongest variation in mobility is seen for protonated monomers of the test compounds used here (DMMP and DIMP). But as we compare IMS1/MS and IMS2, variation in the protonated monomer values is no longer noticeable. Thus, by adjusting the length of the drift tubes consistency between IMS1/MS and IMS2 were achieved through out the measurement range. In Table 2 the reduced mobility values achieved after adjustment procedure are compared with both the reduced mobility values obtained using Eq. (3) and also with some literature values. When calculating the reduced mobility values using Eq. (3), we have used 2,6-D*t*BP as a standard mobility (1.42 cm^2/Vs) and corresponding drift times of each instrument as a standard drift times. Values obtained based on effective drift tube length correspond naturally to ones obtained using the method suggested by Eiceman et al. (Eq. (3)). Comparison of mobility values consist always some factors of uncertainties and hence literature values should be considered as indicative values. Here, the literature values seem to correspond to the measured values after adjustment within acceptable variation.

Close examination of the spectral characteristics reveal some differences between the devices. For one, the reaction ion peak is slightly faster for RAID 1 than for IMS2, and the overall shape of the spectra produced by the test compounds DMMP and DIMP have minor differences. Also the reduced mobility values differ slightly between the devices, especially in the case of protonated monomers. The actual reduced mobility of the protonated monomer of DMMP is dependent on water vapor concentration [15,27]. Thus, the most probable cause for the different mobility values for the protonated monomers is different humidity inside the drift tubes. Other minor differences in the reduced mobilities and in the spectral characteristics are most probably caused by different construction of the devices, minor internal contaminations, and due to the fact that different ionization techniques [28,29] can give slightly different reduced mobility values.

The most sensitive parameter in this calibration method is the value used for the reference compound, in this case for 2,6-D*t*BP. At present, only one literature value by Eiceman et al. [15] is available. 2,6-D*t*BP is shown to have a minor temperature dependency in the scale of −10 to 250 °C [15,18]. This is

Table 2
Reduced mobility values obtained in this study using effective drift tube length and Eiceman et al. [15] methods, and also corresponding literature values in cm^2/Vs

2,6-D*t*BP	$DMMP_1$	$DMMP_2$	$DIMP_1$	$DIMP_2$	Reference
1.42	1.74–1.80	1.38–1.39	1.48–1.53	1.08	This study, effective drift tube length method[a]
1.42	1.76–1.80	1.39	1.49–1.53	1.08–1.09	This study, Eiceman et al. [15] method (Eq. (3))
1.42	1.80	1.39			[15] ~95 °C (2,6-D*t*BP and $DMMP_2$), ~37 °C ($DMMP_1$), air, moisture 2.9 mg/m^3, values are estimations from graphical data
		1.42		1.09	[30] 100 °C, air
	1.82	1.45	1.54–1.55	1.13	[31] Parameters not reported
	1.63–1.81	1.42			[27] Room temperature, air, water vapor concentration 6 ppm, 5×10^2 ppm and 2×10^2 ppm, values are estimations from graphical data

Subscripts 1 and 2 refer to protonated monomer and proton bound dimer, respectively.

[a] The reduced mobility values have been obtained by determining the reduced mobility corresponding to maximum intensity value. When it was possible to detect the mobility peak from the spectra with low and high concentrations, the mobility value shown here is the average from these two.

in good agreement with experiments showing a high entropy change with hydration or dimerisation of 2,6-D*t*BP, due to the loss of rotational freedom of both the water molecule and the *tert*-butyl groups [32]. However, experimental ion mobility data on humidity behavior is not that well reported. Also measurement data with other carrier gases than air are lacking at present. Based on this study, 2,6-D*t*BP is well suited for reference compound in order to adjust the mobility scales. Before reaching the general approved status as an ion mobility reference compound, more measurement data and studies on 2,6-D*t*BP are needed in addition only to IMS methods based on time-of-flight technique.

4. Conclusion

The mobility scales of three different IMS-devices, all based on time-of-flight technique, have been adjusted. The data required for the adjustment, was obtained in a joint measurement campaign. By equalizing the operational parameters, a comparable measurement setup was successfully created. The use of 2,6-D*t*BP as a standard compound enabled us to compare the devices by readjusting the mobility scale. 2,6-D*t*BP was well suited to a reference compound in our experience. By using DMMP and DIMP as a test compounds wider range in mobility scale was investigated, which confirmed the agreement between the instruments. The reduced mobility values also corresponded to the values available in the literature.

Adjustment of the mobility scale is seen as an effective method when comparing different IMS-devices. Naturally, different conditions can still generate difference between the mobility distributions. Thus, the effect of conditions must be recognized. Based on this study, the use of 2,6-D*t*BP as a standard reference compound for IMS applications suggested by Eiceman et al. [15] is supported. For instrument comparison the determination of effective drift tube lengths using 2,6-D*t*BP as a reference compound is suggested. The obtained value can be then verified by measurements of other known compounds.

Acknowledgements

This study was supported by the Finnish Funding Agency for Technology and Innovation (Tekes), Environics Ltd., Orion Pharma, Paavo Ristola Consulting Engineers Ltd., and the National Bureau of Investigation (Finland) and the HERC project “Urban and rural air pollution—response of ecosystem and society (URPO)”. The authors would also like to acknowledge Finnish Defense Forces and Industrial Research Fund at Tampere University of Technology for funding. Dr. Marjamäki was supported by the Academy of Finland, project 109124. Division of Atmospheric Sciences of University of Helsinki is acknowledged for the pressure data.

References

[1] G.A. Eiceman, Z. Karpas, Ion Mobility Spectrometry, second ed., CRC Press, Boca Raton, 2005.
[2] M.J. Cohen, F.W. Karasek, J. Chromatogr. Sci. 8 (1970) 330.
[3] J.I. Baumbach, G.A. Eiceman, Appl. Spectrosc. 53 (1999) 338A.
[4] K. Nagato, C.S. Kim, M. Adachi, K. Okuyama, J. Aerosol. Sci. 36 (2005) 1036.
[5] K. Nagato, D.J. Tanner, H.R. Friedli, F.L. Eisele, J. Geophys. Res. 104 (1999) 3471.
[6] L. Myles, T.P. Meyers, L. Robinson, Atmos. Environ. 40 (2006) 5745.
[7] J.I. Baumbach, M. Westhoff, Spectrosc. Europe 18 (2006) 22.
[8] J. Zeleny, Phys. Rev. 34 (1929) 310.
[9] H.F. Tammet, The Aspiration Method for the Determination of Atmospheric-Ion Spectra, Translated from Russian, Published for the National Science Foundation, Washington, D.C. by the Israel Program for Scientific Translations, Jerusalem, 1970.
[10] M. Zhang, A.S. Wexler, Int. J. Mass Spectrom. 258 (2006) 13.
[11] S. Zimmermann, N. Abel, W. Baether, S. Barth, Sens. Actuators, B 125 (2007) 428.
[12] S. Ude, J.F. de la Mora, J. Aerosol. Sci. 36 (2005) 1224.
[13] T. Seto, K. Okuyama, L. de Juan, J.F. de la Mora, J. Chem. Phys. 107 (1997) 1576.
[14] J.M. Mäkelä, V. Jokinen, T. Mattila, A. Ukkonen, J. Keskinen, J. Aerosol. Sci. 27 (1996) 175.
[15] G.A. Eiceman, E.G. Nazarov, J.A. Stone, Anal. Chim. Acta 493 (2003) 185.
[16] G.A. Eiceman, E.G. Nazarov, J.E. Rodriguez, J.A. Stone, Rev. Sci. Instrum. 72 (2001) 3610.
[17] R.G. Ewing, G.A. Eiceman, J.A. Stone, Int. J. Mass Spectrom. 193 (1999) 57.
[18] A.-K. Viitanen, T. Mattila, J.M. Mäkelä, M. Marjamäki, O. Anttalainen, J. Keskinen, Atmospheric Research (2008), doi:10.1016/j.atmos.res.2007.12.003.
[19] G.E. Spangler, Anal. Chem. 65 (1993) 3010.
[20] J. Viidanoja, A. Sysoev, A. Adamov, T. Kotiaho, Rapid Commun. Mass Spectrom. 19 (2005) 3051.
[21] M. Imanaka, Y. Okada, K. Ehara, K. Takeuchi, J. Aerosol. Sci. 37 (2006) 1643.
[22] S.L. Kaufman, J.W. Skogen, F.D. Dorman, F. Zarrin, Anal. Chem. 68 (1996) 1895.
[23] Z. Karpas, Anal. Chem. 61 (1989) 684.
[24] K. Cottingham, Anal. Chem. 75 (2003) 435A.
[25] J. Laakia, T. Mauriala, A. Adamov, J. Viidanoja, V. Teplov, R.A. Ketola, R. Kostianen, A. Sysoev, T. Kotiaho, ISIMS2007, Mikkeli, Finland (2007).
[26] A. Sysoev, A. Adamov, J. Viidanoja, R.A. Ketola, R. Kostiainen, T. Kotiaho, Rapid Commun. Mass Spectrom. 18 (2004) 3131.
[27] R.G. Ewing, G.A. Eiceman, C.S. Harden, J.A. Stone, Int. J. Mass Spectrom. 255–256 (2006) 76.
[28] H. Borsdorf, E.G. Nazarov, G.A. Eiceman, J. Am. Soc. Mass Spectrom. 13 (2002) 1078.
[29] H. Borsdorf, E.G. Nazarov, G.A. Eiceman, Int. J. Mass Spectrom. 232 (2004) 117.
[30] G.A. Eiceman, Y.-F. Wang, L. Garcia-Gonzalez, C.S. Harden, D.B. Shoff, Anal. Chim. Acta 306 (1995) 21.
[31] P. Rearden, P.B. Harrington, Anal. Chim. Acta 545 (2005) 13.
[32] M. Meot-Ner, L.W. Sieck, J. Am. Chem. Soc. 105 (1983) 2956.

Talanta 76 (2008) 1177–1182

Contents lists available at ScienceDirect

Talanta

journal homepage: www.elsevier.com/locate/talanta

A novel analytical approach for investigation of anthracene adsorption onto mangrove leaves

Ping Wang[a], Ke-Zhao Du[b], Ya-Xian Zhu[b], Yong Zhang[a,*]

[a] State Key Laboratory of Marine Environmental Science, Xiamen University, Xiamen 361005, P. R. China
[b] Department of Chemistry, Xiamen University, Xiamen 361005, P. R. China

ARTICLE INFO

Article history:
Received 22 February 2008
Received in revised form 13 May 2008
Accepted 14 May 2008
Available online 21 May 2008

Keywords:
Solid surface fluorimetry
Anthracene
Adsorption
Mangrove leaves

ABSTRACT

A solid surface fluorimetry approach was established for direct determination of anthracene (An) adsorbed onto fresh mangrove leaves. The experimental results showed that the linear dynamic ranges for determination of An adsorbed onto *Avicennia marina* (*Am*), *Bruguiera gymnorrhiza* (*Bg*), *Kandelia candel* (*Kc*) and *Rhizophors stylosa* (*Rs*) leaves varied from 0.92 to 8.71, 0.089 to 0.70, 0.063 to 5.61 and 0.11 to 1.82 $\mu g\,g^{-1}$, with detection limits of 5.77, 1.79, 4.29 and 1.42 $ng\,g^{-1}$, respectively, and with a relative standard deviation less than 10% ($n = 5$). The experimental recovery results for adsorbed An on *Am*, *Bg*, *Kc* and *Rs* leaves were among 79.2–85.9, 75.1–102.3, 70.2–93.8 and 73.1–110.8%, respectively. Using the established method, we investigated the effects of exposure time of An and the different quantity of leaf-wax among the four species of mangrove on the amount of An adsorbed. Under the same experimental conditions, the adsorption of An on the upper and lower sides of the same mangrove leaf, and at different regions on the upper side of the same mangrove leaf were also studied. The results demonstrated that the leaves of different mangrove species contained different quantities of leaf-wax, and with the same exposure conditions to An, the quantity of leaf-wax among the four species showed a significant positive correlation with the amount of An adsorbed onto the leaves.

1. Introduction

Vegetation plays a key role in the environmental fate of many organic chemicals, from pesticides applied to plants to the air-vegetation exchange and global cycling of atmospheric organic contaminants [1]. Polycyclic aromatic hydrocarbons (PAHs) are widely distributed organic contaminants of great environmental concern, which are known to be teratogenic, carcinogenic and mutagenic [2]. There are many routes by which PAHs from diverse sources reach the environment, such as incomplete combustion of fossil fuels, waste incineration, vehicle exhausts, industrial processes, urban runoff, petroleum spillage and atmospheric fallout [3]. The persistence of PAHs in the environment poses a potential threat to human health through bioaccumulation and biomagnification via food chains [4].

There are mainly two pathways through which PAHs enter into vegetation. One way is by partitioning from contaminated soil to the roots, the other one is from the atmosphere by gas-phase and particle-phase deposition onto the waxy cuticle of the leaves or by uptake through the stomata [5]. Uptake from the atmosphere through plant leaf is the predominant pathway of accumulation for PAHs that have low water solubilities, low Henry's law constants, and high K_{ow} values [3,6,7].

In the last few decades, research on the environmental behavior of PAHs in many different vegetation types has been considerably increased and has also led to some good conclusions [8–11]. However, the behavior of PAHs in some special ecological environments still needs to be further studied. Mangrove ecosystems, important intertidal estuarine wetlands along the coastlines of tropical and subtropical regions, have been considered wastelands and widely used as sites where effluents are discharged, solid wastes are dumped, in addition to the dry and wet deposits from the atmosphere, including anthropogenic contamination by PAHs [12]. The unique features of mangrove ecosystems such as high primary productivity, abundant detritus, rich organic carbon and anoxic/reduced conditions make them a target for the uptake and preservation of PAHs from anthropogenic inputs [13]. PAHs may also be transported to estuarine waters when accumulated by mangroves and concentrated in exported leaf debris, which is an important food source for higher organisms in estuarine food

* Corresponding author at: State Key Laboratory of Marine Environmental Science, Environmental Research Center, Xiamen University, Siming Road, Xiamen 361005, China. Tel.: +86 592 2188685; fax: +86 592 2184977.
E-mail address: yzhang@xmu.edu.cn (Y. Zhang).

0039-9140/$ – see front matter © 2008 Elsevier B.V. All rights reserved.
doi:10.1016/j.talanta.2008.05.021

chains. Mangrove wetland, as a buffer in the estuary, therefore acts as a sink and source of organic pollutants in the coastline ecosystem. Thus, mangrove uptake and storage is a potential key component in the global cycling of persistent organic pollutants, especially the PAHs. Because of their special ecological functions, mangrove wetlands have become a very important research area [14]. However, the published research on PAHs in mangrove wetlands has mainly focused on analysis of the concentrations of individual PAH compounds and total PAHs (ΣPAHs) in the sediment or water; determination of the distribution and proportion of PAHs in different tissues of many mangrove species; evaluation of the possible sources of PAHs in the wetland; and microcosm studies concerning the removal of PAHs from surface- or bottom-contaminated sediments [12,15,16]. As a result, research centered on the mangrove plant as a core of the wetland whose leaves could adsorb the PAHs directly is rarely involved, although it has been reported that leaves are the most important pathways through which atmospheric PAHs enter vegetation. Therefore, it is necessary to develop a rapid, accurate method to determine the quantity of PAHs adsorbed onto mangrove leaves, which, to some extent, can monitor pollution by airborne PAHs.

Traditional research methods for the determination of PAHs on leaves are time-consuming, arduous, and need a large amount of organic solvent with separation and extraction procedures which might cause secondary pollution problems. In addition, the traditional methods utilizing the entirely destructive chemical extraction techniques could destroy the originally existing forms and eliminate the spatial distribution of PAHs in the leaves. Thus, results derived from these traditional methods only reflect the total concentration of PAHs in the whole leaf and it is difficult for them to be used to understand comprehensively the distribution of PAHs in different leaf tissues.

PAHs are suitable for study by luminescence due to their high native fluorescence quantum yield [17]. In this work, anthracene (An) represents certain properties of persistent organic pollutants, notably their hydrophobicity, lipophilicity, and semivolatility and it was selected as a model PAH compound to establish an in situ solid surface fluorimetry (SSF) method for studying the An adsorbed onto the mangrove leaves. The mangrove leaves were immersed into An–acetone solutions directly in order to roughly simulate the depositions of An from the atmosphere and ignored the deposition time, the processing of An and its transportation to the inner leaf tissues.

2. Experimental

2.1. Apparatus and reagents

All the spectra were obtained on a Cary Eclipse fluorescence spectrophotometer (Varian, USA) equipped with a 150-W Xenon flash lamp. The spectrofluorimeter was controlled by Cary Eclipse software for acquiring and processing the spectral data. Fluorescence measurements were performed using a laboratory-made solid substrate holder. The SSF spectra were obtained with the following instrumental parameters: excitation and emission slits were both set at 5 nm; scan speed was 120 nm min^{-1}; PMT voltage was 600 V; and an ultrasonic cleaning device (Model KQ3200, power 150 W, frequency 40 kHz) was also used to extract the An adsorbed onto the mangrove leaves and the leaf-wax on the leaf surface.

The stock solution of An (Aldrich, purity > 99%, USA) was prepared by dissolving the solutes in acetone in a brown volumetric flask, and it was stored at 4 °C in the dark to avoid possible photodegradation. Working solutions of An were prepared by dilution of the stock solution in acetone before use.

2.2. Sample collection

Leaves from four mangrove species (*Am*, *Bg*, *Kc* and *Rs*) were collected from Xiamen Yundang Lake in China (longitude: 24°29′3″; latitude: 118°5′59″; altitude: 0 m above sea level). Leaves of each species were divided into three groups (each group contained four leaves), and each group was sealed into a plastic bag and taken back to the laboratory as soon as possible. In addition, 10 old and 10 young leaves from each species were also collected and taken back to the laboratory for measuring the amounts of leaf-wax.

2.3. Experimental methods

The mangrove leaves from the four species were carefully rinsed with distilled water to remove surface silt. After air-drying, the four sets of leaves were contaminated by immersing each four leaf-sample into a set concentration of An–acetone solution at room temperature. After set intervals of exposure to An, the mangrove leaves were taken out from the acetone solutions and air dried. Then the mangrove leaves were placed into the solid substrate holder to determine the relative SSF intensities of An adsorption onto their surfaces directly. The detection excitation and emission wavelength were set at 253 and 405 nm, respectively. Determination of the amount of An adsorbed involved the four mangrove leaves of each species from each of the 72 locations, that is 72 measurements were made for each species. The value of relative SSF intensity presented represented the average behavior shown by the adsorbed An at different locations in each of the mangrove species.

In order to quantify the actual An adsorption onto the leaves of each species, after determination of the SSF intensities, the An adsorbed was extracted by dichloromethane (100 ml) in a branson ultrasonic water bath for 5 min. Then the An–dichloromethane extracted solutions from the leaves of each mangrove species were measured using fluorimetry and quantified using standard calibration curve for An–dichloromethane solutions. The quantity of An adsorbed (μg g^{-1}) on the leaves of each mangrove species was obtained.

To further investigate the factors influencing An adsorbed on the leaves of the four species, the wax content of the various mangrove leaves was quantified. The samples of the four species, which included 10 old and 10 young leaves, were immersed into dichloromethane (150 ml) in 400 ml beakers. The beakers were sealed using aluminum foil and then the mangrove leaf wax was extracted in a branson ultrasonic water bath for 10 min. After this, the mangrove leaves were removed from the dichloromethane solution and the extraction solution was allowed to evaporate in a gentle flow of high-purity nitrogen gas to remove the solvent. The solid leaf-wax left in the beakers was weighed, and finally the wax content of each species was obtained (mg g^{-1}).

3. Results and discussion

3.1. Fluorescence excitation and emission spectra of An

There are two different modes to detect SSF signals: one is the front-reflection mode, where the excitation light source and detector are at the same side, which is generally adapted for an opaque solid matrix like a plant leaf. The other is the transmission mode, where the excitation light source and detector are on the different sides, which is generally adapted to a transparent solid matrix [18]. In this work, the front-reflection mode was selected. It is reported that leaf autofluorescence is the main interference in the SSF determination of the fluorescence signal when using in vivo plant leaves [19]. Therefore, the excitation and emission spectra of both the uncontaminated and An-contaminated species of mangrove leaves

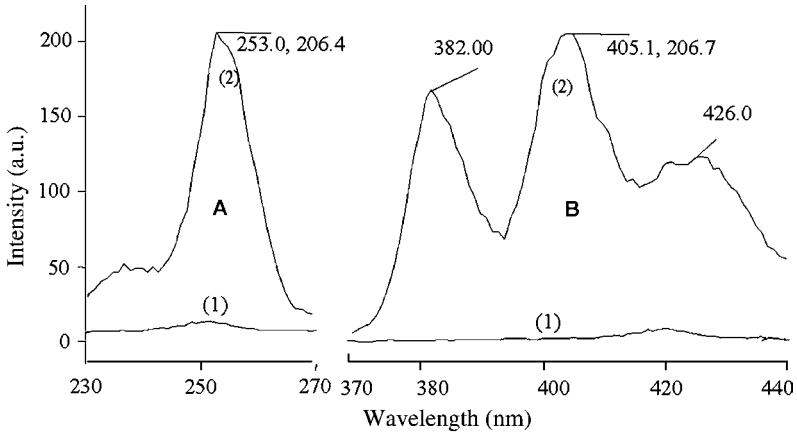

Fig. 1. SSF excitation (A: λ_{em} = 405 nm) and emission (B: λ_{ex} = 253 nm) spectra of An adsorbed on *Am* leaves: (1) uncontaminated leaf and (2) An-contaminated leaf.

were investigated, and the experimental results of *Am* are shown in Fig. 1. As can be seen in this figure, the excitation spectra of An (with λ_{em} = 405 nm) adsorbed on *Am* leaves showed a single peak at 253 nm, while the emission spectra of An adsorbed (with λ_{ex} = 253 nm) showed three peaks at 382, 405 and 426 nm, with the maximum at 405 nm. Compared with the standard aqueous An solution spectra, the shape of the An-SSF excitation and emission spectra were almost accordant, but with about a 4-nm redshift for excitation and emission spectra. Also from Fig. 1, it is clear that the autofluorescence of the uncontaminated *Am* leaf was very weak, which would not interfere with the detection of An adsorbed onto the leaf surface by SSF. This was true of the autofluorescence of the other three species of uncontaminated mangrove leaves, since similar SSF excitation and emission spectra were obtained for the other three species of An-contaminated mangrove leaves, and only their relative fluorescence intensities were different.

During the contamination process of acetone immersion of mangrove leaves, some of the chlorophyll in the mangrove leaves was extracted and dissolved in the immersion solution. However, further experimental results demonstrated that the extracted chlorophyll did not affect the determination by SSF of the An adsorbed. In the next experiment related to the quantity of An adsorbed on each mangrove species leaf surfaces, a certain amount of the wax on the mangrove leaves might also have been extracted by the dichloromethane and dissolved into the extraction solutions. However, based on further experimental validations, the dissolved leaf-wax did not affect An determination in the extraction solution.

Therefore, it can be concluded from the experimental results that SSF is a simple, fast and easy-operation method for determination of An adsorbed onto mangrove leaves, without the necessity for sample pretreatment with a great amount of organic solvent. It might also be a suitable method which could be developed for direct in situ determination of PAHs adsorbed onto mangrove leaves.

3.2. Merits in the determination by SSF of An adsorbed

It is reported that the adsorption of PAHs on leaves has a close relationship with the physical–chemical properties of vegetation and the concentration of the PAHs [20]. For this study, the leaves of four typical mangrove species were selected together with An, representing a model PAH compound. With the same exposure time, the adsorption of An on different species of mangrove leaves was investigated. Fig. 2 shows the relationship between the quantity of An adsorbed onto the leaves of the four mangrove species and their relative SSF intensities, at the same exposure time of 90 min. It was also demonstrated that, under the same experimental conditions, the leaves of the four mangrove species showed different capacities to adsorb An. Within a certain range, the SSF intensity of the An adsorbed on the upper side of leaves from the four mangrove species increased linearly with increments in the exposure quantity of An. The calibration equations, linear ranges, correlation coefficients and detection limits of leaves from the four mangrove species are shown in Table 1. It is reported that whether the surface of the substrate was rough or not influences the detection of relative SSF signals [21–23]. This might be one of the reasons why the SSF intensities of different mangrove leaves shown in Fig. 2 were different from each other despite the same quantity of An being adsorbed. For this reason, the mangrove leaves should always be kept smooth during the course of the measurements. Another factor which might influence the detection of SSF signals was the size of the An-fluorescence dots on the mangrove leaves. If the sizes of the fluorescence dots were so small as to be outside the detection limit of the instrument, they would not be detected. Further studies are needed to investigate the possible reasons which might influence the detection of SSF signals.

3.3. Recovery experiment

In order to understand more about the adsorption of An onto the leaves of the four mangrove species, and to ensure the feasibility of this SSF method for direct determination of An onto mangrove leaves, a recovery experiment should be performed. However, the traditional recovery formula only suits homogeneous systems and, so far, there is no recovery formula applicable to the solid surface substrate of mangrove leaves. Therefore, a revised recovery for-

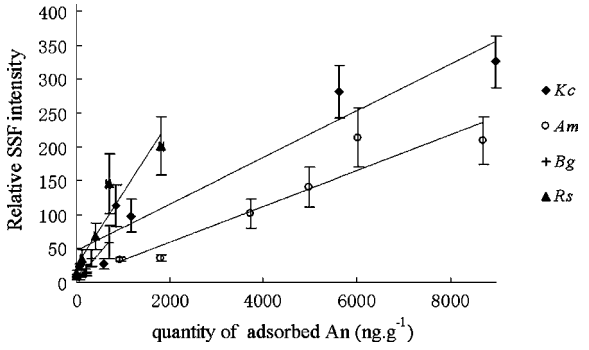

Fig. 2. Dependence of relative SSF intensity on An adsorbed on the upper side of leaves from four mangrove species when the exposure time of An–acetone solution was 90 min. The error bars represent the standard deviation of 72 measurements.

Table 1
Performance data for the leaves of the four mangrove species

An adsorbed on substrates	Calibration equation	Linear range ($\mu g\,g^{-1}$)	Correlation coefficient	Detection limit ($ng\,g^{-1}$)[a]
Am	y[b] = 0.026x[c] + 7.42	0.92–8.71	0.9449	5.77
Bg	$y = 0.084x + 1.85$	0.089–0.70	0.9769	1.79
Rs	$y = 0.106x + 25.56$	0.11–1.82	0.9508	1.42
Kc	$y = 0.035x + 45.93$	0.063–5.61	0.9612	4.29

[a] $q_L = 3S_B/m$ ('S_B' means standard deviation of uncontaminated mangrove leaves; 'm' means slope of the calibration equation).
[b] Relative SSF intensity.
[c] The quantity of adsorbed An ($ng\,g^{-1}$) on mangrove leaves.

mula was adapted to the new system, but without violating the principles. The process was as follows: a prepared clean mangrove leaf was exposed to an An–acetone solution at a concentration of C_1 with an exposure time of 90 min. The quantity of An adsorbed, marked as M_1 ($ng\,g^{-1}$), was measured using the established method mentioned above, then another leaf of the same species and which was similar to the first one was selected to be exposed to an An–acetone solution at a concentration of C_2 ($C_2 = 2C_1$), with the same exposure time, and the same method was used to determine the quantity of An adsorbed, marked as M_2 ($ng\,g^{-1}$). The recovery of the exposure experiment (P) can be calculated using the following formula: $P = ((M_2 - M_1)/M_1) \times 100\%$. The recovery results for An adsorbed onto leaves of the four mangrove species are shown in Table 2, and it is clear that the recoveries for four species were between 70.2 and 110.8%.

Although we attempted to select similar leaves of the same mangrove, such as similar maturity, similar size and so on, these two mangrove leaves were not the same and differences certainly existed. For example, the quantity of leaf-wax, which was considered as one of the important factors governing the capacity for PAH uptake, was generally different among similar mangrove leaves of the same species. This might be one of the reasons why most of the recoveries for the four mangrove species were below 100%, and further studies are therefore needed.

3.4. Effect of exposure time on SSF intensity of An

Plant leaves are covered by a nonliving lipid surface structure called the cuticle, which acts as a barrier against water loss and pathogen invasion [24]. The cuticle consists of a biopolymer framework encrusted by and interspersed with soluble leaf-wax, which as a unit is a formidable barrier to diffusion into the leaf [25]. PAHs are believed to enter the plant primarily via the cuticle because of their high solubilities in lipid [26]. Leaves with a high wax content generally have a high PAH concentration in their tissues, and most of the variation in PAH concentration among different kinds of leaves can be attributed to varying amounts of wax [11]. There is much leaf-wax in the cuticle of mangrove leaves, which can strongly adsorb the lipophilic PAHs. Therefore, in the same exposure concentration of An–acetone solutions ($5 \times 10^{-3}\,mol\,L^{-1}$), the capacities for the leaves of the four mangrove species to adsorb PAHs were investigated. In the range 30–150 min, the effect of exposure time on the quantity of An adsorbed was determined at 30 min intervals. The experimental results showed that in the same exposure time the capacities of different mangrove species were different. There are mainly two "compartments" where leaves take up PAHs: one is the cuticle "compartment", which quickly reaches equilibrium in PAH uptake; and the other is the inner "compartment" of the leaf which can take several weeks to reach equilibrium [27]. Therefore, in high concentrations of An, the An adsorbed onto the mangrove leaves reached equilibrium quickly (several tens of minutes) and, as the exposure time grew, the second inner "compartment" might play a role, and some of the An adsorbed onto the leaf surface might enter into the inner "compartment" of the mangrove leaves. From Fig. 3, we can see that in the range of 30–90 min the relative SSF intensity of *Bg* was basically unchanged, the equilibration time of *Rs* and *Kc* were both at 90 min, while *Am* reached the maximum relative SSF intensity at 120 min. Therefore, 90 min was selected as the best exposure time for the experiments. In order to further illustrate the result shown in Fig. 3, the leaf-wax content of old and young mangrove leaves of the four species were determined [28], and the results for *Am*, *Bg*, *Kc* and *Rs* leaves were 5.050–13.636, 2.618–8.821, 2.637–9.997 and 2.597–9.005 $mg\,g^{-1}$, respectively. It was demonstrated that for the same mangrove species the older the leaf was, the more the leaf-wax it contained. The mean values of leaf-wax content of the four mangrove species were in the order *Am* > *Kc* > *Rs* > *Bg*, which was identical to the order of the maximum relative SSF intensities measured for the four species. Under the same exposure concentration of the An–acetone solution, the *Am* leaf took the longest time to reach adsorption equilibrium, which might be because of its high leaf-wax content. When evaluating the uptake and accumulation of organic pollutants in different species,

Table 2
The experimental recovery results for An adsorbed on the leaves of the four mangrove species

Analyte	C_1 ($mol\,L^{-1}$)	M_1 ($ng\,g^{-1}$)	C_2 ($mol\,L^{-1}$)	M_2 ($ng\,g^{-1}$)	Recovery (%)
Am	1×10^{-5}	454.2	2×10^{-5}	831.6	83.1
	1×10^{-4}	1792.3	2×10^{-4}	3211.8	79.2
	2×10^{-4}	3211.8	4×10^{-4}	5970.7	85.9
Bg	1×10^{-5}	23.1	2×10^{-5}	40.4	75.1
	1×10^{-4}	99.3	2×10^{-4}	200.9	102.3
	2×10^{-4}	200.9	4×10^{-4}	362.8	80.6
Rs	1×10^{-5}	9.5	2×10^{-5}	16.4	73.1
	1×10^{-4}	58.4	2×10^{-4}	123.1	110.8
	2×10^{-4}	135.5	4×10^{-4}	249.7	84.3
Kc	1×10^{-5}	62.7	2×10^{-5}	121.5	93.8
	1×10^{-4}	585.5	2×10^{-4}	1094.3	86.9
	2×10^{-4}	1094.3	4×10^{-4}	1862.5	70.2

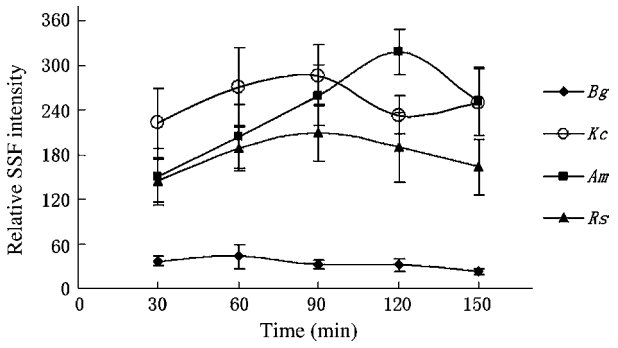

Fig. 3. Effects of exposure time on relative SSF intensity of An adsorbed on the upper side of leaves from four mangrove species with exposure to An–acetone solution concentration of $5 \times 10^{-3}\,mol\,L^{-1}$. The error bars represent the standard deviation of 72 measurements.

the quality of the leaf-wax should also be focused on, in addition to considering the quantity of leaf-wax [29]. The experimental results also showed that the color of the leaf-wax of the leaves of the four mangrove species was different. However, the differences of leaf-wax quality among different species which might influence the uptake of PAHs are still not clear.

With an increment in exposure time, the relative SSF intensities of the leaves of the four mangrove species increased before the equilibration time and decreased after the equilibration time. This could be explained by the fact that, when An accumulation on the mangrove leaf surface achieved a certain level, with the passage of time, the An on the leaf surface might penetrate into the inner leaf tissues [30]. Because the SSF method could only detect fluorescence signals on the surface of the mangrove leaves, this might be one of the reasons why the relative SSF intensities for the adsorbed An decreased as time progressed. However, more studies are needed to confirm this.

3.5. Effect of upper and lower surfaces and different regions of the mangrove leaf on the SSF intensity of the An adsorbed

On the whole, there are two pathways by which PAHs enter into leaves: one is via the waxy cuticle, the other is via the stomata. In the case of a plant with a very permeable cuticle, the importance of the stomatal pathway is predicted to be reduced almost to zero [31]. Riederer and Schreiber show how the relative importance of the stomatal pathway increases as the permeability of the cuticle decreases [25]. In order to investigate the pathways by which An entered into the mangrove leaves, we examined the relative SSF intensities on the upper and lower sides of the leaves of four An-contaminated mangrove species under different An exposure concentration. The results (Fig. 4) show that at any exposure concentration, the relative SSF intensities of the upper side of the *Am* leaf were much stronger than those of the lower side, which has many stomata. Because the mangrove leaves have a large quantity of leaf-wax on both sides of the leaves [32], the stomatal pathway is also important for mangrove leaves. The relative SSF intensities of the upper and lower sides of the An-contaminated leaves of the other three mangrove species were similar to that of *Am*, and the relative SSF intensities of both sides were different. Furthermore, it is reported that the forms of leaf-wax on different sides of the same mangrove leaf are different [32], which might influence the adsorption of An on different sides of a single mangrove leaf. In addition, the *Am* leaf has salt glands on both sides of the leaf surface, and on the lower side, there are many wrinkle-shaped trichomes at the top of which are protuberances, which might make the lower side of the *Am* leaf surface much coarser and so influence the intensity of SSF signals. All these factors might influence the adsorption or detection of An on mangrove leaf surfaces and all of them should be studied more in the future. Wild et al note that a PAH (phenanthrene) distributed on the edges of spinach leaves has a systematically higher concentration than that on the center of the same leaves [33]. In order to further investigate the distribution of An adsorbed onto the mangrove leaf surface, the relative SSF intensities in different regions of the upper surface of the same An-contaminated mangrove leaves were measured. Fig. 5 shows the changes of SSF intensities in different regions of the upper surface of the *Am* leaf, in relation to changes in the exposure concentration of An–acetone solutions. The relative SSF intensities in different regions of the same leaf differed from each other at all the exposure concentrations of An. These experimental results might provide us with more important information concerning how PAHs vary and are distributed on mangrove leaves. The differences of relative SSF intensities in different leaf regions also existed in the other three mangrove species, and only the relative intensities of different regions were different. However, the regularity with which An uptake capacities varied in different regions of the same mangrove leaf was not clear, and so further experimental verification is needed.

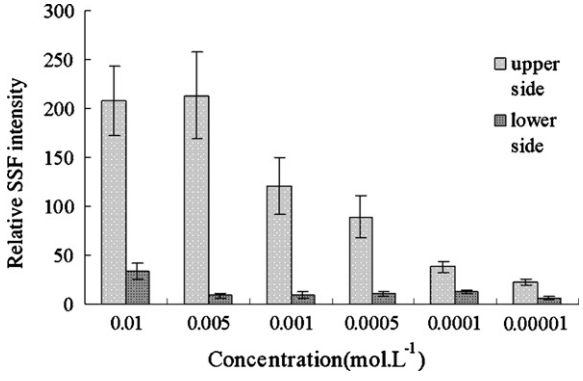

Fig. 4. Comparison of the relative SSF intensities on the upper and lower sides of An-contaminated *Am* leaves when the exposure time of An–acetone solution was 90 min. The error bars represent the standard deviation of 24 measurements.

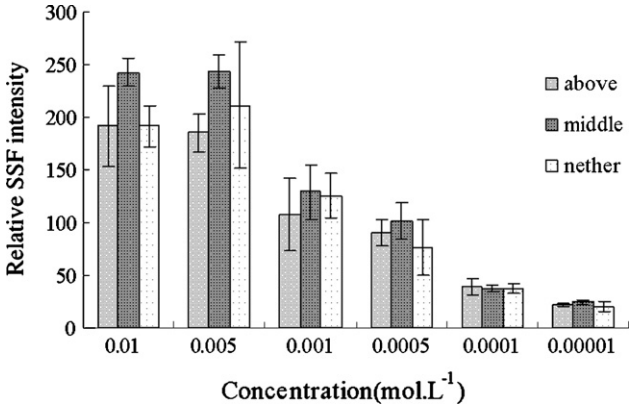

Fig. 5. Changes of relative SSF intensities of the adsorbed An in different regions of the upper side of *Am* leaves when the exposure time of An–acetone solution was 90 min. The error bars represent the standard deviation of 24 measurements.

4. Conclusions

From the above experimental results, it could be concluded that determination of An adsorbed onto four kinds of mangrove leaves by SSF was confirmed to be an easy operation, simple and rapid method. This method had its own distinct advantages that could directly reflect the adsorption of An onto mangrove leaves, without any sample pretreatment that involving a large amount of organic solvent. Thus, the established SSF method has a great potential to be developed as an in situ technique for determination of An or other PAHs adsorbed onto plant's leaves (including mangrove) and distinguish the distribution of An or other PAHs on different regions of the same leaf.

However, much more studied need to be carried out in the near future. For example, PAHs usually existed in a mixture or multi-component in real environment. Firstly, synchronous solid surface fluorimetry might be a good way to be used for determination of multi-component PAHs simultaneously. Secondly, the concentrations of multi-component of PAHs existed in real environment are very low, thus portable laser induced time resolved fluorimetry (Gurtingen Laser Fluorvision, Germany) could be used to develop new methods for simultaneously determination of PAHs in a mixture on plant leaves, through its distinction of PAHs' different life

time. Thirdly, based on primary information provided by SSF, air-to-leaf transfer and within-leaf movement of An or other PAHs could be further studied by two-photon laser confocal scanning microscopy (TPLCSM) which has already been succssfully used to monitor the air-to-leaf transfer, within-leaf movement and distribution of phenanthrene in maize and spinach [33].

It could be prospected that with the development of the mentioned methods, it will be helpful for us to understand more the environmental behavior of PAHs in real environment, and it will also provide us a new way to study on mechanism of phytoremediation of PAHs in mangrove wetland or other contaminated mediums, optimize phytoremediation strategies for both PAHs contaminated soil and air cleanup in the near future.

Acknowledgements

Financial supports from the Natural Science Foundation of China (No. 20777062 and No. 405210003) are gratefully acknowledged. Professor John Hodgkiss is thanked for his assistance with English.

References

[1] E. Wild, J. Dent, J.L. Barber, G.O. Thomas, K.C. Jones, Environ. Sci. Technol. 38 (2004) 4195–4199.
[2] C.D. Simpson, A.A. Mosi, W.R. Cullen, K.J. Reimer, Sci. Tot. Environ. 181 (1996) 265–278.
[3] Q.-Q. Wang, Y.-L. Zhao, Y. Dong, L.-M. Yang, Z.-J. Li, B.-L. Huang, Environ. Sci. Technol. 38 (2004) 4739–4744.
[4] N.T. Edwards, J. Environ. Qual. 12 (1983) 427–441.
[5] S.T. Simonich, R.A. Hites, Environ. Sci. Technol. 29 (1995) 2905–2914.
[6] H. Behrendt, R. Bruggemann, Chemosphere 27 (1993) 2325–2332.
[7] S. Paterson, D. Mackay, C. Mcfarlane, Environ. Sci. Technol. 28 (1994) 2259–2266.
[8] B.-L. Chen, E.J. Johnson, B. Chefetz, L.-Z. Zhu, B.-S. Xing, Environ. Sci. Technol. 39 (2005) 6138–6146.
[9] J.J. Cornejo, F.G. Munoz, C.Y. Ma, A.J. Stewart, Ecotoxicology 8 (1999) 311–320.
[10] C. Collins, M. Fryer, A. Grosso, Environ. Sci. Technol. 40 (2006) 45–52.
[11] S.L. Simonich, R.A. Hites, Environ. Sci. Technol. 28 (1994) 939–943.
[12] L. Ke, W.Q. Wang, T.W.Y. Wong, N.F.Y. Tam, Chemosphere 51 (2003) 25–34.
[13] D. Bernard, H. Pascaline, J.J. Jeremie, Mar. Pollut. Bull. 32 (1996) 734–739.
[14] Z.Q. Lu, W.J. Zheng, L.H. Peng, Mar. Sci. 26 (2002) 26–29.
[15] S. Bayen, O. Wurl, S. Karuppiah, N. Sivasothi, H.K. Lee, J.P. Obbard, Chemosphere 61 (2005) 303–313.
[16] T.G. Luan, S.H. Keith, Y. Zhong, H.W. Zhou, C.Y. Lan, N.F.Y. Tam, Chemosphere 65 (2006) 2289–2296.
[17] F.P. Schwarz, S.P. Waslk, Anal. Chem. 48 (1976) 524–528.
[18] G.-Z. Chen, X.-Z. Huang, J.-G. Xu, Z.-Z. Zheng, Z.-B. Wang, Fluorescent Analysis, Science Press (China), Beijing, 1990, p. 309.
[19] Y.Q. Li, Ph.D. Thesis, Xiamen University, Xiamen, China, 1991.
[20] X. Gao, X. Jiang, Z.-Q. Qu, Chin. J. Appl. Ecol. 13 (2002) 501–504.
[21] Ahmet E. Eroğlu, M. Volkan, O. Yavuz Ataman, Talanta 53 (2000) 89–101.
[22] J.F. Fernández-Sánchez, A. Segura Carretero, C. Cruces-Blanco, A. Fernández-Gutiérrez, Talanta 60 (2003) 287–293.
[23] J.F. García Reyes, P. Ortega Barrales, A. Molina Díaz, Talanta 65 (2005) 1203–1208.
[24] G. Kerstiens, Trends Plant Sci. 1 (1996) 125–129.
[25] M. Riederer, L. Schreiber, J. Exp. Bot. 52 (2001) 2023–2032.
[26] M. Riederer, Environ. Sci. Technol. 24 (1990) 829–837.
[27] J. Tollst, M.S. Mclachlan, Environ. Sci. Technol. 28 (1994) 159–166.
[28] Y.Q. Wang, Q. Zuo, X.C. Jiao, S.P. Wu, S. Tao, Chin. J. Environ. Sci. 25 (2004) 23–27.
[29] F. Böhme, K. Welsch-Pausch, M.S. Mclachlan, Environ. Sci. Technol. 33 (1999) 1805–1813.
[30] P. Komp, M.S. Mclachlan, Sci. Tot. Environ. 250 (2000) 63–71.
[31] J.L. Barber, P.B. Kurt, G.O. Thomas, G. Kerstiens, K.C. Jones, Environ. Sci. Technol. 36 (2002) 4282–4287.
[32] Y.-Y. Li, Ph.D. Thesis, Xiamen University, Xiamen, China, 2006.
[33] E. Wild, J. Dent, G.O. Thomas, K.C. Jones, Environ. Sci. Technol. 40 (2006) 907–916.

Talanta 76 (2008) 1207–1211

Contents lists available at ScienceDirect

Talanta

journal homepage: www.elsevier.com/locate/talanta

Selective enhancement of resonance light-scattering of gold nanoparticles by glycogen

Minghui Xiang, Xiao Xu, Dongxu Li, Feng Liu, Na Li*, Kean Li[1]

Key laboratory of Bioorganic Chemistry and Molecular Engineering of Ministry of Education, Institute of Analytical Chemistry, College of Chemistry and Molecular Engineering, Peking University, Beijing 100871, China

ARTICLE INFO

Article history:
Received 18 March 2008
Received in revised form 12 May 2008
Accepted 18 May 2008
Available online 27 May 2008

Keywords:
Glycogen
Gold nanoparticle
Resonance light-scattering
Plasmon absorption

ABSTRACT

Simple and sensitive methods for the determination of glycogen are desirable. This study was to establish the determination of glycogen based on the enhancement of the light-scattering intensity of gold nanoparticles (AuNPs) at nanogram per milliliter levels. Glycogen enhancement was independent of temperature and was highest at pH 7. The enhancement was linear from 10 to 800 ng mL^{-1} with a 2 ng mL^{-1} detection limit (3 S/N). The standard deviation of the slope for 5 consecutive calibration runs was within 5%. Analysis of three artificial samples with varied glycogen concentrations had 98–102% recovery. Selected amino acids, glucose, lactose, BSA and trichloroacetic acid all showed minor effects on glycogen enhancement demonstrating the potential for glycogen determination in complex samples.

1. Introduction

Carbohydrates, one of the four major classes of biomolecules (proteins, nucleic acids, lipids and carbohydrates) have played important roles in biological processes such as cellular recognition, transmission of information, immunity and tumorigenesis [1]. Polysaccharides and glycoconjugates were not studied intensively until the 1990s when their biological functions were recognized. Glycogen is the major storage form of polysaccharides in animal cells. This polymer has an average molecular weight of several million with $\alpha(1 \rightarrow 4)$-linked glucose subunits and $\alpha(1 \rightarrow 6)$-linked branching [1]. The tissue glycogen content often provides information for diagnosis of disease including glycogen storage diseases, esophageal cancer and cervical cancer as well as general health.

Carbohydrates are a category of molecules that have in the molecular structure only the hydroxyl as an easy to derivatize group. Glycogen content in tissues is usually assayed by microphotometry following periodic acid-schiff (PAS) staining [2–8]. In this method, the periodic acid causes oxidative cleavage of each of the 1, 2-glycol linkages of glycogen to form aldehydes, which are then stained with Schiff's reagent. This primary stain method has been used for the histological quantification of muscle glycogen in frozen tissue sections [3,6]. Iodine-binding spectrophotometric assay has also been used to determine glycogen in solution [9]. Many factors including, temperature, iodine concentration and coexisting substances can affect the signal, thus the application can be limited by its lower sensitivity and specificity. Enzymatic assay methods have been used with the measurement of the glucose released from hydrolyzed glycans as an indirect method of determination [10–12]. The glucose produced from hydrolysis of glycogen by amyloglucosidase was then assayed by glucose oxidase methods. The enzymatic method is sensitive but time consuming and expensive. Because the hydrolysis process can be applied to any polysaccharide, the amount of glucose determined might come from more than one resource other than glycogen [13]. Thus selectivity could be a problem. Near infrared [14], dual isotope technique [15], fluorescence cytometry [16], HPLC with refractive index detection [17] and cytometry [18] have also been used for glycogen analyses. A bioassay for glycogen in biological phosphorus removal systems was developed by Brdjanovic et al. [19]. The glycogen concentration of the sludge was determined indirectly via measuring the maximal total acetate uptake by the activated sludge in anaerobic batch tests to avoid interference from glucose and other carbohydrates. These approaches had many advantages, including good sensitivity and selectivity, but the methods are often time consuming and labor intensive. Other approaches with higher sensitivity and selectivity have been sought to manage better the diverse specimens often available for analysis in limited quantities.

Light-scattering has been widely applied to study the aggregation, size, shape and distribution of particles in solution. When the excitation wavelength is close to the absorption bands, greatly

* Corresponding author. Tel.: +86 10 62761187; fax: +86 10 62751708.
E-mail addresses: lina@pku.edu.cn (N. Li), likean@pku.edu.cn (K. Li).
[1] Tel.: +86 10 62761187; fax: +86 10 62751708.

0039-9140/$ – see front matter © 2008 Elsevier B.V. All rights reserved.
doi:10.1016/j.talanta.2008.05.027

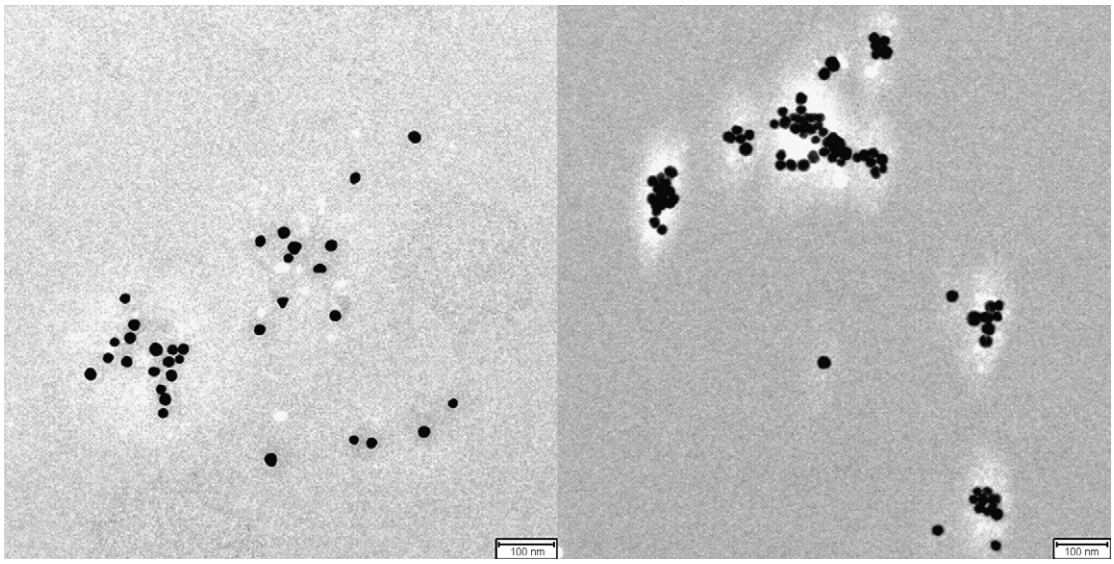

Fig. 1. TEM images of AuNPs (left) and AuNPs with 500 ng mL^{-1} glycogen (right).

enhanced Rayleigh light-scattering signals could be expected, which was called resonance light-scattering (RLS). The plasmons of AuNPs are electron density waves, which propagate along the surface of a typically a metal conductor [20]. The oscillating electrons radiate light with the same frequency of the incident electromagnetic radiation [21], which is the optical characteristic of metal nanoparticles. This process is often referred to as plasmon light-scattering or resonance light-scattering [22,23]. Since 1995 when Pasternack and Collings recommended resonance light-scattering with a conventional fluorescence spectrophotometer, RLS has been used in many biomedical and pharmaceutical analyses [24–27].

In glycan and gold nanoparticles (AuNPs) studies, oligosaccharide conjugated AuNPs were prepared as a biominetic model for study of biomolecular interactions [28,29]. A colorimetric bioassay was developed for Cholera toxin based on a specifically synthesized lactose derivative that was self-assembled onto 16 nm diameter AuNPs [30]. Aslan et al. described a new approach for colorimetric assay of glucose with Con A-aggregated dextran-coated gold colloids [31]. The glycogen light-scattering characteristics were discovered in our early studies that demonstrated glycogen could be measured at concentrations as low as 0.8 μg mL^{-1} [32]. In our current studies, we found that glycogen at the nanogram level could enhance RLS of AuNPs near plasmon absorption wavelength as well as make the plasmon absorption shift to longer wavelength. The purpose of this study was to explore the application of RLS of AuNPs to glycogen and glycoconjugate sensing. The AuNPs resonance light-scattering method may provide an approach to avoid the enzymatic methods and labeling techniques for glycogen analysis.

2. Experimental

2.1. Reagents and instrumentations

$HAuCl_4{\cdot}4H_2O$ (AR) was purchased from Shenyang Research Institute of Nonferrous Metals (China) and trisodium citrate (AR) from Beijing Chemical Plant (China). Glycogen (type II, from oysters) was purchased from Sigma and albumin bovine V (BSA, 98%) was purchased from Amresco. Amino acids (BR) and trichloroacetic acid (TCA, AR) were purchased from Sinopharm Chemical Reagent Beijing Co. Ltd. (China). Glucose (AR)was from Sino-Pharm Co.(China) and lactose (AR) was from Shanghai Chemical Reagent Co. (China). For all experiments, deionized water was filtrated with 0.45 μm microporous filter membrane.

Transmission Electronic Microscopy (TEM) was performed with Hitachi H9000-NAR (Japan). TEM was used to determine the size and mono-dispersity of the resulted nanoparticle solutions. The resonance light-scattering spectra were obtained by synchronous scans on Hitachi F-4500 fluorescence spectrometer (Japan) and the UV–visible absorption spectra were recorded on Hitachi UV-3010 absorption spectrophotometer (Japan).

2.2. Preparation of AuNPs

AuNPs were synthesized by the citrate reduction of $HAuCl_4$ [33]. All glassware was cleaned in aqua regia (3 parts HCl, 1 part HNO_3), rinsed with filtered, deionized water, and oven dried prior to use. One hundred and eight milliliters 0.011% $HAuCl_4$ aqueous solution was brought to a reflux with stirring. Then 20 mL 38.8 mmol L^{-1} trisodium citrate solution was added quickly. The resulted dark red solution was kept refluxing for 15 min, cooled to room temperature, and subsequently filtered through 0.45 μm membrane. The AuNPs obtained were typically 20 nm in diameter (Fig. 1.) and exhibited a characteristic plasmon band centered at about 520 nm (Fig. 2A). The AuNPs molar concentration was calculated to be 0.98 nmol L^{-1} [34].

2.3. Acquisition of RLS and plasmon absorption spectra

A measured volume of glycogen was mixed with 2.5 mL AuNPs. The mixture was diluted to 5 mL with filtered, deionized water and homogenized by vortexing. After 15 min at room temperature, the RLS spectra were obtained on F-4500 fluorescence spectrometer by scanning simultaneously the excitation and emission monochromators at $\Delta\lambda = 0$ nm from 200 to 800 nm and plasmon absorption spectra were measured on UV-3010 spectrophotometer from 400 to 700 nm.

3. Results and discussion

3.1. Plasmon absorption and resonance light-scattering

AuNPs with particle size at 20 nm have plasmon absorption at 520 nm (Fig. 2A) and a RLS peak at 552 nm (Fig. 2B). The addition

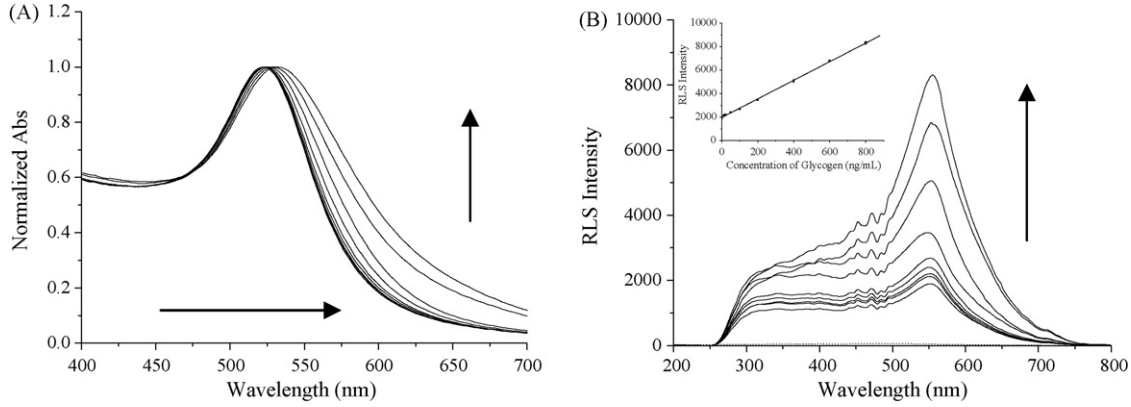

Fig. 2. Plasmon absorption (A) and resonance light-scattering (B) of 0.49 nmol L^{-1} AuNPs in the presence of glycogen with concentrations of 0, 10, 20, 50, 100, 200, 400, 600, and 800 ng mL^{-1}.

of 800 ng mL^{-1} glycogen made plasmon absorption move from 523 to 532 nm in the final solution, suggesting an increased dielectric constant in the environment surrounding the gold particle [35]. The red shift of plasmon absorption wavelength was sensitive to and correlated with glycogen concentration change (Fig. 2A). In addition to the red shift of plasmon absorption, peak broadening was also observed, showing again electric field changes surrounding gold particle surface.

The addition of glycogen increased the RLS intensity in a linear manner ($r^2 = 0.999$) with concentration of glycogen up to 800 ng mL^{-1} (Fig. 2B). When glycogen concentration was greater than 800 ng mL^{-1}, the RLS intensity increase rate slowed down and started to decrease thereafter.

3.2. Optimization of conditions for determination of glycogen

For AuNPs, both plasmon absorption and scattering spectra did not change as pH changed (Fig. 3). The formation of AuNPs–glycogen complexes altered the scattering intensity with maximum intensity at pH 7–8. An observable plasmon absorption red shift occurred pH 7.

The RLS intensity of both AuNPs and AuNPs–glycogen were not sensitive to temperature change (<6%) in 25–50 °C, thus simplifying experimental procedures.

The amount of sodium citrate added to the synthesis solution altered AuNPs particle size, and the RLS intensity of AuNPs. More sodium citrate resulted in more intensively enhanced RLS, especially in the presence of glycogen (Fig. 4). More sodium citrate also resulted in plasmon absorption red shift from 522 to 532 nm as the sodium citrate increased from 10 to 30 mL (Fig. 5).

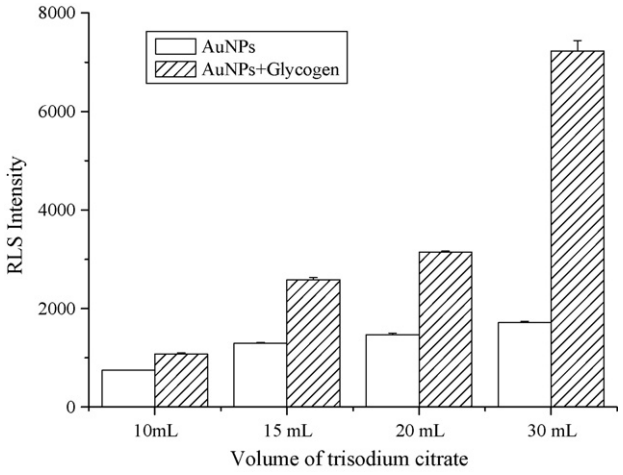

Fig. 4. The RLS intensity of AuNPs and AuNPs with 500 ng mL^{-1} glycogen with varied citrate concentrations used for AuNPs synthesis (0.01% $HAuCl_4$).

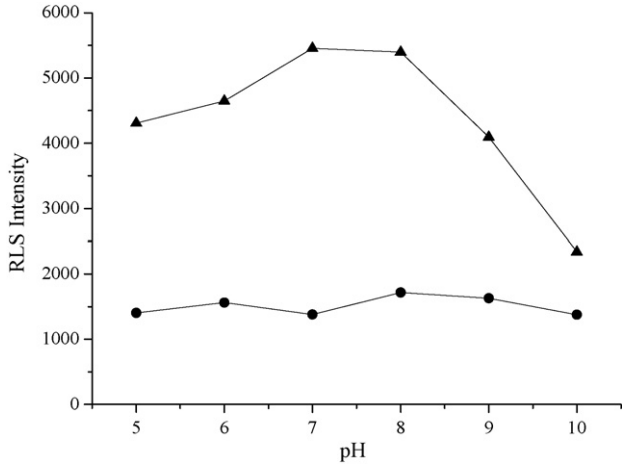

Fig. 3. The pH dependence of the RLS intensity of 0.49 nmol L^{-1} AuNPs (●) and 0.49 nmol L^{-1} AuNPs with 500 ng mL^{-1} glycogen (▲).

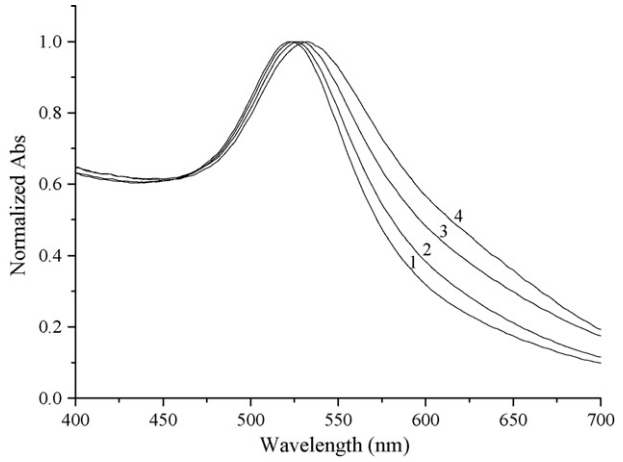

Fig. 5. The plasmon absorption spectra of AuNPs in varied citrate concentrations used for synthesis. Volume of 38.8 mmol L^{-1} trisodium citrate solution: (1) 10 mL, (2) 15 mL, (3) 20 mL, and (4) 30 mL.

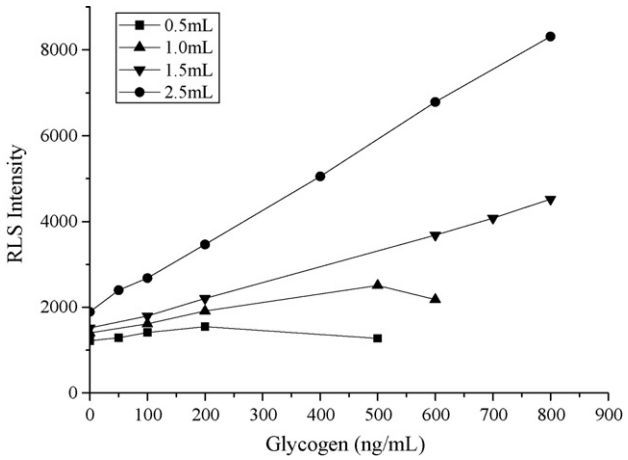

Fig. 6. The RLS intensity of glycogen with varied amounts of AuNPs.

The amount of AuNPs added to the detection solution affected the sensitivity and range of linearity (Fig. 6). Sensitivity and linearity was improved when more AuNPs was used in the test system. In this study, 2.5 mL AuNPs was selected for all tests.

The intensity of RLS started increasing with the addition of glycogen with AuNPs. The reaction rate was glycogen concentration dependant. Higher glycogen concentrations needed more time to reach their maximum. Once the maximum was reached, the mixture was stable for several hours (Fig. 7).

Most of the six tested amino acids, glucose and lactose did not significantly affect the light-scattering intensity of glycogen–AuNPs system (<5%). Cysteine at 1 mg mL^{-1} was the most significant with 15% reduction of the RLS intensity that was probably due to the interaction between the thiol group and AuNPs. At comparable glycogen concentrations, BSA did not change the RLS intensity of glycogen–AuNPs complex. Trichloroacetic acid that was used for the precipitation of proteins in sample preparation had a very minor effect on the RLS intensity of glycogen–AuNPs system (Table 1).

3.3. Analytical parameters

As stated above, the linearity increased with amount of AuNPs used in the determination. For 2.5 mL AuNPs (~20 nm), the calibration curve was linear with glycogen up to 800 ng mL^{-1} with the limit of detection of 2 ng mL^{-1}. The calibration curve was repeated 5 times with the standard deviation at 5% for slope and 4% for the intercept, demonstrating that the method repeatability was acceptable.

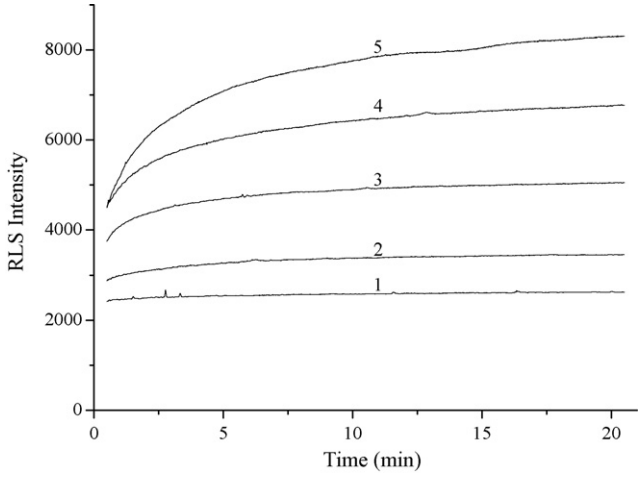

Fig. 7. The time dependence of RLS intensity of AuNPs with varied glycogen concentrations: (1) 100 ng mL^{-1}, (2) 200 ng mL^{-1}, (3) 400 ng mL^{-1}, (4) 600 ng mL^{-1}, and (5) 800 ng mL^{-1} (T = 25 °C).

Table 1
Effect of potential interfering substances on RLS of AuNPs–glycogen system[a]

Foreign substance interference	Intensity ± S.D.	Change %
Glycogen	5930 ± 254	–
Ala	5715 ± 516	−3.6
Phe	5894 ± 73	−0.6
Lys	6223 ± 133	4.9
Asp	6233 ± 51	5.1
Ser	5804 ± 182	−2.1
Cys	5010 ± 140	−15.5
Lactose	5901 ± 160	−0.5
Glucose	5797 ± 102	−2.2
BSA	5930 ± 83	0.0
TCA	6015 ± 124	1.4

[a] [AuNPs] = 0.49 nmol L^{-1} and [glycogen] = 500 ng mL^{-1}; the concentrations of amino acids were 1 mg mL^{-1}, lactose was 1 mg mL^{-1}, glucose was 10 mg mL^{-1}, BSA was 500 ng mL^{-1} and TCA was 0.1% (w/w).

3.4. Artificial sample test

Recovery of glycogen from artificial samples was tested to show accuracy of this method (Table 2). Artificial samples were composed of glycogen (0.5%, 1% and 2%, w/w), BSA (20%, w/w), amino acids (1 mg mL^{-1}), glucose (10 mg mL^{-1}), and lactose (1 mg mL^{-1}). One gram of above artificial sample was diluted to 10 mL. Two milliliters of the diluted sample was then mixed with 2 mL 10% TCA. The mixture was centrifuged at 9000 rpm for 10 min. Fifty microliters supernatant was then diluted to 10 mL with water. 0.5 mL of the diluted supernatant was then mixed with 2.5 mL AuNPs. The mixture was diluted to 5 mL before RLS measurement.

Since proteins are usually present in greater concentrations than glycogen, separation of the proteins is required before analysis. BSA was used in the artificial sample as an example to evaluate effect of TCA protein precipitation. The recovery when the BSA to glycogen mass ratio was in the range of 10–40 was very good.

3.5. Mechanism for light-scattering enhancement

It has been reported [21,36–40] that the aggregation and assembly process could induce enhanced light-scattering. In our study, the RLS enhancement was induced from aggregation of AuNPs with glycogen as shown with TEM (Fig. 1). The about 20 nm AuNPs used for determination was well suspended without contacting glycogen. When the AuNPs were mixed with glycogen, aggregation was observed.

Table 2
Recovery of glycogen from artificial samples

Glycogen, added (%)	Sample no.	Glycogen, found (%)	Recovery (S.D., %)
0.5	1	0.49	98.5 (1.0)
	2	0.49	
	3	0.50	
	4	0.49	
1.0	1	0.98	101.0 (2.6)
	2	1.00	
	3	1.02	
	4	1.04	
2.0	1	2.00	102.0 (3.3)
	2	2.11	
	3	1.97	
	4	2.08	

The optical properties of plasmon-resonant nanoparticles can be well described by the usual dipolar Rayleigh approximation, in which all characteristics of the light absorption and scattering are determined by the electrostatic polarizability calculated with the optical dielectric permittivity [41]. The enhancement of AuNPs resonance light-scattering by glycogen can also be described by Rayleigh approximation because the RLS wavelength is well beyond the particle size of AuNPs. Introducing glycogen to AuNPs system might alter dielectric constant surrounding surface of the AuNPs as indicated by red shifted and broadened plasmon absorption (Fig. 2A). Other than dielectric constant which affects scattering cross-section parameters, the light-scattering intensity also increased with particle size [21,42]. When glycogen was in a concentration range where enhanced light-scattering was observed, glycogen might basically aggregated with AuNPs to yield a "bigger particle" in a loose binding manner [43], which then increased the scattering intensity.

4. Conclusion

The light-scattering technique combined with AuNPs probes has been shown to be a promising method for glycogen analysis with a linear range of 10–800 ng mL^{-1} with 2 ng mL^{-1} detection limit. Tested amino acids, glucose, lactose, BSA and trichloroacetic acid were found to have no effect on the RLS signal at comparable and substantially higher glycogen concentrations. This non-enzymatic approach to glycogen analysis was a simple and low cost method. With 5 consecutive determinations, the relative standard deviation of calibration curves was within 5%. Recovery of glycogen from 3 artificial samples was 98–102% demonstrating the potential for the determination of glycogen in complex mixtures.

More work will be done to show the potential applications of this method for the determination of glycogen status in carbohydrate storage process and related diseases such as muscle glycogen repletion in sports and glycogen storage disorders.

Acknowledgements

This work was supported by the National Nature Sciences Foundation of China (No. 20475004, 90713013 & 20775004) and Instrumental Analysis Fund of Peking University.

References

[1] D.L. Nelson, M.M. Cox, Lehninger Principles of Biochemistry, 4th ed., W.H. Freeman, New York, 2004.
[2] P.S. Cerri, E. Sasso-Cerri, Micron 34 (2003) 365–372.
[3] T.J. Fairchild, P.A. Fournier, Med. Sci. Sports Exerc. 36 (2004) 2053–2058.
[4] J.R. Thogmartin, D. England, C.F. Siebert, Am. J. Forensic Med. Pathol. 22 (2001) 313–318.
[5] M.V. Kudryavtseva, G.A. Sakuta, A.D. Skorina, G.I. Stein, A.V. Emelyanov, B.N. Kudryavtsev, Tissue Cell 28 (1996) 279–285.
[6] J. Halkjaer-Kristensen, T. Ingemann-Hansen, Histochem. J. 11 (1979) 629–638.
[7] B.N. Kudriavtsev, M.V. Kudriavtseva, E.E. Zavadskaia, T.M. Shalakhmetova, S.A. Komarov, Tsitologiia 21 (1979) 74–83.
[8] V.K. Shil'nikova, V.A. Siguta, Biol. Bull. Acad. Sci. USSR 5 (1978) 288–292.
[9] C.R. Krisman, Anal. Biochem. 4 (1962) 17–23.
[10] U. Schulze, M.E. Larsen, J. Villadsen, Anal. Biochem. 228 (1995) 143–149.
[11] M.J. GomezLechon, X. Ponsoda, J.V. Castell, Anal. Biochem. 236 (1996) 296–301.
[12] S.A. Burton, A.L. MacKenzie, T.J. Davidson, A.C. Fraser, J. Shellfish Res. 19 (2000) 841–844.
[13] M.J. Gomez-Lechon, X. Ponsoda, J.V. Castell, Anal. Biochem. 236 (1996) 296–301.
[14] F. Mochaba, P. Torline, B. Axcell, J. Am. Soc. Brew. Chem. 52 (1994) 145–147.
[15] G.W. Goodwin, J.R. Arteaga, H. Taegtmeyer, J. Biol. Chem. 270 (1995) 9234–9240.
[16] K.J. Hutter, M. Remor, S. Muller, Monatsschr. Brauwiss. 53 (2000) 68.
[17] J. Lopez-Hernandez, M.J. Gonzalez-Castro, M. Pereda-Gonzalez, J. Chromatogr. Sci. 38 (2000) 383–385.
[18] K.J. Hutter, J. Inst. Brew. 108 (2002) 52–53.
[19] D. Brdjanovic, M.C.M. van Loosdrecht, C.M. Hooijmans, T. Mino, G.J. Alaerts, J.J. Heijnen, Water Sci. Technol. 37 (1998) 541–547.
[20] G. Doyle, B. Ashall, M. Galvin, M. Berndt, S. Crosbie, D. Zerulla, Appl. Phys. A: Mater. Sci. Process. 89 (2007) 351–355.
[21] C.L. Schofield, A.H. Haines, R.A. Field, D.A. Russell, Langmuir 22 (2006) 6707–6711.
[22] K. Aslan, P. Holley, L. Davies, J.R. Lakowicz, C.D. Geddes, J. Am. Chem. Soc. 127 (2005) 12115–12121.
[23] J. Yguerabide, E.E. Yguerabide, Anal. Biochem. 262 (1998) 137–156.
[24] R.F. Pasternack, P.J. Collings, Science 269 (1995) 935–939.
[25] C.Z. Huang, Y.F. Li, Anal. Chim. Acta 500 (2003) 105–117.
[26] Z.G. Chen, J.B. Liu, Y.L. Han, Talanta 71 (2007) 1246–1251.
[27] X.X. Dai, Y.F. Li, W. He, Y.F. Long, C.Z. Huang, Talanta 70 (2006) 578–583.
[28] J.M. de la Fuente, A.G. Barrientos, T.C. Rojas, J. Rojo, J. Canada, A. Fernandez, S. Penades, Angew. Chem. Int. Edit. 40 (2001) 2257–2261.
[29] S.B. Zhang, Z.S. Wu, M.M. Guo, G.L. Shen, R.Q. Yu, Talanta 71 (2007) 1530–1535.
[30] C.L. Schofield, R.A. Field, D.A. Russell, Anal. Chem. 79 (2007) 1356–1361.
[31] K. Aslan, J.R. Lakowicz, C.D. Geddes, Anal. Biochem. 330 (2004) 145–155.
[32] S.Z. Zhang, F.L. Zhao, K.A. Li, S.Y. Tong, Anal. Chim. Acta 431 (2001) 133–139.
[33] G. Frens, Nat. Phys. Sci. 241 (1973) 20–22.
[34] X.H.N. Xu, S. Huang, W. Brownlow, K. Salaita, R.B. Jeffers, J. Phys. Chem. B 108 (2004) 15543–15551.
[35] J.D.S. Newman, J.M. Roberts, G.J. Blanchard, Anal. Chem. 79 (2007) 3448–3454.
[36] J. Ling, C.Z. Huang, Y.F. Li, Y.F. Long, Q.G. Liao, Appl. Spectrosc. Rev. 42 (2007) 177–201.
[37] Z.L. Jiang, F. Li, H. Liang, Acta Chim. Sin. 58 (2000) 1059–1062.
[38] Z.L. Jiang, Z.W. Feng, T.S. Li, F. Li, F.X. Zhong, J.Y. Xie, X.H. Yi, Sci. China Ser. B: Chem. 44 (2001) 175–181.
[39] Z.L. Jiang, S.J. Sun, A.H. Liang, C.J. Liu, Anal. Chim. Acta 571 (2006) 200–205.
[40] S.P. Liu, Z. Yang, Z.F. Liu, L. Kong, Anal. Biochem. 353 (2006) 108–116.
[41] B.N. Khlebtsova, N.G. Khlebtsov, J. Quant. Spectrosc. Radiat. Transf. 106 (2007) 154–169.
[42] W. Lu, B.S.F. Band, Y. Yu, Q.G. Li, J.C. Shang, C. Wang, Y. Fang, R. Tian, L.P. Zhou, L.L. Sun, Y. Tang, S.H. Jing, W. Huang, J.P. Zhang, Microchim. Acta 158 (2007) 29–58.
[43] N.G. Khlebtsov, V.A. Bogatyrev, B.N. Khlebtsov, L.A. Dykman, P. Englebienne, Colloid J. 65 (2003) 622–635.

Talanta 76 (2008) 1165–1169

Contents lists available at ScienceDirect

Talanta

journal homepage: www.elsevier.com/locate/talanta

The determination of iron as its EDTA complex in *Helix aspera* by hydrophilic interaction liquid chromatography coupled to Fourier transform electrospray ionisation mass spectrometry

L. Zheng, D.G. Watson*, J.N.A. Tettey, C.A. Clements

Strathclyde Institute for Pharmacy and Biomedical Sciences, University of Strathclyde, 27 Taylor Street, Glasgow G4 0NR, United Kingdom

ARTICLE INFO

Article history:
Received 1 February 2008
Received in revised form 5 May 2008
Accepted 14 May 2008
Available online 21 May 2008

Keywords:
FeEDTA
Snail
HILIC chromatography
Fourier transform mass spectrometry

ABSTRACT

Metal complexes of Fe(III) such as Fe(III) ethylene diamine tetraacetic acid (FeETDA) have been observed to be effective molluscicides. The mechanism of toxicity of FeEDTA complex on molluscs is not clear and it is also not known if Fe(III) in the form FeEDTA is absorbed more effectively by snails than simple iron salts. Snails were fed with molluscicide pellets containing the FeEDTA complex and also with pellets containing $FePO_4$ after 3–4 days the hearts, kidneys and dart sacs removed and analysed for Fe(III) content. Hydrophilic interaction liquid chromatography (HILIC) coupled with Fourier transform electrospray ionisation mass spectrometry (FT-ESIMS) was used to analyse the sample extracts. The method had a very wide linear range from 2 to 10,000 ng mL^{-1}, intra- and inter-day precisions of *ca.* ±0.5% were observed for the analysis of extracts from snail tissues spiked with Fe(III). The limit of detection was of 0.5 ng mL^{-1} for a 20 μL injection. The levels of Fe(III) in tissues from snails fed Fe EDTA pellets were 10–100 times higher than the levels in snails fed $FePO_4$ pellets. The analysis of Cu, Zn, Ca and Mn could also be carried out using the same analytical procedure.

1. Introduction

Iron(III) phosphate containing pellets are used as molluscicides but relatively little is known about the mechanism of action of these pellets although iron has been observed to be deposited in digestive gland and body wall of the mollusc [1]. It has been reported that the ability of metals to act as molluscicides was improved when they were formulated as organic complexes [2] and in 1995 a patent was taken out on the use of ferric EDTA and related complexes as molluscicides [3]. Recently, it has been observed that earthworms are also very sensitive to molluscicides based on $FePO_4$ [4]. The aim of the current study was to develop a method for the determination of iron in the organs of *Helix aspera* as a model for what may occur in other molluscs. A number of studies have been conducted to determine whether or not the uptake of iron via the gut is more effective when the iron is administered as a complex such as FeEDTA compared with administration of a simple salt such as $FeSO_4$. In one study [5], it was found that iron was accumulated to a lesser extent in liver and spleen of rat when FeEDTA was administered than when $FeSO_4$ was administered but other organs were not examined. Zhu et al. [6] found that the penetration of iron through Caco-2 cells, used as a model for the cells of the gut, was less effective in the case of Fe(III)EDTA compared with $FeSO_4$ and $FeCl_3$. However, an *in vivo* study by the same group found that NaFeEDTA produced different tissue distributions of iron compared to $FeSO_4$ in the rat [7]. Levels of iron in the kidney were 83% higher when rats were fed NaFeEDTA and levels in the liver were 53% lower when compared with feeding $FeSO_4$.

Among a large number of chelating reagents for formation of complexes with metals, particularly iron, EDTA is considered to be very effective. EDTA can normally be represented as H_4Y, in the fully protonated form because of four acidic groups. The pK_a values of four corresponding hydrogens are pK_{a1} = 1.99, pK_{a2} = 2.67, pK_{a3} = 6.16, and pK_{a4} = 10.26 [8]. The hexadentate ligand has an unusual chelating power with metals forming 1:1 complexes with many metals. Of all the important metals, Fe^{3+} has the highest complexation stability constant (log K of 25.1), followed by Cu (log K 18.8), Zn (log K 16.3), Co^{2+} (log K 16.2) and so on [9]. In aqueous solution EDTA and Fe(III) forms an octahedral complex $[FeY]^-$ exhibiting a negative charge.

The determination of Fe(III) as its FeEDTA complex has been carried out by a number of researchers. Owens et al. [10] studied EDTA complexes by capillary electrophoresis (CE) with UV detection. Complexes of various metal ions were formed prior to analysis including Fe^{3+}, Ca^{2+}, Co^{2+}, Cu^{2+}, Zn^{2+}, Cd^{2+}, and Pb^{2+}. The authors reached a detection limit of $[FeY]^-$ at 4 μg mL^{-1}. Blatny et al. [11]

* Corresponding author. Tel.: +44 1415482651; fax: +44 1415522562.
E-mail address: d.g.watson@strath.ac.uk (D.G. Watson).

0039-9140/$ – see front matter © 2008 Elsevier B.V. All rights reserved.
doi:10.1016/j.talanta.2008.05.018

studied metal ions in water with CE; EDTA was added to water to form a complex which was then detected at 254 nm. The limit of detection for Fe was 13 ng mL^{-1}. Sillanpää et al. [12] performed ion pair HPLC to measure EDTA complexes with ferric ions. They used a buffer solution containing the ion-pairing agent cetrimide as the mobile phase. The complex was detected at 260 nm and the limit detection was 0.5 μg mL^{-1}. A similar ion pair method was used by Lucena et al. with tetrabutylammonium chloride as ion pair reagent and UV detection at 280 nm [13]. Chen et al. [14] developed an analysis of $[FeY]^-$ by CE coupled with electrospray ionization-mass spectrometry. The authors reached a detection of limit at 4 ng mL^{-1} for $[FeY]^-$ in the negative ion mode. Quintana and Reemtsma [15] used liquid chromatography coupled with ESI-MS to detect the EDTA–Fe(III) complex. They added the volatile ion-pairing reagent tributylamine to the mobile phase. A phenyl–hexyl column was used and the detection of limit was 1 ng mL^{-1} with a 50 μL injection volume. Álavarez-Fernández et al. used an ESI-time of flight method to determine a number of Fe(III) chelates used in fertilisers in various agricultural matrices. The used reverse phase chromatography in the negative ion mode, high sensitivity was achieved through the use of ^{57}Fe-labelled internal standards and the LOQ for Fe(III) EDTA achieved was 328 pmol/mL (114.1 ng/mL) [16]. Inductively coupled plasma-mass spectrometry (ICP-MS) has been also used to determine Fe. Yeh and Jiang [17] use ICP-MS to speciate V, Cr and Fe with CE separation, the limit of detection was 10 ng mL^{-1} for $[FeY]^-$. Xuan et al. [18] introduced a ZIC–hydrophilic interaction liquid chromatography (HILIC) column to separate and identify the different phytosiderophores of the mugineic acid family as their metal complexes. Various metals (Zn, Cu, Ni, and Fe) were added to 2′-deoxymugincic acid (DMA) and nicotinamine to form complexes. They used a mobile phase consisting of NH_4AC and CH_3CN at pH 7.3. When authors checked the stability of the complexes during separations using EDTA, they found EDTA–Fe(III) peaks $[FeY]^-$ at 21.7 min with m/z 344.0. However, they had not shown chromatograms or validate the method.

In the current work a HILIC chromatography method interfaced with Fourier transform electrospray ionisation mass spectrometry (FT-ESIMS) was developed for the determination of uptake of iron(III) into tissues of the snail following feeding of a commercially available molluscicide based on iron(III).

2. Experimental

2.1. Chemicals and materials

All chemicals used were analytical grade. EDTA disodium salt dihydrate, EDDS trisodium salt solution, iron chloride hexahydrate were purchased from Sigma–Aldrich. HPLC grade acetonitrile and formic acid were from VWR International, UK. For all eluents and standards preparations, sample preparations, deionised water was provided by a water purification system (Milli-Q system, Millipore). Snails (*H. aspera*) were purchased from Blades Biological Systems (Kent, UK). Ferramol slug pellets (W. Neudorff, Germany) were purchased locally. Iron(III) phosphate pellets (1%, w/w) were provided by Lonza Ltd. and contained iron(III) phosphate without addition of EDTA.

2.2. Microscopy

All snails were dissected under a stereo-binocular microscope from Brunel, UK with magnification power objectives 4× and an eyepiece 10×. A micro-dissection tool kit was used for dissecting the snails. The dissected tissue was homogenised using a hand held homogenizer (LabGen 7B, USA).

2.3. Standards and sample preparation

FeEDTA: $FeCl_3{\cdot}6H_2O$ (*ca.* 77.7 mg; MW = 270.3 g mol^{-1}) and $C_{10}H_{14}O_8N_2Na_2{\cdot}2H_2O$ (*ca.* 106.9 mg; MW = 372.2 g mol^{-1}) were weighed out and both dissolved in 100 mL of water in the same volumetric flask, thus preparing solution A with FeEDTA (referred to hereafter as the FeEDTA complex standard) at a concentration of 1 mg mL^{-1}. Solution A was diluted 1000× with acetonitrile/0.1% (v/v) formic acid (70:30) producing a stock solution of FeEDTA complex standard at a concentration of 1 μg mL^{-1}. From this solution calibration series was prepared with 2, 10, 50, 200, 500, 1000, 5000 and 10,000 ng mL^{-1} of FeEDTA.

2.4. Feeding and dissection of snails

The snails were fed manually with pellets which contained either $FePO_4$ or commercial pellets containing FeEDTA and kept in an aquarium. Once they had died (after 3 days), dissections were carried under the microscope. Firstly, the outer shells were removed by breaking bits of shell away with forceps taking care not to damage the soft tissue. Pieces of the shell and any other surface contamination was removed by washing the body in water (3× 0.5 L). The mantle skirt was located and cut away; another cut was made transversely from the pneumostome to the left side of the mantle along the posterior edge of skirt. The body was cut posteriorly along the left side of the mantle to the posterior end of the lung. Thus, the mantle was laid aside and the atrium, aorta, ventricle and kidney were removed from the lung roof. The dart sac in the body cavity was also removed. The kidney, heart and dart sac were placed into 5 mL vials and extracted with either 1 mL of 0.1% (v/v) formic acid in water in order to determine FeEDTA in the tissues after feeding with FeEDTA pellets or 1 mL of 0.1% (v/v) formic acid in water containing 10 μg mL^{-1} of EDTA where total iron in the tissues was compared between snails fef on FeEDTA pellets, $FePO_4$ pellets and a control group not fed on pellets. The tissue was then homogenised with a hand held homogeniser. A drop of 1% (v/v) Triton solution was added to the vials and the samples were left sonicate for 1 h at 40 °C. Acetonitrile (1.5 mL) was then added to each vial and all vials were vortexed for 5 min. The solutions were filtered using a syringe filter and transferred to HPLC autosampler vials.

2.5. Caco-2 assay system

Caco-2 cells (HTB-37) were obtained from the ATCC. Permeability studies were carried out using the BIOCOAT HTS Caco-2 assay system purchased from Becton Dickinson Labware Europe. This system provides an *in vitro* intestinal model for the transport of drugs and natural compounds consisting of a fibrillar collagen coated 24-well insert plate and a Multiwell feeder tray for culturing cell monolayers; combined with basal seeding medium, Entero-STIM a serum free medium containing butyric acid to induce cell differentiation and MITO + serum extender containing the hormones, growth factors and metabolites required for serum free cell culture.

A suspension of Caco-2 cells at a density of 4×10^5 cells/mL was prepared in basal medium supplemented with MITO + serum extender, 500 μL of which was pipetted into each of the 24 collagen inserts to give a seeding density of 2×10^5 cells per insert. A volume of the same medium (35 mL) was pipetted into the Multiwell feeder tray and the system was incubated at 37 °C, 5% CO_2 and 100% humidity for 24 h The medium was then removed from the feeder tray and from each insert taking care not to damage the cell monolayer. 500 μL of Entero-STIM medium supplemented with MITO + serum extender was added to the interior of each insert and 35 mL of the same medium was added to the feeder tray. The system was then incubated under the conditions previously described

for 48 h to allow formation of the differentiated enterocyte-like monolayer. The Multiwell insert plate was removed from the feeder tray and placed on a 24 well plate. The Entero-STIM medium was carefully removed from each insert and the cell monolayers were washed with PBS. Prior to permeability testing Caco-2 monolayer integrity was confirmed by means of Lucifer yellow rejection. Rejection values of 98.9% were obtained which indicated well-formed cell monolayers. Permeability of EDTA and $FePO_4$ made up in PBS (pH 7.4) was tested at concentrations of 10, 50 and 100 μM in duplicate. The test solutions were added in a volume of 300 μL to the inside of the inserts and 1000 μL PBS was added to each well of the receiving 24-well plate. The test plate was incubated at 37 °C, 5% CO_2, 100% humidity for 120 min, with intermittent shaking at 50 rpm. The insert plate was then removed, and the solutions in the receiving 24-well plate were analysed by LC–MS to determine percentage permeability.

2.6. Statistics

One-way and two-way ANOVA with replication was performed on the results obtained for the analysis of iron(III) as FeEDTA in the snail organs.

2.7. LC/MS instrumentation

The HPLC system consisted of Finnigan Surveyor MS Pump Plus; an online Finnigan Surveyor degasser; Finnigan Surveyor MS Autosampler Plus; Finnigan Surveyor PDA Plus detector (Thermo Finnigan, MA, USA). A ZIC–HILIC column was used (50 mm × 4.6 mm, 5 μm) purchased from HiChrom Ltd., Reading, UK. It was fitted with a ZIC–HILIC guard column (20 mm × 2.1 mm, 5 μm) from the same supplier. The determination of EDTA–Fe(III) was carried out using a mixture of 0.1% (v/v) formic acid in water with acetonitrile (30:70) as the mobile phase at room temperature. The run time was 18 min with a flow rate of 0.5 mL min^{-1} and an injection volume of 10 μL. For the separation of other metal EDTA complexes, the eluent was changed to 0.1% (v/v) formic acid in water:CH_3CN (40:60) and parameters remained the same. The FT-ESIMS instrument was a Finnigan LTQ Orbitrap (Thermo Finnigan, MA, USA) operated in the negative ion mode. The capillary spray voltage was set to 4.5 kV. The temperature of the heated capillary was maintained at 250 °C. Nitrogen gas flow was kept at a flow rate of 41 and auxiliary gas at 28, the tube lens voltage was −100 V. The scan range was set to 100–800 amu at the beginning when confirmation of the peaks of $[FeY]^-$, then set to scan the narrow range of 343–345 amu to monitor FeEDTA.

3. Results and discussion

3.1. Method validation

The measurements of the EDTA–Fe(III) complex were optimised in several steps. The various LC conditions and mass spectrometer conditions were optimised and the mass spectrometer was tuned to the molecular ion for the EDTA complex using standard solutions at a concentration of 1 μg mL^{-1}. The ZIC–HILIC column is particularly effective type of HILIC column based on a Zwitterionic stationary phase; it gives very stable chromatography when used with simple aqueous modifiers such as 0.1% formic acid. The mass spectrum of the $[FeY]^-$ is shown in Fig. 1. The spectrum shows the three major ions. The peak m/z 344.00 (343.9931) is from the $[FeY]^-$ and the lower spectrum shows the MS^2 obtained at normalised collision energy of 35 V. The peaks m/z 299.9931, m/z 256.0435 correspond to successive losses of the carboxylate group starting from the parent ion $[FeY]^-$. These fragmentations confirmed the ion at m/z 344.0 to be due to the $[FeY]^-$. The specificity of the LC–MS method was demonstrated to be free from interference by running an EDTA solution blank which can be compared with the peak for FeEDTA obtained at the LOD (Fig. 2).

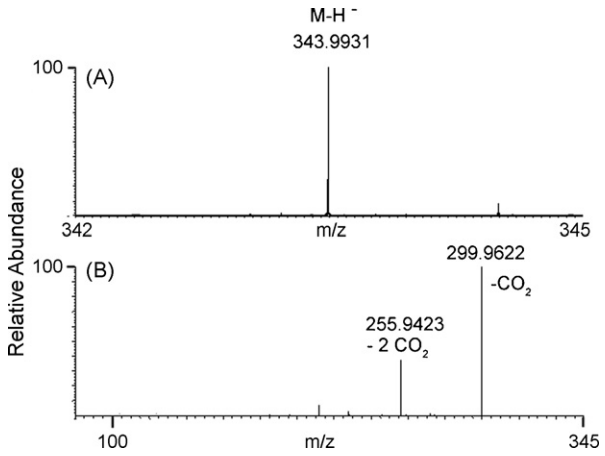

Fig. 1. A representative mass spectrum of FeEDTA obtained in negative ESI mode.

The intra-day instrument precision of the method was evaluated using two concentrations of the FeEDTA complex standard which was spiked into homogenised snail tissue. Nine consecutive runs were carried out. The relative standard deviation (R.S.D.) values obtained are shown in Table 1 and in both cases were *ca.* ±0.5%.

The inter-day precision was evaluated on day 1 and day 2 with spiked solution concentrations of at 12.5 ng mL^{-1} and at 5000 ng mL^{-1}. Six injections were carried on each day. The means and R.S.D. values were similar for day 1 and day 2.

The linearity of the method was obtained for the concentration range 2–10,000 ng mL^{-1}. The calibration curves of the peak area as function of concentration were linear, with a correlation coefficient

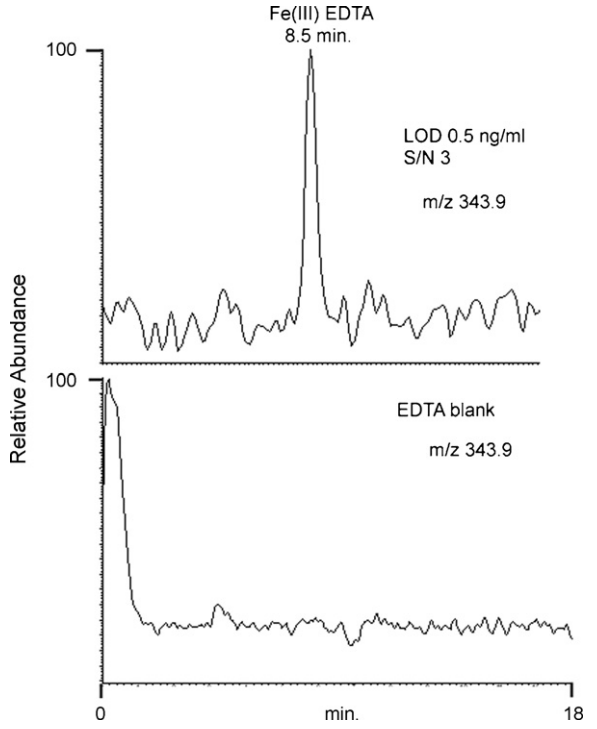

Fig. 2. (A) Selected ion chromatogram of a 0.5 ng/mL $[FeY]^-$ standard solution (20 μL injection). (B) Reagent blank EDTA in water.

Table 1
Inter- and intra-day precision for FeEDTA solution spiked into samples of homogenised snail tissue filtered then analysed by FT-ESIMS

	$[FeY]^-$ = 12.5	$[FeY]^-$ = 5000 ng/mL
Inter-day variation		
Mean	3,48,145	99,281,296
S.D.	2,216	4,91,096
R.S.D. (%)	0.636	0.495
Intra-day variation		
Day 1		
Mean	347759.3	9,92,48,153
S.D.	2048.5	548116.7
R.S.D. (%)	0.589	0.557
Day 2		
Mean	347807.5	9,92,54,116
S.D.	1984.4	6,03,225
R.S.D. (%)	0.571	0.608

Table 2
Calibration curve statistics for slope, intercept and R^2 (n = 3) for calibration in the range 2–10,000 ng mL^{-1}

No.	Slope (K)	Intercept (B)	R^2
1	16,697	92,555	0.9988
2	16,726	78,522	0.9990
3	17,889	85,554	0.9998
Mean	17,104	85,544	0.9992
R.S.D.	3.976	8.202	0.053

of 0.9998. Because the samples were determined during several months, the calibration curves were prepared freshly each time. The R.S.D. values of the line slopes (K), intercept (B) and correlation coefficient R^2 shown in Table 2 indicate good precision for the linearity over the time period.

The observed detection limit was about 0.5 ng mL^{-1} for a 20 μL injection volume (S/N = 3) (Fig. 2). Once the method had been validated the Ferramol slug pellets were analysed for their FeEDTA content and it was found to be 1.08% (w/w) ±0.42% R.S.D. (n = 3). Although the active ingredient in the pellets according to the label claim is $FePO_4$ it is obvious, because of the high stability constant for FeEDTA, that this complex will form as soon as the pellets become wet since the pellets obviously also contain EDTA.

3.2. Studies on Caco-2 cells

Caco-2 cells provide a model for the gut absorption. The permeability of the FeEDTA complex standard was tested on Caco-2 cells. The data in Table 3 indicates that the FeEDTA complex is absorbed intact through a Caco-2 cell monolayer.

3.3. Iron extraction recovery from snail tissues

Aliquots of Fe(III) phosphate solution equivalent to 10, 20, 35, and 175 ng mL^{-1} of FeEDTA were added to 1 mL aliquots of solution containing homogenised snail tissue and EDTA was added into the solution which was heated at 40 °C and sonicated for 1 h. As indicated in Table 4 the recoveries were around 96%. This demonstrated that the free Fe(III) could be recovered from the snail tissues as its FeEDTA complex reproducibly.

Table 3
The permeability of FeEDTA complex through Caco-2 cell monolayers, the complex solution was dissolved in PBS at pH 7.4 and applied to the surface of the monolayer

Feed solution level (mM)	FeEDTA (ng mL^{-1})
100	430
50	210
10	130

Table 4
Extraction recovery studies for Fe(III)

Nominal Concentration of FeEDTA (ng mL^{-1})	Recovery of FeEDTA (%)
10	96.1
20	96.2
35	96.0
175	96.1
Mean	96.1
R.S.D.	0.08

Fe(III) was spiked into snail tissue, EDTA was then added and the solution was filtered and then analysed, in comparison with an unextracted FeEDTA standard at the same concentration.

3.4. Iron and FeEDTA absorption in snails

The snails were fed on lettuce and carrots until they were removed to a separate tank for feeding with pellets. They were either fed with $FePO_4$ (1% w/w) pellets or the commercial pellets, which contained $FePO_4$ (1%, w/w) according to the label claim along with a quantity of EDTA which was not specified on the label. Five snails at a time were transferred to a separate tank and commercial FeEDTA or $FePO_4$ only pellets were introduced into the tank for feeding. After 3 days the snails were removed from the tanks and dissected immediately to acquire the hearts, kidneys and dart sacs. Table 5 shows that the quantities of FeEDTA in heart and kidney after feeding with the commercial slug pellets are significantly higher than the control group with p value below 0.05. In this experiment extraction was carried out with 0.1% formic acid alone thus there did appear to be contamination of the kidneys in the control group with FeEDTA since no FeEDTA had been fed to this group. When dissecting the dead snails, we observed that debris from the pellets adhered to the body and shells of the snails. Thus, it was hard to eliminate the possibility that the FeEDTA might be absorbed via the skin or contaminate the organs and also the instruments during dissection. Although the snails were rinsed with 0.5 L of deionised water three times the sticky pellets were not easily removed. Finally, the snails were fed manually with pellets softened with deionised water until they stopped eating. The snails fed on the FeEDTA pellets were fed 4–5 pellets and died 3 days after this single feeding. The snails fed on the $FePO_4$ pellets were fed 3–4 pellets on three occasions over 3 days since they continued to eat the pellets and suffered no apparent ill effects. In addition the organs were removed from unfed snails, drowned in deionised water as a control. In this experiment the total iron in the tissues was measured by extracting the organs with deionised water con-

Table 5
Statistical evaluation of the results on feeding FeEDTA pellets to *H. aspera* (snails stayed in the tank together with the pellets) in comparison with *H. aspera* which were not fed pellets

No.	Kidney		Heart (ng/organ)	
	Feed	Control	Feed	Control
1	34,786	6	4365	0
2	66,702	394	3654	0
3	9,381	151	5623	0
4	23,596	234	2168	0
5	4,587	1132	1260	0
p-Value	0.035		0.002	

p-Value given for 95% confidence. In this case extraction was carried out with 0.1% formic acid.

Table 6
Results of FeEDTA distribution in organs from feedings to three groups of snails: control (no pellets fed); $FePO_4$ (pellets containing $FePO_4$ alone); FeEDTA (pellets containing $FePO_4$ with EDTA)

Feed group[a]	Heart	Kidney	Dart sac (ng/mg)
Control group	0.117 ± 0.219	0.014 ± 0.021	0.028 ± 0.053
$FePO_4$	41.352 ± 18.080	0.685 ± 0.679	0.982 ± 1.345
Fe EDTA	409.834 ± 196.370	327.131 ± 139.151	144.439 ± 103.975

In this case 0.1% (v/v) formic acid in water containing 10 μg mL^{-1} of EDTA was used to extract all the samples thus determining total iron in the tissues.
[a] $n = 5$, $\mu = X \pm$ S.D.

taining EDTA. Table 6 shows the iron accumulated in snail organs after manual feeding with $FePO_4$ pellets (1%, w/w), FeEDTA pellets (1%, w/w) and after feeding just with a normal diet.

Negligible amounts of iron were found in the snails which had not been fed with pellets and very large differences in iron accumulation in the organs were observed between the snails fed $FePO_4$ pellets and those fed FeEDTA pellets. Snails fed with the 1% (w/w) $FePO_4$ did not suffer any ill or toxic effects and could be maintained on this diet indefinitely. Thus, it would appear that the presence of EDTA in the formulation along with iron(III) is necessary for the absorption of toxic levels of iron. Very high levels of iron were found in hearts and kidney when snails were fed with FeEDTA compared with much lower levels in snails fed with $FePO_4$, as indicated in Table 6. Two-way ANOVA with replication ($n = 5$) was performed on the results. A 95% confidence interval was applied to determine if the variance was statistically significant. From the data in Table 7 the type of feeding had a significant effect (with $p < 0.001$) which means the feedings significantly influence the uptake of Fe or FeEDTA. The snails' organs were differently distributed with complex the significance of which is revealed by $p = 0.01$. Interactions between the type of feedings and organs were not found to be significant ($p = 0.06$) which means the effect of one factor feedings is independent of the organs. This indicates that the different feedings do not affect the distribution of iron. In addition, considering the FeEDTA and $FePO_4$ feeding only, the former significantly increased the absorption of Fe or FeEDTA in snails.

It was found by previous workers that Fe(III) in the form of FeEDTA did not pass through a Caco-2 monolayer any better than Fe(III) as simple iron salts [6]. As seen from the data in Table 6 the Fe(III) was not evenly distributed between heart, kidney and the reproductive system. The hearts always had the highest levels of iron, with lower amounts in the kidney and the smallest amount in reproductive system. Interestingly, the heart and kidneys are both located in the lung cavity and quite adjacent with each other, while the dart sac is close to the stomach in the body cavity. Accumulation of FeEDTA in the kidney reflects the observations of Zhu and Miller with respect to rat kidney [7]. The exact mechanism of iron toxicity in the snails is not known but given that the natural levels of iron in snail tissue appear to be very low and that snails use copper to carry oxygen in their haemolymph rather than iron, they may be very sensitive to the presence of iron in their tissues. Since the FeEDTA is present at very high concentrations in the tissues it may be that, under physiological conditions, where the stability of the FeEDTA complex could change, essential metals such as copper could become complexed by the EDTA.

Table 7
The two way ANOVA with replication ($n = 5$) on the accumulation of Fe(III)/FeEDTA in organs after three feedings to *H. aspera*

Source of variation	SS	d.f.	MS	*F*	*p*-Value	*F* crit
Organs	2091.43	2	1045.71	5.14	0.01	3.26
Feedings	21808.98	2	10904.49	53.6	<0.001	3.26
Interaction	2940.83	4	735.20	2.11	0.06	2.63
Within	7321.04	36	203.36			
Total	34162.28	44				

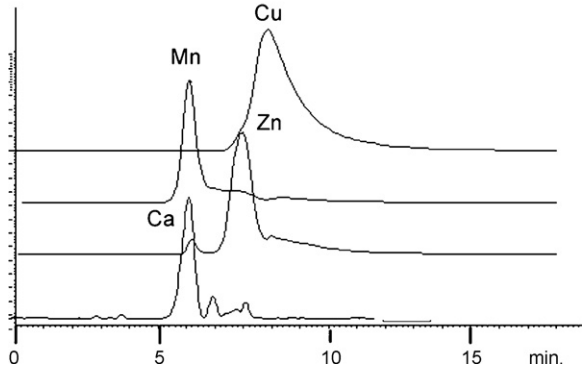

Fig. 3. TIC of Cu, Mn, Zn, Ca after complexation with EDTA run ZIC–HILIC column with 0.1% (v/v) formic acid in water:CH_3CN (40:60).

It was not possible to use the LC–MS method to distinguish between iron(II) and iron(III), in theory the iron(II) EDTA complex should be doubly charged but there was no evidence of this when the iron(II) EDTA complex was analysed. It may be that iron(II) becomes oxidised to iron(III) during the electrospray process. In addition in theory the FT-MS system should be able to measure a difference in mass of one electron but again it was not possible to confidently distinguish between iron(II) EDTA and iron(III) EDTA on the basis of mass when the two complexes were mixed. In fact it might have been expected that in order to maintain a single negative charge the iron(II)EDTA complex would have carried an extra proton and thus would have had a m/z value of 345. The LC–MS analysis of other metals was also observed to be possible and the EDTA complexes of Cu^{2+}, Zn^{2+}, Ca^{2+} and Mn^{2+} could be determined by the current method. Fig. 3 shows extracted ion chromatograms for these complexes which give good peak shapes apart from the Cu^{2+} complex. Thus, method could provide a sensitive general method for metal determination.

Acknowledgement

We thank Lonza Ltd. for sponsoring the research project.

References

[1] R.A. Triebskorn, I.F. Henderson, A.P. Martin, Pest. Sci. 55 (1999) 55.
[2] I.F. Henderson, G.G. Briggs, N.P. Coward, G.W. Dawson, J.A. Pickett, J.J. Bullock, L.F. Larkworthy, BCPC Monogr. 41 (1989) 289.
[3] G.S. Puritch, D.S. Almond, R.M. Matson, W.M. Matson, US Patent 5,437,870 (1995).
[4] A.M. Langan, E.M. Shaw, Appl. Soil Ecol. 34 (2006) 184.
[5] M.J. Appel, C.F. Kuper, R.A. Woutersen, J. Food Chem. Toxicol. 39 (2001) 261.
[6] L. Zhu, R.P. Glan, C.K. Yeung, D.D. Miller, J. Agric. Food Chem. 54 (2006) 7924.
[7] L. Zhu, D.D. Miller, J. Agric. Food Chem. 55 (2007) 8793.
[8] Logarithms of stability constants of miscellaneous complexones, Complexometry, BDH Chemicals Ltd., 1969, pp. 228–230.
[9] A.T. Hubbard, Encyclopaedia of Surface and Colloid Science, CRC Press, 2002, p. 444.
[10] G. Owens, V.K. Ferguson, M.J. McLaughlin, I. Singleton, R.J. Reid, F.A. Smith, Environ. Sci. Technol. 34 (2002) 885.
[11] P. Blatny, F. Kvasnicka, E. Kenndler, J. Chromatogr. A 757 (1997) 297.
[12] M. Sillanpää, R. Kokkonen, M.L. Sihvonen, Anal. Chim. Acta 303 (1995) 187.
[13] J.J. Lucena, P. Barak, L. Hernández, J. Chromatogr. A. 727 (1996) 253.
[14] Z. Chen, M. Megharaj, R. Naidu, J. Microchem. 86 (2007) 94.
[15] J.B. Quintanaa, T. Reemtsma, J. Chromatogr. A 1145 (2007) 110.
[16] A. Álvarez-Fernández, I. Orera, J. Abadía, A. Abadía, J. Am. Soc., Mass Spectrom. 18 (2007) 37–47.
[17] C.-F. Yeh, S.-J. Jiang, J. Chromatogr. A 1029 (2004) 255.
[18] Y. Xuan, E.B. Scheuermann, A.R. Meda, H. Hayen, N. von Wirén, G. Weber, J. Chromatogr. A 1136 (2006) 73.